Transactions of the ASME®

FLUIDS ENGINEERING DIVISION
Editor
JOSEPH KATZ (2005)
Editorial Assistant
LAUREL MURPHY (2005)

Associate Editors
J. BRIDGES (2002)
S. CECCIO (2004)
I. CELIK (2003)
W. COPENHAVER (2004)
T. GATSKI (2003)
E. GRAF (2003)
G. KARNIADAKIS (2002)
J. MARSHALL (2003)
Y. MATSUMOTO (2002)
L. MONDY (2002)
M. ÖTÜGEN (2004)
M. PLESNIAK (2004)
A. PRASAD (2003)
B. SCHIAVELLO (2002)
Y. TSUJIMOTO (2002)

BOARD ON COMMUNICATIONS
Chair and Vice-President
OZDEN OCHOA

OFFICERS OF THE ASME
President, W. A. WEIBLEN
Exec. Director
D. L. BELDEN
Treasurer
R. E. NICKELL

PUBLISHING STAFF
Managing Director, Engineering
THOMAS G. LOUGHLIN
Director, Technical Publishing
PHILIP DI VIETRO
Managing Editor, Technical Publishing
CYNTHIA B. CLARK
Managing Editor, Transactions
CORNELIA MONAHAN
Production Assistant
MARISOL ANDINO

Transactions of the ASME, Journal of Fluids Engineering (ISSN 0098-2202) is published quarterly (Mar., June, Sept., Dec.) by The American Society of Mechanical Engineers, Three Park Avenue, New York, NY 10016. Periodicals postage paid at New York, NY and additional mailing offices.
POSTMASTER: Send address changes to Transactions of the ASME, Journal of Fluids Engineering, c/o THE AMERICAN SOCIETY OF MECHANICAL ENGINEERS, 22 Law Drive, Box 2300, Fairfield, NJ 07007-2300.
CHANGES OF ADDRESS must be received at Society headquarters seven weeks before they are to be effective. Please send old label and new address.
STATEMENT from By-Laws. The Society shall not be responsible for statements or opinions advanced in papers or ... printed in its publications (B7.1, Par. 3).
COPYRIGHT © 2002 by the American Society of Mechanical Engineers. Authorization to photocopy material for internal or personal use under those circumstances not falling within the fair use provisions of the Copyright Act, contact the Copyright Clearance Center (CCC), 222 Rosewood Drive, Danvers, MA 01923, tel: 978-750-8400, www.copyright.com. Request for special permission or bulk copying should be addressed to Reprints/Permission Department.
INDEXED by Applied Mechanics Reviews and Engineering Information, Inc. Canadian Goods & Services Tax Registration #126148048.

Journal of Fluids Engineering

Published Quarterly by The American Society of Mechanical Engineers

VOLUME 124 • NUMBER 1 • MARCH 2002

(Contents continued on inside back cover)

This journal is printed on acid-free paper, which exceeds the ANSI Z39.48-1992 specification for permanence of paper and library materials. ♾™
♻ 85% recycled content, including 10% post-consumer fibers.

Downloaded 03 Jun 2010 to 171.66.16.159. Redistribution subject to ASME license or copyright; see http://www.asme.org/terms/Terms_Use.cfm

Journal of Fluids Engineering Volume 124, Number 1 MARCH 2002

TECHNICAL BRIEFS

ANNOUNCEMENTS

Downloaded 03 Jun 2010 to 171.66.16.159. Redistribution subject to ASME license or copyright; see http://www.asme.org/terms/Terms_Use.cfm

Journal of Fluids Engineering

Editorial

Another year has passed and with it, some Associate Editors have completed their three-year terms and new ones have joined us. I would like to take this opportunity to express my gratitude to the departing Associate Editors, Prof. Peter Bearman, Dr. Khairul Zaman, Prof. Urmila Ghia, Prof. Peter Raad and Prof. Muhammad Hajj for their substantial and very valuable service. Their efforts in selecting referees, obtaining reviews, evaluating the papers based on these reviews, communicating with the authors and overseeing modifications is critical for the successful operation and quality of the journal.

Four new Associate Editors have recently joined us, and I would like to introduce and welcome them to our team. This new group will greatly enhance our range of expertise that is essential for effective reviews of papers, especially in the experimental and complex flows areas. Dr. William Copenhaver from the Air Force Research Laboratory is an accomplished expert on all aspects of flows within axial turbomachines, both computational and experimental. He is joining the presently overloaded group of Associate Editors that handle the growing number of papers focusing on flows within pumps, turbomachines and related complex systems. Prof. Steven Ceccio from the University of Michigan is an experimentalist and has substantial experience in cavitation, multiphase flows, boundary layers, tomography, and applied large-scale experiments. He is joining the multiphase flow group, and will focus mainly on the experimental aspects of this area. Prof. Volkan Ötügen from Polytechnic University is an expert in compressible and incompressible three-dimensional, turbulent shear flows. He also has considerable experience in development of optical diagnostic techniques involving combined scalar and velocity measurements. He is joining the fluid mechanics group, and will handle papers dealing with turbulent shear flows and complex measurement techniques. Last, but not least, Prof. Michael Plesniak from Purdue University is an experimentalist and an expert in turbulent transport and mixing, aerosols, sprays and related pollution problems. He also has substantial experience in a variety of measurement techniques and applied heat transfer. He will mainly handle papers in the turbulent mixing area. As is evident, the diverse experience of the new Associate Editors will enhance our capability to review papers effectively. We promise to take advantage of their expertise and willingness to contribute.

Joseph Katz
Editor

 Copyright © 2002 by ASME

Downloaded 03 Jun 2010 to 171.66.16.150. Redistribution subject to ASME license or copyright; see http://www.asme.org/terms/Terms_Use.cfm

Journal of Fluids Engineering

Editorial

Quantifying Uncertainty in CFD

There has been recently an intense interest in *verification* and *validation* of large-scale simulations and in quantifying uncertainty, and several workshops have been organized to address this subject. Characterization of uncertainty is a complex subject in general, but it can be roughly classified as numerical uncertainty and physical uncertainty. The former includes spatiotemporal discretization errors, errors in numerical boundary conditions (e.g., outflow), errors in solvers or geometry description, etc. On the other hand, physical uncertainty includes errors due to unknown boundary and initial conditions, imprecise transport coefficients or interaction terms, insufficient knowledge of the flow geometry, approximate constitutive laws, etc. Coupled problems involving source and interaction terms tend to be particularly difficult to simulate even deterministically, so providing error bars for such solutions is an even more difficult task. Uncertainty can also be characterized as *epistemic*, i.e., reducible, or as *irreducible*. For example, if much finer simulations are performed or better experiments with higher resolution instruments are conducted, that will provide more accurate boundary conditions. This will reduce the uncertainty level. But even in such cases, and certainly in many simulations of realistic configurations, uncertainty is irreducible beyond some level due to insufficient detail of input, e.g., background turbulence and random roughness. There are no absolutely quiet wind tunnels and the ocean or the atmosphere are not quiet environments either.

Progress, however, has been made. With regards to numerical uncertainty, accuracy tests and error control have been employed in simulations for some time now, at least for the more modern discretizations. While fully-adaptive simulations are limited to some demonstration examples at the moment, at least the algorithmic framework and mesh generation technology exists for routine adaptive CFD in the near future. Also, a posteriori error bounds and other post-processing tools are available and are used (albeit not very often) in CFD. To this end, the editorial policy statement on the control of numerical accuracy that JFE pioneered in 1986 along with more recent enhancements, has positively influenced the field.

With regards to physical uncertainty, it is only recently that a systematic effort has been made to address it. Most of the effort in CFD research so far has been in developing efficient algorithms for different applications, assuming an ideal input with precisely defined computational domains. With the field reaching now some

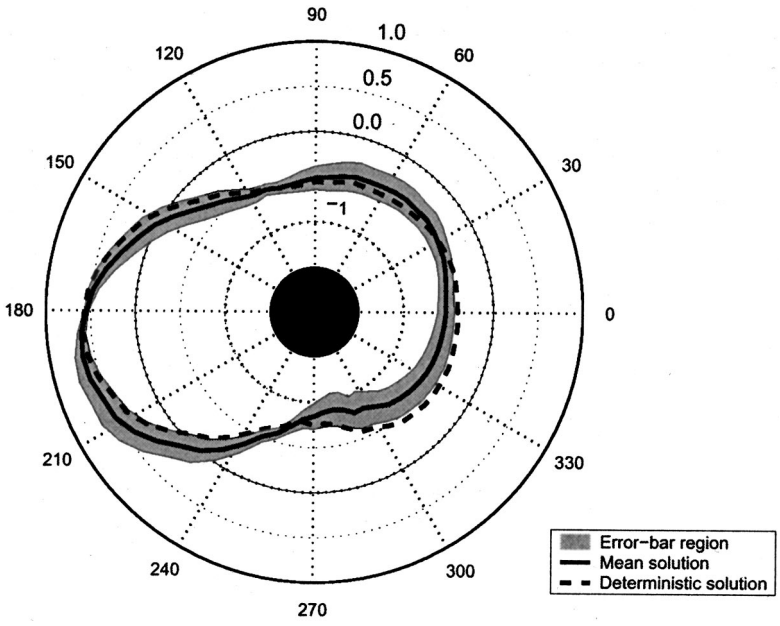

Fig. 1 Stochastic simulation of flow past a vibrating cylinder with a noisy inflow. Shown is the instantaneous pressure distribution on the cylinder. The error band is shown by gray and the deterministic and mean stochastic solutions are superimposed on this polar plot. (Courtesy of Didier Lucor and Dongbin Xiu, Brown University).

 Copyright © 2002 by ASME

Downloaded 03 Jun 2010 to 171.66.16.150. Redistribution subject to ASME license or copyright; see http://www.asme.org/terms/Terms_Use.cfm

degree of maturity, we naturally pose the more general question of how to model uncertainty and stochastic input, and how to formulate algorithms so that the simulation output reflects accurately the propagation of uncertainty. That is, in addition to a posteriori error bounds, the new objective is to model uncertainty from the beginning of the simulation and not simply as an afterthought. Stochastic simulations have been going on in solid mechanics for some time now, especially in the finite elements community, so in that respect CFD is about ten years behind! But stochastic CFD simulations have begun, and the first results have provided very valuable information, as shown in the figure.

This special issue of JFE on quantifying uncertainty in CFD is in response to such pressing needs as error bars in CFD, and for reliable answers even for ''nonsterilized'' problems. The eight invited papers address both numerical accuracy and physical uncertainty issues. They present different techniques and sometimes diverse philosophies, as this is a new field and no absolute consensus exists at the moment.

The first paper by Roache presents a straightforward approach to verification of codes by using manufactured solutions. Roache has been a long-time advocate of verification and validation in CFD and he presents here an overview and new clarifications of his previous work. Of particular interest is the blind study work that he reviews, where his proposed method of manufactured solutions was employed for correcting an intentionally sabotaged code.

The second and third papers deal with numerical accuracy as well. In particular, the paper by Cadafalch et al. is a comprehensive study of solution errors in finite volumes, and addresses laminar flows, turbulent flows with two-equations models, and reactive flows at steady state. The generalized Richardson extrapolation is employed and the grid convergence index is used along with other metrics for providing local and global estimators. The next paper by Pozrikidis addresses convergence of boundary element methods in the presence of sharp corners. This is a notoriously hard problem for any discretization (e.g., Motz problem in finite elements) and the paper presents an effective way of distributing the elements in a geometric fashion to restore uniform convergence.

The fourth paper by DeVolder et al. presents a general framework for quantifying uncertainty in multiscale simulations. It is based on the Bayesian approach for statistical inference and presents methods for determining the Bayesian likelihood and for fast integration. The case of flow in porous media is addressed first, and the shock wave dynamics is then considered. In particular, the stochastic Riemann problem is identified as a fundamental paradigm and analyzed in some detail.

The next two papers address modeling of physical uncertainty and its propagation through the simulation using polynomial chaos expansions. In particular, the paper by Ghanem and Hayek considers the dynamics of overland flow as a model problem. Ghanem pioneered the use of Wiener-Hermite expansions in modeling random input and solving stochastic partial differential equations. In this paper, the use of the Karhunen-Loeve expansion to represent stochastic input reduces significantly the dimensionality of the problem, thus requiring substantially less computational effort compared to Monte Carlo simulation. In the next paper by Xiu et al. a generalized polynomial chaos approach is introduced that extends the work of Wiener to best representations for other non-Gaussian distributions. A new class of polynomial functionals, the Askey family, is introduced and the Wiener-Askey chaos is formulated for the Navier-Stokes equations. The method is used to model flow-structure interaction problems.

The seventh paper by Putko et al. addresses robust design with the uncertainties in the input incorporated into the optimization procedure. Specifically, the approximate statistical moment method is employed for uncertainty propagation and statistical moments involving first-order sensitivity derivatives appear in the objective function and system constraints. The method is applied to shape optimization of a nozzle using a one-dimensional Euler code.

The final paper by Prud'homme et al. is more mathematical and is one of the first attempts to rigorously quantify uncertainty in simulations based on reduced-basis representations. Specifically, this new method involves the a priori generation of several solutions corresponding to different values of the uncertain parameter, and subsequently a fast solution at a specified parameter value based on a projection to the pre-computed solution space. This approach is demonstrated for heat conduction problems but a formulation for the convection-diffusion problem is also discussed.

I hope that the readers of JFE enjoy these exciting papers collected in this volume, as well as similar future publications that address uncertainty quantification. I would like to thank all the authors and referees for their contribution, and also the editor, Joe Katz, for recognizing how timely and important is this subject.

Guest Editor:
George Em Karniadakis
Brown University

Downloaded 03 Jun 2010 to 171.66.16.150. Redistribution subject to ASME license or copyright; see http://www.asme.org/terms/Terms_Use.cfm

Code Verification by the Method of Manufactured Solutions

Patrick J. Roache
Consultant,
P.O. Box 3379,
Los Lunas, NM 87031
e-mail: hermosa@swcp.com

Verification of Calculations involves error estimation, whereas Verification of Codes involves error evaluation, from known benchmark solutions. The best benchmarks are exact analytical solutions with sufficiently complex solution structure; they need not be realistic since Verification is a purely mathematical exercise. The Method of Manufactured Solutions (MMS) provides a straightforward and quite general procedure for generating such solutions. For complex codes, the method utilizes Symbolic Manipulation, but here it is illustrated with simple examples. When used with systematic grid refinement studies, which are remarkably sensitive, MMS produces strong Code Verifications with a theorem-like quality and a clearly defined completion point. [DOI: 10.1115/1.1436090]

Introduction

In the semantic tangle of the subject of ''Quantification of Uncertainty'' (a term which itself generates some disagreement) the three most important terms, and the most universally agreed upon, are Verification of Codes, Verification of Calculations, and Validation. For reasons both logical and practical, these activities must be performed in this order [1,2]. Verification of a Calculation involves error *estimation*, whereas Verification of a Code involves error *evaluation*, from a known solution. Both Verifications are purely mathematical activities, with no concern whatever for the accuracy of physical laws. That is the concern of Validation, i.e., the agreement of the mathematics with science.

Journal Policy Statements on reporting of numerical uncertainty, of which this journal's 1986 statement [3] was the original, refer only to Verification of Calculations; the code used is assumed to be correct. ''Correct'' is perhaps preferable to ''accurate.'' It can be misleading to describe a code as ''accurate,'' because naive users of commercial software may think that, if the code they use is accurate, then their calculation will be accurate. This neglects their own burden to perform systematic discretization convergence tests for their particular calculation, i.e., Verification of a Calculation. Determining the correctness of the code itself can only be done by systematic discretization convergence tests using a known solution or ''benchmark'' (another term with inconsistent connotations). The best benchmark solution or standard of comparison is an exact analytical solution, i.e. a solution expressed in simple primitive functions like sin, exp, tanh, etc. Note that benchmark solutions involving infinite series are not desirable, typically being more numerical trouble to evaluate accurately than the CFD code itself [1]. It is not sufficient that the analytical solution be exact; it is also necessary that the solution structure be sufficiently complex that all terms in the governing equation being tested are exercised. For example, some early and misleading claims of accuracy of commercial codes which used the notoriously inaccurate first-order upstream differencing for advection terms were based on comparisons with Poiseuille, Couette or Rayleigh problems, which do not even ''turn on'' the advection terms.

It has often been stated in research journal articles that general accuracy Verification of Codes for difficult problems, e.g. the full Navier-Stokes equations of fluid dynamics, is not possible because exact solutions exist only for such relatively simple problems that do not fully exercise the code. Many papers and reports approach accuracy Verification of Codes in a haphazard and piecemeal way, comparing single-grid results for a few exact solutions on problems of reduced complexity. In fact, a very general procedure exists for generating analytical solutions for accuracy Verification of Codes. I first presented the method in [4], and later expanded the applications [1,2]. Although a few respected authorities (e.g. [5–9]) have recognized the power of the method, acceptance has been slow and misunderstanding is not uncommon. Based on my experience in many discussions with professional colleagues including teaching short courses with participations by senior researchers, the misunderstanding is due to the deceptive simplicity (elegance?) of the concept. This article is written in an attempt to clarify the concepts with simple examples, to dispel concerns often voiced, to add a few fine points, and to provide some recent references. It is hoped that the reader will bear with the somewhat conversational style, since the paper is part tutorial, part review.

The methodology provides for convincing, rigorous Verification of the numerical accuracy of a code via systematic grid convergence testing. This procedure is straightforward though somewhat tedious to apply, and verifies all accuracy aspects of the code: formulation of the discrete equations (interior and boundary conditions) and their order of accuracy, the accuracy of the solution procedure, and the user instructions.

The Method of Manufactured Solutions

The Method of Manufactured Solutions (MMS) provides a general procedure for generating an analytical solution for code accuracy verification.

The basic idea of the procedure is to simply manufacture an exact solution, without being concerned about its physical realism. (The ''realism'' or lack thereof has nothing to do with the mathematics, and Verification is a purely mathematical exercise.) In the original, most straightforward and most universally applicable version of the method, one simply includes in the code a general source term, $Q(x,y,z,t)$ and uses it to generate a nontrivial but known solution structure. We follow the counsel of G. Polya [10]: *Only a fool starts at the beginning; the wise one starts at the end.*

We first pick a continuum solution. Interestingly enough, we can pick a solution virtually independent of the code or of the hosted equations. That is, we can pick a solution, then use it to verify an incompressible Navier-Stokes code, a Darcy flow in porous media code, a heat conduction code, an electrode design code, a materials code, etc.

We want a solution that is non-trivial but analytic, and that exercises all ordered derivatives in the error expansion and all terms, e.g., cross-derivative terms. For example, chose a solution involving tanh. This solution also defines boundary conditions, to be applied in any (all) forms, i.e., Dirichlet, Neumann, Robin, etc. Then the solution is passed through the governing PDE's to give the production term $Q(x,y,z,t)$ that produces this solution. Since this description sounds circular, we will demonstrate with con-

Contributed by the Fluids Engineering Division for publication in the JOURNAL OF FLUIDS ENGINEERING. Manuscript received by the Fluids Engineering Division July 24, 2001; revised manuscript received November 12, 2001. Associate Editor: G. Karniadakis.

 Copyright © 2002 by ASME

Downloaded 03 Jun 2010 to 171.66.16.150. Redistribution subject to ASME license or copyright; see http://www.asme.org/terms/Terms_Use.cfm

crete examples. In [4] we used Symbolic Manipulation to generate Q, and this is still recommended for complex multidimensional CFD codes. However, for illustration purposes, we can consider simple one-dimensional transient problems and generate the results by hand, in unambiguous steps.

Three Example Problems in MMS. To emphasize the generality of the concept, we pick the first example solution *before we specify the governing equations*. Then we will use this same solution for two different problems, i.e., set of governing PDE's and boundary conditions. The chosen solution $U(t,x)$ is the following.

$$U(t,x)=A+\sin(B), \quad B=x+Ct \tag{1}$$

Example 1. First, let us apply this 1-D transient solution to the nonlinear Burgers equation, often taken as a model for CFD algorithm development [2].

$$u_t=-uu_x+\alpha u_{xx} \tag{2}$$

Incidentally, this specified solution $U(t,x)$ is the exact solution for the constant velocity advection equation with boundary condition of $u(t,0)=A+\sin(Ct)$, so for the high Reynolds number problem (small α) it may look ''realistic'' in some sense, but it is not a solution to our governing Eq. (2), and its ''realism'' or lack thereof is irrelevant to the task of Code Verification.

We determine the source term $Q(t,x)$ which, when added to the Burgers equation for $u(t,x)$, produces the solution $u(t,x)=U(t,x)$. We write the Burgers equation as an operator (nonlinear) of u,

$$L(u)\equiv u_t+uu_x-\alpha u_{xx}=0 \tag{3}$$

Then we evaluate the Q that produces U by operating on U with L.

$$Q(t,x)=L(U(t,x))=\partial U/\partial t+U\partial U/\partial x-\alpha\partial^2 U/\partial x^2 \tag{4}$$

By elementary operations on the manufactured solution $U(t,x)$ stated in Eq. (1),

$$Q(t,x)=C\cos(B)+[A+\sin(B)]\cos(B)+\alpha\sin(B) \tag{5}$$

If we now solve the modified equation

$$L(u)\equiv u_t+uu_x-\alpha u_{xx}=Q(t,x) \tag{6}$$

or

$$u_t=-uu_x+\alpha u_{xx}+Q(t,x) \tag{7}$$

with compatible initial and boundary conditions, the exact solution will be $U(t,x)$ given by Eq. (1).

The initial conditions are obviously just $u(0,x)=U(0,x)$ everywhere. The boundary conditions are determined from the manufactured solution $U(t,x)$ of Eq. (1). Note that we have not even specified the domain of the solution as yet. If we want to consider the usual model $0\leqslant x\leqslant 1$ or something like $-10\leqslant x\leqslant 100$, the same solution Eq. (1) applies, but of course the boundary values are determined at the corresponding locations in x. Note also that we have not even specified the *type* of boundary condition as yet. This aspect of the methodology has often caused confusion. Everyone knows that different boundary conditions on a PDE produce different answers; not everyone recognizes immediately that the same solution $U(t,x)$ can be produced by more than one set of boundary condition types. The following combinations of inflow (left boundary, e.g., $x=0$) or outflow (e.g., $x=1$) boundary conditions will produce the same solution $U(t,x)$ over the domain $0\leqslant x\leqslant 1$.

Dirichlet—Dirichlet:

$$u(t,0)=U(t,0)=A+\sin(Ct), u(t,1)=A+\sin(1+Ct) \tag{8}$$

Dirichlet—Outflow Gradient (Neumann):

$$u(t,0)=U(t,0)=A+\sin(Ct), \partial u/\partial x|(t,1)=\cos(1+Ct) \tag{9}$$

Robin (mixed)—Outflow Gradient (Neumann) at $x=\pi$:

$$\begin{aligned} au+bu_x=c \ \ at \ \ (t,0)\rightarrow given \ \ a \ \ and \ \ b, \ \ select \\ =c[A+\sin(Ct)]+b\cos(Ct) \\ \partial u/\partial x|(t,\pi)=\cos(\pi+Ct) \end{aligned} \tag{10}$$

For this time-dependent solution, the boundary values are time-dependent. It also will be possible to manufacture time-dependent solutions with steady boundary values, if required by the code.

Example 2. To further clarify the concept, we now apply the same solution to a different problem, choosing as the new governing PDE a Burgers-like equation that might be a candidate for a 1-D turbulence formulation based on the mixing length concept.

$$\begin{aligned} u_t&=-uu_x+\alpha u_{xx}+\lambda\partial/\partial x[(x\partial u/\partial x)^2] \\ &=-uu_x+\alpha u_{xx}+2\lambda[x(u_x)^2+x^2u_{xx}] \end{aligned} \tag{11}$$

Writing the mixing-length model equation as a nonlinear operator of u,

$$L(u)\equiv u_t+uu_x-\alpha u_{xx}-2\lambda[x(u_x)^2+x^2u_{xx}]=0 \tag{12}$$

we evaluate the Q_m that produces U by operating on U with L_m.

$$\begin{aligned} Q_m(t,x)=L_m(U(t,x))&=\partial U/\partial t+U\partial U/\partial x-\alpha\partial^2 U/\partial x^2 \\ &-2\lambda[x(\partial U/\partial x)^2+x^2\partial^2 U/\partial x^2] \end{aligned} \tag{13}$$

By elementary operations on the (same) manufactured solution $U(t,x)$ stated in Eq. (1),

$$\begin{aligned} Q(t,x)=C\cos(B)+[A+\sin(B)]\cos(B)+\alpha\sin(B) \\ -2\lambda[x\cos^2(B)-x^2\sin(B)] \end{aligned} \tag{14}$$

If we now solve the modified model equation

$$L_m(u)\equiv u_t+uu_x-\alpha u_{xx}-2\lambda[x(u_x)^2+x^2u_{xx}]=Q_m(t,x) \tag{15}$$

or

$$u_t=-uu_x+\alpha u_{xx}+2\lambda[x(u_x)^2+x^2u_{xx}]+Q_m(t,x) \tag{16}$$

with compatible initial and boundary conditions, the exact solution for this turbulent problem again will be $U(t,x)$ given by Eq. (1), as it was for the previous laminar problem.

Note: the same initial and boundary conditions and boundary values from the previous problem can apply, since these are determined from the solution, not from the governing PDE, nor from Q or Q_m.

Example 3. We have shown how the same solution can be used as the exact solution to verify two different codes with different governing equations, with different source terms being created to Manufacture the same solution. A third example will demonstrate the arbitrariness of the solution form. Rather than the somewhat ''realistic'' solution to the constant velocity advection equation given by Eq. (1), let us consider the ''unrealistic'' but equally valuable solution as follows.

$$U_e(t,x)=\sin(t)e^x \tag{17}$$

Following the same procedure for the Burgers Equation (2), we evaluate the terms in Eq. (4) from the solution U_e of Eq. (17) and obtain

$$Q_e(t,x)=\cos(t)e^x+[\sin(t)e^x]^2-\alpha\sin(t)e^x \tag{18}$$

(arranged for readability rather than compactness). This Q_e, when added to Eq. (2), produces the Manufactured Solution Eq. (17) when compatible initial and boundary conditions are evaluated from Eq. (17).

Application to Verification of Codes. Once a nontrivial exact analytic solution has been generated, by this Method of Manufactured Solutions or perhaps another method, the solution is now used to Verify a Code by performing systematic discretization

Downloaded 03 Jun 2010 to 171.66.16.150. Redistribution subject to ASME license or copyright; see http://www.asme.org/terms/Terms_Use.cfm

convergence tests (usually, grid convergence tests) and monitoring the convergence as $\Delta \to 0$, where Δ is a measure of discretization (e.g., Δx, Δt in a finite difference or finite volume code, and element size in a finite element code, etc.).

The principle definition of ''order of convergence'' is based on behavior of the error of the discrete solution. There are various measures of error, but in some sense we are always referring to the difference between the discrete solution $f(\Delta)$ (or a functional of the solution, such as lift coefficient) and the exact (continuum) solution,

$$E = f(\Delta) - f^{\text{exact}} \tag{19}$$

For an order p method, and for a well-behaved problem (exceptions are discussed in Chapters 6 and 8 of [1]), the error in the solution E asymptotically will be proportional to Δ^p. This terminology applies to every ''consistent'' methodology: finite difference methods (FDM), finite volume methods (FVM), finite element methods (FEM), spectral, pseudo-spectral, vortex-in-cell, etc., regardless of solution smoothness. Thus,

$$E = f(\Delta) - f^{\text{exact}} = C\Delta^p + \text{H.O.T.} \tag{20}$$

where H.O.T. are higher order terms. (For smooth problems, it may be possible in principle to evaluate the coefficient C and the H.O.T. from the continuum solution, but as a practical matter, we do not do this in the accuracy Verification procedure.) We then monitor the numerical error as the grid is systematically refined. Successive grid halving is not required, just refinement. (See [1] for examples, analysis and extensive discussion.) Thorough iterative convergence is required. Theoretically (from Eq. 20), values of $C = error/\Delta^p$ should become constant as the grid is refined for a uniformly p-th order method (''uniformly'' implying at all points for all derivatives). Details and many examples are given in [1].

The following summary points from [1] are worth noting.

The procedure detects all ordered errors. It will not detect coding mistakes that do not affect the answer obtained, e.g. mistakes in an iterative solution routine which affect only the iterative convergence rate. In the present view, these mistakes are not considered as Code Verification issues, since they affect only code efficiency, not accuracy.

The procedure does not evaluate the adequacy of non-ordered approximations, e.g., distance to an outflow boundary, distance to an outer (wind-tunnel wall-like) boundary, use of $\partial p/\partial y = 0$ at a wall as a boundary condition (this is not a rigorous physical boundary condition for Navier-Stokes equations). The errors of these approximations do not vanish as $\Delta \to 0$, hence are ''non-ordered approximations.'' The adequacy of these approximations must be assessed by sensitivity tests which may be described as ''Justification'' exercises [1]; these are similar to Verification of Calculations in that they involve only mathematics, but are simply the results of calculations. If the code manual says it uses a 2nd order accurate discretization of $\partial p/\partial y = 0$ at walls and the MMS procedure shows that it does, then the Code is Verified on this point.

When this systematic grid convergence test is verified (for all point-by-point values), we have verified

1. any equation transformations used (e.g., nonorthogonal boundary fitted coordinates),
2. the order of the discretization,
3. the encoding of the discretization, and
4. the matrix solution procedure.

This technique was originally applied in [4] to long Fortran code produced by Artificial Intelligence (Symbol Manipulation) methods. The original 3-D nonorthogonal coordinate code contained about 1800 lines of dense Fortran. It would be impossible to check this by reading the source code, yet the procedure described Verified the code convincingly. Roundoff error was not a problem.

The arbitrary solution, produced inversely by the specification of the source term Q, has been aptly described by Oberkampf et al. [5] and Reed et al. [9] as a ''Manufactured Solution.'' The approach was independently developed and named the ''Prescribed Solution Forcing Method'' by Dee [11]. Others who independently developed the same philosophy and essentially the same methodology are Ethier and Steinman [12] and Powers [13–16]. The first systematic exposition of the method with application to multidimensional nonlinear problems appears to be [4], but in retrospect, it seems that early instances of the use of what we now call the Method of Manufactured Solutions were cited in 1972 (the original version of [2], pp. 363–365). Although the authors did not mention the method they used, it seems clear that they used this approach to generate an *ad hoc* exact solution for time-dependent model equations. Obviously, the simple solution form was chosen first, then passed through the PDE to generate the problem; see the ''Errata and Addenda'' section of the website www.hermosa-pub.com/hermosa for references and details. Undoubtedly, many of the non-infinite-series classical solutions in engineering were obtained this way, i.e. beginning with a solution form. What is strange is that the notion persisted, often repeated, that we did not have any non-trivial solutions to the full nonlinear Navier-Stokes equations, when all we have to do is ''complicate'' the problem a little with the addition of a source term, and we can generate all the solutions we want. The key concept is that, for Verification of Codes, these solutions need not be physically realistic.

The technique is applicable to systems of equations, including full Navier-Stokes in general non-orthogonal coordinates (e.g., see [17,18]), provided that the code is capable (or modifiable) to treat source terms in each PDE.

The technique of Code Verification by monitoring grid convergence is extremely powerful. Upon initial exposure to the technique, engineers are often negative about the method because they intuit that it cannot be sensitive enough to pick up subtle errors. After exposure to numerous examples, if they remain negative it is usually because the method is *excessively* sensitive, revealing minor inconsistencies such as first-order discretizations at a single boundary point in an elliptic problem that effects the size of the error very little (as correctly intuited) but still reduces the rate of convergence to first order for the entire solution. For examples, see [1].

The fact that the Manufactured Solution may bear no relation to any physical problem does not affect the rigor of the accuracy Verification of Codes. The only important point is that the solution (manufactured or otherwise) be non-trivial, i.e., that it exercise all the terms in the error expansion. The algebraic complexity may be something of a difficulty, but is not insurmountable, and in practice has been easily handled using Symbolic Manipulation packages like Macsyma, Mathematica, Maple, etc. Using the source-code (Fortran) writing capability of Macsyma, it is not even necessary for the analyst to look at the form of Q. Rather, the specification of the solution (e.g., tanh function) to the Symbolic Manipulation code results in some complicated analytical expression that can be directly converted by the Symbolic Manipulation code to a Fortran (or Pascal, *C*, etc.) source code segment, which is then readily emplaced in a source code module (subroutine, function, etc.) that then is called in the accuracy Verification of Code procedure. (This ''emplacement'' can be performed by hand by the analyst, without actually reading the complicated source code expressions, or can itself be automated in the Symbolic Manipulation code.)

The procedure has been applied successfully to nonlinear systems of equations, with separate Q's generated for each equation. Both unsteady and steady solutions are possible. (It may be useful to avoid exponential solution growth in time so as to avoid confusion with instabilities; e.g., see the fully 3D incompressible Navier-Stokes analytical solutions of Ethier and Steinman [12].) Nonlinearity is an issue only because of uniqueness questions;

Downloaded 03 Jun 2010 to 171.66.16.150. Redistribution subject to ASME license or copyright; see http://www.asme.org/terms/Terms_Use.cfm

otherwise, the source term complexity may be worse because of nonlinearity, but that is the job of the Symbolic Manipulation code. Nonuniqueness could be an issue because the code could converge to another legitimate solution other than the Manufactured Solution, producing a false-negative accuracy Verification test for a correct code. However, it would be difficult to contrive a situation in which a false positive accuracy Verification was obtained. In much experience, non-uniqueness has not been an issue. In [4], we applied the procedure to the nonlinear (quasi-linear) PDE's of the elliptic grid generation method for nonorthogonal coordinates. Here, the Manufactured Solution was an analytical 3-D coordinate transformation; see examples in [1].

While the simple example problems herein were chosen for transparency, complex nonlinear systems (like Navier-Stokes equations in non-orthogonal coordinates) benefit from use of computer Symbolic Manipulation routines to perform the differentiation and algebra which generate the source term. As noted above, in this approach it is not necessary to even examine the source term; using the Fortran or C code writing capabilities of software packages like Macsyma, Maple, etc. a subroutine can be produced to generate the pointwise values of the source terms for inclusion in the governing PDE's. For coupled nonlinear PDE's like those of 3-D elliptic grid generation equations, the pointwise evaluation requires simultaneous solution of 3 coupled (non-dimensional) nonlinear equations at each point. We have always used full Newton-Raphson iteration methods, the Jacobians of which are also produced by Symbol Manipulation and Fortran source code writing, so the process remains automated; i.e., one never performs any algebra or calculus manipulations by hand. In fact, for our work in grid generation via variational methods [19–24], we never even looked at the governing PDE's themselves. We considered only the variational principle itself. The Symbolic Manipulation toolkits developed by Prof. Steinberg were used to automatically generate the PDE's by (symbolic) differentiation of the variational equations to produce the Euler-Lagrange equations, to substitute 2nd order difference expressions for the PDE's, to gather terms, to write Fortran subroutines for their evaluation, to generate a specified Manufactured Solution (i.e., ''a continuum grid'' or parameterization which, when discrete values are evaluated, produces a computational grid), to write Fortran code for the source term including Newton-Raphson point solutions, and to perform the entire Code Verification procedure, without the researcher ever having to look at either the continuum or discretized PDE's or source terms.

Note that the Manufactured Solution should be generated in original (''physical space'') coordinates (x,y,z,t). Then the same solution can be used directly with various non-orthogonal grids or coordinate transformations.

The only disadvantage of the procedure is the requirement that the CFD code being Verified must include accurate treatment of a source term and that the code's boundary condition values not be hard-wired. Many codes are built with source terms included, and many algorithms allow trivial extension to include Q's. However, in directionally-split algorithms such as Approximate Factorization [2] the time-accurate treatment of $Q(x,y,z,t)$ involves subtleties and complexities at boundaries, especially for non-orthogonal coordinates [2,18]. Thus, CFD code extensions may be required in order to apply this procedure involving ''Manufactured Solutions'' for Code Verification. Likewise, some groundwater flow codes are built with hard-wired homogeneous Neumann boundary conditions, $\partial f/\partial n=0$. In order to use an arbitrary solution function, nonhomogeneous boundary values like $\partial f/\partial n=g$ would be required. Alternately, one could restrict the choice of Manufactured Solution functions to fit the hard-wired values.

Likewise, to test periodic boundary conditions, one must chose a periodic function for the Manufactured Solution.

The paper by Pelletier and Ignat [8] (see also [1], pp. 162–163) will be of interest to turbulence modelers interested in Code Verification. It provides simple analytical solutions for an incompressible free shear layer applicable to $k-\varepsilon$, $k-\omega$ and $k-\tau$ models.

The practical difficulties arising from large numbers of option combinations are discussed extensively in [1]. Briefly, option combinations are countable, and pessimistic computer science conclusions about complex codes being unverifiable are based on unrealistic conditions like ''arbitrary complexity.'' Furthermore, the number of option combinations required often can be greatly reduced by ''partitioning the option matrix'' [1] based on common sense and knowledge of code structure (a ''glass box'' philosophy [7] as opposed to the more demanding ''black box'' philosophy). Failing this, codes can be Verified only for a subset of option combinations. In any case, these issues are an essential part of Code Verification by any method; they are not unique to the MMS, and in fact the generality of the MMS approach will reduce the difficulties arising from option complexity because less testing will be required for each option combination compared to the usual haphazard and piecemeal approach to Code Verification.

Also see [1] for the following topics: early applications of MMS concepts, discussions and examples of mixed first- and second-order differencing, the small parameter (high Reynolds number) problem, economics of dimensionality, applications of MMS to 3D grid generation codes, effects of strong and inappropriate coordinate stretching, debugging with Manufactured Solutions (when the Code Verification initial result is negative), examples of many manufactured or otherwise contrived analytical solutions in the literature, approximate but highly accurate solutions (often obtained by perturbation methods) that can also be utilized in Code Verification, the possibility of a useful theorem related to MMS, special considerations required for turbulence modeling and other fields with multiple scales, example of MMS Code Verification with a 3-D grid-tracked moving free surface (see [17]), code robustness, examples of the remarkable sensitivity of Code Verification via systematic grid convergence testing, and several methodologies for Verification of Calculations, including the recommended use of the Grid Convergence Index (GCI) for uniform reporting of systematic grid convergence studies.

Recent Work and Further Discussion

Blind Study. Salari and Knupp [17] have exercised the MMS in a blind study, in which one author (Knupp) modified a CFD code previously developed and Verified by the other (Salari), deliberately introducing errors. Then the code author tested the sabotaged code with the MMS. This exercise was not performed on simple model problems, but on a full time-dependent, compressible and incompressible, Navier-Stokes code with plenty of options. In all, 21 cases were studied, including one ''placebo'' (no mistake introduced) and several that involved something other than the solution (e.g., wrong time step, post-processing errors). Several formal mistakes (not order-of-convergence errors) went undetected, as expected.

Two cases showed possible limitations or cautions of MMS. Case E.4 involved an error in a DO loop for updating density arrays. Although MMS was successful, it would not have been if my suggestion (on p. 78 of [1]) had been followed to use exact continuum solutions as the initial conditions to reduce run time. (This is a caution note not just for the MMS but for any Code Verification by systematic grid convergence testing using any benchmark solution.) Also, Case E.12 showed that an error in a convergence test of one variable (a ''.le.'' test replaced with a ''.ge.'' test) could go undetected on a particular problem because the convergence test was successfully implemented for another variable.

All ten of the OAM (Order-of-Accuracy Mistake) errors, i.e., all that could prevent the governing equations from being correctly solved, were successfully detected. In addition, several less serious mistakes were detected using the procedure.

The report also discusses error (and mistake) taxonomies, provides examples and Manufactured Solutions (with source terms)

Downloaded 03 Jun 2010 to 171.66.16.150. Redistribution subject to ASME license or copyright; see http://www.asme.org/terms/Terms_Use.cfm

from compressible Navier-Stokes codes as well as heat conduction and 2-D Burgers equation codes in both Cartesian and curvilinear coordinates, and discusses approaches for developing Manufactured Solutions without using source terms.

From the Abstract: ''The principle advantage of the MMS procedure over traditional methods of Code Verification is that code capabilities are tested in full generality. The procedure thus results in a high degree of confidence that all coding mistakes which prevent the equations from being solved correctly have been identified.''

The understanding and experience of the authors is profound, and the report should be read in its entirety by anyone interested in pursuing the Method of Manufactured Solutions.

Two Multidimensional Features. In the first 1-D example problem above, we noted that the Manufactured Solution, since it is analytic, can be applied over any range of the dependent spatial variable x, e.g. the domain could extend over $x \in [0,1]$ or $x \in [-\pi, +\pi]$ etc. This feature extends to multidimensions, e.g., the same multidimensional analytic solution could be applied to a square driven cavity problem, a rectangular cavity, a backstep, a wing, etc. Also, multidimensional problems might require a little more thought to assure that all terms of the governing equations are exercised. For example, a Manufactured Solution of form $U(t,x,y) = F1(t) \cdot F2(x) \cdot F3(y)$ will not be adequate to exercise governing equations containing cross derivative terms such as $\partial^2 u / \partial x \partial y$ since these are identically zero no matter how complex are the F's.

Mixed Order Methods. Roy [25,26] has shown how to treat mixed-differencing (e.g., first-order upstream differencing for advection and second-order differencing for other terms) in the systematic grid convergence tests. These two papers present the resolution, in an elegant manner, of a long-standing and practical difficulty in grid convergence studies and the GCI (Grid Convergence Index), namely, the treatment of mixed-order convergence. The mixed order behavior can arise either from the explicit use of 1st-order advection discretization and 2nd-order diffusion, or from the 1st-order observed convergence rate of nominally second-order methods caused by shocks. The procedure simply involves another grid level to evaluate the *two* leading coefficients in the error expansion. The analysis includes non-integer grid refinement factors $\mathbf{r}$. The papers also demonstrate how nonmonotonic convergence occurs from mixed-order methods in the non-asymptotic range. The method is applicable to both Verification of Codes and Verification of Calculations, and would enable more accurate (less conservative) error estimation by way of the GCI [1] for QUICK and similar methods using 2nd order accurate diffusion terms and 3rd order accurate advection terms.

Radiation Transport Code Including Eigenvalue Problems Pautz [27] presents his experience applying MMS to the radiation transport code ATTILA. The application was inspired by Salari and Knupp [17] and contains some early 1970's references on the basic ideas, but these are '' . . . more limited than the more recent and general treatment by Salari and Knupp.''

The Code Verification described includes angular flux, scattering cross sections, and spherical harmonics. In the approach used, by choosing the term $f(\mathbf{r}) = 1$ (versus a more general form) in the assumed form of the manufactured Solution, one can isolate spatial differencing terms (they cancel) and Verify whether the code handles angular terms correctly.

The code uses 3-D tetrahedral elements (utilizing linear discontinuous finite element discretization) in space and discrete ordinates in the angular discretization. The study treated the following features: Steady State—Monoenergetic, Steady State—Multigroup, Monoenergetic K-Eigenvalue, Gray Infrared.

The experience with the MMS approach was quite successful. With $f(\mathbf{r}) = 1$, the author discovered coding mistakes in input routines (and a divide by zero for a particular combination of input options). Also, the procedure revealed mistakes in discretization of certain boundary data for the gray infrared problem. The approach Verified 2nd order convergence for norms and 3rd order convergence for average scalar flux. A subtle aspect required for successful application of the MMS procedure was the consistent finite element weighting on the MMS source term. Based on earlier 1-D analysis in the literature, it was expected that all the examined quantities (norms and average scalar flux) would exhibit 3rd order convergence, but the results of the MMS procedure demonstrated only 2nd order convergence for the norms in multidimensions. The author concluded that MMS is '' . . . a very powerful verification tool'' [27]. Further [pers.comm.] the author says ''The power and conceptual simplicity of MMS make it an indispensable tool for code development'' and recommends that MMS be required in any formal Code Verification system.

Nonhomogeneous Boundary Conditions. An arbitrary Manufactured Solution will not necessarily have homogeneous boundary conditions, e.g., $u \neq 0$ or $\partial u / \partial x \neq 0$. To use such a solution, the code would require this capability. This might be inconvenient, e.g., many CFD codes have hard-wired no-slip conditions at a wall, e.g., $u = 0$. Rather than modify the code, some thought will produce Manufactured Solutions with homogeneous boundary values.

Nonlinear Boundary Conditions. So-called ''radiation'' outflow conditions are usually linear and are already covered by the previous discussion. Nonlinear boundary conditions, e.g., simple vortex conditions at outflow, or true (physical) heat-transfer radiation boundary conditions, are possible. It may be possible to select a Manufactured Solution that meets the nonlinear boundary condition; otherwise, a source term would have to be added (if it is not already present) in the nonlinear boundary equations to retain the generality of the MMS.

Shocks. Shock solutions are treatable by the MMS, with additional considerations. See pages 89–90 of [1], which include the work of J. Powers and associates [13–16]. The simplest approach may be to Verify the shock capturing algorithms separately on inviscid benchmark problems such as oblique shock solutions, if shock curvature is not viewed as a major question, or if it is, by using attached curved shock solutions obtained by the method of characteristics and/or detached bow shock solutions obtained by the classical inverse method. The benchmark solutions may involve asymptotic approximations in geometry or Mach number, e.g. an analysis [16] neglecting terms of $O(\varepsilon^2)$ where $\varepsilon = 1/M^2$. This approximation can be made very accurate by choosing high M, say $M \sim 20$, for the Code Verification exercise. Note again the distinction of mathematics versus science; it is not a concern that the code being tested might be built on perfect gas assumptions that are not valid at such high M. This does not affect the mathematics of Code Verification; the code would not be applied at such high M when accuracy of the physics becomes important, during Code Validation.

The assumption involved in this approach is that the option matrix of the code may be partitioned (see [1], Chapter 6 for an example). That is, the Verification of the shock-capturing algorithm and coding will not be affected by the later inclusion of viscous terms, boundary conditions, etc. Other option-partitioning assumptions will occur to the reader: separated Verification of a direct banded Gaussian elimination routine in a FEM code; Verification of shock-capturing algorithm separate from non-ideal gas effects; radioactive decay option (which is dimensionless) verified separately from spatial discretization of flow equations. This partitioning approach requires the ''black-box'' Verification philosophy to be modified to a ''glass-box'' [7], i.e. some knowledge of code structure is required to justify the approach, and it will be more difficult to convince reviewers, editors, contract monitors, regulators, etc. that the approach is justified. The work savings can be enormous, of course, avoiding the factorial increase of complexity inherent in option combinations.

Another straightforward approach for shocks that does not in-

Downloaded 03 Jun 2010 to 171.66.16.150. Redistribution subject to ASME license or copyright; see http://www.asme.org/terms/Terms_Use.cfm

volve partitioning the option matrix is to generate a Manufactured Solution that is in fact (in the continuum) C^{∞} smooth, but that has such strong gradients in some region that it appears as a shock over the targeted range of grid resolutions. The possible difficulty here is that some shock capturing algorithms are based on the conservation equations without source terms, e.g., Godunov's method and modern variants, and these could conceivably fail where source terms are present. Any shock-capturing algorithm based purely on geometric limiters will be oblivious to the source terms and should work without modification.

Requirement for Source Terms. In the version demonstrated, the MMS requires that the code be capable of treating source terms in each PDE. For some engineering codes, this is always the case, e.g. time-dependent chemistry codes, grid generation codes based on elliptic generation. Another approach to MMS developed by Knupp (see [17] and [1], Chapters 3 and 6) is applicable to variable coefficient problems, e.g., groundwater transport codes or heat conduction codes with variable properties. In this method, a Solution is Manufactured by solving directly for the distribution of variable coefficients that produces it. Generally, for Navier-Stokes codes, distributed source terms are nonphysical and would not have been included, so these codes would have to be modified to use the method. For codes developed ''in house,'' this is very little trouble. The only tricky situation we know of occurs with implicit Approximate Factorization codes built for second-order time accuracy, as noted above and in [1]; in this case, the consistently second-order treatment of source terms is subtle. Still, the trouble of adding source terms is small compared to the alternative of a haphazard and piecemeal approach to Code Verification. It is certainly trivial for FEM code using direct solvers. For general purpose commercial codes, it is not an undue hardship on vendors to be required to include source terms so that users can Verify the Codes themselves. (CFD Software vendors are notoriously uninterested in performing V&V and in sharing results with customers, apparently for good reasons.)

Solution Realism. The MMS as presented generates solutions to PDE's, modified to include source terms for all dependent variables, with no concern for realism of the solution. Thus, acceptance requires that the judge recognize that Code Verification is a purely mathematical exercise. Physical realism and even physical realizability are irrelevant. Actually, there is no *requirement* that the Manufactured Solution look unrealistic, and we can invent appealing solutions if necessary to satisfy managers, regulators, public stakeholders, etc. But it is worthwhile to understand that this ''realism'' is mere window dressing. It is also risky, in that it encourages a dangerous misconception and opens the door to criticism and arguments about adequate ''realism,'' which after all is a qualitative concept and again opens the door to piecemeal and perpetual Code Verification exercises.

Furthermore, ''realistic'' solutions can actually be less desirable. For example, a realistic solution for Navier-Stokes equations would have a boundary-layer behavior at walls. But then the terms neglected in classical boundary layer theory (e.g., $\partial p/\partial y$) will not be strongly exercised in the code, and a minor error might conceivably slip by undetected, e.g., a one-sided difference expression for $\partial p/\partial y$ near the wall thought to be 2nd order but actually 1st order will not affect the answer if $\partial p/\partial y = 0 + O(\Delta^2)$ whereas an ''unrealistic'' solution based on tanh, etc. would exercise these terms.

Code Verification With a Clearly Defined Completion Point

As noted earlier, it is now well-recognized that benchmark solutions for Code Verification must exhibit sufficiently complex structure that all terms in the governing equation being tested are exercised. What apparently is not so widely recognized today is that, once a code (or rather, a specific set of code option combinations) has been convincingly Verified on such a solution, it is nearly pointless to continue exercising it on simpler problems. I say ''nearly'' because the exercises have some value, but should not be thought of as Verification, but as Confirmation exercises; see Chapter 1 of [1]. In the present view, Code Verification has a theorem-like quality, and therefore terminates. Like a high-school student plugging numbers into the solution for the quadratic equations, a code user who performs Confirmation exercises gains confidence in the code and in his ability to set up the code and to interpret the results. Such Confirmation exercises are valuable, indeed necessary, as part of user training, but these should not be confused with Code Verification. Similarly, we recognize that simple problems (e.g., 1-D linear wave propagation) are useful in algorithm development, in exploring algorithm and code characteristics, and in comparing performance of different codes, but once again, these comparison exercises should not be confused with Code Verification. For example, one could have three codes of 1st, 2nd, and 4th order accuracy, each of which was rigorously Verified to be so. Then a comparison exercise based on simple wave propagation with a linear advection-diffusion equation would be expected to show increasing accuracy; however, this does not alter the previously determined and completed Code Verifications.

Proof? Does such a Code Verification process deserve the term ''proof''? This is another semantic question whose answer depends on the community context. Logicians, philosophers and pure mathematicians clearly view ''proof'' differently from engineers, with an often other-worldly standard. For example, Fermat's Last Theorem is easily demonstrable; anyone can readily convince themselves of its correctness, and a straightforward computer program can be written to convincingly demonstrate its correctness for systematic millions of cases. No one, not even the philosophers or logicians or pure mathematicians, doubts it. Indeed, if one were to put forward a counter-proof, it would be rejected by all. Yet only recently has a book-length ''proof'' been put forward (and doubts about it remain). Since some philosophers maintain that it is not possible even in principle to prove relativity, or Newton's laws of gravity (which are certainly provable within engineering accuracy) they are not going to accept the notion of proof of correctness of a complex code, i.e., Verification of Code

The notion of proof is at the heart of very important criticisms, not just of the subject MMS, but of the concepts of Code Verification and especially Certification [1] for large public-policy projects. One might agree with some philosophers who maintain it is not possible to prove relativity or Newton's Laws, but would one be willing to cancel a public policy project (e.g., a nuclear waste project) because the modeling used Newton's laws? Presumably not, but stakeholders are willing to cancel such projects under the guise of unprovability of code correctness. The harm is done when these standards for proof of philosophers, mathematicians or logicians are applied to down-to-earth engineering projects. If we accept such out-of-context standards for proof, we cannot do anything, literally. For example, we have no proof of convergence for real systems, because the Lax Equivalence theorem only holds for linear systems. The word ''proof'' is itself a technical term, with different appropriate standards in logic, pure mathematics, applied mathematics, engineering, criminal law vs. torts vs. civil law (e.g., ''beyond a reasonable doubt''), etc. The first definition in one dictionary for ''proof'' is ''The evidence or argument that compels the mind to accept an assertion as true.'' In this sense, if not in a strict mathematical sense, one could claim that the MMS approach can provide proof of Code Verification.

I am unhesitating in claiming ''convincing demonstration'' and ''robust Verification'' for the present MMS approach. A mathematical proof would require the formalism of a theorem; as noted, it would seem that a theorem is possible, for some related problem(s). Further, if one allows the legitimacy of a nonmathematical proof in principle, then I would claim that this method provides it. It is highly unlikely that a code embodying the Burgers equation (2) and passing the Verification test for the so-

Downloaded 03 Jun 2010 to 171.66.16.150. Redistribution subject to ASME license or copyright; see http://www.asme.org/terms/Terms_Use.cfm

lution of the above example could be wrong (without a contrived counter-example). More complex codes with option combinations require more tests, obviously. Computer Scientists like to negate the possibility of complete Code Verification by considering codes of ''arbitrary complexity'' or ''arbitrary number of options,'' but in fact real codes have a countable, exercisable number of options; in any case, a code can be conditionally Verified just for those sets of options exercised. Geometry complexity is hard to address in general, but once again the claim of Code Verification can be conditionally stated to restrict geometry families to those tested. In practice, difficulties with complex geometries (e.g., singularities) are often not Code Verification issues at all, but are simply difficulties with Verification of Calculations; i.e., they are not issues of code correctness.

An Alternative View on Code Verification With a Clearly Defined Completion Point. The present view of Code Verification as a theorem-like process with a fixed termination is not universally accepted. In an alternative view [5–7,28] held by respected authorities, Code Verification (and Validation) are ''ongoing activities that do not have a clearly defined completion point'' [28], more akin to accumulating evidence for a legal case than to proving a theorem [6,7]. Both viewpoints recognize, obviously, that if the code is modified, it is a new code (even if the name of the code remains) and the new code must be re-Verified. Also, both viewpoints recognize that all plausible non-independent combinations of input options must be exercised so that every line of code is executed in order to claim that the entire code is Verified; otherwise, the Verification can be claimed only for the subset of options exercised. And both viewpoints recognize the value of ongoing code exercise by multiple users, both in an evidentiary sense and in user training. In this alternative view these activities could be part of formal Code Verification itself, rather than as Code ''Confirmation'' as in the present view [1].

The decision whether or not to include these activities under ''Code Verification'' rather than ''Code Confirmation'' is semantic but it must be recognized that it has practical and possibly serious consequences. For example, contractual and/or regulatory requirements for delivery or use of a ''Verified Code'' might be ambiguous in this view, since ''Code Verification'' by definition is never-ending. Also, any test (even a superficial one) could be claimed as ''partial Verification.'' However, some advantages exist for this view, e.g., encourages more precision of the meaning of ''Verified Code,'' and it more explicitly recognizes the value of ongoing code exercise by the user community. Both viewpoints recognize that ongoing code use and exercise can possibly uncover mistakes missed in the Code Verification process (just as a theorem might turn out to have a faulty proof or to have been misinterpreted) but in this alternative view Code Verification cannot be completed, except by specification (perhaps negotiated) of the meaning of ''Verified Code.'' Verification of individual calculations, and certainly Validations, are still viewed as ongoing processes in both views, of course. [1,2,5–7,28]

Concluding Remarks

The Method of Manufactured Solutions for Code Verification is typically met with skepticism, but in the experience of Oberkampf and Trucano [7] and my own, people who actually try it are enthusiastic. The MMS enables one to produce many exact analytical solutions for use as benchmarks in systematic discretization refinement tests, which tests are remarkably sensitive for Code Verification. The method is straightforward and, when applied to all option combinations in a code, can lead to complete and final Code Verification, with a well-defined completion point. It eliminates the typical haphazard, piecemeal and never-ending approach of partial Code Verifications with various highly simplified problems that still leave the customer unconvinced.

Acknowledgments

I gratefully acknowledge many clarifying discussions with Dr. W. L. Oberkampf.

References

[1] Roache, P. J., 1998, *Verification and Validation in Computational Science and Engineering*, Hermosa Publishers, Albuquerque, NM.

[2] Roache, P. J., 1999, *Fundamentals of Computational Fluid Dynamics*, Hermosa Publishers, Albuquerque, NM, Chapter 18.

[3] Roache, P. J., Ghia, K., and White, F., 1986, ''Editorial Policy Statement on the Control of Numerical Accuracy,'' ASME J. Fluids Eng., **108**, No. 1, Mar., p. 2.

[4] Steinberg, S., and Roache, P. J., 1985, ''Symbolic Manipulation and Computational Fluid Dynamics,'' J. Comput. Phys., **57**, No. 2, Jan., pp. 251–284.

[5] Oberkampf, W. L., Blottner, F. G., and Aeschliman, D. P., 1995, ''Methodology for Computational Fluid Dynamics Code Verification/Validation,'' AIAA Paper 95-2226, 26th AIAA Fluid Dynamics Conference, 19–22 June, San Diego, California.

[6] Oberkampf, W. L., and Trucano, T. G., 2000, ''Validation Methodology in Computational Fluid Dynamics,'' AIAA Paper 2000–2549, 19–22 June, Denver, CO.

[7] Oberkampf, W. L., and Trucano, T. G., 2002, ''Verification and Validation in Computational Fluid Dynamics,'' AIAA Progress in Aerospace Sciences (to appear).

[8] Pelletier, D., and Ignat, L., 1995, ''On the Accuracy of the Grid Convergence Index and the Zhu-Zienkiewicz Error Estimator,'' pp. 31–36 in ASME FED Vol. 213, Quantification of Uncertainty in Computational Fluid Dynamics, Aug., R. W. Johnson and E. D. Hughes, eds.

[9] Reed, H. L., Haynes, T. S., and Saric, W. S., 1998, ''CFD Validation Issues in Transition Modeling,'' AIAA J., **36**, No. 5, May, pp. 742–749. See also AIAA Paper 96-2051, 27th AIAA Fluid Dynamics Conference, 17–20 June 1996, New Orleans, Louisiana.

[10] Polya, G., 1957, *How to Solve It; A New Aspect of Mathematical Method*, Princeton University Press, Princeton, NJ.

[11] Dee, D. P., 1991, ''Prescribed Solution Forcing Method for Model Verification in Hydraulic Engineering,'' Proc. 1991 National Conference on Hydraulic Engineering, ASCE, Nashville, July 29-August 2.

[12] Ethier, C. R., and Steinman, D. A., 1994, ''Exact Fully 3D Navier-Stokes Solutions for Benchmarking,'' Int. J. Fract., **19**, pp. 369–375.

[13] Powers, J. M., and Gonthier, K. A., 1992, ''Reaction Zone Structure for Strong, Weak Overdriven and Weak Underdriven Oblique Detonations,'' Phys. Fluids A, **4**, No. 9, Sept., pp. 2082–2089.

[14] Powers, J. M., and Stewart, D. S., 1992, ''Approximate Solutions for Oblique Detonations in the Hypersonic Limit,'' AIAA J., **30**, No. 3, Mar., pp. 726–736.

[15] Grismer, M. J., and Powers, J. M., 1992, ''Comparison of Numerical Oblique Detonation Solutions with an Asymptotic Benchmark,'' AIAA J., **30**, No. 12, Dec., pp. 2985–2987.

[16] Grismer, M. J., and Powers, J. M., 1996, ''Numerical Predictions of Oblique Detonation Stability Boundaries,'' Shock Waves, **6**, pp. 147–156.

[17] Salari, K., and Knupp, P., 2000, ''Code Verification by the Method of Manufactured Solutions,'' SAND2000-1444, Sandia National Laboratories, Albuquerque, NM 87185, June.

[18] Salari, K., and Roache, P. J., 1990, ''The Influence of Sweep on Dynamic Stall Produced by a Rapidly Pitching Wing,'' AIAA Paper 90-0581.

[19] Roache, P. J., and Steinberg, S., 1985, ''A New Approach to Grid Generation Using a Variational Formulation,'' AIAA 85-1527-CP, *Proceedings AIAA 7th Computational Fluid Dynamics Conference*, 15–17 July, Cincinnati, Ohio.

[20] Steinberg, S., and Roache, P. J., 1986, ''Using MACSYMA to Write Fortran Subroutines,'' Journal of Symbolic Computation, **2**, pp. 213–216. See also *MACSYMA Newsletter*, Vol. II-2, 1985, pp. 10–12.

[21] Steinberg, S., and Roache, P. J., 1986, ''Variational Grid Generation,'' Numerical Methods for Partial Differential Equations, **2**, pp. 71–96.

[22] Steinberg, S., and Roache, P. J., 1986, ''A Tool Kit of Symbolic Manipulation Programs for Variational Grid Generation,'' AIAA Paper No. 86-0241, AIAA 24th Aerospace Sciences Meeting, 6–9 January 1986, Reno, Nevada.

[23] Steinberg, S., and Roache, P. J., 1986, ''Grid Generation: A Variational and Symbolic-Computation Approach,'' *Proceedings Numerical Grid Generation in Fluid Dynamics Conference*, July, Landshut, W. Germany.

[24] Steinberg, S., and Roache, P. J., 1992, ''Variational Curve and Surface Grid Generation,'' J. Comput. Phys., **100**, No. 1, pp. 163–178.

[25] Roy, C. J., McWherter-Payne, M. A., and Oberkampf, W. L., 2000, ''Verification and Validation for Laminar Hypersonic Flowfields,'' AIAA 2000-2550, June, Denver.

[26] Roy, C. J., 2001, ''Grid Convergence Error Analysis for Mixed-Order Numerical Schemes,'' AIAA Paper 2001–2606, June, Anaheim. See also this issue of ASME JFE.

[27] Pautz, S. D., 2001, ''Verification of Transport Codes by the Method of Manufactured Solutions: the ATTILA Experience,'' Proc. ANS International Meeting on Mathematical Methods for Nuclear Applications, M&C 2001, Salt Lake City, Utah, Sept.

[28] AIAA, 1998, ''Guide for the Verification and Validation of Computational Fluid Dynamics Simulations,'' American Institute of Aeronautics and Astronautics, AIAA-G-077-1998, Reston, VA.

Downloaded 03 Jun 2010 to 171.66.16.150. Redistribution subject to ASME license or copyright; see http://www.asme.org/terms/Terms_Use.cfm

Verification of Finite Volume Computations on Steady-State Fluid Flow and Heat Transfer

J. Cadafalch
C. D. Pérez-Segarra
R. Còsul
A. Oliva

Centre Tecnològic de Transferència de Calor (CTTC),
Lab. de Termotècnia i Energètica,
Universitat Politècnica de Catalunya (UPC),
c/ Colom 11, 08222 Terrassa, Spain
e-mail: labtie@labtie.mmt.upc.es

This work presents a post-processing tool for the verification of steady-state fluid flow and heat transfer finite volume computations. It is based both on the generalized Richardson extrapolation and the Grid Convergence Index (GCI). The observed order of accuracy and a error band where the grid independent solution is expected to be contained are estimated. The results corresponding to the following two and three-dimensional steady-state simulations are post-processed: a flow inside a cavity with moving top wall, an axisymmetric turbulent flow through a compressor valve, a premixed methane/air laminar flat flame on a perforated burner, and the heat transfer from an isothermal cylinder enclosed by a square duct. Discussion is carried out about the certainty of the estimators obtained with the post-processing procedure. They have been shown to be useful parameters in order to assess credibility and quality to the reported numerical solutions.
[DOI: 10.1115/1.1436092]

1 Introduction

During the last decades the numerical methods on heat transfer and fluid flow have been consolidated as an indispensable tool for the resolution of thermal and mechanical engineering problems, being nowadays an essential complement to the experimental studies. The aim of the Computational Fluid Dynamics (CFD) scientific community up to the last years was mainly focussed on improving the performance of the numerical methods in order to increase the range of applications, i.e., larger domains and more and more complex physical phenomena. As a result, many commercial codes have appeared on the market and are being used by many engineers and technicians in their projects and companies for design, evaluation and testing of new equipment and even entire systems (virtual prototyping and virtual testing), decreasing dramatically the time and cost of bringing new products to the market. Together with the increase of the number of users on these techniques, a discussion about the need of assessing the credibility of the numerical results has emerged in the scientific Computational Fluid Dynamics community. Prestigious journals and institutes in the field of CFD and heat transfer have adopted statement policies about this subject [1,2], and many papers have been published concerning the quantification of the numerical errors and the quality of the numerical solutions [3,4].

A numerical solution is the final result of two steps: a modeling of the physical phenomena so as to obtain a set of PDEs (physical or mathematical model), and the conversion of these PDEs to algebraic equations and their solution on a computer (computational model). The first step concerns modeling research such as turbulence modeling and modeling of chemical kinetics. The second step involves the discretization of the PDEs, the numerical procedures to solve the algebraic equations, the programming of the code, the criteria for finishing the convergence procedure and the computer accuracy. Both steps introduce approximations in the solutions, and the resulting errors should be independently understood and quantified, if possible. The errors introduced in the second step are known as computational errors and the process to study these errors as verification process. Once the mathematical model and the computational model have been independently verified, the final validation of the simulation process should be carried out by comparing the results predicted by the simulation with experimental data, which is known as validation process. In this context, validation process is the last step of the overall procedure required to assess credibility. Furthermore, in validation processes, uncertainties arise in both the experimental results and the computational results. Therefore, when analyzing discrepancies between simulation and experimental data attention must be focussed not only on the numerical solution (mathematical model and computational model), but also on the procedure adopted to obtain the experimental data. For example, experimental uncertainties can come about when testing is done under conditions other than the operating conditions of the studied system or equipment.

From the different processes involved to assess the credibility of fluid dynamics and heat transfer computations (the study of the physical model, the verification and the validation), this work focuses on the verification process. The main source of computational errors is the discretization. In steady-state problems, using double precision real numbers with strong enough convergence criteria, and when the code is free of programming errors and bugs, the remaining computational error is caused by the geometric discretization (mesh) and the numerical discretization (numerical scheme). In order to quantify these errors, two different parameters are usually adopted: h, which is representative of the mesh spacing, and p, which stands for the order of accuracy of the numerical scheme. The h-refinement treatment is commonly used to reduce the grid discretization errors in finite volume techniques (i.e., the numerical scheme is fixed and the mesh is refined). In these studies, the Richardson extrapolation can be adopted as a formally upper-order extrapolated solution estimator and as an error estimator [5].

The goal of this work is to show the capability of a post-processing tool for the computational error analysis of the simulations of different kind of steady state flows and physical phenomena: laminar flows, turbulent flows using two equations turbulence models [6] and reactive flows [7]. The studies are based on the generalized Richardson extrapolation for h-refinement studies and on the Grid Convergence Index (GCI) proposed by Roache [8]. First results using this tool for steady state laminar and turbulent flows have already been reported by the authors [9,10].

The post-processing procedure here described, has been designed so as to establish criteria about the sensitivity of the simulation to the computational model parameters that account for the

Contributed by the Fluids Engineering Division for publication in the JOURNAL OF FLUIDS ENGINEERING. Manuscript received by the Fluids Engineering Division May 16, 2001; revised manuscript received November 12, 2001. Associate Editor: G. Karniadakis.

 Copyright © 2002 by ASME

Downloaded 03 Jun 2010 to 171.66.16.150. Redistribution subject to ASME license or copyright; see http://www.asme.org/terms/Terms_Use.cfm

discretization: the mesh spacing and the order of accuracy. For transient calculations, not considered here, an additional parameter should be added in order to account for the order of accuracy of the time-marching scheme. This tool estimates the order of accuracy of the numerical solution (observed order of accuracy) and an error band where the grid independent solution is expected to be contained (uncertainty due to discretization), also giving criteria about the credibility of these estimations. Both global estimators and local estimators are calculated. Local estimators make it possible to find out local source of error such as zones with inadequate mesh concentration or problems with an inadequate formulation of the boundary conditions. Therefore, they are very useful to improve the numerical solutions. However, as they consist of a large amount of data such as maps of observed order of accuracy or maps of estimated local discretization error, they seem to give too much information and usually not clear enough, for the final reporting of the results. For such purposes, the global estimators are easier to be used and reproduced for different authors in different reports.

To show the capability of these tools, different results of two and three dimensional steady state problems solved on a *h*-refinement criteria have been post processed: a flow inside a cavity with moving top wall, an axisymmetric turbulent flow through a compressor valve, a premixed methane/air laminar flat flame on a perforated burner and the heat transfer from an isothermal cylinder enclosed by a square duct. Both structured rectangular or axisymmetric staggered grids, and body fitted non-staggered grids are used. A solution with a very fine grid and high order numerical scheme has been calculated for all the tested cases and it has been considered the ''exact'' or reference solution. With this ''exact'' solution, the ''exact'' errors of the numerical solutions have been calculated and compared to the uncertainty obtained from the post-processing tool. The values of the global estimators are given for all the post processed cases together with the ''exact'' absolute error. The values of some local estimators for one of the cases are also given and discussed.

So as to point out the credibility of the estimators obtained with the post processing tool, a simple case with analytical solution has been solved numerically using an *h*-refinement criteria. The uncertainty due to discretization calculated from the post-processing has been compared to the real discretization error obtained from the comparison of the numerical solution to the analytical solution.

In the following section an overview of the mathematical basis on the evaluation of discretization errors is given. In Section 3 details of the post-processing tool are described. The test problems and the mesh used in each of them are explained in Section 4. Finally, the results are given and discussed in Section 5.

2 Fundamentals

2.1 Estimation of the Discretization Errors: Mathematical Formulation. Assuming that the numerical solution of a problem is free of convergence errors, round-off errors and programming errors, the computational error at a given point $\mathbf{x}$ of the computational domain is only due to the discretization process. Therefore, the absolute error due to discretization can be defined as the absolute difference between the computed solution $\phi(\mathbf{x})$ and the exact solution $\phi_E(\mathbf{x})$:

$$e_D(\mathbf{x}) = |\phi(\mathbf{x}) - \phi_E(\mathbf{x})| \tag{1}$$

As in practical situations the exact solution or an estimation of the exact solution is not available, the discretization error cannot be calculated using Eq. (1). In this section, it is shown how the magnitude of the discretization error can be estimated by means of the Richardson extrapolation theory [5] and the concept of Grid Convergence Index (*GCI*) for uniform reporting of grid refinement studies [4].

In steady state computations, there are two discretization error sources: the mesh and the numerical schemes. In order to quantify each of them, two parameters of the computational model are usually adopted:

h: geometric discretization parameter representative of the mesh spacing

p: order of accuracy of the numerical schemes

According to the Richardson extrapolation theory, at a given point $\mathbf{x}$ of the domain and when the solution is in the asymptotic range (sufficient small *h*), the local absolute discretization error can be expressed in terms of the above mentioned parameters and of a coefficient $C_p(\mathbf{x})$ [5]:

$$e_D(\mathbf{x}) = |C_p(\mathbf{x}) h^p| \tag{2}$$

With three solutions of a problem ($\phi_1(\mathbf{x})$, $\phi_2(\mathbf{x})$ and $\phi_3(\mathbf{x})$) obtained by means of a *h*-refinement treatment on the grids $h_1 = h$ (fine grid), $h_2 = rh$ (middle grid), and $h_3 = r^2 h$ (coarse grid), a three-equation system of the unknown variables $p(\mathbf{x})$, $\phi_E(\mathbf{x})$, and $C_p(\mathbf{x})$ can be posed:

$$e_{Di}(\mathbf{x}) = |\phi_i(\mathbf{x}) - \phi_E(\mathbf{x})| = |C_p(\mathbf{x})[r^{i-1}h]^{p(\mathbf{x})}| \quad i = 1,2,3 \tag{3}$$

where the order of accuracy *p* has been assumed to be dependent on the position $\mathbf{x}$, and *r* is the refinement ratio.

From Eq. (3) it can be determined that:

$$p(\mathbf{x}) = \frac{\ln[(\phi_2(\mathbf{x}) - \phi_3(\mathbf{x}))/(\phi_1(\mathbf{x}) - \phi_2(\mathbf{x}))]}{\ln r} \tag{4}$$

$$e_{D_1}(\mathbf{x}) = |\phi_1(\mathbf{x}) - \phi_E(\mathbf{x})| = \left| \frac{\phi_1(\mathbf{x}) - \phi_2(\mathbf{x})}{1 - r^{p(\mathbf{x})}} \right| \tag{5}$$

where Eq. (4) is meaningful only in case of monotonic convergence to the exact numerical solution as the grid is refined.

With this formulation, a formally upper-order extrapolated value of $\phi_E(\mathbf{x})$ can be calculated [8]. However, the use of the extrapolated value of $\phi_E(\mathbf{x})$ is generally not recommended because of its lack of conservation, and because the assumptions involved in its calculation not always apply in practical problems. On the other hand, the estimator of the absolute discretization error, Eq. (5), is a good parameter in order to assess credibility to the numerical solution. Roache [4] incorporates a safety factor F_s into this estimator and defines the Grid Convergence Index (*GCI*). At a given point $\mathbf{x}$ of the computational domain, the *GCI* corresponding to the fine grid solution $\phi_1(\mathbf{x})$ takes the following form:

$$GCI_1(\mathbf{x}) = F_s \left| \frac{\phi_1(\mathbf{x}) - \phi_2(\mathbf{x})}{1 - r^{p(\mathbf{x})}} \right| \tag{6}$$

In a two-grid convergence study where $p(\mathbf{x})$ must be assumed according to the formal order of accuracy, a conservative value of $F_s = 3$ is recommended. For higher quality studies using three or more grids, as those presented in this work, and where $p(\mathbf{x})$ can be estimated by means of Eq. (4), a value of $F_s = 1.25$ appears to be adequately conservative.

2.2 Classification of the Calculation Nodes. As previously stated, Eq. (4) can only be used for the estimation of $p(\mathbf{x})$ at those nodes with monotone error convergence. Furthermore, as the argument of the logarithm function is the ratio between the solution changes $(\phi_2(\mathbf{x}) - \phi_3(\mathbf{x}))$ and $(\phi_1(\mathbf{x}) - \phi_2(\mathbf{x}))$, numerical problems can arise when analysing $\phi(\mathbf{x})$ values close to 0 or nodes with both solution changes approaching 0.

It is useful to classify the calculation nodes into three groups according to the following conditions:

$$\begin{aligned} &\textit{Richardson node:} && [\phi_2^*(\mathbf{x}) - \phi_3^*(\mathbf{x})] * [\phi_1^*(\mathbf{x}) - \phi_2^*(\mathbf{x})] > C_0 \\ &\textit{Converged node:} && |[\phi_2^*(\mathbf{x}) - \phi_3^*(\mathbf{x})] * [\phi_1^*(\mathbf{x}) - \phi_2^*(\mathbf{x})]| < C_0 \\ &\textit{Oscillatory node:} && [\phi_2^*(\mathbf{x}) - \phi_3^*(\mathbf{x})] * [\phi_1^*(\mathbf{x}) - \phi_2^*(\mathbf{x})] < -C_0 \end{aligned} \tag{7}$$

Downloaded 03 Jun 2010 to 171.66.16.150. Redistribution subject to ASME license or copyright; see http://www.asme.org/terms/Terms_Use.cfm

where the upper-index * indicates that the solutions have been normalized by means of the maximum absolute $\phi(\mathbf{x})$, and C_0 is a positive coefficient approaching 0 ($C_0 = 10^{-30}$ in this work, where all the computations have been performed using double precision real numbers).

From the numerical point of view, the Richardson nodes can be defined as those nodes where Eq. (4) can be calculated. These Richardson nodes do not necessarily fulfill all the requirements for the generalized Richardson extrapolation. In fact, the solution may be outside the asymptotic range (h not small enough).

Formally, the condition of converged nodes is ill-defined because it can also be accomplished by inflection points in the solution where all three solutions cross through the same point, which are obviously not converged nodes. Nevertheless, no relevant effects of these nodes have been observed in the results post-processed by the authors of this work up to now.

2.3 The Observed Order of Accuracy as a Certainty Parameter. The formal or theoretical order of accuracy depends on the accuracy of the numerical schemes used in the inner and boundary nodes for both the diffusive and convective terms. In some cases such as when the numerical scheme is fully first order (upwind differential scheme) or second order (central differences), the accuracy of these terms is formally known. However, when hybrid schemes such as Power Law are used, the order of accuracy is bounded but not fixed and it depends on the nature of the problem. Furthermore, different schemes are usually used in the evaluation of the diffusive and convective terms. Therefore, it is plausible to expect an overall order of accuracy p bounded by the order of accuracy of the schemes used. For example, a numerical solution obtained with a code using the first order accurate upwind difference scheme for convective terms and second order accurate central differences for the diffusive terms, should have an order of accuracy between 1 and 2.

A global observed p calculated using the procedure explained in the following section contained within the expected limits of the theoretical p (i.e., observed order of accuracy equals the theoretical order of accuracy), indicates that the numerical solution is converging asymptotically observing the assumptions of the Richardson extrapolation. When this condition is satisfied, the corresponding *GCI* is expected to be reliable.

3 Post-Processing Tool for the Evaluation of the Discretization Errors

The goal of a tool for the evaluation of the discretization error of a numerical solution is to provide a good estimation of the magnitude of the error. If a grid independent solution is available, this error can be easily calculated. Even for those more extended benchmark problems generally only grid-independent global values are available, such as the average Nu or the velocity distribution in a section of a domain. They are useful for code validation but are still limited for a detailed error evaluation. In fact, in most practical problems the grid independent solution is not available, and it is usually far beyond the available solutions in terms of computational requirements. Therefore, a post-processing tool must deal with concepts such as error estimators and extrapolations, and must also give criteria about the certainty of these estimators and extrapolations as well.

The tool here described is based on the mathematical concepts given in the previous section. This tool not only calculates an error band where the grid-independent solution is expected to be contained, but also the order of accuracy of the numerical solution (observed p). Both local and global estimators are given. When analyzing a problem, local estimators give a detailed information to the CFD code users in order to know where the convergence problems occurs, to find out where more refinement is necessary or to find bugs in the code. However, when reporting the results they seem to give too much information. In this case, global estimators are more useful.

The post-processing procedure is described in the following subsection step by step. All these steps have to be carried out for all the dependent variables of the problem obtaining for each of them a global observed p and *GCI*, local values $p(\mathbf{x})$ and $GCI(\mathbf{x})$, and a measurement of the deviation of the local values from the global values.

Step 1: Interpolation at the Post-Processing Grid. The discretized solution of three consecutive refinement levels of an h-refinement study with a constant refinement ratio r (fine grid solution $\phi_1(\mathbf{x})$, middle grid solution $\phi_2(\mathbf{x})$, and coarse grid solution $\phi_3(\mathbf{x})$), are interpolated at the main nodes of the grid where the estimators are calculated (the post-processing grid). This aspect is specially relevant when the numerical solution has been obtained on non-staggered grids. Typically, this mesh could be the coarsest one (grid 3). So as not to introduce additional uncertainties in the post processed numerical solution, third order accurate Lagrangian interpolations are used. Second-order interpolations could introduce additional inaccuracies in the numerical solutions obtained with high order schemes such as SMART or QUICK. Grids finer than the coarsest are also not recommended because the extrapolations required in this situation could also introduce additional inaccuracies.

Step 2: Classification of the Calculation Nodes. All the calculation nodes of the post processing grid are classified into Richardson nodes, converged nodes and oscillatory nodes according to the conditions described in Eq. (7). The percentage of each type of calculation node is computed. Boundary nodes and the nodes with fixed ϕ value (blocked-off nodes), are not considered as calculation nodes.

Step 3: Calculation of the Local Observed p. The local observed order of accuracy $p(\mathbf{x})$ is calculated at all the Richardson nodes of the post-processing grid using Eq. (4).

Step 4: Calculation of the Global Observed p. The global observed order of accuracy is estimated by means of the average of the local order of accuracy at the Richardson nodes. The standard deviation of the local values from the mean values is also calculated. The standard deviation of $p(\mathbf{x})$ from the global p can be considered as a measure of how close the solutions are to the asymptotic range, and, therefore, of the credibility of the estimates obtained from the post-processing procedure.

Step 5: Calculation of the Local GCI. The local Grid Convergence Index $GCI(\mathbf{x})$ of the fine mesh is calculated at all the Richardson nodes and converged nodes. At the Richardson nodes $GCI(\mathbf{x})$ is calculated by means of Eq. (6) using $F_s = 1.25$ and assuming the order of accuracy $p(\mathbf{x})$ in Eq. (6) to be equal to the global observed p calculated in Step 4. At the converged nodes the $GCI(\mathbf{x})$ is assumed to be 0.

Step 6: Calculation of the Global GCI. The local *GCI* weighted by the fraction of volume (between each control volume and the overall volume occupied by all the Richardson nodes and converged nodes) is calculated. The volume weighted average value is taken as the estimator of the global *GCI*. The standard deviation of the local volume weighted $GCI(\mathbf{x})$ is also calculated. If the global *GCI* is calculated from the statistical moments of the distribution of the local *GCIs* without weighting them by the fraction of volume, when post-processing locally refined grids unexpected high values of the global *GCI* are obtained because the local refinement usually coincide with those zones where the discretization error (and thus the *GCI*) is higher. In these cases, the global *GCIs* corresponding to different meshes cannot be directly compared. Another way to avoid this problem is to use a uniform post processing grid instead of using the coarse grid of the studied set of solution, which in practical problems may be refined in some zones.

Downloaded 03 Jun 2010 to 171.66.16.150. Redistribution subject to ASME license or copyright; see http://www.asme.org/terms/Terms_Use.cfm

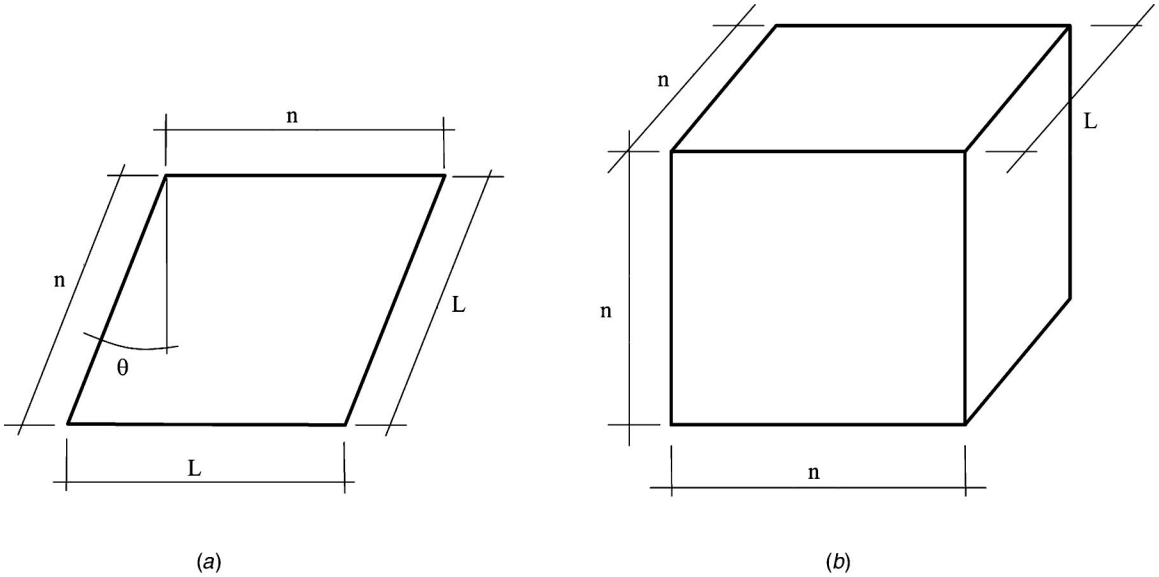

Fig. 1 Case A: Cavity with moving top wall. (*a*) Two-dimensional case. (*b*) Three-dimensional case.

4 Tested Cases

The cases presented in this section have been chosen so as to show the capability of the post-processing tool described in this paper for the evaluation of the computational error of different kind of flows, using different grids and different numerical schemes. All of them have been solved with a *h*-refinement criterion using four, five or six different refinement levels with a refinement ratio $r=2$ (doubling the mesh). Each refinement level is referenced by means of the parameter *n* which is properly defined for each case. The values of some governing parameters are pointed out: reference values of the dependent variables for the normalization of the results, main features of the mesh and numerical schemes used. More details about the numerical procedure, solvers, boundary conditions and so on have been left out in this work. They can be found in the references.

4.1 Case A: Cavity With Moving Top Wall. Laminar forced flow inside a cavity whose top side moves with a uniform velocity in its own plain in the *x* direction. The main parameters describing the test case are: $\mathrm{Re}=10^2$ and $\mathrm{Re}=10^3$; *reference velocity=top wall velocity; reference length=wall length* (*L*). Several variants have been computed: two-dimensional flows with side walls inclined at an angle θ with respect to the vertical, see Fig. 1(*a*), and three-dimensional flow in a cubic cavity, see Fig.

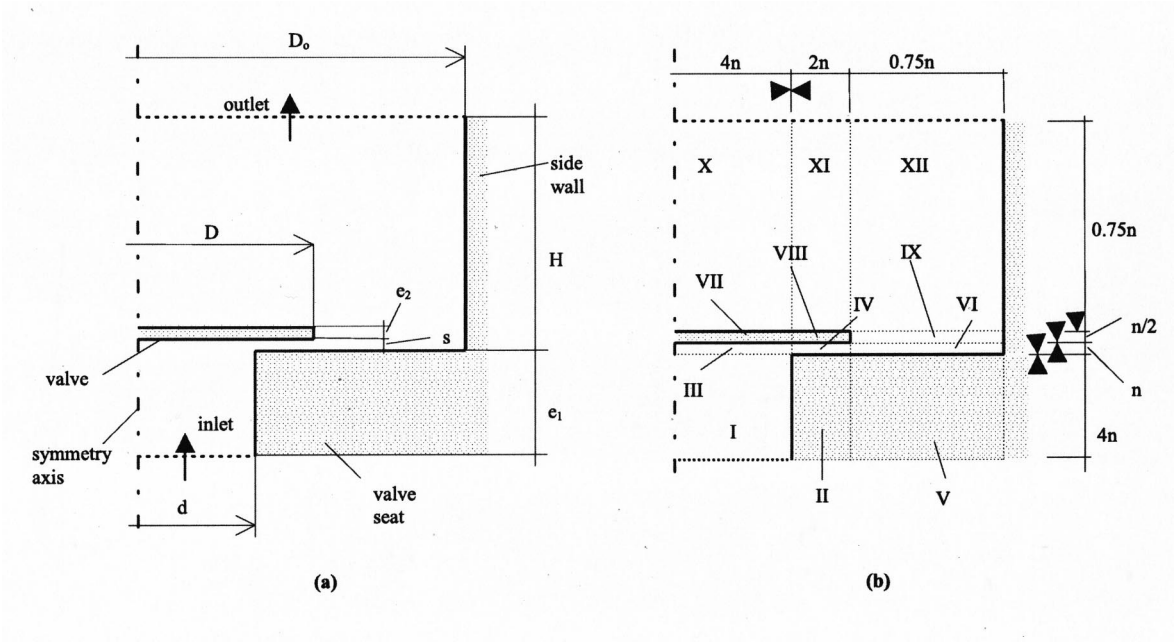

Fig. 2 Case B: Axisymmetric turbulent flow through a compressor valve. (*a*) Idealized valve geometry. (*b*) Mesh and computational domain.

Downloaded 03 Jun 2010 to 171.66.16.150. Redistribution subject to ASME license or copyright; see http://www.asme.org/terms/Terms_Use.cfm

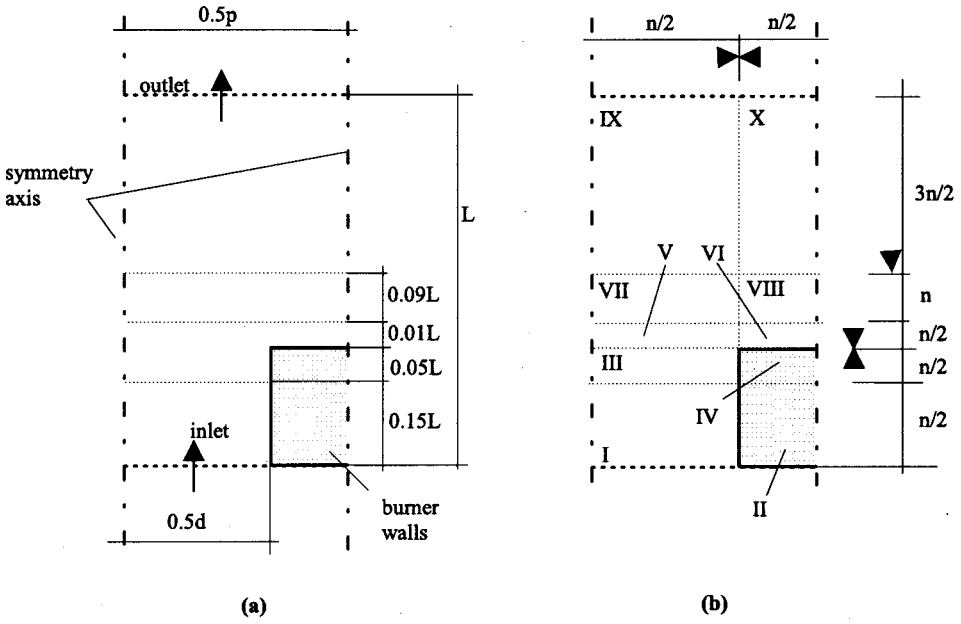

Fig. 3 Case C: Premixed methane/air laminar flat flame on a perforated burner. (*a*) Idealized geometry. (*b*) Mesh and computational domain.

1(*b*). The cavity is discretized with a uniform mesh of $n*n$ control volumes on five levels ($n=10$, 20, 40, 80, and 160) in the two-dimensional variants, see Fig. 1(*a*), and with a uniform mesh of $n*n*n$ control volumes on four levels ($n=10$, 20, 40, and 80) in the three-dimensional variant, see Fig. 1(*b*). Diffusive terms are modeled by means of second order central differences while both the first order accurate UDS scheme (upwind) or the high order accurate SMART scheme are used for the convective terms. For more details see [11,12].

4.2 Case B: Axisymmetric Turbulent Flow Through a Compressor Valve. Modeling of an axisymmetric turbulent flow through an idealized discharge compressor valve by means of low-Reynolds number $k-\epsilon$ turbulence models. The main parameters describing the test case are: $\mathrm{Re}=10^5$; *reference velocity =average velocity at the entrance* (v_{in}); *reference length=inlet diameter* (d); *valve lift*=(s/d); *reference* $k=0.5v_{in}^2$; and *reference* $\epsilon=(d/s)v_{in}^3/d$. The idealized physical domain is described in Fig. 2(*a*). It is divided in zones with different number of nodes and with a concentrated grid where necessary (i.e., in the boundary layer close to the solid walls of the inlet port and the radial diffuser), see Fig. 2(*b*). A concentration tanh-like function with a concentration factor of 1 has been adopted. Roman numbers from I to XII label the zones. The side of the zones with grid concentration are indicated by a solid triangle, and the number of nodes corresponding to each zone are indicated in terms of the grid parameter n (e.g., when $n=10$, 40*40, 40*10, and 20*10 control volumes are used in the zones I, III and IV, respectively). The *h*-refinement study is performed with five levels of refinement ($n=5$, 10, 20, 40, and 80). The post-processing study has been carried out in the zones of interest: the inlet valve port zone and the radial diffuser (zones I, III, and IV in Fig. 2(*b*)). The diffusive terms are modeled by means of central differences, the convective terms of the momentum equations with SMART scheme and the convective terms of the additional convection-diffusion equations for the turbulence modeling ($k-\epsilon$) with the Power-Law scheme. See [6,13] for details.

4.3 Case C: Premixed Methane/Air Laminar Flat Flame on a Perforated Burner. A methane-air homogeneous mixture flows through a drilled burner plate to an open domain. The main parameters describing the test case are: *mass flow rate*=0.05925 g/cm^{2}s; *inlet temperature*=298.2 K; *stoichiometric mixture; reference velocity=mean inlet velocity; reference temperature=inlet temperature*; and *reference mass fractions=ten per cent the mass fractions of the stoichiometric combustion*. The burner plate forms a regular pattern of small drilled holes. This plate may be viewed as an ensemble of tiny premixed Bunsen-like burners of a diameter d ordered in a regular honeycomb structure with pitch p. Choosing a small enough diameter and a small enough pitch, the three-dimensional behavior of the flame is reduced notably adopting a global flat structure disturbed only at the edges of the burner rim and in the vicinity of the drilled holes. Neglecting the effects of the burner rim, the combustion phenomena can be modeled

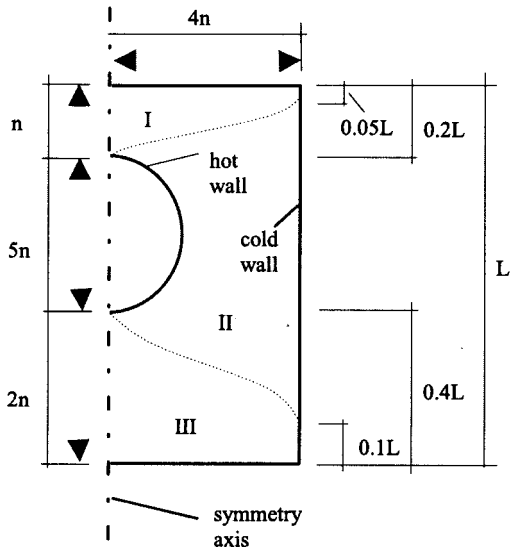

Fig. 4 Case D: Heat transfer from an isothermal cylinder enclosed by a square duct. Mesh and computational domain.

Downloaded 03 Jun 2010 to 171.66.16.150. Redistribution subject to ASME license or copyright; see http://www.asme.org/terms/Terms_Use.cfm

Table 1 Case A: Square cavity with moving top wall, Re=100. Post-processing results. Numerical scheme: UDS and SMART for convective terms and central differences for diffusive terms. (For table description see Section 5.1.)

UDS										
		x-velocity					y-velocity			
grid	θ	Rn	p	$\sigma_{p(x)}$	GCI^*	e_D^*	Rn	p	$\sigma_{p(x)}$	GCI^*	e_D^*
$n_3/n_2/n_1$	[deg]	[%]			[%]	[%]	[%]			[%]	[%]
10/20/40		66	1.0	2.4	1.5	.88	77	1.2	1.5	.96	.81
20/40/80	0	89	1.1	1.3	.57	.43	88	1.2	1.3	.47	.39
40/80/160		96	1.1	0.9	.26	.21	96	1.1	0.8	.22	.18
10/20/40		75	1.5	1.4	.76	.52	68	2.0	2.4	.23	.40
20/40/80	60	84	1.5	1.4	.25	.22	84	2.0	1.9	.09	.18
40/80/160		93	1.4	1.0	.12	.08	90	1.5	1.4	.07	.07
SMART										
		x-velocity					y-velocity			
grid	θ	Rn	p	$\sigma_{p(x)}$	GCI^*	e_D^*	Rn	p	$\sigma_{p(x)}$	GCI^*	e_D^*
$n_3/n_2/n_1$	[deg]	[%]			[%]	[%]	[%]			[%]	[%]
10/20/40		66	1.4	1.9	.76	.21	77	1.6	1.8	.40	.21
20/40/80	0	82	2.4	1.6	.07	.05	83	2.4	1.3	.05	.05
40/80/160		88	2.1	1.4	.02	-	88	2.2	1.4	.02	-
10/20/40		71	1.6	1.7	.64	.27	62	2.1	2.0	.19	.09
20/40/80	60	84	2.0	1.4	.11	.07	82	2.5	1.6	.04	.04
40/80/160		93	1.9	0.8	.03	-	92	2.1	1.0	.02	-

adopting a two-dimensional computational domain enclosed within two symmetry planes, as shown in Fig. 3(*a*), accounting for a half burner hole and the corresponding part of the open domain above the burner ($L=0.4$ cm, $d=0.03$ cm and $p=0.045$ cm). The computational domain is divided in zones with different number of nodes and with a concentrated grid where necessary (i.e. near the burner walls and at the flame front) by means of a tanh-like function. The number of grid nodes in each direction and zones is schematically described in Fig. 3(*b*). Roman numbers from I to X label the zones. The side of the zones with grid concentration are indicated by a solid triangle, and the number of nodes corresponding to each zone are indicated in terms of the grid parameter *n*. The *h*-refinement study is performed with seven levels of refinement ($n=5$, 10, 20, 40, 80, 160, and 320). This means that when $n=360$, the domain is discretized with 332.800 control volumes. The post-processing study has been carried out in the zones of interest: flame front (zones III, V, VI, VII, and VIII in Fig. 3(*b*)). The diffusive terms are modeled by means of central differences and both UDS or SMART scheme are used for the convective terms. For details see [6,14,15].

4.4 Case D: Heat Transfer From an Isothermal Cylinder Enclosed by a Square Duct. Heat transfer from a cylinder whose wall is maintained at a constant temperature and is enclosed by an isothermal square duct. The main parameters describing the test case are: $\mathrm{Ra}=10^6$; $\mathrm{Pr}=10$; *reference length =square duct side* (L); *reference temperature=reference difference of temperature=cylinder temperature—square duct temperature* (ΔT); *reference velocity*$=\sqrt{g\beta\Delta TL}$. Details about the geometry and mesh are given in Fig. 4. The domain is divided

Table 2 Case A: Square cavity with moving top wall, Re=1000. Post-processing results. Numerical scheme: UDS and SMART for convective terms and central differences for diffusive terms. (For table description see Section 5.1.)

UDS										
		x-velocity					y-velocity			
grid	θ	Rn	p	$\sigma_{p(x)}$	GCI^*	e_D^*	Rn	p	$\sigma_{p(x)}$	GCI^*	e_D^*
$n_3/n_2/n_1$	[deg]	[%]			[%]	[%]	[%]			[%]	[%]
10/20/40		84	0.2	1.5	20.	5.3	85	-0.1	1.5	42.	5.4
20/40/80	0	78	0.2	1.5	26.	3.4	91	0.3	1.1	12.	3.3
40/80/160		86	0.7	1.2	3.1	2.0	92	0.8	1.1	2.7	1.9
10/20/40		72	1.6	1.8	1.3	2.4	72	1.8	1.5	.35	1.1
20/40/80	60	82	1.0	1.6	1.6	1.4	80	1.0	1.9	.56	.67
40/80/160		90	1.1	1.3	.71	.78	89	1.1	1.4	.32	.39
SMART										
		x-velocity					y-velocity			
grid	θ	Rn	p	$\sigma_{p(x)}$	GCI^*	e_D^*	Rn	p	$\sigma_{p(x)}$	GCI^*	e_D^*
$n_3/n_2/n_1$	[deg]	[%]			[%]	[%]	[%]			[%]	[%]
10/20/40		81	0.9	1.1	3.5	1.3	80	0.4	1.9	11.	1.4
20/40/80	0	66	1.6	1.8	.70	.29	74	1.5	1.8	.71	.31
40/80/160		93	1.9	1.0	.14	-	96	1.9	0.7	.14	-
10/20/40		65	2.1	1.8	.69	.45	55	1.6	2.2	.45	.30
20/40/80	60	75	2.1	1.9	.18	.10	78	2.0	1.7	.09	.07
40/80/160		78	1.9	1.6	.06	-	82	2.2	1.5	.02	-

Downloaded 03 Jun 2010 to 171.66.16.150. Redistribution subject to ASME license or copyright; see http://www.asme.org/terms/Terms_Use.cfm

Table 3 Case A: Cubic cavity with moving top wall, Re=100. Post-processing results. Numerical scheme: UDS and SMART for convective terms and central differences for diffusive terms. (For table description see Section 5.1.)

UDS														
	x-velocity					y-velocity					z-velocity				
grid	Rn	p	$\sigma_{p(x)}$	GCI^*	e_D^*	Rn	p	$\sigma_{p(x)}$	GCI^*	e_D^*	Rn	p	$\sigma_{p(x)}$	GCI^*	e_D^*
$n_3/n_2/n_1$	[%]			[%]	[%]	[%]			[%]	[%]	[%]			[%]	[%]
10/20/40	85	1.3	1.3	.58	.49	84	0.9	1.1	1.3	.48	84	0.7	1.3	.27	.12
20/40/80	90	1.2	1.2	.32	.22	91	1.1	1.1	.37	.20	91	0.8	1.0	.11	.06
SMART															
	x-velocity					y-velocity					z-velocity				
grid	Rn	p	$\sigma_{p(x)}$	GCI^*	e_D^*	Rn	p	$\sigma_{p(x)}$	GCI^*	e_D^*	Rn	p	$\sigma_{p(x)}$	GCI^*	e_D^*
$n_3/n_2/n_1$	[%]			[%]	[%]	[%]			[%]	[%]	[%]			[%]	[%]
10/20/40	68	1.7	2.3	.30	.14	70	1.3	1.9	.63	.14	77	1.2	1.8	.08	.02
20/40/80	90	1.9	1.2	.07	-	87	2.0	1.2	.08	-	87	1.9	1.3	.01	-

in three different zones. The number of nodes corresponding to each zone is indicated in terms of the grid parameter n. A solid triangle in Fig. 4 indicates the zones where the grid has been concentrated by means of a tanh-like function. The domain is discretized using body fitted coordinates with nonstaggered grids on five levels of refinement ($n=2$, 4, 8, 16, and 32). The diffusive terms are modeled by means of central differences, while both UDS or SMART schemes are used for the convective terms. See [6,11,12] for details.

5 Results

5.1 Description.

Calculation of the "Exact" Computational Error. In order to point out the certainty of the estimators obtained from the post-processing tool, the "exact" computational error has been estimated. To do so, the most accurate solution of each problem (finest mesh with the higher order numerical scheme) has been considered the "exact" solution, $\phi_E(\mathbf{x})$. For each solution i in the h-refinement, the absolute discretization error $e_D(\mathbf{x})$ has been estimated at all the computational nodes of the post-processing grid by means of Eq. (1), and finally a global discretization error (e_D) and the standard deviation of the local values have been calculated. The interpolation of the "exact" solution and the solution i at the nodes of the post-processing grid has been performed as indicated in Step 1 of Section 3, and the global discretization error has been obtained from the local discretization error following the same procedure used for the *GCI*, see Step 6 of Section 3.

Description of the Tables of Global Estimators. For each set of three consecutive meshes on the h-refinement represented by the grid parameter n, the following values are indicated: the percentage of Richardson nodes (Rn), the observed global p, the standard deviation of the local observed $p(\mathbf{x})$ from the global value, the global *GCI* and the global "exact" absolute discretization error e_D. The upper-index * in the *GCI* and e_D indicates that they have been normalized using the reference values given in Section 4 for each of the tested cases (i.e., $GCI^*=GCI/\phi_{ref}$ and $e_D^*=e_D/\phi_{ref}$).

Other data also obtained from the post-processing tool and that have not been included in the tables of global estimators are the percentage of converged nodes and oscillatory nodes, and the standard deviation of the local values of *GCI* and e_D from the global values. For all the post-processing results presented in this work, the percentage of converged nodes was always 0. Therefore, all those nodes that did not accomplish the condition of Richardson node, Eq. (7), were oscillatory nodes. On the other hand, observed deviations of the *GCI* and e_D in all the cases were of similar magnitude and tended to vanish with the mesh refinement.

For example, Table 3 shows the global estimators of the three-dimensional driven cavity with moving top wall (case A). As four refinement levels are used in this case, two sets of solutions can be analyzed. For the set of solutions involving the grids $n=20$, $n=40$ and $n=80$ and the numerical scheme UDS, when evaluating the $x-velocity$, 90 percent of Richardson nodes have been detected (i.e., 10 percent of oscillatory nodes). The global order of accuracy of the finest solution of this set ($n=80$) is 1.2 with a standard deviation of 1.2. The global *GCI* has a good coincidence with the "exact" absolute error e_D, being 0.32 and 0.22 percent of the $x-velocity$ reference value, respectively. As the most accurate solution is used as "exact" solution for the estimation of e_D^*, the e_D^* of these solutions is equal to 0. The cells corresponding to these situations are indicated with a dash (i.e., the set of grids $n=20$, $n=40$ and $n=80$ using the SMART scheme).

Table 4 Case B: Axisymmetric turbulent flow through a valve. Post-processing results. Numerical scheme: central differences for diffusive terms and SMART and PLDS for the momentum and turbulent quantities convective terms, respectively. (For table description see Section 5.1.)

	radial-velocity					axial-velocity				
grid	Rn	p	$\sigma_{p(x)}$	GCI^*	e_D^*	Rn	p	$\sigma_{p(x)}$	GCI^*	e_D^*
$n_3/n_2/n_1$	[%]			[%]	[%]	[%]			[%]	[%]
5/10/20	68	0.8	1.7	8.4	1.1	79	1.3	1.7	.72	.57
10/20/40	70	1.4	1.8	.76	.31	72	1.3	1.6	.35	.23
20/40/80	85	1.4	1.3	.29	-	85	1.4	1.4	.14	-
	turbulent kinetic energy (k)					dissipation rate of k (ϵ)				
grid	Rn	p	$\sigma_{p(x)}$	GCI^*	e_D^*	Rn	p	$\sigma_{p(x)}$	GCI^*	e_D^*
$n_3/n_2/n_1$	[%]			[%]	[%]	[%]			[%]	[%]
5/10/20	88	1.0	1.3	9.7	3.5	84	0.9	1.6	23.	5.8
10/20/40	90	1.1	1.1	3.2	1.0	88	1.0	1.2	5.1	2.0
20/40/80	90	1.2	1.0	.94	-	87	1.3	1.2	1.5	-

Downloaded 03 Jun 2010 to 171.66.16.150. Redistribution subject to ASME license or copyright; see http://www.asme.org/terms/Terms_Use.cfm

Table 5 Case C: Premixed methane/air laminar flat flame on a perforated burner. Post-processing results. Numerical scheme: UDS and SMART for convective terms and central differences for diffusive terms. (For table description see Section 5.1.)

UDS

	radial-velocity					axial-velocity					temperature				
grid	Rn	p	$\sigma_{p(x)}$	GCI^*	e_D^*	Rn	p	$\sigma_{p(x)}$	GCI^*	e_D^*	Rn	p	$\sigma_{p(x)}$	GCI^*	e_D^*
$n_3/n_2/n_1$	[%]			[%]	[%]	[%]			[%]	[%]	[%]			[%]	[%]
5/10/20	82	1.1	1.0	.67	.35	93	1.2	0.9	1.8	3.0	93	0.7	0.6	6.7	4.4
10/20/40	90	1.3	1.0	.18	.17	93	0.7	1.1	3.0	1.6	100	0.8	0.2	3.7	2.3
20/40/80	95	1.2	0.8	.09	.08	98	1.0	0.7	1.0	.86	100	0.9	0.1	1.6	1.2
40/80/160	98	1.1	0.5	.05	.04	98	1.0	0.5	.53	.44	100	1.0	0.2	.77	.61
80/160/320	97	1.0	0.6	.03	.02	98	1.0	0.5	.27	.23	100	1.0	0.1	.37	.31

	CH_4					O_2				
grid	Rn	p	$\sigma_{p(x)}$	GCI^*	e_D^*	Rn	p	$\sigma_{p(x)}$	GCI^*	e_D^*
$n_3/n_2/n_1$	[%]			[%]	[%]	[%]			[%]	[%]
5/10/20	100	0.7	0.8	11.	6.1	100	0.6	0.7	1.2	6.0
10/20/40	98	0.8	0.6	5.4	3.2	100	0.9	0.4	4.4	3.1
20/40/80	99	0.9	0.3	2.2	1.6	100	0.9	0.4	2.3	1.6
40/80/160	100	1.0	0.1	1.1	.84	99	1.0	0.2	1.0	.82
80/160/320	100	1.0	0.1	.53	.42	100	1.0	0.1	.55	.42

	CO_2					H_2O				
grid	Rn	p	$\sigma_{p(x)}$	GCI^*	e_D^*	Rn	p	$\sigma_{p(x)}$	GCI^*	e_D^*
$n_3/n_2/n_1$	[%]			[%]	[%]	[%]			[%]	[%]
5/10/20	93	0.4	0.7	17.	5.7	96	0.6	0.6	13.	6.5
10/20/40	95	0.8	0.3	4.6	3.0	99	0.9	0.4	4.4	3.4
20/40/80	100	0.9	0.3	2.0	1.5	100	1.0	0.3	2.1	1.7
40/80/160	100	0.9	0.2	.99	.79	100	1.0	0.2	1.1	.88
80/160/320	100	1.0	0.1	.51	.40	100	1.0	0.1	.55	.44

SMART

	radial-velocity					axial-velocity					temperature				
grid	Rn	p	$\sigma_{p(x)}$	GCI^*	e_D^*	Rn	p	$\sigma_{p(x)}$	GCI^*	e_D^*	Rn	p	$\sigma_{p(x)}$	GCI^*	e_D^*
$n_3/n_2/n_1$	[%]			[%]	[%]	[%]			[%]	[%]	[%]			[%]	[%]
5/10/20	75	1.8	1.4	.27	.14	70	2.0	2.3	.78	.65	77	0.8	1.3	1.9	.40
10/20/40	81	2.2	1.5	.05	.06	82	1.7	1.3	.34	.20	85	1.8	0.9	.17	.13
20/40/80	58	1.1	2.0	.06	.03	93	1.4	0.9	.11	.06	90	1.8	1.2	.05	.04
40/80/160	89	0.7	1.1	.04	.01	97	1.6	0.6	.03	.02	87	1.5	1.1	.02	.01
80/160/320	98	0.8	0.6	.01	-	95	1.4	0.9	.01	-	92	1.2	0.8	.01	-

	CH_4					O_2				
grid	Rn	p	$\sigma_{p(x)}$	GCI^*	e_D^*	Rn	p	$\sigma_{p(x)}$	GCI^*	e_D^*
$n_3/n_2/n_1$	[%]			[%]	[%]	[%]			[%]	[%]
5/10/20	44	1.8	2.4	.91	.46	44	1.6	2.5	.95	.45
10/20/40	91	2.0	1.0	.15	.13	94	1.8	1.1	.18	.13
20/40/80	87	1.8	1.2	.05	.04	90	1.7	1.2	.05	.05
40/80/160	91	1.5	1.0	.02	.01	93	1.6	1.1	.02	.01
80/160/320	93	1.3	1.0	.01	-	91	1.4	1.2	.01	-

	CO_2					H_2O				
grid	Rn	p	$\sigma_{p(x)}$	GCI^*	e_D^*	Rn	p	$\sigma_{p(x)}$	GCI^*	e_D^*
$n_3/n_2/n_1$	[%]			[%]	[%]	[%]			[%]	[%]
5/10/20	49	0.8	2.4	2.4	.47	39	2.7	1.9	.43	.46
10/20/40	95	1.9	0.9	.16	.14	92	1.9	0.7	.18	.13
20/40/80	93	1.9	1.1	.05	.05	87	1.8	1.2	.05	.04
40/80/160	90	1.8	1.1	.02	.02	90	1.5	1.1	.02	.01
80/160/320	83	1.1	1.1	.02	-	93	1.2	1.0	.01	-

5.2 Discussion About the Tested Cases. Case A is a laminar forced flow mainly dominated by internal forces in the inner regions, and the tangential forces at the boundaries. There are no additional source terms that make the convergence with the grid spacing difficult. When solving the Reynolds number $\mathrm{Re}=10^2$, both for the two-dimensional variants (considering two different inclination angles θ) and the three-dimensional variant, even the most coarse meshes seem to belong to the asymptotic range where the generalized Richardson extrapolation can be applied. Therefore, the calculated estimators are expected to be reliable. The global estimators obtained from the post-processing tool are given in Tables 1 to 3.

The results of the variants corresponding to $\mathrm{Re}=10^2$ are given in Table 1 (two-dimensional flow) and Table 3 (three-dimensional flow). Specially for the finest meshes, a high percentage of Richardson nodes are computed. The use of the SMART scheme generally increases the number of nodes that converge in an oscillatory manner with the mesh, reducing the number of Richardson nodes. As the flow is dominated by the inertial forces (convective terms), the observed order of accuracy tends to be the one corresponding to the formal order of accuracy of the numerical scheme used for the convective terms (1 in case of UDS, and approximately between 2 and 3 for SMART). The e_D^* are pretty well

Downloaded 03 Jun 2010 to 171.66.16.150. Redistribution subject to ASME license or copyright; see http://www.asme.org/terms/Terms_Use.cfm

Table 6 Case D: Heat transfer from an isothermal cylinder enclosed by a square duct. Post-processing results. Numerical scheme: UDS and SMART for convective terms and central differences for diffusive terms. (For table description see Section 5.1.)

UDS															
	x-velocity					y-velocity					temperature				
grid	Rn	p	$\sigma_{p(x)}$	GCI^*	e^*_D	Rn	p	$\sigma_{p(x)}$	GCI^*	e^*_D	Rn	p	$\sigma_{p(x)}$	GCI^*	e^*_D
$n_3/n_2/n_1$	[%]			[%]	[%]	[%]			[%]	[%]	[%]			[%]	[%]
2/4/8	77	2.5	2.3	.05	.06	70	1.6	1.5	.17	.09	85	1.2	1.5	1.2	1.0
4/8/16	77	1.8	1.7	.02	.03	80	1.2	1.4	.06	.05	85	1.2	1.1	.48	.58
8/16/32	68	1.3	1.6	.01	.01	77	1.2	1.4	.02	.02	84	0.9	0.7	.41	.30
SMART															
	x-velocity					y-velocity					temperature				
grid	Rn	p	$\sigma_{p(x)}$	GCI^*	e^*_D	Rn	p	$\sigma_{p(x)}$	GCI^*	e^*_D	Rn	p	$\sigma_{p(x)}$	GCI^*	e^*_D
$n_3/n_2/n_1$	[%]			[%]	[%]	[%]			[%]	[%]	[%]			[%]	[%]
2/4/8	73	2.1	2.6	.10	.05	64	1.9	1.9	.13	.05	41	2.3	2.0	.11	.26
4/8/16	76	2.3	1.9	.02	.01	71	2.0	1.6	.02	.01	65	1.4	1.7	.18	.10
8/16/32	80	1.9	1.2	.01	-	80	1.8	1.2	.01	-	79	1.7	1.1	.03	-

estimated by GCI^*. The biggest discrepancies are found for the coarsest set of meshes when using the SMART scheme, coinciding with the set of meshes with a lower number of Richardson nodes.

More discrepancies are observed in the variants with $\mathrm{Re}=10^3$ (see Table 2). With the uniform meshes used, the low-accurate UDS scheme is inappropriate for the case with $\theta=0$. The observed order of accuracies are significatively lower than the theoretical value of 1 corresponding to this scheme, and they only take values closer to 1 for the finest set of meshes. When using the SMART

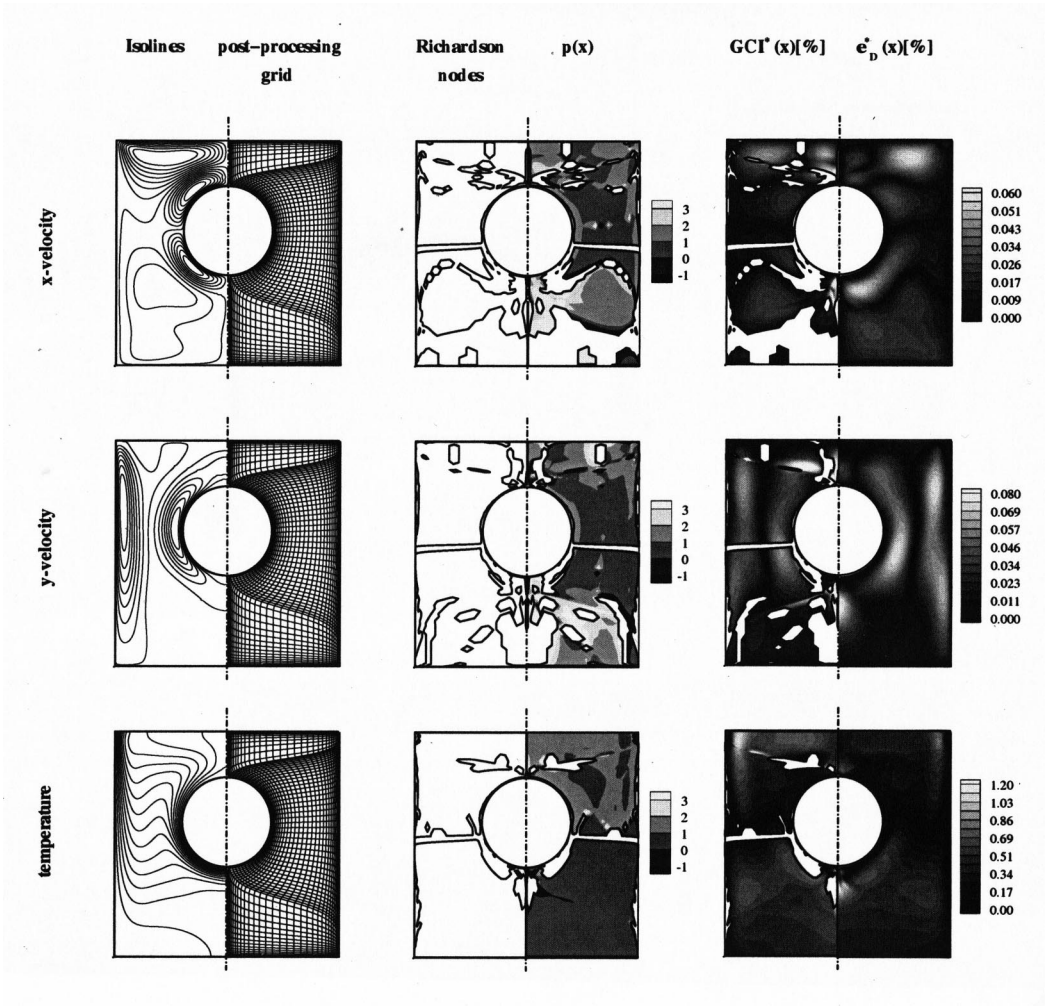

Fig. 5 Case D: Heat transfer from an isothermal cylinder enclosed by a square duct. Post-processing results. Local estimators of the solution with the grid $n=32$ (post-processing grid $n=8$) and the numerical scheme UDS.

Downloaded 03 Jun 2010 to 171.66.16.150. Redistribution subject to ASME license or copyright; see http://www.asme.org/terms/Terms_Use.cfm

scheme, observed order of accuracy only differs from the theoretical value for the coarsest set of meshes. The discrepancies between the observed and theoretical values of p for the coarsest meshes indicate that the corresponding estimators of the computational errors are not very reliable. In fact, when comparing the ''exact'' error to the estimated absolute computational error, differences are observed for the coarsest meshes, which tend to vanish for the higher levels of refinement.

Case B, see Table 4, is a complex turbulent flow impinging a wall with recirculation zones and zones with a high level of turbulence. Therefore, the results with the coarsest meshes may not be contained in the asymptotic range of convergence. In spite of that, the observed order of accuracy has acceptable values even for the coarse meshes. Furthermore, the e_D^* and the GCI^* have similar order of magnitude.

Case C involves, apart from the momentum, energy and continuity equations, the resolution of four additional convection diffusion equations to account for the mass fraction of the products and reactives of the combustion process. Therefore, the resulting algebraic equation system to be solved is highly complicated with a strong coupling between all the variables and with the algebraic coefficients highly dependent on the dependent variables.

The corresponding global estimators are given in Table 5. For all the situations, even for the most coarse set of solutions, the observed order of accuracy approximates the expected theoretical value. Most important discrepancies are found for the coarsest meshes, and for the finest meshes using the SMART schemes (where a degradation of the observed order of accuracy is detected, tending to 1). However, even in these cases, the observed order of accuracy approaches the expected p enough, so as to make the estimator GCI^* reliable. In fact, differences between e_D^* and the GCI^* are quite acceptable for the coarse meshes and tend to vanish for the finest meshes.

Case D is a two-dimensional heat transfer flow. The global estimators obtained from the post-processing are given in Table 6. Reasonable values of observed accuracy are obtained and good accordance between the computational error estimator and the ''exact'' computational error is observed.

Global estimators like those presented in the previously referenced tables, are quite promising in terms of reporting purposes because they can be reproduced by different authors, and they can be reported in a compact manner. When these estimators are obtained from the procedure described in this paper, they arise from a statistical treatment of local estimators. These estimators made up a large amount of data which is difficult to be reported. However, this information is very useful for the user of the computational code, because it makes it possible to find out local source of errors, such as zones with insufficient mesh concentration or problems with the boundary conditions.

As an example, the local estimators corresponding to the solution of case D with the grid $n=32$, and the numerical scheme UDS, are shown in Fig. 5. For each one of the dependent variables of the case (x-velocity, y-velocity, and temperature), the isolines, the post-processing grid ($n=8$), the Richardson nodes, the estimated order of accuracy $p(\mathbf{x})$, the estimated normalized local computational error $GCI^*(\mathbf{x})$, and the ''exact'' normalized local computational error $e_D^*(\mathbf{x})$ are given. In the maps of local p and local GCI^*, the zones corresponding to non-Richardson nodes (all of them oscillatory nodes) and where the post-processing procedure cannot be performed, have been blanked. As expected, local observed p at a given point of the domain can have quite different values from one dependent variable to another, depending on the local nature of the corresponding physical equation. Furthermore, obviously one point in the domain may not fulfill the conditions required for the Richardson nodes when analyzing one of the variables, while being a Richardson node when analyzing the other dependent variables. On the other hand, it can been observed that the maps of $GCI^*(\mathbf{x})$ predict the corresponding maps of ''exact'' normalized absolute computational error quite well. Therefore, these kind of maps are quite useful when analyzing a new problem to be solved by means of computational techniques, giving criteria to the code user about how and where the grid has to be intensified so as to improve the quality of the computational solution.

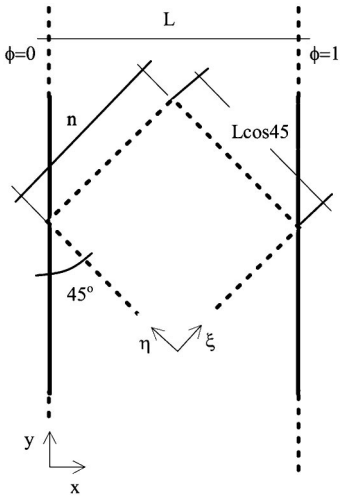

Fig. 6 Case with analytical solution: One dimensional steady state convection-diffusion process without source term, with constant transport properties and with Dirichlet boundary conditions. Computational domain: square domain with an inclination of 45 deg and discretized by means of a uniform mesh of *n*∗*n* control volumes.

Table 7 Case with analytical solution: One-dimensional steady-state convection-diffusion process without source term, with constant transport properties and with Dirichlet boundary conditions, Pe=1 and Pe=10. Post-processing results. (For table description see Section 5.1.)

		UDS					SMART				
grid	Pe	Rn	p	$\sigma_{p(x)}$	GCI^*	e_D^*	Rn	p	$\sigma_{p(x)}$	GCI^*	e_D^*
$n_3/n_2/n_1$		[%]			[%]	[%]	[%]		[%]		[%]
10/20/40		89	1.1	1.1	1.2	1.0	85	1.8	0.9	.48	.32
20/40/80	1	94	1.0	0.8	.69	.52	96	1.8	1.0	.12	.09
40/80/160		97	1.0	0.6	.35	.26	99	1.9	0.7	.03	.02
80/160/320		98	1.0	0.5	.17	.13	100	1.9	0.5	.01	.01
10/20/40		99	0.8	0.4	17.	12.	83	1.8	1.4	1.8	.80
20/40/80	10	99	0.9	0.3	8.7	6.5	89	1.8	0.6	.42	.21
40/80/160		100	0.9	0.2	4.4	3.3	97	1.8	0.7	.09	.05
80/160/320		100	1.0	0.2	2.2	1.7	99	1.9	0.4	.02	.01

Downloaded 03 Jun 2010 to 171.66.16.150. Redistribution subject to ASME license or copyright; see http://www.asme.org/terms/Terms_Use.cfm

5.3 Further Discussion. Results discussed in the previous section show that the estimated discretization error band obtained from the post-processing procedure reproduces the ''exact'' absolute computational error (obtained numerically as indicated in Section 5.1) quite well in all the tested problems. All these results give confidence about the certainty of the estimators. However, the estimated discretization error is compared to a value (the ''exact'' computational error) which may no be free from computational error. Therefore, some doubts about the certainty of the estimators can still remain.

So as to go a step further towards assessing the credibility of the estimator of the discretization error, in this subsection the post-processed results of the numerical solution of a case with analytical solution will be shown. These results will be compared to the exact absolute computational error (take note that now the word exact is not written within quotation marks because it is obtained from the analytical solution).

The evaluated case consists of the steady state convection-diffusion process of a variable $\phi(x,y)$ without source term and constant transport properties within a domain with infinite height (y dimension), a width L (x dimension), and with the Dirichlet boundary conditions in the x direction $\phi(0,y)=\phi_0=0$ and $\phi(L,y)=\phi_L=1$, see Fig. 6. In such conditions the convection-diffusion equation yields to a one-dimensional equation (x dependent) with the well known analytical solution $\phi(x)=(1-e^{\mathrm{Pex}/L})/(1-e^{\mathrm{Pe}})$, where Pe is the Peclet number (ratio between the convective and diffusive coefficients). For more details see [9].

The computational domain is a square domain inclined at an angle of 45 deg with respect to the x direction, with one vertex at $x=0$ and the opposite vertex at $x=L$. Dirichlet boundary conditions have been fixed according to the analytical solution. A uniform mesh of $n*n$ control volumes is used. Both calculations using the UDS and SMART schemes for the convective terms have been performed, while central differences have always been used for the diffusive terms.

Six levels of h-refinement have been solved ($n=10$, 20, 40, 80, 160, and 320). Results of the post-processing of these results are given in Table 7 for two different Pe numbers and the two numerical schemes used for the convective terms. Other Pe numbers not presented herewith have also been studied. The Grid Convergence Index *GCI* and the exact absolute discretization error e_D have been normalized using a reference value of $\Delta\phi=0.01(\phi_L-\phi_0)$. As it is shown, the *GCI* has predicted the exact absolute discretization error for all the studied situations quite well.

6 Conclusions

This work addresses the verification process of finite volume numerical solutions. Even when a code has been previously submitted to a credibility test by comparison with a set of either previously accepted simulations or experimental data, the credibility of the results of new problems or situations is not assessed. Therefore, specific credibility tests must be carried out before the solution can be accepted. The credibility tests encompass the study of the physical model used to represent the physical phenomena, the verification of the numerical solution (accuracy of the computational model) and the validation by comparison to experimental results.

A post-processing tool for the study of the discretization errors (verification process) based on the generalized Richardson extrapolation and on the concept of grid convergence index *GCI* has been presented. This tool not only estimates an error band where the grid-independent solution is expected to be contained, but also the order of accuracy of the numerical solution (observed p). Both local and global estimators are computed. While local estimators are a good tool for the code user in order to improve the quality of the numerical solutions, global error estimators seem easier to be used and reproduced for different authors in the final reporting of the results.

The numerical results of different heat transfer and fluid flow problems involving different phenomena (laminar flow, turbulent flow and reactive flow), adopting different meshes (Cartesian grids in a staggered arrangement, axisymmetric grids in a staggered arrangement, and body fitted coordinates in a nonstaggered arrangement) and different numerical schemes have been post processed. The obtained global error band estimators have been given for all of them. Local absolute error estimators of one of the post processed results have also been shown. The certainty of the error band estimators has been checked comparing its value to the ''exact'' absolute error of the numerical solutions always obtaining very reasonable values. The post-processing results have been discussed in detail in order to give criteria about the credibility of the numerical solutions. Although the error estimators obtained with the post-processing procedure here described have been shown to be quite reliable for all the studied cases, whether these estimators are reliable or not in other kind of flows, will require further research.

Acknowledgments

This work has been financially supported by the Comisión Interministerial de Ciencia y Tecnología, Spain (project TIC1999-0770), and by the Comissionat per Universitats i Recerca de la Generalitat de Catalunya. Detailed comments and suggestions of the reviewers of the *Journal of Fluids Engineering* have been introduced in the text improving some technical aspects and making the paper more comprehensible.

References

[1] AIAA, 1998, ''AIAA Guide for the Verification and Validation of Computational Fluid Dynamics Simulations,'' AIAA, G-077.
[2] Journal of Fluids Engineering, 1993, ''Journal of Fluids Engineering Editorial Policy. Statement on the Control of Numerical Accuracy, Editorial,'' ASME J. Fluids Eng., **115**, pp. 339–342.
[3] AIAA Journal, 1998, ''Special Section: Credible Computational Fluid Dynamics Simulations,'' AIAA J., **36**, No. 5, pp. 665–764.
[4] Roache, P. J., 1998, ''Verification of Codes and Calculations,'' AIAA J., **36**, No. 5, pp. 696–702.
[5] Celik, I., and Zhang, W. M., 1995, ''Calculation of Numerical Uncertainty using Richardson Extrapolation: Application to some Simple Turbulent Flow Calculations,'' ASME J. Fluids Eng., **117**, pp. 439–445.
[6] Pérez-Segarra, C. D., Oliva, A., Costa, M., and Escanes, F., 1995, ''Numerical Experiments in Turbulent Natural and Mixed convection in Internal Flows,'' Int. J. Numer. Methods Heat Fluid Flow, **5**, pp. 13–33.
[7] Còsul, R., Pérez-Segarra, C. D., Cadafalch, J., Soria, M., and Oliva, A., 1998, ''Numerical Analysis of Laminar Flames Using the Domain Decomposition Method,'' Proceedings of the Fourth ECCOMAS Computational Fluid Dynamics Conference, Vol. 1, Part 2, pp. 996–1001, Wiley, Athens, Greece.
[8] Roache, P. J., 1994, ''Perspective: A Method for Uniform Reporting of Grid Refinement Studies,'' ASME J. Fluids Eng., **116**, pp. 405–413.
[9] Cadafalch, J., Oliva, A., Pérez-Segarra, C. D., Costa, M., and Salom, J., 1999, ''Comparative Study of Conservative and Non-Conservative Interpolation Schemes for the Domain Decomposition Method on Laminar Incompressible Flows,'' Numer. Heat Transfer, Part B, **35**, pp. 65–84.
[10] Cadafalch, J., Pérez-Segarra, C. D., Soria, M., and Oliva, A., 1998, ''Fully Conservative Multiblock Method for the Resolution of Turbulent Incompressible Flows,'' Proceedings of the Fourth ECCOMAS Computational Fluid Dynamics Conference, **1**, Part 2, pp. 1234–1239, Wiley, Athens, Greece.
[11] Pérez-Segarra, C. D., Oliva, A., and Còsul, R., 1996, ''Analysis of some Numerical Aspects in the Solution of the Navier-Stokes Equations using Non-Orthogonal Collocated Finite-Volume Methods,'' Proceedings of the Third ECCOMAS Computational Fluid Dynamics Conference, pp. 505–511, Wiley, Paris, France.
[12] Demirdzic, I., Lilek, Z., and Peric, M., 1992, ''Fluid Flow and Heat Transfer Test Problems for Non-Orthogonal Grids: Bench-Mark Solutions,'' Int. J. Numer. Methods Fluids, **15**, pp. 329–354.
[13] Pérez-Segarra, C. D., Cadafalch, J., Rigola, J., and Oliva, A., 1999, ''Numerical Study of Turbulent Fluid Flow through Valves,'' Proceedings of the International Conference on Compressors and Their Systems, City University, London, pp. 13–14 Sept.
[14] Sommers, L. M. T., 1994, PhD thesis, Technical University of Eindhoven.
[15] Soria, M., Cadafalch, J., Còsul, R., and Oliva, A., 2000, ''A Parallel Algorithm for the Detailed Numerical Simulation of Reactive Flows,'' Proceedings of the 1999 Parallel Computational Fluid Dynamics Conference, pp. 389–396, Williamsburg, VA.

Downloaded 03 Jun 2010 to 171.66.16.150. Redistribution subject to ASME license or copyright; see http://www.asme.org/terms/Terms_Use.cfm

Boundary Element Grid Optimization for Stokes Flow With Corner Singularities

C. Pozrikidis
Department of Mechanical and Aerospace Engineering, University of California, San Diego, La Jolla, CA 92093-0411
e-mail: cpozrikidis@ucsd.edu

The accuracy of boundary-element methods for computing Stokes flow past boundaries with sharp corners where singularities occur is discussed. To resolve the singular behavior, a graded mesh of boundary elements whose length increases in a geometrical fashion with respect to distance from the corners according to a prescribed stretch ratio is used. Numerical results for two-dimensional Stokes flow past bodies with polygonal shapes reveal the existence of an optimal value of the stretch ratio for best accuracy in the computation of the force and torque. When the optimal value is used, fast convergence is achieved with respect to the number of boundary elements. [DOI: 10.1115/1.1436091]

1 Introduction

The occurrence of singularities at boundary corners is a major concern in the computation of internal and external viscous flow. When computations are performed using the boundary-integral equation method for Stokes flow, the problem formulation results in an integral equation for the boundary traction, and the numerical method seeks to describe functions that diverge at sharp corners, a seemingly impossible endeavor. Fortunately, numerical results have shown that attempting to capture the singular behavior does not have a catastrophic effect on the overall accuracy of the method, although it diminishes the accuracy, slows down the rate of convergence, and requires a large number of boundary elements or high-order expansions.

The undesirable effect of corner singularities in Stokes flow was first pointed out by Kelmanson, 1983 in the context of the biharmonic equation [1,2]. Kelmanson accounted for the local singular behavior by ingeniously hard-coding it into the boundary-element implementation via a series representation whose coefficients are computed as part of the solution. Hansen and Kelmanson [3] improved the efficiency of the method by restricting the singularity subtraction only to those elements that are located in the vicinity of the singular point. More recently, Kelmanson and Longsdale [4] advocated eliminating the corner singularities by use of a Green's function appropriate for the domain of flow under consideration. This method circumvents the need for custom-made implementation, but requires knowledge of the Green's function which is available only for a small number of boundary geometries.

An alternative is to capture the singular behavior by enhancing the spatial resolution via grid refinement or by increasing the order of the boundary-element expansion near the singularity, using, respectively, *h*- or *p*-adaptation. In practice, it is desirable to keep the number of boundary elements constant and the order of the expansion fixed, and perform optimization with respect to the location of the element nodes in the spirit of *r*-adaptation. A drawback of this method is that, when a small or moderate number of elements is used, the optimal element distribution may be highly skewed. Grid optimization for the boundary-element method was pioneered by Ingber and Mitra [5]. The optimization process involves introducing a norm for the numerical error, and then minimizing the error with respect to the position of the boundary-element end-nodes. Error estimation and adaptive boundary element methods have been developed by numerous subsequent authors, as reviewed by MacKerle [6], Liapis [7], and Abe and Sakuraba [8], and as discussed in a recent volume edited by Muci-Küchler and Miranda-Valenzuela [9].

In this work, we implement and investigate the performance of a method of restricted *r*-type grid optimization in which the boundary element distribution is assigned a particular form determined by a scalar parameter, and the optimal value of this parameter is desired. We assume, in particular, that the size of the boundary elements increases in a geometrical fashion with respect to distance from a corner where a singularity occurs, according to a specified stretch factor. The objective function for the optimization is the force and torque exerted on a two-dimensional body that is held stationary in an incident shear flow. The results will show that the restricted optimization is successful in capturing the nature of the corner singularities, and thereby allows for fast convergence and significant improvement in accuracy.

2 Problem Statement and Formulation

We illustrate the numerical method with reference to two-dimensional simple shear flow of a Newtonian fluid with density ρ and viscosity μ past a stationary body located above an infinite plane wall, as depicted in Fig. 1.

Far from the body, the x and y components of the velocity tend to the unperturbed distributions

$$u_x^\infty = ky, \quad u_y^\infty = 0, \tag{1}$$

where k is the shear rate. The Reynolds number $\mathrm{Re} = \rho k a^2/\mu$, where a is the characteristic size of the body, is assumed to be so small that the effect of fluid inertia is negligible, and the motion of the fluid is governed by the linear equations of Stokes flow. Thus, the velocity $\mathbf{u}$ and dynamic pressure p satisfy the continuity equation and the homogeneous Stokes equation

$$\nabla \cdot \mathbf{u} = 0, \quad \nabla p = \mu \nabla^2 \mathbf{u}. \tag{2}$$

The solution is subject to the no-penetration and no-slip boundary conditions along the solid boundaries of the flow including the body and the plane wall.

It should be noted that the presence of the infinite wall prevents the perturbation velocity from diverging at infinity, although this divergence would not present a paradox due to the linear growth of the incident simple shear flow.

2.1 Corner Singularities. A local analysis of Stokes flow near a corner reveals that the stream function, defined by the equations $u_x = \partial\psi/\partial y$ and $u_y = -\partial\psi/\partial x$, admits solutions of the form

$$\psi(r,\theta) = A r^\lambda f(\theta) + \mathrm{cc}, \tag{3}$$

Contributed by the Fluids Engineering Division for publication in the JOURNAL OF FLUIDS ENGINEERING. Manuscript received by the Fluids Engineering Division May 8, 2001; revised manuscript received November 13, 2001. Associate Editor: G. Karniadakis.

 Copyright © 2002 by ASME

Downloaded 03 Jun 2010 to 171.66.16.150. Redistribution subject to ASME license or copyright; see http://www.asme.org/terms/Terms_Use.cfm

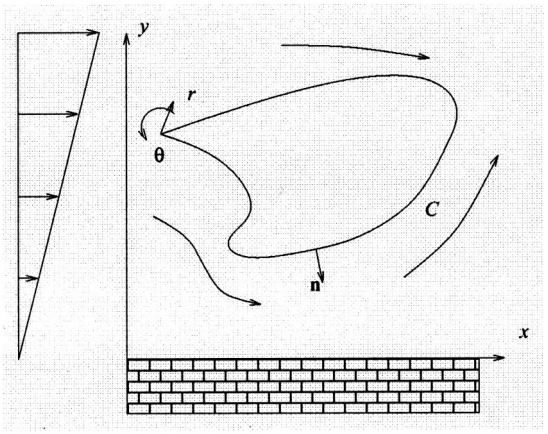

Fig. 1 Illustration of two-dimensional Stokes flow past a stationary body located above an infinite plane wall

where (r,θ) are plane polar coordinates centered at the apex, as illustrated in Fig. 1, A is a complex coefficient determined by the nature of the far flow, and "cc" stands for the complex conjugate of the right-hand side [10–12]. The complex exponent λ and the complex function $f(\theta)$ are to be computed as part of the solution. The analysis shows that λ satisfies the nonlinear algebraic equation

$$\sin[2\alpha(\lambda-1)]=\pm(1-\lambda)\sin(2\alpha), \tag{4}$$

where α is the corner semi-aperture ranging between 0 and π. The plus sign applies in the case of the antisymmetric flow illustrated in Fig. 2(*a*), and the minus sign applies in the case of the symmetric flow illustrated in Fig. 2(*b*). In the case of antisymmetric flow, Eq. (4) has the obvious solution $\lambda=1$, and in the second of symmetric flow, it has the obvious solutions $\lambda=1$ and 2. These values, however, are inadmissible because of the inappropriate functional forms for $f(\theta)$ underlying Eq. (4) [11,12].

Figure 2(*c*) illustrates the solution branch of λ with the smallest real part for antisymmetric flow (thick lines) and symmetric flow (thin lines). The solid lines represent the real part. λ_r, and the

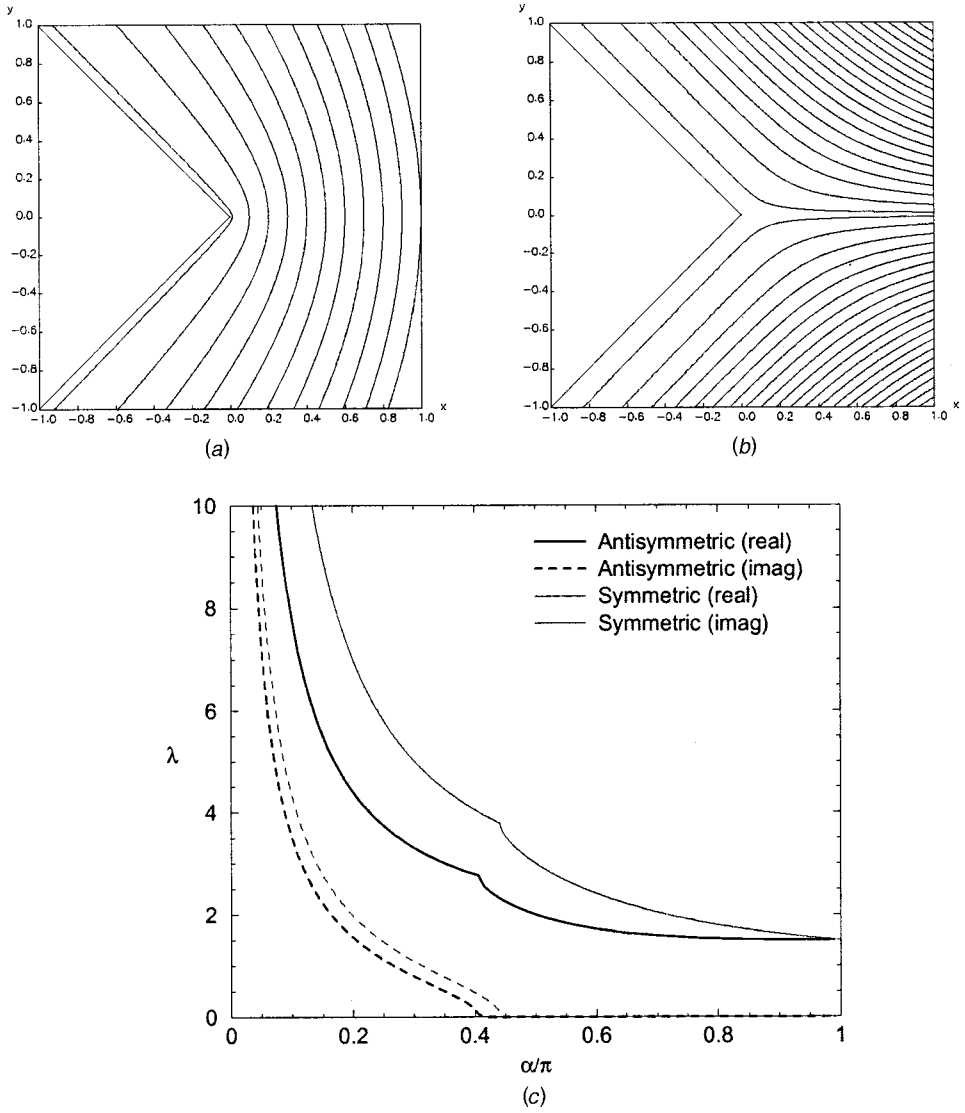

Fig. 2 Streamline pattern of (*a*) antisymmetric and (*b*) symmetric flow around a corner with aperture angle $2\alpha=3\pi/2$. (*c*) Branches of the real and imaginary part of λ for antisymmetric flow (thick lines) and symmetric flow (thin lines); the solid lines represent the real part, and the dashed lines represent the imaginary part.

Downloaded 03 Jun 2010 to 171.66.16.150. Redistribution subject to ASME license or copyright; see http://www.asme.org/terms/Terms_Use.cfm

dashed lines represent the imaginary part, λ_i. In both cases, when the aperture semi-angle α is smaller than a certain threshold, λ is complex, and this suggests that an infinite sequence of eddies develop inside the corner. The real part λ_r expresses the rate by which the streamfunction decays with respect to distance from the apex. When λ_r is less than 2, the wall shear stress diverges at an algebraic rate, behaving like r^{λ_r-2}. For example, when $2\alpha=3\pi/2$, $\lambda_r=1.544484$ in the case of antisymmetric flow, or 1.908529 in the case of symmetric flow. In both cases, the shear stress exhibits an integrable singularity at the apex.

An arbitrary flow around a corner may be expressed as a linear combination of an antisymmetric flow and a symmetric flow whose coefficients are determined by the structure of the flow far from the corner. The results of the local analysis suggest that, because of the lower value of λ_r, the antisymmetric component is expected to dominate near the apex. This will be confirmed by the results of numerical computations presented in Sec. 3.

2.2 Integral Formulation. Considering flow past the body depicted in Fig. 1, we use the boundary integral formulation of Stokes flow and find that the velocity at the point $\mathbf{x}_0=(x_0,y_0)$ that is located in the flow or at the boundaries is given by the integral representation

$$u_j(\mathbf{x}_0)=u_j^{\infty}(\mathbf{x}_0)-\frac{1}{4\pi\mu}\int_C f_i(\mathbf{x})G_{ij}^{2DW}(\mathbf{x},\mathbf{x}_0)dl(\mathbf{x}), \qquad (5)$$

where C is the contour of the body in the xy plane, $\mathbf{f}\equiv\sigma\cdot\mathbf{n}$ is the boundary traction, σ is the Newtonian stress tensor, $\mathbf{n}$ is the unit vector normal to C pointing into the fluid, and $G_{ij}^{2DW}(\mathbf{x},\mathbf{x}_0)$ is the Green's function of two-dimensional Stokes flow representing the velocity field induced by a point force in a semi-infinite domain of flow bounded by an infinite plane wall where the no-slip and no-penetration boundary conditions are required [13].

Placing the point $\mathbf{x}_0=(x_0,y_0)$ on the body contour C, and requiring the no-slip and no-penetration boundary condition $u_j(\mathbf{x}_0)=0$, we obtain a Fredholm integral equation of the first kind for the boundary traction,

$$u_j^{\infty}(\mathbf{x}_0)=\frac{1}{4\pi\mu}\int_C f_i(\mathbf{x})G_{ij}^{2DW}(\mathbf{x},\mathbf{x}_0)dl(\mathbf{x}). \qquad (6)$$

Now, because the Green's function satisfies the integral constraint

$$\int_C n_i(\mathbf{x})G_{ij}^{2DW}(\mathbf{x},\mathbf{x}_0)dl(\mathbf{x})=0, \qquad (7)$$

as required by the continuity equation, the integral equation (7) does not have a unique solution: any particular solution may be enhanced with an arbitrary multiple of the normal vector. Since the single-layer operator expressed by the right-hand side of (6) is self-adjoint, the solvability condition requires

$$\int_C u_j^{\infty}(\mathbf{x})n_j(\mathbf{x})dl(\mathbf{x})=0, \qquad (8)$$

which is satisfied by any solenoidal incident velocity field.

2.3 Boundary Element Method. To solve the integral equation (6), we use a standard boundary element method. The numerical procedure involves dividing the contour of the body into boundary elements that are straight segments or circular arcs, and approximating the Cartesian components of the traction with constant functions over the elements. Requiring the satisfaction of the integral equation at the mid-points of the boundary elements, we derive a system of linear equations for the element tractions composing the vector $\mathbf{f}$,

$$\mathbf{M}\cdot\mathbf{f}=\mathbf{b}, \qquad (9)$$

where $\mathbf{M}$ is the influence matrix containing integrals of the Green's function over the boundary elements. In the numerical method, the influence matrix is computed by numerical quadrature after the logarithmic singularity of the Green's function has been subtracted out. The right-hand side $\mathbf{b}$ contains the velocity components of the incident flow evaluated at the collocation points.

The occurrence of the singular eigensolution $\mathbf{n}$, as shown in (7), suggests that the matrix $\mathbf{M}$ is nearly singular, and the condition number increases as the numerical error due to discretization and integration are made smaller. When the body contour is polygonal, consisting of straight segments, the boundary elements have corresponding straight shapes, and the six-point quadrature is used to carry out the numerical integration, $\mathbf{M}$ is singular virtually to machine precision, and any attempt to solve system (9) fails.

To circumvent this difficulty, we note that, in the discretized version of the problem, the solvability condition (6) is expressed by the inner product of the vector $\mathbf{b}$ and a vector $\mathbf{w}$ whose elements are defined in terms of integration weights that depend on the particular method chosen to carry out the numerical integration. Because of discretization and integration error, the inner product $\mathbf{b}\cdot\mathbf{w}$ will not be equal to zero to machine precision.

To ensure that the linear system shares the properties of the integral equation regarding solvability, we perform singular preconditioning. This is done by projecting both sides of (9) onto the space that is orthogonal to the eigenvector $\mathbf{w}$, thereby replacing the nearly-singular system (9) with the singular system

$$\mathbf{B}\cdot\mathbf{z}=\mathbf{c}, \qquad (10)$$

where $\mathbf{B}\equiv\mathbf{P}\cdot\mathbf{M}$, $\mathbf{c}\equiv\mathbf{P}\cdot\mathbf{b}$, and the matrix $\mathbf{P}\equiv\mathbf{I}-ww/|w|^2$ carries out the projection [14,15]. Since the vector $\mathbf{w}$ is an eigenvector of the transpose of $\mathbf{B}$ corresponding to the null eigenvalue, the solvability condition $\mathbf{w}\cdot\mathbf{c}=0$ is satisfied to machine precision, the coefficient matrix $\mathbf{B}$ is rank-one deficient, and system (10) has a one-parameter family of solutions. One of the components of the unknown traction vector $\mathbf{f}$ may then be assigned an arbitrary value, and one equation of the linear system may be dismissed without prejudice. The solution of the rest of the equations is guaranteed to satisfy the discarded equation to machine precision. In the present implementation, the reduced non-singular system is solved by Gauss elimination.

It should be emphasized that, for bodies with polygonal shapes, the numerical eigenvector $\mathbf{w}$ is exact, and singular preconditioning is imperative. Without it, the linear system is singular even when each side is discretized into one boundary element whose endnodes are located at the corners.

2.4 Boundary Element Distribution. To capture the singular behavior of the traction at the corners, we use a graded mesh of boundary elements whose length increases in a geometrical fashion with respect to distance from a corner. Specifically, if Δl_i is the size of the ith boundary element on a segment of the body contour, then

$$\Delta l_{i+1}=\beta\Delta l_i, \qquad (11)$$

where $\beta\geq 1$ is the element stretch ratio, and Δl_1 is the length of the boundary element whose first node is a corner. In the numerical implementation, we specify the total number of elements and the ratio between the largest and smallest element size along each segment, denoted by γ, and compute β to fit the specified number of elements to the segment. An option is provided for the element distribution to be symmetric or non-symmetric with respect to the mid-point of each segment. In the first case, γ is equal to the ratio of the length of the mid-element(s) to the length of the corner element; in the second case, γ is equal to the ratio of the length of the first element to the length of the last element.

When an integrable singularity occurs at a corner, the traction behaves like l^{λ_r-2}, where l is the arc length with origin at the corner, and $\lambda_r>1$ is the real exponent. The integrated traction over the ith element scales with

Downloaded 03 Jun 2010 to 171.66.16.150. Redistribution subject to ASME license or copyright; see http://www.asme.org/terms/Terms_Use.cfm

$$J_i(\beta,\lambda_r) \equiv l_{i+1}^{\lambda_r-1} - l_i^{\lambda_r-1}$$
$$= \frac{\Delta l_1^{\lambda_r-1}}{(\beta-1)^{\lambda_r-1}}[(\beta^{i+1}-1)^{\lambda_r-1} - (\beta^i-1)^{\lambda_r-1}]. \quad (12)$$

Ideally, the boundary elements should be distributed so that the right-hand side of (12) is constant, independent of i. As λ_r tends to 2 corresponding to the mildest singular behavior, $J_i(\beta,\lambda_r) \simeq \Delta l_1 \beta^i$; demanding that the boundary elements make comparable contributions requires evenly-spaced elements corresponding to $\beta=1$. On the other hand, as λ_r tends to 1 corresponding to the strongest singular behavior, $J_i(\beta,\lambda_r) \simeq \Delta l_1 \ln[(\beta^{i+1}-1)/(\beta^i-1)] \simeq \Delta l_1 \ln \beta$. Consideration of these two asymptotic limits suggests that the value of β should be selected according to the value of λ_r; that is, according to the corner angle defined by the body shape.

3 Results and Discussion

Consider shear flow past a square cylinder with side length a, where the center of the cylinder is placed at a distance a above a plane wall, and the two sides of the cylinder are parallel to the wall, as illustrated in Fig. 4(*a*). Figure 3 shows graphs of the x component of the dimensionless force per unit length exerted on the cylinder, $F_x/(\mu k a)$, and the corresponding z component of the dimensionless torque with respect to the center of the cylinder, $T_z/(\mu k a^2)$, plotted against the boundary element stretch ratio β, for $N_s=8$, 16, 32 and 64 boundary elements along each side. The highest curve in Fig. 3(*a*) and the lowest curve in Fig. 3(*b*) correspond to $N_s=64$.

The results confirm that, given the number of boundary elements, there is an optimal value of the element stretch ratio for best accuracy. Moreover, the optimal value converges rapidly to the exact value with respect to N_s. In contrast, when the boundary elements are evenly spaced, corresponding to $\beta=1$, the force and

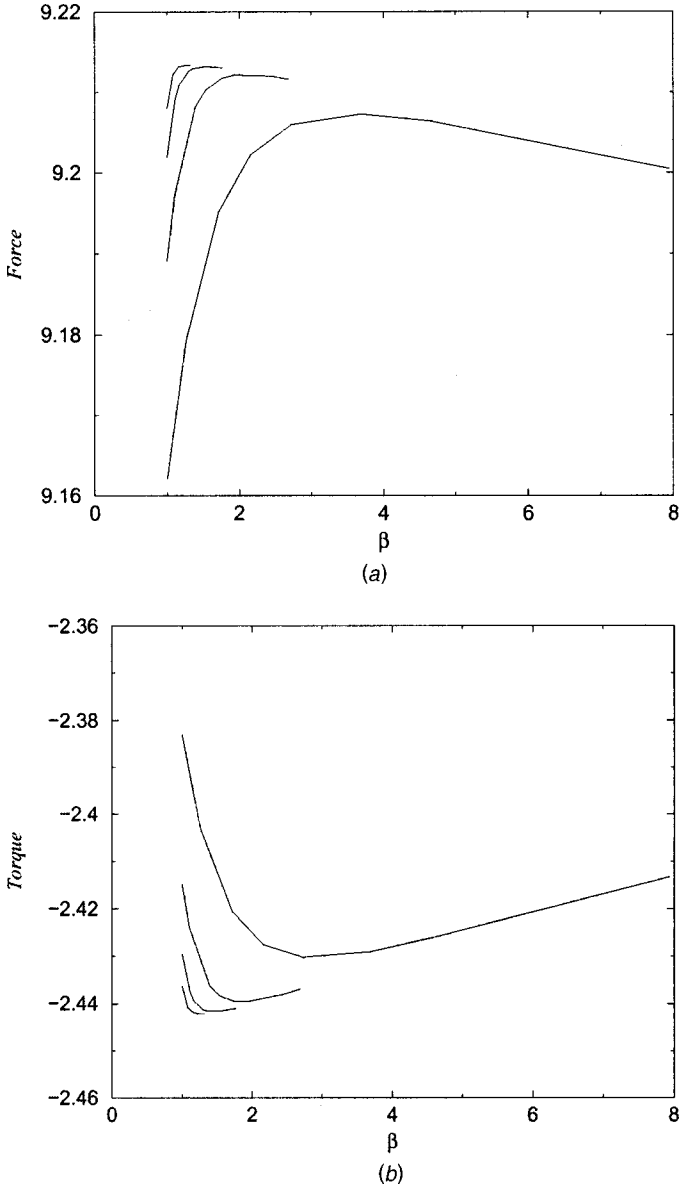

Fig. 3 Force and torque exerted on a square cylinder with side length *a* whose center is located at distance *a* above the plane wall, plotted against the element stretch ratio β for $N_s=8$, 16, 32, and 64 boundary elements along each side. The highest curve in (*a*) and the lowest curve in (*b*) correspond to $N_s=64$.

Downloaded 03 Jun 2010 to 171.66.16.150. Redistribution subject to ASME license or copyright; see http://www.asme.org/terms/Terms_Use.cfm

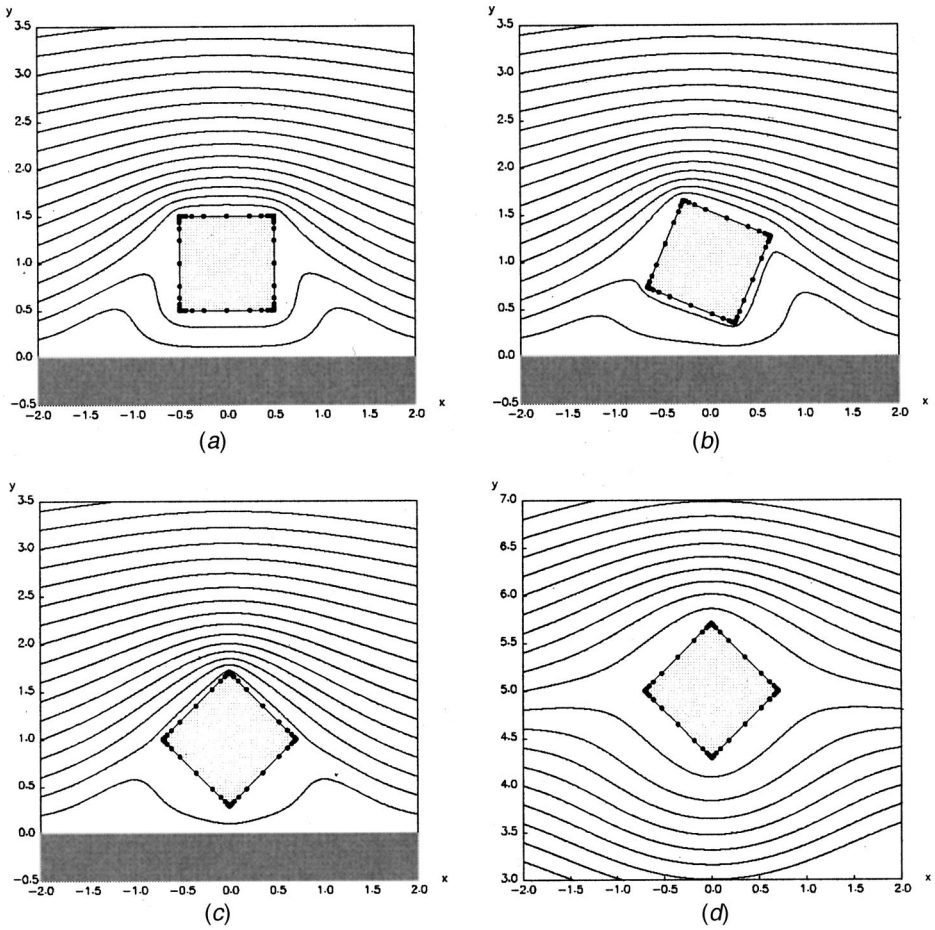

Fig. 4 Streamline pattern of shear flow past a square computed with the nearly optimal element distribution of 16 elements along each side, for inclination angle (*a*) 0, (*b*) $\pi/4$, and (*c*) $\pi/2$. (*d*) Flow past an inclined square whose center is located at a distance equal to five times the side length above the wall. The dots mark the location of the boundary element nodes.

torque converge only slowly. The nearly optimal distribution of the boundary-element nodes for $N_s=16$ is depicted in Fig. 4(*a*). The ratio between the length of the largest boundary elements located in the middle of each side and the length of the smallest boundary element located next to a corner is $\gamma=100$.

To understand the effect of the element stretch ratio, it is helpful to consider the contribution of each element to the line integral of the traction around the body defining the force. Figure 5 shows a graph of the contributions of the boundary elements on the top side of the cylinder to the x component of the force, for $N_s=32$. The circles, squares, diamonds and crosses correspond to $\gamma=1$, 5, 500, and 1000, where $\gamma=500$ is nearly optimal. The best results are obtained when the elements in the vicinity of the corners make comparable contributions, and a local maximum does not arise.

Figure 6 shows the distribution of the shear stress along the upper side of the square cylinder illustrated in Fig. 4(*a*), plotted against the arc length measured from the northwestern corner near Alaska, computed with $N_s=32$. The circles, squares and diamonds correspond, respectively, to element ratios $\gamma=5$, 50, and 500, and associated stretch factors $\beta=1.113$, 1.298, and 1.513. The straight line represents the predictions of the local solution for antisymmetric flow corresponding to $\lambda_r=1.544$. The results illustrate that boundary-element distributions with large stretch factors

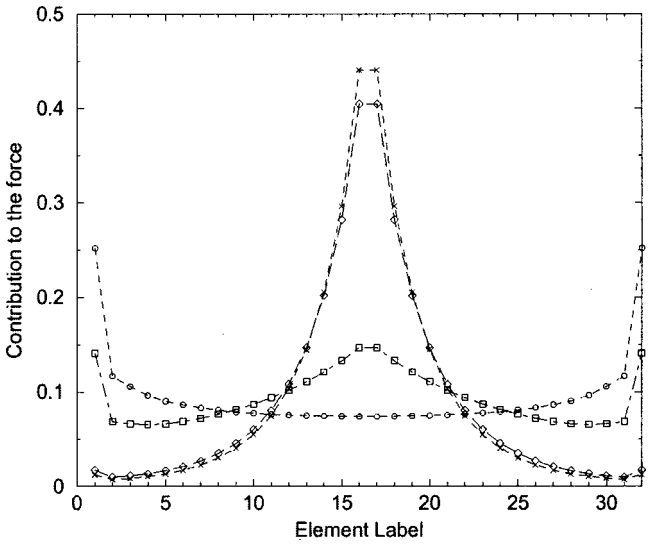

Fig. 5 Contribution of the top elements to the line integral of the traction defining the force corresponding to Fig. 4(*a*)

Downloaded 03 Jun 2010 to 171.66.16.150. Redistribution subject to ASME license or copyright; see http://www.asme.org/terms/Terms_Use.cfm

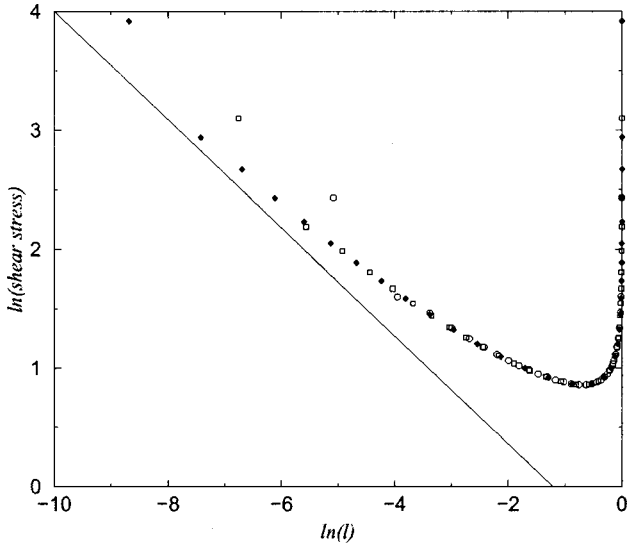

Fig. 6 Distribution of the shear stress along the upper side of the square illustrated in Fig. 4(*a*), plotted against the arc length measured from the northwestern corner

successfully probe the singular nature of the shear stress after the second corner element.

Similar results are obtained when the body is inclined with respect to the wall, as illustrated in Fig. 4(*b*,*c*). To demonstrate the effect of orientation, we consider shear flow past a square cylinder whose center is located at a distance equal to five time the side length above the plane wall, and the sides of the cylinder are rotated by $\pi/4$ with respect to the horizontal, as illustrated in Fig. 4(*d*). Figure 7 shows a graph of the shear stress plotted against the arc length measured from the left and top corner on a log-log scale, computed with $N_s=64$ elements along each side and $\gamma=1000$. The local flow around the left corner is similar to the symmetric flow illustrated in Fig. 2(*b*), whereas the local flow around the top corner is similar to the antisymmetric flow illustrated in Fig. 2(*a*). Accordingly, the distribution of shear stress around the left and top corner, corresponding to the circles and squares, fall on straight lines with slope λ_r-2, where $\lambda_r=1.544$ or 1.909, respectively, for antisymmetric or symmetric flow. The

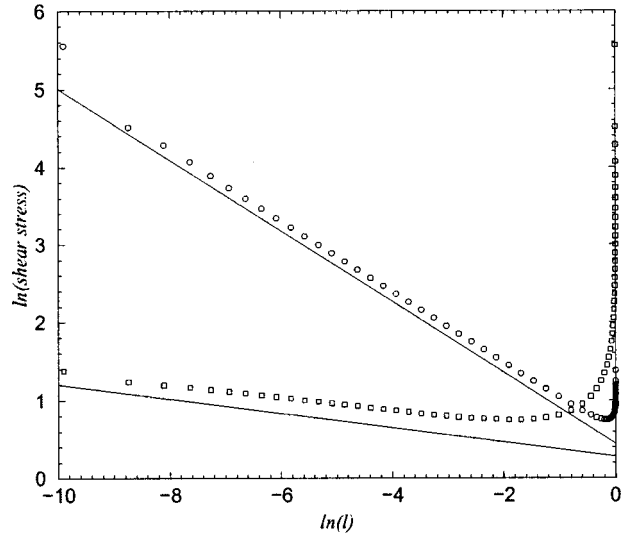

Fig. 7 Distribution of shear stress with respect to arc length measured from the left and top corners for the flow illustrated in Fig. 4(*d*)

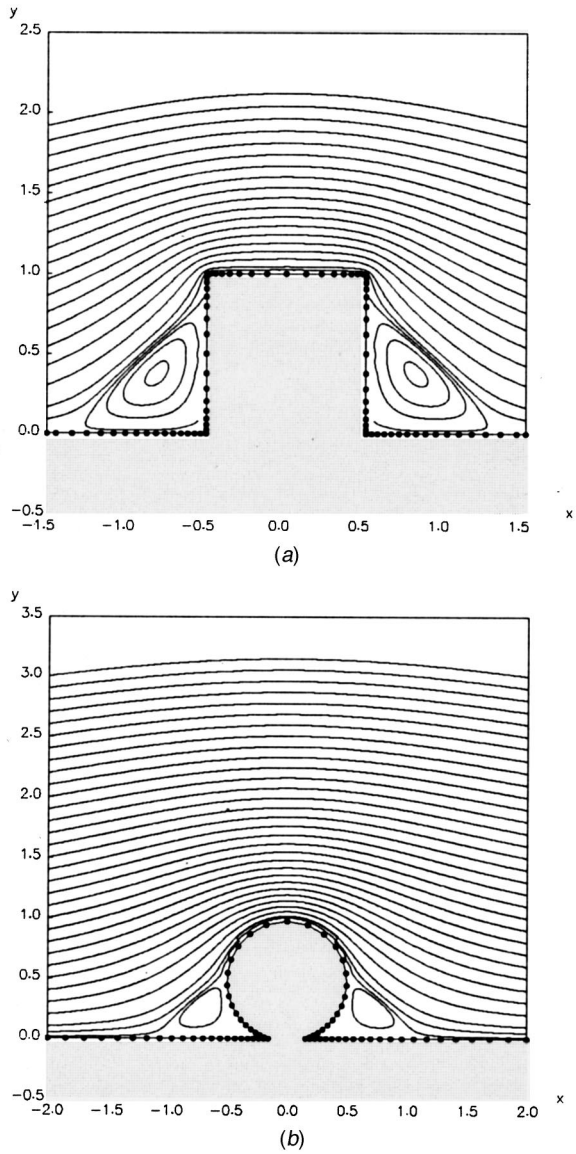

Fig. 8 Streamline patterns of simple shear flow past a surface-mounted square and section of a circular cylinder

singular behavior near the left corner is weaker than that near the top corner. Because of the presence of the infinite wall, the flow around the left corner is not perfectly symmetric, but contains a small antisymmetric component whose strength is proportional to the perturbation flow due to the wall. The results in Fig. 7 suggest that the antisymmetric component becomes apparent at much higher resolutions.

The numerical method, and variations of it, were applied to investigate several other types of two-dimensional Stokes flow. Figure 8(*a*) illustrates the streamline pattern of simple shear flow past a surface-mounted square obstacle. The numerical results show that, given the number of boundary elements along each side, the force and torque exerted on the obstacle are computed with best accuracy when the boundary elements over the three sides are distributed with a stretch ratio that is comparable to that for the square cylinder discussed earlier. As a second illustration, Fig. 8(*b*) shows the streamline pattern of simple shear flow past a truncated circular cylinder mounted on a plane wall. In this case, the boundary elements have circular shapes over the cylinder and flat shapes over the wall, and the elements are concentrated near the points of contact.

Downloaded 03 Jun 2010 to 171.66.16.150. Redistribution subject to ASME license or copyright; see http://www.asme.org/terms/Terms_Use.cfm

4 Concluding Remarks

We have discussed the implementation and optimization of the boundary-element method for two-dimensional Stokes flow past bodies with corner singularities. In the numerical method, the boundary element distribution is determined by the scalar stretch ratio β, and the objective functions are the force and torque exerted on the body. The choice of these objective functions is dictated by their relevance in studies of suspension dynamics and micro-hydrodynamics with small-scale topography. Extensions of the numerical method to three dimensions is straightforward in principle but tedious in implementation. To compute a three-dimensional Stokes flow past a body with corners and edges, we use elements whose size increases by a certain factor with respect to distance from the singular lines or points.

The boundary element procedure described in this paper may be extended to the case of Stokes flow through narrow passages where strong lubrication forces develop. In that case, the boundary elements should be concentrated near regions of maximum normal traction associated with high shear stress and lubrication pressure. The method was tested for flow due to a circular cylinder translating parallel to, or rotating about its center, above a plane wall. When the gap between the cylinder and the wall is 2 percent of the cylinder radius, and 64 circular elements are used, the dimensionless force exerted on a cylinder translating with velocity U along the x axis parallel to the wall is found to be $F_x/(\mu U) = -59.42$, -62.00, -62.08 and -61.72, respectively, for $\gamma = 1$, 10, 100 and 1000; the exact value due to Wannier is -62.30 [16].

Overall, the *r*-adaptive boundary element method with restricted optimization emerges as a desirable practical alternative to its more rigorous but much more demanding unrestricted counterpart.

Acknowledgment

I thank George Karniadakis for inviting me to contribute to this volume. This research was supported by a grant provided by the National Science Foundation.

References

[1] Kelmanson, M. A., 1983, "Modified Integral Equation Solution of Viscous Flows Near Sharp Corners," Comput. Fluids, **11**, No. 4, pp. 307–324.

[2] Kelmanson, M. A., 1983, "An Integral Equation Method for the Solution of Singular Stokes Flow Problems," J. Comput. Phys., **51**, pp. 139–158.

[3] Hansen, E. B., and Kelmanson, M. A., 1994, "An Integral Equation Justification of the Boundary Conditions of the Driven-Cavity Problem," Comput. Fluids, **23**, No. 1, pp. 225–240.

[4] Kelmanson, M. A., and Longsdale, B., 1995, "Annihilation of Boundary Singularities Via Suitable Green's Functions," Comput. Math. Appl., **29**, No. 4, pp. 1–7.

[5] Ingber, M. S., and Mitra, A. K., 1986, "Grid Optimization for the Boundary Element Method," Int. J. Numer. Methods Fluids, **23**, pp. 2121–2136.

[6] Mackerle, J., 1993, "Mesh Generation and Refinement for FEM and BEM—A Bibliography (1990–1993)," Finite Elem. Anal. Design, **15**, pp. 177–188.

[7] Liapis, S., 1994, "A Review of Error Estimation and Adaptivity in the Boundary-Element Method," Eng. Anal. Boundary Elem., **14**, No. 4, pp. 315–323.

[8] Abe, K., and Sakuraba, S., 1999, "An HR-Adaptive Boundary Element for Water Free-Surface Problems," Eng. Anal. Boundary Elem., **23**, pp. 223–232.

[9] Muci-Küchler, K. H., and Miranda-Valenzuela, J. C., 2001, "Guest Editorial," Eng. Anal. Boundary Elem., **25**, pp. 477–487.

[10] Dean, W. R., and Montagnon, P. E., 1949, "On the Steady Motion of Viscous Liquid in a Corner," Proc. Cambridge Philos. Soc., **45**, pp. 389–394.

[11] Moffatt, H. K., 1964, "Viscous and Resistive Eddies Near a Sharp Corner," J. Fluid Mech., **18**, pp. 1–18.

[12] Pozrikidis, C., 1997, *Introduction to Theoretical and Computational Fluid Dynamics Flow*, Cambridge University Press.

[13] Pozrikidis, C., 1992, *Boundary Integral and Singularity Methods for Linearized Viscous Flow*, Cambridge University Press.

[14] Pozrikidis, C., 1999, "A Spectral-Element Method for Particulate Stokes Flow," J. Comput. Phys., **156**, pp. 360–381.

[15] Pozrikidis, C., 2001, "Dynamical Simulation of the Shear Flow of Suspensions of Particles with Arbitrary Shapes," Eng. Anal. Boundary Elem., **25**, pp. 19–30.

[16] Wannier, G. H., 1950, "A Contribution to the Hydrodynamics of Lubrication," Q. Appl. Math., **8**, No. 1, pp. 1–32.

Downloaded 03 Jun 2010 to 171.66.16.150. Redistribution subject to ASME license or copyright; see http://www.asme.org/terms/Terms_Use.cfm

B. DeVolder[2]
Los Alamos National Laboratory,
Los Alamos, NM 87545

J. Glimm[3,4]
Department of Applied Mathematics
and Statistics,
State University of New York
at Stony Brook,
Stony Brook, NY 11794-3600;
Center for Data Intensive Computing,
Brookhaven National Laboratory,
Upton, NY 11973

J. W. Grove[2]
Los Alamos National Laboratory,
Los Alamos, NM 87545

Y. Kang[5]

Y. Lee[4]

Department of Applied Mathematics
and Statistics,
State University of New York
at Stony Brook,
Stony Brook, NY 11794-3600

K. Pao[2]

D. H. Sharp[2]

Los Alamos National Laboratory
Los Alamos, NM 87545

K. Ye
Department of Applied Mathematics
and Statistics,
State University of New York
at Stony Brook,
Stony Brook, NY 11794-3600

Uncertainty Quantification for Multiscale Simulations[1]

A general discussion of the quantification of uncertainty in numerical simulations is presented. A principal conclusion is that the distribution of solution errors is the leading term in the assessment of the validity of a simulation and its associated uncertainty in the Bayesian framework. Key issues that arise in uncertainty quantification are discussed for two examples drawn from shock wave physics and modeling of petroleum reservoirs. Solution error models, confidence intervals and Gaussian error statistics based on simulation studies are presented. [DOI: 10.1115/1.1445139]

1 Introduction

Simulation based prediction will play an increasing role in support of global climate studies, assessment of the performance, safety, and reliability of the nuclear stockpile, engineering design, infrastructure modeling, environmental remediation projects, and other critical problems. To be effective in this role, predictive simulations must be accompanied by reliable and defensible estimates of their level of accuracy, limits of applicability, and of the level of confidence that can be placed in such estimates. In short, simulation results must come with good error bars, just as is expected of experimental results. This condition is rarely met in practice, and to do so requires the development of systematic methods for uncertainty quantification in large scale simulations.

We refer to errors as a deterministic measure of the inaccuracy in input parameters, physical models, or numerical solutions of the governing equations in each realization of an ensemble of problems. A probability model for errors refers to the distribution of errors in any quantity, taken over the ensemble. Of course, the ensemble of errors can be averaged to obtain a mean error, which is again a deterministic quantity. Uncertainty refers to the variability in any quantity over the ensemble. Thus a probability model for errors and uncertainty of errors are basically identical concepts, and both have a probabilistic and deterministic aspect. Normally we are interested in uncertainty in quantities which are not errors (such as uncertainty in mean annual sea surface tempera-

[1]Los Alamos National Laboratory Report LA-UR 01-4022.
[2]Supported by the U.S. Department of Energy.
[3]Supported in part by the NSF Grant DMS-0102480, the Army Research Office Grant DAAL-03-91-0027, and the U.S. Department of Energy Grants DE-FG02-90ER25084 and DE-AC02-98CH10886.
[4]Supported in part by U.S. Department of Energy Grant DE-FG02-98ER25363.
[5]Supported in part by U.S. Department of Energy Grant DE-FG03-98DP00206.
Contributed by the Fluids Engineering Division for publication in the JOURNAL OF FLUIDS ENGINEERING. Manuscript received by the Fluids Engineering Division August 7, 2001; revised manuscript received November 12, 2001. Associate Editor: G. Karniadakis.

 Copyright © 2002 by ASME

Downloaded 03 Jun 2010 to 171.66.16.150. Redistribution subject to ASME license or copyright; see http://www.asme.org/terms/Terms_Use.cfm

ture); such uncertainty is of course not an error nor is it a probability model of an error.

Potential sources of uncertainty in simulation based predictions include poorly known input parameters, incomplete physical models, and limited accuracy of numerical solutions of the governing equations. Incomplete knowledge of the properties of complex systems frequently leads to the need for a probabilistic description of each source of error. Thus error and uncertainty are both probabilistic concepts, and differ, as used here, only in the scope of variables to which they apply.

Especially for complex systems, the bedrock test of simulation based prediction is comparison with experimental data. This comparison generally needs to go beyond a simple yes/no verdict as to whether a prediction agrees with data, to include an inverse step that uses data to constrain uncertainties in the choice of a model or its parameters. This inverse step, which maps probabilities in observations or in solutions back to probabilities in the problem inputs, *i.e.*, to its formulation, is a stochastic version of the much studied inverse problem, equivalently called the parameter determination problem or the history problem, depending on the context.

The purpose of uncertainty quantification is to identify and quantify each source of error, and to assess their net, or integrated, effect on the simulation results. Assessment of experimental error is of course an essential part of the overall procedure when comparing with data.

This brief description clearly shows that uncertainty quantification is an inherently multidisciplinary undertaking, drawing on physical modeling, stochastic modeling and statistics, and applied mathematics.

In this paper, we briefly review some of the main components of uncertainty quantification. The Bayesian framework for statistical inference is discussed in Section 2. This is a convenient way to formulate the probabilistic inverse procedure used to constrain model uncertainties on the basis of experimental data, especially when the data are obtained from diverse sources. Solution error is the novel feature that arises in quantifying uncertainty in simulations. Some of the principal issues that arise in constructing probabilistic models for solution errors are discussed in Section 3. Uncertainty quantification invariably requires evaluation of results for a frequently large ensemble of runs. This can be very costly, so methods for fast integration, both in forward simulations and for evaluation of ensemble averages of various kinds in high dimensional probability spaces are a high priority. A brief overview of some of the available methods is given in Section 4.

In Section 5 we discuss two examples. The first concerns the flow of oil in an (idealized) petroleum reservoir. The purpose of the example is to show how data on observed oil production could be used to reduce uncertainty in the geological description of the reservoir, and to improve predictions of future oil production. This example illustrates the use of probability models for solution errors in Bayesian statistical inference. The second example discusses the diagnosis and modeling of solution errors arising in shock wave dynamics. These examples are simple enough that the main ideas and results can be presented succinctly. They illustrate some, though by no means all, parts of the uncertainty quantification framework presented earlier in the paper.

2 The Bayesian Framework

The Bayesian framework [1] for statistical inference provides a systematic procedure for updating our current knowledge of a system on the basis of new information. In the engineering and natural science applications that we shall consider, the system is represented by a simulation model m that is intended to be a complete specification of all information needed to solve a given problem. Thus m includes the governing evolution equations for the physical model, initial and boundary conditions, and modeling parameters; *i.e.*, m contains sufficient information to make the solution $s(m)$ well posed in the sense of Hadamard [2,3]. Any or all of the information in m can be either deterministic or uncertain to some degree. To represent the uncertainty that may be present in the specification of the system, we introduce an ensemble of models $\mathcal{M}$, with $m \in \mathcal{M}$, and define a probability distribution on $\mathcal{M}$, called the prior distribution, and denoted by $p(m)$. We note that determinism in the sense of Hadamard for $s(m)$ can be lost due to lack of detailed deterministic knowledge of m.

If additional information about the system is supplied by an observation, $\mathcal{O}$, one can determine an updated estimate of the probability for m, called the posterior distribution and denoted by $p(m|\mathcal{O})$, using Bayes' formula

$$p(m|\mathcal{O}) = \frac{p(\mathcal{O}|m)p(m)}{\int_{\mathcal{M}} p(\mathcal{O}|m)p(m)dm}. \tag{1}$$

It is important to realize that the Bayesian procedure does not determine the choice of $p(m)$. Thus to use Bayesian analysis, one must supply the prior from an independent data source or a more fundamental theory, or else use a noninformative ''flat'' prior.

The factor $p(\mathcal{O}|m)$ in (1) is called the likelihood. The likelihood is the unnormalized probability for the observation $\mathcal{O}$, *given* the model m. In the cases of interest here, model predictions are determined by solutions, $s(m)$, of the governing equations, typically partial differential equations. The simulated observables are functionals $\mathcal{O}(s(m))$. If both the experimentally measured observable $\mathcal{O}$ and the solution $s(m)$, hence $\mathcal{O}(s(m))$, are exact, the likelihood $p(\mathcal{O}|m)$ is a delta function concentrated on the hypersurface in $\mathcal{M}$ defined by the equation

$$\mathcal{O} = \mathcal{O}(s(m)).$$

In other words, the likelihood selects exactly those models m which agree with the observation $\mathcal{O}$ and with no others.

Real world observations and simulations of course contain errors and a discrepancy will invariably be observed between $\mathcal{O}$ and $\mathcal{O}(s(m))$. Because the likelihood is evaluated subject to the hypothesis that the model $m \in \mathcal{M}$ is correct, any such discrepancy can be attributed either to errors in the solution or in the measurements. The likelihood is defined by assigning probabilities to solution or measurement errors of different sizes. The required probability models for these errors must be supplied by an independent analysis.

This discussion shows that the role of the likelihood in simulation based prediction is to assign a weight to a model m based on a probabilistic measure of the quality of the fit of the model predictions to the data. Probability models for solution and measurement errors play a similar role in determining the likelihood.

This point is so fundamental and sufficiently removed from common approaches to error analysis that we repeat it for emphasis: *Numerical and observation errors are the leading contribution to the determination of the Bayesian likelihood, needed for uncertainty quantification*. When quantifying uncertainty, one cannot make errors small and then neglect them, as is the goal of classical numerical analysis, rather we must of necessity study and model these errors. They supply critical information needed for uncertainty quantification.

Bayesian inference can be extended to include multiple sources of information and multiple stages of inference, leading to hierarchical Bayesian models based on inference graphs. These capabilities are very important; since data is often in short supply and expensive to acquire, it is essential to make full use of all possible sources of data.

Alternative approaches to inference include the use of interval analysis, possibility theory, fuzzy sets, and theories of evidence. We do not survey these alternatives here, but simply mention that they are based on different assumptions about what is known and what can be concluded. For example, interval analysis assumes that unknown parameters vary within an interval (known exactly), but that the distribution of possible values of the parameter within

Downloaded 03 Jun 2010 to 171.66.16.150. Redistribution subject to ASME license or copyright; see http://www.asme.org/terms/Terms_Use.cfm

the interval is not known even in a probabilistic sense. This method yields error bars but not confidence intervals.

A primary focus of the present article is the determination of probability models for solution errors, along with a sketch of how they are used in uncertainty quantification within the Bayesian framework. This work is an outgrowth of earlier studies on uncertainty quantification for simulation based predictions [4–7], which the reader may wish to consult for further information.

3 Probability Models for Solution Errors

Several requirements must be kept in mind when formulating models for solution errors for use in simulations of complex phenomena.

First, use of moderate to coarse grids is a fact of life in simulations of complex phenomena for the foreseeable future. In view of the increasingly powerful computer hardware that is becoming available, one might wonder why the use of relatively coarse grids needs to continue. The answer is that the faster hardware must be used for more demanding problems (*e.g.*, three space dimensions, more detailed models, ensembles of runs for statistical studies) and cannot be used simply to run old problems at higher resolution. Thus many, or most, simulations of key problems will continue to be under resolved, and consequently useful models of solution errors must be applicable in such circumstances.

Incomplete knowledge about important details of complex systems is another fact of life, and this leads to the need for a probabilistic treatment of solution errors. This is a somewhat revolutionary concept, so we explain the motivation. The operation of a solution algorithm is, of course, basically deterministic: a given input leads to a given output. However, the *accuracy* of a solution can depend on the *value* of an input parameter or other problem feature, so an uncertain input parameter will lead not only to an uncertain solution, but to an uncertain solution *error* as well. For example, chance alignments of propagating or interacting waves relative to a discrete mesh contribute a random, *i.e.*, unpredictable, component to numerical error. For equations with stiff parameters or problems with sensitive dependence on initial conditions, errors or uncertainty in these parameters or initial conditions can be greatly amplified by the solution process, to the point that some aspects of the solution, and hence of the error, become essentially unpredictable. Fluid instabilities provide examples of this phenomena. They depend sensitively on their initial conditions, which are often given as perturbations of some unstable (equilibrium) solution. Here we suppose that the perturbation is given by a finite Fourier expansion. If the grid is sufficiently fine relative to the amplitude and wavelength of a perturbation, an accurate solution can be obtained for some time interval. If the wavelength or amplitude of the perturbation is unknown, their ratios to the grid size are uncertain, and the accuracy will also be uncertain.

Like experimental errors, solution errors will generally have a systematic and a random part. Systematic errors might reflect the grid resolution, while the random errors would reflect aspects of the solution for which insufficient detail is available for a deterministic characterization of the error. In some cases, the error model for a particular problem can be fine tuned so that it is nearly deterministic. This advantage must usually be purchased at the price of wider applicability of the error model, so that problem dependent trade-offs are necessary.

In this paper, we begin the construction of solution error models meeting the requirements outlined above. As examples, we consider flow in porous media (Section 5.1) and shock wave dynamics (Section 5.2). Our basic approach, similar in spirit to that of an experimental scientist, is to study errors in an ensemble of solutions, generated by variation of input parameters and other aspects of the solution procedure (grid size, solution algorithm). Errors are evaluated by comparing the solution whose accuracy one wishes to assess to something that is accepted as correct; either a fine grid ''fiducial'' solution or, when possible, experimental data. We compute and analyze the error statistics and discuss probability models that describe the observed error statistics.

A fiducial solution can often (not always) be found for problems of small to moderate complexity. But how does one get a solution error model for a truly complex problem, where it is most needed, since for such problems a fine grid fiducial solution is almost surely not feasible? This is a hard problem. To do this requires an algorithm, or method, for composition of errors based on three steps: (i) decomposition of a complex problem into elementary pieces; (ii) construction of error models for each of the simple pieces, and (iii) recombination of the error models for the simple pieces to obtain an error model for the complete problem.

To elaborate this set of ideas, we imagine a full simulation problem to consist of successive stages, each described by a limited range of physics models. In some cases the successive stages couple only through a few macroscopic variables, and the computation of errors can be mediated through their influence on these key variables. An example is given by the decomposition of a global climate model into separate ocean and atmospheric models, communicating through the ocean surface layer. In other cases, the composition of errors is achieved through an approximate spatial localization of errors. Thus for full field oil reservoir models, the global error model can be decomposed into local error models associated with the transport of oil in the vicinity of single wells. For hyperbolic problems, solutions typically decompose into wave-like structures, with distinct error models for each of these, and for their interactions. Thus shock wave interaction problems also allow localized treatment of errors arising from simpler problems.

Established methods for the analysis of errors in the numerical solution of partial differential equations include asymptotic analysis of truncation errors and *a posteriori* error analysis [8–10]. These methods surely have much to contribute to the overall problem. The questions motivating these approaches are, for the most part, somewhat different from those of concern here, and the different approaches to error modeling are complementary rather than competitive.

4 Fast Integration Methods

Uncertainty quantification requires the statistical study of multiple simulations, generated using data obtained by sampling probability distributions for the relevant physical variables. The overall accuracy of an uncertainty study reflects not only the numerical accuracy of each simulation, but the accuracy with which an ensemble is sampled (sample size). For complex problems, both the forward simulation and integration over a probability measure are computationally expensive, and efficient ways for performing both steps are essential for the success of uncertainty quantification at the practical level. In Section 4.1 we discuss methods for speeding the convergence of ensemble integration, and in Section 4.2 we discuss the role of subgrid models and up scaling in achieving rapid solution of the governing equations.

4.1 Posterior Integration. This discussion will touch on the following points: methods to sample from the posterior distribution, which is generally more complex than the prior; parallelized random sampling; accelerated sampling from a simple distribution, such as the prior; and methods for screening variables to reduce the dimensionality of the integration.

The generic prediction problem can be formulated as the evaluation of the integral

$$\int_{\mathcal{M}} f(s(m))d_{\mathrm{Post}}m \tag{2}$$

with the posterior measure $d_{\mathrm{Post}}m$ defined by (1). For example, (2) gives the expected value, also denoted $\langle f\rangle$, of the function f. Monte Carlo integration

$$\langle f\rangle = \int_{\mathcal{M}} f(s(m))d_{\mathrm{Post}}m = \lim_{N\to\infty}\frac{1}{N}\sum_{i=1}^{N} f(s(m_i)), \tag{3}$$

Downloaded 03 Jun 2010 to 171.66.16.150. Redistribution subject to ASME license or copyright; see http://www.asme.org/terms/Terms_Use.cfm

with the models m_i sampled from the posterior distribution, provides a general method for the evaluation of integrals such as (2) relative to the posterior measure. The integrals (3) are basic to the quantification of uncertainty. They provide mean values and higher moments for outcomes, defined by a functional f of the solution $s=s(m)$. The posterior measure allows calculation of confidence intervals and other performance measures. Monte Carlo integration converges at the rate $O(N^{-1/2})$.

Usually the likelihood in (1) does not have a simple structure, and so the construction of the random samples $\{m_i\}$ from the posterior distribution is not elementary. One approach to this problem is given by Markov chain Monte Carlo methods [11]. In a Markov chain, the choice of the new state m_i is a random event that only depends on the previous state m_{i-1}, with a transition probability $P(m_i|m_{i-1})$. In this algorithm, a move proposing Markov chain $q=q(\cdot|m_{i-1})$ defines the transition probability for the selection of a candidate move m_i. For example q could be chosen to generate samples from the prior distribution. In this case $q(m_i|m_{i-1})=p(m_i)$ is independent of i. Let Post(m_i) denote the posterior probability of m_i. When a move is accepted, m_i is defined with probability $\alpha(m_i,m_{i-1})$, where

$$\alpha(m_i,m_{i-1})=\min\left(1,\frac{\text{Post}(m_i)q(m_i|m_{i-1})}{\text{Post}(m_{i-1})q(m_{i-1}|m_i)}\right). \tag{4}$$

Otherwise, the move is rejected, and $m_i=m_{i-1}$. A significant advantage of the Markov chain Monte Carlo method is the cancellation of the denominator in (1), so that only the likelihood $P(\mathcal{O}|m)$ in (1) has to be evaluated.

While the Markov chain Monte Carlo method provides a way to sample from the posterior, as a method for evaluation of integrals based on the posterior it will not converge more rapidly (in the limit $N\to\infty$) than typical Monte Carlo methods. It may actually be slower, as the Markovian move to a new state will be rejected with probability $1-\alpha$ if the new state results in an increase in the ratio of Bayes likelihoods in the definition of α. Thus we discuss faster methods.

As one way to speed convergence of the Markov chain Monte Carlo algorithm, we propose a parallelized version of the algorithm, whereby independent Markov chains evolve in parallel, with occasional Metropolis weighted sampling (as in the sampling choice based on α in (4)) of the chains with replacement to give new starting points for the Markov chains. By this we mean that the selection of states from the ensemble computed in parallel is probabilistic, through a weighting function of the form $\exp(E/T)$ for some choice of temperature T. The idea is that the ensemble, computed in parallel, achieves thermal equilibrium before the individual processes computed on separate processors, so that the sample is from the parallel ensemble. This suggestion is motivated by the success of a similar algorithm for parallel simulated annealing [12].

An alternative to Markov chain Monte Carlo is to sample from the prior directly and to multiply the integrand by the normalized Bayesian likelihood. Often the prior has a relatively simple structure, allowing faster integration methods. In the case where $\mathcal{M}$ is a product of distinct factors and $p(m)dm$ is a product measure, Latin hypercube sampling can be used to improve the convergence rate in comparison to Monte Carlo integration [13–17]. A Latin hypercube is a stratified sample where each of the product variables is divided into N equiprobable pieces. The sample design assures that each variable occurs once in each of the equiprobable pieces. Therefore, each one-dimensional projection of the sample is uniform. Latin hypercube sampling converges at least as fast as the Monte Carlo method, *i.e.*, $O(N^{-1/2})$ [14]. In practice, it often converges considerably faster through reduction of the coefficient multiplying the $O(N^{-1/2})$ rate but without change in the rate itself. Further improvement can be achieved through Latin hypercubes that stratify on several variables simultaneously [15,16], or that control the correlation among the variables [17,18]. We use Latin hypercubes for sampling from the prior distribution for evaluation of ensemble averages.

The quasi Monte Carlo method [19] is another fast integration method, valid for a bounded domain of integration. This method uses a deterministic sequence that minimizes the Kolmogorov-Smirnov distance between the empirical cumulative distribution function and the uniform distribution. Therefore, the sample spread is nearly uniformly over the domain of integration. Quasi Monte Carlo sampling converges with order $O(N^{-1}\log(N)^{d-1})$ where d is the dimension of the space of integration, significantly faster than Monte Carlo and Latin hypercube sampling. The generation of the sequence is quite involved and, because a deterministic sequence is used, there are no established error estimates.

Sensitivity analysis is used to identify significant variables (possibly leading to a reduction in the dimension of the integration space), to construct a localized linear response surface approximating the graph of $s(m)$ near the evaluation point, and to propagate linearized uncertainty from inputs to outputs. Sensitivity studies, as usually formulated, depend on evaluation of the gradient $\mathcal{G}=\partial s/\partial m$. The gradient defines a linear response surface, or a linear approximation as a tangent plane, valid in a neighborhood of the sample point where $\mathcal{G}$ is evaluated. For small variations in m (or variation of m with a linear influence on s), the covariance of the solution C_s can be computed from the covariance of the input, C_m, by the formula

$$C_s=\mathcal{G}C_m\mathcal{G}^*.$$

Experimental design is used to identify significant variables and to construct a response surface model approximating $s(m)$. Its main virtues are robust and efficient predictions from limited data. Assumptions typical in the practice of experimental design are; (*a*) sparsity, in that only a limited number of variables will ultimately be needed and (*b*) approximate linearity, in that the higher order interactions among the variables are weak. Experimental design methods are based on a finite step size rather than the infinitesimal step size used in construction of the gradient. Polynomial or other types of nonlinear response surfaces, as well as nonparametric response surfaces, can also be constructed by these methods.

The response surface is used for evaluation of integrals or whenever repeated function evaluations are required. These evaluations generally involve the solution of a partial differential equation and can be expensive. Instead, one calculates the function value from its approximation by the response surface. In this sense, the surface pre-evaluates the function, and stores enough information to determine its value at an arbitrary point through interpolation. This method works best if the function being evaluated is not too complex and if many function evaluations are required, so that the expense of constructing the response surface is amortized over many response surface evaluations. The construction of a response surface for systems of partial differential equations is discussed in [17,20,21]. Tabulated functions are an equivalent method that has been used for fluid dynamics problems that require an equation of state for real materials.

4.2 Subgrid Models. Multiscale problems have a wealth of fine scale detail, but it is often the macroscopic behavior that is of primary interest. However, the fine scale structures cannot be ignored, since they can have a significant influence on the macroscopic behavior. A number of related methods with a variety of names including subgrid modeling, up scaling, averaged equations, effective equations, or parameterized equations each involve some kind of averaging to suppress the irrelevant fine scale while still capturing the influence of this detail on the macroscale variables.

Subgrid models are usually derived by a formal procedure of averaging, introduction of moments, truncation of the hierarchy of moment equations, and closure to complete the system of equations, which is otherwise under determined due to the truncation of the moment hierarchy. Of these steps, all but the closure can be

Downloaded 03 Jun 2010 to 171.66.16.150. Redistribution subject to ASME license or copyright; see http://www.asme.org/terms/Terms_Use.cfm

performed at a mathematical level and are formally exact. Closure is a physics dependent modeling step. It introduces new relations, independent of the primitive equations, *i.e.*, those that result directly from the averaging process. Closure restricts the validity of the equations to the regime where the closure itself is valid. Closure relations are to some extent constrained by general considerations of covariance, symmetry, dimensionality, *etc*. They are subject to confirmation by experiment or direct numerical simulation, but are normally beyond the scope of mathematical derivation. Experimental validation of closure relations is common. An example occurring within the authors' program is given by the buoyancy drag differential equations for the edge of a turbulent mixing zone, given for example in [22]. In this example both the functional form (known from general principles of fluid dynamics) and the specific values of the drag coefficient (which depends on shape and cannot be predicted from general principles) are validated by comparison to experiment.

Subgrid models reduce the number of degrees of freedom in a model. For this reason they can lead to more rapid solution methods. Subgrid models are studied in a number of contexts: for example in climate modeling subgrid models are used for precipitation, cloud cover, and other meteorological phenomena. Turbulence subgrid models aim to capture the effects of small scale vortices on the macroscale flow. We will discuss subgrid models for flow in porous media in Section 5.1.

It is useful to contrast subgrid models with response surface methods, as these very different methods have the common purpose of speeding solution evaluations, and thus the integration over the ensemble of solutions. A response surface is constructed by data fitting and interpolation, while the subgrid model leads to a coherent, self contained description of the macroscopic physics. In general, we expect response surfaces to be faster in execution and easier to implement but to be less general and robust in their application to modified problems, and to offer less insight into the physical processes being studied.

5 Examples

5.1 Flow in Porous Media. Spatial variability is an inherent property of petroleum reservoirs. The variability manifests itself starting from properties on the scale of the rock pore size (microns) and extends to geologic properties at the field scale of kilometers. Over the past two decades, it has become clear that even relatively fine scale variability, on the order of a meter, can have a significant impact on large scale flow and transport of oil, gas, and other materials. In particular, predictions of oil production depend on a knowledge of the reservoir geology, which is generally uncertain and described by a geostatistical model. The problem examined here is that of using observational data on past oil production to constrain uncertainties in the geology and thereby improve prediction of future oil production.

The reservoir geology is linked to oil production data by simulations. This presents the following problem. Statically accurate reservoir descriptions that incorporate fine scale heterogeneities have been developed, but reservoir simulations that could resolve this level of detail are generally too expensive for practical engineering use. As an example, a statistically accurate description for a typical formation may require a grid of ten to fifty million cells, whereas routine simulations on modern reservoir simulators are currently limited to about 100,000 to 250,000 cells. A version of subgrid modeling known as scale up has been developed to bridge this gap. The porous formation is characterized on a fine scale; the scale up algorithm transforms the fine grid description into a coarse grid description in a way that captures some, but of course not all, of the crucial fine scale information; and the problem is simulated on the coarse grid. In the work reviewed here, we use a version of up scaling developed in [23–26], with typical results as shown in Fig. 1 (left), in which the fine grid solution is compared with solutions obtained with several levels of coarsening. A discussion of the physical and mathematical motivation and the details of the formulation for the scale up algorithm are outside the scope of this paper.

We focus on a different point here. Even good up scaling methods introduce solution errors; coarse grid solutions without the use of up scaling introduce even more. Our objective is to examine the effect of these solution errors on our ability to constrain uncertainties in the geology using observational data, along the lines discussed in Section 2 and Section 3. For this purpose we conducted a study [27–29] based on an ensemble of 500 reservoirs, with the permeability function $K(x,y)$ (to describe the geology) taken as a random field. We consider two-dimensional flow in a unit square, $0 \leqslant x,\ y \leqslant 1$. The K's were drawn from a log normal distribution with a vertical (y direction) correlation length of 0.02 and a horizontal correlation length Λ, where Λ is one of 0.2, 0.4, 0.6, 0.8, 1.0 (100 realizations each).

The simplest reservoir equations were considered. Darcy's law and the condition for incompressible flow

$$\mathbf{v} = -\lambda K \nabla p; \quad \nabla \cdot \mathbf{v} = 0,$$

where p is the pressure, define the total seepage velocity $\mathbf{v} = \mathbf{v}(x,y,t)$, while the saturation or local water fraction $s(x,y,t)$ is a solution of the Buckley-Leverett equation

$$\partial_t s + \nabla \cdot \mathbf{v} f(s) = 0.$$

Boundary conditions are $p=1$ for $x=0$ and $p=0$ for $x=1$, while the vertical component of $\mathbf{v}$ is zero on the lower and upper boundaries $y=0$ or $y=1$, respectively. The functions λ and f are the mobility and saturation flux, respectively, and, taken in their simplest form, are defined by quadratic relative permeabilities. An oil to water viscosity ratio of 5:1 was assumed.

The solutions were computed on a fine grid (100×100 cells), and this solution was regarded as exact. They were also computed on coarse grids of size 20×20, 10×10 and 5×5 with up scaled K's, f's, and λ's. The ratio of outflow (flux at $x=1$) oil to water (the oil cut) was recorded as a function of time, see Fig. 1. We write the error as

$$\mathbf{e} = \mathbf{s}_f - \mathbf{s}_c$$

where $\mathbf{s}_f$ and $\mathbf{s}_c$ are the fine and coarse grid solutions state vectors. We define $\bar{\mathbf{e}} = \langle \mathbf{e} \rangle$ as the ensemble average error. Since $\bar{\mathbf{e}}$ is known independently of the choice of the correct reservoir, denoted below by j_0, we can use it for history matching and prediction purposes. Thus we regard $\mathbf{s}_c + \bar{\mathbf{e}}$ as the coarse grid solution and $\delta\mathbf{e} = \mathbf{e} - \bar{\mathbf{e}} = \mathbf{s}_f - \mathbf{s}_c - \bar{\mathbf{e}}$ as the error. With this convention, $\langle \delta_{\mathbf{e}} \rangle = 0$, and the ensemble mean value of the redefined error is zero. With this data the error, *i.e.*, the difference between the fine and the coarse grid solutions, is a time series.

We next specify the data to be used in the analysis of prediction. We seek to improve estimates of future oil production by using observations of the oil produced (oil cut) up to a specified time (the present) and the statistics of solution errors. In the present study we obtain this data as follows. We first identify a specific reservoir with permeability $K = K_{j_0}$ as "correct." The oil cut resulting from the fine grid solution with permeability $K = K_{j_0}$ is taken as a stand in for actual observational data. A time T_0 for which the oil cut had a given value, c_0, in realization j_0 is called the "present time." All observed data, *i.e.*, the exact oil cut for times $t \leqslant T_0$ are used in the analysis and errors for all times $0 \leqslant t$ are used to calibrate the error model. Thus the solution error model pertains to both the past and future solution behavior. We emphasize that the solution error model is used twice. Errors for times $t < T_0$ (the past) are used to obtain revised probabilities (the posterior) for the model geology. Errors for $t > T_0$ (the future) are used to assess the accuracy of forward simulations, used for prediction.

We assume a Gaussian error model and use the observed error statistics to define the mean and covariance that characterize this Gaussian. Because the errors are observed in a finite sample, we need to restrict the dimension of the error model (to avoid over

Downloaded 03 Jun 2010 to 171.66.16.150. Redistribution subject to ASME license or copyright; see http://www.asme.org/terms/Terms_Use.cfm

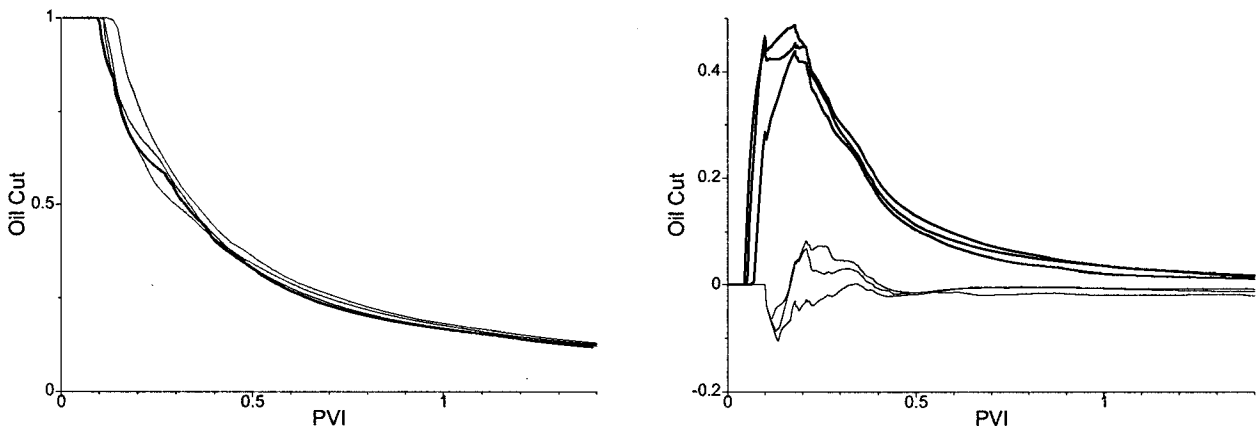

Fig. 1 Left: Fine grid and several coarse grid solutions. Here fractional oil production rate (oil cut) is plotted vs. a dimensionless time variable, the total pore volumes of fluid injected, or PVI. Right: Typical errors (lower curves) and discrepancies (upper curves) plotted vs. PVI. The two families of curves on the right are clearly separable.

fitting of the data). This means that errors are projected onto a finite dimensional space and the covariance is projected onto a finite rank matrix. This finite matrix defines the Gaussian error model.

In addition to errors, *i.e.*, the difference between the fine and coarse grid solutions, we need to consider discrepancies, which are the difference between the fine grid solution for one geology and the coarse grid solution for another. In our methodology, we cannot know which of the geologies is ''correct,'' and we cannot know which of the discrepancies is actually an error (through choice of the correct geology for the coarse grid). Fortunately, this problem is avoided in the Bayesian approach, where the likelihood is constructed *assuming that the model m is correct*. This means that we can take a discrepancy, and assume it is an error and evaluate its probability based on this assumption. Doing this defines the posterior probability. The posterior probability and the solution error model for forward simulations define all quantities needed for the uncertainty quantification analysis, including mean prediction values and confidence intervals.

In Fig. 1 (right) we show typical discrepancies and errors. Evidently the errors are often systematically smaller, so that the correct geology (and any others with similar solution properties, hence with small discrepancies similar to errors) will show a larger probability in the posterior distribution, and thus be favored in the Bayesian predictions.

We illustrate the use of this construction of the posterior in two ways. First we use the posterior to predict future oil production rates (the oil cut as a function of time). The prediction error reduction relative to the prior probability prediction is expressed in percent in Table 1. This quantity is defined as $1-PE_{\text{posterior}}/PE_{\text{prior}}$ where PE is a prediction error for the posterior or prior ensemble. The prediction error is defined as the absolute value of the prediction error integrated over some future time interval, and is the difference between the fine grid solution for the chosen geology with index j_0 and the prediction. Since the ratio is a function of the index j_0 of the chosen (''correct'') geology, we average the ratio over all choices of j_0 to obtain the values reported in Table 1. In this table, we show results for three levels of scale up, and also the predicted results for no scale up. To define the posterior for the latter, we use a windowing method, and select all geologies whose solution for $0 \leqslant t \leqslant T_0$ lies in a small window about the exact solution for geology j_0. See Fig. 2.

Table 1 Percent reduction in the oil cut prediction error relative to prediction based on the prior distribution. The fine grid results and three levels of scale up are presented.

c_0	100×100	20×20	10×10	5×5
0.8	42	21	19	14
0.6	51	39	32	20
0.4	57	55	45	34

In Table 2 we show expected confidence intervals for the prediction of future oil production, expressed as a percent of predicted future oil production. The confidence interval depends on the choice of correct geology j_0, and so it is a random variable. The mean value of this random variable, expressed as a percent deviation from the predicted production, is presented in Table 2. In Table 1, absolute values of error are integrated in time, so that cancellation of errors between under and over prediction within a given simulation does not occur. In Table 2, we are dealing with total oil production and errors in this quantity. Thus cancellation of errors occurring at different times within a given simulation can occur. This appears to be the reason that the results on scale up in Table 2 appear to be more favorable than those in Table 1.

Table 2 shows a generally very satisfactory accuracy for the scaleup predictions, with possible difficulties only for the very extreme 5×5 scaleup and the very early time scaleup, $c_0=0.8$. The authors believe that the results summarized in Table 1 and Table 2 provide the first quantitative assessment of the statistics of prediction errors associated with scaleup (*i.e.*, uncertainty quantification) and could provide a model for future assessments of scaleup.

5.2 Shock Wave Interactions. Compressible hydrodynamics, in addition to its intrinsic importance in modeling physical flows, is also the prototypical example of a hyperbolic system of equations. Equations of this type occur in many types of problems, and the quantification of uncertainty in such problem is of fundamental importance to applications.

We focus on the case of compressible gas dynamics where the flow is described by the system of partial differential equations:

$$\mathbf{u}_t+\nabla\cdot\mathbf{f}=\mathbf{b} \tag{5}$$

where $\mathbf{u}=(\rho,\rho\mathbf{v},\rho E)$, ρ is the mass density, $\mathbf{v}$ the fluid velocity, $E=v^2/2+e$ the specific total energy, and e the specific internal energy. The flux tensor $\mathbf{f}$ is given by

$$\mathbf{f}=\left(\rho\mathbf{v},\rho\mathbf{v}\otimes\mathbf{v}+P,\rho\mathbf{v}\left(\frac{v^2}{2}+e\right)+P\mathbf{v}\right),$$

where P is the pressure. The components of $\mathbf{b}$ describe body forces, viscous forces, and heat conduction. In this discussion we assume inviscid flow, so $\mathbf{b}\equiv 0$. The system is closed by a thermodynamic equation of state that relates pressure, density, and inter-

Downloaded 03 Jun 2010 to 171.66.16.150. Redistribution subject to ASME license or copyright; see http://www.asme.org/terms/Terms_Use.cfm

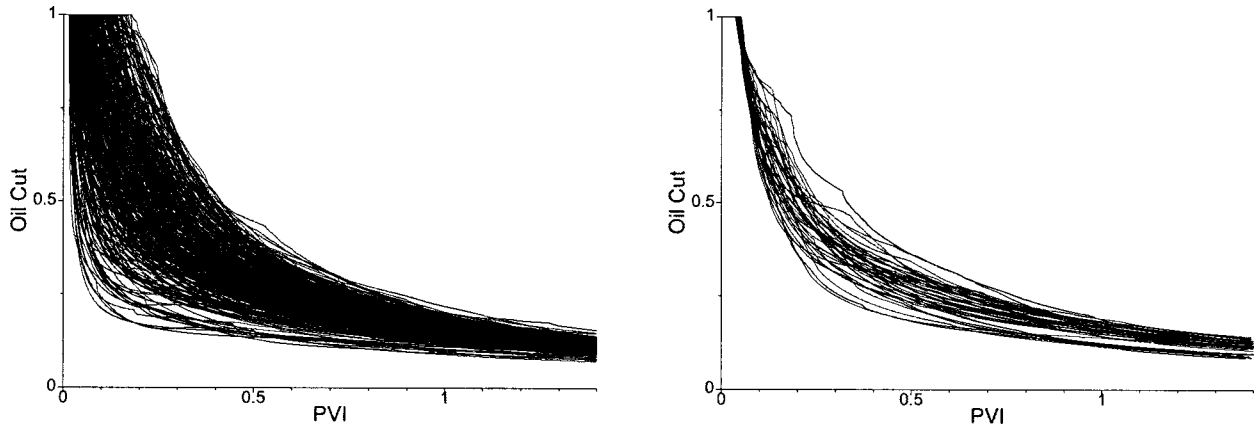

Fig. 2 Illustration of the window method to construct the posterior ensemble. Left: full ensemble of oil cut curves. Right: Posterior ensemble defined as those geologies whose oil cut curves agree with the solution for geology j_0 within the window error, for the past times.

nal energy. For simplicity we assume a perfect gas equation of state $P=(\gamma-1)\rho e$. Furthermore, we will only consider one-dimensional flows.

We are interested in solving the initial boundary value problem for system (5):

$$\mathbf{u}(x,0)=\mathbf{u}_0(x), \quad a\leqslant x\leqslant b$$

with appropriate boundary conditions at $x=a$ and $x=b$. Most commonly three types of boundary conditions are considered, periodic, reflecting, or flow specified. A fourth type of boundary condition is also often used and can be a significant source of solution error. This is the so-called open boundary condition. The intent is to model a one-way door that couples the computational region to an external reservoir so as to allow waves to propagate from inside the computational region into the external reservoir but not produce reflected signals back into the computational region. This type of boundary condition is often used in situations where the region of interest is relatively small, and the simulation of the entire flow regime is prohibitively expensive. The open boundary condition involves the loss of information of the flow state outside the domain and is often implemented as an extrapolation from the interior to the exterior.

In contrast to the porous media example of the previous subsection, where stochasticity in terms of the unknown geology is an inherent part of the system, error mechanisms in hydrodynamics tend to be either numerical, or due to a lack of knowledge concerning the initial, boundary conditions, or the constitutive models (*e.g.*, γ) describing the materials in the flow.

Relatively little is known about error propagation in nonlinear hyperbolic systems. A formal prototype theory can be developed using the notion of the modified equation for a numerical method, (see for example [30] chapter 12, section 14). It can be shown that for a given finite difference numerical method, an approximate solution $\mathbf{u}$ satisfies an alternate partial differential equation to higher order than the original system. More specifically $\mathbf{u}$ satisfies a system of the form

$$\mathbf{u}_t+\nabla\cdot\mathbf{f}(\mathbf{u})=\mathbf{Q}\mathbf{u}, \tag{6}$$

where $\mathbf{Q}$ is a differential operator that depends on the numerical method. If the numerical method has order of accuracy α, then $\mathbf{Q}=O(\Delta x^{\alpha})$. For example, for a scalar conservation law in one space dimension and the first order Lax-Friedrichs method:

$$u(x,t+\Delta t)=\frac{u(x+\Delta x,t)+u(x-\Delta x,t)}{2}-\frac{\Delta t}{\Delta x}\frac{f(x+\Delta x,t)-f(x-\Delta x,t)}{2},$$

and for fixed $\lambda=\Delta t/\Delta x$,

$$Qu=\frac{\Delta x}{2\lambda}\partial_x((1-(\lambda f'(u))^2)u_x)+O(\Delta x^2).$$

If we assume that $\mathbf{w}$ is the exact solution to (5) then the error $\mathbf{e}=\mathbf{w}-\mathbf{u}$ satisfies the system

$$\begin{aligned}\mathbf{u}_t+\nabla\cdot\mathbf{f}(\mathbf{u})&=\mathbf{Q}\mathbf{u}\\ \mathbf{e}_t+\nabla\cdot(\mathbf{f}(\mathbf{u}+\mathbf{e})-\mathbf{f}(\mathbf{u}))&=-\mathbf{Q}\mathbf{u}.\end{aligned} \tag{7}$$

The combined system forms a diffusive hyperbolic system with characteristic speeds given by the eigenvalues of the flux derivatives $\mathbf{f}'(\mathbf{u})$ and $\mathbf{f}'(\mathbf{w})$.

Our ultimate goal is to develop a tractable differential system whose solution characterizes the distributions of $\mathbf{u}$ and $\mathbf{e}$. Since this goal is almost certainly unattainable, a more reasonable approach is to develop models that quantitatively approximate the distribution properties. More specifically, we seek parametric models for the error distribution and equations that govern the evolution of distribution parameters.

Generally pointwise estimates are less useful than averaged measures of error. Indeed convergence under mesh refinement for systems of nonlinear conservation laws does not occur in L^{∞} but rather locally in L^1. Furthermore, averaging can improve the regularity of the error distribution, increasing the validity of parametric models (such as Gaussian). With this in mind we introduce an averaging kernel $K(x,t)$ and convolve (7) with this kernel. Since convolution commutes with differentiation, we have

$$\begin{aligned}(K*\mathbf{u})_t+\nabla\cdot(K*\mathbf{f}(\mathbf{u}))&=K*\mathbf{Q}\mathbf{u}\\ (K*\mathbf{e})_t+\nabla\cdot(K*\mathbf{f}(\mathbf{u}+\mathbf{e})-K*\mathbf{f}(\mathbf{u}))&=-K*\mathbf{Q}\mathbf{u}.\end{aligned}$$

Table 2 Confidence intervals for future oil production, centered about the predicted value and expressed as a percent of predicted production. Mean values for the upper and lower endpoints of the confidence intervals are given here for three choices of c_0, with the fine grid results and three levels of scale up presented.

c_0	100×100	20×20	10×10	5×5
0.8	[−15,22]	[−17,32]	[−20,30]	[−23,31]
0.6	[−14,20]	[−16,23]	[−19,26]	[−22,30]
0.4	[−14,17]	[−15,19]	[−19,22]	[−23,26]

Downloaded 03 Jun 2010 to 171.66.16.150. Redistribution subject to ASME license or copyright; see http://www.asme.org/terms/Terms_Use.cfm

Nonlinearity leads to the introduction of new unknowns, $K*\mathbf{f}(\mathbf{u})$, $K*\mathbf{Q}\mathbf{u}$, and $K*\mathbf{f}(\mathbf{u}+\mathbf{e})$. For each such quantity it is possible to derive a system similar to (7) which when convolved with K gives an additional set of equations for the given quantity. Ultimately the process leads to an infinite set of equations and closure models are needed to terminate this process. For example, closure would seek to express the new unknown $K*\mathbf{f}(\mathbf{u})$ as a function of the primitive averaged unknowns, such as $K*\mathbf{u}$. This process leads to a Reynolds stress, approximate models for which define the k, ϵ and other well studied turbulent models. From the perspective of the present article, we regard the approximate solution $\mathbf{u}$ and its regularization $K*\mathbf{u}$ as known, and so the above is an equation for $\mathbf{e}$. Closure is also required for this $\mathbf{e}$ equation, so that the flux in the error equation can be expressed in terms of the primitive smoothed error variable $K*\mathbf{e}$ and the known $\mathbf{u}$.

Given a model for the convolved error, we can form equations for the statistical moments of the error distribution. Nonlinearity again introduces higher order terms that require closure models to truncate the moment equations. Closed equations typically involve first or second order moments. Our contribution to this topic at the present time is simply to note that the computational studies reported here suggest that the distribution of $\mathbf{e}$ is approximately Gaussian, a fact that simplifies the search for closures.

Obviously the procedure outlined above is deficient in a number of ways. For example the operator $\mathbf{Q}$ depends on the numerical method used to solve the system. For simple finite difference methods like the Lax-Friedrichs or Lax-Wendroff methods [30] it is possible to use symbolic mathematics software such as Mathematica or Maple to derive explicit formulas for $\mathbf{Q}$. However, for more complex methods like the Godunov type schemes (see for example the book of Godlewski and Raviat [31]), an explicit determination of $\mathbf{Q}$ may be difficult. An alternate approach is to realize that system (7) is only semi-coupled, and that $\mathbf{u}$ does not depend on $\mathbf{e}$. To formulate the error equation we regard the approximate solution $\mathbf{u}$ as known and use (6) as the definition of the operator $\mathbf{Q}$. In this case the equation for $\mathbf{e}$ can be rewritten as:

$$\mathbf{e}_t+\nabla\cdot(\mathbf{F}(\mathbf{u},\mathbf{e})\mathbf{e})=-(\mathbf{u}_t+\nabla\cdot\mathbf{f}(\mathbf{u})), \tag{8}$$

where

$$\mathbf{F}(\mathbf{u},e)=\int_0^1\frac{d\mathbf{f}}{d\mathbf{u}}(\mathbf{u}+\alpha\mathbf{e})d\alpha.$$

We see that the degree to which $\mathbf{u}$ does not satisfy the original partial differential equation is a source term for the error, and that the flux in the error equation is the average action of the solution flux derivative on the error.

It is important to note that the above discussion is formal and its translation into a viable numerical method for the computation of solution error is an open question. Since one numerically solves for an ensemble of $\mathbf{u}$'s to approximate the distribution of the solution, and each such simulation is performed at finite accuracy, typically either first or second order in the mesh size, the source term in (8) is $O(\Delta x^\alpha)$, where α is the order of accuracy of the numerical method. Furthermore, the flux $\mathbf{F}(\mathbf{u},\mathbf{e})$ differs from the flux derivative $d\mathbf{f}/d\mathbf{u}(\mathbf{u})$ by this same order of magnitude. Thus if one naively attempts to solve (8) to this same order of accuracy, you are effectively solving the linearized system:

$$\mathbf{e}_t+\nabla\cdot\left(\frac{d\mathbf{f}}{d\mathbf{u}}(\mathbf{u})\mathbf{e}\right)=0.$$

Since the initial conditions are $\mathbf{e}(\mathbf{x},0)=0$, this system has the trivial solution $\mathbf{e}\equiv 0$, *i.e.,* we obtain no additional information about the error. This is hardly surprising since solving for $\mathbf{e}$ is equivalent to finding the exact solution $\mathbf{w}$ to the original system. Methods analogous to the up scaling described in the previous section might eventually provide a means to solve system (8) to sufficient accuracy for error estimation, but for the present we solve for the ''exact'' solution $\mathbf{w}$ using extreme mesh refinement and regard the above formal procedure as a theoretical guide towards developing quantifiable approximation models for error statistics rather than as an explicit method for computing solution error.

Our approach is to use the computer as a computational laboratory to gain insight into the error distribution. We compute an ensemble of solutions using extremely fine grids, as a stand-in for the ''exact'' solution. We then compute the error explicitly using the differences between the fine grid and various coarse grid solutions. This approach requires ensembles of fine grid solutions which would be prohibitively expensive even for relatively simple two and three dimensional problems.

As mentioned in Section 3, our approach to extending our solution error methodology to complex problems is based on the idea of transferability of error models. As will be seen below, our simulations confirm the known facts that errors in shock physics simulations arise primarily within the interacting wave zone, and propagate largely unchanged along solution waves or characteris-

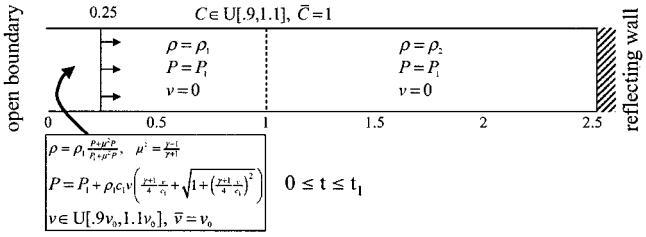

Fig. 3 Test problem. A piston-driven shock moves to the right. The shock is incident on a contact discontinuity, where it produces a reflected and a transmitted shock. A reflecting wall is placed at the downstream end of the shock tube. All parameters of the problem are fixed (deterministic) except the shock velocity and the contact position. Each of these are allowed a uniform variation by ±10 percent about a base value.

Table 3 Mean initial conditions for the shock tube simulations

	Incident shock Mach number	ρ_0	P_0	$\overline{v_0}$	ρ_1	P_1	v_1	ρ_2	P_2	v_2
				Step Up						
1	32.70	3.974	1.33725	1	1	0.001	0	10	0.001	0
2	18.65	3.951	434.787	18	1	1	0	10	1	0
3	32.70	3.974	1.33725	1	1	0.001	0	100	0.001	0
4	18.65	3.951	434.787	18	1	1	0	100	1	0
				Step Down						
1	103.3	39.84	13.3523	1	10	0.001	0	1	0.001	0
2	58.82	39.82	4327.65	18	10	1	0	1	1	0
3	326.7	398.5	133.502	1	100	0.001	0	1	0.001	0
4	186.0	398.5	43256.3	18	100	1	0	1	1	0

Downloaded 03 Jun 2010 to 171.66.16.150. Redistribution subject to ASME license or copyright; see http://www.asme.org/terms/Terms_Use.cfm

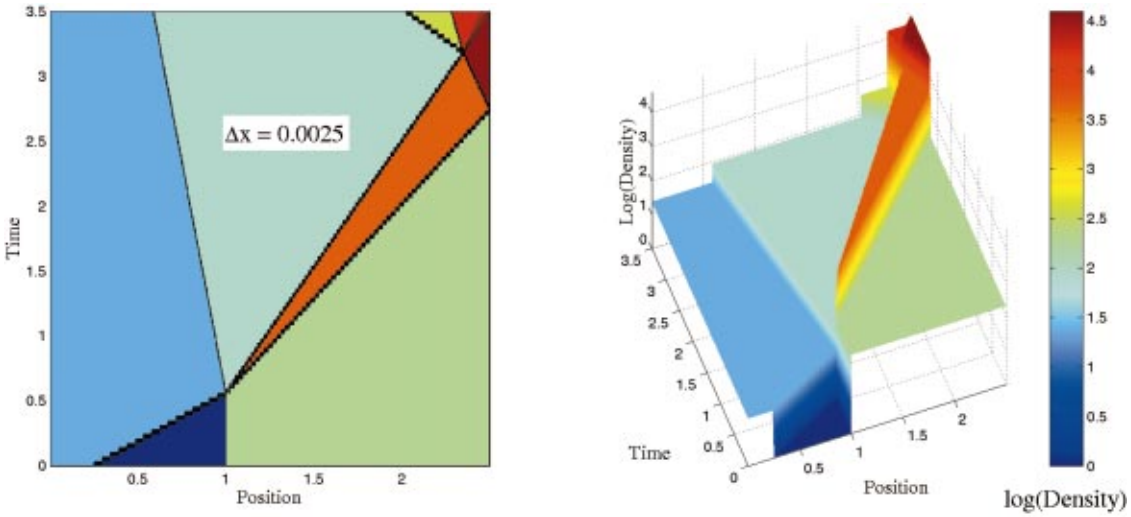

Fig. 4 A space time plot of the logarithm of density for one of the step up cases, selecting the base case from the ensemble. The finest grid result (1000 cells) is displayed.

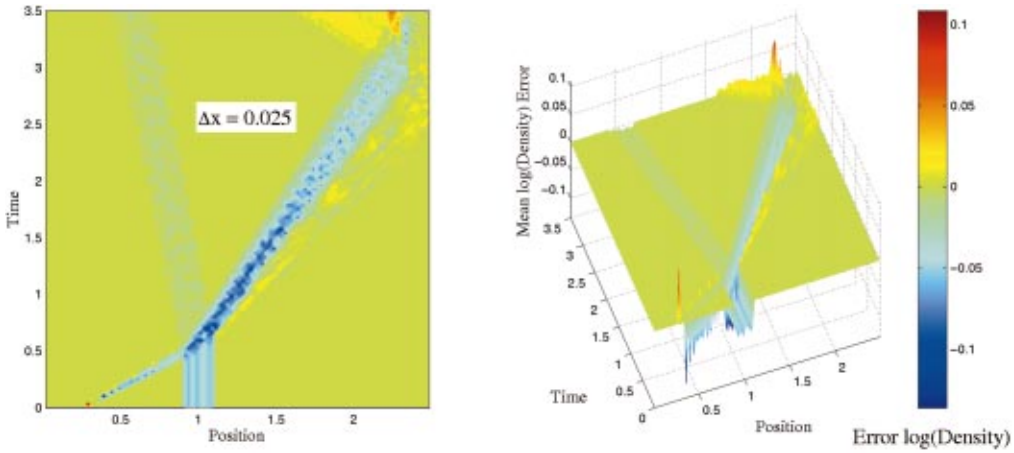

Fig. 5 A space time plot of the mean error in the logarithm of density, integrated over the ensemble, step up case, finest coarse grid errors

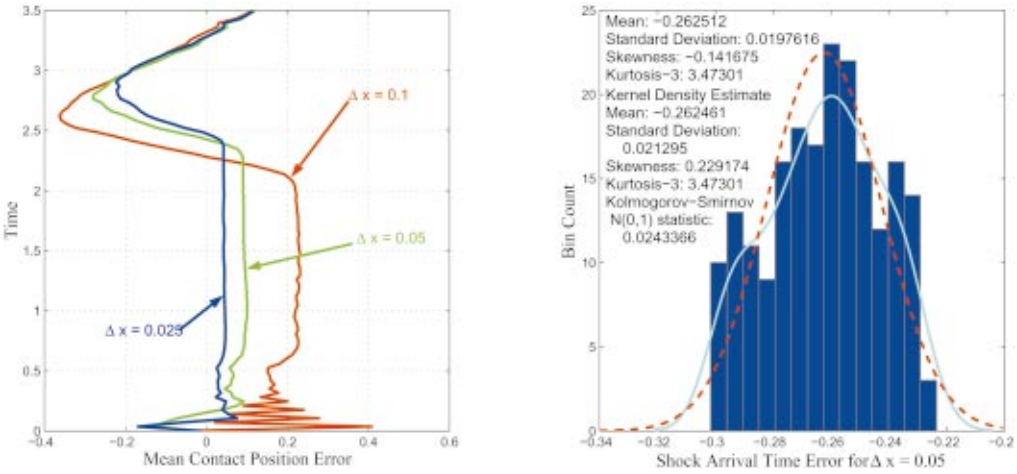

Fig. 7 Left: mean errors as a function of time for the contact location for three levels of grid refinement. Right: histogram of errors in the shock arrival time at the wall, for $\Delta x = 0.05$.

Downloaded 03 Jun 2010 to 171.66.16.150. Redistribution subject to ASME license or copyright; see http://www.asme.org/terms/Terms_Use.cfm

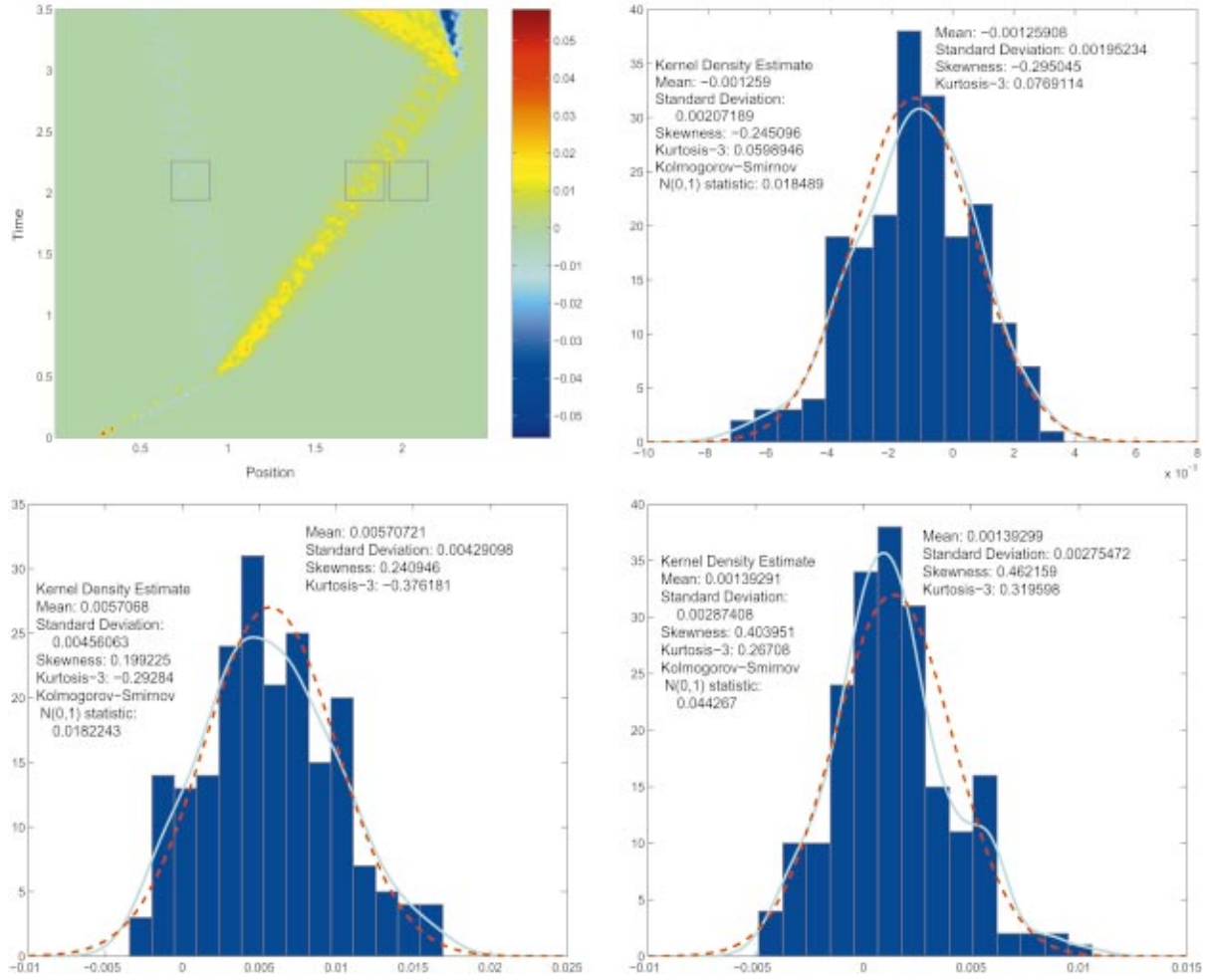

Fig. 6 Histograms of space-time averaged errors. Upper left: the specific internal energy error field. The boxes from left to right show regions centered about the reflected shock, deflected contact, and transmitted shock respectively. HISTOGRAMS: Upper right—reflected shock region. Lower left—contact region, Lower right—transmitted shock region. The solid and dashed curves show the kernel density estimate and the best Gaussian fit to the distributions respectively.

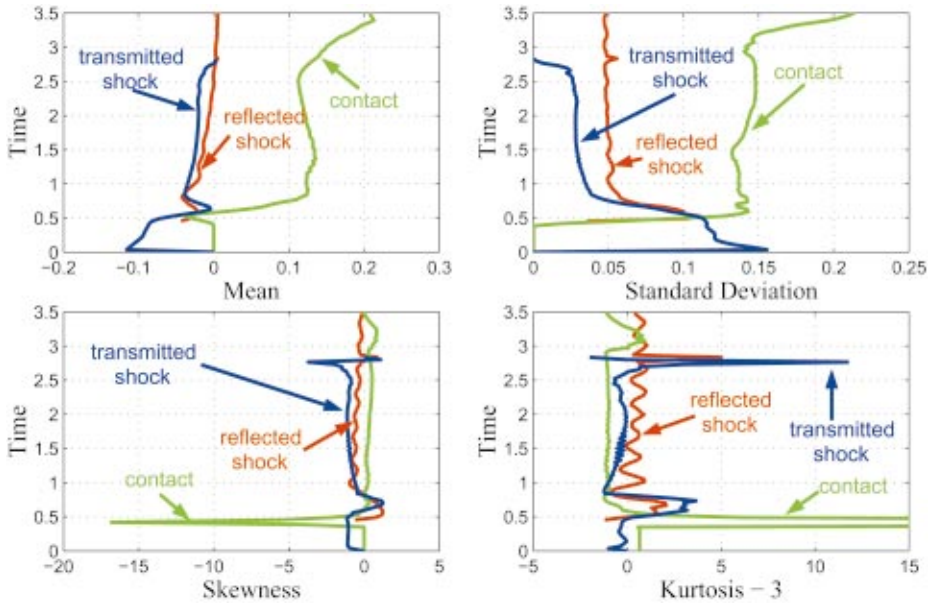

Fig. 8 Time dependence of the localized specific internal energy error for $\Delta x = 0.05$

Downloaded 03 Jun 2010 to 171.66.16.150. Redistribution subject to ASME license or copyright; see http://www.asme.org/terms/Terms_Use.cfm

Table 4 Specific internal energy errors localized within major waves. Statistics taken at time=2.1.

Error statistics		Reflected shock	Contact	Transmitted shock
100	mean	0.00459241	0.0921823	−0.0185576
	standard deviation	0.0474799	0.12871	0.0285532
50	mean	−0.00427657	0.119411	−0.0202767
	standard deviation	0.0492499	0.14564	0.0284457
25	mean	−0.0193008	0.142649	−0.0472504
	standard deviation	0.0499294	0.136949	0.0318628
Solution statistics		Reflected shock	Contact	Transmitted shock
1000	mean	0.640088	0.368899	0.0652551
	standard deviation	0.119341	0.109465	0.0553988

Table 5 Mean wave widths at time=1.26.

Mesh	Reflected shock	Contact	Transmitted shock	Δx
		Mean Wave Widths		
25	0.096738	0.096825	0.14615	0.1
50	0.047094	0.072744	0.065469	0.05
100	0.022	0.0058225	0.034831	0.025
		Ensemble Wave Width		
1000	0.25125	0.29125	0.26625	0.0025

tics until further interactions occur. These features lead naturally to the point of view that errors are generated in the solutions of Riemann problems [32–34] embedded within the simulation. Moreover, the statistics of the errors likewise arise from statistics of errors in the Riemann problem solution, i.e. the stochastic map from an ensemble of Riemann problems to an ensemble of Riemann problem solutions. In this sense, the stochastic Riemann problem is a fundamental tool for the analysis of errors in simple shock physics problems.

Errors in complex shock physics problems can be addressed by composition of errors in simple problems. This step is not taken here, but we note the analogous role of the Riemann problem solution as the fundamental building block for the construction of deterministic numerical methods for the solution of compressible flows [33,35,36].

In this paper we present an analysis of solution errors in the simple Riemann problem. We find a number of solution observables for which the solution error has an approximately Gaussian form. The Bayesian modeling step discussed in Section 2 is not taken in this example. The Riemann problem we study is defined by the refraction of a shock wave through a material interface in a semi-closed shock tube. Figure 3 illustrates the basic configuration. The flow is one dimensional and the shock tube is semi-infinite on the left with a rigid wall on the right. The shock tube is filled with two gases, initially at rest, separated by a contact discontinuity/material interface near the middle of the tube. A shock driven by a piston of specified velocity is initiated to the left of the interface. For simplicity we take both gases to be perfect gases with $\gamma=5/3$.

A total of eight configurations were computed, divided into two classes depending on whether the density of the unshocked gas increases (steps up) or decreases (steps down) when moving from left to right across the interface. These two families are further divided into strong or extremely strong incident shock cases. Stochastic variations in the simulations are added by giving the shocked gas velocity and the contact position 10 percent uniform distributions about their means. Table 3 shows the initial values for the mean shocked gas velocity used in the simulations. The units are arbitrary, but the interpretation of pressure as bars, and density as 0.1 grams/liter corresponds to a 2.5 centimeter long test section and velocities measured in centimeters per 10^{-5} seconds.

Solutions were computed on grids of 25, 50, 100, and 1000 equal sized mesh zones in the spatial direction. Several gas dynamics simulation codes were used including CLAWPACK [37], CHAD [38,39], and *FronTier* [40,41]. In addition the simulations were performed using a combination of various solution options such as the choice of Riemann solver for computing the numerical flux, and tracking or capturing of the main waves in the flow. An ensemble of 200 realizations were performed for each of the eight basic setups using Latin hypercube sampling from the piston velocity and contact position distributions. Spatial averaging is used to map the fine grid solution onto the coarse grids and the error is computed as the difference between the coarse grid value and averaged fine grid solution.

Space limitations prohibit a discussion of all of the cases described above, so we will simply report on the first step up case and simulations using interface tracking in *FronTier*. Figure 4 shows space time plots of the logarithm of density for this case. The refraction produces reflected and transmitted shock waves and deflects the material interface toward the wall. Subsequently, the transmitted shock is reflected by the right hand wall and then collides with the deflected contact interface, where it is refracted into a reflected rarefaction wave and a transmitted shock. The simulation is halted shortly after this second refraction.

Figure 5 shows a space-time plot of the mean error in the logarithm of the density for the first step up case. As expected, the errors are concentrated near the wave fronts where the solution gradients are large. It is interesting to note that the error regions for the transmitted shock and deflected contact overlap. Since the velocities of these two waves are relatively close, some samples from the solution ensemble actually have faster contact speeds than the transmitted shock speed from other samples.

Not all functionals of the solution have useful statistical properties. A consequence of the lack of pointwise (L^∞) convergence of the numerical solutions is generally uninformative statistical properties of pointwise error values. One of our main conclusions is that a very modest amount of spacetime averaging yields useful statistics and approximately Gaussian behavior for the errors. A similar statement applies to wave position and arrival time statistics.

A variety of diagnostic tools were used to study the selected observables. Using the MATLAB [42] package an interactive program was developed that allows the user to plot histograms of the error distribution at selected points in space and time. These histograms are produced by averaging the error over user defined regions. The histogram plot includes a graph of the probability density for the best Gaussian fit as well as a kernel probability density estimate [43] obtained by convolving the discrete sample distribution with a Gaussian kernel. Figure 6 shows histograms of the error distribution in three selected regions centered about the principal waves produced by the shock refraction. The upper left hand figure shows the specific internal energy error field. From left to right the three boxes indicate averaging regions about the reflected shock, deflected contact, and transmitted shock. It is significant to note that the discrete distribution is well fit by a Gaussian. The Kolmogorov-Smirnov statistic, which is the L^∞ distance between the N(0,1) cumulative distribution and the normalized

Downloaded 03 Jun 2010 to 171.66.16.150. Redistribution subject to ASME license or copyright; see http://www.asme.org/terms/Terms_Use.cfm

empirical distribution of the sample, shows that the probability differences between the Gaussian fit and kernel density estimate are less than 10 percent. Although the deviation from Gaussian is statistically significant, the relatively small value for the Kolmogorov-Smirnov statistic is encouraging for the development of approximately Gaussian models for the space-time averaged solution error.

Solution errors can be roughly divided into two classes, position errors, *i.e.*, errors in wave velocity, and local errors about the waves. As we have seen, significant error is generally associated with the presence of a wave, or equivalently a large flow gradient. Consider a fixed location in space and time. We divide the simulation ensemble into two populations depending on whether or not the given location lies within a wave profile at the given time. Only those elements of the ensemble with wave profiles crossing this location will generate significant errors in that location. We employ a filter to separate these two populations, and analyze the wave localized errors, *i.e.*, the errors conditioned on being located within a wave. The filter is constructed as follows. Given a discrete time level i, a spatial mesh index j, and a given realization, let $\mathbf{s}_j^i=(\rho_j^i,v_j^i,e_j^i)$ denote the state in this mesh block. For a specified spatial offset m (here $m=3$), we solve the Riemann problem with data $\mathbf{s}_{j-m}^i$ and $\mathbf{s}_{j+m}^i$. The solution to this Riemann problem yields a set of wave strengths $W_j^i(k)$, where $k=-1,0,1$ corresponding to the backward, contact, or forward wave family, respectively. A variety of measures of wave strength are possible, here we use the quantity:

$$W_j^i(k)=\frac{|\Delta P|}{P_a}+\frac{|\Delta\rho|}{2\overline{\rho}},$$

where Δ denotes the jump across the wave, P_a is the pressure ahead of the wave, and $\overline{\rho}$ is the average of the density on either side of the wave. We then compute normalized wave strengths:

$$w_j^i(k)=\frac{W_j^i(k)}{W_j^i(-1)+W_j^i(0)+W_j^i(1)},$$

and say that the mesh block (i,j) lies inside a wave of family k if $w_j^i(k)$ is greater than twice the maximum of the other two wave strengths. The width of a wave is defined as the width of the region of cells inside that wave, and the wave position is the midpoint of the width interval. The filter is defined relative to the coarse grid wave width region, *i.e.*, a realization from the ensemble is taken to be within the wave localized population at the given point if this location lies inside the coarse grid wave profile.

When conditioned upon being in a specific wave we find that error magnitude is nearly independent of the mesh spacing and comparable to the jump discontinuity in the solution. The errors are also nearly constant in time, except during periods of wave interactions. Table 4 shows conditional error statistics for the reflected shock, contact, and transmitted shock from the step up 1 simulation using tracking.

Table 5 shows the mean widths for the principal waves at time 1.26. Since all three waves were tracked for the simulations shown, their widths are all approximately equal to Δx. Results for captured waves (not shown) would show an approximately time constant shock width of a few mesh blocks and a contact width that increases in time.

In Fig. 7 we plot mean errors in the contact position (left) and the shock arrival time at the wall (right). The contact location and the shock arrival time are both potentially observable quantities. Such observations lead to a Bayesian posterior. We note that the simulation errors in these observables are more sharply localized than is the spread in the observable quantities associated with the variation within the ensemble, see Table 5. The fact that the ensemble mean width is larger than a single realization wave width means that a posterior distribution constructed on the basis of observation of wave position or arrival time is more informative than the prior. As a result, wave position and arrival time observations will result in a refinement of the ensemble. The posterior would be strictly more informative than the prior, leading to a prediction of improved precision.

Figure 8 plots localized error statistics for specific internal energy. Except during periods of wave interactions, such as the initial shock-contact collision or when the wall reflection collides with the contact, the statistics are generally consistent with a Gaussian approximation, skewness relatively small, and kurtosis approximately equal to three.

6 Conclusions

We have presented a general framework for uncertainty quantification applicable to multiscale simulations. The Bayesian likelihood is determined by a probability model for the solution and measurement errors. In the case of numerical simulation errors, which are the focus of attention here, the probability model is constructed on the basis of numerical experiments.

Two examples were discussed. The first concerns flow in porous media. The multiscale aspects of the simulation are addressed through up scaling. Predictions with confidence intervals are constructed. This construction is formally exact within the mathematical framework employed, and is verified by observing that the true solution lies within the confidence interval approximately the expected number of times. Some details and approximations in this study are documented in the cited literature, but omitted here in the interests of brevity.

The second example concerns shock wave physics. We identify a fundamental paradigm for the analysis of solution errors in shock physics simulations: the stochastic Riemann problem. We have analyzed several versions of the stochastic Riemann problem, one of which is reported here. We have observed approximate Gaussian behavior for errors in wave location and arrival times and for local space time averages of pointwise errors. The Gaussian property holds up to about 1.5σ (data not shown here), and the occurrence of larger errors has a definitely sub Gaussian character. We also observed that solution errors were significantly smaller than the ensemble variability for the problem and ensemble considered. This fact will support a nontrivial posterior, with resulting improved prediction, uncertainty quantification and confidence intervals.

References

[1] S. French and J. Q. Smith, eds., 1997, *The Practice of Bayesian Analysis*, Arnold, London.

[2] Hadamard, J., 1936, ''Equations aux dérivées partielles. les conditions définies en général. le cas hyperboliqaue,'' Enseignement Math., **35**, pp. 5–42.

[3] R. Courant and D. Hilbert, 1962, *Methods of Mathematical Physics II*. Interscience, New York.

[4] J. Glimm and D. H. Sharp, 1997, ''Stochastic partial differential equations: Selected applications in continuum physics,'' R. A. Carmona and B. L. Rozovskii, eds., *Stochastic Partial Differential Equations: Six Perspectives*, Mathematical Surveys and Monographs, American Mathematical Society, Providence.

[5] Glimm, J., and Sharp, D. H., 1997, ''Multiscale science,'' SIAM News, Oct.

[6] Glimm, J., and Sharp, D. H., 1998, ''Stochastic methods for the prediction of complex multiscale phenomena,'' Q. Appl. Math., **56**, pp. 741–765.

[7] Glimm, J., and Sharp, D. H., 1999, ''Prediction and the quantification of uncertainty,'' Physica D, **133**, pp, 152–170.

[8] I. Babuska, A. Miller, and M. Vogelius, 1983, ''Adaptive methods and error estimation for elliptic problems of structural mechanics,'' In I. Babuska, J. Chandra, and J. Flaherty, eds., *Adaptive Computational Methods for Partial Differential Equations*, pp. 57–73. SIAM, Philadelphia.

[9] Babuska, I., and Rheinboldt, W., 1978, ''Error estimates in adaptive finite element computations,'' SIAM (Soc. Ind. Appl. Math.) J. Numer. Anal., **15**, pp. 736–754.

[10] Cockburn, B., 1998, ''A simple introduction to error estimation for nonlinear hyperbolic conservation laws,'' Technical report, University of Minnesota.

[11] W. R. Gilks, S. Richardson, and D. J. Spiegelhalter, ed. 1996, *Markov Chain Monte Carlo in Practice*, Chapman and Hall, London and New York.

[12] Chu, K., Deng, Y., and Reinitz, J., 1999, ''Parallel simulated annealing by mixing of states,'' J. Comput. Phys., **148**, pp. 646–662.

[13] McKay, M. D., Conover, W. J., and Beckman, R. J., 1979, ''A comparison of three methods for selecting values of INput variables in the analysis of output from a computer code,'' Technometrics, **21**, pp. 239–245.

Downloaded 03 Jun 2010 to 171.66.16.150. Redistribution subject to ASME license or copyright; see http://www.asme.org/terms/Terms_Use.cfm

[14] Stein, M., 1987, ''Large sample properties of simulations using latin hypercube sampling,'' Technometrics, **29**, pp. 143–151.
[15] Owen, A. B., 1992, ''Orthogonal arrays for computer experiments, integration and visualization,'' Statistica Sinica, **2**, pp. 439–452.
[16] Tanveer, S., 1993, ''Singularities in the classical Rayleigh-Taylor flow: Formation and subsequent motion,'' Proc. R. Soc. London, Ser. A, **441**, pp. 501–525.
[17] Ye, K. Q., 1998, ''Column orthogonal latin hypercube design and their application in computer experiments,'' J. Am. Stat. Assoc., **93**, pp. 1430–1439.
[18] Owen, A. B., 1994, ''Lattice sampling revised: Monte carlo variance of means over randomized orthogonal arrays,'' Appl. Ocean. Res., **22**, pp. 930–945.
[19] Harald Niederreiter, 1992, *Random number generation and quasi-Monte Carlo methods*, Society for Industrial and Applied Mathematics (SIAM), Philadelphia, PA.
[20] J. R. Koehler and A. B. Owen, 1996, ''Computer experiments,'' *Design and analysis of experiments*, pp. 261–308, North-Holland, Amsterdam.
[21] Sacks, J., Welch, W., Mitchell, T., and Wynn, P., 1989, ''Design and analysis of computer experiments,'' Stat. Sci., **4**, pp. 409–435.
[22] Cheng, B., Glimm, J., and Sharp, D. H., 2000, ''Density dependence of Rayleigh-Taylor and Richtmyer-Meshkov mixing fronts,'' Phys. Lett. A, **268**, pp. 366–374.
[23] Wallstrom, T., Hou, S., Christie, M. A., Durlofsky, L. J., and Sharp, D. H., 1999, ''Accurate scale up of two phase flow using renormalization and nonuniform coarsening,'' Comput. Geosci., **3**, pp. 69–87.
[24] T. Wallstrom, S. Hou, M. A. Christie, L. J. Durlofsky, and D. H. Sharp, 1999, ''Application of a new two-phase upscaling technique to realistic reservoir cross sections,'' *Proceedings of the SPE 15th Symposium on Reservoir Simulation*, pp. 451–462, SPE 51939.
[25] Wallstrom, T., Hou, S., Christie, M. A., Durlofsky, L. J., Sharp, D. H., and Zou, Q., 2001, ''Effective medium boundary conditions for upscaling relative permeabilities,'' Transp. Porous Media, Accepted for Publication.
[26] M. A. Christie, T. C. Wallstrom, L. J. Durlofsky S. Hou, D. H. Sharp, and Q. Zou, 2000, ''Effective medium boundary conditions in upscaling,'' *Proceedings of the 7th European Conference on the Mathematics of Oil Recovery, Baveno, Italy, Sept. 5–8.*
[27] J. Glimm, S. Hou, H. Kim, D. Sharp, and K. Ye, 1999, ''A probability model for errors in the numerical solutions of a partial differential equation,'' *CFD Journal*, 9, 2000. Proceedings of the 8th International Symposium on Computational Fluid Dynamics, Bremen, Germany, SUNY-SB Preprint Number SUNYSB-AMS-99-11.
[28] Glimm, J., Hou, S., Kim, H., Lee, Y., Sharp, D., Ye, K., and Zou, Q., 2000, ''Risk management for petroleum reservoir production: A simulation-based study of prediction,'' Report No. SUNYSB-00-12, State University of New York at Stony Brook, J. Comp. Geosciences (to appear).
[29] J. Glimm, S. Hou, Y. Lee, D. Sharp, and K. Ye, 2001. ''Prediction of oil production with confidence intervals,'' SPE 66350, SPE Reservoir Simulation Symposium held in Houston, Texas, 11–14 Feb.
[30] R. Richtmyer and K. Morton, 1967, *Difference Methods for Initial Value Problems*, Interscience, New York, second edition.
[31] E. Godlewski and P. A. Raviart, 1991, *Numerical Approximation of Hyperbolic Systems of Conservation Laws*, Springer Verlag, New York.
[32] Riemann, B., 1958, ''Uber die fortpflanzung ebener luftwellen von endlicher schwingungsweite,'' Göttingen Abhandlungen, **8**, pp. 43.
[33] Glimm, J., 1965, ''Solutions in the large for nonlinear hyperbolic systems of equations,'' Commun. Pure Appl. Math., **18**, pp. 697–715.
[34] Glimm, J., and Sharp, D., 1986, ''An S-matrix theory for classical nonlinear physics,'' Found. Phys., **16**, pp. 125–141.
[35] Goduno, S. K., 1959, ''A difference method for numerical calculation of discontinuous solutions of the equations of hydrodynamics,'' Mat. Sb., **47**, pp. 271–306.
[36] van Leer, B., 1979, ''Towards the ultimate conservative difference scheme: V. A second order sequel to Godunov's method,'' J. Comput. Phys., **32**, pp. 101–136.
[37] R. J. LeVeque, J. O. Langseth, M. Berger, and S. Mitran, ''CLAWPACK, conservation law package,'' http://www.amath.washington.edu/~claw/.
[38] O'Rourke, P. J., and Sahota, M. S., 1998, ''A variable explicit/implicit numerical method for calculating advection on unstructured meshes,'' J. Comput. Phys., **143**, p. 312.
[39] DeVolder, B. G., Sahota, M. S., and Cline, M. C., 2000, ''Verification of the CHAD hydrodynamics code,'' Report No. LA-UR-00-6039, Los Alamos National Laboratory, Los Alamos, NM.
[40] Grove, J. W., 1994, ''Applications of front tracking to the simulation of shock refractions and unstable mixing,'' J. Appl. Num. Math., **14**, pp. 213–237.
[41] Glimm, J., Grove, J. W., Li, X. L., Oh, W., and Sharp, D. H., 2001, ''A critical analysis of Rayleigh-Taylor growth rates,'' J. Comput. Phys., **169**, pp. 652–677, LANL report No. LA-UR-99-5582.
[42] The MathWorks. MATLAB. http://www.mathworks.com/.
[43] M. P. Wand and M. C. Jones, 1995, *Kernel Smoothing*. Chapman & Hall, 2–6 Boundary Row, London SE1 8HN, UK.

Downloaded 03 Jun 2010 to 171.66.16.150. Redistribution subject to ASME license or copyright; see http://www.asme.org/terms/Terms_Use.cfm

Probabilistic Modeling of Flow Over Rough Terrain

Roger Ghanem
Associate Professor

Bernard Hayek
Graduate Student

Department of Civil Engineering,
The Johns Hopkins University,
Baltimore, MD 21218

This paper presents a method for the propagation of uncertainty, modeled in a probabilistic framework, through a model-based simulation of rainflow on a rough terrain. The adopted model involves a system of conservation equations with associated nonlinear state equations. The topography, surface runoff coefficient, and precipitation data are all modeled as spatially varying random processes. The Karhunen-Loeve expansion is used to represent these processes in terms of a denumerable set of random variables. The predicted state variables in the model are identified with their coordinates with respect to the basis formed by the Polynomial Chaos random variables. A system of linear algebraic deterministic equations are derived for estimating these coordinates.
[DOI: 10.1115/1.1445138]

1 Introduction

Overland flow has significant consequences on the fate of environmental pollutants as well as the performance of water supply and drainage infrastructure. The ability to accurately predict the dynamics of surface runoff can thus be critical to the design of reliable watershed management and environmental monitoring systems. A major obstacle to achieving a desirable level of accuracy derives from variabilities and heterogeneities observed over a wide spectrum of space and time scales.

Formalisms are needed that facilitate the adaptive quantification of uncertainty and of its effect on mechanics-based predictions. In addition to the more traditional quest for estimating the probability of extreme events such as failure, attention must begin to focus on estimating the confidence in model predictions and to designing adaptive schemes for improving this confidence through model refinement as well as data refinement. The possibility of performing such an adaptation can play a significant role in shaping performance-based design practice in science and engineering by quantifying the information, and its associated worth, required to achieve a target confidence in the predicted behavior of some contemplated design. The concept of combined stochastic-deterministic error and its estimation must be introduced that will permit the development of optimal numerical optimization strategies such as adaptive mesh refinement that are consistent with the level of accuracy justified by available data. Concepts must be developed that will guide the simultaneous refinement of mesh and data. Recent work in the above direction has capitalized on the possibility of developing common mathematical representations for probabilistic and deterministic approximations [1]. This has permitted the development of a framework that allows models of data to be integrated into models of computational mechanics.

A critical component of the above development consists of the ability to propagate uncertainty through model-based simulations. This problem can be conceptually described in terms of events in the set generated by the parameters of the system under investigation, being mapped into events in the set generated by the state of the system. Variability in the set of basic events induces variability in the set of predictions, with the correspondence specified through a deterministic mapping, which is typically derived from first principles by relying on a mechanistic representation of the phenomena involved. Probabilistic statements about the parameters of the model are associated, through this mapping, with probabilistic statements about the predictions of the model.

Hydrological systems involve a multitude of spatial scales, exhibiting heterogeneity and variability at both the local and regional levels. This complexity not-withstanding, hydrologic analysis and design have primarily been based on a significant level of empiricism combined with data assimilation and parameter calibration techniques [2–6] This empirical approach is often reflected in a significant scatter in the parameters of the associated predictive models. This scatter is in turn propagated into a significant level of uncertainty in the predictions from these models. An assessment of the manner in which uncertainty is propagated through predictive models of hydrological systems is essential for the ability to rely on them for risk and reliable resources management. A probabilistic context for representing the uncertainty is commonly used, placing at the disposal of the analyst a significant machinery associated with the underlying mathematical theory.

A number of techniques are available for treating this uncertainty propagation problem. While the Monte Carlo sampling and analysis procedure is essentially valid for a wide range of problems, it is computer-intensive. While this constraint is becoming increasingly insignificant, another more intrinsic drawback of the Monte Carlo approach is the fact that it does not yield a manageable representation of the predicted processes. These can be very useful for propagating the information from one computational module through a complex network of interacting modules, representing the multi-physics nature of the physical world. An alternative to the Monte Carlo procedure, and one which results in an approximate representation of the solution, is the perturbation approach [7,8]. This approach represents the prediction as a perturbation around its nominal value, usually associated with the mean deterministic problem. Perturbation techniques are known to provide reliable results only when the associated perturbations are small. Variations on the perturbation techniques have also been developed [9]. An alternative procedure, and one which capitalizes on the mathematical foundation of probability theory will be implemented in the present analysis. It consists of representing the random variables and processes associated with the problem in terms of convergent expansions in a manner similar to the representations common to deterministic approximation theory [10–14].

In the next section, the mechanics of overland flow and its finite element implementation are presented. Following that, numerically efficient representations of stochastic processes are reviewed. Next, the spectral stochastic finite element expansion is applied to the model. Finally, a numerical example demonstrating the methodology described in the paper is presented.

2 The Overland Flow Problem

Overland flow modeling is important for a number of applications ranging from environmental watershed pollution manage-

Contributed by the Fluids Engineering Division for publication in the JOURNAL OF FLUIDS ENGINEERING. Manuscript received by the Fluids Engineering Division September 4, 2001; revised manuscript received November 12, 2001. Associate Editor: G. Karniadakis.

 Copyright © 2002 by ASME

Downloaded 03 Jun 2010 to 171.66.16.150. Redistribution subject to ASME license or copyright; see http://www.asme.org/terms/Terms_Use.cfm

ment to urban storm routing and control. The problem also presents a challenging system of hyperbolic partial differential equations that will be used as a vehicle to demonstrate the generality of the probabilistic methodology presented in the paper. The governing equations are presented in the first part of this section along with some simplifications that are consistent with the physical phenomenon being described.

2.1 The Governing Equations. The partial differential equations governing the surface runoff problem consist of the following continuity equation,

$$\frac{\partial H}{\partial t}+\frac{\partial q_x}{\partial x}+\frac{\partial q_y}{\partial y}=r, \tag{1}$$

and the following equilibrium equations,

$$\frac{\partial q_x}{\partial t}+\frac{\partial}{\partial x}\left(\frac{q_x^2}{h}\right)+\frac{\partial}{\partial y}\left(\frac{q_x q_y}{h}\right)=\frac{\partial p}{\partial x}-gh\left(S_{fx}+\frac{\partial H}{\partial x}\right), \tag{2}$$

$$\frac{\partial q_y}{\partial t}+\frac{\partial}{\partial y}\left(\frac{q_y^2}{h}\right)+\frac{\partial}{\partial x}\left(\frac{q_x q_y}{h}\right)=\frac{\partial p}{\partial y}-gh\left(S_{fy}+\frac{\partial H}{\partial y}\right), \tag{3}$$

where q_x, q_y are flow rates per unit width, S_{fx}, S_{fy} are friction slopes in the x and y directions, respectively, H is the free water surface elevation, h is the flow depth, p is the pressure, g is the gravitational acceleration, and r is the precipitation rate [2,4,15]. The above equations are based on the assumptions that the fluid is incompressible and the bottom slopes are relatively uniform. Grouping together the acceleration terms in Eqs. (2) and (3) and dividing throughout by gh the equations of motion can be rewritten as,

$$m_z-\frac{1}{gh}\frac{\partial p}{\partial z}+\left(S_{fz}+\frac{\partial H}{\partial z}\right)=0, \quad z=x,y. \tag{4}$$

In this last equation, m_z refers to the combined inertial terms. The kinematic wave assumption is next invoked to simplify the above equations. This assumption states that the inertial and pressure effects are insignificant and that the weight of the fluid is only balanced by the resistive forces of the bed friction [3,16]. Equation (4) is thus approximated by,

$$S_{fz}+\frac{\partial H}{\partial z}=0, \quad z=x,y, \tag{5}$$

Assuming steady flow conditions, the friction slope S_{fz} is estimated from the Manning's equation for uniform flow,

$$q_z=\frac{b}{n}h^{5/3}S_{fz}^{1/2}, \tag{6}$$

where n represents the Manning resistance coefficient and b is an empirically computed normalization factor equal to 1 or 1.486 depending on whether SI units or English units are used, respectively. Substituting the value of S_{fz} from Eq. (5) into Eq. (6) yields,

$$q_z=-K_z\frac{\partial H}{\partial z} \tag{7}$$

where

$$K_z=\frac{b}{n}h^{5/3}\Big/\left|\frac{\partial H}{\partial z}\right|^{1/2}. \tag{8}$$

Substituting Eq. (8) into Eq. (1) results in the governing equation of the model,

$$\frac{\partial H}{\partial t}-\frac{\partial}{\partial x}\left(K_x\frac{\partial H}{\partial x}\right)-\frac{\partial}{\partial y}\left(K_y\frac{\partial H}{\partial y}\right)=r, \quad \mathbf{x},\mathbf{y}\in\Omega, \tag{9}$$

where

$$K_x=\frac{b}{n}h^{5/3}\Big/\left|\frac{\partial H}{\partial x}\right|^{1/2} \quad K_y=\frac{b}{n}h^{5/3}\Big/\left|\frac{\partial H}{\partial y}\right|^{1/2}, \tag{10}$$

subjected to the following initial and boundary conditions,

$$H(t,\mathbf{x})=T_0 \quad \mathbf{x}\in\Gamma_1, \quad -K\frac{\partial H}{\partial n}=q_b \quad \mathbf{x}\in\Gamma_2, \tag{11}$$

where H is the free water elevation, Ω represents the spatial extent of the problem, Γ_1 and Γ_2 represent, respectively, portions on the boundary where essential and natural boundary conditions are applied, and $\mathbf{x}$, $\mathbf{y}$ are the spatial coordinates. In what follows, the topographic elevation of the surface, the Manning coefficient, and the rain intensity will all be modeled as stochastic processes with spatially varying random fluctuations.

The numerical approximation of the solution to Eq. (9) is developed in accordance with the finite element method, and equality in Eq. (9) is construed as equality in the weak sense. Multiplying this equation by a test function w and invoking the divergence theorem results in,

$$\begin{aligned}\int_\Omega\left[w\frac{\partial H}{\partial t}+\frac{\partial w}{\partial x}K_x\frac{\partial H}{\partial x}+\frac{\partial w}{\partial y}K_y\frac{\partial H}{\partial y}-r\right]dxdy\\ =\oint_\Gamma wK_x\frac{\partial H}{\partial x}n_x ds+\oint_\Gamma wK_y\frac{\partial H}{\partial y}n_y ds\\ =q_b\end{aligned} \tag{12}$$

where K_z is given by:

$$K_z=\frac{b}{n}(H-T)^{5/3}\Big/\left|\frac{\partial H}{\partial z}\right|^{1/2}, \quad z=x,y, \tag{13}$$

where T is the topographic elevation of the ground surface to which the model is being applied. By choosing the test functions to be polynomials with local support, and projecting the solution on the finite dimensional span of these polynomials, the above integration is reduced to integration over subdomains, $\Omega^{(e)}$, in Ω.

3 Representation of Stochastic Processes

The integration of stochastic processes into the numerical solution of differential equations, requires their representation in efficient and computationally tractable schemes. When viewed as measurable functions, elements of a Hilbert space, random variables can be approximated by their projections on subspaces spanned by appropriate basis sets. In this section, two such approximation procedures are reviewed, consisting, respectively, of the Karhunen-Loeve and the Polynomial Chaos representations [11,13,14].

3.1 The Karhunen-Loeve Expansion. When second-order statistical information in the form of a correlation function, is available regarding a stochastic process, the Karhunen-Loeve expansion can be used to optimally discretize it in terms of a denumerable set of uncorrelated random variables. The expansion hinges on the spectral decomposition of the covariance function which is, by definition, symmetrical and positive definite. Accordingly, and using the argument θ to label probabilistic quantities, a stochastic process, $T(\mathbf{x},\theta)$ is represented as,

$$T(\mathbf{x},\theta)=\overline{T}(\mathbf{x})+\sum_{i=1}^{n}\sqrt{\lambda_i}\xi_i(\theta)\phi_i(\mathbf{x}) \tag{14}$$

where $\overline{T}(\mathbf{x})$ denotes the mean value of the process at a point $\mathbf{x}$ in its spatial domain of definition, $\xi_i(\theta)$ denotes a set of uncorrelated random variables and λ_i and $\phi_i(\mathbf{x})$ denote the eigenvalues and eigenfunctions of the covariance kernel obtained as the solution to the following integral eigenvalue problem,

Downloaded 03 Jun 2010 to 171.66.16.150. Redistribution subject to ASME license or copyright; see http://www.asme.org/terms/Terms_Use.cfm

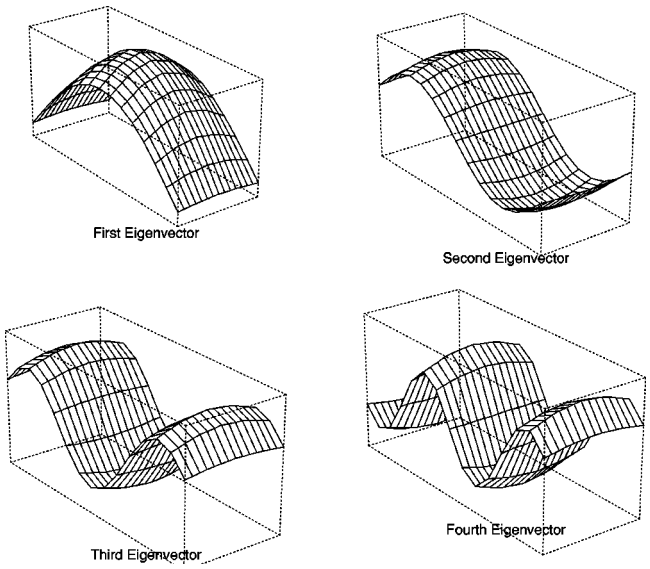

Fig. 1 Three first four normalized eigenvectors ($b=25$)

$$\int_{\Omega} R_{TT}(\mathbf{x}_1,\mathbf{x}_2)\phi_i(\mathbf{x}_2)d\mathbf{x}_2=\lambda_i\phi_i(\mathbf{x}_1). \tag{15}$$

In this last equation, Ω denotes the spatial extent of the problem. Note that in the case of a Gaussian process, the random variables $\{\xi_i\}$ form a set of independent normal random variables.

As an example of using the Karhunen-Loeve expansion, Fig. 1 shows the first four normalized eigenvectors corresponding to the covariance function given by the equation

$$R_{TT}=\sigma_T^2 e^{-|\mathbf{x}_1-\mathbf{x}_2|/b}, \tag{16}$$

where σ_T^2 denotes the variance of the process and b its correlation length, and $|\mathbf{x}_1-\mathbf{x}_2|$ denotes the euclidian distance between the two spatial locations $\mathbf{x}_1$ and $\mathbf{x}_2$. This model of the correlation function clearly implies an assumed isotropy in the stochastic process being represented. In this figure, the horizontal axes correspond to the spatial extent being investigated and the vertical axis corresponds to the normalized magnitude of the eigenfunctions. These eigenfunctions can be thought of as the deterministic scales of fluctuation contributing to the randomness of the stochastic process. Figure 2 shows the corresponding eigenvalues for two different correlation lengths. The monotonic decay of the eigenvalues is the result of the positive-definiteness of the covariance kernel. It should noted that the rate of decay is related to the correlation length of the process in question.

3.2 The Polynomial Chaos Decomposition. As clearly indicated in the previous section, information regarding a stochastic process, in the form of its covariance structure, permits the customization of a representation that is optimal for that process. In many situations, however, such information is not known a-priori, such as in the case of the predictions from a model-based simulation. In such cases, a generic basis in the vector space of random variables can be identified and used for their representation. The Polynomial Chaos [11] decomposition provides the basic construction of such a basis. In essence, the Polynomial Chaos decomposition states that the set of random variables consisting of multi-dimensional Hermite polynomials in Gaussian variables forms a basis in the vector space of second-order random variables. These are the random variables with finite variance. The Polynomial Chaos representation is mean-square convergent. A random variable $H(\theta)$ can therefore be represented as,

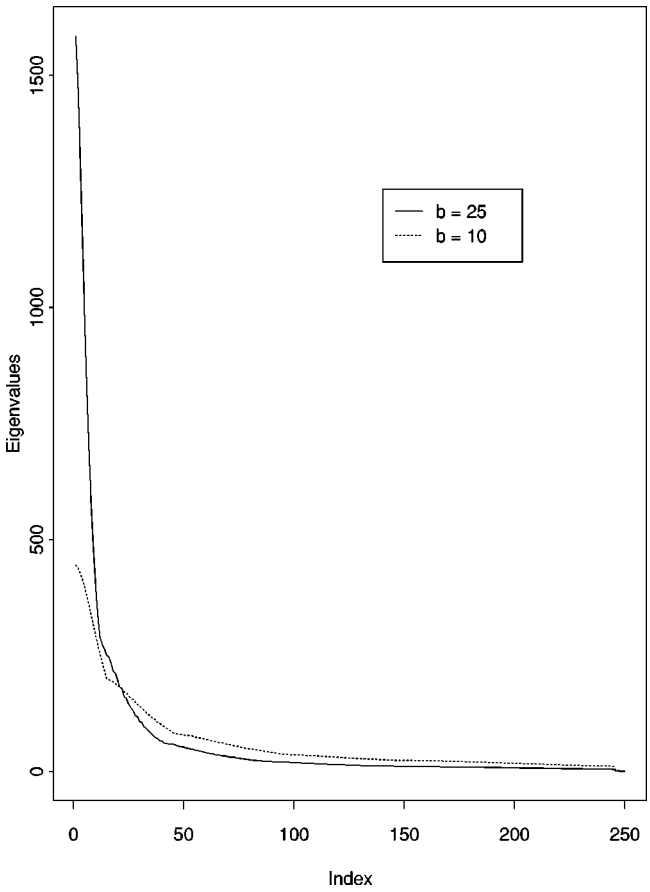

Fig. 2 The eigenvalues associated with the shapes of Fig. 1

Table 1 Four-dimensional polynomial chaos

ith Polynomial chaos	Order of polynomial chaos	Ψ_i	$\langle\Psi_i^2\rangle$
0	0	1	1
1	1	ξ_1	1
2		ξ_2	1
3		ξ_3	1
4		ξ_4	1
5	2	ξ_1^2-1	2
6		$\xi_1\xi_2$	1
7		$\xi_1\xi_3$	1
8		$\xi_1\xi_4$	1
9		ξ_2^2-1	2
10		$\xi_2\xi_3$	1
11		$\xi_2\xi_4$	1
12		ξ_3^2-1	2
13		$\xi_3\xi_4$	1
14		ξ_4^2-1	2

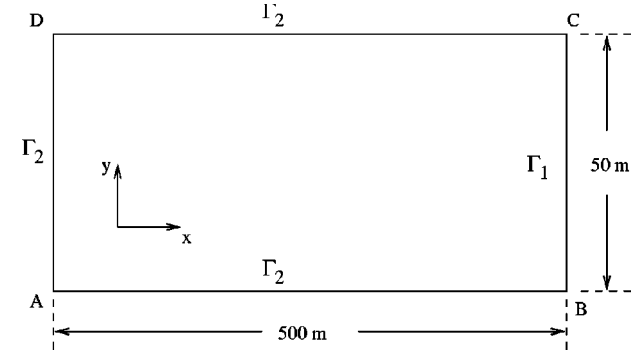

Fig. 3 The spatial domain of the problem

Downloaded 03 Jun 2010 to 171.66.16.150. Redistribution subject to ASME license or copyright; see http://www.asme.org/terms/Terms_Use.cfm

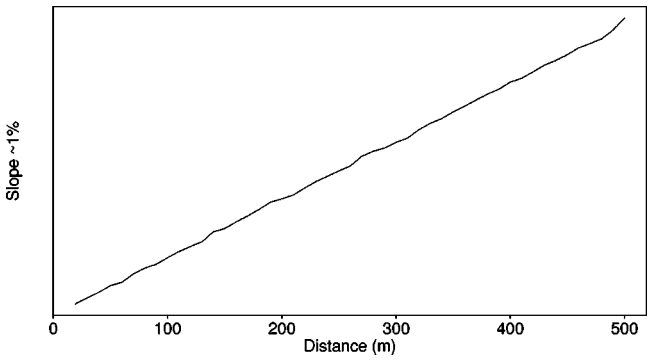

Fig. 4 The elevation profile of the surface

$$H(\theta)=a_0\Gamma_0+\sum_{i_1=1}^{\infty} a_i\Gamma_1[\xi_{i_1}(\theta)] + \sum_{i_1=1}^{\infty}\sum_{i_2=1}^{i_1} a_{i_1 i_2}\Gamma_2[\xi_{i_1}(\theta),\xi_{i_2}(\theta)]+\ldots, \quad (17)$$

where $\Gamma_n[\xi_{i_1}(\theta),\ldots,\xi_{i_n}(\theta)]$ represents the multi-dimensional Hermite polynomial of order n in the variables $(\xi_{i_1},\ldots,\xi_{i_n})$. If a one-to-one mapping to a set ordered indices $\{\Psi_i\}$ is introduced, the polynomial chaos expansion can be rewritten as,

$$H(\theta)=\sum_{i=1}^{M} H_i\Psi_i(\theta) \quad (18)$$

where the representation has been truncated after the Mth term. Table 1 shows few terms of the four-dimensional polynomial chaos [11].

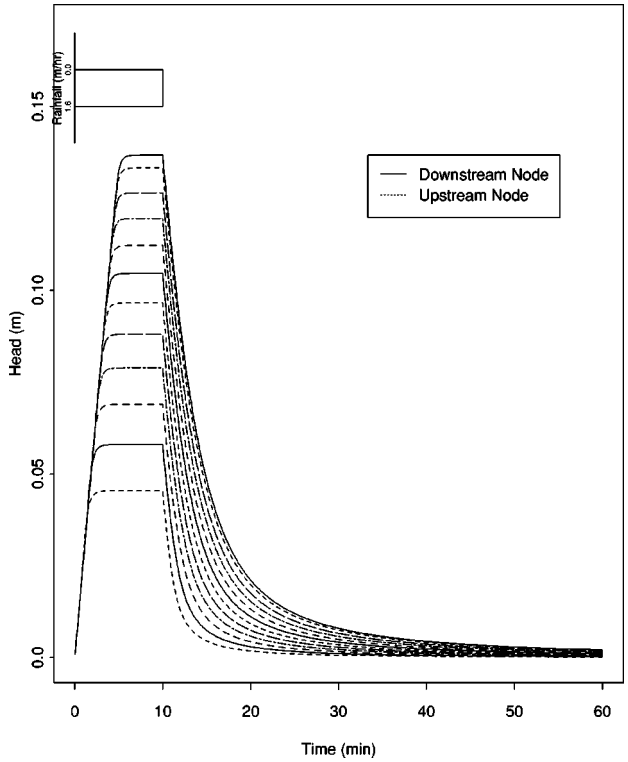

Fig. 5 Mean of H; COV=0.1 for all parameters

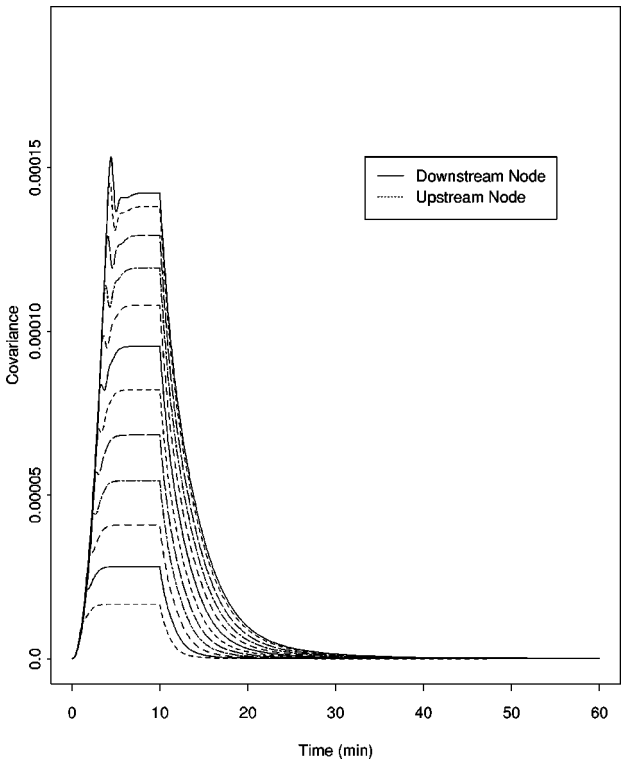

Fig. 6 Standard Deviation of H; COV=0.1 for all parameters

The coefficients H_i's in the expansion are evaluated by means of a weighted residual scheme presented in the following section. Once these coefficients have been computed, a complete probabilistic characterization of the process H is obtained.

4 Implementation of the Spectral Expansion to the Model

In this problem, T, n and r are modeled as independent random processes and will be treated according to the presentation in Section (3.1). Accordingly, these quantities are expanded as follows,

$$T(\mathbf{x},\theta)=\overline{T}(\mathbf{x})+\sum_{i=1}^{N_t}\xi_i(\theta)T_i(\mathbf{x})=\sum_{i=0}^{N_t}\xi_i(\theta)T_i(\mathbf{x}),$$

$$n(\mathbf{x},\theta)=\overline{n}(\mathbf{x})+\sum_{i=1}^{N_n}\xi_i(\theta)n_i(\mathbf{x})=\sum_{i=0}^{N_n}\xi_i(\theta)n_i(\mathbf{x}), \quad (19)$$

$$r(\mathbf{x},\theta)=\overline{r}(\mathbf{x})+\sum_{i=1}^{N_r}\xi_i(\theta)r_i(\mathbf{x})=\sum_{i=0}^{N_r}\xi_i(\theta)r_i(\mathbf{x}),$$

where T_i, n_i, and r_i are the product of the ith eigenfunction by the square root of the corresponding ith eigenvalue of the corresponding process. Note that $\xi_0=1$ and the random variables ξ_i appearing in each of the above equations are independent from those appearing in the others due to the assumption of independence between the processes T, n and r. Moreover, upon defining $N=N_t+N_n+N_r$, the above expansions can be rewritten as,

$$T(\mathbf{x},\theta)=\sum_{i=0}^{N}\xi_i(\theta)T_i(\mathbf{x}), \quad T_i=0, \quad i>N_t,$$

$$n(\mathbf{x},\theta)=\sum_{i=0}^{N}\xi_i(\theta)n_i(\mathbf{x}), \quad n_i=0, \quad N_n<i\leqslant N_t, \quad i\neq 1, \quad (20)$$

Downloaded 03 Jun 2010 to 171.66.16.150. Redistribution subject to ASME license or copyright; see http://www.asme.org/terms/Terms_Use.cfm

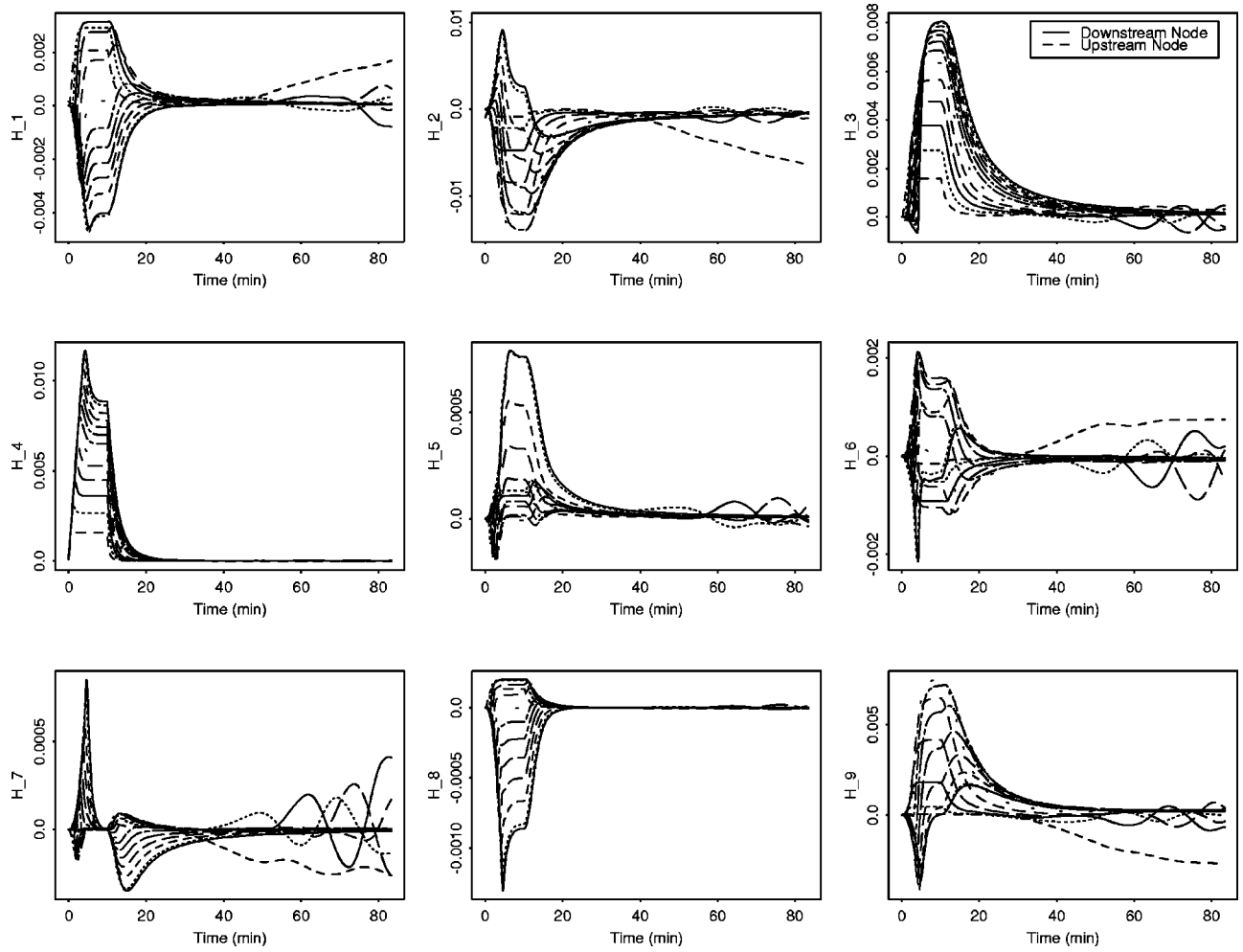

Fig. 7 Coefficients from the expansion of H; COV=0.1 for all parameters; Correlation length $b=500$

$$r(\mathbf{x},\theta)=\sum_{i=0}^{N}\xi_i(\theta)r_i(\mathbf{x}),\quad r_i=0,\quad i\leqslant N_n,\quad i\neq 1.$$

which will be substituted in the model equations (9)–(11). In order to yield a computationally tractable implementation, K_z, which is nonlinear function of the defining random process is represented in an expansion similar to those in Eq. (20). This is achieved by first expanding $K_z(H,T,n)$ in a Taylor series around the mean values of H, T, and n, resulting in

$$K_z\approx K_z(\overline{H},\overline{T},\overline{n})+\left.\frac{\partial K_z}{\partial H}\right|_{(\overline{H},\overline{T},\overline{n})}(H-\overline{H})+\left.\frac{\partial K_z}{\partial T}\right|_{(\overline{H},\overline{T},\overline{n})}(T-\overline{T})+\left.\frac{\partial K_z}{\partial n}\right|_{(\overline{H},\overline{T},\overline{n})}(n-\overline{n})+O(H,T,n). \tag{21}$$

After evaluating the partial derivatives, $\partial K_z/\partial H$, $\partial K_z/\partial T$, and $\partial K_z/\partial n$, at the mean values of the variables H, T and n, respectively, these variables are replaced by their corresponding expansions from Eqs. (18) and (20). After substitution and simplification, K_z is rewritten as follows,

$$K_z=\sum_{i=0}^{M}\overline{K_{zi}}\Psi_i. \tag{22}$$

Clearly, accuracy of this approximation can be improved by either including a higher order Taylor expansion in the approximation, or by computing the coefficients in Eq. (22) directly through a spectral projection on the Polynomial Chaos basis [17]. Substituting the above expansion along with the expansion of r from Eq. (20) into Eq. (12) yields,

$$\int_\Omega\left[w\frac{\partial H}{\partial t}+\frac{\partial w}{\partial x}\left(\sum_{i=0}^{M}K_{xi}\Psi_i\right)\frac{\partial H}{\partial x}+\frac{\partial w}{\partial y}\left(\sum_{i=0}^{M}K_{yi}\Psi_i\right)\frac{\partial H}{\partial y}-\sum_{i=0}^{N}r_i\xi_i\right]dxdy=q_b. \tag{23}$$

Choosing the test functions w to be polynomials with bounded support and projecting the above equation on the span of these polynomials, results in the following finite element projection of Eq. (23),

$$\mathbf{C}\dot{\mathbf{H}}+\sum_{i=0}^{M}\Psi_i\mathbf{K}_i\mathbf{H}-\sum_{i=0}^{N}\xi_i\mathbf{F}_i=\mathbf{q} \tag{24}$$

where $\mathbf{C}$, $\mathbf{K}_i$, and $\mathbf{F}_i$ are obtained from assembling their element-level counterparts given by,

$$\mathbf{C}^{(e)}=\int_{\Omega^{(e)}}\mathbf{N}\mathbf{N}^T d\mathbf{A}$$

$$\mathbf{K}_i^{(e)}=\int_{\Omega^{(e)}}\nabla\mathbf{N}^T\mathbf{K}_i\nabla\mathbf{N}d\mathbf{A} \tag{25}$$

Downloaded 03 Jun 2010 to 171.66.16.150. Redistribution subject to ASME license or copyright; see http://www.asme.org/terms/Terms_Use.cfm

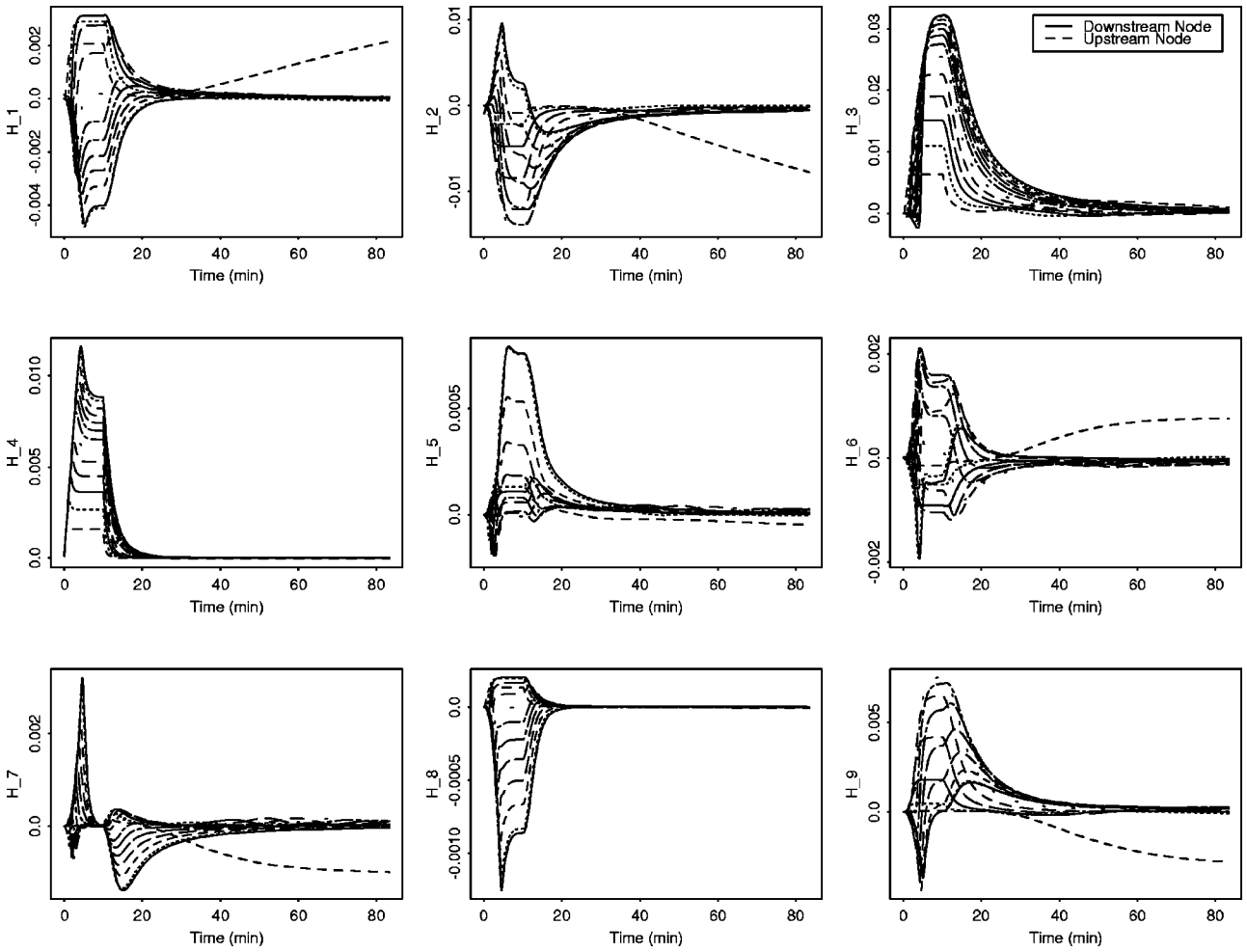

Fig. 8 Coefficients from the expansion of H; COV topography=0.1; COV Manning coefficient=0.4; COV rain=0.1; Correlation length $b=500$

$$\mathbf{F}_i^{(e)} = \int_{\Omega^{(e)}} \mathbf{N}\mathbf{N}^T r_i \mathbf{A}$$

and the right-hand side vector $\mathbf{q}$ is obtained by assembling the element-level vectors,

$$\mathbf{q}^{(e)} = \int_{\Gamma^{(e)}} \mathbf{N} d\mathbf{\Gamma}. \tag{26}$$

In the above equations, $\mathbf{N}$ denotes a vector whose components consist of the polynomial basis functions used in projecting the partial differential equation, and Ω^e denotes the bounded subset of Ω over which the integration is nonzero. As described in Section (3.2), the solution process being the free surface elevation $\mathbf{H}$, is represented in its polynomial chaos decomposition as follows,

$$\mathbf{H} = \sum_{j=1}^{m} \Psi_j \mathbf{H}_j . \tag{27}$$

Substituting this expansion into Eq. (24) yields,

$$\sum_{j=0}^{M} \Psi_j \mathbf{C}\dot{\mathbf{H}}_j + \sum_{j=0}^{M}\sum_{i=0}^{M} \Psi_i \Psi_j \mathbf{K}_i \mathbf{H}_j - \sum_{i=0}^{N} \xi_i \mathbf{F}_i = \mathbf{q}, \tag{28}$$

multiplying this last equation by Ψ_k and taking the ensemble averages, the following deterministic system of equations is obtained,

$$\sum_{j=0}^{M} \langle \Psi_j \Psi_k \rangle \mathbf{C}\dot{\mathbf{H}}_j + \sum_{j=0}^{M}\sum_{i=0}^{M} \langle \Psi_i \Psi_j \Psi_k \rangle \mathbf{K}_i \mathbf{H}_j - \sum_{i=0}^{N} \langle \xi_i \Psi_k \rangle \mathbf{F}_i = \langle \Psi_k \mathbf{q} \rangle, \quad k = 0, \ldots, M. \tag{29}$$

The above system of ordinary differential equations is solved for the polynomial chaos coefficients, $\mathbf{H}_i$ of the solution process. An implicit time-stepping scheme is used along with an Euler iterative scheme to resolve the nonlinear dependencies of the problem. The mean value of the solution is given by $\mathbf{H}_0$ and its corresponding covariance matrix can be computed as,

$$\mathbf{R}_{HH} = \sum_{i=1}^{M} \mathbf{H}_i \mathbf{H}_i^T \langle \Psi_i^2 \rangle. \tag{30}$$

The variance of the solution at the nodal points can then be obtained from the diagonal entries of $\mathbf{R}_{HH}$.

5 Numerical Example

The method presented in this paper has been applied to a two-dimensional inclined surface. A plan view of the domain is shown in Fig. 3 while the profile, indicating the random fluctuations around the mean is shown in Fig. 4. The average value of the Manning coefficient is chosen to be 0.016, and the average slope of the terrain is 1 percent. The domain is subjected to a constant head boundary condition $H=T$ along the boundary Γ_1 applied

Downloaded 03 Jun 2010 to 171.66.16.150. Redistribution subject to ASME license or copyright; see http://www.asme.org/terms/Terms_Use.cfm

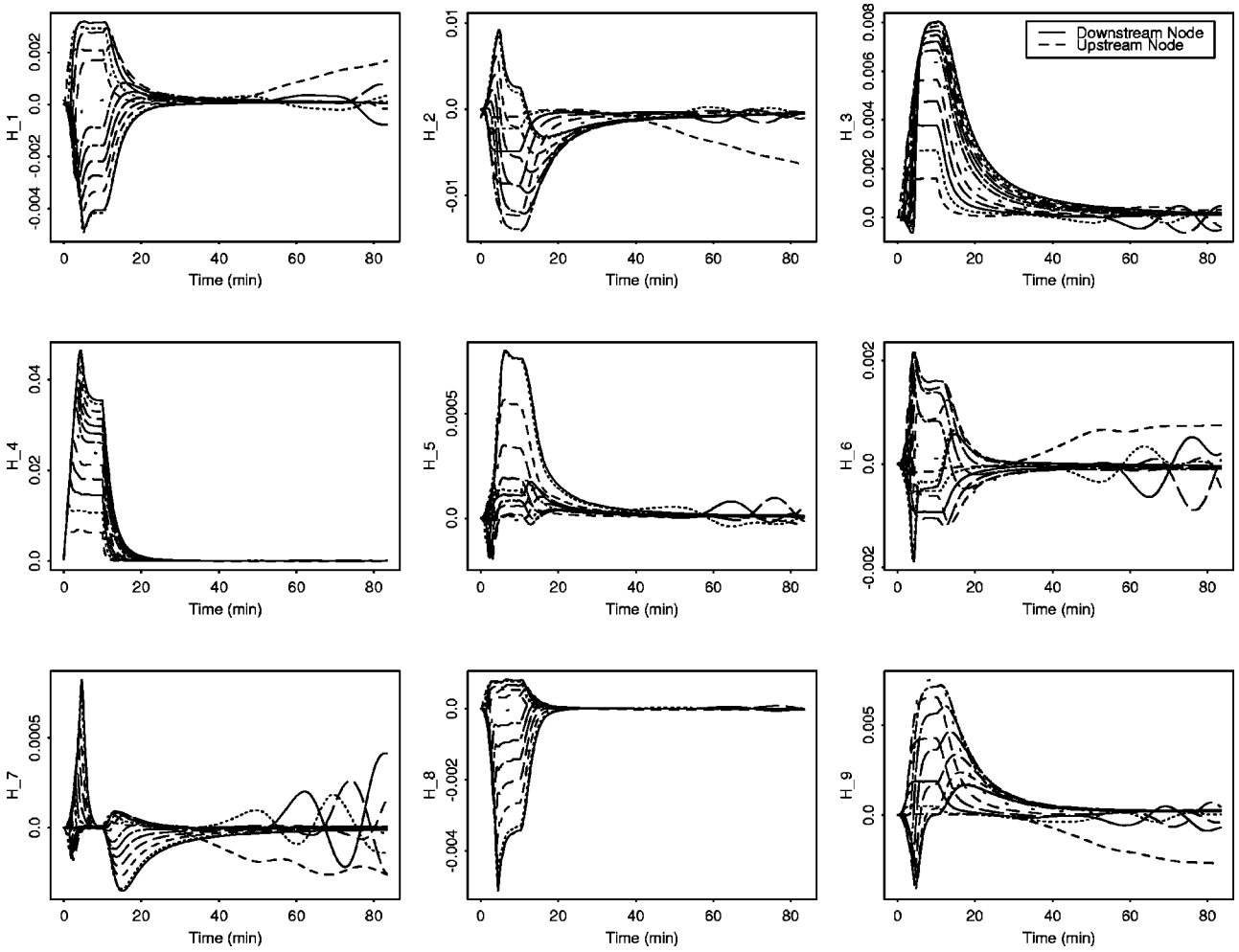

Fig. 9 Coefficients from the expansion of H; COV topography =0.1; COV Manning coefficient=0.1; COV rain=0.4; Correlation length b=500

with a probability equal to one and a flux boundary condition $q_b = c$ along the boundary Γ_2. The domain is discretized into a uniform mesh of 250 elements.

The model parameters T, n and r are all assumed to be random processes and their corresponding covariance functions are assumed to have similar form to the function in Eq. (16). For the purpose of this example problem, these three processes are represented as follows,

$$\mathbf{T} = \overline{\mathbf{T}} + \mathbf{T}_1\xi_1 + \mathbf{T}_2\xi_2 + \mathbf{0}\xi_3 + \mathbf{0}\xi_4 = \sum_{i=0}^{4} \mathbf{T}_i\xi_i$$

$$\mathbf{n} = \overline{\mathbf{n}} + \mathbf{0}\xi_1 + \mathbf{0}\xi_2 + \mathbf{n}_3\xi_3 + \mathbf{0}\xi_4 = \sum_{i=0}^{4} \mathbf{n}_i\xi_i \tag{31}$$

$$\mathbf{r} = \overline{\mathbf{r}} + \mathbf{0}\xi_1 + \mathbf{0}\xi_2 + \mathbf{0}\xi_3 + \mathbf{r}_4\xi_4 = \sum_{i=0}^{4} \mathbf{r}_i\xi_i$$

A single term representation of the Manning coefficient and the precipitation reflects their assumed uniformity over the spatial domain. They are being modeled as random variables. Two terms representation of the topography process reflects a more rapid spatial fluctuations. The above representations result in a four-dimensional polynomial chaos representation of the solution process, H. A second order four-dimensional representation is adopted for this representation resulting in,

$$\begin{aligned}\mathbf{H} = \overline{\mathbf{H}} &+ \mathbf{H}_1\xi_1 + \mathbf{H}_2\xi_2 + \mathbf{H}_3\xi_3 + \mathbf{H}_4\xi_4 + \mathbf{H}_5(\xi_1^2 - 1) + \mathbf{H}_6\xi_1\xi_2 \\ &+ \mathbf{H}_7\xi_1\xi_3 + \mathbf{H}_8\xi_1\xi_4 + \mathbf{H}_9(\xi_2^2 - 1) + \mathbf{H}_{10}\xi_2\xi_3 + \mathbf{H}_{11}\xi_2\xi_4 \\ &+ \mathbf{H}_{12}(\xi_3^2 - 1) + \mathbf{H}_{13}\xi_3\xi_4 + \mathbf{H}_{14}(\xi_4^2 - 1) \\ &= \sum_{i=0}^{14} \mathbf{H}_i\Psi_i\,. \end{aligned} \tag{32}$$

The significance of the higher order terms and their impact on the estimation of the solution process is investigated throughout this section. The results shown in the figures to follow are all plotted at equidistantly selected nodes along the longitudinal direction of the domain in Fig. 3 unless indicated otherwise. Also, the three processes making up the properties of the model are assumed to be Gaussian. Non-Gaussian processes could be integrated into the model, however they are not investigated in this particular study [14].

The evolution with time of the mean solution is shown in Fig. 5. The physical event associated with this prediction corresponds to a rainfall of constant magnitude and finite duration equal to 10 minutes as shown in the storm hyetograph included in the figure. The time evolution of the standard deviation is shown in Fig. 6. These results correspond to a coefficient of variation equal to 0.1 in all three random processes.

Figure 7 shows the results associated with all three processes, T, n, and r, having a coefficient of variation equal to 0.1. The plots

Downloaded 03 Jun 2010 to 171.66.16.150. Redistribution subject to ASME license or copyright; see http://www.asme.org/terms/Terms_Use.cfm

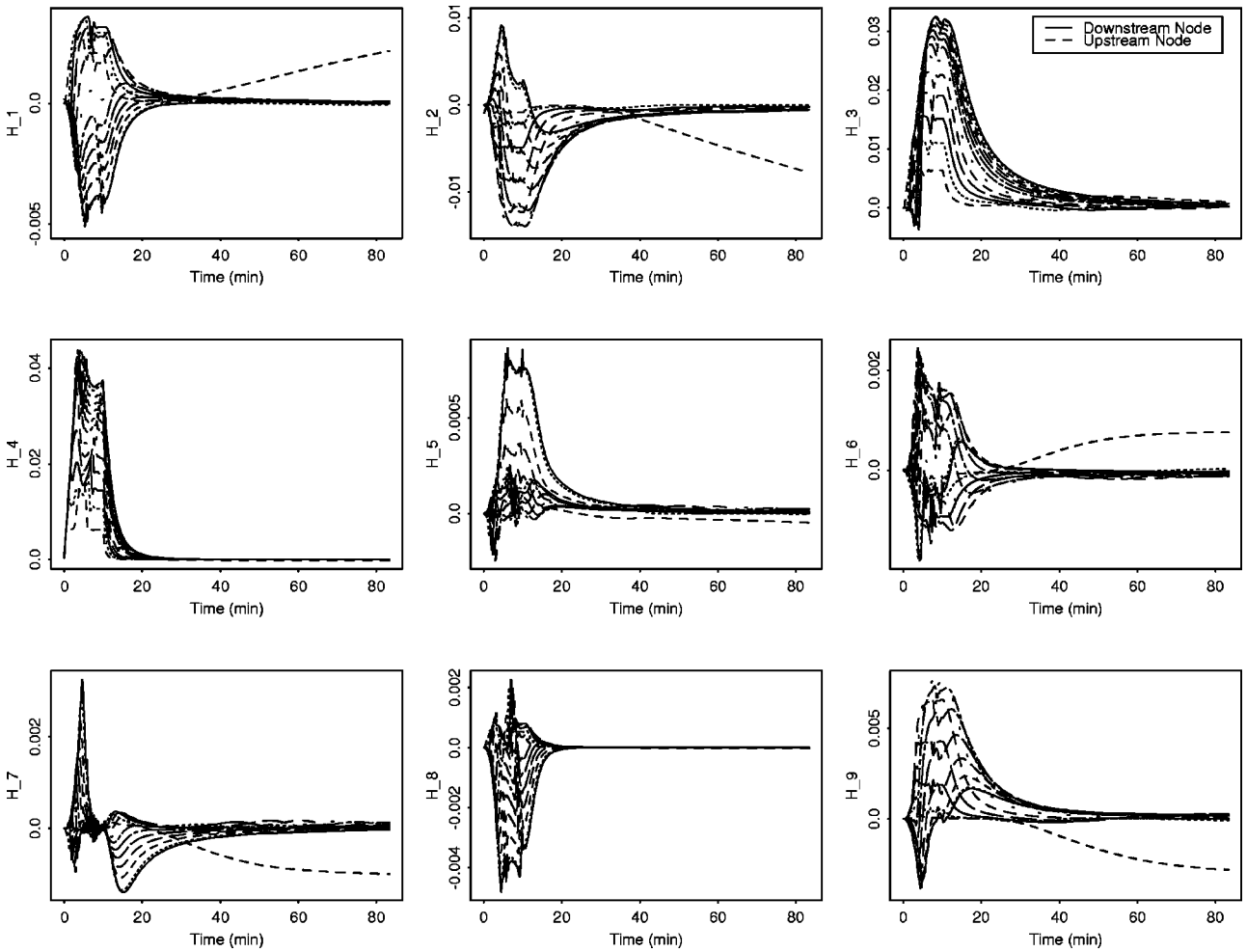

Fig. 10 Coefficients from the expansion of H; COV topography=0.1; COV Manning coefficient=0.4; COV rain=0.4; Correlation length $b=500$

are labeled according to the indices associated with the coefficients of H_i in Eq. 32. Comparing the plots of the first order terms, H_1, H_2, H_3, and H_4, it is clear that the solution is more sensitive to the topography (H_1,H_2) and the rain (H_4) than to the Manning roughness coefficient (H_3). However, after the rain ceases, H_4 drops very quickly to zero and the magnitude of H_3 then becomes comparable to that of H_2. This observation is consistent with the kinematic wave assumption used in the model which states that the gravity forces are only balanced by the resistive forces of friction along the bed. Note also that in this case, the second order terms, the H_5 and higher, are at least an order of magnitude smaller than their corresponding first order terms and their effect can be neglected in the second moment evaluations. Figure 8 shows the results associated with an increased COV of the Manning coefficient to 0.4. In this case, the Manning coefficient's contribution to the first order terms of H becomes quite significant in contrary to the observation from the previous results. Figure 9 shows the results of a reversed scenario where the COV of Manning's coefficient has been fixed at 0.1 and the COV for the rain has been increased to 0.4. The plot shows that the rain in this case dominates the higher order terms of the solution. However, in both Figs. 8 and 9, the contributions of the second order terms, H_5 and higher, are still an order of magnitude smaller than their counterparts in the first order terms of the solution making their contribution insignificant for the evaluation of the higher order moments of the solution. In Fig. 10, the COV for both the Manning coefficient and the rain have been fixed at 0.4. At this high value of COV for these two parameters, the contribution becomes comparable to that of the topographic data parameters. Such predictions are expected since at this high level of rain intensity and friction, higher water head is expected and the effect of the surface fluctuation becomes less significant. These predictions also allow us to study in more detail the limitation of the problem under severe natural conditions and whether or not the model can be accurately applied to these events.

6 Conclusion

An integration of the Karhunen-Loeve and Polynomial Chaos decompositions was implemented for the problem of surface flow over a rough terrain. The decomposition of the stochastic processes making up topographic data, Manning coefficient and rain intensity was achieved using the Karhunen-Loeve expansion. The probabilistic information regarding the predicted values of the water head over the spatial extent of the domain is computed in terms of the Polynomial Chaos decomposition of the head. This methodology for uncertainty propagation lays a mathematically sound foundation for the uncertainty quantification in the predictions from physics-based models. A sound quantification of the uncertainty is essential for reliable decision making. Moreover the format of the predicted solution, through its Chaos decomposition, lends itself easily to further manipulations required for risk and resource management.

References

[1] Ghanem, R., and Pellissetti, M., 2001, ''Adaptive data refinement in the spec-

Downloaded 03 Jun 2010 to 171.66.16.150. Redistribution subject to ASME license or copyright; see http://www.asme.org/terms/Terms_Use.cfm

tral stochastic finite element method,'' to appear, Communications in Numerical Methods in Engineering.
[2] Horton, R. E., *Surface Runoff Phenomena*, Edwards Brothers Inc., Ann Arbor, MI, 1935.
[3] Henderson, F. M., and Woodings, R. A., 1964, ''Overland Flow and Groundwater Flow from a Steady Rainfall of Finite Duration,'' J. Geophys. Res., **69**, No. 8, 1531–1540.
[4] Overton, D. E., and Meadows, M. E., 1976, *Stormwater Modeling*, Academic Press, NY, 11976.
[5] Emmerich, W. E., Woolhiser, D. A., and Shirley, D. E., 1989, ''Comparison of Lumped and Distributed Models for Chemical Transport by Surface Runoff,'' J. Environ. Qual., **18**, pp. 120–126.
[6] Bedient, P., and Huber, W., 1992, *Hydrology and Floodplain Analysis*, Addison-Wesley, 1992.
[7] Liu, W. K., Belytschko, T., and Mani, A., 1986, ''Random Field Finite Elements,'' Int. J. Numer. Methods Eng., **23**, pp. 1831–1845.
[8] Emery, A. F., and Fadale, T. D., 1997, ''Handling Temperature Dependent Properties and Boundaries Conditions in Stochastic Finite Element Analysis,'' Numer. Heat Transfer, Part A, **31**, pp. 37–51.
[9] Adomian, G., 1983, *Stochastic Systems*, Academic Press, NY.
[10] Spanos, P. D., and Ghanem, R., 1989, ''Stochastic Finite Element Expansion for Random Media,'' J. Eng. Mech., **115**, No. 5.
[11] Ghanem, R. G., and Spanos, P.D., 1991, ''Stochastic Finite Elements: A Spectral Approach,'' Springer-Verlag.
[12] Ghanem, R., and Dham, S., 1998, ''Stochastic Finite Element Analysis for Multiphase Flow in Heterogeneous Porous Media,'' Transp. Porous Media, **32**, pp. 239–262.
[13] Ghanem, R., 1998, ''Scales of fluctuation and the propagation of uncertainty in random porous media,'' Water Resour. Res., **34**, No. 9, pp. 2123–2136.
[14] Ghanem, R., 1999, ''Higher-Order Sensitivity of Heat Conduction Problems to Random Data Using the Spectral Stochastic Finite Element Method,'' ASME J. Heat Transfer, **121**, May, pp. 290–299.
[15] Hromadka, H., and Nestlinger, A. J., 1986, ''Estimating water shed S-graphs using a diffusion flow model,'' Adv. Water Resour., **8**, No. 4, pp. 214–218.
[16] Akan, A. O., and Yen, B. C., 1981, ''Diffusion-Wave Flood Routing in Channel Networks,'' J. Hydraul. Div., Am. Soc. Civ. Eng., **107**, No. HY6, June.
[17] Le Maitre, O., Knio, O., Najm, H., and Ghanem, R., 2002, ''A stochastic projection method for fluid flow: Basic formulation,'' to appear, J. Comput. Phys.

Downloaded 03 Jun 2010 to 171.66.16.150. Redistribution subject to ASME license or copyright; see http://www.asme.org/terms/Terms_Use.cfm

Stochastic Modeling of Flow-Structure Interactions Using Generalized Polynomial Chaos

Dongbin Xiu
Didier Lucor
C.-H. Su
George Em Karniadakis[1]

Division of Applied Mathematics,
Brown University,
Providence, RI 02912

We present a generalized polynomial chaos algorithm to model the input uncertainty and its propagation in flow-structure interactions. The stochastic input is represented spectrally by employing orthogonal polynomial functionals from the Askey scheme as the trial basis in the random space. A standard Galerkin projection is applied in the random dimension to obtain the equations in the weak form. The resulting system of deterministic equations is then solved with standard methods to obtain the solution for each random mode. This approach is a generalization of the original polynomial chaos expansion, which was first introduced by N. Wiener (1938) and employs the Hermite polynomials (a subset of the Askey scheme) as the basis in random space. The algorithm is first applied to second-order oscillators to demonstrate convergence, and subsequently is coupled to incompressible Navier-Stokes equations. Error bars are obtained, similar to laboratory experiments, for the pressure distribution on the surface of a cylinder subject to vortex-induced vibrations. [DOI: 10.1115/1.1436089]

1 Introduction

In the last decade there has been substantial progress in simulations of flow-structure interactions involving the full Navier-Stokes equations, e.g. [1,2]. While such simulations are useful in complementing experimental studies in the low Reynolds number range, they are based on *ideal* boundary conditions and *precisely* defined properties of the structure. In practice, such flow conditions and properties can only be defined approximately. As an example, the internal structural damping for the structure is typically taken as 1–3 percent of the critical damping since it cannot be quantified by direct measurements. It is, therefore, of great interest to formally model such uncertainty of stochastic inputs, and to formulate algorithms that reflect accurately the propagation of this uncertainty [3].

To this end, the Monte Carlo approach can be employed but it is computationally expensive and is only used as the last resort. The sensitivity method is a more economical approach, based on the moments of samples, but it is less robust and depends strongly on the modeling assumptions [4]. One popular technique is the perturbation method where all the stochastic quantities are expanded around their mean via Taylor series. This approach, however, is limited to small perturbations and does not readily provide information on high-order statistics of the response. The resulting system of equations becomes extremely complicated beyond second-order expansion. Another approach is based on expanding the inverse of the stochastic operator in a Neumann series, but this too is limited to small fluctuations, and even combinations with the Monte Carlo method seem to result in computationally prohibitive algorithms for complex systems [5].

A more effective approach pioneered by Ghanem and Spanos [6] in the context of finite elements for solid mechanics is based on a spectral representation of the uncertainty. This allows high-order representation, not just first-order as in most perturbation-based methods, at high computational efficiency. It is based on the original theory of Wiener (1938) on homogeneous chaos [7,8]. This approach was employed in turbulence in the 1960s [9–11]. However, it was realized that the chaos expansion converges slowly for turbulent fields [12–14], so the polynomial chaos approach did not receive much attention for a long time.

In more recent work [15,16] the polynomial chaos concept was extended to represent many different distribution functions. This generalized polynomial chaos approach, also referred as the Askey-chaos, employs the orthogonal polynomials from the Askey scheme [17] as the trial basis in the random space. The original polynomial chaos can be considered as a subset of the generalized polynomial chaos, as it employs Hermite polynomials, a subset of the Askey scheme, as the trial basis. In [15], the framework of Askey-chaos was proposed and convergence properties of different random bases were examined. In [16] the Askey-chaos was applied to model uncertainty in incompressible Navier-Stokes equations. Various tests were conducted to demonstrate the convergence of the chaos expansion in prototype flows.

For flow-structure interactions the interest on stochastic modeling so far has primarily been on the dynamics of lumped systems, i.e., single- or two-degree-of-freedom second-order oscillators [18,19]. The effect of the flow has been modeled via an interaction (source) term as either white noise or as a Gaussian distribution if the loading is caused by wind [20–23]. However, non-Gaussian distribution behavior for the response has been documented with *the excess index* well above or below zero (sharp or flat intermittency) [18]. For example, even for a velocity field following a Gaussian distribution, which is a reasonable assumption for maritime winds [21], the corresponding force given by the Morison formula

$$F_V(t) = \tfrac{1}{2}\rho D C_d V(t)|V(t)|$$

does not follow a Gaussian distribution. This is because the above formula defines a nonlinear (memoryless) transformation [20], and its first-density function is given by

$$f_1(v) = \frac{1}{2\sigma_V\sqrt{2\pi|v|}}\exp\left[-\frac{1}{2}\left(\frac{sign(v)\sqrt{|v|}-m_V}{\sigma_V}\right)^2\right],$$

where m_V and σ_V are the mean value and standard deviation of the the Gaussian distribution for the velocity $V(t)$.

In this paper we apply the chaos expansions to coupled Navier-Stokes/structure equations. We first demonstrate the convergence of chaos expansions by solving a second-order ordinary differential equation. We then present the stochastic modeling of the fully coupled flow-structure interaction problem for vortex-induced vi-

[1]Corresponding author, e-mail: gk@cfm.brown.edu

Contributed by the Fluids Engineering Division for publication in the JOURNAL OF FLUIDS ENGINEERING. Manuscript received by the Fluids Engineering Division September 13, 2001; revised manuscript received October 29, 2001. Associate Editor: J. Katz.

Downloaded 03 Jun 2010 to 171.66.16.150. Redistribution subject to ASME license or copyright; see http://www.asme.org/terms/Terms_Use.cfm

brations in flow past a cylinder. The algorithms developed here are general and can be applied to any type of distributions although our applications are concentrated on Gaussian type random inputs.

In the next section we review the theory of the generalized polynomial chaos. In Section 3 we apply it to second-order oscillators, and in Section 4 we present its application to Navier-Stokes equations. In Section 5 we present the computational results of stochastic flow-structure interactions, and we conclude with a brief discussion in Section 6.

2 The Generalized Polynomial Chaos

In this section we introduce the generalized polynomial chaos expansion along with the Karhunen-Loeve (KL) expansion, another classical technique for representing random processes. The KL expansion can be used in some cases to represent efficiently the known stochastic fields, i.e., the stochastic inputs.

2.1 The Askey Scheme. The Askey scheme, which is represented as a tree structure in Fig. 1 (following [24]), classifies the hypergeometric orthogonal polynomials and indicates the limit relations between them. The ''tree'' starts with the Wilson polynomials and the Racah polynomials on the top. The Wilson polynomials are continuous while the Racah polynomials are discrete. The lines connecting different polynomials denote the limit transition relationships between them; this implies that the polynomials at the lower end of the lines can be obtained by taking the limit of one of the parameters from their counterparts on the upper end. For example, the limit relation between Jacobi polynomials $P_n^{(\alpha,\beta)}(x)$ and Hermite polynomials $H_n(x)$ is

$$\lim_{\alpha\to\infty} \alpha^{-1/2n} P_n^{(\alpha,\alpha)}\left(\frac{x}{\sqrt{\alpha}}\right) = \frac{H_n(x)}{2^n n!},$$

and between Meixner polynomials $M_n(x;\beta,c)$ and Charlier polynomials $C_n(x;a)$ is

$$\lim_{\beta\to\infty} M_n\left(x;\beta,\frac{a}{a+\beta}\right) = C_n(x;a).$$

For a detailed account of definitions and properties of hypergeometric polynomials, see [17]; for the limit relations of Askey scheme, see [25] and [24].

The orthogonal polynomials associated with the generalized polynomial chaos, include: Hermite, Laguerre, Jacobi, Charlier, Meixner, Krawtchouk, and Hahn polynomials.

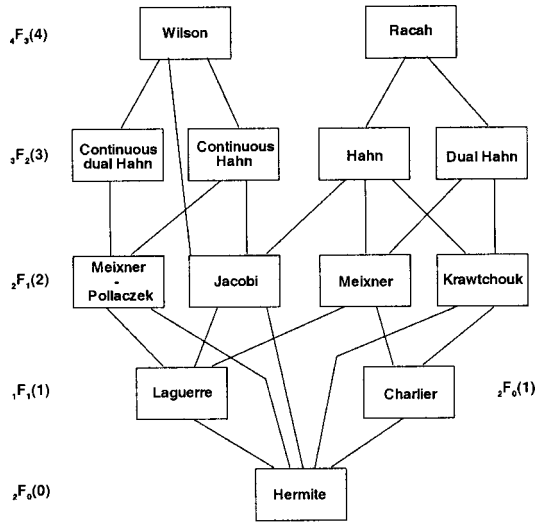

Fig. 1 The Askey scheme of orthogonal polynomials

Table 1 Correspondence of the type polynomials and random variables for different Askey-chaos ($N \geq 0$ is a finite integer).

	Random variables $\boldsymbol{\xi}$	Orthogonal polynomials $\{I_n\}$	Support
Continuous	Gaussian	Hermite	$(-\infty,\infty)$
	Gamma	Laguerre	$[0,\infty)$
	Beta	Jacobi	$[a,b]$
	Uniform	Legendre	$[a,b]$
Discrete	Poisson	Charlier	$\{0,1,2,\ldots\}$
	Binomial	Krawtchouk	$\{0,1,\ldots,N\}$
	Negative Binomial	Meixner	$\{0,1,2,\ldots\}$
	Hypergeometric	Hahn	$\{0,1,\ldots,N\}$

2.2 The Generalized Polynomial Chaos: Askey-Chaos. The original polynomial chaos [7,8] employs the Hermite polynomials in the random space as the trial basis to expand the stochastic processes. Cameron and Martin proved that such expansion converges to any second-order processes in the L_2 sense [26]. It can be seen from Fig. 1 that Hermite polynomial is a subset of the Askey scheme. The generalized polynomial chaos, or the Askey-Chaos, was proposed in [15,16] and employs more polynomials from the Askey scheme. Convergence to second-order stochastic processes can be readily obtained as a generalization of Cameron-Martin theorem [26].

A general second-order random process $X(\theta)$, viewed as a function of $\theta\in(0,1)$, i.e., the random event, can be represented in the form

$$X(\theta) = a_0 I_0 + \sum_{i_1=1}^{\infty} c_{i_1} I_1(\xi_{i_1}(\theta)) + \sum_{i_1=1}^{\infty}\sum_{i_2=1}^{i_1} c_{i_1 i_2} I_2(\xi_{i_1}(\theta),\xi_{i_2}(\theta)) + \sum_{i_1=1}^{\infty}\sum_{i_2=1}^{i_1}\sum_{i_3=1}^{i_2} c_{i_1 i_2 i_3} I_3(\xi_{i_1}(\theta),\xi_{i_2}(\theta),\xi_{i_3}(\theta)) + \ldots, \tag{1}$$

where $I_n(\xi_{i_1},\ldots,\xi_{i_n})$ denotes the Askey-chaos of order n in terms of the multi-dimensional random variables $\boldsymbol{\xi} = (\xi_{i_1},\ldots,\xi_{i_n})$. In the original polynomial chaos, $\{I_n\}$ are *Hermite* polynomials and $\boldsymbol{\xi}$ are *Gaussian* random variables. In the Askey-chaos expansion, the polynomials I_n are not restricted to Hermite polynomials and $\boldsymbol{\xi}$ not Gaussian variables. The corresponding type of polynomials and their associated random variables are listed in Table 1.

For notational convenience, we rewrite Eq. (1) as

$$X(\theta) = \sum_{j=0}^{\infty} \hat{c}_j \Phi_j(\boldsymbol{\xi}), \tag{2}$$

where there is a one-to-one correspondence between the functions $I_n(\xi_{i_1},\ldots,\xi_{i_n})$ and $\Phi_j(\boldsymbol{\xi})$, and their coefficients $\hat{c}_j$ and $c_{i_1,\ldots,i_r}$. Since each type of polynomials from the Askey scheme form a complete basis in the Hilbert space determined by their corresponding support, we can expect each type of Askey-chaos to converge to any L_2 functional in the L_2 sense in the corresponding Hilbert functional space as a generalized result of Cameron-Martin theorem ([26] and [27]). The orthogonality relation of the generalized polynomial chaos takes the form

$$\langle \Phi_i \Phi_j \rangle = \langle \Phi_i^2 \rangle \delta_{ij}, \tag{3}$$

where δ_{ij} is the Kronecker delta and $\langle\cdot,\cdot\rangle$ denotes the ensemble average which is the inner product in the Hilbert space of the random variables $\boldsymbol{\xi}$

$$\langle f(\boldsymbol{\xi}) g(\boldsymbol{\xi}) \rangle = \int f(\boldsymbol{\xi}) g(\boldsymbol{\xi}) W(\boldsymbol{\xi}) d\boldsymbol{\xi}, \tag{4}$$

or

Downloaded 03 Jun 2010 to 171.66.16.150. Redistribution subject to ASME license or copyright; see http://www.asme.org/terms/Terms_Use.cfm

$$\langle f(\boldsymbol{\xi})g(\boldsymbol{\xi})\rangle = \sum_{\xi} f(\boldsymbol{\xi})g(\boldsymbol{\xi})W(\boldsymbol{\xi}) \tag{5}$$

in the discrete case. Here $W(\boldsymbol{\xi})$ is the weighting function corresponding to the Askey polynomials chaos basis $\{\Phi_i\}$. Each type of orthogonal polynomials from the Askey-chaos has weighting functions of the same form as the probability function of its associated random variables $\boldsymbol{\xi}$, as shown in Table 1.

For example, as a subset of the Askey-chaos, the original polynomial chaos, also will be termed the Hermite-chaos, employs the Hermite polynomials defined as

$$I_n(\xi_{i_1}, \ldots, \xi_{i_n}) = e^{1/2\boldsymbol{\xi}^T\boldsymbol{\xi}}(-1)^n \frac{\partial^n}{\partial\xi_{i_1}\ldots\partial\xi_{i_n}} e^{-1/2\boldsymbol{\xi}^T\boldsymbol{\xi}}, \tag{6}$$

where $\boldsymbol{\xi}=(\xi_{i_1}, \ldots, \xi_{i_n})$ are multi-dimensional independent Gaussian random variables with zero mean and unit variance. The weight function in the orthogonality relation (4) is

$$W(\boldsymbol{\xi}) = \frac{1}{\sqrt{(2\pi)^n}} e^{-1/2\boldsymbol{\xi}^T\boldsymbol{\xi}}, \tag{7}$$

where n is the dimension of $\boldsymbol{\xi}$. It can seen that this is the same as the probability density function (PDF) of the n-dimensional Gaussian random variables. For example, the one-dimensional Hermite polynomials are:

$$\Psi_0 = 1, \quad \Psi_1 = \xi, \quad \Psi_2 = \xi^2 - 1, \quad \Psi_3 = \xi^3 - 3\xi, \ \ldots \tag{8}$$

2.3 The Karhunen-Loeve Expansion. The Karhunen-Loeve (KL) expansion [28] is another way of representing a random process. It is a spectral expansion based on the decomposition of the covariance function of the process. Let us denote the process by $h(\mathbf{x}, \theta)$ and its covariance function by $R_{hh}(\mathbf{x},\mathbf{y})$, where $\mathbf{x}$ and $\mathbf{y}$ are the spatial or temporal coordinates. By definition, the covariance function is real, symmetric, and positive definite. All eigenfunctions are mutually orthogonal and form a complete set spanning the function space to which $h(\mathbf{x}, \theta)$ belongs. The KL expansion then takes the following form:

$$h(\mathbf{x}, \theta) = \overline{h(\mathbf{x})} + \sum_{i=1}^{\infty} \sqrt{\lambda_i}\phi_i(\mathbf{x})\xi_i(\theta), \tag{9}$$

where $\overline{h(\mathbf{x})}$ denotes the mean of the random process, and $\xi_i(\theta)$ forms a set of independent random variables. Also, $\phi_i(\mathbf{x})$ and λ_i are the eigenfunctions and eigenvalues of the covariance function, respectively, i.e.,

$$\int R_{hh}(\mathbf{x},\mathbf{y})\phi_i(\mathbf{y})d\mathbf{y} = \lambda_i\phi_i(\mathbf{x}). \tag{10}$$

Among many possible decompositions of a random process, the KL expansion is optimal in the sense that the mean-square error of the finite term representation of the process is minimized. Its use, however, is limited as the covariance function of the solution process is often not known *a priori*. Nevertheless, the KL expansion provides an effective means of representing the input random processes when the covariance structure is known.

3 Second-order Random Oscillator

3.1 Governing Equations. We consider the second-order linear ordinary differential equation (ODE) system with both external and parametric random excitations.

$$\frac{dx}{dt} = y,$$

$$\frac{dy}{dt} + c(\theta)y + k(\theta)x = f(t, \theta), \tag{11}$$

where the parameters and forcing are functions of random event θ. We assume

$$c = \overline{c} + \sigma_c\xi_1, \quad k = \overline{k} + \sigma_k\xi_2,$$

$$f(t) = F\cos(\omega t) = (\overline{f} + \sigma_f\xi_3)\cos(\omega t), \tag{12}$$

where $(\overline{c}, \sigma_c)$, $(\overline{k}, \sigma_k)$ and $(\overline{f}, \sigma_f)$ are the mean and standard deviation of c, k and F, respectively. The random variables ξ_1, ξ_2, and ξ_3 are assumed to be independent standard *Gaussian* random variables.

3.2 Chaos Expansions. By applying the generalized polynomial chaos expansion, we expand the solutions as

$$x(t) = \sum_{i=0}^{P} x_i(t)\Phi_i(\boldsymbol{\xi}), \quad y(t) = \sum_{i=0}^{P} y_i(t)\Phi_i(\boldsymbol{\xi}), \tag{13}$$

where we have replaced the infinite summation of $\boldsymbol{\xi}$ in infinite dimensions in Eq. (2) by a truncated finite-term summation of $\boldsymbol{\xi}$ in finite dimensional space. In this case, $\boldsymbol{\xi}=(\xi_1,\xi_2,\xi_3)$ is a three-dimensional *Gaussian* random vector according to the random inputs. This results in a three-dimensional *Hermite*-chaos expansion. The most important aspect of the above expansion is that the random processes have been decomposed into a set of deterministic functions in the spatial-temporal variables multiplied by the random basis polynomials which are independent of these variables:

$$\sum_{k=0}^{P} \frac{dx_k}{dt}\Phi_k = \sum_{k=0}^{P} y_k\Phi_k,$$

$$\sum_{k=0}^{P} \frac{dy_k}{dt}\Phi_k + \sum_{i=0}^{P}\sum_{j=0}^{P} c_i y_j \Phi_i\Phi_j + \sum_{i=0}^{P}\sum_{j=0}^{P} k_i x_j \Phi_i\Phi_j = \sum_{k=0}^{P} f_k(t)\Phi_k, \tag{14}$$

where c_i, k_i, and f_i are the chaos expansion, similar to Eq. (13), of c, k, and f, respectively. A Galerkin projection of the above equation onto each polynomial basis $\{\Phi_i\}$ is then conducted in order to ensure the error is orthogonal to the functional space spanned by the finite-dimensional basis $\{\Phi_i\}$. By projecting with Φ_k for each $k=\{0, \ldots, P\}$ and employing the orthogonality relation (3), we obtain for each $k=0, \ldots, P$,

$$\frac{dx_k}{dt} = y_k,$$

$$\frac{dy_k}{dt} + \frac{1}{\langle\Phi_k^2\rangle}\sum_{i=0}^{P}\sum_{j=0}^{P}(c_i y_j + k_i x_j)e_{ijk} = f_k(t), \tag{15}$$

where $e_{ijk} = \langle\Phi_i\Phi_j\Phi_k\rangle$. Together with $\langle\Phi_i^2\rangle$, the coefficients e_{ijk} can be evaluated analytically from the definition of Φ_i. Equation (15) is a set of $(P+1)$ coupled ODEs. The total number of equation is determined by the dimensionality of the chaos expansion (n), in this case $(n=3)$, and the highest order (p) of the polynomials $\{\Phi\}$ [6]:

$$P = \sum_{s=1}^{p} \frac{1}{s!}\prod_{r=0}^{s-1}(n+r). \tag{16}$$

3.3 Numerical Results. The above set of equations can be integrated by any conventional method, e.g., Runge-Kutta. Here we employ the Newmark scheme which is second-order accurate in time. We define two error measures for the mean and variance of the solution

Downloaded 03 Jun 2010 to 171.66.16.150. Redistribution subject to ASME license or copyright; see http://www.asme.org/terms/Terms_Use.cfm

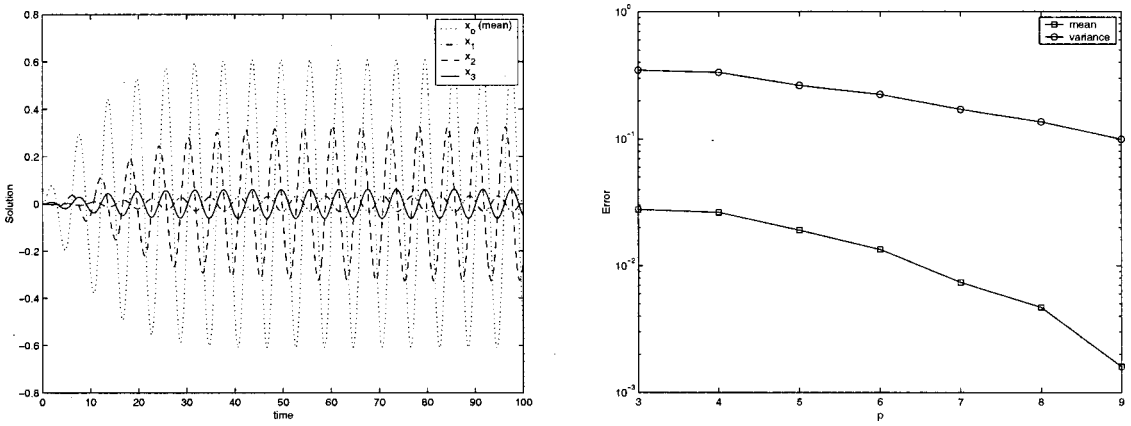

Fig. 2 Solution with Gaussian random inputs by Hermite-chaos. Left: solution of the dominant random modes, right: error convergence of the mean and the variance.

$$\varepsilon_{\text{mean}}(T)=\left|\frac{\overline{x}(T)-\overline{x}_{\text{exact}}(T)}{\overline{x}_{\text{exact}}(T)}\right|,\quad \varepsilon_{\text{var}}(T)=\left|\frac{\sigma^2(T)-\sigma^2_{\text{exact}}(T)}{\sigma^2_{\text{exact}}(T)}\right|, \tag{17}$$

where $\overline{x}(t)=E[x(t)]$ is the mean value of $x(t)$ and $\sigma^2(t)=E[(x(t)-\overline{x}(t))^2]$ is the variance. Integration is performed up to $T=100$ (nondimensional time units) when the solution reaches an asymptotic periodic state. The computation parameters are set as: $(\overline{c},\sigma_c)=(0.1,0.01)$, $(\overline{k},\sigma_k)=(1.05,0.105)$ and $(\overline{f},\sigma_f)=(0.1,0.01)$, with frequency $\omega=1.05$ and zero initial conditions. Here the standard deviations are set to be reasonably small to ensure the well-posedness of Eq. (11) in some stochastic sense. The exact stochastic solution is obtained from the exact deterministic solution and the known probability distribution functions of the random inputs. The exact mean and variance of the solution are obtained by integrating the solution over the support defined by the Gaussian distribution. These integrations are performed numerically using a Gauss-Hermite quadrature; a quadrature with 30 points provides high accuracy.

In Fig. 2 (left) we plot the development of the solution of the *mean* (zero mode) as well as the first three random modes, i.e., the modes contribution to a Gaussian distribution in this case. On the right figure we plot the error in the *mean* and the *variance*. We see from the semi-log plot that as the order of Hermite-chaos expansion increases, the error of mean and variance decreases exponentially fast. This is due to the fact that the chaos expansion is a spectral expansion in the random space. Similar exponential convergence rate has been demonstrated for first-order ODE for various Askey-chaos basis in [15]. It is worth noting that if the appropriate chaos basis, in this case the Hermite-chaos corresponding to the Gaussian inputs, is not chosen, the exponential convergence may not be maintained [15].

4 Incompressible Navier-Stokes Equations

In this section we present the solution procedure for solving the stochastic Navier-Stokes equations by generalized polynomial chaos expansion. The randomness in the solution can be introduced through boundary conditions, initial conditions, forcing, etc.

4.1 Governing Equations. We employ the incompressible Navier-Stokes equations

$$\nabla\cdot\mathbf{u}=0, \tag{18}$$

$$\frac{\partial\mathbf{u}}{\partial t}+(\mathbf{u}\cdot\nabla)\mathbf{u}=-\nabla\Pi+\mathrm{Re}^{-1}\nabla^2\mathbf{u}, \tag{19}$$

where Π is the pressure and Re the Reynolds number. All flow quantities, i.e., velocity and pressure are considered as stochastic processes. A random dimension, denoted by the parameter θ, is introduced in addition to the spatial-temporal dimensions $(\mathbf{x},t)$, thus

$$\mathbf{u}=\mathbf{u}(\mathbf{x},t;\theta);\quad \Pi=\Pi(\mathbf{x},t;\theta). \tag{20}$$

4.2 Chaos Expansion. We apply the generalized polynomial chaos expansion, or the Askey-chaos (2), to these quantities and obtain

$$\mathbf{u}(\mathbf{x},t;\theta)=\sum_{i=0}^{P}\mathbf{u}_i(\mathbf{x},t)\Phi_i(\boldsymbol{\xi}(\theta));$$

$$\Pi(\mathbf{x},t;\theta)=\sum_{i=0}^{P}\Pi_i(\mathbf{x},t)\Phi_i(\boldsymbol{\xi}(\theta)). \tag{21}$$

Substituting (21) into Navier-Stokes equations we obtain the following equations

$$\sum_{i=0}^{P}\nabla\cdot\mathbf{u}_i(\mathbf{x},t)\Phi_i=0, \tag{22}$$

$$\sum_{i=0}^{P}\frac{\partial\mathbf{u}_i(\mathbf{x},t)}{\partial t}\Phi_i+\sum_{i=0}^{P}\sum_{j=0}^{P}[(\mathbf{u}_i\cdot\nabla)\mathbf{u}_j)]\Phi_i\Phi_j=-\sum_{i=0}^{P}\nabla\Pi_i(\mathbf{x},t)\Phi_i+\mathrm{Re}^{-1}\sum_{i=0}^{P}\nabla^2\mathbf{u}_i\Phi_i\,. \tag{23}$$

We then project the above equations onto the random space spanned by the basis polynomials $\{\Phi_i\}$ by taking the inner product of above equation with each basis. By taking $\langle\cdot,\Phi_k\rangle$ and utilizing the orthogonality condition (3), we obtain the following set of equations:

For each $k=0,\ldots P$,

$$\nabla\cdot\mathbf{u}_k=0, \tag{24}$$

$$\frac{\partial\mathbf{u}_k}{\partial t}+\frac{1}{\langle\Phi_k^2\rangle}\sum_{i=0}^{P}\sum_{j=0}^{P}e_{ijk}[(\mathbf{u}_i\cdot\nabla)\mathbf{u}_j)]=-\nabla\Pi_k+\mathrm{Re}^{-1}\nabla^2\mathbf{u}_k\,, \tag{25}$$

where $e_{ijk}=\langle\Phi_i\Phi_j\Phi_k\rangle$. The set of equations consists of $(P+1)$ system of deterministic 'Navier-Stokes-like' equations for each random mode coupled through the convective terms.

4.3 Numerical Discretization. Discretization in space and time can be carried out by any conventional method. Here we

Downloaded 03 Jun 2010 to 171.66.16.150. Redistribution subject to ASME license or copyright; see http://www.asme.org/terms/Terms_Use.cfm

employ the spectral/hp element method in space in order to have better control of the numerical error [29]. The high-order splitting scheme together with properly defined consistent pressure boundary conditions are employed in time [30]. In particular, the spatial discretization is based on Jacobi polynomials on triangles or quadrilaterals in two-dimensions, and tetrahedra, hexahedra or prisms in three-dimensions.

4.4 Post-Processing. After solving the *deterministic* expansion coefficients, we obtain the analytical form (in random space) of the solution process. It is possible to perform a number of analytical operations on the stochastic solution in order to carry out other analysis such as the sensitivity analysis. The *mean* solution is contained in the expansion term with index of zero. The *second-moment*, i.e., the *covariance function* is given by

$$R_{\mathbf{uu}}(\mathbf{x}_1,t_1;\mathbf{x}_2,t_2)=\langle \mathbf{u}(\mathbf{x}_1,t_1)-\overline{\mathbf{u}(\mathbf{x}_1,t_1)},\mathbf{u}(\mathbf{x}_2,t_2)-\overline{\mathbf{u}(\mathbf{x}_2,t_2)}\rangle$$
$$=\sum_{i=1}^{P}[\mathbf{u}_i(\mathbf{x}_1,t_1)\mathbf{u}_i(\mathbf{x}_2,t_2)\langle\Phi_i^2\rangle]. \quad (26)$$

Note that the summation starts from index ($i=1$) instead of 0 to exclude the mean, and that the orthogonality of the Askey-chaos basis $\{\Phi_i\}$ has been used in deriving the above equation. Similar expressions can be obtained for the pressure field.

Implementation details and verifications of the stochastic Navier-Stokes solver can be found in [16].

5 Flow-Structure Interactions

In this section we consider two-dimensional vortex-induced vibrations of an elastically-mounted circular cylinder subject to stochastic inputs. The computational domain is shown in Fig. 3 where the circular cylinder with unit diameter ($D=1$) is located at the origin. The size of the domain is $[-15,25]\times[-9,9]$. There are 412 triangular elements and sixth-order Jacobi polynomials in each element are found to be sufficient to resolve the flow in the physical space in the range of $\mathrm{Re}<200$. The Reynolds number is defined as $\mathrm{Re}=U_\infty D/\nu$, where U_∞ is the inflow and ν the kinematic viscosity.

5.1 Structure Problem. In this paper we will focus on the cross-flow displacement of the cylinder, i.e., the cylinder is free to move in the y-direction but not in the x-direction. For a linear structure, the governing equation is the second-order ordinary differential equation

$$\rho\frac{d^2\eta}{dt^2}+b\frac{d\eta}{dt}+K\eta=F(t), \quad (27)$$

where ρ, b and K are the mass, damping and stiffness of the cylinder, and the natural frequency of this system is $\omega_n=\sqrt{K/\rho}$. For clarity, we rewrite Eq. (27) in the same form as in (11):

$$\frac{d^2\eta}{dt^2}+c\frac{d\eta}{dt}+k\eta=f(t), \quad (28)$$

where $c=b/\rho$, $k=K/\rho$ and $f(t)=F(t)/\rho$. The external force $f(t)$ comes from the flow and we incorporate uncertain components in c and k in the following simulations.

5.2 Transformed Navier-Stokes Equations. To couple the flow with moving boundaries of the structure, one can employ Arbitrary Lagrangian-Eulerian (ALE) method. Although general, this approach is computationally expensive so we consider a boundary-fitted coordinate approach for the specific problem we solve here. By attaching the coordinate system to the cylinder, the cylinder appears stationary in time (with respect to that coordinate system). Following [31], we define two coordinate systems: (x',y',t') and (x,y,t), where (x',y',t') is the original coordinate system and (x,y,t) is the transformed one. The mapping between the two systems is

$$x=x',$$
$$y=y'-\eta(t'),$$
$$t=t'.$$

In two-dimensional flow, this simply reduces to the v velocities being shifted by the reference frame velocity,

$$u=u',$$
$$v=v'-\frac{d\eta}{dt'},$$
$$p=p'.$$

It is worth noting that this mapping is stochastic when the cylinder motion is random and needs to be represented by the chaos expansion as well.

The incompressible Navier-Stokes equations are transformed into:

$$\nabla\cdot\mathbf{u}=0, \quad (29)$$

$$\frac{\partial\mathbf{u}}{\partial t}+(\mathbf{u}\cdot\nabla)\mathbf{u}=-\nabla\Pi+\mathrm{Re}^{-1}\nabla^2\mathbf{u}+\mathbf{A}(t), \quad (30)$$

where $A_x=0$ and $A_y=-d^2\eta/dt^2$.

In the following simulations, we assume the damping c and stiffness k in Eq. (28) to be random variables. Then the structure response becomes a random process, so does the psuedoforcing $\mathbf{A}(\mathbf{t})$ in the transformed Navier-Stokes equations. This, in turn, makes the flow field random, which exerts a stochastic dynamic forcing $f(t)$ back onto the cylinder. The entire coupled system

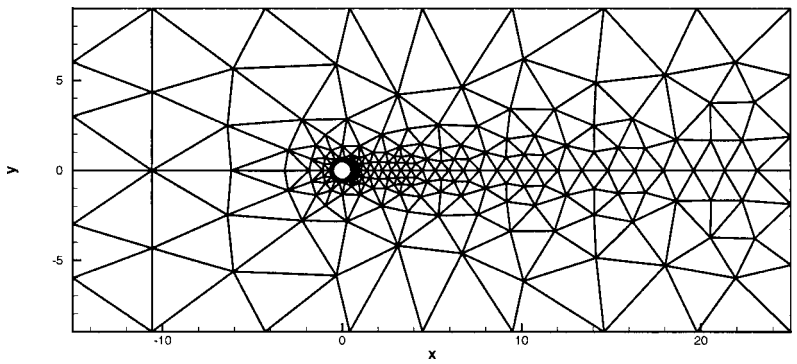

Fig. 3 Schematic of the domain for flow past an elastically mounted circular cylinder

Downloaded 03 Jun 2010 to 171.66.16.150. Redistribution subject to ASME license or copyright; see http://www.asme.org/terms/Terms_Use.cfm

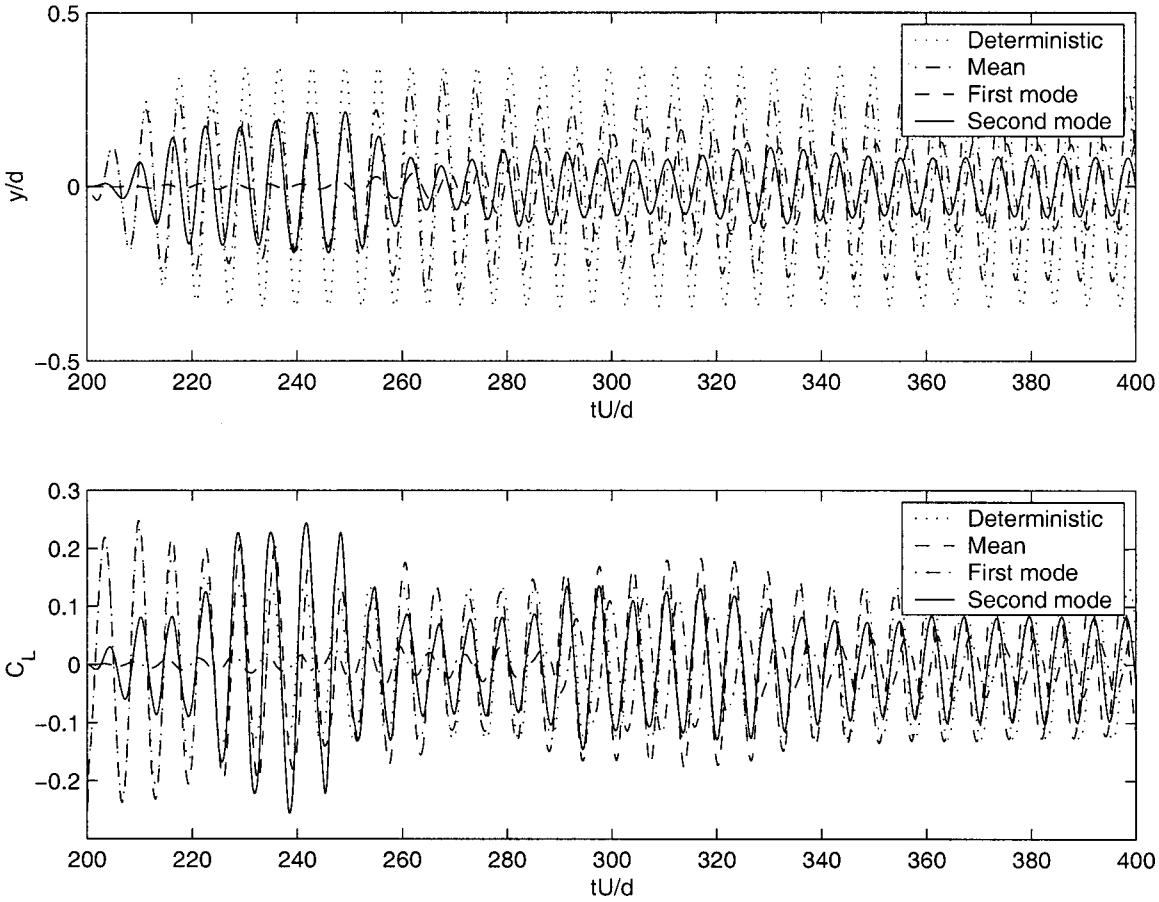

Fig. 4 Dominant random modes of the cylinder motion. Upper: modes of the cross-flow displacement y/D; lower: modes of the lift coefficient C_L.

then becomes stochastic. The same expansion procedure as in Section 4 is employed, with the psuedo-forcing $\mathbf{A}(t)$ and the mapping expanded appropriately, too.

5.3 Numerical Results. We assume that the Reynolds number is fixed at Re=100, and we also assume that the input parameters of the cylinder are uncertain, i.e., $c=\bar{c}+\sigma_c\xi_1$ and $k=\bar{k}+\sigma_k\xi_2$, where ξ_1 and ξ_2 are two independent standard Gaussian random variables with zero mean and unit variance. The mean and standard deviation of c and k are set as $(\bar{c},\sigma_c)=(0.1,0.01)$ and $(\bar{k},\sigma_k)=(1.0,0.2)$, respectively. We choose $k=1.0$ such that the natural frequency of the oscillator is close to the frequency of the vortex shedding of the fixed cylinder at Re=100, and the cylinder response is maximized. According to the uncertain inputs, we employ the two-dimensional $(n=2)$ Hermite-chaos, the corresponding Askey-chaos for Gaussian inputs as shown in Table 1, as the trial basis in random space. A third-order Hermite-chaos $(p=3)$ is employed which results in a 10-term chaos expansion $(P=9$ according to Eq. (16)). Therefore, the computational cost (serial) of this run is about 10 times more than the cost of the corresponding deterministic simulation. In particular, the cost of the structure solver, even if it is nonlinear, is negligible compared to the flow solver. The fluid forces on the cylinder are computed using

$$\mathbf{F}=\oint[-\mathbf{n}\Pi+\mathrm{Re}^{-1}(\nabla\mathbf{u}+\nabla\mathbf{u}^T)\cdot\mathbf{n}]ds,$$

where $\mathbf{n}$ is the outward normal on the cylinder and ds is the arc length on the surface of the cylinder. The corresponding force coefficients are computed by nondimensionalizing the forces with the fluid density ρ_f, free-stream velocity U_∞ and the cylinder diameter D:

$$C_D=\frac{F_D}{\frac{1}{2}\rho_f DU_\infty^2},\quad C_L=\frac{F_L}{\frac{1}{2}\rho_f DU_\infty^2}.$$

In Fig. 4 we plot the time evolution of the first few coefficients of the dominant random modes of the nondimensional cross-flow displacement (y/D) and the lift coefficient (C_L), together with the deterministic solution. We see that due to the effective diffusion of the randomness, the mean response of y/D has smaller amplitude compared to its deterministic counterpart. The first and second random modes, as shown in the figure, correspond to the Gaussian part of the response.

In Fig. 5 we show the time evolution of the variances of the cross-flow displacement y/D and lift coefficient C_L. We see that the variance peaks at the early transition stage before it settles to the asymptotic periodic state. The peak value is 2–3 times larger than that of the final periodic state. This suggests that the system responses to the uncertain inputs are important in the early transition stage and also non-negligible in the final asymptotic state.

Figure 6 shows the instantaneous contours of the rms of the vorticity field at $t=600$ (nondimensional time units) corresponding to more than 100 shedding cycles. The center location of the cylinder is not at the origin as shown in the figure. It is interesting that the regions with the largest uncertainty are regions of the most importance from the fluid dynamical point of view, i.e., the shear layer and near-wake but not the far-field.

In Fig. 7 the instantaneous pressure distribution along the surface of the cylinder at $t=600$ is shown. Here θ is the angle of the location on the surface with $\theta=0$ the rear stagnation point and $\theta=\pi$ the front stagnation point. The error-bar curve is centered at the mean of the stochastic pressure solution and the length of the

Downloaded 03 Jun 2010 to 171.66.16.150. Redistribution subject to ASME license or copyright; see http://www.asme.org/terms/Terms_Use.cfm

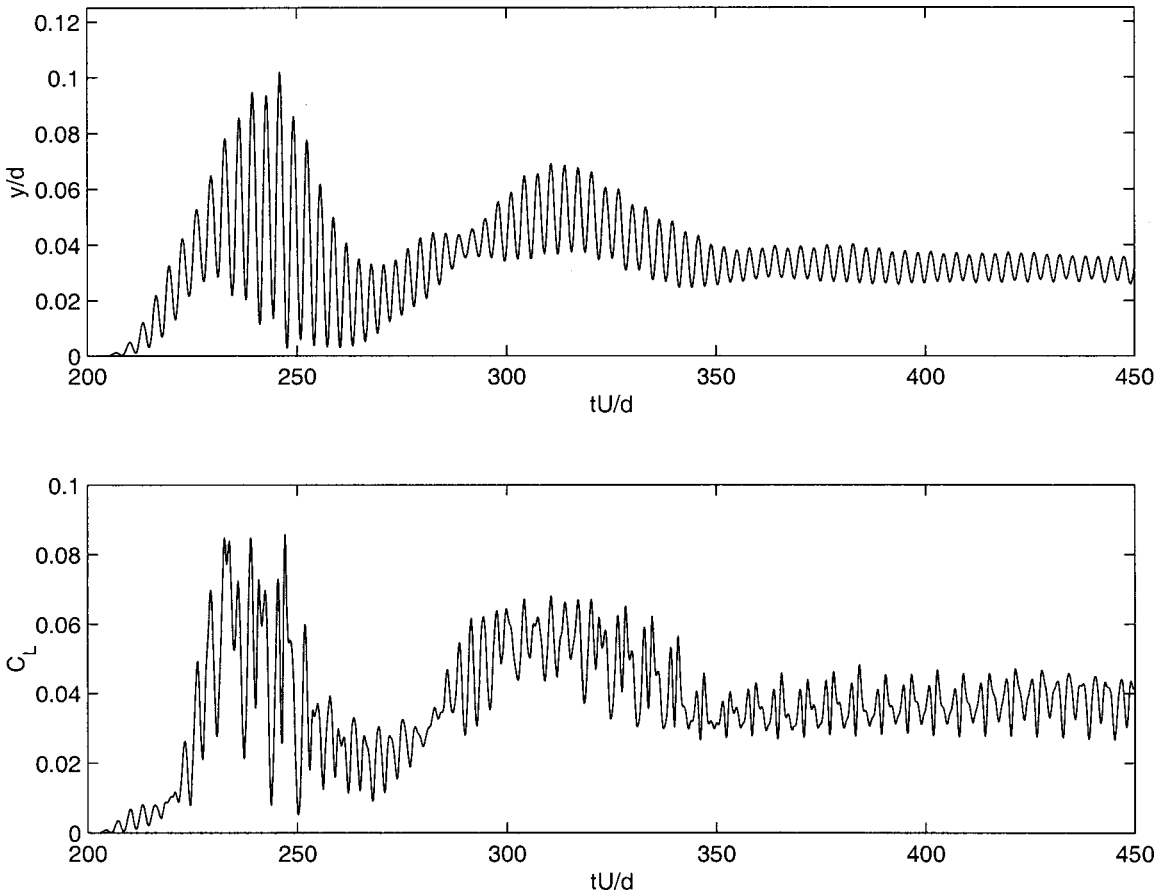

Fig. 5 Variance of the cylinder motion. Upper: variance of the cross-flow displacement *y/D*, lower, variance of the lift coefficient C_L.

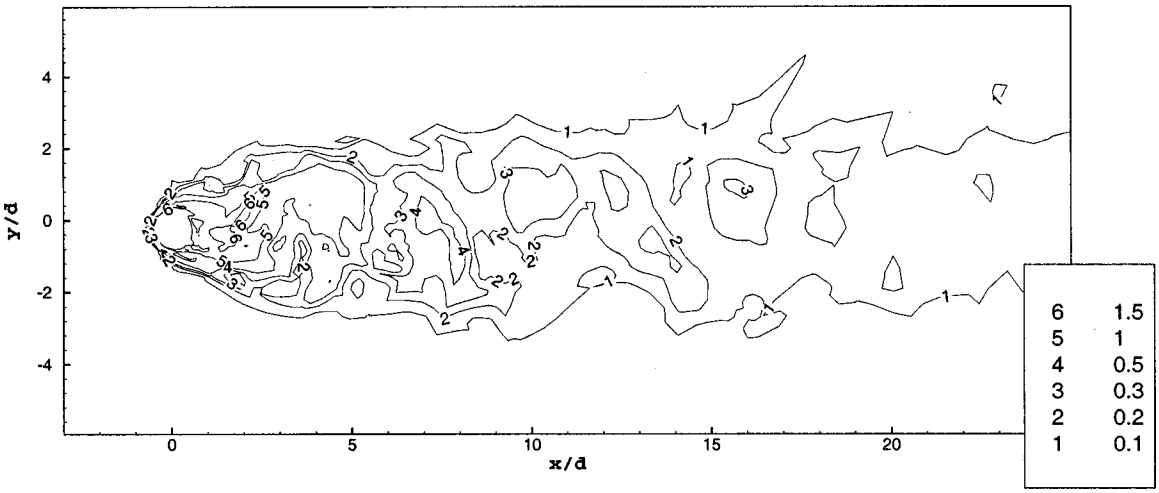

Fig. 6 Regions of uncertainty: instantaneous *rms* of vorticity

bars indicates two standard deviations around the mean (i.e., one above and one below the mean). For comparison, the deterministic pressure distribution at the same instance is shown as well. The difference compared with stochastic mean solution is noticeable; for the chosen magnitudes of variance of the stochastic inputs, the deterministic signal remains inside the ''envelope'' of the stochastic solution at this instance.

6 Summary and Discussion

We have developed a stochastic spectral method to model uncertainty and its propagation in flow simulations. More specifically, we have generalized the original polynomial chaos idea of Wiener and proposed a broader framework, i.e., the Askey-chaos, which includes Wiener's Hermite-chaos as a subset. Numerical examples were presented for relatively simple systems, such as a second-order ordinary differential equation and a more complicated flow-structure interaction problem at relatively low Reynolds number. We do not yet have experience with such stochastic simulations at high Reynolds number.

The method we developed here is general and can also be applied to model uncertainty in the boundary domain, e.g., a rough

Downloaded 03 Jun 2010 to 171.66.16.150. Redistribution subject to ASME license or copyright; see http://www.asme.org/terms/Terms_Use.cfm

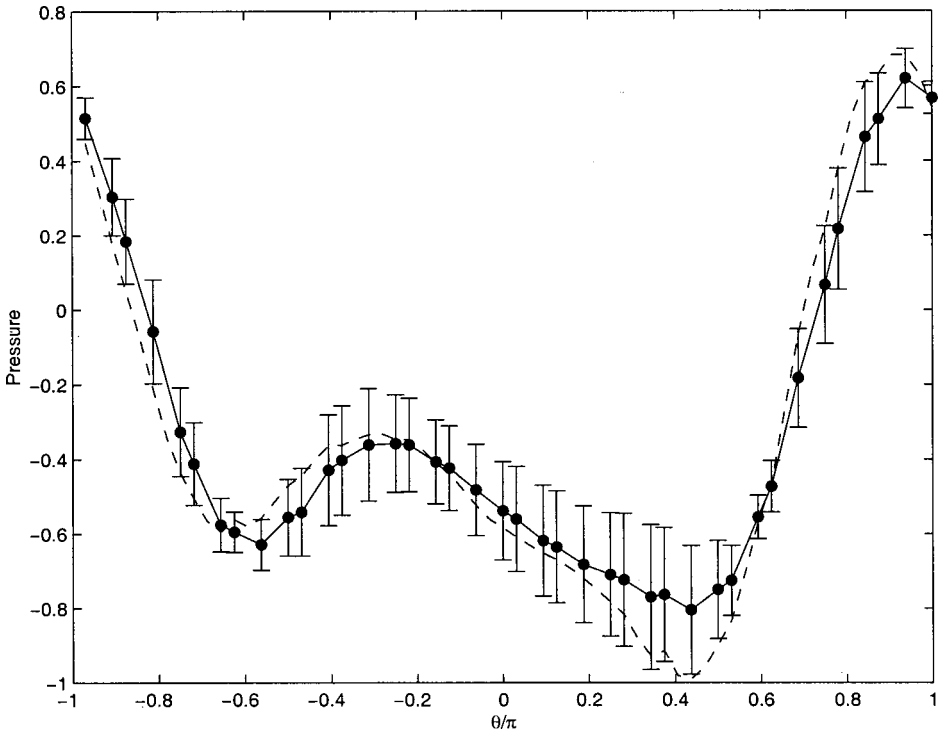

Fig. 7 Instantaneous pressure distribution along the surface of the cylinder; error-bar: stochastic solution, dashed line: deterministic solution

surface, in the transport coefficients, e.g., the eddy viscosity in large eddy simulations, and other problems. It provides a formal procedure for constructing a *composite error bar* for CFD applications, as proposed in [32], that includes, in addition to the discretization errors, contributions due to imprecise physical inputs to the simulations.

As regards efficiency, a single Askey-chaos based simulation, albeit computationally more expensive than the corresponding deterministic solver, is able to generate the solution statistics in a single run. In contrast, for the Monte Carlo simulation, tens of thousands of realizations are required for converged statistics, which is prohibitively expensive for most CFD problems in practice. Further work will include simulations with different distribution functions and their corresponding Askey-chaos expansion as presented here.

Acknowledgments

This work was supported by ONR. Computations were performed at Brown's TCASCV, DoD NaAVO and NCSA's (University of Illinois) facilities.

References

[1] Ziada, S. and Staubli, T., (editors), 2000, ''Flow-Induced Vibration,'' Proc. 7th Int. Conf., FIV2000, Lucerne, Switzerland, 19–22 June, A. A. Balkema.
[2] Leweke, T. (editor), 2001, ''Special Issue on Proc. of IUTAM Symposium on Bluff Body Wakes and Vortex-Induced Vibrations, Marseille, France, 13–16 June 2000,'' J. Fluids Struct. .
[3] Shlesinger, M. F. and Swean, T., 1998, *Stochastically Excited Nonlinear Ocean Structures*, World Scientific.
[4] Hills, R. G., and Trucano, T. G., 1999, ''Statistical Validation of Engineering and Scientific Models: Background,'' Technical Report SAND99-1256, Sandia National Laboratories.
[5] Shinozuka, M., and Deodatis, G., 1986, ''Response Variability of Stochastic Finite Element Systems,'' Technical Report, Dept. of Civil Engineering, Columbia University, New York.
[6] Ghanem, R. G., and Spanos, P., 1991, *Stochastic Finite Elements: A Spectral Approach*, Springer-Verlag.
[7] Wiener, N., 1938, ''The Homogeneous Chaos,'' Am. J. Math., **60**, pp. 897–936.
[8] Wiener, N., 1958, *Nonlinear Problems in Random Theory*, MIT Technology Press Wiley, New York.
[9] Meecham, W. C., and Siegel, A., 1964, ''Wiener-Hermite Expansion in Model Turbulence at Large Reynolds Numbers,'' Phys. Fluids, **7**, pp. 1178–1190.
[10] Siegel, A., Imamura, T., and Meecham, W. C., 1965, ''Wiener-Hermite Expansion in Model Turbulence in the Late Decay Stage,'' J. Math. Phys., **6**, pp. 707–721.
[11] Meecham, W. C., and Jeng, D. T., 1968, ''Use of the Wiener-Hermite Expansion for Nearly Normal Turbulence,'' J. Fluid Mech., **32**, pp. 225–249.
[12] Orszag, S. A., and Bissonnette, L. R., 1967, ''Dynamical Properties of Truncated Wiener-Hermite Expansions,'' Phys. Fluids, **10**, p. 2603.
[13] Crow, S. C., and Canavan, G. H., 1970, ''Relationship Between a Wiener-Hermite Expansion and an Energy Cascade,'' J. Fluid Mech., **41**, pp. 387–403.
[14] Chorin, A. J., 1974, ''Gaussian Fields and Random Flow,'' J. Fluid Mech., **85**, pp. 325–347.
[15] Xiu, D., and Karniadakis, G. E., 2001, ''The Wiener-Askey Polynomial Chaos for Stochastic Differential Equations,'' SIAM J. Sci. Comput. (USA), submitted.
[16] Xiu, D., and Karniadakis, G. E., 2001, ''Modeling Uncertainty in Flow Simulations Via Generalized Polynomial Chaos,'' J. Comput. Phys., to appear.
[17] Askey, R., and Wilson, J., 1985, ''Some Basic Hypergeometric Polynomials that Generalize Jacobi Polynomials,'' Memoirs Amer. Math. Soc., AMS, Providence RI, **54**, No. 319, pp. 1–55.
[18] Hou, Z., Zhou, Y., Dimentberg, M. F., and Noori, M., 1996, ''A Stationary Model for Periodic Excitation with Uncorrelated Random Disturbances,'' Probab. Eng. Mech., **11**, pp. 191–203.
[19] Yim, S. C. S., and Lin, H., 1998, ''A Methodology for Analysis and Design of Sensitive Nonlinear Ocean Systems, *Stochastically Excited Nonlinear Ocean Structures*, World Scientific, p. 105.
[20] Soong, T. T., and Grigoriu, M., 1993, *Random Vibration of Mechanical and Structural Systems*, Prentice Hall.
[21] Fei, C.-Y., and Vandiver, J. K., 1995, ''A Gaussian Model for Predicting the Effect of Unsteady Windspeed on the Vortex-Induced Vibration Response of Structural Members,'' J. Struct. Mech., ASME, Proc. 14th Int. Conf. on Offshore Mechanics and Arctic Engineering, Book No. H00939:57–65.
[22] Shinozuka, M., Yun, C., and Vaicatis, R., 1977, ''Dynamic Analysis of Fixed Offshore Structures Subject to Wind Generated Waves,'' J. Struct. Mech., **5**, No. 2, pp. 135–146.
[23] Grigoriu, M., 1984, ''Extremes of Wave Forces,'' J. Eng. Mech., **110**, pp. EM12:1731–1742.
[24] Schoutens, W., 2000, *Stochastic Processes and Orthogonal Polynomials*, Springer-Verlag New York.
[25] Koekoek, R., and Swarttouw, R. F., 1998, ''The Askey-Scheme of Hypergeometric Orthogonal Polynomials and its Q-Analogue,'' Technical Report 98-17, Department of Technical Mathematics and Informatics, Delft University of Technology.

Downloaded 03 Jun 2010 to 171.66.16.150. Redistribution subject to ASME license or copyright; see http://www.asme.org/terms/Terms_Use.cfm

[26] Cameron, R. H., and Martin, W. T., 1997, ''The Orthogonal Development of Nonlinear Functionals in Series of Fourier-Hermite Functionals,'' Ann. Math., **48**, p. 385.
[27] Ogura, H., 1972, ''Orthogonal Functionals of the Poisson Process,'' IEEE Trans. Inf. Theory, **IT-18**, pp. 473–481.
[28] Loève, M., 1977, *Probability Theory, Fourth edition*, Springer-Verlag.
[29] Karniadakis, G. E., and Sherwin, S. J., 1999, *Spectral/hp Element Methods for CFD*, Oxford University Press.
[30] Karniadakis, G. E., Israeli, M., and Orszag, S. A., 1991, ''High-Order Splitting Methods for Incompressible Navier-Stokes Equations,'' J. Comput. Phys., **97**, p. 414.
[31] Newman, D. J., and Karniadakis, G. E., 1997, ''Simulations of Flow Past a Freely Vibrating Cable,'' J. Fluid Mech., **344**, pp. 95–136.
[32] Karniadakis, G. E., 1995, ''Towards an Error Bar in CFD,'' ASME J. Fluids Eng., **117**, pp. 7–9.

Downloaded 03 Jun 2010 to 171.66.16.150. Redistribution subject to ASME license or copyright; see http://www.asme.org/terms/Terms_Use.cfm

Michele M. Putko
Ph.D. Candidate

Arthur C. Taylor III
Associate Professor

Department of Mechanical Engineering,
Old Dominion University,
Norfolk, VA 23529

Perry A. Newman
Senior Research Scientist

Lawrence L. Green
Research Scientist

NASA Langley Research Center,
Hampton, VA 23681

Approach for Input Uncertainty Propagation and Robust Design in CFD Using Sensitivity Derivatives[1]

An implementation of the approximate statistical moment method for uncertainty propagation and robust optimization for quasi 1-D Euler CFD code is presented. Given uncertainties in statistically independent, random, normally distributed input variables, first- and second-order statistical moment procedures are performed to approximate the uncertainty in the CFD output. Efficient calculation of both first- and second-order sensitivity derivatives is required. In order to assess the validity of the approximations, these moments are compared with statistical moments generated through Monte Carlo simulations. The uncertainties in the CFD input variables are also incorporated into a robust optimization procedure. For this optimization, statistical moments involving first-order sensitivity derivatives appear in the objective function and system constraints. Second-order sensitivity derivatives are used in a gradient-based search to successfully execute a robust optimization. The approximate methods used throughout the analyses are found to be valid when considering robustness about input parameter mean values.
[DOI: 10.1115/1.1446068]

1 Introduction

Gradient-based optimization of complex aerodynamic configurations and their components, utilizing high-fidelity Computational Fluid Dynamics (CFD) tools, continues as a very active area of research (see, for example, [1–3]). In most of the CFD-based aerodynamic optimization and design studies to date, the input data and parameters have been assumed precisely known; we refer to this as deterministic or conventional optimization. When statistical uncertainties exist in the input data or parameters, however, these uncertainties affect the design and therefore must be accounted for in the optimization. Such optimizations under uncertainty have been studied and used in structural design disciplines (see, for example [4–8]); we refer to these as nondeterministic or robust design optimization procedures.

Derivatives of code output with respect to code input and parameters are called sensitivity derivatives and they contain information which can be used to direct an optimization search. In a fluid flow optimization problem, the objective and constraint gradients are functions of the CFD sensitivity derivatives. Such derivatives can also be used to accurately approximate the CFD output in a small region, such as that near the mean value of a random variable. In [9], it is shown that a statistical First Order Second Moment (FOSM) method and automatic differentiation can be used to efficiently propagate input uncertainties through finite element analyses to approximate output uncertainty. This uncertainty propagation method is demonstrated herein for CFD code.

An integrated strategy for mitigating the effect of uncertainty in simulation-based design is presented in [10]; this strategy consists of uncertainty quantification, uncertainty propagation, and robust design tasks or modules. Two approaches are discussed there for propagating uncertainty through sequential analysis codes: an extreme condition approach and a statistical approach. Both approaches can be efficiently implemented using sensitivity derivatives. For CFD code, the former approach is demonstrated in [11], whereas the latter approach is demonstrated herein using second moment approximations. These uncertainty propagation methods have been developed and are being investigated as an alternative to propagation by direct Monte Carlo simulation for potentially expensive CFD analyses.

The present paper shows how the approximate statistical second moment methods, FOSM and the Second Order Second Moment (SOSM) counterpart, can be used in conjunction with sensitivity derivatives to propagate input data uncertainties through CFD code to estimate output uncertainties. The FOSM approximation is then used to perform sample robust optimizations. For demonstration purposes, the method is illustrated on a simple design example which contains the important elements of more complex design problems. We assume that the input uncertainty quantification is given by independent normally-distributed random variables, and we demonstrate the strategy of [10] as applied to a CFD code module. This strategy is also applicable to correlated and/or non-normally distributed variables; however, the analysis and resulting equations become much more complex.

The gradient-based robust optimization demonstrated herein requires second-order sensitivity derivatives from the CFD code. In [12], we present, discuss, and demonstrate the efficient calculation of second-order derivatives from CFD code using a method proposed, but not demonstrated, in [13]. This method, used herein, incorporates first-order derivatives obtained by both forward-mode and reverse-mode differentiation in a noniterative scheme to obtain second-order sensitivity derivatives.

To date, the only other demonstration or application of gradient-based, robust optimization involving advanced or high-fidelity (nonlinear) CFD code that we have found was just recently presented in [14–15]. The analytical statistical approximation of their objective function for robust optimization also required second-order sensitivity derivatives. However, these studies employed a direct numerical random sampling technique to compute expected values at each optimization step in order to

[1]This paper is declared a work of the U.S. Government and is not subject to copyright protection in the United States.

Contributed by the Fluids Engineering Division for publication in the JOURNAL OF FLUIDS ENGINEERING. Manuscript received by the Fluids Engineering Division July 20, 2001; revised manuscript received November 12, 2001. Associate Editor: G. Karniadakis.

 Copyright © 2002 by ASME

Downloaded 03 Jun 2010 to 171.66.16.150. Redistribution subject to ASME license or copyright; see http://www.asme.org/terms/Terms_Use.cfm

avoid the second derivatives. An example of linear aerodynamics involved in multidisciplinary performance optimization subject to uncertainty is found in [16].

Two other aspects need to be pointed out in regard to the robust optimization demonstrations for CFD code modules presented herein and also in [14,15]. First, the sources of uncertainty considered were only those due to code input parameters involving geometry and/or flow conditions; i.e., due to sources external to the CFD code simulation. Other computational simulation uncertainties, such as those due to physical, mathematical, and numerical modeling approximations [17,18]—essentially internal model error and uncertainty sources, were not considered. That is, the discrete CFD code analysis results were taken to be deterministically "certain" herein. Ultimately, all of these modeling sources of error and uncertainty must be assessed and considered. Sensitivity derivatives can also aid in this assessment [19] since the adequacy of an internal model's (i.e., algorithm, turbulence, etc.) prediction capability generally depends, to some extent, on the modeling parameter values specified as input.

Second, as discussed in [15], uncertainty classification with respect to an event's impact (from performance loss to catastrophic) and frequency (from everyday fluctuation to extremely rare) sets the problem formulation and solution procedure. Structural reliability techniques typically deal with risk assessment of infrequent but catastrophic failure modes, identifying the most probable point of failure and its safety index. Here, we are addressing the assessment of everyday operational fluctuations on performance loss, not catastrophe. Consequently, we are most concerned with aero performance behavior due to probable fluctuations, i.e., near the mean of probability density functions (pdf). Structural reliability assessment is most concerned with improbable catastrophic events, i.e., probability in the tails of the pdf. Simultaneous consideration of both types of uncertainty is discussed in [16].

2 Integrated Statistical Approach

In [10] an integrated methodology for dealing with uncertainty in a simulation-based design is proposed and demonstrated for a linkage mechanism design. The integrated strategy of [10] for mitigating the effect of uncertainty includes (a) uncertainty quantification, (b) uncertainty propagation, and (c) robust design. The present study utilizes the strategy proposed in [10], but differs in regard to uncertainty propagation and application. Here, we are considering the influence of uncertainty in CFD code input; that is, the effect of uncertainty in input geometry on aerodynamic shape-design optimization and the effect of uncertainty in flow conditions on design for flow control.

2.1 Uncertainty Quantification. In this study, we consider the influence of uncertainty in CFD input parameterization variables. We have assumed that these input variables are statistically independent, random, and normally distributed about a mean value. This assumption not only simplifies the resulting algebra and equations, but also serves to quantify input uncertainties. Furthermore, it is not an unreasonable assumption for input geometric variables subject to random manufacturing errors nor for input flow conditions subject to random fluctuations.

2.2 Uncertainty Propagation. Uncertainty propagation is accomplished by approximate statistical second moment methods [9] and [20] where the required sensitivity derivatives are obtained by hand or by automatic differentiation. The first step in second moment analyses is to approximate the CFD system output solutions of interest in Taylor series form, truncated to the desired order. These approximations are formed to estimate the output value for small deviations of the input.

Given input random variables $\mathbf{b}=\{b_1,\ldots,b_n\}$ with mean values, $\overline{\mathbf{b}}=\{\overline{b}_1,\ldots,\overline{b}_n\}$, and standard deviations, $\sigma_b=\{\sigma_{b_1},\ldots,\sigma_{b_n}\}$, first- and second-order Taylor series approximations of the CFD output function, **F**, are given by

$$\mathbf{F}(\mathbf{b})=\mathbf{F}(\overline{\mathbf{b}})+\sum_{i=1}^{n}\frac{\partial\mathbf{F}}{\partial b_i}(b_i-\overline{b}_i) \tag{1}$$

and

$$\mathbf{F}(\mathbf{b})=\mathbf{F}(\overline{\mathbf{b}})+\sum_{i=1}^{n}\frac{\partial\mathbf{F}}{\partial b_i}(b_i-\overline{b}_i)+\frac{1}{2!}\sum_{j=1}^{n}\sum_{i=1}^{n}\frac{\partial^2\mathbf{F}}{\partial b_i\partial b_j}(b_i-\overline{b}_i)(b_j-\overline{b}_j), \tag{2}$$

respectively. Both first and second derivatives are evaluated at the mean values, $\overline{\mathbf{b}}$.

One then obtains expected values for the mean (first moment) and variance (second moment) of the output function, **F**, which depend on the sensitivity derivatives and input variances, $\sigma^2_{\mathbf{b}}$. The mean of the output function, $\overline{\mathbf{F}}$, and standard deviation $\sigma_{\mathbf{F}}$, are approximated as
First Order:

$$\overline{\mathbf{F}}=\mathbf{F}(\overline{\mathbf{b}})$$

$$\sigma^2_{\mathbf{F}}=\sum_{i=1}^{n}\left(\frac{\partial\mathbf{F}}{\partial b_i}\sigma_{b_i}\right)^2 \tag{3}$$

Second Order:

$$\overline{\mathbf{F}}=\mathbf{F}(\overline{\mathbf{b}})+\frac{1}{2!}\sum_{i=1}^{n}\frac{\partial^2\mathbf{F}}{\partial b_i^2}\sigma^2_{b_i}$$

$$\sigma^2_{\mathbf{F}}=\sum_{i=1}^{n}\left(\frac{\partial\mathbf{F}}{\partial b_i}\sigma_{b_i}\right)^2+\frac{1}{2!}\sum_{j=1}^{n}\sum_{i=1}^{n}\left(\frac{\partial^2\mathbf{F}}{\partial b_i\partial b_j}\sigma_{b_i}\sigma_{b_j}\right)^2, \tag{4}$$

where both first and second derivatives are evaluated at the mean values, $\overline{\mathbf{b}}$. Note in Eq. (4) that the second-order mean output, $\overline{\mathbf{F}}$, is not at the mean values of input $\overline{\mathbf{b}}$, i.e., $\overline{\mathbf{F}}\neq\mathbf{F}(\overline{\mathbf{b}})$.

Equations (3) and (4) are the FOSM and SOSM approximations, respectively, for the uncertainty propagation. The methods are straightforward with the difficulty largely lying in computation of the sensitivity derivatives. The very efficient and effective method used here to obtain such derivatives is presented in [12].

2.3 Robust Design. Conventional optimization for an objective function, Obj, that is a function of the CFD output, **F**, state variables, **Q**, and input variables, **b**, is expressed in Eq. (5). Herein, the CFD state equation residuals, **R**, are represented as an equality constraint, and other system constraints, **g**, are represented as inequality constraints. The input variables, **b**, are precisely known, and all functions of **b** are therefore deterministic.
min Obj,

$$\mathrm{Obj}=\mathrm{Obj}(\mathbf{F},\mathbf{Q},\mathbf{b})$$

subject to

$$\mathbf{R}(\mathbf{Q},\mathbf{b})=0$$

$$\mathbf{g}(\mathbf{F},\mathbf{Q},\mathbf{b})\leqslant 0 \tag{5}$$

For robust design, the conventional optimization, Eq. (5), must be treated in a probabilistic manner. Given uncertainty in the input variables, **b**, all functions in Eq. (5) are no longer deterministic. The design variables are now the mean values, $\overline{\mathbf{b}}=\{\overline{b}_1,\ldots,\overline{b}_n\}$, where all elements of $\overline{\mathbf{b}}$ are assumed statistically independent and normally distributed with standard deviations $\sigma_{\mathbf{b}}$. The objective function is cast in terms of expected values and becomes a function of $\overline{\mathbf{F}}$ and $\sigma_{\mathbf{F}}$. The state equation residual equality constraint, **R**, is deemed to be satisfied at the expected values of **Q** and **b**, that is the mean values $\overline{\mathbf{Q}}$ and $\overline{\mathbf{b}}$ for the FO approximation. The other constraints are cast into a probabilistic statement: the probability that the constraints are satisfied

Downloaded 03 Jun 2010 to 171.66.16.150. Redistribution subject to ASME license or copyright; see http://www.asme.org/terms/Terms_Use.cfm

is greater than or equal to a desired or specified probability, P_k. This probability statement is transformed [10] into a constraint involving mean values and standard deviations under the assumption that variables involved are normally distributed. The robust optimization can be expressed as
min Obj,

$$\text{Obj} = \text{Obj}(\overline{\mathbf{F}}, \sigma_{\mathbf{F}}, \overline{\mathbf{Q}}, \overline{\mathbf{b}})$$

subject to

$$\mathbf{R}(\overline{\mathbf{Q}}, \overline{\mathbf{b}}) = 0$$

$$\mathbf{g}(\overline{\mathbf{F}}, \overline{\mathbf{Q}}, \overline{\mathbf{b}}) + k\sigma_{\mathbf{g}} \leqslant 0, \tag{6}$$

where k is the number of standard deviations, $\sigma_{\mathbf{g}}$, that the constraint **g** must be displaced in order to achieve the desired or specified probability, P_k. For the FOSM approximation, standard deviations $\sigma_{\mathbf{F}}$ and $\sigma_{\mathbf{g}}$ are of the form given in Eq. (3) involving first-order sensitivity derivatives. Therefore, a gradient-based optimization will then require second-order sensitivity derivatives to compute the objective and constraint gradients. Note that for the SOSM approximation, third-order sensitivity derivatives would be required for these gradients.

The calculation of second-order sensitivity derivatives for CFD code, such as those required for SOSM and robust optimization with FOSM, was demonstrated in [13]; the efficient calculation method used herein is demonstrated and discussed in [12]. Both hand differentiation and automatic differentiation via the ADIFOR tool [21–23] were used in [12] and [13]. Both conventional and robust optimizations were performed using the Sequential Quadratic Programming method option in the Design Optimization Tools, DOT [24].

3 Application to Quasi 1-D Euler CFD

A very simple example has been chosen to demonstrate the propagation of input uncertainty through CFD code and its effect on optimization. The quasi one-dimensional Euler equations and approximate boundary conditions are solved in a discretized CFD form (see Appendix). Of course, modern CFD methods are not required to solve the quasi 1-D Euler equations; exact analytical solutions are available in any basic textbook on gas dynamics. However, these quasi 1-D equations are commonly and effectively used as the initial test platform in the development of CFD algorithms and methods.

Two separate applications are presented; the first involving propagation of geometric uncertainties, the second involving propagation of flow parameter uncertainties. Both uncertainty analyses are performed with quasi one-dimensional CFD Euler equations and boundary conditions describing subsonic flow through a variable area nozzle. The nozzle inlet is located at $x=0$ with area $A(x=0)=1$; the nozzle outlet is at $x=1$. The area distribution is given by

$$A(x) = 1 - ax + bx^2.$$

The volume, V, occupied by the nozzle, is the integration of $A(x)$ over the length $x=0$ to $x=1$

$$V = 1 - \frac{a}{2} + \frac{b}{3},$$

where a and b are the input geometric parameters. Three flow parameters are specified as input boundary conditions: the stagnation enthalpy, inlet entropy, and outlet static (back) pressure. The discretized quasi 1-D Euler equation set is symbolically written as the state equation in Eq. (5); its residual, **R** is driven to (machine) zero for a solution (see Appendix).

For supersonic flow through a variable area nozzle, shock waves generally appear and the flow solution (objective, constraint, etc.) becomes noisy or non-smooth (see [25] and the references cited therein). Care must be exercised with respect to obtaining and using the sensitivity derivatives needed for gradient-based optimization [25,26]. Therefore, we chose to bypass issues related to this supersonic flow non-smoothness in these initial demonstrations of the present approach for uncertainty propagation and robust design for CFD code modules.

3.1 Geometric Uncertainty Propagation. For the discussion of geometric uncertainty propagation, geometric shape parameters a and b will represent the statistically independent random input variables, **b**. The Mach number distribution through the nozzle, **M**, is viewed here as a component of the state variable, **Q**; its value at the inlet, **M**, is the CFD output, **F**. Applying the approach previously outlined (recall Eqs. (3) and (4)) yields the following first-and second-order approximations of the output function, M.
Input random variables: $\mathbf{b}=\{a,b\}$
CFD output function: $\mathbf{F}=\{\text{M}\}$
First-order Taylor series:

$$\text{M}(a,b) = \text{M}(\overline{a},\overline{b}) + \frac{\partial \text{M}}{\partial a}(a-\overline{a}) + \frac{\partial \text{M}}{\partial b}(b-\overline{b}) \tag{7}$$

Second-order Taylor series:

$$\text{M}(a,b) = M(\overline{a},\overline{b}) + \frac{\partial \text{M}}{\partial a}(a-\overline{a}) + \frac{\partial \text{M}}{\partial b}(b-\overline{b}) + \frac{\partial^2 \text{M}}{\partial a\,\partial b}(a-\overline{a}) \times (b-\overline{b}) + 0.5\left(\frac{\partial^2 \text{M}}{\partial a^2}(a-\overline{a})^2\right) + 0.5\left(\frac{\partial^2 \text{M}}{\partial b^2}(b-\overline{b})^2\right) \tag{8}$$

The mean, $\overline{\text{M}}$, and standard deviation σ_M of the output function are expressed as
FOSM:

$$\overline{\text{M}} = \text{M}(\overline{a},\overline{b})$$
$$\sigma_M^2 = \left(\frac{\partial \text{M}}{\partial a}\sigma_a\right)^2 + \left(\frac{\partial \text{M}}{\partial b}\sigma_b\right)^2 \tag{9}$$

SOSM:

$$\overline{\text{M}} = \text{M}(\overline{a},\overline{b}) + 0.5\left(\frac{\partial^2 \text{M}}{\partial a^2}\right)\sigma_a^2 + 0.5\left(\frac{\partial^2 \text{M}}{\partial b^2}\right)\sigma_b^2$$
$$\sigma_M^2 = \left(\frac{\partial \text{M}}{\partial a}\sigma_a\right)^2 + \left(\frac{\partial \text{M}}{\partial b}\sigma_b\right)^2 + 0.5\left(\frac{\partial^2 \text{M}}{\partial a^2}\sigma_a^2\right)^2 + 0.5\left(\frac{\partial^2 \text{M}}{\partial b^2}\sigma_b^2\right)^2 + \left(\frac{\partial^2 \text{M}}{\partial a\,\partial b}\sigma_a\sigma_b\right)^2. \tag{10}$$

Predictions of $\text{M}(a,b)$, $\overline{\text{M}}$ and σ_M for FOSM (Eqs. (7) and (9)) and SOSM (Eqs. (8) and (10)) are compared with CFD solutions and Monte Carlo analyses based on CFD solutions, as given and discussed in the results section.

3.2 Robust Shape Optimization. Applying the conventional optimization previously described yields
min Obj,

$$\text{Obj} = \text{Obj}(\text{M},a,b)$$

subject to

$$\mathbf{R}(\mathbf{M},a,b) = 0$$
$$V(a,b) \leqslant 0, \tag{11}$$

where the system constraint, V, is a constraint on the nozzle volume and depends only on a and b; our objective does not explicitly depend on **M**.

Applying the robust optimization previously described yields
min Obj, $\text{Obj} = \text{Obj}(\overline{\text{M}}, \sigma_M, \overline{a}, \overline{b})$
subject to

Downloaded 03 Jun 2010 to 171.66.16.150. Redistribution subject to ASME license or copyright; see http://www.asme.org/terms/Terms_Use.cfm

$$\mathbf{R}(\overline{\mathbf{M}},\overline{a},\overline{b})=0$$
$$V(\overline{a},\overline{b})+k\sigma_V\leqslant 0, \tag{12}$$

where

$$\sigma_V^2=\left(\frac{\partial V}{\partial a}\sigma_a\right)^2+\left(\frac{\partial V}{\partial b}\sigma_b\right)^2. \tag{13}$$

With a and b subject to statistical uncertainties (which may be due to measurement, manufacturing, etc.), V becomes uncertain. Since V is linearly dependent on a and b, it is also normally distributed. Therefore, its standard deviation, σ_V, is given exactly by Eq. (13).

To demonstrate the optimizations, a simple target-matching problem is selected; a unique answer is obtained when an equality volume constraint is enforced. The CFD code is run for given a and b; the resulting $\mathrm{M}(a,b)$ and corresponding $V(a,b)$ are taken as the target values Mt and Vt, respectively. For this conventional optimization, the objective function and constraint function for V of Eq. (11) become

$$\mathrm{Obj}(\mathrm{M},a,b)=[\mathrm{M}(a,b)-\mathrm{Mt}]^2$$
$$V(a,b)-\mathrm{Vt}=0$$

enforced as

$$V(a,b)-\mathrm{Vt}\leqslant 0 \quad \text{and} \quad \mathrm{Vt}-V(a,b)\leqslant 0 \tag{14}$$

for the convenience of the optimizer.

For robust optimization using the FOSM approximation, the corresponding objective and constraint on V of Eq. (12) become

$$\mathrm{Obj}(\overline{\mathrm{M}},\sigma_M,\overline{a},\overline{b})=[\overline{\mathrm{M}}(\overline{a},\overline{b})-\mathrm{Mt}]^2+\sigma_M^2$$
$$V(\overline{a},\overline{b})-\mathrm{Vt}+k\sigma_V=0$$

similarly enforced as

$$V(\overline{a},\overline{b})-\mathrm{Vt}+k\sigma_V\leqslant 0 \quad \text{and} \quad \mathrm{Vt}-V(\overline{a},\overline{b})-k\sigma_V\leqslant 0. \tag{15}$$

Note that for $\sigma_a=\sigma_b=0$ in Eq. (15), the conventional optimization is obtained. Also, in the probabilistic statement of the constraint on V, it is assumed that the desired volume is less than or equal to Vt.

3.3 Flow Parameter Uncertainty Propagation. A second example of uncertainty in CFD involves fluctuations in input flow parameters. For the discussion of flow parameter uncertainty propagation, the free-stream Mach number, Minf, and the nozzle static back pressure, Pb, will be taken as statistically independent random variables. Specifying the free-stream Mach number sets the stagnation enthalpy. The Mach number distribution through the nozzle, **M**, is again viewed as a component of the state variable, **Q**; its value at the inlet, M, is the CFD output, **F**. Applying the approach previously outlined yields equations which are similar to Eq. (7) through (10) but with

Input random variables: $\mathbf{b}=\{\mathrm{Minf},\mathrm{Pb}\}$
CFD output function: $\mathbf{F}=\{\mathbf{M}\}$

Again, predictions of M, $\overline{\mathrm{M}}$, and σ_M for the FOSM and SOSM approximations are compared with CFD solutions and Monte Carlo analyses based on CFD solutions, as given and discussed in the next section.

3.4 Robust Design for Flow Control. The conventional optimization is expressed as

min Obj $\quad \mathrm{Obj}=\mathrm{Obj}(\mathrm{M},\mathrm{Minf},\mathrm{Pb})$
subject to

$$\mathbf{R}(\mathbf{M},\mathrm{Minf},\mathrm{Pb})=0$$
$$q(\mathrm{Minf},\mathrm{Pb})\leqslant 0, \tag{16}$$

where q is a constraint on the mass flux through the nozzle.

The robust optimization is expressed as

min Obj, $\quad \mathrm{Obj}=\mathrm{Obj}(\overline{\mathrm{M}},\sigma_M,\overline{\mathrm{Minf}},\overline{\mathrm{Pb}})$
subject to

$$\mathbf{R}(\overline{\mathrm{M}},\overline{\mathrm{Minf}},\overline{\mathrm{Pb}})=0$$
$$q(\overline{\mathrm{Minf}},\overline{\mathrm{Pb}})+k\sigma_q\leqslant 0. \tag{17}$$

For the free-stream Mach number, Minf, and the nozzle back pressure, Pb, subject to statistical uncertainties, the mass flux, q, becomes uncertain. Since q is dependent on Minf and Pb, its standard deviation, σ_q, may be approximated by

$$\sigma_q^2=\left(\frac{\partial q}{\partial \mathrm{Minf}}\sigma_{\mathrm{Minf}}\right)^2+\left(\frac{\partial q}{\partial \mathrm{Pb}}\sigma_{\mathrm{Pb}}\right)^2. \tag{18}$$

Since q is not a linear function of Minf and Pb, Eq. (18) is not exact.

To demonstrate the optimizations, a simple target-matching problem is again chosen. The CFD code is run for given Minf and Pb, the resulting M and corresponding q are taken as the target values Mt and qt, respectively. For this conventional optimization, the objective function and constraint functions of Eq. (16) are

$$\mathrm{Obj}(\mathrm{M},\mathrm{Minf},\mathrm{Pb})=[\mathrm{M}(\mathrm{Minf},\mathrm{Pb})-\mathrm{Mt}]^2$$
$$q(\mathrm{Minf},\mathrm{Pb})-qt=0$$

enforced as

$$q(\mathrm{Minf},\mathrm{Pb})-qt\leqslant 0 \quad \text{and} \quad qt-q(\mathrm{Minf},\mathrm{Pb})\leqslant 0. \tag{19}$$

For robust optimization using the FOSM approximation, the corresponding objective and constraint on q of Eq. (17) can be shown as

$$\mathrm{Obj}=\mathrm{Obj}(\overline{\mathrm{M}},\sigma_M,\overline{\mathrm{Minf}},\overline{\mathrm{Pb}})=[\overline{\mathrm{M}}(\overline{\mathrm{Minf}},\overline{\mathrm{Pb}})-\mathrm{Mt}]^2+\sigma_M^2$$
$$q(\overline{\mathrm{Minf}},\overline{\mathrm{Pb}})-qt+k\sigma_q=0$$

enforced as

$$q(\overline{\mathrm{Minf}},\overline{\mathrm{Pb}})-qt+k\sigma_q\leqslant 0 \quad \text{and} \quad qt-q(\overline{\mathrm{Minf}},\overline{\mathrm{Pb}})-k\sigma_q\leqslant 0. \tag{20}$$

Again note that for $\sigma_{\mathrm{Minf}}=\sigma_{\mathrm{Pb}}=0$ in Eq. (20), the conventional optimization is obtained. Also, in the probabilistic statement of the constraint on q, it is assumed that the desired mass flux is less than or equal to qt.

4 Sample Results and Discussion

Presentation and discussion of results for the sample quasi 1-D Euler CFD problems are divided into four topics: function approximations, uncertainty propagation, pdf approximations, and robust optimization. For the first three topics, the FOSM and SOSM approximations are assessed by comparison with direct CFD simulations. Note that the CFD code and its corresponding derivative codes are executed at the mean values of the random input variables to obtain the functions and sensitivity derivatives needed for construction of the statistical approximations.

4.1 Function Approximations. It is important to assess the Taylor series output function approximations with direct nonlinear CFD code simulations prior to presenting uncertainty propagation. If the CFD output function, M, is quasi-linear with respect to the input variables of interest, one can expect first-order approximations to be reasonably good; that is, the first-order moments given by Eq. (3) should match well with the moments produced by a Monte Carlo simulation. For a more nonlinear system, one naturally expects better accuracy with second-order approximations; that is, uncertainty analyses which include second-order terms should yield results which better predict the statistical moments produced by the Monte Carlo simulation.

Downloaded 03 Jun 2010 to 171.66.16.150. Redistribution subject to ASME license or copyright; see http://www.asme.org/terms/Terms_Use.cfm

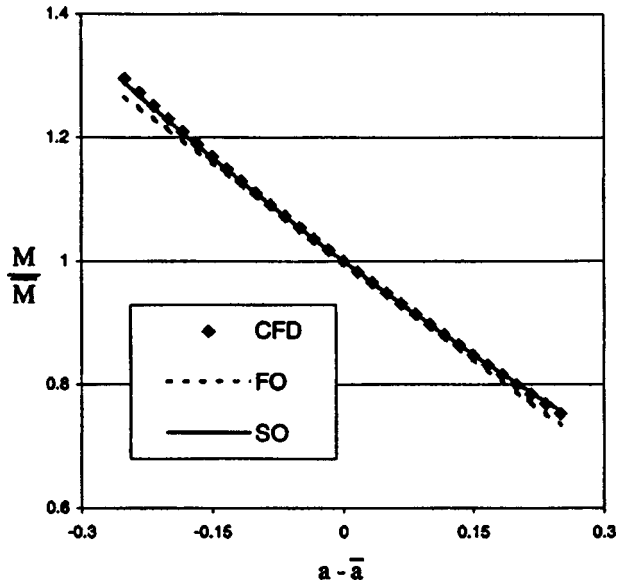

Fig. 1 Comparison of function approximations versus CFD solution, input variable $b=\bar{b}$

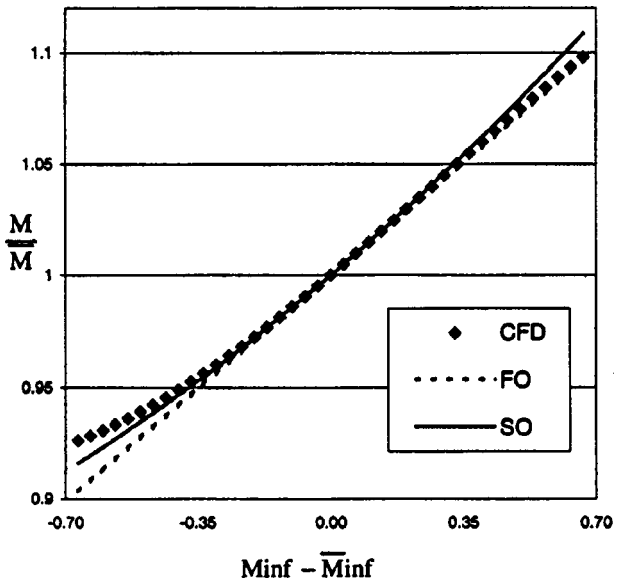

Fig. 3 Comparison of function approximations versus CFD solution, input variable Pb=P̄b

Figures 1–4 show that for $\mathbf{F}=\mathrm{M}(a,b)$, M behaves as a quasi-linear function in the neighborhood of $(\bar{a},\bar{b})$, whereas for $\mathbf{F}=\mathrm{M}(\mathrm{Minf},\mathrm{Pb})$, M is more nonlinear in the neighborhood of $(\overline{\mathrm{Minf}},\overline{\mathrm{Pb}})$. In these figures, approximations of the CFD output functions, $\mathrm{M}(a,b)$ and M(Minf,Pb), using the first- (FO) and second-order (SO) Taylor series (as given in Eqs. (7) and (8) for $\mathrm{M}(a,b)$), are compared to direct solution of the Euler CFD. In each example, two traces were considered through the design space. Trace 1 varied the first input variable, while the second remained fixed at its mean value, and vice versa for trace 2. The required first- and second-order sensitivity derivatives needed for construction of the first-and second-order approximations were obtained by hand differentiation and automatic differentiation as discussed and presented in [12].

Nonlinear behavior of the CFD result is reasonably well approximated by the SO result in all plots; however, there does appear to be an inflection point in the CFD results given in Fig. 3. Note that the linear FO result is a good approximation in the geometric example; the flow parameter example is more nonlinear. At larger deviations from the mean, a linear approximation for M(Minf,Pb) loses accuracy.

4.2 Uncertainty Propagation. Approximation of the statistical first and second moments is done using equations Eq. (9) and (10) (geometric example), and corresponding equations for the flow parameter example. Again, both first- and second-order sensitivity derivatives are required and the prediction is straightforward, given these derivatives. An independent verification of these approximate mean and standard deviation values is obtained here using direct Monte Carlo (MC) simulation with the quasi 1-D Euler CFD code and standard statistical analyses of these Monte Carlo results. The standard statistical analyses used were from MicroSoft ® Excel 2000 and the random number generator MZRAN used was from [27]. Tables 1 and 2 give results for the mean (first moment) and Tables 3 and 4 give results for the stan-

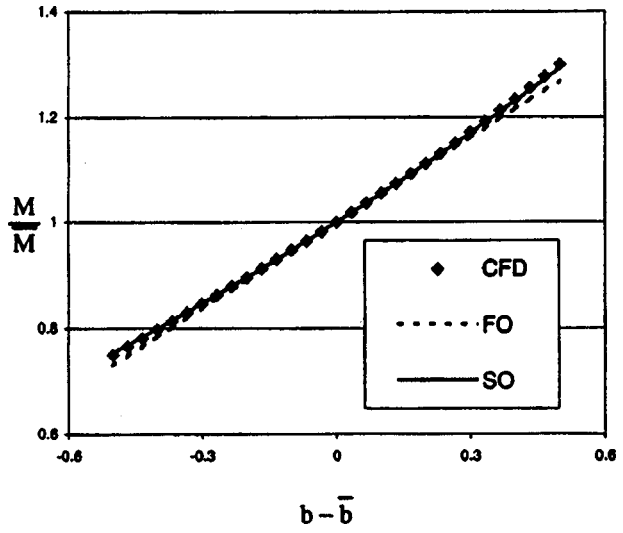

Fig. 2 Comparison of function approximations versus CFD solution, input variable $a=\bar{a}$

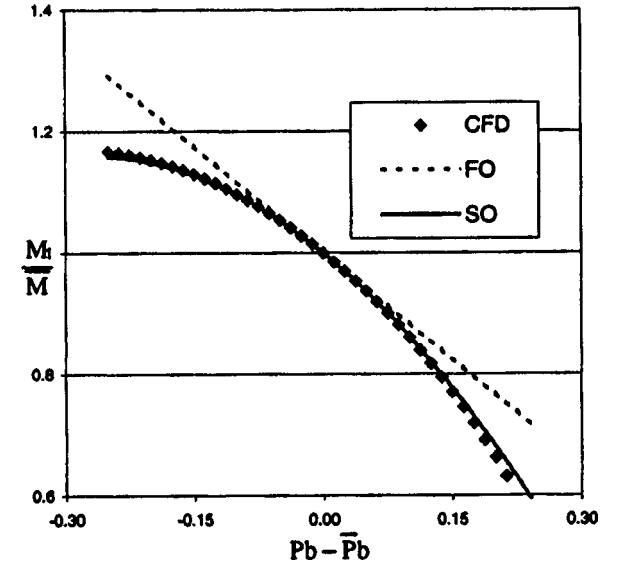

Fig. 4 Comparison of function approximations versus CFD solution, input variable Minf=Minf

Downloaded 03 Jun 2010 to 171.66.16.150. Redistribution subject to ASME license or copyright; see http://www.asme.org/terms/Terms_Use.cfm

Table 1 Percent difference from MC for FO and SO predictions of $\bar{M}$ ($\bar{a}$,$\bar{b}$)

Case	Input σ $\sigma_a=\sigma_b$	$\bar{M}$ MC	% Error MC	% diff w/MC FO Predict	% diff w/MC SO Predict
1	0.01	0.4041	0.0187	−0.0105	0.0656
2	0.02	0.4040	0.0379	0.0716	0.1531
3	0.04	0.4054	0.0756	−0.2867	0.0383
4	0.06	0.4055	0.1142	−0.3012	0.4301
5	0.08	0.4096	0.1557	−1.3078	−0.0209

Table 2 Percent difference from MC for FO and SO predictions of $\bar{M}$ ($\bar{M}$inf,$\bar{P}$b)

Case	Input σ $\sigma_{Minf}=\sigma_{Pb}$	$\bar{M}$ MC	% Error MC	% diff w/MC FO Predict	% diff w/MC SO Predict
1	0.01	0.3933	0.0056	0.0037	−0.0269
2	0.02	0.3932	0.0114	0.0187	−0.1034
3	0.04	0.3898	0.0229	0.8917	0.3991
4	0.06	0.3889	0.0364	1.1251	0.0141

Table 3 Percent difference from MC for FO and SO predictions of σ_M, geometric example

Case	Input σ $\sigma_a=\sigma_b$	σ_M MC	% diff w/MC FO Predict	% diff w/MC SO Predict
1	0.01	0.0102	−0.5773	−0.5708
2	0.02	0.0207	−1.7026	−1.6769
3	0.04	0.0414	−1.5794	−1.4766
4	0.06	0.0625	−2.2590	−2.0296
5	0.08	0.0853	−4.3987	−4.0001

Table 4 Percent difference from MC for FO and SO predictions of σ_M, flow parameter example

Case	Input σ $\sigma_{Minf}=\sigma_{Pb}$	σ_M MC	% diff w/MC FO Predict	% diff w/MC SO Predict
1	0.01	0.0030	1.1815	1.2473
2	0.02	0.0062	−1.5093	−1.2533
3	0.04	0.0125	−4.1604	−3.1680
4	0.06	0.0199	−4.4070	−2.1938

dard deviation (second moment) value comparisons. The input deviations (σ_a and σ_b) or (σ_{Minf} and σ_{Pb}), are taken to be equal and given in the second column of each table. The third column in each table gives the result from the MC simulation, where the sample size (N) used was 3000. The MC error in its predicted mean is $\sigma_M/\sqrt{N}$, which is given in the fourth column of Tables 1 and 2. The first-order (FO) and second-order (SO) approximate predictions are given in the last two columns of each table as percent difference from the MC results.

Results from the last two columns of Tables 1–4 are plotted in Figs. 5 and 6. Note that mean and standard deviation approximations for output M agree well with the MC results for small standard deviations in input variables, (σ_a,σ_b) or (σ_{Minf},σ_{Pb}), for both the FO and SO predictions. At higher standard deviations, the SO results tend to agree better with the MC results, especially in the flow parameter example.

As expected, the SO approximations are generally better than those for FO and an increase in the standard deviation of input parameters monotonically increases the error associated with both predictions. Both FO and SO approximations predict the mean more accurately than the standard derivation. Also note that the MC simulation with a sample size of 3000 limits accuracy of the MC results. This is apparent in the raggedness of the pdfs shown in the following section.

4.3 Probability Density Function Approximations. Given a mean and standard deviation of the CFD output function (from either an MC simulation or an FO or SO prediction) and assuming a normal distribution, one may then construct a pdf to approximate the behavior of the nondeterministic output function. This approximation is compared to pdf histograms generated from MC simulations in Figs. 7, 8, and 9. The bars depict the MC histogram, and the solid curve is a normal distribution at the MC mean value and MC standard deviation as given in the previous tables. The MC simulation size of 3000 is certainly not sufficient to obtain a smooth pdf. We note that both the first-order and second-order normal distributions are indistinguishable from this normal MC curve at this scale so neither is shown in the figure. It is apparent that for either the quasi-linear functional dependence on *a* and *b* (Fig. 7), or for small input standard deviations of the flow parameters (Fig. 8), the statistical approximations are good for a significant region about the mean but tend to break down in predicting the tails of the distribution. This is significant, for if one is primarily interested in reliable failure predictions, as for structural design, this prediction may not be good enough. It is felt, how-

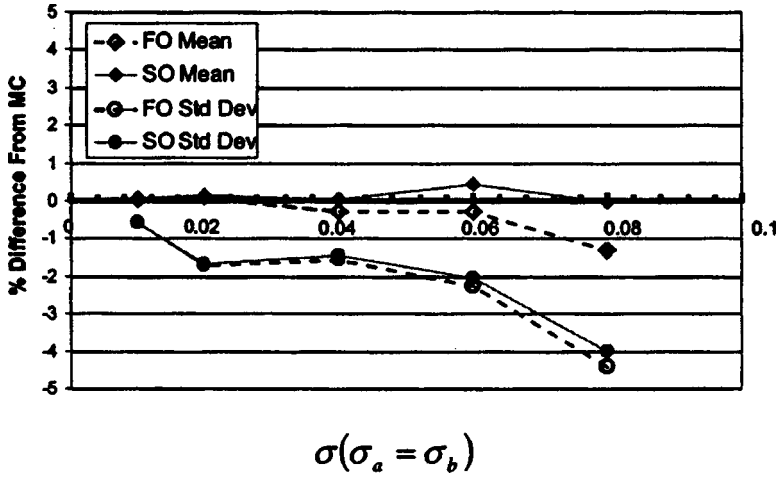

Fig. 5 Comparison of statistical moment approximations with Monte Carlo simulation results, geometric examples

Downloaded 03 Jun 2010 to 171.66.16.150. Redistribution subject to ASME license or copyright; see http://www.asme.org/terms/Terms_Use.cfm

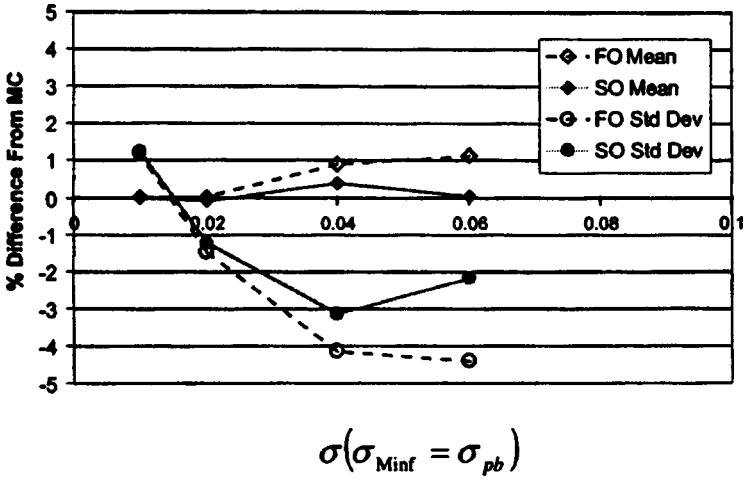

Fig. 6 Comparison of statistical moment approximations with Monte Carlo simulation results, flow parameter examples

ever, that in aerodynamic performance optimization using CFD, where robustness about the mean is desired, these approximations may be good enough.

It is not surprising that a nonlinear CFD output function behaves differently for randomness in different input variables. For M(Minf, Pb) at higher input standard deviations ($\sigma_{\text{Minf}} = \sigma_{Pb} = 0.06$), the pdf of the output function is no longer normal. In Fig. 9 one can see the non-normal behavior of CFD output given normally distributed input variables Minf and Pb.

4.4 Robust Optimizations. Optimization results were generated using the quasi 1-D Euler CFD code and the procedure given by Eqs. (5) and (6). As noted earlier, conventional optimization is obtained for $\sigma_a = \sigma_b = 0$ or for $\sigma_{\text{Minf}} = \sigma_{\text{Pb}} = 0$. For the FOSM approximation, first-order sensitivity derivatives are required to obtain σ_M and σ_V (Eqs. (9) and (13)) or σ_q (Eqs. (9) and (18)); therefore, second-order sensitivity derivatives will be required for their gradients, which are used in the optimization. The second-order derivatives were obtained by the manner presented in [12], except for those associated with Eq. (18) where the first-order derivatives were finite differenced simply for convenience.

It is seen from Eqs. (12) and (17) that the robust optimization results should depend on the probabilistic parameters (σ_a, σ_b) or ($\sigma_{\text{Minf}}, \sigma_{Pb}$), and k. The desired probability, P_k, is that from the normal cumulative distribution function since σ_V and σ_q here are assumed to be normally distributed. For each robust optimization example, two cases are presented. For case 1, P_k is fixed at $k = 1$, i.e., $P_1 = 84.13\%$, and the effect of increasing the input variable standard deviations is addressed. For case 2, the standard deviations of the input variables are fixed at 0.01 and P_k increases.

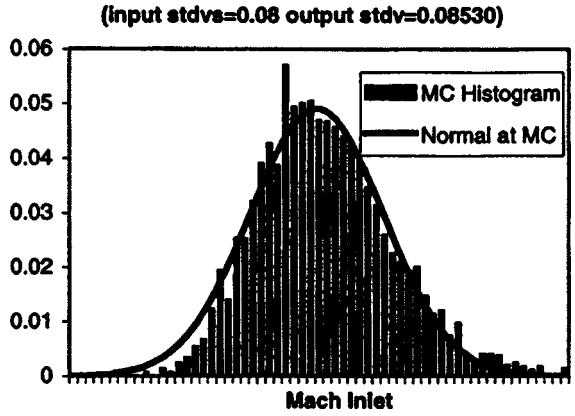

Fig. 7 Probability density function for M(a, b) for $\sigma_a = \sigma_b = 0.08$

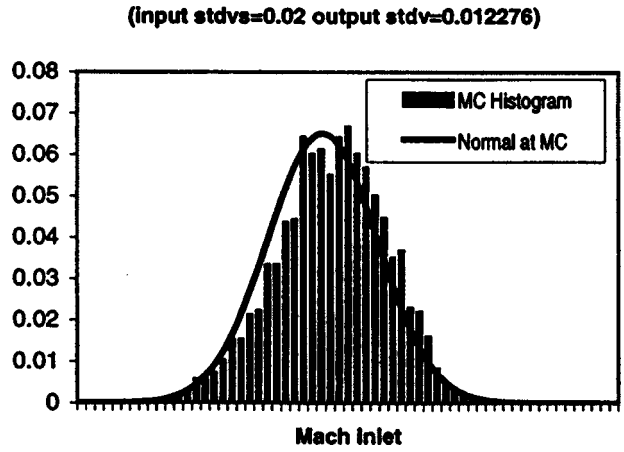

Fig. 8 Probability density function for M (Minf, Pb) for $\sigma_{\text{Minf}} = \sigma_{Pb} = 0.02$

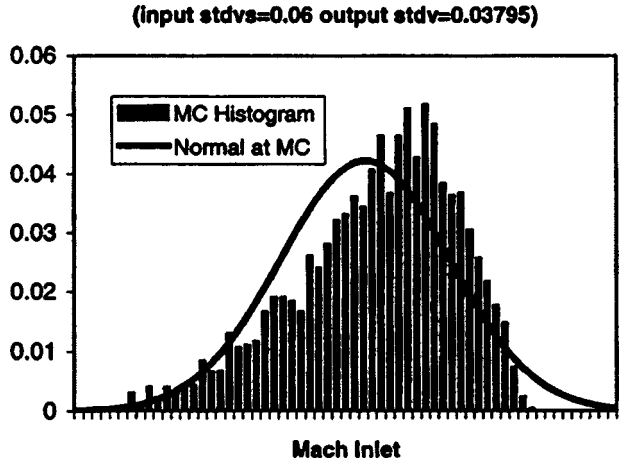

Fig. 9 Probability density function for M (Minf, Pb) for $\sigma_{\text{Minf}} = \sigma_{Pb} = 0.06$

Downloaded 03 Jun 2010 to 171.66.16.150. Redistribution subject to ASME license or copyright; see http://www.asme.org/terms/Terms_Use.cfm

Table 5 Robust shape optimization results with increasing input parameter σ for k=1

$\sigma_a=\sigma_b$	$\bar{a}$	$\bar{b}$	Obj	$\bar{M}$	σ_M	σ_V
0.00	0.6001	0.3001	0.0000	0.4043	0.0000	0.0000
0.02	0.6685	0.3667	0.0004	0.4036	0.0203	0.0120
0.04	0.7338	0.4286	0.0016	0.4018	0.0406	0.0240
0.06	0.7948	0.4841	0.0037	0.3984	0.0607	0.0360
0.08	0.8534	0.5358	0.0065	0.3941	0.0804	0.0480

Table 6 Robust shape optimization results with increasing P_k for $\sigma=0.01$

K	P_k	$\bar{a}$	$\bar{b}$	Obj	$\bar{M}$	σ_M	σ_V
0	0.5000	0.5996	0.2995	0.000104	0.4041	0.0101	0.006
1	0.8413	0.6246	0.3189	0.000118	0.4004	0.0101	0.006
2	0.9772	0.6698	0.3687	0.000104	0.4041	0.0101	0.006
3	0.9986	0.7052	0.4037	0.000104	0.4042	0.0102	0.006
4	0.9999	0.7406	0.4388	0.000104	0.4043	0.0102	0.006

4.4.1 Robust Shape Optimization Results. In Table 5, results for case 1 of the robust shape optimization are displayed. For $\sigma_a=\sigma_b$ ranging from 0 to 0.08, optimal values for the input variables $(\bar{a},\bar{b})$ are listed. As $\sigma_a=\sigma_b$ increases, so does σ_V. Accordingly, the mean values, $(\bar{a},\bar{b})$, which minimize the objective function and satisfy the probabilistic constraint, become increasingly displaced from the target volume, Vt. This is shown in Fig. 10. Mean values $(\bar{a},\bar{b})$ change, keeping the mean value, $\bar{M}(\bar{a},\bar{b})$, of the probabilistic output near the target value, Mt. The robust design points track the dashed curve for $\bar{M}=Mt$ with some displacement due to the $\sigma_M{}^2$ term of the objective, Eq. (15). The volume, $V(\bar{a},\bar{b})$, is displaced from the solid curve $V=Vt$ by $k\sigma_V$, as required by the probabilistic constraint. This displacement can be viewed as the solution dependent or ''effective'' safety factor.

In Fig. 11 the changing area distribution of the robust optimization is illustrated. As the standard deviations of design variables $(\bar{a},\bar{b})$ increase, the optimal nondeterministic volume, $V(\bar{a},\bar{b})$, significantly decreases.

The results for case 2 of the robust shape optimization, where $\alpha_a=\sigma_b$ is fixed at 0.01, and P_k increases from 50 percent to 99.99 percent ($k=0$ to 4) are given in Table 6. Again mean values $(\bar{a},\bar{b})$ change, keeping the mean value, $\bar{M}(\bar{a},\bar{b})$, of the probabilistic output near the target value, Mt. Since $\sigma_a=\sigma_b$ remains small, the $\sigma_{\bar{M}}^2$ term of the objective remains small, and the displacement of $\bar{M}$ from the dashed line depicting Mt due to the σ_M^2 term remains small as shown in Fig. 12. With an increase in P_k, $V(\bar{a},\bar{b})$ is displaced from the solid curve $V=Vt$ by $k\sigma_V$, as required by the probabilistic constraint. Accordingly, the mean values, $(\bar{a},\bar{b})$, which minimize the objective function and satisfy the constraint, again become increasingly displaced from those at the target volume, Vt. Note the significant displacement of the solution from the target volume when P_k is large, i.e., when one is attempting to incorporate the tails of the pdf. In order to increase the probability of constraint satisfaction from 97.77 percent to 99.99 percent, one sees a significant change in $(\bar{a},\bar{b})$ for a mere gain of 2 percent in constraint satisfaction.

4.4.2 Robust Design for Flow Control Results. Similar results are seen in the flow parameter example. In Table 7, the

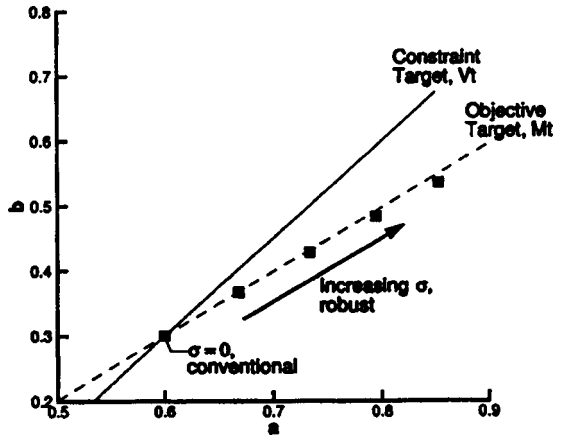

Fig. 10 Optimization results in design space (a,b), P_k fixed at P_1

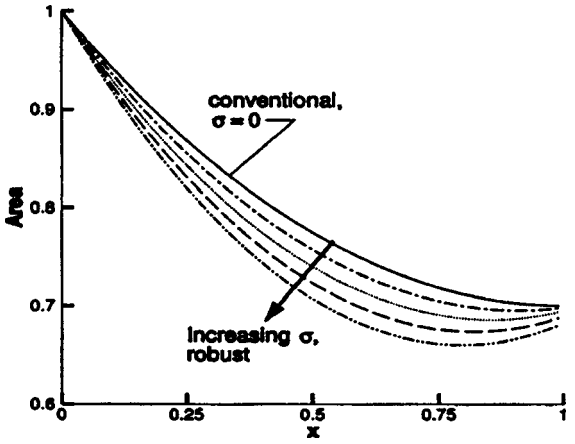

Fig. 11 Nozzle area distributions, P_k fixed at P_1

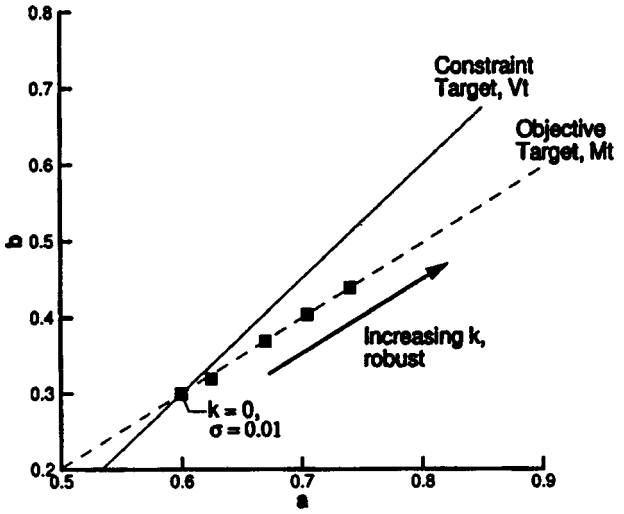

Fig. 12 Optimization results in design space (a,b), σ fixed at 0.01

Table 7 Robust design for flow control results with increasing input parameter σ for k=1

$\sigma_{Min}=\sigma_{Pb}$	$\bar{M}$inf	Pb	Obj	$\bar{M}$	σ_M	σ_q
0	0.3000	0.8000	0.0000	0.3933	0.0000	0.0000
0.02	0.2861	0.7883	0.0001	0.3974	0.0116	0.0058
0.04	0.2655	0.7801	0.0005	0.3985	0.0231	0.0112
0.06	0.2555	0.7653	0.0012	0.4050	0.0327	0.0163
0.08	0.2468	0.7498	0.0020	0.4118	0.0407	0.0209

Downloaded 03 Jun 2010 to 171.66.16.150. Redistribution subject to ASME license or copyright; see http://www.asme.org/terms/Terms_Use.cfm

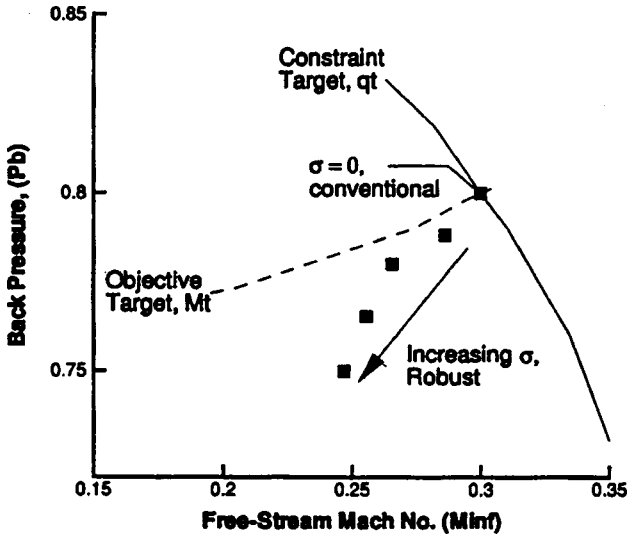

Fig. 13 Optimization results in design space (Minf,Pb), P_k fixed at P_1

results for case 1 are displayed. For $\sigma_{\text{Minf}} = \sigma_{\text{Pb}}$ ranging from 0 to 0.08, optimal values for the input variables ($\overline{\text{M}}\text{inf},\overline{\text{P}}\text{b}$) are listed. As $\sigma_{\text{Minf}} = \sigma_{Pb}$ increases, so does σ_q. Accordingly, the mean values, ($\overline{\text{M}}\text{inf},\overline{\text{P}}\text{b}$), which minimize the objective function and satisfy the constraint, become increasingly displaced from the target mass flux, qt. This is shown in Fig. 13. Mean values ($\overline{\text{M}}\text{inf},\overline{\text{P}}\text{b}$) change, keeping the mean value, $\overline{\text{M}}(\overline{\text{M}}\text{inf},\overline{\text{P}}\text{b})$, of the probabilistic output near the target value, Mt. The robust design points track the dashed curve for $\overline{\text{M}} = \text{Mt}$ with displacement due to the σ_{M}^2 term of the objective, Eq. (17). The optimized mass flux, $q(\overline{\text{M}}\text{inf},\overline{\text{P}}\text{b})$, is displaced from the solid curve $q = qt$ by $k\sigma_q$ as required by the probabilistic constraint.

Table 8 Robust design for flow control results with increasing P_k for $\sigma = 0.01$

K	P_k	$\overline{\text{M}}$inf	$\overline{\text{P}}$b	Obj	$\overline{\text{M}}$	σ_{M}	σ_{q}
0	0.5000	0.3000	0.8000	0.00003	0.3933	0.0060	0.0030
1	0.8413	0.2919	0.7953	0.00003	0.3945	0.0059	0.0029
2	0.9772	0.2825	0.7916	0.00003	0.3949	0.0059	0.0029
3	0.9986	0.2688	0.7896	0.00003	0.3936	0.0060	0.0028
4	0.9999	0.2598	0.7867	0.00003	0.3938	0.0060	0.0028

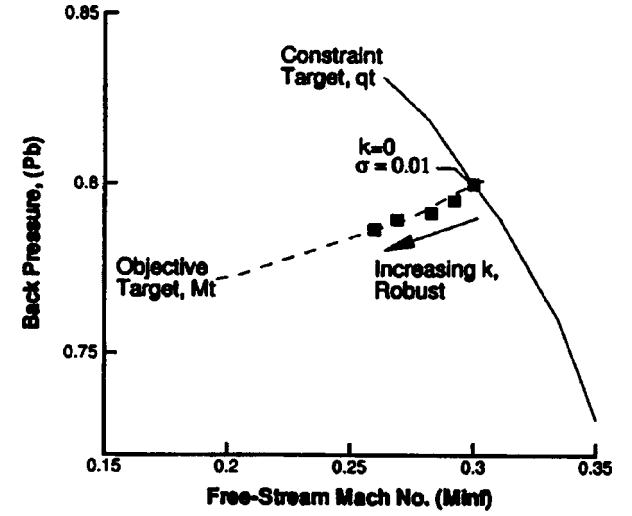

Fig. 14 Optimization results in design space (Minf,Pb), σ fixed at 0.01

The results for case 2 of the robust design for flow control, where $\sigma_{\text{Minf}} = \sigma_{Pb}$ is fixed at 0.01, and P_k increases from 50 percent to 99.99 percent, ($k = 0$ to 4) are given in Table 8. Again, mean values ($\overline{\text{M}}\text{inf},\overline{\text{P}}\text{b}$) change, keeping the mean value, $\overline{\text{M}}(\overline{\text{M}}\text{inf},\overline{\text{P}}\text{b})$, of the probabilistic output near the target value, Mt. As in the preceding example, since $\sigma_{\text{Minf}} = \sigma_{\text{Pb}}$ remains small, the σ_M^2 term of the objective remains small and the displacement due to the σ_M^2 term remains small, as shown in Fig. 14. With an increase in P_k, $q(\overline{\text{M}}\text{inf},\overline{\text{P}}\text{b})$ is displaced from the solid curve $q = qt$ by $k\sigma_q$, as required by the probabilistic constraint. Accordingly, the mean values, ($\overline{\text{M}}\text{inf},\overline{\text{P}}\text{b}$), which minimize the objective function and satisfy the constraint again become increasingly displaced from the target mass flux, *qt*. Again, note the significant displacement from the target mass flux incurred in the higher probability optimizations, i.e., when one is attempting to incorporate the tails of the pdf.

5 Concluding Remarks and Challenges

The present results represent an implementation of the approximate statistical moment method for uncertainty propagation and robust optimization for a quasi 1-D Euler CFD code. Assuming statistically independent, random, normally distributed input variables, first- and second-order statistical moment procedures were performed to approximate the uncertainty in the CFD output. Efficient calculation of both first- and second-order sensitivity derivatives was employed and the validity of the approximations was assessed by comparison with statistical moments generated through Monte Carlo simulations. The uncertainties in the CFD input variables were incorporated into a robust optimization procedure where statistical moments involving first-order sensitivity derivatives appeared in the objective function and system constraints. Second-order sensitivity derivatives were used in a gradient-based robust optimization. The approximate methods used throughout the analyses were found to be valid when considering robustness about input parameter mean values.

Collectively, these results demonstrate the possibility for an approach to treat input parameter uncertainty and its propagation in gradient-based design optimization that is governed by complex CFD analysis solutions. It has been demonstrated on a very simple CFD code and problem; there are computational resource issues to be addressed in application to significant 2-D and 3-D CFD codes and problems. Conventional optimization in 2-D and 3-D already requires significantly more resources than in 1-D and obtaining second-order sensitivity derivatives for more design variables will add even more work. Some of these are addressed in [12] and work is presently in progress regarding application and demonstration using 2-D and 3-D Euler CFD code.

Acknowledgments

The authors wish to thank Dr. Luc Huyse of the Institute for Computer Applications in Science and Engineering (ICASE) at NASA Langley for many helpful discussions regarding statistical aspects related to this study, and also Dr. Thomas Zang of the Multidisciplinary Optimization Branch at NASA Langley for his encouragement and support. One author (ACT III) was partially supported by an ASEE Grant during the summer of 2000 at NASA Langley.

Nomenclature

- A = nozzle area
- a = geometric shape parameter
- b = geometric shape parameter
- **b** = vector of independent input variables

Downloaded 03 Jun 2010 to 171.66.16.150. Redistribution subject to ASME license or copyright; see http://www.asme.org/terms/Terms_Use.cfm

$\mathbf{F}$ = vector of CFD output functions
g = vector of conventional optimization constraints
k = number of standard deviations
M = Mach number at nozzle inlet
$\mathbf{M}$ = vector of Mach number at each grid point
Minf = free-stream Mach number
Mt = target inlet Mach number
N = Monte Carlo sample size
Pb = normalized nozzle static back (outlet) pressure
$\mathbf{Q}$ = vector of flow-field variables (state variables)
q = mass flux through nozzle
qt = target mass flux through nozzle
$\mathbf{R}$ = vector of state equation residuals
V = nozzle volume
Vt = target nozzle volume used for optimization
x = normalized axial position within nozzle
σ = standard deviation
σ^2 = variance

Superscript

- = mean value

Appendix-Quasi One-Dimensional Euler CFD

The steady-state, quasi 1-D Euler equations are

$$\frac{\partial E(Q)}{\partial x} + S(Q) = 0$$

where

$$Q = [\rho, \rho u, \rho e_0]^T,$$

$$E(Q) = [\rho u, \rho u^2 + P, (\rho e_0 + P)u]^T,$$

$$S(Q) = -\frac{dA}{dx}\frac{1}{A}[\rho u, \rho u^2, (\rho e_0 + P)u]^T.$$

In these equations, ρ is density, u is flow speed, P is pressure, e_0 is the specific total energy (i.e., $e_0 = e + u^2/2$, where e is the specific internal energy), and $A(x)$ is the local cross-sectional area. The ideal gas law with a constant ratio of specific heats γ (taken to be 1.4) is used for closure, which implies $P = (\gamma - 1)(\rho e_0 - \rho u^2/2)$. The governing equations are discretized and solved numerically with the upwind flux-vector-splitting method of Van Leer [28], which includes the use of higher order accuracy to approximate the flux terms. A more complete discussion of these numerical procedures is presented in [29]. The flow field was discretized with 100 grid points. This discretiztion of the governing equations, together with the numerical treatment of the boundary conditions, results in a large set of coupled nonlinear algebraic equations with the form of Eq. (5). In this study, the procedure for solving the discrete nonlinear flow equations is Newton's method.

References

[1] Newman, P. A., Hou, G. J.-W., and Taylor, A. C., III, 1997 "Observations Regarding Use of Advanced CFD Analysis, Sensitivity Analysis, and Design Codes in MDO," N.M. Alexandrov, and M.Y. Hussaini, eds., *Multidisciplinary Design Optimization: State of the Art*, SIAM Proceedings Series, SIAM, Philadelphia, pp. 263–279; also ICASE Report 96-16, NASA CR 198293 (available electronically at www.icase.edu).

[2] Newman, J. C., III, Taylor, A. C., III, Barnwell, R. W., Newman, P. A., and Hou, G. J.-W., 1999, "Overview of Sensitivity Analysis and Shape Optimization for Complex Aerodynamic Configurations," J. Aircr., **36**, No. 1, pp. 87–96.

[3] Jameson, A., and Vassberg, J. C., 2001, "Computational Fluid Dynamics for Aerodynamic Design: Its Current and Future Impact," AIAA-2001-0538, Jan.

[4] Thanedar, P. B., and Kodiyalam, S., 1992, "Structural Optimization Using Probabilistic Constraints," Struct. Optim., **4**, pp. 236–240 (also AIAA-91-0922-CP, 1991).

[5] Parkinson, A., Sorensen, C., and Pourhassan, N., 1993, "A General Approach for Robust Optimal Design," ASME J. Mech. Des., **115**, No. 1, pp. 74–80.

[6] Chen, X., Hasselman, T. K., and Neill, D. J., 1997, "Reliability Based Structural Design Optimization for Practical Applications," AIAA-97-1403, Apr.

[7] Du, X., and Chen, W., 1999, "Towards a Better Understanding of Modeling Feasibility Robustness in Engineering Design," American Society of Mechanical Engineers, Paper DAC-8565, Sept.

[8] A Collection of Technical Papers, 40th AIAA/ASME/ASCE/AHS/ASC Structures, Structural Dynamics, and Materials Conference and Exhibit, AIAA Forum on Non-Deterministic Approaches, St. Louis, MO, April 12–15, 1999.

[9] Chinchalkar, S., and Taylor, D. L., 1994, "Geometric Uncertainties in Finite Element Analysis," Computing Systems in Engineering, **5**, No. 2, pp. 159–170.

[10] Du, X., and Chen, W., 2000, "Methodology for Managing the Effect of Uncertainty in Simulation-Based Design," AIAA J., **38**, No. 8, pp. 1471–1478.

[11] Turgeon, E., Pelletier. D., and Borggaard, J., 2001, "Sensitivity and Uncertainty Analysis for Variable Property Flows," AIAA 2001-0139, Jan.

[12] Taylor, A. C., III, Green, L. L., Newman, P. A., and Putko, M. M., "Some Advanced Concepts in Discrete Aerodynamic Sensitivity Analysis," AIAA-2001-2529.

[13] Sherman, L., Taylor, A., III, Green, L., Newman, P., Hou, G., and Korivi, M., 1996, "First-and Second-Order Aerodynamic Sensitivity Derivatives via Automatic Differentiation with Incremental Iterative Methods," J. Comput. Phys., **129**, No. 2, pp. 307–336.

[14] Huyse, L., and Lewis, R. M., 2001, "Aerodynamic Shape Optimization of Two-dimensional Airfoils Under Uncertain Conditions," ICASE Report No. 2001-1, NASA CR-2001-210648, Jan.

[15] Huyse, L., 2001, "Solving Problems of Optimization Under Uncertainty as Statistical Decision Problems." AIAA 2001-1519, Apr.

[16] Oakley, D. R., Sues, R. H., and Rhodes, G. S., 1998, "Performance Optimization of Multidisciplinary Mechanical Systems Subject to Uncertainties," Probabilistic Engineering Mechanics, **13**, No. 1, pp. 15–26.

[17] Alvin, K. F., Oberkampf, W. L., Rutherford, B. M., and Diegert, K. V., 2000, "Methodology for Chacterizing Modeling and Discretization Uncertainties in Computational Simulation," Sandia Report SAND2000-5015, Mar.

[18] Oberkampf, W. L., DeLand, S. M., Rutherford, B. M., Diegert, K. V., and Alvin, K. F., 1999, "A New Methodology for the Estimation of Total Uncertainty in Computational Simulation," AIAA-99-1612, Apr. (see Ref. [8], pp. 3061–3083).

[19] Green, L. L., Newman, P. A., and Haigler, K. J., 1996, "Sensitivity Derivatives for Advanced CFD Algorithm and Viscous Modeling Parameters via Automatic Differentiation," J. Comput. Phys., **125**, No. 2, pp. 313–324 (also AIAA 93-3321).

[20] Robinson, D. G., 1998, "A Survey of Probabilistic Methods Used in Reliability, Risk and Uncertainty Analysis: Analytical Techniques I," Sandia Report SAND98-1189, June.

[21] Bischof, C. H., Carle, A., Corliss, G. F., Griewank, A., and Hovland, P., 1992, "ADIFOR: Generating Derivative Codes from Fortran Programs," Sci. Prog., **1**, No. 1, pp. 1–29.

[22] Bischof, C., Carle, A., Khademi, P., and Mauer, A., 1996, "Automatic Differentiation of FORTRAN," IEEE Comput. Sci. Eng., Fall.

[23] Carle, A., and Fagan, M., 2000, "Overview of Adifor 3.0," Department of Computational and Applied Mathematics, Rice University, CAAM-TR 00-02, Jan.

[24] Anon., 1995, *Design Optimization Tools-DOT Users Manual: Version 4.20*, Vanderplaats Research & Development, Inc., Colorado Springs, May.

[25] Dadone, A., Valorani, M., and Grossman, B., 2000, "Smoothed Sensitivity Equation Method for Fluid Dynamic Design Problems," AIAA J., **38**, No. 3, pp. 418–426.

[26] Zhang, X., Pelletier, D., Trepanier, J., and Camarero, R., 2000, "Verification of Error Estimators for the Euler Equations," AIAA-2000-1001, Jan.

[27] Marsaglia, G., and Zaman, A., 1994, "Some Portable Very-Long-Period Random Number Generators," Comput. Phys., **8**, No. 1, pp. 117–121.

[28] Van Leer, B., 1982, "Flux-Vector Splitting for Euler Equations," ICASE Report 82-30, Sept. (Also *Lecture Notes in Physics*, **170**, pp. 507–512, 1982).

[29] Thomas, J. L., Van Leer, B., and Walters, R. W., 1990, "Implicit Flux-Split Schemes for the Euler Equations," AIAA J., **28**, pp. 973–974.

Downloaded 03 Jun 2010 to 171.66.16.150. Redistribution subject to ASME license or copyright; see http://www.asme.org/terms/Terms_Use.cfm

C. Prud'homme

D. V. Rovas

K. Veroy

L. Machiels

Department of Mechanical Engineering,
Massachusetts Institute of Technology,
Cambridge, MA 02139

Y. Maday

Laboratoire d'Analyse Numérique,
Université Pierre et Marie Curie,
Boîte courrier 187, 75252 Paris,
Cedex 05, France

A. T. Patera

Department of Mechanical Engineering,
Massachusetts Institute of Technology,
Cambridge, MA 02139

G. Turinici

ASCI-CNRS Orsay,
and INRA Rocquencourt M3N,
B.P. 105, 78153 LeChesnay Cedex France

Reliable Real-Time Solution of Parametrized Partial Differential Equations: Reduced-Basis Output Bound Methods

We present a technique for the rapid and reliable prediction of linear-functional outputs of elliptic (and parabolic) partial differential equations with affine parameter dependence. The essential components are (i) (provably) rapidly convergent global reduced-basis approximations—Galerkin projection onto a space W_N spanned by solutions of the governing partial differential equation at N selected points in parameter space; (ii) a posteriori error estimation—relaxations of the error-residual equation that provide inexpensive yet sharp and rigorous bounds for the error in the outputs of interest; and (iii) off-line/on-line computational procedures methods which decouple the generation and projection stages of the approximation process. The operation count for the on-line stage in which, given a new parameter value, we calculate the output of interest and associated error bound, depends only on N (typically very small) and the parametric complexity of the problem; the method is thus ideally suited for the repeated and rapid evaluations required in the context of parameter estimation, design, optimization, and real-time control.
[DOI: 10.1115/1.1448332]

1 Introduction

The optimization, control, and characterization of an engineering component or system requires the prediction of certain ''quantities of interest,'' or performance metrics, which we shall denote *outputs*—for example deflections, maximum stresses, maximum temperatures, heat transfer rates, flowrates, or lift and drags. These outputs are typically expressed as functionals of field variables associated with a parametrized partial differential equation which describes the physical behavior of the component or system. The parameters, which we shall denote *inputs*, serve to identify a particular ''configuration''of the component: these inputs may represent design or decision variables, such as geometry—for example, in optimization studies; control variables, such as actuator power—for example in real-time applications; or characterization variables, such as physical properties—for example in inverse problems. We thus arrive at an implicit *input-output* relationship, evaluation of which demands solution of the underlying partial differential equation.

Our goal is the development of computational methods that permit *rapid* and *reliable* evaluation of this partial-differential-equation-induced input-output relationship *in the limit of many queries*—that is, in the design, optimization, control, and characterization contexts. The ''many queries'' limit has certainly received considerable attention: from ''fast loads'' or multiple right-hand side notions (e.g., Chan and Wan [1], Farhat et al. [2]) to matrix perturbation theories (e.g., Akgun et al. [3], Yip [4]) to continuation methods (e.g., Allgower and Georg [5], Rheinboldt [6]). Our particular approach is based on the reduced-basis method, first introduced in the late 1970s for nonlinear structural analysis (Almroth et al. [7], Noor and Peters [8]), and subsequently developed more broadly in the 1980s and 1990s (Balmes [9], Barrett and Reddien [10], Fink and Rheinboldt [11], Peterson [12], Porsching [13], Rheinboldt [14]). The reduced-basis method recognizes that the field variable is not, in fact, some arbitrary member of the infinite-dimensional solution space associated with the partial differential equation; rather, it resides, or ''evolves,'' on a much lower-dimensional manifold induced by the parametric dependence.

The reduced-basis approach as earlier articulated is local in parameter space in both practice and theory. To wit, Lagrangian or Taylor approximation spaces for the low-dimensional manifold are typically defined relative to a particular parameter point; and the associated *a priori* convergence theory relies on asymptotic arguments in sufficiently small neighborhoods (Fink and Rheinboldt [11]). As a result, the computational improvements—relative to conventional (say) finite element approximation—are often quite modest (Porsching [13]). Our work differs from these earlier efforts in several important ways: first, we develop (in some cases, provably) *global* approximation spaces; second, we introduce rigorous *a posteriori error estimators*; and third, we exploit *off-line/on-line* computational decompositions (see Balmes [9] for an earlier application of this strategy within the reduced-basis context). These three ingredients allow us, for the restricted but important class of ''parameter-affine'' problems, to reliably decouple the generation and projection stages of reduced-basis approximation, thereby effecting computational economies of several orders of magnitude.

In this expository review paper we focus on these new ingredients. In Section 2 we introduce an abstract problem formulation and several illustrative instantiations. In Section 3 we describe, for coercive symmetric problems and ''compliant'' outputs, the reduced-basis approximation; and in Section 4 we present the associated *a posteriori* error estimation procedures. In Section 5 we

Contributed by the Fluids Engineering Division for publication in the JOURNAL OF FLUIDS ENGINEERING. Manuscript received by the Fluids Engineering Division September 13, 2001; revised manuscript received November 2, 2001. Associate Editor. G. Karmadakis.

 Copyright © 2002 by ASME

Downloaded 03 Jun 2010 to 171.66.16.150. Redistribution subject to ASME license or copyright; see http://www.asme.org/terms/Terms_Use.cfm

consider the extension of our approach to noncompliant outputs and nonsymmetric operators; eigenvalue problems; and, more briefly, noncoercive operators, parabolic equations, and nonaffine problems. A description of the system architecture in which these numerical objects reside may be found in Veroy et al. [15].

2 Problem Statement

2.1 Abstract Formulation. We consider a suitably regular domain $\Omega \subset \mathbb{R}^d$, $d=1$, 2, or 3, and associated function space $X \subset H^1(\Omega)$, where $H^1(\Omega)=\{v \in L^2(\Omega),\ \nabla v \in (L^2(\Omega))^d\}$, and $L^2(\Omega)$ is the space of square-X integrable functions over Ω. The inner product and norm associated with X are given by $(\cdot,\cdot)_X$ and $\|\cdot\|_X=(\cdot,\cdot)_X^{1/2}$, respectively. We also define a parameter set $\mathcal{D} \in \mathbb{R}^P$, a particular point in which will be denoted μ. Note that Ω does *not* depend on the parameter.

We then introduce a bilinear form a: $X\times X\times \mathcal{D}\rightarrow \mathbb{R}$, and linear forms f: $X\rightarrow\mathbb{R}$, ℓ: $X\rightarrow\mathbb{R}$. We shall assume that a is continuous, $a(w,v;\mu)\leq \gamma(\mu)\|w\|_X\|v\|_X \leq \gamma_0\|w\|_X\|v\|_X$, $\forall \mu\in\mathcal{D}$; furthermore, in Sections 3 and 4, we assume that a is coercive,

$$0<\alpha_0\leq\alpha(\mu)=\inf_{w\in X}\frac{a(w,w;\mu)}{\|w\|_X^2},\quad \forall \mu\in\mathcal{D}, \tag{1}$$

and symmetric, $a(w,v;\mu)=a(v,w;\mu)$; $\forall w,v\in X$, $\forall\mu\in\mathcal{D}$. We also require that our linear forms f and ℓ be bounded; in Sections 3 and 4 we additionally assume a "compliant" output, $f(v)=\ell(v)$, $\forall v\in X$.

We shall also make certain assumptions on the parametric dependence of a, f, and ℓ. In particular, we shall suppose that, for some finite (preferably small) integer Q, a may be expressed as

$$a(w,v;\mu)=\sum_{q=1}^{Q}\sigma^q(\mu)a^q(w,v),\quad \forall w,v\in X,\forall\mu\in\mathcal{D}, \tag{2}$$

for some σ^q: $\mathcal{D}\rightarrow\mathbb{R}$ and a^q: $X\times X\rightarrow\mathbb{R}$, $q=1,\ldots,Q$. This "separability," or "affine," assumption on the parameter dependence is crucial to computational efficiency; however, certain relaxations are possible—see Section 5.3.3. For simplicity of exposition, we assume that f and ℓ do not depend on μ; in actual practice, affine dependence is readily admitted.

Our abstract problem statement is then: for any $\mu\in\mathcal{D}$, find $s(\mu)\in\mathbb{R}$ given by

$$s(\mu)=\ell(u(\mu)), \tag{3}$$

where $u(\mu)\in X$ is the solution of

$$a(u(\mu),v;\mu)=f(v),\quad \forall v\in X. \tag{4}$$

In the language of the Introduction, a is our partial differential equation (in weak form), μ is our parameter, $u(\mu)$ is our field variable, and $s(\mu)$ is our output. For simplicity of exposition, we may on occasion suppress the explicit dependence on μ.

2.2 Particular Instantiations. We indicate here a few instantiations of the abstract formulation; these will serve to illustrate the methods (for coercive, symmetric problems) of Sections 3 and 4.

2.2.1 A Thermal Fin. In this example, we consider the two- and three-dimensional thermal fins shown in Fig. 1; these examples may be (interactively) accessed on our web site.[1] The fins consist of a vertical central "post" of conductivity $\tilde{k}_0$ and four horizontal "subfins" of conductivity $\tilde{k}^i$, $i=1,\ldots,4$. The fins conduct heat from a prescribed uniform flux source $\tilde{q}''$ at the root $\tilde{\Gamma}_{\text{root}}$ through the post and large-surface-area subfins to the surrounding flowing air; the latter is characterized by a sink temperature $\tilde{u}_0$ and prescribed heat transfer coefficient $\tilde{h}$. The physical model is simple conduction: the temperature field in the fin, $\tilde{u}$, satisfies

$$\sum_{i=0}^{4}\int_{\tilde{\Omega}_i}\tilde{k}^i\tilde{\nabla}\tilde{u}\cdot\tilde{\nabla}\tilde{v}+\int_{\partial\tilde{\Omega}\setminus\tilde{\Gamma}_{\text{root}}}\tilde{h}(\tilde{u}-\tilde{u}_0)\tilde{v}=\int_{\tilde{\Gamma}_{\text{root}}}\tilde{q}''\tilde{v},$$

$$\forall\tilde{v}\in\tilde{X}\equiv H^1(\tilde{\Omega}), \tag{5}$$

where $\tilde{\Omega}_i$ is that part of the domain with conductivity $\tilde{k}^i$, and $\partial\tilde{\Omega}$ denotes the boundary of $\tilde{\Omega}$.

We now (*i*) nondimensionalize the weak equations (5), and (*ii*) apply a continuous piecewise-affine transformation from $\tilde{\Omega}$ to a fixed (μ-independent) reference domain Ω (Maday et al. [16]). The abstract problem statement (4) is then recovered for $\mu=\{k^1,k^2,k^3,k^4,\text{Bi},L,t\}$, $\mathcal{D}=[0.1,10.0]^4\times[0.01,1.0]\times[2.0,3.0]\times[0.1,0.5]$, and $P=7$; here $k^1,\ldots,k^4$ are the thermal conductivities of the "subfins" (see Fig. 1) relative to the thermal conductivity of the fin base; Bi is a nondimensional form of the heat transfer coefficient; and, L, t are the length and thickness of each of the "subfins" relative to the length of the fin root $\tilde{\Gamma}_{\text{root}}$. It is readily verified that a is continuous, coercive, and symmetric; and that the "affine" assumption (2) obtains for $Q=16$ (two-

[1] FIN2D: http://augustine.mit.edu/fin2d/fin2d.pdf and FIN3D: http://augustine.mit.edu/fin3d_1/fin3d_1.pdf

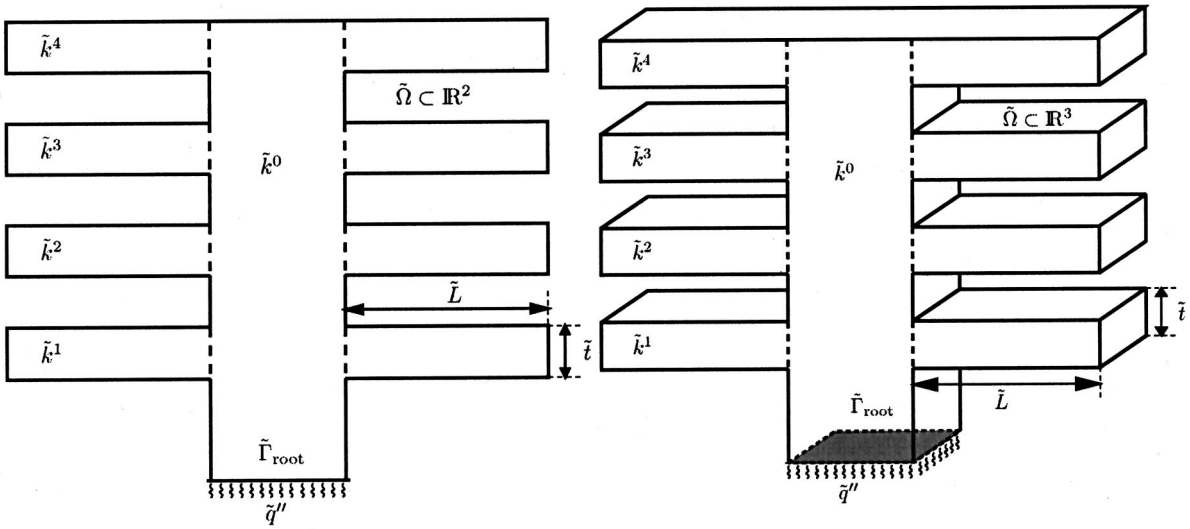

Fig. 1 Two- and three-dimensional thermal fins

Downloaded 03 Jun 2010 to 171.66.16.150. Redistribution subject to ASME license or copyright; see http://www.asme.org/terms/Terms_Use.cfm

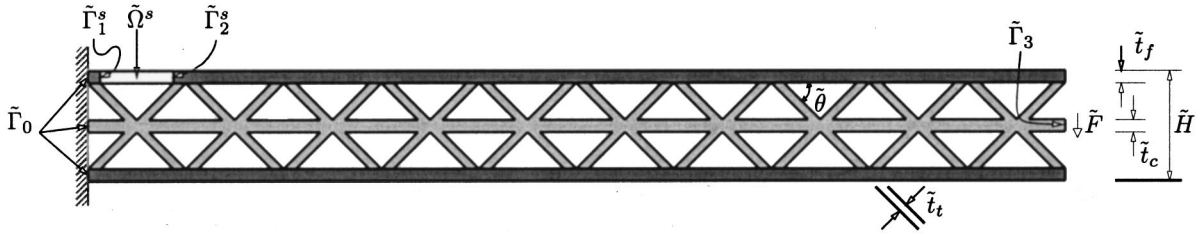

Fig. 2 A truss structure

dimensional case) and $Q=25$ (three-dimensional case). Note that the geometric variations are reflected, via the mapping, in the $\sigma^q(\mu)$.

For our output of interest, $s(\mu)$, we consider the average temperature of the root of the fin nondimensionalized relative to $\tilde{q}''$, $\tilde{k}^0$, and the length of the fin root. This output may be expressed as $s(\mu)=\ell(u(\mu))$, where $\ell(v)=\int_{\Gamma_{\text{root}}} v$. It is readily shown that this output functional is bounded and also "compliant": $\ell(v)=f(v)$, $\forall v\in X$.

2.2.2 A Truss Structure. We consider a prismatic microtruss structure (Evans et al. [17], Wicks and Hutchinson [18]) shown in Fig. 2; this example may be (interactively) accessed on our web site.[2] The truss consists of a frame (upper and lower faces, in dark gray) and a core (trusses and middle sheet, in light gray). The structure transmits a force per unit depth $\tilde{F}$ uniformly distributed over the tip of the middle sheet $\tilde{\Gamma}_3$ through the truss system to the fixed left wall $\tilde{\Gamma}_0$. The physical model is simple plane-strain (two-dimensional) linear elasticity: the displacement field u_i, $i=1,2$, satisfies

$$\int_{\tilde{\Omega}} \frac{\partial \tilde{v}_i}{\partial \tilde{x}_j} \tilde{E}_{ijkl} \frac{\partial \tilde{u}_k}{\partial \tilde{x}_l} = -\left(\frac{\tilde{F}}{\tilde{t}_c}\right) \int_{\tilde{\Gamma}_3} \tilde{v}_2, \quad \forall v \in \tilde{X}, \tag{6}$$

where $\tilde{\Omega}$ is the truss domain, $\tilde{E}_{ijkl}$ is the elasticity tensor, and $\tilde{X}$ refers to the set of functions in $H^1(\tilde{\Omega})$ which vanish on $\tilde{\Gamma}_0$. We assume summation over repeated indices.

We now (*i*) nondimensionalize the weak equations (6), and (*ii*) apply a continuous piecewise-affine transformation from $\tilde{\Omega}$ to a fixed (μ-independent) reference domain Ω. The abstract problem statement (4) is then recovered for $\mu=\{t_f,t_t,H,\theta\}$, $\mathcal{D}=[0.08,1.0]\times[0.2,2.0]\times[4.0,10.0]\times[30.0°,60.0°]$, and $P=4$. Here t_f and t_t are the thicknesses of the frame and trusses (normalized relative to $\tilde{t}_c$), respectively; H is the total height of the microtruss (normalized relative to $\tilde{t}_c$); and θ is the angle between the trusses and the faces. The Poisson's ratio, $\nu=0.3$, and the frame and core Young's moduli, $E_f=75$ GPa and $E_c=200$ GPa, respectively, are held fixed. It is readily verified that a is continuous, coercive, and symmetric; and that the "affine" assumption (2) obtains for $Q=44$.

Our outputs of interest are (*i*) the average downward deflection (compliance) at the core tip, Γ_3, nondimensionalized by $\tilde{F}/\tilde{E}_f$; and (*ii*) the average normal stress across the critical (yield) section denoted Γ_1^s in Fig. 2. These compliance and noncompliance outputs can be expressed as $s^1(\mu)=\ell^1(u(\mu))$ and $s^2(\mu)=\ell^2(u(\mu))$, respectively, where $\ell^1(v)=-\int_{\Gamma_3} v_2$, and

$$\ell^2(v)=\frac{1}{t_f}\int_{\Omega^s} \frac{\partial \chi_i}{\partial x_j} E_{ijkl} \frac{\partial u_k}{\partial x_l}$$

are bounded linear functionals; here χ_i is any suitably smooth function in $H^1(\Omega^s)$ such that $\chi_i \hat{n}_i=1$ on Γ_1^s and $\chi_i \hat{n}_i=0$ on Γ_2^s, where $\hat{n}$ is the unit normal. Note that $s^1(\mu)$ is a compliant output, whereas $s^2(\mu)$ is "noncompliant."

3 Reduced-Basis Approach

We recall that in this section, as well as in Section 4, we assume that a is continuous, coercive, symmetric, and affine in μ—see (2); and that $\ell(v)=f(v)$, which we denote "compliance."

3.1 Reduced-Basis Approximation. We first introduce a sample in parameter space, $S_N=\{\mu_1,\ldots,\mu_N\}$, where $\mu_i\in\mathcal{D}$, $i=1,\ldots,N$; see Section 3.2.2 for a brief discussion of point distribution. We then define our Lagrangian (Porsching [13]) reduced-basis approximation space as $W_N=\text{span}\{\zeta_n\equiv u(\mu_n), n=1,\ldots,N\}$, where $u(\mu_n)\in X$ is the solution to (4) for $\mu=\mu_n$. In actual practice, $u(\mu_n)$ is replaced by an appropriate finite element approximation on a suitably fine truth mesh; we shall discuss the associated computational implications in Section 3.3. Our reduced-basis approximation is then: for any $\mu\in\mathcal{D}$, find $s_N(\mu)=\ell(u_N(\mu))$, where $u_N(\mu)\in W_N$ is the solution of

$$a(u_N(\mu),v;\mu)=\ell(v), \quad \forall v\in W_N. \tag{7}$$

Non-Galerkin projections are briefly described in Section 5.3.1.

3.2 *A Priori* Convergence Theory.

3.2.1 Optimality. We consider here the convergence rate of $u_N(\mu)\to u(\mu)$ and $s_N(\mu)\to s(\mu)$ as $N\to\infty$. To begin, it is standard to demonstrate optimality of $u_N(\mu)$ in the sense that

$$\|u(\mu)-u_N(\mu)\|_X \leq \sqrt{\frac{\gamma(\mu)}{\alpha(\mu)}} \inf_{w_N\in W_N} \|u(\mu)-w_N\|_X. \tag{8}$$

(We note that, in the coercive case, stability of our ("conforming") discrete approximation is not an issue; the noncoercive case is decidedly more delicate (see Section 5.3.1).) Furthermore, for our compliance output,

$$\begin{aligned} s(\mu)&=s_N(\mu)+\ell(u-u_N)=s_N(\mu)+a(u,u-u_N;\mu)\\ &=s_N(\mu)+a(u-u_N,u-u_N;\mu) \end{aligned} \tag{9}$$

from symmetry and Galerkin orthogonality. It follows that $s(\mu)-s_N(\mu)$ converges as the square of the error in the best approximation and, from coercivity, that $s_N(\mu)$ is a lower bound for $s(\mu)$.

3.2.2 Best Approximation. It now remains to bound the dependence of the error in the best approximation as a function of N. At present, the theory is restricted to the case in which $P=1$, $\mathcal{D}=[0,\mu_{\max}]$, and

$$a(w,v;\mu)=a_0(w,v)+\mu a_1(w,v), \tag{10}$$

where a_0 is continuous, coercive, and symmetric, and a_1 is continuous, positive semi-definite ($a_1(w,w)\geq 0$, $\forall w\in X$), and symmetric. This model problem (10) is rather broadly relevant, for

[2] TRUSS: http://augustine.mit.edu/simple_truss/simple_truss.pdf

Downloaded 03 Jun 2010 to 171.66.16.150. Redistribution subject to ASME license or copyright; see http://www.asme.org/terms/Terms_Use.cfm

Table 1 Error, error bound (Method I), and effectivity as a function of N, at a particular representative point $\mu \in \mathcal{D}$, for the two-dimensional thermal fin problem (compliant output)

N	$\lvert s(\mu)-s_N(\mu)\rvert/s(\mu)$	$\Delta_N(\mu)/s(\mu)$	$\eta_N(\mu)$
10	1.29×10^{-2}	8.60×10^{-2}	2.85
20	1.29×10^{-3}	9.36×10^{-3}	2.76
30	5.37×10^{-4}	4.25×10^{-3}	2.68
40	8.00×10^{-5}	5.30×10^{-4}	2.86
50	3.97×10^{-5}	2.97×10^{-4}	2.72
60	1.34×10^{-5}	1.27×10^{-4}	2.54
70	8.10×10^{-6}	7.72×10^{-5}	2.53
80	2.56×10^{-6}	2.24×10^{-5}	2.59

Table 2 Error, error bound (Method II), and effectivity as a function of N, at a particular representative point $\mu \in \mathcal{D}$, for the truss problem (compliant output)

N	$\lvert s(\mu)-s_N(\mu)\rvert/s(\mu)$	$\Delta_N(\mu)/s(\mu)$	$\eta_N(\mu)$
10	3.26×10^{-2}	6.47×10^{-2}	1.98
20	2.56×10^{-4}	4.74×10^{-4}	1.85
30	7.31×10^{-5}	1.38×10^{-4}	1.89
40	1.91×10^{-5}	3.59×10^{-5}	1.88
50	1.09×10^{-5}	2.08×10^{-5}	1.90
60	4.10×10^{-6}	8.19×10^{-6}	2.00
70	2.61×10^{-6}	5.22×10^{-6}	2.00
80	1.19×10^{-6}	2.39×10^{-6}	2.00

example to variable orthotropic conductivity, variable rectilinear geometry, variable piecewise-constant conductivity, and variable Robin boundary conditions.

We now suppose that the μ_n, $n=1,\ldots,N$, are logarithmically distributed in the sense that

$$\ln(\bar{\lambda}\mu_n+1)=\frac{n-1}{N-1}\ln(\bar{\lambda}\mu_{\max}+1),\quad n=1,\ldots,N, \tag{11}$$

where $\bar{\lambda}$ is an upper bound for the maximum eigenvalue of a_1 relative to a_0. (Note $\bar{\lambda}$ is perforce bounded thanks to our assumption of continuity and coercivity; the possibility of a continuous spectrum does not, in practice, pose any problems.) We can then prove (Maday et al. [19]) that, for $N>N_{\text{crit}}\equiv e\,\ln(\bar{\lambda}\mu_{\max}+1)$,

$$\inf_{w_N\in W_N}\|u(\mu)-w_N\|_X\leq(1+\mu_{\max}\bar{\lambda})\|u(0)\|_X \times\exp\left\{\frac{-(N-1)}{(N_{\text{crit}}-1)}\right\},\quad \forall\,\mu\in\mathcal{D}. \tag{12}$$

We observe exponential convergence, uniformly (globally) for all μ in $\mathcal{D}$, with only very weak (logarithmic) dependence on the range of the parameter ($\mu_{\max}$). (Note the constants in (12) are for the particular case in which $(\cdot,\cdot)_X=a_0(\cdot,\cdot)$.)

The proof exploits a parameter-space (nonpolynomial) interpolant as a surrogate for the Galerkin approximation. As a result, the bound is not always "sharp:" we observe many cases in which the Galerkin projection is considerably better than the associated interpolant; optimality (8) chooses to "illuminate" only certain points μ_n, automatically selecting a best "subapproximation" among all (combinatorially many) possibilities. We thus see why reduced-basis *state-space* approximation of $s(\mu)$ via $u(\mu)$ is preferred to simple *parameter-space* interpolation of $s(\mu)$ ("connecting the dots") via $(\mu_n, s(\mu_n))$ pairs. We note, however, that the logarithmic point distribution (11) implicated by our interpolant-based arguments is *not* simply an artifact of the proof: in numerous numerical tests, the logarithmic distribution performs considerably (and in many cases, provably) better than other more obvious candidates, in particular for large ranges of the parameter. Fortunately, the convergence rate is not *too* sensitive to point selection: the theory only requires a log "on the average" distribution (Maday et al. [19]); and, in practice, $\bar{\lambda}$ need not be a sharp upper bound.

The result (12) is certainly tied to the particular form (10) and associated regularity of $u(\mu)$. However, we do observe similar exponential behavior for more general operators; and, most importantly, the exponential convergence rate degrades only very slowly with increasing parameter dimension, P. We present in Table 1 the error $\lvert s(\mu)-s_N(\mu)\rvert/s(\mu)$ as a function of N, at a particular representative point μ in $\mathcal{D}$, for the two-dimensional thermal fin problem of Section 2.2.1; we present similar data in Table 2 for the truss problem of Section 2.2.2. In both cases, since tensor-product grids are prohibitively profligate as P increases, the μ_n are chosen "log-randomly" over $\mathcal{D}$: we sample from a multivariate uniform probability density on $\log(\mu)$. We observe that, for both the thermal fin ($P=7$) and truss ($P=4$) problems, the error is remarkably small even for very small N; and that, in both cases, very rapid convergence obtains as $N\to\infty$. We do not yet have any theory for $P>1$. But certainly the Galerkin optimality plays a central role, automatically selecting "appropriate" scattered-data subsets of S_N and associated "good" weights so as to mitigate the curse of dimensionality as P increases; and the log-random point distribution is also important—for example, for the truss problem of Table 2, a *non-logarithmic* uniform random point distribution for S_N yields errors which are larger by factors of 20 and 10 for $N=30$ and 80, respectively.

3.3 Computational Procedure. The theoretical and empirical results of Sections 3.1 and 3.2 suggest that N may, indeed, be chosen very small. We now develop off-line/on-line computational procedures that exploit this dimension reduction.

We first express $u_N(\mu)$ as

$$u_N(\mu)=\sum_{j=1}^{N}u_{Nj}(\mu)\zeta_j=(\underline{u}_N(\mu))^T\underline{\zeta}, \tag{13}$$

where $\underline{u}_N(\mu)\in\mathbb{R}^N$; we then choose for test functions $v=\zeta_i$, $i=1,\ldots,N$. Inserting these representations into (7) yields the desired algebraic equations for $\underline{u}_N(\mu)\in\mathbb{R}^N$,

$$\underline{A}_N(\mu)\underline{u}_N(\mu)=\underline{F}_N, \tag{14}$$

in terms of which the output can then be evaluated as $s_N(\mu)=\underline{F}_N^T\underline{u}_N(\mu)$. Here $\underline{A}_N(\mu)\in\mathbb{R}^{N\times N}$ is the SPD matrix with entries $A_{N\ i,j}(\mu)\equiv a(\zeta_j,\zeta_i;\mu)$, $1\leq i,j\leq N$, and $\underline{F}_N\in\mathbb{R}^N$ is the "load" (and "output") vector with entries $F_{N\ i}\equiv f(\zeta_i)$, $i=1,\ldots,N$.

We now invoke (2) to write

$$A_{N\ i,j}(\mu)=a(\zeta_j,\zeta_i;\mu)=\sum_{q=1}^{Q}\sigma^q(\mu)a^q(\zeta_j,\zeta_i), \tag{15}$$

or

$$\underline{A}_N(\mu)=\sum_{q=1}^{Q}\sigma^q(\mu)\underline{A}_N^q,$$

where the $\underline{A}_N^q\in\mathbb{R}^{N\times N}$ are given by $A_{N\ i,j}^q=a^q(\zeta_j,\zeta_i)$, $i\leq i,j\leq N$, $1\leq q\leq Q$. The off-line/on-line decomposition is now clear. In the *off-line* stage, we compute the $u(\mu_n)$ and form the $\underline{A}_N^q$ and $\underline{F}_N$: this requires N (expensive) "a" finite element solutions and $O(QN^2)$ finite-element-vector inner products. In the *on-line* stage, for any given new μ, we first form $\underline{A}_N$ from (15), then solve (14) for $\underline{u}_N(\mu)$, and finally evaluate $s_N(\mu)=\underline{F}_N^T\underline{u}_N(\mu)$: this requires $O(QN^2)+O(2/3\ N^3)$ operations and $O(QN^2)$ storage.

Thus, as required, the incremental, or marginal, cost to evaluate $s_N(\mu)$ for any given new μ—as proposed in a design, optimization, or inverse-problem context—is very small: first, because N is very small, typically $O(10)$—thanks to the good convergence properties of W_N; and second, because (14) can be very rapidly

Downloaded 03 Jun 2010 to 171.66.16.150. Redistribution subject to ASME license or copyright; see http://www.asme.org/terms/Terms_Use.cfm

assembled and inverted—thanks to the off-line/on-line decomposition (see Balmes [9] for an earlier application of this strategy within the reduced-basis context). For the problems discussed in this paper, the resulting computational savings relative to standard (well-designed) finite-element approaches are significant, at least $O(10)$, typically $O(100)$, and often $O(1000)$ or more.

4 A Posteriori Error Estimation: Output Bounds

From Section 3 we know that, in theory, we can obtain $s_N(\mu)$ very inexpensively: the on-line computational effort scales as $O(2/3\ N^3)+O(QN^2)$; and N can, *in theory*, be chosen quite small. However, *in practice*, we do not know *how* small N can be chosen: this will depend on the desired accuracy, the selected output(s) of interest, and the particular problem in question; in some cases $N=5$ may suffice, while in other cases, $N=100$ may still be insufficient. In the face of this uncertainty, either too many or too few basis functions will be retained: the former results in computational inefficiency; the latter in unacceptable uncertainty---particularly egregious in the decision contexts in which reduced-basis methods typically serve. We thus need *a posteriori* error estimators for s_N. Surprisingly, *a posteriori* error estimation has received relatively little attention within the reduced-basis frame-work (Noor and Peters [8]), even though reduced-basis methods are particularly in need of accuracy assessment: the spaces are *ad hoc* and pre-asymptotic, thus admitting relatively little intuition, ''rules of thumb,'' or standard approximation notions.

Recall that, in this section, we continue to assume that a is coercive and symmetric, and that ℓ is ''compliant.''

4.1 Method I. The approach described in this section is a particular instance of a general ''variational'' framework for *a posteriori* error estimation of outputs of interest. However, the reduced-basis instantiation described here differs significantly from earlier applications to finite element discretization error (Maday et al. [20], Machiels et al. [21]) and iterative solution error (Patera and Rønquist [22]) both in the choice of (energy) relaxation and in the associated computational artifice.

4.1.1 Formulation. We assume that we are given a positive function $g(\mu):\mathcal{D}\rightarrow\mathbb{R}_+$, and a continuous, coercive, symmetric (μ-independent) bilinear from $\hat{a}:X\times X\rightarrow\mathbb{R}$, such that

$$\underline{\alpha}_0\|v\|_X^2\leqslant g(\mu)\hat{a}(v,v)\leqslant a(v,v;\mu),\quad \forall v\in X,\forall\mu\in\mathcal{D} \tag{16}$$

for some positive real constant $\underline{\alpha}_0$. We then find $\hat{e}(\mu)\in X$ such that

$$g(\mu)\hat{a}(\hat{e}(\mu),v)=R(v;u_N(\mu);\mu),\quad \forall v\in X, \tag{17}$$

where for a given $w\in X$, $R(v;w;\mu)=\ell(v)-a(w,v;\mu)$ is the weak form of the residual. Our lower and upper output estimators are then evaluated as

$$s_N^-(\mu)\equiv s_N(\mu),\ \text{ and }\ s_N^+(\mu)\equiv s_N(\mu)+\Delta_N(\mu), \tag{18}$$

respectively, where

$$\Delta_N(\mu)\equiv g(\mu)\hat{a}(\hat{e}(\mu),\hat{e}(\mu)) \tag{19}$$

is the estimator gap.

4.1.2 Properties. We shall prove in this section that $s_N^-(\mu)\leqslant s(\mu)\leqslant s_N^+(\mu)$, and hence that $|s(\mu)-s_N(\mu)|=s(\mu)-s_N(\mu)\leqslant\Delta_N(\mu)$. Our lower and upper output estimators are thus lower and upper output *bounds*; and our output estimator gap is thus an output *bound* gap—a rigorous bound for the error in the output of interest. It is also critical that $\Delta_N(\mu)$ be a relatively *sharp* bound for the true error: a poor (overly large) bound will encourage us to refine an approximation which is, in fact, already adequate—with a corresponding (unnecessary) increase in off-line and on-line computational effort. We shall prove in this section that $\Delta_N(\mu)\leqslant(\gamma_0/\underline{\alpha}_0)(s(\mu)-s_N(\mu))$, where γ_0 and $\underline{\alpha}_0$ are the *N-independent* a-continuity and $g(\mu)\hat{a}$-coercivity constants defined earlier. Our two results of this section can thus be summarized as

$$1\leqslant\eta_N(\mu)\leqslant\text{Const},\quad\forall N, \tag{20}$$

where

$$\eta_N(\mu)=\frac{\Delta_N(\mu)}{s(\mu)-s_N(\mu)} \tag{21}$$

is the *effectivity*, and Const is a constant independent of N. We shall denote the left (bounding property) and right (sharpness property) inequalities of (20) as the lower effectivity and upper effectivity inequalities, respectively.

We first prove the lower effectivity inequality (bounding property): $s_N^-(\mu)\leqslant s(\mu)\leqslant s_N^+(\mu)$, $\forall\mu\in\mathcal{D}$, for $s_N^-(\mu)$ and $s_N^+(\mu)$ defined in (18). The lower bound property follows directly from Section 3.2.1. To prove the upper bound property, we first observe that $R(v;u_N;\mu)=a(u(\mu)-u_N(\mu),v;\mu)=a(e(\mu),v;\mu)$, where $e(\mu)\equiv u(\mu)-u_N(\mu)$; we may thus rewrite (17) as $g(\mu)\hat{a}(\hat{e}(\mu),v)=a(e(\mu),v;\mu),\forall v\in X$. We thus obtain

$$\begin{aligned}g(\mu)\hat{a}(\hat{e},\hat{e})&=g(\mu)\hat{a}(\hat{e}-e,\hat{e}-e)+2g(\mu)\hat{a}(\hat{e},e)-g(\mu)\hat{a}(e,e)\\&=g(\mu)\hat{a}(\hat{e}-e,\hat{e}-e)+(a(e,e;\mu)-g(\mu)\hat{a}(e,e))\\&\quad+a(e,e;\mu)\\&\geqslant a(e,e;\mu)\end{aligned} \tag{22}$$

since $g(\mu)\hat{a}(\hat{e}(\mu)-e(\mu),\hat{e}(\mu)-e(\mu))\geqslant 0$ and $a(e(\mu),e(\mu);\mu)-g(\mu)\hat{a}(e\mu),e(\mu))\geqslant 0$ from (16). Invoking (9) and (22), we then obtain $s(\mu)-s_N(\mu)=a(e(\mu),e(\mu);\mu)\leqslant g(\mu)\hat{a}(\hat{e}(\mu),\hat{e}(\mu))$; and thus $s(\mu)\leqslant s_N(\mu)+g(\mu)\hat{a}(\hat{e}(\mu),\hat{e}(\mu))\equiv s_N^+(\mu)$, as desired.

We next prove the upper effectivity inequality (sharpness property):

$$\eta_N(\mu)=\frac{\Delta_N(\mu)}{s(\mu)-s_N(\mu)}\leqslant\frac{\gamma_0}{\underline{\alpha}_0},\quad\forall N.$$

To begin, we appeal to a-continuity and $g(\mu)\hat{a}$-coercivity to obtain

$$a(\hat{e}(\mu),\hat{e}(\mu);\mu)\leqslant\frac{\gamma_0 g(\mu)}{\underline{\alpha}_0}\hat{a}(\hat{e}(\mu),\hat{e}(\mu)). \tag{23}$$

But from the modified error equation (17) we know that $g(\mu)\hat{a}(\hat{e}(\mu),\hat{e}(\mu))=a(e(\mu),\hat{e}(\mu);\mu)$. Invoking the Cauchy-Schwartz inequality, we obtain

$$\begin{aligned}g(\mu)\hat{a}(\hat{e},\hat{e})&=a(e,\hat{e};\mu)\\&\leqslant(a(\hat{e},\hat{e};\mu))^{1/2}(a(e,e;\mu))^{1/2}\\&\leqslant\left(\frac{\gamma_0}{\underline{\alpha}_0}\right)^{1/2}(g(\mu)\hat{a}(\hat{e},\hat{e}))^{1/2}(a(e,e;\mu))^{1/2};\end{aligned}$$

the desired result then directly follows from (19) and (9).

We now provide empirical evidence for (20). In particular, we present in Table 1 the bound gap and effectivities for the thermal fin example. Clearly, $\eta_N(\mu)$ is always greater than unity for any N, and bounded---indeed, quite close to unity---as $N\rightarrow\infty$.

4.1.3. Computational Procedure. Finally, we turn to the computational artifice by which we can efficiently compute $\Delta_N(\mu)$ in the on-line stage of our procedure. We again exploit the affine parameter dependence, but now in a less transparent fashion. To begin, we rewrite the ''modified'' error equation, (17), as

$$\hat{a}(\hat{e}(\mu),v)=\frac{1}{g(\mu)}\left(\ell(v)-\sum_{q=1}^{Q}\sum_{j=1}^{N}\sigma^q(\mu)u_{N\ j}(\mu)a^q(\zeta_j,v)\right),\quad\forall v\in X,$$

Downloaded 03 Jun 2010 to 171.66.16.150. Redistribution subject to ASME license or copyright; see http://www.asme.org/terms/Terms_Use.cfm

where we have appealed to our reduced-basis approximation (13) and the affine decomposition (2). It is immediately clear from linear superposition that we can express $\hat{e}(\mu)$ as

$$\hat{e}(\mu)=\frac{1}{g(\mu)}\left(\hat{z}_0+\sum_{q=1}^{Q}\sum_{j=1}^{N}\sigma^q(\mu)u_{N\ j}(\mu)\hat{z}_j^q\right), \tag{24}$$

where $\hat{z}_0\in X$ satisfies $\hat{a}(\hat{z}_0,v)=\ell(v)$, $\forall v\in X$, and $\hat{z}_j^q\in X$, $j=1,\ldots,N$, $q=1,\ldots,Q$, satisfies $\hat{a}(\hat{z}_j^q,v)=-a^q(\zeta_j,v)$, $\forall v\in X$. Inserting (24) into our expression for the upper bound, $s_N^+(\mu)=s_N(\mu)+g(\mu)\hat{a}(\hat{e}(\mu),\hat{e}(\mu))$, we obtain

$$\begin{aligned}s_N^+(\mu)&=s_N(\mu)+\frac{1}{g(\mu)}\left(c_0+2\sum_{q=1}^{Q}\sum_{j=1}^{N}\sigma^q(\mu)u_{N\ j}(\mu)\Lambda_j^q\right.\\&\left.+\sum_{q=1}^{Q}\sum_{q'=1}^{Q}\sum_{j=1}^{N}\sum_{j'=1}^{N}\sigma^q(\mu)\sigma^{q'}(\mu)u_{N\ j}(\mu)u_{N\ j'}(\mu)\Gamma_{jj'}^{qq'}\right)\end{aligned} \tag{25}$$

where $c_0=\hat{a}(\hat{z}_0,\hat{z}_0)$, $\Lambda_j^q=\hat{a}(\hat{z}_0,\hat{z}_j^q)$, and $\Gamma_{jj'}^{qq'}=\hat{a}(\hat{z}_j^q,\hat{z}_{j'}^{q'})$.

The off-line/on-line decomposition should now be clear. In the *off-line* stage we compute $\hat{z}_0$ and $\hat{z}_j^q$, $j=1,\ldots,N$, $q=1,\ldots,Q$, and then form c_0, Λ_j^q, and $\Gamma_{jj'}^{qq'}$: this requires $QN+1$ (expensive) "$\hat{a}$" finite element solutions, and $O(Q^2N^2)$ finite-element-vector inner products. In the *on-line* stage, for any given new μ, we evaluate s_N^+ as expressed in (25): this requires $O(Q^2N^2)$ operations and $O(Q^2N^2)$ storage (for c_0, Λ_j^q, and $\Gamma_{jj'}^{qq'}$). As for the computation of $s_N(\mu)$, the marginal cost for the computation of $s_N^{\pm}(\mu)$ for any given new μ is quite small—in particular, it is *independent* of the dimension of the truth finite element approximation space X.

There are a variety of ways in which the off-line/on-line decomposition and output error bounds can be exploited. A particularly attractive mode incorporates the error bounds into an on-line adaptive process, in which we successively approximate $s_N(\mu)$ on a sequence of approximation spaces $W_{N_j'}\subset W_N$, $N_j'=N_0 2^j$---for example, $W_{N_j'}$ may contain the N_j' samples points of S_N closest to the new μ of interest---until $\Delta_{N_j'}$ is less than a specified error tolerance. This procedure both minimizes the on-line computational effort and reduces conditioning problems—while simultaneously ensuring accuracy and certainty.

The essential advantage of the approach described in this section is the guarantee of rigorous bounds. There are, however, certain disadvantages. The first set of disadvantages relates to the choice of $g(\mu)$ and $\hat{a}$. In many cases, simple inspection suffices: for example, in our thermal fin problem of Section 2.2.1, $g(\mu)=\min_{q=1,\ldots,Q}\sigma^q(\mu)$ and $\hat{a}(w,v)=\Sigma_{q=1}^{Q}a^q(w,v)$ yields the very good effectivities summarized in Table 1. In other cases, however, there is no self-evident (or readily computed, Maday et al. [23]) good choice: for example, for the truss problem of Section 2.2.2, the existence of almost-pure rotations renders $g(\mu)$ very small relative to $\gamma(\mu)$, with corresponding detriment to $\eta_N(\mu)$. The second set of disadvantages relates to the computational expense—the $O(Q)$ off-line and the $O(Q^2)$ on-line scaling induced by (24) and (25), respectively. Both of these disadvantages are eliminated in the "Method II" to be discussed in the next section; however "Method II" only provides *asymptotic* bounds as $N\to\infty$. The choice thus depends on the relative importance of absolute certainty and computational efficiency.

4.2. Method II. As already indicated, Method I has certain limitations; we discuss here a Method II which addresses these limitations, albeit at the loss of complete certainty.

4.2.1. Formulation. To begin, we set $M>N$, and introduce a parameter sample $S_M=\{\mu_1,\ldots,\mu_M\}$ and associated reduced-basis approximation space $W_M=\text{span}\{\zeta_m\equiv u(\mu_m),m=1,\ldots,M\}$; for both theoretical and practical reasons we require $S_N\subset S_M$ and therefore $W_N\subset W_M$. The procedure is very simple: we first find $u_M(\mu)\in W_M$ such that $a(u_M(\mu),v;\mu)=f(v)$, $\forall v\in W_M$; we then evaluate $s_M(\mu)=\ell(u_M(\mu))$; and, finally, we compute our upper and lower output estimators as

$$s_{N,M}^-(\mu)=s_N(\mu),\quad s_{N,M}^+(\mu)=s_N(\mu)+\Delta_{N,M}(\mu), \tag{26}$$

where $\Delta_{N,M}(\mu)$, the estimator bound gap, is given by

$$\Delta_{N,M}(\mu)=\frac{1}{\tau}(s_M(\mu)-s_N(\mu)) \tag{27}$$

for some $\tau\in(0,1)$. The effectivity of the approximation is defined as

$$\eta_{N,M}(\mu)=\frac{\Delta_{N,M}(\mu)}{s(\mu)-s_N(\mu)}. \tag{28}$$

For our purposes here, we shall consider $M=2N$.

4.2.2. Properties. As for Method I, we would like to prove the effectivity inequality $1\leqslant\eta_{N,2N}(\mu)\leqslant\text{Const}$, $\forall N$. However, we will only be able to demonstrate an asymptotic form of this inequality. Furthermore, the latter shall require, and we shall make, the hypothesis that

$$\varepsilon_{N,2N}(\mu)\equiv\frac{s(\mu)-s_{2N}(\mu)}{s(\mu)-s_N(\mu)}\to 0,\quad \text{as } N\to\infty. \tag{29}$$

We note that the assumption (29) is certainly plausible: if our *a priori* bound of (12) in fact reflects asymptotic behavior, then $s(\mu)-s_N(\mu)\sim c_1e^{-c_2N}$, $s(\mu)-s_{2N}(\mu)\sim c_1e^{-2c_2N}$, and hence $\varepsilon_{N,2N}(\mu)\sim e^{-c_2N}$, as desired.

We first prove the lower effectivity inequality (bounding property): $s_{N,2N}^-(\mu)\leqslant s(\mu)\leqslant s_{N,2N}^+(\mu)$, as $N\to\infty$. To demonstrate the lower bound we again appeal to (9) and the coercivity of a; indeed, this result (still) obtains for *all* N. To demonstrate the upper bound, we write

$$s_{N,2N}^+(\mu)=s(\mu)+\left(\frac{1}{\tau}-1\right)(s(\mu)-s_N(\mu))-\frac{1}{\tau}(s(\mu)-s_{2N}(\mu)) \tag{30}$$

$$=s(\mu)+\left(\frac{1}{\tau}[1-\varepsilon_{N,2N}(\mu)]-1\right)(s(\mu)-s_N(\mu)). \tag{31}$$

We now recall that $s(\mu)-s_N(\mu)\geqslant 0$, and that $0<\tau<1$—that is, $1/\tau>1$; it then follows from (31) and our hypothesis (29) that there exists a finite N^* such that

$$s_{N,2N}^+(\mu)-s(\mu)\geqslant 0,\quad \forall N>N^*. \tag{32}$$

This concludes the proof: we obtain *asymptotic* bounds.

We now prove the upper effectivity inequality (sharpness property). From the definitions of $\eta_{N,2N}(\mu)$, $\Delta_{N,2N}(\mu)$ and $\varepsilon_{N,2N}(\mu)$, we directly obtain

$$\eta_{N,2N}(\mu)=\frac{1}{\tau}\frac{s_{2N}(\mu)-s_N(\mu)}{s(\mu)-s_N(\mu)}$$

$$=\frac{1}{\tau}\frac{(s_{2N}(\mu)-s(\mu))-(s_N(\mu)-s(\mu))}{(s(\mu)-s_N(\mu))} \tag{33}$$

$$=\frac{1}{\tau}(1-\varepsilon_{N,2N}(\mu)). \tag{34}$$

It is readily shown that $\eta_{N,2N}(\mu)$ is bounded from above by $1/\tau$ for all N: we know from (9) that $\varepsilon_{N,2N}(\mu)$ is strictly non-negative. It can also readily be shown that $\eta_{N,2N}(\mu)$ is non-negative: since

Downloaded 03 Jun 2010 to 171.66.16.150. Redistribution subject to ASME license or copyright; see http://www.asme.org/terms/Terms_Use.cfm

$W_N \subset W_{2N}$, it follows from (8) (for $(\cdot,\cdot)_X = a(\cdot,\cdot;\mu)$) and (9) that $s(\mu) \geq s_{2N}(\mu) \geq s_N(\mu)$, and hence $\varepsilon_{N,2N}(\mu) \leq 1$. We thus conclude that $0 \leq \eta_{N,2N}(\mu) \leq 1/\tau$ for all N. Furthermore, from our hypothesis on $\varepsilon_{N,2N}(\mu)$, (29), we know that $\eta_{N,2N}(\mu)$ will *tend* to $1/\tau$ as N increases.

The essential approximation enabler is exponential convergence: we obtain bounds even for rather small N and relatively large τ. We thus achieve both "near" certainty *and* good effectivities. We demonstrate this claim in Table 2, in which we present the bound gap and effectivity for our truss example of Section 2.2.2; the results tabulated correspond to the choice $\tau = 1/2$. We clearly obtain bounds for all N; and we observe that $\eta_{N,2N}(\mu)$ does, indeed, rather quickly approach $1/\tau$.

4.2.3. Computational Procedure. Since the error bounds are based entirely on evaluation of the output,we can directly adapt the off-line/on-line procedure of Section 3.3. Note that the calculation of the output approximation $s_N(\mu)$ and the output bounds are now integrated: $\underline{A}_N(\mu)$ and $\underline{F}_N(\mu)$ (yielding $s_N(\mu)$) are a sub-matrix and sub-vector of $\underline{A}_{2N}(\mu)$ and $\underline{F}_{2N}(\mu)$ (yielding $s_{2N}(\mu)$, $\Delta_{N,2N}(\mu)$, and $s^{\pm}_{N,2N}(\mu)$), respectively. In the *off-line* stage, we compute the $u(\mu_n)$ and form the $\underline{A}^q_{2N}$ and $\underline{F}_{2N}$: this requires $2N$ (expensive) "a" finite element solutions, and $O(4QN^2)$ finite-element-vector inner products. In the *on-line* stage, for any given new μ, we first form $\underline{A}_N(\mu)$, $\underline{F}_N$ and $\underline{A}_{2N}(\mu)$, $\underline{F}_{2N}$, then solve for $\underline{u}_N(\mu)$ and $\underline{u}_{2N}(\mu)$, and finally evaluate $s^{\pm}_{N,2N}(\mu)$: this requires $O(4QN^2) + O(16/3\ N^3)$ operations and $O(4QN^2)$ storage. The on-line effort for this Method II predictor/error estimator procedure (based on $s_N(\mu)$ and $s_{2N}(\mu)$) will thus require eightfold more operations than the "predictor-only" procedure of Section 3.

Method II is in some sense very naïve: we simply replace the true output $s(\mu)$ with a finer-approximation surrogate $s_{2N}(\mu)$. (There are more obscure ways to describe the method—in terms of a reduced-basis approximation for the error—however, there is little to be gained from these alternative interpretations.) The essential computation enabler is again exponential convergence, which permits us to choose $M = 2N$—hence controlling the additional computational effort attributable to error estimation—while simultaneously ensuring that $\varepsilon_{N,2N}(\mu)$ tends rapidly to zero. Exponential convergence also ensures that the cost to compute both $s_N(\mu)$ and $s_{2N}(\mu)$ is "negligible." In actual practice, since $s_{2N}(\mu)$ is available, we can of course take $s_{2N}(\mu)$, rather than $s_N(\mu)$, as our output prediction; this greatly improves not only accuracy, but also certainty—$\Delta_{N,2N}(\mu)$ is almost surely a bound for $s(\mu) - s_{2N}(\mu)$, albeit an exponentially conservative bound as N tends to infinity.

5. Extensions

5.1. Noncompliant Outputs and Nonsymmetric Operators. In Sections 3 and 4 we formulate the reduced-basis method and associated error estimation procedure for the case of compliant outputs, $\ell(v) = f(v)$, $\forall v \in X$. We briefly summarize here the formulation and theory for more general linear bounded output functionals; moreover, the assumption of symmetry (but not yet coercivity) is relaxed, permitting treatment of a wider class of problems---a representative example is the convection-diffusion equation, in which the presence of the convective term renders the operator nonsymmetric. We first present the reduced-basis approximation, now involving a dual or adjoint problem; we then formulate the associated *a posteriori* error estimators; and we conclude with a few illustrative results.

As a preliminary, we first generalize the abstract formulation of Section 2.1. As before, we define the "primal" problem as in (4), however we of course no longer require symmetry. But we also introduce an associated adjoint or "dual" problem: for any $\mu \in X$, find $\psi(\mu) \in X$ such that

$$a(v,\psi(\mu);\mu) = -\ell(v), \quad \forall v \in X; \tag{35}$$

recall that $\ell(v)$ is our output functional.

5.1.1. Reduced-Basis Approximation. To develop the reduced-basis space, we first choose, randomly or log-randomly as described in Section 3.2, a sample set in parameter space, $S_{N/2} = \{\mu_1, \ldots, \mu_{N/2}\}$, where $\mu_i \in \mathcal{D}$, $i = 1, \ldots, N/2$ (N even). We next define an "integrated" Lagrangian reduced-basis approximation space, $W_N = \text{span}\{(u(\mu_n), \psi(\mu_n)), n = 1, \ldots, N/2\}$.

For any $\mu \in \mathcal{D}$, our reduced basis approximation is then obtained by standard Galerkin projection onto W_N (though for highly nonsymmetric operators minimum residual and Petrov-Galerkin projections are attractive—stabler—alternatives). To wit, for the primal problem, we find $u_N(\mu) \in W_N$ such that $a(u_N(\mu),v;\mu) = f(v)$, $\forall v \in W_N$; and for the adjoint problem, we define (though, unless otherwise indicated, do *not* compute) $\psi_N(\mu) \in W_N$ such that $a(v,\psi_N(\mu);\mu) = -\ell(v)$, $\forall v \in W_N$. The reduced-basis output approximation is then calculated from $s_N(\mu) = \ell(u_N(\mu))$.

Turning now to the *a priori* theory, it follows from standard arguments that $u_N(\mu)$ and $\psi_N(\mu)$ are "optimal" in the sense that

$$\|u(\mu) - u_N(\mu)\|_X \leq \left(1 + \frac{\gamma(\mu)}{\alpha(\mu)}\right) \inf_{w_N \in W_N} \|u(\mu) - w_N\|_X,$$

$$\|\psi(\mu) - \psi_N(\mu)\|_X \leq \left(1 + \frac{\gamma(\mu)}{\alpha(\mu)}\right) \inf_{w_N \in W_N} \|\psi(\mu) - w_N\|_X.$$

The best approximation analysis is then similar to that presented in Section 3.2. As regards our output, we now have

$$\begin{aligned} |s(\mu) - s_N(\mu)| &= |\ell(u(\mu)) - \ell(u_N(\mu))| \\ &= |a(u - u_N, \psi; \mu)| \\ &= |a(u - u_N, \psi - \psi_N; \mu)| \leq \gamma_0 \|u - u_N\|_X \|\psi - \psi_N\|_X \end{aligned} \tag{36}$$

from Galerkin orthogonality, the definition of the primal and the adjoint problems, and the Cauchy-Schwartz inequality. We now understand why we include the $\psi(\mu_n)$ in W_N: to ensure that $\|\psi(\mu) - \psi_N(\mu)\|_X$ is small. We thus recover the "square" effect in the convergence rate of the output, albeit (and unlike the symmetric case) at the expense of some additional computational effort—the inclusion of the $\psi(\mu_n)$ in W_N; typically, even for the very rapidly convergent reduced-basis approximation, the "fixed error-minimum cost" criterion favors the adjoint enrichment.

For simplicity of exposition (and to a certain extent, implementation),we present here the "integrated" primal-dual approximation space. However, there are significant computational and conditioning advantages associated with a "nonintegrated" approach, in which we introduce *separate* primal ($u(\mu_n)$) and dual ($\psi(\mu_n)$) approximation spaces for $u(\mu)$ and $\psi(\mu)$, respectively. Note in the "nonintegrated" case we are obliged to compute $\psi_N(\mu)$, since to preserve the output error "square effect" we must modify our predictor with a residual correction, $f(\psi_N(\mu)) - a(u_N(\mu),\psi_N(\mu);\mu)$ (Maday et al. [23]). Both the "integrated" and "nonintegrated" approaches admit an off-line/on-line decomposition similar to that described in Section 3.3 for the compliant, symmetric problem; as before, the on-line complexity and storage are independent of the dimension of the very fine ("truth") finite element approximation.

5.1.2. Method I A Posteriori Error Estimators. We extend here the method developed in Section 4.1.2 to the more general case of noncompliant and nonsymmetric problems. We begin with the formulation.

We first find $\hat{e}^{\text{pr}}(\mu) \in X$ such that

$$g(\mu)\hat{a}(\hat{e}^{\text{pr}}(\mu),v) = R^{\text{pr}}(v;u_N(\mu);\mu), \quad \forall v \in X,$$

where $R^{\text{pr}}(v;w;\mu) \equiv f(v) - a(w,v;\mu)$, $\forall v \in X$; and $\hat{e}^{\text{du}}(\mu) \in X$ such that

Downloaded 03 Jun 2010 to 171.66.16.150. Redistribution subject to ASME license or copyright; see http://www.asme.org/terms/Terms_Use.cfm

$$g(\mu)\hat{a}(\hat{e}^{\rm du}(\mu),v)=R^{\rm du}(v;\psi_N(\mu);\mu),\quad \forall v\in X,$$

where $R^{\rm du}(v;w;\mu)\equiv -\ell(v)-a(v,w;\mu)$, $\forall v\in X$. We then define

$$\overline{s_N}(\mu)=s_N(\mu)-\frac{g(\mu)}{2}\hat{a}(\hat{e}^{\rm pr}(\mu),\hat{e}^{\rm du}(\mu)),\quad \text{and} \tag{37}$$

$$\Delta_N(\mu)=\frac{g(\mu)}{2}[\hat{a}(\hat{e}^{\rm pr}(\mu),\hat{e}^{\rm pr}(\mu))]^{1/2}[\hat{a}(\hat{e}^{\rm du}(\mu),\hat{e}^{\rm du}(\mu))]^{1/2}. \tag{38}$$

Finally, we evaluate our lower and upper estimators as $s_N^{\pm}(\mu)=\overline{s_N}(\mu)\pm\Delta_N(\mu)$. Note that, as before, $g(\mu)$ and $\hat{a}$ still satisfy (16); and that, furthermore, (16) will only involve the *symmetric* part of a. We define the effectivity as

$$\eta_N(\mu)=\frac{\Delta_N(\mu)}{|s(\mu)-s_N(\mu)|}; \tag{39}$$

note that $s(\mu)-s_N(\mu)$ now has no definite sign.

We now prove that our error estimators are bounds (the lower effectivity inequality): $s_N^-(\mu)\leq s(\mu)\leq s_N^+(\mu)$, $\forall N$. To begin, we define $\hat{e}^{\pm}(\mu)=\hat{e}^{\rm pr}(\mu)\mp 1/\kappa\ \hat{e}^{\rm du}(\mu)$, and note that, from the coercivity of $\hat{a}$,

$$\begin{aligned}\kappa g(\mu)\hat{a}&\left(e^{\rm pr}-\frac{1}{2}\hat{e}^{\pm},e^{\rm pr}-\frac{1}{2}\hat{e}^{\pm}\right)\\&=\kappa g(\mu)\hat{a}(e^{\rm pr},e^{\rm pr})\\&\quad+\frac{\kappa g(\mu)}{4}\hat{a}(\hat{e}^{\pm},\hat{e}^{\pm})-\kappa g(\mu)\hat{a}(\hat{e}^{\pm},e^{\rm pr})\geq 0,\end{aligned} \tag{40}$$

where $e^{\rm pr}(\mu)=u(\mu)-u_N(\mu)$, $e^{\rm du}(\mu)=\psi(\mu)-\psi_N(\mu)$, and κ is a positive real number. From the definition of $\hat{e}^{\pm}(\mu)$ and $\hat{e}^{\rm pr}(\mu)$, $\hat{e}^{\rm du}(\mu)$, we can express the "cross-term" as

$$\begin{aligned}g(\mu)\hat{a}(\hat{e}^{\pm},e^{\rm pr})&=R^{\rm pr}(e^{\rm pr};u_N;\mu)\mp\frac{1}{\kappa}R^{\rm du}(e^{\rm pr};\psi_N;\mu)\\&=a(e^{\rm pr},e^{\rm pr};\mu)\mp\frac{1}{\kappa}a(e^{\rm pr},e^{\rm du};\mu)\\&=a(e^{\rm pr},e^{\rm pr};\mu)\pm\frac{1}{\kappa}(s(\mu)-s_N(\mu)),\end{aligned} \tag{41}$$

since $R^{\rm pr}(e^{\rm pr};u_N;\mu)=a(u,e^{\rm pr};\mu)-a(u_N,e^{\rm pr};\mu)=a(e^{\rm pr},e^{\rm pr};\mu)$, $R^{\rm du}(e^{\rm pr};\psi_N;\mu)=a(e^{\rm pr},\psi;\mu)-a(e^{\rm pr},\psi_N;\mu)=a(e^{\rm pr},e^{\rm du};\mu)$, and $\ell(u)-\ell(u_N)=-a(u-u_N,\psi;\mu)=-a(u-u_N,\psi-\psi_N;\mu)$ (by Galerkin orthogonality)$=-a(e^{\rm pr},e^{\rm du};\mu)$. We then substitute (41) into (40) to obtain

$$\begin{aligned}\pm(s(\mu)-s_N(\mu))&\leq-\kappa(a(e^{\rm pr},e^{\rm pr};\mu)-g(\mu)\hat{a}(e^{\rm pr},e^{\rm pr}))\\&\quad+\frac{\kappa g(\mu)}{4}\hat{a}(\hat{e}^{\pm},\hat{e}^{\pm})\leq\frac{\kappa g(\mu)}{4}\hat{a}(\hat{e}^{\pm},\hat{e}^{\pm}),\end{aligned}$$

since $\kappa>0$ and $a(e^{\rm pr}(\mu),e^{\rm pr}(\mu);\mu)-g(\mu)\hat{a}(e^{\rm pr}(\mu),e^{\rm pr}(\mu))\geq 0$ from (16).

Expanding $\hat{e}^{\pm}(\mu)=\hat{e}^{\rm pr}(\mu)\mp 1/\kappa\ \hat{e}^{\rm du}(\mu)$ then gives

$$\begin{aligned}&\pm(s(\mu)-s_N(\mu))\\&\quad\leq\frac{g(\mu)}{4}\left[\kappa\hat{a}(\hat{e}^{\rm pr},\hat{e}^{\rm pr})+\frac{1}{\kappa}\hat{a}(\hat{e}^{\rm du},\hat{e}^{\rm du})\mp 2\hat{a}(\hat{e}^{\rm pr},\hat{e}^{\rm du})\right],\end{aligned}$$

or

$$\begin{aligned}&\pm\left(s(\mu)-\left(s_N(\mu)-\frac{g(\mu)}{2}\hat{a}(\hat{e}^{\rm pr},\hat{e}^{\rm du})\right)\right)\\&\quad\leq\frac{\kappa g(\mu)}{4}\hat{a}(\hat{e}^{\rm pr},\hat{e}^{\rm pr})+\frac{g(\mu)}{4\kappa}\hat{a}(\hat{e}^{\rm du},\hat{e}^{\rm du}).\end{aligned} \tag{42}$$

We now choose $\kappa(\mu)$ as

$$\kappa(\mu)=\left(\frac{\hat{a}(\hat{e}^{\rm du}(\mu),\hat{e}^{\rm du}(\mu))}{\hat{a}(\hat{e}^{\rm pr}(\mu),\hat{e}^{\rm pr}(\mu))}\right)^{1/2}$$

so as to minimize the right-hand side (42); we then obtain

$$|s(\mu)-\overline{s_N}(\mu)|\leq\Delta_N(\mu), \tag{43}$$

and hence $s_N^-(\mu)\leq s(\mu)\leq s_N^+(\mu)$.

We now turn to the upper effectivity inequality (sharpness property). If the primal and dual errors are a-orthogonal, or become increasingly orthogonal as N increases, then the effectivity will not, in fact, be bounded as $N\to\infty$. However, if we make the (plausible) hypothesis that $|s(\mu)-s_N(\mu)|\geq\underline{C}\|e^{\rm pr}(\mu)\|_X\|e^{\rm du}(\mu)\|_X$, then it is simple to demonstrate that

$$\eta_N(\mu)\leq\frac{\gamma_0^2}{2\underline{C}\underline{\alpha}_0}. \tag{44}$$

In particular, it is an easy matter to demonstrate that $g^{1/2}(\mu)\times(\hat{a}(\hat{e}^{\rm pr}(\mu),\hat{e}^{\rm pr}(\mu)))^{1/2}\leq\gamma_0/\underline{\alpha}_0^{1/2}\|e^{\rm pr}(\mu)\|_X$ (note we lose a factor of $\gamma_0^{1/2}$ relative to the symmetric case); similarly, $g^{1/2}(\mu)\times(\hat{a}(\hat{e}^{\rm du}(\mu),\hat{e}^{\rm du}(\mu)))^{1/2}\leq\gamma_0/\underline{\alpha}_0^{1/2}\|e^{\rm du}(\mu)\|_X$. The desired result then directly follows from the definition of $\Delta_N(\mu)$ and our hypothesis on $|s(\mu)-s_N(\mu)|$.

Finally, turning to computational issues, we note that the off-line/on-line decomposition described in Section 4.1 for compliant symmetric problems directly extends to the noncompliant, nonsymmetric case—except that we must compute the norm of both the primal and dual "modified errors," with a concomitant doubling of computational effort.

5.1.3 Method II A Posteriori Error Estimators. We discuss here the extension of Method II of Section 4.2 to noncompliant outputs and nonsymmetric operators.

To begin, we set $M>N$, M even, and introduce a parameter sample $S_{M/2}=\{\mu_1,\ldots,\mu_{M/2}\}$ and associated "integrated" reduced-basis approximation space $W_M=\text{span}\{u(\mu_m),\psi(\mu_m),m=1,\ldots,M/2\}$. We first find $u_M(\mu)\in W_M$ such that $a(u_M(\mu),v;\mu)=f(v)$, $\forall v\in W_M$; we then evaluate $s_M(\mu)=\ell(u_M(\mu))$; and finally, we compute our upper and lower output estimators as

$$s_{N,M}^{\pm}(\mu)=s_N(\mu)+\frac{1}{2\tau}(s_M(\mu)-s_N(\mu))\pm\frac{1}{2}\Delta_{N,M}(\mu), \tag{45}$$

$$\Delta_{N,M}(\mu)=\frac{1}{\tau}|s_M(\mu)-s_N(\mu)|, \tag{46}$$

for $\tau\in(0,1)$. The effectivity of the approximation is defined as

$$\eta_{N,M}(\mu)=\frac{\Delta_{N,M}(\mu)}{|s(\mu)-s_N(\mu)|}. \tag{47}$$

We shall again only consider $M=2N$.

As in Section 4.2, we would like to prove that $1\leq\eta_{N,2N}(\mu)\leq$Const for sufficiently large N; and, as in Section 4.2, we must again make the hypothesis (29). We first consider the lower effectivity inequality (bounding property), and prove that

$$s_{N,2N}^-(\mu)\leq s(\mu)\leq s_{N,2N}^+(\mu),\quad \text{as}\quad N\to\infty. \tag{48}$$

In particular, simple algebraic manipulations yield

$$\begin{aligned}s_{N,2N}^-(\mu)=s(\mu)-\frac{1}{1-\varepsilon_{N,2N}}|s_N(\mu)-s_{2N}(\mu)|\\\times\begin{cases}1 & s_{2N}(\mu)\geq s_N(\mu)\\ \dfrac{1}{\tau}(1-\varepsilon_{N,2N})-1 & s_{2N}(\mu)<s_N(\mu)\end{cases},\end{aligned} \tag{49}$$

Downloaded 03 Jun 2010 to 171.66.16.150. Redistribution subject to ASME license or copyright; see http://www.asme.org/terms/Terms_Use.cfm

Table 3 Error, error bound (Method II), and effectivity as a function of N, at a particular representative point $\mu \in \mathcal{D}$, for the truss problem (noncompliant output)

N	$\lvert s(\mu)-s_N(\mu)\rvert/s(\mu)$	$\Delta_{N,2N}(\mu)/s(\mu)$	$\eta_{N,2N}(\mu)$
20	2.35×10^{-2}	4.67×10^{-2}	1.99
40	1.74×10^{-4}	3.19×10^{-4}	1.83
60	5.59×10^{-5}	1.06×10^{-4}	1.90
80	1.44×10^{-5}	2.73×10^{-5}	1.89
100	7.45×10^{-6}	1.40×10^{-5}	1.88

$$s^+_{N,2N}(\mu) = s(\mu) + \frac{1}{1-\varepsilon_{N,2N}}\lvert s_N(\mu)-s_{2N}(\mu)\rvert \times \begin{cases} \frac{1}{\tau}(1-\varepsilon_{N,2N})-1 & s_{2N}(\mu)\geq s_N(\mu) \\ 1 & s_{2N}(\mu)<s_N(\mu) \end{cases}. \quad (50)$$

The desired result then directly follows from our hypothesis on $\varepsilon_{N,2N}$, (29), and the range of τ.

The proof for the upper effectivity inequality (sharpness property) parallels the derivation of Section 4.2.2. In particular, we write

$$\eta_{N,2N}(\mu) = \frac{\frac{1}{\tau}\lvert s_{2N}-s_N\rvert}{\lvert s-s_N\rvert} = \frac{\frac{1}{\tau}\lvert s_{2N}-s+s-s_N\rvert}{\lvert s-s_N\rvert} \quad (51)$$

$$= \frac{1}{\tau}\lvert 1-\varepsilon_{N,2N}\rvert; \quad (52)$$

from our hypothesis (29) we may thus conclude that $\eta_{N,2N}(\mu) \rightarrow 1/\tau$ as $N\rightarrow\infty$. Note in the noncompliant, nonsymmetric case we can make no stronger statement.

We demonstrate our effectivity claims in Table 3, in which we present the error, bound gap, and effectivity for the noncompliant output ($s^2(\mu)$, average stress) of the truss example of Section 2.2.2; the results tabulated correspond to the choice $\tau=1/2$. We clearly obtain bounds for all N; and the effectivity rather quickly approaches $1/\tau$ (for $N\geq120$, $\eta_{N,2N}(\mu)$ remains fixed at $1/\tau=2.0$).

5.2 Eigenvalue Problems. We next consider the extension of our approach to symmetric positive definite eigenvalue problems. The eigenvalues of appropriately defined partial-differential-equation eigenproblems convey critical information about a physical system: in linear elasticity, the critical buckling load; in dynamic analysis of structures, the resonant modes; in conduction heat transfer, the equilibrium timescales. Solution of large-scale eigenvalue problems is computationally intensive: the reduced-basis method is thus very attractive.

The abstract statement of our eigenvalue problem is: find $(u_i(\mu),\lambda_i(\mu)) \in X\times\mathbb{R}$, $i=1,\ldots,$ such that

$$a(u_i(\mu),v;\mu) = \lambda_i(\mu)m(u_i(\mu),v;\mu), \quad \forall v\in X,$$
$$\text{and } m(u_i(\mu),u_i(\mu);\mu)=1. \quad (53)$$

Here a is the continuous, coercive, symmetric form introduced earlier, and m is (say) the L^2 inner product over Ω. The assumptions on a and m imply the eigenvalues $\lambda_i(\mu)$ will be real and positive. We order the eigenvalues (and corresponding eigenfunctions u_i) such that $0<\lambda_1(\mu)<\lambda_2(\mu)\leq\ldots$; we shall assume that $\lambda_1(\mu)$ and $\lambda_2(\mu)$ are distinct. We suppose that our output of interest is the minimum eigenvalue,

$$s(\mu)=\lambda_1(\mu); \quad (54)$$

other outputs may also be considered.

Following (Machiels et al. [24]), we present here a reduced-basis predictor and a Method I error estimator for symmetric positive-definite eigenvalue problems; we also briefly describe the simpler Method II approach.

5.2.1 Reduced-Basis Approximation. We sample, randomly or log-randomly, our design space $\mathcal{D}$ to create the parameter sample $S_{N/2}=\{\mu_1,\ldots,\mu_{N/2}\}$; we then introduce the reduced-basis space $W_N=\text{span}\{u_1(\mu_1),u_2(\mu_1),\ldots,u_1(\mu_{N/2}),u_2(\mu_{N/2})\}$, where we recall that $u_1(\mu)$ and $u_2(\mu)$ are the eigenfunctions associated with the first (smallest) and second eigenvalues $\lambda_1(\mu)$ and $\lambda_2(\mu)$, respectively. Note that W_N has good approximation properties both for the first and second lowest eigenfunctions, and hence eigenvalues; this is required by the Method I error estimator to be presented below. Our reduced-order approximation is then: find $(u_{Ni}(\mu),\lambda_{Ni}(\mu))\in W_N\times\mathbb{R}$, $i=1,\ldots,N$, such that

$$a(u_{Ni}(\mu),v;\mu)=\lambda_{Ni}(\mu)m(u_{Ni}(\mu),v;\mu), \quad \forall v\in W_N,$$
$$\text{and } m(u_{Ni}(\mu),u_{Ni}(\mu);\mu)=1; \quad (55)$$

the output approximation is then $s_N(\mu)=\lambda_{N1}(\mu)$.

The formulation admits an on-line/off-line decomposition (Machiels et al. [24]) very similar to the approach described for equilibrium problems in Section 3.

5.2.2 Method I A Posteriori Error Estimators. As before, we assume that we are given a positive function $g(\mu):\mathcal{D}\rightarrow\mathbb{R}_+$ and a continuous, coercive, symmetric bilinear form $\hat{a}(w,v):X\times X\rightarrow\mathbb{R}$, that satisfy the inequality (16). We then find $\hat{e}(\mu)\in X$ such that

$$g(\mu)\hat{a}(\hat{e}(\mu),v)=[\lambda_{N1}m(u_{N1}(\mu),v;\mu)-a(u_{N1}(\mu),v;\mu)], \quad \forall v\in X, \quad (56)$$

in which the right-hand side is the eigenproblem equivalent of the residual. We then evaluate our estimators as

$$s^+_N(\mu)=\lambda_{N1}(\mu), \quad s^-_N(\mu)=\lambda_{N1}(\mu)-\Delta_N(\mu),$$
$$\Delta_N(\mu)=\frac{g(\mu)}{\tau\delta(\mu)}\hat{a}(\hat{e}(\mu),\hat{e}(\mu)),$$

where $\delta(\mu)=1-\lambda_{N1}(\mu)/\lambda_{N2}(\mu)$ and $\tau\in(0,1)$. The effectivity is defined as $\eta_N(\mu)=\Delta_N(\mu)/(\lambda_{N1}(\mu)-\lambda_1(\mu))$.

We now consider the lower and upper effectivity inequalities. As regards the lower effectivity inequality (bounding property), we of course obtain $s^+_N(\mu)\geq\lambda_1(\mu)$, $\forall N$. The difficult result is the lower bound: it can be proven (Machiels et al. [24]) that there exists an $N^*(S_{N/2},\mu)$ such that $s^-_N(\mu)\leq\lambda_1(\mu)$, $\forall N>N^*$. In practice, $N^*=1$, due to the good (theoretically motivated) choice for $\delta(\mu)$; there is thus very little uncertainty in our (asymptotic) bounds. We also prove in Machiels et al. [24] a result related to the upper effectivity inequality (sharpness property); in, practice, very good effectivities are obtained. To demonstrate these claims we consider the eigenvalue problem associated with (the homogeneous version) of our two-dimensional thermal fin example of Section 2.2.1. We present in Table 4 the error, error

Table 4 Error, error bound (Method I), and effectivities as a function of N, at a particular representative point $\mu\in\mathcal{D}$, for the thermal fin eigenproblem

N	$\lvert\lambda_1(\mu)-\lambda_{N1}(\mu)\rvert/\lambda_1(\mu)$	$\Delta_N(\mu)/\lambda_1(\mu)$	$\eta_N(\mu)$
10	1.19×10^{-2}	6.66×10^{-2}	5.63
20	1.08×10^{-3}	7.19×10^{-3}	6.65
30	6.20×10^{-4}	3.19×10^{-3}	5.17
40	1.72×10^{-4}	1.55×10^{-3}	9.44
50	3.47×10^{-5}	4.06×10^{-4}	11.74

Downloaded 03 Jun 2010 to 171.66.16.150. Redistribution subject to ASME license or copyright; see http://www.asme.org/terms/Terms_Use.cfm

bound, and effectivity as a function of N at a particular point $\mu \in \mathcal{D}$. We observe rapid convergence, bounds for all N, and good effectivities.

Finally, we note that our output estimator admits an off-line/on-line decomposition similar to that for equilibrium problems; the additional terms in (56) are readily treated through our affine expansion/linear superposition procedure.

5.2.3 Method II A Posteriori Error Estimators. For Method II, we no longer require an estimate for the second eigenvalue. We may thus define $S_N=\{\mu_1,\ldots,\mu_N\}$, $W_N=\text{span}\{u_1(\mu_i),i=1,\ldots,N\}$, and (for $M=2N$) $S_{2N}=\{\mu_1,\ldots,\mu_{2N}\}\supset S_N$, $W_{2N}=\text{span}\{u_1(\mu_i),i=1,\ldots,2N\}\supset W_N$. The reduced basis approximation now takes the form (53), yielding $s_N(\mu)=\lambda_{N1}(\mu)$ and (for $N\to 2N$) $s_{2N}(\mu)=\lambda_{2N1}(\mu)$. Our estimators are then given by

$$s^+_{N,2N}(\mu)=\lambda_{N1}(\mu),\quad s^-_{N,2N}=\lambda_{N1}(\mu)-\Delta_{N,2N}(\mu),$$

$$\Delta_{N,2N}(\mu)=\frac{1}{\tau}(s_N(\mu)-s_{2N}(\mu)) \tag{57}$$

for $\tau\in(0,1)$. The effectivity $\eta_{N,2N}(\mu)$ is defined as for Method I.

For the lower effectivity inequality (bounding property), we of course retain $s^+_{N,2N}(\mu)\geq\lambda_1(\mu)$, $\forall N$. We also readily derive $s^-_{N,2N}(\mu)=\lambda_1-(\lambda_{N1}-\lambda_1)(1/\tau(1-\varepsilon_{N,2N})-1)$; under our hypothesis (29), we thus obtain asymptotic bounds as $N\to\infty$. For the upper effectivity inequality (sharpness property), we directly obtain $\eta_{N,2N}=1/\tau(1-\varepsilon_{N,2N})$. By variational arguments it is readily shown that $0\leq\varepsilon_{N,2N}\leq 1$: we thus conclude that $0\leq\eta_{N,2N}\leq 1/\tau$, $\forall N$. Additionally, under hypothesis (29), we deduce that $\eta_{N,2N}\to 1/\tau$ as $N\to\infty$.

5.3 Further Generalizations. In this section we briefly describe several additional extensions of the methodology. In each case we focus on the essential new ingredient; further details (in most cases) may be found in the referenced literature.

5.3.1 Noncoercive Linear Operators. The archetypical noncoercive linear equation is the Helmholtz, or reduced-wave, equation; many (e.g., inverse scattering) applications of this equation arise, for example, in acoustics and electromagnetics. The essential new mathematical ingredient is the loss of coercivity of a. In particular, well-posedness is now ensured only by the inf-sup condition: there exists positive β_0, $\beta(\mu)$, such that

$$0<\beta_0\leq\beta(\mu)=\inf_{w\in X}\sup_{v\in X}\frac{a(w,v;\mu)}{\|w\|_X\|v\|_X},\quad\forall\mu\in\mathcal{D}. \tag{58}$$

Two numerical difficulties arise due to this "weaker" stability condition.

The first difficulty is preservation of the inf-sup stability condition for finite dimensional approximation spaces. To wit, although in the coercive case restriction to the space W_N actually increases stability, in the noncoercive case restriction to the space W_N can easily decrease stability: the relevant supremizers may not be adequately represented. Loss of stability can, in turn, lead to poor approximations—the inf-sup parameter enters in the denominator of the *a priori* convergence result. The second numerical difficulty is estimation of the inf-sup parameter, which for noncoercive problems plays the role of $g(\mu)$ in Method I *a posteriori* error estimation techniques. In particular, $\beta(\mu)$ can not typically be deduced analytically, and thus must be evaluated (via an eigenvalue formulation) as part of the reduced-basis approximation. Our resolution of both these difficulties involves two elements (Maday et al. [23]): first, we consider projections other than standard Galerkin; and second, we consider "enriched" approximation spaces.

In one approach (Maday et al. [23]), we pursue a minimum-residual projection: the (low-dimensional) infimizing space contains both the solution u and also the inf-sup infimizer at the μ_n sample points; and the (high-dimensional) supremizing space is taken to be X. Stability is ensured and rigorous (sharp) error bounds are obtained—though technically the bounds are only asymptotic due to the approximation of the inf-sup parameter; and, despite the presence of X, the on-line complexity remains independent of the dimension of X—as in Section 3.3, we exploit affine parameter dependence and linear superposition to precompute the necessary inversions. In a second suite of much simpler and more general approaches (see Maday et al. [23] for one example in the symmetric case), we exploit minimum-residual or Petrov-Galerkin projections with infimizer-supremizer enriched, but still very low-dimensional, infimizing and supremizing spaces. Plausible but not yet completely rigorous arguments, and empirical evidence, suggest that stability is ensured and rigorous asymptotic (and sharp) error bounds are obtained.

In Maday et al. [23] we focus entirely on Method I *a posteriori* error estimator procedures; but Method II techniques are also appropriate. In particular, Method II approaches do not require accurate estimation of the inf-sup parameter; we thus need be concerned only with stability in designing our reduced-basis spaces.

5.3.2 Parabolic Partial Differential Equations. The next extension considered is the treatment of parabolic partial differential equations of the form $m(u_t,v;\mu)=a(u,v;\mu)$; typical examples are time-dependent problems such as unsteady heat conduction—the "heat" or "diffusion" equation. The essential new ingredient is the presence of the time variable, t.

The reduced-basis approximation and error estimator procedures are similar to those for noncompliant nonsymmetric problems, except that we now include the time variable as an additional parameter. Thus, as in certain other time-domain model-order-reduction methods (Antoulas and Sorensen [25], Sirovich and Kirby [26]), the basis functions are "snapshots" of the solution at selected time instants; however, in our case, we construct an *ensemble* of such series corresponding to different points in the non-time parameter domain $\mathcal{D}$. For rapid convergence of the output approximation, the solutions to an adjoint problem, which evolves *backward* in time, must also be included in the reduced-basis space.

For the temporal discretization method, many possible choices are available. The most appropriate method, although not the only choice, is the discontinuous Galerkin method (Machiels et al. [27]). The variational origin of the discontinuous Galerkin approach leads naturally to rigorous output bounds for Method I *a posteriori error* estimators; the Method II approach is also directly applicable. Under our affine assumption, off-line/on-line decompositions can be readily crafted; the complexity of the on-line stage (calculation of the output predictor and associated bound gap) is, as before, independent of the dimension of X.

5.3.3 Locally Nonaffine Parameter Dependence. An important restriction of our methods is the assumption of affine parameter dependence. Although many property, boundary condition, load, and even geometry variations can indeed be expressed in the required form (2) for reasonably small Q, there are many problems, for example, general boundary shape variations, which do not admit such a representation. One simple approach to the treatment of this more difficult class of nonaffine problems is (*i*) in the off-line stage, store the $\zeta_n\equiv u(\mu_n)$, and (*ii*) in the on-line stage, directly evaluate the reduced-basis stiffness matrix as $a(\zeta_j,\zeta_i,\mu)$. Unfortunately, the operation count (respectively, storage) for the on-line stage will now scale as $O(N^2\dim(X))$ (respectively, $O(N\dim(X))$, where $\dim(X)$ is the dimension of the truth (very fine) finite element approximation space: the resulting method may no longer be competitive with advanced iterative techniques; and, in any event, "real-time" response may be compromised.

We prefer an approach which is slightly less general but potentially much more efficient. In particular, we note that in many cases—for example, boundary geometry modification—the non-

Downloaded 03 Jun 2010 to 171.66.16.150. Redistribution subject to ASME license or copyright; see http://www.asme.org/terms/Terms_Use.cfm

affine parametric dependence can be restricted to a small subdomain of Ω, Ω_{II}. We can then express our bilinear form a as an affine/nonaffine sum,

$$a(w,v;\mu) = a_I(w,v;\mu) + a_{II}(w,v;\mu). \tag{59}$$

Here a_I, defined over Ω_I, the majority of the domain, is affinely dependent on μ; and a_{II}, defined over Ω_{II}, a small portion of the domain, is not affinely dependent on μ. It immediately follows that the reduced-basis stiffness matrix can be expressed as the sum of two stiffness matrices corresponding to contributions from a_I and a_{II}, respectively; that the stiffness matrix associated with a_I admits the usual on-line/off-line decomposition described in Section 3.3; and that the stiffness matrix associated with a_{II} requires storage (and inner product evaluation) *only of* $\zeta_i|_{\Omega_{II}}$ (ζ_i restricted to Ω_{II}). The nonaffine contribution to the on-line computational complexity thus scales only as $O(N^2 \dim(X|_{\Omega_{II}}))$, where $\dim(X|_{\Omega_{II}})$ refers (in practice) to the number of finite-element nodes located within Ω_{II}, often extremely small. We thus recover a method that is (almost) independent of $\dim(X)$, though clearly the on-line code will be more complicated than in the purely affine case.

In the above we focus on approximation. As regards *a posteriori* error estimation, the nonaffine dependence of a (even locally) precludes the precomputation and linear superposition strategy required by Method I (unless domain decomposition concepts are exploited (Machiels et al. [28]); however, Method II directly extends to the locally nonaffine case.

Acknowledgments

We would like to thank Mr. Thomas Leurent (formerly) of MIT for his many contributions to the work described in this paper; thanks also to Shidrati Ali of the Singapore-MIT Alliance and Yuri Solodukhov of MIT for very helpful discussions. We would also like to acknowledge our longstanding collaborations with Professor Jaime Peraire of MIT and Professor Einar Rønquist of the Norwegian University of Science and Technology. This work was supported by the Singapore-MIT Alliance, by DARPA and AFOSR under Grant F49620-01-1-0458, by DARPA and ONR under Grant N00014-01-1-0523 (Subcontract 340-6218-3), and by NASA under Grant NAG-1-1978.

References

[1] Chan, T. F., and Wan, W. L., 1997, "Analysis of projection methods for solving linear systems with multiple right-hand sides," SIAM J. Sci. Comput. (USA), **18**, No. 6, p. 1698.
[2] Farhat, C., Crivelli, L., and Roux, F., 1994, "Extending substructure based iterative solvers to multiple load and repeated analyses," Comput. Methods Appl. Mech. Eng., **117**, No. 1–2, pp. 195–209.
[3] Akgun, M. A., Garcelon, J. H., and Haftka, R. T., 2001, "Fast exact linear and non-linear structural reanalysis and the Sherman-Morrison-Woodbury formulas," Int. J. Numer. Methods Eng., **50**, No. 7, pp. 1587–1606.
[4] Yip, E. L., 1986, "A note on the stability of solving a rank-*p* modification of a linear system by the Sherman-Morrison-Woodbury formula," SIAM (Soc. Ind. Appl. Math.) J. Sci. Stat. Comput., **7**, No. 2, pp. 507–513.
[5] Allgower, E., and Georg, K., 1980, "Simplicial and continuation methods for approximating fixed-points and solutions to systems of equations," SIAM Rev., **22**, No. 1, pp. 28–85.
[6] Rheinboldt, W., 1981, "Numerical analysis of continuation methods for nonlinear structural problems," Comput. Struct., **13**, No. 1–3, pp. 103–113.
[7] Almroth, B. O., Stern, P., and Brogan, F. A., 1978, "Automatic choice of global shape functions in structural analysis," AIAA J., **16**, pp. 525–528.
[8] Noor, A. K., and Peters, J. M., 1980, "Reduced basis technique for nonlinear analysis of structures," AIAA J., **18**, No. 4, pp. 455–462.
[9] Balmes, E., 1996, "Parametric families of reduced finite element models theory and applications," Mech. Syst. Signal Process., **10**, No. 4, pp. 381–394.
[10] Barrett, A., and Reddien, G., 1995, "On the reduced basis method," Z. Angew. Math. Mech., **75**, No. 7, pp. 543–549.
[11] Fink, J. P., and Rheinboldt, W. C., 1983, "On the error behaviour of the reduced basis technique for nonlinear finite element approximations," Z. Angew. Math. Mech., **63**, pp. 21–28.
[12] Peterson, J. S., 1989, "The reduced basis method for incompressible viscous flow calculations," SIAM (Soc. Ind. Appl. Math.) J. Sci. Stat. Comput., **10**, No. 4, pp. 777–786.
[13] Porsching, T. A., 1985, "Estimation of the error in the reduced basis method solution of nonlinear equations," Math. Comput., **45**, No. 172, pp. 487–496.
[14] Rheinboldt, W., 1993, "On the theory and error estimation of the reduced basis method for multi-parameter problems," Nonlinear Analysis, Theory, Methods and Applications, **21**, No. 11, pp. 849–858.
[15] Veroy, K., Leurent, T., Prud'homme, C., Rovas, D., and Patera, A., 2002, "Reliable real-time solution of parametrized elliptic partial differential equations: Application to elasticity," *Proceedings SMA Symposium 2002*.
[16] Maday, Y., Machiels, L., Patera, A. T., and Rovas, D. V., 2000, "Blackbox reduced-basis output bound methods for shape optimization," *Proceedings 12th International Domain Decomposition Conference*, eds. T. Chan, et al., ddm.org, pp. 429–436.
[17] Evans, A. G., Hutchinson, J. W., Fleck, N. A., Ashby, M. F., and Wadley, H. N. G., 2001, "The topological design of multifunctional cellular metals," Prog. Mater. Sci., **46**, No. 3–4, pp. 309–327.
[18] Wicks, N., and Hutchinson, J. W., 2001, "Optimal truss plates," Int. J. Solids Struct., **38**, No. 30–31, pp. 5165–5183.
[19] Maday, Y., Patera, A., and Turinici, G., "Global a priori convergence theory for reduced-basis approximation of single-parameter symmetric coercive elliptic partial differential equations," C. R. Acad. Sci. Paris Série I. Submitted.
[20] Maday, Y., Patera, A. T., and Peraire, J., 1999, "A general formulation for a posteriori bounds for output functionals of partial differential equations; Application to the eigenvalue problem," C. R. Acad. Sci. Paris, Série I, **328**, pp. 823–828.
[21] Machiels, L., Peraire, J., and Patera, A. T., 2001, "A posteriori finite element output bounds for the incompressible Navier-Stokes equations; Application to a natural convection problem," J. Comput. Phys., **172**, pp. 401–425.
[22] Patera, A. T., and Rønquist, E. M., 2001, "A general output bound result: Application to discretization and iteration error estimation and control," Math. Models Methods Appl. Sci., **11**, No. 4, pp. 685–712.
[23] Maday, Y., Patera, A. T., and Rovas, D. V., 2001, "A blackbox reduced-basis output bound method for noncoercive linear problems," *Seminaive du College de France J. L. Lions, Series in Applied Mathematics*, eds. P. G. Ciarlet and P. L. Lions, Elsevier–Gauthier–Villars, Vol. 7, accepted, July 2002.
[24] Machiels, L., Maday, Y., Oliveira, I. B., Patera, A., and Rovas, D., 2000, "Output bounds for reduced-basis approximations of symmetric positive definite eigenvalue problems," C. R. Acad. Sci. Paris, Série I, **331**, No. 2, pp. 153–158.
[25] Antoulas, A., and Sorensen, D., 2001 "Approximation of large-scale dynamical systems: An overview," Technical report, Rice University.
[26] Sirovich, L., and Kirby, M., 1987, "Low-dimensional procedure for the characterization of human faces," J. Opt. Soc. Am. A, **4**, No. 3, pp. 519–524.
[27] Machiels, L., Patera, A., and Rovas, D., 2001, "Reduced basis output bound methods for parabolic problems," Comput. Methods Appl. Mech. Eng., Submitted.
[28] Machiels, L., Maday, Y., and Patera, A. T., 2000, "A flux-free nodal Neumann subproblem approach to output bounds for partial differential equations," C. R. Acad. Sci. Paris, Série I, **330**, No. 3, pp. 249–254.

Downloaded 03 Jun 2010 to 171.66.16.150. Redistribution subject to ASME license or copyright; see http://www.asme.org/terms/Terms_Use.cfm

Large Eddy Simulation of Turbulent Wake Behind a Square Cylinder With a Nearby Wall

Tong-Miin Liou
Professor,
Fellow ASME
College of Engineering,
Feng Chia University,
Taichung, Taiwan 407, ROC

Shih-Hui Chen
Graduate Student

Po-Wen Hwang
Graduate Student

Department of Power Mechanical Engineering,
National Tsing Hua University,
Hsinchu, Taiwan 30013, ROC

Computations of the time-averaged and phase-averaged fluid flow and heat transfer based on large eddy simulation (LES) are presented for turbulent flows past a square cylinder with and without a nearby wall at a fixed Reynolds number of 2.2×10^4. The finite-volume technique was used to solve the time-dependent filtered compressible Navier-Stokes equations with a dynamic subgrid-scale turbulence model, and the numerical fluxes were computed using alternating in time the second-order, explicit MacCormack's and the modified Godunov's scheme. Results show some improvements in predicting the streamwise evolutions of the long-time-averaged streamwise mean velocity and total fluctuation intensity along the centerline over those predicted by using Reynolds stress models. A better overall centerline streamwise mean velocity distribution is also predicted by the present LES than by other LES. The wall proximity effect is studied through the comparison of turbulent wake flow past one free standing cylinder and one with a nearby wall, and is illustrated by the phase-averaged spanwise vorticity components and the vortex celerity of spanwise vortices. Moreover, documentation is given on the mechanisms responsible for the augmentation of heat transfer through the spanwise and longitudinal vortices as well as periodic and random fluctuations. [DOI: 10.1115/1.1445797]

Introduction

In addition to being a model for fundamental studies of challenging fluid mechanics problems, the flow over bluff bodies is widely encountered in practical applications such as a combustor installed with flame holders, a heat exchanger system with bluff-body turbulator arranged along the length of a passage to periodically disrupt the flow, a building in a crossflow, etc. Oscillating flow resulting from the spanwise vortices behind bluff bodies arranged near a heating wall can enhance the heat transfer along the wall due to periodically sweeping the thermal boundary layer [1–2]. The streamwise vortices are naturally generated in a number of flows, e.g., flow along a concave wall (Goertler vortex), boundary layer transition to turbulence, mixed convective flow through a bottom heated horizontal rectangular duct. It can also be produced by mounting vortex generators, e.g., two-dimensional(2-D) broken ribs, delta wings [3], v-shaped ribs [4], and three-dimensional(3-D) bodies(cube, hemisphere, cone) on the heat exchange wall. The secondary flow induced by streamwise vortices can entrain the fresh or cooler fluids from the main stream toward near wall region and thus effectively enhance the wall heat transfer. The design of a heat exchanger requires, therefore, a thorough understanding of the aforementioned vortex structures and their role in affecting heat transfer. For turbulent flows past bluff bodies, which usually occur in practice, stochastic three-dimensional turbulent fluctuations are superimposed on the periodic vortex-shedding motion in the wake region. The simulation of large coherent structures in the turbulent wake flow is difficult because of the wide-spread spectrum of scales. Phenomenological turbulence modeling is a practical alternative choice but needs further improvements. Large eddy simulation(LES) is a promising one to solve this problem and attracts much attention.

Firstly, some works relevant to turbulent flow past a free-standing cylinder are cited. For numerical studies, Rodi [5] reviewed the simulations of turbulent flows past a bluff body and concluded the general superiority of Reynolds stress model over $k-\varepsilon$ model and the promising application of LES. Franke and Rodi [6] calculated the turbulent flow past a square cylinder behind which a von Karman vortex street existed according to the experiments. They compared four different turbulence models: $k-\varepsilon$ model and Reynolds stress model(RSM), each with wall function and one-equation near wall treatment. In using the RSM the wall-related pressure-strain model of Gibson and Launder [7] was adopted. They found that the $k-\varepsilon$ model with wall function did not produce any vortex shedding at all whereas the other three models predicted vortex shedding. Among them, the RSM variants produced results in fairly good agreement with experiments. Tamura et al. [8] calculated 2-D and 3-D unsteady flows around a cylinder (circular, square, and rectangular) by a finite difference method without a turbulence model. The convection terms were discretized with a third-order upwind scheme which introduces numerical damping and basically takes over the role of a subgrid-scale model in a LES. Murakami et al. [9] reported 2-D and 3-D LES results of vortex shedding flow past a square cylinder using the Smagorinsky subgrid-scale (SGS) model. Rodi et al. [10] compiled the LES results from a workshop to assess the present state-of-the-art in LES of complex flows. The test cases selected were the flow over a free-standing square cylinder and the flow over a cube mounted on one wall of a channel.

For experimental studies, Durao et al. [11] measured the turbulent wake flow field of a square cylinder using laser-Doppler velocimetry (LDV). The experiments were performed in a water channel with a blockage ratio of 0.14 and Reynolds number based on the cylinder height of 1.4×10^4. They showed that in the zone of highest velocity oscillations the energy associated with the turbulent fluctuations is about 40 percent of the total energy, including periodic and turbulent fluctuations. Lyn and Rodi [12] and Lyn et al. [13] measured the turbulent wake flow of a square cylinder using LDV. The experiments were performed in a water channel with a blockage ratio of 0.07 and Reynolds number based on the cylinder height of 2.2×10^4. Lyn and Rodi [12] focused on the the turbulent shear layer and the associated recirculation region on the top and bottom walls of the cylinder due to the flow separation from the forward corner of the cylinder. Lyn et al. [13] focused on the turbulent near-wake flow around the cylinder.

Some works relevant to turbulent flow past a cylinder with a nearby wall (Fig. 1) are also worthy of being cited. Durao et al. [14] investigated the flow around a square cylinder near a wall

Contributed by the Fluids Engineering Division for publication in the JOURNAL OF FLUIDS ENGINEERING. Manuscript received by the Fluids Engineering Division November 16, 1999; revised manuscript received October 15, 2001. Associate Editor: P. E. Raad.

 Copyright © 2002 by ASME

Downloaded 03 Jun 2010 to 171.66.16.150. Redistribution subject to ASME license or copyright; see http://www.asme.org/terms/Terms_Use.cfm

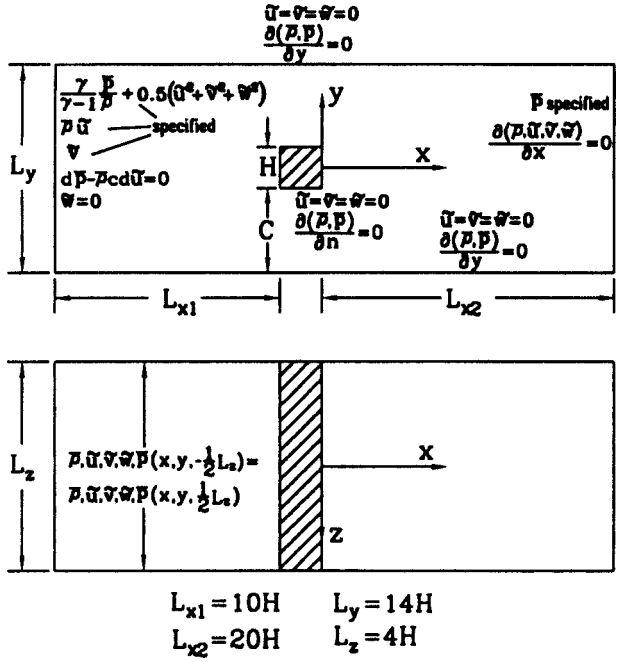

Fig. 1 Coordinate system and schematic drawing of the computational domain and boundary conditions

with a two-component LDV at $Re=1.4\times10^4$. They found that vortex shedding activity is suppressed for gap sizes smaller than $C/H=0.375$. The mean flow field were measured for $C/H=0.25$ and 0.50. Devarakonda and Humphrey [15] investigated the near wall streamwise velocity component and the pressure forces acting on the square cylinder as a function of the gap height at $Re=1.0\times10^4$. The results showed that the drag coefficient decreases while the lift coefficient and Strouhal number increase with decreasing gap height for $Re=1.0-2.75\times10^4$. Bosch et al. [16] and Bosch and Rodi [17] conducted experimental and numerical studies of vortex shedding past a square cylinder near a wall at $Re=2.2\times10^4$. Detailed two-component LDV measurements were carried out for $C/H=0.75$. In addition to time-averaged mean-velocity and stress components, phase-averaged components were presented. Bosch and Rodi [17] compared the standard $k-\varepsilon$ model and the modification attributable to Kato and Launder [18] (abbreviated as KL model). The KL model yielded reasonable predictions over the standard $k-\varepsilon$ model.

The dynamics of 3-D spanwise and streamwise vortical structures behind a nominally 2-D circular cylinder attracts much attention in the recent years. However, very little attention has been given to high Reynolds number turbulent wake flows behind a square cylinder. It is clear that the applications of LES to the systematic study of fluid flows past a square cylinder with and without wall proximity are still limited, a fact motivating the present investigation. LES is adopted in the present study since the fluid flow and heat transfer behind the bluff-body cylinder are expected to be dominated by the large-scale coherent structures prevailing there. Previously, LES with the Smagorinsky SGS model had been successfully applied by authors to simulate compressible turbulent free mixing layers [19] and confined reacting shear layers [20,21]. In the present study, we extend its application with, however, a dynamic SGS turbulence model to investigate the wake flow behind a square cylinder with and without a nearby wall.

In the following text, code verifications are performed through comparisons with the measurements. The time-averaged mean velocities and turbulence fluctuation intensities are compared with the measured data of Lyn et al. [13]. The gap between the cylinder and the wall yields a profound influence on the interaction between the wake flow behind the cylinder and the boundary layer along the wall and thus the design of an efficient heat transfer enhancement system [2,22]. The effect of wall on turbulent wake is examined through the comparison of flow past one free standing cylinder and one with a nearby wall. For the latter case, the value of C/H is 0.75. The choice of $C/H=0.75$ is based on the measurements of Bosch et al. [16]. Finally, the fluid dynamic mechanisms responsible for the augmentation of heat transfer is documented.

Theoretical Analysis

Governing Equations. The flow variables are decomposed into a large-scale (or resolved) part which can be solved explicitly and a SGS part which is modeled with a SGS model. The filtering operation

$$\overline{g}(\mathbf{x})=\int_\Omega G_\Delta(\mathbf{x}-\zeta)g(\zeta)d\zeta, \tag{1}$$

where G is a filter function, decomposes a variable g into a large-scale component $\overline{g}$ and a subgrid-scale component g', which accounts for the scales not resolved by the filter width Δ:

$$g=\overline{g}+g' \tag{2}$$

A mass-weighted filter that simplifies the mathematical expressions for compressible flow simulations is defined by

$$\tilde{g}=\frac{\overline{\rho g}}{\overline{\rho}} \tag{3}$$

This implies a second decomposition of g:

$$g=\tilde{g}+g'' \tag{4}$$

Assuming that there are no external heat additions and body forces, the filtered forms of compressible mass, momentum, and total energy equations with a dynamic subgrid scale model in Cartesian coordinates can be respectively written as

$$\frac{\partial\overline{\rho}}{\partial t}+\frac{\partial}{\partial x}(\overline{\rho}\tilde{u})+\frac{\partial}{\partial y}(\overline{\rho}\tilde{v})+\frac{\partial}{\partial z}(\overline{\rho}\tilde{w})=0, \tag{5}$$

$$\frac{\partial}{\partial t}(\overline{\rho}\tilde{u})+\frac{\partial}{\partial x}(\overline{\rho}\tilde{u}\tilde{u}-\overline{\tau}_{xx}-\tau_{s_{xx}})+\frac{\partial}{\partial y}(\overline{\rho}\tilde{u}\tilde{v}-\overline{\tau}_{xy}-\tau_{s_{xy}})+\frac{\partial}{\partial z}(\overline{\rho}\tilde{u}\tilde{w}-\overline{\tau}_{xz}-\tau_{s_{xz}})=0, \tag{6}$$

$$\frac{\partial}{\partial t}(\overline{\rho}\tilde{v})+\frac{\partial}{\partial x}(\overline{\rho}\tilde{v}\tilde{u}-\overline{\tau}_{yx}-\tau_{s_{yx}})+\frac{\partial}{\partial y}(\overline{\rho}\tilde{v}\tilde{v}-\overline{\tau}_{yy}-\tau_{s_{yy}})+\frac{\partial}{\partial z}(\overline{\rho}\tilde{v}\tilde{w}-\overline{\tau}_{yz}-\tau_{s_{yz}})=0, \tag{7}$$

$$\frac{\partial}{\partial t}(\overline{\rho}\tilde{w})+\frac{\partial}{\partial x}(\overline{\rho}\tilde{w}\tilde{u}-\overline{\tau}_{zx}-\tau_{s_{zx}})+\frac{\partial}{\partial y}(\overline{\rho}\tilde{w}\tilde{v}-\overline{\tau}_{zy}-\tau_{s_{zy}})+\frac{\partial}{\partial z}(\overline{\rho}\tilde{w}\tilde{w}-\overline{\tau}_{zz}-\tau_{s_{zz}})=0, \tag{8}$$

$$\frac{\partial\hat{E}}{\partial t}+\frac{\partial}{\partial x}(\hat{E}\tilde{u}-\overline{u\tau}_{xx}-\overline{v\tau}_{yx}-\overline{w\tau}_{zx}-\tilde{u}\tau_{s_{xx}}-\tilde{v}\tau_{s_{yx}}-\tilde{w}\tau_{s_{zx}}-\kappa\partial\overline{T}/\partial x-q_{s_x})+\frac{\partial}{\partial y}(\hat{E}\tilde{v}-\overline{u\tau}_{xy}-\overline{v\tau}_{yy}-\overline{w\tau}_{zy}-\tilde{u}\tau_{s_{xy}}-\tilde{v}\tau_{s_{yy}}-\tilde{w}\tau_{s_{zy}}-\kappa\partial\overline{T}/\partial y-q_{s_y})+\frac{\partial}{\partial z}(\hat{E}\tilde{w}-\overline{u\tau}_{xz}-\overline{v\tau}_{yz}-\overline{w\tau}_{zz}-\tilde{u}\tau_{s_{xz}}-\tilde{v}\tau_{s_{yz}}-\tilde{w}\tau_{s_{zz}}-\kappa\partial\overline{T}/\partial z-q_{s_z})=0 \tag{9}$$

where viscous stresses τ_{ij} are defined as

Downloaded 03 Jun 2010 to 171.66.16.150. Redistribution subject to ASME license or copyright; see http://www.asme.org/terms/Terms_Use.cfm

$$\tau_{xx} = -p + 2\mu\left[\frac{\partial u}{\partial x} - \frac{1}{3}\left(\frac{\partial u}{\partial x} + \frac{\partial v}{\partial y} + \frac{\partial w}{\partial z}\right)\right],$$

$$\tau_{yy} = -p + 2\mu\left[\frac{\partial v}{\partial y} - \frac{1}{3}\left(\frac{\partial u}{\partial x} + \frac{\partial v}{\partial y} + \frac{\partial w}{\partial z}\right)\right],$$

$$\tau_{zz} = -p + 2\mu\left[\frac{\partial w}{\partial y} - \frac{1}{3}\left(\frac{\partial u}{\partial x} + \frac{\partial v}{\partial y} + \frac{\partial w}{\partial z}\right)\right],$$

$$\tau_{xy} = \tau_{yx} = \mu\left(\frac{\partial u}{\partial y} + \frac{\partial v}{\partial x}\right), \quad \tau_{yz} = \tau_{zy} = \mu\left(\frac{\partial v}{\partial z} + \frac{\partial w}{\partial y}\right),$$

$$\tau_{xz} = \tau_{zx} = \mu\left(\frac{\partial w}{\partial x} + \frac{\partial u}{\partial z}\right). \tag{10}$$

The terms $\tau_{s_{ij}}$ and q_{s_j} are subgrid-scale stresses and heat fluxes, respectively, and can be modeled as

$$\tau_{s_{xx}} = \overline{\rho}(\widetilde{u}\widetilde{u} - \widetilde{uu}) = 2\overline{\rho}\nu_s\left[\frac{\partial \widetilde{u}}{\partial x} - \frac{1}{3}\left(\frac{\partial \widetilde{u}}{\partial x} + \frac{\partial \widetilde{v}}{\partial y} + \frac{\partial \widetilde{w}}{\partial z}\right)\right] - \frac{2}{3}\overline{\rho}k_s,$$

$$\tau_{s_{yy}} = \overline{\rho}(\widetilde{v}\widetilde{v} - \widetilde{vv}) = 2\overline{\rho}\nu_s\left[\frac{\partial \widetilde{v}}{\partial y} - \frac{1}{3}\left(\frac{\partial \widetilde{u}}{\partial x} + \frac{\partial \widetilde{v}}{\partial y} + \frac{\partial \widetilde{w}}{\partial z}\right)\right] - \frac{2}{3}\overline{\rho}k_s,$$

$$\tau_{s_{zz}} = \overline{\rho}(\widetilde{w}\widetilde{w} - \widetilde{ww}) = 2\overline{\rho}\nu_s\left[\frac{\partial \widetilde{w}}{\partial z} - \frac{1}{3}\left(\frac{\partial \widetilde{u}}{\partial x} + \frac{\partial \widetilde{v}}{\partial y} + \frac{\partial \widetilde{w}}{\partial z}\right)\right] - \frac{2}{3}\overline{\rho}k_s,$$

$$\tau_{s_{xy}} = \tau_{s_{yx}} = \overline{\rho}(\widetilde{u}\widetilde{v} - \widetilde{uv}) = \overline{\rho}\nu_s\left(\frac{\partial \widetilde{u}}{\partial y} + \frac{\partial \widetilde{v}}{\partial x}\right),$$

$$\tau_{s_{xz}} = \tau_{s_{zx}} = \overline{\rho}(\widetilde{u}\widetilde{w} - \widetilde{uw}) = \overline{\rho}\nu_s\left(\frac{\partial \widetilde{u}}{\partial z} + \frac{\partial \widetilde{w}}{\partial x}\right),$$

$$\tau_{s_{yz}} = \tau_{s_{zy}} = \overline{\rho}(\widetilde{v}\widetilde{w} - \widetilde{vw}) = \overline{\rho}\nu_s\left(\frac{\partial \widetilde{v}}{\partial z} + \frac{\partial \widetilde{w}}{\partial y}\right), \tag{11}$$

$$q_{s_x} = \overline{\rho}c_p(\widetilde{T}\widetilde{u} - \widetilde{Tu}) = \frac{c_p\overline{\rho}\nu_s}{Pr_s}\frac{\partial \widetilde{T}}{\partial x},$$

$$q_{s_y} = \overline{\rho}c_p(\widetilde{T}\widetilde{v} - \widetilde{Tv}) = \frac{c_p\overline{\rho}\nu_s}{Pr_s}\frac{\partial \widetilde{T}}{\partial y},$$

$$q_{s_z} = \overline{\rho}c_p(\vec{T}\widetilde{w} - \widetilde{Tw}) = \frac{c_p\overline{\rho}\nu_s}{Pr_s}\frac{\partial \widetilde{T}}{\partial z} \tag{12}$$

where ν_S, the subgrid kinematic viscosity, and k_S, the subgrid turbulent kinetic energy, prescribed by the eddy viscosity model of Smagorinsky [23] are

$$\nu_s = c_s\Delta^2\left(2\widetilde{S}_{ij}\frac{\partial \widetilde{u}_i}{\partial x_j}\right)^{1/2}, \tag{13}$$

$$k_s = \nu_s^2/(c_k\Delta)^2. \tag{14}$$

In the equations, $c_k(=0.094)$ is a model constant, Δ the average size of the computational cell, and c_S determined by a least-squares approach proposed by Lilly [24], a modification to the original formulation of Germano et al. [25]. Spatial averaging of c_S along the homogeneous spanwise direction and clipping of negative eddy viscosities were performed to avoid the numerical instability. The basic idea of the dynamic model is to improve the Smagorinsky model by setting the constant at a different value at each mesh node and at each time step, in an attempt to adjust the induced dissipation to the local state of the flow.

Equations (5)–(9) can be put into the following general form

$$\frac{\partial \mathbf{Q}}{\partial t} + \frac{\partial \mathbf{F}}{\partial x} + \frac{\partial \mathbf{G}}{\partial y} + \frac{\partial \mathbf{H}}{\partial z} = 0 \tag{15}$$

For an ideal gas, the total energy $\hat{E}$ per unit volume is related to the filtered pressure $\overline{P}$ and axial($\widetilde{u}$), transverse($\widetilde{v}$), and spanwise($\widetilde{w}$) velocity components via $\hat{E} = \overline{P}/(\gamma - 1) + 0.5\overline{\rho}(\widetilde{u}^2 + \widetilde{v}^2 + \widetilde{w}^2)$. The filtered temperature $\widetilde{T}$ is related to $\overline{\rho}$ and $\overline{P}$ by ideal gas law $\widetilde{T} = \overline{P}/\overline{\rho}R$. In the above R and γ are the gas constant and specific heat ratio, respectively. Equations (5)–(9) are used to solve $\overline{\rho}$, $\widetilde{u}$, $\widetilde{v}$, $\widetilde{w}$, $\overline{p}$, $\hat{E}$, and $\widetilde{T}$ can be further calculated from aforementioned definition and ideal gas law.

Decomposition of an Instantaneous Quantity. Following the concept of Reynolds decomposition an instantaneous quantity φ is split into

$$\varphi = \langle\varphi\rangle_p + \varphi'^s \tag{16}$$

where $\langle\varphi\rangle_p$ is the mean value and φ'^s the stochastic turbulent fluctuation. It is expected from previous studies mentioned in Introduction that the large-scale coherent vortex shedding may appear behind the square cylinder. The mean value $\langle\varphi\rangle_p$ may therefore vary slowly with time and must be the so called ensemble (or phase) averaged value. Due to the periodic vortex shedding behind the cylinder bluff bodies, the ensemble averaged value $\langle\varphi\rangle_p$, as suggested by Hussain and Reynolds [26], can be further decomposed into

$$\langle\varphi\rangle_p = \langle\varphi\rangle_t + \varphi'^p = \overline{\varphi}^t + \varphi'^p \tag{17}$$

where $\langle\varphi\rangle_t$ or $\overline{\varphi}^t$ is the long-time-averaged value and φ'^p the periodic fluctuation. In summary, an instantaneous quantity can be expressed as

$$\varphi(t) = \langle\varphi\rangle_t + \varphi'^p(t) + \varphi'^s(t) = \langle\varphi\rangle_t + \varphi'^t(t) \tag{18}$$

where $\varphi'^t(t)$ stands for the total fluctuation.

Numerical Method. The finite-volume technique is adopted in the present code. The conservation variables $\overline{\rho}$, $\overline{\rho\widetilde{u}}$, $\overline{\rho\widetilde{v}}$, $\overline{\rho\widetilde{w}}$, and $\hat{E}$ are calculated at the center of each computational cell whereas flux vectors **F**, **G**, and **H** in Eq. (15) are calculated at the cell edges using alternating in time the second-order, explicit MacCormack's and the modified Godunov's scheme [27]. Reduction in phase error can be achieved by temporal switching of these two schemes since MacCormack's scheme has a lagging phase error and Godunov's scheme a leading phase error [28]. Hence, using the alternating in time the MaCormack's and modified Godunov's schemes is less dissipative than using the modified Godunov's scheme alone. In Godunov's scheme, characteristic information is used to solve forward in time the Riemann problem. From the solution of the Riemann problem the numerical flux at the cell edges can thus be calculated. To improve the order of spatial accuracy of Godunov's original scheme, the piecewise initial states to the left and right of the cell edges are obtained by a second-order extrapolation [27] in the present work.

Note that since the Mach number is low, many time-steps and long run-times are necessary to achieve statistically stationary flow. In the present study, the time step of only 0.27 μsec was necessary (giving a maximum CFL number of 0.6). 30,000 steps were used to start up the LES calculations from a zero velocity initial field.

Boundary and Initial Conditions. The computational domain, coordinate system and boundary conditions are shown in Fig. 1. At the solid wall of bluff body, Werner and Wengle's approach [29] for instantaneous velocity parallel to the solid wall, zero normal pressure gradient, and adiabatic wall conditions are used for the primitive variables ($\widetilde{u}$,$\widetilde{v}$,$\widetilde{w}$), $\overline{p}$, and $\overline{\rho}$, respectively. Along the upper and lower boundaries of computational domain for the free standing cylinder, the slip (symmetry) conditions are applied. Along the lower wall adjacent to the cylinder, the same conditions as cylinder wall are used except the heating condition. Periodic conditions are implemented to the side boundaries of the computational domain. Characteristic-based boundary conditions are enforced on the inflow and outflow boundaries. At the inflow, transverse and spanwise velocities, mass flux, and energy flux are

Downloaded 03 Jun 2010 to 171.66.16.150. Redistribution subject to ASME license or copyright; see http://www.asme.org/terms/Terms_Use.cfm

kept constant since there are four incoming and one outgoing characteristics for the subsonic inlet velocity. To simulate the inflow turbulence existed in the experiments, a perturbation with amplitude of 2 percent of U_{ref} was given to inflow transverse velocity. At the exit, there are four outgoing and one incoming characteristics for the subsonic outlet velocities, and the pressure boundary condition is specified. The initial condition is specified from still condition.

Grid Independence. The computations to be reported in the following sections were performed on a $122\times90\times34$ grid. Additional runs for the coarser ($92\times68\times26$) and finer ($182\times134\times50$) meshes were undertaken for a check of grid independence. The distance from the near-wall node to the nearest wall was kept constant for the three runs. A comparison of the results showed that the maximum changes of 1.8 percent in the time-mean axial velocity profiles on the central plane $z=0$ between $122\times90\times34$ and $182\times134\times50$ grid sizes were smaller than 9.4 percent found between $92\times68\times26$ and $182\times134\times50$ mesh sizes. Consequently, the accuracy of the solutions on a $122\times90\times34$ grid size is deemed satisfactory. In fact, in LES the grid size is the filter scale which separates the computed large scales from the modeled small scales. This grid size should lie in the inertial range of scales, beyond the energetic but larger than the dissipation scales. The velocity power spectrum shown shortly in Fig. 3(*b*) was based on the $122\times90\times34$ grid and does resolve the inertial range of scales. Hence, the mean quantities obtained from $122\times90\times34$ grid and $182\times134\times50$ grid should be grid independent in LES.

Results and Discussion

Turbulent Wake Behind a Free-Standing Cylinder. *Time-Averaged Flow.* Statistics for time averaged and phase-averaged flow were compiled over 15 vortex shedding cycles. The results shown below are on the central plane of $z/H=0$. Figure 2 depicts the variation of the computed time-averaged streamwise mean velocity along the centerline for $Re=2.2\times10^4$. For comparison with the results of RANS, the experimental data of Lyn et al. [13], computational results of Franke and Rodi [6] based on a RSM model, and our previous results [30] computed using a RSM model with the wall-related pressure-strain model of Craft and Launder [31] are included in Fig. 2(*a*). In addition, four representative predictions, KAWAMU(Kawamura, H., Kawashima, N., Science Univ. of Tokyo, Japan), UMIST-2 (Archambeau, F., Laurence, D., EDF/LNH Chatou, France and Leschziner, M.A., UMIST, Manchester, U.K.), UKAHY-2 (Pourquie, M., Breuer, M., Rodi, W., Univ. of Karlsruhe/Inst. for Hydromechanics, Germany) and TAMU-2 (Tamura, T., Itoh, Y., Takakuwa, A., Tokyo Inst. of Technology, Japan) taken from the LES data bank compiled by Rodi et al. [10] are included in Fig. 2(*b*) to illustrate the current status of LES in the prediction of turbulent wake flow behind a square cylinder. Note that the negative time-averaged mean velocities behind the cylinder indicate the wake recirculation flow and the zero streamwise mean velocity position represents the wake saddle point. The distance between the rear face of the cylinder and the saddle point is the wake length which is an important characteristic length often used for validating computation. The dimensionless mean wake lengths (L_R/H) obtained by the present calculations and measured by Lyn et al. [13] are 0.91 and 0.88, respectively. As a comparison, the wake lengths based on the RSM model computed by Liou and Chen [30] and Franke and Rodi [6] are 1.10 and 0.48 respectively. The measured data (triangle symbol in Fig. 2(*a*) and (*b*)) of Lyn et al. [13] indicate that the time mean velocity recovers fast as x/H increases from 1 to 2 and gradually levels off beyond $x/H=3$ with the velocity defect recovering to about 60 percent of the bulk mean velocity. Figure 2(*a*) further shows that the present LES of the time-averaged streamwise centerline mean velocity distribution is superior to the previous RSM simulations. As for the above-mentioned four LES

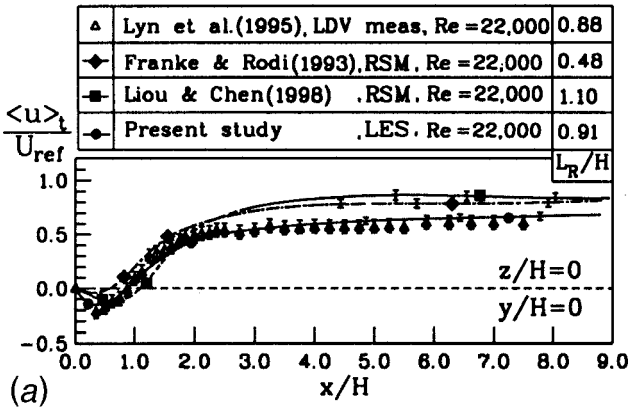

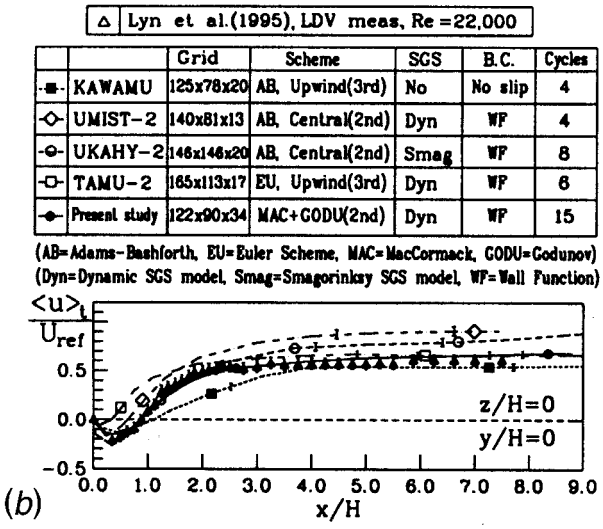

Fig. 2 (*a*) Streamwise time-averaged mean velocity variation along the centerline behind the free-standing cylinder for Re $=2.2\times10^4$ (comparison with RANS). (*b*) Streamwise time-averaged mean velocity variation along the centerline behind the free-standing cylinder for $Re=2.2\times10^4$ (comparison with other LES)

results [10], Fig. 2(*b*) shows that UKAHY-2 gives a better prediction of wake region and TAMU-2 attains a better velocity recovery downstream of wake. The present LES predicts a better overall centerline streamwise mean velocity distribution. As shown in the top table of Fig. 2(*b*), finer grid resolution in the spanwise direction, more cycles for time or phase average, and different numerical schemes adopted are the possible reasons for the better centerline mean velocity predictions attained in the present study.

Table 1 shows a comparison of some predicted and measured flow parameters for turbulent wake flow past a square cylinder with and without wall proximity, including mean recirculation wake length (L_R/H), maximum negative $\langle u\rangle_t/U_{ref}$ in the wake region, $\langle u\rangle_t/U_{ref}$ at $x/H=9.0$ along the centerline, Strouhal number (St), and mean drag coefficient ($\overline{c_d}$). Comparing with the data of Lyn et al. [13], the present LES results in discrepancies in L_R/H of about 3 percent while other LES in the range of 8–50 percent, in maximum negative $\langle u\rangle_t/U_{ref}$ of 23 percent while other LES in the range of 19 percent–71 percent, in centerline $\langle u\rangle_t/U_{ref}$ at $x/H=9.0$ of 12 percent while other LES in the range of 8 percent–52 percent. In the prediction of St, the predicted values of most LES lie in the range of 0.13 ± 0.02 with a discrepancy smaller than 15 percent compared with the experimental data, except 0.09 predicted by UMIST-2. The present computed power spectra of the fluctuating lift coefficient acting on the cylinder and

Downloaded 03 Jun 2010 to 171.66.16.150. Redistribution subject to ASME license or copyright; see http://www.asme.org/terms/Terms_Use.cfm

Table 1 Predictions or measurements of fluid flow parameters

Authors	TEC	Re $\times 10^4$	L_R/H	Max. negative $\langle u \rangle_t / U_{ref}$	$\langle u \rangle_t / U_{ref}$ (X/H=9.0, Y/H=0.0, Z/H=0.0)	St	$\overline{c_d}$	Wall Proximity
Durao et al. [11]	LDV	1.4	0.83			0.14		No
Lyn et al. [13]	LDV	2.2	0.88	−0.21	0.60	0.132	2.1	No
Devarakonda and Humphrey [15]	LDV	2.75					2.35	Yes $C/H=0.95$
Bosch et al. [16]	LDV	2.2	1.10	−0.28		0.139		Yes $C/H=0.75$

Authors	TURB model	Re $\times 10^4$	L_R/H	Max. negative $\langle u \rangle_t / U_{ref}$	$\langle u \rangle_t / U_{ref}$ (X/H=9.0, Y/H=0.0, Z/H=0.0)	St	$\overline{c_d}$	Wall Proximity
Franke and Rodi [6]	RSM	2.2	0.48	−0.04	0.82	0.136	2.15	No
	Two-layer RSM	2.2	0.48			0.159	2.43	No
Liou and Chen [30]	RSM	2.2	1.1	−0.12	0.84			No
Bosch and Rodi [17]	KL	2.2	1.73	−0.17	0.56			Yes $C/H=0.75$
KAWAMU	LES	2.2	0.70	−0.13	0.55	0.15	2.58	No
UKAHY2	LES	2.2	0.96	−0.25	0.91	0.13	2.30	No
UMIST2	LES	2.2	0.71	−0.17	0.90	0.09	2.02	No
TAMU2	LES	2.2	0.44	−0.06	0.66	0.14	2.77	No
Present study	LES	2.2	0.91	−0.16	0.67	0.133	2.14	No
Present study	LES	2.2	1.06	−0.15	0.50	0.139	2.41	Yes $C/H=0.75$

TEC: Technique TURB: Turbulence

the fluctuating velocity component are plotted in Fig. 3. There is a distinct peak with a value of St=0.133, as also shown in Table 1. In the present prediction of $\overline{c_d}$ the discrepancy compared with the experimental data of Lyn et al. [13] is about 8.6 percent, and the predicted $\overline{c_d}$ of other LES are in the range of 4–32 percent.

Figure 4 depicts the total streamwise and transverse velocity fluctuation distributions along the centerline downstream of the cylinder for $Re=2.2\times10^4$. The peak of transverse total velocity fluctuation occurs at a position slightly downstream of the streamwise one, and the peak value of the former is about twice that of the latter. The discrepancy in u'^t/U_{ref} between the LES results and the measured data of Lyn et al. [13] is larger in the region immediately behind the cylinder. The poor prediction of the streamwise mean velocity $\langle u \rangle_t / U_{ref}$ recovery by the RSM, as mentioned above, results in a poor u'^t/U_{ref} prediction downstream of $x/H=2$. Overall speaking, the LES results are in a better agreement with the measured data of Lyn et al. [13] than the RSM results. Some possible explanations for the discrepancies of $\langle u \rangle_t / U_{ref}$,

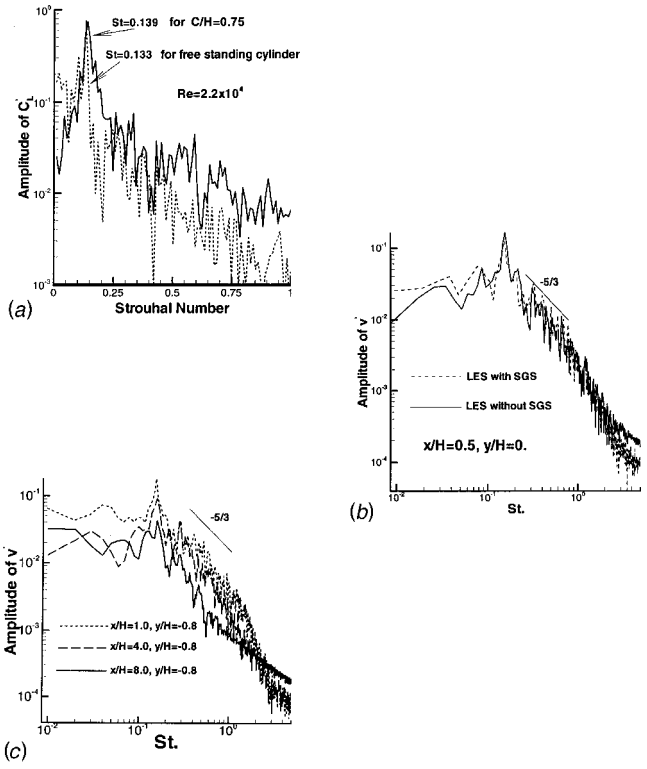

Fig. 3 (*a*) Power spectra of fluctuating lift coefficient for cylinder with and without a nearby wall. (*b*) Power spectra of transverse fluctuating velocity component with and without SGS model. (*c*) Power spectra of transverse fluctuating velocity component at different locations.

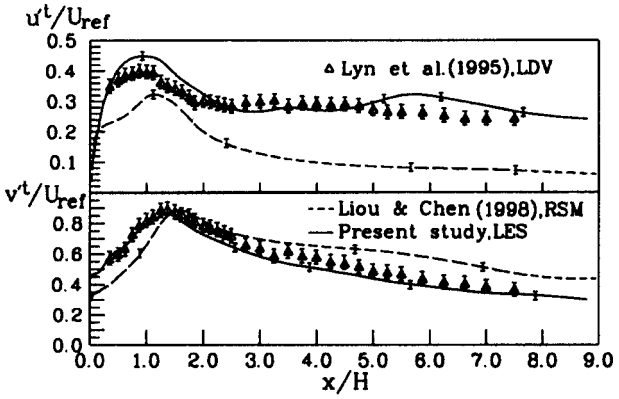

Fig. 4 Streamwise and transverse total fluctuation intensity variation along the centerline downstream of the free-standing cylinder for $Re=2.2\times10^4$

Downloaded 03 Jun 2010 to 171.66.16.150. Redistribution subject to ASME license or copyright; see http://www.asme.org/terms/Terms_Use.cfm

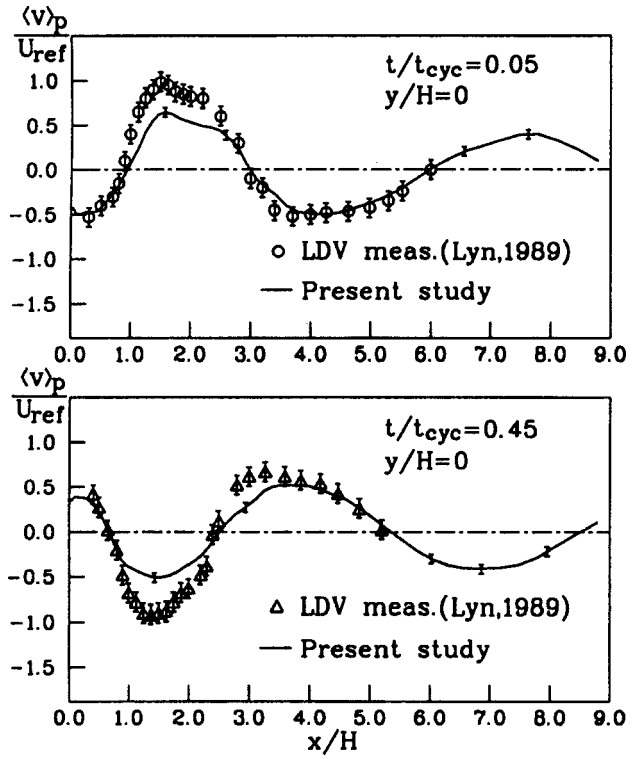

Fig. 5 Phase-averaged transverse velocity variation along the centerline behind the free-standing cylinder at two selected phases ($t/t_{cyc}=0.05$ and 0.45) for $Re=2.2\times10^4$

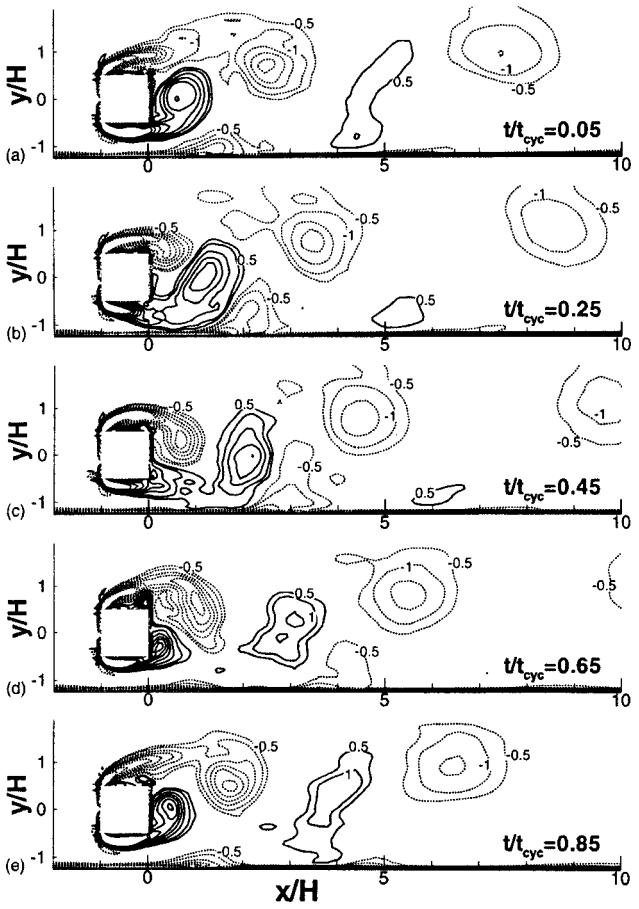

Fig. 6 Nondimensionalized phase-averaged spanwise vorticity contours at five selected phases ($t/t_{cyc}=0.05$, 0.25, 0.45, 0.65, and 0.85) for $C/H=0.75$ and $Re=2.2\times10^4$

u'^t/U_{ref}, and v'^t/U_{ref} in the reversal flow zone immediately behind the cylinder between the present LES results and the experimental data of Lyn et al. [13] may be attributable to the uncertainties associated with measurements, in particular the insufficient inlet conditions provided, and to the SGS model adopted in modeling the unresolved part of the turbulence scales.

Phase-Averaged Flow. The vortex shedding phenomenon can not be revealed by the above long-time-averaged flow field; however, it can be demonstrated by the phase-averaged flow field. Figure 5 shows the phase averaged transverse velocity along the centerline at two selected phases. It is seen that the calculated results are in reasonable agreement with the measured data of Lyn [32]. At both selected phases, the first positive peak values of the phase-averaged transverse velocities are located between $x/H=1$ and $x/H=2$, which is in accordance with the distribution of time-averaged transverse total velocity fluctuation shown in Fig. 4. However, Fig. 5 reveals alterative positive and negative peaks with a decreasing amplitude as the flow proceeds downstream, a piece of information lacking in Fig. 4.

Turbulent Wake With A Nearby Wall. Attention is now focused on the effect of wall proximity ($C/H=0.75$) and the interaction of turbulent wake behind a cylinder and the wall boundary layer. The mechanism responsible for heat transfer augmentation is also an important topic in the cylinder-wall interaction.

Time-Averaged Flow. In Table 1, it can be seen that limited literature on wake flow with wall proximity is available. Comparing with the data of Bosch et al. [16], the present LES and the prediction with KL model of Bosch and Rodi [17] result in discrepancies in L_R/H of 4 percent and of 57 percent, respectively, and in maximum negative $\langle u\rangle_t/U_{ref}$ of 46 percent and 39 percent, respectively. The computed power spectra of the fluctuating lift coefficient acting on the cylinder and the transverse fluctuating velocity component are plotted in Fig. 3(*a*) and Figs. 3(*b*)–3(*c*), respectively. There is a distinct peak with a peak frequency of $St=0.139$, which is close to the experimental data shown in Table 1. In the present prediction of $\overline{c_d}$, the discrepancy compared with the experimental data of Devarakonda and Humphrey [15] is about 3 percent.

Phase-Averaged Flow. Figure 6 depicts the phase-averaged spanwise vorticity contours on $z/H=0$ plane at 5 selected phases ($t/t_{cyc}=0.05$, 0.25, 0.45, 0.65, and 0.85) for $C/H=0.75$ and $Re=2.2\times10^4$. The vortex shedding phenomenon is clearly demonstrated. The vortex shed from the upper side of the cylinder is nearly circular and is similar to the The vortex shed from a free-standing cylinder, while the vortex shed from the lower side is stretched and generally smaller than the vortex shed from the upper side when reached the same streamwise position. Moreover, the lower-side-shed vortex induces a wall vortex. The wall vortex originates from the wall boundary layer and connects to the wall layer over the entire shedding cycle without isolating from the wall layer. Both the lower-side-shed vortex and wall vortex have the same vortex celerity, as will be further shown later. Figure 7 depicts the trajectory (x_c/H,y_c/H) of vorticity peak and the variation of vortex peak value with x/H. The location of the vorticity peak can be identified as the vortex center. Three vortices including upper, lower, and wall vortices are traced to reveal the vortex motion. The upper vortex is the upper-side-shed vortex and almost moves along the upper edge of the cylinder but gradually directs away from the wall. The lower vortex is the lower-side-shed vortex and moves along the center line in a somewhat back and forth way. Note that the wall vortex is not an isolated vortex but it still can be identified during $t/t_{cyc}=0.25$, 0.45, and 0.65. The trajectory of wall vortex is in pace with the lower vortex, indicating that the

Downloaded 03 Jun 2010 to 171.66.16.150. Redistribution subject to ASME license or copyright; see http://www.asme.org/terms/Terms_Use.cfm

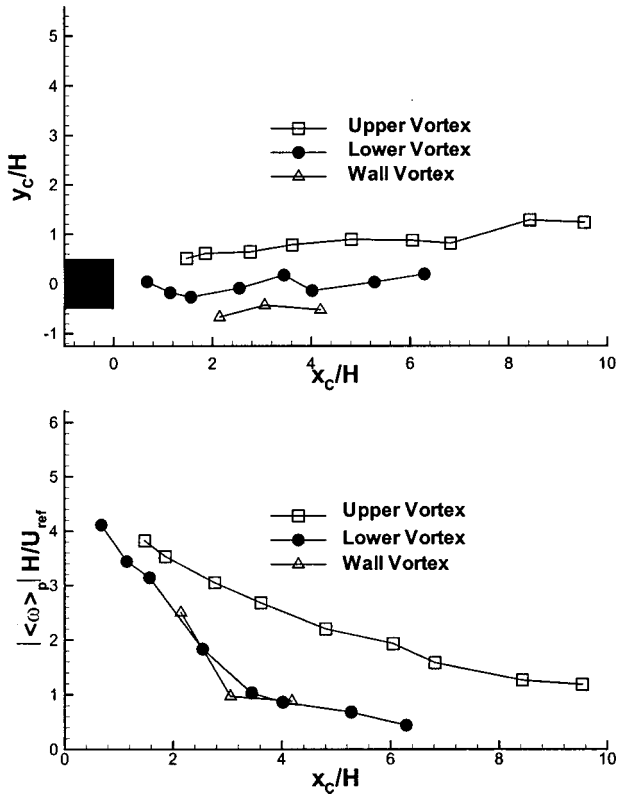

Fig. 7 Trajectory of vortex peak and variation of spanwise vorticity peak value with x/H for C/H=0.75 and Re=2.2×10^4

wall vortex is induced by the lower vortex. The vortex peak value ($\langle\omega\rangle_p H/U_{ref}$) decays with increasing streamwise coordinate; it decays rapidly at the base region (immediately behind the cylinder) and at a slower rate downstream of x/H=3. The decay profile along the flow direction is different between the upper and lower vortices. The upper vortex has a slower rate of decay while the lower and wall vortices have a rapid decay rate. The lower and wall vortices have about the same decay profile which means that the interaction between them is a mutual process. It should be pointed out that the large-scale vortex decay can also be shown by the power spectra of the fluctuating velocity component at different x/H stations in Fig. 3(c). As the flow proceeds from x/H $=-0.48$ through x/H=4.0 to x/H=8.0, the decrease and increase of the amplitudes of the large- (lower frequency part) and small-scale (higher frequency part) eddies indicates the evolution of the large-scale vortex to the random small-scale eddies.

Figure 8 depicts the variation of the streamwise location of the vortex peak (x_c/H) with time. The slope of the curve gives the vortex celerity [30]. Within the range of x/H>2.0, the vortex celerity is almost a constant of $u_c=0.78U_{ref}$ for the upper vortex which is equal to that of a free-standing cylinder measured by Lyn et al. [13] and a constant of $u_c=0.66U_{ref}$ for the lower and wall vortices. The vortex celerity of the upper vortex is larger than that of the lower and wall vortices. This indicates the retardation effect of the wall on the shedding vortex. Within the range of x/H <2.0, the vortex celerity is almost a constant of $u_c=0.31U_{ref}$ for the three vortices, which is lower than $0.43U_{ref}$ of Lyn et al. [13]. The slower vortex celerities for x/H<2.0 means that the wall effect is imposed on alternating vortex formation at the base region via the mutual interaction of upper and lower vortices, as the basic mechanism of Von-Karman vortex shedding is.

Time-Averaged Heat Transfer. Figure 9 shows the time-averaged Nusselt number distribution along the bottom heated wall. Two distinct peaks of time-averaged Nu exist. The first one

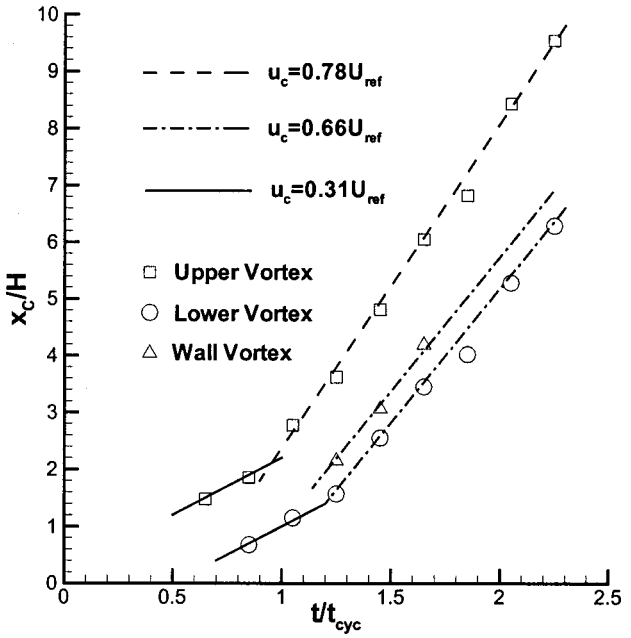

Fig. 8 Time history of spanwise vorticity peak along the streamwise direction for C/H=0.75 and Re=2.2×10^4

is located at x/H=−0.48, and is attributed to the fluid flow between the cylinder and the bottom wall. Because of the high speed flow there, the forced convection is dominating. The second peak is related to the wall vortices which are shown in Fig. 6(*b*–*d*). The wall vortex is induced by the lower vortex and has the same nature as the upper vortex in the sense that they are characterized by negative spanwise vorticity or clockwise fluid motion. The clockwise fluid motion entrains fresh or cooler fluid from its downstream side to the space between itself and the channel wall. This is called the washing action, as also experimentally visualized using intermittent dye injection method by Yao et al. [33]. In the range of x/H=2.0–5.0, where the wall vortex can be clearly

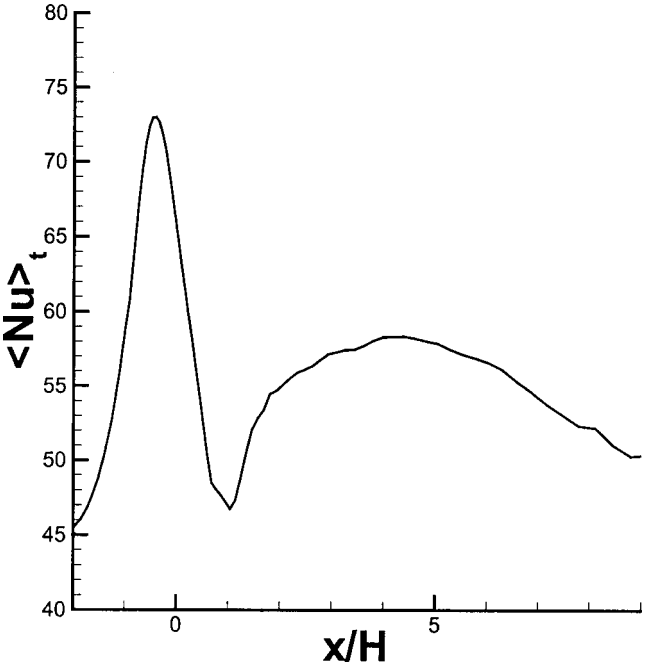

Fig. 9 Streamwise time-averaged Nusselt number variation along the wall on z/H=0 plane for C/H=0.75 and Re=2.2×10^4

Downloaded 03 Jun 2010 to 171.66.16.150. Redistribution subject to ASME license or copyright; see http://www.asme.org/terms/Terms_Use.cfm

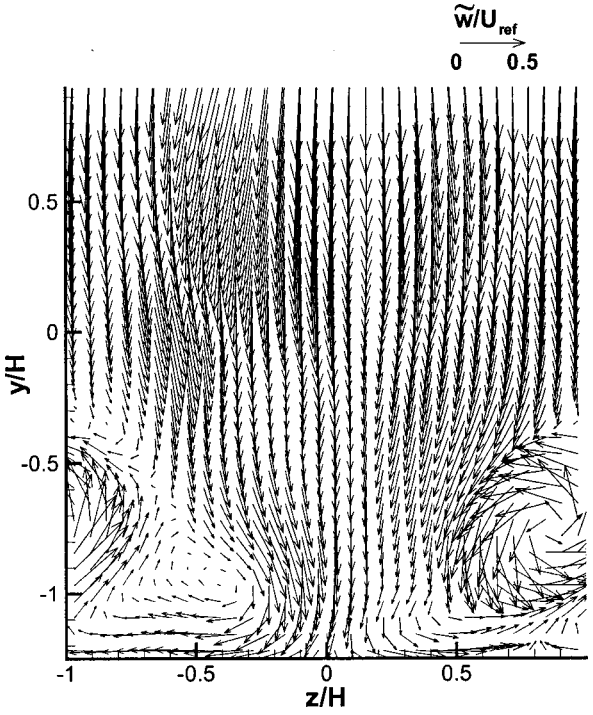

Fig. 10 Instantaneous secondary velocity vector plot at x/H = 4.0 for $C/H = 0.75$ and $Re = 2.2\times10^4$

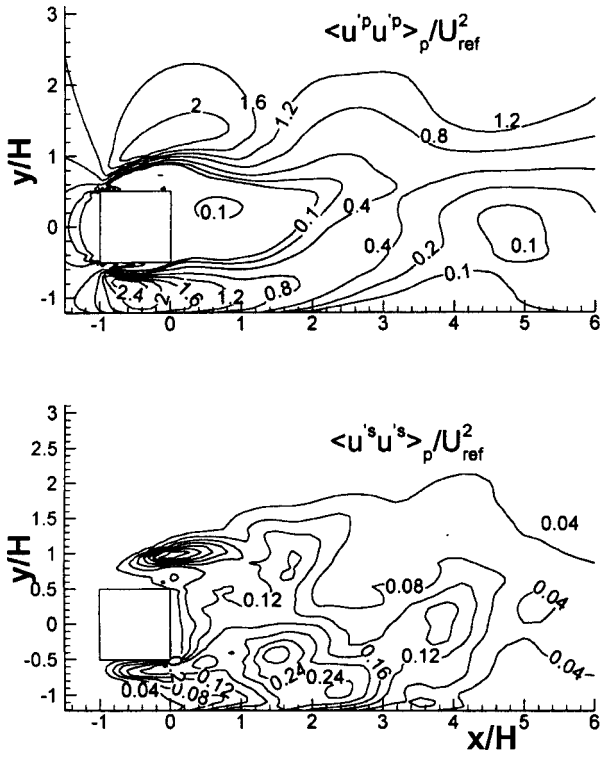

Fig. 11 Nondimensionalized phased-averaged contours of the streamwise periodic $\langle u'^p u'^p \rangle_p / U_{ref}^2$ and random $\langle u'^s u'^s \rangle_p / U_{ref}^2$ fluctuations at a selected phase $t/t_{cyc} = 0.45$ for $C/H = 0.75$ and $Re = 2.2\times10^4$

identified in Fig. 6, the time-averaged Nu attains its second peak value, and the clockwise-rotating spanwise vortex can contribute heat transfer augmentation by the aforementioned washing action. In exploring the possible method for augmenting heat transfer, an appropriate control of the evolution of the spanwise and streamwise vortices is helpful. For instance, the streamwise vortices with common-flow-down are especially important [34]. The streamwise vortices with common-flow-down, denoting the counter-rotating vortices with the direction of the secondary flow between them that are directed toward the wall, are found to be essential for elevating heat transfer [34]. The streamwise vortices for the present case of $C/H = 0.75$ are counter-rotating vortices with secondary flow directed toward the wall, as evidenced by the secondary flow pattern (Fig. 10) at x/H = 4.0. These vortices produce strong distortion of the normal 2-D boundary layer structure. As the secondary flow is directed toward the wall, the boundary layer is thinned and the heat transfer is elevated. Among the flow dynamic factors relevant to heat transfer augmentation, such as main stream convective velocity, near-wall turbulence, and secondary flow induced by longitudinal vortices, the direction (relative to the wall) and strength of the aforementioned secondary flow have been experimentally found to be more influential on enhancing the local heat transfer for duct flows with wall-mounted vortex generators [4]. For a square cylinder detached a dimensionless distance of $C/H = 0.75$ from the heated wall, the computed results further indicate that spanwise and longitudinal vortices are also able to generate washing action and favorable secondary flow direction relative to the heated wall, which thus attains a better local heat transfer elevation.

It is interesting to know the relative contributions of the periodic and random fluctuations to the cooling enhancement while approaching the wall. Thus, the contour maps of their streamwise components at a selected phase $t/t_{cyc} = 0.45$ are depicted in Fig. 11. The relatively high values of the streamwise periodic fluctuation component $\langle u'^p u'^p \rangle_p / U_{ref}^2$, more than 10 times those of the random fluctuation component $\langle u'^s u'^s \rangle_p / U_{ref}^2$, in the region between the cylinder and bottom wall certainly contribute to the first Nu peak at x/H = −0.48 (Fig. 9). Adjacent to the bottom wall and proceeding downstream, the $\langle u'^p u'^p \rangle_p / U_{ref}^2$ decreases rapidly from a value of 2.4 at x/H = −0.48 to 0.1 at x/H = 4 where Nu attains its second peak (Fig. 9). Correspondingly, $\langle u'^s u'^s \rangle_p / U_{ref}^2$ drops slower from 0.16 at x/H = −0.48 to 0.08 at x/H = 4. It is now clear that both the periodic and random fluctuations contribute to the second Nu peak at x/H = 4. Note that the transverse and spanwise components of the periodic and random fluctuations are typically an order of magnitude smaller than their streamwise counterparts. Hence, they contribute little to the cooling enhancement.

Concluding Remarks

The following conclusions are drawn from the data presented:

1 The present three-dimensional large eddy simulations of the turbulent wake behind a square cylinder attain a better overall agreement with the available experimental data in predicting the streamwise variation of centerline mean velocity and turbulence intensity components than the previous computations.

2 Strouhal number is increased and drag coefficient is decreased when a nearby wall is present. The celerity of the lower vortex is smaller than that of the upper vortex due to the interaction with the wall boundary layer. The mutual interaction between the lower and wall vortices can be identified through the vortex peak trajectory, the decay profile of vortex peak value, and the vortex celerity.

3 For a turbulent flow past a square cylinder with a nearby wall located at an adequate dimensionless distance, such as C/H = 0.75 examined, the wall vortex induced by the lower-side-shed vortex can cause a washing effect and direct the secondary flow in the cross-sectional (y-z) plane toward the heat transfer wall. These physical mechanisms are responsible for the observed local heat transfer augmentation and are revealed computationally for the first time by using LES.

Downloaded 03 Jun 2010 to 171.66.16.150. Redistribution subject to ASME license or copyright; see http://www.asme.org/terms/Terms_Use.cfm

4 Among the periodic and random fluctuation components, the streamwise periodic fluctuation component is found to have a dominant contribution to the major peak of Nusselt number distribution. Both the streamwise periodic and random fluctuation components have about the same contribution to the second Nusselt number peak.

Acknowledgment

This research was supported by the National Science Council of the Republic of China under Contracts NSC83-0401-E007-014 and NSC84-2212-E007-049.

Nomenclature

C = gap between the cylinder and the wall
c_k = model constant
c_s = Smagorinsky constant
$\hat{E}$ = $\overline{p}/(\gamma-1)+0.5\overline{\rho}(\tilde{u}^2+\tilde{v}^2+\tilde{w}^2)$, filtered total energy per unit volume, J/m^3
$\mathbf{F}$ = convective flux vector in x direction of Navier-Stokes equations
f = vortex shedding frequency
G = spatial filter function
$\mathbf{G}$ = convective flux vector in y direction of Navier-Stokes equations
g = flow variable
$\mathbf{H}$ = convective flux vector in z direction of Navier-Stokes equations
H = cylinder height (4 mm)
h = local heat transfer coefficient $\equiv q_w/(T_w-T_\infty)$
k = turbulent kinetic energy, m^2/s^2
k_s = subgrid turbulent kinetic energy, m^2/s^2
L_R = mean reattachment length, wake length
Nu = local Nusselt number ($\equiv hH/\kappa$)
p = pressure, N/m^2
$\mathrm{Pr_S}$ = SGS Prandtl number
$\mathbf{Q}$ = conservation variables vector of Navier-Stokes equations
q_s = subgrid-scale heat flux, W/m^2
q_w = local wall heat flux, W/m^2
Re = Reynolds number based on cylinder height ($\equiv \rho U_{\mathrm{ref}} H/\mu$)
St = Strouhal number ($\equiv fH/U_{\mathrm{ref}}$)
S_{ij} = $1/2(\partial u_i/\partial x_j+\partial u_j/\partial x_i)-1/3\delta_{ij}\partial u_k/\partial x_k$, strain rate tensor
T = temperature, K
T_w = local wall temperature, K
T_∞ = freestream temperature, K
t = time coordinate, s
t_{cyc} = period of a vortex shedding cycle, s
u = streamwise velocity, m/s
$\langle u\rangle_t$ = long-time mean streamwise velocity
$\langle u\rangle_p$ = phase-averaged streamwise velocity
u''^t = streamwise velocity total fluctuation$=(\langle u'^p u'^p\rangle_t+\langle u'^s u'^s\rangle_t)^{1/2}$
U_{ref} = inlet mean velocity as a reference velocity
u_c = vortex celerity
v = transverse velocity, m/s
$\langle v\rangle_t$ = long-time mean transverse velocity
$\langle v\rangle_p$ = phase-averaged transverse velocity
v''^t = transverse velocity total fluctuation$=(\langle v'^p v'^p\rangle_t+\langle v'^s v'^s\rangle_t)^{1/2}$
w = spanwise velocity, m/s
$\mathbf{x}$ = position vector
x = streamwise coordinate
y = transverse coordinate
z = spanwise coordinate
$'$ = filter width
δ_{ij} = Kronecker delta function
γ = specific heats ratio
κ = thermal conductivity, W/(m·K)
μ = dynamic viscosity, kg/(m·s)
ν = kinematic viscosity, m/s^2
ν_s = subgrid kinematic viscosity, m/s^2
Ω = flow domain
ω = vorticity
ρ = density, kg/m^3
τ = viscous shear stress, N/m^2
τ_s = subgrid-scale shear stress, N/m^2
τ_w = shear stress at wall, N/m^2
ζ = dummy variable
ε = dissipation rate of turbulence kinetic energy, m^2/s^3

Subscripts

e = exit plane
w = wall

Superscripts

$'$ = subgrid component
$'^p$ = periodic fluctuation component
$'^s$ = stochastic turbulent fluctuation component
$'^t$ = total fluctuation component
$''$ = mass-weighted subgrid component
$\overline{}$ = spatially filtered quantity
$\overline{}^t$ = long-time averaged quantity
$\sim$ = mass-weighted spatially filtered quantity
$\langle\rangle_p$ = phase-averaged quantity
$\langle\rangle_t$ = time-averaged quantity$=\overline{}^t$

References

[1] Suzuki, K., 1996, "Flow Modification and Heat Transfer Enhancement with Vortices," The Ninth International Symposium on Transport Phenomena in Thermal-Fluids Engineering, Singapore, June 25–28, pp. 72–83.
[2] Liou, T. M., Wang, W. B., and Chang, Y. J., 1995, "Holographic Interferometry Study of Spatially Periodic Heat Transfer in a Channel with Ribs Detached from One Wall," ASME J. Heat Transfer, **117**, 1995, pp. 32–39.
[3] Fiebig, M., 1996, "Embedded Vortices in Internal Flow: Heat Transfer and Pressure Loss Enhancement," Int. J. Heat Fluid Flow, **16**, pp. 376–388.
[4] Liou, T. M., Chen, C. C., and Tsai, T. W., 2000, "Heat Transfer and Fluid Flow in a Square Duct with 12 Different Shaped Vortex Generators," ASME J. Heat Transfer, **122**, pp. 327–335.
[5] Rodi, W., 1993, "On the Simulation of Turbulent Flow Past Bluff Bodies," J. Wind. Eng. Ind. Aerodyn., **46,47**, pp. 3–19.
[6] Franke, R., and Rodi, W., 1993, "Calculation of Vortex Shedding Past a Square Cylinder with Various Turbulence Models," *Turbulent Shear Flow 8*, Durst, F. et al., eds, Springer-Verlag, New York, pp. 189–204.
[7] Gibson, M. M., and Launder, B. E., 1978, "Ground Effects on Pressure Fluctuations in the Atmospheric Boundary Layer," J. Fluid Mech., **86**, pp. 491–511.
[8] Tamura, T., Ohta, I., Kuwahara, K., 1990, "On the reliability of Two-Dimensional Simulation for Unsteady Flows Around a Cylinder-type Structure," J. Wind. Eng. Ind. Aerodyn., **35**, pp. 275–298.
[9] Murakami, S., Mochida, A., Rodi, W., Franke, R., 1993, "Large Eddy Simulation of Turbulent Vortex Shedding Flow Past 2D Square Cylinders," Engineering Applications of Large Eddy Simulation, FED-Vol. 162, ASME, pp. 113–120.
[10] Rodi, W., Ferziger, J. H., Breuer, M., and Pourquie, M., 1997, "Status of Large Eddy Simulation: Results of a Workshop," ASME J. Fluids Eng., **119**, No. 2, pp. 248–262.
[11] Durao, D. F. G., Heitor, M. V., and Pereira, J. C. F., 1988, "Measurements of Turbulent and Periodic Flows Around a Square Cross-Section Cylinder," Exp. Fluids, **6**, pp. 298–304.
[12] Lyn, D. A., and Rodi, W., 1994, "The Flapping Shear Layer Formed by Flow Separation from the Forward Corner of a Square Cylinder," J. Fluid Mech., **267**, pp. 353–376.
[13] Lyn, D. A., Einav, S., Rodi, W., and Park, J. H., 1995, "A Laser-Doppler Velocimetry Study of Ensemble-Averaged Characteristics of the Turbulent Near Wake of a Square Cylinder," J. Fluid Mech., **304**, pp. 285–319.
[14] Durao, D. F. G., Gouveia, P. S. T., and Pereira, J. C. F., 1991, "Velocity Characteristics of the Flow Around a Square Cross Section Cylinder Placed Near a Channel Wall," Exp. Fluids, **11**, pp. 341–350.
[15] Devarakonda, R., and Humphrey, J. A. C., 1996, "Turbulent Flow in the Near Wakes of Single and Tandem Prisms," Int. J. Heat Fluid Flow, **17**, pp. 219–227.
[16] Bosch, G., Kappler, M., and Rodi, W., 1996, "Experiments on the Flow Past a Square Cylinder Placed Near a Wall," Exp. Therm. Fluid Sci., **13**, pp. 292–305.

Downloaded 03 Jun 2010 to 171.66.16.150. Redistribution subject to ASME license or copyright; see http://www.asme.org/terms/Terms_Use.cfm

[17] Bosch, G., and Rodi, W., 1996, ''Simulation of vortex shedding past a square cylinder near a wall,'' Int. J. Heat Fluid Flow, **17**, pp. 267–275.
[18] Kato, M., and Launder, B. E., 1993, ''The Modelling of Turbulent Flow Around Stationary and Vibrating Square Cylinders,'' Proceeding 9th Symposium on Turbulent Shear Flows, Kyoto, Japan, 10-4, 1993.
[19] Liou, T. M., Lien, W. Y., and Hwang, P. W., 1995, ''Compressibility Effects and Mixing Enhancement in Turbulent Free Shear Flows,'' AIAA J., **33**, No. 12, pp. 2332–2338.
[20] Liou, T. M., Lien, W. Y., and Hwang, P. W., 1994, ''Large-Eddy Simulations of Turbulent Reacting Flows in a Chamber with Gaseous Ethylene Injection through the Porous Wall,'' Combust. Flame, **99**, pp. 591–600.
[21] Liou, T. M., Lien, W. Y., and Hwang, P. W., 1997, ''Flammability Limits and Probability Density Functions in Simulated Solid-Fuel Ramjet Combustors,'' J. Propul. Power, **13**, No. 5, pp. 643–650.
[22] Liou, T. M., Yang, C. P., and Lee, H. L., 1997, ''LDV Measurements of Spatially Periodic Flows Over a Detached Solid-Rib Array,'' ASME J. Fluids Eng., **119**, pp. 383–389.
[23] Smagorinsky, J., 1963, ''General Circulation Experiments with the Primitive Equations,'' Mon. Weather Rev., **91**, No. 3, pp. 99–164.
[24] Lilly, D. K., 1992, ''A Proposed Modification of the Germano Subgrid-Scale Closure Method,'' Phys. Fluids A, **4**, No. 3, pp. 633–635.
[25] Germano, M., Piomelli, U., Moin, P., and Cabot, W. H., 1991, ''A Dynamic Subgrid-Scale Eddy Viscosity Model,'' Phys. Fluids A, **3**, No. 7, pp. 1760–1765.
[26] Hussain, A. K. M. F., and Reynolds, W., 1970, ''The Mechanics of an Organized Wave in Turbulent Shear Flow,'' J. Fluid Mech., **41**, pp. 241–258.
[27] Liou, T. M., Lien, W. Y., and Hwang, P. W., 1994, ''A Modified Godunov's Scheme for Shock Tube Flows and Turbulent Combustion Flows,'' The Fourth National Conference on Combustion Science and Technology, Hsinchu, Taiwan, Republic of China, pp. 242–247.
[28] Tsai, Y. P., and Christiansen, W. H., 1990, ''Two-Dimensional Numerical Simulation of Shear-Layer Optics,'' AIAA J., **28**, No. 12, pp. 2092–2097.
[29] Werner, H., and Wengle, H., 1993, ''Large-Eddy Simulations of Turbulent Flow Over and Around a Cube in a Plate Channel,'' *Turbulent Shear Flow 8*, Durst, F. et al., eds, Springer-Verlag, New York, pp. 155–168.
[30] Liou, T. M., and Chen, S. H., 1998, ''Turbulent Flow Past an Array of Bluff Bodies Aligned Along the Channel Axis,'' ASME J. Fluids Eng., **120**, No. 3, pp. 520–530.
[31] Craft, T. J., and Launder, B. E., 1992, ''New Wall-Reflection Model Applied to the Turbulent Impinging Jet,'' AIAA J., **30**, pp. 2970–2975.
[32] Lyn, D. A., 1989, ''Phase-Averaged Turbulence Measurements in the Separated Shear Layer Region of Flow Around a Square Cylinder,'' Proceedings of 23rd Congress of International Association for Hydraulic Research, Ottawa, Canada, 21–25 August, A85–A92.
[33] Yao, M., Nakatani, M., and Suzuki, K., 1995, ''Flow Visualization and Heat Transfer Experiments in a Turbulent Channel Flow Obstructed With an Inserted Square Rod,'' Int. J. Heat Fluid Flow, **16**, pp. 389–397.
[34] Pauley, W. R., and Eaton, J. K., 1994, ''The Effect of Embedded Longitudinal Vortex Arrays on Turbulent Boundary Layer Heat Transfer,'' ASME J. Heat Transfer, **116**, pp. 871–879.

Downloaded 03 Jun 2010 to 171.66.16.150. Redistribution subject to ASME license or copyright; see http://www.asme.org/terms/Terms_Use.cfm

Large Eddy Simulation of a Flow Past a Free Surface Piercing Circular Cylinder

T. Kawamura[1]

S. Mayer

A. Garapon

L. Sørensen

International Research Centre for Computational Hydrodynamics (ICCH), Agern Allé 5, 2970 Hørsholm, Denmark

Interactions between surface waves and underlying viscous wake are investigated for a turbulent flow past a free surface piercing circular cylinder at Reynolds number $Re=2.7\times10^4$ using large eddy simulation (LES). The computations have been performed for three Froude numbers $Fr=0.2$, 0.5 and 0.8 in order to examine the influence of the Froude number. A second-order finite volume method coupled with a fractional step method is used for solving the grid-filtered incompressible Navier-Stokes equations. The computational results are found to be in good agreement with the available experimental data. At low Froude numbers $Fr=0.2$ and 0.5, the amplitude of generated surface wave is small and the influence on the wake is not evident. On the other hand, strong wave-wake interactions are present at $Fr=0.8$, when the generated free surface wave is very steep. It is shown that structures of the underlying vortical flow correlate closely with the configuration of the free surface. Computational results show presence of a recirculation zone starting at the point where the surface slope changes discontinuously. Above this zone the surface elevation fluctuates intensively. The computed intensity of the surface fluctuation is in good agreement with the measurements. It is also shown that the periodic vortex shedding is attenuated near the free surface at a high Froude number. The region in which the periodic vortex shedding is hampered extends to about one diameter from the mean water level. It is qualitatively shown that the separated shear layers are inclined outward near the free surface due to the generation of the surface waves. This change in the relation between two shear layers is suggested to be responsible for the attenuation of the periodic vortex shedding. [DOI: 10.1115/1.1431545]

1 Introduction

Numerical simulations of turbulent flows can be classified into three groups. The most accurate approach is direct numerical simulation (DNS), which resolves all the scales of motions in a turbulent flow. However, because of the large difference between the largest and smallest scales, it is generally impossible at present to apply DNS to flows of realistic industrial or environmental interest. The approach that is most commonly used for practical applications is Reynolds averaged Navier-Stokes (RANS) simulation. There are a variety of turbulence models for RANS simulation from algebraic models to higher order models. The advanced models such as Reynolds stress models are generally more accurate than the simpler ones, and can be applied to a wider range of turbulent flows. However, the complexity of the advanced models decreases their utility as an engineering approximation.

The approach called large eddy simulation (LES) determines the large scales of turbulent motions while modeling only the small scale motions. LES can be applied to more complex flows than DNS, since LES requires much less computational effort. On the other hand, since the small scale motions modeled in LES are much less energetic than explicitly solved large scale motions, it is expected that relatively simple models can represent a wide range of turbulent flows. The application of LES was limited to simple flows in its early years since it was first applied to an engineering flow by Deardorff [1]. However, the importance of LES is increasing as the growing capability of computers enlarges the feasible range of its application.

In the present study we investigate an unsteady flow past a circular cylinder vertically piercing a free surface using LES. A surface-piercing bluff body placed in a steady current creates quite a complex flow. At a high Froude number, the generated surface waves become very steep and also unsteady. The process of the periodic vortex shedding has been noted to be significantly altered by the generation of surface waves [2]. Triantafyllou and Dimas [3] have analytically shown an instability of the wave-wake interaction about a horizontal cylinder piercing a free surface. Sheridan et al. [4] have experimentally shown that the wake of a horizontal cylinder submerged beneath a free surface at various depths can have several different states. Unlike the cases with a horizontal cylinder, the case with a vertical cylinder is a fully three-dimensional problem, and analytical treatment becomes much more difficult.

Inoue et al. [2] have experimentally investigated cases with a vertical cylinder at high Froude numbers. They carried out a towing tank experiment using a cylinder of 5 cm in diameter for two Froude numbers, Fr= 0.8 and 1.0. The experimental data suggest that the periodic vortex shedding is attenuated near the free surface, while an instability mechanism different from the Karman mode plays an important role in that region. The measurement of the velocity shows that the periodic vortex shedding is apparent in the deeper region. However, the periodic component of the fluctuations is small in the region near the free surface, while more random fluctuations of higher frequency are more prominent in that region. Intensive oscillations of the free surface are also present in the wake region. They also presented numerical simulations using a finite volume method, however the results are limited to a laminar case at the Reynolds number Re=50, and the unsteady feature of the free surface was not captured. Laminar cases have been studied also by Chiba and Kuwahara [5] using a finite difference method.

The primary objective of the present study is to provide a better understanding of the three-dimensional wave-wake interactions

[1]Present address: Department of Environmental and Ocean Engineering, School of Engineering, The University of Tokyo, 7-3-1 Hongo, Bunkyo-ku, Tokyo 113-8656 Japan.

Contributed by the Fluids Engineering Division for publication in the JOURNAL OF FLUIDS ENGINEERING. Manuscript received by the Fluids Engineering Division May 22, 2000; revised manuscript received August 24, 2001. Associate Editor: P. W. Bearman.

 Copyright © 2002 by ASME

Downloaded 03 Jun 2010 to 171.66.16.150. Redistribution subject to ASME license or copyright; see http://www.asme.org/terms/Terms_Use.cfm

using LES. The flow over a circular cylinder exhibits many different features as the Reynolds number increases. The Reynolds number based on the cylinder diameter, free-stream velocity, and the kinematic viscosity is set to 2.7×10^4 in this study. At this subcritical Reynolds number, the boundary layer on the cylinder surface is laminar, and the transition to turbulence occurs in the wake region [6]. Several researchers have applied LES to the flow over an infinite circular cylinder at subcritical Reynolds numbers [7–10]. Beaudan and Moin [7] have shown that LES provides better predictions of the hydrodynamic forces and the near wake mean flow statistics than RANS. While Kravchenko and Moin [10] have indicated that a high grid resolution is required for accurate prediction of the flow statistics in the near wake region, the results of the LES computations are generally in a good agreement with the experimental data.

Although LES has been applied to various kinds of flows by many researchers, there have been small number of applications to flows with a free surface. Zanden et al. [11] and Thomas and Williams [12] have separately applied LES to open channel flows, and Salvetti et al. [13] have studied the decay process of turbulence under a free surface by LES with dynamic-type SGS models. Most previous applications including the examples above have dealt with a rigid free surface. But very little work has been done for cases with finite amplitude free surface waves. Therefore, one of the objectives of this paper is to verify the accuracy of the LES method applied to a problem involving strong interactions between free surface waves and vortices through comparisons with experimental data.

This paper is organized as follows. Section 2 describes the governing equation; Section 3 gives the outline of the numerical method. The results of the numerical simulation are shown and discussed in Section 4. In Section 5 we summarize our main conclusions.

2 Governing Equation

The governing equations are the grid-filtered incompressible Navier-Stokes equations,

$$\frac{\partial\overline{u_i}}{\partial t}=-\frac{\partial\overline{u_i}\overline{u_j}}{\partial x_j}+\frac{\partial}{\partial x_j}\left\{\nu\left(\frac{\partial\overline{u_i}}{\partial x_j}+\frac{\partial\overline{u_j}}{\partial x_i}\right)\right\}-\frac{\partial\overline{p}}{\partial x_i}-\frac{\partial\tau_{ij}}{\partial x_j} \tag{1}$$

and

$$\frac{\partial\overline{u_i}}{\partial x_i}=0, \tag{2}$$

where t, x_i, u_i and ν are the time, the Cartesian coordinate, the fluid velocity, and the kinematic viscosity, respectively, and the filtering operation is denoted by the overbar. The filtering operation gives rise to the SGS stress tensor τ_{ij} written as

$$\tau_{ij}=\overline{u_iu_j}-\overline{u_i}\,\overline{u_j}. \tag{3}$$

The Smagorinsky model [14] is used to model the SGS stress tensor in this study. The SGS stress tensor is given by

$$\tau_{ij}=-2\nu_T\overline{S}_{ij}=-2(C_s\Delta)^2\sqrt{2\overline{S}_{lm}\overline{S}_{lm}}\,\overline{S}_{ij}, \tag{4}$$

where ν_T, C_s, and Δ are the eddy viscosity, the model coefficient, and the cubic root of the volume of the cell, respectively. S_{ij} is the strain rate tensor defined as

$$\overline{S}_{ij}=\frac{1}{2}\left(\frac{\partial\overline{u_i}}{\partial x_j}+\frac{\partial\overline{u_j}}{\partial x_i}\right). \tag{5}$$

The optimum value of the coefficient C_s is known to be around 0.1 for a channel flow and 0.2 for a wake or jet flow [15]. Since the primary objective of this study is to investigate the interaction between the turbulent wake and the free surface, C_s is set to 0.2 with an appropriate damping function to account for the near-wall effects.

The pressure variable p is defined as the deviation from the hydrostatic pressure, that is,

$$p=\tilde{p}+gx_3, \tag{6}$$

in which $\tilde{p}$ is the pressure divided by the fluid density ρ, g is the gravitational acceleration, and x_3 is the vertical coordinate.

The position of the free surface, denoted as h, is expressed by a single-valued function of time and the horizontal coordinates x_1 and x_2. The time evolution of the height h is governed by the kinematic condition of the free surface,

$$\frac{\partial\overline{h}}{\partial t}+\overline{u}_1\frac{\partial\overline{h}}{\partial x_1}+\overline{u}_2\frac{\partial\overline{h}}{\partial x_2}=\overline{u}_3. \tag{7}$$

The contribution of the SGS terms in the above equation is assumed to be small [16], and is neglected in this study.

3 Numerical Method

3.1 Discretization and Solution Procedure. The governing equations are discretized by a finite-volume formulation on a boundary-adapted structured curvilinear grid, where all the flow variables are defined at cell centers. A second-order central interpolation is used for calculating fluxes except for the convective flux for which the second-order QUICK scheme is used. The effect of the numerical schemes on the calculated flow field has been investigated by Breuer [9], who carried out LES computations of the flow past an infinite circular cylinder at Re=3900 with five different numerical schemes. That work shows that the turbulent fluctuations are sustained in the simulations with the second-order QUICK scheme, while a better agreement with the experimental data is obtained with a second-order central scheme. Although the nondissipative nature of the central schemes are preferable, preparatory simulations carried out with central schemes failed to converge because of the additional nonlinearity of the flow due to the higher Reynolds number and the presence of the deformable free surface. Therefore, the second-order QUICK scheme is used in the following computations. The dissipative nature of the QUICK scheme acts as an additional SGS term [9], and the influence on the simulated flow field should be carefully investigated.

The computational grid is fitted to the free surface and updated every time step by moving the grid points in the vertical direction. The volume flux due to this movement of the grid is taken into account in the momentum equation. Since the details of the method and validations are found in Mayer et al. [17] and Kawamura [18], we give only a brief outline of the solution procedure and the treatment of the viscous free surface condition.

Given the velocity, the pressure and the free surface elevation at time step n, the free surface elevation at the next time step is obtained first by explicitly integrating Eq. (7) by a second-order explicit scheme. The free surface elevation h is defined at the centers of cell boundaries at the free surface, and Eq. (7) is discretized by a second-order finite-difference scheme in space. The resulting height of the free surface at the next time step is used to regenerate the grid.

Time integration of the momentum equation is performed by a semi-implicit second-order fractional step method. First in the predictor step, the intermediate velocity $\overline{u}_i^*$ is obtained from

$$\frac{\overline{u}_i^*-\overline{u}_i^n}{\Delta t}=\frac{3C_i^n-C_i^{n-1}}{2}+\frac{D_i^*+D_i^n}{2}+\frac{G_i^*+G_i^n}{2}+\frac{3P_i^n-P_i^{n-1}}{2}, \tag{8}$$

where C, D, G, and P represent the convective terms, viscous terms including the SGS stress, convective terms due to the movement of the grid, and pressure gradient terms respectively. The superscripts n and $n-1$ denote the time levels, and* refers to the

Downloaded 03 Jun 2010 to 171.66.16.150. Redistribution subject to ASME license or copyright; see http://www.asme.org/terms/Terms_Use.cfm

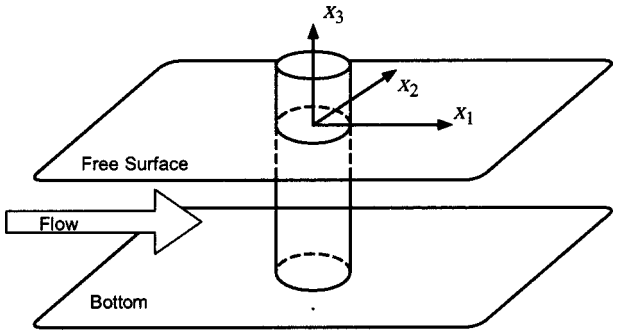

Fig. 1 Definition of the coordinate system

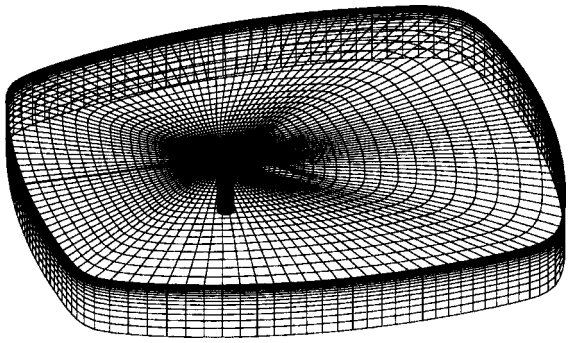

Fig. 2 Grid system (Grid-B) used for the simulations of a flow past a surface-piercing circular cylinder at Re=2.7×10^4

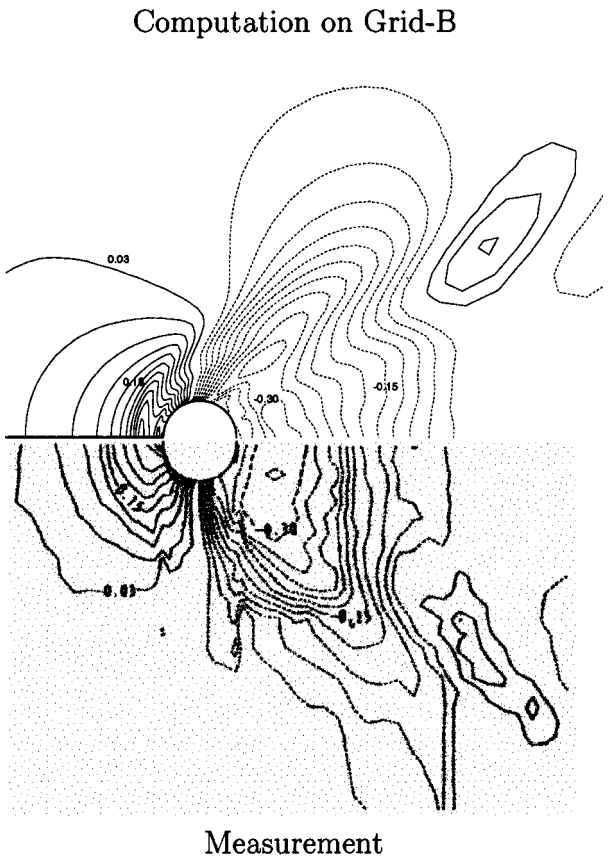

Fig. 3 Computed and measured mean surface elevation around a surface-piercing circular cylinder at Re=2.7×10^4 and Fr=0.8

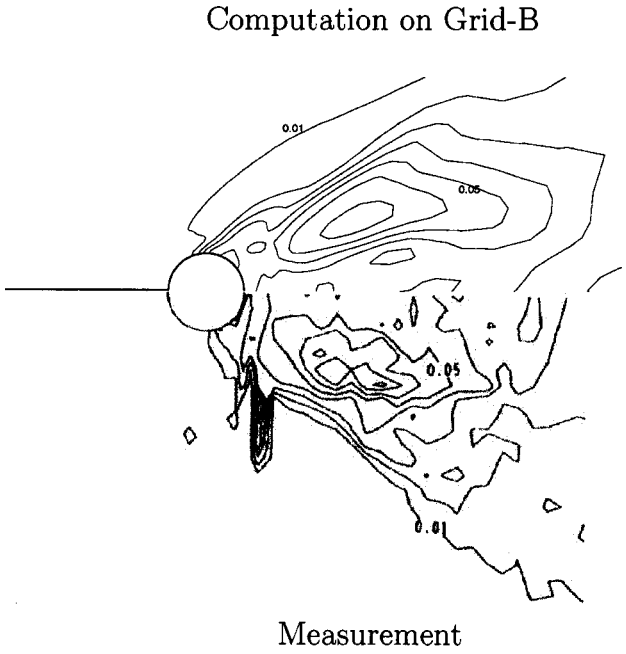

Fig. 4 Computed and measured r.m.s of the surface fluctuation around a surface-piercing circular cylinder at Re=2.7×10^4 and Fr=0.8

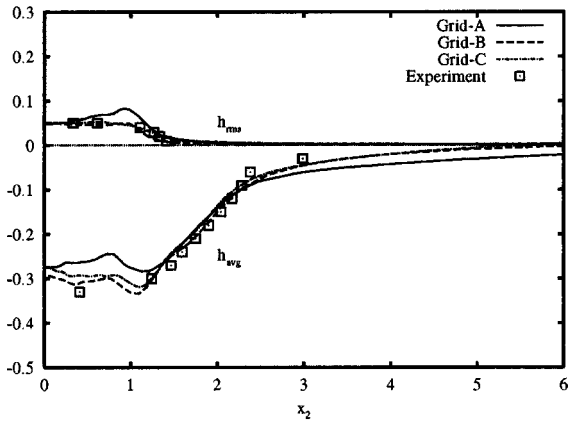

(*a*) $x_1 = 0.9$

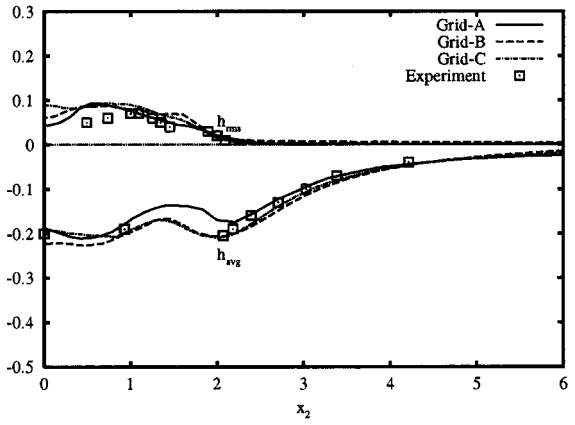

(*b*) $x_1 = 2.0$

Fig. 5 Profiles of the time-averaged elevation and r.m.s. fluctuation of the surface at Fr=0.8: (*a*) x_1=0.9, (*b*) x_1=2.0

Downloaded 03 Jun 2010 to 171.66.16.150. Redistribution subject to ASME license or copyright; see http://www.asme.org/terms/Terms_Use.cfm

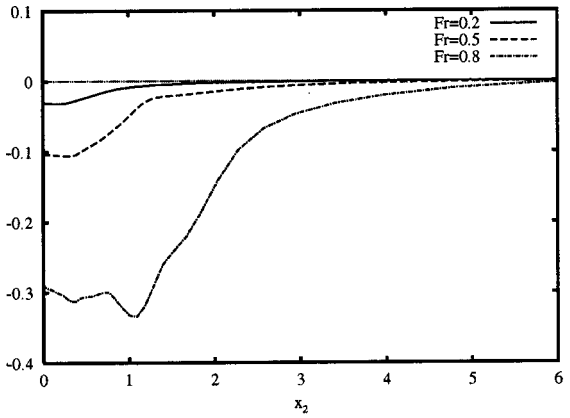

(a) $x_1 = 0.9$

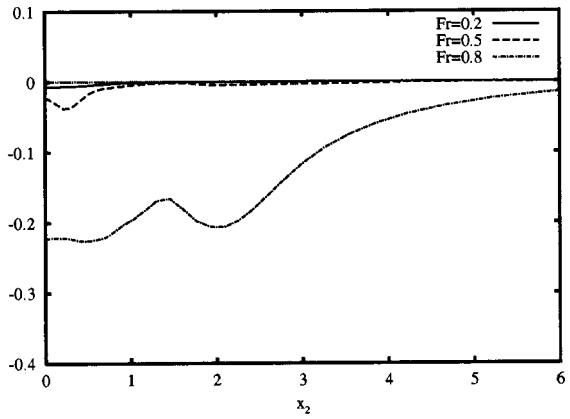

(b) $x_1 = 2.0$

Fig. 6 Profiles of the time-averaged elevation of the surface: (*a*) $x_1=0.9$, (*b*) $x_1=2.0$

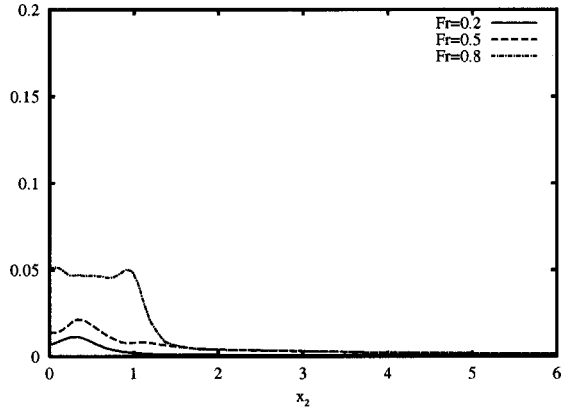

(a) $x_1 = 0.9$

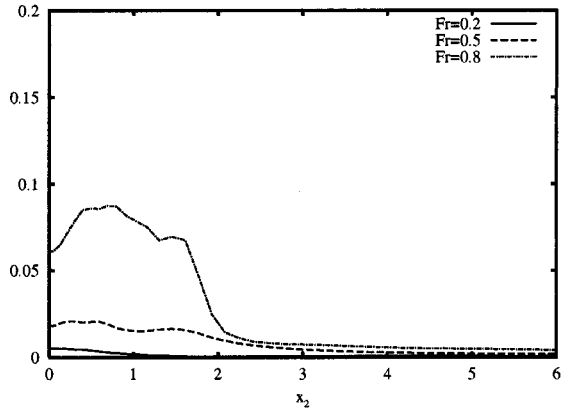

(b) $x_1 = 2.0$

Fig. 7 Profiles of the r.m.s. fluctuation of the surface elevation: (*a*) $x_1=0.9$, (*b*) $x_1=2.0$

intermediate time step between the steps n and $n+1$. The implicit terms D_i^* and G_i^* are expressed by a 19-point stencil. The system of Eq. (8) is solved for u_i^* by a line relaxation.

The velocity at the next time step is obtained by correcting the intermediate velocity $\overline{u_i}^*$ to enforce the divergence free condition,

$$\overline{u_i}^{n+1} = \overline{u_i}^* - \frac{\partial \overline{\phi}^{n+1}}{\partial x_i}, \tag{9}$$

where ϕ is a scalar variable obtained by solving a Poisson equation,

$$\nabla^2 \overline{\phi}^{n+1} = \frac{\partial \overline{u_i}^*}{\partial x_i}. \tag{10}$$

Finally, the pressure field is obtained by solving the Poisson equation, which is derived by taking the divergence of the momentum equation,

$$\nabla^2 \overline{p}^{n+1} = \frac{\partial}{\partial x_i}\left[-\frac{\partial \overline{u_i}^{n+1}\overline{u_j}^{n+1}}{\partial x_j} + \frac{\partial}{\partial x_j}\left\{ (\nu+\nu_T)\left(\frac{\partial \overline{u_i}^{n+1}}{\partial x_j} + \frac{\partial \overline{u_j}^{n+1}}{\partial x_i} \right) \right\} \right]. \tag{11}$$

The Poisson equations are solved by a multigrid method employing an incomplete line LU factorization (ILLU) as the smoother on each level.

3.2 Dynamic Free Surface Condition. When the surface tension is neglected, the dynamic condition of the free surface can be written as

$$(\nu+\nu_T)\left(\frac{\partial \overline{u_i}}{\partial x_j} + \frac{\partial \overline{u_j}}{\partial x_i} \right) n_j - \tilde{p} n_i = 0, \tag{12}$$

where n_i is the unit normal vector of the free surface. The unknown velocity components at the free surface are solved for from the condition Eq. (12), and the results are then used in solving the momentum equation and the kinematic condition of the free surface. Discretizing Eq. (12) using a second-order one sided differencing scheme at the free surface yields a set of three equations. Since there are four unknowns including the pressure $\tilde{p}$, this equation system is closed by coupling with the continuity equation discretized at the free surface. The obtained value of $\tilde{p}$ is used as a Dirichlet boundary condition in solving the Poisson equation for the pressure.

3.3 Other Boundary Conditions. The computational domain is discretized using an O-H-type mesh. The boundary of the computational domain consists of the free and body surfaces, the bottom, and the outer boundary. The outer boundary is divided into in- and outflows at $\theta=120$ and $\theta=240$ deg, in which θ is the tangential angle starting from the upstream direction. The stress free condition is applied at the free surface as described in the previous section, while a symmetry condition is applied at the bottom boundary. On the body surface, the no-slip condition is imposed and surface elevation is linearly extrapolated from the two points nearest to the body surface. Since the grid spacing in the direction normal to the body surface is very small in order to resolve the boundary layer, the numerical results are insensitive to the treatment of the surface elevation at the body boundary.

At the inflow boundary, the velocity components are fixed at the free-stream value, while a homogeneous Neumann condition

Downloaded 03 Jun 2010 to 171.66.16.150. Redistribution subject to ASME license or copyright; see http://www.asme.org/terms/Terms_Use.cfm

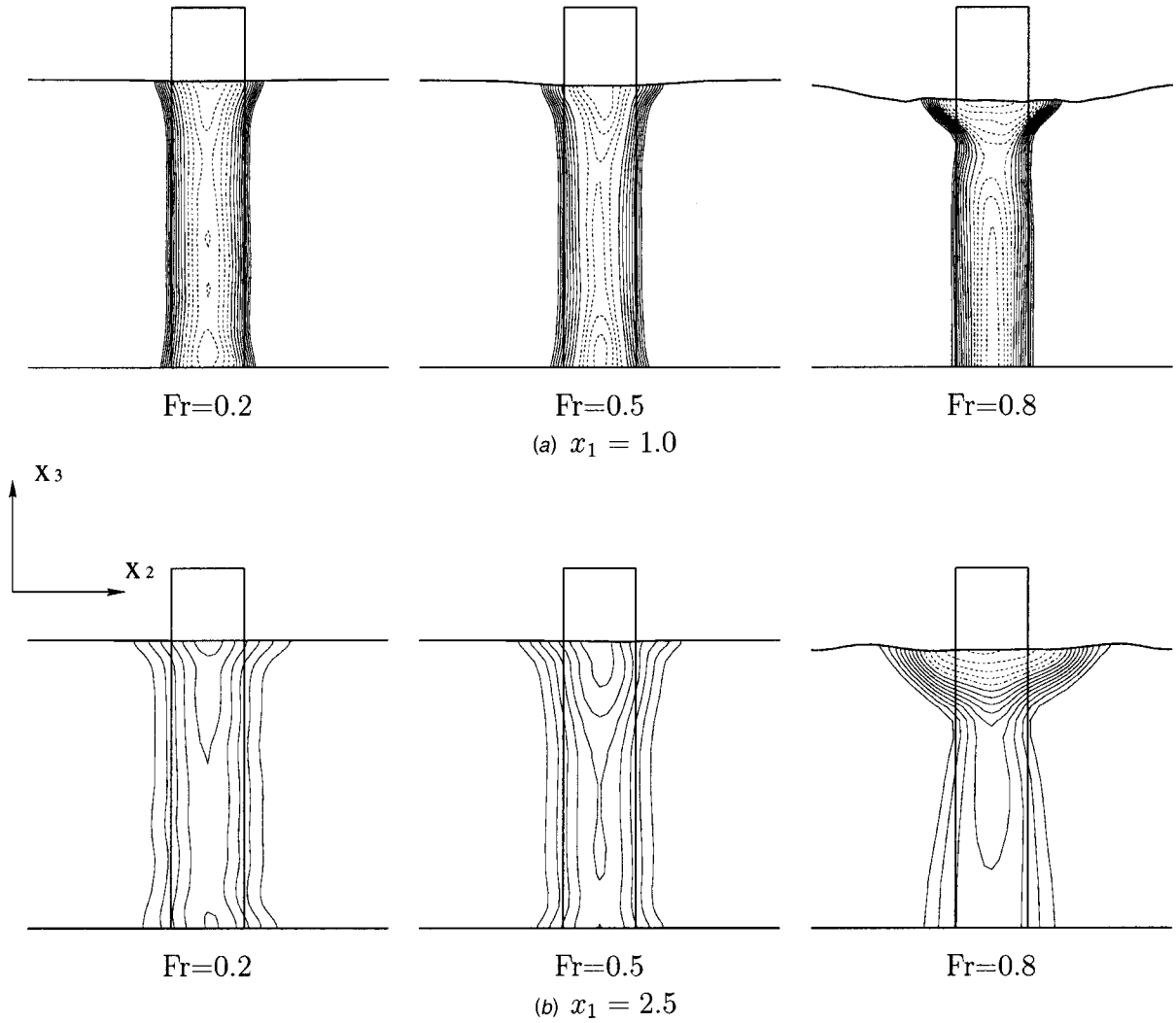

Fig. 8 Contours for the time-averaged streamwise velocity component at Fr=0.8: (*a*) x_1=1.0, (*b*) x_1=2.5. The contour interval is 0.1. Dotted lines denote negative values.

is applied to pressure. At the outflow, the velocity components are extrapolated and pressure is kept at zero. The vortices reaching the outflow boundary undergo deformations due to this rather crude outflow boundary condition. However, the effect is limited within the region very close to the outer boundary due to the numerical dissipation resulting from the large grid spacing in this region. The boundary condition for ϕ is a homogeneous Neumann condition at body and in-flow boundaries, and a homogeneous Dirichlet condition at the free surface and outflow boundaries.

An artificial damping function is applied to the surface elevation near the outer boundary as described in [17]. The surface elevation $\overline{h}$ and the vertical component of the velocity $\overline{u}_3$ are relaxed towards zero by a procedure of the form

$$\overline{h}=(1-\alpha)\overline{h}, \quad \overline{u}_3=(1-\alpha)\overline{u}_3. \tag{13}$$

α denotes a relaxation parameter, which is zero at the entrance of the damping region and one at the outer boundary. The variation of α in the damping region is prescribed as

$$\alpha(x)=\left(\frac{x-x_{start}}{x_{end}-x_{start}}\right)^3, \tag{14}$$

in which the local coordinate x is taken in the direction normal to the outer boundary, and x_{start} and x_{end} are the locations of the starting and ending points of the damping region. The width of the damping region is set to four times the diameter of the cylinder. Throughout the LES computations no significant reflection waves at the outer boundary was observed.

4 Numerical Simulation

4.1 Condition of Computation. We carried out a LES computation of the steady flow past a free surface piercing circular cylinder. Figure 1 shows the definition of the Cartesian coordinate system. The origin is the center of the cylinder at the still water level, and the x_1, x_2, and x_3 axes are taken in the longitudinal, the transverse, and the vertical direction, respectively.

Hereafter, all the quantities are nondimensionalized with respect to the diameter of the cylinder D, and the uniform velocity U. Since the surface tension is neglected, there are two nondimensional parameters, the Froude number and the Reynolds number, defined as

$$\mathrm{Fr}=\frac{U}{\sqrt{gD}} \tag{15}$$

and

$$\mathrm{Re}=\frac{UD}{\nu}, \tag{16}$$

Downloaded 03 Jun 2010 to 171.66.16.150. Redistribution subject to ASME license or copyright; see http://www.asme.org/terms/Terms_Use.cfm

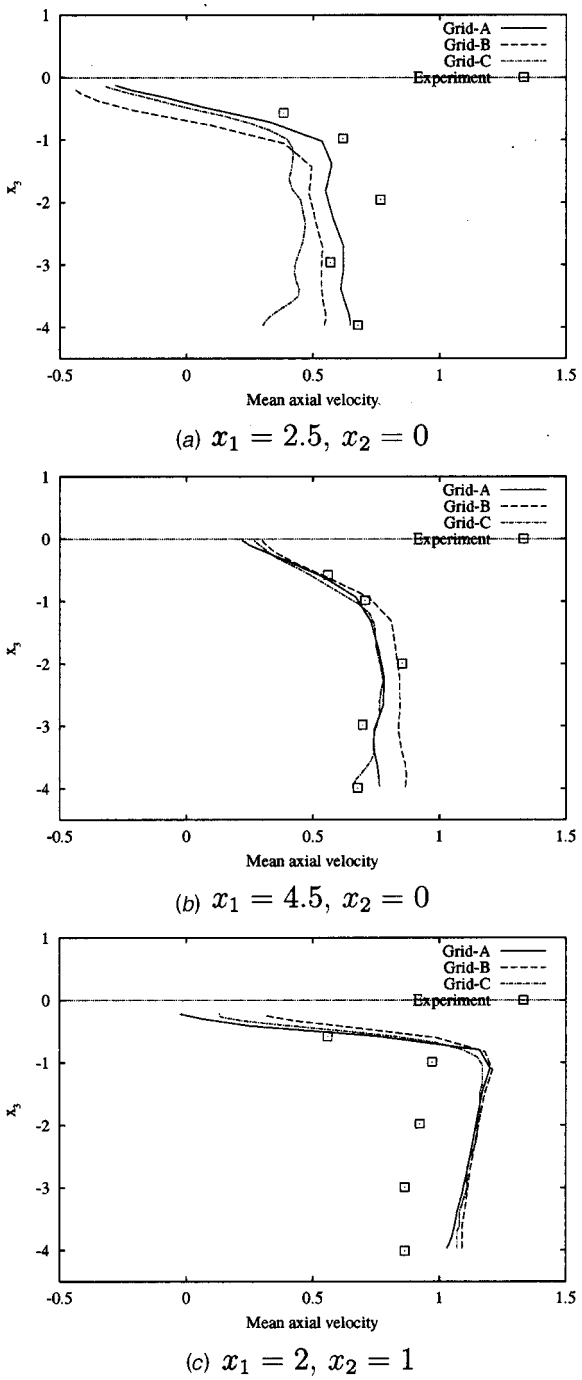

Fig. 9 The vertical profiles of the computed and measured mean streamwise velocity at Fr=0.8: (*a*) $x_1=2.5$, $x_2=0$, (*b*) $x_1=4.5$, $x_2=0$, (*c*) $x_1=2$, $x_2=1$

respectively.

In order to investigate the influence of the Froude number on the flow, simulations were carried out for three Froude numbers Fr=0.2, 0.5 and 0.8, while the Reynolds number was set to 2.7×10^4 in all cases. The case at Fr=0.8 and Re=2.7×10^4 was also investigated experimentally by Inoue et al. [2].

The influence of the grid resolution is investigated by performing computations for Fr=0.8 using three different grid resolutions. The coarse grid, referred to as Grid-A, has $81\times49\times17$ points in the tangential, radial and vertical directions, respectively, while the medium grid (Grid-B) and the fine grid (Grid-C) have $129\times65\times17$ and $161\times99\times33$ points, respectively. Figure 2 shows the medium grid, Grid-B. The results from the computations using Grid-B are most extensively shown, while the results obtained using Grid-A and -C are used for investigating the influence of the grid resolution. The numerical results presented hereafter are from the computations using Grid-B unless otherwise mentioned.

The depth of the domain H is set to 4. A deep draft is assumed in the present case, and the depth of four diameters was confirmed to be sufficient. The distance from the front and side outer boundaries to the center of the cylinder is 10, while that from the rear outer boundary is set to 15 following the studies by Breuer [9] and Kravchenko and Moin [10].

The flow initially at rest is gradually accelerated from $t=0$ to 10. A statistically steady state is achieved at about $t=50$, which corresponds to about ten vortex-shedding periods. The computations are continued until $t=200$ with the time increment being 0.005; the results from the latter 100 non-dimensional time is used for calculating the statistics.

4.2 Surface Waves. Contours of the computed and measured time-averaged surface elevation at Fr=0.8 are shown in Fig. 3. The shape of the time-averaged free surface is characterized by the hump on the upstream side of the body, an almost constant slope leading to the large depression on the downstream side, and the diverging Kelvin wave system. These features are well reproduced in the LES computation. The root mean square (r.m.s.) of the computed and measured fluctuations of the free surface are symmetrically compared in Fig. 4. The fluctuation of the surface starts near the end of the slope from the hump to the hollow. The peak value is located near the edge of the flat hollow part on the downstream side of the body. The results of the LES computation agree well with the measurements.

The influence of the grid resolution on the computation of surface waves is examined in Fig. 5(*a*) and (*b*), which compare the profiles of the time-averaged elevation and r.m.s. fluctuation of the surface at Fr=0.8 at two transverse sections on the downstream side of the body. Although some discrepancies are observed in the results from Grid-A, the difference between the results from Grid-B and Grid-C is small.

The dependencies of the mean elevation and fluctuation of the surface on the Froude number are examined Figs. 6 and 7. Naturally, both elevation and fluctuation decrease as the Froude number Fr is decreased. The deformation of the surface at Fr=0.2 is an order of magnitude smaller than that at Fr=0.8. The effect of this difference on the viscous flow beneath the surface is examined hereafter.

4.3 Wave-Wake Interactions. Figure 8 shows distribution of the wake by contours of the computed time-averaged streamwise velocity at two transverse sections. At low Froude numbers Fr=0.2 and 0.5 the wake distribution is almost symmetrical with respect to the horizontal mid-depth plane, indicating that the free surface acts like a rigid free-slip boundary. On the other hand, the influence of the surface deformation in the wake is clearly observed at Fr=0.8. At $x_1=1.0$ shown in Fig. 8(*a*), the lateral width of the wake is nearly constant from the bottom boundary to the level about 0.6 diameter below the mean water level; beyond that level the width increases rapidly. The section at $x_1=1.0$ is located within the recirculation region; the mean velocity near the center line is negative from the bottom to the free surface. Observe that the lateral spread of the wake is not uniform in the vertical direction. Figure 8(*b*) shows that the width of the wake is narrowest at the level about one diameter below the mean water level, and that it increases in both directions toward the free surface and the bottom. Negative streamwise velocity is seen only near the free surface.

Unfortunately, only a few velocity measurements were provided, but the comparisons of the time-averaged streamwise velocity at Fr=0.8 shown in Fig. 9 indicate fair agreement with the computation. The decrease in the streamwise velocity near the

Downloaded 03 Jun 2010 to 171.66.16.150. Redistribution subject to ASME license or copyright; see http://www.asme.org/terms/Terms_Use.cfm

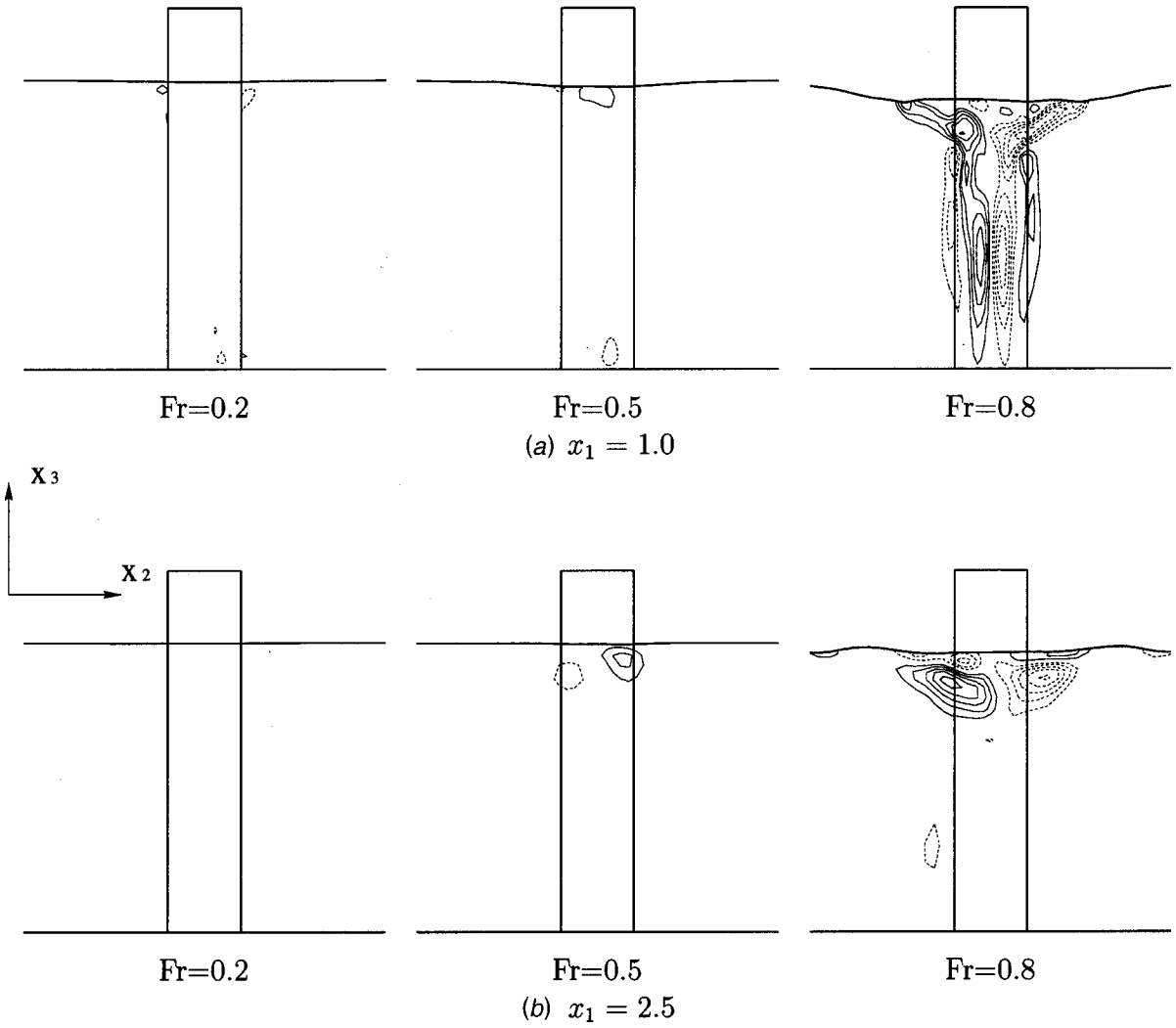

Fig. 10 Time-averaged streamwise vorticity at Fr=0.8: (*a*) $x_1=1.0$, (*b*) $x_1=2.5$. Solid and dotted lines denote clockwise and counterclockwise rotation, respectively. Contour interval is 0.5.

free surface is clearly seen both in the computation and the measurement. It is also noted that the differences among the computational results using different grid resolutions are also small.

The contour plots of the time-averaged streamwise vorticity shown in Fig. 10 for the same sections as Fig. 8 indicate that there are a pair of counter rotating streamwise vortices under the free surface at Fr=0.8. There are also weaker secondary vortices between the primary vortex pair and the free surface. The locations of the strong streamwise vortices and the constriction of the wake shown in Fig. 8 correlate well, indicating that the secondary flow characterized by streamwise vortices contributes to the distortion of the wake. On the other hand, three-dimensionality of the mean flow is small at low Froude numbers Fr=0.2 and 0.5.

Figures 11(*a*) and (*b*) show the contours of the time-averaged transverse component of the vorticity $\overline{\omega}_2$ at Fr=0.8 for two sections of $x_2=1.0$ and $x_2=2.0$, respectively. The large magnitude of the negative vorticity seen at $x_2=1.0$ clearly exhibits the presence of a recirculation zone starting from the point where the surface slope changes suddenly. The surface fluctuation is probably related to instabilities of shear layers under a free surface (see for example [19,20]). On the other hand, the weak vorticity seen under the crest and the trough is due to the curvature of the free surface [21].

Figure 12 shows an instantaneous field of computed vertical vorticity component $\overline{\omega}_3$ at Fr=0.8 at different depths. At $x_3=-4.0$, the flow pattern is very similar to that for an infinitely long cylinder, where periodic vortex-shedding is apparent. As the free surface is approached, the large scale interaction between two separated shear layers becomes less prominent, and more random smaller scale vortices come to the fore. The variation of the flow pattern in the vertical direction is due to the change in the relation between the two separated shear layers. At a deep level, the shear layers stretch straight in the downstream direction, while near the free surface due to the deformation of the surface the shear layers are inclined outward prohibiting the formation of the large scale vortex shedding.

At the Reynolds number of $Re=2.7\times10^4$, the boundary layer along the cylinder surface is laminar, and the transition to turbulence occurs in the wake. However, this feature is not well reproduced in the present LES computations, since the SGS stresses do not vanish in laminar region. This results in an overestimation of the growth of the boundary layer and an erroneous prediction of the separation point. Use of the dynamic SGS model [22] or an ad hoc damping function on the Smagorinsky coefficient in the laminar region may improve the quality of the solution.

4.4 Velocity Fluctuation. The vertical distribution of the computed r.m.s. velocity fluctuation at Fr=0.8 is shown in Figs. 13(*a*), (*b*), and (*c*) for three locations in the wake. The velocity fluctuation u_i' is defined as

Downloaded 03 Jun 2010 to 171.66.16.150. Redistribution subject to ASME license or copyright; see http://www.asme.org/terms/Terms_Use.cfm

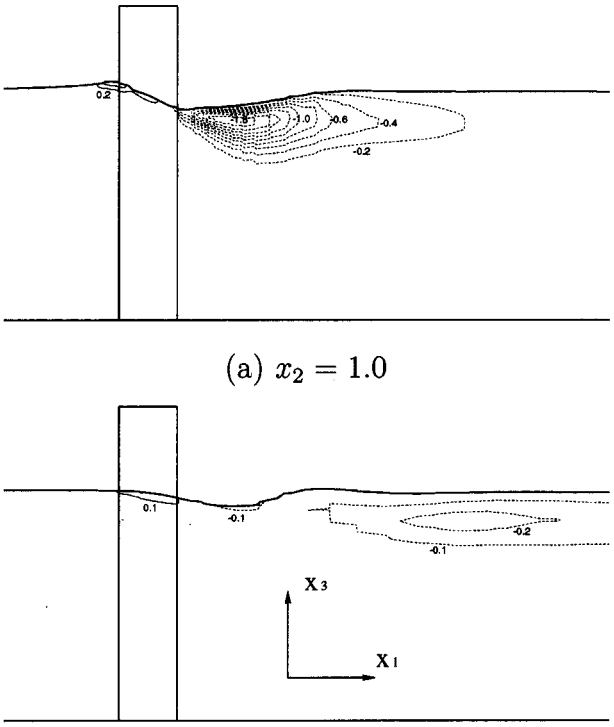

Fig. 11 Contours of the transverse component of the time-averaged vorticity at Fr=0.8: (*a*) $x_2=1.0$, (*b*) $x_2=2.0$.

$$u_i' = \overline{u_i} - \langle \overline{u_i} \rangle, \tag{17}$$

in which the angle brackets denote time-averaging. Both periodic and random components are included, but the subgrid scale fluctuation is assumed to be small and is not included in the statistics. Phase-averaging can separate the periodic and random components. However it was not performed because the periodicity is not perfectly regular and it requires very long simulation time to converge.

On the center symmetry plane ($x_2=0$) shown in Figs. 13(*a*) and (*b*), the transverse component $u_{2\,\mathrm{rms}}'$ decreases near the free surface, while $u_{1\,\mathrm{rms}}'$ and $u_{3\,\mathrm{rms}}'$ exhibit small variation in the vertical direction.

On the other hand, under the trough of the surface wave shown in Fig. 13(*c*), $u_{1\,\mathrm{rms}}'$ and $u_{2\,\mathrm{rms}}'$ first decrease in the region from the bottom to the level about one diameter below the still water level ($x_3=-1.0$), whereas the intensities of all the three components increase sharply near the free surface. The fluctuation of the free surface is also intensive at this point.

The vertical profile of the time-averaged velocity at this point shown in Fig. 9(*c*) also indicates the existence of a strong shear layer beneath the free surface. Figure 14 shows the time history of the transverse velocity component $\overline{u_2}$ for the same point. At the bottom boundary ($x_3=-4.0$) the periodic component of the fluctuation is dominant while, at the level $x_3=-1.0$, the intensity of the fluctuation becomes small and more random fluctuations of higher frequencies stand out. The intensity of the random fluctuation increases at the level $x_3=-0.6$ near the mean free surface level. The same tendency was also confirmed qualitatively in the experiment by Inoue et al. [2]. An analysis of the time history of the measured velocity showed the decay of the periodic component and the increase in the random component toward the free surface. The results of the present LES suggests that the fluctuation due to the shear flow instability near a free surface are locally predominant while the periodic vortex shedding is attenuated.

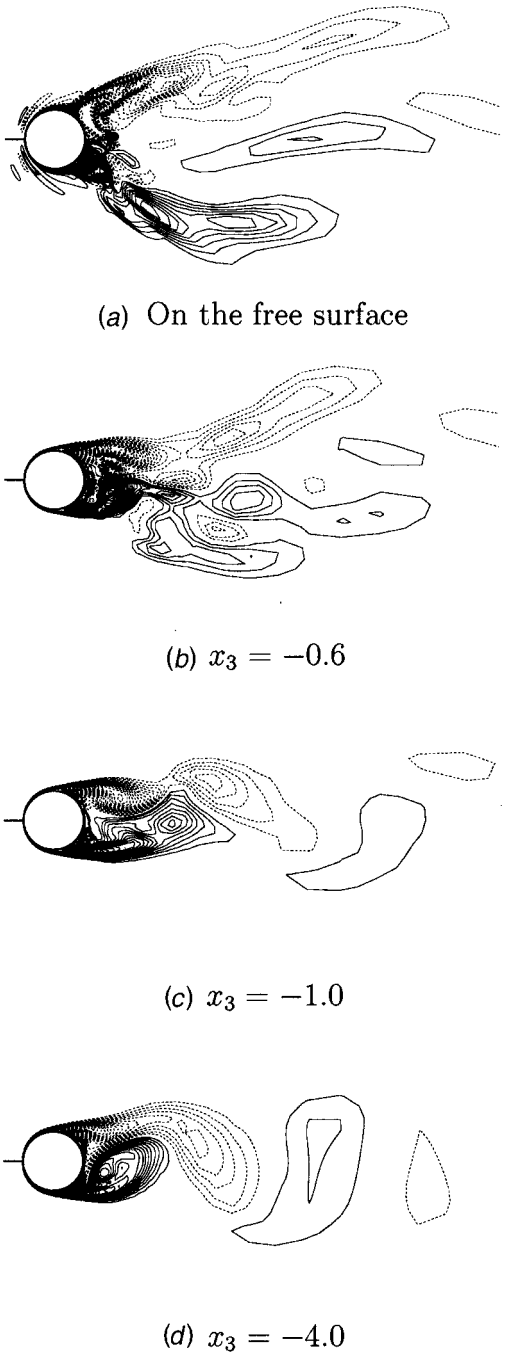

Fig. 12 Comparison of the instantaneous vertical vorticity component at Fr=0.8 on horizontal planes: (*a*) on the free surface, (*b*) $x_3=-0.6$, (*c*) $x_3=-1.0$, (*d*) $x_3=-4.0$. Contour interval is 0.4

4.5 Hydrodynamic Forces. The drag coefficient C_D and the lift coefficient C_L are defined as

$$C_D = \frac{F_1}{1/2\rho U^2 DH} \tag{18}$$

and

Downloaded 03 Jun 2010 to 171.66.16.150. Redistribution subject to ASME license or copyright; see http://www.asme.org/terms/Terms_Use.cfm

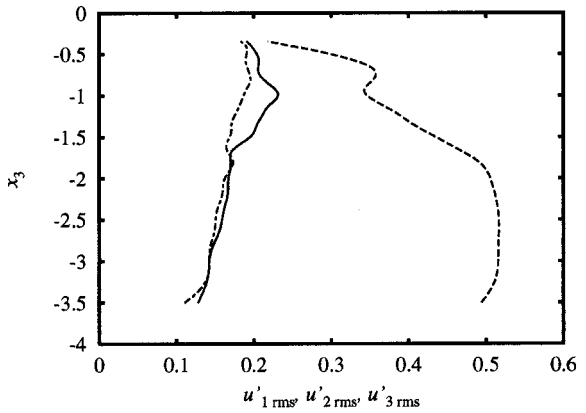

(a) $x_1 = 2.5,\ x_2 = 0$

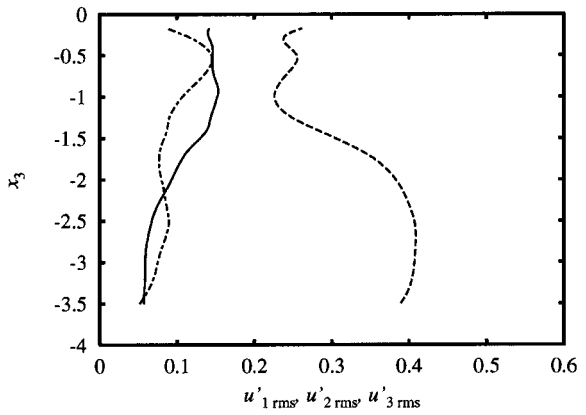

(b) $x_1 = 4.5,\ x_2 = 0$

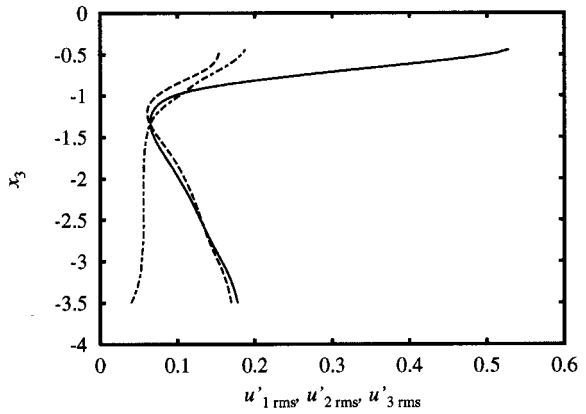

(c) $x_1 = 2,\ x_2 = 1$

Fig. 13 Profiles of the computed r.m.s. velocity fluctuations, $u'_{1\mathrm{rms}}$ (solid), $u'_{2\mathrm{rms}}$ (dashed), and $u'_{3\mathrm{rms}}$ (dot-dashed) at Fr=0.8: (*a*) $x_1=2.5$, $x_2=0$, (*b*) $x_1=4.5$, $x_2=0$, (*c*) $x_1=2$, $x_2=1$

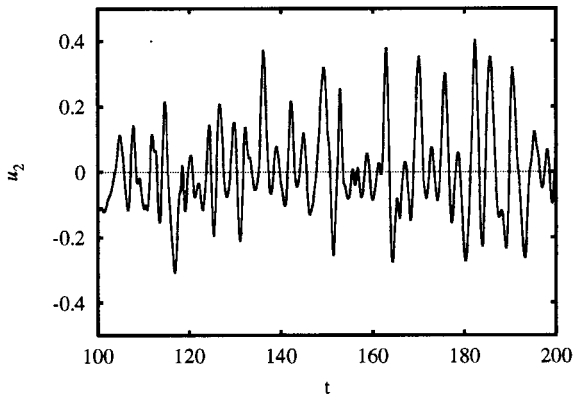

(a) $x_3 = -0.6$

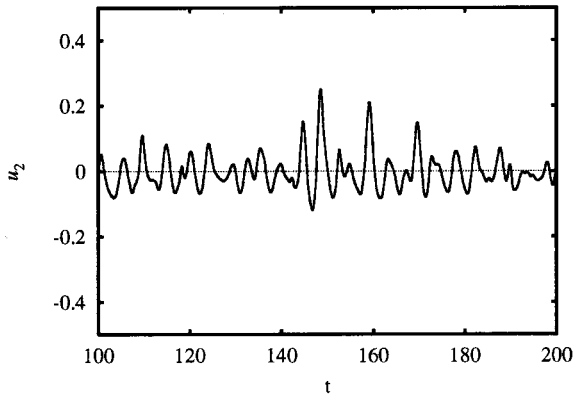

(b) $x_3 = -1.0$

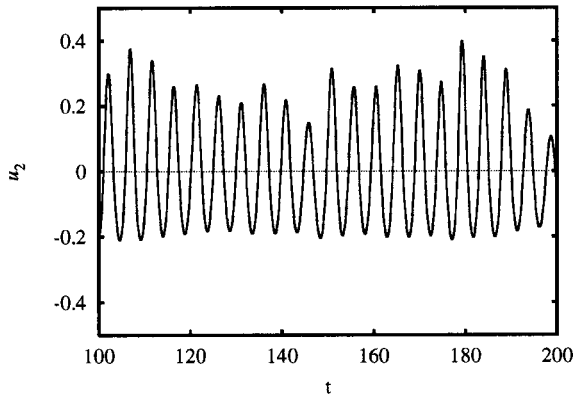

(c) $x_3 = -4.0$

Fig. 14 Vertical variation of the velocity signals in the wake ($x_1=2, x_2=1$) at Fr=0.8

$$C_L = \frac{F_2}{1/2\rho U^2 DH}, \tag{19}$$

in which F_1 and F_2 are the forces in the x_1 and x_2 directions, respectively. Table 1 shows the mean value of the drag coefficient $C_{D\ \mathrm{mean}}$ and the r.m.s. of the lift coefficient $C_{L\ \mathrm{rms}}$ from the LES computations. The forces are calculated by integrating the normal and tangential stresses on the body surface.

It is shown that the dependencies of the computed hydrodynamic forces for a case at Fr=0.8 on the grid resolution is small. The experimental value of $C_{D\ \mathrm{mean}}$ for an infinite cylinder is about 1.2 [23,24]. The influence of the aspect ratio on vortex shedding from a circular cylinder has been investigated by Szepessy and Bearman [24], and their results indicate that the influence of the end condition on $C_{D\ \mathrm{mean}}$ at $H/D=4$ and $\mathrm{Re}=2.7\times10^4$ is small. The values of $C_{D\ \mathrm{mean}}$ from the LES computations are smaller than the experimental value probably due to the deformation of free surface. As the Froude number is decreased, the influence of the deformation of the free surface decreases, and the value of $C_{D\ \mathrm{mean}}$ approaches the experimental value for an infinite cylinder. The computed values of $C_{D\ \mathrm{mean}}$ for a surface-piercing cylinder include the wave making resistance. However, from the observed wave pattern, the contribution of the wave making resistance on $C_{D\ \mathrm{mean}}$ is estimated to be less than 1% [25] at Fr=0.8 and $H/D=4$.

The experimental value of $C_{L\ \mathrm{rms}}$ at $H/D=4$ and Re=2.7

Downloaded 03 Jun 2010 to 171.66.16.150. Redistribution subject to ASME license or copyright; see http://www.asme.org/terms/Terms_Use.cfm

Table 1 Hydrodynamic forces on a circular cylinder vertically piercing a free surface at Re=2.7×10^4

Fr	Grid	$C_{D\ \mathrm{mean}}$	$C_{L\ \mathrm{rms}}$
0.2	Grid-B	1.12	0.32
0.5	Grid-B	1.05	0.30
0.8	Grid-A	1.00	0.28
0.8	Grid-B	0.99	0.26
0.8	Grid-C	0.97	0.24

$\times10^4$ is about 0.45 [24], while the computed values of $C_{L\ \mathrm{rms}}$ range between 0.24 and 0.32. The difference between the experiment and the LES computation becomes smaller, as the Froude number in the computation is decreased. It is also noted that the dependency of $C_{L\ \mathrm{rms}}$ on the Froude number is larger than that of $C_{D\ \mathrm{mean}}$.

Figure 15 shows the distributions of sectional $C_{D\ \mathrm{mean}}$ and $C_{L\ \mathrm{rms}}$ along the cylinder span. The values of $C_{D\ \mathrm{mean}}$ increase toward the bottom and the free surface boundaries probably due to the restriction of the three-dimensionality [24], while the effect of the free surface is not apparent. On the other hand, the variation of the sectional $C_{L\ \mathrm{rms}}$ at Fr=0.8 is more obvious. The minimum value observed at $x_3=-1.5$ is less than a half of its maximum value near the bottom boundary, and the value increases towards the free surface and bottom boundaries. This trend is consistent with the trend of the velocity fluctuations shown in Fig. 14.

5 Summary and Conclusions

Turbulent flow around a surface piercing circular cylinder at Re=2.7×10^4 has been investigated using LES. The objective has been to gain deeper insight into the wave-wake interaction about a surface piercing bluff body while validating the computational method through comparisons with experimental data. The computations have been performed for three Froude numbers Fr=0.2, 0.5 and 0.8 in order to examine the influence of the Froude number.

The computational results are generally in good agreement with the available experimental data with respect to the mean velocity profiles and the surface elevation. At Fr=0.2 and 0.5 surface deformations are small, and the mean flow near the surface is similar to that near the bottom symmetry boundary. On the other hand, the generated surface waves at Fr=0.8 is very large and strongly unsteady. The computational results show that the distribution of the surface fluctuation and the structure of the vertical structure beneath correlate closely with the mean configuration of the surface. Computational results show the presence of a recirculation zone starting at the point where the surface slope changes discontinuously. Above this zone the surface elevation fluctuates intensively. Very good agreement with experimental results has been obtained in the intensity of the surface fluctuation.

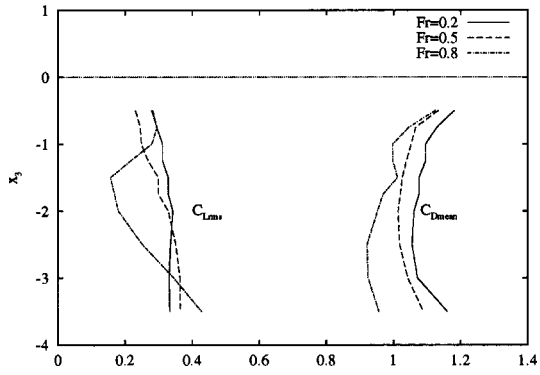

Fig. 15 Sectional drag and lift coefficients of a surface-piercing circular cylinder at Re=2.7×10^4 and Fr=0.8

It has been also shown that the periodic vortex shedding is attenuated near the free surface in the high Froude number case Fr=0.8. This is clearly shown by the plots of the instantaneous vertical vorticity component, the time history of the velocity, and the profiles of the intensity of the velocity fluctuation. This feature is consistent with the experimental observations [2]. The region in which the periodic vortex shedding is hampered extends to about one diameter from the mean water level. It is qualitatively shown that the separated shear layers are inclined outward near the free surface due to the generation of the surface waves. This change in the relation between two shear layers is suggested to be responsible for the attenuation of the periodic vortex shedding.

Acknowledgment

This work was partly financed by the Danish National Research Foundation and partly by the Danish Technical Research Council (STVF grant no. 9801635). Their financial support is greatly appreciated.

References

[1] Deardorff, J. W., 1970, ''A numerical study of three-dimensional turbulent channel flow at large Reynolds numbers,'' J. Fluid Mech., **41**, pp. 453–480.
[2] Inoue, M., Baba, N., and Himeno, Y., 1993, ''Experimental and numerical study of viscous flow field around an advancing vertical circular cylinder piercing a free-surface,'' J. Kansai Soc. Naval Archit. of Japan, **220**, pp. 57–64.
[3] Triantafyllou, G. S., and Dimas, A. A., 1989, ''Interaction of two-dimensional separated flows with a free surface at low Froude numbers,'' Phys. Fluids A, **1**, No. 11, pp. 1813–1821.
[4] Sheridan, J., Lin, J.-C., and Rockwell, D., 1997, ''Flow past a cylinder close to a free surface,'' J. Fluid Mech., **330**, pp. 1–30.
[5] Chiba, S., and Kuwahara, K., 1989, ''Numerical analysis for free surface flow around a vertical circular cylinder,'' *Proceedings of Third Symposium on Computational Fluid Dynamics*, Tokyo, Japan, pp. 295–299.
[6] Williamson, C. H. K., 1996, ''Vortex dynamics in the cylinder wake,'' Annu. Rev. Fluid Mech., **28**, pp. 477–539.
[7] Beaudan, P., and Moin, P., 1994, ''Numerical experiments on the flow past a circular cylinder at sub-critical Reynolds number,'' Technical Report TF-62, Department of Mechanical Engineering, Stanford University.
[8] Mittal, R., and Moin, P., 1997, ''Suitability of upwind-biased finite-difference schemes for large-eddy simulation of turbulent flows,'' AIAA J., **35**, pp. 1415–1417.
[9] Breuer., M., 1997, ''Numerical and modeling influences on large eddy simulations for the flow past a circular cylinder,'' *Proceedings of 11th Symposium on Turbulent Shear Flows*, 8–10 Sept. Grenoble, France, pp. 26–27.
[10] Kravchenko, A. G., and Moin, P., 2000, ''Numerical studies of flow over a circular cylinder at Re_D=3900,'' Phys. Fluids, **12**, pp. 403–417.
[11] Van Der Zanden, J., Simons, H., and Nieuwstadt, F. T. M., 1992, ''Application of large-eddy simulation to open-channel flow,'' Eur. J. Mech. B/Fluids, **11**, No. 31, pp. 337–347.
[12] Thomas, T. G., and Williams, J. J. R., 1995, ''Turbulent simulation of open channel flow at low Reynolds number,'' Int. J. Heat Mass Transf., **38**, No. 2, pp. 259–266.
[13] Salvetti, M., Zang, Y., Street, R., and Banerjee, S., 1996, ''Large-eddy simulation of decaying free-surface turbulence with dynamic mixed subgrid-scale models,'' *Proceedings of Twenty-First Symposium on Naval Hydrodynamics*, Trondheim, Norway, National Academy Press, pp. 1018–1032.
[14] Smagorinsky, J., 1963, ''General circulation experiments with the primitive equations I. The basic experiment,'' Mon. Weather Rev., **91**, pp. 99–164.
[15] Piomelli, U., Moin, P., and Ferziger, J. H., 1988, ''Model consistency in large eddy simulation of turbulent channel flows,'' Phys. Fluids A, **31**, pp. 1884–1891.
[16] Dommermuth, D., and Novikov, E. A., ''Direct-numerical and large-eddy simulation of turbulent free surface flows,'' *Proceedings of the Sixth International Conference on Numerical Ship Hydrodynamics*, Iowa City.
[17] Mayer, S., Garapon, A., and Sørensen, L., 1998, ''A fractional step method for unsteady free surface flow with applications to non-linear wave dynamics,'' Int. J. Numer. Methods Fluids, **28**, pp. 293–315.
[18] Kawamura, T., 1998, ''*Numerical simulation of 3D turbulent free-surface flows*,'' PhD thesis, Department of Naval Architecture and Ocean Engineering, School of Engineering, University of Tokyo.
[19] Dimas, A. A., and Triantafyllou, G. S., 1994, ''Nonlinear interaction of shear flow with a free surface,'' J. Fluid Mech., **260**, pp. 211–246.
[20] Longuet-Higgins, M. S., 1998, ''Instabilities of a horizontal shear flow with a free surface,'' J. Fluid Mech., **364**, pp. 147–162.

Downloaded 03 Jun 2010 to 171.66.16.150. Redistribution subject to ASME license or copyright; see http://www.asme.org/terms/Terms_Use.cfm

[21] Batchelor, G. K., 1967, *Introduction to Fluid Dynamics*, Cambridge University Press.
[22] Germano, M., Piomelli, U., Moin, P., and Cabot, W. H., 1991, ''A dynamic subgrid-scale eddy viscosity model,'' Phys. Fluids A, **3**, pp. 1760–1765.
[23] Wieselsberger, C., 1921, ''Neuere Festellungen über die Gesetze des Flüssigkeits-und Luftwiderstands,'' Phys. Z., **22**, pp. 321–328.
[24] Szepessy, S., and Bearman, P. W., 1992, ''Aspect ratio and end plate effects on vortex shedding from a circular cylinder,'' J. Fluid Mech., **234**, pp. 191–217.
[25] Baba, E., 1969, ''Study on separation of ship resistance components,'' J. Soc. Naval Archit. Japan, **125**, pp. 9–22.

Downloaded 03 Jun 2010 to 171.66.16.150. Redistribution subject to ASME license or copyright; see http://www.asme.org/terms/Terms_Use.cfm

A Finite-Mode PDF Model for Turbulent Reacting Flows

Kuochen Tsai

Paul A. Gillis

Subrata Sen

The Dow Chemical Company,
2301 N. Brazosport Blvd., B-1225,
Freeport, TX 77541
e-mail: ktsai@dow.com

Rodney O. Fox

Chemical Engineering Department,
Iowa State University,
Ames, Iowa 50011-2230
e-mail: rofox@iastate.edu

The recently proposed multi-environment model, R. O. Fox, 1998, "On the Relationship between Lagrangian Micromixing Models and Computational Fluid Dynamics," Chem. Eng. Proc., Vol. 37, pp. 521–535. J. Villermaux and J. C. Devillon, 1994, "A Generalized Mixing Model for Initial Contacting of Reactive Fluids," Chem. Eng. Sci., Vol. 49, p. 5127, provides a new category of modeling techniques that can be employed to resolve the turbulence-chemistry interactions found in reactive flows. By solving the Eulerian transport equations for volume fractions and chemical species simultaneously, the local concentrations of chemical species in each environment can be obtained. Assuming micromixing occurs only in phase space, the well-known IEM (interaction by exchange with the mean) model can be applied to close the micromixing term. This simplification allows the model to use micromixing timescales obtained from more sophisticated models and can be applied to any number of environments. Although the PDF shape doesn't change under this assumption, the interaction between turbulence and chemistry can be resolved up to the second moments without any ad-hoc assumptions for the mean reaction rates. Furthermore, the PDF shape is found to have minimal effect on mean reaction rates for incompressible turbulent reacting flows. In this formulation, a spurious dissipation term arises in the transport equation of the scalar variances due to the use of Eulerian transport equations. A procedure is proposed to eliminate this spurious term. The model is applied to simulate the experiment of S. Komori, et al., 1993, "Measurements of Mass Flux in a Turbulent Liquid Flow With a Chemical Reaction," AIChE J., Vol. 39, pp. 1611–1620, for a reactive mixing layer and the experiment of K. Li and H. Toor, 1986, "Turbulent Reactive Mixing With a Series Parallel reaction: Effect of Mixing on Yield," AIChE J., Vol. 32, pp. 1312–1320, with a two-step parallel/consecutive reaction. The results are found to be in good agreement with the experimental data of Komori et al. and the PDF simulation of K. Tsai and R. Fox, 1994, "PDF Simulation of a Turbulent Series-Parallel Reaction in an Axisymmetric Reactor," Chem. Eng. Sci., Vol. 49, pp. 5141–5158, for the experiment of Li and Toor. The resulting model is implemented in the commercial CFD code, FLUENT,[1] and can be applied with any number of species and reactions.
[DOI: 10.1115/1.1431546]

Introduction

Micromixing and chemical reactions in turbulence have long been a challenging topic in both academia and industry due to its importance in many industrial processes and combustion. Recent work shows that the problem can be divided into two parts (e.g., Tsai and O'Brien, [1]; Tsai et al. [2]): the shape of scalar PDF and the micromixing timescale that governs the rate of change of the scalar PDF.

Monte-Carlo PDF methods (Pope [3]; Fox [4]) are considered the state-of-the-art technique for such problems. Unfortunately, the computational cost severely hinders their application for practical problems (e.g., Tsai and Fox [5]). The advantage of a full PDF simulation is that the interaction between micromixing and reaction terms is resolved exactly. While neglecting the change in micromixing timescales due to chemical reactions, the PDF methods are able to provide more accurate predictions than conventional moment-method based closures. The widely used model of Magnussen and Hjertager [6] assumes the rate limiting timescale to be the eddy-breakup time and thus provides a measure for mixing-controlled reactions. However, such measure strongly depends on the local structure of the scalar field. Since the concentration fluctuations are not accounted for, empirical parameters are needed for reasonable predictions. The uncertainty of determining the empirical parameters exacerbates when applied to high Schmidt number flows. It is very difficult (if not impossible) to have universal parameters that account for the structure differences in concentration fluctuations due to Schmidt number effects.

Conceptually, the Magnussen model can be considered as using a single delta function in state space to represent the bulk reaction rates. Since only mean equations are solved, rate-limiting parameters must be introduced to represent the effect of turbulence. However, it is possible to use multiple delta functions in state space to represent both the concentration means and fluctuations in a deterministic manner (Fox [7]). The micromixing timescale can be embedded using the dissipation rate of scalar variance, thus, eliminating the need for empirical parameters. Furthermore, it has been found that, for incompressible flows, the effects of PDF shape may be of little consequence to the prediction of mean reaction rates (Tsai et al. [2]). This evidence further confirms the adequacy of using a finite number of delta functions as a representation of scalar PDF. The details are described below.

Scalar Transport Equations. For simplicity, the following discussion is limited to constant-density flows (i.e., density fluctuation not considered). However, the method is general and can be easily extended to flows with variable density.

Using the concept of probability (described below) in constant-density flows, the equations that govern the probability flow from inlet stream (environment) i can be written as

$$\rho \frac{DP_i}{Dt} = 0, \tag{1}$$

[1]FLUENT is a trade designation of Fluent Incorporated

Contributed by the Fluids Engineering Division for publication in the JOURNAL OF FLUIDS ENGINEERING. Manuscript received by the Fluids Engineering Division August 30, 1999; revised manuscript received April 25, 2001. Associate Editors: C. Merkle, J. Katz.

 Copyright © 2002 by ASME

Downloaded 03 Jun 2010 to 171.66.16.150. Redistribution subject to ASME license or copyright; see http://www.asme.org/terms/Terms_Use.cfm

where capital D on the left denotes the material derivative and ρ is the density. This equation can be also used to describe the mass fraction transport in reactive flows without molecular diffusion and is the basis for the FMPDF model. In comparison, the transport of composition joint PDF equation without reaction and micromixing can be described below (Pope [3], Section 7)

$$\frac{\partial}{\partial t}[\rho f_\phi]+\frac{\partial}{\partial x_i}[\rho\langle u_i|\phi=\psi\rangle f_\phi]=0, \tag{2}$$

where f_ϕ is the composition joint PDF and $\langle u_i|\phi=\psi\rangle$ denotes the mean velocity conditioned on composition ϕ. If f_ϕ is assumed as a sum of delta functions from each inlet stream j, then

$$f_\phi=\sum_j G_j\delta(\psi-\psi_j), \tag{3}$$

where G_j is the magnitude of the delta function $\delta(\psi-\psi_j)$. Using the gradient diffusion assumption and Reynolds' averaging the second term in the bracket can be rewritten as

$$\rho\langle u_i|\phi=\psi\rangle f_\phi=\rho\overline{u_i}f_\phi-\Gamma_T\frac{\partial f_\phi}{\partial x_t}, \tag{4}$$

where $\overline{u_i}$ is the ensemble average of u_i, and Γ_T the eddy diffusivity, defined as

$$\Gamma_T=\rho\frac{C_\mu}{\eta_t}\frac{k^2}{\varepsilon}. \tag{5}$$

In Eq. (5), C_μ is a model constant (=0.09), η_t the turbulent Schmidt number (=0.7), k the turbulent kinetic energy, and ε the turbulent dissipation rate. Substituting Eq. (3) in Eq. (2), the following equation is obtained:

$$\rho\frac{\partial}{\partial t}\left(\sum_j G_j\delta(\psi-\psi_j)\right)+\rho\overline{u_i}\frac{\partial}{\partial x_i}\sum_j G_j\delta(\psi-\psi_j)$$
$$=\frac{\partial}{\partial x_i}\Gamma_T\frac{\partial}{\partial x_i}\sum_j G_j\delta(\psi-\psi_j). \tag{6}$$

One possible solution is that each $G_j\delta(\psi-\psi_j)$ satisfies Eq. (6). This leads to

$$\rho\frac{\partial}{\partial t}[G_j\delta(\psi-\psi_j)]+\rho\overline{u_i}\frac{\partial}{\partial x_i}[G_j\delta(\psi-\psi_j)]$$
$$=\frac{\partial}{\partial x_i}\Gamma_T\frac{\partial}{\partial x_i}[G_j(\psi-\psi_j)]. \tag{7}$$

Integrating over phase space ψ, Eq. (7) is reduced to

$$\rho\frac{\partial G_j}{\partial t}+\rho\overline{u_i}\frac{\partial G_j}{\partial x_i}=\frac{\partial}{\partial x_i}\Gamma_T\frac{\partial}{\partial x_i}G_j \tag{8}$$

Equation (8) is identical to Eq. (1) when the gradient assumption is used to model the turbulent flux. It is therefore assumed that the transport of mass fraction can also be interpreted as the probability flow from stream i without micromixing. Equation (6) can be regarded as the transport equation for the discrete representation of $f_\phi(\psi)$, similar to the Monte-Carlo PDF equation without micromixing. Note that G_j in Eq. (8) will be referred as P_j hereafter.

If (7) is multiplied by ψ and then integrated over phase space, the transport equation for the total concentration of species k from inlet stream i

$$S_k^i=P_i\psi_k^i \tag{9}$$

can be written as follows:

$$\rho\frac{\partial S_k^i}{\partial t}+\rho\overline{u_j}\frac{\partial S_k^i}{\partial x_j}=\frac{\partial}{\partial x_j}\Gamma_T\frac{\partial S_k^i}{\partial x_j}+\rho M_k^i(\mathbf{P},\mathbf{S}_k)+\rho R_k(P_i,\mathbf{S}^i) \tag{10}$$

with $M\equiv R\equiv 0$, where M and R represent the source terms due to micromixing and chemical reactions, respectively, and **P** and **S** are the vector form of P and S. The proposed M and R terms are also taken hint from the transport equation of $f_\phi(\psi)$, which reads (Pope [3])

$$\frac{\partial}{\partial t}[\rho f_\phi]+\frac{\partial}{\partial x_j}(\rho\overline{u_j}f_\phi)=\frac{\partial}{\partial\psi}\left[\left\langle\frac{\partial J_j}{\partial x_j}\middle|\psi\right\rangle f_\phi\right]-\frac{\partial}{\partial\psi}[\rho R(\psi)f_\phi], \tag{11}$$

where J is the molecular diffusion flux, $\langle\partial J_j/\partial x_j|\psi\rangle$ the micromixing term conditioned on ψ, and $R(\psi)$ the reaction source term (for simplicity, only a single scalar is considered). Since the terms on the right-hand side only depend on ψ, it is therefore assumed that M and R can be modeled as functions of ψ (i.e., functions of **P** and **S**).

Since Eqs. (8) and (10) are identical with $M\equiv R\equiv 0$, ψ_k^i will remain the same as in inlet stream i. This is similar to the Lagrangian concentration described in the Monte-Carlo PDF method. Thus, by definition, the following relations must be satisfied,

$$\sum_i P_i=1 \tag{12}$$

and

$$\overline{\phi_k}=\sum_i S_k^i. \tag{13}$$

Note that ϕ_k is the physical counterpart of the phase variable ψ and is used hereafter to represent both the phase (Lagrangian) and physical concentration variables. Furthermore, since micromixing does not change scalar concentration means, the micromixing term M must satisfy the following criterion:

$$\sum_i M_k^i=0. \tag{14}$$

Equation (14) provides the first guideline for modeling the micromixing term. Since both the mean and Lagrangian values of ϕ_k can be obtained through Eqs. (8), (9), and (10), M_k^i can be modeled using the IEM (interaction by exchange with the mean) closure (Villermaux and Devillon [8]; Dopazo [9]), which gives

$$M_k^i=-\gamma P_i(\phi_k^i-\overline{\phi_k}), \tag{15}$$

where γ is the scaling factor for the micromixing timescale. With Eqs. (9) and (13), Eq. (15) can be rewritten as

$$M_k^i=\gamma\left(S_k^i-P_i\sum_j S_k^j\right) \tag{16}$$

Note that in this formulation, γ needs to be provided as a model input as in the other one-point closures (e.g., Tsai and OBrien [1], Tsai and Fox [5]). The last term in Eq. (10) can be obtained by multiplying the regular expression of chemical source term with P_i. For instance, let ϕ_a^i and ϕ_b^i be the Lagrangian molar concentrations of reacting species A and B in environment i, a bimolar reaction rate for species A in can be expressed as

$$-k_c\phi_A^i\phi_B^i, \tag{17}$$

where k_c is the reaction rate constant. Multiply Eq. (17) by P_i, the source term $R_k(\mathbf{S}^i,P^i)$ in Eq. (10) can be expressed as

$$R_a^i=-P_ik_c\phi_a^i\phi_b^i=-\frac{k_cS_a^iS_b^l}{P_i}, \tag{18}$$

thus closes Eq. (10). Equations (8) and (10) are implemented in Fluent using the user-defined subroutines. For a problem with two PDF modes (i.e., inlet streams) and two species, a total of 5 (1 PDF mode and two S_k in each PDF mode) user-defined scalars need to be solved since one PDF mode can be obtained using Eq. (12).

Downloaded 03 Jun 2010 to 171.66.16.150. Redistribution subject to ASME license or copyright; see http://www.asme.org/terms/Terms_Use.cfm

Mixture Fraction Variance. Using the definition of P_i and S^i, the mixture fraction variance σ^2 can be found by

$$\sigma^2 = \sum_i \phi^{i^2} P_i - \left(\sum_i \phi^i P_i \right)^2, \tag{19}$$

where ϕ^i is the Lagrangian concentration of a inert tracer from inlet stream i. Differentiating Eq. (19) with respect to time and applying Eqs. (8) and (10), the transport equation for σ^2 can be derived as

$$\rho \frac{\partial \sigma^2}{\partial t} + \rho \overline{u}_j \frac{\partial \sigma^2}{\partial x_j} = \frac{\partial}{\partial x_j} \left[\Gamma_T \frac{\partial \sigma^2}{\partial x_j} \right] + 2\Gamma_T \frac{\partial \overline{\phi}}{\partial x_j} \frac{\partial \overline{\phi}}{\partial x_j} - 2\Gamma_T \sum_i P_i \frac{\partial \phi^i}{\partial x_j} \frac{\partial \phi^i}{\partial x_j} + 2\rho \sum_i \phi^i M^i. \tag{20}$$

The last two term on the right-hand side are the ''spurious'' dissipation term and the scalar dissipation term due to micromixing (Fox [7]), respectively. Applying the definition of M^i (Eq. (16)) and Eq. (13), the last term can be rewritten as

$$2 \sum_i \phi^i M_i = -2\gamma \sum_i P_i (\overline{\phi} - \phi^i)^2, \tag{21}$$

which has the same form as the IEM model (Villermaux and Devillon [8], Dopazo [9]). In the absence of the ''spurious'' dissipation term, γ can be defined as

$$\gamma = \frac{1}{\tau_m}, \tag{22}$$

where τ_m is the characteristic timescale for micromixing. Details of determining the value for τ_m can be found elsewhere (Fox [10]). The scope of this paper is limited to evaluating the FMPDF model. Several different expressions of τ_m will be exploited to compare with the full PDF simulation (Tsai and Fox [11]), Magnussen model, and Baldyga and Henczka's model based on mixture fraction variance [12].

With the gradient-diffusion assumption, the correct transport equation for mixture fraction variance can be written as

$$\rho \frac{\partial \sigma^2}{\partial t} + \rho \overline{u}_j \frac{\partial \sigma^2}{\partial x_j} = \frac{\partial}{\partial x_j} \left[\Gamma_T \frac{\partial \sigma^2}{\partial x_j} \right] + 2\Gamma_T \frac{\partial \overline{\phi}}{\partial x_j} \frac{\partial \overline{\phi}}{\partial x_j} - \frac{2\rho}{\tau_m} \sigma^2. \tag{23}$$

Compared with Eq. (10), it is clear that the ''spurious'' term is indeed an extra dissipation term that should be eliminated. It is argued that this term is relatively small (Fox [7]). However, there are several ways to eliminate this term. One possibility is to solve both Eq. (20) and Eq. (23) simultaneously and redefine γ using σ^2 solved in Eq. (23). This method thus forces the solutions of Eq. (23) and Eq. (20) to be identical. For numerical implementation, only Eq. (23) needs to be solved explicitly because Eq. (20) is implied by the solution of Eqs. (8) and (10). It is found this correction is essential for a correct modeling of turbulence-chemistry interactions since the spurious dissipation term can enhance micromixing. Another advantage with this method is that the models for timescale (e.g., Baldyga and Henczka [12], Fox [10]) can be implemented through Eq. (23). It is found that this method provides a stable and accurate solution for σ^2 and is adopted for all simulations performed in this paper.

The velocity and turbulence fields are solved using both the standard and the RNG $k-\varepsilon$ model (Launder and Spalding [13], Yakhot and Orszag [14]). For results presented below, there is little difference found between these two models.

Results and Discussion

The Experiment of Komori et al. [15]. The FMPDF model is compared with the Magnussen model and Baldyga's model for the reactive mixing layer experiment of Komori et al. [15]. The experiment was conducted in a water tunnel with both inert tracer and a one-step irreversible acid-base neutralization reaction

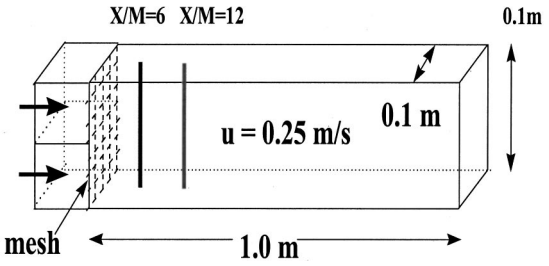

Fig. 1 Schematic diagram for the experiment of Komori et al. [15]

$$A + B \xrightarrow{k_c} \text{product}, \tag{24}$$

where $k_c \to \infty$. In the model, k_c is assumed to be 10^{15} (m^3/mole-s). However, k_c can be as small as 10^8 without altering the results significantly.

A Experimental Configuration. The water tunnel has a square cross section and the inlet streams have equal volume ratio. The Reynolds number is about 25,000 and Schmidt number is 800. This experiment is chosen because of its relatively high Schmidt and Reynolds numbers, and because the measurements can be more accurately taken with few complications from the effects of wall boundary layers. Figure 1 is a schematic diagram of the experiment configuration. The two vertical lines shown in Fig. 1 are the locations ($X/M=6$ and $X/M=12$ with $M=0.02$ m) where concentration profiles of species A are compared (Eq. (13)). The X value is measured from the splitter tip.

The micromixing timescale, τ_m, for the FMPDF model is given by the classic formula of Corssin [16]:

$$\tau_m = \frac{3}{2} \frac{k}{\varepsilon} + \frac{1}{2} \ln(Sc) \left(\frac{\nu}{\varepsilon} \right)^{1/2}, \tag{25}$$

where ε is the turbulent dissipation rate, k the turbulent kinetic energy and v the kinematic viscosity ($\approx 10^{-6}$ for water). This timescale contains the correct scaling for fluids with high Schmidt numbers, and is derived for a fully developed turbulence at high Reynolds number where a viscous-convective spectrum is present. For liquid flows, this is the only timescale accounts for the well-known scaling of -1 for the inertial-viscous range at high-Schmidt numbers. The initial concentrations of two reacting species, C_{A0} and C_{B0}, have the same values of 10 mole/m^3.

B Boundary Conditions. The experiment has two streams and two reactants, thus a total of 7 (2 environments + 2 species in each environment and 1 variance) variables need to be solved. By applying Eq. (12), the variables can be reduced to 5. The boundary conditions are summarized below:

Inlet\Variable	P_1	P_2	S_A^1 (mol/m3)	S_B^1	^2_A	S_B^2
1	1.0	0.0	10.0	0.0	0.0	0.0
2	0.0	1.0	0.0	0.0	0.0	10.0

The mean values can be obtained according to Eq. (13).

Results and Discussion. The predictions of the FMPDF model for the inert tracer is shown in Fig. 2 and the reactive mixing layer case shown in Fig. 3. Both results match quite well with the experimental data.

Both the Magnussen model and Baldyga's mixture fraction reaction model predict almost identical results as shown in Fig. 2 for the inert tracer case (not shown). For the case of reactive mixing layer, the Magnussen model requires adjustment of the empirical

Downloaded 03 Jun 2010 to 171.66.16.150. Redistribution subject to ASME license or copyright; see http://www.asme.org/terms/Terms_Use.cfm

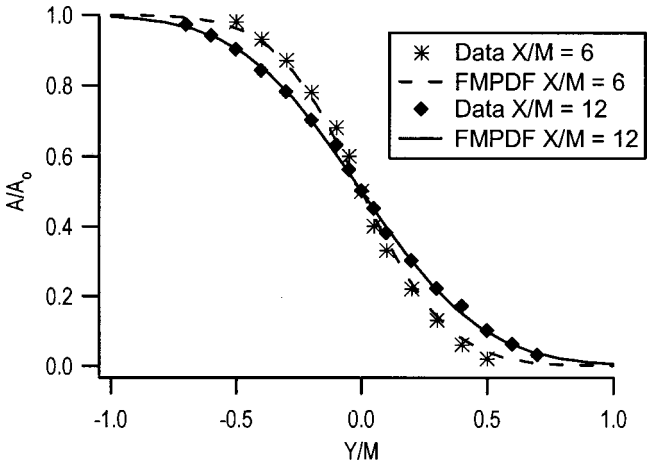

Fig. 2 Vertical profiles of inert tracer at the position of X/M =6 and X/M=12 predicted by Eq. (3). X is the axial distance and M is the mesh size (=0.02 m).

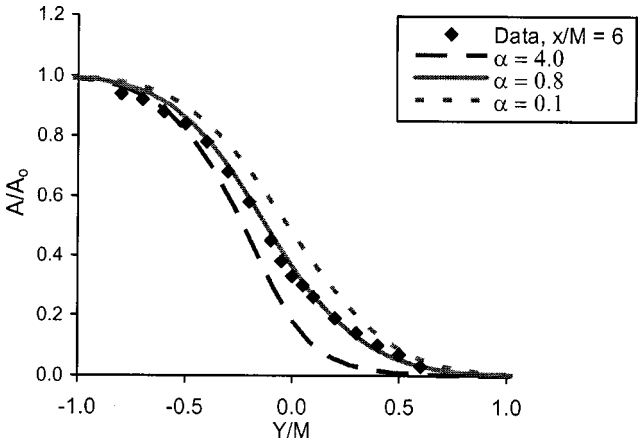

Fig. 4 Vertical profiles of species A mean concentration at X/M=6 predicted with different values of empirical parameters using the Magnussen model

parameters to fit the data correctly. The Magnussen model assumes the limiting reaction rate has the following form for one-step irreversible reactions:

$$R_i = \nu_i' W_i \alpha \rho \frac{\varepsilon}{k} \frac{P_R}{\nu_R' W_R}, \tag{26}$$

where ν_i' is the stochiometric coefficient for species i, α the empirical parameter, W_i the molecular weight of species i, ρ the fluid density, and P_R the mass fraction of reactant R. After some trial and error, α is found to be 0.8. The effect of α is shown in Fig. 4. With $\alpha=0.8$, both profiles at $X/M=6$ (Fig. 4) and $X/M=12$ (not shown) fits the data closely. However, determining the value of α is highly empirical and a universal value for different reactions and flows might not be possible.

Baldyga's model contains two parts. Part one is a cascade model for the decay of mixture fraction variance, which includes the effects of dissipation rate at different stages of the scalar spectrum, and therefore does not require any empirical constants. However, the model requires solving three stages of variance cascade and the final variance is the sum of the three stages. Equation (23) is used as the first stage. Depending on the Reynolds number, Baldyga's model always predicts a larger variance when the same τ_m is chosen. The second part is a model for the mean reaction rates based on the PDF shape of mixture fraction. A beta distribution is assumed for the mixture fraction PDF. By solving the mean and the three-stage variance equations, a beta density function is assigned as the mixture fraction PDF and a linear relationship is assumed between reactants and the mixture fraction. This gives the mean reaction rates for reactants and products. Details can be found elsewhere (Baldyga and Henczka [12]) and is not repeated. The results are shown in Fig. 5. Significant deviations can be found at both locations ($X/M=6$ and $X/M=12$). The reason for the deviation is not clear since both the models for the mixture fraction variance and the mean reaction rates could contribute to the error.

The simulations are performed in 2-D since the mixing layer thickness is relatively small compared to the equipment dimension. Three resolutions are used (241×40, 120×30, and 50×20). The two higher-density grids produced almost identical results within 2500 iterations with an error tolerance of 10^{-8} for scalars.

Li and Toor's Experiment. The experiment of Li and Toor [17] is conducted using a coaxial jet reactor with the following parallel/consecutive reaction:

$$A + B \xrightarrow{k_1} Q,$$
$$B + Q \xrightarrow{k_2} T, \tag{27}$$

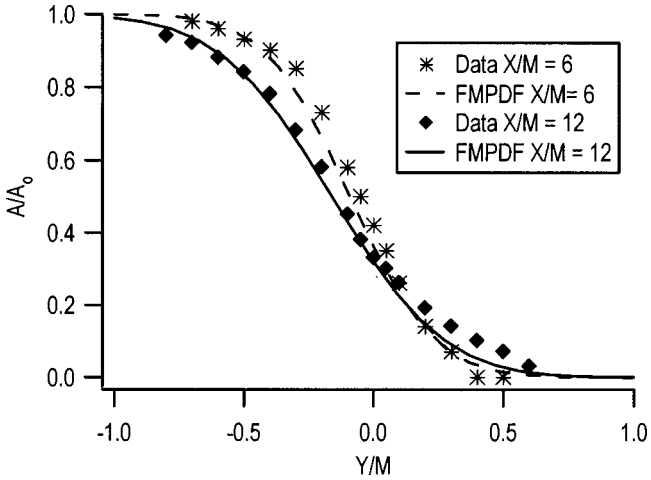

Fig. 3 Vertical profiles of species A for the reactive mixing layer experiment predicted by the FMPDF model

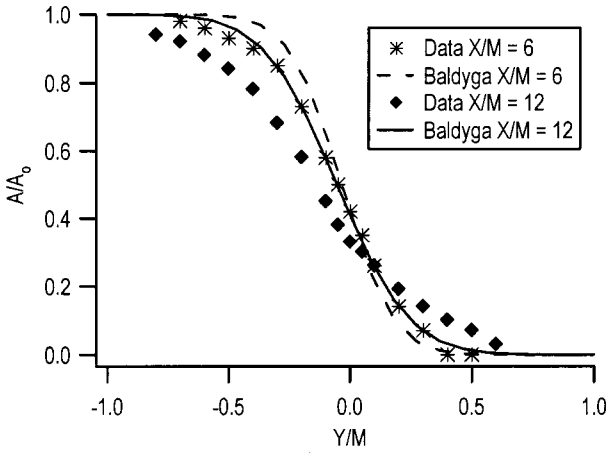

Fig. 5 Vertical profiles of species A predicted by Baldyga's model

Downloaded 03 Jun 2010 to 171.66.16.150. Redistribution subject to ASME license or copyright; see http://www.asme.org/terms/Terms_Use.cfm

Table 1 Summary of results from the FMPDF and the Monte-Carlo simulations using Eq. (29)

B (gmol/m3)	Re	FMPDF/PDF/EXP B in jet	FMPDF/PDF/EXP A in jet	$C_{\phi 1}$
2.86	3530	80.40/81.0/82.05 %	79.9/80/84.92	1.65
2.86	7552	88.11/88.3/88.33	87.43/88.38/90.86	1.65
0.964	3530	91.28/91.8/88.95	91.0/90.0/91.13	1.65
0.964	7552	95.14/95.4/93.45	95.06/95.3/94.88	1.65

Table 2 Summary of results from the FMPDF and the Monte-Carlo Simulations using Eq. (30)

B (gmol/m3)	Re	FMPDF/PDF B in jet	FMPDF/PDF A in jet	$C_{\phi 2}$
2.86	3530	85.6/82.5 %	n/a	0.525
2.86	7552	88.8/88.53	88.11/87.14	0.37
0.964	3530	93.9/92.49	n/a	0.525
0.964	7552	95.4/95.18	95.4/95.08	0.37

where $k_1 = 10^{15}(m^3/\text{gmole-s})$ and $k_2 = 1800$. This reaction is well-known for its sensitivity to micromixing. The formation of species T is highly dependent on flow parameters. The reaction source terms for FMPDF can be expressed as follows:

$$R_A^i = -k_1 \frac{S_A^i S_B^i}{P_i}$$

$$R_B^i = -k_1 \frac{S_A^i S_B^i}{P_i} - k_2 \frac{S_B^i S_Q^i}{P_i} \tag{28}$$

$$R_R^i = k_1 \frac{S_A^i S_B^i}{P_i} - k_2 \frac{S_B^i S_Q^i}{P_i}$$

Concentration values for species T is obtained through molar balance. For this reaction, a total of seven variables need to be solved plus Eq. (23). The inlet boundary conditions can be derived as discussed in the previous section.

The initial volume ratio of species A and B is equal to one. The experiment uses a single-jet reactor consisted of a smaller tube centered with four vanes in a larger tube. The smaller tube has a 0.004 m inner diameter and 0.0048 m outer diameter. The larger tube has an inner diameter of 0.0066 m and a length of 1.8m. More details of the experimental configuration can be found in Li and Toor [17]. In order to demonstrate that the turbulence-chemistry interactions are correctly modeled, the FMPDF model adopts identical micromixing timescales used in the Monte-Carlo PDF simulations performed by Tsai and Fox [11]. Interested readers should refer to that paper for more details. Only results relevant to this study are outlined here. Three different timescales are used in their study:

$$T_{m1} = C_{\phi 1} \frac{d}{\sqrt{k}} \tag{29}$$

$$\tau_{m2} = C_{\phi 2} \frac{k}{\varepsilon} \tag{30}$$

$$\tau_{m3} = C_{\phi 3} \sqrt{\frac{\nu}{\varepsilon}}, \tag{31}$$

where d is the inner diameter of the larger tube. In the PDF simulations, these three timescales are chosen to predict the yield defined below

$$Y_Q = \frac{\overline{\phi}_Q}{\overline{\phi}_Q + 2\overline{\phi}_T}, \tag{32}$$

It is concluded that Eq. (29) provides the best fit since the PDF simulations are able to reproduce the yield within 2 percent accuracy with a constant value of $C_{\phi 1}(=1.65)$ for several configurations (Table 1). The other two timescales require different values of $C_{\phi 2}$ and $C_{\phi 3}$ to predict the correct yield at different Reynolds numbers. In order to show that the proposed model correctly resolves the turbulence-chemistry interactions, all three timescales are used to reproduce the results predicted by the PDF simulations.

It should be noted that the three timescales are significantly different from Eq. (25). Equations (29) to (31) contain no information about the Schmidt number and thus should only be considered as a best fit to the experimental data. Since the Reynolds numbers in Li and Toor's experiment are relatively low, a reasonable prediction of the time scale is difficult. As pointed out by Kruis and Falk [18] even with sophisticated models (e.g., spectral relaxation model of Fox [10]), the prediction is still less than desirable. Furthermore, as mentioned earlier, the FMPDF model is a one-point closure and thus incapable of predicting timescale information. The purpose of this comparison is to demonstrate that the interaction between turbulence and chemistry can be modeled reasonably well without resorting to the full PDF simulation, which is known for its analytical formulation for turbulence-chemistry interactions (Pope [3]).

The results shown in Table 1 to Table 3 contain eight cases, including two different inlet concentrations of A and B at two Reynolds numbers (3530 and 7552), and cases in which species A and B are switched at the inlet. In Table 1, the experimental data are attached in the last column of each data field marked EXP for comparison.

In Table 1, the first column shows the concentration of species B (species A is always 4 percent in excess to ensure the completion of species B). The second column indicates the Reynolds number. The third column summarizes the results with species B injected through the center jet, and the fourth column shows the results with species A injected through the center jet. In column 3 and 4, the numbers on the left are the results predicted by the FMPDF model and the numbers on the right are the results predicted by the Monte-Carlo PDF simulation. While a constant $C_{\phi 1}$ can be used with timescale $d/\sqrt{k}$, at different Reynolds numbers, the commonly used timescale, k/ε, requires two different values of $C_{\phi 2}$ (0.525 and 0.37 as shown in Table 2) to predict the experimental results correctly. Table 3 shows the results with the third timescale, $\sqrt{\nu/\varepsilon}$, with a constant value of $C_{\phi 3}$ (0.028), but the results are less satisfactory at the low Reynolds number.

For all cases shown here, the predicted results from these two models differ less than 2 percent with identical values of C_ϕ. This is remarkable considering the fact that FMPDF takes a completely different approach then the full PDF formulation and the difference in CPU time consumed. Since FMPDF is formulated in an Eulerian frame, it can be easily integrated into many commercial CFD codes and solved as a steady-state solution. In contrast, the Monte-Carlo PDF simulation can only obtain time-averaged stationary solutions because of the randomness in particle movement. The Monte-Carlo PDF simulation requires approximately 5

Table 3 Summary of results from the FMPDF and the Monte-Carlo simulations using Eq. (31)

B (gmol/m3)	Re	FMPDF/PDF B in jet	FMPDF/PDF A in jet	$C_{\phi 3}$
2.86	3530	76.1/74.5 %	n/a	0.028
2.86	7552	88.46/88.5	88.04/87.6	0.028
0.964	3530	88.86/86.6	n/a	0.028
0.964	7552	94.4/95.1	95.2/95.2	0.028

Downloaded 03 Jun 2010 to 171.66.16.150. Redistribution subject to ASME license or copyright; see http://www.asme.org/terms/Terms_Use.cfm

hr on a HP-Appolo 735[2] workstation (with optimization) for each simulation while the FMPDF model uses less than 15 minutes on a Sun Ultra 30[3] workstation for a simulation with an identical mesh.

Numerically, the simulations are performed in a 2-D axisymmetric domain due to the co-axial jet configuration. The simulation dimension and grid density are chosen to be identical to the full PDF simulations. The grid coordinates and velocity fields are available in Tsai and Fox [11].

Conclusions

A simple deterministic model based on the concept of finite-mode PDF is proposed to resolve the turbulence-chemistry interactions in turbulent reacting flows. By using delta functions representing the probability flow from each inlet streams, both concentration mean and variance can be solved. This new technique allows a more physically sound methodology for resolving the turbulence-chemistry interactions. The model is validated against the experimental data of Komori et al. [15] using the timescale formulated by Corrsin [16], which includes the high Schmidt effects of liquids used in the experiment. The results match reasonably well with the experimental data. The Magnussen model requires adjustment of empirical parameters with which good results cannot always be assured. The model of Baldyga and Henczka does not predict the experimental data well. This may be a result of either the cascade micromixing model or the mean reaction rate model based on the beta mixture fraction PDF, and a simplified interpolation between infinite and zero reaction rate constants.

The comparison with the Monte-Carlo PDF simulation is also satisfactory. In all the cases compared, the FMPDF results match closely with the full PDF method under different micromixing timescales and model constants. This clearly indicates that the micromixing effect on reaction is correctly coupled. The short CPU time requirement will also allow simulations for realistic industrial problems.

The formulation presented in this paper can be easily extended to compressible flows. However, since only a small number of PDF modes have been tested, the model's ability to predict mean reaction rates with nonlinear temperature dependency remains uncertain, especially for flows with high density and temperature variations, which can alter the probability density greatly. More investigation in the area of combustion may be a worthwhile venture.

Acknowledgments

The authors would like to thank Prof. Phil Smith (University of Utah) for many stimulating discussions regarding Baldyga's model.

Nomenclature

A = chemical species A
B = chemical species B
C_ϕ = micromixing coefficient
C_μ = model constant for Eddy diffusivity
D_m = molecular diffusion coefficient
G_j = magnitude of probability density at ψ_j
J_j = molecular diffusion flux at direction j
P_i = volume fraction of environment i
$\mathbf{P}$ = vector of P
M = mesh size
M_k^i = micromixing source term for species k in environment i
Q = chemical species Q
T = chemical species T
R_k = reaction source term for species k
S_k^i = total concentration of species k in environment i
$\mathbf{S}$ = vector of S
W = molecular weight
Y_Q = yield of product Q
Y = vertical distance
X = axial distance
$f_\phi(\psi)$ = composition joint PDF
k = turbulent kinetic energy
k_c, k_1, k_2 = reaction rate constant
t = time
$\overline{u}$ = mean velocity
Γ_T = turbulent diffusion coefficient
α = empirical constant in Magnussen's model
σ^2 = mixture fraction variance
γ = micromixing scaling factor
η_t = turbulent Schmidt number
ϕ_k^i = concentration of species k in environment i
ψ = phase variable of ϕ
τ_m = micromixing timescale
ε = turbulent energy dissipation rate
ν = kinematic viscosity
ν' = stoichiometric ratio
Sc = Schmidt number

[2]HP-Apollo 735 is a trade designation of Hewlett Packard.
[3]Sun Ultra 30 is a trade designation of Sun Microsystems.

References

[1] Tsai, K., and O'Brien, E. E., 1993, "A Hybrid One- and Two-Point Approach for Isothermal Reacting Flows in Homogeneous Turbulence," Phys. Fluids, **5**, pp. 2901–2910.
[2] Tsai, K., Charkrabarti, M., Fox, R. O., and Hill, J. C., 2001, "Evaluation of Micromixing Models for a Series-Parallel Reaction in Simulated Homogeneous Turbulence," in preparation.
[3] Pope, S., 1985, "PDF Methods for Turbulent Reactive Flows," Prog. Energy Combust. Sci., **28**, pp. 119–192.
[4] Fox, R. O., 1992, "The Fokker-Plank Closure for Turbulent Molecular Mixing: Passive Scalars," Phys. Fluids A, **4**, pp. 1230–1244.
[5] Tsai, K., and Fox, R. O., 1996, "PDF Modeling of Turbulent-Mixing Effects on Initiator Efficiency in a Tubular LDPE Reactor," AIChE J., **42**, pp. 2926–2940.
[6] Magnussen, B. F., and Hjertager, B. H., 1976, "On Mathematical Models of Turbulent Combustion with Special Emphasis on Soot Formation and Combustion," 16th Symp. (Int'l.) on Combustion, Cambridge, MA, Aug. 15–20.
[7] Fox, R. O., 1998, "On the Relationship Between Lagrangian Micromixing Models and Computational Fluid Dynamics," Chem. Eng. Process., **37**, pp. 521–535.
[8] Villermaux, J., and Devillon, J. C., 1972, "Représentation de la Coalescence et de la Redispersion des Domaines de Ségrégation dans un Fluide Par un Modèle d'interaction Phénoménologique," 2nd Int'l. Symp. Chem. React. Engng., Amsterdam B, pp. 1–13.
[9] Dopazo, C., 1975, "Probability Density Function Approach for a Turbulent Axisymmetric Heated Jet Centerline Evolution," Phys. Fluids, **18**, pp. 397–404.
[10] Fox, R. O., 1995, "The Spectral Relaxation Model of the Scalar Dissipation Rate in Homogeneous Turbulence," Phys. Fluids, **6**, pp. 334–348.
[11] Tsai, K., and Fox, R. O., 1994, "PDF Simulation of a Turbulent Series-Parallel Reaction in an Axisymmetric Reactor," Chem. Eng. Sci., **49**, pp. 5141–5158.
[12] Baldyga, J., and Henczka, M., 1997, "Turbulent Mixing and Parallel Chemical Reactions in a Pipe-Application of a Closure Model," Récents Progrès en Génie des Procédés, **11**, pp. 341–348.
[13] Launder B. E., and Spalding D. B., 1972, *Lecture in Mathematical Models of Turbulence*, Academic Press, London, England.
[14] Yakhot, V., and Orszag, S. A., 1986, "Renormalization Group Analysis of Turbulence: I Basic Theory," J. Sci. Comput., **1**, pp. 1–51.
[15] Komori, S., Nagata, K., Kanzaki, T., and Murakami, Y., 1993, "Measurements of Mass Flux in a Turbulent Liquid Flow with a Chemical Reaction," AIChE J., **39**, pp. 1611–1620.
[16] Corssin, S., 1964, "The Isotropic Turbulent Mixer: Part II. Arbitrary Schmidt Number," AIChE J., **10**, pp. 870–877.
[17] Li, K., and Toor, H. L., 1986, "Turbulent Reactive Mixing with a Series-Parallel Reaction: Effect of Mixing on Yield," AIChE J., **32**, pp. 1312–1320.
[18] Kruis, F. E., and Falk, L., 1996, "Mixing and Reaction in a Tubular Jet Reactor: A Comparison of Experiments with a Model Based on a Prescribed PDF," Chem. Eng. Sci., **51**, pp. 2439–2448.
[19] Tsai, K., and Fox, R. O., 1998, "The BMC/GIEM Model for Micromixing in Non-Premixed Turbulent Reacting Flows," Ind. Eng. Chem. Res., **37**, pp. 2131–2141.
[20] Villermaux, J., and Falk, L., 1994, "A Generalized Mixing Model for Initial Contacting of Reactive Fluids," Chem. Eng. Sci., **49**, p. 5127.

Downloaded 03 Jun 2010 to 171.66.16.150. Redistribution subject to ASME license or copyright; see http://www.asme.org/terms/Terms_Use.cfm

S. Becker
Lehrstuhl für Strömungsmechanik (LSTM),
Friedrich-Alexander Universität,
Cauerstr. 4,
D-95058 Erlangen-Nuremberg, Germany

C. M. Stoots
Idaho National Engineering and Environmental
Laboratory (INEEL),
Idaho Falls, ID 83415-3890;
Lehrstuhl für Strömungsmechanik (LSTM),
Friedrich-Alexander Universität,
Cauerstr. 4,
D-95058 Erlangen-Nuremberg, Germany

K. G. Condie
Idaho National Engineering and Environmental
Laboratory (INEEL),
Idaho Falls, ID 83415-3890

F. Durst
Lehrstuhl für Strömungsmechanik (LSTM),
Friedrich-Alexander Universität,
Cauerstr. 4,
D-95058 Erlangen-Nuremberg, Germany

D. M. McEligot
Fellow ASME,
Idaho National Engineering and Environmental
Laboratory (INEEL),
Idaho Falls, ID 83415-3885;
University of Arizona,
Tucson, AZ 85721

LDA-Measurements of Transitional Flows Induced by a Square Rib

New fundamental measurements are presented for the transition process in flat plate boundary layers downstream of two-dimensional square ribs. By use of laser Doppler anemometry (LDA) and a large Matched-Index-of-Refraction (MIR) flow system, data for wall-normal fluctuations and Reynolds stresses were obtained in the near wall region to $y^+ < 0.1$ *in addition to the usual mean streamwise velocity component and its fluctuation. By varying velocity and rib height, the experiment investigated the following range of conditions:* $k^+ = 5.5$ *to 21,* $0.3 < k/\delta_1 < 1$, $180 < \mathrm{Re}_k < 740$, $6 \times 10^4 < \mathrm{Re}_{x,k} < 1.5 \times 10^5$, $\mathrm{Re}_\Theta 660$, $-125 < (x - x_k)/k < 580$. *Consequently, results covered boundary layers which retained their laminar characteristics through those where a turbulent boundary layer was established shortly after reattachment beyond the forcing rib. For "large" elements, evolution of turbulent statistics of the viscous layer for a turbulent boundary layer* ($y^+ < \sim 30$) *was rapid even in flows where the mean velocity profile still showed laminar behavior.* [DOI: 10.1115/1.1446067]

1 Introduction

Laminar-to-turbulent flow transition is a phenomenon which continues to be of interest to fluid mechanics scholars. In many technical applications, laminary boundary layers are induced, by roughnesses, to undergo transition to a turbulent flow at lower Reynolds numbers than the natural flow transition in order to enhance heat, mass or momentum transfer. This situation also has some flow phenomena in common with separation bubbles and the blockage of film cooling on turbine blades, both of which can induce early transition. Although investigations of laminar-to-turbulent flow transition have been going on for many decades, there are still many open questions that await answers. In general, the present studies were initiated to extend the knowledge of the structure of the transition process induced by a square roughness element.

A few studies of boundary layer development examined the process from transition through to the resulting turbulent boundary layer via hot wire anemometry. However, of these, Purtell et al. [1], Murliss et al. [2] and Erm and Joubert [3] all concentrated on behavior after the turbulent flow was established. Data on the evolution of the boundary layer structure during transition are sparse. Suder et al. [4] observed the flow structure in the case of ''bypass'' transition due to ''high'' freestream turbulence, examining the development of the streamwise velocity component and its mean turbulence statistics from laminar through turbulent flow. The evolution of integral parameters in comparable experiments by Roach and Brierley of Rolls Royce is presented by Savill [5]. Qui and Simon [6] measured profiles of streamwise velocity, turbulence intensity and intermittency through transition on a model of the suction surface of a gas turbine blade; they concluded that their transition started in the shear layer of a separation bubble and propagated to the wall. Transition characteristics were measured for an NACA 0012 airfoil by Lee and Kang [7], with and without another airfoil upstream.

Most studies of transition induced by roughness elements have concentrated on determining the resultant reduction in transition Reynolds number (Fage [8], Schlichting [9], Masad [10]). Conventional wisdom is that, for single circular elements, transition is not affected if $k^+ < \sim 7$ and it occurs at the element itself if $k^+ > \sim 20$. As noted by Schlichting, such criteria for transition induced by sharp elements become smaller than for cylindrical ones. This observation is demonstrated by comparable studies recently conducted at the Lehrstuhl für Strömungsmechanik (LSTM) to extend knowledge to include the structure of the transition process caused by a rectangular element (Durst et al. [11]); one of their objectives was to characterize the dependence of a transition Reynolds number on the size of the roughness element to determine the increased effectiveness of a square obstacle compared to a circular cylinder for forcing transition.

The measurements were carried out in a wind tunnel with five

Contributed by the Fluids Engineering Division for publication in the JOURNAL OF FLUIDS ENGINEERING. Manuscript received by the Fluids Engineering Division October 4, 2000; revised manuscript received August 8, 2001. Associate Editor: D. R. Williams.

 Copyright © 2002 by ASME

Downloaded 03 Jun 2010 to 171.66.16.150. Redistribution subject to ASME license or copyright; see http://www.asme.org/terms/Terms_Use.cfm

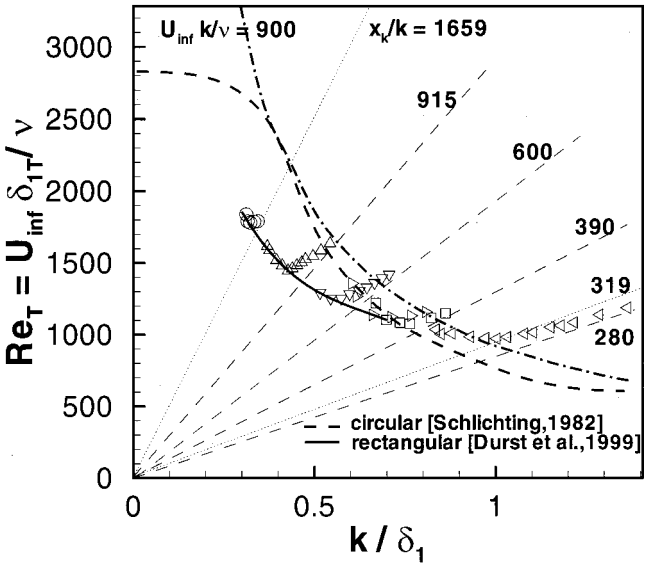

Fig. 1 Comparison of transition induced by a square rib (Durst et al. [10]) to that by a circular wire (Schlichting [8])

different roughness heights ($k=0.25$, 0.52, 0.72, 0.8 and 1.1 mm) and a range of free stream velocities. A pressure signal corresponding to the velocity gradient close to the wall was obtained with a Preston tube (a Pitot tube held against the wall); for given flow conditions it is a measure of the local wall shear stress or skin friction coefficient. Because the laminar-turbulent transition leads to an increase of the wall velocity gradient, the transition location was defined as the streamwise location where this local pressure was a minimum. Results are compared to experiments reported by Schlichting [9] in Fig. 1. One sees that the square, sharp-edged roughness elements are more effective, especially at small values of k/δ_1. As the nondimensional roughness size increases, the difference becomes smaller.

Due to the curved surface of a cylinder, it will perturb the base flow less than a rectangular element of equal height. Recirculating regions with shear layers and their inflectional profiles are established before and after the circular element. For the sharp-edged element these regions are larger and there is likely to be an additional separation bubble on top of the element. The radius of curvature of the cylinder is larger than that of the corner of a square element so the former can be expected to introduce a narrower spectrum of disturbance frequencies than the rectangular rib and the dominant frequency would be lower. Consequently, the ''receptivity'' of the boundary layer should be greater for a rectangular rib than for such a rounded shape.

Some details of the structure of the transition process downstream of a roughness element have been determined by Klebanoff and Tidstrom [12] with a single hot wire sensor; these investigators examined the response to the presence of a circular wire. However, their main emphasis was on the ''recovery zone'' where the flow could be considered to be essentially laminar. In addition to mean velocity and turbulence intensity distributions in the freestream direction, the spectral density distributions were reported for a range of Reynolds numbers. This investigation showed that it is possible to understand the behavior of a disturbed boundary layer as if the effect of the element is ''that of a strong wavelike disturbance which vigorously destabilizes the boundary layer and thus has the same effect as an increase in turbulence intensity of the free stream'' (Schlichting [9]).

In measuring low-Reynolds-number turbulent boundary layers, Erm and Joubert [3] demonstrated that mean-flow profiles are sensitive to the shape of tripping device used to induce the transition to turbulent flow. From the report of Arnal et al. [13], Arnal [14] presented limited measurements of the development of U/U_{inf} and u'/U_{inf} downstream of a band of carborundum grains employed as a near-rectangular roughness element. Little information exists about the behavior of the transition process and its flow structure very close to the wall, especially in other flow directions.

Phenomenologically, the Reynolds shear stress $-\rho\overline{uv}$ can be interpreted as the turbulent contribution to momentum transfer towards and away from a surface. In order to determine its evolution in the key viscous layer, simultaneous measurements of u and v are desired for the range of about $3<y^+<40$; none of the experiments mentioned above had the instrumentation or spatial resolution necessary to deduce v and uv accurately through this range. Most used single sensors ($\sim u$); the few that measured the normal component were constrained, by the configuration of their X-wire probes, to obtain data at locations greater than y^+ of about fifty (Murliss et al. [2], Erm and Joubert [3]) and concentrated on the fully turbulent region. Use of two-component laser anemometry in the large Matched-Index-of-Refraction flow system at the Idaho National Engineering and Environmental Laboratory (INEEL) has made possible such measurements for the present paper.

A present *aim* is to obtain fundamental data for the evolution of the Reynolds stresses in transition processes induced by roughnesses, especially in the near-wall region. The very high velocity gradients near the wall can raise questions regarding data accuracy for both numerical and experimental investigations. For example, even results of the DNS boundary layer flow simulations of Kim et al. [15] and Horiuhi [16] differ significantly from each other near the wall. With the present well-defined geometry, the results should also be valuable for benchmarking direct numerical simulations of transition (Laurien and Kleiser [17], Fasel et al. [18], Spalart [19], Narasimha [20]) enhanced by the presence of roughness elements. Patel [21] calls flow over rough surfaces an Achilles heel of computational fluid dynamics (CFD). For a first application to transition induced by roughness, a two-dimensional geometry would be most convenient for the DNS modeler. However, representing a circular element on a flat plate could involve undesirable complications with the numerical grid. A rectangular or square rib should be much easier for the analysts to represent; however, detailed data on the structure of the transition process have not been available for this case.

The present paper describes the experimental arrangements and uncertainties, behavior for a smooth plate without a roughness element, typical results for the streamwise component for a range of (nondimensional) roughness heights and detailed examination of the streamwise development for an example with ''laminar recovery'' and one that undergoes transition to a turbulent boundary layer. The presentation ends with a few remarks summarizing the study and its new results.

2 Experiment

The *objectives* of the present work include

- Obtaining laser Doppler velocimeter (LDV) measurements of the development of laminar, transitional and/or turbulent boundary layers evolving behind roughness elements of heights k^+ ranging from less than six to over twenty,
- Determining the wall-normal velocity component v and its mean statistics in the near-wall region downstream (as well as the usual streamwise velocity component) and
- Determining the evolution of the viscous layer (typically $y^+<30$ or so in an unheated turbulent boundary layer).

In contrast to the study of Klebanoff and Tidstrom [12], emphasis also includes the transition from laminar to turbulent conditions as well as the recovery of a laminar boundary layer.

Quantification of boundary layer flows requires measurements very close to the wall for determination of the wall shear stress. Hot wires for near-wall velocity studies are intrusive and pose wall conduction problems; the inherent difficulty of measuring v

Downloaded 03 Jun 2010 to 171.66.16.150. Redistribution subject to ASME license or copyright; see http://www.asme.org/terms/Terms_Use.cfm

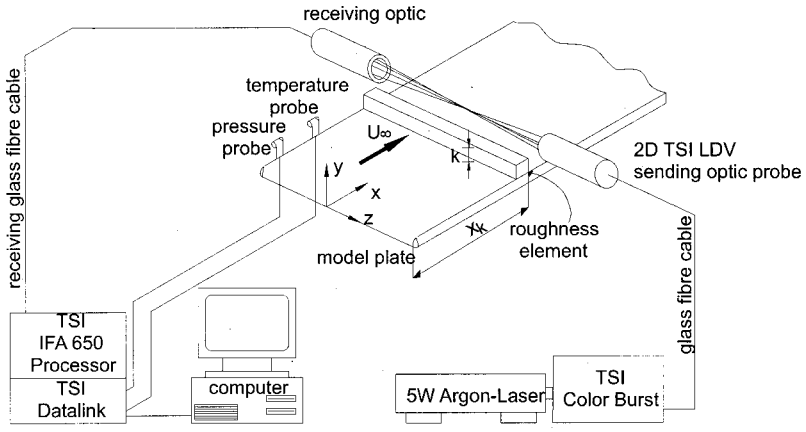

Fig. 2 Experimental apparatus, model configuration and nomenclature

and uv at small values of y^+ has been mentioned above. With hot-wire and hot-film X- or slant-probes to deduce Reynolds shear stresses, the sensor volume required has a dimension of the order of a millimeter perpendicular to the surface plus the additional space necessary for the support prongs. With laser Doppler anemometry (LDA), an effective sensor diameter of about 60 μm or less can be achieved so measurements can be obtained to $y \approx 30$ μm before ''intersecting'' the surface. LDA measurements usually suffer from optical interference of the laser beams, especially when systems for two and three component measurements are employed. One way to eliminate optical interference of multicomponent LDA systems is by employing suitable transparent wall materials together with fluids that possess the same refractive index as the wall material itself (Corino and Brodkey [22], Budwig [23]). In this way, the wall disappears optically (and therefore has no influence on the laser beams) but maintains its full mechanical influence on the flow.

To measure the wall-normal component close to the surface, two-component laser Doppler anemometry (LDA) was used with the INEEL Matched-Index-of-Refraction (MIR) flow system. This facility has the world's largest test section for an MIR system; previous systems were about an order-of-magnitude smaller in size. Consequently, the INEEL MIR system allows significantly improved spatial resolution (in terms of sensor diameter relative to the characteristic dimension). The working fluid is a light mineral oil (Penreco Drakeol #5) which has the same refractive index as quartz glass near room temperature, has almost no odor and is almost non-toxic, relatively inflammable and nonvolatile, cheap, and very stable. Further details of the system are provided elsewhere (Condie et al. [24], Stoots et al. [25]).

2.1 Apparatus. The configuration of the experiment is sketched in Fig. 2. The cross section of the MIR test section is about 61 cm by 61 cm and is 2.44 m long. At the entrance, for a velocity of 1.4 m/s the nonuniformity in velocity has been found to be about one percent of the mean velocity. At 1.2 m downstream, this nonuniformity decreased to about 0.1 percent outside the wall boundary layers. Freestream turbulence levels at the inlet have been measured with a hot film anemometer; turbulence intensities ranged from 0.4 to 0.6 percent. Thus, the facility is *not* appropriate for experiments concerning *natural* transition. However, it can be employed for ''bypass'' transition experiments (Suder et al. [4]) and for flows where induced disturbances have effects significantly greater than the background freestream turbulence—as in the present experiments. At $x \approx 2.3$ m and $U_{\text{inf}} \approx 1.25$ m/s for a flat plate without a roughness element, the mean velocity agrees with the Blasius profile and the maximum streamwise turbulent fluctuation in the boundary layer, as measured with the LDV, is $u'/U_{\text{inf}} \approx 0.01$ or $u'/u'_{\text{inf}} \approx 1.3$ at $\eta \approx 1.3$ to 3.

Based on guidance from an earlier study of Durst et al. [26], it was estimated that the oil temperature must be controlled to be steady and uniform to within 0.3 C to match the refractive index of quartz adequately for high-quality LDV measurements. A computer-controlled auxiliary system accomplishes this task. Temperature sensing is via precision thermistor probes and LabView software from National Instruments provides the necessary data acquisition and control of the heating and cooling components.

Figure 2 is a simple illustration of the experimental model and measurement orientation. The flat plate is about 60 mm wide, 12 mm thick and 2.4 m long with the forward face of the roughness element located at $x = 1150$ mm. Flow across the plate is from left to right. The leading edge of the plate is a NACA 0009 air foil. The plate was oriented horizontally at the centerplane of the tunnel test section and spanned almost the entire width. A small gap ($\sim$5 mm) was designed between the test section walls and the plate edges to reduce the propagation of disturbances from that region across the flow (Strunz [27], Wiegand [28]). The plate material upstream of a square quartz roughness element is anodized aluminum, with quartz glass downstream from this rib. Element heights of 2, 4 and 6 mm were used as well as runs without a rib in order to obtain measurements for comparison to accepted boundary layer theory for laminar flows. This experimental fixture was designed and constructed at the LSTM. An adjustable flap (not pictured) is located on the downstream end of the model to adjust the flow to yield a negligible streamwise pressure gradient.

Velocity and turbulence measurements are primarily obtained with a TSI two-component, fiberoptic-based laser Doppler velocimeter operated in the forward scattering mode with custom LSTM receiving optics (see Fig. 2). Transmitting optics are provided by a Model 9832-XX fiber optics probe with a collimating lens option included and a lens of 350 mm focal distance. With this configuration, the diameter of the LDV measurement control volume (MCV) is approximately 60 μm. Since the receiving optics were designed to focus on a region of about 50 μm in diameter, the effective MCV was smaller yet. A traversing system is integrated with the LDV to allow movement in all three axes. Data processing is accomplished via a TSI IFA 655 digital burst correlator and their FIND-W software.

2.2 Procedures. Most of the data were acquired with the two-component LDV operating in the forward scattering mode, thereby permitting simultaneous streamwise and normal velocity component measurements and calculations of their higher-order moments to be performed. For calculating mean quantities, so-called ''transit-time weighting'' was employed to counter velocity bias (Hoesel and Rodi [29], Tummers [30]).

The LDA data acquisition was normally operated in the ''coincidence mode'' requiring near simultaneous detection of samples

Downloaded 03 Jun 2010 to 171.66.16.150. Redistribution subject to ASME license or copyright; see http://www.asme.org/terms/Terms_Use.cfm

in both coordinate directions, i.e., from the same scattering particle. For each point, data collection was programmed to acquire 50,000 to 100,000 samples or to measure for a duration of two minutes, whichever came first. Normally, the former criterion was satisfied except in the vicinity of the wall and in the recirculating region after the rib where particle arrival rates were reduced (for example, for a typical reattached boundary layer, a duration of two minutes yielded about 12,000 samples at $y \approx 0.5$ mm and 21,000 samples at $y \approx 1$ mm).

The database provides a series of profiles downstream (and upstream) from the rib at each run combination of rib height and freestream velocity. Traversing for a profile was conducted vertically in the upward direction (y). Small bubbles in the quartz wall cause continuous signals on the oscilloscope; observing such a signal served a criterion to indicate that the MCV was touching the quartz wall. Data then were acquired at locations spaced 50 μm apart until well into the boundary layer where the spacing was increased. Velocity measurements could be made at the plate surface, with part of the laser probe volume located within the quartz plate (such velocity data are not included in the results due to the biasing of their statistics). Streamwise and normal velocity components were measured, and the calculation of their higher-order moments was performed, for wall proximities of $y^+ \approx 0.1$ and less. For the immediate vicinity of the wall the resulting mean streamwise velocity profile was plotted (Condie et al. [24]) and a straight line was manually fit through the linear region of the profile. The extrapolation of this line defined the effective surface, $y=0$, and its slope provided the velocity gradient at the wall for deducing the friction velocity, u_τ. Thus, it was possible to determine the local apparent mean wall shear stress accurately from the measured gradient $\partial U/\partial y$.

3 Experimental Uncertainties

The following uncertainty analysis is derived largely following the approach of MacManus et al. [31]. Instead of presenting a single overall uncertainty value, individual sources of uncertainty are discussed.

3.1 Particle Behavior. LDV measurements require seeding of the flow field with a second phase such as particles, bubbles or droplets. In this work, microbubbles were the seeding particles. There are two criteria that must be met to ensure that the movement of the bubbles truly represents the turbulent movement of the continuous phase. First, the size of the bubbles must be smaller than the Kolmogorov microscale. Second, the inertial relaxation time of the bubbles should be less than the Kolmogorov time scale. The procedure recommended by Calabrese and Middleman [32] was used to estimate the inertial relaxation time.

The smallest Kolmogorov microscale is estimated to be 250 μm. The Kolmogorov time scale is estimated to be 0.0048 seconds. For the inertial relaxation time of the bubbles to be less than the Kolmogorov time scale, their diameter must be less than 1500 μm. The bubbles in the flow field were estimated to be the order of ten μm in diameter or less, smaller than the measuring control volume of the LDV. The ''oversize level'' control of the LDV was also adjusted to avoid measurements from the largest particles in the size distribution.

3.2 Frequency Measurement. The manufacturer's specifications claim that their IFA 655 digital burst correlator has a resolution of 0.05 percent of the reading.

3.3 Optical Errors. Great care has been taken by the investigators to ensure that the alignment and intersection of the beams within the flow field are correct. Since the index of refraction of the oil is wavelength-dependent as well as temperature-dependent, matching indices of refraction for both beam wavelengths simultaneously is impossible, the optimum temperature for the green component of laser light is not exactly the optimum for the blue. Thus, some misalignment can be expected when more than one beam passes through quartz and oil. The temperature at which the indices are matched best for both components was ultimately determined experimentally. In order to match the refractive indices, the refractive index of the oil was varied by adjusting the oil temperature via the temperature control system. With the LDV placed so one blue beam passed through the quartz rib and one green beam passed through the quartz horizontal plate of the present test model, the LDV data acquisition was operated in the two velocity coincidence mode for short time series and the oil temperature was gradually varied. The maximum sampling rate that was obtained served to indicate the best temperature for operation so that the blue and green measuring control volumes are most coincident. For the oil in the MIR flow system this maximum in coincidence sampling rate occurred at about 23.7 C. At this condition the reduction in overlap of the two MCVs is estimated to be about thirty percent of their lengths, thereby reducing the size of the effective MCV when operating with the coincidence mode. There is also an uncertainty in the crossing angles of the beam (and focal distances) in air or oil that leads to uncertainties in the velocities (Schwartz et al. [33]). The value is an approximately constant error but usually our normalized presentation will cause this error to cancel from the results presented.

3.4 Statistical Uncertainties Due to Finite Sample Size. Estimation of the statistical errors encountered due to a finite sample size followed the approach presented by Bendat and Piersol [34] and used a typical sample size of 50,000 and measurement time of 120 seconds. For a peak velocity of 1.7 m/s and peak turbulence intensity of 15 percent of that velocity, the absolute maximum statistical uncertainties for the mean and rms velocity measurements were estimated to be ± 0.015 m/s and 0.010 m/s or 0.9 and 0.6 percent of that velocity, respectively. This approach utilized half the channel height as a typical length scale. A more conservative length scale is the maximum boundary layer thickness (approximately 50 mm) and a more characteristic turbulence intensity is 5 percent of the mean velocity, resulting in typical uncertainties of ± 0.0019 m/s and ± 0.0013 m/s for the mean and rms velocities, respectively.

3.5 Positional Accuracy. The vertical motion is accomplished with a traversing mechanism consisting of a spindle and a stepper motor. The spindle advance is 5 mm per revolution and the manufacturer's inspection report shows the measured motion to agree within about 0.015 percent or less of the setting. The stepper motor gives 500 steps per revolution, corresponding to an advance of 10 μm per step. While the resolution would appear to be 10 μm, the uncertainty in vertical position is believed to be less since all LDV measurements were accomplished with the traversing mechanism moving in the same direction to avoid backlash difficulties. The positional accuracy becomes important in deducing the wall shear stress and the wall location from fitting the measurements for $y^+ < \sim 3$. For the highest wall shear stress measured, this distance corresponds to $y \approx 400$ μm so with an uncertainty of 10 μm this contribution to the uncertainty in Δy would be about four percent or less. The uncertainty of the extrapolation to $y \approx 0$ is also thought to be about 10 μm. For the streamwise direction the uncertainty of reading the scale is estimated to be about 0.5 mm.

3.6 Temperature Accuracy. The index of refraction for the oil is a relatively strong function of temperature (Orr et al. [35]). Mismatch of the indices of refraction for the oil and quartz plate can result in movement of the measurement volume as well as distortion of the fringes within the measurement volume. Durst et al. [26] recommended that the indices of refraction should be matched to the fourth decimal point (i.e., 0.0001). For the oil used in this work, the temperature control must therefore be better than $+/-0.3$ C. Temperature control tests were conducted with both water and oil in the loop. Measurements of the spatial and temporal variation with a precision thermistor probe have shown spanwise uniformity and steadiness within 0.1 °C.

Downloaded 03 Jun 2010 to 171.66.16.150. Redistribution subject to ASME license or copyright; see http://www.asme.org/terms/Terms_Use.cfm

3.7 Uncertainties in Oil Properties. The properties of the light mineral oil were measured by Orr et al. [35]. An indication of the precision of these data is provided by their variations for 3σ; these were 0.002 g/cm^2 and 0.3 centistokes or about 0.3 and two percent of typical values, respectively. The latter uncertainty would dominate the uncertainties in Reynolds numbers, making them of the order of two percent of their calculated values.

3.8 Calibration. To obtain a measure of the accuracy of the overall LDV system, the mean velocity indicated by the data processing system was compared to that of a rotating ''calibration wheel'' passing through the measuring volume formed by the laser beams. The indicated velocity agreed with this standard to within about 0.3 percent. The variation along the axis of the measuring volume was less than one percent of its average value; this variation is a contributor to the apparent turbulence intensities of the LDV technique (Condie et al. [24]).

4 Experimental Results

As noted, conventional wisdom concerning detailed investigations in the past has been limited to only two dimensional circular wire roughness elements (Klebanoff and Tidstrom [12]). These measurements were carried out by one-dimensional hot-wire techniques. In addition to mean velocity and turbulence intensity distributions in the free stream direction, the spectral density distributions were reported for a range of Reynolds numbers. They concentrated on disturbance growth in a ''laminar recovery'' before transition. Their investigation showed that it is possible to understand the behavior of the boundary layer in their flows through comparison of the influence with a kind of wave disturbance. Stability theory supported these conclusions. Little information exists about the behavior of the transition process and the flow structure very close to the wall, especially for other velocity components.

Detailed velocity and turbulence measurements were obtained for a range of laminar and transitional flows. Schlichting [9] shows that the influence of a roughness element upon the transition process can extend through two limits. He suggests that in the case where the disturbance by the roughness element is less than the freestream turbulence intensities, the effect upon transition is negligible. Then the transition process is located at the same streamwise location as would be predicted for transition on a smooth plate with the same freestream turbulence level. The other extreme is when the transition process begins directly behind the roughness element. Data for two-dimensional circular roughness elements indicate that these limits are approximately given by $k^+<7$ and $k^+>20$, respectively. The present authors' interest centers upon the transition process between these two cases.

The measurements with a square rib were carried out at three different roughness heights k and three different freestream velocities, resulting in the following ranges of nominal parameters:

$$k^+=5.5 \text{ to } 21, \quad 0.3<k/\delta_1<1, \quad 180<\mathrm{Re}_k<740,$$

$$6\times10^4<\mathrm{Re}_{x,k}<1.5\times10^5, \quad \mathrm{Re}_\Theta<660,$$

$$-125<(x-x_k)/k<580.$$

For comparison to accepted analytical results, measurements were also conducted without installing a rib in the model, i.e., as a smooth flat plate. The nominal parameters for each of the eight sets of experimental conditions are listed in Table 1.

4.1 Smooth Plate. First experiments were conducted with a smooth plate model—(1) to qualify the facility as providing data in agreement with existing theory and (2) to serve as a reference condition ($k=0$) for the effects of square roughness elements. Figure 3 summarizes some of the results. The subfigure examines the variation of freestream velocity in the streamwise direction along the length of the plate. Values from the location where the rib would be placed and further downstream varied less than one percent, indicating a near constant freestream velocity distribution along the plate and a negligible streamwise pressure gradient. Following a procedure outlined by Lienhart and Becker [36], we used the displacement thickness of the boundary layer at each streamwise measurement position to calculate a virtual plate origin (x_v) of -209 mm. From this information, the streamwise mean velocity distribution can be compared to predictions from the boundary layer theory of Blasius (Schlichting [9]). Figure 3 demonstrates excellent agreement.

Table 1 Nominal values of experiment parameters

k (mm)	$U_{\inf}$ (m/sec)	$\mathrm{Re}_{x,k}$	k/δ_1	k^+	Re_k
None	1.25	101000	0	0	0
2	1.25	103000	0.297	5.53	179
2	1.75	145000	0.351	7.11	251
4	1.25	103000	0.593	11.05	358
4	1.75	145000	0.702	14.22	502
6	0.75	61200	0.683	11.16	318
6	1.25	102000	0.882	16.37	529
6	1.75	143000	1.043	21.07	741

The streamwise variation of the shape factor H is included in later figures for comparison purposes (e.g., Figs. 4–6). From $x=400$ to 2100 mm, H falls in the range between 2.49 and 2.60, compared to 2.59 for the Blasius solution. The measured skin friction coefficient varied from 0.98 to about 1.1 times the theoretical value. At these locations the rms fluctuations in the streamwise component, u', varied smoothly from near zero at the wall to its freestream value as η increased. The last two profiles at $x=2200$ and 2300 mm show a slight increase to $u'/U_{\inf}\approx0.01$ or $u'/u'_{\inf}\approx1.3$ at $\eta\approx1.3$–2.2 and a slight increase in shape factor. These last locations may be affected by the control flap at the end of the plate.

4.2 Development of Transitional Boundary Layers. The typical evolution of the flow and the effects of the roughness element on the streamwise component are demonstrated in Fig. 4. These measurements were obtained with the largest roughness element, $k\approx6$ mm, and nominal freestream velocities of 0.75, 1.25 and 1.75 m/s. Results are normalized with the roughness height and the freestream velocity. (The numbers in parentheses indicate the scaling of the quantities relative to the scale on the abscissa.) In addition, the local values of the shape factor are compared to the value predicted for a laminar boundary layer and to the values measured at the same location without an element installed.

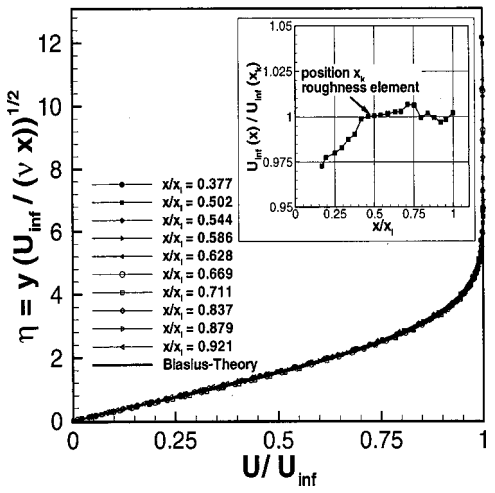

Fig. 3 Velocity distribution in the flat plate boundary layer without a roughness element

Downloaded 03 Jun 2010 to 171.66.16.150. Redistribution subject to ASME license or copyright; see http://www.asme.org/terms/Terms_Use.cfm

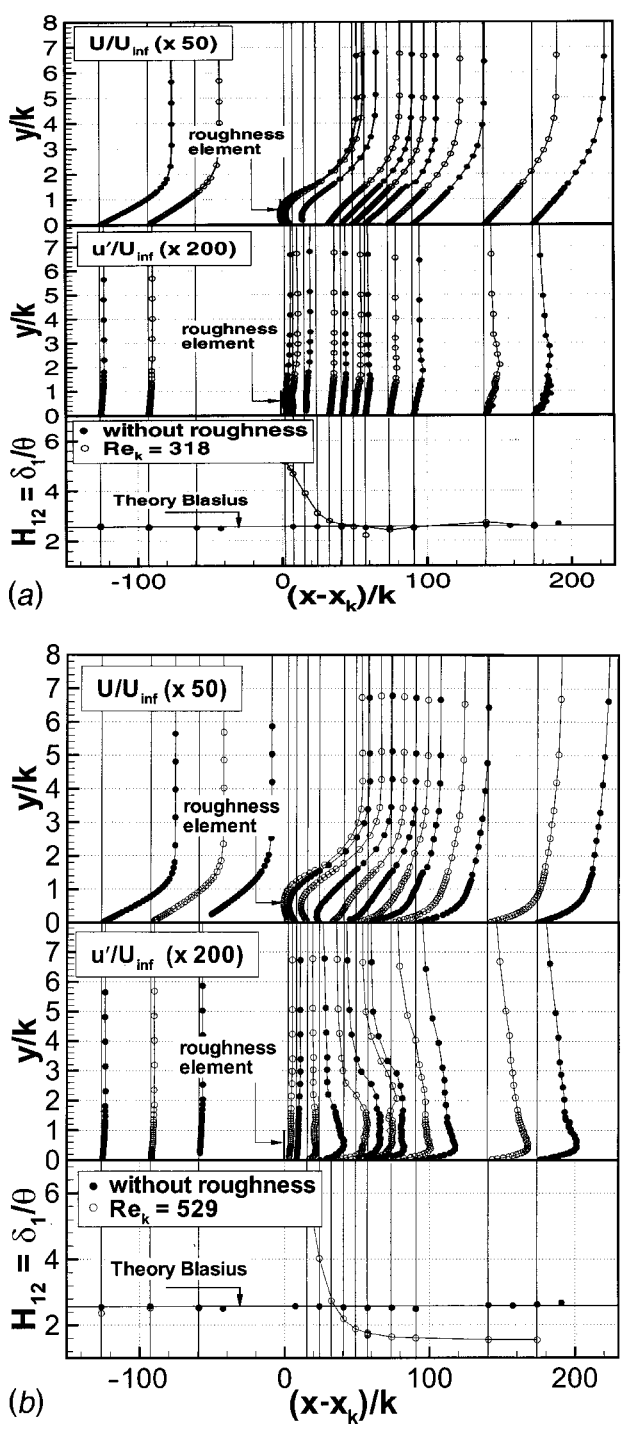

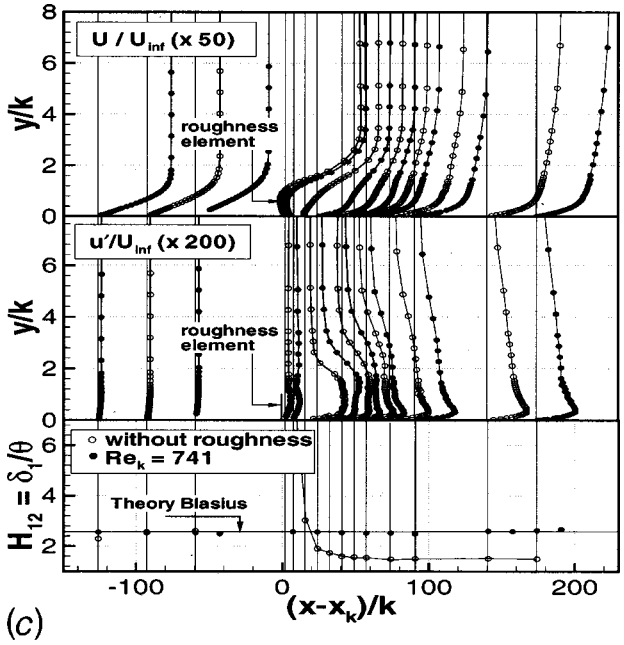

Fig. 4 Evolution of flow over a two-dimensional square rib. (*a*) $Re_{x,k} \approx 6 \times 10^4$, $k^+ \approx 11$, $k/\delta_1 \approx 0.7$, $Re_k \approx 318$; (*b*) $Re_{x,k} \approx 1 \times 10^5$, $k^+ \approx 16$, $k/\delta_1 \approx 0.9$, $Re_k \approx 529$; (*c*) $Re_{x,k} \approx 1.4 \times 10^5$, $k^+ \approx 21$, $k/\delta_1 \approx 1$, $Re_k \approx 741$.

In each case the mean velocity profiles upstream from the rib appear to be laminar and the shape factors there agree with the Blasius theory. The freestream turbulence levels u'/U_{inf} measured with the LDV are about 1.5, 1.3 and 1.2 percent or less for nominal freestream velocities of 0.75, 1.25 and 1.75 m/s, respectively, upstream of the rib. The mean velocity profiles show expected recirculating flows immediately following the rib with reattachments occurring between 13 and 34 heights downstream. A separated profile yields higher values of the shape factor than for the attached flow. Values of the fluctuating component u' within the recirculating region and development downstream of reattachment vary with the Reynolds number and roughness parameters.

The first case shown ($k^+ \approx 11$, Fig. 4(*a*)) appears to correspond to the study of Klebanoff and Tidstrom [12] with recovery to a laminar mean velocity profile following reattachment at 16 to 25 heights. In the recirculating region and in the boundary layer above it u' is low, approaching the freestream value gradually as y increases. Downstream the shape factors agree with the Blasius theory but the u' distributions show evidence of growth of disturbances evolving from the level of the inflectional region of the separated profiles ($y/k \approx 1.5$ or so). At $(x-x_k)/k \approx 140$ or $x \approx 2000$ mm, the maximum value of u' in the boundary layer is about twice the freestream value; the quantity u'/u'_{inf} is about 2.5 times its value at the same location on the smooth plate.

Downloaded 03 Jun 2010 to 171.66.16.150. Redistribution subject to ASME license or copyright; see http://www.asme.org/terms/Terms_Use.cfm

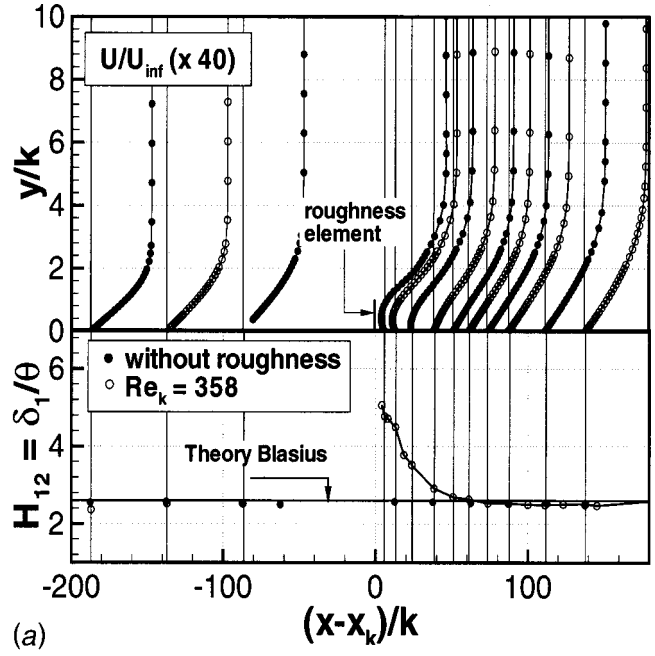

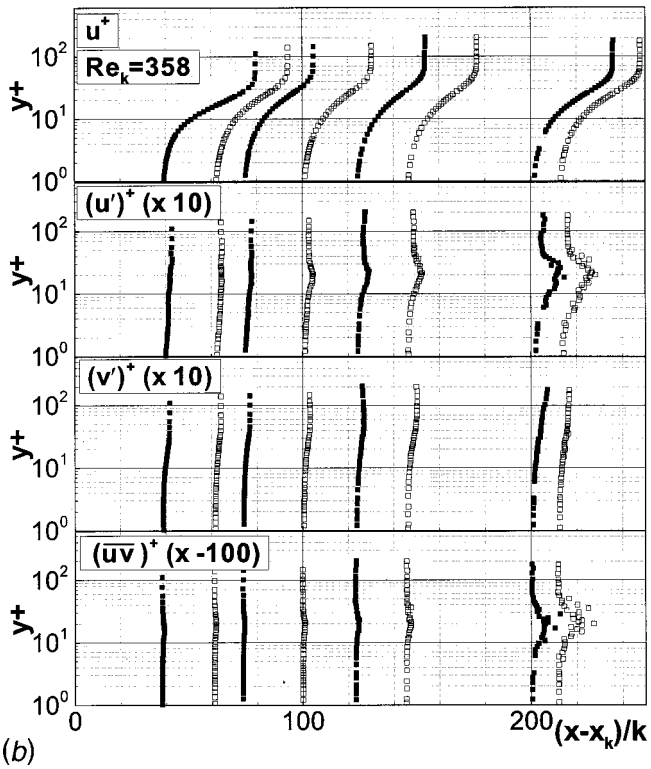

Fig. 5 (*a*) **Development of boundary layer and turbulence statistics for flow with "laminar recovery." Results normalized by freestream velocity and rib height.** (*b*) **Development of boundary layer and turbulence statistics for flow with "laminar recovery." Wall coordinates.**

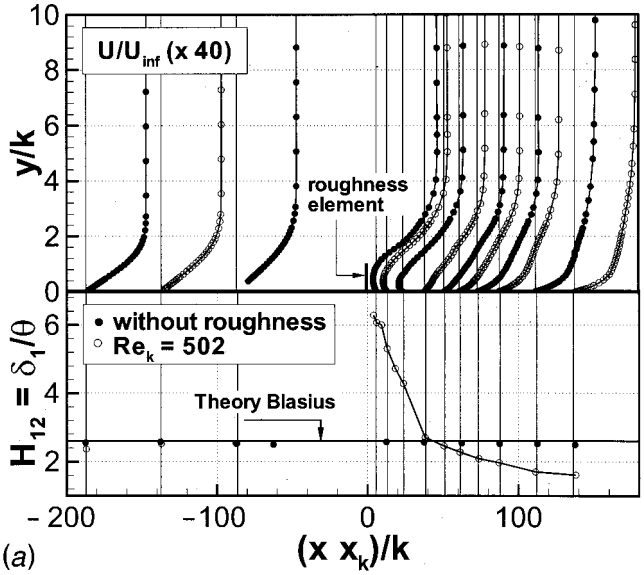

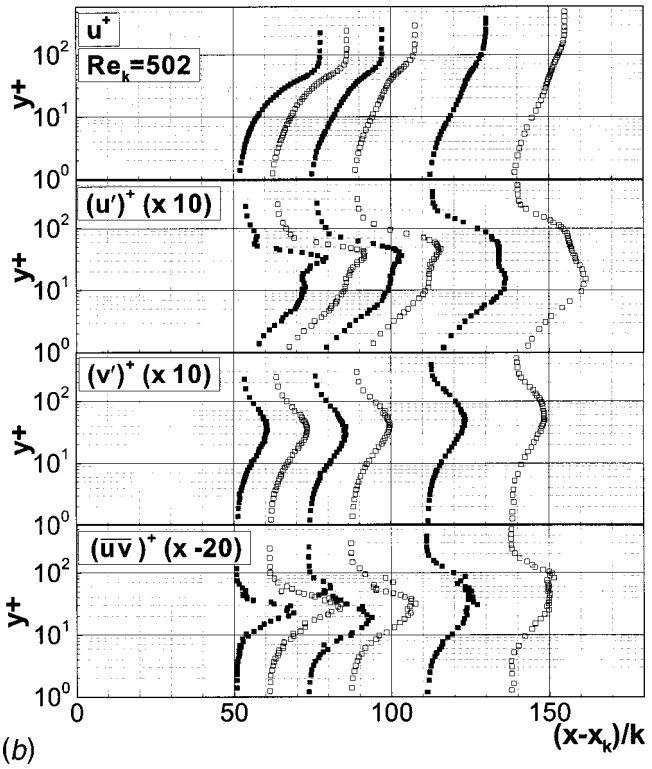

Fig. 6 (*a*) **Evolution of turbulent boundary layer. Results normalized by freestream velocity and rib height.** (*b*) **Evolution of turbulent boundary layer. Wall coordinates.**

In the second and third cases ($k^+ \approx 16$ and 21, Figs. 4(*b*) and (*c*)), the profiles and shape factors indicate a more obvious transition toward a turbulent boundary layer. After reattachment, the shape factors decrease to values of about 1.5 to 1.6, characteristic of fully-developed turbulent boundary layers. For the range $75 < (x - x_k)/k < 175$ the deduced local skin friction coefficients agreed with a correlation for a fully-developed turbulent boundary layer,

$$c_f = 0.0256 \ \mathrm{Re}_\Theta^{-1/4},$$

(Schlichting, Eq. 21.12 [9]) to within five percent. In both cases u' profiles show evidence of disturbance growth within and above the recirculating region; after reattachment both demonstrate rapid development of near-wall peaks in the u' profiles.

Klebanoff and Tidstrom [12] suggested that, for much "larger" roughness elements than in their investigation, the inflectional nature of the velocity profile may be such that the instability will be characteristic of a free shear layer rather than the boundary-layer type they studied. The third case likely represents such a situation. In the last profile before reattachment, over a range from near the wall to $y/k \approx 1.6$—which corresponds to the inflectional point in

Downloaded 03 Jun 2010 to 171.66.16.150. Redistribution subject to ASME license or copyright; see http://www.asme.org/terms/Terms_Use.cfm

the mean velocity profile at that location—u' is approximately six times its freestream value. Reattachment appears to be closer to the rib than for the first and second cases, despite the higher Reynolds number. At $(x-x_k)/k \approx 25$, the first station after reattachment, normalization by wall variables shows the near-wall region already to be approaching the behavior of the viscous layer of a fully-developed turbulent flow. The distribution of $(u')^+$ reaches a level of about 2.6–2.7 near $y^+ \approx 15$ as in a pipe flow (Durst et al. [37]). One may surmise that transition occurred in the shear layer of one of the three ''separation bubbles'' formed around the rib; this idea would be consistent with the suggestion of Qui and Simon [6] that their transition on the suction surface of a turbine blade model started in the shear layer of a separation bubble and propagated to the wall.

4.3 Structure of the Transition Process. Detailed results are presented to examine the evolution of turbulent momentum transport, as represented by the Reynolds shear stress, for two situations. By operating the LDV in the ''coincidence mode'' while measuring both u and v, one can determine the instantaneous and mean values of the product uv. The first case with $k^+ \approx 11$ corresponds approximately to Fig. 4(*a*) and to some extent to the study of Klebanoff and Tidstrom. The second is with $k^+ \approx 14$, or a slightly ''smaller'' roughness element than the middle case in Fig. 4, in order to review the development from an apparent near-laminar flow after reattachment to a nearly fully-developed turbulent boundary-layer.

Data are for a physical rib height of 4 mm at nominal freestream velocities of 1.25 and 1.75 m/s. The presentations provide distributions in two forms: normalized by freestream velocity and rib height first and then by wall variables. The former is useful in identifying inflectional profiles, reattachment and recirculation while the latter emphasizes the evolution of the viscous layer after reattachment. In both flows valid measurements were obtained to values of y^+ as low as 0.5 and less.

The *first example* can be considered to be a case of ''laminar recovery.'' Nominal values of roughness parameters were $k^+ \approx 11$, $k/\delta_1 \approx 0.6$, $\mathrm{Re}_k \approx 358$ and $\mathrm{Re}_{x,k} \approx 1 \times 10^5$. Figure 5(*a*) presents the results with vertical distance normalized by the rib height k so unity corresponds to the top of the element. Reynolds normal stresses, u^2 and v^2, are represented by their root mean square values, u' and v', and they are scaled equally in the figure. Mean streamwise velocity profiles show mean reattachment between 24 and 38 heights downstream, closer to the latter (Fig. 5(*a*)). The rib induces inflectional profiles above the recirculating region with the inflection points in the range $1.4 < y/k < 1.8$ relative to the rib. The shape factors show agreement with the Blasius value after $(x-x_k)/k \approx 60$, corresponding to the appearance of the mean profiles; before that station, the other profiles show evidence of inflectional regions. Freestream turbulence values are about one percent for u'/U_{inf} and about 0.8 percent for v'/U_{inf}. In general, v' decreases smoothly from its freestream value to zero at the wall, displaying no evident peaks or growth. In the third profile one sees a slight peak in u' near the wall though it is less than the freestream value; its location corresponds approximately to the dividing mean streamline. However, in the reversed flow towards the rib, u' decreases and both u' and v' are small, indicating a laminar recirculating flow.

In the flow after reattachment, the peak in u' near the wall can be seen to persist and spread outward slightly but, in the profile at $(x-x_k)/k \approx 60$, one can discern additional growth of u' (near $y/k \approx 1.5$). Further downstream, this latter growth persists at roughly the same height as the earlier inflectional region and its peak moves slightly further from the wall while spreading both inward and outward (not shown). The magnitudes of the maxima of u'/u'_{inf} at $(x-x_k)/k \approx 140$ ($\sim$1700 mm) and $(x-x_k)/k \approx 210$ ($\sim$2000 mm) are about 1.6 and 3.9, respectively, compared to less than 1.3 for the smooth plate at $x \approx 2200$ mm. From their experiments, Suder et al. [4] concluded that once the peak rms of velocity fluctuations in the boundary layer reached 3 to 3.5 percent, turbulent bursting started regardless of the bursting mechanism. Consequently, an effect of the rib has been to accelerate the growth of the streamwise fluctuations, leading to an earlier transition than for the smooth plate at the present freestream turbulence level.

In Fig. 5(*b*) one sees that downstream from $(x-x_k)/k \approx 60$ the mean velocity profiles demonstrate the characteristic shape of a Blasius profile when plotted in terms of semi-logarithmic coordinates. The boundary layer thickness δ^+ is about sixty for this flow. Again v' shows a mostly monotonic increase from the wall to its freestream value. At $(x-x_k)/k \approx 40$, u' does as well. But at $(x-x_k)/k \approx 60$ and 75 there is a flattening of $(u')^+$ for $y^+ > \sim 15$ and then for $(x-x_k)/k \approx 100$ a slight but distinctive peak appears. This peak grows and spreads but remains in the region $y^+ \approx 15$ to 30. The maximum value of $(u')^+$ at $(x-x_k)/k \approx 210$ is about 1.6 and is located at y^+ about 20; for fully-developed pipe flow the respective values would be about 2.6 at $y^+ \approx 15$ (Durst et al. [37]). Evidence of turbulent transport can be imagined in the profile of $(\overline{uv})^+$ at $y^+ \approx 15$ as early as $(x-x_k)/k \approx 40$. Though small, a peak can be seen in the profiles to $(x-x_k)/k \approx 145$. It appears to grow significantly by $(x-x_k)/k \approx 200$ (the intermediate region is hidden by the structure of the test section). Neglecting possibly spurious points, one sees that at $(x-x_k)/k \approx 210$ the peak value of $(\overline{uv})^+$ is about 0.1 and is in the region $15 < y^+ < 30$. Though not evident in the mean profiles, in this layer the turbulent momentum transport is already about ten percent of the molecular value near the wall (since $(\overline{uv})^+$ is defined as $\overline{uv}/u_\tau^2 = \rho\overline{uv}/\tau_w$).

The *second example* involves development of a turbulent boundary layer. Nominal values of roughness parameters were $k^+ \approx 14$, $k/\delta_1 \approx 0.7$, $\mathrm{Re}_k \approx 502$ and $\mathrm{Re}_{x,k} \approx 1.5 \times 10^5$. Mean streamwise velocity profiles again show mean reattachment between 24 and 38 heights downstream (Fig. 6(*a*)). Profiles above the recirculating region have inflection points in the range $1.6 < y/k < 1.7$ relative to the rib. The first profiles of u' and v' after the rib are at about six heights downstream. The value of u' decreases from its freestream value to near zero above the level of the rib; its magnitude is approximately the same or less than for the smooth plate at the same location. Since the flow must accelerate to clear the rib ahead of this region, a decrease would not be surprising. The values of v' show a smooth decrease from the freestream value to near zero as well. Thus, the flow passing over the rib can be considered to be a laminar flow despite the separated regions before and above the square element.

The Reynolds stresses mostly grow as the flow progresses downstream, as expected. The last station before reattachment displays a substantial increase in u' and a moderate increase in v'. The peak value of u' is about four times the freestream value. This peak is approximately at the dividing mean streamline and values then decrease as y increases towards the inflection point in the mean velocity profile. For v', the profile is smoother and broader with a peak of about 1.7 times its freestream value falling at $y/k \approx 2$, a bit beyond the inflection point of the mean velocity profile. Examining the u' and v' distributions in the recirculating region at the second and first profiles, one sees u' and v' decay in the reverse flow towards the rib as with the example for $k^+ \approx 11$.

After reattachment, the first mean velocity profile at $(x-x_k)/k \approx 40$ appears, to the eye, almost like a Blasius profile and the shape factor is near the value for laminar flow with a negligible streamwise pressure gradient. However, the turbulent fluctuations have grown substantially. Two peaks appear in the u' profile, one near the wall and the other at $y/k \approx 1.4$, near the upstream inflectional region. Both are approximately six times the freestream value and both grow as the flow proceeds downstream. The outer grows more rapidly at first but eventually the highest

Downloaded 03 Jun 2010 to 171.66.16.150. Redistribution subject to ASME license or copyright; see http://www.asme.org/terms/Terms_Use.cfm

values occur near the wall at $y/k \approx 1/2$ as the shape factor decreases to 1.6 and the mean velocity profile becomes more representative of a turbulent boundary layer. From $(x-x_k)/k \approx 50$ on, the v' distribution has smooth profiles with gentle maxima varying in position from $y/k \approx 2$ to 1.4 to 1.9–2 again, corresponding to the upstream inflectional region. It is not clear to this author whether there is any significance to the latter observation; once a fully-developed turbulent flow is established without "memory" of the rib, it would be fortuitous.

One might ask how the important viscous layer is established. Further insight is obtained by presenting the data of Fig. 6(*a*) in terms of wall coordinates, as done in Fig. 6(*b*). Only the stations following reattachment are shown since the wall shear stress is in the opposite direction in the recirculating region. At $(x-x_k)/k \approx 50$, the mean velocity profile still appears to correspond to a Blasius profile in semi-logarithmic coordinates with $\delta^+ \approx 80$. However, u^+ diverges from y^+ near $y^+ \approx 5$ as for the viscous layer of a turbulent boundary layer and values are below the old "buffer layer" approximation (Kays, Eq. 6-32 [38]) until $y^+ \approx 20$; this observation is an indication of significant momentum transport by other than molecular means in this range. The two peaks in $(u')^+$ are about 2.2 at $y^+ \approx 10$ and 2.9 at $y^+ \approx 35$. The maximum for $(v')^+$ is about unity at $y^+ \approx 40$. For fully-developed, high-Reynolds-number pipe flow, the values would be $(u')^+ \approx 2.6$ at $y^+ \approx 15$ and $(v')^+$ about unity at $y^+ \approx 100$ (Durst et al. [36]). The Reynolds shear stress demonstrates significant turbulent momentum transport in a thin layer, say $10 < y^+ < 40$; it increases smoothly to a maximum value $(\overline{uv})^+ \approx 0.9$ at $y^+ \approx 25$ and then decreases to the edge of the boundary layer.

As the flow progresses downstream, the mean velocity profiles evolve to the logarithmic-"law" shape characteristic of a turbulent boundary layer and δ^+ increases to about 200 at the last profile. In terms of wall coordinates, the $(v')^+$ maximum retains its value near unity and gradually shifts to higher y^+ without a change in profile shape; this trend corresponds to the peaks at larger y/k in Fig. 6(*a*) and to an increase in τ_w with x. The outer peak in $(u')^+$ retains its magnitude until $(x-x_k)/k \approx 90$ and then decreases and loses its identity. The inner peak grows slightly and becomes established at $(u')^+ \approx 2.5$ at $y^+ \approx 15$. The layer of turbulent momentum transport broadens as the flow proceeds downstream but after $(x-x_k)/k \approx 60$ it does not "penetrate" closer to the wall; the profile becomes approximately self-preserving in wall variables from the wall to $y^+ \approx 20$. The Reynolds shear stress distribution shows the maximum turbulent momentum transport located in a range about $20 < y^+ < 40$ until $(x-x_k)/k \approx 90$ with $(\overline{uv})^+$ values near unity, corresponding to a constant stress layer; then at later stations it "spreads" and decreases in magnitude. As a first approximation, one may say that the important viscous layer becomes established rapidly while the turbulent transport is developing and spreading in the outer region.

4 Concluding Remarks

With transitions induced by a square rib, new measurements of the evolution of the Reynolds stresses, v^2 and $\overline{uv}$, have been obtained at $y^+ < 30$ in transitional boundary layers on a flat plate. To our knowledge, such data were not previously available so close to the wall (in nondimensional terms) for transitional boundary layers. These data were made possible by use of the unique large Matched-Index-of-Refraction flow system at INEEL in conjunction with two-component laser Doppler velocimetry. Tabulated mean results are available for eight sets of experimental conditions, spanning a range from flows that do not undergo significant transition to ones which become turbulent in a short distance. These measurements extend the study of Klebanoff and Tidstrom to larger non-dimensional roughnesses, square ribs, moderate freestream turbulence levels and larger downstream distances. For small ribs (e.g., $k^+ \approx 11$), turbulence evolved from the inflectional region above the separated region downstream of the rib but laminar mean velocity profiles were recovered as in their case. For larger ribs ($k^+ > 14$) significant turbulence appeared in the reattaching shear layer as well and the viscous layer of a turbulent boundary layer began evolving soon after reattachment. The new data showed the development of the turbulent momentum transport across the boundary layer.

Acknowledgments

This research received financial support through the Laboratory Directed Research and Development Program of the INEEL under the United States Department of Energy Idaho Field Office Contracts DE-AC07-94ID13223 and DE-AC-99ID13727 and the Deutsche Forschungsgemeinschaft under projects Be 2129/1 and Du 101/44. The authors gratefully acknowledge this support of their work.

Nomenclature

H = shape factor, δ_1/Θ
k = roughness height
u,v = velocity, streamwise and wall-normal components
u',v' = rms fluctuations of velocity components; $u'_{\inf}$, value in freestream
u_τ = friction velocity, $(\tau_w/\rho)^{1/2}$
$\overline{uv}$ = Reynolds shear stress
U = mean velocity in streamwise direction; $U_{\inf}$, freestream value
x,y = spatial coordinates, streamwise and wall-normal; x_k, localization of trailing face of rib
δ = boundary layer thickness; δ_1, displacement thickness
Θ = momentum thickness
ν = kinematic viscosity
ρ = density
τ_w = wall shear stress

Nondimensional Variables and Parameters

c_f = local skin friction coefficient, $2\tau_w/(\rho U_{\inf}^2)$
k^+, y^+, δ^+ = value in wall coordinates, $(\ )u_\tau/\nu$
Re = Reynolds number; Re_k, roughness Reynolds number, $U_{\inf}k/\nu$; $\mathrm{Re}_{x,k}$, value at rib, $U_{\inf}x_k/\nu$; Re_Θ, based on momentum thickness
u^+ = streamwise velocity, U/u_τ
$(u')^+, (v')^+$ = rms fluctuations of velocity components, $(\ )/u_\tau$
$(\overline{uv})^+$ = Reynolds shear stress, $\overline{uv}/u_\tau^2$
η = Blasius variable, $y(vx/U_{\inf})^{-1/2}$

References

[1] Purtell, L. P., Klebanoff, P. S., and Buckley, F. T., 1981, "Turbulent Boundary Layer at Low Reynolds Number," Phys. Fluids, **24**, pp. 802–811.
[2] Murlis, J., Tsai, H. M., and Bradshaw, P., 1982, "The Structure of Turbulent Boundary Layers at Low Reynolds Numbers," J. Fluid Mech., **122**, pp. 13–56.
[3] Erm, L. P., and Joubert, P. N., 1991, "Low-Reynolds-Number Turbulent Boundary Layers," J. Fluid Mech., **230**, pp. 1–44.
[4] Suder, K. L., O'Brien, J. E., and Reshotko, E., 1988, "Experimental Study of Bypass Transition in a Boundary Layer," NASA TM 100913.
[5] Savill, A. M., 1993, "Some Recent Progress in the Turbulence Modelling of By-Pass Transition," *Near-Wall Turbulent Flows*, R.M.C. So, C. G. Speziale and B. E. Launder, eds., Elsevier, Amsterdam, pp. 829–848.
[6] Qui, S., and Simon, T. W., 1997, "An Experimental Investigation of Transition as Applied to Low Pressure Turbine Suction Surface Flows," ASME paper 97-GT-455. Also Simon, T. W., Qui, S., and Yuan, K., 2000, "Measurements in a Transitional Boundary Layer Under Low-Pressure Turbine Airfoil Conditions," NASA-CR-2000-209957.
[7] Lee, H., and Kang, S.-H., 2000, "Flow Characteristics of Transitional Boundary Layers on an Airfoil in Wakes," ASME J. Fluids Eng., **122**, pp. 522–532.
[8] Fage, A., 1943, "The Smallest Size of Spanwise Surface Corrugation Which Affects Boundary Layer Transition on an Airfoil," (British) Aero. Research Council, R&M 2120.
[9] Schlichting, H., 1979, *Boundary Layer Theory*, 7th ed., McGraw-Hill, New York.

Downloaded 03 Jun 2010 to 171.66.16.150. Redistribution subject to ASME license or copyright; see http://www.asme.org/terms/Terms_Use.cfm

[10] Masad, J. A., 1995, ''On the Roughness Reynolds Number Transition Criterion,'' ASME J. Fluids Eng., **117**, pp. 727–729.
[11] Durst, F., Fischer, M., Becker, S., Jovanovic, J., and Schenck, T., 1999, ''Untersuchung des laminar-turbulenten Strömungsumschlags hinter Rauigkeitselementen mit der Laser-Doppler-anemometrie,'' Tech. Report Du 101/44-2, LSTM Erlangen, Juli.
[12] Klebanoff, P. S., and Tidstrom, K. D., 1972, ''Mechanism by Which a Two-Dimensional Roughness Element Induces Boundary-Layer Transition,'' Phys. Fluids, **15**, pp. 1173–1188.
[13] Arnal, D., Juillen, J. C., and Olive, M., 1979, ''Etude expe'rimentale du de'clenchement de la transition par rugosite's en e'coulement uniforme incompressible,'' Tech. Report OA No. 4/5018 AYD, ONERA.
[14] Arnal, D., 1984, ''Description and Prediction of Transition in Two-Dimensional Incompressible Flow,'' AGARD-R-709, pp. 2–1 to 2–71.
[15] Kim, J., Moin, P., and Moser, R. D., 1987, ''Turbulence Statistics in Fully-Developed Channel Flow at Low Reynolds Number,'' J. Fluid Mech., **177**, pp. 133–166.
[16] Horiuhi, K., 1992, ''Establishment of the DNS Database of Turbulent Transport Phenomena,'' Report, Grants-in-aid for Scientific Research, No. 02302043.
[17] Laurien, E., and Kleiser, L., 1989, ''Numerical Simulation of Boundary-Layer Transition and Transition Control,'' J. Fluid Mech., **199**, pp. 403–440.
[18] Fasel, H., Rist, U., and Konzelmann, U., 1990, ''Numerical Investigation of the Three-Dimensional Development in Boundary-Layer Transition,'' AIAA J., **28**, pp. 29–37.
[19] Spalart, P. R., 1993, ''Numerical Study of Transition Induced by Suction Devices,'' *Near-Wall Turbulent Flows*, R. M. C. So, C. G. Speziale, and B. E. Launder, eds., Elsevier, Amsterdam, pp. 849–858.
[20] Narasimha, R., 1998, Post Workshop Summary, Minnowbrook II, 1997 Workshop on Boundary Layer Transition in Turbomachines, J. E. laGraff and D. E. Ashpis, eds., NASA/CP-1998-206958, pp. 485–495.
[21] Patel, V. C., 1998, ''Perspective: Flow at High Reynolds Number and Over Rough Surfaces—Achilles Heel of CFD,'' ASME J. Fluids Eng., **120**, pp. 434–444.
[22] Corino, E. R., and Brodkey, R. S., 1969, ''A Visual Investigation of the Wall Region in Turbulent Flow,'' J. Fluid Mech., **37**, pp. 1–30.
[23] Budwig, R., 1994, ''Refractive Index Matching Methods for Liquid Flow Investigations,'' Exp. Fluids, **17**, pp. 330–335.
[24] Condie, K. G., Stoots, C. M., Becker, S., Alahyari, A. A., Durst, F., and McEligot, D. M., 1998, ''The Structure of Boundary Layer Transition Induced by a Square Rib (A New Large-Scale MIR Flow System for Measurements of Boundary Layer Transition,'' Tech. Report INEEL/EXT-98-01039, Idaho National Engineering and Environmental Laboratory.
[25] Stoots, C. M., Becker, S., Condie, K. G., Durst, F., and McEligot, D. M., 2001, ''A Large-Scale Matched-Index-of-Refraction Flow Facility for LDA Studies Around Complex Geometries,'' Exp. Fluids, **30**, pp. 391–398.
[26] Durst, F., Keck, T., and Kleine, R., 1979, ''Turbulence Quantities and Reynolds Stress in Pipe Flow of Polymer Solutions Measured by Two-Channel Laser-Doppler Anemometry,'' Proc., 6th Symp. On Turbulence, Rolla, Mo.
[27] Strunz, M., 1987, Ein Laminarwasserkanal zur Untersuchung von Stabilitätsproblemen in der Strömungsgrenzschicht, Doctoral thesis, U. Stuttgart.
[28] Wiegand, T., 1996, ''Experimentelle Untersuchungen zum laminar-turbulenten Transitionsprozeß eines Wellenzuges in einer Plattengrenzschict,'' Doctoral thesis, U. Stuttgart.
[29] Hoesel, W., and Rodi, W., 1977, ''New Biasing Elimination Method for Laser Doppler Velocimeter Counter Processing,'' Rev. Sci. Instrum., **48**, pp. 910–919.
[30] Tummers, M. J., 1999, ''Investigation of a Turbulent Wake in an Adverse Pressure Gradient Using Laser Doppler Anemometry,'' Ph.D. thesis, Tech. Univ. Delft.
[31] MacManus, Eaton, D. J., Barrett, R., Rickards, J., and Swales, C., 1996, ''Mapping the Flow Field Induced by a HLFC Perforation Using a High Resolution LDV,'' AIAA paper 96-0097.
[32] Calabrese, R. V., and Middleman, S., 1979, ''The Dispersion of Discrete Particles in a Turbulent Flow Field,'' AIChE J., **25**, No. 6, pp. 1025–1035.
[33] Schwartz, A. C., Plesniak, M. W., and Murthy, S. N. B., 1999, ''Turbulent Boundary Layers Subjected to Multiple Strains,'' ASME J. Fluids Eng., **121**, pp. 526–532.
[34] Bendat, J. S., and Piersol, A. G., 1986, *Random Data Analysis and Measurement Procedures*, Wiley, New York.
[35] Orr, B., Thomson, E., and Budwig, R. S., 1997, ''Drakeol 5 Thermophysical Property Measurements,'' Mech. Engr. Dept. U. Idaho, Moscow, 18 Dec.
[36] Lienhart, H., and Becker, S., 1994, ''LDA-Untersuchungen zur Grenzschichttransition,'' 9 DGLR-Fach-Symposium, Strömung mit Ablösung, DGLR—Bericht 94-04, Bonn, pp. 25–31.
[37] Durst, F., Jovanovic, J., and Sender, J., 1995, ''LDA Measurements in the Near Wall Region of a Turbulent Pipe Flow,'' J. Fluid Mech., **295**, pp. 303–335.
[38] Kays, W. M., 1966, *Convective Heat and Mass Transfer*, McGraw-Hill, New York.

Downloaded 03 Jun 2010 to 171.66.16.150. Redistribution subject to ASME license or copyright; see http://www.asme.org/terms/Terms_Use.cfm

Modification of Near-Wall Structure in a Shear-Driven 3-D Turbulent Boundary Layer

Robert O. Kiesow
Westinghouse Govt. Services Co. LLC,
Electro-Mechanical Division,
1000 Cheswick Ave.,
Cheswick, PA 15024

Michael W. Plesniak[1]
Purdue University,
School of Mechanical Engineering,
Maurice J. Zucrow Laboratories,
West Lafayette, IN 47907

The near-wall physics of a planar, shear-driven, 3-D turbulent boundary layer with varying strengths of crossflow are examined. Flow visualization data reveals a reduction of mean streak length by as much as 50% with increasing spanwise shear. Power spectra of velocity confirm this shift towards higher temporal frequencies, corresponding to decreased streamwise length scales. PIV measurements indicate a significant modification of the inner region of the boundary layer with increasing spanwise shear. Streamwise velocity profiles exhibit an increasing velocity deficit with increased crossflow. Increased levels of the normal Reynolds stresses $\overline{u'^2}$ *and* $\overline{v'^2}$ *and an increase in the* $-\overline{u'v'}$ *Reynolds shear stress are also observed. Modifications in the spanwise and transverse vorticity were also observed at higher shear rates.* [DOI: 10.1115/1.1431269]

Introduction

Most high Reynolds number flows of engineering interest are three-dimensional and their extra rates of strain result in complex flow fields that are not fully understood (see reviews by Johnston and Flack [1], Eaton [2], Ölçmen and Simpson [3]). Key features include noncolateral shear stress and strain rate vectors and decreasing ratio of the shear stresses to the turbulent kinetic energy with increasing three-dimensionality. These are indicators that the skewing has a significant effect on the structure of turbulence. A common feature of previous shear-driven experiments (e.g., Driver and Johnston [4]) is their complex geometry and multiple strain rates. Computational studies (Moin et al. [5], Sendstad and Moin [6]) have used direct numerical simulation (DNS) to examine planar channel flows subject to transverse pressure gradient. A study by Coleman et al. [7] includes both spanwise shear and transverse pressure gradient effects on a plane channel flow. More recent large eddy simulations (LES) by Le et al. [8] and Kannepalli and Piomelli [9] of shear-driven three-dimensional turbulent boundary layers (3DTBLs) have provided further insight into the near-wall flow physics of such flows. These computational studies, along with pressure-driven and shear-driven experimental investigations, have contributed to the understanding of 3DTBLs.

Complete comprehension of near-wall phenomena in these complex flows is still elusive, indicating a continued need for experimental and computational studies to expand the understanding of 3DTBLs and their associated turbulence structure. The objective of the current study is to investigate the flow physics of a nonequilibrium, planar, shear-driven 3DTBL having a simple geometry and also variation in the strength of the crossflow. The effects of crossflow are thus isolated from the confounding effects of streamwise pressure gradient, allowing closer examination of the near-wall structural features of the 3DTBL. Examination of the separate effects of skewing and streamwise pressure gradient in this apparatus will complement numerical studies, e.g. the DNS of Coleman et al. [7]. This investigation is performed using flow visualization and particle image velocimetry (PIV) as well as using hot-film anemometry to evaluate the power spectra of the streamwise velocity.

Experimental Apparatus and Techniques

The planar, shear-driven 3DTBL is studied in a low-speed recirculating water tunnel specifically designed for this purpose. This facility provides a flat and smooth test surface along which a canonical 2-D boundary layer develops and is subsequently subjected to spanwise shear to generate a 3-D boundary layer. The Reynolds number, based on the momentum thickness, at the measurement location is $\mathrm{Re}_\theta = 1450$, and the boundary layer thickness is $\delta = 50$ mm. A schematic of the 3-D turbulent boundary layer test plate is shown in Fig. 1. This test plate supports a shearing device integrated into a section of the sidewall to provide a spanwise-translating motion, with variable speed capability. The shearing device is an enclosed spanwise-translating belt mechanism embedded in the wall with a 12.7 cm wide by 38.1 cm high section of the belt exposed in the plane of the test section side wall. This corresponds to 50% of the span of the test section height and approximately two and a half boundary layer thicknesses in the streamwise direction. Considerable attention was given to the design of the shearing mechanism in order to minimize flow disturbances other than the desired spanwise translation of the belt. The entire belt mechanism was submersed in water to eliminate air entrainment. In addition, tensioning and tracking features were included in the design of the belt mechanism to control both the flatness and positioning of the belt during operation. The shear-generating mechanism was operated at belt velocity ratios of $W_r = 0$, 1.0, 2.0 and 2.75, where W_r is the spanwise belt speed divided by the freestream velocity of the boundary layer, $U_\infty = 27$ cm/s.

Flow visualization using direct dye injection was performed to examine the structural features of the shear-driven boundary layer. The dye was introduced into the flow by means of two 20.3 cm long dye slots located approximately one and a half boundary layer thicknesses upstream and downstream of the translating wall, respectively. The dye solution consisted of fluorescein disodium salt dissolved in water at a concentration of 4 ppm. A laser light sheet, formed using a Coherent I-90 5W Argon-Ion cw laser and sheet-forming optics, was oriented in the xz-plane at $y = 0.5$ mm and $y = 1.5$ mm and was used to illuminate the fluorescent dye in the near-wall region.

Hot-film anemometry measurements were used to obtain the power spectral density of the streamwise velocity over a range of belt operating conditions. A DANTEC model R01 hot-film probe was used in conjunction with a TSI IFA-300 constant temperature anemometry system. The hot-film probe was positioned along the spanwise centerline approximately 1.5 δ downstream of the trail-

[1]Corresponding Author.

Contributed by the Fluids Engineering Division for publication in the JOURNAL OF FLUIDS ENGINEERING. Manuscript received by the Fluids Engineering Division June 2, 2000; revised manuscript received August 24, 2001. Associate Editor: P. W. Bearman.

 Copyright © 2002 by ASME

Downloaded 03 Jun 2010 to 171.66.16.150. Redistribution subject to ASME license or copyright; see http://www.asme.org/terms/Terms_Use.cfm

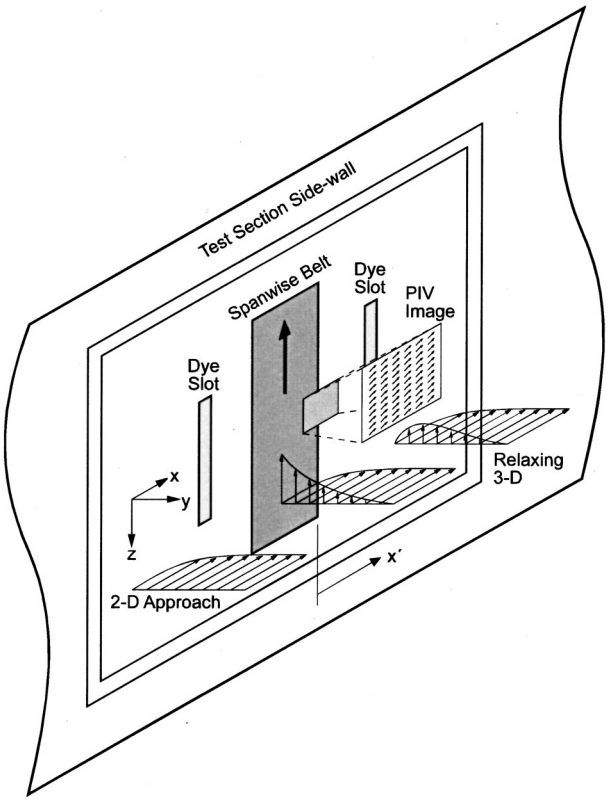

Fig. 1 Schematic of 3-D turbulent boundary layer test plate

ing edge of the translating belt. Measurements were acquired at a sampling rate of 20 Hz and filtered at 10 Hz to obtain spectra over a 10 Hz range at a resolution of 0.005 Hz. A sampling rate of 200 Hz and filtering at 100 Hz was also used to examine a larger frequency range at a resolution of 0.05 Hz.

Additionally, a DANTEC FlowMap PIV 2100 processor was used to obtain instantaneous measurements of two components of velocity in the *xy*-plane (side view) and *xz*-plane (plan view). The optical system consists of a NewWave 100mJ Nd:YAG laser with software-driven controls for the pulse separation time. Resolution of particle movement was found to be optimal with a pulse separation time of $\Delta t = 0.9$ ms. The laser beam propagates through sheet-forming optics to form a sheet that is approximately 1 mm thick and 150 mm wide. A Kodak® MEGAplus ES 1.0 CCD cross-correlation camera with a $1008(\mathrm{H}) \times 1018(\mathrm{V})$ pixel array provides on-line imaging capability. Controlled image acquisition, storage and display, and processing of the image to obtain the velocity data are accomplished on a personal computer running FlowManager software. The flow was seeded with 5 micron silicon carbide particles at a concentration of approximately 20 particles per mm^3. Typically, thirty images were ensemble-averaged to provide the mean flow velocities that were subtracted from an instantaneous flow image to reveal secondary structures. In addition, up to 250 images were ensemble-averaged to obtain statistics for the mean flow velocity, rms velocities and Reynolds stresses.

Velocity vectors were determined from interrogation regions having a size of $0.84\,\mathrm{mm} \times 0.84\,\mathrm{mm}$. The overall uncertainty in the velocity measurements can be determined at a 95% confidence level following the methods of Moffat [10]. The uncertainty in the U and V velocities is estimated at $\pm 3\%$ of the local measurement. Uncertainties in the Reynolds normal stresses $\overline{u'^2}$ and $\overline{v'^2}$ are estimated to be $\pm 9\%$ of the local value. The uncertainty in the primary Reynolds shear stress, $-\overline{u'v'}$, is estimated to be on the order of $\pm 30\%$ of the local measurement. This is a consequence of the limited ensemble size of 250 images used to estimate statistical quantities such as second order moments.

Results

Laser-induced fluorescence (LIF) flow visualization studies were performed to investigate the flow structure in the near-wall region of the 3DTBL. The dye was introduced into the flow through the downstream dye slot located approximately one and a half boundary layer thickness downstream of the translating belt. The illuminating light sheet was positioned parallel to the wall at wall-normal locations of approximately $y = 0.5$ mm ($y^+ \approx 6$) and $y = 1.5$ mm ($y^+ \approx 18$) and allowed a 150 mm streamwise $\times$ 200 mm spanwise section of the near-wall region to be visualized with the fluorescent dye. Photographs of the LIF flow visualization at $y = 0.5$ mm revealed a modification of the near-wall streak structure due to the crossflow as reported in Kiesow and Plesniak [11,12]. In the presence of crossflow, the streak length is reduced by as much as 50% compared to the 2-D base with no spanwise shear. However, there does not appear to be any significant modification of the streak spanwise spacing.

In order to quantify the observations of the LIF flow visualization, LIF images were digitized and with image enhancement, the wall streaks were identified, counted, and measured. The length of the individual low-speed streaks was measured along the imposed flow direction. Although this procedure entailed a certain amount of subjectivity in identifying streaks and determining their beginning and ends, the procedure was applied consistently to all of the images. Therefore, the resulting trends represent a reasonable picture of modifications to the streak structure. The image analysis resulted in sample sizes of approximately 900 streaks for the $W_r = 0$ case and 1300 streaks for the $W_r = 2.0$ case. The resulting histograms for the streak length for the base case and at a velocity ratio of 2.0 are shown in Fig. 2. These histograms clearly show a shift towards smaller streamwise length scales with increasing spanwise shear and a narrower distribution of streak sizes compared to the 2-D base case. Both histograms are asymmetric; however, the $W_r = 2.0$ case exhibits higher skewness and kurtosis compared to the base case. Smaller standard deviations for the sheared cases, along with the reduction in mean streak length, are strong indications of a reduction in the streamwise length scales of the wall streaks in the near-wall region. Similar results were reported in a DNS of a channel flow with spanwise pressure gradient by Sendstad and Moin [6] as well as by Le et al. [8] of a DNS and LES of a 3DTBL generated by a spanwise-moving wall in a channel. Kannepalli and Piomelli [9] observed similar modifications of flow structures in their large-eddy simulation of a shear-driven 3DTBL with significant disruption of near-wall streak structures occurring at the moving/stationary wall junction as the flow transitions to the stationary wall condition.

Plots of the one-dimensional normalized power spectra over a frequency range of 0 to 10 Hz for the 2-D base case and for $W_r = 2.0$ are shown in Fig. 3. In these plots the power spectral density is premultiplied by the frequency and divided by the variance, so that the peak is centered about the most energetic frequencies. The effect of increasing spanwise shear is to shift the energy peak towards higher temporal frequencies, or smaller streamwise scales. For the 2-D base case, the most energetic frequencies are centered at 4 Hz. In contrast, for the $W_r = 2.0$ case, the peak energy has not only shifted to around 10 Hz, but the boundary layer has also become more energetic at these flow scales. Additional power spectra over a frequency range of 0 to 100 Hz were acquired to examine the energy content over a broader frequency range. These power spectra exhibited the expected dissipation and eventual drop-off of the flow energy at the higher frequencies but are not included here since the focus of the measurements was at the lower frequencies associated with the modifications of the streak structure. Based on the aforementioned spectra and the two other cases examined, i.e., $W_r = 1.0$ and 2.75 (not shown), the effect of increasing spanwise shear is to cause a progressive

Downloaded 03 Jun 2010 to 171.66.16.150. Redistribution subject to ASME license or copyright; see http://www.asme.org/terms/Terms_Use.cfm

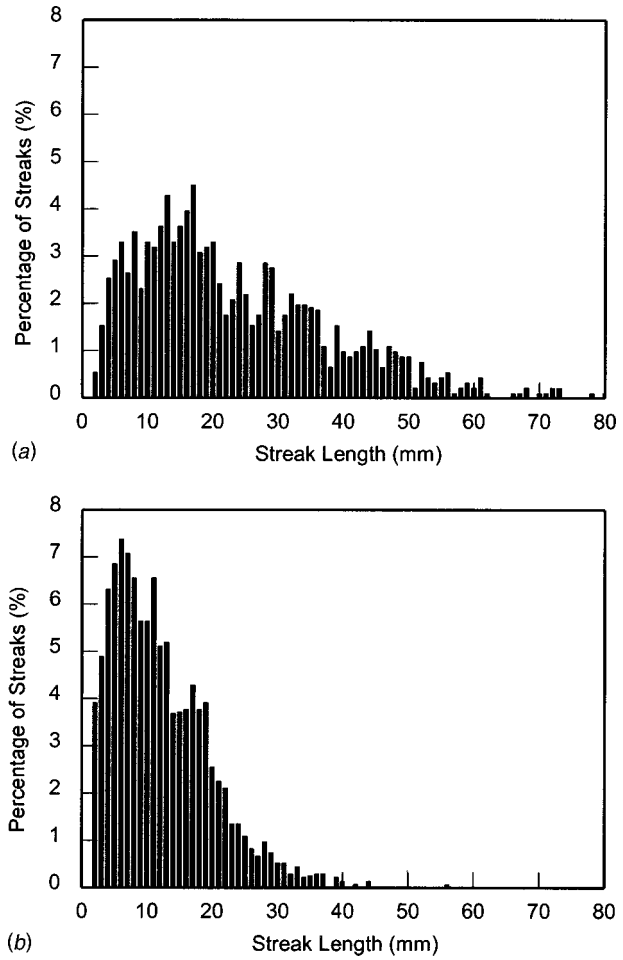

Fig. 2 Histograms of streak length for (*a*) $W_r=0$ and (*b*) $W_r=2.0$

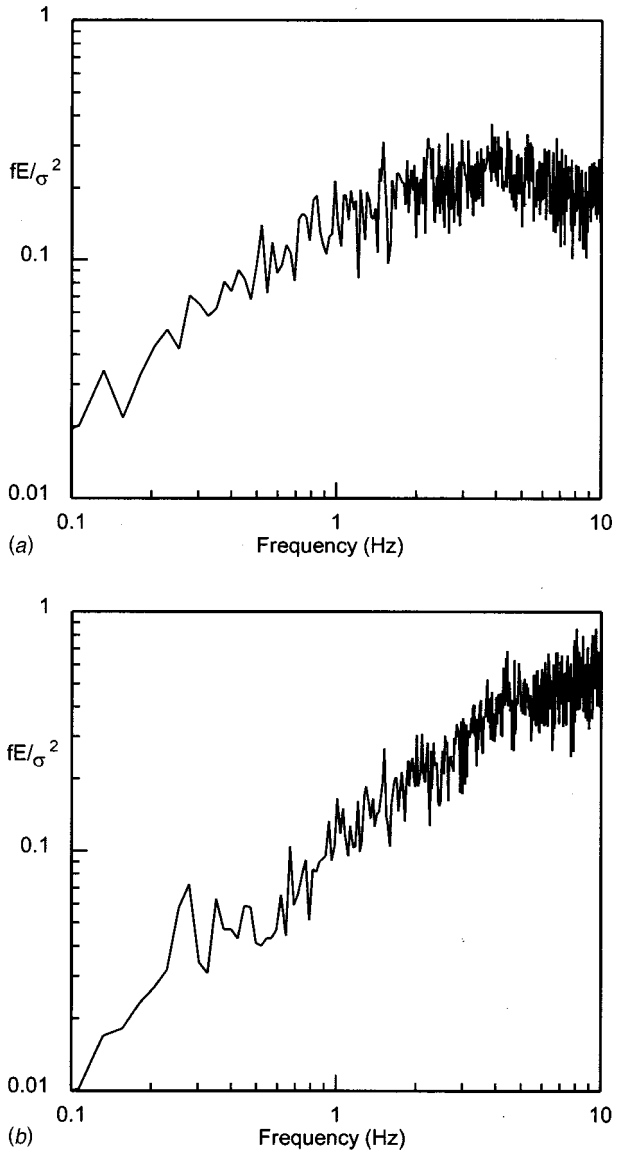

Fig. 3 Nondimensionalized power spectra at 1.5 δ downstream of belt edge at y=6 mm for (*a*) $W_r=0$ and (*b*) $W_r=2.0$

growth of the flow energy and to shift the peak energy to higher frequencies. This observation of more energy at the higher frequencies and corresponding smaller scales corroborates the observed shift towards smaller streamwise length scales in the LIF flow visualization results.

Particle image velocimetry measurements were obtained in a plane parallel to the approach flow and parallel to the wall (*xz*-plane) and in a plane that is parallel to the flow and perpendicular to the wall (*xy*-plane). Image analysis produced simultaneous measurements of *U* and *W* components of velocity in the *xz*-plane or *U* and *V* velocities in the *xy*-plane at a maximum of 6972 points over a uniform grid in an image region approximately 54 mm square. Measurements were obtained with the belt stationary in order to establish the base case for the 2-D boundary layer and with the belt operating at velocity ratios of $W_r=1.0$, 2.0 and 2.75. The image region discussed here was located approximately on the spanwise centerline at a streamwise location that extended from $x'/\delta=-0.4$ upstream to $x'/\delta=0.6$ downstream of the translating wall reference ($x'=0$ at the trailing edge of the belt). Additional PIV measurements were acquired at streamwise locations extending from $0.8\leqslant x'/\delta\leqslant 1.8$ and $1.8\leqslant x'/\delta\leqslant 2.8$. Results of these measurements have been reported in Kiesow and Plesniak [12,13] and indicated the relaxation of the 3DTBL back to a 2DTBL with extended streamwise distance.

Representative plots of the instantaneous velocity field in the *xz*-plane at $x'/\delta=-0.4$ and $y/\delta\approx 0.01$ for velocity ratios of $W_r=0.0$ and 2.75, are presented in Fig. 4. Only the lower half of the total spanwise extent of the image region is plotted to better highlight flow structures. The trailing edge of the belt at $x'=0$ ($x'/\delta=0$) is indicated by the dashed line and the motion of the belt is in the plane of the paper and upward. Although the wall friction velocity is the preferred parameter for normalizing turbulence data, the friction velocity could not be reliably determined in this experimental study. Therefore, the normalization was performed in terms of outer variables using the freestream velocity, U_∞, and the boundary layer thickness, δ. The instantaneous flow field for the 2-D base case (in Fig. 4(*a*)) exhibits several regions of lower velocity, which are associated with the near-wall streaky structure of the turbulent boundary layer. With increased spanwise shear, as in the $W_r=2.75$ case shown in Fig. 4(*b*) the flow field becomes increasingly non-uniform (i.e., unequal velocities) with more numerous organized regions of strong fluctuating velocities, particularly over the belt surface at $x'/\delta<0$. The velocity vectors indicate significant flow turning but the flow field is highly perturbed and nonuniform, with numerous concentrated regions of reduced velocity that do not appear to have any preferential alignment with the mean flow direction. These perturbed regions extend upstream over the belt surface, as well as downstream of the belt/stationary wall junction.

Downloaded 03 Jun 2010 to 171.66.16.150. Redistribution subject to ASME license or copyright; see http://www.asme.org/terms/Terms_Use.cfm

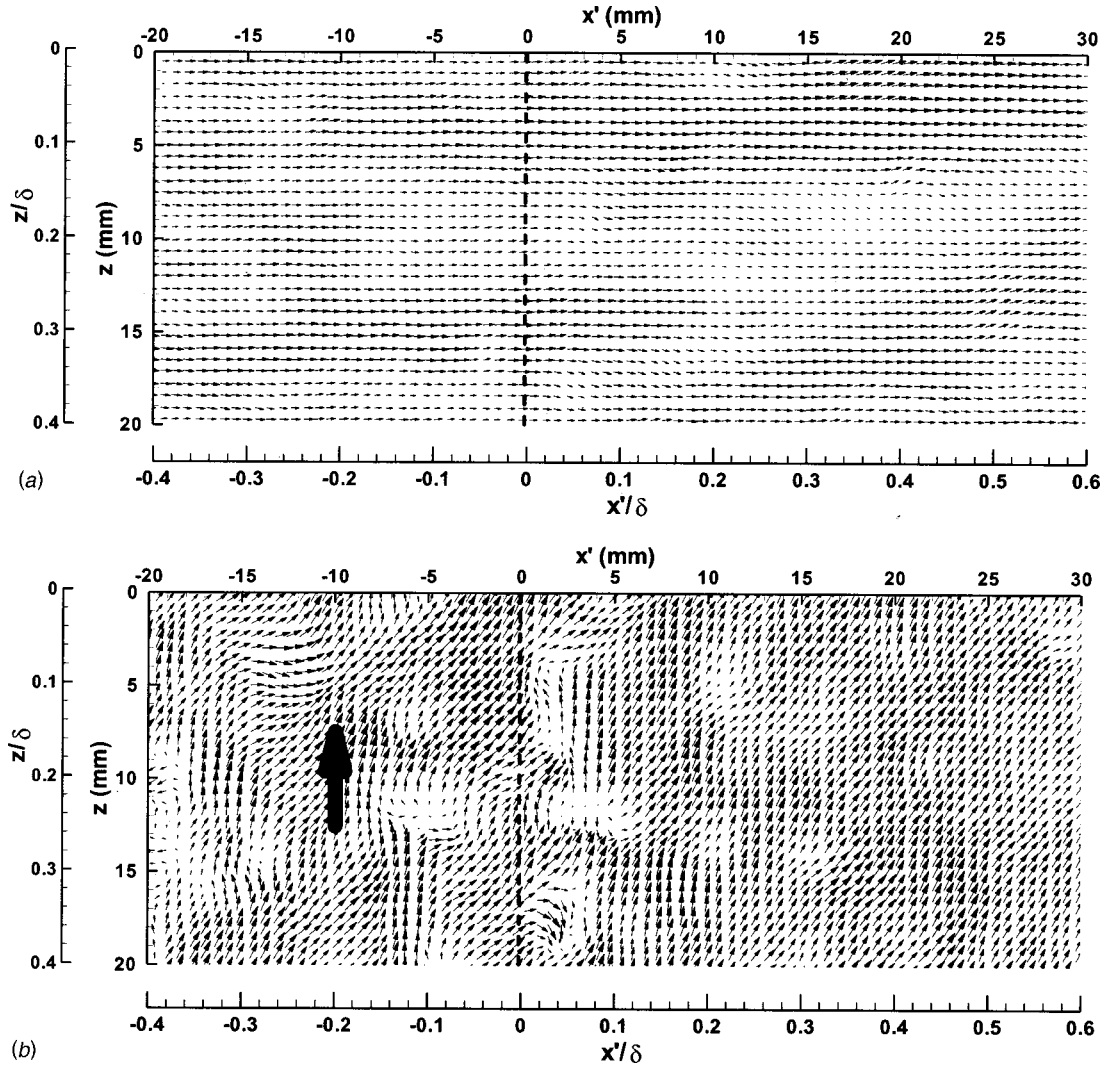

Fig. 4 Instantaneous velocity field in *xz*-plane at y/δ=0.01 from x′/δ=−0.4 to 0.6 for (*a*) stationary belt (W_r=0.0) and (*b*) W_r=2.75

Contours of the instantaneous transverse vorticity, ω_y, corresponding to the *xz*-plane vector plots are shown in Fig. 5 for the stationary belt case ($W_r=0.0$) and belt velocity ratio $W_r=2.75$ at $x'/\delta=-0.4$ and $y/\delta\approx 0.01$. The transverse vorticity in the 2-D base case typically ranges from ± 40 s^{-1} and the vorticity contours are somewhat elongated and aligned horizontally with the mean flow direction. In the case of the more highly sheared flow, with $W_r=2.75$ (in Fig. 5(*b*)), the fluctuating transverse vorticity occurs in smaller, more concentrated regions with strong negative and positive values exceeding 100 s^{-1}, particularly over the belt surface and belt-wall junction. These regions do not tend to have any preferential alignment with respect to the mean flow direction and the disruption of near-wall vorticity with spanwise shear is associated with the observed break-up of streak structure.

Representative plots of the secondary flow fields in the *xy*-plane for the 2-D base case of $W_r=0$ and for the most strongly sheared case of $W_r=2.75$ are shown in Fig. 6. The secondary velocity field is obtained by subtracting the local mean velocity at each *y*-normal location in order to reveal secondary flow patterns. The secondary velocity field for $W_r=0$ is fairly uniform with minimal variations in the magnitude of the secondary velocities and some regions of mild recirculation. In contrast, the secondary velocity field for the most strongly sheared case ($W_r=2.75$) exhibits much larger variations in the secondary velocity magnitude. More frequent and significantly stronger regions of recirculation are also observed. These regions extend further into the boundary layer (out to $y\approx 15$ mm or $y/\delta\approx 0.3$) compared to the 2-D case.

Contour plots of the instantaneous spanwise vorticity, ω_z, for the aforementioned vector fields, are shown in Fig. 7. The spanwise vorticity for the 2-D base case ($W_r=0$) is concentrated in a layer (of negative vorticity) near the surface ($y<5$ mm), where the velocity gradients are highest. The addition of spanwise shear results in a significant alteration of the ω_z distribution. With increased crossflow, the layer of spanwise vorticity along the surface is broken up and more isolated regions of both positive and negative sign extend further into the boundary layer. For the most strongly sheared case ($W_r=2.75$) numerous counter-rotating vortices of similar magnitude appear to exist. They are lifted off the surface and extend out into the boundary layer (out to $y\approx 15$ mm or $y/\delta\approx 0.3$). It is hypothesized that these counter-rotating vortices are representative of cross-sections of hairpin vortices that have been skewed in the spanwise direction due to the spanwise velocity in this region. These counter-rotating structures observed in these contour plots share many similarities with studies by Zhow et al. [14] in which PIV was used to reveal the formation of hairpin vortices in a turbulent channel flow. The lifting of vortical flow regions is associated with increased momentum transfer between high and low momentum fluid leading to the observed thickening of the inner region of the turbulent boundary layer.

Downloaded 03 Jun 2010 to 171.66.16.150. Redistribution subject to ASME license or copyright; see http://www.asme.org/terms/Terms_Use.cfm

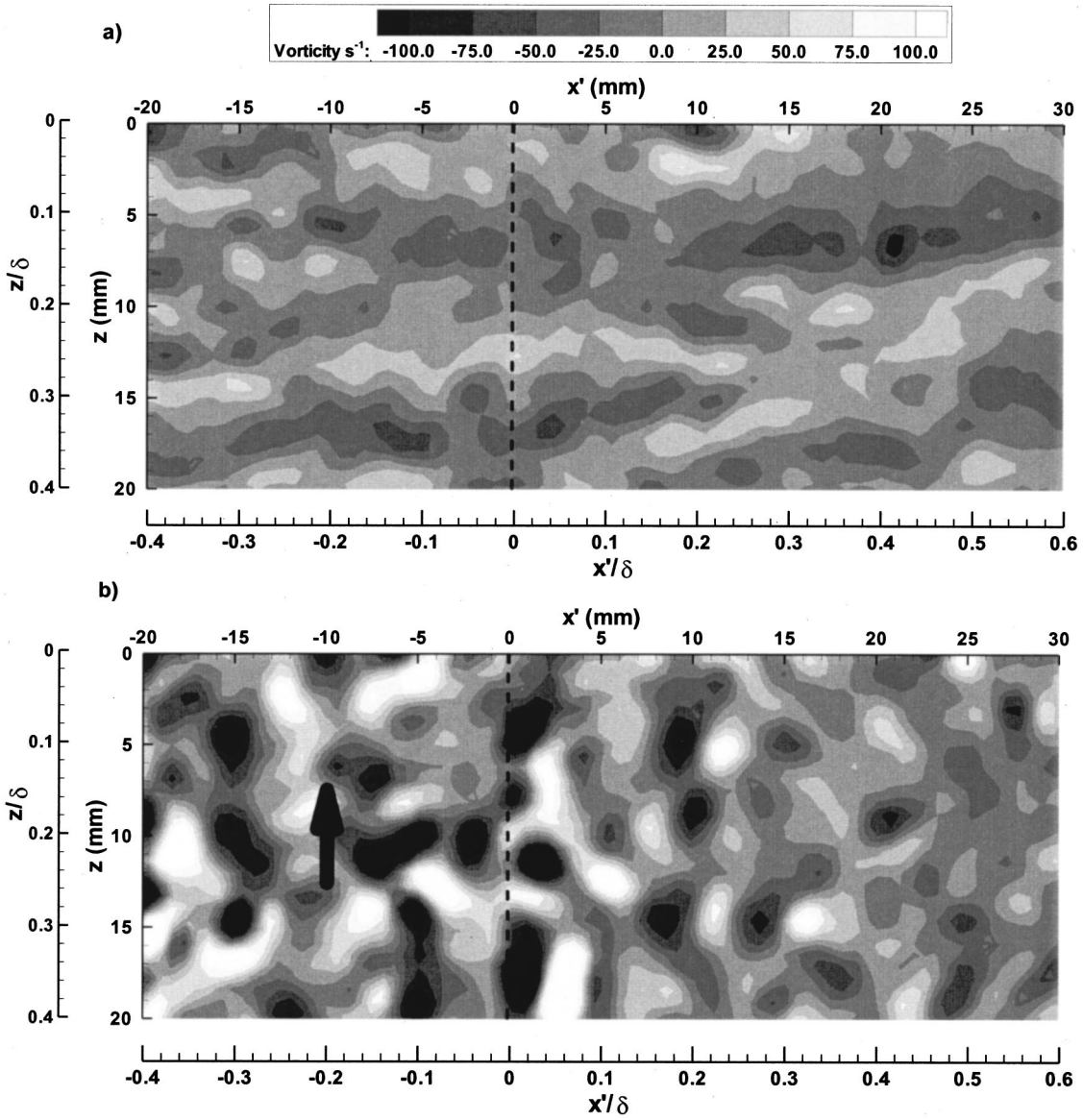

Fig. 5 Contour plots of instantaneous transverse vorticity, ω_y, at belt trailing edge for velocity ratios (*a*) $W_r=0$ and (*b*) $W_r=2.75$

Mean statistics were determined from an ensemble average of 250 vector maps with 3969 points in each image. Profiles obtained by Spalart [15] using DNS of a 2-D flat plate boundary layer are plotted with solid lines to provide a benchmark for the PIV profiles. Note that exact agreement is not expected because of the difference in freestream turbulence levels between the experiment and simulation. Boundary layer profiles for the four operating conditions at a streamwise location of $x'/\delta=0.5$, corresponding to approximately half a boundary layer thickness downstream of the belt, are shown in Fig. 8. These profiles of the mean streamwise velocity develop an increasingly severe velocity deficit in the inner region of the boundary layer with increasing spanwise shear. This velocity deficit is not very pronounced for the $W_r=1.0$ case with mild crossflow. However, for the higher imposed shear ($W_r=2.0$ and 2.75) the deceleration of the streamwise velocity is significant, with the deficit region extending out to a y/δ of approximately 0.4. This velocity deficit is attributed to increased turbulence and a corresponding increase in the wall shear stress resulting in increased drag on the wall surface. This velocity deficit can be further explained by considering a momentum balance since the increased turbulence must be compensated for by a velocity decrease in order to conserve momentum. Increased turbulence production and an associated increase in the streamwise drag are features reported for a fully developed shear layer in the LES of a 3DTBL by Le et al. [8]. In the outer region of the boundary layer ($y/\delta>0.4$) the profiles essentially collapse onto a common curve. A strong velocity deficit is still evident for highly sheared cases at subsequent downstream locations (Kiesow and Plesniak [13]). However, the magnitude of the streamwise velocity deficit begins to decrease, indicating a relaxation of the 3-D flow.

Profiles of the normal Reynolds stress $\overline{u'^2}$ are shown in Fig. 9 for $W_r=0$, 1.0, 2.0, and 2.75 at a streamwise location of $x'/\delta=0.5$. These profiles were obtained from the ensemble average of three columns of PIV velocity vectors to reduce the scatter, i.e., spatially averaged over 1.7 mm, or 0.04 δ. For the 2-D base case, the peak in the $\overline{u'^2}$ profile occurs near the wall, at approximately the same location as the benchmark [15], but with higher intensity. Weak spanwise shear ($W_r=1.0$) causes an initial decrease in the magnitude of the $\overline{u'^2}$ normal stress in the near-wall region, compared to the 2-D case. However, the more highly sheared cases

Downloaded 03 Jun 2010 to 171.66.16.150. Redistribution subject to ASME license or copyright; see http://www.asme.org/terms/Terms_Use.cfm

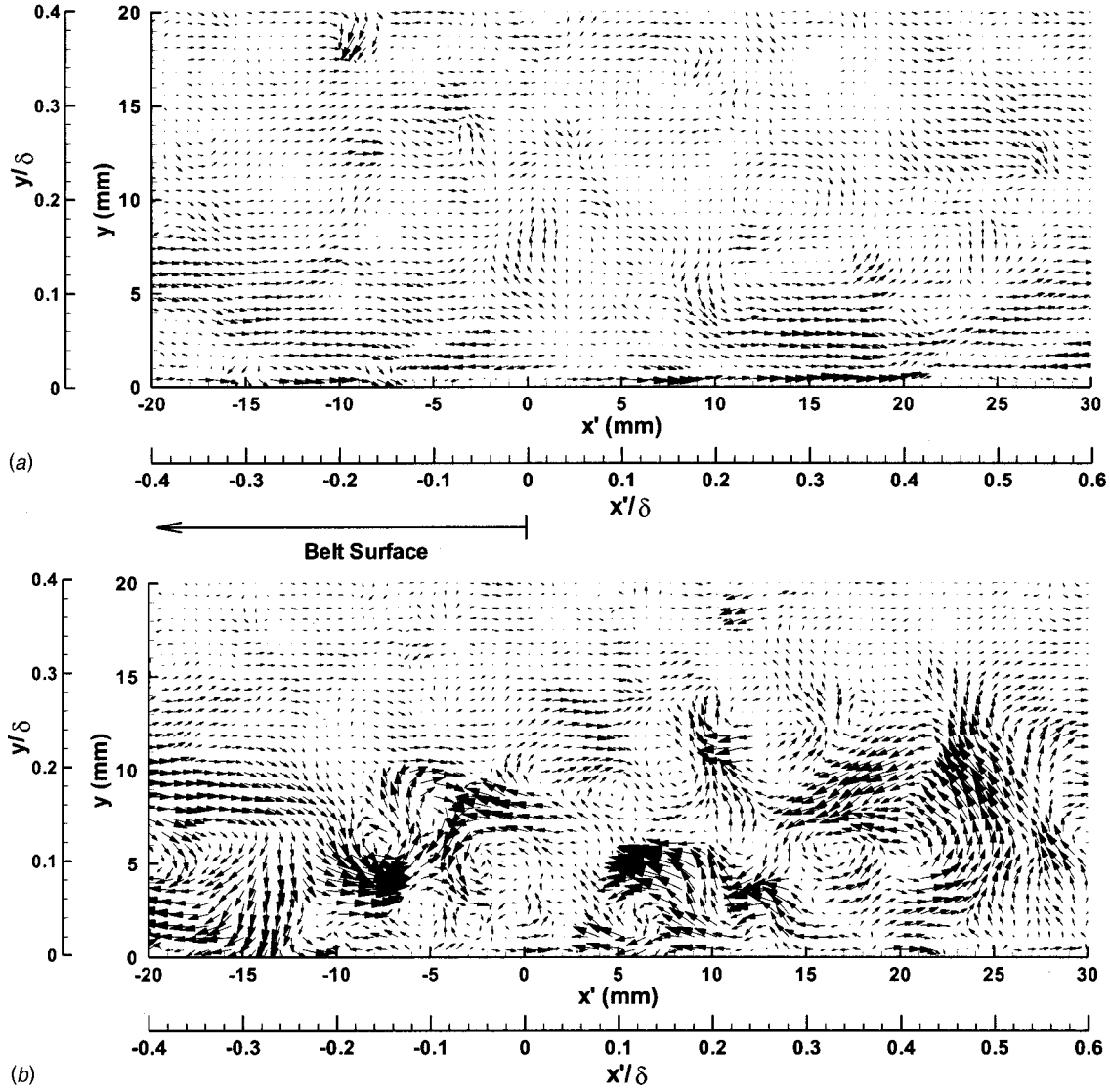

Fig. 6 Secondary velocity fields in the *xy*-plane at belt trailing edge for belt velocity ratios (*a*) $W_r=0$ and (*b*) $W_r=2.75$

($W_r=2.0$ and 2.75) experience an increase in $\overline{u'^2}$ out to $y/\delta \approx 0.4$ with an associated monotonic shift in the peak value away from the wall as spanwise shear increases. For the most highly sheared case ($W_r=2.75$) the peak has shifted out to $y/\delta \approx 0.2$. In the outer region of the boundary layer ($y/\delta > 0.4$) the profiles are similar and collapse onto a common curve.

Corresponding profiles for the $\overline{v'^2}$ normal Reynolds stress at $x'/\delta=0.5$ for all four belt velocity ratios are presented in Fig. 10. The effect of increasing spanwise shear is a monotonic increase of the $\overline{v'^2}$ normal stress away from the wall. For the most highly sheared case ($W_r=2.75$) the magnitude of $\overline{v'^2}$ is almost an order of magnitude higher compared to the 2-D base case. A second effect of increased spanwise shear is to shift the peak in the $\overline{v'^2}$ stress away from the wall. For the mildly sheared case ($W_r=1.0$) the peak value occurs at $y/\delta \approx 0.1$ while for the most strongly sheared case ($W_r=2.75$) the peak value has shifted out to $y/\delta \approx 0.2$. However, in the outer region of the boundary layer ($y/\delta > 0.4$) the profiles again collapse onto a common curve.

Profiles of the primary Reynolds shear stress $-\overline{u'v'}$ are shown in Fig. 11 for $W_r=0$, 1.0, 2.0, and 2.75 at a streamwise location of $x'/\delta=0.5$. These profiles were also obtained from the ensemble average of three columns of PIV velocity vectors to reduce the scatter in the shear stress profiles. The effect of imposed spanwise shear appears to be twofold. First, with increasing spanwise shear, the magnitude of the $-\overline{u'v'}$ Reynolds stress steadily increases below $y/\delta < 0.5$. For the most strongly sheared case ($W_r=2.75$) the peak magnitude in $-\overline{u'v'}$ is 130% greater than the 2-D case. Second, the crossflow causes a shift of the peak in the $-\overline{u'v'}$ stress away from the wall with increased spanwise shear. For the 2-D base case, the peak in the $-\overline{u'v'}$ stress is located at $y/\delta \approx 0.10$ while for the most highly sheared case of $W_r=2.75$ the peak has shifted out to a $y/\delta \approx 0.25$. Although three-dimensionality generally results in a reduction of the Reynolds stresses and a_1 parameter, the regions where the boundary layer is initially skewed exhibit an overshoot of $-\overline{u'v'}$. This trend has been reported in other studies e.g., Flack and Johnston [16] and Compton and Eaton [17]. At subsequent downstream locations the peak in the $-\overline{u'v'}$ stress continues to shift further into the outer region of the boundary layer. However, the magnitude of the

Downloaded 03 Jun 2010 to 171.66.16.150. Redistribution subject to ASME license or copyright; see http://www.asme.org/terms/Terms_Use.cfm

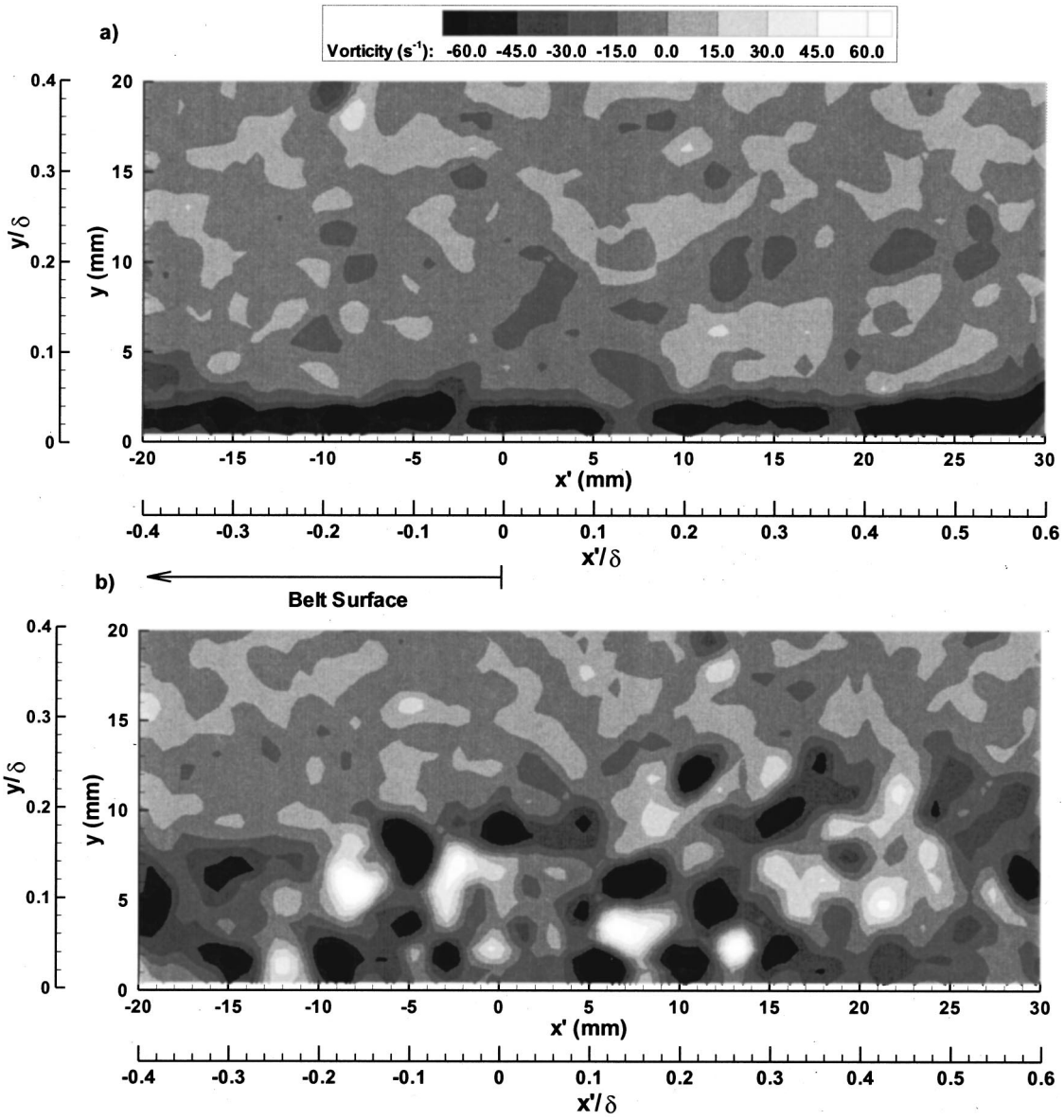

Fig. 7 Contour plots of instantaneous spanwise vorticity, ω_z, at belt trailing edge for belt velocity ratios (*a*) $W_r=0$ and (*b*) $W_r=2.75$

$-\overline{u'v'}$ stress begins to decrease, showing signs of a relaxing flow field (Kiesow and Plesniak [13]).

Conclusions

A specialized facility for generating a shear-driven 3DTBL allowed the near-wall turbulence structure to be examined for varying degrees of crossflow. LIF flow visualization reveals a modification of the near-wall streak structure when the turbulent boundary layer is subjected to spanwise shear. A reduction of mean streak length with increasing spanwise shear was measured, while streak spacing remained relatively constant. Histograms of streak length show a reduction of approximately 50% in mean streak length for a belt-to-freestream velocity ratio of $W_r=2.0$. Power spectra of the streamwise velocity downstream of the belt confirm this shift toward smaller streamwise length scales, or higher temporal frequencies. The imposition of spanwise shear causes a shift of the peak energy to higher frequencies, or smaller scales. PIV measurements in the *xz*-plane and *xy*-plane, at the trailing edge of the translating wall, revealed modifications of the inner region of the boundary layer due to the crossflow. Instantaneous velocity fields in the *xz*-plane exhibit significant disruption of flow structures at higher imposed shear compared to the 2-D base case. This distortion of the near-wall velocity field is also evidenced by the marked disruption of the transverse vorticity, particularly at the most highly sheared case, $W_r=2.75$. Secondary velocity fields in the *xy*-plane exhibit an increase in magnitude and stronger regions of recirculation throughout the inner region of the boundary layer with increasing spanwise shear. Another observed effect of the crossflow is the breakup of the spanwise vorticity layer in the near-wall region compared to that in the 2-D base case. With increasing spanwise shear, the spanwise vorticity is distributed into smaller pockets that extend throughout the inner region of the boundary layer with both positive and negative signs. The interaction of secondary flow structures and increased levels and distortion of both spanwise and transverse vorticity disrupt the usual alignment of near-wall vortical structures (e.g., legs of hairpins) which are associated with elongated streak structures. Instead, the disruption of near-wall vorticity (by the secondary structures) results in the breakup of the near-wall streaks and lifts them into the inner region of the boundary layer at an advanced stage compared to the 2-D case.

Boundary layer profiles show a significant velocity deficit at

Downloaded 03 Jun 2010 to 171.66.16.150. Redistribution subject to ASME license or copyright; see http://www.asme.org/terms/Terms_Use.cfm

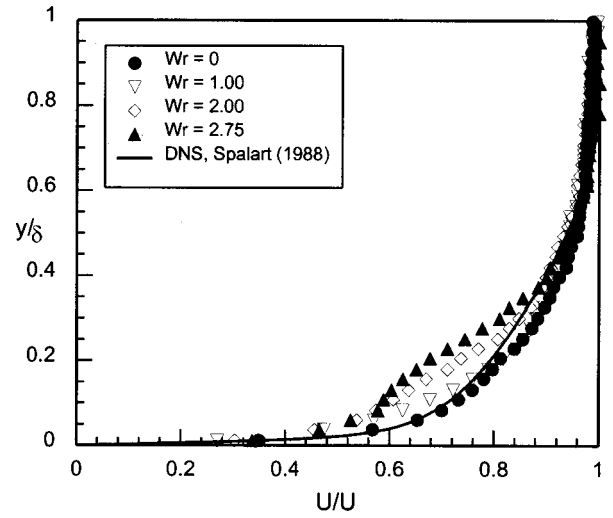

Fig. 8 Boundary layer profiles of streamwise velocity at $x'/\delta = 0.5$ downstream of belt trailing edge for velocity ratios of $W_r = 0$, 1.0, 2.0, and 2.75

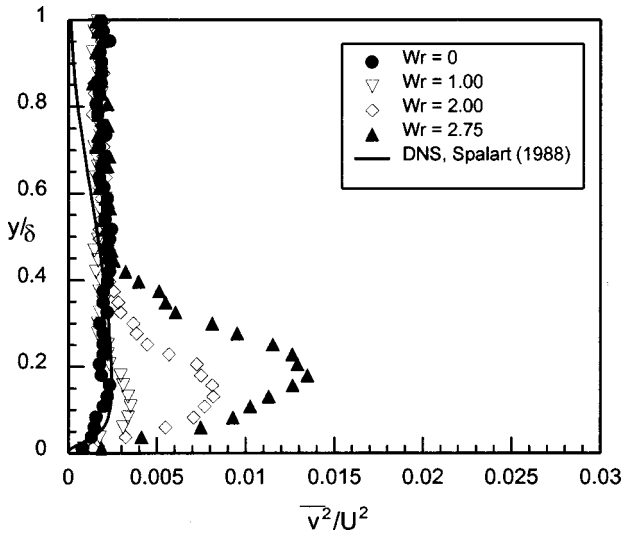

Fig. 10 Profiles of $\overline{v'^2}$ Reynolds stress at $x'/\delta = 0.5$ downstream of belt trailing edge for velocity ratios of $W_r = 0$, 1.0, 2.0, and 2.75

$y/\delta < 0.4$ for the higher spanwise shear cases ($W_r = 2.0$ and 2.75). Profiles of turbulence quantities also exhibit significant changes of the turbulence in the inner region of the boundary layer. Profiles of the normal Reynolds stresses indicate increased levels of $\overline{u'^2}$ and $\overline{v'^2}$ out to $y/\delta < 0.4$ with increasing spanwise shear. However, an initial decrease in $\overline{u'^2}$ is observed in the near-wall region for the most weakly sheared case. The $-\overline{u'v'}$ stress exhibits an overshoot of approximately 130% for the most highly sheared case ($W_r = 2.75$) and its peak shifts away from the wall with increasing spanwise shear. The overall effect of the crossflow in this planar, shear-driven 3DTBL is to disrupt near-wall coherent structures, resulting in a shift to smaller length scales and an increase of the $\overline{u'^2}$ and $\overline{v'^2}$ normal Reynolds stresses, and of the $-\overline{u'v'}$ Reynolds shear stress in the inner region of the boundary layer.

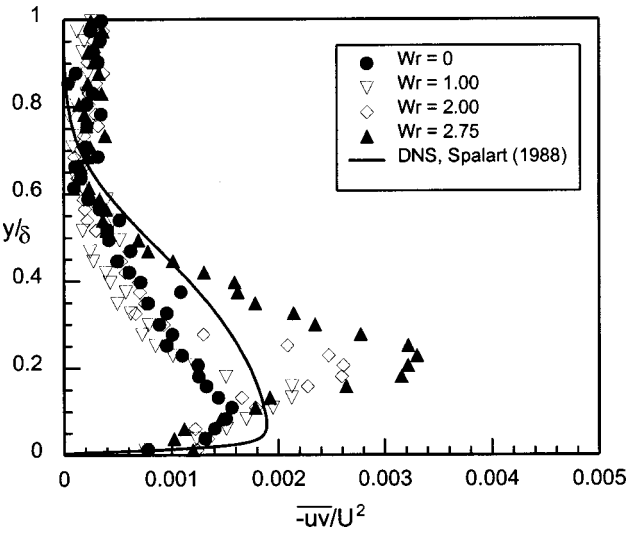

Fig. 11 Profiles of $-\overline{uv}$ Reynolds stress at $x'/\delta = 0.5$ downstream of belt trailing edge for velocity ratios of $W_r = 0$, 1.0, 2.0, and 2.75

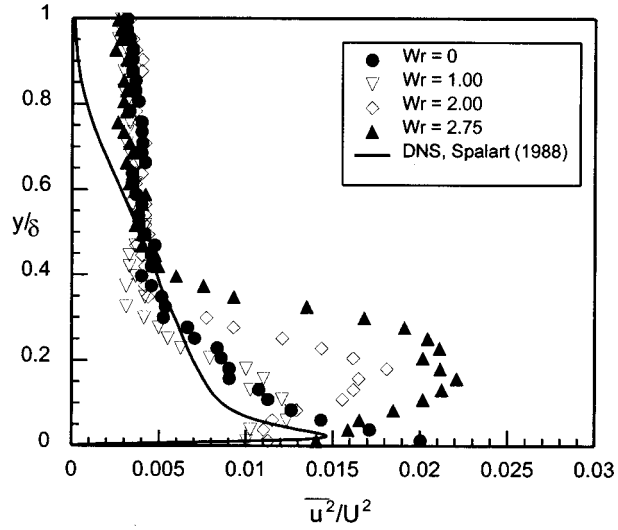

Fig. 9 Profiles of $\overline{u'^2}$ Reynolds stress at $x'/\delta = 0.5$ downstream of belt trailing edge for velocity ratios of $W_r = 0$, 1.0, 2.0, and 2.75

Nomenclature

Re_θ = momentum thickness Reynolds number
Δt = laser pulse separation time
U = streamwise mean velocity
U_∞ = edge velocity of boundary layer
$\overline{u'^2}$ = streamwise normal shear stress component
$-\overline{u'v'}$ = primary Reynolds shear stress
V = wall-normal mean velocity
$\overline{v'^2}$ = transverse normal shear stress component
W = spanwise mean velocity
W_b = translating wall velocity
W_r = velocity ratio, W_b/U_∞
x = streamwise coordinate
x' = distance downstream of trailing edge of belt
y = wall-normal coordinate
$y+$ = wall-normal coordinate in viscous units
z = spanwise coordinate

Downloaded 03 Jun 2010 to 171.66.16.150. Redistribution subject to ASME license or copyright; see http://www.asme.org/terms/Terms_Use.cfm

δ = boundary layer thickness, $U/U_\infty = 0.99$
ω_y = transverse vorticity
ω_z = spanwise vorticity

References

[1] Johnston, J., and Flack, K., 1996, ''Advances in three-dimensional turbulent boundary layers with emphasis on the wall-layer regions,'' ASME J. Fluids Eng., **118**, pp. 219–232.

[2] Eaton, J., 1995, ''Effects of mean flow three dimensionality on turbulent boundary-layer structure,'' AIAA J., **33**, pp. 2020–2025.

[3] Ölçmen, M., and Simpson, R., 1992, ''Perspective: On the near wall similarity of three-dimensional turbulent boundary layers,'' ASME J. Fluids Eng., **114**, pp. 487–495.

[4] Driver, D., and Johnston J., 1990, ''Experimental study of a three-dimensional shear-driven turbulent boundary layer with streamwise adverse pressure gradient,'' *NASA Technical Memorandum* 102211.

[5] Moin, P., Shih, T., Driver, D., and Mansour, N., 1990, ''Direct numerical simulation of a three-dimensional turbulent boundary layer.'' Phys. Fluids, **2**, pp. 1846–1853.

[6] Sendstad, O., and Moin, P., 1992, ''The near-wall mechanics of three-dimensional turbulent boundary layers,'' *Report* TF 57, Thermosciences Div. of Mech. Engng, Stanford University.

[7] Coleman, G., Kim, J., and Le, A., 1996, ''A numerical study of three-dimensional wall-bounded flows,'' Int. J. Heat Fluid Flow, **17**, pp. 333–342.

[8] Le, A., Coleman, G., and Kim, J., 1999, ''Near-wall turbulence structures in three-dimensional boundary layers,'' *Proceedings of the First Intl. Symp. on Turbulence and Shear Flow Phenomena*, pp. 147–152.

[9] Kannepalli, C., and Piomelli, U., 2000, ''Large-eddy simulation of a three-dimensional shear-driven turbulent boundary layer,'' J. Fluid Mech., **423**, pp. 175–203.

[10] Moffat, R., 1988, ''Describing the uncertainties in experimental results,'' Exp. Therm. Fluid Sci., **1**, pp. 3–17.

[11] Kiesow, R., and Plesniak, M., 1997, ''Near-wall physics and structure of a shear-driven 3-D turbulent boundary layer,'' *ASME FED Symp. on Complex and Separated Flows*, FEDSM97-3282.

[12] Kiesow, R., and Plesniak, M., 1998, ''Modification of near-wall turbulence structure in a shear-driven three-dimensional turbulent boundary layer,'' Exp. Fluids, **25**, pp. 233–242.

[13] Kiesow, R., and Plesniak, M., 1999, ''Structural modifications and near-wall physics of a shear-driven 3-D turbulent boundary layer,'' *ASME FED Symp. on Complex and Separated Flows*, FEDSM99-7068.

[14] Zhow, J., Adrian, R., Balachandar, S., and Kendall, T., 1999, ''Mechanism for generating coherent packets of hairpin vortices in channel flow,'' J. Fluid Mech., **387**, pp. 353–396.

[15] Spalart, P., 1988, ''Direct simulation of a turbulent boundary layer up to $R_\theta = 1410$,'' J. Fluid Mech., **187**, pp. 66–98.

[16] Flack, K., and Johnston, J., 1994, ''Near-wall flow in a three-dimensional turbulent boundary layer on the endwall of a rectangular bend,'' *ASME Fluids Engineering Division* **184**, pp. 1–19.

[17] Compton, D., and Eaton, J., 1997, ''Near-wall measurements in a three-dimensional turbulent boundary layer,'' J. Fluid Mech., **350**, pp. 189–208.

Downloaded 03 Jun 2010 to 171.66.16.150. Redistribution subject to ASME license or copyright; see http://www.asme.org/terms/Terms_Use.cfm

Surface Roughness Effects on Turbulent Boundary Layer Structures

L. Keirsbulck
L. Labraga
A. Mazouz
C. Tournier

Laboratoire de Mécanique et d'Energétique,
Université de Valenciennes
et du Hainaut Cambrésis,
le Mont Houy, B.P.311, 59304 Valenciennes,
Cedex France

A turbulent boundary layer structure which develop over a k-type rough wall displays several differences with those found on a smooth surface. The magnitude of the wake strength depends on the wall roughness. In the near-wall region, the contribution to the Reynolds shear stress fraction, corresponding to each event, strongly depends on the wall roughness. In the wall region, the diffusion factors are influenced by the wall roughness where the sweep events largely dominate the ejection events. This trend is reversed for the smooth-wall. Particle Image Velocimetry technique (PIV) is used to obtain the fluctuating flow field in the turbulent boundary layer in order to confirm this behavior. The energy budget analysis shows that the main difference between rough- and smooth-walls appears near the wall where the transport terms are larger for smooth-wall. Vertical and longitudinal turbulent flux of the shear stress on both smooth and rough surfaces is compared to those predicted by a turbulence model. The present results confirm that any turbulence model must take into account the effects of the surface roughness.
[DOI: 10.1115/1.1445141]

1 Introduction

Experimental investigations into a turbulent boundary layer over rough-wall have shown that the turbulence structure depends on the roughness surface and differ from that in smooth-wall boundary layers (Bandyopadhyay and Watson [1], Krogstad and Antonia [2], Krogstad et al. [3], Krogstad and Antonia [4], Antonia [5], Shafi and Antonia [6], Shafi et al. [7], Shafi and Antonia [8].

The principal effect on a rough surface is to alter the structure of the boundary layer near the wall thereby increasing the surface skin friction. This is felt in the roughness sublayer of the order of a few roughness heights away from the wall (Rotta [9], Raupach [10]). In the remainder of the inner layer and in the outer layer, the flow obeys a familiar similarity law with respect to roughness surface. In a recent experimental investigation, Krogstad et al. [3] have shown that the strength of the rough-wall outer region ''wake'' is larger than that of a smooth-wall. The wake strength Π was found to be 0.51 for the smooth-wall and 0.70 for the rough-wall. Krogstad et al. [3] have underlined that the larger value of Π on the rough-wall was linked to a greater entertainment of irrotational fluid. This rather high value of Π is nearly the same as the value obtained by Osaka and Mochizuki [11] and Tani et al. [12] for *d*-type roughness. For the *k*-type roughness, the values of the wake strength Π evaluated by Tani [13] range from 0.4 to 0.7. The results of Raupach [10] on the smooth-wall and rough-wall boundary layers indicate that normalized second moments of the velocity are independent of the roughness. This similarity was questioned by other authors. Krogstad et al. [3] found that the longitudinal turbulence intensity distribution is essentially the same for both surfaces, but there is a significant increase in the normal intensity v and a moderate increase in the Reynolds stress over the rough-wall. For the same nominal velocity, the mean velocity profiles on the rough-wall are not as full as those obtained on a smooth-wall. The data available of higher-order moments of the fluctuating component of the velocity are scared. However, Antonia and Luxton [14], found that the flatness factors of u and v are the same on both rough- and smooth-walls. The latter authors showed that the effect of increasing the Reynolds number results in small changes in the distributions of the skewness and the flatness factors of the u and v fluctuating components of the velocity. Krogstad and Antonia [4] have shown that the major effect of the roughness is to tilt the inclination of the structures toward the wall-normal direction and that the roughness tends to reduce the overall anisotropy of the large-scale motion.

In light of the studies above, the main aim of the present work is to investigate the effects of a rough surface on the statistics of the turbulent boundary layer at Reynolds numbers sufficiently large to satisfy the Reynolds number similarity. Measurements on rough-wall boundary layers have been compared with corresponding measurements in smooth-wall boundary layers. For a rough-wall, we consider one surface characterized by spanwise two-dimensional square grooves regularly spaced. This type of roughness, referred to as ''k-type,'' has been largely investigated but the physics of this flow, especially the effect of roughness on the higher-order statistics, is not clearly understood. The diffusion of the turbulent energy is strongly affected by the wall roughness. The turbulence production mechanisms in the near-wall region also depend on the wall roughness. The roughness classification scheme based solely on the mean velocity profiles may be reviewed using structural considerations. The energy transfer mechanism between the turbulence and the mean flow is strongly dependent on the wall roughness. These results confirm the wall similarity hypothesis; ''that outside the roughness sublayer, the turbulent motions are independent from the wall roughness'' (Perry et al. [15], Raupach [10], and Raupach et al. [16]). The mean velocity and the turbulence characteristics on smooth and rough walls were obtained using single hot wire and X-wire probes.

2 Experimental Details

The experiments were carried out in an open wind tunnel with a 0.6×0.6 m^2 square test section and with a 5 m long. The working section is made up of five plates each 1 m long with a width of 0.6 m. The boundary layer develops on one of the walls of the test section, thus the opposite wall is used to maintain a zero pressure gradient for all the values of the free-stream velocity U_∞. The transition of the flow is tripped to obtain a fully developed turbulent boundary layer at the measuring location. For experiments on the rough-wall, the *k*-type roughness consisted of two-dimensional

Contributed by the Fluids Engineering Division for publication in the JOURNAL OF FLUIDS ENGINEERING. Manuscript received by the Fluids Engineering Division June 5, 2000; revised manuscript received October 15, 2001. Associate Editor: J. Lasheras.

 Copyright © 2002 by ASME

Downloaded 03 Jun 2010 to 171.66.16.150. Redistribution subject to ASME license or copyright; see http://www.asme.org/terms/Terms_Use.cfm

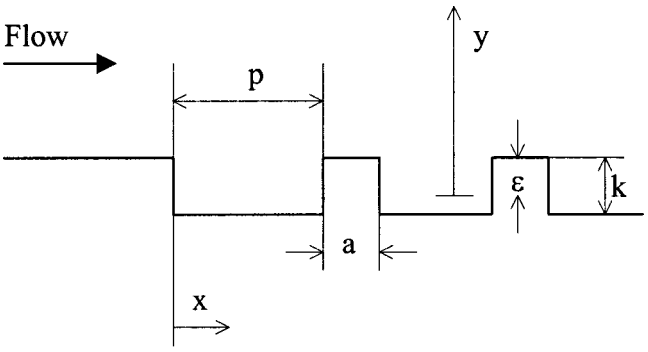

Fig. 1 Two-dimensional roughness geometry

bars of square cross-section normally placed in the flow direction. The transversely grooved surface is illustrated in Fig. 1. The gap between consecutive elements was $p=7$ mm. The *k*-type roughness elements have a $k(=a)=3$ mm height and spanned the entire section. Note that, in the *k*-type roughness, $p/k>1$. Most of the measurements were taken at a distance of $x=4.5$ m from the end of the tunnel contraction. At this position, the boundary layer behaved accordingly to the criteria for self-similarity of the turbulent boundary layers. The values of U_∞ for smooth-wall and rough-wall boundary layers are 21.5 m/s and 11.83 m/s, respectively. The free-stream turbulence of the wind tunnel was 0.5 percent. Mean flow integral parameters for both smooth-wall and rough-wall, inferred from the velocity profiles, are summarized in Table 1. Mean and fluctuating velocities were measured using hot-wire anemometry with single and X-probes. The sensing wire had a 2.5 μm diameter and was made of platinum-tungsten. The length l of the sensing wire was 0.5 mm. This corresponds to a ratio $l/d=200$, large enough for end conduction effects. Table 1 also shows the values of the sampling frequency and active length l^+ of a hot-wire probe in inner scaling for different experiments. The $+$ superscript denotes nondimensionalization with friction velocity U_τ and kinematic viscosity ν. The hot wire probes were operated with a DANTEC CTA 90C10 constant temperature anemometers at a overheat ratio of 0.8. The outputs were linearized and digitized at an appropriate sampling rate. The signal from the wires were filtered at a cut-off frequency (F_c) to minimize the contamination from high-frequency electronic noise. The value of F_c was identified, after examining the spectra of the differentiated signals. Hence, the cut off frequency was evaluated. The sampling frequency used is $F_s=2F_c$. The hot-wire probes were always calibrated within the free stream of the wind tunnel with a compensating temperature system. The wind tunnel was run at 10 different free-stream velocities, but only two of them (same Reynolds number for smooth and rough case) were analyzed. The free-stream velocities were measured using a Pitot tube and a differential transducer with a 0.01 mm H_2O resolution. A typical record duration of nearly 25 s was used. This total time was found to be sufficient to ensure a good statistic convergence. Digital data files were stored and processed on a computer. The system used for PIV measurements is a TSI device, which allows two-dimensional basic planar measurements. A double-pulsed laser (SpectraPhysics Nd: YAG/2.5 J/8 ns) produces light pulses in a sheet from an articulated arm and the optical system. The frequency of the double-pulse is 15 Hz. The camera (PIVCAM 10-30) with a CCD matrix (1000×968 pixels) records images by pairs and transmits them to a computer. The synchronization between the laser and the camera is ensured by the synchronizer (Laser Pulse synchronizer). In view of improving the accuracy of the measurements, the cross-correlation between images is carried out on a 32×32 pixels zone. An optimal time interval Δt between pulses was chosen. The fluctuating velocity fields is then determined by subtracting the mean velocity field from the instantaneous velocity fields.

Table 1

	U_∞	δ	θ	Re_θ	U_τ	$C_f\times10^3$	k^+	ε/k	ΔU^+	Π	ℓ^+	Fs
	m/s	mm	mm		m/s							kHz
Smooth	21.55	55	5.85	8405	0.81	2.825	--------	--------	--------	0.51	27	42
Rough	11.83	79	10.84	8549	0.75	8.040	150	0.37	11.9	0.68	25	40

3 Boundary-Layer Profiles

For both smooth-wall and rough-wall, the mean streamwise velocity distribution across the entire region is given by

$$U^+=\frac{1}{\kappa}\ln y^+ + A - \Delta U^+ + \frac{2\Pi}{\kappa}\omega(\eta) \tag{1}$$

$y^+=(y+\varepsilon)U_\tau/\nu$ and $\eta=(y+\varepsilon)/\delta$ (Krogstad et al. [3]). ε is the shift at the origin for the rough-wall (zero for smooth-wall) and y is measured from the top of the roughness. κ and A are presumed to be constant and are empirically determined for both rough-wall and smooth-wall boundary layers to be 0.41 and 5, respectively. $\Delta U^+=(U_r-U_s)/U_\tau$ is the roughness function (zero for smooth-wall) and parameter Π determines the strength of the wake function $\omega(\eta)$. The description of the measured mean velocity requires the determination of the four parameters U_τ, ε, ΔU^+, and Π. For smooth-wall, Hama's decomposition [17] proposed that the wake gives a universal value of strength wake $\Pi=0.52$. Many authors have shown that the value thus obtained is not optimal for a rough-wall boundary layer (Osaka and Mochizuki [11], Tani [13], Tani et al. [12], Krogstad et al. [3] and Antonia and Krogstad [18]). Hama's formulation may be applied with confidence for rough-wall boundary layers. A formulation proposed by Finley et al. [19] and later by Granville [20] is used to fit the profiles and to give values of these parameters presented in Table 1. It is shown that the magnitude of the strength of the wake for the rough-wall ($\cong0.7$) is higher that the universal value ($\cong0.51$) for the smooth-wall. The much higher C_f in rough-wall boundary layers implies a faster growth rate of the layer. Because of the positioning error that will be reflected in the shift of the origin in rough-wall, a large scatter was found in ε. The shift obtained from the fit is $\varepsilon\cong0.37$ k. Figure 2 shows the mean velocity profiles in wall coordinates for both smooth-wall and rough-wall boundary

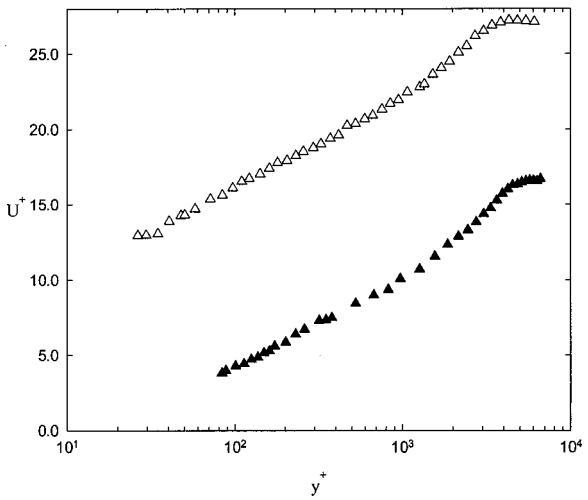

Fig. 2 Mean velocity profiles. Smooth-wall: △, Re_θ=8405. Rough-wall: ▲, Re_θ=8549.

Downloaded 03 Jun 2010 to 171.66.16.150. Redistribution subject to ASME license or copyright; see http://www.asme.org/terms/Terms_Use.cfm

layers. Therefore, the main effect of the roughness results in an increase of both the skin friction (shown in Fig. 2) and the strength of the wake (Π values in Table 1).

4 Higher-Order Statistics of the Velocity Fluctuations

4.1 Second-Order Moments. Figures 3(*a*) and 3(*b*) show the profiles of the normalized turbulence intensities of the fluctuating streamwise u'^{+2} and vertical v'^{+2} components. Differences are observed near the wall region where turbulence intensity u'^{+2} is higher for smooth-wall. Raupach [10] found that outside the roughness sublayer (a region extending to about two times the roughness height) the normalized second-order moments of the velocity are universal. The present results indicate that in the inner region, the turbulent motions strongly depend on the wall roughness. Figures 3(*a*) and 3(*b*) show that the results obtained in the present study agree well with the data of Krogstad et al. [3] in both smooth- and rough-walls boundary layers. The normal stress v'^{+2} is affected in the region ($y/\delta \leqslant 0.4$) and remains unaffected outside this region. The present results for u'^{+2} are slightly higher for smooth wall than for rough wall in the inner regions $y/\delta > 0.8$. The results found by Krogstad et al. [3] are lower than those of the present study. This difference was possibly attributed to a higher free-stream turbulence in the present wind tunnel. The Reynolds shear stress as shown in Fig. 3(*c*), is more important in the case of smooth wall than in the case of rough wall. It is worth noting that these distributions appear to have a peak value at different locations (Antonia and Luxton [14]).

4.2 Third-Order Moments. The distributions of the skewness factors, $S_u = \overline{u^3}/(u')^3$ and $S_v = \overline{v^3}/(v')^3$ are shown in Figs. 4(*a*) and 4(*b*) for both smooth and rough walls (a prime denotes an rms value). In the near-wall region, high positive values of S_u are observed indicating the dominance of sweep events. This shows the occurrence of high-speed fluids from regions distant from the wall. The higher values on rough-wall compared to smooth-wall underline a strong activity of the sweep events on rough surfaces. Further away from the wall, the value of S_u is negative, consistent with the arrival of low-speed fluids from the wall (ejection events). For $y/\delta > 0.5$, the distribution of S_u in the two layers as shown in Fig. 4(*a*) appears to be similar. In the $0 \leqslant y/\delta < 0.5$ range, the distribution of S_u is significantly different over the two layers. The influence of the roughness is emphasized as the distance from the wall decreases. In the inner regions, for rough-wall, there is a higher probability of finding large positive u fluctuation, consistent with strong sweep events already observed by Grass [21] using flow visualizations. For the rough-wall, S_u changes sign far from the wall comparing to the smooth-wall and increases abruptly as the distance from the wall decreases. Figure 4(*b*) shows that the values of S_v are lower on rough-wall than on smooth-wall everywhere in the boundary layer. The present results

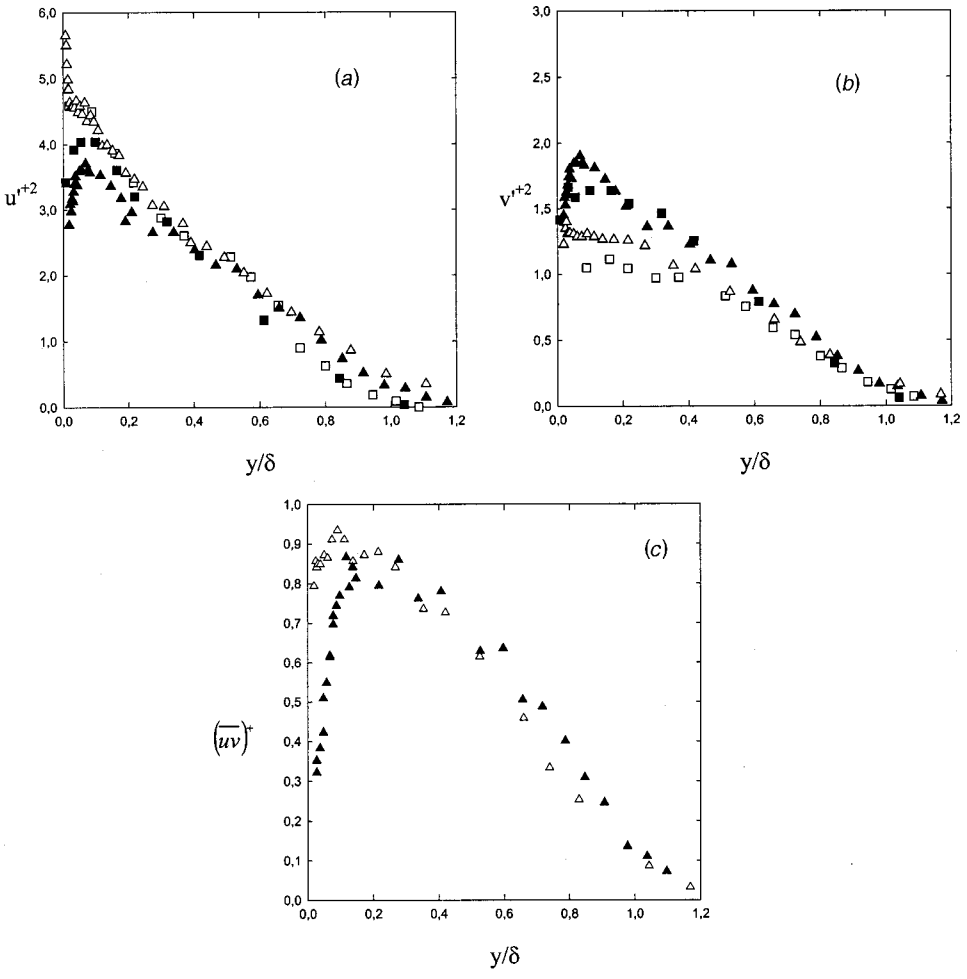

Fig. 3 Reynolds stresses distributions on smooth and rough walls boundary layers. The same symbols as Fig. 2 for the present measurements. Smooth-wall: □, Re_θ=9630 (Krogstad et al. [3]). Rough-wall: ■, Re_θ=13040 (Antonia and Krogstad [18]).

Downloaded 03 Jun 2010 to 171.66.16.150. Redistribution subject to ASME license or copyright; see http://www.asme.org/terms/Terms_Use.cfm

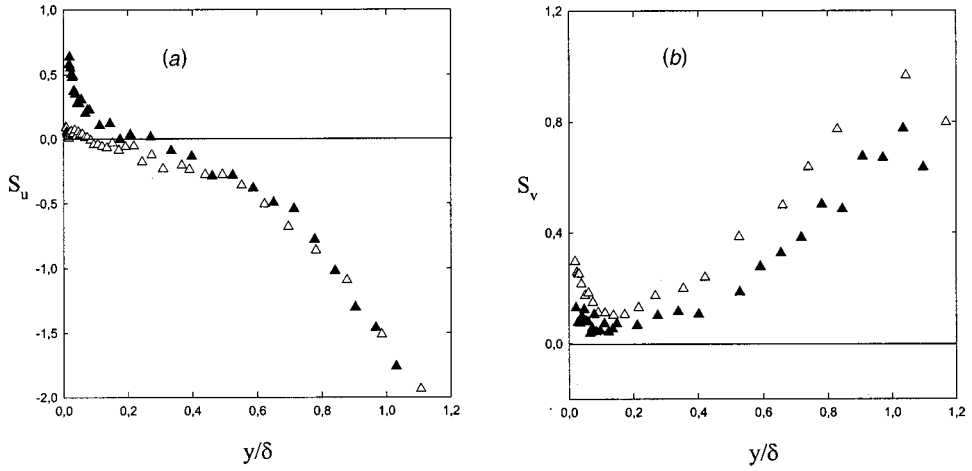

Fig. 4 Profiles of skewness of u and v in outer-law scaling for both smooth and rough walls' boundary layers. Symbols are same as that of Fig. 2.

are in good agreement with those found by Bandyopadhyay and Watson [1]. They observed that the S_u distributions are much the same in the smooth- and rough-walls, but the S_v values tend to be lower all over the rough surfaces. They concluded that the hairpin vortices shape induces different vertical motions and different vertical diffusions of turbulence in the rough case compared to the smooth case.

Figure 5 shows the distribution of the turbulent diffusion $D_u = (\overline{uv^2})/(u_\tau)^3$ and $D_v = (\overline{vu^2})/(u_\tau)^3$ in the x and y directions compared with those obtained by HL model (Hanjalic and Launder [22]). Note, that the relations between D_u and D_v resemble that between S_u and S_v. Figures 5(a) and 5(b) show that, in the outer region ($y/\delta > 0.8$). In the wall region, the effect of the wall-roughness is remarkable with $D_u > 0$ and $D_v < 0$ which underlines the importance of sweep events for the rough-wall. Like the distributions of S_u, the point of cross-over from the sweep to ejection events occurs at $y/\delta \approx 0.2$ over the rough-wall. The smooth-wall shows an opposite tendency in the turbulent energy transport. For the smooth-wall, D_u remains negative in this region and significantly decreases at $y/\delta < 0.1$. These distributions show that for the smooth-wall, the flux is outward and is associated with a streamwise deceleration (corresponding to a negative sign of the u component). For the rough-wall, the flow is wallward and is associated with a streamwise acceleration (corresponding to a positive sign of the u component) in the inner region. These results are in good agreement with those reported by Bandyopadhyay and Watson [1]. D_v distributions are similar for both smooth and rough walls. D_v distribution is positive in the overall boundary layer for the smooth wall. In the inner region, D_v is negative for $y/\delta < 0.1$. Large positive values of D_v are consistent with a predominance of ejection, which is in agreement with results given by S_u. Negative values of D_v are related to the predominance of sweeps which are more intense in the case of the rough wall. These results are compared to those obtained by a turbulent model suggested by Hanjalic and Launder [22] for the diffusion by turbulent velocity fluctuation. One of the contribution to the diffusive transport of the Reynolds stress has been approximated as follows:

$$\overline{u_i u_j u_k} = -0{,}11 \times \frac{k}{\varepsilon}\left[\overline{u_i u_l}\frac{\partial \overline{u_j u_k}}{\partial x_l} + \overline{u_j u_l}\frac{\partial \overline{u_i u_k}}{\partial x_l} + \overline{u_k u_l}\frac{\partial \overline{u_j u_i}}{\partial x_l}\right]$$

where k is the average kinetic energy and ε is the dissipation rate of turbulence kinetic energy obtained by using $\varepsilon = f(E_{11}, u', f_r)$ where E_{11} is the longitudinal spectrum and f_r is the frequency taken in the inertial range. Taylor's hypothesis and local isotropy are assumed. The expressions for the diffusive transport of u and v reduce to:

$$(\overline{uv^2})^+ = -c_s \times \left[\frac{k}{\varepsilon} \times \left[2 \times \overline{v^2} \times \frac{\partial \overline{uv}}{\partial y} + \overline{uv} \times \frac{\partial \overline{v^2}}{\partial y}\right]\right]^+$$

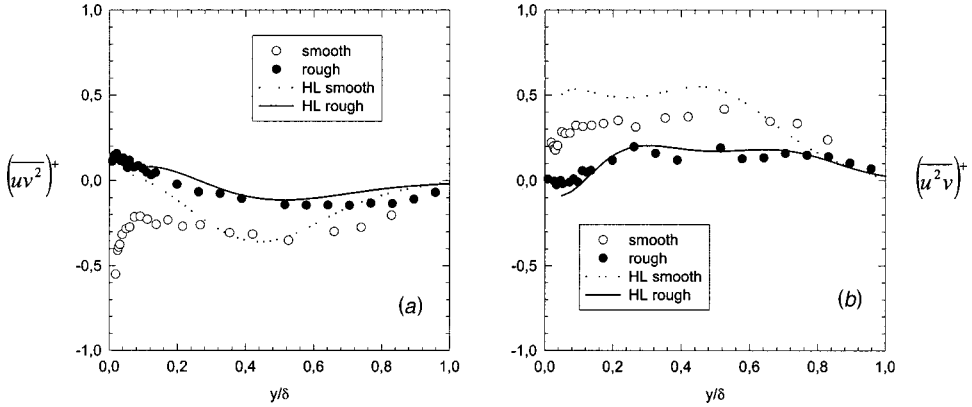

Fig. 5 Vertical and longitudinal turbulent flux of the shear stress for both smooth-wall and rough-wall boundary layers. Symbols are same as that of Fig. 2. ◇ Smooth-wall; Solid line $Re_\theta = 4750$ (Bandyopadhyay and Watson [1]). ♦ Rough-wall (Bandyopadhyay and Watson [1])

Downloaded 03 Jun 2010 to 171.66.16.150. Redistribution subject to ASME license or copyright; see http://www.asme.org/terms/Terms_Use.cfm

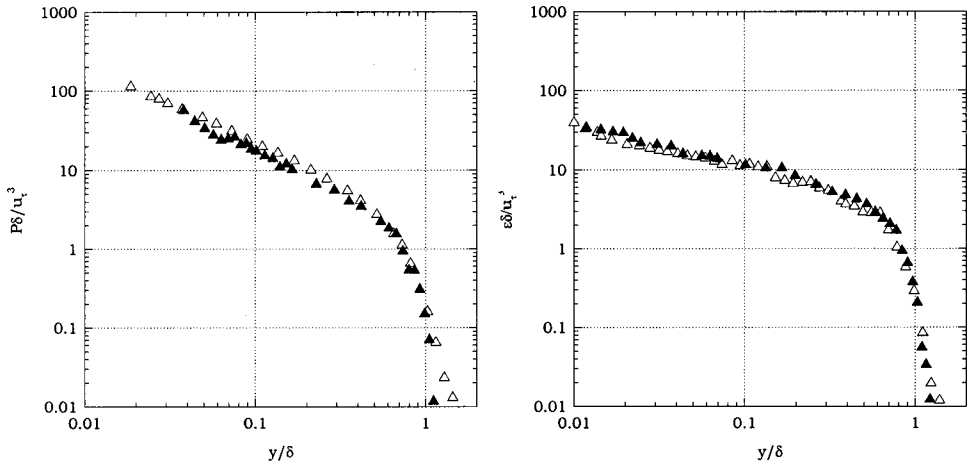

Fig. 6 Production and dissipation on smooth- and rough-wall. Smooth-wall: open symbols; rough-wall: filled symbols.

$$(\overline{u^2v})^+ = -c_s \times \left[\frac{k}{\varepsilon} \times \left[2 \times \overline{uv} \times \frac{\partial \overline{uv}}{\partial y} + \overline{v^2} \times \frac{\partial \overline{u^2}}{\partial y}\right]\right]^+$$

with a value of $c_s = 1.1$ proposed by Hanjalic and Launder.

The comparison of prediction suggested by HL model with the present experiments are reported on Fig. 5 for the vertical and longitudinal turbulent fluxes of the shear stress on smooth and rough walls. Figure 5(*a*) shows that, except for a narrow region $0.3 \leqslant y/\delta \leqslant 0.5$, D_u exhibits a consistent disagreement between the measurements on the smooth wall and the prediction. A better agreement for D_u between predictions and measurements is observed in the case of the rough wall throughout the boundary layer. Figure 5(*b*) shows that, except in the outer regions, the prediction of D_v distributions display large departure from the measured values on the smooth wall. As for the rough wall, the agreement between predicted and measured values of D_v is excellent for $y/\delta \geqslant 0.1$. The reason for the rather poor prediction of D_u and D_v on smooth wall and a good prediction of these quantities on rough wall can be attributed to a more isotropic behavior of the large scale structure in the rough wall layer (Shafi and Antonia [8]). An efficient way to evaluate the anisotropy degree of the turbulent flow is to use the anisotropy Reynolds stress map invariant suggested by Lumley and Newman. The results, not reported here, confirm a tendency towards isotropy of the Reynolds stress tensor for the rough wall.

5 Turbulent Kinetic Energy Transport

Equations of the turbulent kinetic energy transport may be written in the following form:

$$\underset{①}{\overline{U^+}\frac{\partial k^+}{\partial(x/\delta)}} + \underset{②}{\overline{V^+}\frac{\partial k^+}{\partial(y/\delta)}} - \underset{③}{(-\overline{uv})^+\frac{\partial \overline{U^+}}{\partial(y/\delta)}} + \underset{④}{\frac{\varepsilon\delta}{u_\tau^3}} - \frac{\partial}{\partial(y/\delta)} \times \left(\underset{⑤}{-\overline{\left(\frac{u^{+2}+v^{+2}+w^{+2}}{2}\right)v'^+}} - \underset{⑥}{\frac{(\overline{pv})^+}{u_\tau^2}} + \frac{\partial k^+}{\partial y^+} \right) = 0$$

The first and the second terms are the advection, the third and the fourth terms are, respectively, the production and dissipation of mean turbulent energy and the last term is diffusion. Note that the gradient of D_v is the primary diffusion term in the transport equation for $\overline{u^2}$ and its distribution appears to be very sensitive to the surface condition (Fig. 5). The diffusion due to the pressure-

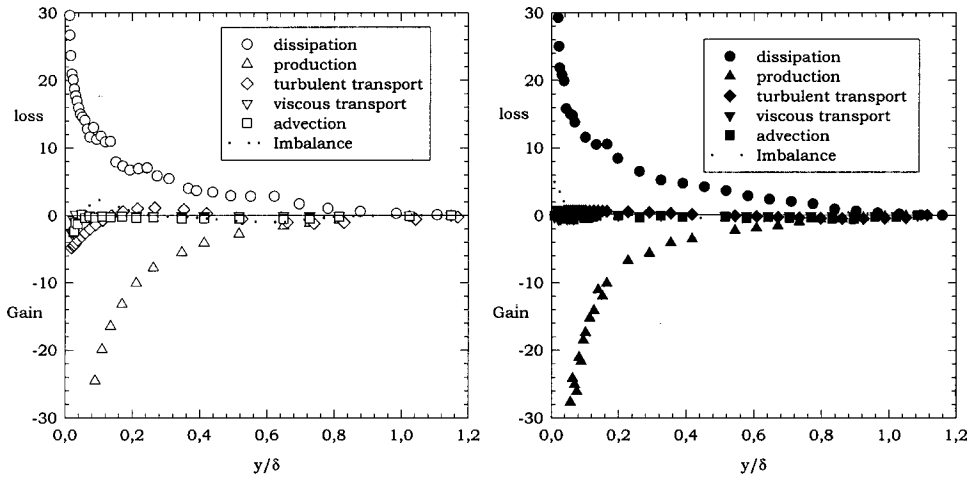

Fig. 7 Turbulent kinetic energy budget. Smooth-wall: open symbols; rough-wall: filled symbol.

Downloaded 03 Jun 2010 to 171.66.16.150. Redistribution subject to ASME license or copyright; see http://www.asme.org/terms/Terms_Use.cfm

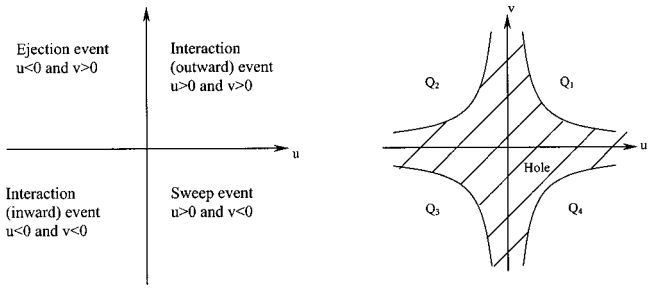

Fig. 8 Schematic of quadrant decomposition

strain term and the advection in the x direction could not be measured using the present techniques. The diffusion term $\partial(\overline{w^2v})^+/\partial(y/\delta)$ was approximated by $3/4\partial(\overline{u^2v}+\overline{v^3})^+/\partial(y/\delta)$. In Figs. 6($a$) and 6($b$) the rate of production and dissipation of the mean turbulent energy normalized with the inner variables is plotted as a function of y/δ and appear to be unaffected by the surface type. The approximate turbulent kinetic energy for the both surfaces are plotted on Figs. 7(a) and 7(b). The production and dissipation of the turbulent kinetic energy are nearly balanced throughout the layer in both cases. It appears, from Fig. 7, that the transport terms are larger in the inner region than in the outer part of the log region. The advection, viscous transport and turbulent transport terms are much smaller than the production and dissipation terms for both smooth and rough-walls. The main difference between smooth and rough-wall is observed in the inner region. These terms decrease, reaching negative values within the inner region close to the wall. This trend is emphasized for the turbulent diffusion. This behavior corresponds to a loss or a gain of kinetic energy near the smooth wall due to ejection motions and is quantified by using a quadrant analysis. From these observations, it appears once more that the turbulent transport mechanisms near the wall strongly depend on the surface geometry.

6 Quadrant Decomposition

On the basis of the qualitative results obtained by the flow visualization on the Reynolds shear stress production (Corino and Bordkey [23], Grass [21]) some researchers have attempted to obtain more quantitative knowledge about the structure of the Reynolds shear stress, using the quadrant decomposition (Wallace et al. [24], Brodkey et al. [25], Willmarth and Lu [26], and Lu and Willmarth [27]). This method consists in dividing the plane of the streamwise and normal fluctuating velocity components u and v into four quadrants, as shown in Fig. 8, in order to evaluate the contributions of the ejections and sweeps to the Reynolds shear stress production.

Figures 9(a) and 9(b) exhibit the contributions of the outward and inward interactions for $H=0$ on smooth-wall and rough-wall turbulent boundary layers. It is interesting to note that the roughness surface significantly increases the relative intensity of each event at $H=0$ in inner and outer region of the flow. Figures 9(c)

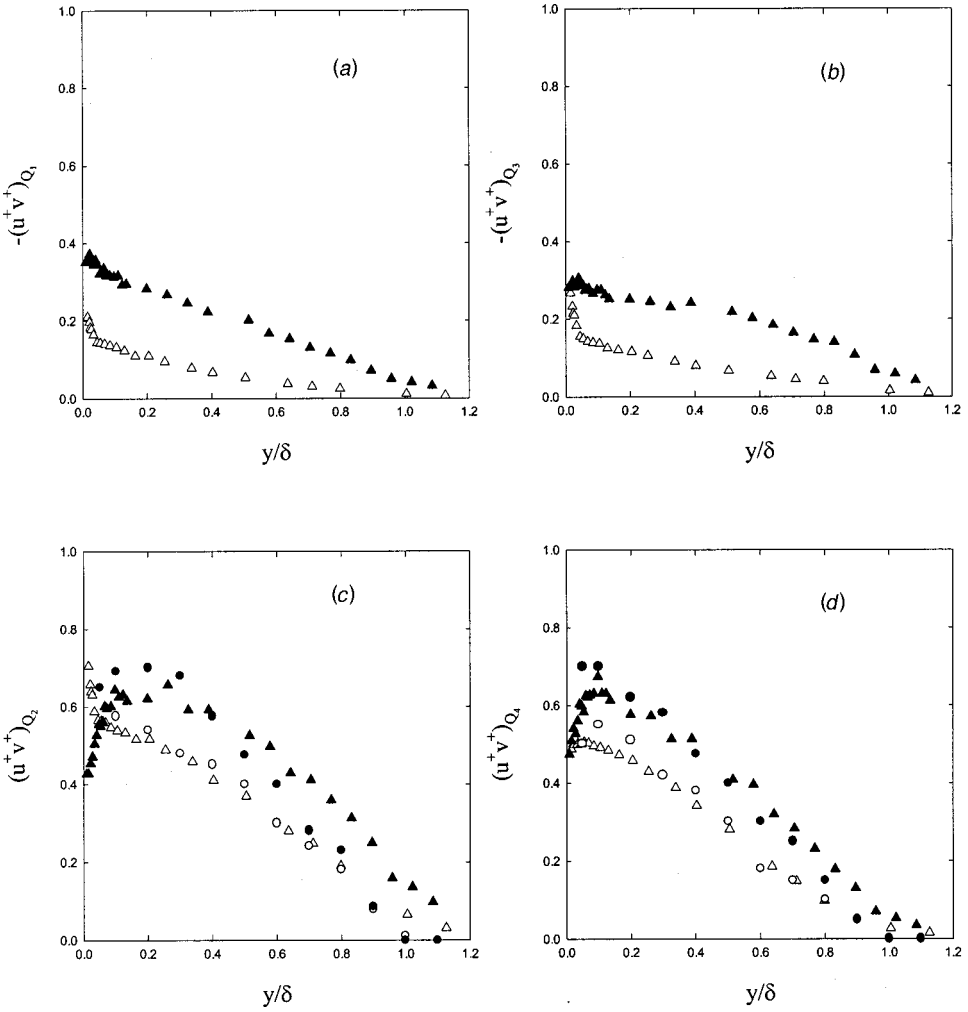

Fig. 9 Shear stress contributions from quadrants Q_2 and Q_4 for H=0 on smooth- and rough-wall. Symbols are same as in Fig. 2.

Downloaded 03 Jun 2010 to 171.66.16.150. Redistribution subject to ASME license or copyright; see http://www.asme.org/terms/Terms_Use.cfm

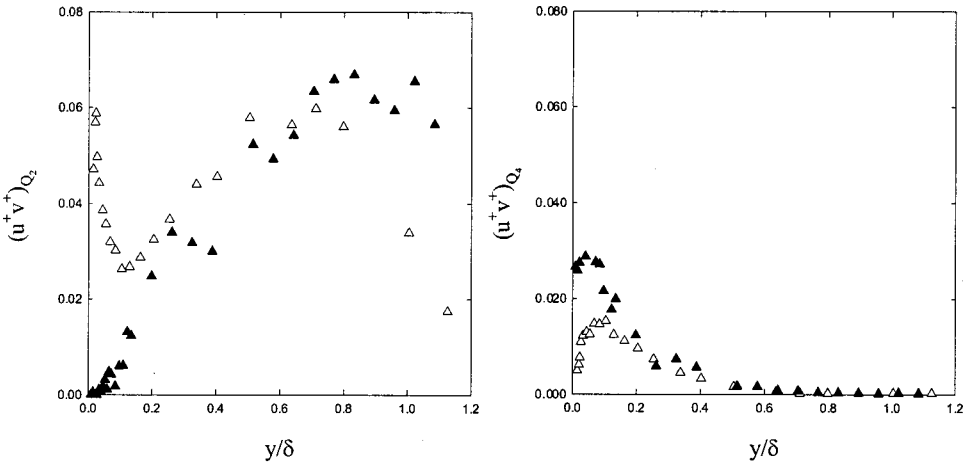

Fig. 10 Shear stress contribution from quadrants Q_2 and Q_4 for H=5 on smooth and rough wall

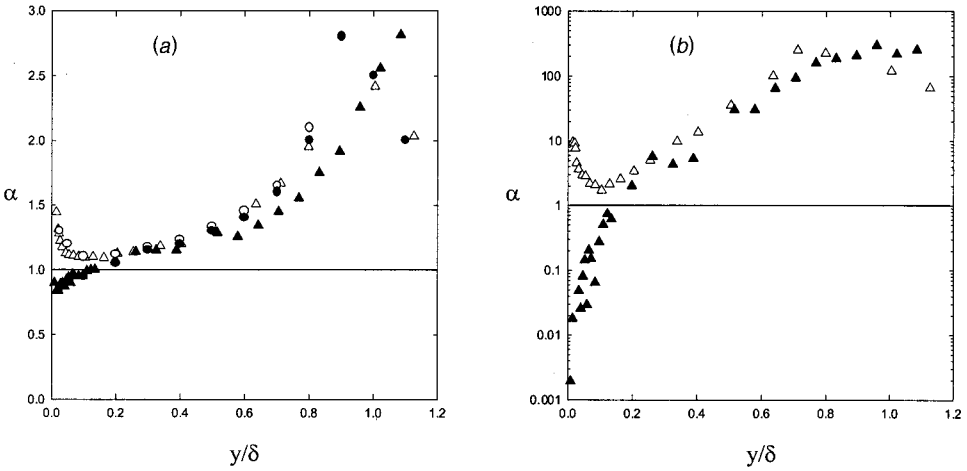

Fig. 11 Ratio of contributions to $\overline{uv}$ from quadrants Q_2 and Q_4 for H=0 and H=5

and 9(*d*) show the profiles of the intensities of ejection and sweep events normalized by inner scaling. For both walls, the sweeps and ejections decrease while increasing y/δ. The data of Krogstad et al. [3] on smooth and rough walls agree with the present results except for the ejection values on smooth-wall which show some differences for $y/\delta > 0.6$. This difference is probably linked to a relatively high free-stream turbulence for the present measurements. Figures 9(*c*) and 9(*d*) show that both ejection and sweep events are affected by the wall-roughness. The conditional analysis allows us to underline that the effect of the wall-roughness is not confined only in the sublayer.

In the wall region ($y/\delta < 0.2$), Fig. 10(*a*) shows that the magnitude of $\overline{(u^+v^+)}_{Q_2}$ is significantly larger for the smooth-wall than the rough-wall for strong events ($H=5$) confirming the predominance of strong ejection events on the smooth wall. In the same region, Fig. 10(*b*) shows that sweep events are stronger on the rough wall. However, for ($y/\delta \geq 0.2$) the distributions of these contributions on smooth-wall and rough-wall are nearly the same. The difference between the present results and the data of Krogstad et al. [3] for ($H=4$), however, suggest that the strong events decrease while H increases.

Figures 11(*a*) and 11(*b*) indicate the distributions of the ratio $\alpha = \overline{(uv)}_{Q_{2,H}} / \overline{(uv)}_{Q_{4,H}}$ on smooth and rough walls for $H=0$ and $H=5$, respectively. This ratio is useful because it highlights the importance of sweeps and ejections on smooth and rough walls. Figure 12 shows that for $y/\delta \leqslant 0.2$, α is larger in the smooth wall layer reflecting the importance of the ejection motion. The lower values of α on the rough wall confirm the importance of the sweep events. The distributions of α for $H=0$ measured in smooth and rough walls boundary layers by Krogstad et al. [3] are also shown in Fig. 11(*a*). The present data on the smooth wall agree well with their results.

7 PIV Results

Qualitative measurements have been achieved using the PIV technique. Figure 12 shows a typical fluctuating velocity field for smooth- and rough-walls in xy-plane. In the case of the smooth-wall, ejections are predominant in the near wall regions (Fig. 12(*a*)) and opposite to that, for the rough-wall case, sweeps are predominant in the near wall regions (Fig. 12(*b*)). This behavior is in good agreement with the quadrant's results. This may be interpreted by the fact that near roughness elements, viscous sublayer becomes thinner or completely disappears. Moreover the cavities between the roughness elements lead to fewer severe constraints for the v-component as it has been suggested by Krogstad et al. [3]. In the same way, Krogstad and Antonia [2], concluded that the v-component of the velocity was more sensitive to the roughness effect than the u-component, especially in the near wall regions.

Downloaded 03 Jun 2010 to 171.66.16.150. Redistribution subject to ASME license or copyright; see http://www.asme.org/terms/Terms_Use.cfm

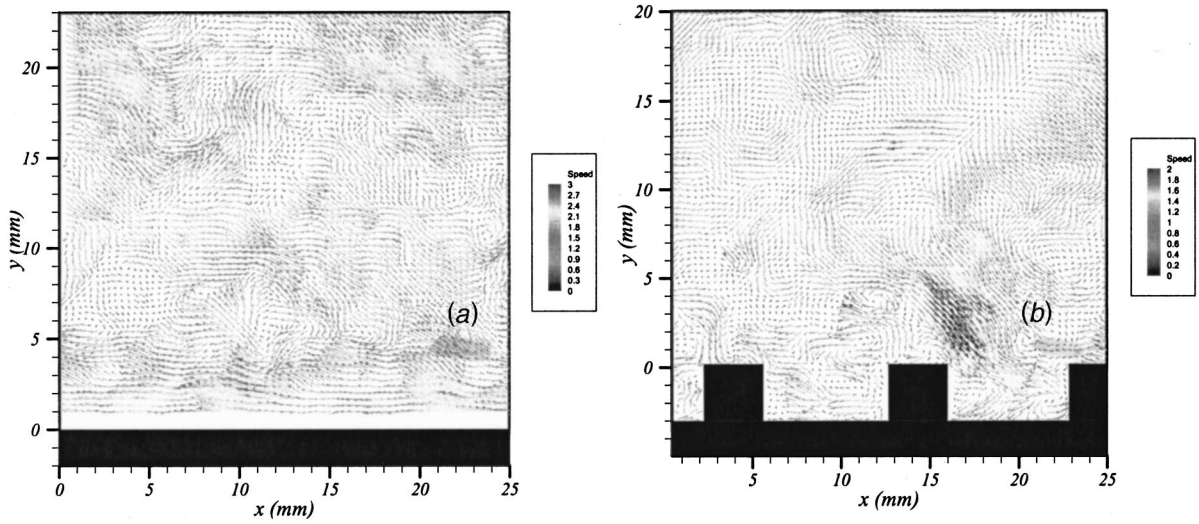

Fig. 12 Fluctuating velocity field on smooth and rough walls

The results found by PIV measurements did not permit to underline the ejection of low speed fluid between roughness elements away from the wall as it has been suggested by Grass [21].

8 Conclusion

The present results on smooth- and rough-walls turbulent boundary layers indicate considerable effects of surface condition in the inner layers. In the inner region, the Reynolds stress shows a significant increase on smooth-wall for u'^{+2}. The present results show that the effects of the *k*-type roughness on the Reynolds stresses u'^{+2}, v'^{+2} and $(uv)^{+}$ are mainly confined to the near wall region. The distribution of the triple velocity correlation and the quadrant analysis indicate that the ejection events represent the major contribution to the turbulent diffusion for the Reynolds stress. The distributions of these quantities over the k-type roughness highlight the presence of violent ejections and sweeps. The prediction by a turbulent model of vertical and longitudinal turbulent fluxes is in better agreement with the results on the rough wall than those on the smooth wall. This is probably due to the more isotropic character of the large scale structure on the rough wall. This feature suggests that modeling higher-order moments should be considered. The PIV velocity fields confirm the behavior of the structures predicted by the quadrant analysis in the wall regions. It seems that the v-component of the velocity is more sensitive to the roughness effect than the u-component, especially in the near wall regions as it has been observed earlier by other authors. It is most likely due to the less severe constraints for the v-component in the case of rough-wall than in the case of smooth-wall.

Nomenclature

A = constant in the logarithm law
C_f = local skin friction coefficient
D_u, D_v = turbulent diffusion in the x and y directions
F_c = cut off frequency
F_s = sampling frequency
H = threshold level required for the Quadrant method
P = turbulent energy production
Re_θ = Reynolds-number based on the free-stream or centerline velocity U_0 and momentum thickness θ
S_u, S_v = skewness factor of the longitudinal and vertical velocity fluctuations
t = time
x,y,z = Cartesian coordinates
U_∞ = free-stream or centerline velocity
u_τ = skin friction velocity
u, v = velocity components respectively in the longitudinal and normal direction
$\overline{(uv)_{Qi}}$ = contribution to $\overline{uv}$ from a particular quadrant $i (i = 1 \ldots 4)$

Greek

α = ratio of contributions to Reynolds shear stress from quadrants 2 and 4
δ = boundary layer thickness
ε = dissipation rate or roughness parameter
κ = Von Karman's constant (=0.41)
ν = kinematic viscosity
ω = wake function
ρ = density
θ = momentum thickness
τ_0 = mean wall shear stress
Π = wake parameter
ΔU = roughness function

Superscripts

$+$ = made dimensionless with inner variables
$'$ = rms value
$\overline{\ }$ = mean value

References

[1] Bandyopadhyay, P. R., and Watson, R. D., 1987, "Structure of Rough-Wall Turbulent Boundary Layers," Phys. Fluids, **31**, pp. 1877–1883.
[2] Krogstad, P.-Å., and Antonia, R. A., 1999, "Surface Roughness Effects in Turbulent Boundary Layers," Exp. Fluids, **27**, pp. 450–460.
[3] Krogstad, P.-A., Antonia, R. A., and Browne, L. W. B., 1992, "Comparison between Rough- and Smooth-wall Turbulent Boundary Layers," J. Fluid Mech., **245**, pp. 599–617.
[4] Krogstad, P.-A., and Antonia, R. A., 1994, "Structure of Turbulent Boundary Layers on Smooth and Rough Walls," J. Fluid Mech., **277**, pp. 1–21.
[5] Antonia, R. A., 1994, "The Effect of Different Types of Surfaces Conditions on a Turbulent Boundary Layer," *1st International Conference on Flow Interaction cum Exhibition on Interaction of Science & Art, Hong Kong*, pp. 64–79.
[6] Shafi, H. S., and Antonia, R. A., 1995, "Anisotropy of the Reynolds Stress in a Turbulent Boundary Layer on a Rough Wall," Exp. Fluids, **18**, pp. 213–215.
[7] Shafi, H. S., Antonia, R. A., and Krogstad, P-Å., 1995, "Influence of Surface Roughness on the Turbulence Characteristics of a Boundary Layer," *Proc. Tenth Symposium on Turbulent Shear Flows*, J. C. Wyngaard, F. Durst, R. M. So, and J. H. Whitelaw, eds., pp. 5.13–5.18.
[8] Shafi, H. S., and Antonia, R. A., 1997, "Small-scale Characteristics of a Turbulent Boundary Layers over a Rough Wall," J. Fluid Mech., **342**, pp. 263–293.
[9] Rotta, J. C., 1962, "Turbulent Boundary Layers in Incompressible Flow," *Progress in Aeronautical Science*, A. Feric, D. Kucheman, and L. H. G. Stone, eds., Pergamon, 2, pp. 1–20.

Downloaded 03 Jun 2010 to 171.66.16.150. Redistribution subject to ASME license or copyright; see http://www.asme.org/terms/Terms_Use.cfm

[10] Raupach, M. R., 1981, ''Conditional Statistics of Reynolds Stresses in Rough-wall and Smooth-wall Turbulent Boundary Layers,'' J. Fluid Mech., **108**, pp. 363–382.
[11] Osaka, H., and Mochizuki, S., 1988, ''Coherent Structures of a d-type Rough Wall Boundary Layer,'' *Transport Phenomena in Turbulent Flows: Theory, Experimental and Numerical Simulation*, M. Hirata and N. Kasagi, eds., Hemisphere, pp. 199–211.
[12] Tani, I., Munakata, H., Matsumoto, A., and Abe, K., 1988, ''Turbulence Management by Groove Roughness,'' *Turbulence Management and Relaminarisation*, H. W. Liepman, and R. Narasimha, eds., Springer, pp. 161–172.
[13] Tani, I., 1988, ''Turbulent Boundary Layer Development over Rough Surfaces,'' *Perspectives in Turbulence Studies*, H. U. Meier and P. Bradshaw, eds., Springer, pp. 223–249.
[14] Antonia, R. A., and Luxton, R. E., 1971, ''Some Statistical Properties of Turbulence in Smooth and Rough Wall Boundary Layers,'' *Charles Kolling Research Laboratory, T.N F31, University of Sydney*.
[15] Perry, A. E., Schofield, W. H., and Joubert, P. N., 1969, ''Rough Wall Turbulent Boundary Layer,'' J. Fluid Mech., **177**, pp. 383–413.
[16] Raupach, M. R., Antonia, R. A., and Rajagopalan, S., 1991, ''Rough-wall Turbulent Boundary Layers,'' Appl. Mech. Rev., **44**, pp. 1–25.
[17] Hama, F. R., 1954, ''Boundary Layer Characteristics for Smooth and Rough Surfaces,'' Trans. Soc. Naval Archit. Mar. Engrs., **62**, pp. 233–255.
[18] Antonia, R. A., and Krogstad, P-Å., 1993, ''Scaling of the Bursting Period in Turbulent Rough Wall Boundary Layers,'' T.N. in Exp. Fluids, **15**, pp. 82–84.
[19] Finley, P. J., Khoo, Chong Phoe, and Chin, Jeck Poh., 1966, ''Velocity Measurements in a Thin Turbulent Wake Layer,'' La Houille Blanche, **21**, pp. 713–721.
[20] Granville, P. S., 1976, ''A Modified Law of the Wake for Turbulent Shear Layers,'' ASME J. Fluids Eng., **98**, pp. 578–580.
[21] Grass, A. J., 1971, ''Structural Features of Turbulent Flow over Smooth and Rough Boundaries,'' J. Fluid Mech., **50**, pp. 233–255.
[22] Hanjalic, K., and Launder, B. E., 1972, ''Asymmetric Flow in Plane Channel,'' J. Fluid Mech., **51**, p. 301.
[23] Corino, E. R., and Brodkey, R. S., 1969, ''A Visual Investigation of the Wall Region in Turbulent Flow,'' J. Fluid Mech., **37**, pp. 1–30.
[24] Wallace, J. M., Eckelmann, H., and Brodkey, R. S., 1972, ''The Wall Region in Turbulent Flow,'' J. Fluid Mech., **54**, pp. 39–48.
[25] Brodkey, R. S., Wallace, J. M., and Eckelmann, H., 1974, ''Some Properties of Truncated Turbulence Signals in Bounded Shear Flows,'' J. Fluid Mech., **63**, pp. 209–224.
[26] Willmarth, W. W., and Lu, S. S., 1972, ''Structure of the Reynolds Stress Near the Wall,'' J. Fluid Mech., **55**, pp. 65–92.
[27] Lu, S. S., and Willmarth, W. W., 1973, ''Measurements of the Structure of the Reynolds Stress in a Turbulent Boundary Layer,'' J. Fluid Mech., **60**, pp. 481–571.

Downloaded 03 Jun 2010 to 171.66.16.150. Redistribution subject to ASME license or copyright; see http://www.asme.org/terms/Terms_Use.cfm

R. K. Sullerey
Professor,
Department of Aerospace Engineering,
Indian Institute of Technology,
Kanpur-208 016, India
e-mail: suller@iitk.ac.in

Sourabh Mishra
Former Graduate Student

A. M. Pradeep
Graduate Student

Department of Aerospace Engineering,
Indian Institute of Technology, Kanpur, India

Application of Boundary Layer Fences and Vortex Generators in Improving Performance of S-Duct Diffusers

An experimental investigation was undertaken to study the effect of various fences and vortex generator configurations in reducing the exit flow distortion and improving total pressure recovery in two-dimensional S-duct diffusers of different radius ratios. Detailed measurements including total pressure and velocity distribution, surface static pressure, skin friction, and boundary layer measurements were taken in a uniform inlet flow at a Reynolds number of 7.8×10^5*. These measurements are presented here along with static pressure rise, distortion coefficient, and the transverse velocity vectors at the duct exit determined from the measured data. The results indicate that substantial improvement in static pressure rise and flow quality is possible with judicious deployment of fences and vortex generators.* [DOI: 10.1115/1.1436096]

Introduction

Combat aircrafts have one or two engines, which are generally integrated with the fuselage. Supplying them with the necessary quantity of air for generating thrust takes place by means of specially designed inlets, through which air is taken from the external flow and supplied to the engines. Numerous modern combat aircraft designs are equipped with inlets that act as two dimensional air intakes. The inlets are attached to the side of the fuselage as two dimensional air intakes with basically horizontal orientation. Connecting the inlet to the engine compressor face is a subsonic diffuser that converts rectangular cross section to a circular cross section (for a twin engine aircraft) or to a semi-circular cross section in the case of a single engine aircraft. As the shift in the axis is required between the inlet and the engine, the subsonic diffuser is generally an S-duct. Due to space limitations, a short duct is desired, resulting in high degrees of centerline curvature. Due to centerline curvature, there are cross-stream pressure gradients giving rise to secondary flows. Within the boundary layer this imparts cross-flow velocities creating non-uniform total pressure profiles. In addition, there is a stream-wise pressure gradient resulting from increasing cross-sectional area. The combined effect may result in an increased total pressure nonuniformity (i.e., distortion) and total pressure loss at the duct exit. The engine response to the flow delivered by the intake depends not only on the total pressure provided but also, more significantly, on the quality of the flow at the compressor face.

Guo and Seddon [1] investigated the swirl in an S-shaped duct of typical aircraft intake proportions at different incidences and through flow ratios. In order to reduce the magnitude of swirl at high angles of incidences, two methods were studied. One, to change the distortion of the pressure by means of a spoiler and two, to re-energize the separated flow and inflow of free stream air through auxiliary inlets. Of the anti-swirl devices, the spoiler was found to be more powerful and could be sized to either reverse the swirl direction or to eliminate the swirl completely. Weng and Guo [2] presented a new approach of swirl control in an S-shaped diffuser called automatic adjustable blade (AAB) method that offered an effective swirl control at the expense of an acceptable total pressure loss.

Taylor et al. [3] have reported measurements of flow in circular and square cross-section S-ducts using a Laser Doppler Anemometer for both laminar and turbulent flows. The results of this study have been used for comparison with computational studies by McConnaughey et al. [4].

Majumdar et al. [5] have reported experimental measurements in a diffusing S-duct having an area ratio of two. The duct was fabricated by joining two 90-degree identical diffusing ducts with an offset. A small pocket of flow reversal at the inflection plane was observed in their measurements. Secondary motions were present throughout the diffuser passage. The curvature and area ratios of the diffusers were too high for aircraft intakes.

Benchmark aerodynamic data for compressible flow through a representative S-duct were presented by Wellborn et al. [6]. Details of separated flow region, including the mechanism, which drives complicated flow phenomenon, were discussed. The measurements indicated that the duct curvature induces strong pressure driven secondary flows, evolving into counter-rotating vortices.

Wendt and Reichert [7] have experimentally studied the effect of nonuniform upstream flow arising due to vortex ingestion in a diffusing S-duct inlet with and without an array of surface mounted vortex generators. The ingested vortex was observed to have a strong influence on duct flow field, but only when the vortex trajectory was near the region of separation that existed in the baseline S-duct.

Seddon [8] investigated the effect of wall fences of various sizes and combinations in reducing the swirl in an S-duct arising due to high angles of attack. It was concluded that large swirl reduction with an improvement of the total pressure distortion at high incidence was possible with modest size fences and a small effect on mean pressure recovery at low incidence. In contrast, Sullerey and Mishra [9] have studied the effectiveness of boundary layer fences in improving the performance of S-duct diffusers of rectangular cross-section in a uniform inlet flow. Significant improvement in performance of the diffusers was observed with top and bottom wall fences. Various fence heights were tried to achieve optimum performance of the duct.

Reichert and Wendt [10] could improve the total pressure distortion and recovery performance of a diffusing S-duct using low-

Contributed by the Fluids Engineering Division for publication in the JOURNAL OF FLUIDS ENGINEERING. Manuscript received by the Fluids Engineering Division November 17, 2000; revised manuscript received August 24, 2001. Associate Editor: P. W. Bearman.

 Copyright © 2002 by ASME

Downloaded 03 Jun 2010 to 171.66.16.150. Redistribution subject to ASME license or copyright; see http://www.asme.org/terms/Terms_Use.cfm

profile vortex generators (so-called wishbone types). In a further study, Reichert and Wendt [11] used tapered-fin type vortex generators with an objective of controlling the development of secondary flows. The application of vortex generators here differed from conventional point of view of vortex generators as devices that re-energize the boundary layer by mixing free stream and boundary layer fluids, rather the objective was to control the development of secondary flows. Later Reichert and Wendt [12] presented the compilation of previous two studies with additional data on the effectiveness of various vortex generator configurations in reducing exit flow distribution of circular S-ducts. Foster et al. [13] conducted measurements in flow through rectangular-to-semi annular transition duct to demonstrate the effectiveness of vortex generators to reduce the circumferential total pressure distortion.

Wendt and Dudek [14] described the development of an effective design strategy for surface-mounted vortex generator arrays in a subsonic diffuser using both computational and experimental analysis for transitioning high-speed inlet flow. While, a substantial reduction in circumferential total pressure distortion was obtained by proper placement of vortex generators using computational results, experimental measurements were used to determine proper vortex generator sizing to minimize total pressure recovery losses associated with vortex generator device drag.

The objective of the present investigations was to study the effect of fences [9] and vortex generators in controlling secondary flows in an S-duct diffuser with a uniform inlet flow for radius and area ratios that are typical of combat aircraft intakes. Two S-duct diffusers of rectangular cross-section were studied. Both the diffusers had the same centerline arc length and area ratio thereby keeping the streamwise pressure gradient nearly constant. However, the radius of curvature of the centerline arc was different in the two cases. The diffuser with greater radius of curvature of the centerline arc was subject to increased secondary flows. In both the diffuser configurations, fences and vortex generators were used to assess the improvement in pressure recovery and exit flow distortion.

Earlier Reichert and Wendt [11,12] had conducted tests on circular S-ducts of radius ratio 10 with tapered-fin vortex generators. Significant improvement in performance of the diffuser with proper placement of tapered-fin vortex generators was observed as a result of reduced secondary flows. Usually, aircraft intakes have radius ratios between 4 and 6. In the present investigations, a series of tests was undertaken to investigate the effectiveness of tapered-fin vortex generators in diffusers with rectangular cross sections of lower radius ratios (increased curvatures). The tapered-fin vortex generators were employed such that each vortex generator produced a single trailing axial vortex in the direction opposing the naturally occurring secondary flows thus reducing secondary flow effects.

The height of the boundary layer fences was varied to obtain an optimum performance in fence alone configurations. Two types of vortex generators were tried, namely, wishbone type and tapered-fin type. The wishbone type vortex generators were used on the curved walls for the purpose of energizing the boundary layer in regions of high adverse pressure gradients. The tapered-fin vortex generators were used with a primary intention to control secondary flows. These were deployed on top and bottom walls. The tapered-fin vortex generator angles (refer Fig. 2(*a*)) were varied for best performance.

Experimental Setup and Procedure

The measurements were carried out in an open-circuit wind tunnel. A blower discharged air through a diffuser into a large settling chamber having a honeycomb and three sets of wire mesh screens. A contraction section of an area ratio of 17 accelerated the flow into the test section entrance of cross-section area of 380 mm (width)$\times$305 mm (height). A large contraction ratio ensured a uniform flow at the inlet. The measured free stream turbulence level of the inlet flow was less than 0.5 percent. Between the contraction and the S-duct diffuser, a straight duct of 300 mm length was provided to obtain fully developed, zero pressure gradient turbulent boundary layer at the diffuser inlet. Detailed velocity measurements were carried out across the diffuser inlet (free-stream) and in the inlet boundary layers. The diffuser inlet flow was uniform with an average wall boundary layer momentum thickness equal to 0.2 percent of the inlet width. The tests were carried out at a Reynolds number of 7.8×10^5 based on the diffuser inlet width. A constant area duct extension of 300 mm length was also placed at the diffuser exit to provide smooth, continuos flow exiting the duct.

Diffusing S-Duct. The diffusers investigated had a rectangular cross-section with an aspect ratio (diffuser inlet height to width ratio) of 0.8. The area ratio (diffuser exit to inlet area ratio) for both the diffusers was 1.35. The diffuser geometries are shown in Fig. 1 and Fig. 2. The two diffusers were designed for radius ratios 4 and 6 and so experienced different curvature effects. However as the area ratio and the centerline arc lengths were same in the two cases, the streamwise pressure gradient was similar. The centerline arc length of both the diffusers corresponded to a 6-degree semi-divergence angle of an equivalent straight diffuser of same area ratio. To increase the duct area, the diffuser width was linearly varied along the duct centerline while keeping the height constant. The width was equally distributed normal to the centerline. The top and bottom duct walls were made of plywood and the curved sidewalls were of Perspex sheets. For the first diffuser (Fig. 1), the centerline radius of curvature to half width ratio was 6 and for the second diffuser (Figs. 2(*a*) and 2(*b*)) it was 4. Two planar circular arcs with identical radii defined the duct centerline. However, as the arc radius was different in two cases, the two diffusing ducts subtended different angles (16 and 24 degrees, respectively).

Fences and Vortex Generators. The different fence configurations with which S-duct diffuser flow measurements have been taken are shown in Fig. 1. The fences were made of 1.5 mm thick aluminum sheet. The edges of the fences were rounded off. Based on initial observations in the S-duct diffuser ($R/r=6$), the fence height was kept uniform at 120 percent of the measured boundary layer thickness in the bare duct (diffuser without any flow control devices) at the inflection plane. This choice of fence height was based on detailed preliminary measurements. From these measurements, it was concluded that this fence height gave the best performance improvement. The fences were inserted through slots along the top and bottom wall centerlines. Four different fence

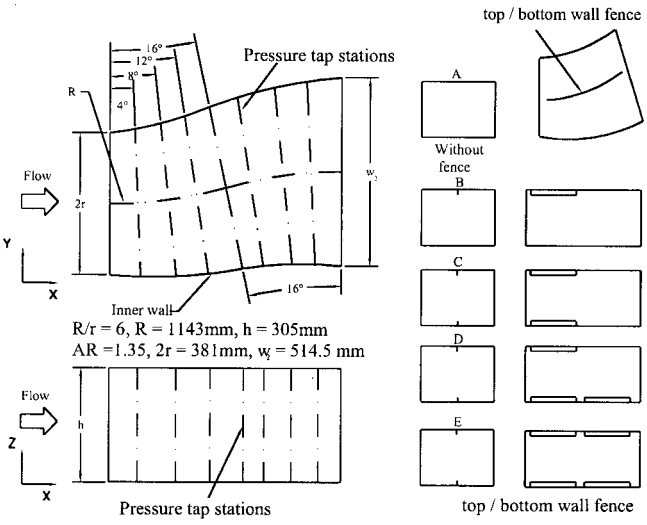

Fig. 1 Layout of S-duct diffuser 1 and fence configurations

Downloaded 03 Jun 2010 to 171.66.16.150. Redistribution subject to ASME license or copyright; see http://www.asme.org/terms/Terms_Use.cfm

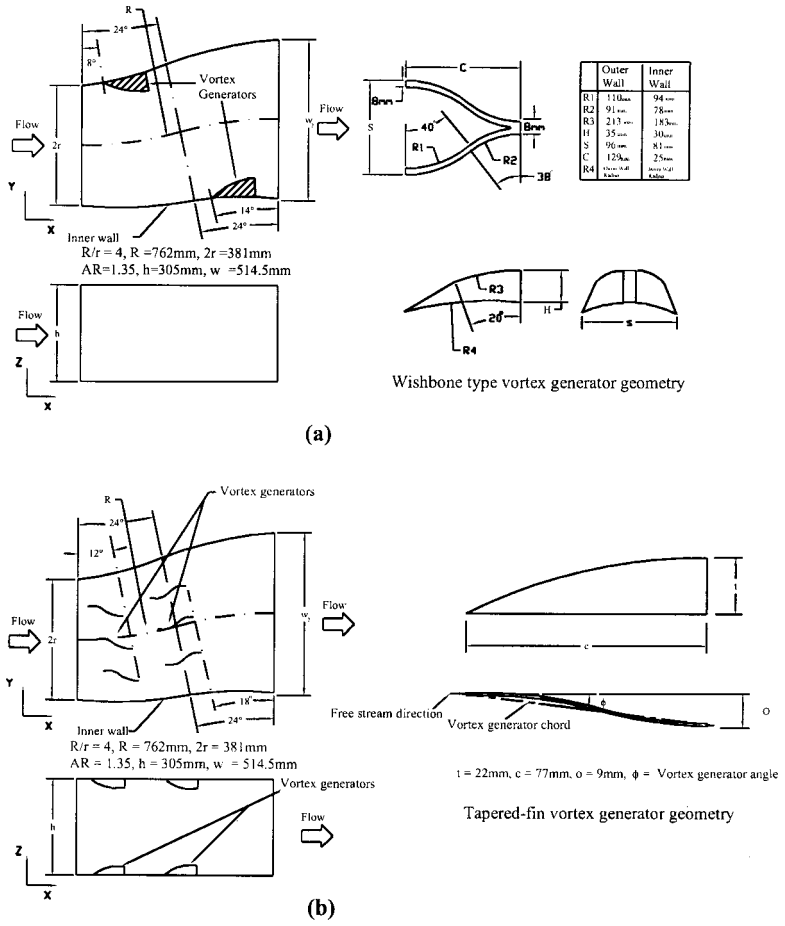

Fig. 2 Diffuser 2 geometry with wishbone and tapered-fin vortex generators

configurations used were B, C, D, and E. The configuration A was the diffuser without any wall-mounted fences. For the second diffuser ($R/r=4$), the fence height was further increased (based on measurements with different fence heights) and only configuration E was tested. Experimental measurements with fences on the curved walls did not result in any improvement in diffuser performance. Therefore, detailed measurements were made only with fences on top and bottom walls.

The vortex generator designs are shown in Figs. 2(*a*) and 2(*b*) alongside the diffuser geometry. The wishbone type vortex generator geometry chosen was similar to the one given by Wendt and Hingst [15]. The height of the wishbone type vortex generator was about 60 percent of the boundary layer thickness (of the bare duct) at the point where the vortex generator (tip) was fitted. The base of the vortex generator was curved in accordance with the wall profile. The locations of the vortex generators were selected on the basis of wall pressure distribution. The most appropriate location was considered to be just prior to the region of high adverse pressure gradients (the boundary layer grows rapidly in this region). At each location, a pair of vortex generators was used (details of flow structure in the wake of such vortex generators given in [15]).

The tapered-fin vortex generators were designed as given by Wendt and Reichert [11]. The height of the vortex generators was about 50 percent of the boundary layer thickness at the inflection plane. The vortex generators were made from 1.5 mm thick aluminum sheet and were fixed firmly on the top and bottom walls of the diffusers. The location of the vortex generators was decided based on the wall static pressure distribution (maximum pressure difference between the inner and outer walls) in the bare duct. The vortex generators were fixed in such a way that the tip of the trailing edge pointed towards the high-pressure side so that the vortices shed by the vortex generators opposed the naturally occurring secondary flows and thus aiding in control of secondary flow losses. At each location a set of three vortex generators were used. The vortex generator angle (ref. Fig. 2(*b*)) was varied so as to achieve optimum performance.

Instrumentation and Measurement Techniques. The measurements included diffuser wall static pressure distributions, mean velocities, boundary layer and skin friction measurements and flow angularity measurements. A Furness (FC012 model) digital multi-channel micro-manometer was used for all pressure measurements. The static pressure measurements were taken with wall pressure tappings at eight stations on each diffuser. Each station had nine pressure taps of 0.8 mm diameter (three on each curved walls and three on the top wall). There were thirteen pressure taps at the inflection plane. The last station was at some distance from the diffuser exit on the straight duct attached at diffuser exit. The C_p values were expected to be within one percent accuracy (on the basis of multiple measurements at a given station).

The skin friction measurements were made using wall mounted Preston tubes of 0.8 mm diameter. These tubes were fitted along the centerline of inner and outer walls at eight stations. The skin friction coefficient was estimated based on the procedure given by Patel [16]. The skin friction measurements were expected to be within 2 percent accuracy. More than the skin friction measurements, the basic purpose of using Preston tubes in the present experiments was to detect regions of flow separation. The bound-

Downloaded 03 Jun 2010 to 171.66.16.150. Redistribution subject to ASME license or copyright; see http://www.asme.org/terms/Terms_Use.cfm

ary layer measurements were made on all four walls at inlet, inflection and the exit planes of the S-duct diffuser. A 0.8 mm diameter pitot probe was used for this purpose.

The total pressure and velocity measurements (including flow angularity) were made using a five-hole conical probe of diameter 6.4 mm. For probe traverse, an accurate three-dimensional traverse system (least count 0.5 mm) was used. The five-hole probe was calibrated (using a three dimensional calibration rig as in [17]) with one-degree interval and hence the accuracy in flow angularity was expected to be within one degree. Detailed flow measurements using five-hole probe were made at the inflection and the diffuser exit plane for different fence and vortex generator configurations tested. The total pressure measurements were expected to be within one percent accuracy.

Results and Discussions

The first set of tests was carried out on bare S-duct diffusers. The boundary layer measurements at the inflection plane and the duct exit did not indicate flow separation in either of the diffusers. These measurements along with the wall static pressure distribution provided an estimate of the boundary layer thickness and the severity of adverse pressure gradients in the diffusers. The selection of particular fence configurations and the location of the vortex generators were based on these measurements.

Tapered-fin vortex generators and boundary layer fences were tried on both the diffusers as devices for control of secondary flows. However wishbone type vortex generators find application more as devices to energize the boundary layer. Hence, it was considered appropriate to use wishbone type vortex generators only for the diffuser $2(R/r=4)$ as it had a much greater adverse pressure gradient on the curved surfaces compared to diffuser $1(R/r=6)$. Presented below are the results of the two diffusers of radius ratio 6 and 4 in that order.

Diffuser 1 ($R/r=6$). The C_p distribution on the inner and outer walls for the diffuser is shown in Fig. 3 for all five cases with and without fences. The inner and outer wall pressures at a particular station can be seen to differ considerably. This pressure distribution is typical of S-duct diffusers [8]. In the first bend, the inner wall pressure was considerably higher than the outer. However, after the inflection plane (where there was change of curvature), outer wall pressures became higher than those on inner wall. The wall pressure differentials between the inner and outer wall created secondary flows by causing slow moving boundary layer fluid to move from high pressure to low-pressure region. Except near the inflection plane, everywhere else the wall pressure differentials were high. The fences were placed in regions of high-pressure differentials. It was observed that the pressure recovery improved significantly both on the inner and outer walls, especially with fence configurations *D* and *E*. The fences are expected to prevent secondary motion and this is confirmed by these results.

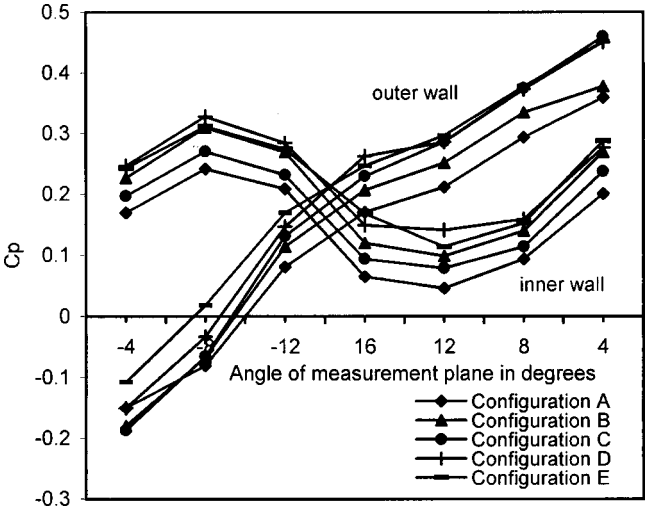

Fig. 3 C_p distribution of diffuser 1 for different fence configurations

On the basis of average static pressure at the exit of the duct, an 18.6 percent improvement in the C_p value was obtained for the configuration *E* as compared with the bare duct. A fence height 120 percent of the inflection plane boundary layer thickness was found to be optimum for this diffuser based on measurements carried out for various fence heights. It was the migration of low energy boundary layer fluid towards the low-pressure wall (responsible for increased losses) that was prevented by the fences (by physically blocking the cross flow). However, fences add to the wetted surface of the duct, so any increase in fence height beyond what is necessary would give rise to additional frictional losses.

It may be mentioned that the measurements of Seddon [8] were confined to application of fences for countering swirl in S-ducts at high angle of attacks and fences were used only in the first bend. The fences extended almost to the mid-section of the duct. However, the present application of fences was to improve the S-duct performance by reducing secondary flows and fence heights were of the order of the boundary layer thickness.

The bare diffuser exit momentum thickness (as percentage of inlet width) was 2.2 percent on outer wall and 1.0 percent on the inner wall. Both these measurements were at the midsections. For configuration E the corresponding values are 1.9 percent and 0.4 percent. The reduced momentum thickness is indicative of lower losses when the fences are employed.

The exit total pressure nonuniformity was measured in terms of distortion coefficient, D_C, which reduces from a value of 0.662 for the bare duct to 0.588 for the diffuser with fences. The total

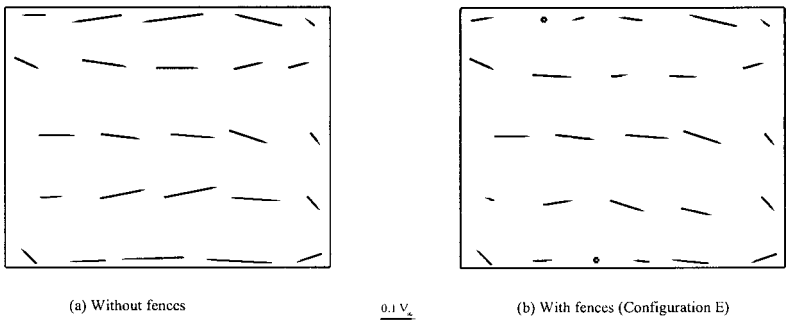

Fig. 4 Transverse velocity distribution at the diffuser 1 exit. (*a*) Without fences, (*b*) with fences (Configuration E).

Downloaded 03 Jun 2010 to 171.66.16.150. Redistribution subject to ASME license or copyright; see http://www.asme.org/terms/Terms_Use.cfm

Table 1 Summary of results for diffuser 1 ($R/r=6$)

Exit flow property	Bare duct	With fences	With tapered-fin vortex generators
C_P	0.343	0.407	0.372
ϖ	0.16	0.10	0.142
D_C	0.662	0.588	0.602

pressure loses were expressed in terms of average total pressure loss coefficient, ϖ (mass average of 25 point measurements at duct exit). The exit pressure loss coefficient was 0.16 for the bare duct and 0.1 for the diffuser with fence configuration E. The expected accuracy of loss coefficient values was within 2 percent.

Figures 4(*a*) and 4(*b*) show the transverse velocity vectors at the exit of the bare duct and diffuser with fences (configuration *E*). The angles of the velocity vectors were in the range 2 to 8 degrees. The magnitude of the transverse velocity vectors reduced with the employment of fences as is clear from these figures.

The vortex generators were placed on the top and bottom walls of the diffuser. Their exact location was chosen from the C_p distribution of the bare duct. The vortex generators were placed at locations where the difference between the inner and outer wall C_p was maximum. The vortex generators were placed at two planes with three vortex generators (the number of vortex generator and their spacing to chord ratio was based on [10,11]) in each plane (Fig. 2(*b*)). The vortex generator angle was varied (in the range 2 to 8 degrees as obtained from transverse velocity distribution) so as to achieve optimum performance improvement. There was a modest improvement in performance, (as measured by static pressure rise, total pressure loss coefficient, ϖ and distortion coefficient, D_C) but to a lesser extent as compared to fences. The optimum angle of the vortex generators was observed to be three degrees on both planes where they were placed.

The consolidated results for the bare diffuser, diffuser with fences for configuration *E* and diffuser with tapered-fin vortex generators at three degrees chord angle are given in Table 1. Significant improvement in performance of the diffuser with fences can be observed. Tapered-fin vortex generators also lead to improvement in all the parameters measured but to a lesser extent in comparison to fences.

Diffuser 2 ($R/r=4$). This diffuser had a higher centerline curvature than diffuser1. Secondary flows in curved ducts arise due to the pressure difference between the inner and outer wall. Hence diffuser 2 experienced increased cross flows and consequently more losses. After initial measurements on the bare duct, measurements were carried out with fence configuration E for varying fence heights. In addition, as a steep adverse pressure gradient was observed on the curved sidewalls, it was considered appropriate to use wishbone type vortex generators on the curved walls so as to energize the boundary layers. The wishbone type vortex generators were used with and without top and bottom wall fences.

Figure 5(*a*) presents the inner and outer wall C_p distribution with and without fences. A fence height of 130 percent of boundary layer thickness (50 mm fence height) at inflection plane gave an optimum performance. Fence heights greater than this value did not result in any further performance improvement. Hence the results of this configuration have not been included in Fig. 5(*a*). Measurements with wishbone type vortex generators gave a C_p value of 0.269 at the exit of the duct. The C_p value of the bare duct was 0.267. The average total pressure loss coefficient was 0.147 and the distortion coefficient was found to be 0.744. On comparing these values to those with fences, it was observed that the wishbone type vortex generators did not lead to much improvement in performance, as flow control by mixing was ineffective in an S-duct diffuser. For bare diffuser 2, the momentum thickness (as percentage of inlet width) was 2.50 percent on the outer wall and 1.20 percent on the inner wall. For the diffuser with fences of height 50 mm the corresponding values were 2.0 percent, and 0.60 percent respectively.

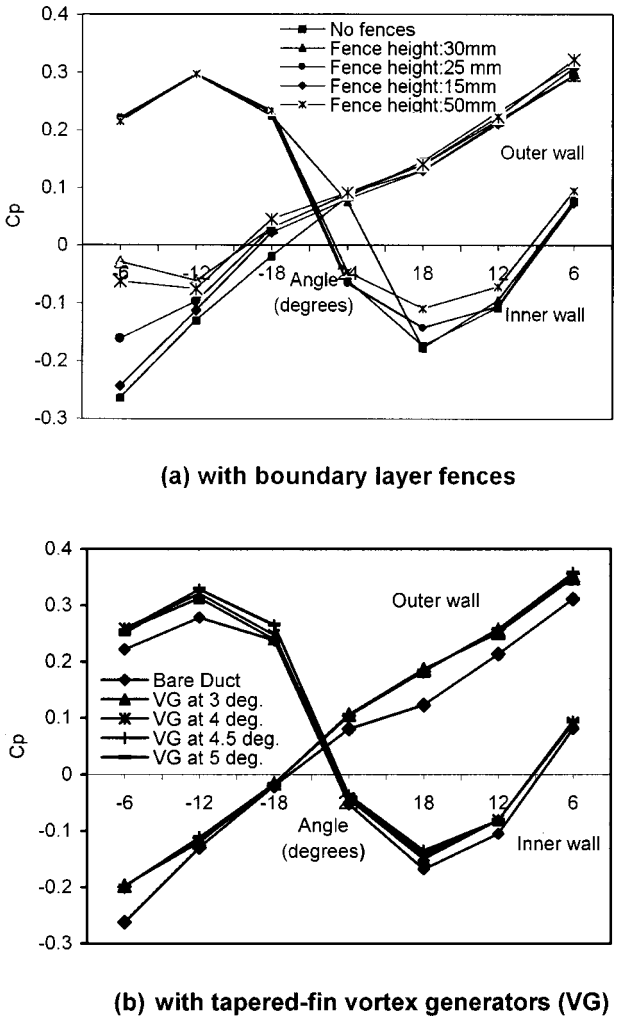

Fig. 5 Inner and outer wall C_p distribution with angle of measurement plane for diffuser 2. (*a*) With boundary layer fences, (*b*) with tapered-fin vortex generators (VG).

Next, measurements were carried out using tapered fin vortex generators. The tapered fin vortex generators were placed in a similar manner as for the diffuser 1. The exact location was obtained from the C_p distribution of the bare diffuser 2. The C_p distribution for the diffuser 2 with various tapered fin vortex generators configurations is given in Fig. 5(*b*). The vortex generator angle was varied on both the planes so as to obtain optimum performance. Vortex generator angle of 4.5 degrees on both the planes gave the most optimum performance. Comparing 5(*a*) and 5(*b*), it can be noted that for diffuser 2, the performance improvement with tapered fin vortex generators is better than with fences.

In Fig. 6, centerline C_p distributions of bare diffuser1 and 2 are presented together with their most optimum configurations of fences and vortex generators. There is significantly higher-pressure recovery for diffuser 1 as compared to diffuser 2. As both were of same area ratio and semi-divergence angle, reduced performance of diffuser 2 was due to increased centerline curvature. It was observed from these results that fences were more effective in improving performance for diffuser 1 where centerline curvature was less and tapered-fin vortex generators in the case of diffuser 2 where centerline curvature was more.

The total pressure loss coefficient contours are given in Figs. 7(*a*) and 7(*b*) without and with tapered-fin vortex generators re-

Downloaded 03 Jun 2010 to 171.66.16.150. Redistribution subject to ASME license or copyright; see http://www.asme.org/terms/Terms_Use.cfm

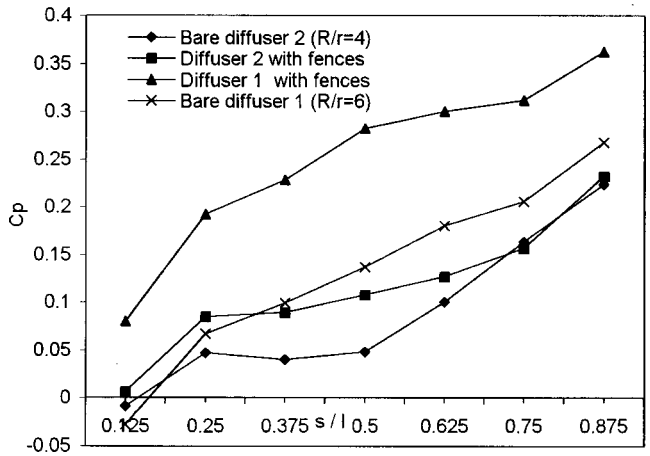

Fig. 6 Comparison of centerline C_p distribution for the two diffusers

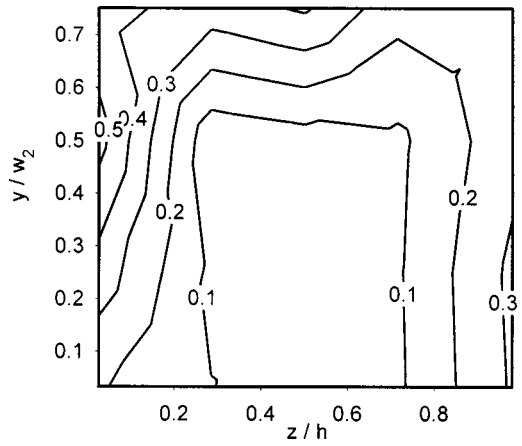

(a) bare duct

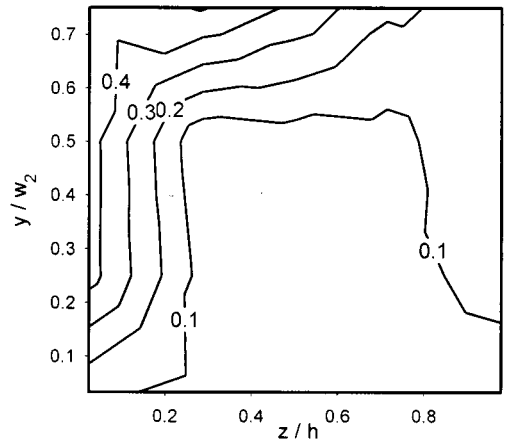

(b) with tapered-fin vortex generators

Fig. 7 Total pressure loss coefficient distribution at the diffuser 2 exit. (*a*) Bare duct, (*b*) with tapered-fin vortex generators.

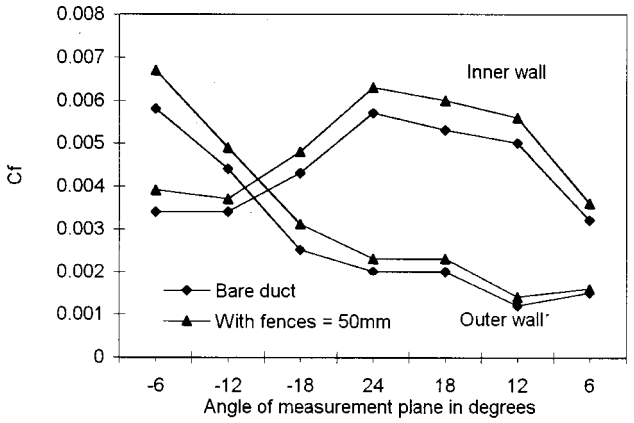

(a) Diffuser 1

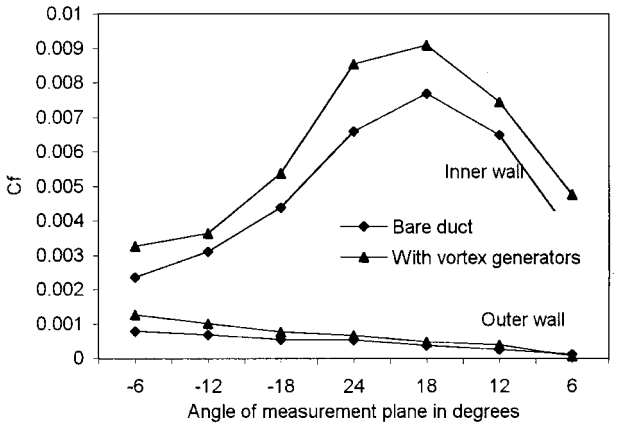

(b) Diffuser 2

Fig. 8 Variation of skin fraction coefficient along the sidewalls. (*a*) Diffuser 1, (*b*) Diffuser 2.

Table 2 Summary of results for diffuser 2 ($R/r=4$)

Exit flow property	Bare duct	With tapered-fin vortex generators	With fences
C_P	0.267	0.322	0.30
ϖ	0.17	0.104	0.121
D_C	0.786	0.651	0.707

spectively. The extent of low loss regions ($0.1<\omega<0.2$) is more extensive in Fig. 7(*b*) as compared to Fig. 7(*a*). In Figs. 8(*a*) and 8(*b*), the skin friction measurements for the two diffusers are shown. The outer wall C_f for diffuser 2 approached zero toward the exit of the duct. Comparing with diffuser 1, C_f values were lower for diffuser 2. The skin friction coefficients were observed to increase with the use of fences on diffuser 1 and tapered-fin vortex generator on diffuser 2.

The summary of results for the bare diffuser 2, diffuser with fences at 50 mm height and with tapered-fin vortex generators at 4.5 degrees chord angle are listed in Table 2. Significant improvement in performance of the diffuser can be observed with the employment of tapered-fin vortex generators. The improvement in performance with fences is less as compared to the tapered-fin vortex generators.

Conclusions

In diffuser 1 ($R/r=6$) the use of fences significantly improved the diffuser performance for the entire fence configurations tested. The best configuration, *E*, having fences along both top and bottom wall centerlines, gave an increase of 18.6 percent in the static pressure recovery, improved the total pressure loss coefficient

Downloaded 03 Jun 2010 to 171.66.16.150. Redistribution subject to ASME license or copyright; see http://www.asme.org/terms/Terms_Use.cfm

from 0.16 to 0.10 and decreased the flow distortion coefficient at the duct exit from 0.662 to 0.588. A fence height equal to 120 percent of boundary layer thickness at the inflection plane resulted in best diffuser performance. The improvement in the diffuser performance was brought about by the reduction in the secondary flows by the fences. The employment of tapered-fin vortex generators (a set of three vortex generators in two planes) in the same diffuser resulted in an increase in static pressure by 8.4 percent, reduction in total pressure loss coefficient from 0.16 to 0.142 and improvement in the flow distortion coefficient from 0.662 to 0.602. Thus it is observed that tapered-fin vortex generators are less effective as compared to fences for the diffuser 1.

In diffuser 2 $(R/r=4)$, the maximum improvement in static pressure recovery was obtained with the configuration employing tapered fin vortex generators. An improvement of 20.6 percent in C_p value at the diffuser exit was obtained with this configuration. The distortion coefficient decreased from 0.786 to 0.651. The employment of fences (most optimum fence height being 130 percent of boundary layer thickness at inflection plane) on diffuser 2 resulted in a modest improvement in performance. A static pressure rise of 12.3 percent was obtained with fences. The reduction in total pressure loss coefficient and distortion coefficient was also by a lesser factor as compared to that of tapered-fin vortex generators. The wishbone type vortex generators that were employed with diffuser 2 gave only marginal improvement in all the parameters as compared to the fences or tapered-fin vortex generators. A reason for these results seems to be that the improvement in the case of fences and tapered-fin vortex generators arises due to reduction in secondary flows. While the wishbone type vortex generators created their own losses, the fences and tapered fin vortex generators being very thin in cross section generate very less losses.

It was observed that the fence height and tapered fin vortex generators orientation giving the best performance would vary depending upon the centerline curvature. The present experimental investigation reveals that fences perform better when used with diffusers of greater radius ratio while tapered-fin vortex generators would perform better when used with diffusers of lesser radius ratio.

Nomenclature

AR = area ratio of the diffuser
C_p = pressure coefficient $=(p-p_{\text{ref}})/(1/2\rho V_\infty^2)$
C_f = skin fiction coefficient
D_c = distortion coefficient $=(p_{\text{oav}}-p_{\text{omin}})/q_{\text{av2}}$
R = duct centerline radius of curvature
Re = Reynolds number based on inlet diffuser width
V = fluid velocity
Y = distance along duct centerline radius from inner wall of the diffuser
Z = distance along diffuser height from the bottom of the diffuser
h = diffuser height (constant)
l = duct centerline length
p = static pressure
p_o = total pressure
q = dynamic head
r = inlet half width
s = distance along the duct centerline from diffuser inlet
ρ = fluid density
ϖ = average total pressure loss coefficient $=(p_{o1}-p_{o2av})/(1/2\rho V_\infty^2)$

Subscript

av = average value
max = maximum value
min = minimum value
ref = inlet plane (reference)
1,2 = notations for inlet and exit planes
∞ = free stream value
o = total pressure

References

[1] Guo, R.W., and Seddon, J., 1983, ''The Swirl in an S-duct of Typical Air Intake Proportions,'' Aeronaut. Q., **34**, pp. 99–129.
[2] Weng, P.F., and Guo, R.W., 1994, ''New Method of Swirl Control in a Diffusing S-duct,'' AIAA J., **30**, No. 7, Technical Notes, pp. 1918–1919.
[3] Taylor, A.M.K.P., Whitelaw, J.H., and Yianeskis, M., 1982, ''Curved Ducts with Strong Secondary Motion: Velocity Measurements of Developing Laminar and Turbulent Flow,'' ASME J. Fluids Eng., **104**, pp. 350–359.
[4] McConnaughey, P., Cornelison, J., and Barker, L., ''The Prediction of Secondary Flows in Curved S-ducts of Square Cross-Section,'' 1989, AIAA Paper 89-0276.
[5] Majumdar, B., Singh, S.N., and Agarwal, D.P., 1997, ''Flow Characteristics in S-Shaped Diffusing Duct,'' International Journal of Turbo and Jet Engines, **14**, pp. 45–57.
[6] Wellborn, S.R., Reichert, B.A., and Okiishi, T.H., 1992, ''An Experimental Investigation of the Flow in a Diffusing S-Duct,'' AIAA Paper 92-3622.
[7] Wendt, B.J., and Reichert, B.A., 1996, ''Vortex Ingestion in a Diffusing S-Duct Inlet,'' J. Aircr., **33**, No. 1, pp. 149–154.
[8] Seddon, J., 1984, ''Understanding and Countering the Swirl in S-Ducts: Tests on the Sensitivity of Swirl to Fences,'' Aeronaut. Q., **88**, pp. 117–127.
[9] Sullerey, R.K., and Mishra, S., 2000, ''Performance Improvement in S-duct diffusers with boundary layer fences,'' FEDSM2000-11240, Proceedings, 2000 ASME Fluids Engineering Summer Meeting, Boston.
[10] Reichert, B.A., and Wendt, B.J., 1993, ''An Experimental Investigation of S-Duct flow Control Using arrays of Low Profile Vortex Generator,'' AIAA Paper 93-0018.
[11] Reichert, B.A., and Wendt, B.J., 1994, ''Improving Diffusing S-Duct Performance by Secondary Flow Control,'' NASA Technical Memorandum 106492.
[12] Reichert, B.A., and Wendt, B.J., 1996, ''Improving Curved Subsonic Diffuser with Vortex Generators,'' AIAA J., **34**, No. 1, pp. 65–72.
[13] Foster, J., Wendt, B.J., Reichert, B.A., and Okiishi, T.H, 1997, ''Flow Through a Rectangular-to-Semiannular Diffusing Transition Duct,'' J. Propul. Power, **13**, No. 2, pp. 312–317.
[14] Wendt, B.J., and Dudek, J.C., 1998, ''Development of Vortex Generator Use for a Transitioning High-Speed Inlet,'' J. Aircr., **35**, No. 4, pp. 536–543.
[15] Wendt, B.J., and Hingst, W.R., 1994, ''Flow structure in the Wake of a Wishbone Vortex Generator,'' AIAA J., **32**, No. 11, pp. 2234–2240.
[16] Patel, V.C., 1965, ''Calibration of Preston tubes and its Limitations on its Use in Pressure Gradients,'' J. Fluid Mech., **23**, Part 1, pp. 185–208.
[17] Novak, C.F.R., 1970, ''Improved Calibration Method for a Five-hole Spherical Pitot Probe,'' Journal of Physics, Sec. E, **3**, No. 1–2, p. 21.

Downloaded 03 Jun 2010 to 171.66.16.150. Redistribution subject to ASME license or copyright; see http://www.asme.org/terms/Terms_Use.cfm

Measurement of the Instantaneous Velocity Gradients in Plane and Axisymmetric Turbulent Wake Flows

T. Schenck
Ph.D. Student

J. Jovanović
Senior Research Scientist

Lehrstuhl für Strömungsmechanik,
Universität Erlangen-Nürnberg,
Cauerstrasse 4, 91058 Erlangen, Germany

All first-order spatial derivatives of the turbulent velocity fluctuations were measured using a pair of X hot-wire probes. Measurements were performed in the self-preserving region of a turbulent plane wake downstream of a cylinder and in an axisymmetric wake behind the sphere. Good spatial resolution of the measurements was ensured by choosing small values for the cylinder/sphere diameter and a low flow speed. Errors due to the finite hot-wire length and the wire and probe separation were analyzed using Wyngaard's correction method. The derived corrections were verified experimentally. The measuring technique and the experimental results were systematically checked and compared with the results available in the literature. The assumptions of local isotropy and local axisymmetry were examined. Both investigated flows deviate only moderately from local isotropy and local axisymmetry. Support for the measured results is provided by plotting the data on an anisotropy invariant map. The budgets of the turbulent kinetic energy were computed from the measured data. In contrast to the results obtained in the plane wake, where the pressure transport is nearly negligible, in the axisymmetric wake it was found to play an important role and closely follows the estimate made by Lumley, $\overline{u_i p}/\rho \approx -0.2\overline{q^2 u_i}$.
[DOI: 10.1115/1.1428330]

1 Introduction

The dissipation correlations $\epsilon_{ij} = \nu\overline{\partial u_i/\partial x_k\, \partial u_j/\partial x_k}$ play an important role in turbulence modeling, since these represent a sink term in the Reynolds stress equations. The trace of the dissipation tensor ϵ[1] appears in nearly all turbulent models. Modeling of the dissipation rate correlations is the weakest part of the turbulence closures since the dynamics of ϵ_{ij} are extremely complicated. Often they are modeled assuming local isotropy, as proposed by Kolmogorov [1]. An exception is the near-wall region where empirical wall functions are used to recast the data. One of many difficulties also originates from an insufficient amount of numerical or experimental data that can be of some use for direct validation of the closure assumptions used to construct a transport equation for the dissipation rate. Although direct numerical simulations have been available for almost 20 years, only very few data sets contain useful information about terms in the transport equation of the turbulent dissipation rate. In this respect, two-point statistics would be extremely useful but are not available. Experimental data are also rare, since measurements of the relevant terms are very difficult or even impossible.

The first dissipation measurements were made by Simmons and Salter [2] using hot-wire probes together with Taylor's frozen flow hypothesis and assuming isotropy in the dissipation range. In a similar way, the turbulent dissipation rate was measured in a turbulent jet by Corrsin [3] and Corrsin and Uberoi [4] and in a plane wake by Townsend [5,6]. Townsend measured statistics of the streamwise derivatives which provided support for the applicability of the assumption of local isotropy. Laufer [7] and Klebanoff [8] measured five of the nine terms of the turbulent dissipation rate in a turbulent pipe flow and in a flat plate boundary layer, respectively. For the determination of the remaining terms they applied isotropic relationships. All three components of the temperature dissipation rate were measured in a turbulent wake flow by Uberoi and Freymuth [9] and Antonia and Browne [10]. The same quantities were also measured by Tavoularis and Corrsin [11,12] in a homogeneous shear flow and by Krishnamoorthy and Antonia [13] in a turbulent boundary layer.

Using a pair of X hot-wire probes, Browne et al. [14] measured all nine terms of the turbulent dissipation rate. Instead of ϵ the authors determined the dissipation from $\overline{\epsilon}$ and assumed local isotropy for the three remaining terms. George and Hussein [15] and Hussein et al. [16] used the flying hot-wire technique for measuring five of the nine dissipation terms in a round jet at high Reynolds numbers. A similar experiment was performed by Hussein [17], who measured seven of nine terms of ϵ in a plane jet. The results obtained in this study showed that local axisymmetry is a better approximation than local isotropy.

Ye [18] measured all nine terms of the turbulent dissipation rate and three components of the dissipation tensor in a turbulent plane wake using the same technique as Browne et al. [14]. The measurements described in this paper are an extension of the work of Browne et al. [14] and Ye [18]. Instead of a fixed X hot-wire configuration, two probes with variable separation were employed, allowing precise relative alignment and the possibility of performing various test measurements. The paper focuses mainly on experimental aspects such as corrections and accuracy tests. At the end of the paper we provide distributions of the individual terms involved in the transport equation for turbulent kinetic energy. A detailed investigation and validation turbulence closure of the dissipation correlations using the experimental data will be the subject of a future paper.

[1] ϵ and the total average turbulent dissipation rate $\overline{\epsilon}$ are related as follows:

$$\overline{\epsilon} = \nu\overline{\frac{\partial u_i}{\partial x_k}\left(\frac{\partial u_i}{\partial x_k} + \frac{\partial u_k}{\partial x_i}\right)} = \nu\overline{\frac{\partial u_i}{\partial x_k}\frac{\partial u_i}{\partial x_k}} + \nu\frac{\partial^2\overline{u_i u_k}}{\partial x_i \partial x_k}.$$

The second term on the right-hand side is negligible in the wake flows under consideration.

Contributed by the Fluids Engineering Division for publication in the JOURNAL OF FLUIDS ENGINEERING. Manuscript received by the Fluids Engineering Division January 7, 2000; revised manuscript received September 13, 2001. Associate Editor: J. Bridges.

Downloaded 03 Jun 2010 to 171.66.16.150. Redistribution subject to ASME license or copyright; see http://www.asme.org/terms/Terms_Use.cfm

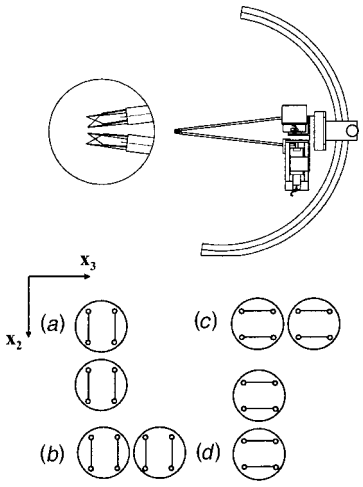

Fig. 1 Different configurations of X hot-wire probes employed for measurements of the instantaneous velocity derivatives. (*a*) $u_{1,1}$, $u_{1,2}$, $u_{2,1}$, $u_{2,2}$; (*b*) $u_{1,1}$, $u_{1,3}$, $u_{3,1}$, $u_{3,3}$; (*c*) $u_{1,1}$, $u_{1,3}$, $u_{2,1}$, $u_{2,3}$; (*d*) $u_{1,1}$, $u_{1,2}$, $u_{3,1}$, $u_{3,2}$.

2 Experimental Technique for Measuring Velocity Derivatives

Spatial derivatives of the fluctuating velocities can be obtained experimentally by measuring the velocity difference at two closely spaced points, $u_{i,j}=\partial u_i/\partial x_j \approx \Delta u_i/\Delta x_j$. This technique, known as the finite-difference method, was used in several studies by Browne et al. [14], Ye [18], and Zhu and Antonia [19]. Using a pair of X hot-wire probes of different configurations all nine components of the turbulent dissipation rate ϵ can be measured, as shown in Fig. 1, which provide details of a wind-tunnel arrangement of two closely separated X hot-wire probes used for the velocity derivative measurements. The sketch shows probe holders, the device used for calibration of hot wires at known yaw angles in the wind tunnel (top) and different configurations of X hot-wire probes (bottom). Here, the coordinates x_2 and x_3 lie in the plane peperdicular to the flow which is along the x_1 direction.

In the analysis of the data measured by different hot-wire configurations shown in Fig. 1, it was necessary to account for the spatial filtering arising from the finite length (l) of the hot wires and also for the wire (d) and probe (s) separation. For this purpose, the correction procedure suggested by Wyngaard [20,21], and extended by Zhu and Antonia [19], was applied. Here we provide a brief summary of the correction method used to evaluate the data.

Assuming that turbulence is homogeneous, the derivative $\overline{(\partial u_1/\partial x_2)^2}$ can be expressed by

$$\overline{\left(\frac{\partial u_1}{\partial x_2}\right)^2}=\int_{-\infty}^{\infty}\int_{-\infty}^{\infty}\int_{-\infty}^{\infty}k_2^2\phi_{11}(\mathbf{k})dk_1dk_2dk_3, \tag{1}$$

where $\mathbf{k}$ is the wavenumber vector, $\mathbf{k}=(k_1,k_2,k_3)$, and ϕ_{11} is the energy spectral tensor. The measured velocity derivative spectrum $\phi^m_{u_{1,2}}$ for the hot-wire configuration (a) shown in Fig. 1 and 2 can be represented by

$$\begin{aligned}\phi^m_{u_{1,2}}(\mathbf{k})=1/s^2\sin^2(k_2s/2)\{&\phi_{11}[(X_a^2+X_b^2)+2X_aX_b\cos(k_3d)]\\&+2\cot\vartheta\phi_{12}(X_b^2-X_a^2)+\cot^2\vartheta\phi_{22}[(X_a^2+X_b^2)\\&-2X_aX_b\cos(k_3d)]\},\end{aligned} \tag{2}$$

where $X_a=\sin(\mathbf{kl}_a)/(\mathbf{kl}_a)$ originate from the filtering effect due to the finite length of the hot wire (Zhu and Antonia, [19]). The use of the above equation assumes homogeneity of turbulence, uniformity of the mean velocity field across the hot wire and small turbulence intensity. With Eqs. (1) and (2) one can estimate the ratio

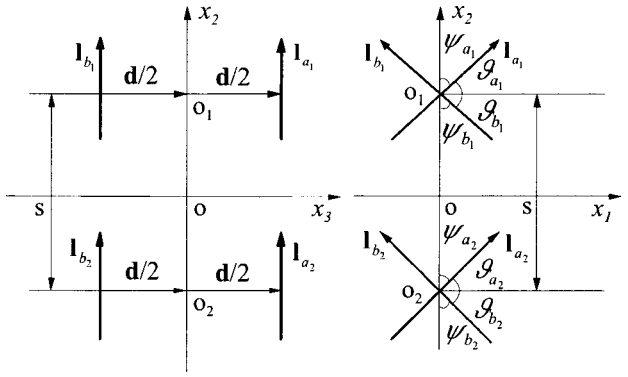

Fig. 2 Schematic of the X hot-wire configuration shown in Fig. 1(*a*). Here *d* is the distance between the hot wires, *l* is the hot-wire length, *s* is the distance between two probes and ψ is the effective wire angle.

$$r_{12}=\frac{\overline{(\partial u_1/\partial x_2)^{2^m}}}{\overline{(\partial u_1/\partial x_2)^2}}=\frac{\int\int\int_{-\infty}^{\infty}\phi^m_{u1,2}(\mathbf{k})dk_1dk_2dk_3}{\int\int\int_{-\infty}^{\infty}k_2^2\phi_{11}(\mathbf{k})dk_1dk_2dk_3}, \tag{3}$$

by integrating Eq. (3) numerically with the assumed isotropic form for ϕ_{ij}:

$$\phi_{ij}(\mathbf{k})=\frac{E(k)}{4\pi k^4}(k^2\delta_{ij}-k_ik_j), \tag{4}$$

where $E(k)$ is the three-dimensional energy spectrum. In the same way, corrections for all other gradients can be defined.

Zhu and Antonia [19] used $E(k)$ from the DNS data for a turbulent channel flow to evaluate the data. In the present study the form of $E(k)$ suggested by Pao [22] was used to estimate the influence of the wire length and the wire and probe separation on measured statistics of the velocity derivatives. Because of the implied isotropy assumption involved in approximation of the energy spectrum, $E(k)$ corrections must be verified before they can be applied.

2.1 Wind Tunnel Setup and Instrumentation. The experiments were carried out in the closed test section of a return-type wind tunnel at the Lehrstuhl für Strömungsmechanik, Erlangen. Its test section is 1.87 m wide, 1.40 m high, and 2.0 m long. The flow uniformity in the wind tunnel and two-dimensionality of the plane wake were systematically investigated before performing the measurements. The free stream turbulence level in the empty test section was approximately 0.07% in the streamwise direction and 0.04% in the normal and lateral directions. Since the free stream turbulence level was very low, no interference with the wake turbulence was expected.

The plane wake was generated by a steel tube of diameter $D=3$ mm which was installed in the middle of the tunnel test section. The velocity U_∞ in the free stream was 6.6 m/s, corresponding to a Reynolds number based on the cylinder diameter of $R_D=1340$. For generating the axisymmetric wake a sphere of diameter $D=16$ mm was suspended using four thin wires. In order to avoid vortex shedding from the suspending wires, their diameter was only 50 μm. With a free stream velocity of 6.1 m/s the wire Reynolds number was 20, which is well below $\mathrm{Re}_{\mathrm{crit}}\approx 50$. The Reynolds number based on the sphere diameter was 6550.

The axisymmetry of the mean flow field was measured using a single hot-wire probe. Figure 3 shows distributions of turbulence intensity, skewness and flatness factors of the streamwise velocity component. Data from the contour plots shown in this figure display small radial asymmetries in the narrow region of the upper

Downloaded 03 Jun 2010 to 171.66.16.150. Redistribution subject to ASME license or copyright; see http://www.asme.org/terms/Terms_Use.cfm

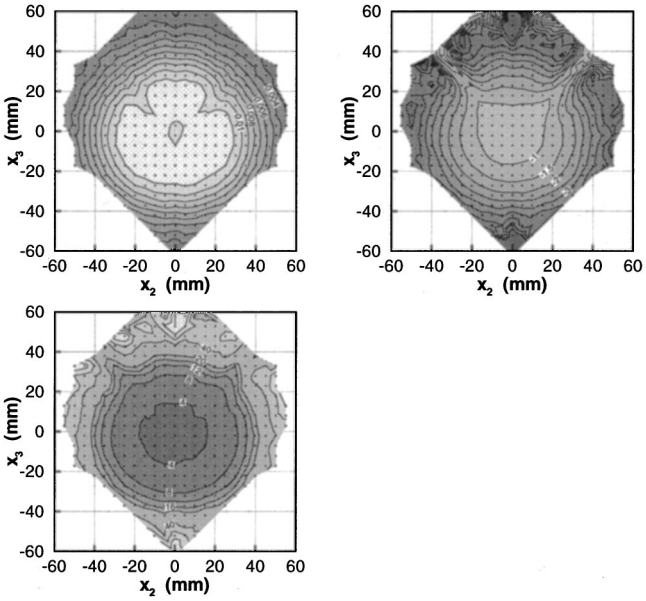

Fig. 3 Contour plot of relative turbulence intensity u_1'/U_1 (top left), the skewness factor (top right) and the flatness factor (bottom) of the streamwise velocity component in the axisymmetric wake at $x_1/D=101$

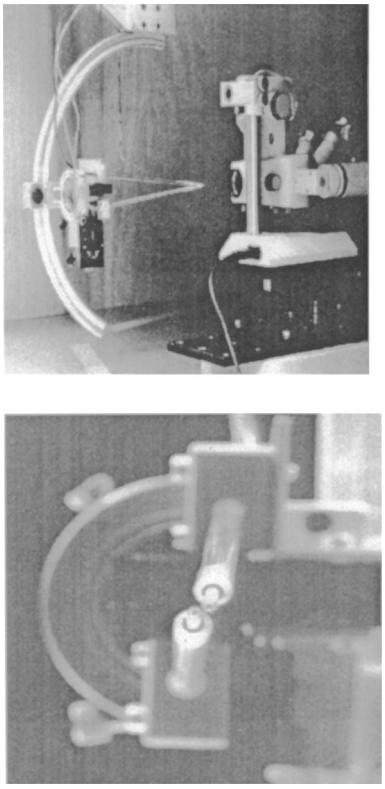

Fig. 4 Photograph of the hot-wire mounting and the microscope for probe positioning in the wind tunnel (top). Enlarged front view of the hot-wire probes (bottom).

part of the wake which originate from disturbances caused by the suspending wires. Detailed profiles of mean velocity and turbulence quantities taken by horizontal and vertical traverses across the wake showed very small deviations and nearly perfect symmetry in the measured data (Schenck [23]). It was decided, therefore, that data obtained from vertical traverses are good representatives to quantify turbulence in the axisymmetric wake flow.

Detailed experimental investigations reported here were performed in the self-preserving region: 400 diameters downstream from the circular cylinder and 75 diameters behind the sphere. The self-similarity in the wake was checked by comparing mean velocity profiles, second- and third-order moments and statistics of the longitudinal gradient of the fluctuating u_1 velocity component taken at different streamwise locations.

All measurements were made using standard DANTEC hot-wire probes operated with Dantec StreamLine constant temperature anemometers at an overheat ratio of 0.6. The output signals from the anemometers were passed through back-up amplifiers, low-pass filtered and then digitized and stored on a PC for further processing. For measurements of the mean velocity and turbulence intensities, single and X hot -wire probes (DANTEC 55P11 and 55P61[2]) were used.

To ensure the statistical independence of the sampled data, the integral time-scale was measured from the autocorrelation function at various positions across the wake. This information was used to set the sampling interval to about two integral time-scales of the flow. The sample size at each measuring point was 25,000 data taken at rate of 250 Hz. This sample size corresponds to a sampling error of 0.03% for the mean velocity and 2.3% for the second-order moments calculated on the basis of a 99% confidence level.

Hot wires were calibrated *in situ* in the wind tunnel by fitting the anemometer output voltage (E) to the effective cooling law $E^2=A+BU_{\text{eff}}^{0.45}$. The coefficients A and B, that were determined from the linear regression of the calibration data taken over the relatively small speed range, provided high accuracy (0.2%) of the voltage to velocity conversion. Owing to the small turbulence levels encountered in the investigated wake flows, the cosine law for the effective cooling velocity U_{eff} was used for splitting the signals from cross wires into the velocity components. For yaw calibration, the method proposed by Bradshaw [24] was utilized. The cross wires were employed for measurements of the normal and lateral intensity components, shear stress and triple velocity correlations, which contribute to the balance of the turbulent kinetic energy. Townsend's [6] method for measuring the triple correlation $\overline{\mu_3^2 u_2}$ was employed (see Wygnanski and Fiedler [25] and Ye [18]).

The gradients of fluctuating velocities in the normal and lateral directions, which contribute to the dissipation rate correlations, were measured using a pair of either single or cross hot-wire probes (see Fig. 4). The two cross hot wires were each yawed by 5 deg to allow a small separation between the probes ($\approx$ 1.6 mm). The inclination of the probes to the flow was accounted for during the data processing by adding the yaw angle to the effective wire angle to compute the effective cooling velocity using the stored calibration data. Taylor's hypothesis was used to determine the derivatives in the streamwise direction from recorded time traces of the measured fluctuations. The outputs of the hot-wire anemometers were first low-pass filtered at 5 kHz and then digitized at a sampling frequency f_S of 12 kHz. Prior to computing time derivatives, the data were additionally digitally low-pass filtered at the Kolmogorov frequency $f_k=U_1/2\pi L_k$ [$L_k=(\nu^3/\epsilon)^{1/4}$] using the NERD filter routines described by Kaiser and Reed [26]. The derivatives were then evaluated using $\Delta t=2/f_S$ and subsequently corrected for the effects of finite hotwire length, probe and wire separation.

[2]The hot-wire probes employed were made from Pt-plated tungsten wire, diameter 5 μm, length $l=1.16\pm0.02$ mm and the separation between the wires was $d=0.4\pm0.05$ mm.

Downloaded 03 Jun 2010 to 171.66.16.150. Redistribution subject to ASME license or copyright; see http://www.asme.org/terms/Terms_Use.cfm

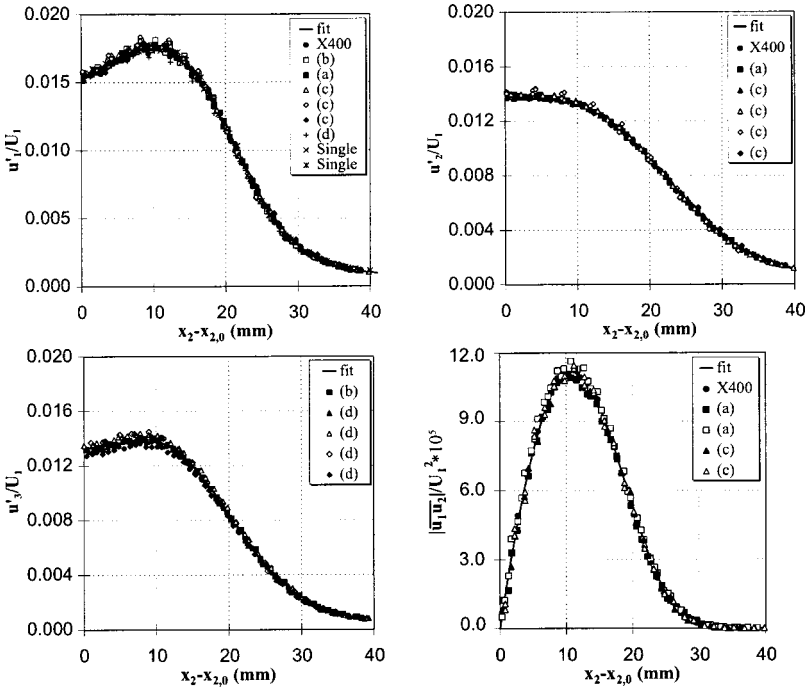

Fig. 5 Comparisons of the intensity and shear stress distributions across the plane wake measured using single wire (denoted single), cross wire (denoted X400) and configurations (*a*), (*b*), (*c*), and (*d*) shown in Fig. 1. Displayed data includes both side of the wake which cannot be distinguished owing to perfect symmetry of the flow.

3 Experimental Results

3.1 Mean Flow Field. In order to ensure high reliability of the measured data, a number of qualifying tests were made. Several profiles of $u_1'=\sqrt{\overline{u_1^2}}, u_2', u_3'$ were compared to check the repeatability of the measurements. For the plane wake flow most of the measured profiles are shown in Fig. 5. This figure shows complete profiles, i.e., both sides of the wake, and includes the data measured by all hot-wire configurations shown in Fig. 1. Note that for measurements of the instantaneous velocity derivatives it is important that both probes give nearly identical responses. The deviations between the individual curves are within a few percent and the agreement between single and cross-wire measurements is seen to be very good. The data for the axisymmetric wake (not presented here) show nearly the same degree of agreement.

An additional check of the measured data can be made from the mean momentum equation. For the two-dimensional small-deficit wake this equation is

$$U_\infty \frac{\partial U_1}{\partial x_1} + \frac{\partial \overline{u_1 u_2}}{\partial x_2} = 0, \tag{5}$$

which can be rearranged in the form

$$\frac{\overline{u_1 u_2}}{U_S^2} = -\frac{A_L}{2A_U}\,\eta f, \tag{6}$$

where A_L and A_U are the similarity constants. These can be expressed as

$$\frac{U_S}{U_\infty} = A_U \left(\frac{x_1 - x_{1,0}}{D}\right)^{-1/2}, \quad \frac{L}{D} = A_L \left(\frac{x_1 - x_{1,0}}{D}\right)^{1/2}, \tag{7}$$

where U_S is the centerline mean-velocity defect, which measures the difference between the free stream and local mean velocities, $x_{1,0}$ is the virtual flow origin, η is the nondimensional normal coordinate $\eta = x_2/L$, L is the half-width of the wake (where U_S

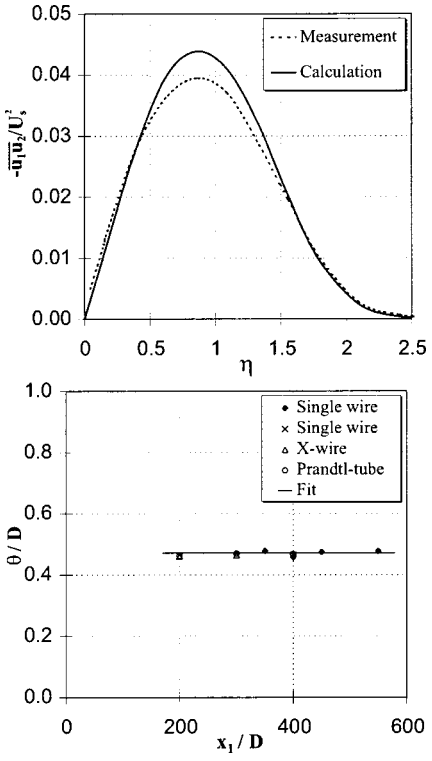

Fig. 6 Normalized distributions of measured and calculated shear stress (top). Momentum thickness in the plane wake computed at different locations behind the cylinder (bottom).

Downloaded 03 Jun 2010 to 171.66.16.150. Redistribution subject to ASME license or copyright; see http://www.asme.org/terms/Terms_Use.cfm

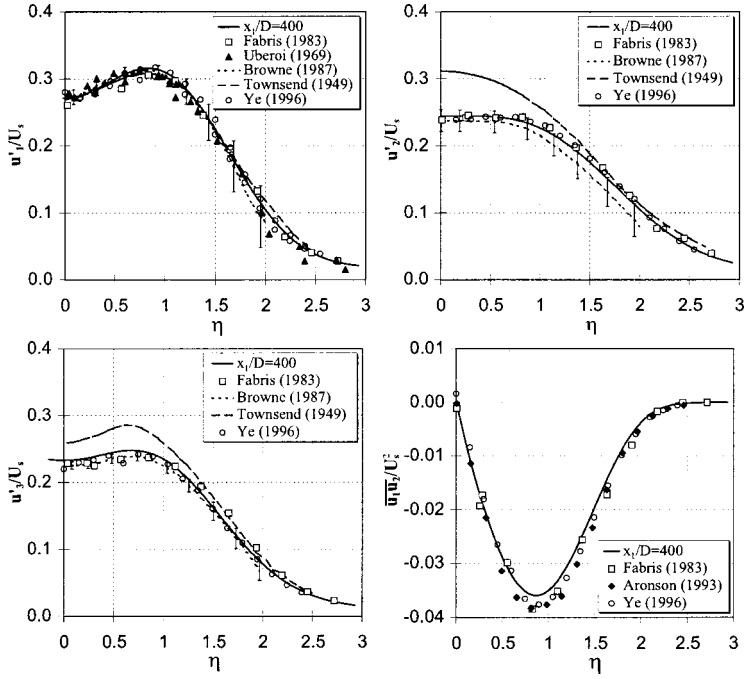

Fig. 7 Comparisons of the measured intensity components and shear stress across the plane wake with the data available in the literature

$=0.5$) and $f(\eta)$ is the normalized mean velocity distribution $f(\eta)=(U_\infty-U_1)/U_S$. Figure 6 shows the comparison between the measured data and values computed from Eq. (6). At the position of maximum shear stress the deviation is about 10% and originates from uncertainties in the determination of the similarity constants involved in Eq. (7), which were obtained by fitting the measured data at different streamwise positions in the wake (see Schenck [23]). In the case of the axisymmetric wake the maximum deviation between the measured and calculated shear stress was 8%.

The measured mean velocity profiles were used to compute the momentum thickness:

$$\theta=\int_{-\infty}^{\infty}\frac{U_1}{U_\infty}\left(1-\frac{U_1}{U_\infty}\right)dx_2, \tag{8}$$

which must be constant. Figure 6 (bottom) shows the computed values of θ at different locations behind the cylinder. The average value $\theta=1.42\pm0.02$ mm corresponds to a drag coefficient $c_D=2\theta/D$ of 0.95, which is identical with the result obtained by Wygnanski et al. [27] and is close to the value suggested in the literature (see Hoerner [28]). The value of drag inferred from the measurements in the wake behind the sphere, $c_D=0.42$, is in good agreement with the data from the literature (Hoerner [28], $c_D=0.42$; Schlichting and Gersten [29], $c_D=0.40$).

The measured data were also compared with the results available from other studies reported in the literature. Since the shape of the self-similar profiles depends on the initial conditions, as shown by Wygnanski et al. [27], only the data from wake flows behind circular cylinders from Townsend [6], Fabris [30], Aronson and Löfdahl [31], Browne et al. [14], Uberoi and Freymuth [32] and Ye [18] were used for comparisons. However, only in the studies reported by Fabris [30] and Ye [18] were all stresses directly measured. Figure 7 shows comparisons of the turbulence intensities and the shear stress in the plane wake. The data from Browne et al. [14] are shown with error bars which indicate the maximum deviations between their data sets. The agreement is seen to be good, in particular with the data of Fabris [30] and Ye [18]. The source of the deviations of the present data from those measured by Townsend [6] could not be found. An attempt to apply the extended similarity theory proposed by George [33] was not successful and the data emerging from this analysis are not shown here.

3.2 Statistics of the Velocity Derivatives. In order to test the validity of the corrections discussed in the previous section, measurements with variable separation between hot-wire probes were performed. The derivatives in the streamwise direction were computed from the recorded time traces using the Taylor hypothesis. Figure 8 shows the measured and corrected derivatives $u'_{1,1}=\sqrt{\overline{(\partial u_1/\partial x_1)^2}}$, $u'_{3,1}$ and $u'_{1,3}$ as a function of the separation distance between the probes normalized by the Kolmogorov microscale L_k.[3] The displayed data correspond to the centerline region and the outer part of the wake and were obtained using the single hot wire ($u'_{1,1}$), cross wire ($u'_{3,1}$) and a pair of single hot wires ($u'_{1,3}$). If the corrections were exact, the corrected derivatives would exhibit no dependence on the separation distance between the probes. In the centerline region of the wake the correction procedure works very well whereas in the outer part it underestimates expectations. This may be attributed to larger deviations from local isotropy in the outer part of the wake. Because the Kolomogorov length scale L_k increases with the distance from the wake centerline by a factor of about two, the relative separation between the sensors $\Delta x/L_k$ decreases and the poor performance of the corrections in the outer part of the wake is not so critical.

For very small separations between the probes, the influence of noise causes the derivatives to increase. Owing to the decreasing signal-to-noise ratio, this effect is noticeable in the outer part of the wake. An average separation between the probes of 1.7 mm corresponding to $\approx 4L_k$ near the centerline and $\approx 2L_k$ near the edge of the wake was found to be an optimal compromise between sufficient signal-to-noise ratio and a small amount of correction (3–5%) due to spatial averaging.

The separation between the individual X hot-wire probes was estimated from the average of the measured distances between the

[3]For the plane case the values of L_k were 0.44 mm near the wake centerline ($\eta\approx0$) and 0.75 mm in the outer part ($\eta\approx2$) of the wake. The corresponding values for the axisymmetric case were 0.55 and 1.05 mm, respectively.

Downloaded 03 Jun 2010 to 171.66.16.150. Redistribution subject to ASME license or copyright; see http://www.asme.org/terms/Terms_Use.cfm

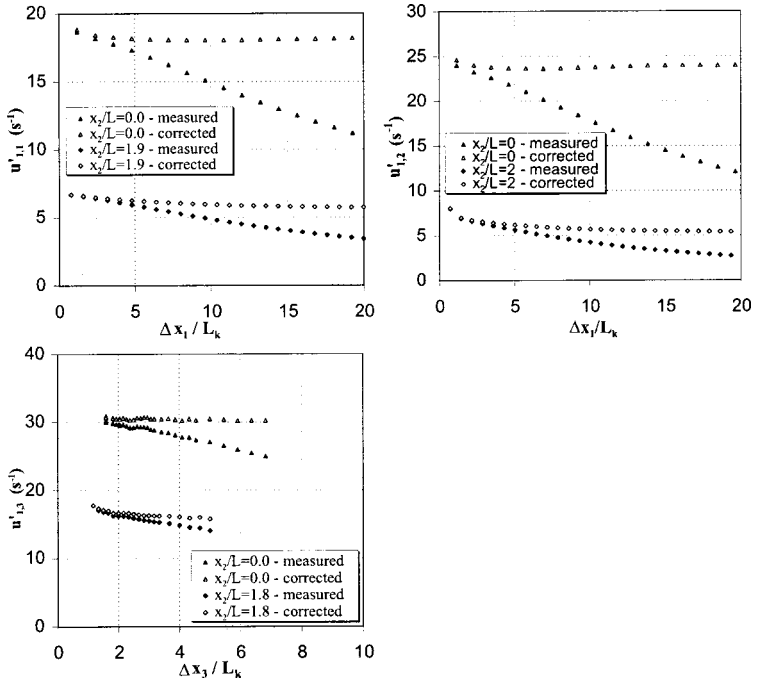

Fig. 8 Measured and corrected statistics of the velocity derivatives $u'_{1,1}$, $u'_{3,1}$, and $u'_{1,3}$ at the centerline ($x_2/L \simeq 0$) and in the outer part ($x_2/L \simeq 1.8-2$) of the plane wake

four pairs of supporting prongs. However, it was also possible to find an effective probe distance by shifting the statistics measured with hot-wire configurations shown in Fig. 1(*a*) and (*d*). Figure 9 (top) shows the measured profiles of the u'_1 and u'_2 intensities in the plane wake. By matching the measured profiles one obtains the effective probe distance as shown in Fig. 9 (bottom). This method was found to be reliable and the separation distance estimated in this way was always within ± 0.08 mm of the geometrical distance measured between the probes.

Figure 10 shows comparisons between the statistics of $u'_{1,2}$ and $u'_{1,3}$ using the probe configurations shown in Fig. 1 and the data obtained from a pair of two single hot wires. This figure also includes the statistics for $u'_{1,1}$ obtained by invoking Taylor's hypothesis. The displayed data were obtained in the axisymmetric wake and include profiles measured across both sides of the wake. The agreement achieved between various measurements of $u'_{1,1}$ is very good. A similar degree of agreement was obtained for $u'_{2,1}$ and $u'_{3,1}$ using different *X* hot-wire configurations (not shown). The agreement between the data for $u'_{1,2}$ and $u'_{1,3}$ measured using a pair of single hot wires and configurations (*a*) and (*b*) shown in Fig. 1 is also good. However, there is some discrepancy in the data measured with configuration (*d*) shown in Fig. 1. The same observations were made in the plane wake, with the exception that deviations of about 10% were obtained between the measured data for configurations (*b*) and (*c*). The origin of these deviations cannot be explained by spatial filtering effects due to the finite resolution of the hot wires employed. It might be associated with the phase differences between signals related to the separation between the wires which cannot be accounted for using the spectral corrections. In general, however, the accuracy can be considered to be satisfactory.

Figure 11 shows comparisons with the results from Browne et al. [14] and Ye [18]. Statistics of the streamwise derivatives from Ye [18] show qualitatively the same behavior but are 5–10%

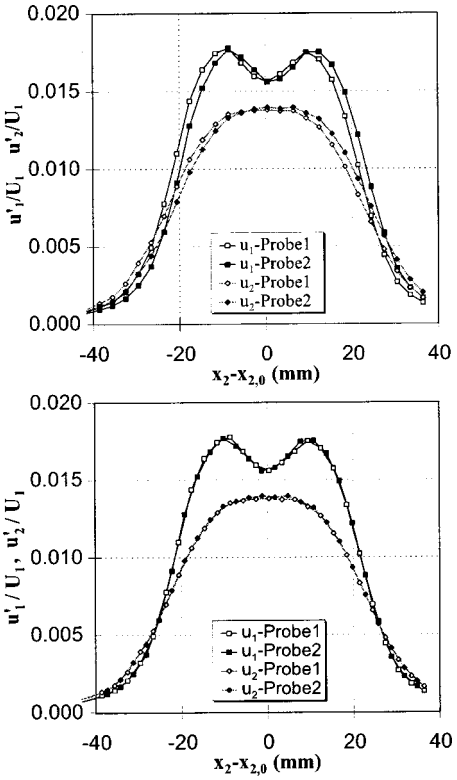

Fig. 9 Determination of an "effective" separation between the probes from the measured single point statistics using two X hot wires; profiles before matching (top) and after matching (bottom)

Downloaded 03 Jun 2010 to 171.66.16.150. Redistribution subject to ASME license or copyright; see http://www.asme.org/terms/Terms_Use.cfm

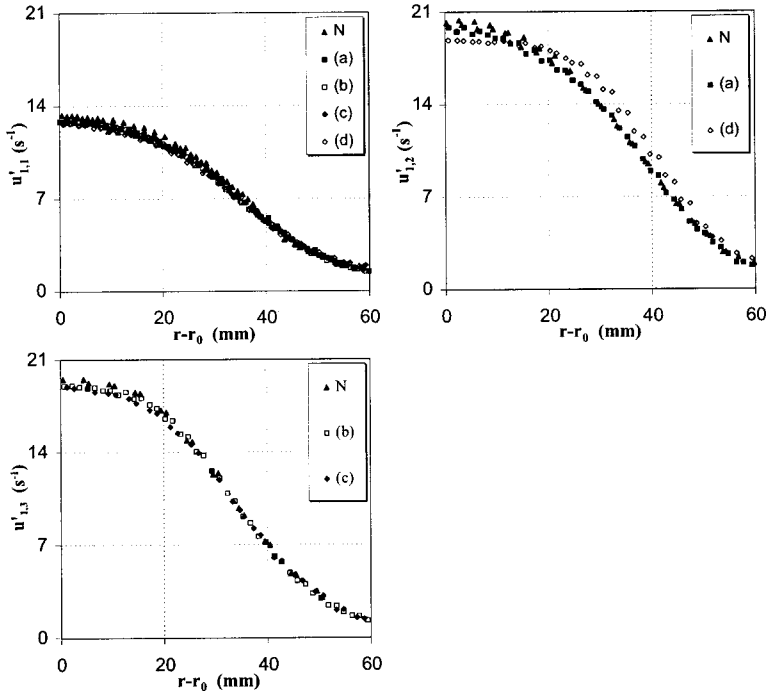

Fig. 10 Comparisons of $u'_{1,1}$, $u'_{1,2}$ and $u'_{1,3}$ measured with hot-wire configurations (*a*), (*b*), (*c*), and (*d*) shown in Fig. 1 with measurements taken using a single wire and a pair of single hot wires (denoted N) in the axisymmetric wake

higher than the present values. The reason for this can be attributed to the electronic noise, since Ye [18] used a 3 dB filter and computed the derivatives directly from time series sampled at 10 kHz. Browne et al. [14] did not apply any corrections to the measured data that were sampled at a frequency of 4800 Hz, which corresponds to $\Delta x_1 / L_k \approx 3$. Measured statistics for the derivatives in the x_2 and x_3 directions are in good agreement with the data from Ye [18]. Deviations from the data measured by Ye are in the outer part of the wake and most probably originate from uncertainties in the position of the centerline, since she measured only half of the wake width. It must be mentioned, however, that Ye [18] did not correct her data for the finite length of the hot wires

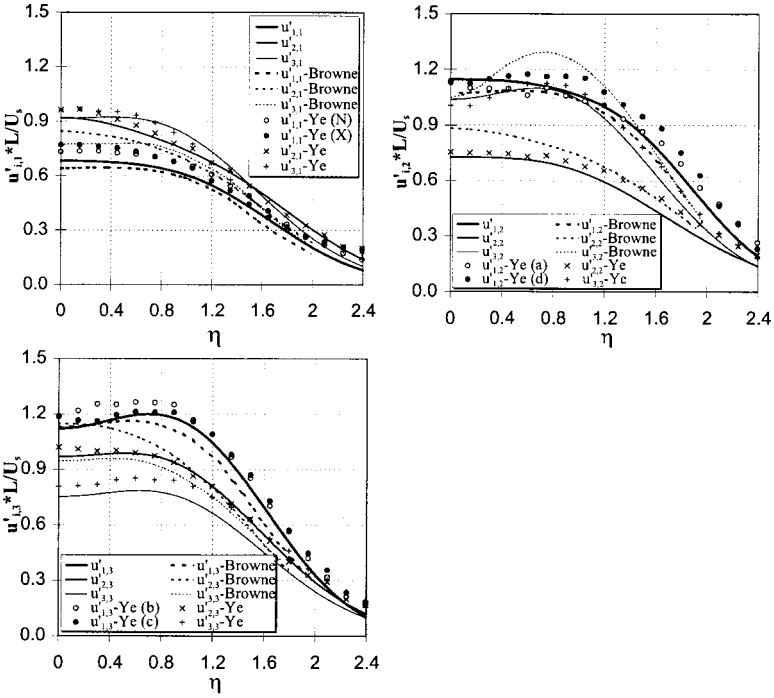

Fig. 11 Comparisons of the statistics of all nine derivatives $u'_{i,j}$ in the plane wake with the data of Browne et al. [14] and Ye [18]

Downloaded 03 Jun 2010 to 171.66.16.150. Redistribution subject to ASME license or copyright; see http://www.asme.org/terms/Terms_Use.cfm

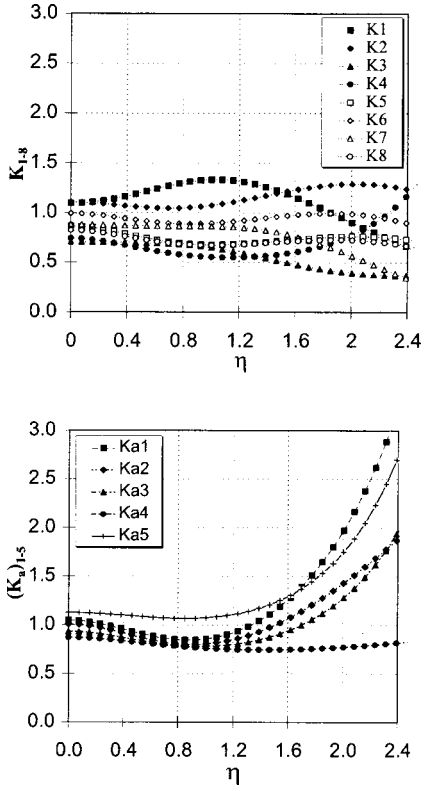

Fig. 12 Distributions of the isotropic ratios K_1-K_8 (top) and the axisymmetric ratios $K_{a1}-K_{a5}$ (bottom) across the plane wake

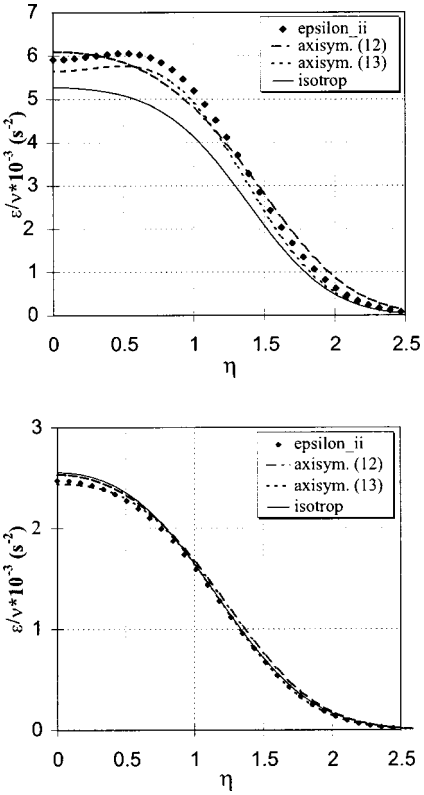

Fig. 13 Comparison of the measured dissipation rate ϵ_{ii} with its isotropic and axisymmetric approximations in the plane (top) and axisymmetric (bottom) wake

and probe and wire separation effects. The agreement of $u'_{1,2}$ and $u'_{1,3}$ with the data of Browne et al. [14] is good. The remaining statistics for the derivatives $u'_{2,2}$, $u'_{2,3}$, $u'_{3,2}$ and $u'_{3,3}$ show significant deviations. The reason for this lies in the experimental difficulties associated with derivative measurements. In the next section we provide support for our measurements based on rational arguments.

3.3 Validation of the Assumptions of Local Isotropy and Local Axisymmetry. The measured statistics of the velocity derivatives were used to check the assumptions of local isotropy and local axisymmetry. Local isotropy requires

$$\overline{\left(\frac{\partial u_i}{\partial x_k}\right)\left(\frac{\partial u_j}{\partial x_l}\right)}=\frac{1}{2}\overline{\left(\frac{\partial u_1}{\partial x_1}\right)^2}(4\delta_{ij}\delta_{kl}-\delta_{il}\delta_{jk}-\delta_{jl}\delta_{ik}), \tag{9}$$

from which it follows that in such a turbulence the ratios K_i must be equal to unity:

$$K_1=\frac{2\overline{(\partial u_1/\partial x_1)^2}}{\overline{(\partial u_2/\partial x_1)^2}},\quad K_2=\frac{2\overline{(\partial u_1/\partial x_1)^2}}{\overline{(\partial u_3/\partial x_1)^2}},\quad K_3=\frac{2\overline{(\partial u_1/\partial x_1)^2}}{\overline{(\partial u_1/\partial x_2)^2}},$$

$$K_4=\frac{2\overline{(\partial u_1/\partial x_1)^2}}{\overline{(\partial u_1/\partial x_3)^2}},\quad K_5=\frac{2\overline{(\partial u_1/\partial x_1)^2}}{\overline{(\partial u_3/\partial x_2)^2}},\quad K_6=\frac{2\overline{(\partial u_1/\partial x_1)^2}}{\overline{(\partial u_2/\partial x_3)^2}},$$

$$K_7=\frac{\overline{(\partial u_1/\partial x_1)^2}}{\overline{(\partial u_2/\partial x_2)^2}},\quad K_8=\frac{\overline{(\partial u_1/\partial x_1)^2}}{\overline{(\partial u_3/\partial x_3)^2}}. \tag{10}$$

In a similar way, one can derive the ratios K_{ai} for the case of locally axisymmetric turbulence (George and Hussein [15]):

$$K_{a_1}=\frac{\overline{(\partial u_1/\partial x_2)^2}}{\overline{(\partial u_1/\partial x_3)^2}},\qquad K_{a_2}=\frac{\overline{(\partial u_2/\partial x_1)^2}}{\overline{(\partial u_3/\partial x_1)^2}},$$

$$K_{a_3}=\frac{\overline{(\partial u_2/\partial x_2)^2}}{\overline{(\partial u_3/\partial x_3)^2}},$$

$$K_{a_4}=\frac{\overline{(\partial u_2/\partial x_3)^2}}{\overline{(\partial u_3/\partial x_2)^2}},\quad K_{a_5}=\frac{3\overline{(\partial u_2/\partial x_2)^2}}{\overline{(\partial u_1/\partial x_1)^2}+\overline{(\partial u_2/\partial x_3)^2}}. \tag{11}$$

Figure 12 shows profiles of the individual ratios K_1-K_8 and $K_{a1}-K_{a5}$ in the plane wake. According to the results reported in the literature, the deviations from local isotropy and local axisymmetry grow with increasing distance from the wake centerline. Our results show relatively small deviations from local isotropy near the wake centerline and are in agreement with measurements of Townsend [6] and Ye [18] but at variance with the results of Browne et al. [14]. Owing to moderate deviations from local isotropy, the isotropic estimate of the dissipation rate $\epsilon^{iso}=15\nu\overline{(\partial u_1/\partial x_1)^2}$, shown in Fig. 13, is about 12% lower than the true value of ϵ at the wake centerline.

Figure 12 (bottom) suggests that local axisymmetry is a better approximation than local isotropy. In the inner part of the wake all ratios and $K_{a1}-K_{a5}$ are within experimental accuracy close to unity. In the outer part of the wake the deviations from local axisymmetry increase. Figure 13 (top) indicates that the axisymmetric estimates of ϵ, which may be defined in different ways owing to the identities (11) (Rotta [34]):

$$\epsilon^{axi}=\nu[-\overline{(\partial u_1/\partial x_1)^2}+2\overline{(\partial u_1/\partial x_2)^2}+2\overline{(\partial u_2/\partial x_1)^2}+8\overline{(\partial u_2/\partial x_2)^2}], \tag{12}$$

or

Downloaded 03 Jun 2010 to 171.66.16.150. Redistribution subject to ASME license or copyright; see http://www.asme.org/terms/Terms_Use.cfm

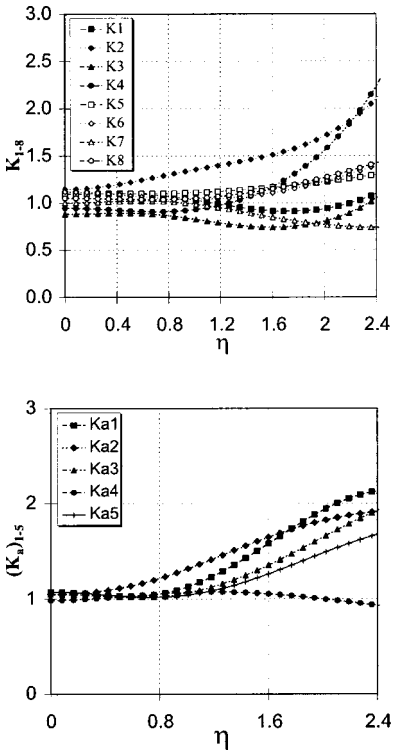

Fig. 14 Distributions of the isotropic ratios K_1-K_8 (top) and the axisymmetric ratios $K_{a1}-K_{a5}$ (bottom) across the axisymmetric wake

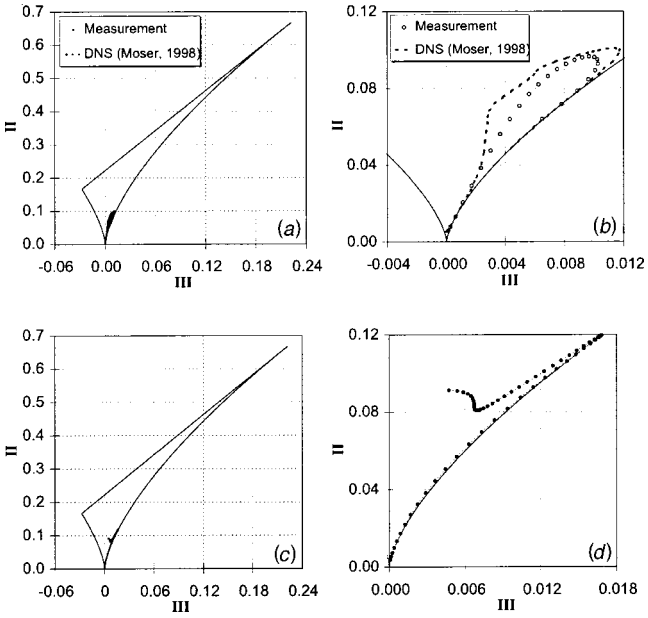

Fig. 15 Traces of joint variations of the invariants across the plane wake (top, left-right) and the axisymmetric wake (bottom, left-right) within the anisotropy-invariant map

$$\epsilon^{axi}=\nu\left[\frac{5}{3}\overline{(\partial u_1/\partial x_1)^2}+2\overline{(\partial u_1/\partial x_3)^2}+2\overline{(\partial u_2/\partial x_1)^2}+\frac{8}{3}\overline{(\partial u_2/\partial x_3)^2}\right], \tag{13}$$

are in good agreement with the results of direct measurements.

The data for the axisymmetric wake are displayed in Fig. 14. Deviations from local isotropy and local axisymmetry in the centerline region of the wake are even smaller than in the plane case. Both isotropic and axisymmetric estimates for ϵ are in very good agreement with the true value of ϵ deduced from direct measurements of all nine terms involved in ϵ (see Fig. 13, bottom).

We may provide additional support for the results shown in Fig. 12–14 by exploring the results obtained from invariant theory. Using this theory, Jovanović and Otić [35] derived the exact relation between the anisotropies of the large and small scales in axisymmetric turbulence:

$$e_{ij}=\mathcal{A}a_{ij}, \tag{14}$$

where a_{ij} and e_{ij} are defined as follows:

$$a_{ij}=\frac{\overline{u_iu_j}}{q^2}-\frac{1}{3}\delta_{ij}, \tag{15}$$

$$e_{ij}=\frac{\epsilon_{ij}}{\epsilon}-\frac{1}{3}\delta_{ij}, \tag{16}$$

and $\mathcal{A}$ is a scalar function. Equation (14) shows that anisotropy of turbulence in the dissipation range is directly proportional to the anisotropy of turbulence at large scales. To quantify anisotropy, Lumley [36] introduced scalar invariants of a_{ij}:

$$\mathrm{II}=a_{ij}a_{ji}, \tag{17}$$

$$\mathrm{III}=a_{ij}a_{jk}a_{ki}, \tag{18}$$

to show that these can be interrelated analytically for two-component turbulence:

$$\mathrm{II}=2/9+2\mathrm{III}, \tag{19}$$

and axisymmetric turbulence:

$$\mathrm{II}=(2/3)[(4/3)|\mathrm{III}|]^{2/3}. \tag{20}$$

The cross-plot of II versus III constructed from Eqs. (19) and (20) defines the anisotropy invariant map which bounds all physically realizable turbulence.

By plotting the experimental data on the anisotropy invariant map (Fig. 15), one can clearly observe that, in the inner part of the wake behind the sphere, turbulence is almost exactly axisymmetric. Also, the data of the plane wake show only moderate deviations from the axisymmetric state. Figure 15 shows that these results are supported by the DNS data of Moser et al. [37], who performed direct numerical simulations of the plane wake flow. Taking these results into account, it follows from Eq. (14) that the anisotropy at small scales and therefore of ϵ_{ij} must vanish near the wake centerline.

3.4 The Balance of the Energy Equation. The experimental data were used to compute the budget of the turbulent kinetic energy $k=\overline{u_ku_k}/2=\overline{q^2}/2$. For the two-dimensional wake flow the transport equation for k is

$$\underbrace{U_1\frac{\partial}{\partial x_1}\frac{\overline{q^2}}{2}}_{\text{Convection}}=\underbrace{-\overline{u_1u_2}\frac{\partial U_1}{\partial x_2}}_{\text{Production}}\underbrace{-\frac{1}{2}\frac{\partial}{\partial x_2}\overline{q^2u_2}}_{\overline{q^2}\text{-Diffusion}}\underbrace{-\frac{1}{\rho}\frac{\partial}{\partial x_2}\overline{pu_2}}_{\text{Pressure-Diffusion}}\underbrace{-\epsilon}_{\text{Dissipation}}. \tag{21}$$

The viscous diffusion was neglected in Eq. (21) since it was found to be much smaller than the other terms involved in the budget of k.

The convection term was estimated from the self-similarity of the profiles, $\overline{q^2}/U_S^2=\widetilde{\overline{q^2}}(\eta)$. Production and diffusion terms were computed directly from the measured profiles of the mean velocity, shear stress and triple moments. The pressure diffusion was deduced from the balance of Eq. (21) by difference.

Downloaded 03 Jun 2010 to 171.66.16.150. Redistribution subject to ASME license or copyright; see http://www.asme.org/terms/Terms_Use.cfm

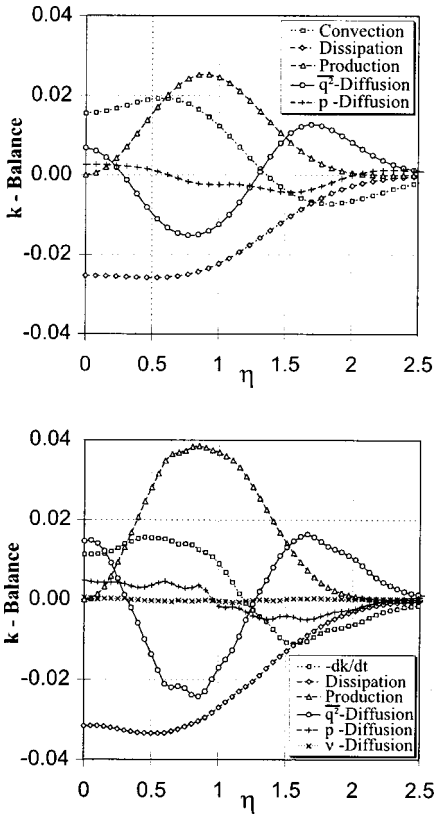

Fig. 16 Budget of the turbulent kinetic energy in the plane wake: measurements (top); DNS of Moser et al. [37] (bottom)

The distributions of all terms involved in the balance of Eq. (21), normalized by L/U_S^3, are shown in Fig. 16 (top). At the wake centerline convection and turbulent diffusion are balanced by the dissipation. The pressure-diffusion is small compared with the other terms. A similar observation was made by Ye [18] and Browne et al. [14]. The integral constraints for the diffusion terms

$$\int_0^\infty \frac{\partial}{\partial \eta}(\overline{q^2 u_2})\,d\eta = 0 \quad \text{and} \quad \int_0^\infty \frac{\partial}{\partial \eta}(\overline{p u_2})\,d\eta = 0, \qquad (22)$$

were satisfied within 1.5% and 15%, respectively, relative to the absolute value of the corresponding integral. One should note that the pressure-diffusion is small compared with the turbulent diffusion and therefore is strongly influenced by small measuring errors of the terms dominating the balance of k. For example, the integral of the pressure-diffusion term tends to zero if the dissipation rate is underestimated by 2%.

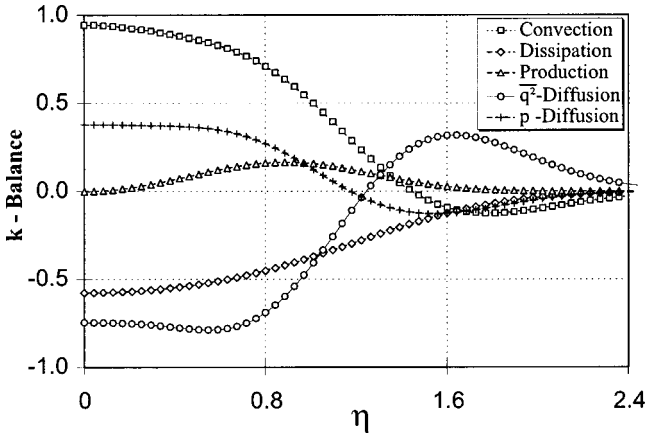

Fig. 17 Budget of the turbulent kinetic energy in the axisymmetric wake

The DNS data of Moser et al. [37], which are plotted in Fig. 16 (bottom), show nearly the same trends in the behavior of the individual terms of the energy balance (21) as our experimental results. One should note that Moser et al. [37] simulated the time-developing wake whereas our experimental investigations correspond to the spatially developing wake.

For the axisymmetric wake the energy equation is

$$\underbrace{U_1 \frac{\partial}{\partial x_1}\frac{\overline{q^2}}{2}}_{\text{Convection}} = \underbrace{-\overline{u_1 u_2}\frac{\partial U_1}{\partial r_2}}_{\text{Production}} \underbrace{-\frac{1}{2r}\frac{\partial}{\partial r} r \overline{q^2 u_2}}_{\overline{q^2}\text{-Diffusion}} \underbrace{-\frac{1}{\rho}\frac{1}{r}\frac{\partial}{\partial r} r \overline{p u_2}}_{\text{Pressure-Diffusion}} \underbrace{-\epsilon}_{\text{Dissipation}}. \qquad (23)$$

Figure 17 shows the distributions of the individual terms involved in Eq. (23), normalized by L/U_S^3. The production of k is seen to be much smaller than in the plane case. This observation and the whole energy balance is in very good agreement with the data of Uberoi and Freymuth [38]. It should be mentioned, however, that they computed the diffusion terms directly from the balance of Eq. (23) and found that these do not satisfy the integral constraints. An explanation for this might lie in the uncertainty of the estimated convection term. We encountered a similar problem and therefore decided to estimate the convection term directly by computing the streamwise derivative from the measured longitudinal intensity component assuming that the changes of the anisotropy in the streamwise direction are negligible. The turbulent and pressure diffusion which were obtained by difference from Eq. (23) satisfy the integral constraints within 1.5% and 6%, respectively. Figure 17 implies that in the axisymmetric wake the pressure diffusion cannot be neglected and follows qualitatively the suggestion made by Lumley [36], $\overline{u_i p}/\rho \approx -0.2\overline{q^2 u_i}$.

4 Conclusion

Measurements of all first-order spatial derivatives of the instantaneous velocity fluctuations in plane and axisymmetric small-deficit turbulent wakes were performed using a pair of X wires. Errors due to finite length of the hot wires and due to the wire and probe spacing effects were analyzed and accounted for in evaluation of the data.

The experimental results were systematically checked and were found to be consistent with the dynamic equations for the turbulence quantities and also with the data available in the literature. The assumptions of local isotropy and local axisymmetry were examined. Both investigated wake flows deviate only moderately from local isotropy and local axisymmetry.

The assumption of local axisymmetry was found to be a better approximation than the assumption of local isotropy. The axisymmetric estimate of the turbulent dissipation rate was found to be a good approximation for both plane and axisymmetric wake flows. The results presented demonstrate that the isotropic approximation of the dissipation rate underestimates the true value of ϵ between 10% near the wake centerline and 25% in the outer part of the plane wake. In the case of the axisymmetric wake the isotropic dissipation computed by assuming local isotropy gives an excellent estimate in comparison with direct measurements.

The budget of the turbulent kinetic energy was computed from the data. The individual terms of the k equation show the plausible distributions with the diffusion terms which satisfy the integral constraints. While the pressure transport is nearly negligible in the plane wake, it plays an important role in the axisymmetric wake and follows closely Lumley's [36] suggestion, $\overline{u_i p}/\rho \approx -0.2\overline{q^2 u_i}$.

Downloaded 03 Jun 2010 to 171.66.16.150. Redistribution subject to ASME license or copyright; see http://www.asme.org/terms/Terms_Use.cfm

Acknowledgments

This research received financial support in part from the Volkswagen-Stiftung within the project ''Development of statistical models of turbulence using the experimental and numerical databases'' (I/72 857) and by the Deutsche Forschungsgemeinschaft (Grant Jo 240/1-3).

References

[1] Kolmogorov, A. N., 1941, ''Local Structure of Turbulence in an Incompressible Fluid at Very High Reynolds Numbers,'' Comptes Rendus (Doklady) de l'Académie des Sciences de l'U.R.S.S., **30**, pp. 299–303.
[2] Simmons, L. F. G., and Salter, C., 1934, ''Experimental Investigation and Analysis of the Velocity Variations in Turbulent Flow,'' Proc. R. Soc. London, Ser. A, pp. 145–212.
[3] Corrsin, S., 1943, ''Investigation of Flow in Axially Symmetrical Heated Jet of air,'' The National Advisory Committee for Aeronautics, War-time Report W-94, Washington D.C.
[4] Corrsin, S., and Uberoi, M. S., 1951, ''Spectra and Diffusion in a Round Jet,'' The National Advisory Committee for Aeronautics, Technical Note 1040, Washington D.C.
[5] Townsend, A. A., 1948, ''Local Isotropy in the Turbulent Wake of a Cylinder,'' Australian Journal of Scientific Research, Series A, **1**, pp. 161–174.
[6] Townsend, A. A., 1949, ''The Fully Developed Turbulent Wake of a Circular Cylinder,'' Australian Journal of Scientific Research, Series A, **2**, pp. 451–468.
[7] Laufer, J., 1954, ''The Structure of Turbulence in Fully Developed Pipe Flow,'' The National Advisory Committee for Aeronautics, Report 1174, Washington D.C., pp. 417–433.
[8] Klebanoff, J., 1953, ''Characteristics of Turbulence in a Boundary Layer with Zero Pressure Gradient,'' The National Advisory Committee for Aeronautics, Technical note 3178, Washington D.C.
[9] Uberoi, M. S., and Freymuth, P., 1973, ''Temperature Fluctuations in the Turbulent Wake Behind an Optically Heated Sphere,'' Phys. Fluids, **16**, pp. 161–168.
[10] Antonia, R. A., and Browne, L. W. B., 1986, ''Anisotropy of the Temperature Dissipation in a Turbulent Wake,'' J. Fluid Mech., **163**, pp. 393–403.
[11] Tavoularis, S., and Corrsin, S., 1981, ''Experiments in Nearly Homogeneous Turbulent shear Flow with Uniform Mean Temperature Gradient. Part 1,'' J. Fluid Mech., **104**, pp. 311–347.
[12] Tavoularis, S., and Corrsin, S., 1981, ''Experiments in Nearly Homogeneous Turbulent Shear Flow with Uniform Mean Temperature Gradient. Part 2,'' J. Fluid Mech., **104**, pp. 349–367.
[13] Krishnamoorthy, L. V., and Antonia, R. A., 1987, ''Temperature-Dissipation Measurements in a Turbulent Boundary Layer,'' J. Fluid Mech., **176**, pp. 265–281.
[14] Browne, L. W. B., Antonia, R. A., and Shah, D. A., 1987, ''Turbulent Energy Dissipation in a Wake,'' J. Fluid Mech., **179**, pp. 307–326.
[15] George, W. K., and Hussein, H. J., 1991, ''Locally Axisymmetric Turbulence,'' J. Fluid Mech., **233**, pp. 1–23.
[16] Hussein, H. J., Capp, S. P., and George, W., 1994, ''Velocity Measurements in a High Reynolds Number, Momentum-Conserving, Axisymmetric, Turbulent Jet,'' J. Fluid Mech., **258**, pp. 31–75.
[17] Hussein, H. J., 1994, ''Evidence of Local Axisymmetry in the Small Scales of a Turbulent Planar Jet,'' Phys. Fluids, **6**, pp. 2058–2070.
[18] Ye, Q.-Y., 1996, ''Die Tturbulente Dissipation Mechanischer Energie in Scherschichten,'' *Dissertation*, Universität Erlangen-Nürnberg.
[19] Zhu, Y., and Antonia, R. A., 1996, ''The Spatial Resolution of Hot-Wire Arrays for the Measurement of Small-Scale Turbulence,'' Meas. Sci. Technol., **7**, pp. 1349–1359.
[20] Wyngaard, J. C., 1968, ''Measurement of Small-Scale Turbulence Structure with Hot Wires,'' J. Sci. Instrum., **1**, pp. 1105–1108.
[21] Wyngaard, J. C., 1969, ''Spatial Resolution of the Vorticity Meter and Other Hot-Wire Arrays,'' J. Sci. Instrum., **2**, pp. 983–987.
[22] Pao, Y.-H., 1965, ''Structure of Turbulent Velocity and Scalar Fields in Large Wave Numbers,'' Phys. Fluids, **8**, pp. 1063–1075.
[23] Schenck, T. C., 1999, ''Messung der Turbulenten Dissipationsrate in Ebenen und Achsensymmetrischen Nachlaufströmungen,'' *Dissertation*, Universität Erlangen-Nürnberg.
[24] Bradshaw, P., 1971, *An Introduction to Turbulence and its Measurement*, Pergamon Press, Oxford.
[25] Wygnanski, I., and Fiedler, H., 1969, ''Some measurements in the Self-Preserving Jet,'' J. Fluid Mech., **38**, pp. 577–612.
[26] Kaiser, J. F., and Reed, W. A., 1977, ''Data Smoothing Using Low-Pass Digital Filters,'' Rev. Sci. Instrum., **48**, No. 11, pp. 1447–1457.
[27] Wygnanski, I., Champagne, F., and Marasli, B., 1986, ''On the Large-Scale Structures in Two-Dimensional, Small-Deficit, Turbulent Wake,'' J. Fluid Mech., **168**, pp. 31–71.
[28] Hoerner, S. F., 1965, *Fluid-Dynamic Drag*, Hoerner Fluid Dynamics, P.O. Box 342, Brick Town, NJ 08723.
[29] Schlichting, H., and Gersten, K., 1997, *Grenzschicht-Theorie*, Springer-Verlag, Berlin, Heidelberg.
[30] Fabris, G., 1983, ''Third-Order Conditional Transport Correlations in the Two-Dimensional Turbulent Wake,'' Phys. Fluids, **26**, pp. 422–427.
[31] Aronson, D., and Löfdahl, L., 1993, ''The Plane Wake of a Cylinder: Measurements and Inferences on Turbulence Modeling,'' Phys. Fluids A, **5**, pp. 1433–1437.
[32] Uberoi, M. S., and Freymuth, P., 1969, ''Spectra of Turbulence in Wakes Behind Circular Cylinders,'' Phys. Fluids, **12**, pp. 1359–1363.
[33] George, W. K., 1989, ''The Self-Preservation of Turbulent Flows and its Relation to Initial Conditions and Coherent Structures,'' *Advances in Turbulence*, (W. K. George and R. Arndt), eds., Hemisphere, pp. 39–73.
[34] Rotta, J. C., 1972, *Turbulent Strömungen*, B. G. Taubner, Stuttgart.
[35] Jovanović, J., and Otić, I., 2000, ''On the Constitutive Relation for the Reynolds Stresses and the Prandtl-Kolmogorov Hypothesis of Effective Viscosity in Axisymmetric Strained Turbulence,'' ASME J. Fluids Eng., **122**, pp. 48–50.
[36] Lumley, J., 1978, ''Computational Modeling of Turbulent Flows,'' Adv. Appl. Mech., **18**, pp. 123–176.
[37] Moser, R. D., Rogers, M. M., and Ewing, D. W., 1998, ''Self-Similarity of Time-Evolving Plane Wakes,'' J. Fluid Mech., **367**, pp. 255–289.
[38] Uberoi, M. S., and Freymuth, P., 1970, ''Turbulent Energy Balance and Spectra of the Axisymmetric Wake,'' Phys. Fluids, **13**, pp. 2205–2210.

Downloaded 03 Jun 2010 to 171.66.16.150. Redistribution subject to ASME license or copyright; see http://www.asme.org/terms/Terms_Use.cfm

An Investigation of Flow Fields Over Multi-Element Aerofoils

S. R. Maddah

H. H. Bruun

Department of Mechanical and Medical Engineering,
Fluid Flow Division,
University of Bradford,
Bradford, BD7 1DP, United Kingdom

This paper presents results obtained from a combined experimental and computational study of the flow field over a multi-element aerofoil with and without an advanced slat. Detailed measurements of the mean flow and turbulent quantities over a multi-element aerofoil model in a wind tunnel have been carried out using stationary and flying hot-wire (FHW) probes. The model configuration which spans the test section (600 mm $\times$600 mm), is made of three parts: 1) an advanced (heel-less) slat, 2) a NACA 4412 main aerofoil and 3) a NACA 4415 flap. The chord lengths of the elements were 38, 250 and 83 mm, respectively. The results were obtained at a chord Reynolds number of 3×10^5 and a free Mach number of less than 0.1. The variations in the flow field are explained with reference to three distinct flow field regimes: attached flow, intermittent separated flow, and separated flow. Initial comparative results are presented for the single main aerofoil and the main aerofoil with a nondeflected flap at angles of attacks of 5, 10, and 15 deg. This is followed by the results for the three-element aerofoil with emphasis on the slat performance at angles of attack $\alpha=10$, 15, 20, and 25 deg. Results are discussed both for a nondeflected flap ($\delta_f=0$ deg) and a deflected flap ($\delta_f=25$ deg). The measurements presented are combined with other related aerofoil measurements to explain the main interaction of the slat/main aerofoil and main aerofoil/flap both for nondeflected and deflected flap conditions. These results are linked to numerically calculated variations in lift and drag coefficients with angle of attack and flap deflection angle.
[DOI: 10.1115/1.1431267]

Keywords: Turbulent Flow, Flying Hot-Wire, Advanced and Conventional Slats, Multi-Element Aerofoil

1 Introduction

High-lift systems are used on aircraft to provide adequate low speed performance in terms of approach speed and take-off and landing field lengths. Leading-edge devices, such as slats and the Kruger flap, are commonly used to delay stall to higher angles of attack and consequently increase the maximum lift performance, C_{lmax}. For aviation purposes, the significant features are the total (integrated) lift and drag forces. Consequently, there are many reported direct measurements of the lift and drag coefficients for two- and three-element aerofoils e.g., Innes et al. [1] and Moens and Capbern [2]. However, such integrated quantities cannot provide direct insight into the occurring velocity and pressure fields. As the primary fluid mechanics feature is the flow field over the aerofoil, the emphasis of this paper is on the mean and turbulent flow fields. There are a number of other related investigations. Two-element configurations have been studied by e.g. [3–5] and the performance of a conventional slat in high lift systems has been investigated e.g., Nakayama et al. [6] and Braden et al. [7]. The slat and flap gap flows have been reported by Savory et al. [8] and Alemdaruglu [9]. These studies confirm the presence of slat cove separation, which has some effects on the boundary layer development over the wing and the mean velocity and turbulence fields over the main aerofoil, Maddah et al. [10]. The slat cove separation is minimized for the advanced slat due to its smooth and heel-less lower surface and it therefore produces less drag compared to a conventional slat with lower surface discontinuity, Jones [11].

The majority of experiments on multi-element aerofoils have been conducted for attached flow conditions with only limited data at near stall conditions. Even if there was separation, it was on the flap at low angles of attack. The work of Braden et al. [7] appears to be the most detailed and extensive experimental data set covering attached as well as separated flows both for single and two-element aerofoils. However, there remains a need for similar detailed measurements of mean velocity and turbulent quantities of the flow field over three-element aerofoils with emphasis on the effect of the flap and the slat (in particular a heel-less slat) at low to high angles of attack ranging from $\alpha=5$ to 25 deg. This paper presents results for a single, two-element, and three-element aerofoil and highlights the variation in the mean and turbulent quantities as the flow changes from attached flow to intermittently separated flow and finally to separated flow. The interpretation from the observed flow phenomena in this investigation is combined with related flow field results and vortex concepts to highlight the varying interaction between upstream/downstream elements with angles of attack and flap deflection angle in a high lift system, and the resulting effect on the lift and drag of multi-element aerofoils.

2 Experimental Arrangement and Test Conditions

The experiments were conducted in a low speed wind tunnel with a cross section of 600 mm$\times$600 mm located at the University of Bradford. The model configuration spans the test section and it is made of three parts: 1) an advanced (heel-less) slat, 2) a NACA 4412 main aerofoil and 3) a NACA 4415 flap. The chord lengths of the elements were 38, 250 and 83 mm, respectively. The slat gap and overlap and the flap gap and overlap were set to $0.02\%c$, $-0.025\%c$, $0.015\%c$, and $0.04\%c$, respectively. The free-stream velocity was 18 m/s and the corresponding Reynolds number based on the main aerofoil chord length was 3×10^5. By using extra screens, at the inlet to the wind tunnel, the free stream turbulence intensity was reduced to 0.4%.

The main experimental technique of the present research was a flying hot-wire mounted on a precise computer-controlled mechanism. The technique is based on moving the probe along a prescribed path with a large enough velocity to avoid hot wire signal

Contributed by the Fluids Engineering Division for publication in the JOURNAL OF FLUIDS ENGINEERING. Manuscript received by the Fluids Engineering Division January 23, 2001; revised manuscript received August 27, 2001. Associate Editor: T. Gatski.

 Copyright © 2002 by ASME

Downloaded 03 Jun 2010 to 171.66.16.150. Redistribution subject to ASME license or copyright; see http://www.asme.org/terms/Terms_Use.cfm

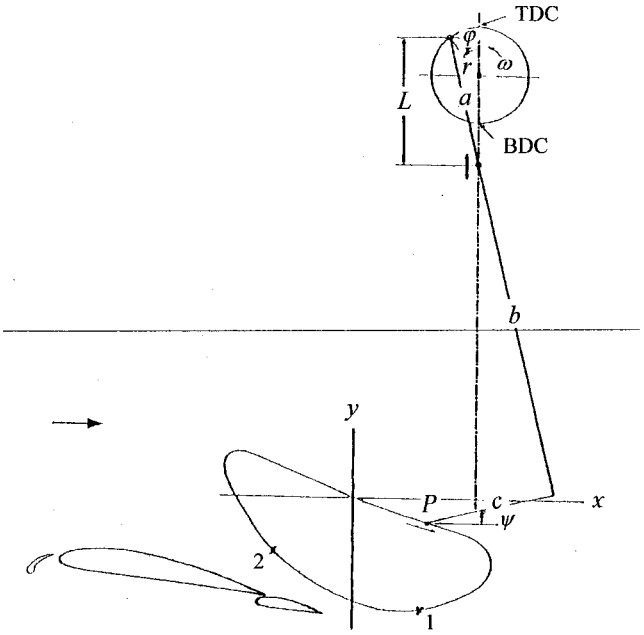

Fig. 1 Four-bar flying hot-wire mechanism, notation, and wind tunnel measurement coordinate system. The geometry is that which is used at the University of Bradford: $r=60$ mm, $a=160$ mm, $c=146$ mm, $b=468$ and 548 mm for old and new flying arm, respectively.

rectification associated with stationary hot-wire probes in reversing flow, Bruun [12]. The FHW probe was calibrated in the "stationary" mode as explained by e.g., Bruun [12] and Maddah [13]. Temperature effect and calibration drift were minimized by calibration checks before and after test runs.

The installation of the multi-element aerofoil in the wind tunnel, and the principle of the mechanical implementation for the bean shaped curve path used at Bradford University is illustrated in Fig. 1. Measurements were obtained from a number of points on the lower part of the probe curve path during a single sweep, and for the study of the slat and multi-element aerofoil performance, 20 evenly spaced points were selected for detailed analysis. Each sweep was repeated 200 times. Using the (X,Y) wind tunnel aligned coordinate system shown in Fig. 1, ensemble averaging was used to calculate the mean velocity components, $\overline{U}$ and $\overline{V}$, and the turbulent quantities, $\overline{u^2}$, $\overline{v^2}$, and $\overline{uv}$. Using a plated DANTEC X hot-wire probe, the minimum (safe) distance from the center of the probe to the aerofoil surface was 2.5 mm. The minimum mean velocity $\overline{U}_{\min}$ discussed in Sections 4 to 6 refers to this probe path position. The maximum mean velocity obtained within the measurement region near the front of the main aerofoil is denoted by $\overline{U}_{\max}$. The attached flow over the nose of the aerofoil was not included in this investigation. The capability of the FHW for acquiring high quality experimental data enabled this technique to be used for cases with or without separation. Details of Bradford University's flying hot-wire system are given by Maddah [13].

Two-Dimensionality. The flow over the multi-element aerofoil in the wind tunnel may deviate from two-dimensional flow. The deviation is associated with the growth of the secondary flows in the corners formed by the model and the side walls of the wind tunnel and it will increase directly with angle of attack and flap deflection angles. Aerofoil models with aspect ratios of about 2 or less have been used [6,9,14] with consequently significant three-dimensional effects. For the present investigation, the aspect ratio for the main aerofoil was ~2.5 which resulted in much weaker three-dimensional effects. Comparative measurement of the mean velocity profiles at different spanwise locations showed negligible variation with and without the slat. For the nondeflected flap case ($\delta_f=0$ deg), the two-dimensionality of the flow was validated for about 90% of the span. However, for the highly deflected flap ($\delta_f=25$ deg) cases, in particular for $\alpha \geqslant 20$ deg, splitter plates were used to maintain two-dimensional flow for 80% of the span.

3 The Measurement Matrix and Flow Regime Classification

The test matrix is shown in Table 1. It includes the two-element aerofoil (main aerofoil and the flap) cases and the three-element aerofoil cases incorporating the advanced slat. Four configurations are considered for the two-element aerofoil: three cases with the main aerofoil set at 5, 10, and 15 deg with a nondeflected flap and one case for $\alpha=10$ deg with a highly deflected flap. The flow field at each angle of attack, i.e., 5, 10, and 15 deg, is compared with the corresponding flow field measured by Mahmood et al. [15,16] for the same single NACA 4412 aerofoil.

The effect of the leading edge slat on the aerofoil flow field is explained with reference to the three-element aerofoil configuration at angles of attack of 10, 15, 20, and 25 deg, using both a non-deflected flap ($\delta_f=0$ deg) and two deflection angles $\delta_f=10$ and 25 deg (see test matrix, Table 1).

For the description in this paper, the flow over the aerofoils will be classified as attached flow, intermittent separated flow and small and large scale separated flow. The notation, attached flow, is self explanatory. Separated flow is identified as a spatially permanent flow region (usually toward the rear part of the main aerofoil) with reversed (negative) mean velocities. Intermittent separated flow is explained below.

Intermittent Separation. If a small positive streamwise mean velocity component $\overline{U}$ and a relatively high turbulence intensity occur near the trailing edge of the main aerofoil, then a separated flow condition might exist for short periods of time in this region. For example, with reference to the test matrix in Table 1 for case B5 (three-element aerofoil at $\alpha=25$ deg and $\delta_f=0$ deg), the acquired data for the streamwise component of the velocity, U, at a point located 90% c from the leading edge of the main aerofoil demonstrated that no steady reverse flow situations exist. From corresponding pdf results, it was observed that about one sixth of the total sampling size correspond to negative values of U. This can indicate the existence of an intermittent small sepa-

Table 1 Test configurations

α	Single main aerofoil	Two-element aerofoil		Three-element aerofoil		
		$\delta_f=0$ deg	$\delta_f=25$ deg	$\delta_f=0$ deg	$\delta_f=10$ deg	$\delta_f=25$ deg
5 deg	S1	A1				
10 deg	S2	A2	AD2	B2	C2	D2
15 deg	S3	A3		B3	C3	D3
20 deg				B4	C4	D4
25 deg				B5	C5	D5

Downloaded 03 Jun 2010 to 171.66.16.150. Redistribution subject to ASME license or copyright; see http://www.asme.org/terms/Terms_Use.cfm

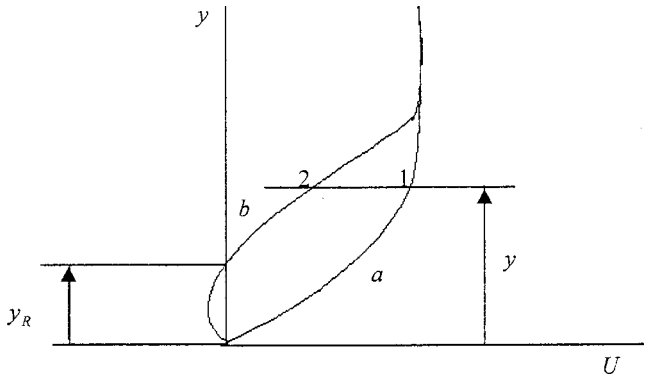

Fig. 2 Velocity profiles for a position near the trailing edge of the aerofoil containing an intermittent unstable separation bubble: (i) curve a: velocity profile when the boundary layer is attached, and (ii) curve b: velocity profile when the flow is separated. A hot-wire probe placed at position *y* will detect velocities U_1 and U_2 corresponding to the two flow states.

ration bubble which starts to grow and remain attached for a short period of time before it is swept downstream with the flow in the streamwise direction, temporarily creating an attached unstable boundary layer flow in this region. That the separation region was of a limited axial extent was demonstrated by considering a point at 60% *c* from the leading edge of the main aerofoil. The related acquired data for the same configuration showed no negative value for *U*, indicating the limited spatial extent of the intermittent separation bubble.

Consequently, it is justifiable to suggest that the flow field varies between two extreme conditions: 1) an attached unstable boundary layer flow and 2) a separation bubble containing reversed flow (negative *U* values). These two conditions can be illustrated by the velocity profile curves *a* (attached) and *b* (separated) in Fig. 2. A single hot-wire probe placed in the outer part of the boundary layer at a distance $y > y_R$ from the surface where no negative velocities occur can be used to indicate the existence of the two flow states corresponding to curves *a* and *b*. (As a single normal hot-wire probe cannot detect negative velocities it is important that it is placed at a distance *y* greater than the maximum vertical extent y_R of the reverse flow region.) For such a position the average level of the hot-wire output should change related to the velocities $\overline{U}_1$ and $\overline{U}_2$ as shown in Fig. 3. Measurements were carried out for a number of probe positions corresponding to this flow condition, and the expected change in the output voltage level from E_1 to E_2 was observed as shown in Fig. 3. These and similar results demonstrate the existence of the two extreme conditions of 1) an attached unstable boundary layer flow and 2) a temporal intermittent separation bubble. This flow situation will be referred to as intermittent separation.

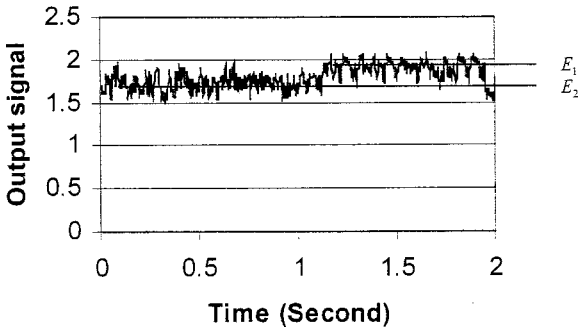

Fig. 3 Output signal from a single normal hot-wire probe located just outside the edge of an intermittent unstable separation bubble, demonstrating two quasi-steady flow conditions corresponding to (1) E_1: an attached unstable boundary layer flow and (2) E_2: an intermittent separation bubble.

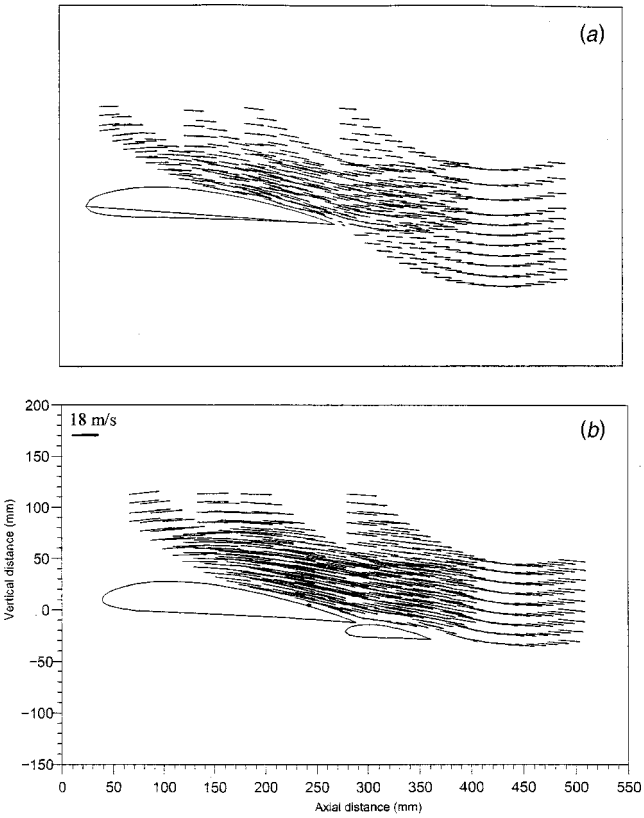

Fig. 4 Mean velocity values for: (*a*) Single aerofoil at $\alpha = 5$ deg; (*b*) two-element aerofoil at $\alpha = 5$ deg and $\delta_f = 0$ deg

4 Three Distinct Flow Regimes

As described above the flow field over the investigated aerofoil combinations will be described in terms of three types of flow regimes. Examples are given below.

4.1 Attached Flow

Single and Two-Element Aerofoils at $\alpha = 5$ Deg (Cases S1 and A1) Mean Velocity. Figures 4(*a*) and 4(*b*) show the mean velocity vectors for the single aerofoil and the two-element aerofoil at an angle of attack of $\alpha = 5$ deg respectively. In general, the mean velocity vectors for the single aerofoil, presented in Fig. 4(*a*), are similar to the corresponding velocity field over the main aerofoil for the two-element case A1, depicted in Fig. 4(*b*). These velocity vector plots for both aerofoils, indicate that the flows are attached to the model surfaces and there are no signs of separation. For both configurations, accelerated flows over the leading edge of the main aerofoil are responsible for creating suction and lift. The measured maximum velocities in this region reach peak values of $\sim 1.27U_\infty$ and $\sim 1.30U_\infty$ for the single and the two-element aerofoil configurations respectively. The velocity deficits in a small region close to the trailing edge of the main aerofoil are slightly larger for the single aerofoil (case S1) compared to the two-element aerofoil (case A1). Comparing the vector plots for these configurations, it can be concluded that introduction of the flap creates higher velocities over the trailing edge of the main aerofoil, thus slightly enhancing the flow field. The total lift for the two-element aerofoil is higher than for the single aerofoil due to a slightly enhanced flow field and the extra area of the flap.

Downloaded 03 Jun 2010 to 171.66.16.150. Redistribution subject to ASME license or copyright; see http://www.asme.org/terms/Terms_Use.cfm

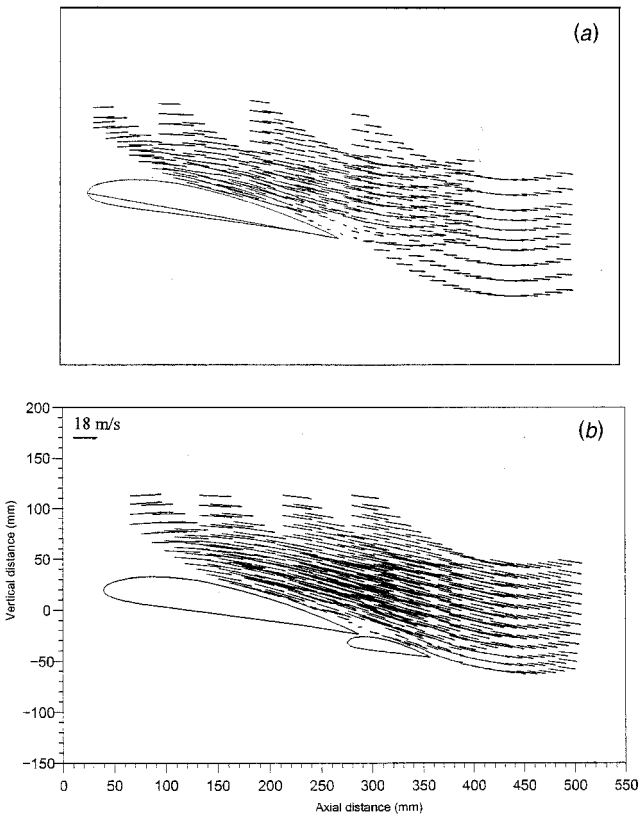

Fig. 5 Mean velocity values for: (*a*) Single aerofoil at $\alpha = 10$ deg; (*b*) two-element aerofoil at $\alpha = 10$ deg and $\delta_f = 0$ deg

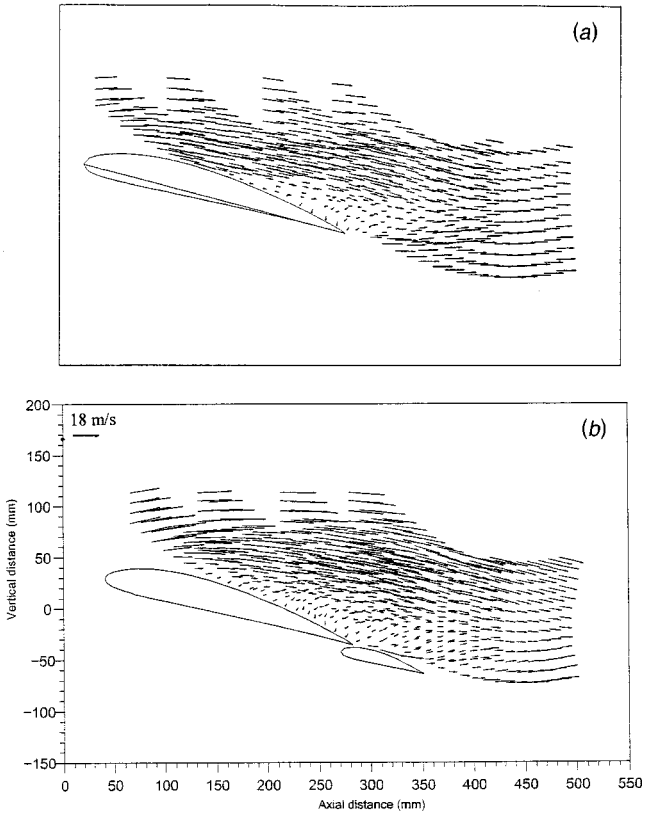

Fig. 6 Mean velocity values for: (*a*) Single aerofoil at $\alpha = 15$ deg; (*b*) two-element aerofoil at $\alpha = 15$ deg and $\delta_f = 0$ deg

Reynolds Stresses. The values of the Reynolds stresses for these configurations (S1 and A1) are small. For example, the peak values of the normalized streamwise Reynolds stresses, $(\overline{u^2}/U_\infty^2) \times 10^3$ occurring over the trailing edge of the main aerofoil are of the order of $\sim 10 \times 10^{-3}$ for both the single and the two-element aerofoils. This corresponds to a local turbulence intensity Tu $\approx 10\%$. The development of $(\overline{v^2}/U_\infty^2)$ and $(\overline{uv}/U_\infty^2)$ exhibits similar trends with smaller peak values. The small magnitudes of these stresses are consistent with the mean velocity results indicating the existence of an attached boundary layer for both cases S1 and A1.

4.2 Intermittent Separation

Single and Two-Element Aerofoils at $\alpha = 10$ Deg (Cases S2 and A2) Mean Velocity. The mean velocity vectors for the single aerofoil and the two-element aerofoil at an angle of attack of 10 deg are shown in Figs. 5(*a*) and 5(*b*), respectively. Similar flow fields are observed for both cases S2 and A2 with high velocities over the top front and low velocities over the trailing edge of the main aerofoil. The measured streamwise components of mean velocity reach peak values of $\sim 1.38 U_\infty$ and $\sim 1.40 U_\infty$ over the front of the main aerofoil for the single and the two-element aerofoil respectively. The extent of the low velocity region over the trailing edge of the main aerofoil is larger for the single aerofoil compared to that of the two-element aerofoil, but the minimum values of the measured mean velocities are as low as 10% of the free-stream velocity for both cases. As for the attached flow case, it can be concluded that the total lift for the two-element aerofoil with a nondeflected flap is higher than for the single aerofoil.

Reynolds Stresses. The highest values of the normalized streamwise Reynolds stress $\overline{u^2}/U_\infty^2$ for the two-element case reaches $\sim 35 \times 10^{-3}$, corresponding to a local turbulence intensity Tu $\approx 20\%$, located in a region over the trailing edge of the main aerofoil and the flap. This value is about four times higher than the corresponding values for $\alpha = 5$ deg. The local turbulence intensity in the low mean velocity region measured closest to the aerofoil surface exceeds 30% which is consistent with intermittent separation. Similar trends are observed for the cross normal Reynolds stress $\overline{v^2}$ and turbulent shear stress $\overline{uv}$ with peak values of $\sim 15 \times 10^{-3}$ and $\sim -16 \times 10^{-3}$, respectively. For the single aerofoil (case S2), the peak values of $\overline{u^2}/U_\infty^2$ are observed over the trailing edge of the main aerofoil with almost the same magnitudes as the corresponding values for the two-element aerofoil.

4.3 Separated Flow

4.3a Small Scale Separation

Single and Two-Element Aerofoil at $\alpha = 15$ Deg (Cases S3 and A3) Mean Velocity. The mean velocity vector fields for the single and the two-element aerofoils at an angle of attack $\alpha = 15$ deg are shown in Fig. 6(*a*) and 6(*b*). The experimental data for the flow over the two-element aerofoil clearly shows a larger region of low velocities over the main aerofoil including reversed flow close to the surface compared to the corresponding mean velocity field for the single aerofoil (case S3). The commencement of flow detachment is at 50%c and 35%c from the leading edge of the main aerofoil for cases S3 and A3, respectively. The large velocity deficits are seen to persist downstream of the aerofoil, beyond a distance of a half chord length from the trailing edge of the main aerofoil for the single case and twice that for the two-element aerofoil case. For the two-element case, the flap gap flow is observed to be responsible for a limited improvement in the velocity field over and beyond the flap.

Downloaded 03 Jun 2010 to 171.66.16.150. Redistribution subject to ASME license or copyright; see http://www.asme.org/terms/Terms_Use.cfm

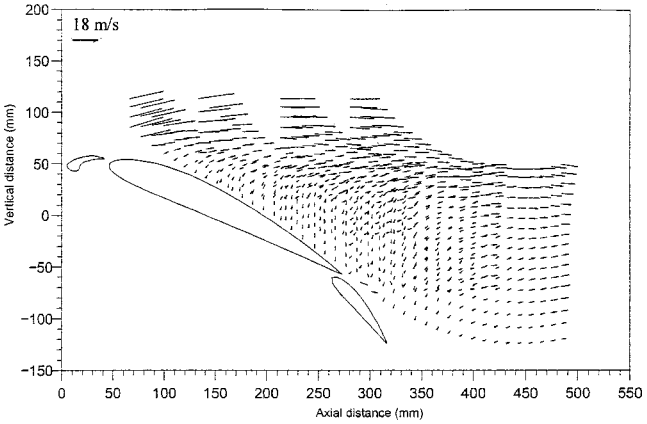

Fig. 7 Mean velocity vectors for three-element aerofoil at $\alpha = 25$ deg and $\delta_f = 25$ deg

Reynolds Stresses. For the two-element aerofoil at an angle of attack of 15 deg, the spatial distribution of the turbulence field has been changed substantially, when compared to the attached flow case (e.g., case A1) and to the flow with a small intermittent separation (e.g., case A2). The separation bubble causes the free shear layer (surrounding the separation bubble) to move a substantial distance in the cross-stream direction away from the two-element aerofoil surface. Consequently, the viscous-inviscid interaction region and the locations of the maximum stresses have also changed. The normalized stress $\overline{u^2}/U_\infty^2$ reaches a peak value of $\sim 180\times 10^{-3}$ corresponding to a local turbulence intensity Tu of $\sim$70%, while the normalized $\overline{v^2}$ and $\overline{uv}$ have increased to $\sim 70 \times 10^{-3}$ and $\sim -55\times 10^{-3}$, respectively. These results are consistent with a region of separated flow.

Similar trends are observed for the peak values of the Reynolds stresses for the single aerofoil at the same angle of attack of 15 deg. However, the extent of the separated region is smaller and the peak locations are closer to the aerofoil surface, which is consistent with the corresponding mean velocity results.

4.3b Large Scale Separation (Stall)

Main Aerofoil at α=25 Deg Slat at δ_s=15 Deg, Flap at δ_f=25 Deg (Case D5) Mean Velocity. The velocity vectors for the three-element aerofoil at $\alpha = 25$ deg with a flap deflection angle set to 25 deg are shown in Fig. 7. Almost 80% of the main aerofoil and the whole flap are stalled. The large region of recirculating flow over the main aerofoil and the flap is an indication of a drastic loss of lift. As shown in Section 5.1b for an intermittent separated flow (case B5) over the three-element aerofoil, the mean velocity $\overline{U}$ reaches values as high as $\sim 1.65U_\infty$. However, for the flow with large scale separation (case D5), the accelerated flow over the leading edge of the main aerofoil has been reduced and the maximum measured mean velocity has dropped to $\sim 1.40U_\infty$, which indicates a loss of lift over the leading edge of the main aerofoil.

Reynolds Stresses. The normalized $\overline{u^2}$ and $\overline{v^2}$ contour plots for the three-element aerofoil at $\alpha = 25$ deg with a highly deflected flap are shown in Figs. 8(*a*) and 8(*b*). It was found that except for a spatially much larger separated flow (stall), and slightly larger Reynolds stresses the turbulence structure is similar to the small scale separated flow observed on the two-element aerofoil at $\alpha = 15$ deg with a nondeflected flap, case A3. The normalized streamwise Reynolds stress $\overline{u^2}/U_\infty^2$ reaches a peak value of $\sim 220\times 10^{-3}$ and it occurs towards the front end of the aerofoil. This large value represents violent axial oscillations of the front part of the separation bubble. The development of $\overline{v^2}$, depicted in Fig. 8(*b*) has a maximum value, $\sim 80\times 10^{-3}$ and it is located in the free shear layer above the rear part of the flap and wake. These high values represent vertical oscillations of the free shear layer.

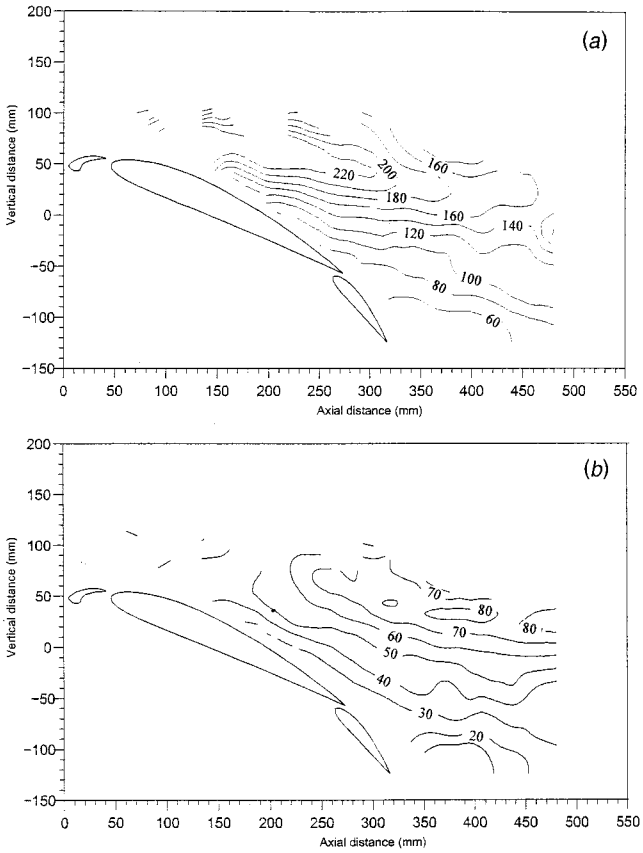

Fig. 8 Three-element aerofoil at $\alpha = 25$ deg and $\delta_f = 25$ deg: (*a*) Normalized streamwise normal Reynolds stress $(\overline{u^2}/U_\infty^2)\times 10^3$; (*b*) normalized cross-stream normal Reynolds stress $(\overline{v^2}/U_\infty^2)\times 10^3$

5 Three-Element Aerofoil Configurations

This section presents the experimental results for the mean velocity $\overline{U}$ and $\overline{u^2}$ Reynolds stress for the three-element aerofoil placed with a slat at $\delta_s = 15$ deg and the main aerofoil at angles of attack α of 10, 15, 20, 25 deg. Section 5.1 contains results for the nondeflected flap ($\delta_f = 0$ deg) while results for the deflected flap at $\delta_f = 25$ deg are described in Section 5.2. For the related attached and intermittent separated flow cases, the peak values of the other two measured Reynolds stresses $\overline{v^2}$ and $\overline{uv}$ occurred at the same locations as $\overline{u^2}_{\max}$, thus only the results for $\overline{u^2}$ are presented. For the separated flow case, e.g., the three-element aerofoil at an angle of attack of $\alpha = 25$ deg with a highly deflected flap ($\delta_f = 25$ deg), as discussed in section 4.3b, the peak locations of the Reynolds stresses are different, hence results were presented for $\overline{u^2}$ and $\overline{v^2}$ in Figs. 8(*a*) and 8(*b*).

5.1 Nondeflected Flap, $\delta_f = 0$ Deg

5.1a Attached Flow Cases

Main Aerofoil at $\alpha = 10$, 15, and 20 Deg With a Slat and a Flap (Cases B2, B3, and B4) Mean Velocity. The vector plot of the mean velocity for the three-element aerofoil at angles of attack of $\alpha = 10$ deg (case B2), 15 deg (case B3) and 20 deg (case B4) are shown in Fig. 9(*a*)–11(*a*). For all three configurations, the flow is attached. When the angle of attack is increased the maximum measured velocity over the front of the main aerofoil reaches val-

Downloaded 03 Jun 2010 to 171.66.16.150. Redistribution subject to ASME license or copyright; see http://www.asme.org/terms/Terms_Use.cfm

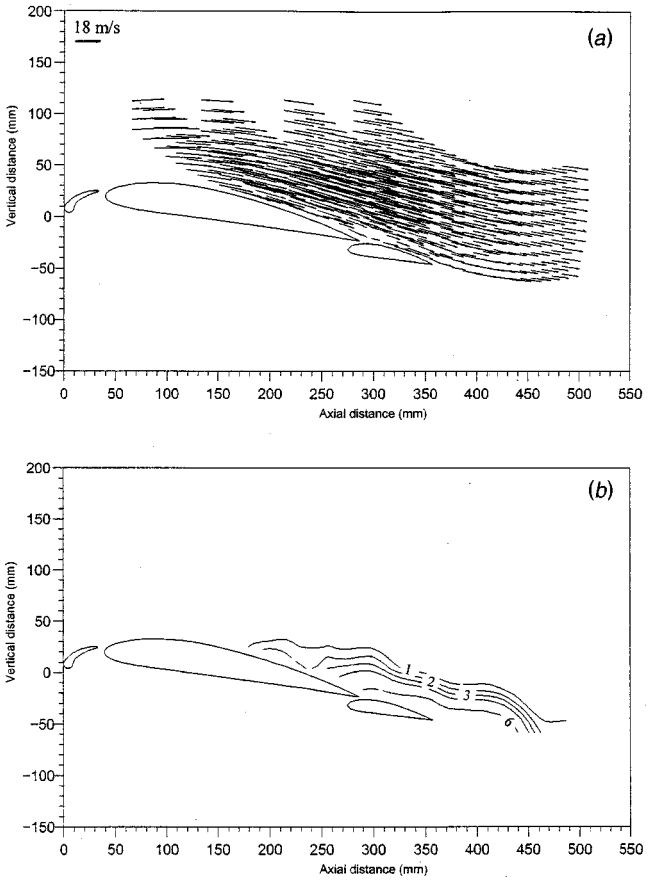

Fig. 9 Three-element aerofoil at $\alpha=10$ deg and $\delta_f=0$ deg: (*a*) Mean velocity vectors; (*b*) normalized streamwise normal Reynolds stress $(\overline{u^2}/U_\infty^2)\times 10^3$

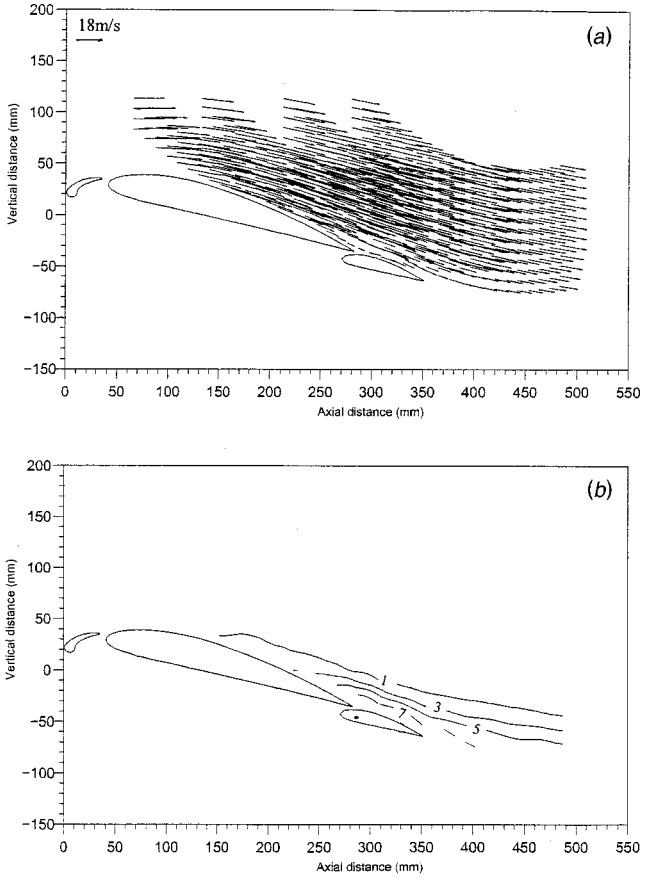

Fig. 10 Three-element aerofoil at $\alpha=15$ deg and $\delta_f=0$ deg: (*a*) Mean velocity vectors; (*b*) normalized streamwise normal Reynolds stress $(\overline{u^2}/U_\infty^2)\times 10^3$

ues of $\sim 1.41U_\infty$, $\sim 1.47U_\infty$ and $\sim 1.55U_\infty$ for configurations B2, B3, and B4, respectively. The following additional features for each of these three cases are discussed below:

$\alpha=10$ deg. The introduction of a deflected advanced slat for the three-element aerofoil at $\alpha=10$ deg, is observed, in general, to have only a small effect on the flow field compared to the corresponding two-element flow case A2, except over the trailing edge of the main aerofoil (Fig. 9(*a*)). In this region, small velocity vectors are found to occur for case A2, as depicted in Fig. 5(*b*), while the corresponding velocity vectors for the three-element aerofoil case B2 have improved to as high as 50% of the free-stream velocity. However, overall the lift coefficients for the two- and three-element aerofoils are very similar as discussed in Section 6.

$\alpha=15$ deg. The introduction of a deflected slat at $\alpha=15$ deg, is seen to enhance the whole flow field compared to the two-element case A3 and to re-establish large velocity vectors over the multi-element aerofoil and in the wake, Fig. 10(*a*). The difference in the streamwise component of the mean velocity for this case and for the one without the slat, $\overline{U}_{with\text{-}slat}-\overline{U}_{without\text{-}slat}$, is shown in Fig. 12. It is observed that the slat causes the U component of the mean velocity at the rear of the main aerofoil to recover up to 75% of the free stream velocity with a resulting thin shear layer and a narrow wake.

$\alpha=20$ deg. The three-element aerofoil at $\alpha=20$ deg is more heavily loaded and consequently, the velocity deficit over the trailing edge of the main aerofoil and over the flap (see Fig. 11(*a*)) is larger than that of the three-element aerofoil at $\alpha=15$ deg with a nondeflected flap, case B3. At this angle of attack the single and two-element aerofoils are stalled, while an enhanced lift coefficient is observed for the three-element aerofoil.

Reynolds Stresses. The contour plot for $\overline{u^2}$ for the three-element aerofoil at angles of attack of $\alpha=10$ deg (case B2), 15 deg (case B3) and 20 deg (case B4) are shown in Figs. 9(*b*)–11(*b*). The normalized streamwise normal Reynolds stress reaches peak values of $\sim 9\times 10^{-3}$, $\sim 12\times 10^{-3}$ and $\sim 20\times 10^{-3}$ over the trailing edge of the main aerofoil and the flap for cases B2, B3, and B4, respectively. Compared to the results without the slat, the peak value for $\overline{u^2}$ has decreased significantly from $\sim 35\times 10^{-3}$ at 10 deg and $\sim 180\times 10^{-3}$ at 15 deg. Similar trends were also observed from contour plots of $\overline{v^2}$ and $\overline{uv}$. These ''slatted'' results indicate a thinner attached boundary layer which is consistent with narrower wakes as observed from the velocity vectors plots, in Figs. 9(*a*)–11(*a*).

5.1b Intermittent Separation. As the angle of attack α is increased further, the extent of the low velocity region increases leading to an intermittent separated flow condition.

Main Aerofoil at $\alpha=25$ Deg With a Slat and a Flap (Case B5) Mean Velocity. The mean velocity vector plot for the three-element aerofoil at $\alpha=25$ deg is shown in Fig. 13(*a*). Increasing the angle of attack to 25 deg is seen to have deteriorated the flow field over the trailing edge of the main aerofoil resulting in a moderate intermittent separated flow region. However, due to the general enhancement of the flow field a higher lift is achieved.

Downloaded 03 Jun 2010 to 171.66.16.150. Redistribution subject to ASME license or copyright; see http://www.asme.org/terms/Terms_Use.cfm

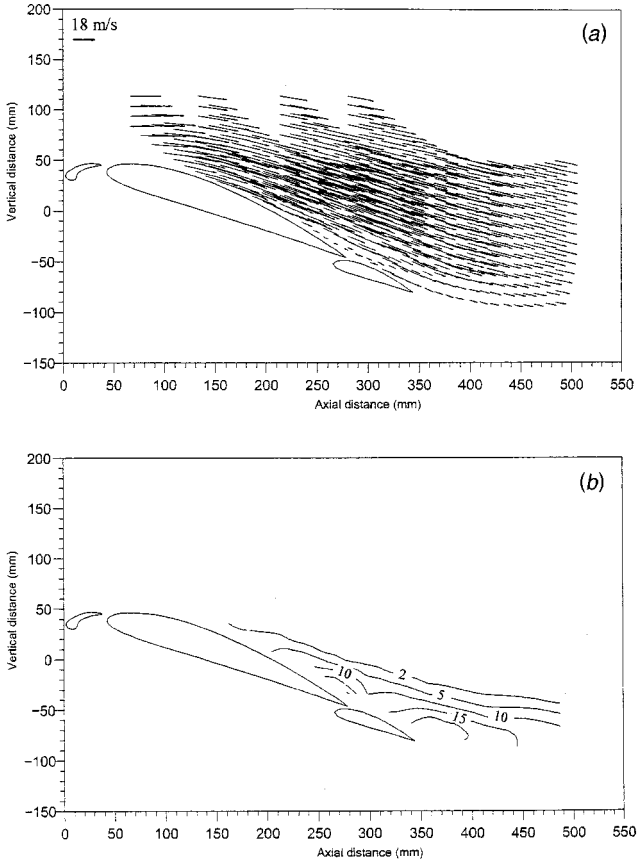

Fig. 11 Three-element aerofoil at $\alpha=20$ deg and $\delta_f=0$ deg: (*a*) Mean velocity vectors; (*b*) normalized streamwise normal Reynolds stress $(\overline{u^2}/U_\infty^2)\times 10^3$

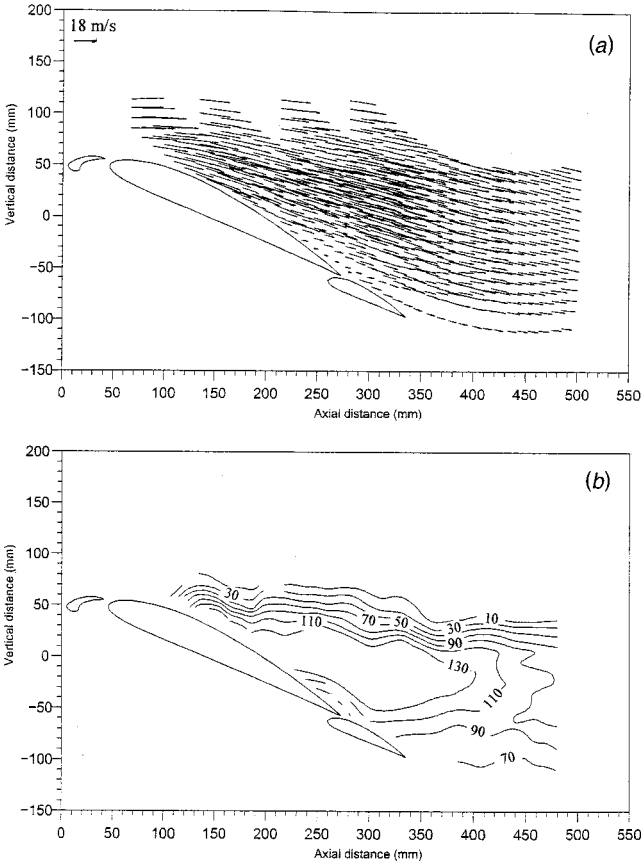

Fig. 13 Three-element aerofoil at $\alpha=25$ deg and $\delta_f=0$ deg: (*a*) Mean velocity vectors; (*b*) normalized streamwise normal Reynolds stress $(\overline{u^2}/U_\infty^2)\times 10^3$

The measured mean velocity over the front of the main aerofoil reaches a maximum of $\sim 1.65U_\infty$ which is 7% higher than the corresponding value for $\alpha=20$ deg, case B4.

Reynolds Stresses. Figure 13(*b*) shows the normalized Reynolds stresses $\overline{u^2}$ for the three-element aerofoil at $\alpha=25$ deg with a nondeflected flap. The presence of intermittent separation and small mean velocities over the rear part of the main aerofoil are consistent with high values for the Reynolds stresses. The normalized stress $\overline{u^2}/U_\infty^2$ reaches a peak value of $\sim 130\times 10^{-3}$, corresponding to a local turbulence intensity Tu≈55%, which is approximately three times higher than the corresponding value for the three-element aerofoil at $\alpha=20$ deg (case B4). Similar trends were also observed for $\overline{v^2}$ and $\overline{uv}$. The observed trends in the mean velocity and Reynolds stresses for the three-element aerofoil associated with the change of the flow regime from attached flow ($\alpha=20$ deg) to intermittent separation ($\alpha=25$ deg) are similar to the changes that occurred for the two-element aerofoil at $\alpha=5$ deg (attached flow, case A1) and $\alpha=10$ deg (intermittent separation, case A2).

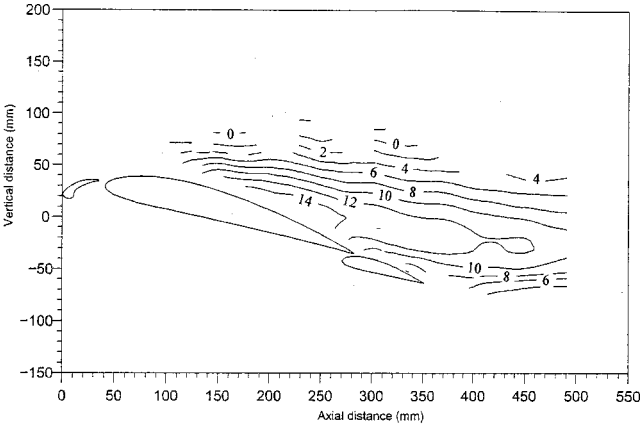

Fig. 12 The difference between streamwise mean velocity components, $\bar{U}_{with\text{-}slat}-\bar{U}_{without\text{-}slat}$, for multi-element aerofoil at $\alpha=15$ deg and $\delta_f=0$ deg

5.2 Deflected Flap, $\delta_f=25$ Deg

Main Aerofoil at $\alpha=10$, 15, and 20 Deg With a Slat and a Flap (Cases D2, D3, and D4) Mean Velocity. For the three-element aerofoil at angles of attack of $\alpha=10$ deg (case D2), 15 deg (case D3) and 20 deg (case D4) with a highly deflected flap ($\delta_f=25$ deg), the flow is attached for cases D2 (shown in Fig. 14(*a*)) and D3, and is intermittently separated for case D4. Compared to the nondeflected flap cases (B2, B3, and B4), setting the flap deflection to 25 deg creates larger velocities over the main aerofoil and the flap, resulting in lift enhancement. Consequently, the measured mean velocity over the front of the main aerofoil reaches larger peak values of $\sim 1.5U_\infty$, $\sim 1.55U_\infty$, and $\sim 1.63U_\infty$ for configurations D2, D3, and D4, respectively, compared with the corresponding results for the nondeflected flap described in Section 5.1a. The measured minimum velocity over the trailing edge of the main aerofoil for the deflected flap cases also exhibited higher values than those observed for the corresponding nondeflected flap cases.

Downloaded 03 Jun 2010 to 171.66.16.150. Redistribution subject to ASME license or copyright; see http://www.asme.org/terms/Terms_Use.cfm

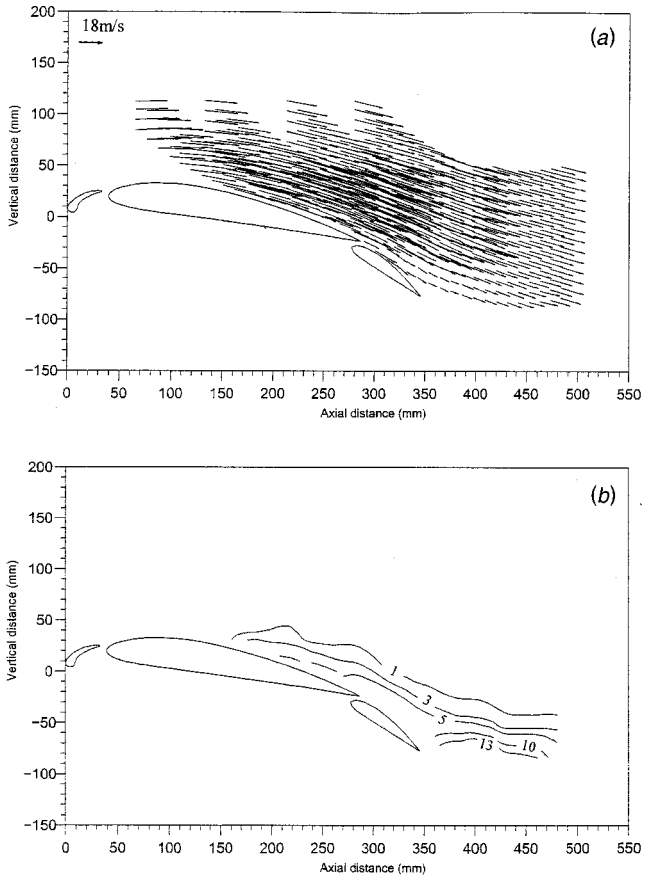

Fig. 14 Three-element aerofoil at $\alpha=10$ deg and $\delta_f=25$ deg: (*a*) Mean velocity vectors; (*b*) normalized streamwise normal Reynolds stress $(\overline{u^2}/U_\infty^2)\times 10^3$

The results for $\alpha=10$ and 15 deg are compared with the following two investigations:

$\alpha=10$ deg. The mean velocity field over a three-element aerofoil incorporating a conventional slat has been reported by Nakayama et al. [6] for $\alpha=10$ deg using a smaller flap deflection angle, $\delta_f=15$ deg. Their results demonstrated a similar trend (as for case D2 shown in Fig. 14(*a*)) in both the spatial velocity distribution and the wake width.

$\alpha=16$ deg. The mean velocity field over a three-element aerofoil reported by Braden et al. [7] at an angle of attack $\alpha=16$ deg incorporating a conventional slat with a higher flap deflection angle, $\delta_f=30$ deg, demonstrated a similar overall trend (as for case D3) in the flow field. However, the higher flap deflection angle and the conventional slat caused a small separated region commencing at the trailing edge of the main aerofoil and extending downstream into the wake and this resulted in a wider wake.

$\alpha=20$ deg. Although, for the three-element aerofoil at $\alpha=20$ deg, with a highly deflected flap, higher velocities were observed over the trailing edge of the main aerofoil compared to the corresponding nondeflected flap case, the direction of the flow indicated that the flow did not follow the surface in this region. This boundary layer behavior is indicative of an intermittent flow separation. It was also observed that the flow does not follow the surface of the flap.

Reynolds Stresses. For the three-element aerofoil at angles of attack of $\alpha=10$ deg (case D2), 15 deg (case D3) and 20 deg (case D4) with a highly deflected flap ($\delta_f=25$ deg), the normalized streamwise normal Reynolds stress $\overline{u^2}/U_\infty^2$ reaches peak values of $\sim 13\times 10^{-3}$, $\sim 16\times 10^{-3}$, and $\sim 60\times 10^{-3}$, respectively, over the trailing edge of the main aerofoil and the flap. The peak value for $\overline{u^2}$ has increased significantly for the three-element aerofoil at 20 deg due to the change of the flow regime from attached (case B4) to intermittently separated flow (case D4). Similar trends were also observed from contour plots of $\overline{v^2}$ and $\overline{uv}$. The results for $\alpha=10$ deg are compared with the following investigation:

$\alpha=10$ deg. A comparison of the $\overline{u^2}$ results shown in Fig. 14(*b*) with the comparative data reported by Nakayama et al. [6] demonstrates similar trends regarding the spatial distribution of the turbulence intensity and the width of the shear layer. However, the peak values of the Reynolds stresses in their experiment are approximately 60% higher than the corresponding values in the present research. This is most likely caused by the heel effect of the conventional slat used.

6 Summary of Aerofoil Measurements

As has been shown, the measured mean and fluctuating velocity fields have clearly identified three types of flow fields over the multi-element aerofoil, i.e., attached flow, intermittent separation over parts of the aerofoil/flap and separated flow including stall.

The following features are particularly helpful in describing the observed flow fields:

Mean Velocities

(i) The value of the maximum mean velocity $\overline{U}_{\max}$ obtained within the measurement region near the front of the aerofoil.

(ii) The measured minimum velocity $\overline{U}_{\min}$ close to the surface of the trailing edge of the main aerofoil, as defined in section 2.

An increase in both values will correspond to enhanced lift conditions. In contrast, low values at the rear of the aerofoil would indicate adverse flow conditions such as intermittent separation. The corresponding measured values for $\overline{U}_{\max}$ and $\overline{U}_{\min}$ are plotted in Figs. 15(*a*) and 15(*b*), respectively, as functions of angle of attack α and flap deflection angle δ_f.

For the front of the aerofoil, the results for $\overline{U}_{\max}$ corresponding to $\delta_f=0$ deg in Fig. 15(*a*), show that the data for the two-element (A1 and A2) and the three-element aerofoil (B2 to B5) lay on the same straight line, demonstrating lift enhancement as a function of α due to the increase in $\overline{U}$ on the front part of the main aerofoil.

For the same flap setting, at the rear of the aerofoil, there is a major difference between the two-element and the three-element results (see Fig. 15(*b*)). The two-element results show a rapid deterioration in the flow field with α, resulting in a separated flow region when $\alpha=15$ deg. In contrast, for the three-element aerofoil substantial positive values for $\overline{U}_{\min}$ ($\sim$6 m/s) are maintained for $\alpha=10-20$ deg, and even at 25 deg, $\overline{U}_{\min}$ is as high as 2 m/s. Consequently, for $\delta_f=0$ deg the lift will increase with α over the complete angle range listed. Compared with a single aerofoil, the flap has the advantage of providing an additional surface area for creating lift and the utilization of a slat ensures that both the main aerofoil and the flap contribute positively to the lift by maintaining an attached boundary layer over both.

For a flap deflection angle $\delta_f=25$ deg, the $\overline{U}_{\max}$ data in Fig. 15(*a*) demonstrate an enhancement in the velocity field in the α range 10–20 deg. However for $\alpha=25$ deg, we notice a rapid decrease in $\overline{U}_{\max}$ and hence in the lift performance. This is consistent with the minimum velocity $\overline{U}_{\min}$ at the rear of the aerofoil, Fig. 15(*b*), having values as high as 9 m/s for $\alpha=10-17.5$ deg and poor separated flow conditions for $\alpha=25$ deg. Consequently, the aerofoil will experience an enhanced lift in the range $\alpha=10$ to 20 deg and a reduction in lift at $\alpha=25$ deg due to virtually stall conditions.

Turbulent Quantities. The maximum value for $\overline{u^2}$ [plotted as $(\overline{u^2}/U_\infty^2)\times 10^3$] can be used to describe the occurring turbulent flow fields. From this value the corresponding local turbulence

Downloaded 03 Jun 2010 to 171.66.16.150. Redistribution subject to ASME license or copyright; see http://www.asme.org/terms/Terms_Use.cfm

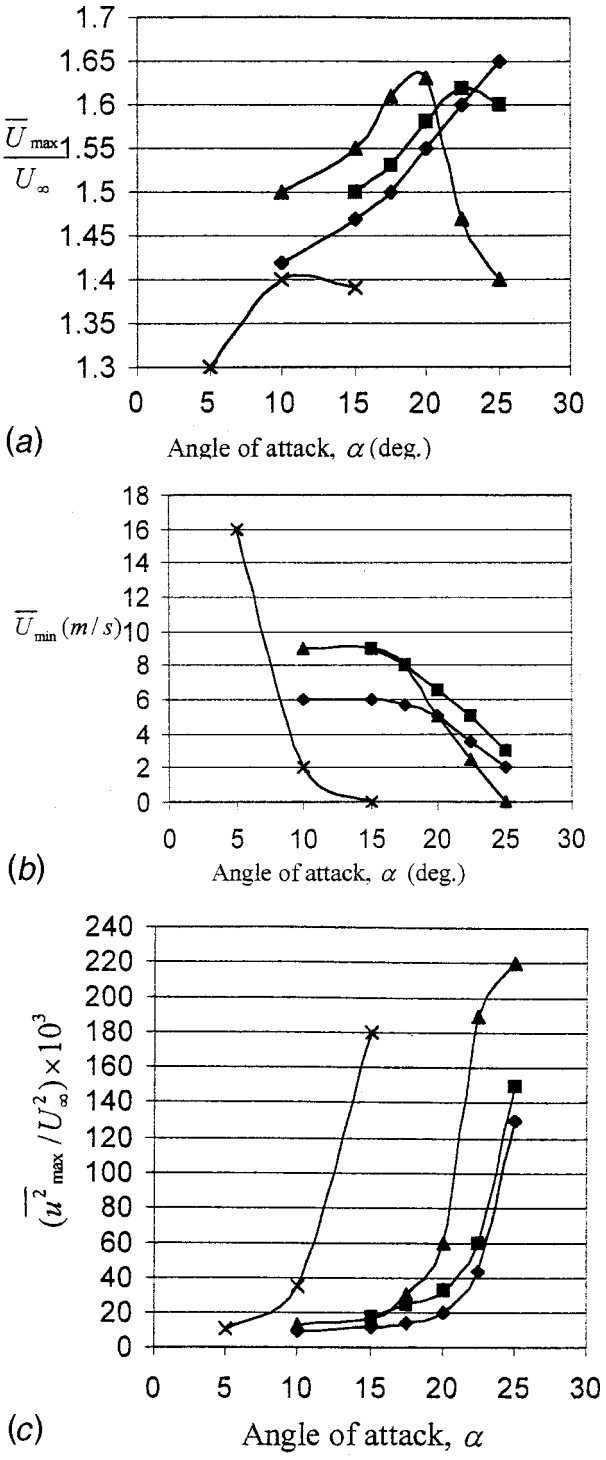

Fig. 15 (*a*) Maximum mean velocity over the top front of the main aerofoil for four aerofoil configurations: Three-element aerofoil, α=10, 15, 20, 25 deg: series 1: ♦, δ_f=0 deg; series 2: ■, δ_f=10 deg, series 3: ▲, δ_f=25 deg. Series 4: ×, Two-element aerofoil, α=5, 10, 15, and δ_f=0 deg. (*b*) Minimum mean velocity over the trailing edge of the main aerofoil for four aerofoil configurations: (legend as in Fig. 15(*a*)). (*c*) ($\overline{u^2}_{max}/U_\infty^2$) as a function of angle of attack for four aerofoil configurations: (legend as in Fig. 15(*a*))

intensity Tu=$u'/\overline{U}$ (where $u'=(\overline{u^2})^{1/2}$ and $\overline{U}$ is the local mean velocity) could be calculated. If the turbulent flow field has a Gaussian distribution, a value of Tu>30% would indicate intermittent flow separation.

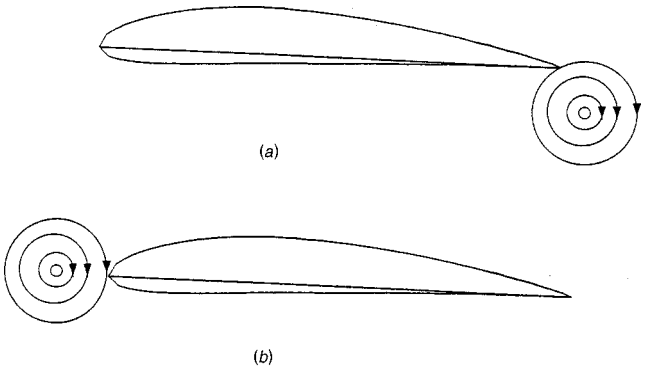

Fig. 16 Representation of the flap and slat by vortices: (*a*) Flap representation; (*b*) slat representation

The change in the flow conditions and related turbulence field can be summarized using a plot of $(\overline{u^2_{max}}/U_\infty^2)\times 10^3$ as a function of the angle of attack α for four aerofoil conditions: two-element aerofoil and three multi-element aerofoil conditions with $\delta_f=0$, 10, and 25 deg. These results are shown in Fig. 15(*c*).

From the Turbulence Results in Fig. 15(c), it was found in general:

(i) When $\overline{u^2_{max}}/U_\infty^2<40\times 10^{-3}$, the corresponding local turbulence intensity Tu<30% and the flow over the aerofoil would be attached. It is observed that these conditions apply to the configurations A1, B2-B4, C2-C4, and D2-D3.

(ii) When $\overline{u^2_{max}}/U_\infty^2\sim(40-60)\times 10^{-3}$, then small scale intermittent separation occurred (flow cases S2, A2 and D4). This was observed to correspond to a relatively small intermittent separation region towards the trailing edge of the main aerofoil. As the value of $\overline{u^2_{max}}$ increases, the extent of the intermittent separation region grows, the longitudinal oscillations become more violent and $\overline{u^2}/U_\infty^2$ reaches values of 130–140 (cases B5 and C5).

(iii) When the value of normalized $\overline{u^2_{max}}$ reaches values of 180×10^{-3} (case A4), then the flow is separated with a permanent region of reversed flow. For $\overline{u^2_{max}}$ values larger than this (case D5), the main aerofoil is, for all practical purposes, stalled.

7 General Discussion and Conclusion

The observed flow fields described in this paper can be related to the interaction between the slat/main aerofoil and the main aerofoil/flap and the consequent variations in the lift and drag. In aerofoil theory it has been common practice to describe the circulation and related lift of an aerofoil according to vortex theory. It is therefore useful to replace the flap and slat with vortices as shown in Figs. 16(*a*) and 16(*b*) and to consider the change in the circulation and hence in the velocity fields for the interacting slat/main aerofoil or main aerofoil/flap. Using a fixed aerofoil configuration and a fixed angle of attack α, Smith [17] has used this vortex concept to explain the upstream/downstream element interaction. However no explanation, based on vortices, has been presented for the variation of this interaction with α and δ_f.

First, the effect of a flap on the flow field over the main aerofoil will be considered. Then the effect of the flap deflection angle is ascertained. Finally, an explanation for the slat effect is provided.

Flap. The simulation of the flap by a clockwise vortex as shown in Fig. 16(*a*), will create a stronger circulation over the main aerofoil which will attempt to create higher velocities over its top surface. The following observations can be made from this figure:

1. Using a flap will attempt to increase the velocity over the whole of the upper surface of the main aerofoil;

Downloaded 03 Jun 2010 to 171.66.16.150. Redistribution subject to ASME license or copyright; see http://www.asme.org/terms/Terms_Use.cfm

2 The increase in the velocity is largest over the leading edge of the main aerofoil.

For attached flow, the first trend is consistent with our comparative experimental results for the mean velocity field over a single aerofoil and two-element aerofoil (with a nondeflected flap). For example, this effect can be observed from a comparison of the flow field over the single aerofoil (case S1) and over the two-element aerofoil (case A1) at an angle of attack of $\alpha=5$ deg. This demonstrates an enhanced flow field for the two-element case.

The second effect causes the front of the main aerofoil to be more heavily loaded. This effect works against the attachment of the flow, and causes the pressure distribution over the main aerofoil to deteriorate in terms of a more unfavorable pressure gradient dp/dx. As α is increased and the aerofoil becomes more heavily loaded (higher velocities on the front), the unfavourable pressure gradient will increase faster than for the single aerofoil, resulting in an earlier separation at the rear of the aerofoil. This is demonstrated by the results for $\alpha=15$ deg.

Flap Deflection. The above concepts also apply to the deflected flap. Provided that the flow remains attached then the second effect will be dominant when the flap is deflected. The deflection of the flap increases the strength of the assumed vortex, thereby creating higher velocities (particularly at the front of the aerofoil), a general enhancement of the flow field and an increase in the lift.

On the other hand, if prior to the flap being deflected, a detached boundary layer or an intermittent separated flow, (however small in size) exists, then the case of the deflected flap will have a worse flow field than the situation with a nondeflected flap. The already unfavorable pressure distribution over the top surface of the main aerofoil will deteriorate further when the flap is deflected, causing a larger low velocity/reverse flow region. For example, the intermittently separated flow field for the three-element aerofoil at $\alpha=25$ deg with a nondeflected flap (case B5) will deteriorate by setting the flap deflection angle to 25 deg (case D5), thus causing a large scale separated flow (stall) and a loss of lift.

Therefore, as long as the flow can cope with the change in the pressure distribution over the aerofoil surface, the flow will remain attached and the deflected flap will enhance the flow field.

When the flow over the main aerofoil starts to deteriorate due to the stronger adverse pressure gradient, then a pressure modifier is needed to restore the pressure distribution, particularly over the nose of the main aerofoil and to smooth the pressure rise in the streamwise direction. This pressure modifier can be a slat and its main effect is explained in the following section.

Slat. As pointed out by Smith [17], a common misconception of the working principle of the slat is that it blows high energy flow into the boundary layer. However, to a large extent the slat has the opposite effect. The effect of the slat can be demonstrated by simulating it using a clockwise vortex as shown in Fig. 16(*b*). The resulting pressure distribution over the main aerofoil and the related lift are functions of the strength of this vortex which is itself a function of: Slat deflection angle, slat gap, slat overlap and slat shape. From Fig. 16(*b*) it is observed that the direction of the circulation over the slat (as represented by the vortex) and over the main aerofoil are in opposite directions in the gap region between the slat and the main aerofoil. This causes lower velocities over the leading edge of the main aerofoil and hence less suction and a consequent reduction in local lift. The effect of the slat on the pressure distribution is shown in Fig. 17 for an aerofoil at $\alpha=10$ deg with and without a deflected slat, Savory et al. [8]. This figures demonstrates three effects:

1 That the slat causes a substantial reduction in the pressure suction and hence in the velocities over the nose of the aerofoil.
2 More importantly, that the pressure recovery on the top front of the aerofoil is much smoother for the slatted aerofoil, causing a much more favorable boundary layer on the top front of the aerofoil.
3 As a consequence, the pressure gradient dp/dx is reduced considerably for the slatted aerofoil, enabling attached flow to be maintained for much larger angles of attack than for the single aerofoil.

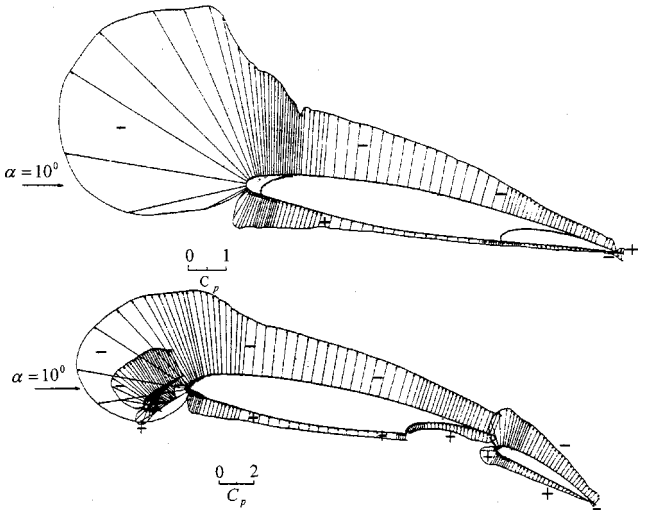

Fig. 17 Pressure distribution for aerofoils at $\alpha=10$ deg: (*a*) Aerofoil with retracted slat and flap; (*b*) three-element aerofoil with extended and deflected slat and flap (from Savory et al. [8])

This is consistent with the measured higher mean velocities in the rear part of the aerofoil for the slatted case and it can be clearly observed from the comparison of the mean velocity results for the two- and three-element aerofoil at an angle of attack of $\alpha=10$ deg, shown in Figs. 5(*b*) and 9(*a*), respectively.

Lift and Drag. In the current experiment it was not possible to directly measure the lift and drag and thereby evaluate the corresponding lift and drag coefficients C_l and C_d.

However, there is sufficient evidence to demonstrate that, provided the flow is attached, then current CFD codes will produce adequate solutions of the mean velocity field and pressure distribution. By integrating the pressure distribution the corresponding C_l and C_d coefficients can be derived.

As described in Maddah [13] such a numerical calculation was carried out using the CFX code, for two-element and three-element aerofoils to demonstrate the variation in C_l and C_d with α in the range 10 to 25 deg and $\delta_f=0$, 10, and 25 deg. The experimental results in this investigation, have shown that the flow is attached for cases B2-B4 and D2-D3, and intermittently separated for cases B5 and D4. Separated flow was identified for case D5 and hence the numerical prediction for this case is significantly less accurate.

Prior to stall occurring for any of the investigated aerofoil configurations ($\alpha<15$ deg), the lift for the single- and the two- and three-element aerofoils with a nondeflected flap is almost the same. This can be explained by considering the interaction of upstream and downstream elements. The circulation increases on the upstream element, while the circulation decreases on the downstream element. Thus, adding a nondeflected flap increases the circulation over the main aerofoil, while the circulation around the flap is decreased, thus, the overall effect is a slight increase in C_l. In addition, there is a considerable increase in the lift due to the extra area provided by the flap. Adding a slat to the single aerofoil, results in higher circulation over the slat and the unloading of the front of the main aerofoil. The overall effect is a slight

Downloaded 03 Jun 2010 to 171.66.16.150. Redistribution subject to ASME license or copyright; see http://www.asme.org/terms/Terms_Use.cfm

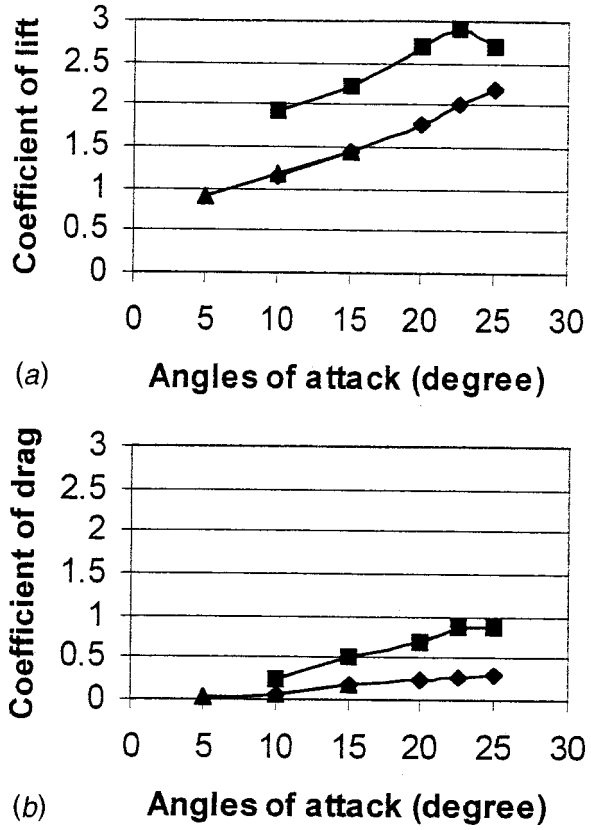

Fig. 18 Numerical prediction of: (*a*) Coefficient of lift C_l for three aerofoil configurations: Three-element aerofoil, $\alpha=10$, 15, 20, 25 deg: series 1: ♦, $\delta_f=0$ deg; series 2: ■, $\delta_f=25$ deg; series 3: ▲, Two-element aerofoil, $\alpha=5$, 10, 15, and $\delta_f=0$ deg; (*b*) coefficient of drag C_d for three aerofoil configurations: (legend as in *a*)

decrease in C_l. For the three-element aerofoil, the overall effect on the main aerofoil is a balance between the increase and decrease in circulation due to the flap and slat, respectively, resulting in values for C_l similar to those observed with the single aerofoil. Figure 18(*a*) shows that for the nondeflected flap case, C_l increases linearly to $\alpha=25$ deg, and the experimental results confirmed that the flow remained attached for all values of α in this range. The delay in the stall angle is caused by the presence of the slat producing a benificial pressure modification on the main aerofoil. The variation of C_l for the three-element aerofoil with a deflected flap, is similar to the three-element aerofoil with a nondeflected flap, but with a shift in C_l at each angle of attack due to the strong circulation effect of the deflected flap on the main aerofoil. However, as the aerofoil is more heavily loaded, the flow field was observed to have deteriorated, with stall occurring at $\alpha=25$ deg and a resulting loss in lift.

The drag for a multi-element aerofoil is different from the drag for a single element aerofoil. In multi-element aerofoil flows the flap and slat are usually extended and often deflected. The deflected leading and trailing edge devices cause a considerable increase in the drag. Consequently, the resulting drag for a multi-element aerofoil, even at low angles of attack, will be higher than the corresponding value for a single element aerofoil as has been reported by several researchers. Deflecting the flap will increase C_d as shown in Fig. 18(*b*).

Acknowledgments

The principle author wishes to acknowledge a study grant from the government of the Islamic Republic of Iran.

Nomenclature

A1 to A3 = two-element aerofoil configurations with a non-deflected flap
B2 to B5 = three-element aerofoil configurations with a non-deflected flap
c = chord length of the main aerofoil
C_d = drag coefficient
C_l = lift coefficient
C_p = pressure coefficient
D2 to D5 = three-element aerofoil configurations with a highly deflected flap
dp/dx = streamwise pressure gradient
E_1, E_2 = output voltage of anemometer
S1 to S3 = single aerofoil configurations
$\overline{U}$ = streamwise mean velocity component
$\overline{U}_{\max}$ = maximum measured streamwise mean velocity component
$\overline{U}_{\min}$ = minimum measured streamwise mean velocity component
Tu = turbulence intensity defined as $u'/\overline{U}=\sqrt{\overline{u^2}}/\overline{U}$
U_∞ = mean free stream velocity
$\overline{u^2}$ = streamwise normal Reynolds stress
$\overline{uv}$ = Reynolds shear stress
$\overline{v^2}$ = cross-stream normal Reynolds stress
y = cross-stream distance
y_R = cross-stream extent of reversed flow region
α = angle of attack
δ_f = flap deflection angle
δ_s = slat deflection angle

Appendix 1-Experimental Uncertainty

The FHW traveling mechanism enabled the location of the longitudinal and vertical positions with an accuracy of ± 0.1 mm. Overall, taking the stiffness of the FHW system into account the accuracy of the absolute spatial resolution of each point was estimated to be within ± 0.25 mm.

The output from a hot-wire sensor is a time varying signal typically representing a velocity component. For a turbulent flow the anemometer signal will be of a random nature. When using digital data analysis, the continuous signal is replaced by a digital finite time record. Thus, errors are introduced by a time series analysis of a finite time history record.

The uncertainty in the evaluated velocity quantities $\overline{U}$ and $\overline{u^2}$ can be estimated as

$$\frac{\hat{\overline{U}}}{\overline{U}}=1\pm Z_{\alpha/2}\varepsilon(\hat{\overline{U}})$$

and

$$\frac{\hat{\overline{u^2}}}{\overline{U}}=1\pm Z_{\alpha/2}\varepsilon(\hat{\overline{u^2}})$$

where $Z_{\alpha/2}$ is the standardized variable used in the Gaussian probability distribution described by Bruun [12]. For N independent samples, we have

$$\varepsilon(\hat{\overline{U}})=\frac{1}{\sqrt{N}}\frac{(\overline{u^2})^{1/2}}{\overline{U}} \quad \text{and} \quad \varepsilon(\hat{\overline{u^2}})=\frac{1}{\sqrt{N}}$$

In the present study, the FHW data was evaluated for $N=200$ statistically independent sweeps with a 10 s dormant period between each sweep.

Downloaded 03 Jun 2010 to 171.66.16.150. Redistribution subject to ASME license or copyright; see http://www.asme.org/terms/Terms_Use.cfm

For all flow cases a large proportion of the flow field has low/moderate turbulence intensity. For illustrative purposes consider flow regimes with a maximum turbulence intensity of 20% (this is the case everywhere except near or inside a separated flow region).

Specifying $Z_{\alpha/2}=2.33$ for a 98% confidence level, it therefore follows that

$$\frac{\hat{U}}{\overline{U}}=1\pm 2.33\frac{1}{\sqrt{200}}0.2=1\pm 3\%$$

$$\frac{\hat{\overline{u^2}}}{\overline{u^2}}=1\pm 2.33\frac{1}{\sqrt{200}}=1\pm 16\%$$

References

[1] Innes, F., Pearcey, H. H., and Sykes, D. M., 1995, ''Improvements in the performance of a three element high lift system by the application of airjet vortex generators,'' Proc. Conference High Lift and Separation Control, Royal Aeronautical Society, University of Bath, UK, pp 25.1–25.11.

[2] Moens, F., and Capbern, P., 1995, ''Design and testing of leading-edge high-lift device for laminar flow wing applications,'' Proc. Conference on High Lift and Separation Control, Royal Aeronautical Society, University of Bath, UK, pp. 7.1–7.13.

[3] Seetharam, H. C., and Wentz, W. H. J., 1977, ''A low speed two-dimensional study of flow separation on the GA(W)-1 airfoil with 30-percent chord Fowler flap,'' NASA CR-2844.

[4] Olson, L. E., and Orlow, K. L., 1981, ''On the structure of turbulent wakes and merging shear layers of multielement aerofoils,'' AIAA paper 81-1238.

[5] Biber, K., and Zumwalt, G. W., 1993, ''Flowfield measurements of a two-element airfoil with large separation,'' AIAA J., **31**, No. 3, pp. 459–464.

[6] Nakayama, A., Kreplin, H. P., and Morgan, H. L., 1990, ''Experimental investigation of flowfield about a multielement airfoil,'' AIAA J., **28**, No. 1, pp. 14–21.

[7] Braden, J. A., Whipkey, R. R., Jones, G. S., and Lilley, D. E., 1986, ''Experimental study of the separating confluent boundary layer,'' NASA CR-3655. also AIAA paper 86-0505.

[8] Savory, E., Toy, N., Tahouri, and Dalley, S., 1992, ''Flow regimes in the cove regions between a slat and wing and between a wing and a flap of a multielement aerofoil,'' Exp. Therm. Fluid Sci., **5**, pp. 307–316.

[9] Alemdaroglu, N., 1993, ''Experimental investigation of flow around a multi-element airfoil,'' AGARD-CP-515.

[10] Maddah, S. R., Gough, T., and Bruun, H. H., 2001, ''Investigation of slat heel effect on flow field over multi-element aerofoils,'' Proc. ASME FEDSM 2001 Conference, New Orleans, USA, session F-252-03.

[11] Jones, J. B. C., 1993, ''An optimised slat to maximise performance in both aircraft take-off and landing,'' PhD thesis, University of Hertfordshire, UK.

[12] Bruun, H. H., 1995, *Hot-wire anemometry*, Oxford University Press, Oxford London.

[13] Maddah, S. R., 2000, ''Study of the flow field over the multi-element aerofoils,'' PhD thesis, Dept. of Mech. and Med. Engineering, Univ. of Bradford.

[14] Coles, D., and Wadcock, A. J., 1979, ''Flying hot-wire study of flow past an NACA 4412 airfoil at maximum lift,'' AIAA J., **17**, No. 4, pp. 321–329.

[15] Mahmood, Z., Khan, M. K., Seale, W. J., and Bruun, H. H., 1995a, ''Comparison of measured and computed velocity fields over a high lift aerofoil,'' Proc. Seventh International Conference on computational methods and experimental measurements, Computational Mechanics Publications, Southampton, UK, Capri, pp 203–211.

[16] Mahmood, Z., Khan, M. K., and Bruun, H. H., 1995b, ''Flow over high lift multiple aerofoils,'' Proc. of Conference on High Lift and Separation Control, Royal Aeronautical Society.

[17] Smith, A. M. O., 1974, ''High lift aerodynamics,'' AIAA paper 74-039.

Downloaded 03 Jun 2010 to 171.66.16.150. Redistribution subject to ASME license or copyright; see http://www.asme.org/terms/Terms_Use.cfm

J. Estevadeordal
Mechanical Engineer

S. Gogineni
Senior Engineer

L. Goss
Analytical Chemist, President ISSI

Innovative Scientific Solutions, Inc.,
2766 Indian Ripple Rd.,
Dayton, OH 45440

W. Copenhaver
Principal Aerospace Research Engineer

S. Gorrell
Aerospace Engineer

Air Force Research Laboratory,
AFRL/PRTF, Bldg. 18,
Wright-Patterson Air Force Base, OH 45433

Study of Wake-Blade Interactions in a Transonic Compressor Using Flow Visualization and DPIV

Flow-field interactions are studied in a high-through-flow, axial-flow transonic compressor using Digital Particle Image Velocimetry (DPIV). Measurement of instantaneous velocities in two-dimensional (2D) planes in the main flow direction allows characterization of the unsteadiness of spatial structures from an upstream blade row and their interaction with the downstream rotor. The measurement system is specially designed for a large transonic environment, which introduces conditions that differ from those generally encountered by traditional DPIV systems. Viewing windows on the compressor housing are used to allow optical access, and the design of a special optical probe permits laser-sheet delivery through one of the wake generators (WG). The system is synchronized with the blade passage and is remotely monitored and controlled. Through flow visualization and instantaneous and ensemble-averaged quantities, it clearly captures the interactions of the wake with the potential field of the rotor leading edge (LE) and its bow shock, vortex shedding, vortex-blade synchronization, wake chopping, and boundary-layer flow at the housing for several configurations. [DOI: 10.1115/1.1429638]

1 Introduction

Turbomachines are typically designed with closely spaced and heavily loaded blade rows to reduce weight; as a result, blade-row/wake interactions are a common source of unsteady aerodynamic excitation. Often-observed unsteady phenomena such as shock-vortex and shock-surface interactions produce nonuniformities and irregular flow patterns that result in blade-row vibrations and high-cycle blade fatigue and influence compressor performance.

A variety of design tools for rotating machinery are currently in use. Some are based on steady Navier-Stokes analysis, with unsteady interactions between blade rows being modeled as ''deterministic stresses.'' Others simulate the time-resolved flow field and analyze the time-averaged solution to avoid problems associated with models for the deterministic stresses. Experimental results for validating these design tools are needed for capturing unsteady flow effects; however, such results are limited. These results would also aid the understanding of the physical phenomena and interaction processes involved in turbomachinery. An experimental technique for capturing the instantaneous nature of unsteady flow structures is needed.

Advanced laser-based diagnostic techniques are very useful for providing quantitative evidence of unsteady effects on the blade-passage scale and identifying the relative importance of the length and time scales of unsteady-flow phenomena in turbomachinery. Two pointwise velocimetry techniques that have been applied to compressor research are Laser Transit Anemometry (LTA) (Calvert et al. [1]) and Laser Doppler Velocimetry (LDV) (Stratizar et al. [2]). However, issues associated with low data rates (long run times), slow mapping due to the pointwise nature of these techniques, and measurement uncertainties associated with unsteady flow fields make these methods difficult to apply outside the basic-research environment. Recent advances in Particle Image Velocimetry (PIV) have allowed researchers to extend this technique to turbomachinery flow fields. This method has been demonstrated in transonic compressors and used for accurate measurements of instantaneous velocity fields (Balzani et al. [3]; Estevadeordal et al. [4]; Sanders et al. [5]; Wernet [6]). Two-color digital PIV (DPIV) has also been developed and implemented for turbomachinery flows (Estevadeordal et al. [4,7]). The advantages of PIV as a diagnostic tool are associated with its instantaneous nature and two-dimensionality (in its simplest form). However, it cannot provide temporal evolution of the flow field because of the relatively slow repetition rate of the lasers. Therefore, statistical analysis of flow fields and calculation of quantities such as turbulence intensity must be done carefully.

In the present study a system was developed to obtain high-resolution velocity data from a high-through-flow, axial-flow transonic compressor (Law and Wadia [8]) located in the Compressor Aerodynamic Research Laboratory (CARL) at Wright-Patterson AFB (Fig. 1). The transonic environment introduces conditions that differ from those generally encountered by traditional DPIV systems, including vibrations, high flow and rotational speeds, high temperatures, compressibility, and shock systems. The DPIV measurement system consists of two Nd:YAG lasers, transmitting and receiving optics, seed particles, camera, and a synchronization setup. The sytem is remotely monitored and controlled.

The main goals of this investigation were to evaluate and develop a DPIV system for turbomachinery studies that could be used to identify and investigate the flow structures from wake generators, the wake-blade interaction, and the wake-shock interaction in transonic-compressor rotors. The interactions of the wake with the potential field of the rotor LE are captured using flow visualizations and instantaneous and ensemble averages for various configurations. The data also characterize the bow shock, wake chopping, and the boundary layer near the compressor case.

2 Stage-Matching-Investigation (SMI) Rig

The SMI rig is a high-speed, highly loaded compressor consisting of three blade rows--a wake generator, a rotor, and a stator (Fig. 2). The rig was designed such that the wake generator-to-rotor axial spacing can be set to three values, denoted by ''close,'' ''mid,'' and ''far'' (Gorrell et al. [9]), as shown in Fig. 2. The spacings normalized by the WG chord are given in Table 1. This DPIV study concentrates on WG blade counts of 24 and 40, close and mid spacings, and no stator.

Contributed by the Fluids Engineering Division for publication in the JOURNAL OF FLUIDS ENGINEERING. Manuscript received by the Fluids Engineering Division January 29, 2001; revised manuscript received August 24, 2001. Associate Editor: A. K. Prasad.

 Copyright © 2002 by ASME

Downloaded 03 Jun 2010 to 171.66.16.150. Redistribution subject to ASME license or copyright; see http://www.asme.org/terms/Terms_Use.cfm

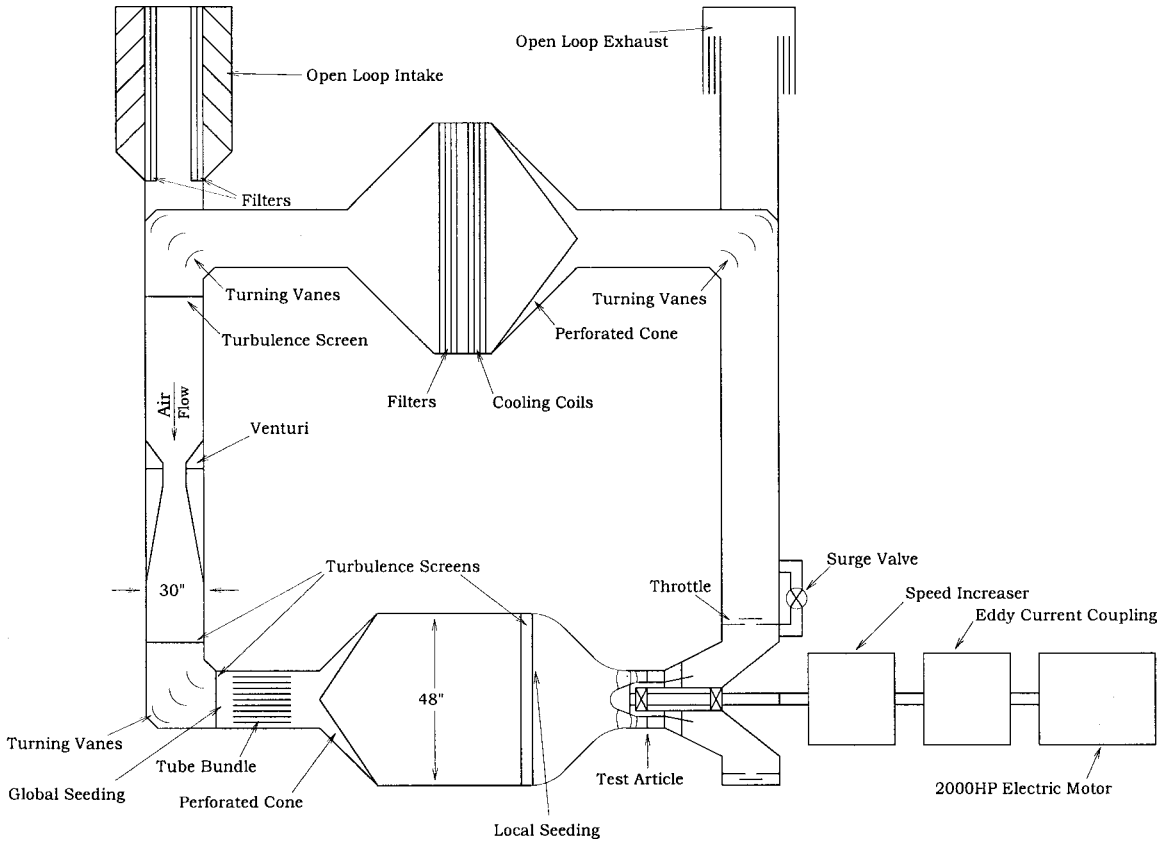

Fig. 1 Flow path of the 2000-hp Compressor Aerodynamic Research Laboratory facility (CARL) and locations for global and local seeding

The WGs were designed to produce wakes typical of modern, highly loaded, low-aspect-ratio, front-stage compressor stators. To simplify the experiment, the WGs were designed as uncambered airfoils that do not turn the flow. Results from measurements of stator wakes from rig tests were used as the design target (Creason and Baghdadi [10]). These wakes were produced in a stator that had no bow or sweep, with a hub Mach number of 0.95, a hub D-Factor of 0.55, and a solidity of 1.64. For simplicity and for isolating the effects of various wake parameters, a 2D representation of the wake was desired. The airfoils have a small LE radius and a relatively blunt trailing-edge (TE) radius, as shown in Fig. 3. In the design process this produced the optimum combination of profile and base drag for matching the desired highly loaded stator wake. Since the wake width and loss are strong functions of solidity, the solidity of the WGs was held constant from hub to tip, resulting in a tapered airfoil-chord along the radius, as seen in the figure. Also, the ratio of WG chord to the gap between the WG TE and rotor LE was designed to be constant from hub to tip for the mid-spacing configuration. This required that the WG TE be swept from hub to tip. However, slight variations in the ratio of axial separation to WG chord occur across the span for close and far spacing. With no diffusion in the flow path, the end-wall losses were expected to be low. There is neither clearance and nor fillet at either the hub or the tip.

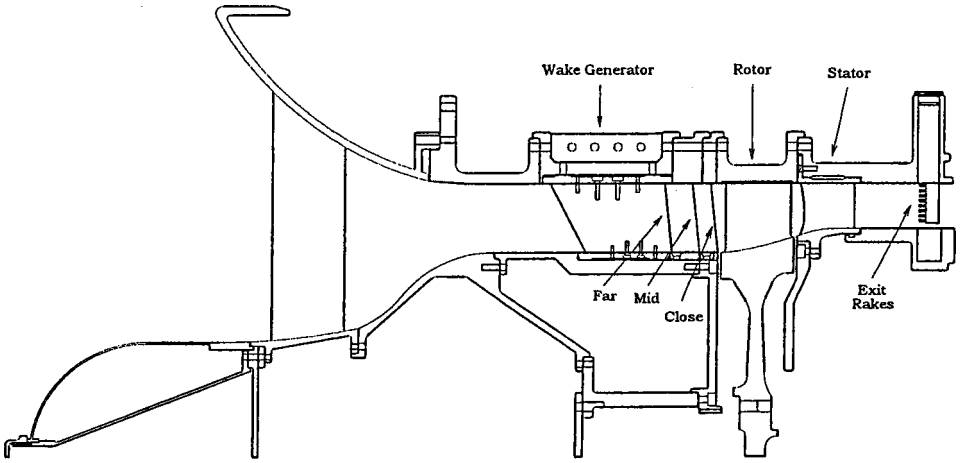

Fig. 2 Cross section of Stage-Matching-Investigation (SMI) rig in general configuration

Downloaded 03 Jun 2010 to 171.66.16.150. Redistribution subject to ASME license or copyright; see http://www.asme.org/terms/Terms_Use.cfm

Table 1 WG axial spacing (normalized by local WG chord)

Spacing	x/c (mean)	x/c (hub)	x/c (tip)
Close	0.13	0.10	0.14
Mid	0.26	0.26	0.26
Far	0.55	0.60	0.52

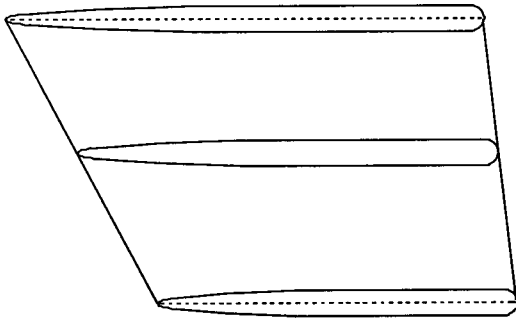

Fig. 3 WG meridional profile with cross sections (flow from left to right)

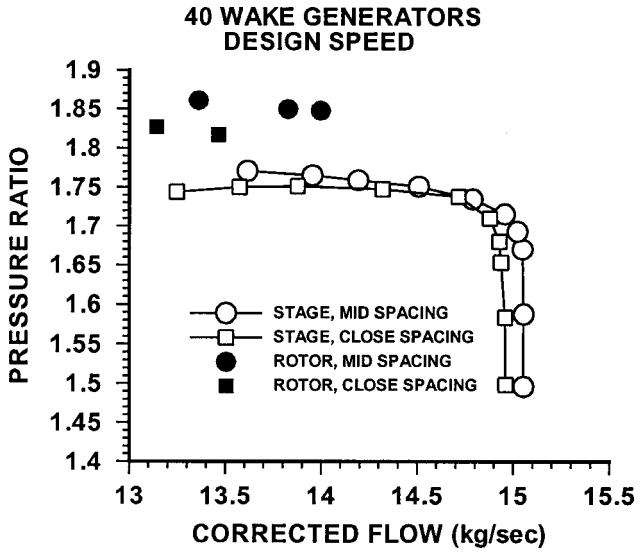

Fig. 4 Stage and rotor pressure ratios for 40 WG configurations

Table 2 SMI aerodynamic design parameters

PARAMETER	ROTOR	STATOR
Number of Airfoils	33	49
Aspect Ratio – Average	0.961	0.892
Inlet Hub/Tip Ratio	0.750	0.816
Flow/Annulus Area, Kg/sec/m^2	195.04	--
Flow/Frontal Area, Kg/sec/m^2	85.34	--
Flow Rate, Kg/sec	15.63	--
Tip Speed, Corrected (m/sec)	341.6	--
M_{rel} LE Hub	0.963	0.82
M_{rel} LE Tip	1.191	0.69
PR, Rotor	1.88	--
PR, Stage	--	1.84
D Factor, Hub	0.545	0.502
D Factor, Tip	0.530	0.491
LE Tip Dia., (m)	0.48260	0.48260
LE Hub Dia., (m)	0.36195	0.39375
Wake-Generator Counts: 24, 40	--	--

The rotor and stator were designed at the CARL facility (Law and Wennerstrom [11]). A compressor map of the stage and rotor pressure ratios for 40 WG configurations is shown in Fig. 4. A summary of the aerodynamic design parameters is given in Table 2.

3 DPIV Sytem

A DPIV system was developed for the present investigation. Figure 5 contains photographs of the system at the rig section, and Fig. 6 contains schematics of the optical sytem. Two frequency-doubled Nd:YAG lasers are used for instantaneous marking of the seed particles in the flow field. Combined by a polarizing cube, the beams are directed through sheet-forming optics and illuminate the test section with a 2D plane of thickness <1 mm. The scattering from the seed particles is recorded on a ES1.0 Kodak CCD sensor (1008×1012 pixels). The camera maximum repetition rate is 15 double exposures per second, and the rate was set to 10 Hz for synchronization with the laser repetition rate. The time delay between the two lasers can be varied, depending on the magnification and the flow speed, to <1 μs. A 105-mm Nikon lens was used. Typical magnifications for the present experiments ranged from ~20 to ~50 pixels/mm, which corresponds to viewing widths ranging from ~50 to ~20 mm, respectively.

Once the PIV image has been captured and digitized, the velocity field is obtained using cross-correlation techniques. The correlation function is calculated over small segments (interrogation domains) of the PIV image. The dimensions of each interrogation domain are dependent on particle density, estimated local velocity gradients, particle-image size, and desired spatial resolution. For the present study, the interrogation domain measured 64×64 pixels; this window yielded to areas ranging from 4.5 mm^2 (40 WG/Close-spacing) to 6 mm^2 (24 WG/Mid-spacing) in the measured flow. The interrogation domains are overlapped by three-quarters the domain size. This implies the use of redundant information but yields to more vectors in the overall velocity field. The peak of the correlation map corresponds to the average velocity displacement

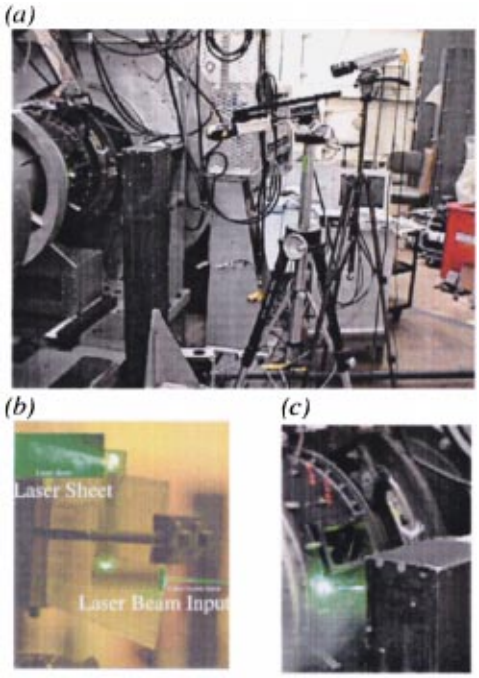

Fig. 5 Detail of DPIV system and rig (*a*); prototype of WG and laser-sheet delivery system (*b*); laser-sheet delivery and receiving window (*c*)

Downloaded 03 Jun 2010 to 171.66.16.150. Redistribution subject to ASME license or copyright; see http://www.asme.org/terms/Terms_Use.cfm

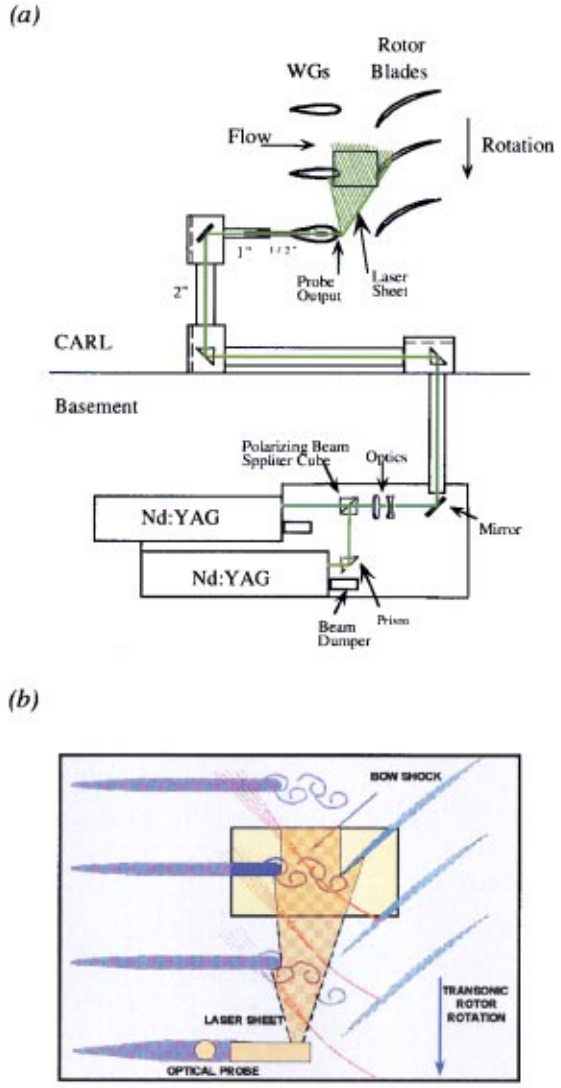

Fig. 6 Schematics of optical path (*a*) and flow features at scale (*b*) with DPIV delivery and receiving optics

within the interrogation spot. An intensity-weighted peak-searching routine is used to determine the exact location of the peak to sub-pixel accuracy.

Laser-Sheet Delivery and Receiving. A compact laser-sheet delivery system was designed, and the prototype is shown in Fig. 5(*b*). This system consists of an enlarged WG, light-sheet-forming optics, prisms, and probe holders for mounting the optics and for protecting them from contaminated seed materials. The Nd:YAG-laser-beam input and the laser-sheet output are also shown. The outside diameter of the probe is 12.7 mm. The modified WG is located two WGs below the WG that is centered at the receiving window. Three receiving windows made of Pyrex substitute the portion of the compressor case of interest and accommodate the three WG-rotor spacings. Figure 5(*c*) shows the location of the window and the laser-beam input. The optical path from the laser room to the CARL test rig was ~8 m long and was fully covered to avoid exposure. The prisms were covered by specially designed boxes that were connected through 50.8-mm-diameter pipes and isolated from the floor vibrations by gaskets and vibration isolators. Figure 6 contains schematics of the path for the laser system. The portion of the path that directs the beam to the rotor rig is covered by a smaller diameter pipe that matches the diameter of the WG probe.

Although the path was relatively long, the laser power required for laser-sheet illumination was very low (~10 mJ/pulse) because the optical losses were minimal. The regions of interest in the present experiments had areas from ~175 mm^2 (close-spacing) to ~750 mm^2 (mid-spacing). The F stop was 5.6 for these experiments. This allowed us to use low laser power which is important for the safety of the lenses in the optical probe when the beam begins to focus.

The combined beam enters the rotor housing perpendicularly through the center of the WG optical probe. The beam is then turned 90 degrees inside the WG by a prism and directed to a spherical lens and a cylindrical lens to form a laser sheet. A prism at the tip of the probe turns the laser sheet 90 degrees and exits the probe normal to the spanwise (radial) direction. The shape of the laser sheet (thickness, width, focal distance) can be altered through various combinations of the spherical-lens focal length, the cylindrical-lens diameter, and the distance between them inside the WG as well as through external optics (e.g., a spherical lens) located in the laser path. The spanwise location of the laser sheet can be changed by rotating the probe. The length of probe that is outside the WG can also be changed to provide further flexibility for moving the laser-sheet streamwise. This probe movement is possible by loosening two screws accessible from outside the housing that hold the probe tight inside the WG. The probe was set manually before each experiment. A device for remote control of the probe motion to allow changes within the experiment is currently being designed. Future modifications will also include remote control of the last prism of the probe to permit further changes in the streamwise laser-sheet extent. This will allow, for example, more illumination between the blades.

The ES1.0 camera was aligned and focused on the laser sheet prior to each run and was set in a tripod to minimize the effect of rig vibrations. Mounting the camera on the rig was not desirable; even though the rig vibration frequency does not affect the ''instantaneous'' laser pulses, it could eventually loosen the camera supports or even damage the camera. Remote control of the camera position and focus is desirable for full utilization of the system. To account for motion of the camera with respect to the laser sheet that might occur for unknown reasons, the camera in the present experiments was set in a translation stage that was remotely controlled to allow small corrections. Large changes in the camera location with respect to the laser sheet would produce magnification changes that would have to be taken into account. After each experiment the laser-sheet and camera locations were verified for possible misplacements. The present experiments did not require major changes.

The rotor one-per-revolution signal was used for triggering the synchronization system. A digital pulse generator (Stanford DG535) and an ES1.0 camera interface (ISSI PIV2000) were used. Programming and operation of the camera frame-grabber (National Instruments PCI-1424) and the delay generator were accomplished using drivers that were specially written for the National Instruments LabWindows/CVI development language; this facilitated integration with the DPIV analysis software (ISSI) which was also written in this environment.

In addition, the experiments were monitored and recorded throughout with a video camera to allow continuous recording and surveillance of the system and flow.

Seeding. For seeding a high-through-flow facility efficiently, a seeder must be capable of supplying a large number of particles that are both small flow tracers and efficient light scatterers. Agglomeration must be avoided, and assurance of uniform distribution is important. Also flammability and exposure limits should be considered in seeder techniques, as well as cost and availability.

Several options for seeding the high-flow CARL facility (~14 kg/s) were evaluated, including the use of various seeding units and seed materials. Both local and global seeding were considered. The seed material used in the low-speed automotive-cooling fan by Estevadeordal et al. [7] was sub-micron-size

Downloaded 03 Jun 2010 to 171.66.16.150. Redistribution subject to ASME license or copyright; see http://www.asme.org/terms/Terms_Use.cfm

smoke particles generated from a glycerin and water mixture. This system also produced sufficient seed particles during its use in the CARL facility when introduced at the end of the settling chamber, before the contraction, and at the height of the receiving window (Fig. 1). The machine can be remotely controlled. The seed material was introduced through a 50.4-mm-diameter port located under the contraction entrance through a 50.4-mm pipe. Because of the location of the port (away from the window), the pipe had to be first directed to the chamber center radially and then turned 90 degrees radially to match the window height. The end of the pipe was perforated with holes of increasing diameter toward the end, with a honeycomb and screen for optimal uniformity and spreading of seed. Calculations based on the flow speed at the beginning of the contraction (which is the area of maximum diameter and minimum speed), the distance from the test area, and the pipe diameter were performed to confirm that the wake behind the pipe was exerting negligible perturbation on the flow.

Global seeding techniques based on particles such as alumina powder (Al_2O_3) and polystyrene latex (PSL) microspheres (Wernet [6]) are under development. The system consists of a pressurized tank with an ethanol and particle mixture, compressed air, and six spray nozzles. Atomization of the mixture releases particles as ethanol evaporates. The system, tested with PSL microspheres, was located upstream of the settling chamber (Fig. 1) in a specially machined flange that allows the spray nozzles to be mounted externally rather than inside the plenum (to minimize interference with the flow). Only the tip of the nozzles enters the plenum, and the injection is perpendicular. Optimal atomization for seeding can be accomplished by changing various settings to produce the smallest possible droplets, maximum fluid injection, and maximum PSL concentration. Although sufficient for LDV (where these systems have been used successfully), the amount of seed was insufficient for PIV in preliminary tests. This low seed level at the test section was attributed to the nature of the facility. First, the settling chamber has many smoothing devices (tube bundles, hollowed plates, honeycombs, and screens) that can prevent the PSL material from reaching the test area. Second, the PSL seed experiments were performed during the hot summer season when humidity was very high, which reduces ethanol evaporation and its positive effects. Other systems for global seeding (e.g., smoke machines upstream of the settling chamber) are also under investigation.

4 Results

To characterize the unsteady flow field between the WGs and the rotor blades, the instantaneous velocity field in the present experiments was measured at two spanwise locations (75% and 90% span), for two WG counts (24 and 40), and at two axial spacings (''close'' and ''mid'') over one rotor-blade period. Blade period refers to the one-per-revolution period divided by the number of blades (33). Since the mass flow for the 24- and 40-WG configurations in the present experiments was not matched, the two cases will be treated independently. Data presented here were acquired at 100% corrected speed ($\sim$13000 rpm), which corresponds to a blade period of $\sim$140 μs. The synchronization system allows study of the blade passage in front of the WG, and specific features such as vortex-blade interaction and wake chopping can be characterized as a function of blade location. Figure 6(*b*) is a schematic of the flow-field features and the DPIV system at the window area. Figure 7 is a schematic of the WGs, the blade passage, and the laser-sheet relative locations for the 40-WG configuration. Results are discussed in terms of flow visualization and DPIV data.

Flow Visualization. Flow visualization often provides the first insight into the flow features. As designed, the present DPIV system allows flow visualization in the interior of the transonic compressor. For purposes of visualization, the amount of seeding can be controlled to permit the marking of flow features such as vortical structures and wake traces.

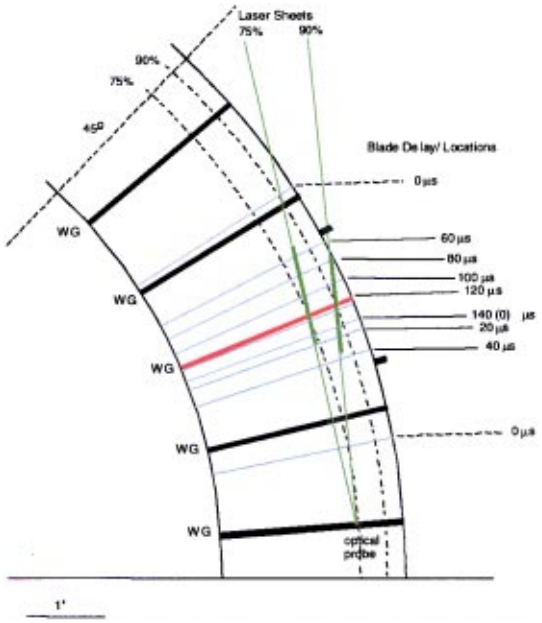

Fig. 7 Blade, WGs, and laser-sheet spanwise locations for 40-WG configuration. Thinner WG line corresponds to WG centered at viewing window (marked by two small lines), and thicker portions of laser sheets (green) denote DPIV image location. Blade-to-blade period is 140 μs. Delays relevant to paper are shown.

The flow behind the WG is depicted for the 24- and 40-WG configurations for various blade positions at 20-μsec intervals in Figs. 8 and 9, respectively. The scale is $\sim$1:1 in most of the figures presented here and emphasizes the actual size of the wake. Because of the tilted laser sheet and the rotor curvature (Fig. 7), the spanwise location of the images varies as a function of image height. This effect is less pronounced in the ''75%-span'' configuration than in the ''90%-span'' configuration. In the latter, the laser sheet is at 90% span at the position of the WG TE and at 100% span as it intersects the viewing window. This allowed boundary-layer data to be obtained in the ''90%-span'' configuration.

At 75% span ((*a*,*c*) in Figs. 8 and 9), vortex shedding can be tracked as a function of blade passage. For ease in following the vortices, the letter ''a'' indicates one of the vortices as it is convected dowstream. The vortices can be seen forming at the WG TE, growing as they are convected downstream, and eventually colliding with the blade LE. It can be observed in these figures that in these 75%-span cases, one vortex interacts with the blade LE and the next is convected downstream between the blades; this process is repeated for every pair of vortices shed from the WG TE. The images depict approximately a half period of the blade passage and show the wake-blade interaction. The other half period is of no interest here because it shows only the convection of the second vortex through the blades and does not show the blade LE in the viewing window. At the 24-WG count (Fig. 8(*a*,*c*)), the vortex interacting with the blade LE does not receive a direct hit, whereas at the 40-WG count (Fig. 9 (*a*,*c*)) that vortex is always destroyed. Thus, in the present experiments, wake chopping occurs by the wake braids in the 24-WG cases and by the vortex in the 40-WG cases. A pair of vortices in the 24-WG cases and a single vortex in the 40-WG cases pass between the blades. This difference between the two configurations is attributed to the difference in mass flows. These features appear to be synchronized with the blade passage. The vortices grow as they convect downstream; and in mid-spacing configurations (*c*,*d*), they can be estimated to be 30% larger than the WG thickness (which varies as

Downloaded 03 Jun 2010 to 171.66.16.150. Redistribution subject to ASME license or copyright; see http://www.asme.org/terms/Terms_Use.cfm

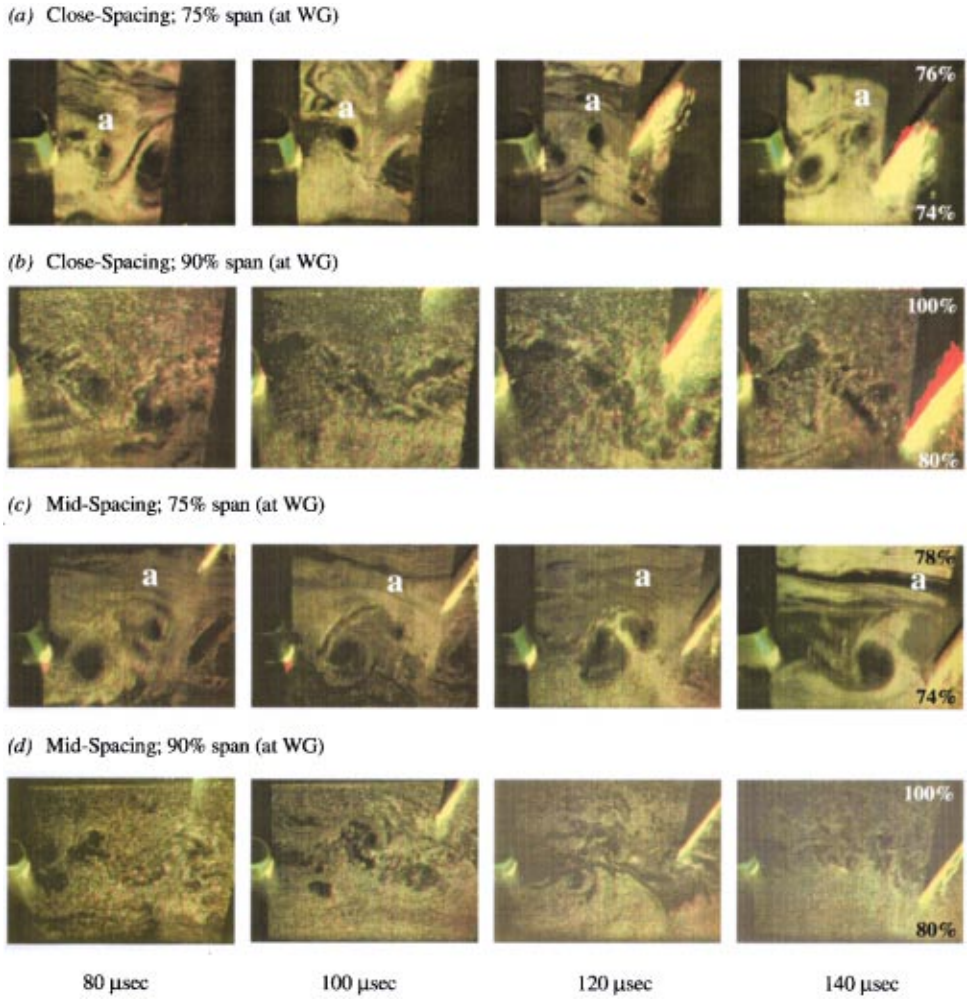

Fig. 8 Flow visualization for half period of blade passage in front of the WG at 20-μs intervals for 24-WG configuration at 75% span (*a*,*c*) and 90% span (*b*,*d*) for close-spacing (*a*,*b*) and mid-spacing (*c*,*d*). Scale is 1:1, except for *b* (2:1). Percentages at top and bottom of last frames of each set indicate span of laser sheet. Letter "a" above vortices indicates their location and convection.

a function of the spanwise location) as they hit the blade LE. These vortices are expected since they are shed from a blunt-body-shaped WG.

At 90% span ((*b*,*d*) in the figures), the wake has a smaller scale and appears to be more turbulent and the shed vortices are smaller. This is attributed to three-dimensionality and the influence of the boundary-layer flow near the compressor case. Measurements (Copenhaver et al. [12]) revealed that the boundary layer penetrates to about 92% span. The wake trace follows a trend similar to that of the vortex shedding and can be seen to grow and convect downstream, interact with the shock, and be ''chopped'' (as shown in the last frame of each set).

Even though the photographs in each set are non-sequential (because of the limitation on the laser frequency), vortex shedding appears to be synchronized with (or forced by or locked with) the blade passage. This vortex-blade synchronization is apparent for both WG counts and spacings. It was observed that qualitative flow patterns such as the number and location of the vortices were always similar for a given blade delay. The main source of the ''synchronization'' appears to be the strong perturbation provided by the blade passage, which induces pressure-field variations at the blade-passage frequency. Measurements of pressure variations at the WG surface (Koch et al. [13]) have shown that they are significant near the WG TE (where the perturbation takes on a hydrodynamic effect). A velocity-field study using DPIV can quantify the variation that exists between wakes for a given blade position and as a function of blade position. Such a study can also determine the amount of wake motion that occurs as the wake approaches the shock and the blade LE. Locking of the frequency of the vortex shedding on the blade-passing frequency in a multi-blade row environment has been investigated numerically in a turbine stage by Sondak and Dorney [14].

During flow visualization the shock effect is observed as the vortices and wake become predominantly smaller and random motion increases [e.g., Fig. 9(*a*,*b*) at 140 μs]. Only those vortices that move downtream between two blades without colliding with the LE preserve their large-scale structure and evolution [e.g., the farther dowstream vortex in Fig. 9(*a*)]. They avoid not only the blade-LE interaction but also the strongest portion of the shock.

DPIV. Typical instantaneous velocity fields in the absolute reference frame are shown for 75% and 90% span, 24-WG/Mid-spacing and 40-WG/Close-spacing in Figs. 10 and 11. Various blade positions at 20-μsec intervals are depicted. A common feature is the sharp change in velocity and flow direction at the bow-shock location, which is clearly discernible. The passage of the shock is clearly visible from the vector fields at the various blade positions. The flow-velocity increase observed after the shock at

Downloaded 03 Jun 2010 to 171.66.16.150. Redistribution subject to ASME license or copyright; see http://www.asme.org/terms/Terms_Use.cfm

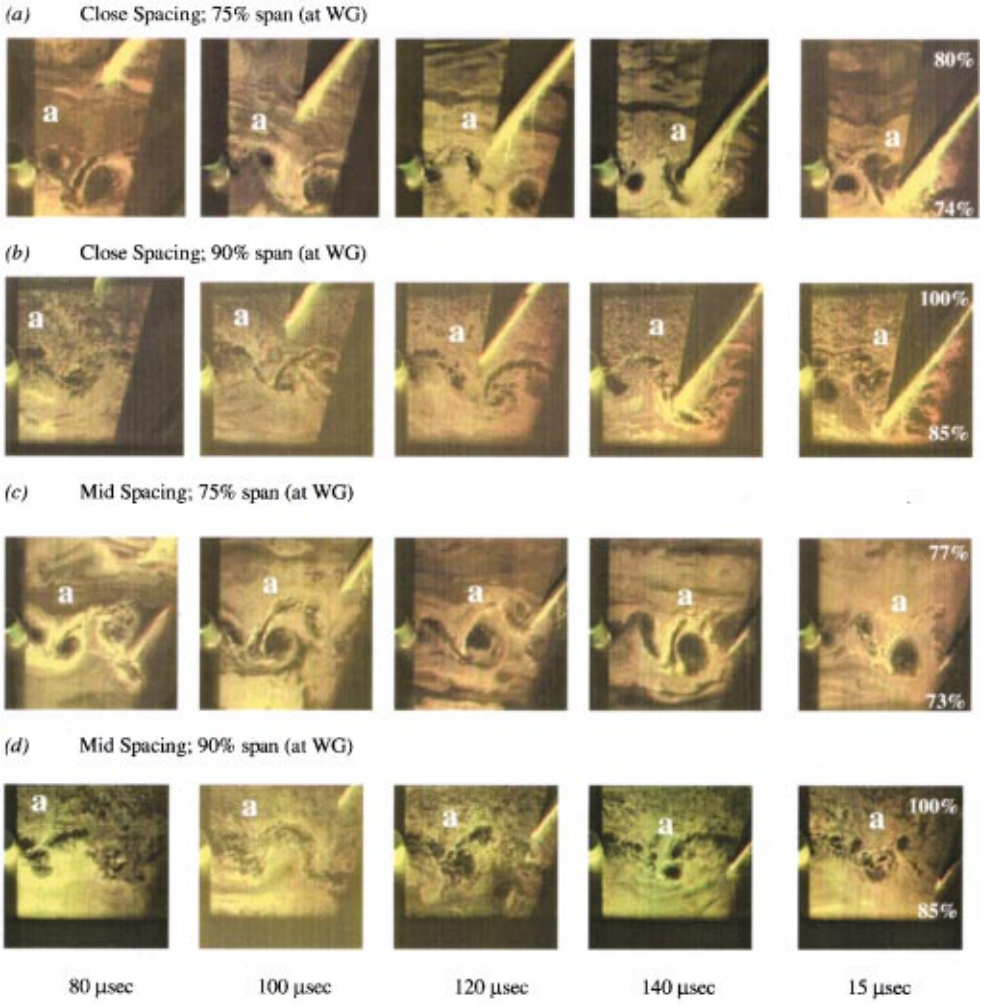

Fig. 9 Flow visualization of half period of blade passage through WG in 20-μsec intervals (except last frame) for 40-WG, close-spacing (*a*,*b*) and mid-spacing (*c*,*d*) at 75% (*a*,*c*) and 90% span (*b*,*d*). Scales are 1:1 (*a*,*b*) and 3:4 (*c*,*d*). Percentages at the top and bottom of the last frames of each set indicate span of laser sheet.

the passage between blades is typical for transonic compressors. Areas with missing vectors in the wake correspond mainly to the vortices. It is difficult to entrain seed particles inside the vortex by seeding the main flow only. Seeding the vortex using local injection of particles through the WG is under investigation. At 90% span the wake turbulence has entrained more seed particles into the wake. The lower speed area on top of the frames at 90% span is due to the boundary layer. Other areas with missing vectors (especially in Fig. 11(*a*)) resulted from a lack of particles or poor correlation due to noise during that particular experimental run; this problem is addressed later in the paper.

Wake-shock interactions are observed where low velocity from the wake crosses the shock front, which appears to be broken as a result of the wake passage. Boundary layer-shock interactions are observed in the 90% spans where the shock appears to be less sharp in the wall region as a result of the interaction with the curved wall and boundary-layer flow. Another feature captured by the velocity field is the upward direction of the velocity immediately below the WG, especially when the blade LE is above the WG. This feature is attributed to the angle of incidence of the flow to the WG row.

The wake-blade interaction can be further analyzed by drawing streamtraces, as shown in Fig. 12 (40WG, close-spacing, and 90% span configuration). An example is shown for three delays, 10 μs apart, as the blade LE passes in front of the WG while the wake is being chopped. These streamtraces indicate the direction of the flow during wake chopping. They are overlayed on vorticity, which is highest in the wake, in the boundary layer, and also at the shock (a consequence of the sharp gradient).

The repeatibility of the wake features and turbulence quantities can be analyzed by comparing several images and their velocity fields and averages. Averaging the instantaneous velocity fields for a given blade delay has the effect of smoothing the wake flow while still revealing a sharp shock location. Averaging was also used to complete the vector map in areas without vectors, such as those of Fig. 11(a); Figure 13(*a*) and (*b*) provide a comparison of the mean and the median over 50 realizations for the flow of Fig. 11(*a*) at a blade delay of 120 μs. The median is a more robust statistic for removal of outliers (points with ''bad'' vectors or ''no'' vectors) and produces a cleaner map. The most common reasons for ''bad'' vectors are lack of particles (e.g., center of vortices), three-dimensionality (e.g., in the wake and tip regions), and loss of correlation (e.g., as a result of excessive glare, blurriness, and sharp local gradients). The mean also produces a clean map (and more similar to the median map) when the number of realizations is increased, and it is used in Fig. 13(*c*) and (*d*) with 150 realizations. Five transversal velocity profiles are included. An estimate of turbulence intensity is calculated through the standard deviation of velocity (Fig. 13(*d*)) and indicates that the larg-

Downloaded 03 Jun 2010 to 171.66.16.150. Redistribution subject to ASME license or copyright; see http://www.asme.org/terms/Terms_Use.cfm

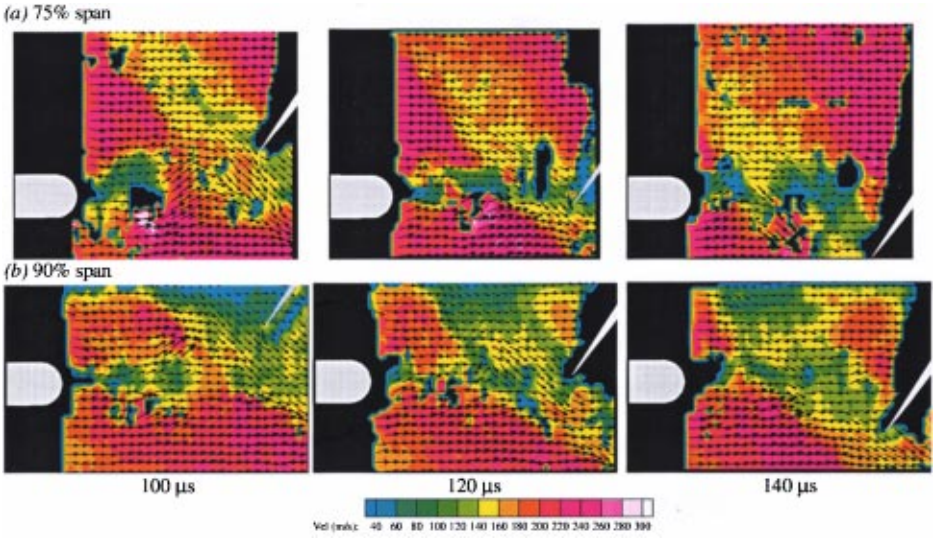

Fig. 10 DPIV instantaneous velocity fields for blade passage at 20-μs intervals for 24-WG and mid-spacing configuration at 75% (*a*) and 90% (*b*) spans. More detailed color maps are available in the online version.

est variation occurs at the wake boundaries--a place of higher unsteadiness. The shock-location variation is small.

Other techniques were used for removing outlier vectors; these included filtering values that fell beyond two standard deviations in the mean distribution and using the Chauvenet's criterion (Coleman and Steele [15]) which employs a filter statistic that depends on the number of realizations. Both techniques assume a normal or Gaussian parent population. The two produced similar mean distributions. In highly unsteady flows filtering must be performed with caution to avoid removing vectors that are real. This constitutes a minor problem in the present experiments because of the synchronization between the vortex shedding and blade passage, which produces high flow repeatibility for a given blade location. This natural synchronization acts as a ''phase-lock,'' and averaging produces results similar to those obtained from ''phase-averaging'' techniques (Estevadeordal and Kleis [16]). This synchronization is best for close spacing because of the proximity between the blade and the WG.

5 Conclusions

A DPIV system was developed for transonic turbomachinery studies and applied to investigation of the unsteady phenomena in the wake region and the interaction of the wake with the blade LE.

The system captures vortex shedding, vortex-blade synchronization, wake chopping, wake-shock interaction, and boundary-

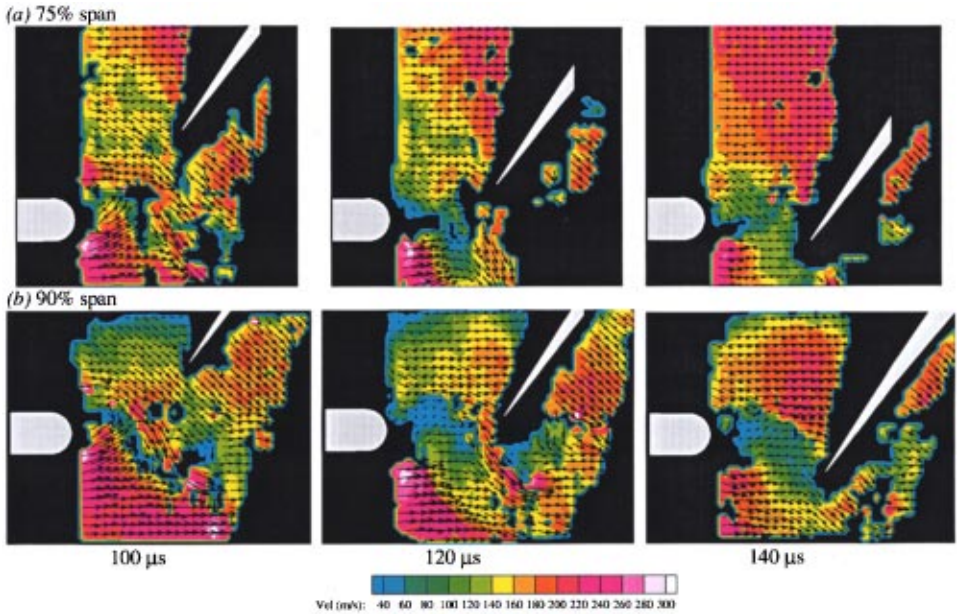

Fig. 11 DPIV instantaneous velocity fields for blade passage at 20-μs intervals for 40-WG and close-spacing configuration at 75% (*a*) and 90% (*b*) spans. More detailed color maps are available in the online version.

Downloaded 03 Jun 2010 to 171.66.16.150. Redistribution subject to ASME license or copyright; see http://www.asme.org/terms/Terms_Use.cfm

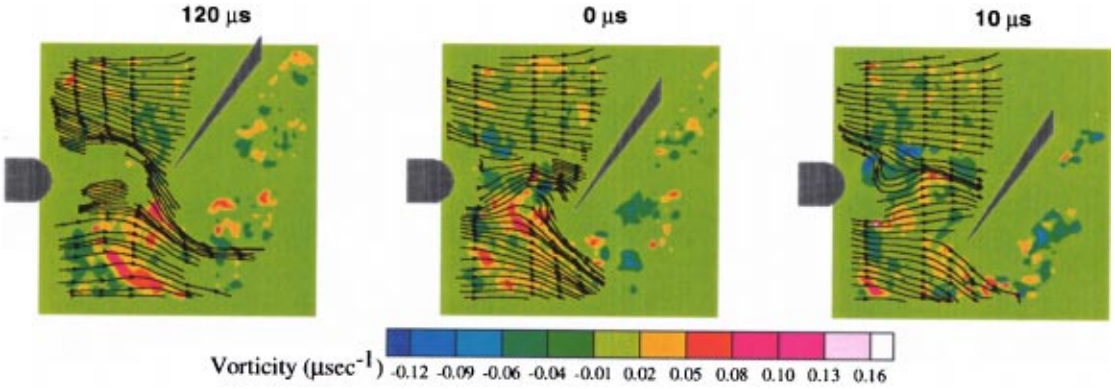

Fig. 12 Streamtraces overlayed on vorticity (μs^{-1}) for three blade delays 10 μs apart during wake-blade interaction for 40 WG, close spacing, and 90% span. More detailed color maps are available in the online version.

layer flow near the housing. The interactions of the wake with the potential field of the rotor LE and its bow shock were shown using instantaneous and ensemble-averaged quantities.

The system will be improved and used for further study of flow interactions in transonic compressors of various configurations.

Acknowledgments

The help of ISSI and CARL staff is greatly appreciated. Pratt & Whitney is acknowledged for fabricating the WGs, rotor, and stator and NASA Glenn for manufacturing the receiving windows.

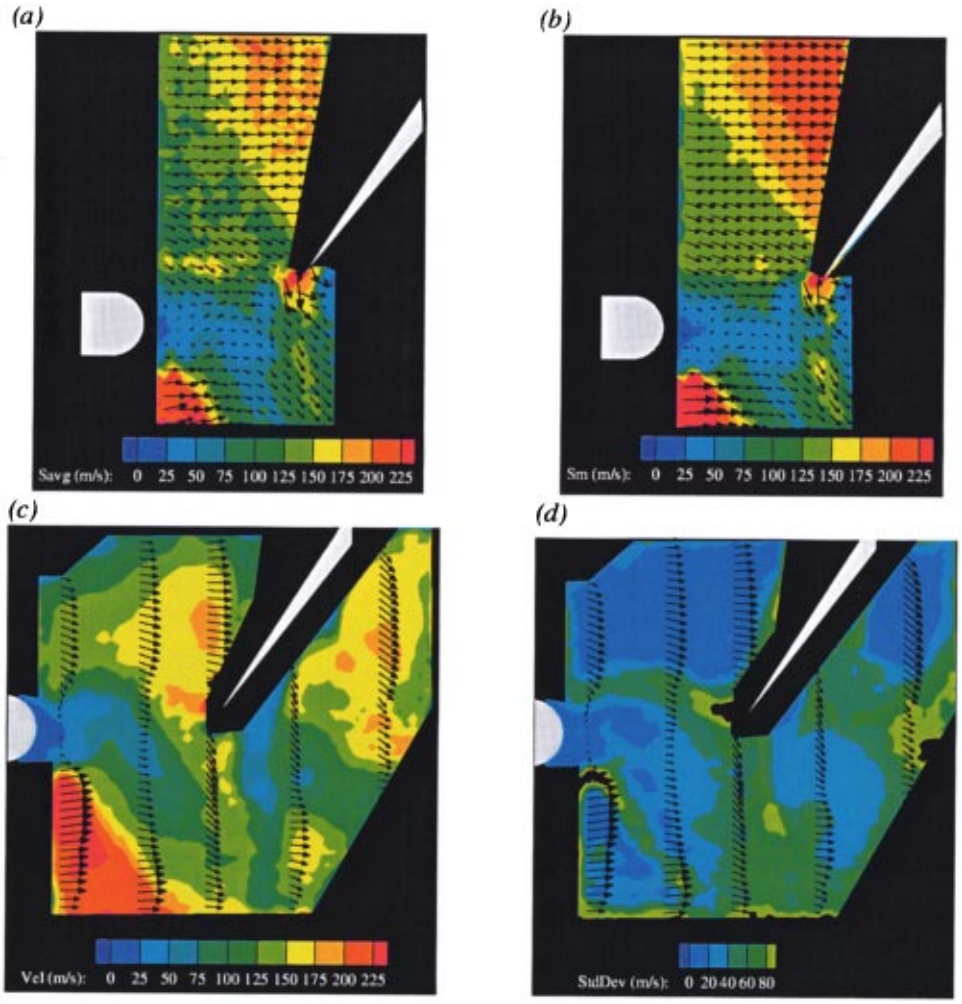

Fig. 13 Average quantities. Mean (*a*) and median (*b*) over 50 realizations at 75% span; mean (*c*) and standard deviation (*d*) over 150 realizations at 90% span. Both for close spacing, 40 WG, and blade delay of 120 μs. Five velocity profiles are overlayed on (*c*) and (*d*). More detailed color maps are available in the online version.

Downloaded 03 Jun 2010 to 171.66.16.150. Redistribution subject to ASME license or copyright; see http://www.asme.org/terms/Terms_Use.cfm

References

[1] Calvert, W. J., 1994, ''Detailed Flow Measurement and Predictions for a Three-Stage Transonic Fan,'' ASME J. Turbomach., **116**, No. 2, pp. 298–305.

[2] Strazisar, A. J., 1985, ''Investigation of Flow Phenomena in a Transonic Fan Rotor Using Laser Anemometry,'' ASME J. Eng. Gas Turbines Power, **107**, No. 2, pp. 427–435.

[3] Balzani, N., Scarano, F., Riethmuller, M. L., and Breugelmans, F. A. E., 2000, ''Experimental Investigation of the Blade-to-Blade Flow in a Compressor Rotor by Digital Particle Image Velocimetry,'' ASME J. Turbomach., **122**, pp. 743–750.

[4] Estevadeordal, J., Gogineni, S., Goss, L., Copenhaver, W., and Gorrell, S., 2000, ''Study of Flow-Field Interactions in a Transonic Compressor Using DPIV,'' 38th AIAA Aerospace Sciences Meeting and Exhibit, January 10-13, Reno, NV, AIAA 00-0378.

[5] Sanders, A. J., Papalia, J., and Fleeter, S., 1999, ''A PIV Investigation of Rotor-IGV Interactions in a Transonic Axial-Flow Compressor,'' 35th AIAA/ASME/SAE/ASEE Joint Propulsion Conference & Exhibit, June 20-23, Los Angeles, AIAA-99-2674.

[6] Wernet, M. P., 2000, ''Development of Digital Particle Imaging Velocimetry for Use in Turbomachinery,'' Exp. Fluids, **28**, pp. 97–115.

[7] Estevadeordal, J., Gogineni, S., Copenhaver, W., Bloch, G., and Brendel, M., 2000, ''Flow Field in a Low-Speed Axial Fan: a DPIV Investigation,'' Exp. Therm. Fluid Sci., **23**, pp. 11–21.

[8] Law, C. H., and Wadia, A. R., 1993, ''Low Aspect Ratio Transonic Rotors: Part 1 - Baseline Design and Performance,'' ASME J. Turbomach., **115**, p. 218.

[9] Gorrell, S., Copenhaver, W., and Chriss, R., 2001, ''Upstream Wake Influences on the Measured Performance of a Transonic Compressor Stage,'' J. Propul. Power, **17**, No. 1, pp. 43–48.

[10] Creason, T., and Baghdadi, S., 1988, ''Design and Test of a Low Aspect Ratio Fan Stage,'' AIAA 88-2816.

[11] Law, C.H., and Wennerstrom, A. J., 1989, ''Two Axial Compressor Designs for a Stage Matching Investigation,'' AFWAL-TR-89-2005, Air Force Wright Aeronautical Laboratories, Wright-Patterson AFB, OH.

[12] Copenhaver, W., Gorrell, S., and Chriss, R., 1999, ''Transonic Compressor Blade-Row Interactions: Spacing Influences on Flow Swallowing and Performance,'' Fourteenth International Symposium on Air Breathing Engines, Florence, Italy (ISABE 7030).

[13] Koch, P, Probasco, D., Wolff, M., Copenhaver, W., and Chriss, R., 1999, ''Transonic Compressor Influences on Upstream Surface Pressures with Axial Spacing,'' International Gas Turbine & Aeroengine Congress & Exhibition, Indianapolis, IN, June 7-10 (ASME Paper No. 99-GT-384).

[14] Sondak, D. L., and Dorney, D. J., 1999, ''Simulation of Vortex Shedding in a Turbine Stage,'' ASME J. Turbomach., **121**, No. 3, pp. 428–435.

[15] Coleman, H. W., and Steele, W. G., 1989, *Experimentation and Uncertainty Analysis for Engineers*, J. Wiley, New York.

[16] Estevadeordal, J., and Kleis, S. J., 1999, ''High-Resolution Measurements of Two-Dimensional Instabilities and Turbulence Transition in Plane Mixing Layers,'' Exp. Fluids, **27**, No. 4, pp. 378–390.

Downloaded 03 Jun 2010 to 171.66.16.150. Redistribution subject to ASME license or copyright; see http://www.asme.org/terms/Terms_Use.cfm

Fluid Flow Equations for Rotordynamic Flows in Seals and Leakage Paths

Y. Hsu

C. E. Brennen
Professor

Division of Engineering and Applied Science,
California Institute of Technology,
Pasadena, CA 91125

Fluid-induced rotordynamic forces produced by the fluid in an annular seal or in the leakage passage surrounding the shroud of a pump or turbine, are known to contribute substantially to the potential excitation forces acting on the rotor. The present research explores some of the important features of the equations governing bulk-flow models of these flows. This in turn suggests methods which might be used to solve these bulk-flow equations in circumstances where the linearized solutions may not be accurate. This paper presents a numerical method for these equations and discusses comparison of the computed results with experimental measurements for annular seals and pump leakage paths. [DOI: 10.1115/1.1436093]

Introduction

Over the last few years a substantial body of experimental data has been gathered on fluid-induced rotordynamic forces [1] generated in narrow, fluidfilled annuli such as occur in turbulent annular seals (for example, Childs and Dressman [2], Nordmann and Massmann [3]) or in the leakage flows surrounding the shrouded impellers of pumps or turbines (for example, Guinzburg et al. [4]). To allow for greater understanding of the underlying fluid mechanics of such flows, it is clearly valuable to view this data in the context of an accurate analytical model and, if necessary, to tune the frictional and other parameters in the model to provide a reliable tool for the designer.

The problem with this strategy is that the available analytical models have not yet shown themselves capable of accurate and reliable predictions. Perhaps the most promising approach has been the bulk flow model developed by Childs [5,6] and subsequently used by others [7]. This linearized model appears to give reasonable results in some cases and unreasonable, even bizarre results, in others. Nevertheless, it represents a coherent and rational starting point from which to begin. Some of the inherent problems with this model are summarized in the following section.

Bulkflow Models of Rotordynamic Flows

Based on Hirs [8] lubrication equations, the bulk flow model of Childs [6] uses simple correlations for the shear stresses based on the gap averaged flow velocities. This model, in its perturbation solution form, is widely regarded as a useful rotordynamic analysis tool for problems with relatively simple computational domains. As presented by Childs, the bulk flow model assumes that the three-dimensional, unsteady, turbulent flow in an annulus can be accurately approximated by reducing the dimensions of the flow from three to two, by using a simple correlation between the shear stresses and gap averaged velocities, and by treating the rotordynamic flow as a linear perturbation on the mean flow. Each of these assumptions should be carefully considered when using this approach to model the flow in a more complex computational domain such as a centrifugal pump leakage annulus.

The assumption that the dimensions of the flow can be reduced from three to two implies that the velocity profiles within the annulus are self-similar and therefore, that the equations of the flow can be averaged over the gap without excessive error. This may have limitations under certain conditions noted in experiments in which flow reversals and recirculation zones occur in the leakage path (Sivo et al. [9], Guelich et al. [10]). These changes in flow direction may lead to frictional stresses which are acting in a direction different from that predicted by the gap averaged velocity. Certain 3-D computational analyses, such as Baskharone and Hensel [11], have observed these flow reversals.

The Reynolds number of most leakage flows is very high. This means the bulk flow model requires expressions which relate the turbulent shear stresses to the averaged velocities in the gap. In the current form of the bulk flow model, the shear stresses on the rotor and the stator are calculated using friction coefficients [8]. These are defined by:

$$\frac{\tau}{\frac{1}{2}\rho u^2} = n\left(\frac{\rho u h}{\eta}\right)^m \tag{1}$$

where u is the gap-averaged velocity relative to the surface under consideration, and the m and n are denoted by m_S and n_S for the stator and m_R and n_R for the rotor. These expressions, which are a simple and heuristic extrapolation from the correlations for turbulent flow in a pipe, are taken from the work of Hirs who recommends that the coefficients m and n be ''fitted to individual experiments.'' The frictional coefficients are dependent on six physical parameters, including the curvature of the surface, inertial effects, and roughness. Thus, the coefficients may not fully account for the curvature of the flow path in a particular leakage geometry. As stated previously any reversal in flow direction near the impeller implies a serious error in the correlation of Eq. (1). The sign of the wall-shear stress term for the rotor should change in a region of reverse flow.

In addition, the use of the above expressions for the turbulent shear stresses are subject to an even more general criticism. They are correlations for steady turbulent flows based, primarily, on experimental observations of steady flows. In contrast, the rotordynamic flows of concern here are fundamentally unsteady. The problem is that very little is known about turbulent flows which are unsteady in the sense that the flow is being externally excited. Therefore, correlations such as that given above are only useful because there are no alternatives, and it must be recognized that the unsteady flows of the present context may lead to substantial deviations from these correlations. At present, this issue can only be resolved by careful comparison of the experimental and model results.

Finally, Childs treats the rotordynamic flow as a linear perturbation on the mean flow in the annulus. While this may be an

Contributed by the Fluids Engineering Division for publication in the JOURNAL OF FLUIDS ENGINEERING. Manuscript received by the Fluids Engineering Division April 17, 2001; revised manuscript received October 15, 2001. Associate Editor: Y. Tsujimoto.

 Copyright © 2002 by ASME

Downloaded 03 Jun 2010 to 171.66.16.150. Redistribution subject to ASME license or copyright; see http://www.asme.org/terms/Terms_Use.cfm

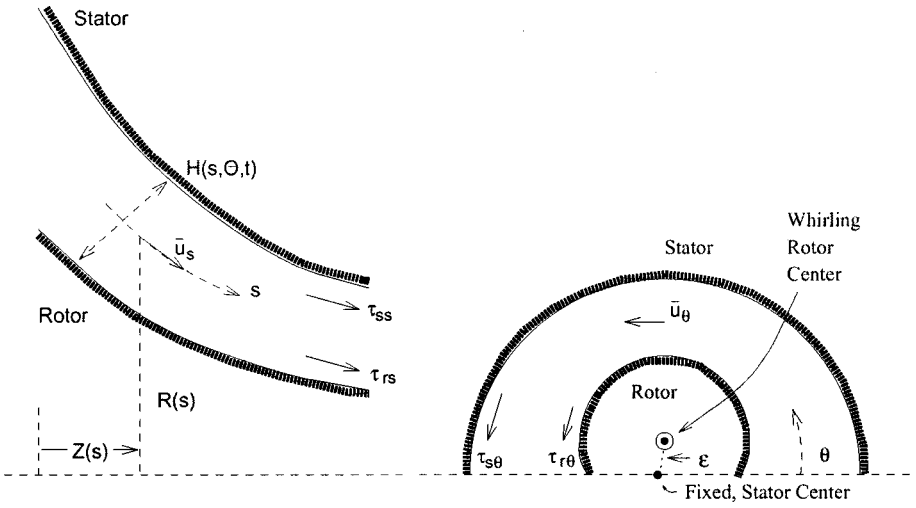

Fig. 1 Sketch of fluid filled annulus between a rotor and a stator for turbulent lubrication analysis

accurate assumption for very small eccentricities, there is currently no way to know at what eccentricity this linearization begins to lose accuracy. This paper will present a solution method that will solve the full bulk flow flow equations and will provide some idea as to the contribution of the nonlinear terms.

The Bulk Flow Model Equations

Black and his co-workers [12,13] were the first to attempt to identify and model the rotordynamics of turbulent annular seals. Bulk flow models (similar to those of Reynolds lubrication equations) were used. Several deficiencies in this early work caused Childs [14,15] to publish a revised version of the bulk flow model for turbulent annular seals [16] and, later, to extend this model [5,6] to examine the rotordynamic characteristics of discharge-to-suction leakage flows around shrouded centrifugal pump impellers. A general geometry is sketched in Fig. 1, and is described by coordinates of the meridian of the gap as given by $Z(s)$ and $R(s)$, $0<s<S$, where the coordinate, s, is measured along that meridian. The clearance is denoted by $H(s,\Theta,t)$ where the mean, nonwhirling clearance is given by $H(s)$.

The equations governing the bulk flow are averaged over the gap. This leads to a continuity equation of the form

$$\frac{\partial H}{\partial t}+\frac{\partial}{\partial s}(Hu_s)+\frac{1}{R}\frac{\partial}{\partial\Theta}(Hu_\Theta)+\frac{Hu_s}{R}\frac{\partial R}{\partial s}=0 \tag{2}$$

where u_s and u_Θ are gap-averaged velocities in the s and Θ directions. The meridional and circumferential momentum equations are

$$-\frac{1}{\rho}\frac{\partial p}{\partial s}=\frac{\tau_{Ss}}{\rho H}+\frac{\tau_{Rs}}{\rho H}-\frac{u_\Theta^2}{R}\frac{\partial R}{\partial s}+\frac{\partial u_s}{\partial t}+\frac{u_\Theta}{R}\frac{\partial u_s}{\partial\Theta}+u_s\frac{\partial u_s}{\partial s} \tag{3}$$

$$-\frac{1}{\rho R}\frac{\partial p}{\partial\Theta}=\frac{\tau_{S\Theta}}{\rho H}+\frac{\tau_{R\Theta}}{\rho H}+\frac{\partial u_\Theta}{\partial t}+\frac{u_\Theta}{R}\frac{\partial u_\Theta}{\partial\Theta}+u_s\frac{\partial u_\Theta}{\partial s}+\frac{u_\Theta u_s}{R}\frac{\partial R}{\partial s} \tag{4}$$

These are the equations used by Childs [5,6]. Note that they include not only the viscous terms commonly included in Reynolds lubrication equations (see for example Pinkus and Sternlicht [17]) but also the inertial terms (see Fritz [18]) which are necessary for the evaluation of the rotordynamic coefficients.

Using Hirs' [8] approach, the turbulent shear stresses, τ_{Ss} and $\tau_{S\Theta}$, applied to the stator by the fluid in the s and Θ directions are given by:

$$\frac{\tau_{Ss}}{\rho u_s}=\frac{\tau_{S\Theta}}{\rho u_\Theta}=\frac{n_S}{2}[u_s^2+u_\Theta^2]^{m_S+1/2}(H/\nu)^{m_S} \tag{5}$$

and the stresses, τ_{Rs} and $\tau_{R\Theta}$, applied to the rotor by the fluid in the same directions:

$$\frac{\tau_{Rs}}{\rho u_s}=\frac{\tau_{R\Theta}}{\rho(u_\Theta-\Omega R)}=\frac{n_R}{2}[u_s^2+(u_\Theta-\Omega R)^2]^{m_R+1/2}(H/\nu)^{m_R} \tag{6}$$

where the constants n_S, n_R, m_S and m_R are chosen to fit the available data on turbulent shear stresses. Childs [14] uses typical values of these constants from simple pipe flow correlations:

$$n_S=n_R=0.079;\quad m_S=m_R=-0.25 \tag{7}$$

Childs then proceeds to linearize the equations by dividing the clearance, pressure, and velocities into mean components (subscript 0) that would pertain in the absence of whirl, and small, linear perturbations (subscript 1) due to an eccentric motion of the rotor at an eccentricity ϵ and a whirl frequency of ω. He develops differential equations for the coefficients which are functions of r only, with the perturbation velocities restrained to simple harmonic functions of Θ.

For a case with a steady whirl of frequency ω, and constant eccentricity ϵ, superimposed on the shaft rotation of radian frequency Ω, a method of solving the bulk flow equations using a stream function and vorticity will now be formulated. With this set of assumptions, the fluid flow in a frame of reference rotating at ω is steady and it is appropriate to rewrite the equations and solve them in this rotating frame. Defining, therefore, a new angular variable, θ, and a new angular velocity, u_0, in this rotating frame such that

$$\theta=\Theta-\omega t;\quad u_\theta=u_\Theta-\omega R \tag{8}$$

it follows that the continuity equation, Eq. (2) can be written as

$$\frac{\partial}{\partial\theta}\{Hu_\theta\}+\frac{\partial}{\partial s}\{RHu_s\}=0 \tag{9}$$

and this is most easily satisfied by defining a stream function, $\psi(s,\theta)$ such that

Downloaded 03 Jun 2010 to 171.66.16.150. Redistribution subject to ASME license or copyright; see http://www.asme.org/terms/Terms_Use.cfm

$$u_s = \frac{1}{RH}\frac{\partial \psi}{\partial \theta}; \quad u_\theta = -\frac{1}{H}\frac{\partial \psi}{\partial s} \tag{10}$$

It follows that the total volume flow rate, Q, at any meridional location, s, is given by

$$Q = \psi(s,2\pi) - \psi(s,0) \tag{11}$$

and this provides a periodic boundary condition on ψ in the θ direction.

In the rotating frame of reference, the equations of motion are usefully written using an appropriate total pressure, P, instead of the static pressure, p, where

$$\frac{P}{\rho} = \frac{p}{\rho} + \frac{1}{2}(u_s^2 + u_\theta^2 - R^2\omega^2) \tag{12}$$

and the equations of motion, Eqs. (3) and (4), then become

$$\frac{\partial}{\partial s}\left(\frac{P}{\rho}\right) = -Hu_\theta\Gamma - u_s(g_S + g_R) \tag{13}$$

$$\frac{1}{R}\frac{\partial}{\partial \theta}\left(\frac{P}{\rho}\right) = Hu_s\Gamma - (u_\theta + \omega R)(g_S + g_R) + \Omega R g_R \tag{14}$$

where the functions, g_S and g_R, are the shear stress terms for the stator and rotor respectively. Using correlations (5) and (6)

$$g_S = \frac{n_S}{2H}\left(\frac{H}{\nu}\right)^{m_S}\{u_s^2 + (u_\theta + \omega R)^2\}^{m_S + 1/2} \tag{15}$$

$$g_R = \frac{n_R}{2H}\left(\frac{H}{\nu}\right)^{m_R}\{u_s^2 + (u_\theta + \omega R - \Omega R)^2\}^{m_R + 1/2} \tag{16}$$

The quantity, Γ, given by

$$\Gamma = \frac{1}{H}\left[-\frac{1}{R}\frac{\partial}{\partial s}(Ru_\theta + \omega R^2) + \frac{1}{R^2}\frac{\partial}{\partial \theta}(Ru_s)\right] \tag{17}$$

plays a crucial role both in understanding the fluid mechanics of these flows and in the solution methodology. This quantity, Γ, can be termed an ''effective vorticity'', and the existence of such a quantity has led to the development of the current methodology.

The vorticity, Γ, is a fundamental property of the flow; this can be discerned by eliminating P from Eqs. (13) and (14) to obtain the basic convection equation for Γ:

$$u_s\frac{\partial \Gamma}{\partial s} + u_\theta\frac{1}{R}\frac{\partial \Gamma}{\partial \theta} = \frac{1}{RH}\left[\frac{\partial}{\partial s}\{R(u_\theta + \omega R)(g_S + g_R) - \Omega R^2 g_R\} - \frac{\partial}{\partial \theta}\{u_s(g_S + g_R)\}\right] \tag{18}$$

which demonstrates that, in the absence of viscous effects ($g_S = g_R = 0$), the vorticity is invariant along any streamline. Conversely, the shear stresses are alone responsible for any change in Γ along a streamline. The total pressure is obtained by integration similar to that for the vorticity, Γ. From Eqs. (13) and (14) it follows that

$$u_s\frac{\partial P}{\partial s} + u_\theta\frac{1}{R}\frac{\partial P}{\partial \theta} = \frac{1}{(u_s^2 + u_\theta^2)^{1/2}} \times [\Omega R u_\theta g_R - \{u_s^2 + u_\theta(u_\theta + \omega R)\}(g_R + g_S)] \tag{19}$$

which demonstrates that the total pressure (or energy in the flow) is constant along a streamline in the absence of viscous effects. Furthermore, when written in the above manner, the governing equations, (18) and (19), indicate a physically reasonable approach to their numerical solution by iterative means.

Boundary Conditions and Numerical Methods

It follows from the above that one method for the numerical solution of the equations for a rotordynamic flow would be to proceed as follows:

(1) First, for given or guessed values of the vorticity, $\Gamma(s,\theta)$, the Poisson-like Eq. (17), rewritten as

$$\frac{\partial}{\partial s}\left\{\frac{R}{H}\frac{\partial \psi}{\partial s} - \omega R^2\right\} + \frac{1}{R}\frac{\partial}{\partial \theta}\left\{\frac{1}{H}\frac{\partial \psi}{\partial \theta}\right\} = RH\Gamma \tag{20}$$

must be solved to obtain the stream function, $\psi(s,\theta)$. From this solution new values for $\psi(s,\theta)$, $u_s(s,\theta)$ and $u_\theta(s,\theta)$ can then be calculated. Appropriate boundary conditions on ψ for use in the solution of Eq. (20) are:

(i) Along $s = 0$, we specify an inlet swirl velocity, $u_\theta(0,\theta)$, which, in order to satisfy conservation of angular momentum, should normally be put equal to the swirl velocity in the reservoir upstream of the inlet.

(ii) An appropriate boundary condition at discharge, $s = S$, would be that the pressure in the flow exiting the annulus should be uniform for all θ,

$$\frac{\partial}{\partial \theta}(p + \zeta u_s^2)_{s=S} = 0 \tag{21}$$

for a given exit loss coefficient, ζ. This parameter, ζ, can also be used to simulate an exit seal.

(iii) The periodic conditions on boundaries at $\theta = 0$ and $\theta = 2\pi$ such that

$$\psi(s,2\pi) - \psi(s,0) = Q \tag{22}$$

(2) Second, given the new values of $\psi(s,\theta)$, $u_s(s,\theta)$ and $u_\theta(s,\theta)$, we can integrate to find new values for $\Gamma(s,\theta)$ using Eq. (18). This requires evaluation of the shear stress functions, g_R and g_S and values of Γ at inlet, $\Gamma(0,\theta)$. Clearly this becomes more cumbersome when there is reverse flow either at inlet or at discharge. Here, we restrict our attention to the simpler circum-

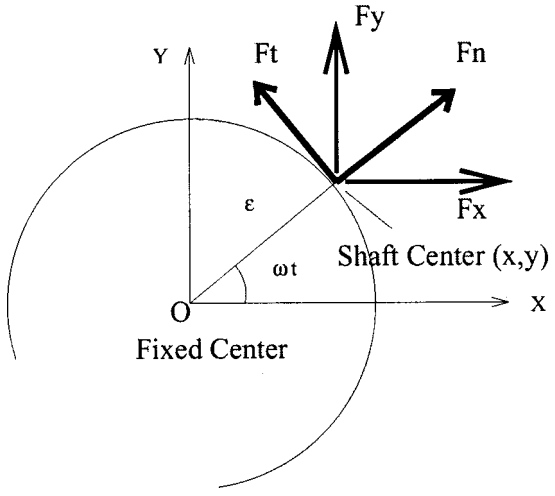

Fig. 2 Force diagram in plane normal to the shaft axis

Downloaded 03 Jun 2010 to 171.66.16.150. Redistribution subject to ASME license or copyright; see http://www.asme.org/terms/Terms_Use.cfm

stances in which there is no flow reversal at the inlet. Then, assuming that the viscous stresses upstream of the inlet are negligible and that the inlet flow is circumferentially uniform, Eq. (14) provides an initial value for Γ,

$$\Gamma(0,\theta)=\frac{1}{Hu_s}[(u_\theta+\omega R)(g_S+g_R)+\Omega R g_R] \tag{23}$$

given the results from step 1.

These two steps are then repeated to convergence.

As the viscous terms were found to be small, Eq. (19) can be integrated in parallel to the Γ integration to obtain the total pressure throughout the domain. If entrance losses are neglected between the upstream reservoir and the inlet plane ($s=0$), then the integration begins with a uniform value of $P(0,\theta)$ equal to the total pressure in the reservoir, P_{res}, and this can conveniently be chosen to be zero without loss of generality. On the other hand if entrance losses are to be included then $P(0,\theta)$ can be set to a value smaller than P_{res} by an amount equal to the entrance loss at that particular θ position. Other complications which could be incorporated include a non-uniform upstream reservoir (such as the volute of a pump operating off-design) which would imply a circumferentially varying $P(0,\theta)$.

Having obtained the pressure (and the viscous shear stresses), it only remains to integrate these to obtain the normal and tangential forces acting on the rotor. With the sign convention as defined in Fig. 2, it follows that:

$$F_n=\int_0^S\left\{1-\left(\frac{dR}{ds}\right)^2\right\}^{1/2}\int_0^{2\pi}(p\cos\theta+\tau_{R\theta}\sin\theta)Rd\theta ds \tag{24}$$

$$F_t=\int_0^S\left\{1-\left(\frac{dR}{ds}\right)^2\right\}^{1/2}\int_0^{2\pi}(p\sin\theta-\tau_{R\theta}\cos\theta)Rd\theta ds \tag{25}$$

In the results quoted in this paper the contributions from the τ_{R0} parts of these integrals are very small and can often be neglected. Finally, the rotordynamic coefficients are obtained by fitting quadratics to the functions, $F_n(\omega/\Omega)$ and $F_t(\omega/\Omega)$,

$$F_n=M\left(\frac{\omega}{\Omega}\right)^2-c\left(\frac{\omega}{\Omega}\right)-K \tag{26}$$

$$F_t=-C\left(\frac{\omega}{\Omega}\right)+k \tag{27}$$

The coefficients are termed the direct added mass (M), direct damping (C), cross-coupled damping (c), direct stiffness (K), and cross-coupled stiffness (k). The forces and coefficients are nondimensionalized as described by Brennen [1].

Results

The computational model was tested on two sets of geometries for which reliable experimental data is available. One comparison was with the seal tests conducted by Marquette and Childs [19]. This seal had an axially uniform radius, with a length to radius ratio of 0.914 and an average clearance of 0.0029 of the radius. Rotor speed varied from 10400 rpm to 41600 rpm and pressure drops from 4 MPa to 12 MPa. The other comparison is with the conical dummy pump impeller tested by Uy [20] whose eye-to-tip ratio is 0.474 and its average leakage path clearance is 0.03 times the tip radius. One difference between the two flows is the presence of the exit seal for the impeller tests. About half of the total pressure drop in the leakage path for the conical impeller occurs in the exit seal. Another difference is that the clearance is about an order of magnitude smaller for the seal experiments than for the impeller experiments. This will affect the acceleration of u_θ.

Using the same parameter values as Marquette and Childs, $n_s=n_r=0.079$ and complete exit loss ($\zeta=0$), the rotordynamic force for the seal in the tangential direction is predicted very well by the current model as shown in Fig. 3. The normal force, however, exhibits a large but uniform offset from the experimental data as manifested by the discrepancy in K. The predictions are similar to those using the Childs' perturbation approach, suggesting dominance of the primary mode in this simple geometry.

Adjusting the exit loss coefficient, ζ, can mostly eliminate the discrepancy in the normal forces. Indeed the forces seem very sensitive to small changes in the exit condition. Whether the source of the large offset between theory and experiment can be appropriately attributed to the exit conditions remains unknown.

An examination of the accuracy of the calculated results from the bulk flow model was also carried out by comparing the rotordynamic forces for the conical impeller to the experimental data. As a result of direct measurements of inlet swirl [21], an inlet swirl velocity of $u_\theta(0,\theta)=0.26$ was used for calculations of rotordynamic forces with the conical pump impeller geometry. Nu-

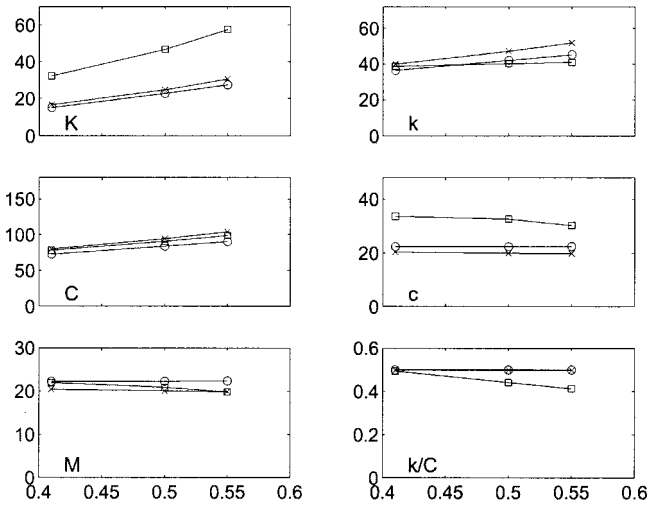

Fig. 3 Comparison of rotordynamic coefficients versus flow coefficient ϕ between experiment (□), and current model (○), and Childs' perturbation model (×) for the seal, with eccentricity equaling 10 percent of average clearance

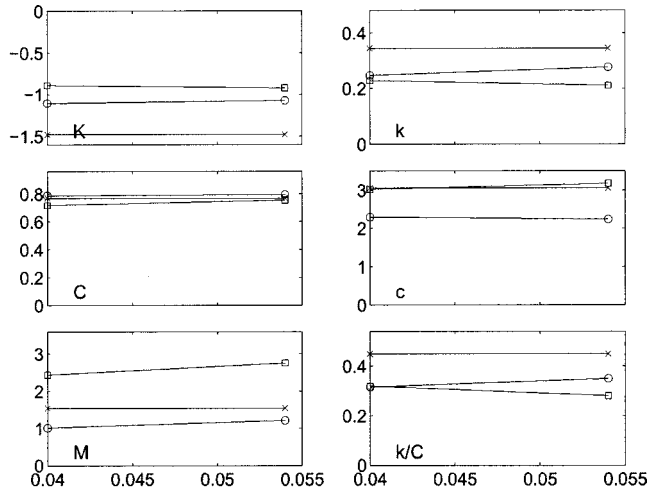

Fig. 4 Comparison of rotordynamic coefficients versus flow coefficient ϕ between experiment (□), and current model (○), and Childs' perturbation model (×) for the conical impeller

Downloaded 03 Jun 2010 to 171.66.16.150. Redistribution subject to ASME license or copyright; see http://www.asme.org/terms/Terms_Use.cfm

merical results for flow coefficients of 0.04 and 0.053 are compared with experimental measurements in Fig. 4. This data uses $n_s = n_r = 0.079$ for the shear stress coefficients and no pressure recovery at exit ($\zeta = 0$). The tangential forces agree reasonably well with the experimental data. The calculated normal forces, however, exhibit added mass, M, and cross-coupled damping, c, coefficients that are much smaller than the experimental results. The direct stiffness, K, agrees well with the experiments.[1]

Figure 4 also shows the calculated rotordynamic coefficients using Childs' perturbation model. Compared with the Childs' model, the current model gives better predictions for the direct stiffness and cross-coupled stiffness coefficients as well as the whirl ratio, k/C. The direct damping coefficient, C, is well predicted by both, while both underpredict the added mass term significantly. Childs' model gives more accurate results for the cross-coupled damping coefficient. Calculations of the rotordynamic coefficients for two other contoured dummy impellers tested by Uy [20] yielded similar comparisons.

Conclusions

This paper has explored some of the basic characteristics of the bulkflow model equations for the turbulent flow in a fluid-filled annulus generated by a combination of rotational and whirling motions. The analysis unveils the definition of the appropriate vorticity for these flows and develops evolutionary equations both for the vorticity and for the total pressure, without resorting to linearization. Among other features demonstrated by these equations is the fact that the changes in vorticity and total pressure along a streamline are entirely due to the shear stresses imposed on the flow.

This equation structure naturally suggests a way in which numerical solutions to these equations might be sought, by iterating between a Poisson-like equation for the streamfunction using a preliminary vorticity distribution and forward integration to revise that distribution. Several sample calculations are used to illustrate this technique.

The numerical solutions are compared to experimental results for a seal geometry in addition to discharge-to-inlet leakage geometries. Results for the seal show very good agreement for the tangential forces. Predictions for the normal forces, however, exhibited a large offset to the experimental results, which can be reduced by changing the exit loss coefficient. Questions remain as to the reason for this discrepancy.

For leakage path geometries, good agreement with experimental results for the conical impeller was found with the exception of the added mass term. Compared to the Childs' perturbation solution method, the current method is more computationally intensive, though still relatively fast. It also provided better predictions for most of the rotordynamic coefficients with the exception of cross-coupled damping term.

Nomenclature

C = direct damping coefficient, normalized by $\rho\pi\Omega R_2^2 L\varepsilon$
c = cross-coupled damping coefficient, normalized by $\rho\pi\Omega R_2^2 L\varepsilon$
F_n = force normal to whirl orbit, normalized by $\rho\pi\Omega^2 R_2^2 L\varepsilon$
F_t = force tangent to whirl orbit, normalized by $\rho\pi\Omega^2 R_2^2 L\varepsilon$
H = clearance between impeller shroud and housing
K = direct stiffness coefficient, normalized by $\rho\pi\Omega^2 R_2^2 L\varepsilon$
k = cross-coupled stiffness coefficient, normalized by $\rho\pi\Omega^2 R_2^2 L\varepsilon$
L = axial length of the impeller
M = direct added mass coefficient, normalized by $\rho\pi R_2^2 L\varepsilon$
m_r, m_s = empirical exponent for rotor and stator respectively
n_r, n_s = empirical constants for rotor and stator respectively
P = total pressure
p = static pressure
Q = volumetric leakage flow rate
R = radius of rotor
R_2 = tip radius of the rotor
u_s = meridional velocity of fluid
u_θ = circumferential velocity of fluid, nondimensionalized by ΩR_2
Γ = effective vorticity defined by Eq. (17)
η = fluid viscosity
ε = eccentricity of whirl orbit
ζ = exit loss coefficient
ρ = fluid density
ϕ = leakage flow coefficient, $Q/2\pi H\Omega R_2^2$
ψ = stream function, defined by Eq. (10)
ω = whirl radian frequency
Ω = main shaft radian frequency
τ = wall shear stress

[1]The highest inlet swirl ratio presented was 0.27, because this is the highest experimental data available [21]. At higher inlet swirl ratios, resonances occur in Childs' perturbation calculations. The current method also exhibits some resonance behavior, but the rotordynamic force curves always remain smooth. Further details can be found in [21].

References

[1] Brennen, C. E., 1994, *Hydrodynamics of Pumps*, Concepts ETI and Oxford University Press.
[2] Childs, D. W., and Dressman, J. B., 1982, "Testing of Turbulent Seals for Rotordynamic Coefficients," *Proc. Workshop on Rotordynamic Instability Problems in High-Performance Turbomachinery, NASA Conf. Publ. 2250*, 157–171.
[3] Nordmann, R., and Massmann, H., 1984, "Identification of Dynamic Coefficients of Annular Turbulent Seals," *Proc. Workshop on Rotordynamic Instability Problems in High Performance Turbomachinery, NASA Conf. Publ. 2338*, 295–311.
[4] Guinzburg, A., Brennen, C. E., Acosta, A. J., and Caughey, T. K., 1994, "Experimental Results for the Rotordynamic Characteristics of Leakage Flows in Centrifugal Pumps," ASME J. Fluids Eng., **116**, pp. 110–115.
[5] Childs, D. W., 1987, "Fluid Structure Interaction Forces at Pump-Impeller-Shroud Surfaces for Rotordynamic Calculations," *ASME Symp. on Rotating Machinery Dynamics*, **2**, 581–593.
[6] Childs, D. W., 1989, "Fluid Structure Interaction Forces at Pump-Impeller-Shroud Surfaces for Rotordynamic Calculations," ASME J. Vibr. Acoust. Stress, Reliab. Des. **111**, pp. 216–225.
[7] Guinzburg, A., 1992, *Rotordynamic Forces Generated by Discharge-to-Suction Leakage Flows in Centrifugal Pumps*, Ph.D. thesis, Calif. Inst. of Tech, Pasadena, CA.
[8] Hirs, G. G., 1973, "A Bulk-Flow Theory for Turbulence in Lubricant Films," ASME J. Lubr. Technol., Apr, pp. 137–146.
[9] Sivo, J., Acosta, A. J., Brennen, C. E., Caughey, T. K., Ferguson, T., and Lee, G., 1994, "Laser Velocimeter Measurements in the Leakage Annulus of a Whirling Centrifugal Pump," *ASME Laser Anemometry-1994, Advances and Applications*, **FED-191**, 111–117.
[10] Guelich, J., Florjancic, D., and Pace, S., 1989, "Influence of Flow Between Impeller and Casing on Part-Load Performance of Centrifugal Pumps, Pumping Machinery," 3rd Joint ASCE/ASME Mechanics Conference, **81**, 227–235.
[11] Baskharone, E., and Hensel, S., 1993, "Flow Field in the Secondary, Seal-Containing Passages of Centrifugal Pumps," ASME J. Fluids Eng., **115**, pp. 702–709.
[12] Black, H. F., 1969, "Effects of Hydraulic Forces in Annular Pressure Seals on the Vibrations of Centrifugal Pump Rotors," J. Mech. Eng. Sci., **11**, No. 2, pp. 206–213.
[13] Black, H. F., and Jensen, D. N., 1970, "Dynamic Hybrid Properties of Annular Pressure Seals," Proc. J. Mech. Eng., **184**, pp. 92–100.
[14] Childs, D. W., 1983, "Dynamic Analysis of Turbulent Annular Seals Based on Hirs' Lubrication Equation," ASME J. Lubr. Technol., **105**, pp. 429–436.
[15] Childs, D. W., 1983, "Finite Length Solutions for Rotordynamic Coefficients of Turbulent Annular Seals," ASME J. Lubr. Technol., **105**, pp. 437–445.
[16] Childs, D. W., and Scharrer, J. K., 1986, "Experimental Rotordynamic, Coef-

Downloaded 03 Jun 2010 to 171.66.16.150. Redistribution subject to ASME license or copyright; see http://www.asme.org/terms/Terms_Use.cfm

ficient Results for Teeth-on-Rotor and Teeth-on-Stator Labyrinth Gas Seals,''*Proc. Adv. Earth-to-Orbit Propulsion Tech. Conf., NASA Conf. Publ. 2436*, 327–345.
[17] Pinkus, O., and Sternlicht, B., 1961, *Theory of Hydrodynamic Lubrication*, McGraw-Hill, New York.
[18] Fritz, R. J., 1970, ''The Affects of an Annular Fluid on the Vibrations of a Long Rotor,'' ASME J. Basic Eng., **92**, pp. 923–937.
[19] Marquette, O. R., Childs, D. W., SanAndres, L., 1997, ''Eccentricity Effects on the Rotordynamic Coefficients of Plain Annular Seals: Theory Versus Experiment,'' ASME J. Tribol., **119**, pp. 443–447.
[20] Uy, R. V., and Brennen, C. E., 1999, ''Experimental Measurements of Rotordynamic Forces Caused by Front Shroud Pump Leakage,'' ASME J. Fluids Eng., **121**, pp. 633–637.
[21] Hsu, Y., 2001, *Studies of Rotordynamic Forces Generated by Discharge-to-Suction Leakage Flows in Centrifugal Pumps*, Ph.D. thesis, Calif. Inst. of Tech, Pasadena, CA.

Downloaded 03 Jun 2010 to 171.66.16.150. Redistribution subject to ASME license or copyright; see http://www.asme.org/terms/Terms_Use.cfm

On the Theoretical Prediction of Fuel Droplet Size Distribution in Nonreactive Diesel Sprays

Jianming Cao
Associate Professor,
Faculty of Automobile,
Chang'an University,
Xi'an, 710064, P. R. China
e-mail: jmcao@pub.xaonline.com

Droplet size distribution function and mean diameter formulas are derived using information theory. The effects of fuel droplet evaporation and coalescence within combustion chamber on the droplet size are emphasized in nonreactive diesel sprays. The size distribution function expressions at various spray axial cross sections are also formulated. The computations are compared with experimental data and KIVA-II code. A good agreement is obtained between numerical and experimental results. Droplet size distribution and mean diameter at various locations from injector exit and at various temperature conditions are predicted. The decreases of droplet number and variations of mean diameter are computed at downstream and higher temperature. [DOI: 10.1115/1.1445140]

1 Introduction

The characteristics of fuel injection and atomization have been known to influence diesel engine performance, such as fuel economy and pollutant emissions. The theoretical modeling of droplet size probability distribution and mean diameter is very important in the analysis of the atomization and combustion processes in diesel engines. Due to the complexities involved in the spray process, there still remains a paucity of systematic mathematical descriptions of the droplet size distributions and their evolutions in the diesel spray. Sellens and Brzustowski [1], Li and Tankin [2] obtained expressions for droplet size distribution in sprays by using the maximum entropy formalism. In these studies, the conservation laws of mass, momentum and energy were applied. However, they did not consider evaporation and coalescence of the droplets within an engine combustion chamber, and their model results were not compared with experimental measured in practical diesel engines.

In practical internal combustion engines, the droplet evolution is controlled not only by liquid bulk break-up, but also by evaporation of the droplets and coalescence resulting from droplet collisions. Droplet evaporation and coalescence will cause a decrease in the droplet number, the variations of D_{30} and D_{32} as well as a redistribution of droplet sizes. In this paper, some droplet size distribution expressions in a closed form by using information theory and the mass conservation law are obtained, Sauter mean diameter, D_{32} or SMD, is also derived. In these derivations, the effects of droplet evaporation and coalescence are incorporated into the model, and the droplet size distribution at various axial cross sections is formulated. The numerical results agree well with the experimental correlation of Levy and Amara [3]. The droplet size distribution predicted by the KIVA-II code [4] is also presented.

2 Model Formulation

In the present study, the constraint imposed for the atomization process is the conservation of liquid mass. Consider a spray produced by an orifice atomizer, a liquid jet is produced at the nozzle exit. As the liquid proceeds downstream, oscillations cause jet breakup into ligaments and finally droplets. When the liquid velocity exceeds a certain value, the atomization process starts almost at the nozzle exit and no observable solid jet develops. Since the droplets in a spray are usually small, surface tension will cause them to be spherical. Thus, $v=\pi D^3/6$, $dv=(\pi D^2/2)dD$. If liquid density is constant ($\rho_i=\rho$), then $v_t=m/\rho$. Assuming droplets are uniform distributed within the spray cone, the droplet volume flux at an axial cross section in a spray per cycle is $v_s=3v_tD_{30}/H$ and droplet number in a spray per cycle is $n_j=6v_j/\pi D_{30}^3$. Then the initial droplet size distribution following the spray formation can be obtained by maximizing the information entropy, subject to the normalization requirement of the probability distribution function and the mass conservation law as follows

$$\text{Information entropy } S=-K\sum_i P_i \ln P_i \tag{1}$$

$$\text{Greatest probability } \sum_i P_i \ln P_i=\text{Extremum} \tag{2}$$

$$\text{Mass conservation } \sum_i P_i v_i n_j=v_j \tag{3}$$

$$\text{Normalization } \sum_i P_i=1 \tag{4}$$

For the conditional extremum problem, we can use the method of Lagrangian multipliers. If the minimum diameter of droplets can be taken as zero, the number fraction of the droplet size can be obtained in a closed form

$$\frac{dN_j}{dD}=\frac{3\alpha_j n_j^2}{1-\exp(-\alpha_j n_j D_{\max}^3)}D^2\exp(-\alpha_j n_j D^3) \tag{5}$$

where α denotes Lagrangian multiplier. It can be determined by

$$m_j=\frac{\pi}{6}\left[\frac{1}{\alpha_j}-\frac{D_{\max}^3\exp(-\alpha_j n_j D_{\max}^3)}{1-\exp(-\alpha_j n_j D_{\max}^3)}\cdot n_j\right] \tag{6}$$

If integrate over droplet size space from the droplet diameter of $(D-\Delta D/2)$ to $(D+\Delta D/2)$, Eq. (5) yields the number distribution of droplet size as following closed form

$$N_{D,j}=\frac{\exp\left[-\alpha_j n_j\left(D-\frac{\Delta D}{2}\right)^3\right]-\exp\left[-\alpha_j n_j\left(D+\frac{\Delta D}{2}\right)^3\right]}{1-\exp(-\alpha_j n_j D_{\max}^3)}\cdot n_j \tag{7}$$

Then a number percentage of the total droplets in the droplets that diameters are between $(D-\Delta D/2)$ and $(D+\Delta D/2)$ must be evaluated as

Contributed by the Fluids Engineering Division for publication in the JOURNAL OF FLUIDS ENGINEERING. Manuscript received by the Fluids Engineering Division June 27, 2000; revised manuscript received August 8, 2001. Associate Editor: Y. Matsumoto.

 Copyright © 2002 by ASME

Downloaded 03 Jun 2010 to 171.66.16.150. Redistribution subject to ASME license or copyright; see http://www.asme.org/terms/Terms_Use.cfm

$$p_{i,j}=\frac{N_{D,j}}{n_j}$$
$$=\frac{\exp\left[-\alpha_j n_j\left(D-\frac{\Delta D}{2}\right)^3\right]-\exp\left[-\alpha_j n_j\left(D+\frac{\Delta D}{2}\right)^3\right]}{1-\exp(-\alpha_j n_j D_{\max}^3)} \quad (8)$$

The volume fraction of the droplet size is

$$\frac{dV_{D,j}}{dD}=\frac{\pi D^2}{2}\cdot N_{D,j} \quad (9)$$

Droplet volume between $(D-\Delta D/2)$ and $(D+\Delta D/2)$, the volume distribution of droplet size, can also be expressed as

$$V_{D,j}=\frac{\pi D^3}{6}\cdot N_{D,j} \quad (10)$$

Sauter mean diameter can be expressed as

$$D_{32}=\frac{\int_0^{D_{\max}} D^3 dN_j}{\int_0^{D_{\max}} D^2 dN_j}$$
$$=\frac{\int_0^{D_{\max}} D^5\exp(-\alpha_j n_j D^3)dD}{\int_0^{D_{\max}} D^4\exp(-\alpha_j n_j D^3)dD}$$
$$=\frac{1-(1+\alpha_j n_j D_{\max}^3)\exp(-\alpha_j n_j D_{\max}^3)}{(\alpha_j n_j)^{1/3}\gamma(5/3,\alpha_j n_j D_{\max}^3)} \quad (11)$$

For a practical engine spray, effects of evaporation and coalescence of the fuel drops within combustion chamber on droplet size are of fundamental importance. Evaporation will promote large droplets to be reduced and small droplets to be vanished. Coalescence is due to collisions: several small drops can gather to create a large droplet. Either of them will cause decrease of the droplet number, variation of the mean diameters and redistribution of the droplet size.

According to the conservations of mass and energy and mass diffusion equation, a relation between a droplet diameter after evaporation and an initial droplet diameter can be obtained as follows [5]

$$D=\sqrt{d^2-K_v\tau} \quad (12)$$

where d is an initial droplet diameter for calculating droplet diameter, D, after evaporation and collisions coalesce. The range is from zero to maximum and K_v is an evaporation coefficient in nonreactive sprays which determined by fuel property and temperature difference between gas within combustion chamber and environment.

$$K_v=\frac{8\lambda}{\rho C_p}\ln\left[1+\frac{C_p}{L}(t_f-t_0)\right] \quad (13)$$

Following procedures present the formulas of the collision influence. Assuming droplets are uniform distributed within the spray cone, a relation between droplet number at a generatrix of the conical liquid jet and total droplet number is

$$\frac{n_l}{n_t}=\frac{3}{\pi RH\sin\frac{\theta}{2}} \quad (14)$$

A relation between droplet number at a generatrix of the spray cone and at an axial cross section is

$$\frac{n_l}{n_s}=\frac{1}{\pi R\sin\frac{\theta}{2}} \quad (15)$$

In the conical liquid jet, since there is a distinct deference on droplet diameters along radial direction and a smaller deference along droplet track, we could assume an efficient distance between a larger droplet and a smaller droplet in a collision to be equal to a droplet diameter. Due to the extremely high fuel concentration in the diesel spray, we could assume that almost all droplets are affected by collision coalescence. According to the collision theory, the collision times of a liquid droplet in an injected duration can be presented as

$$Z=\frac{\pi d^2 R n_l}{\tau_0}=\frac{3n_t}{\tau_0 H\sin\frac{\theta}{2}}d^2=\frac{n_s}{\tau_0\sin\frac{\theta}{2}}d^2 \quad (16)$$

Thus, relation between a droplet diameter after collisions and an initial droplet diameter is

$$D=K_c d^{5/3} \quad (17)$$

where K_c could be called collision coefficient. It can be presented by collision times to multiply penetrated duration

$$K_c=\sqrt[3]{\frac{\tau}{\tau_0}\frac{3n_t}{H\sin\frac{\theta}{2}}}=\sqrt[3]{\frac{\tau}{\tau_0}\frac{n_s}{\sin\frac{\theta}{2}}} \quad (18)$$

Because evaporation takes place immediately at the beginning of the fuel discharged from nozzle exit, evaporation is earlier than coalescence. Thus

$$D=K_c(d^2-K_v\tau)^{5/6} \quad (19)$$

Substituting Eq. (19) into Eqs. (5) through (11), we have formulas of the size redistribution and mean diameters then.

Table 1 Prediction parameters at various axial cross sections and temperatures

t_f= / H=	20 (℃) 10 (mm)	20 (℃) 20 (mm)	20 (℃) 30 (mm)	170 (℃) 10 (mm)	170 (℃) 20 (mm)	170 (℃) 30 (mm)	325 (℃) 10 (mm)	325 (℃) 20 (mm)	325 (℃) 30 (mm)
τ (ms)	0.1	0.35	0.9	0.09	0.3	0.8	0.08	0.25	0.7
n_s	11259	4282	2525	10157	2969	780	9192	2478	366
D_L (μm)	0	0	0	6	12	20	7	13	23
D_{30} (μm)	16.2	18.5	19.6	11.5	13.0	14.7	11.5	12.4	14.1

3 Results and Discussion

The main goals of this study are to calculate the $p_{i,j}$, D_{30}, and D_{32} for sprays produced by pressure hole nozzle of the diesel engines and to compare with experimental results. The calculations have been conducted by using a computer program. The calculation step of the initial droplet diameter, d, is 1 μm. Integral calculus applies rectangle integral method and integral calculation step is 0.01 μm. Initial guess parameter is D_{30}. When difference of D_{30} or D_{32} between two continual calculations is within 0.01 μm and sum of $p_{i,j}$ in all droplet sizes is 100 percent $\pm 10^{-6}$, the computation will be stopped. First, we computed an initial total droplet number, n_t, and initial droplet numbers, n_s, at three locations under $D_{\max}=50$ μm, and got $p_{i,j}$, D_{30}, and D_{32}. The reduced droplet numbers at various axial locations and temperatures were computed according to evaporation and coalescence. Second, we recalculated these parameters under reduced droplet numbers. It should be pointed out that penetrated duration, τ, is a very important parameter. Penetrated duration means the time that spray jet reaches the axial position. It affects the n_s, D_L, mean diameter and droplet size distribution after evaporation and coalescence of droplets significantly. The penetrated duration shown in Table 1 is gotten by empirical relation of Chiu et al. [6] and validation of this law was achieved in Levy and Amara' experiments. It can be seen that n_s decreases, D_L and mean diameter increase in Table 1 and peak of size distribution moves toward lager size in Fig. 1 as τ increases according to our computations. However, the effects of the penetrated duration will reduce as temperature increases gradually because of influences of evaporation. It should be explained that we also conducted the calcula-

Downloaded 03 Jun 2010 to 171.66.16.150. Redistribution subject to ASME license or copyright; see http://www.asme.org/terms/Terms_Use.cfm

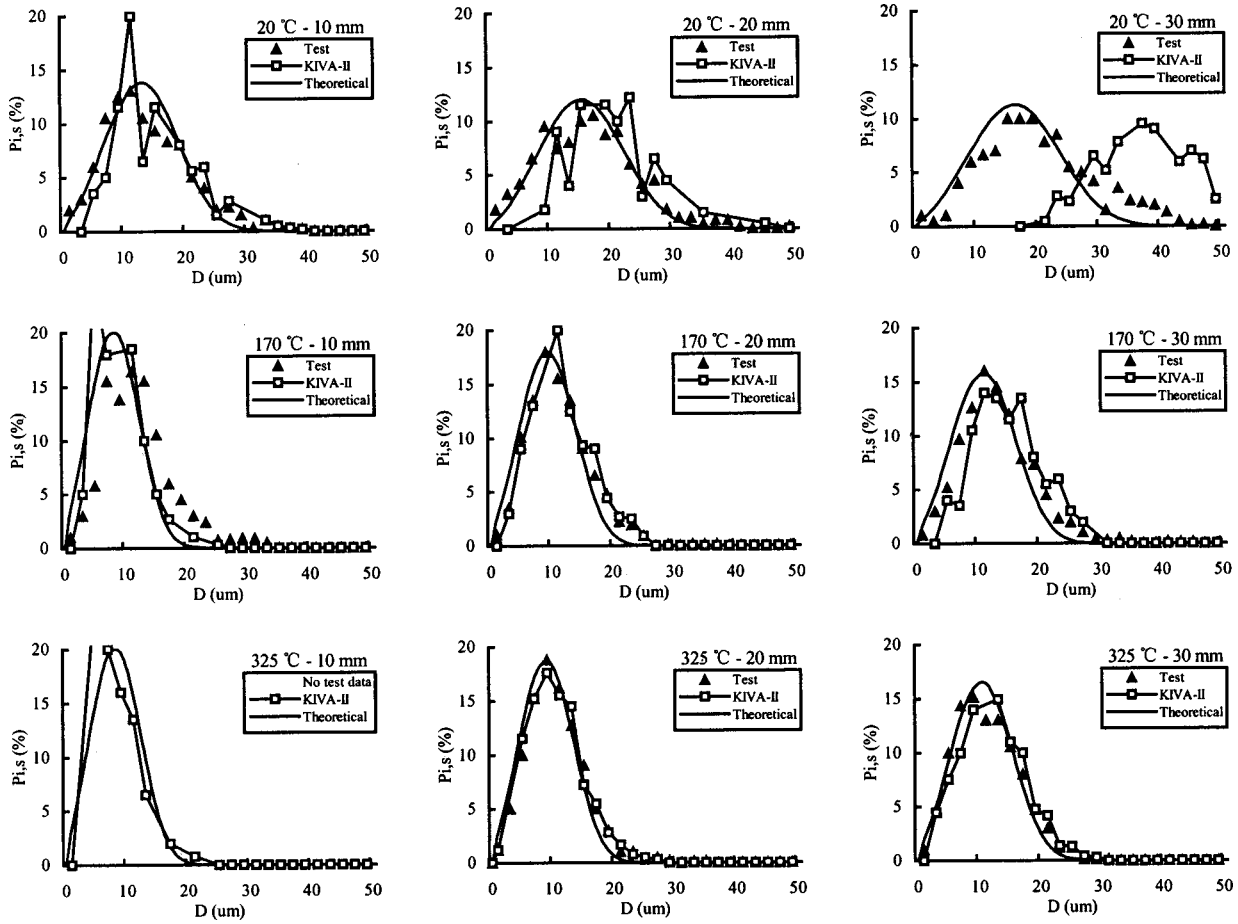

Fig. 1 Droplet size distributions at various locations and temperatures

tions under $D_{max}=200\,\mu$m for validating the sensitivity of the initial value of D_{max} to the calculation results and no notable differences from results under $D_{max}=50\,\mu$m. The initial guess value of $D_{max}=200\,\mu$m is good enough for the common diesel engine sprays.

Levy and Amara performed experiments and predictions of KIVA-II. In their paper, droplet sizes were measured by using Particle Doppler Analyzer instrument. The mean diameter was observed downstream of the break up region. In those tests, diesel fuel was introduced in a cylindrical chamber with two glass windows by using a Bosch type rotative injection pump and a single hole injector. Injected fuel mass in a spray per cycle was 4 mg and injected duration continued 1.1 ms. Experimental conditions are given in Table 2. The KIVA-II code was used to achieve spray computations. This computer program solves the three-dimensional time-dependent conservation equations of the gaseous phase with a finite volume method.

Figure 1 illustrates a comparison with experimental data and results of KIVA-II code. It is clear that a good agreement is obtained between our numerical and experimental results. As can be seen in this figure, the theoretical curves almost coincide with experimental points. In the $t_f=20°$C, $H=30$ mm case, The computation of KIVA-II code shows a large difference. The disagreement shows that the predicted droplet sizes are quite large than the measured ones. However our numerical prediction is suitable.

Table 2 Test conditions

Test case	t_0 (℃)	t_f (℃)	θ
1	20	20	13
2	20	170	11
3	20	325	10

The comparisons of the SMD evolution versus spray axial distance are represented in Fig. 2. It can be seen that our computations fit these experimental data points well. There exists a difference in the $t_f=20°$C case. The growth of the computed SMD with increase of the axial distance is less than growth of the experimental data, the KIVA-II code large than that of test. Because that case is only due to collision modeling, it substantiates that our estimated value for influence of coalescence is smaller than experimental value, that KIVA-II the larger. In other cases, Sauter mean diameters are almost coincide except for $t_f=170°$C, $H=10$ mm. The tested SMD in that case is larger than SMD at $H=20$ mm unexpectedly.

The calculated initial total droplet number is about 2.17×10^7. The droplet numbers of three axial cross sections at various temperatures are represented in Table 1. The computation indicates in Fig. 1 that peak of size distribution slightly moves toward large size, and D_{30} and SMD increase as increase of axial distance in the cold case (20°C), but the small drops are still existence. The decrease of the droplet number is entirely depended on the coalescence. With temperature growth, the influence of the evaporation is to be apparent gradually. Evaporation makes completely vanished droplet diameter, limited droplet diameter, increase quickly as time evolution. Hence, the droplet number will be rapidly reduced by joint influence of the evaporation and coalescence. The peak of size distribution moves toward small size versus temperature, and D_{30} and SMD are reduced. It can be also observed in Fig. 2. As temperature grows, SMD changes are very small with increase of the axial distance because of the droplet

Downloaded 03 Jun 2010 to 171.66.16.150. Redistribution subject to ASME license or copyright; see http://www.asme.org/terms/Terms_Use.cfm

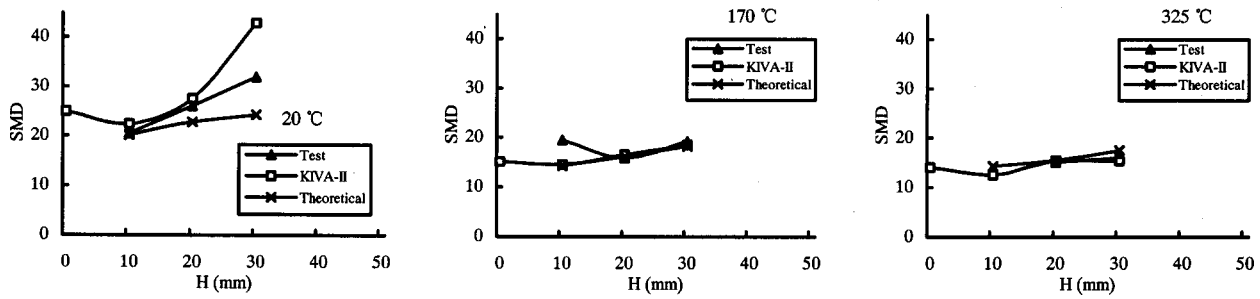

Fig. 2 Sauter mean diameter versus axial location

evaporation. It seems that evaporative influence on the droplet sizes is almost as much as collision coalescent effect under a higher temperature and a more far away position.

It can be imagined that because fuel burned as it delivered within the combustion chamber of engines, the penetration distance of the fuel jet is going to decrease much more with combustion. The smaller drops at a little far from nozzle exit will be almost fully vanished by vaporization. Perhaps, only few drops due to larger initial diameter of several hundred micrometers or coalesced larger diameter are existence [7]. Because the longer the held up time of the droplets, the more the particles pollution due to splitting fuel, the droplet number and diameter will directly effect economy and emissions of the engines.

4 Conclusions

The droplet size distribution functions, droplet numbers, D_{30} and SMD expressions considered evaporation and coalescence have been derived mathematically to atomization processes. The results exhibit a good agreement between numerical and experimental data for the nonreactive diesel sprays. Simulations have shown that droplet size can be predicted downstream of the atomization region. A diesel spray can thus be modeled, when we apply the appropriate initial droplet conditions to the complex processes.

Nomenclature

C_p = specific heat of fuel-air mixture (kJ/kg·°C)
dN_j/dD = number fraction of the droplet size (percent)
dV_j/dD = volume fraction of the droplet size (percent)
d = initial droplet diameter (cm)
D = droplet diameter (cm)
D_{30} = volume mean diameter of the droplets (cm)
D_{32} = Sauter mean diameter of the droplets (cm)
D_L = limited droplet diameter (cm)
$D_{\max}$ = maximum droplet diameter (cm)
H = axial distance from nozzle exit (cm)
K_c = collision coefficient
K_v = evaporation coefficient of the droplets (m^2/s)
L = vaporization heat of the fuel (kJ/kg)
m = injected fuel mass in a spray per cycle (mg/cycle)
n_j = droplet number produced in a spray per cycle
n_l = droplet number at a generatrix within the spray cone
$N_{D,j}$ = droplet number between $(D-\Delta D/2)$ and $(D+\Delta D/2)$
$p_{i,j}$ = a number percentage of the total droplets in the droplets between $(D-\Delta D/2)$ and $(D+\Delta D/2)$
P_i = number-based droplet probability
R = radius at the bottom within the spray cone (cm)
S = information entropy
t_0 = environment temperature (°C)
t_f = gas temperature within combustion chamber (°C)
v_i = a droplet volume [ml]
v_j = droplet volume in a spray per cycle (ml/cycle)
$V_{D,j}$ = droplet volume between $(D-\Delta D/2)$ and $(D+\Delta D/2)$ (ml)
Z = collision times
α_j = Lagrangian multiplier
ΔD = increment of the droplet diameter (cm)
θ = spray cone angle
λ = heat conduct coefficient of the fuel (kW/m·°C)
ρ = fuel density (kg/m^3)
ρ_i = a droplet density (kg/m^3)
τ = penetrated duration (s)
τ_0 = injected duration (s)

Subscripts

i = a droplet property
j = t,s
t = property of the total droplets
s = property of the droplets at an axial cross section within the spray field

References

[1] Sellens, R. W., and Brzustowski, T. A., 1985, "A Prediction of the Drop Size Distribution in a Spray from First Principle," Atomization and Spray Technology, **1**, pp. 89–102.
[2] Li, X., and Tankin, R. S., 1987, "Droplet Size Distribution: A Derivation of a Nukiyama-Tanasawa Type Distribution Function," Combust. Sci. Technol., **56**, No. 1–3, pp. 65–76.
[3] Levy, N., Amara, S., Champoussin, J. C., and Guerrassi, N., 1997, "Non-Reactive Diesel SprayComputations Supported by PDA Measurements," *SAE* paper No. 970049.
[4] Amsden, A. A., Orourke, P. J., and Butler, T. D., 1989, "A Computer Program for Chemically Reactive Flows with Sprays," Los Alamos Laboratory, Report La-11560-MS.
[5] Chang, H., Zhang, Y., and Shen, J, 1993, *Fuel and Combustion, Press of Shanghai Jiaotong University*. Shanhai.
[6] Chiu, W. S., Shahed, S. M., and Lyn, A., 1976, "Transient Spray Mixing Model for Diesel Combustion," *SAE* paper No. 760128.
[7] Quoc, H. X., and Brun, M., 1994, "Study on Atomization and Fuel Drop Size Distribution in Direct Injection Diesel Spray," *SAE* paper No. 940191.

Downloaded 03 Jun 2010 to 171.66.16.150. Redistribution subject to ASME license or copyright; see http://www.asme.org/terms/Terms_Use.cfm

Scale Effect of Cavitation Inception on a 2D Eppler Hydrofoil

E. L. Amromin
Mechmath LLC, Edmond, OK 73034
e-mail: amromin@aol.com

Cavitation inception on an E817 hydrofoil issued from an inverse calculus for ideal fluid has been numerically analyzed for speeds and scales inherent to both model test and full-scale marine conditions. The computations have been carried out with account to the Reynolds number effect on hydrofoil lift and combined effect of the Reynolds number and Weber number on the equilibrium of sheet cavities in the hydrofoil boundary layer. Different levels of scale effects for cavitation inception on suction and pressure sides of E817 hydrofoil are shown. Comparison with the scale effect of cavitation inception on conventional NACA-0012 hydrofoil has helped to explain this difference. Issues in blade design with sections similar to E817 are discussed. [DOI: 10.1115/1.1427689]

1 Introduction

Design of a new hydrofoil with improved performances must include three phases. First, solving an inverse hydrodynamic problem to determine the hydrofoil shape. Such a problem is usually formulated for ideal fluid. Second, model tests that take place in a water tunnel of a relatively small size, where the Reynolds number is not high enough. The third one is an extrapolation of the test results for full-scale conditions in unbounded flows. This phase demands both a theoretical concept of extrapolation and appropriate data of model tests.

For the E817 hydrofoil (designed by Eppler [1] to suppress cavitation inception), the first phase gave a hydrofoil that generates an ordered lift with the minimal value of K in 2D uniform steady incoming flow of ideal fluid. According to [2], such a hydrofoil must have an arc of constant minimal pressure $Cp=-K$. One can see the shape of this hydrofoil in Fig. 1. The value of K has usually been considered as the upper limit for the cavitation number inherent to the hydrofoil at a fixed α, and σ_1 must be smaller than K at any real value of Reynolds number. Eppler's design was carried out for ideal fluid, but the attendant estimations of σ_1 are less favorable than reality.

At a real value of Re, the difference between K and σ_1 depends on many parameters and it is an issue of theoretical estimation of this difference, as well as for an optimal use of hydrofoils in blade design. Because of this, the model test is currently the main basis to predict σ_1 for novel hydrofoils. For E817 hydrofoil, recently Astolfi et al. [3,4] measured σ_1, lift coefficient and other characteristics at $\mathrm{Re}<5\times10^5$ in a water tunnel. This research gave useful initial information about singularities of cavitation inception on E817 that significantly differ from an earlier described [5,6] cavitation inception on conventional hydrofoils of the same thickness (like NACA-4412 or NACA-0012). Particularly, the difference between K and σ_1 for E817 is much higher in a large range of angles of attack (lift coefficients).

For full-scale conditions (usually, for cavitating marine propeller blades, $\mathrm{Re}\sim3\times10^7$), there is neither measured data nor extrapolation results in the quoted papers. The goal of the present paper is to predict the full-scale value of σ_1 for E817, emphasizing special properties of such hydrofoils. An analysis of scale effects on cavitation is done with use of a numerical method developed for sheet cavitation in viscous fluid (Amromin [7,8]). This method allows a comparison of numerical results and model test data [3,4] taking into account the relevant scales.

Contributed by the Fluids Engineering Division for publication in the JOURNAL OF FLUIDS ENGINEERING. Manuscript received by the Fluids Engineering Division November 9, 2000; revised manuscript received September 13, 2001. Associate Editor: J. Katz.

2 Two Modeling Concepts for Cavitation Inception

Traditionally, cavitation inception number has been defined as an upper limit of an increasing succession of σ related to cavities on a hydrofoil/body in stable conditions (a decreasing succession is usually less accurate because of the random appearance of a nuclei). This definition is accepted in both experimenting and modeling. Nevertheless, there are two diverse concepts of modeling cavitation inception. The first concept assumes no influence of the appearing cavity on the pressure on the hydrofoil. Besides, there is no influence of surface tension on σ. According to this concept, the value of σ_1 is completely predetermined by the pressure distribution over the cavitation-free body. Locating cavities in regions of the lowest pressure, one must obtain in the framework of this concept the evident result: $\sigma_1=K$ for $L=B=0$. Examples of such dependencies $\sigma_1(\alpha)$ for hydrofoils E817 and NACA-0012 are shown in Fig. 2 (the thickness of E817 is 11.4%; so, it is close to NACA-0012 thickness), and $\sigma_1=K$ there. Contemporary improvements in hydrofoil/blade design [9,10] are really assigned to minimize K. The value of σ_1 tends to coincide with K at the angle of attack selected for design of such hydrofoils, but hydrofoils usually operate in quite wide ranges of α, and a problem is to predict σ_1 for the whole range of operations. A significant difference between K and σ_1 often appears in such a range. Its values depend on the hydrofoil/body shape and size, as well as on the speed and quality of water. The concept of negligibly small appearing cavities cannot explain such dependencies.

It is evident that there are physically based down limits on cavity sizes, and the second concept includes determination of these sizes and inverse influence of appearing cavities on surrounding flow. The Laplace formula shows that for fixed pressure in the region of cavity location and cavitation number, the cavity surface curvature cannot be higher than

$$\chi=-C^{-1}(Cp+\sigma)\mathrm{We} \tag{1}$$

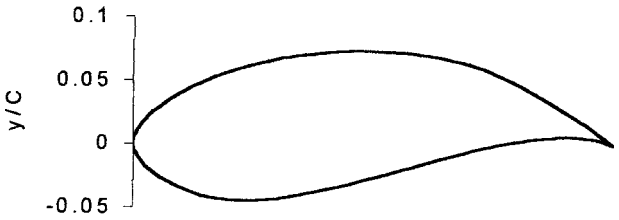

Fig. 1 Shape of hydrofoil E817

 Copyright © 2002 by ASME

Downloaded 03 Jun 2010 to 171.66.16.150. Redistribution subject to ASME license or copyright; see http://www.asme.org/terms/Terms_Use.cfm

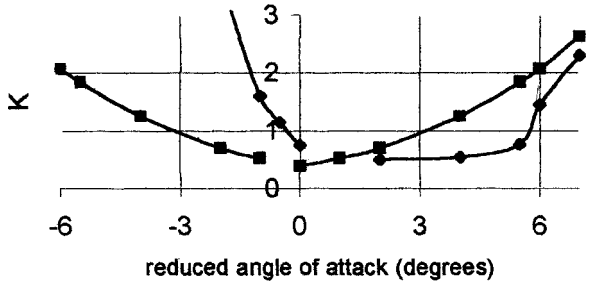

Fig. 2 Minimal pressure on E817 (♦) and NACA0012 (■) in ideal fluid as function of α-α_0 ($\alpha_0=-4$ degree for E817)

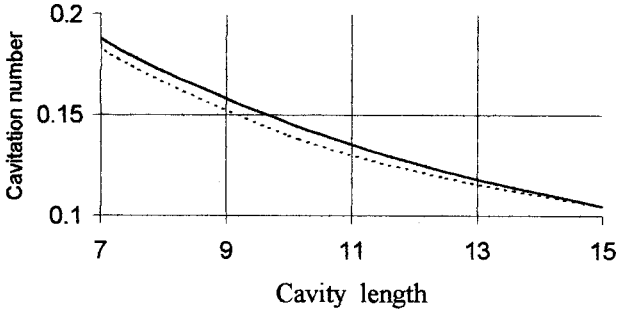

Fig. 3 Computed cavitation number as function of cavity length past disk. Author's result (solid curve) is compared with Brennen's [14] results (dashed curve)

This formula defines a lower limit of cavity size. Such a cavity affects whole flow and, particularly, *Cp*. It is possible to find *Cp* and σ for a succession of decreasing cavities in the traditional framework of theory of ideal fluid by solving the following problem for velocity potential Φ:

$$\Delta\Phi=0 \tag{2}$$

$$(\nabla\Phi,N)_{|s}=0 \tag{3}$$

$$\nabla\Phi(\infty)=\{1,\alpha\} \tag{4}$$

$$(\nabla\Phi,\nabla\Phi)|_{S*}=1+\sigma \tag{5}$$

Here the surface S includes S^*, the hydrofoil wetted surface, a surface of fictitious body that is used for cavity closing, and walls of tunnel/channel (if it exists). A condition for lift determination must be added to Eqs. (2)–(5); usually, it is Kutta-Joukovski condition. It is possible to find a corresponding value of σ for any pair of L and X_L by solving the problem (2)–(5) that is nonlinear because the shape of S^* is initially unknown. There are several contemporary numerical techniques for such solving [11,12].

The author has used a modification of a perturbation method [11] to solve such problems. The method is based on subsequent corrections of S^* by small steps. It is assumed that a tried surface of a length L is close to the initially unknown cavity surface S^* that satisfies to Eq. (5). Let U is a solution of the linear problem (2)–(4) out of a contour S_o that includes the tried surface, and there is no any special condition. According to the above assumption, the velocity U over this part of S_o is close to a constant, and $|1-U/(1+\sigma)^{1/2}|\ll 1$; besides, a distance h between S_o and S^* is much smaller than L. Consequently, it is possible to determine this small distance with use of an auxiliary potential φ of a small density in perturbed Eqs. (3) and (5):

$$\frac{\partial\varphi}{\partial N}+\frac{\partial}{\partial T}Uh=0; \tag{6}$$

$$\frac{\partial\varphi}{\partial T}=U-\sqrt{1+\sigma} \tag{7}$$

The distance h has also to satisfy conditions

$$h(X_L)=0, \tag{8}$$

$$\mathrm{d}h/\mathrm{d}T(L+X_L)=0 \tag{9}$$

For the selected L, σ must be found during computations.

For the initial iteration, S can coincide with the hydrofoil surface, and for relatively thin cavities the solely iteration may be sufficient (like in [13]). Generally, S is the known flow boundary that is the result of previous iteration. Thus, N and T generally relate to S that undergoes changes during iterations, as well as U. Although the auxiliary problem (6)–(9) is linear, iterations certainly go to a solution of the nonlinear problem (2)–(5) because U comes closer to $(1+\sigma)^{1/2}$. In the addition, U is always a solution of the linear problem (2)–(4) outside of the known boundary. Such a solution can be determined with a high accuracy for both unbounded flow and flows in channels/tunnels.

First validation of this perturbation method was performed for axissymmetric cavities with the Riabushinsky scheme of closure (see Fig. 3) because axissymmetric flows are simpler for modeling. Nevertheless, this flow is a hard exam for methods to solve nonlinear problems, and one can see a satisfactory accordance with result of [14] in this figure.

For thin cavities on hydrofoil, a possibility to select its contour as the tried surface makes formulas shorter (it is possible even to suppose $B=h$), with keeping all mathematical singularities inherent to the general case. Let φ is the potential of sources. The problem (6)–(9) has then the following solution [15]:

$$h(x)=\frac{1}{U(x)}\int_{X_L}^{X}\frac{R(x)}{\pi}\int_{X_L}^{X+X_L}\frac{\sqrt{1+\sigma}-U(z)}{R(z)(x-z)}dzdx \tag{10}$$

Here $R(x)=[(x-X_L)(X_L+L-x)]^{1/2}$. This formula allows smooth corrections of S, and solutions weakly depend on discretization, but the following condition must be satisfied:

$$\sqrt{1+\sigma}=\frac{1}{\pi}\int_{X_L}^{L+X_L}\frac{U(z)}{R(z)}dz \tag{11}$$

One cannot find the maximal σ by using minimal L or B in Eqs. (10)–(11) because there is no possibility to determine X_L. Determination of X_L is a key issue for attempts to study the inception of attached cavitation. It is sometimes possible to satisfactorily predict σ_1 with an appropriate selection of X_L in ideal fluid [5], but small changes of X_L significantly affect the dependencies $\sigma(L)$ for the hydrofoils [16].

However, it is possible to determine X_L with consideration of cavitation as a special case of viscous separation. As was shown [17], the minimal cavity thickness and the boundary layer thickness are comparable. Thereby a small cavity induces viscous separation, like an obstacle embedded in the boundary layer. Location of appearing cavities depends on the pressure distribution over a cavitation-free foil, as well as on thickness of both boundary layer and cavity head. Consequently, both the Reynolds number and the Weber number must be considered as significant parameters for sheet cavitation in viscous fluid. Then $\sigma_1=\max\{\sigma(\mathrm{Re},\mathrm{We})\}$. The definitions of Re and We show that $C=\mathrm{const}\times\mathrm{Re}^2/\mathrm{We}$, and $U_\infty=\mathrm{const}\times\mathrm{We}/\mathrm{Re}$, where constants are known. Thus, a pair {Re, We} predetermines the pair $\{C,U_\infty\}$, and scale effects can be analyzed.

Downloaded 03 Jun 2010 to 171.66.16.150. Redistribution subject to ASME license or copyright; see http://www.asme.org/terms/Terms_Use.cfm

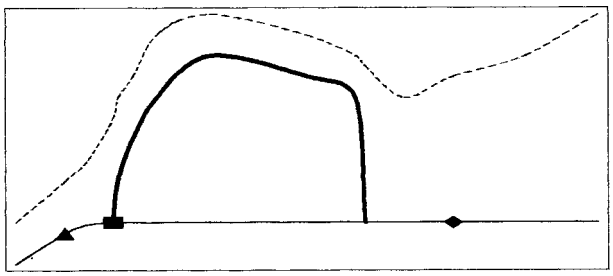

Fig. 4 Sketch of partial cavity on a body in viscous fluid. Thin solid curve is body surface, thick solid curve is cavity surface. Boundary layer is limited by dashed curve, ▲-its separation section, ♦-its reattachment, ■-X_L.

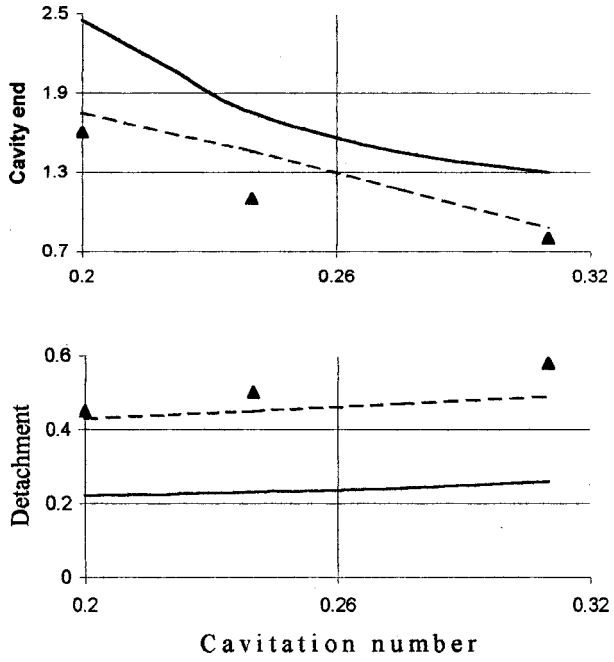

Fig. 5 Cavity leading (bottom) and trailing (top) edge abscissas past axissymmetric ellipsoid $(2x/C\text{-}1)^2+(4y/C)^2=1$: ▲-observations [11]; author's computation for ideal fluid is shown by solid curves, for viscous fluid-by dashed curves

It is important to emphasize the main aspects of relevant modeling cavitation in viscous fluid. A sketch in Fig. 4 helps to understand differences in cavitation schemes for ideal and viscous fluid. First, the cavity surface is not a free boundary of inviscid flow, but the surface of the body of displacement is the free boundary. A distance between S^* and this boundary equals δ^*. Second, a tangent to the fluid surface is broken in the cavity detachment point $x=X_L$. An angle β describes this break. Finally, the velocity over the mentioned free boundary is not constant, but decreases along this boundary. Moreover, U is an implicit function of Re, because its derivative depends on the δ^* values in two zones of viscous separation (upstream of the cavity and downstream from the cavity).

Looking for the relevant mathematical technique, the author found no possibility to use custom CFD codes for this complex, viscous, unsteady, two-phase flow with a high pressure gradient in a very small zone [17] between boundary layer detachment upstream of the cavity and with significant capillary effect on a part of the free boundary. Several attempts to study viscous effects on cavitation ([18,19], etc) have shown that such codes are not adapted to examine this very complex flow. There is, however, a possibility to use the basic equations of ideal cavitation with certain modifications and supplementary conditions.

In order of these modifications, S in Eq. (3) becomes the surface of the displacement body, and the surface S^* in Eq. (5) includes boundaries of viscous separation zones upstream of the cavity and downstream from it (where separation is caused by reentry jet). Further, a constant in the right-hand side of Eq. (5) must be replaced by a more complex function U^{*2} that decreases near the edges of S^*. Fixing values of L and X_L, one does not define the whole length of the free surface, because this length (and values of Xo and Xr) has to be determined. The leading edge of this surface (the curve in 3D flows) is not attached to the hydrofoil, but placed on the distance $\delta^*(X_L)$ from the hydrofoil surface.

A key innovation in this modeling is consideration of equilibrium conditions in a zone between cavity detachment and boundary layer separation upstream of the cavity. This consideration makes it possible to represent Xo and X_L as implicit functions of Re and We for a fixed L.

The separation time-averaged criterion in a point Xo can be written as $F_f/\partial P/\partial x=\text{const}$, where the constant values are different for laminar and turbulent boundary layers, and F_f has to be differently represented in these layers. As a result, there are two kinds of condition with two different empirical coefficients in their right-hand sides:

$$\frac{\delta^{*2}}{\mu U}\cdot\frac{\partial P}{\partial x}=A_{LAM} \tag{12}$$

$$\frac{\delta^*}{\rho U^2}\cdot\frac{\partial P}{\partial x}=A_{\mathrm{TURB}} \tag{13}$$

These conditions have the same general form for both cavitating and cavitation-free flows, and it is acceptable to use the same right-hand sides in Eqs. (12)-(13). A singularity of cavitating flows is the dependency of pressure derivative on a curvature of the cavity surface in the vicinity of cavity detachment. An analogy between cavity head and a source allowed qualitative analysis of the phenomenon [7] and deduction of an approximate formula with a new semi-empirical coefficient for the mentioned derivative. Its substitution in Eq. (12) leads to the following criterion:

$$\left(\frac{X_L-Xo}{\delta^* C_2}\right)^3\left(\frac{C_1}{\mathrm{Re}}-\delta^*\hat{U}\frac{\partial\hat{U}}{\partial x}\right)=[\hat{U}(1+\cos\beta)]^2 \tag{14}$$

Here $\hat{U}$ is value of U in the point $x=X$o, and $C_1=1.1$, as it is commonly used for the cavitation-free laminar boundary layer. The value $C_2=61.2$ is tuned with use of the experimental data [11] for axissymmetric cavitation. For metals, $\beta=2\pi$.

The value δ^* implicitly depends on the cavity shape, because it depends on the pressure derivative upstream of cavity. Thus, value of X_L can be found from Eq. (14). On the other hand, an approximate integration of Eq. (1) in vicinity of cavity detachment gives [7] a simple formula:

$$(X_L-Xo)^2\mathrm{We}\hat{U}\frac{\partial\hat{U}}{\partial x}=C_3 \tag{15}$$

Here $C_3=8.5$ is tuned with use the same experimental data. Successive solving Eqs. (14), (15) actually allows determination of We for given L and Re.

The problem of computation of attached cavitation continues to be nonlinear, and iterations with modified Eq. (10), (11) are the basis of numerical technique for this problem too. The function U can initially be taken from the solution of the ideal cavitation problem with the same pair $\{L,X_L\}$. The necessity to operate with

Downloaded 03 Jun 2010 to 171.66.16.150. Redistribution subject to ASME license or copyright; see http://www.asme.org/terms/Terms_Use.cfm

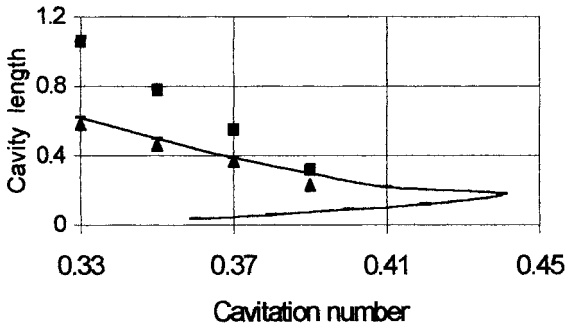

Fig. 6 Comparison of computed and measured [26] cavity length for ITTC-body. Solid curve shows computed L, ▲ and ■ show minimal and maximal observed L.

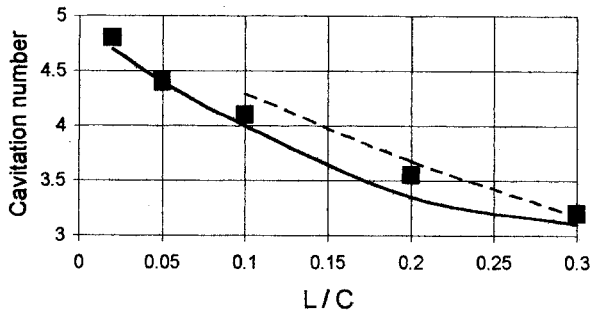

Fig. 8 Comparison of L(σ) for NACA-0010 hydrofoil (H=C, α=6.5 degree). Solid curve-author's computation, dashed curve-computation [21], ■-measurements [15].

δ^* values leads to including a boundary layer computation in every iteration. Besides, the function U^* must be defined. It is accurate enough to suppose that above the cavity $U^*=(1+\sigma)^{1/2}$, but for the viscous separation zone $U^*(x)=(x\text{-}X_1)^2A+(1+\sigma)^{1/2}$, where $A=\text{const}$, $(X_1-X_L)/(X_1-X\text{o})=\text{const}$. This approximation of U^* was used in Eqs. (14), (15).

There are options in modeling flow downstream from the cavity. For a relatively large cavity, it is possible to combine Eqs. (14), (15) with traditional closure schemes of ideal cavitation. Initial validations of the described innovation were carried out with this combination. Their typical results are shown in Fig. 5 for an ellipsoid. One may see that a significant improvement in the prediction of cavity detachment leads to an improvement in computation of cavity lengths. For shorter cavities, the boundary layer reattachment in a point $x=X_3$ must also be taken into account, and consequently:

$$\sum_m h_m(X_3)=\delta^*(X_3) \tag{16}$$

$$\delta^* dU^*/dx(X_3)=C_a U^*(X_3) \tag{17}$$

Here m is iteration's number, and generally, $h_m \neq B$; $Co=\text{const}$. It is necessary to vary X_3 and the difference $U^*(X_3)-(1+\sigma)^{1/2}$ to satisfy Eqs. (16), (17) taking into account a jump of δ^* at the cavity end that is associated with the influence of re-entry jet. There is a scheme with a steady water inlet in the cavity back and a steady water outlet in boundary layer over the cavity, where Karman momentum equation obtains the following form:

$$d\delta^{**}/dx=Vo(Uo/U-1) \tag{18}$$

Here δ^{**} is momentum thickness, and Vo and Uo are normal and tangent velocity components on the cavity. It is necessary to introduce a profile of the tangent velocity and a "friction law" over the cavity to determine δ^* from Eq. (18). Modeling [7] shown that numerical results weekly depend on a Vo profile along the cavity.

Initial validation of computations with Eqs. (16), (17) was also done for axissymmetric flows. Comparison of cavity length is shown in Fig. 6 (maybe, with an underestimation of the wall effect on cavities in the author's computations). It is important to emphasize that there are two solutions for the same σ (with different cavity detachment points). The computed maximum σ does not correspond to a minimum cavity length, because it is mathematically possible to attain an equilibrium of smaller cavities at a smaller cavitation number than σ_1. However, only the top theoretical curve in Fig. 6 corresponds to the physically possible phenomenon.

Such validations for hydrofoils are shown in Figs. 7 and 8. These validations do not include comparisons with distinct published computations for cavitation in viscous fluid, because such computations (like [18]) do not represent dependencies in a certain range of σ. For hydrofoils, there are comparisons with experimental data [20] in Fig. 8.

There is also the comparison with the most successful computations for ideal fluid [21]. Computation [21] includes a precise tuning the ideal fluid closure scheme to a particular hydrofoil. However, the same scheme occurs unsuccessfully for another hy-

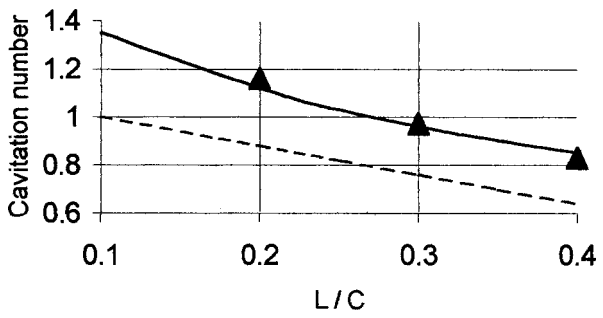

Fig. 7 Comparison of L(σ) for EN-hydrofoil ($\alpha_0=0$) for α=4°. Solid curve-author's computation, dashed curve-computation [21], ▲-measurements [20].

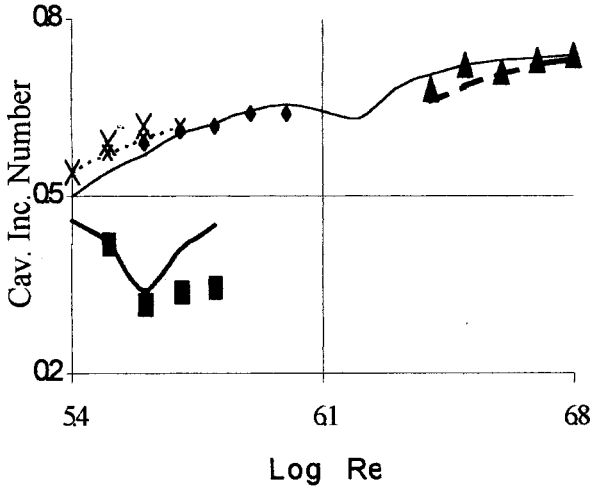

Fig. 9 Cavitation inception number for body with semispherical head. Computed results are plotted by solid curve for body diameter D=0.05 m, by thick solid curve-for D=0.05 m and stimulated laminar-turbulent transition; by dashed curve-for D=0.02 m; by thick dashes-for D=0.4 m. Experimental data are shown: by ♦-for D=0.05 m [6]; by ■-for D=0.05 m and stimulated laminar-turbulent transition [28]; by ▲-for D=0.4 m [27]; by ×-for D=0.02 m [27].

Downloaded 03 Jun 2010 to 171.66.16.150. Redistribution subject to ASME license or copyright; see http://www.asme.org/terms/Terms_Use.cfm

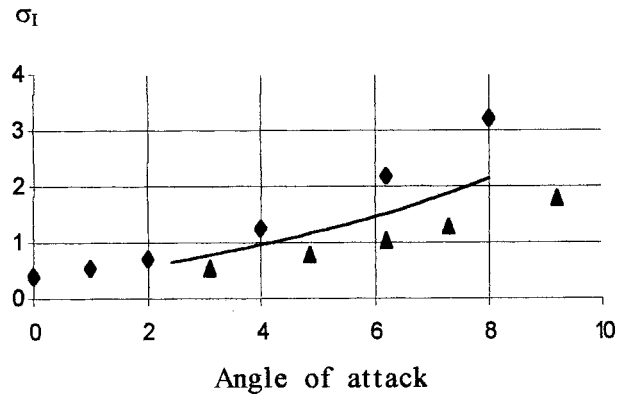

Fig. 10 Computed dependencies $\sigma_1(\alpha)$ for NACA-0012 hydrofoil in infinite flow: ♦-for ideal fluid curve-for FS (C=1 m, U_∞ =27 m/s), ▲-for MT (C=0.1 m, U_∞=6.5 m/s)

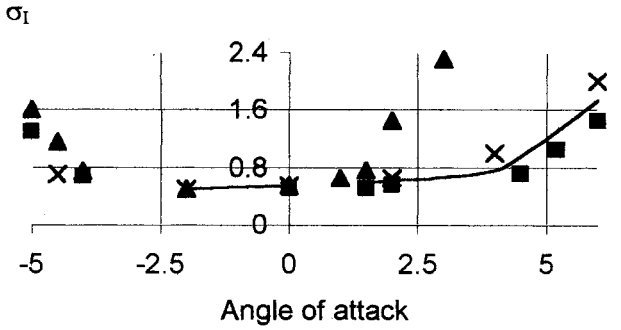

Fig. 11 Cavitation inception number for E817 hydrofoil as function of the angle of attack. ▲-computation for ideal fluid with measured [3] C_L that implicitly (and incompletely) takes into account the wall influence on hydrofoil cavitation, ■-computation for FS with measured [3] C_L, solid curve-computation for MT with C_L (Re) and without an account of the wall effect, x-measured [4] data.

drofoil (see Fig. 7). The suggested method for viscous fluid is uniformly good with the same coefficients determined for axisymmetric flow.

Several recent papers include numerical modeling of viscous effects on cavitation performed without consideration of cavitation effect on viscous separation upstream of cavity. The results (like in [22]) were obtained for $L/C>0.1$ and given location of cavity detachment. Such approach is basically very close to considered earlier [5], and has evident limitation for extrapolations to FS.

Validation of computations $\sigma_1=\max\{\sigma(\mathrm{Re,We})\}$ for axisymmetric flow in Fig. 9 are, perhaps, the most convincing because there are experimental data for a large variety of body sizes (body diameters from 0.02 m up to 0.4 m) and diverse kinds of boundary layers (in turbulent boundary layer Eq. (14) was replaced by $X_L - X_o = 2\delta^*$ [7]). This figure manifests that scale effect on cavitation cannot be completely described by Re.

There is no possibility of such wide comparison for hydrofoils, but similar computed dependencies are plotted in Fig. 10 to show general tendencies. FS data are higher than MT data, and ideal fluid data are the highest. Because NACA-0012 is a symmetric hydrofoil ($\alpha_0=0$), this plot can be symmetrically prolonged to negative α (or negative C_L).

3 Analysis of Real Model Tests

A large difference between K and σ_I for hydrofoils usually occurs because of combination of two effects. The first effect is a viscous effect on cavitation itself. This effect is illustrated in Fig. 9 for the lift-free body, but such illustration can also be considered as an example for a fixed lift. The second effect is a viscous effect on K, and this effect is caused by a dependency of C_L on Re (and C_L evidently affects K). According to Mishkevich [23] approximate formula, E817 at for $\alpha<\pi/15$ and $\mathrm{Re}=5\times10^5$, C_L is 0.64 of ideal C_L and 0.77 of C_L in FS. However, for MT in the quite narrow water tunnel, C_L rises with the ratio of C to the distance H between upper and lower walls and with α. Particularly, according to [16], for $H/C=1.9$ (for conditions of model test [3,4]), the C_L rise is about 30% for $\alpha-\alpha_0=6.5$ degrees. Because of the opposite effects, the measured values of C_L are very close to the theoretical line for ideal fluid until $\alpha.-\alpha_0<\pi/20$ in the actual MT [3]. Therefore, the use of the variable α in plotting buckets for σ_I is acceptable for these particular MT, as is done in Fig. 11; but there is no walls and opposite effects in FS. Although computations for MT are close to the measured data in Fig. 11, some experimental values of σ_I are higher than both measured K [4] and computed values for viscous fluid. Thus, it is appropriate to remember that measured σ_I can significantly depends also on the water quality (on size of nucleus and air content). Currently, theory of cavitation in viscous fluid has not been developed enough to take into account these water properties, and presented dependencies $\sigma_I(\mathrm{Re,We})$ have to be considered as results for a low or moderate air content.

It is necessary to add that gaseous bubbles introduce difficulties in the analysis of data measured in MT. The bubbles appear at $\sigma=2(P_\infty-P_G)/\rho U_\infty^2$, but the gas pressure P_G is generally unknown, and that forces use of the vapor pressure P_C instead of P_G in calculation of σ. This introduces a random error $2(P_G-P_C)/\rho U_\infty^2$ in determination of σ and σ_I. Although this error sharply drops in FS flows (because of much higher U_∞), its existence in MT flows makes difficulties in determination of a basis for extrapolations.

How the Velocity Peak Predetermines the Scale Effect

As noted, there is no tunnel wall's effect in FS, and C_L is much lower than at the same α and much smaller Re in a narrow water tunnel. Therefore, the full scale values of $\sigma_I(\alpha)$ are lower than model values in Fig. 11. This paradox can be deleted by using C_L instead of α in plotting buckets for σ_I (as is done in [10] and in Fig. 12).

It is also useful to supply these buckets by information about location of the cavity edges at $\sigma=\sigma_I$. These computed data for E817 are shown in Fig. 13. There is a gap in computed data for the model hydrofoil E817 because computed $\max\{\sigma\}$ is too small (in comparison with K) in the related range of lift; and there is also no sheet cavitation in model tests [4]. Out of the mentioned gap of angles, a distance between the cavity and the hydrofoil's leading edge is small (see Fig. 14).

For cavities over full-scale hydrofoil in the range of small lifts, the boundary layer becomes turbulent upstream from cavities. Because of high pulsation of pressure, it is possible to define the

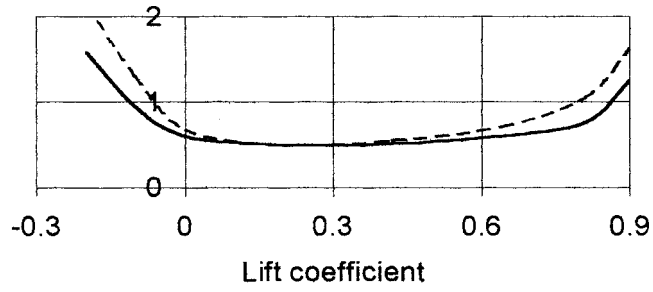

Fig. 12 Computed dependencies $\sigma_I(C_L)$ for E817 hydrofoil. Dashed curve relates to FS flow, solid curve-to MT.

Downloaded 03 Jun 2010 to 171.66.16.150. Redistribution subject to ASME license or copyright; see http://www.asme.org/terms/Terms_Use.cfm

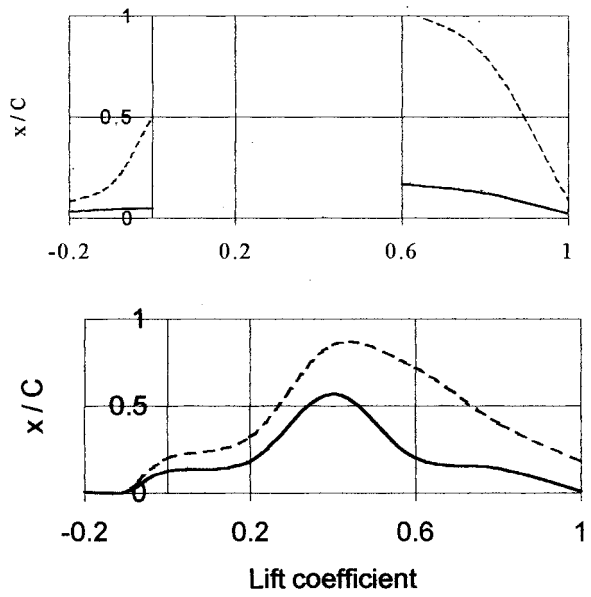

Fig. 13 Computed cavity leading edges (solid curves) and trailing edges (dashed curves) on E817 hydrofoil at MT conditions (top; C=0.1 m and U_∞=6.5 m/s) and FS conditions (bottom; C=1 m and U_∞=27 m/s) for $\sigma=\sigma_I$

leading edges of cavitation zones (usually, with groups of attached cavities), but there is no continuous cavity detachment line, and the zone can be located far enough from the hydrofoil leading edge (in Fig. 15).

As noted, hydrofoil design is usually an inverse problem of ideal fluid theory, and it would be useful to understand what kind of scale effect is associated with a pressure distribution that is selected for this problem. The buckets $\sigma_I(C_L)$ for advanced hydrofoil E817 and conventional hydrofoil NACA-0012 (in Fig. 10) are very different. The unusual dependency of K on $\alpha-\alpha_0$ for E817 and similar hydrofoils was unexpected by blade designers. As a result, cavitation inception occurs on the pressure side much earlier than on suction side [9,24] and the silence operation speed does not attain its accessible limit.

Basically, the difference in scale effects can be explained with regards to pressure distributions on these hydrofoils in ideal fluid at the same values C_L as real flows. Fixation of C_L does not give the complete coincidence of flows, but this fixation allows examination of the main properties of pressure distribution for the diverse α. One can see in Fig. 16 that C_p distributions near the leading edges are similar enough for the suction side of NACA-0012 at α=4° and the pressure side of E817 at $\alpha=-6°$. This similarity results in a certain similarity of dependencies K-σ_I on C_L in such ranges of C_L (or α). The distribution $C_p(x)$ over the suction side for E817 at α=4° is dissimilar to $Cp(x)$ of NACA-

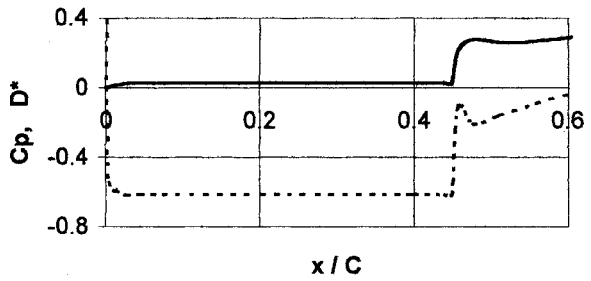

Fig. 14 Computed distribution Cp (dashed curve) and D*=100δ* (solid curve) on the pressure side of E817 hydrofoil at $\alpha=-6°$ for C=0.1 m and U_∞=6.5 m/s

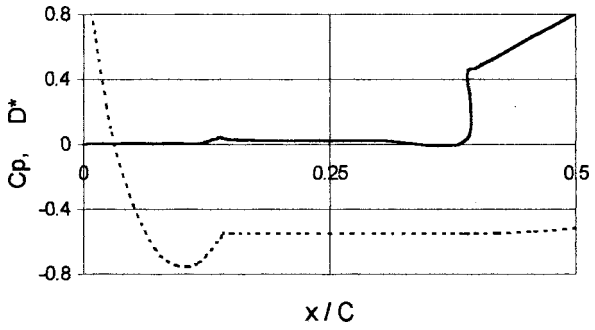

Fig. 15 Computed distribution of Cp (dashed curve) and D*=100δ* (solid curve) on the suction side of E817 hydrofoil with cavity of at α=4° for C=1 m and U_∞=27 m/s

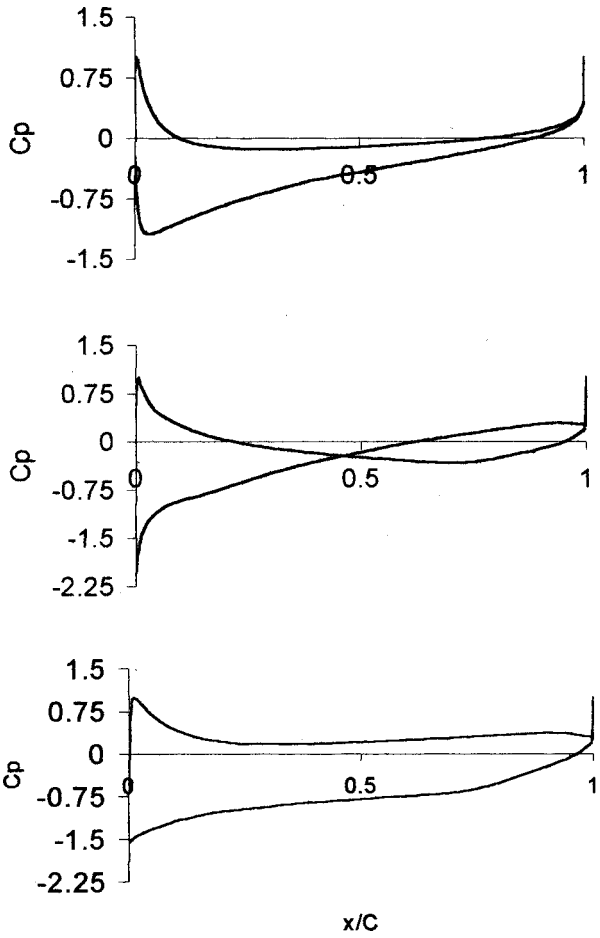

Fig. 16 Distributions of Cp in ideal fluid on NACA-0012 hydrofoil at α=4° (top) and on E817 at α=6° (middle) and at $\alpha=-6°$ (bottom)

0012 at the positive α-α_0 (that coincides with the pressure distribution over its pressure side at negative angle of attack).

The curves $Cp(x)$ for C_L between 0.5 and 0.8 include a small arc of sharp rise and a large plateau there. Ideally, a very thin cavity could spread along this plateau. Really, surface tension prevents such spreading if $\max\{h\}$ is too small. This results in a relatively high difference K-σ_I for any realistic pair $\{C, U_\infty\}$.

Such a difference can be useful. A designer may attain it and reduce σ_I for both model and full-scale Re and We by a relevant rise of hydrofoil camber line. However, it is necessary to consider scale effects on cavitation inception for two sides of hydrofoil. Therefore, in blade design with the use of such 2D sections, the

Downloaded 03 Jun 2010 to 171.66.16.150. Redistribution subject to ASME license or copyright; see http://www.asme.org/terms/Terms_Use.cfm

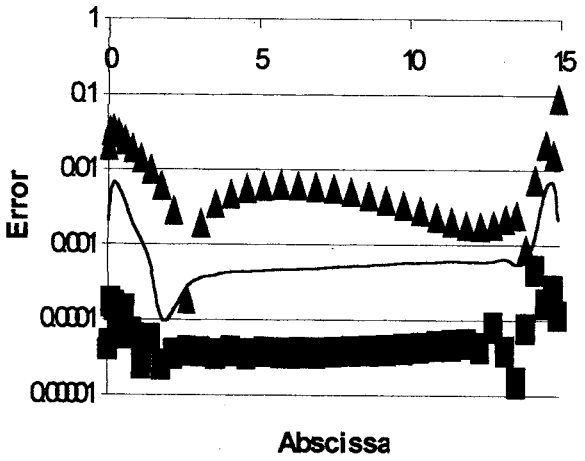

Fig. 17 Error distributions along a axis-symmetric cavity affected by centrifugal force. Triangles corresponds to iteration number 10, curve to iteration number 30, squares to 90th iteration. Cavitator is located at x=15.

center of the K-buckets must be displaced from the center of the interval of angles of attack (or lift coefficients), where the values of K are low and close to a constant.

5 Conclusions

Analyzing scale effects on cavitation inception on hydrofoils in flows with low or moderate air content, one can compose an analysis of cavitation in full-scale conditions from two parts. The first part relates to the Re effect on the hydrofoil lift. The second part relates to the combined effect of boundary layer and surface tension on cavity equilibrium. According to this analysis:

(a) The real envelope $\sigma_1(C_L)$ of the E817 hydrofoil is much wider than its ideal bucket (mainly because of properties of pressure distribution on the suction side).
(b) Scale effects on cavitation inception are very different for suction and pressure sides of E817 hydrofoil due to different ''fullness'' of the velocity peaks near leading edge. It is important to keep in mind such a difference in design of hydrofoils/blades with suppressed cavitation inception.

Acknowledgment

The author thanks the reviewers for their excellent comments that helped to improve the paper.

Appendix

One may require additional illustrations of convergence of the described iterative method to solve nonlinear problems with free boundaries. The author would like to present an illustration that does not relate to hydrofoils, but manifests iteration convergence in the most difficult case [25] where the velocity of ideal fluid drops in the middle of cavity (for abscissa equal 0) down to zero.

The author assumes that Fig. 17 gives a sufficient illustration of the ability of diverse modifications of the iterative method [11] to describe nonlinear effects.

Nomenclature

B = cavity thickness
C = hydrofoil chord
C_L = lift coefficient
Cp = pressure coefficient
Ff = wall friction
FS = full-scale conditions
H = distance between tunnel walls
K = min Cp
MT = model test conditions
L = cavity length
N and T = normal and tangent to S
P, P_∞ and U_∞ = pressure, unperturbed pressure and free-stream speed
S^* = cavity surface
S = whole flow boundary
$U=(1-Cp)^{1/2}$ = velocity in inviscid fluid
Re = Reynolds number
$\mathrm{We}=\rho U_\infty^2 C/\gamma$ = Weber number
γ = coefficient of surface tension
Xo and Xr = abscissas of boundary layer's separation and reattachment
X_L = abscissa of cavity leading edge (cavity detachment)
α and α_0 = angles of the attack and zero lift
β = angle between exterior normal to body and interior normal to cavity at X_L
δ = ratio of hydrofoil thickness to C
δ^* = displacement thickness
σ = cavitation number
σ_1 = cavitation inception number
ρ = fluid density
χ = curvature of cavity surface

References

[1] Eppler, R., 1990, *Airfoil Design and Data*, Springer-Verlag, Berlin.
[2] Garabedian, P. R., and Spencer, D. C., 1952, ''Extermal methods in cavitation flow,'' J. Rational Mech. Analysis, **1**, pp. 309–320.
[3] Dorange, P., Astolfi, J. A., Billard, J. Y. and Fruman, D. H., 1988, ''Cavitation inception and development on two-dimensional hydrofoils,'' Third Int. Symp. On Cavitation, Grenoble, Vol. 1, pp. 227–232.
[4] Astolfi, J. A., Dorange, P., Billard, J. Y., and Cid Tomas, I., 2000, ''An Experimental Investigation of Cavitation Inception and Development on a Two-Dimensional Eppler Hydrofoi,'' ASME J. Fluids Eng., **122**, pp. 164–173.
[5] Huang, T. T., and Peterson, F. B., 1976, ''Influence of Viscous Effects on Model/Full Scale Cavitation Scaling,'' J. Ship Res., **20**, pp. 215–223.
[6] Billet, M. L., and Holl, J. W., 1981, ''Scale Effects on Various Types of Limited Cavitation,'' ASME J. Fluids Eng., **103**, pp. 405–414.
[7] Amromin, E. L., 1985, ''On Cavitation Flow Calculation for Viscous Capillary Fluid,'' Fluid Dyn., **20**, pp. 891–899.
[8] Amromin, E. L., 2000, ''Analysis of Viscous Effects on Cavitation,'' Appl. Mech. Rev., **53**, pp. 307–322.
[9] Jessup, S. D., and Wang, H. C., 1997, ''Propeller design and evaluation for a high speed patrol boat incorporating iterative analysis with panel method,'' SNAME Propeller/shafting '97 Symp., Virginia-Beach, pp. 1101–1125.
[10] Cox, B. D., Kimball, R. W. and Scherer, O., 1997, ''Hydrofoil section with think trailing edges,'' SNAME Propeller/Shafting '97 Symp., Virginia-Beach, pp. 1801–1818.
[11] Ivanov, A. H., 1980, *Hydrodynamic of Developed Cavitating Flow*, Sydostroenie, Leningrad (in Russian).
[12] Kinnas, S. A., 1998 ''The prediction of unsteady sheet cavitation'' Third Intern. Symp. on Cavitation, Grenoble, Vol. 1, pp. 19–38.
[13] Tulin, M. P., and Hsu, C. C., 1980, ''New Application of Cavity Flow Theory,'' 13 Symp. Nav. Hydr., Tokyo.
[14] Brennen, C. E., 1969, ''A numerical solution for axisymmetric cavity flows,'' J. Fluid Mech., **37**, pp. 671–688.
[15] Gakhov, F. D., 1966, *Boundary Value Problems*, Pergamon, New York.
[16] Pellone, C., and Rowe, A., 1988, ''Effect of Separation on Partial Cavitation,'' ASME J. Fluids Eng., **110**, pp. 182–189.
[17] Arakeri, V. H., 1975, ''Viscous effects on the position of cavitation separation from smooth bodies,'' J. Fluid Mech., **68**, pp. 779–799.
[18] Dupont, P., Parkinson, E., and Avellan, F., 1993, ''Cavitation development in a centrifugal pump: numerical and model tests predictions,'' ASME FED, Vol. 177, pp. 63–72.
[19] Dieval, L., Arnaud, M., and Marcer, R., 1998, ''Numerical modeling of unsteady cavitating flows by a VOF method.'' Third Intern. Symp. on Cavitation, Grenoble, Vol. 2, pp. 243–248.
[20] Yamaguchi, H., and Kato, H., 1983, ''Non-linear theory for partially cavitating hydrofoils,'' J. Soc. Nav. Arch. Jap., **152**, pp. 117–124.
[21] Rowe, A., and Blottiaux, O., 1993, ''Aspects of Modelling Partially Cavitating Flows,'' J. Ship Res., **37**, pp. 39–50.
[22] Brewer, J., and Kinnas, S., 1997, ''Experiment and viscous flow analyss on a partially cavitating hydrofoi,'' J. Ship Res., **41**, pp. 161–171.
[23] Mishkevich, V. G., 1995, ''Scale and roughness effects in ship performances in designer's viewpoint,'' Marine Technology, **32**, pp. 126–131.

Downloaded 03 Jun 2010 to 171.66.16.150. Redistribution subject to ASME license or copyright; see http://www.asme.org/terms/Terms_Use.cfm

[24] Amromin, E. L., Vasilyev, A. V., and Syrkin, E. N., 1995, ''Propeller Blade Cavitation Inception Prediction and Problems of Blade Geometry Optimization: Recent Investigation at the Krylov Shipbuilding Research Institute,'' J. Ship Res., **39**, pp. 202–212.
[25] Amromin, E. L., 2001, ''Stokes Wave Over Cavitating Vortex,'' Book of Abstracts, Fourth Intern. Symp. on Cavitation, Pasadena.
[26] Ceccio, S. L., and Brennen, C. E., 1992, ''Dynamics of Sheet Cavities on Bodies of Revolution'' ASME J. Fluids Eng., **114**, pp. 93–99.
[27] Goncharov, O., and Gorshkov, A. S., 1970, ''Cavitation Inception on a Body of Revolution,'' Proc. Krylov Ship. Res. Inst., St Petersburg **258** (in Russian).
[28] Arakeri, V. H., and Acosta, A. J., 1976, ''Cavitation Inception Observation on Axissymmetric Bodies at Supercritical Reynolds Numbers,'' J. Ship Res., **20**, pp. 40–50.

Downloaded 03 Jun 2010 to 171.66.16.150. Redistribution subject to ASME license or copyright; see http://www.asme.org/terms/Terms_Use.cfm

Models for Analysis of Water Hammer in Piping With Entrapped Air

M. A. Chaiko

K. W. Brinckman

PPL Corporation,
Nuclear Technology Group,
Allentown, PA 18101

Water hammer transients in a pipe line with an entrapped air pocket are analyzed with three one-dimensional models of varying complexity. The most simple model neglects the influence of gas-liquid interface movement on wave propagation through the liquid region and assumes uniform compression of the entrapped noncondensable gas. In the most complex model, the full two-region wave propagation problem is solved for adjoining gas and liquid regions with time varying domains. An intermediate model which allows for time variation of the liquid domain, but assumes uniform gas compression, is also considered. Calculations are carried out for a wide range of initial system pressure ranging from 0.101 MPa (14.7 psia) to 6.89 MPa (1000 psia). A step increase in pressure equal to 5 times the initial system pressure is imposed at the pipe inlet and the pressure response of the system is investigated. Results show that time variation of the liquid domain and nonuniform gas compression can be neglected for initial air volumes comprising 5% or less of the initial pipe volume. The uniform compression model with time-varying liquid domain captures all of the essential features predicted by the full two-region model for the entire range of pressure and initial gas volume considered in the study, and it is the recommended model for analysis of waterhammer in pipe lines with entrapped air.
[DOI: 10.1115/1.1430668]

1 Introduction

The prediction of pressure transients in separated gas-liquid systems is of particular interest in the power and process industries. For example, a gas accumulator, which in its simplest form consists of a vertical tube with noncondensable gas trapped against the top closed section of the tube, may be employed on the discharge piping of a positive displacement pump to dampen pressure pulses in piping networks. In some cases, a trapped gas pocket in a dead-end section of process piping can produce undesirable hydraulic interactions between pumps and check valves. The accumulated gas increases the compressibility of the inventory in the pump discharge piping, which can result in a flow/pressure surge during a rapid pump start. The flow surge causes the pump discharge check valve to quickly swing open. As the fluid momentum is arrested, over-compression of the gas pocket can produce a reverse flow in the pipe causing the check valve to slam closed, resulting in a waterhammer transient. In contrast, gas pockets can be used to lessen the severity of waterhammer transients in voided systems by providing a cushioning affect for an accelerating water slug. A study by the Electric Power Research Institute (EPRI) of hydraulic transients in cooling-water systems found that the presence of free air in water systems may be sufficient itself to limit the severity of a pressure surge and make the addition of vacuum breakers unnecessary [1]. The EPRI study reviewed data from a number of plant transients involving pump trips and liquid-column separation. In most cases, owing to vacuum breaker operation and the presence of free air in the system, a waterhammer was avoided following pump restart. While the air is effective in mitigating severe loads in voided systems, the peak pressure resulting from the rapid pressurization of a closed system with entrapped air can be significantly higher than in a purely liquid system [2, 3]. Since pressurization of the piping system will cause movement of the gas-liquid interface, a rigorous treatment of hydraulic transients in pipelines with entrapped air involves the solution of coupled pressure-wave propagation problems on time-varying domains.

In order to simplify engineering analyses, it is commonly assumed that the entrapped air will compress and expand uniformly, i.e., no spatial variation in the gas region, so that the pressure-wave propagation problem for the gas phase can be eliminated. With the assumption of uniform gas compression, effects of the entrapped air appear in the model as a nonlinear boundary condition imposed on the liquid-phase problem. For relatively small amounts of air, it is further assumed that the displacement of the interface can be considered small in comparison to the length of the liquid region, and therefore, pressure-wave transmission through the liquid is computed on the unperturbed spatial domain [4]. Interface displacement is derived from the computed liquid-phase velocity on the unperturbed interfacial boundary. The displacement is then incorporated into the calculation of the gas pressure which in turn feeds back into the liquid-region problem through the interfacial pressure boundary condition.

Martin [2] used a lumped parameter model to compute the pressure rise for an entrapped air pocket at the closed downstream end of a pipe caused by sudden pressurization at the upstream end. The model neglected liquid compressibility and assumed uniform gas compression. Calculations showed that the peak air pressure can be significantly higher than the driving pressure imposed at the upstream end of the pipe.

Qiu and Burrows [5] analyzed pressure surges caused by pump shutdown in pipe lines with entrapped air. Their model considered liquid compressibility and cavitation using the discrete cavity model described by Wiley and Streeter [3]; however, the entrapped gas was treated as a lumped system and the variation of the liquid column length was neglected. Their results showed that small amounts of entrapped air can cause an increased pressure surge as compared to the case of no entrapped air.

Lee and Martin [6] analytically and experimentally studied the pressurization of an air pocket trapped against the closed end of a

Contributed by the Fluids Engineering Division for publication in the JOURNAL OF FLUIDS ENGINEERING. Manuscript received by the Journal of Fluids Engineering Division, January 23, 2001; revised manuscript received October 30, 2001. Associate Editor: E. Graf.

 Copyright © 2002 by ASME

Downloaded 03 Jun 2010 to 171.66.16.150. Redistribution subject to ASME license or copyright; see http://www.asme.org/terms/Terms_Use.cfm

horizontal pipe containing water. Rapid pressurization of the air pocket was accomplished by the sudden opening of a valve separating the air, initially at atmospheric pressure, from the pressurized liquid. Liquid pressure was set by a pressure tank connected to the pipe inlet. Peak air pressure was determined for various tank pressures and for different volumes of entrapped air. Experimental results were compared to predictions obtained by solving the water hammer equations on the time-dependent liquid domain using a uniform compression/expansion model to account for the presence of the entrapped air. A simpler model which neglects compressibility of the liquid (rigid column analysis) was also considered. As shown by the Lee and Martin, rigid column theory breaks down for systems with small entrapped air pockets while water hammer theory shows fairly good overall agreement with the experiments.

Brinckman and Chaiko [7] evaluated the capability of the nuclear thermal-hydraulics code TRAC-BF1 for predicting peak pressure in an air-water-system pressurization transient. TRAC results for peak system pressure were compared against water-hammer solutions obtained by the method of characteristics for a pipe with small initial air volume ($\leqslant$10% of pipe volume). Results for peak pressure agreed favorably with the method of characteristics; however, on longer time scales TRAC tends to exaggerate the oscillation period and the solution suffers from artificial damping.

The present study examines the range of validity associated with certain approximations which are commonly made in carrying out water hammer analyses for systems with entrapped air. First, the study determines the conditions for which it is appropriate to neglect the movement of the gas-liquid interface in the solution of the water hammer equations for liquid pressure and velocity. If a method of characteristics approach is used to solve the water hammer equations, this simplification greatly reduces solution complexity because characteristics become linear paths in the x-t plane, and no interpolation is required to determine the origination points of characteristics on the previous time level. Clearly, the error associated with solving the waterhammer equations on the unperturbed liquid domain diminishes as the initial volume of the entrapped air decreases. The study determines the range of liquid fraction λ for which the fixed-liquid-domain approximation remains valid and discusses the error incurred by using the approximation for systems with large entrapped air pockets.

The second approximation that is examined in this study is the use of a uniform gas compression model to account for the influence of the entrapped air. To the best of the authors' knowledge, none of the water hammer analyses reported in the literature has quantitatively examined the importance of pressure-wave transmission within the gas region. Owing to its simplicity, the standard approach taken in water hammer analysis with entrapped air is to assume uniform compression and expansion of the gas pocket. The present study determines the effect of nonuniform gas compression on peak system pressure for systems with large entrapped air volumes.

While a lumped-parameter model for the entire air-water system can be obtained by neglecting the liquid compressibility and thereby treating the liquid phase as a rigid column along with assuming uniform gas compression, this model is not considered here as it has already been shown by Lee and Martin and by Guarga et al. [8] that rigid-column theory can significantly overpredict peak gas pressure for systems with small entrapped air pockets. Analyses of pressure surge in piping with entrapped air using the lumped-parameter model have also been carried out by Carrera et al. [9] and Hashimoto et al. [10].

Three different mathematical models for water hammer transients in a pipe line with entrapped air are compared in order to assess the range of validity associated with the fixed-liquid-domain and uniform gas compression approximations. The three models consist of:

I. Time-varying liquid length and nonuniform gas compression

II. Time-varying liquid length and uniform gas compression, and

III. Fixed liquid length and uniform gas compression

The physical model considered in this study consists of a vertical pipe containing liquid with an entrapped noncondensable gas pocket at the top closed end of the pipe. The gas pressure response to a sudden pressure disturbance imposed at the bottom open end of the pipe is investigated with respect to the initial fraction of the pipe length occupied by liquid. Gas compression is assumed to be isentropic regardless of whether it occurs uniformly or nonuniformly. Potential vapor formation in the liquid region is not considered. Based on subsidiary calculations carried out with a two-fluid (vapor/liquid), two-component (air/water) method, transient pressure can drop to saturation resulting in some liquid vaporization; however, void fractions in the liquid region are extremely small (10^{-10} to 10^{-6}), and the void formation was found to have no appreciable effect on the computed peak air pressure.

Use of Model I involves solving the one-dimensional, isentropic, compressible-flow equations on the time-varying gas domain. The classical waterhammer equations are solved on the time-varying liquid domain, and the gas and liquid-phase solutions are coupled at the moving interface by appropriate matching conditions. Rather than working explicitly with the time-varying domains, mappings are introduced to transform the governing gas-phase and liquid-phase equations to fixed spatial domains, and the resultant equations are solved using a first-order-accurate, method-of-characteristics approach. The influence of gas-phase wave transmission on system response is determined by comparing results for models I and II. Similarly, a comparison of results for models II and III indicates the importance of including interface movement in the solution of the liquid phase pressure and velocity. Solutions are compared over a wide range of the dimensionless parameter λ which is defined as the fraction of the tube length initially occupied by liquid. Values of λ range from 0.1 to 0.98. Calculations are carried out for three initial pipe pressures: 0.101 MPa (14.7 psia), 0.689 MPa (100 psia), and 6.89 MPa (1000 psia). The dimensionless parameter δ quantifies the magnitude of the pressure disturbance imposed at the inlet of the pipe. δ is defined as the ratio of the imposed disturbance to the initial system pressure. Values of δ ranging from 1 to 10 were considered in this study. Representative results for $\delta=5$ are presented.

Solutions to the governing equations for models I, II, and III are obtained using the method of characteristics. Solution of the model I and model II equations by the method of characteristics involves the use of linear interpolation to determine the origination points of characteristics on previous time levels. It is well known that the use of linear interpolation in the method of characteristics solution of waterhammer problems can introduce numerical damping into the solution. As reported by Wiley and Streeter [3] and confirmed in this study, the use of a higher-order interpolation scheme (second order interpolation) introduces extraneous fluctuations into the solution when applied to problems involving steep wave fronts. A linear interpolation scheme was therefore selected for use with the method of characteristics. Model II equations are also solved using a spectral method to assess the influence of numerical diffusion on the results obtained by using the method of characteristics with linear interpolation. Although the spectral method is not as computationally efficient as the method of characteristics, it does not introduce numerical damping into the solution and it is therefore a useful technique for assessing the degree of artificial damping present in the method of characteristics solution.

Calculation results for models I, II, and III are compared to the experimental results of Lee and Martin [6] obtained using an air/

Downloaded 03 Jun 2010 to 171.66.16.150. Redistribution subject to ASME license or copyright; see http://www.asme.org/terms/Terms_Use.cfm

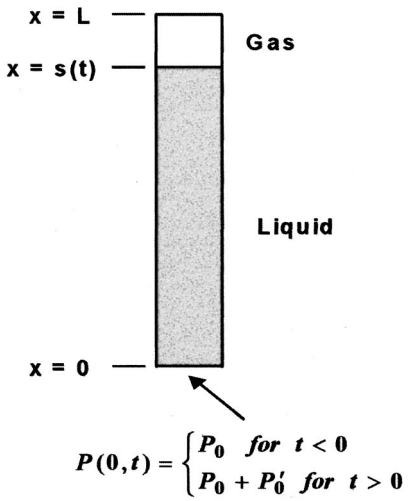

Fig. 1 Schematic of gas-liquid system

water system similar to that considered in this study. The experimental apparatus used by Lee and Martin contained a flow meter which produced a large irreversible pressure loss in the liquid region of the tube. For purposes of comparing against the experimental data, the inlet boundary condition in Eq. (2) was modified to include a large irreversible loss coefficient, and the liquid-phase wave speed was adjusted to be consistent with the value corresponding to the experimental apparatus. Unfortunately, the inclusion of the large loss coefficient had the effect of masking any differences between the three models. The comparison against experimental data does however demonstrate that all three models considered here can give an accurate prediction of peak pressure in air/water systems with large frictional resistances.

As part of this work, guidance is developed with regard to the range of validity of the simplified models II and III. Discussion is presented concerning the magnitude and type of errors which may be incurred if models II and III are employed for gas-liquid systems with relatively large air volumes.

2 Physical Model

The system considered in this work consists of a vertical pipe containing water with air entrapped at the top closed end of the pipe (see Fig. 1). Complete separation of the air from the liquid phase is assumed. Pipe length is 3.05 m (10 ft) and initial pressure ranges from 0.101 MPa (14.7 psia) to 6.89 MPa (1000 psia). The pipe has uniform cross-sectional flow area, and the pipe has an inside diameter of 0.0254 m (1 in). There is no heat transfer from the fluid to the pipe walls. Initially, the water and entrapped air are stationary and at a uniform pressure p_0 (gravity effects are neglected). At $t=0$, a step increase in pressure to p_0+p_0' is imposed at the pipe inlet ($x=0$), and the interaction between the entrapped air and the pressure disturbance is computed. In the model, the magnitude of the imposed pressure disturbance is described by the dimensionless parameter $\delta \equiv p_0'/p_0$. The initial temperature of the system is 294 K (70°F), and within the gas region, wall friction is neglected. The sound speed in the liquid phase is constant and taken equal to 1423 m/s (4670 ft/s) corresponding to the sound speed of 70°F water in a 0.0254 m (1 in.) steel pipe accounting for pipe wall elasticity. The air is assumed to obey the ideal gas equation of state, and compression and expansion of the air occurs isentropically.

3 Governing Equations

3.1 Model I. In the liquid region, the pressure and velocity are governed by the classical waterhammer equations [4],

$$\frac{\partial p_\ell}{\partial t} + \rho_\ell c_\ell^2 \frac{\partial u_\ell}{\partial x} = 0 \quad \text{and} \quad \frac{\partial u_\ell}{\partial t} + \frac{1}{\rho_\ell}\frac{\partial p_\ell}{\partial x} = -\frac{f}{2D} u_\ell |u_\ell| \quad (1)$$

where the subscript ℓ denotes the liquid phase, p is the pressure, u is the velocity, t is the time, x is the spatial coordinate, ρ is the density, f is the Darcy-Weisbach pipe friction factor, and D is the pipe diameter. The density in (1) is the unperturbed liquid density which differs negligibly from the actual fluid density. Liquid phase sound speed c_ℓ is assumed constant. Convection effects are neglected in the liquid phase since the liquid velocity is much less than the wave speed c_ℓ. The pipe friction factor f depends on the local Reynolds number and the relative roughness of the tube. These dependencies are incorporated into the model by using the single-phase friction factor correlations employed in the TRAC-BF1 thermal-hydraulics code [11]. The effects of viscous heating at the pipe wall are not incorporated into the friction factor calculation as sensitivity studies showed that varying fluid temperature and associated viscosity in the applicable range had a negligible effect on the computed peak gas pressures. At $t=0$, the pressure at the inlet of the pipe ($x=0$) begins to increase from p_0 to p_0+p_0' according to the relation

$$p_\ell(0,t) = p_0 + p_0'(1-e^{-bt}) \quad (2)$$

where the constant b is chosen so that the rise in pressure closely approximates a step increase. Physically, this boundary condition could correspond to the opening of a valve at the inlet of the pipe where the valve separates the pipe from a constant-pressure tank. The time-varying liquid domain is defined by $0<x<s(t)$ where $s(t)$ is the location of the gas-liquid interface (see Fig. 1).

In the gas region, one-dimensional isentropic flow of the noncondensable, ideal gas is governed by the respective continuity and momentum equations,

$$\frac{\partial c_g}{\partial t} + u_g \frac{\partial c_g}{\partial x} + \frac{(\gamma-1)}{2} c_g \frac{\partial u_g}{\partial x} = 0$$

and

$$\frac{\partial u_g}{\partial t} + u_g \frac{\partial u_g}{\partial x} + \frac{2}{(\gamma-1)} c_g \frac{\partial c_g}{\partial x} = 0, \quad (3)$$

where the adiabatic index $\gamma=1.4$ is the ratio of the gas specific heats. For the gas region, the domain is $s(t)<x<L$ where L is the total length of the pipe. Pressure in the gas phase is related to wave speed by the isentropic relations for an ideal gas,

$$\left(\frac{c_g}{c_{g^0}}\right)^2 = \left(\frac{p_g}{p_0}\right)^{1-1/\gamma} \quad \text{and} \quad c_{g^0}^2 = \frac{\gamma R T_0}{\omega}, \quad (4)$$

where R is the ideal gas constant, T is the absolute temperature, and ω is the molecular weight of the gas. The subscript g refers to the gas phase, and the subscript 0 refers to the initial state of the fluid. The top of the pipe is closed, and therefore, the appropriate boundary condition on the gas region is

$$u_g(L,t) = 0. \quad (5)$$

Since the pipe diameter is assumed large enough for surface tension effects to be negligible, and since there is no flow across the gas-liquid interface, the pressure and fluid velocity are continuous across the interface. Thus, matching conditions for pressure and velocity consist of

$$P_\ell[s(t),t] = P_g[s(t),t] \quad \text{and} \quad u_\ell[s(t),t] = u_g[s(t),t]. \quad (6)$$

The kinematic relation for the interface,

Downloaded 03 Jun 2010 to 171.66.16.150. Redistribution subject to ASME license or copyright; see http://www.asme.org/terms/Terms_Use.cfm

$$\frac{ds(t)}{dt} = u_\ell[s(t),t], \tag{7}$$

with $s(0)=s_0$, follows from the fact that the time rate of change of the interface location is equal to the liquid (or gas) velocity at the interface. Finally, initial conditions consistent with the assumption of uniform initial pressure and no fluid motion at $t=0$ consist of

$$p_\ell(x,0)=p_0, \quad u_\ell(x,0)=0, \quad \text{for } x\in(0,s_0) \tag{8}$$

$$p_g(x,0)=p_0, \quad \text{and } u_g(x,0)=0 \quad \text{for } x\in(s_0,L). \tag{9}$$

Governing equations are nondimensionalized and transformed to time-independent gas and liquid domains by introducing the following dimensionless variables and parameters:

$$\begin{gathered}\tau=\frac{tc_\ell}{L}, \quad y=\frac{x}{s}, \quad z=\frac{x-s}{L-s}, \quad U=\frac{u_\ell}{c_\ell}, \quad V=\frac{u_g}{c_{g^0}},\\ \varphi=\frac{p_\ell}{p_0}, \quad \psi=\frac{c_g}{c_{g^0}}, \quad \eta=\frac{s}{L}, \quad \delta=\frac{p_0'}{p_0}, \quad \kappa=\frac{c_{g^0}}{c_\ell},\\ \varepsilon=\frac{g_0p_0}{\rho_\ell c_\ell^2}, \quad \beta=\frac{bL}{c_\ell}, \quad \mu=\frac{fL}{2D}, \text{ and } \lambda=\frac{s_0}{L}.\end{gathered} \tag{10}$$

For the present study, $1\leqslant\delta\leqslant 10$, $\kappa=0.243$, $\beta=100$, and $\varepsilon=3.41\times10^{-4}$. The parameter λ is introduced to define the fraction of the pipe length initially occupied by liquid. In this study λ ranges from 0.1 to 0.98. Dimensionless continuity and momentum equations, respectively, for the liquid region become

$$\frac{\partial\varphi}{\partial\tau}+\frac{1}{\varepsilon\eta}\frac{\partial U}{\partial y}-y\frac{\dot\eta}{\eta}\frac{\partial\varphi}{\partial y}=0 \tag{11}$$

and

$$\frac{\partial U}{\partial\tau}+\frac{\varepsilon}{\eta}\frac{\partial\varphi}{\partial y}-y\frac{\dot\eta}{\eta}\frac{\partial U}{\partial y}=-\mu U|U| \tag{12}$$

where the liquid domain is now fixed such that $y\in(0,1)$. For the gas region, the dimensionless continuity and momentum equations are

$$(1-\eta)\frac{\partial\psi}{\partial\tau}+[\kappa V-(1-z)\dot\eta]\frac{\partial\psi}{\partial z}+\frac{\kappa(\gamma-1)}{2}\psi\frac{\partial V}{\partial z}=0 \tag{13}$$

and

$$(1-\eta)\frac{\partial V}{\partial\tau}+[\kappa V-(1-z)\dot\eta]\frac{\partial V}{\partial z}+\frac{2\kappa}{(\gamma-1)}\psi\frac{\partial\psi}{\partial z}=0, \tag{14}$$

where again the domain is now fixed with $z\in(0,1)$. The dimensionless kinematic relation for the interface response is

$$\dot\eta=U(1,\tau), \tag{15}$$

and the nondimensionalized initial, boundary, and matching conditions, respectively, consist of

$$\varphi(y,0)=1, \quad U(y,0)=0, \quad \psi(z,0)=1, \quad V(z,0)=0, \quad \eta(0)=\lambda, \tag{16}$$

$$\varphi(0,\tau)=1+\delta(1-e^{-\beta\tau}), \quad V(1,\tau)=0, \tag{17}$$

$$\varphi(1,\tau)=[\psi(0,\tau)]^{2\gamma/(\gamma-1)}, \text{ and } U(1,\tau)=\kappa V(0,\tau), \tag{18}$$

3.2 Model II. Model II is similar to model I in that it incorporates the effects of interface displacement on the transmission of pressure-waves through the liquid region; however, in the gas region, a simplified approach of assuming that the gas compresses and expands uniformly is taken, i.e., there is no spatial variation in the gas region. Liquid region governing equations consist of (11) and (12) along with boundary conditions,

$$\varphi(0,\tau)=1+\delta(1-e^{-\beta\tau}) \text{ and } \varphi(1,\tau)=\left[\frac{1-\lambda}{1-\eta(\tau)}\right]^\gamma, \tag{19}$$

and initial conditions,

$$\varphi(y,0)=1 \text{ and } U(y,0)=0. \tag{20}$$

The non-linear interfacial boundary condition in (19) which involves the dimensionless interface location $\eta(\tau)$, describes the pressure change in the gas as a result of adiabatic, uniform compression and expansion. $\eta(\tau)$ is determined from the solution of (15) with initial condition $\eta(0)=\lambda$.

3.3 Model III. As in the case of model II, the gas phase is assumed to compress and expand uniformly. An additional simplification is incorporated which involves solving the water hammer equations for the liquid-phase on the unperturbed domain, $x\in(0,s_0)$, i.e., the length of the liquid region remains constant. This approximation is equivalent to setting $\dot\eta=0$ and $\eta=\lambda$ in the transformed Eqs. (11) and (12). The governing equations become

$$\frac{\partial\varphi}{\partial\tau}+\frac{1}{\varepsilon\lambda}\frac{\partial U}{\partial y}=0 \text{ and } \frac{\partial U}{\partial\tau}+\frac{\varepsilon}{\lambda}\frac{\partial\varphi}{\partial y}=-\mu U|U| \tag{21}$$

where $y\in(0,1)$. Boundary and initial conditions consist of (19) and (20).

4 Solution Techniques

4.1 Method of Characteristics for Model I. The dimensionless governing Eqs. (11)–(18) for Model I are solved by the numerical method of characteristics. Liquid-phase equations are expressed in characteristic form through the standard approach of multiplying (11) by an unknown function Λ_1 and (12) by a second unknown function Λ_2 and then adding the resultant equations. It is found that if the ratio Λ_2/Λ_1 satisfies the relation $(\Lambda_2/\Lambda_1)^2=(\varepsilon\eta)^{-2}$, then the linear combination of (11) and (12) can be expressed in terms of total derivatives of φ and U along a curve in the $y-\tau$ plane. It then follows that φ and U are related by the compatibility equations,

$$\frac{d\varphi}{d\tau}\pm\frac{1}{\varepsilon}\frac{dU}{d\tau}\pm\frac{\mu}{\varepsilon}U|U|=0, \tag{22}$$

which hold along characteristic curves defined by solutions to

$$\frac{dy}{d\tau}=-\frac{\dot\eta}{\eta}y\pm\frac{1}{\eta}. \tag{23}$$

Note that if there is no movement of the interface then $\dot\eta=0$ and $\eta=\lambda$, and the characteristics for the liquid region become linear paths in the $y-\tau$ plane. It is the movement of the interface which introduces curvature into the liquid-phase characteristics. Also, note that $\dot\eta=1$ corresponds to movement of the interface at the sonic velocity. For the problem of interest, the interface moves at speeds much smaller than the sound speed, and therefore, $\dot\eta\ll1$. For the gas region, the compatibility equations,

$$\frac{d\psi}{d\tau}\pm\frac{(\gamma-1)}{2}\frac{dV}{d\tau}=0, \tag{24}$$

relate the dimensionless wave speed ψ for the gas to the dimensionless gas velocity V along the characteristics defined by solutions to

$$\frac{dz}{d\tau}=-\frac{(1-z)\dot\eta}{(1-\eta)}+\frac{\kappa(V\pm\psi)}{(1-\eta)}. \tag{25}$$

Initial conditions for (22)–(25) are derived from the initial, boundary and matching conditions (16)–(18). The gas region solution is coupled to that of the liquid region through the interfacial matching conditions (18).

Characteristic Eqs. (23) and (25) are solved numerically on a fixed spatial grid using first-order, semi-implicit temporal integra-

Downloaded 03 Jun 2010 to 171.66.16.150. Redistribution subject to ASME license or copyright; see http://www.asme.org/terms/Terms_Use.cfm

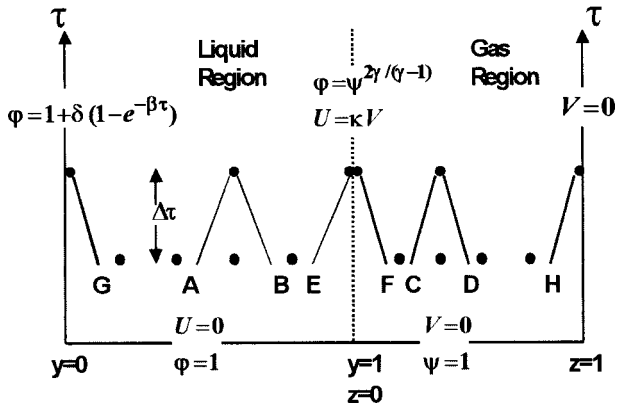

Fig. 2 Computational grid for method of characteristics solution of model I equations

tion. Integration is implicit with respect to the interface location η and the interface velocity $\dot{\eta}=U(1,\tau)$. The remaining variables on the right-hand side of (23) and (25) are treated explicitly. This approach is taken to avoid numerical instabilities in problems where stability constraints on the interface relation (15) are more restrictive, for the case of purely explicit integration, than they are for the characteristic equations. If purely explicit integration was used to solve the characteristic equations, the time step size could be limited by stability constraints on (15) rather than by constraints on the much more computationally intensive characteristic equations, and this could lead to unnecessarily large computation times.

In the present semi-implicit formulation, time step size is variable, and is determined at each time level such that a disturbance does not travel farther than the spatial separation between grid points during a single time step. Figure 2 shows the computational grid used in solving the governing Eqs. (22)–(25) by the numerical method of characteristics. In the interior of the gas and liquid regions, the solution is advanced in time by forcing the right-moving and left-moving characteristics to intersect on an interior grid point at the next time level. Over a single time step, characteristics are approximated by straight line segments. Characteristics will intersect at the target grid point, on the next time level, only if they originate from specific locations on the current time level. Origination points are denoted in Fig. 2 by A through D for the interior mesh points, by E and F for the interfacial grid points, and by G and H for the boundaries. Points of origination for the characteristics are computed as part of the solution. At interior mesh points where the right-moving and left-moving characteristics intersect, the compatibility Eqs. (22) for the liquid and (24) for the gas, are used to compute the dependent variables. When advancing the solution on the boundaries at $y=0$ and $z=1$, only the characteristic and compatibility relations corresponding to wave propagation into the boundary are used; the appropriate boundary condition from (17) provides the additional constraint needed to determine the solution. At the interface, interfacial matching conditions (18) are used in conjunction with the liquid-phase and gas-phase characteristic and compatibility relations which correspond to wave motion into the interface. Note that solution of the compatibility equations requires the values of the dependent variables at the characteristic origination points. Since characteristics do not, in general, originate from grid points at the previous time level, the dependent variables, at points A through H in Fig. 2, are determined by linear interpolation. There are M mesh points in the liquid region and N mesh points in the gas region.

In the solution scheme, the interface problem is solved first. Determining the interface location, velocity, and pressure involves only one characteristic from each region: the right-moving characteristic from the liquid and the left moving characteristic from the gas. Additional constraints are provided by the associated compatibility relations and by the two matching conditions (18). In solving for the interface location η^j at the new time level, and the interface velocity U_M^j which is equal to $\dot{\eta}^j$, the second-order accurate, finite-difference formula (trapezoid rule),

$$\eta^j=\eta^{j-1}+\frac{\Delta\tau}{2}[U_M^j+U_M^{j-1}] \tag{26}$$

is used to approximate the interface relation (15). Here the superscript denotes the time level, and the subscript denotes the spatial grid point. Although the remaining differential equations are integrated using a first-order accurate approach, a second-order method is used for the interface equation because it adds no computational complexity. Moreover, the interface location and interface velocity feed into all of the characteristic relations.

The finite-difference approximations to the compatibility, characteristic, and matching relations at the interface consist of:

$$\varphi_M^j-\varphi_E+\frac{1}{\varepsilon}(U_M^j-U_E)+\frac{\mu}{\varepsilon}U_E|U_E|=0, \tag{27}$$

$$1-y_E=\frac{\Delta\tau}{\eta^j}-\left(\frac{U_M^j}{\eta^j}\right)y_E\Delta\tau, \tag{28}$$

$$\psi_1^j-\psi_F-\frac{(\gamma-1)}{2}(V_1^j-V_F)=0, \tag{29}$$

$$z_F=\frac{\Delta\tau\nu}{(1-\eta^j)}(V_F-\psi_F)+\frac{(z_F-1)U_M^j\Delta\tau}{(1-\eta^j)}, \tag{30}$$

$$\varphi_M^j=(\psi_1^j)^{2\gamma/(\gamma-1)}, \text{ and} \tag{31}$$

$$U_M^j=\kappa V_1^j. \tag{32}$$

In addition, linear interpolation formulas are used to express φ_E, U_E, ψ_F, and V_F in terms of known values at neighboring mesh points on the same time level. Routine algebraic manipulations lead to the following relations for the dimensionless liquid pressure and the gas-phase wave speed at the interface:

$$\varphi_M^j=a_2-\frac{1}{\varepsilon}(U_M^j-a_3)-\frac{\mu}{\varepsilon}a_3|a_3|\Delta\tau, \tag{33}$$

and

$$\psi_1^j=a_{14}+\frac{\gamma-1}{2}a_{16}, \tag{34}$$

where the coefficients a_i are defined sequentially in the Appendix. Note that the coefficients a_i depend on the interface location η^j and the interface velocity U_M^j at the current time level. Therefore, an iterative procedure is used to compute the interface location, velocity, and pressure. The procedure begins with a guess for the interface velocity U_M^j. The interface location η^j is then computed from (26). Coefficients a_i are computed, and φ_M^j and ψ_1^j are calculated from (33) and (34). It is then determined if φ_M^j and ψ_1^j satisfy the matching condition (31); if not, an improved estimate for U_M^j is made and the process is repeated until (31) is satisfied to the desired degree of accuracy. In this work an outer-loop bisection procedure was used to determine U_M^j, and the magnitude of the error in the matching condition (31) was required to be less than 10^{-8}.

Once the interface problem is solved, η and $\dot{\eta}=U_M^j$, are known on the next time level. The solution is then advanced on the boundaries and interior grid points of the gas and liquid regions. Using first-order, finite-difference approximations for the characteristic and compatibility relations (22)–(25), and incorporating the boundary conditions (17), leads to the following results

Downloaded 03 Jun 2010 to 171.66.16.150. Redistribution subject to ASME license or copyright; see http://www.asme.org/terms/Terms_Use.cfm

$$U_1^j = \varepsilon \varphi_1^j + b_4, \tag{35}$$

$$\psi_N^j = d_4 + \frac{(\gamma-1)}{2} d_5 \tag{36}$$

$$\varphi_i^j = \frac{1}{2}(g_7+g_8), \quad U_i^j = \frac{\varepsilon}{2}(g_7-g_8) \quad \text{for} \quad i \in \{2,3,\ldots M-1\}, \tag{37}$$

$$\psi_i^j = \frac{1}{2}(h_{11}+h_{22}), \quad \text{and} \quad V_i^j = \frac{h_{11}-h_{22}}{\gamma-1} \quad \text{for} \quad i \in \{2,3,\ldots N-1\}, \tag{38}$$

where the b_i, d_i, g_i, and h_i are defined in the Appendix, and φ_1^j and V_N^j are determined based on the boundary conditions (17).

4.2 Method of Characteristics for Model II. In model II, the response of the gas region is described by the uniform-compression boundary condition (19) specified for φ on $y=1$. The interface problem consists of the compatibility and characteristic equations from (22) and (23) which correspond to wave propagation from the liquid into the interface (sign is "+") along with the second boundary condition in (19) and the linear interpolation formulas which express φ_E and U_E in terms of neighboring mesh point values. Approximating the characteristic and compatibility equations with first-order-accurate, finite-difference equations leads to the following expression for the liquid pressure at the interface:

$$\varphi_M^j = a_2 - \frac{1}{\varepsilon}(U_M^j - a_3) - \frac{\mu}{\varepsilon} a_3 |a_3| \tag{39}$$

As for model I, the solution scheme involves guessing the interface velocity U_M^j and then computing the interface location η^j from (26). The interfacial pressure φ_M^j is then calculated from (39). It is then determined if the relation

$$\varphi_M^j - \left(\frac{1-\lambda}{1-\eta^j}\right)^\gamma = 0 \tag{40}$$

from (19) is satisfied to the desired degree of accuracy. If it is not, then a root-finding scheme is used to obtain an improved estimate for U_M^j, which corresponds to $\dot{\eta}^j$, and the process is repeated until convergence is obtained. In this work, a bisection procedure is used to compute the interface velocity.

On the boundary $y=0$ and in the interior of the liquid region, the solution is advanced in the same manner as described for model I.

4.3 Method of Characteristics for Model III. In model III, uniform compression and expansion of the gas phase is assumed. In addition, the liquid-phase equations are solved on the unperturbed liquid domain. The liquid-phase equations in characteristic form consist of the compatibility Eqs. (22) and the associated characteristic equations,

$$\frac{dy}{d\tau} = \pm \frac{1}{\lambda} \tag{41}$$

With this model, the characteristics are lines of constant slope in the $y-\tau$ plane. This approximation greatly simplifies the solution because all characteristics originate and terminate at mesh points. Therefore, no interpolation is required.

4.4 Spectral Method for Model II. The uniform compression problem with time-varying liquid domain is also solved by means of finite Fourier transforms. This alternate solution approach is chosen to quantify the effects of artificial damping in the method-of-characteristics solution of the model II governing Eqs. (11), (12), (19), and (20). In the spectral solution, the dimensionless liquid pressure $\varphi(y,\tau)$ is expressed in terms of the uniformly convergent Fourier sine series,

$$\varphi(y,\tau) = \varphi(0,\tau) + y[\varphi(1,\tau)-\varphi(0,\tau)] + 2\sum_{k=1}^{\infty}\left[\frac{(-1)^k\varphi(1,\tau)-\varphi(0,\tau)}{k\pi} + \varphi_k(\tau)\right]\sin(k\pi y) \tag{42}$$

and the dimensionless velocity $U(y,\tau)$ is represented by the cosine series,

$$U(y,\tau) = U_0(\tau) + 2\sum_{k=1}^{\infty} U_k(\tau)\cos(k\pi y), \tag{43}$$

which is also uniformly convergent for $y \in [0,1]$. Series (42) is obtained by expanding $\varphi_y(y,\tau)$ as a cosine series on $y \in (0,1)$ and then integrating the series term-by-term. In (42) and (43), k represents a wave number for the monochromatic constituents of φ and U. k is the number of waves in an interval of length 2, and the associated wave length is $2/k$. The time-dependent coefficients $\varphi_k(\tau)$ and $U_k(\tau)$ are given by

$$\varphi_k(\tau) = \int_0^1 dy\, \sin(k\pi y)\varphi(y,\tau) \quad \text{and}$$

$$U_k(\tau) = \int_0^1 dy\, \cos(k\pi y) U(y,\tau). \tag{44}$$

Equations (44) define finite sine and cosine transforms for the dimensionless pressure and velocity; inversion formulas are given by (42) and (43).

Taking the sine transform of (11) and the cosine transform of (12) leads to the amplitude equations

$$\frac{d\varphi_k(\tau)}{d\tau} = \frac{k\pi}{\varepsilon\eta} U_k(\tau) + \frac{\dot{\eta}}{\eta}[\varphi(1,\tau)-\varphi(0,\tau)]J(0,k) + 2\frac{\dot{\eta}}{\eta}\sum_{j=1}^{\infty}[(-1)^j\varphi(1,\tau)-\varphi(0,\tau)+j\pi\varphi_j(\tau)]J(j,k), \tag{45}$$

$$\frac{dU_0(\tau)}{d\tau} = \frac{\dot{\eta}}{\eta}[U(1,\tau)-U_0(\tau)] + \frac{\varepsilon}{\eta}[\varphi(0,\tau)-\varphi(1,\tau)] - \int_0^1 dy\,\mu U(y,\tau)|U(y,\tau)|, \tag{46}$$

and

$$\frac{dU_k(\tau)}{d\tau} = -\frac{k\pi\varepsilon}{\eta}\varphi_k(\tau) + \frac{\varepsilon}{\eta}[\varphi(0,\tau)-(-1)^k\varphi(1,\tau)] - 2\pi\frac{\dot{\eta}}{\eta}\sum_{j=1}^{\infty} U_j(\tau) j J(k,j) - \int_0^1 dy\,\mu\cos(k\pi y)U(y,\tau)|U(y,\tau)|, \tag{47}$$

where $k \in \{1,2,3,\ldots\}$ and

$$J(j,k) \equiv \int_0^1 dy\, y\cos(j\pi y)\sin(k\pi y). \tag{48}$$

Initial conditions consist of

$$\varphi_k(0) = \frac{[1-(-1)^k]}{k\pi}, \quad U_0(0)=0, \quad \text{and} \quad U_k(0)=0 \quad \text{for} \quad k \in \{1,2,3,\ldots\}. \tag{49}$$

The kinematic interface relation (15) and a truncated set of amplitude equations are integrated numerically to obtain the time-

Downloaded 03 Jun 2010 to 171.66.16.150. Redistribution subject to ASME license or copyright; see http://www.asme.org/terms/Terms_Use.cfm

dependent Fourier coefficients $\varphi_k(\tau)$, $U_0(\tau)$, and $U_k(\tau)$ where k is restricted such that $k \in \{1,2,3,\ldots,K\}$. Converged solutions were obtained using $K=2^6=64$. The mode coupling integrals $J(j,k)$ are evaluated analytically.

When the cosine series (43) is truncated to $K+1$ Fourier modes, the smallest scale for spatial variations in the liquid velocity $U(y,\tau)$ is $2/K$ which corresponds to the minimum wave length which can be resolved by the series representation of U. Since the Fourier decomposition of U is band limited to wave lengths which are $\geqslant 2/K$, the computed liquid velocity $U(y,\tau)$ can be determined everywhere within the range $y \in [0,1]$ by sampling U at $K+1$ equally-spaced points spanning the range $y \in [0,1]$. At each time step during the numerical integration of the amplitude and interface equations, the $K+1$ values of U are obtained from the truncated form of (43) where the $K+1$ Fourier cosine coefficients are determined from the numerical integration of (46) and (47). Note that the nonlinear friction integrals which appear in (46) and (47) are the Fourier cosine coefficients of the function $W(y,\tau) \equiv \mu U(y,\tau)|U(y,\tau)|$. The Fourier cosine coefficients of W, and hence the friction integrals, can be expressed in terms of the discrete Fourier cosine transform,

$$\int_0^1 dy \cos(k\pi y)\mu U(y,\tau)|U(y,\tau)|$$

$$= \frac{1}{2K}[W(0,\tau)+W(1,\tau)(-1)^k] + \frac{1}{K}\sum_{p=1}^{K-1} W(y_p,\tau)\cos(k\pi y_p), \quad (50)$$

where $y_p = p/K$. Values of W at the $K+1$ discrete points required in (50) are determined from the definition of W and the values of U computed from the truncated form of (43) on the $K+1$ evenly spaced grid points spanning the range $y \in [0,1]$. Rather than evaluating the friction integral by the computationally-inefficient defining expression for the discrete Fourier cosine transform given in (50), a standard Fast Fourier Transform algorithm, which requires K to be an integral power of 2, is used [12]. Likewise, the inverse transform (43) is performed using a Fast Fourier inversion formula rather than directing performing the summation in (43) at each of the $K+1$ mesh points.

5 Results

Figure 3 compares predictions of peak gas pressure for models I, II, and III against the experimental results of Lee and Martin [6]. The experimental apparatus used by Lee and Martin to measure peak gas pressure in air-water systems is similar to the physical system considered in this work (Fig. 1). It consists of a horizontal pipe containing water and an entrapped air pocket at the closed downstream end of the pipe. Initially, the liquid and gas regions are separated by a closed valve. Gas pressure is 0.101 MPa (14.7 psia) at the start of the transient.

Liquid pressure is 0.608 MPa (88.2 psia) (6 times the initial gas pressure) prior to opening the valve separating the gas and liquid phases. At the inlet of the pipe, liquid pressure is maintained at 88.2 psia for the duration of the transient. A flow meter in the liquid region is responsible for a large irreversible pressure loss. Liquid region boundary and initial conditions presented in §3 were modified to emulate the experiments. As shown in Fig. 3, all three models predict peak gas pressures consistent with the experimental results. The small variation among the predictions is due to the large flow resistance associated with the flow meter. A large irreversible pressure loss tends to make the results rather insensitive to modeling assumptions. Specifically, the peak pressure is essentially independent of whether or not the model includes time variation of the liquid domain. Models I and II allow for changes in the liquid region length whereas model III does not. As will be shown from the calculation results presented below,

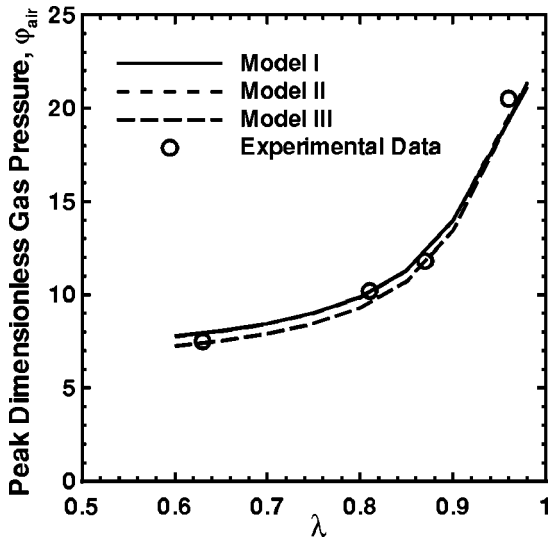

Fig. 3 Comparison of peak gas pressure predicted with models I, II, and III against experimental data of Lee and Martin [5]. Initial gas pressure is 0.101 MPa (14.7 psia) and liquid pressure at pipe inlet is 0.608 MPa (88.2 psia)

liquid region variation strongly affects peak pressure in systems where frictional effects are not dominant. This finding points out that model assessments based on experimental results from systems with strong frictional damping will not capture the limitations of relatively simple models which do not account for variation in the liquid region length.

Figure 4 compares the predicted temporal response of interfacial pressure for models I, II, and III. Results in Fig. 4 correspond to the case where 10 percent of the tube is initially filled with liquid ($\lambda = 0.1$). Initial pressure within the tube is 6.89 MPa (1000 psia), and at $t=0$, the inlet boundary pressure rises rapidly from 6.89 MPa (1000 psia) to 41.4 MPa (6000 psia) corresponding to $\delta = 5$. A high initial system pressure is chosen because predictions of system response have been found to be more sensitive to modeling assumptions in high-pressure systems. For $\lambda = 0.1$, the pressure disturbance imposed on the inlet of the tube at $\tau = 0$ reaches the gas-liquid interface at $\tau = 0.1$; at this time the gas pressure begins to increase. Because of the relatively large entrapped gas pocket considered in this case, the time scale associated with the change in gas pressure is considerably slower than the time scale associated with pressure wave transmission through the liquid region. As a result, there are many wave reflections which take place within the liquid region during a single gas compression cycle. Predicted gas-pressure oscillations decay with time because of the influence of wall friction within the liquid region. As can be seen from the model I results in Fig. 4, pressure-wave transmission within the gas region has a significant effect on the details of the interfacial pressure response. Pressure disturbances propagating through the gas region produce fluctuations in gas pressure not observed in the results obtained with uniform gas compression models (model II and model III); however, the leading order pressure response, which is generally the parameter of interest in engineering applications, shows excellent agreement with the prediction of model II; peak gas pressure and the dominant frequency component of the pressure oscillation match closely. Model III, on the other hand, significantly underpredicts the peak pressure and overpredicts the oscillation frequency. The spectral and method of characteristics solutions for model II show excellent agreement which indicates that numerical diffusion is not a factor in the method of characteristics solution of the model II equations for this value of λ. All of the method of characteristics solutions were carried out using 100 mesh points for the liquid region. For model I, 50 mesh points were found to be adequate for the gas region in

Downloaded 03 Jun 2010 to 171.66.16.150. Redistribution subject to ASME license or copyright; see http://www.asme.org/terms/Terms_Use.cfm

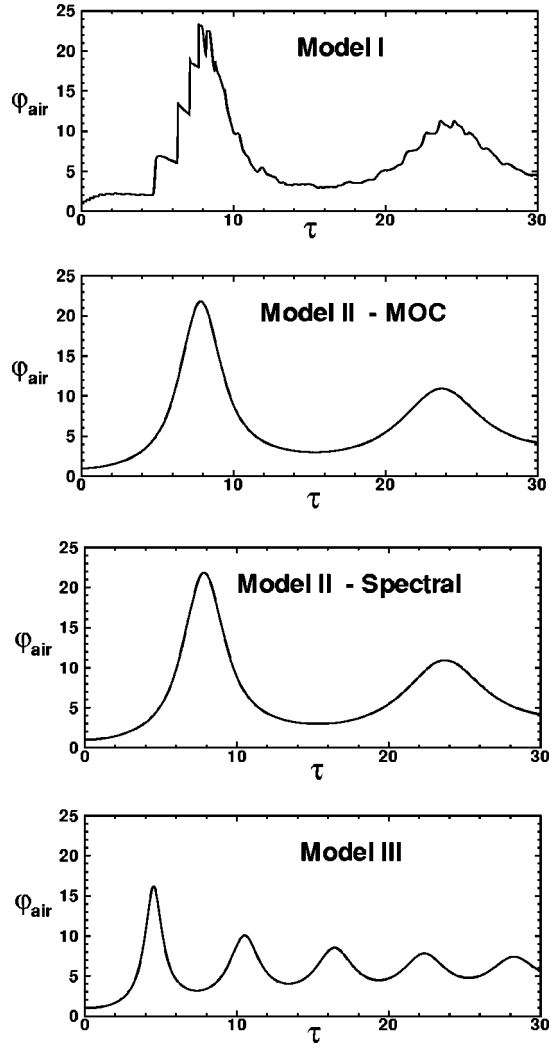

Fig. 4 Temporal response of dimensionless gas pressure for $\lambda = 0.1$, $\delta = 5$, and $P_0 = 6.89$ MPa (1000 psia)

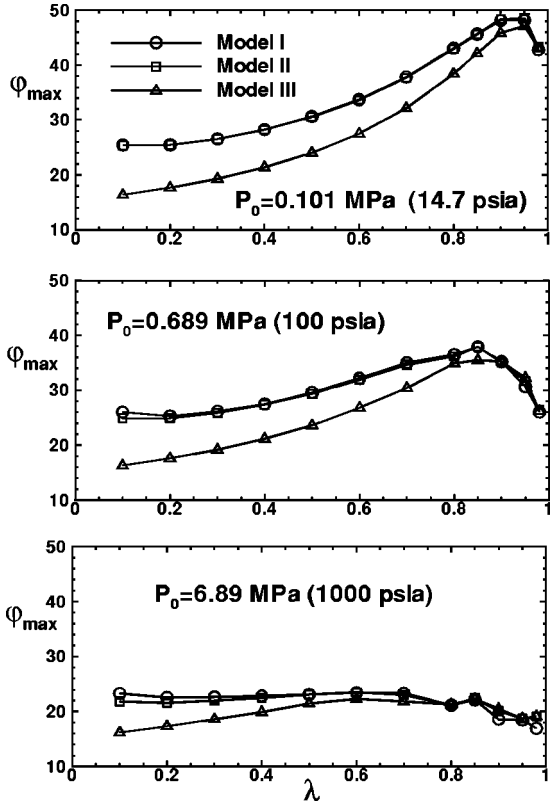

Fig. 5 Peak gas pressure predicted with models I, II, and III as a function of λ and initial air pressure with $\delta = 5$

all problems except for those in which $\lambda \rightarrow 1$. For other than the noted limit, doubling the mesh in the liquid and gas regions produced negligible changes in the calculated results. In the limit as $\lambda \rightarrow 1$, the gas pressure predicted by model I became sensitive to the gas-phase mesh spacing, and mesh-independent solutions could not be obtained. This encountered difficulty is attributed to numerical diffusion and is discussed later in this section. Mode-independent spectral solutions were obtained using 64 Fourier modes.

In waterhammer analyses, a key result is peak system pressure. Figure 5 compares peak interfacial pressure calculated with the three models for λ ranging from 0.1 to 0.98. Initial system pressure ranges from 0.101 MPa (14.7 psia) to 6.89 MPa (1000 psia). Results in Fig. 5 demonstrate that model II agrees very well with Model I over the entire range of initial pressure and λ with the exception of $\lambda \rightarrow 1$ at high initial pressure (6.89 MPa = 1000 psia). The good overall agreement between models I and II for peak pressure indicates that the uniform gas compression approximation remains valid even when the initial length of the gas region is comparable to, or larger than, the length of the liquid region. The fixed-liquid-domain approximation employed in model III can introduce significant, nonconservative error into the peak pressure when $\lambda < \sim 0.95$.

The discrepancy between the results predicted by models I, II, and III for the high-pressure system with $\lambda \rightarrow 1$ is unexpected based on physical considerations. When the initial length of the gas region is small compared to that of the liquid region, nonuniform compression of the gas and variation of the liquid length should become unimportant, and all three models should produce identical results. The source of disagreement can be seen from the temporal response of the interfacial pressure shown in Fig. 6 for an initial system pressure of 6.89 MPa (1000 psia) and $\lambda = 0.98$. Comparison of the pressure trace corresponding to model I against the response predicted by models II and III shows that there is strong numerical damping in the method of characteristics solution of the model I equations. The linear interpolation scheme used in the method of characteristics solution of the model I equations eliminates all of the fine structure in the pressure response. Even the method of characteristics solution of the model II governing equations shows some numerical damping when compared to the spectral solution for model II, although the degree of numerical damping is weak, and none of the important features of the solution are lost. For $\lambda = 0.98$, the spectral solution of the model II equations shows excellent agreement with the method of characteristics solution of model III. No numerical damping is present in the model III solution since the liquid-region characteristics are linear paths in the y-τ plane and no interpolation is required to determine the origination points of characteristics on previous time levels.

6 Conclusions

The presence of air in voided liquid systems can be effective in mitigating severe waterhammer loads due to rapid void collapse. For this reason, it is common to incorporate vacuum breakers into piping systems which are susceptible to liquid-column separation and void formation. Caution must be exercised when introducing air into liquid systems as the peak pressure resulting from the rapid pressurization of a closed system with entrapped air can be significantly higher than in a purely liquid system due to compres-

Downloaded 03 Jun 2010 to 171.66.16.150. Redistribution subject to ASME license or copyright; see http://www.asme.org/terms/Terms_Use.cfm

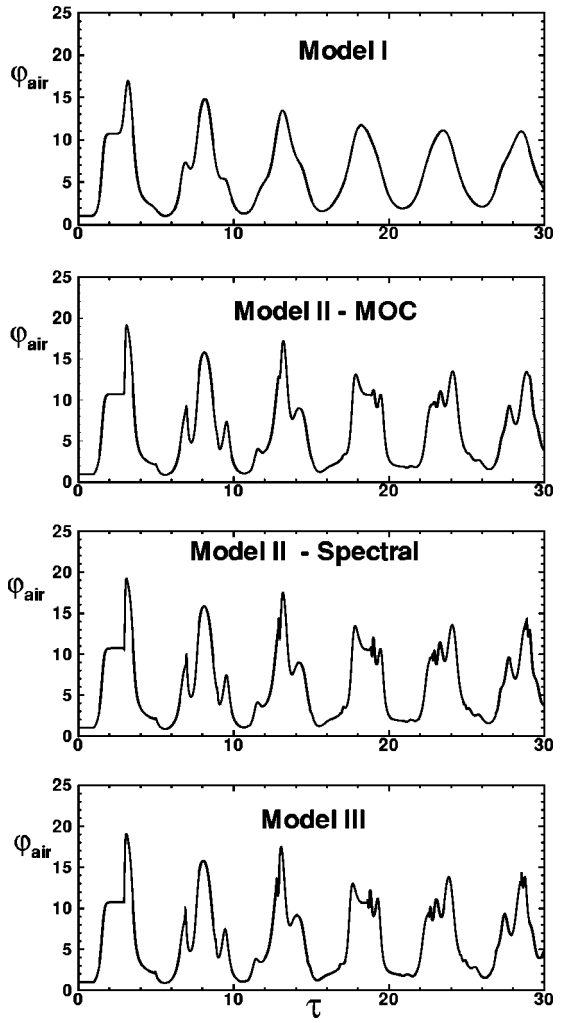

Fig. 6 Temporal response of dimensionless gas pressure for $\lambda = 0.98$, $\delta = 5$, and $P_0 = 6.89$ Mpa (1000 psia)

sion of the air as it arrests the momentum of the moving liquid. The consequences of introducing air into liquid systems should be analyzed in order to verify that the measures taken are effective in mitigating potential waterhammer events and to assess the impact of the air pocket on hydraulic transients. The present study compares models of varying complexity for analyzing pressure transients with entrapped air. The simplest model (model III) does not account for the influence of gas-liquid interface movement on pressure-wave transmission through the liquid region and assumes that the gas phase compresses and expands uniformly. It is found that this fixed-liquid-length approximation can introduce significant error into the predicted response when the initial gas region length is comparable to that of the liquid region. Approximating the time-varying liquid length with a fixed solution domain leads to an over-prediction in the frequency of interfacial pressure oscillations and an under-prediction of the pressure amplitude which is nonconservative for engineering considerations. For systems with $\lambda \geq 0.95$, it is appropriate to neglect variation of the liquid domain as there is negligible error introduced by this approximation. In fact, for $\lambda \geq 0.95$, use of model III is the most suitable approach because it produces results with higher resolution than more complex models considered. Model III underpredicts the peak gas pressure in systems with significant initial gas volume ($\lambda < 0.95$) and should not be used in these cases.

For systems with larger gas pockets, the effect of the change in liquid length with interface movement must be accounted for in the liquid-region model to produce an accurate system simulation. Present results demonstrate that the model with variable liquid length and uniform gas compression (model II) captures all of the essential features of the full two-region model (model I) for systems in which the gas region initially occupies a large fraction of the pipe length. Small-amplitude fluctuations in interfacial pressure predicted by model I for high-pressure systems with large gas volumes are not captured by model II; however, these fluctuations are generally not of interest in practical applications. Typically, the peak pressure and the dominant pressure oscillation frequency are the results of interest. For $\lambda \rightarrow 1$, results obtained with Model II show a small degree of artificial diffusion characterized by a loss of fine detail in the solution.

Table 1 Range of validity for waterhammer models

Model I – Time varying liquid domain, nonuniform gas compression
Model II – Time varying liquid domain, uniform gas compression
Model III – Fixed liquid domain, uniform gas compression

λ	Acceptable	Preferred	Remarks
≥0.95	II, III	III	Model I shows strong numerical diffusion as λ→1. Model II shows some numerical diffusion in this limit.
0.4<λ<0.95	I, II	II	Model III somewhat underpredicts peak pressure.
λ≤0.4	I, II	I	Model III significantly underpredicts peak pressure. Fine solution structure due to wave propagation in gas region is absent in models II and III.

The most complete model considered in the present study accounts for interface movement and tracks pressure wave propagation in both the gas and liquid regions. This model (model I) is capable of capturing small-amplitude, high-frequency fluctuations in the interfacial pressure which the other models are incapable of predicting. However, with model I, the effects of numerical diffusion are much more severe for $\lambda \rightarrow 1$; all of the fine solution structure is lost and at high system pressures this diffusion can lead to a slight under-prediction in peak pressure.

Results of the present study suggest that an appropriate model for pressure prediction in liquid systems with an entrapped gas pocket must account for the effect of interface movement on the liquid domain length if the model is to be valid for cases where gas pockets occupy greater than 5% of the pipe volume. It is further shown that the uniform gas compression model is valid over a range of system pressures and gas volumes and does not suffer from the numerical diffusion of the more complicated model which tracks pressure wave propagation in the gas space. These findings suggest that model II considered in the present study will provide a robust methodology for analyzing waterhammer transients in systems with entrapped gas. Conclusions regarding the range of applicability for each of the three models assessed are summarized in Table 1.

Appendix

The Coefficients a_i, b_i, d_i, g_i, and h_i

$$a_1 = \frac{\eta^j - \Delta\tau}{\eta^j - \Delta\tau U_M^j},$$

$$a_2 = \varphi_{M-1}^{j-1} + \left(\frac{\varphi_M^{j-1} - \varphi_{M-1}^{j-1}}{\Delta y}\right)(a_1 - y_{M-1}),$$

$$a_3 = U_{M-1}^{j-1} + \left(\frac{U_M^{j-1} - U_{M-1}^{j-1}}{\Delta y}\right)(a_1 - y_{M-1}),$$

Downloaded 03 Jun 2010 to 171.66.16.150. Redistribution subject to ASME license or copyright; see http://www.asme.org/terms/Terms_Use.cfm

$$a_4=\frac{\Delta\tau\kappa}{1-\eta^j+\Delta\tau U_M^j},$$

$$a_5=\frac{\Delta\tau U_M^j}{1-\eta^j+\Delta\tau U_M^j},$$

$$a_6=\frac{\psi_2^{j-1}-\psi_1^{j-1}}{\Delta z},$$

$$a_7=1-a_4a_6,$$

$$a_8=a_4a_6,$$

$$a_9=\psi_1^{j-1}+a_5a_6,$$

$$a_{10}=\frac{V_2^{j-1}-V_1^{j-1}}{\Delta z},$$

$$a_{11}=-a_4a_{10},$$

$$a_{12}=1+a_4a_{10},$$

$$a_{13}=V_1^{j-1}+a_5a_{10},$$

$$a_{14}=\frac{a_9a_{12}-a_8a_{13}}{a_7a_{12}-a_8a_{11}},$$

$$a_{15}=\frac{a_7a_{13}-a_9a_{11}}{a_7a_{12}-a_8a_{11}}$$

$$a_{16}=\frac{U_M^j}{\kappa}-a_{15},$$

$$b_1=\frac{\Delta\tau}{\eta^j-\Delta\tau U_M^j},$$

$$b_2=\varphi_1^{j-1}+(\varphi_2^{j-1}-\varphi_1^{j-1})\frac{b_1}{\Delta y},$$

$$b_3=U_1^{j-1}+(U_2^{j-1}-U_1^{j-1})\frac{b_1}{\Delta y},$$

$$b_4=-\varepsilon b_2+b_3-\Delta\tau\mu b_3|b_3|,$$

$$d_1=\frac{\Delta\tau\kappa}{1-\eta_j+\Delta\tau U_M^j},$$

$$d_2=\frac{d_1}{\Delta z}(\psi_N^{j-1}-\psi_{N-1}^{j-1}),$$

$$d_3=\frac{d_1}{\Delta z}(V_N^{j-1}-V_{N-1}^{j-1}),$$

$$d_4=\frac{\psi_N^{j-1}(1+d_3)-d_2V_N^{j-1}}{(1+d_2)(1+d_3)-d_2d_3},$$

$$d_5=\frac{V_N^{j-1}(1+d_2)-d_3\psi_N^{j-1}}{(1+d_2)(1+d_3)-d_2d_3},$$

$$g_1=\frac{y_i\eta^j-\Delta\tau}{\eta^j-\Delta\tau U_M^j},$$

$$g_2=\frac{y_i\eta^j+\Delta\tau}{\eta^j-\Delta\tau U_M^j},$$

$$g_3=\varphi_{i-1}^{j-1}+\frac{\varphi_i^{j-1}-\varphi_{i-1}^{j-1}}{\Delta y}(g_1-y_{i-1}),$$

$$g_4=U_{i-1}^{j-1}+\frac{U_i^{j-1}-U_{i-1}^{j-1}}{\Delta y}(g_1-y_{i-1}),$$

$$g_5=\varphi_i^{j-1}+\frac{\varphi_{i+1}^{j-1}-\varphi_i^{j-1}}{\Delta y}(g_2-y_i),$$

$$g_6=U_i^{j-1}+\frac{U_{i+1}^{j-1}-U_i^{j-1}}{\Delta y}(g_2-y_i),$$

$$g_7=g_3+\frac{g_4}{\varepsilon}-\frac{\mu}{\varepsilon}\Delta\tau g_4|g_4|,$$

$$g_8=g_5-\frac{g_6}{\varepsilon}+\frac{\mu}{\varepsilon}\Delta\tau g_6|g_6|,$$

$$h_1=\frac{z_i(1-\eta^j)+\Delta\tau U_M^j}{1-\eta^j+\Delta\tau U_M^j},$$

$$h_2=\frac{\kappa\Delta\tau}{1-\eta^j+\Delta\tau U_M^j},$$

$$h_3=\frac{h_2}{\Delta z}(V_i^{j-1}-V_{i-1}^{j-1}),$$

$$h_4=1+h_3,$$

$$h_5=V_{i-1}^{j-1}+\frac{h_1-z_{i-1}}{\Delta z}(V_i^{j-1}-V_{i-1}^{j-1}),$$

$$h_6=\frac{h_2}{\Delta z}(\psi_i^{j-1}-\psi_{i-1}^{j-1}),$$

$$h_7=1+h_6,$$

$$h_8=\psi_{i-1}^{j-1}+\frac{h_1-z_{i-1}}{\Delta z}(\psi_i^{j-1}-\psi_{i-1}^{j-1}),$$

$$h_9=\frac{h_5h_7-h_3h_8}{h_4h_7-h_3h_6},$$

$$h_{10}=\frac{h_4h_8-h_5h_6}{h_4h_7-h_3h_6},$$

$$h_{11}=h_{10}+\frac{\gamma-1}{2}h_9,$$

$$h_{12}=\frac{z_i(1-\eta^j)+\Delta\tau U_M^j}{1-\eta^j+\Delta\tau U_M^j},$$

$$h_{13}=\frac{\Delta\tau\kappa}{1-\eta^j+\Delta\tau U_M^j},$$

$$h_{14}=\psi_i^{j-1}+\frac{h_{12}-z_i}{\Delta z}(\psi_{i+1}^{j-1}-\psi_i^{j-1}),$$

$$h_{15}=h_{13}(\psi_{i+1}^{j-1}-\psi_i^{j-1})/\Delta z,$$

$$h_{16}=1-h_{15},$$

$$h_{17}=V_i^{j-1}+\frac{h_{12}-z_i}{\Delta z}(V_{i+1}^{j-1}-V_i^{j-1}),$$

$$h_{18}=h_{13}(V_{i+1}^{j-1}-V_i^{j-1})/\Delta z,$$

$$h_{19}=1+h_{18},$$

$$h_{20}=\frac{h_{14}h_{18}+h_{16}h_{17}}{h_{15}h_{18}+h_{16}h_{19}},$$

$$h_{21}=\frac{h_{14}h_{19}-h_{15}h_{17}}{h_{15}h_{18}+h_{16}h_{19}},\ \text{and}$$

$$h_{22}=h_{21}-(\gamma-1)h_{20}/2.$$

Downloaded 03 Jun 2010 to 171.66.16.150. Redistribution subject to ASME license or copyright; see http://www.asme.org/terms/Terms_Use.cfm

References

[1] Martin, C. S., and Wiggert, D. C., 1989, ''Hydraulic Transients in Cooling-Water Systems,'' EPRI GS-6427, Electric Power Research Institute, June.

[2] Martin, C. S., 1976, ''Entrapped Air in Pipelines,'' Second BHRA International conference on pressure surges, The City University, London, Sept. 22–24, Paper F2.

[3] Wylie, E. B., and Streeter, V. L., 1978, *Fluid Transients*, McGraw-Hill, New York.

[4] Moody, F. J., 1990, *Introduction to Unsteady Thermofluid Mechanics*, Wiley, New York.

[5] Qiu D. Q., and Burrows R., 1996, ''Prediction of Pressure Transients with Entrapped Air in a Pipeline,'' Seventh International Conference on Pressure Surges, BHR Group, Harrogate, England, Apr., Paper 251–263.

[6] Lee N. H., and Martin, C. S., 1999, ''Experimental and Analytical Investigation of Entrapped Air in a Horizontal Pipe,'' Proceedings of the 3rd ASME/JSME Joint Fluids Engineering Conference, July 18–23, San Francisco, CA.

[7] Brinckman, K. W., and Chaiko, M. A., 2001, ''Assessment of TRAC-BF1 for Waterhammer Calculations with Entrapped Air,'' J. Nucl. Sci. Technol., **133**, No. 1, Jan., pp. 133–139.

[8] Guarga, R., Acosta, A., and Lorenzo, E., 1996, ''Dynamic Compression of Entrapped Air Pockets by Elastic Water Columns,'' *Hydraulic Machinery and Cavitation*, pp. 710–719, E. Cabrera et al. eds., Kluwer Academic Publishers, The Netherlands.

[9] Cabrera, E., Abreu, J., Pérez, R., and Vela, A., 1992, ''Influence of Liquid Length Variation in Hydraulic Transients,'' J. Hydraul. Eng., **118**, No. 12, Dec., pp. 1639–1650.

[10] Hashimot, K., Imaed, M., and Osayam, A., 1988, ''Transients of Fluid Lines Containing an Air Pocket or Liquid Column,'' Journal of Fluid Control, **18**, No. 4, June, pp. 38–54.

[11] Borkowski, J. A., and Wade, N. L., ed., 1992, TRAC-BF1/MOD1 Models and Correlations, NUREG/CR-4391.

[12] Press, W. H., Teukolsky, S. A., Vetterling, W. T., and Flannery, B. P., 1992, *Numerical Recipes in FORTRAN: The Art of Scientific Computing*, 2nd Edition, pp. 508–515, Cambridge University Press.

Downloaded 03 Jun 2010 to 171.66.16.150. Redistribution subject to ASME license or copyright; see http://www.asme.org/terms/Terms_Use.cfm

An Experimentally Validated Model for Two-Phase Pressure Drop in the Intermittent Flow Regime for Circular Microchannels

S. Garimella[1]
e-mail: garimell@iastate.edu

J. D. Killion

J. W. Coleman

Department of Mechanical Engineering,
Iowa State University,
2030 H. M. Black Engineering Building,
Ames, IA 50011

This paper reports the development of an experimentally validated model for pressure drop during intermittent flow of condensing refrigerant R134a in horizontal microchannels. Two-phase pressure drops were measured in five circular channels ranging in hydraulic diameter from 0.5 mm to 4.91 mm. For each tube under consideration, pressure drop measurements were first taken over the entire range of qualities from 100% vapor to 100% liquid. In addition, the tests for each tube were conducted for five different refrigerant mass fluxes between 150 kg/m^2-s and 750 kg/m^2-s. Results from previous work by the authors on condensation flow mechanisms in microchannel geometries were then used to identify data that corresponded to the intermittent flow regime. A pressure drop model was developed for a unit cell in the channel based on the observed slug/bubble flow pattern for these conditions. The unit cell comprises a liquid slug followed by a vapor bubble that is surrounded by a thin, annular liquid film. Contributions of the liquid slug, the vapor bubble, and the flow of liquid between the film and slug to the pressure drop were included. Empirical data from the literature for the relative length and velocity of the slugs and bubbles, and relationships from the literature for the pressure loss associated with the mixing that occurs between the slug and film were used with assumptions about individual phase friction factors, to estimate the total pressure drop in each unit cell. A simple correlation for non-dimensional unit-cell length based on slug Reynolds number was then used to estimate the total pressure drop. The results from this model were on average within ±13.4% of the measured data, with 88% of the predicted results within ±25% of the 77 measured data points. [DOI: 10.1115/1.1428327]

Keywords: Two-Phase, Pressure Drop, Microchannel, Intermittent Flow

Introduction

Heat transfer coefficients and pressure drop in phase-change processes are a strong function of the local vapor quality. For condensation inside tubes, different flow patterns are established at different regions of the condenser as the fluid undergoes a transition from vapor to liquid along the length of the tube. Accurate heat transfer and pressure drop predictions require an approach that accounts for the variation in flow patterns as the quality changes. Circular and noncircular microchannel tubes are being used in space-conditioning condensers, particularly by the automotive industry. There is also considerable interest in heat transfer and pressure drop in microchannel geometries for a variety of applications because of the extremely high heat transfer coefficients that these geometries offer. Coleman and Garimella [1–3] demonstrated in a study on two-phase flow of air-water mixtures and refrigerant R134a through small diameter circular and noncircular geometries that flow regime transitions in such geometries are different from those observed in larger diameter circular tubes. This is because of significant differences between large round tubes and the smaller tubes in the relative magnitudes of gravity, shear, and surface tension forces, which determine the flow regime established at a given combination of liquid and vapor-phase velocities. Thus, extrapolation of large round tube correlations to smaller diameters and noncircular geometries could introduce substantial errors into pressure drop and heat transfer predictions.

Limited research has been conducted on addressing the effect of tube hydraulic diameter on pressure drop and heat transfer coefficients during condensation. The relatively few studies on two-phase flow in small diameter round tubes have primarily used isothermal air-water mixtures. Suo and Griffith [4] investigated intermittent flow of several gas-liquid combinations in horizontal tubes with hydraulic diameters ranging from 1.03 to 1.6 mm. They found that, in this flow regime, the bubbles are long cylindrical shapes separated from the wall by a surrounding liquid film. Also, all the bubbles travel at nearly the same velocity and thus do not agglomerate, but are separated by a liquid slug. Dimensional analysis was used to choose seven non-dimensional groups to characterize the system. However, it was found experimentally that the ratio of the velocity of the bubble (equivalent to the translation velocity of the slug/plug when there is no vapor entrainment in the liquid slug) to the velocity in the slug (the sum of the superficial velocity of the liquid and gas phases) could be correlated with just two of the parameters, which are functions of surface tension, liquid density, liquid viscosity, tube diameter and bubble velocity. Their analysis assumes laminar flow and it was shown that if the bubble-to-slug velocity ratio is known, then the cross-sectional area of the film around the bubbles may be calculated. In their analysis, the authors assumed that the liquid in the film around the bubble was effectively stagnant, noting that, for all the gas-liquid combinations considered, the viscosity of the gas

[1]Author to whom all correspondence should be addressed.

Contributed by the Fluids Engineering Division for publication in the JOURNAL OF FLUIDS ENGINEERING. Manuscript received by the Fluids Engineering Division January 26, 2001; revised manuscript received September 12, 2001. Associate Editor: A. K. Prasad.

 Copyright © 2002 by ASME

Downloaded 03 Jun 2010 to 171.66.16.150. Redistribution subject to ASME license or copyright; see http://www.asme.org/terms/Terms_Use.cfm

is much lower than that of the liquid. A corollary of this assumption is that the pressure drop in the bubble/film region is negligible. They suggest that their experimental results corroborate this assumption and the implication is that the velocity ratio is ''determined at the nose of the bubble.'' Finally, the authors showed that as the non-dimensional bubble velocity increases, the ratio of bubble velocity to the average liquid velocity in the slug obtains a nearly constant value of about 1.19 which compares well with the literature.

Dukler and Hubbard [5] developed a model for the pressure drop in intermittent flow through 38-mm diameter horizontal tubes using air-water mixtures. They used several methods to collect data from this system including fast-response pressure transducers, photography, motion pictures and dye tracers. For most of the conditions tested, the pressure loss associated with accelerating the slow-moving liquid film as it is overtaken by the faster-moving liquid slug was a significant portion of the total pressure drop. Their model consists of a slug of liquid with some gas entrained, which has a blunt nose due to the take-up of the liquid film. The bubble/film portion of the flow was assumed to be stratified and cause negligible pressure drop. The nose of the bubble is tapered reflecting a more gradual shedding process forming the liquid film. The authors assumed a turbulent velocity profile in the slug and assumed that the portion of the liquid slug which is moving at less than the average velocity determines the ''shedding'' rate of the slug, or the rate at which the film is left behind. Using this approach, they fit the following simple logarithmic expression to their more complex analytical solutions for the ratio of the shape-translation velocity (bubble velocity if the slug is assumed to contain no gas) to slug velocity as a function of slug Reynolds number:

$$U_{\text{translation}}/U_{\text{slug}} = 0.021 * \ln(\text{Re}_{\text{slug}}) + 1.022 \quad (1)$$

For the Re_{slug} range considered in their work, $30{,}000 < \text{Re}_{\text{slug}} < 400{,}000$, the resulting velocity ratio varied from 1.25 to 1.30. The authors also developed expressions for the relative slug length and pressure loss due to the acceleration of the film to complete the model. The independent variables required to calculate the total pressure drop, in addition to the physical properties and tube dimensions, are simply the liquid and gas flow rates, the slug frequency (which is used to calculate the total length of a slug and bubble pair), and the fractional entrainment of gas in the liquid slug. The latter two values were obtained from their data.

Fukano et al. [6] investigated the flow of air and water though horizontal tubes with diameters ranging from 1.0 to 4.9 mm. They used visualization and pressure drop experiments to develop empirical two-phase pressure-drop multipliers for several flow regimes and to validate an intermittent flow model. They showed from their visualization work that, in the slug/plug regime, the ratio of bubble velocity to slug velocity is about 1.2 for all test conditions. Furthermore, for each tube diameter, they were able to correlate the relative slug length as a function of superficial velocities using a simple proportionality constant; that is, $L_{\text{slug}}/(L_{\text{slug}}+L_{\text{bubble}}) = kj_L/(j_L+j_V)$. They neglected the pressure drop in the bubble/film region and assumed a simple expression for the losses associated with the film-to-slug transitions. The method to calculate slug length (or frequency) is not described, but they showed that the losses associated with the film-to-slug transitions could be a significant portion of the total pressure drop.

In the study by Coleman and Garimella [1], the effect of tube diameter and shape on flow patterns and flow regime transitions for air-water mixture flow in tubes with small hydraulic diameters (1.3 mm to 5.5 mm) was investigated. Gas and liquid superficial velocities were varied from 0.1 m/s to 100 m/s, and 0.01 m/s to 10.0 m/s, respectively. They showed that while pipe diameter and surface tension may have a negligible effect on flow regime transitions in tubes with diameters greater than 10 mm ([7]; [8]), for smaller tubes these factors play an important role. Therefore, flow regime maps such as those developed by Mandhane et al. [7] based upon data from larger tubes may not be applicable for a smaller tube diameter range. It was also shown that the theoretical results of Taitel and Dukler [9] and the assumptions inherent in these analyses may not be valid for tube diameters less than about 5 mm. It was shown that as the tube diameter decreases, the transition to a dispersed flow regime occurs at a higher value of the superficial liquid velocity. Also, the transition to annular flow occurs at a nearly constant value of the superficial gas velocity, which approaches a limiting value as the tube diameter decreases. Another effect of surface tension and tube diameter is to suppress the stratified regime in small diameter tubes and to increase the size of the intermittent regime. Thus, this study showed that the flow patterns and the respective transitions change significantly with tube diameter and shape.

Coleman and Garimella [2,3] studied the influence of tube miniaturization on two-phase flow mechanisms during condensation of refrigerant R134a in a 4.91-mm round tube and four square tubes with hydraulic diameters ranging from 1 mm–4 mm. For each tube under consideration, flow mechanisms were recorded over the entire range of qualities $0 < x < 1$, and for five different mass fluxes between 150 kg/m^2-s and 750 kg/m^2-s. Approximately 50 data points were recorded for each tube to obtain a comprehensive understanding of the effects of geometry, mass flux and quality on the phase-change flow mechanisms. The flow mechanisms were categorized into four different flow regimes: intermittent, wavy, annular, and dispersed flow. In addition, the large amount of data over a wide range of test conditions enabled the delineation of several different flow patterns within each flow regime, which provided a clearer understanding of the different modes of two-phase flow. For example, the annular regime was divided into the mist, annular film, annular ring, wave ring and wave packet flow patterns. The wavy flow regime was divided into the discrete- and disperse-wave flow patterns. The dispersed flow regime primarily consisted of the bubble flow pattern. The intermittent regime was divided into the plug and slug flow patterns. Transition lines between the respective flow patterns and regimes on these maps were established based on the experimental data. It was found that the hydraulic diameter has a substantial effect on the flow patterns and transitions. As the hydraulic diameter decreases, the overall size of the annular regime increases, and conversely, the wavy regime decreases in size. Progressing from a hydraulic diameter of 3 mm to 2 mm, the disperse wave pattern disappears and only the discrete wave pattern remains. A further decrease in hydraulic diameter to 1 mm causes the wavy regime to disappear completely, and is replaced by the annular film flow pattern. The size of the intermittent regime increases as the hydraulic diameter decreases, with a particularly large intermittent regime for the 1-mm tube, indicating a diminishing influence of gravity forces.

In the present study, the work of Coleman and Garimella [2,3] was extended to investigate pressure drop during condensation of refrigerant R134a in small diameter round tubes. Two-phase pressure drops in fourteen different circular and noncircular (square, rectangular, triangular and other shapes) tubes of hydraulic diameters ranging from 0.4 mm to 4.9 mm were investigated by the present authors to span the range of flow rates that covered each of the flow regimes described above. However, the focus of the present work is the measurement and modeling of two-phase pressure drop during condensation in the **intermittent** flow regime for round tubes of varying diameters. Tran et al. [10] have recently reported similar measurements of pressure drop in **boiling** flow of three refrigerants including R-134a in small diameter tubes over a wide range of conditions and have developed a correlation which is an enhancement and modification of existing large-tube correlations.

Experimental Approach

The test facility used by Coleman and Garimella [2,3] for the R134a phase-change flow visualization studies was also used in

Downloaded 03 Jun 2010 to 171.66.16.150. Redistribution subject to ASME license or copyright; see http://www.asme.org/terms/Terms_Use.cfm

the present study. A detailed description of the facility and the experimental techniques used was provided in those papers. A brief summary of the experimental approach is presented here. A schematic of the test loop is shown in Fig. 1. Subcooled liquid refrigerant exiting the set of postcondensers flows through the coriolis mass flowmeter. The refrigerant is pumped through a tube-in-tube evaporator, in which hot water flows counter-current to the refrigerant to boil and superheat it. The superheated state is ensured by a combination of a sight glass, temperature and pressure measurements. Temperature and pressure measurements at the superheated state enable measurement of the refrigerant enthalpy. The superheated vapor enters one of two precondensers, where city water of the desired (variable) flow rate is used to partially condense the vapor. Each precondenser is a tube-in-tube heat exchanger, with the difference being that one of the heat exchangers is approximately 3 times longer than the other. These two precondensers and varying cooling water flow rates through them help establish a wide range of refrigerant conditions at the test section inlet. The outlet state of the test section was calculated using a different independent measurement of this state. Thus, the set of postcondensers downstream of the test section is used to completely condense and subcool the refrigerant. The subcooled refrigerant enthalpy at the exit of the postcondenser and an energy balance on this condenser are used to deduce the refrigerant enthalpy and quality at the test section outlet. The measured pressure drop in the test section is characteristic of the average quality in the test section.

Refrigerant exiting the precondensers enters the test section. The circular geometries tested in this study are shown in Fig. 2. For the two largest diameter (4.91 mm and 3.05 mm) tubes, the test sections consisted of counterflow, tube-in-tube heat exchangers. For the smaller tubes, the test sections were fabricated as flat tubes with multiple extruded parallel channels. Three such tubes were brazed together, as shown in Fig. 3, with refrigerant flowing through the center tube, and coolant flowing in counterflow through the top and bottom tubes. This method of using multiple parallel channels ensured that the refrigerant flow rates used were large enough to be adequately controlled and measured, with accurate heat balances around the test loop. Coriolis mass flow meters ($\pm 0.15\%$ uncertainty for the refrigerant, and $\pm 0.2\%$ uncertainty for the air) were used for the measurement of refrigerant and air flow rates. Cooling water flow rates for the pre- and postcondensers were measured using banks of precision rotameters with a maximum uncertainty of $\pm 2\%$. The flow rate ranges covered by these rotameters were: 0.2–4.5 liters per min, 0.2–2.2 liters per min, and 100–780 ml per min. For each data point, the cooling water was routed through the rotameter that yielded the highest accuracy. Integral precision valving with high turndown ratios allowed steady control of the cooling water flow rates. Absolute pressure transducers with uncertainties of $\pm 0.25\%$ of the span were used to measure pressures of the refrigerant at various locations and also the pressure of the compressed air used as the coolant. Pressure drops across the test section were measured using a bank of three selectable differential pressure transducers, with maximum ΔP values of 6.22 kPa, 62.2 kPa, and 248.2 kPa, respectively, and an accuracy of $\pm 0.25\%$ of the span. As the geometry, mass flux and quality was varied, the pressure drop for a particular data point was measured using the most accurate of the three transducers and averaged over a two minute time interval. All temperatures were measured using Platinum RTDs.

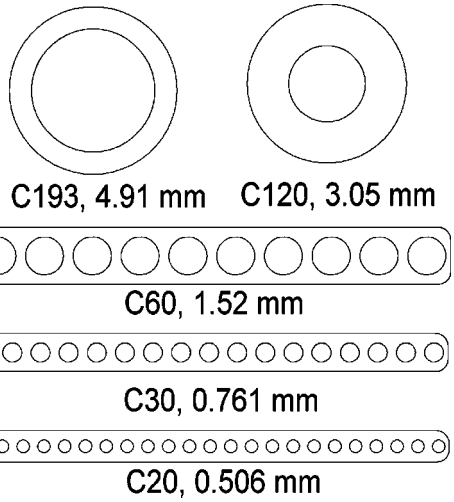

Fig. 2 Tubes investigated in the present study

For each of the test sections investigated in this study, single-phase tests were first conducted to calculate the single-phase friction factors for comparison with correlations found in the literature. Both single-phase liquid and vapor data were taken to span a wide range of data in the laminar, transition and turbulent flow regimes. Contraction and expansion losses at the inlet and outlet were subtracted from the total measured pressure drop using the appropriate loss coefficients. The residual frictional component of the pressure drop was compared with the values predicted by the Churchill [11] correlation as shown in Fig. 4. Relative roughness values were assumed based on typical surface roughness values for drawn tubing. In every case, the roughness values needed to match the Churchill [11] correlation values were well within the range of roughnesses for such tubes, which validates the approach used in this study. Similar results were also obtained for the other tubes. The excellent agreement between the single-phase data and this correlation validates the test procedures.

Because a portion of the total pressure drop (change) in two-phase flow can be attributed to deceleration/acceleration of the fluid due to the changing quality and fluid properties, pressure

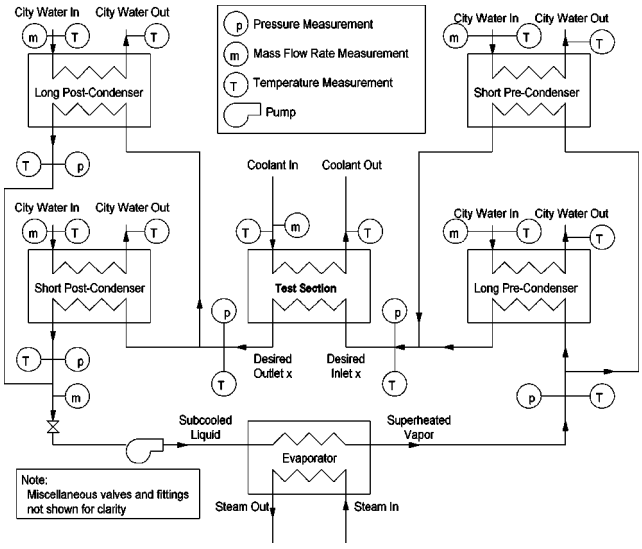

Fig. 1 Test section schematic

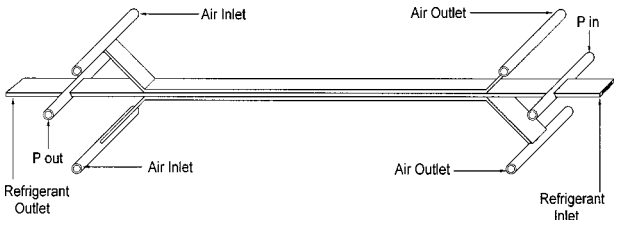

Fig. 3 Test section schematic

Downloaded 03 Jun 2010 to 171.66.16.150. Redistribution subject to ASME license or copyright; see http://www.asme.org/terms/Terms_Use.cfm

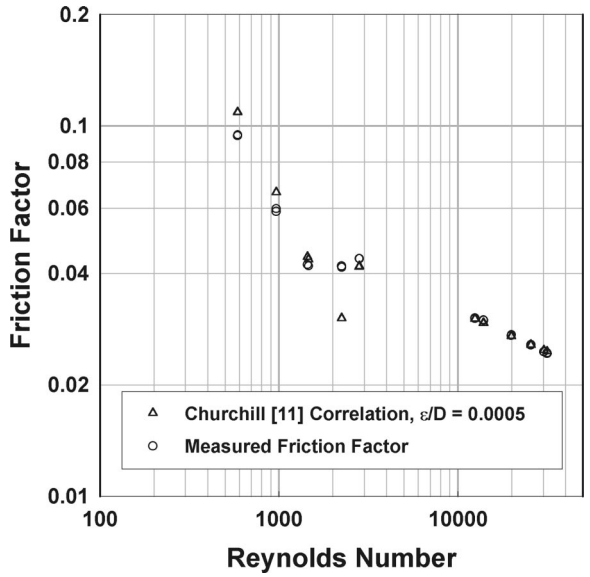

Fig. 4 Single-phase pressure drop validation (tube C30)

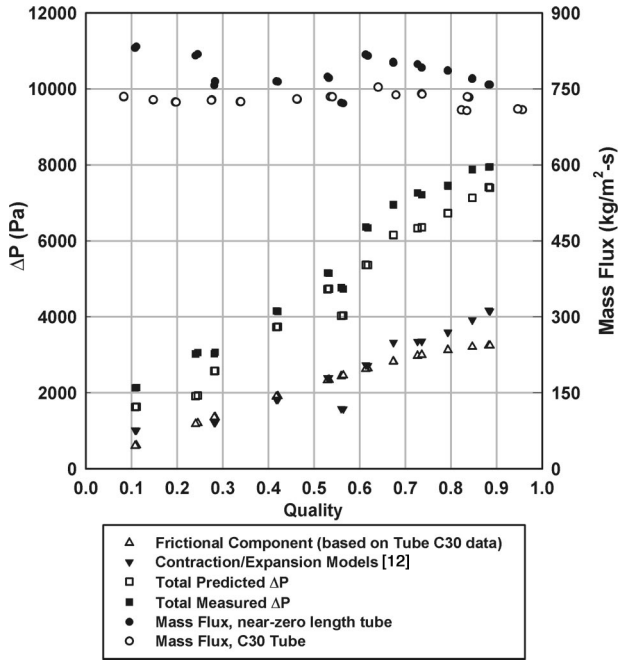

Fig. 5 Validation of contraction/expansion contributions using near-zero length tube

drop tests were conducted with and without coolant flow in the test sections. With the test section inlet and outlet quality known, the acceleration/deceleration component can be estimated from void fraction and momentum change analyses. The results from these tests with and without condensation in the test section provide additional validation of these estimates. These analyses are described in more detail in the next section. Contraction/expansion losses at the inlet and outlet of the test section must also be estimated to enable the calculation of the frictional component of the pressure drop. These contributions were estimated using two-phase ''minor loss'' models available in the literature (described in the next section). For additional validation, tests were also conducted on a ''near-zero'' length test section (with a tube length of 0.022 m). Thus, the bulk of the pressure drop in this test section was due to the contraction and expansion losses, and these data served to corroborate the ''minor loss models'' used to estimate these contributions.

Data Analysis

Quality and Pressure Drop Calculation. As stated above, energy balance calculations were performed on the pre- and post-condensers to obtain independently determined values of the test section inlet and outlet qualities, which suffice to calculate the test section average quality for each data point. However, for the tests in which there was coolant flow in the test section also, the test section heat duty was measured from the coolant flow rate and temperature difference. This test section duty measurement provided another redundant value of the inlet (or outlet) quality, and therefore, a method to confirm the test section average quality measurement. The difference between the average test section quality calculated from the precondenser water-side duty, and the quality calculated from the combination of the postcondenser water-side duty and the test-section duty, was typically less than 1–2 percent, with a few data points at the extreme conditions showing slightly higher discrepancies. An uncertainty analysis was conducted to estimate the uncertainty in the test section quality measurement using the error propagation approach. Representative uncertainties for the range of mass flux and qualities studied are as follows:

$G = 150\ \text{kg/m}^2\text{-s}$:

$$x_{\text{avg}} = 0.13 \pm 0.032 \quad x_{\text{avg}} = 0.50 \pm 0.027 \quad x_{\text{avg}} = 0.91 \pm 0.021$$

$G = 450\ \text{kg/m}^2\text{-s}$:

$$x_{\text{avg}} = 0.12 \pm 0.045 \quad x_{\text{avg}} = 0.48 \pm 0.014 \quad x_{\text{avg}} = 0.88 \pm 0.026$$

$G = 750\ \text{kg/m}^2\text{-s}$:

$$x_{\text{avg}} = 0.11 \pm 0.039 \quad x_{\text{avg}} = 0.51 \pm 0.022 \quad x_{\text{avg}} = 0.74 \pm 0.035$$

For each data point, the measured pressure drop data can be represented by:

$$\Delta P_{\text{measured}} = \Delta P_{\text{frictional}} + \Delta P_{\text{expansion+contraction}} + \Delta P_{\text{deceleration}} \tag{2}$$

where the expansion and contraction losses are due to the headers at both ends of the test section, and the pressure change due to deceleration is a result of the changing vapor fraction as condensation takes place. The latter two terms in above equation must be estimated before a model for the frictional contribution to the total pressure drop can be developed. The pressure drop due to contraction into the test section was estimated using a homogeneous flow model recommended by Hewitt et al. [12]:

$$\Delta P_{\text{contraction}} = \frac{G^2}{2\rho_L}\left[\left(\frac{1}{C_c} - 1\right)^2 + 1 - \gamma^2\right]\Psi_H \tag{3}$$

where γ is the area ratio ($A_{\text{test section}}/A_{\text{header}}$), C_C is a function of this ratio, and Ψ_H is the homogeneous flow multiplier, which is in turn a function of the phase densities and the quality. For the expansion into the header from the test section, the following separated flow model recommended by Hewitt et al. [12] was used:

$$\Delta P_{\text{expansion}} = \frac{G^2\gamma(1-\gamma)\Psi_S}{\rho_L} \tag{4}$$

where Ψ_S, the separated flow multiplier, is also a function of the phase densities and the quality. As stated above, these estimates were validated using pressure drop measurements on a ''near-zero'' length test section. The results are shown in Fig. 5. This graph shows excellent agreement between the measured total pressure drop in the near-zero length test section and the contraction/expansion plus frictional component predictions.

Downloaded 03 Jun 2010 to 171.66.16.150. Redistribution subject to ASME license or copyright; see http://www.asme.org/terms/Terms_Use.cfm

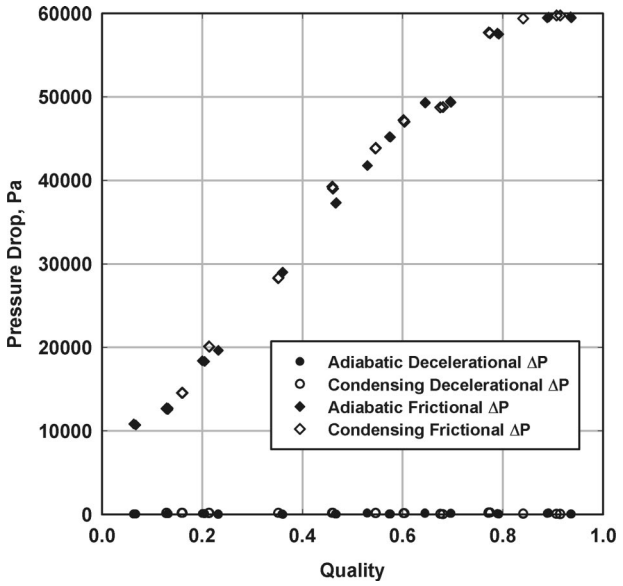

Fig. 6 Delineation of acceleration/deceleration contributions, tube C30, 600 kg/m^2-s

Here, the frictional component of the short, 0.022 m length section necessary to cause the contraction and expansion is estimated from the corresponding data for the C30 tube (which has the same 0.761 mm diameter channels) based on the ratio of their respective lengths. The scatter in these graphs can be attributed to the slight fluctuations in the mass fluxes for the data points, which are also shown for reference in this figure. Once this approach was validated in this manner, it was used to subtract the contraction and expansion contributions from all the measured data points. It should be noted that contraction and expansion loss contributions were less than 5 percent of the total measured pressure drop for almost all the data points because of the relatively long test section lengths used.

The slight change in quality between the inlet and outlet of the test section results in acceleration or deceleration of the fluid, which can be estimated using the following expression [13]:

$$\Delta P_{\text{acceleration}} = \left[\frac{G^2x^2}{\rho_V\alpha} + \frac{G^2(1-x)^2}{\rho_L(1-\alpha)}\right]_{x=x_{\text{out}}} - \left[\frac{G^2x^2}{\rho_V\alpha} + \frac{G^2(1-x)^2}{\rho_L(1-\alpha)}\right]_{x=x_{\text{in}}} \quad (5)$$

where α is the void fraction which was evaluated using the Baroczy [14] correlation. Because the quality at the outlet is lower than at the inlet (condensation), $\Delta P_{\text{acceleration}}$ is generally negative and, when subtracted from the measured pressure drop, adds to the value of the measured pressure drop. As can be seen in Fig. 6 for a mass flux of 600 kg/m^2-s for Tube C30, however, in all the tests conducted in this study, this term is extremely small compared to the overall pressure drop. These estimates of the negligible (and within measurement error) contribution of the acceleration term were also corroborated by tests conducted with and without condensation in the test section. (In Fig. 6, a deceleration/acceleration term is shown even for the adiabatic tests because at the same enthalpy, the refrigerant quality could be slightly different as the pressure changes from the inlet to the outlet.)

Flow Regime Determination. Experiments on the tubes under consideration were conducted over a nominal quality range of 5 percent to 95 percent for each of the mass fluxes of interest. However, the focus of the present study is the intermittent flow regime; therefore, only data points belonging to this regime were

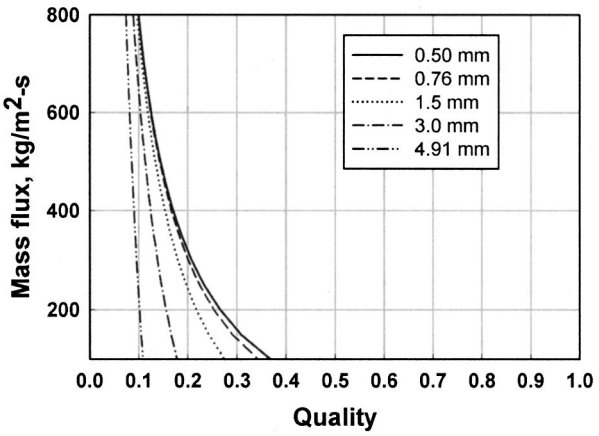

Fig. 7 Intermittent flow regime boundaries for tubes under consideration

included for this pressure drop model. The transition criteria developed by Coleman and Garimella [3] from flow visualization studies were used to identify the flow regime established for each data point. They found that intermittent flow occurs at low vapor qualities, with this flow regime persisting at higher qualities as the mass flux decreases. In addition, they developed individual transition equations for each tube ($1 < D_h < 4.91$ mm) on which flow visualization tests were conducted, and showed that the size of the intermittent regime increases as D_h decreases. In the present study, which covers a similar range of D_h values, interpolation equations as a function of D_h were developed from their transition criteria to address the specific tubes shown in Fig. 2. The general equation for the transition criteria is as follows:

$$x \leqslant \frac{a}{G+b} \quad (6)$$

where G is the total mass flux expressed in kg/m^2-s and a and b are geometry dependent constants given by:

$$a = 69.5673 + 22.595 \cdot \exp(0.2586 \cdot D_h) \quad (7)$$

$$b = -59.9899 + 176.8137 \cdot \exp(0.3826 \cdot D_h) \quad (8)$$

where D_h is the hydraulic diameter of the tubes in mm. These criteria for transition from intermittent flow for each of the tubes under consideration are shown on a G-x plot in Fig. 7. The points of interest for this study are those that lie to the left of these lines; points lying to the right are either in the wavy regime or the annular regime, depending on tube diameter. A total of 77 pressure drop data points belonging to this intermittent regime were identified for model validation using these criteria.

Model Development. Table 1 shows photographs of the plug/slug flow expected in the region of the G-x map identified above from the flow visualization work of Coleman and Garimella [3]. It can be seen that solitary bubbles travel as long, nearly cylindrical shapes between slugs of liquid with virtually no vapor entrainment. In the 1-mm tube, the effect of gravity does not appear to be

Table 1 Representative patterns in the intermittent regime

D_h (mm)	CONDITION	FLOW PATTERN	REMARKS
1	G = 334 kg/m^2-s, x = 0.07		Four square tubes, viewed at an angle
2	G = 154 kg/m^2-s, x = 0.11		Two square tubes, viewed from side
3	G = 293 kg/m^2-s, x = 0.06		One square tube
4	G = 597 kg/m^2-s, x = 0.02	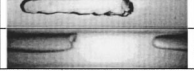	One square tube
4.91	G = 146 kg/m^2-s, x = 0.09	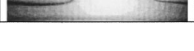	One round tube

Downloaded 03 Jun 2010 to 171.66.16.150. Redistribution subject to ASME license or copyright; see http://www.asme.org/terms/Terms_Use.cfm

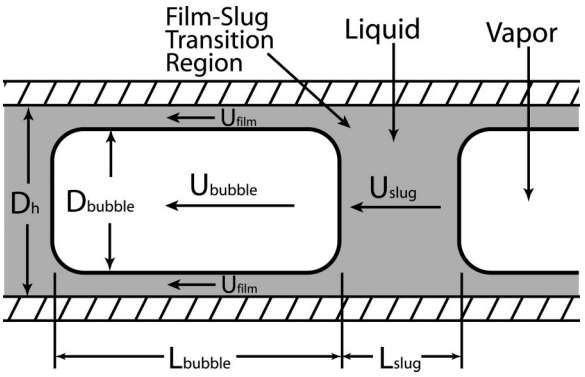

Fig. 8 Cross section of assumed flow pattern for model unit cell

significant, as evidenced by bubbles that are surrounded by a very thin annular film of uniform thickness around the tube circumference. Surface tension forces ostensibly have a significant effect for such small diameter tubes. In the larger tubes, the flow exhibits more stratification and the film becomes thicker beneath the bubbles. These observed flow patterns are used as a basis for the development of the intermittent regime pressure drop model. As a starting point, the assumptions about the shape of the bubble, film, and slug regions proposed by Suo and Griffith [4] and Fukano et al. [6] were used. Essentially, a long, cylindrical bubble of vapor with a uniform annular film of liquid surrounding it is assumed to flow somewhat faster than the liquid slugs which bound it on either end (see Fig. 8); the annular film flows very slowly compared to both the bubble and the slug. Thus liquid is continually shed into the film from the posterior of the slug and picked up from the film at the anterior of the slug. The liquid slugs are assumed to contain no entrained vapor, and the bubbles are assumed to be uniform and constant throughout the test section. The total pressure drop due to this flow mechanism is the sum of the purely frictional pressure drop in the slug and film/bubble regions and the losses associated with the flow between the film and the slug.

Frictional Losses in the Slug. The total mass flux and average quality in the test section are known from the measurements and comprise the independent variables input to the model. As has been shown by Suo and Griffith [4] from mass conservation, the average velocity in the liquid slugs can be readily obtained from the sum of the superficial liquid and vapor velocities. Thus the average slug velocity and slug Reynolds number can be calculated as follows:

$$j_L = \frac{(\mathbf{1}-x)G}{\rho_L} \tag{9}$$

$$j_v = \frac{xG}{\rho_V} \tag{10}$$

$$U_{slug} = j_{\mathbf{v}} + j_L \tag{11}$$

$$\mathrm{Re}_{slug} = \frac{\rho_L U_{slug} D_h}{\mu_L} \tag{12}$$

For all of the test conditions considered here, $2740 < \mathrm{Re}_{slug} < 34{,}400$. Therefore a power-law turbulent velocity profile with exponent $n=7$ was assumed for this region [15]:

$$u(r) = U_{max}\left(1-\frac{r}{R}\right)^{1/n} \tag{13}$$

$$U_{average} = U_{max}\frac{2n^2}{(n+\mathbf{1})(2n+\mathbf{1})} \tag{14}$$

Since $U_{average}$ is known for the slug, the velocity profile in this region is defined. Also, the pressure drop per unit length in the slug is easily calculated assuming the Blasius equation as follows:

$$\left(\frac{dP}{dx}\right)_{slug} = \frac{\mathbf{0.3164}}{\mathrm{Re}_{slug}^{\mathbf{0.25}}}\frac{\rho_L U_{slug}^{\mathbf{2}}}{\mathbf{2}D_h} \tag{15}$$

Frictional Losses in the Bubble/Film Region. Fukano et al. [6] and Suo and Griffith [4] studied flow in tubes of approximately the same diameter as in the present study and concluded that the ratio between bubble and slug velocity is approximately 1.2. Dukler and Hubbard [5] used much larger tubes and suggested a relationship (see Eq. 1) for this relative velocity that was not intended to extend to the lower values of Re_{slug} encountered in the present work. However, extrapolating their equation to the current Re range yields relative velocity values of 1.18–1.24, which is in remarkably good agreement with the results from the other authors, in spite of the fact that it was based on a stratified model of the film. For the present work, therefore, it was assumed that, for all cases:

$$\frac{U_{bubble}}{U_{slug}} = \mathbf{1.2} \tag{16}$$

Each of the aforementioned authors suggest that the pressure drop in the film/bubble region may be negligible compared to the total pressure drop. However, since these investigators only considered air-water systems, the physical properties of the system that led them to this conclusion may not apply to phase-change refrigerant flow under consideration here. In particular, the ratio of the liquid to vapor densities for R134a is much lower (approximately 16:1 versus 850:1 for air-water) as is the ratio of liquid and vapor viscosities (approximately 10:1 versus 50:1). Therefore, the contribution of the film/bubble region was not neglected in the present work. Several other unknowns in this region can be calculated using the assumed relative velocity ratio, and continuity and momentum balances. Based on the Re ranges encountered in this work, $8 \leqslant \mathrm{Re}_{film} \leqslant 541$ and $1900 \leqslant \mathrm{Re}_{bubble} \leqslant 18{,}000$, the flow in the film was assumed to be laminar and the flow in the bubble turbulent. Here,

$$\mathrm{Re}_{film} = \frac{\rho_L U_{film}(D_h - D_{bubble})}{\mu_L} \tag{17}$$

$$\mathrm{Re}_{bubble} = \frac{\rho_V (U_{bubble} - U_{interface}) D_{bubble}}{\mu_V} \tag{18}$$

The film flow was assumed to be driven by the combination of the pressure gradient in the film/bubble region and shear at the film/bubble interface. The velocity profile for combined Couette-Poiseuille flow through an annulus where the inner surface moves at the interface velocity, $U_{interface}$, is represented by the superposition of the pressure-driven and the shear-driven components [16,17]:

$$u_{film}(r) = \frac{-\left(\frac{dP}{dx}\right)_{f/b}}{\mathbf{4}\mu_L}\left[R_{tube}^{\mathbf{2}} - r^{\mathbf{2}} - (R_{tube}^{\mathbf{2}} - R_{bubble}^{\mathbf{2}}) \times \frac{\ln(R_{tube}/r)}{\ln(R_{tube}/R_{bubble})}\right] + U_{interface}\frac{\ln(R_{tube}/r)}{\ln(R_{tube}/R_{bubble})} \tag{19}$$

Within the bubble, a power-law profile is again assumed with $n=7$:

$$u_{bubble}(r) = \frac{(n+\mathbf{1})(2n+\mathbf{1})}{\mathbf{2}n^{\mathbf{2}}}(U_{bubble} - U_{interface})\left(\mathbf{1} - \frac{r}{R_{bubble}}\right)^{1/n} + U_{interface} \tag{20}$$

Downloaded 03 Jun 2010 to 171.66.16.150. Redistribution subject to ASME license or copyright; see http://www.asme.org/terms/Terms_Use.cfm

Note that both of these profiles satisfy the boundary condition that $u(r=R_{\text{bubble}})=U_{\text{interface}}$. The shear stress boundary condition at the interface is as follows:

$$\tau_{\text{interface}}=\mu_L\left(\frac{du_{\text{film}}}{dr}\right)_{r=R_{\text{bubble}}}=\tau_{\text{bubble}}(r=R_{\text{bubble}}) \tag{21}$$

Since the bubble is purely driven by the pressure gradient, the shear in the bubble at the interface is given by:

$$\tau_{\text{bubble}}(r=R_{\text{bubble}})=-\frac{R_{\text{bubble}}}{\mathbf{2}}\left(\frac{dP}{dx}\right)_{f/b} \tag{22}$$

This allows the evaluation of the interface velocity, $U_{\text{interface}}$, by differentiating Eq. (19) for du_{film}/dr. Therefore:

$$U_{\text{interface}}=\frac{-(dP/dx)}{\mathbf{4}\mu_L}(R_{\text{tube}}{}^2-R_{\text{bubble}}{}^2) \tag{23}$$

The corresponding film velocity profile is:

$$u_{\text{film}}(r)=\frac{-\left(\frac{dP}{dx}\right)_{f/b}}{\mathbf{4}\mu_L}(R_{\text{tube}}{}^2-r^2) \tag{24}$$

Thus the film has a parabolic velocity profile driven by the pressure gradient in the film/bubble region. The average film flow rate is therefore:

$$U_{\text{film}}=\frac{-\left(\frac{dP}{dx}\right)_{f/b}}{\mathbf{8}\mu_L}(R_{\text{tube}}{}^2-R_{\text{bubble}}{}^2) \tag{25}$$

The pressure drop per unit length in the bubble/film region is not readily apparent, however it is known that (again assuming the Blasius friction factor):

$$\left(\frac{dP}{dx}\right)_{f/b}=\frac{\mathbf{0.3164}}{\text{Re}_{\text{bubble}}{}^{\mathbf{0.25}}}\frac{\rho_V(U_{\text{bubble}}-U_{\text{interface}})^{\mathbf{2}}}{\mathbf{4}R_{\text{bubble}}} \tag{26}$$

At this point, there are five equations (17, 18, 23, 25, 26) for six unknowns: R_{bubble}, $(dP/dx)_{f/b}$, $U_{\text{interface}}$, U_{film}, $\text{Re}_{\text{bubble}}$, Re_{film}. To complete the problem, continuity is enforced over a control volume noting that the volumetric flow rate through any plane must be constant:

$$U_{\text{slug}}=U_{\text{bubble}}\left(\frac{R_{\text{bubble}}}{R_{\text{tube}}}\right)^{\mathbf{2}}+U_{\text{film}}\left(\mathbf{1}-\left(\frac{R_{\text{bubble}}}{R_{\text{tube}}}\right)^{\mathbf{2}}\right) \tag{27}$$

For the conditions of interest here, these calculations yield $0.899 \leqslant R_{\text{bubble}}/R_{\text{tube}} \leqslant 0.911$; thus the predicted bubble diameter is about 90 percent of the tube diameter.

Fractional Contributions of Slug and Bubble/Film Regions. With the pressure drop per length known in both the slug and the film/bubble regions, knowing the relative length of the bubble to slug is all that is required to calculate the frictional component of the pressure drop for any length of tube. For this, the measurements of Fukano et al. [6] were used. For each of the tube diameters they tested (1.0, 2.4, and 4.9 mm), they showed that the relative length of the slug could be closely approximated by:

$$\frac{L_{\text{slug}}}{L_{\text{slug}}+L_{\text{bubble}}}=k\frac{j_L}{j_L+j_V} \tag{28}$$

where k is a different constant for each tube diameter. The following expression fits the reported values of k:

$$k=0.7228+0.4629^{*}\exp(-0.9604^{*}D_h) \tag{29}$$

where D_h is expressed in mm.

Thus the pressure drop due to frictional losses is known:

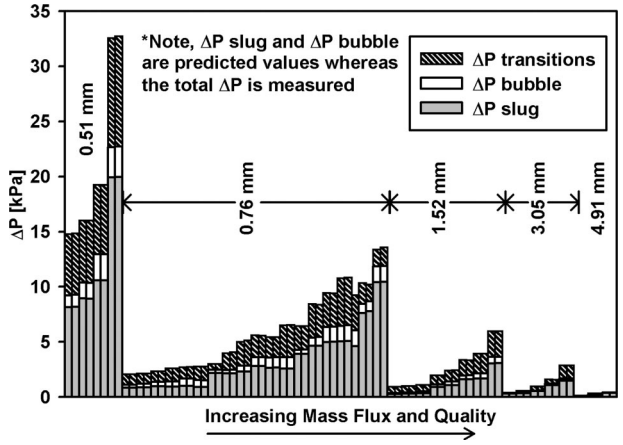

Fig. 9 Contribution of each pressure drop mechanism to total pressure drop for each test point

$$\Delta P_{\text{friction only}}=L_{\text{tube}}\left[\left(\frac{dP}{dx}\right)_{f/b}\left(\mathbf{1}-\frac{L_{\text{slug}}}{L_{\text{slug}}+L_{\text{bubble}}}\right)+\left(\frac{dP}{dx}\right)_{\text{slug}}\left(\frac{L_{\text{slug}}}{L_{\text{slug}}+L_{\text{bubble}}}\right)\right] \tag{30}$$

For the conditions tested, this value is typically about 64% of the total measured pressure drop. Figure 9 illustrates how the calculated values of $\Delta P_{\text{friction only}}$ from both the slug and bubble/film regions compare with the total measured pressure drop.

Calculation of Pressure Loss From Film-to-Slug Flow. The remaining contribution to the total pressure drop is the loss associated with the flow of liquid between the film and the slug. Because the film moves slowly, the front of the liquid slug is constantly taking up fluid from the film. A pressure loss is associated with the acceleration and subsequent mixing of this liquid [5]. The total pressure loss from these transitions can be expressed as:

$$\Delta P_{\text{film/slug transitions}}=N_{UC}\cdot\Delta P_{\text{one transition}} \tag{31}$$

where $\Delta P_{\text{one transition}}$ is the loss associated with a single film-to-slug transition, and the number of these transitions that occur within the test section is N_{UC}. Fukano et al. [6] assume that the pressure loss as the film enters the slug region is the same as the dynamic pressure calculated using the relative average velocity between the slug and the film:

$$\Delta P_{\text{one transition}}=\rho_L\frac{(U_{\text{slug}}-U_{\text{film}})^{\mathbf{2}}}{\mathbf{2}} \tag{32}$$

They postulate that the pressure loss is due to an expansion of the film into the slug at the rear of the bubble. Conversely, Dukler and Hubbard [6] derive $\Delta P_{\text{one transition}}$ by considering the force required to accelerate the portion of the liquid film overtaken by the rear of the bubble from the average film velocity to the average slug velocity. The resulting expression can be shown to be equivalent to:

$$\Delta P_{\text{one transition}}=\rho_L\left(\mathbf{1}-\left(\frac{R_{\text{bubble}}}{R_{\text{tube}}}\right)^{\mathbf{2}}\right)\frac{(U_{\text{slug}}-U_{\text{film}})(U_{\text{bubble}}-U_{\text{film}})}{\mathbf{2}} \tag{33}$$

They suggest that a region of mixing at the front of the slug generates the blunt interface often seen between the bubble and slug at the front of the slug/rear of the bubble. For the cases considered here, $\Delta P_{\text{one transition}}$ calculated in the manner of Fukano et al. [6] is typically 2.1–2.4 times the value obtained using the expression from Dukler and Hubbard [5]. In the present work, the Dukler and Hubbard [5] expression is adopted due to its mecha-

Downloaded 03 Jun 2010 to 171.66.16.150. Redistribution subject to ASME license or copyright; see http://www.asme.org/terms/Terms_Use.cfm

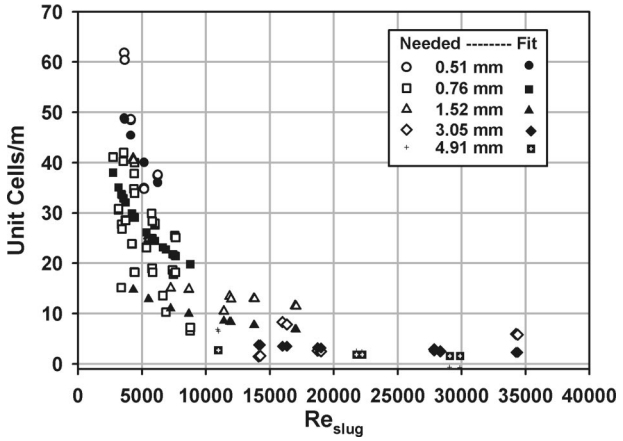

Fig. 10 Number of unit cells per meter derived from measured data and model as a function of slug Reynolds number, comparison with curve fit

nistic basis. N_{UC} is simply the number of slug/bubble pairs, or unit cells, since there is one mixing zone per unit cell. Knowing the length or frequency of the unit cells would be sufficient to determine N_{UC} for any test section. Unfortunately, neither of these parameters is easily available *a priori*. Dukler and Hubbard [5] derive empirical values of slug frequency from their prior work and present these graphically, though they suggest a correlation from Grescovich and Shrier [18] may be applicable when data are unavailable. Fukano et al. [6] do not specify how they calculate the number of unit cells; presumably they, too, derive it from their experimental work. In the present work, there is no obvious manner in which to calculate the number of unit cells from the flow conditions. Therefore, this parameter was initially calculated using the experimental data to account for the difference between $\Delta P_{\text{friction only}}$ and the measured values in the following manner:

$$N_{UC}=\frac{\Delta P_{\text{measured}}-\Delta P_{\text{friction only,predicted}}}{\Delta P_{\text{one transition}}} \tag{34}$$

The number of unit cells for any given length generally decreases with increasing quality, increasing mass flux, and increasing tube diameter. Because Re_{slug} is a function of each of these parameters, the number of unit cells per meter ($1/L_{UC}$ where L_{UC} is the length of a unit cell) were plotted against Re_{slug}, as shown in Fig. 10. Based on the trends observed in this figure, the following expression was developed to correlate the number of unit cells:

$$N_{UC}\left(\frac{D_h}{L_{\text{tube}}}\right)=\left(\frac{D_h}{L_{UC}}\right)=a(\text{Re}_{\text{slug}})^b \tag{35}$$

with the following coefficients: $a=2436.9$, $b=-0.5601$. Although the resulting regression coefficient is quite low, $R^2=0.75$, the fit is close enough to significantly improve the accuracy of the overall results (see Fig. 11). The maximum number of unit cells per meter predicted by this equation for all the data points considered in this study was about 50, resulting in a minimum unit cell length of about 20 mm. The maximum unit cell length predicted for the 0.51, 0.76 and 1.52-mm tubes was about 50 mm. The unit-cell-length-to-tube-diameter ratio ranged from 34 to 66 for the data points for these tubes, which had the three smallest tube diameters from among those investigated here. In the two larger tubes, the number of unit cells predicted was very small (corresponding to longer unit cells) since the predicted $\Delta P_{\text{friction only}}$ was near, or in some cases, exceeding the actual measured pressure drop. (It should be noted that the measured pressure drops in these tubes with the larger cross sections were relatively low, particularly for this low vapor-quality region.) This result suggests a limitation of the model for larger tubes, which will be discussed further in the following sections.

Results and Discussion

Figure 9 illustrates the relative contribution of the three pressure drop mechanisms: viscous losses in the slug, viscous losses in the bubble/film region, and transitional losses from film take-up at the front of the slug. For the test conditions modeled, typically the slug flow accounts for 53 percent of the total pressure drop, the film/bubble region 12 percent, and the transitional losses 35 percent. As shown in Fig. 11, the pressure drop values predicted with the model described above agree well with the measured data; 88 percent of the predicted pressure drop values fall within ± 25 percent of the measured values with an average error of 13.4 percent. Figure 11 also shows that, in general, as the tube diameter increases and the measured pressure drop decreases, the variance between the measured and predicted values increases. One explanation for this is that when the total pressure drop is very small, measurement precision may be a limiting factor. In addition, the assumptions utilized for the model regarding the shape of the bubble and film become less valid as the tube diameter increases due to the increasing role of gravity which produces a more stratified flow pattern (see Table 1). Since the model presented here neglects the effects of gravity compared to surface tension forces, when stratification of the flow occurs, the assumptions in the model are less representative, leading to lower accuracies. Clearly though, the model developed here is quite successful in predicting intermittent-regime pressure drops in microchannel tubes with hydraulic diameter on the order of 1 mm.

One of the weaknesses in the model is in the calculation of the length of the unit cells. As was shown in Fig. 10, the number of unit cells per unit length calculated from the measured data and the modeled pressure drop in the bubble/film and slug region is a strong function of the Reynolds number of the slug, which accounts for quality, mass flux, tube diameter and liquid density and viscosity. However, this correlation did not completely collapse the data into a single trend. This suggests that, in addition to errors introduced due to measurement uncertainties in these relatively low-pressure drop flows, there are other phenomena not accounted for in this simple model. The effect of surface tension may also be an important parameter to consider in future work.

Effect of Hydraulic Diameter. Figure 12 illustrates the effects of quality, mass flux and hydraulic diameter on pressure drop predicted using the model developed here for a constant representative L_{tube}/D_h ratio of 500. The significant features of these plots are as follows:

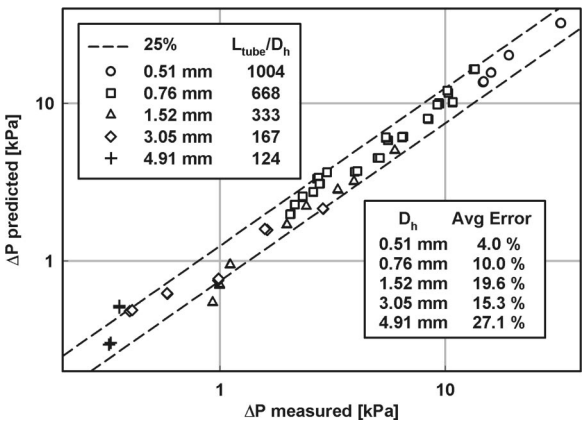

Fig. 11 Comparison of total predicted pressure drop with measurements

Downloaded 03 Jun 2010 to 171.66.16.150. Redistribution subject to ASME license or copyright; see http://www.asme.org/terms/Terms_Use.cfm

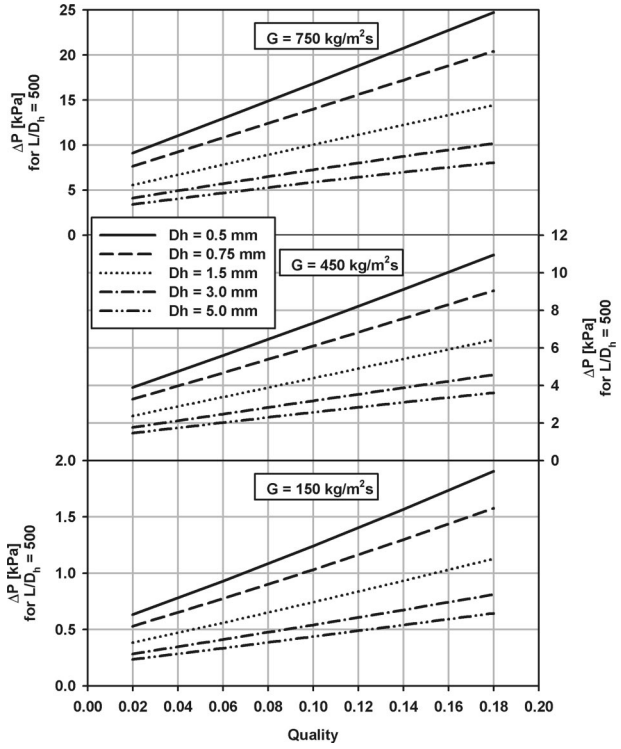

Fig. 12 Predicted effect of hydraulic diameter, mass flux, and quality on pressure drop for constant L/D_h

• Smaller diameter tubes produce higher pressure drop at any given quality and mass flux for a constant L_{tube}/D_h, and the effect of diameter becomes increasingly significant as the tube diameter decreases.

• The increase in pressure drop with quality is nearly linear, but the slope depends on the diameter and mass flux.

• Pressure drop increases with increasing mass flux, and the effect of mass flux becomes increasingly significant as the mass fluxes increases.

Conclusions

An experimentally validated pressure drop model for intermittent flow of condensing refrigerant R134a in horizontal tubes with hydraulic diameters from 0.5 to 5 mm was developed. The experimental work presented here in conjunction with prior flow visualization studies of condensing refrigerant flows provided an accurate set of measured pressure drop data for intermittent flow that was used for model validation. Using assumptions based on the observed slug/bubble flow pattern for these conditions and empirical data from the literature for the relative length and velocity of the slugs and bubbles, the contributions of the slug and bubble/film regions to the pressure drop were quantified. A simple correlation for non-dimensional unit-cell length based on slug Reynolds number was used with relationships from the literature to calculate the pressure loss associated with the mixing that occurs as the liquid slugs overtake the annular liquid film surrounding the bubble. Besides tube dimensions and thermophysical properties, the only input required for the model are the quality and mass flux of the refrigerant. The results of this model were within ± 13.4 percent of the measured data on average, with 88 percent of the predicted results within ± 25 percent of the 77 measured data points. The model was validated over a large range of mass fluxes. Furthermore, criteria for predicting the existence of intermittent flow were presented, based on earlier flow visualization work by the authors. It was noted that the assumed flow pattern more accurately represents the observed flow pattern for smaller tube diameters; the agreement of the model with the experimental data was shown to degrade somewhat for the larger tube diameters considered. Finally, the model was used to characterize the effect of hydraulic diameter, mass flux and quality on pressure drop in a systematic way. It was found that pressure drop for the same L_{tube}/D_h ratio increases almost linearly with increasing quality, and more sharply with decreasing tube diameter and increasing mass flux. Although the results of the model were satisfactory, as with other models proposed in the literature [5,6], modeling the variation of unit cell length or slug frequency with flow conditions, tube dimensions, and fluid properties is an area that needs further investigation.

Acknowledgments

This study was supported through a research grant from Modine Manufacturing Company, Racine, WI.

Nomenclature

A = cross sectional area [m^2]
a, b = variable constants
C_C = constant in Eq. 3 [12]
D = diameter [m] (or [mm] as noted)
d = ordinary differential operator
ΔP = pressure drop [kPa]
dP/dx = pressure drop per unit length [kPa/m]
G = mass flux [kg/m^2s]
j = superficial velocity [m/s] (see Eqs. 9 and 10)
k = constant from Fukano et al. [6] (see Eq. (28))
L = tube length [m]
n = power law exponent (see Eq. (13))
N_{UC} = number of unit cells
R = radius [m]
r = radial coordinate [m]
Re = Reynolds Number
u = velocity [m/s] position dependent
U = velocity [m/s] cross-sectional average
x = vapor quality

Greek Symbols

α = void fraction
Ψ_H = homogeneous flow multiplier Eq. 3 [12]
Ψ_S = separated flow multiplier Eq. 4 [12]
ρ = mass density [kg/m^3]
μ = dynamic viscosity [Ns/m^2]
τ = shear stress [N/m^2]

Subscripts

avg = average within test section
f/b = film/bubble region
h = hydraulic diameter of tube
L = liquid
UC = unit cell
V = vapor

References

[1] Coleman, J. W., and Garimella, S., 1999, "Characterization of Two-phase Flow Patterns in Small Diameter Round and Rectangular Tubes," Int. J. Heat Mass Transf., **42**, No. 15, pp. 2869–2881.
[2] Coleman, J. W., and Garimella, S., 2000, "Visualization of Refrigerant Two-Phase Flow During Condensation," *Proceedings of the 34th National Heat Transfer Conference*, *NHTC2000-12115*.
[3] Coleman, J. W., and Garimella, S., 2000, "Two-Phase Flow Regime Transitions in Microchannel Tubes: The Effect of Hydraulic Diameter," *Proc. ASME Heat Transfer Division-2000 HTD*, Vol. 366-4, pp. 71–83.
[4] Suo, M., and Griffith, P., 1964, "Two-Phase Flow in Capillary Tubes," ASME J. Basic Eng., **86**, pp. 576–582.
[5] Dukler, A. E., and Hubbard, M. G., 1975, "A Model for Gas-Liquid Slug Flow in Horizontal and Near Horizontal Tubes," Ind. Eng. Chem. Fundam., **14**, No. 4, pp. 337–347.
[6] Fukano, T., Kariyasaki, A., and Kagawa, M., 1989, "Flow Patterns and Pressure Drop in Isothermal Gas-Liquid Concurrent Flow in a Horizontal Capillary Tube," *ANS Proceedings 1989 National Heat Transfer Conference*, Vol. 4, pp. 153–161.

Downloaded 03 Jun 2010 to 171.66.16.150. Redistribution subject to ASME license or copyright; see http://www.asme.org/terms/Terms_Use.cfm

[7] Mandhane, J. M., Gregory, G. A., and Aziz, K., 1974, ''A Flow Pattern Map for Gas-Liquid Flow in Horizontal Pipes,'' Int. J. Multiphase Flow, **1**, pp. 537–553.
[8] Weisman, J., Duncan, D., Gibson, J., and Crawford, T., 1979, ''Effects of Fluid Properties and Pipe Diameter on Two-Phase Flow Patterns in Horizontal Lines,'' Int. J. Multiphase Flow, **5**, pp. 437–462.
[9] Taitel, Y., and Dukler, A. E., 1976, ''A Model for Predicting Flow Regime Transitions in Horizontal and Near Horizontal Gas-Liquid Flow,'' AIChE J., **22**, No. 1, pp. 47–55.
[10] Tran, T. N., Chyu, M.-C., Wambsganss, M. W., and France, D. M., 2000, ''Two-Phase Pressure Drop of Refrigerants During Flow Boiling in Small Channels: An Experimental Investigation and Correlation Development,'' Int. J. Multiphase Flow, **26**, No. 11, pp. 1739–1754.
[11] Churchill, S. W., 1977, ''Friction Factor Equation Spans All Fluid Flow Regimes,'' Chem. Eng., **84**, No. 24, pp. 91–92.
[12] Hewitt, G. F., Shires, G. L., and Bott, T. R., 1993, *Process Heat Transfer*, CRC Press, Ann Arbor, MI.
[13] Carey, V. P., 1992, *Liquid-Vapor Phase Change Phenomena*, Taylor & Francis Series in Mechanical Engineering, Hemisphere Publishing, New York.
[14] Baroczy, C. J., 1965, ''Correlation of Liquid Fraction in Two-Phase Flow with Applications to Liquid Metals,'' Chem. Eng. Prog., Symp. Ser., **61**, No. 57, pp. 179–191.
[15] Schlichting, H., 1955, *Boundary Layer Theory*, Pergamom Press Ltd., London.
[16] White, F. M., 1990, *Viscous Fluid Flow*, McGraw, Hill, New York.
[17] Berker, A. R., 1963, ''*Intégration des équations du mouvement d'un fluide visqueux incompressible*,'' *Encyclopedia of Physics*, S. Flügge, Ed., Springer, Berlin, p. 1–384.
[18] Greskovich, E. J., and Shrier, A. L., 1972, Ind. Eng. Chem. Process Des. Dev. **11**, p. 317, as referenced by [5].

Downloaded 03 Jun 2010 to 171.66.16.150. Redistribution subject to ASME license or copyright; see http://www.asme.org/terms/Terms_Use.cfm

Tzung-hang Lee
Associate Professor,
Department of Mechanical Engineering,
Tamkang University, Tamsui, Taiwan, R.O.C.
e-mail: zouhan@mail.tku.edu.tw

Zhengquan Zhou
Graduate Student,
School of Naval Architecture and
Marine Engineering,
University of New Orleans,
New Orleans, LA 70148
e-mail: zhengqzhou@yahoo.com

Yusong Cao[1]
Principal Consultant,
C-Z Marine Technology, Inc.,
2100 Jefferson Ave., New Orleans, LA 70115
e-mail: yusong@czmarine.com

Numerical Simulations of Hydraulic Jumps in Water Sloshing and Water Impacting

A numerical investigation on Glimm's method as applied to water sloshing and impacting is carried out. Emphasis is given to the handling and predicting hydraulic jumps. The effects of the spatial and temporal discretizations are examined. Three shallow water problems, 1) dam-breaking problem, 2) water sloshing in a rolling tank, and 3) impact of breaking of a water reservoir, are studied. It is shown numerically that Glimm's method is stable and converged solutions can be obtained. The characteristics of the hydraulic jumps are well captured by the numerical calculations. The numerical results are in good agreement with either analytical solutions or experimental data.
[DOI: 10.1115/1.1436097]

1 Introduction

It is well known that liquid sloshing has a very significant effect on dynamic behavior of moving vehicles (or vessels) containing liquids. For example, a ship in heavy seas usually receives a large amount of seawater on its deck. The flow of the water on the deck profoundly affects the motion of the ship in the seaway in which it operates (Buchner [1]). An oil tanker traveling in rough seas may suffer from dynamic instabilities due to the coupling of the fluid oscillation in its internal tanks (De Kat [2]). A rocket using liquid fuel is also subject to the effect of the sloshing of the liquid in the fuel tanks after some of the fuel has been used (Graham and Rodriguez [3]). Generally speaking, partially filled tanks in moving vehicles are prone to violent sloshing motions (Abramson [4], Pilipchuk and Ibrahim [5]). If the liquid in a tank undergoing oscillatory motion is relatively shallow and the oscillation frequency is close to the natural frequency of the liquid sloshing, a hydraulic jump (an abrupt change in the elevation of the liquid surface in a very narrow region) may occur (Verhagen Van Wijngaarden [6]). A hydraulic jump can create localized high impact pressure on tank walls, which not only affects the motion of the vessel but may also cause structure damages (Hamlin et al. [7]). Verhagen Van Wijngaarden [6] observed the formation of a hydraulic jump in a tank of an oil tanker at some resonant frequency. The hydraulic jump traveled periodically back and forth between the walls of the tank. The motion of the oil tanker was affected significantly by the movement of the hydraulic jump. Since the formation and movement of a hydraulic jump are caused by the motion of the supporting vessel, it is clear that the motion of the vessel and the movement of the hydraulic jump are strongly coupled.

Water impacting is another phenomenon in which the surface of an object is hit by a large amount of water with high velocity. In many cases, there is a similarity between water impacting and water sloshing in terms of formation of hydraulic jumps. For instance, as a tidal wave moves closer to a shoreline where the water depth becomes shallower, the wave becomes steeper and its front evolves into a hydraulic jump (Stoker [8], Yih [9]). This hydraulic jump soon turns into an overturning plunging wave with a very high tip flow velocity. This overturning wave may hit the shore (or coastal structures) with a very large impact, which is a major cause of damage to the shore (or coastal structures). Another example of water impacting is impact of so-called green water on structures or equipments on deck of a ship or offshore platform (Bunchner [1,10]). At times, on a side of the deck, an almost vertical wall of water can rise above the deck due to large relative motions of the ship and severe waves. This water wall soon falls onto the deck (the water on the deck is called green water) similar to the water flow of a dam-breaking (Bunchner [10]). The water on the deck can evolve into a hydraulic jump, resulting in a high speed water jet shooting onto the structures on the deck. This impact of green water can cause severe damages to the structures or sensitive equipments on the deck.

Both liquid sloshing and water impacting are very important issues in design and operation of ships and marine structures. The water sloshing and water impacting concerned by ship and marine structure designers are physically similar flows, all involving hydraulic jumps. The size of the hydraulic jump, its location and movement are clear to have significant influence on the hydrodynamic impact on the structures. Therefore, an accurate modeling and simulation of the hydraulic jumps is the key to accurate prediction of the effects of liquid sloshing on the motion of ship and prediction of water impacting on the marine structures.

Like shock waves in gas dynamics, hydraulic jumps have been modeled mathematically with a discontinuity in liquid surface elevation. Many researchers, including Stoker [8] and Verhangen and Van Wijngaarden [6], have studied flows involving hydraulic jumps with use of shallow water wave theories. The analytical approaches used in these early works were based on shallow water wave theories and Taylor series expansions about the undisturbed liquid surface. Most of the solution methods were derived for some particular, simple problems. It is difficult for these approaches to find applications in the analysis and prediction of water sloshing and water impacting in practical engineering problems where nonlinear effects are often so strong that these methods are not expected to give good solutions.

Research on numerical simulations of shallow water flows and the associated loading on structures has been carried out recently (Faltinsen [11,12], Lou et al. [13], Lee et al. [14] and Buchner [1]). Finite difference scheme and boundary integral equation method (or boundary element method) are two major types of

[1]Former Associate Professor, School of Naval Architecture and Marine Engineering, University of New Orleans.

Contributed by the Fluids Engineering Division for publication in the JOURNAL OF FLUIDS ENGINEERING. Manuscript received by the Fluids Engineering Division November 13, 2000; revised manuscript received September 13, 2001. Associate Editor: J. Marshall.

 Copyright © 2002 by ASME

Downloaded 03 Jun 2010 to 171.66.16.150. Redistribution subject to ASME license or copyright; see http://www.asme.org/terms/Terms_Use.cfm

methods used in most of the numerical simulations. These researches aimed at solving more practical problems. There are three major difficulties associated with simulating a hydraulic jump. The first difficulty is handling the discontinuity of water elevation on two sides of the jump (keeping the sharp shape of the water front of a hydraulic jump, and maintaining the amplitude of the jump accurately). The second difficulty is handling the propagation of the hydraulic jump (ensuring the moving hydraulic jump propagate in the right direction). The third difficulty is associated with accurately predicting the magnitude and phase of the propagation velocity of the hydraulic jump, thus the location of the jump. In many cases, however, too much numerical damping (or artificial dissipation) is introduced by these two types of the numerical methods near the hydraulic jump. These methods, therefore, often fail to predict the formation of the jump or smear an initial jump (Faltinsen [12]).

These difficulties may be overcome by using Glimm's method [15] (also known as Random-choice method, Chorin [16,17]). The method was introduced by Glimm [15] as part of the proof of the existence of solutions to a class of systems of hyperbolic differential equations. It was later developed by Chorin [16,17] into a useful tool to obtain the numerical solutions to systems of hyperbolic differential equations. One of the distinctive features of Glimm's method is its superiority over the early methods mentioned above in handling discontinuities in the solution. Since the governing equations for the shallow water waves are of hyperbolic type, Glimm's method should be very well suitable for solving the hydraulic jump problems.

Dillingham [18] was probably the first one to use Glimm's method to investigate the effect of the sloshing of the shallow deck water on the sway and roll of a ship. The problem was simplified as two-dimensional. His results using Glimm's method for the water sloshing in a rolling tank compared reasonably well with the experimental measurement. But, the comparison was made for a narrow time span. Pantazopoulous and Adee [19] used Glimm's method to calculate the water height of a two-dimensional dam-breaking problem for which there is an analytical solution (Stoker [8]). His result was not smooth and did not compare well with the analytical solution even for a very narrow time span. Pantazopoulos [19,20] also attempted applying Glimm's method to three-dimensional sloshing of water on ship decks. Similar to the two-dimensional problem, the results for the three-dimensional problem were not smooth. Besides, no detailed information on the pressure on the bottom and walls of the tank was presented in Dillingham [18] and Pantazopoulous and Adee [19] and Pantazopoulous [20]. Since then, little had been reported on the application of Glimm's method in water sloshing and water impacting until more recently when Zhou [21] and Zhou et al. [22] reported their work on green water dynamics on deck using Glimm's method. Their calculations compared fairly well with the experiment measurement. This rekindled the interest in Glimm's method for water sloshing and water impacting, especially those involving hydraulic jumps.

Like any numerical method, the accuracy of the numerical solutions using Glimm's method is affected by a number of factors. These factors include geometric discretization, time step size, numerical time stepping algorithm used, Courant-Friderichs-Levy (CFL) condition (the ratio of the time step and the spatial resolution, as a stability criterion for the time stepping), and correct implementation of the algorithm in computer code programming, etc. More thorough investigation of these factors on the solution accuracy is needed before a fair assessment can be made on Glimm's method as applied to water sloshing and water impacting.

The present paper further extends the numerical investigation on Glimm's method. The effects of the spatial and temporal discretizations on the numerical solution are examined. Also examined is the effect of the CFL condition on the stability of the numerical time stepping procedure. The method is investigated with an emphasis on handling the hydraulic jump (the height of the jump and its propagation direction and speed) encountered in water sloshing and water impacting. For sake of simplicity, only two-dimensional cases are considered. Excellent agreement with the analytical solution of Stoker [8] is achieved for the dam-breaking problem. The result for the water sloshing is in good agreement with experimental data. In addition, the paper also presents a simulation of the movement of the hydraulic jump traveling between the walls of the rolling tank (the water surface profile at a series of time instants), and the sloshing moment acting on the tank as a function of time. Glimm's method is also applied to study the hydrodynamic impact due to breaking of a water reservoir. The computed water height and the impact pressure as functions of time at several locations on the walls and bottom are compared with available experimental data.

2 Mathematical Model

2.1 Coordinate System. Three coordinate systems are employed to describe the shallow water flow on board of the deck of a vessel with a general three-degree-of-freedom motion in a plane, as depicted in Fig. 1.

(a) Earth-fixed coordinate system

Coordinate system $O_0-y_0z_0$ is fixed in space, with y_0 axis pointing in the horizontal direction and z_0 axis pointing upwards.

(b) Moving coordinate system

Coordinate system $G-y_gz_g$ is attached to the vessel with its origin G at the vessel's gravity center. The directions of the axes are: y_g in the lateral port side direction and z_g upwards. This coordinate system moves with the vessel.

(c) Deck-Flow coordinate system

Coordinate system Z_d-yz is used to describe the shallow water flow on the deck. y axis is parallel to the y_g axis of the $G-y_gz_g$ coordinate system and coincides with the undisturbed calm water surface. The z axis is inline with the z_g axis.

Figure 2 shows a two-dimensional water wave flow deck in the Z_d-yz system. The water surface elevation is defined as $\eta(y,t)$ measured from $z=0$.

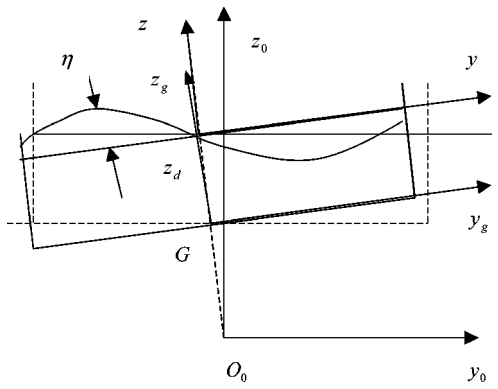

Fig. 1 Coordinate system configuration

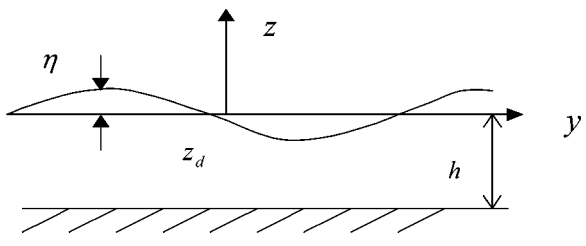

Fig. 2 Shallow water flow coordinate system

Downloaded 03 Jun 2010 to 171.66.16.150. Redistribution subject to ASME license or copyright; see http://www.asme.org/terms/Terms_Use.cfm

2.2 Governing Equations. The problem of the shallow water flow in a container can be formulated as a nonlinear hyperbolic system of equations using shallow water wave theory. The nonlinear shallow water wave equations derived in Stoker [8] are used in our study,

$$\frac{\partial v}{\partial t}+v\frac{\partial v}{\partial y}=-g\frac{\partial \eta}{\partial y} \tag{1}$$

$$\frac{\partial[v\cdot(\eta+h)]}{\partial y}=-\frac{\partial \eta}{\partial t} \tag{2}$$

in which $v(y,t)$ is the vertically-averaged flow velocity in the y-direction. h is the water depth when the water is undisturbed. g is the gravitational acceleration. In the derivation of Eqs. (1) and (2), the water is assumed inviscid and incompressible. The water depth is assumed shallow as compared to the radius of curvature of the water surface. It is not necessary to assume that the displacement and slope of the water surface are small. As a result, the theory is not necessarily linear. The above two equations are derived based on the fluid mass and momentum conservation laws (the Euler equations for ideal fluid), and satisfy the nonpenetration condition on the solid bottom and the kinematic and dynamic boundary conditions on the free surface. The free surface kinematic condition ensures that the fluid particles on the surface remain on the surface. The free surface dynamic condition requires the fluid pressure on the free surface equal to the atmospheric pressure usually set to zero.

Equations (1) and (2) represent the movement of the water in a stationary and leveled vessel. Since the Z_d-yz coordinate system is non-inertial for a moving vessel, it is necessary to take into account the apparent body forces arising as a result of the accelerations and rotations of the vessel in order to correctly describe the flow in the Z_d-yz system. Therefore, Eq. (1) and Eq. (2) are modified as (Zhou [22]),

$$\frac{\partial v}{\partial t}+v\frac{\partial v}{\partial y}=-a(y,t)\frac{\partial \eta}{\partial y}+f(y,t) \tag{3}$$

$$\frac{\partial[v(\eta+h)]}{\partial y}=-\frac{\partial \eta}{\partial t}. \tag{4}$$

where

$$f(y,t)=-\ddot{Y}_G\cos\phi-\ddot{Z}_G\sin\phi+\omega^2 y+\dot{\omega}z-g\sin\phi \tag{5}$$

and

$$a(y,t)=-\ddot{Y}_G\sin\phi+\ddot{Z}_G\cos\phi-\omega^2 z+2\omega v+\dot{\omega}y+g\cos\phi \tag{6}$$

where (Y_G,Z_G) is the location of the origin of the $G-y_gz_g$ system in the earth-fixed system $O_0-y_0z_0$. ϕ and ω are the rotation angle and the angular velocity of the $G-y_gz_g$ system relative to the earth-fixed system $O_0-y_0z_0$. The single dot and double dot over the variables in Eq. (5) and Eq. (6) indicate the first and second derivatives with respect to time. $f(y,t)$ and $a(y,t)$ are the body forces, in y and z directions respectively, acting on the water due to the gravitation and acceleration of the $G-y_gz_g$ system.

Defining water height as $\lambda=\eta+h$, one has $\partial\lambda/\partial t=\partial\eta/\partial t$. Equations (3) and (4) can then be expressed as,

$$\frac{\partial v}{\partial t}+v\frac{\partial v}{\partial y}+a(y,t)\frac{\partial \lambda}{\partial y}=f(y,t) \tag{7}$$

$$\frac{\partial \lambda}{\partial t}+v\frac{\partial \lambda}{\partial y}+\lambda\frac{\partial v}{\partial y}=0 \tag{8}$$

With proper initial conditions and boundary conditions on the tank walls, the shallow water flow field can be solved numerically. Initial conditions are given as:

$$\lambda=\lambda(y,t_0),\quad v=v(y,t_0)\quad \text{at}\quad t=t_0 \tag{9}$$

where $t_0<t<t_0+Dt$ in Eq. (7) and Eq. (8), Dt is a time interval of the motion of the vessel. The boundary conditions on the free surface and the bottom are automatically satisfied under the long wave assumption (Stoker [8]). The remaining boundary conditions to be satisfied are those on the side walls of the tank. On the side walls, the usual non-penetration of flow condition is imposed,

$$v=V_w \tag{10}$$

where V_w is the velocity of a side wall. Numerical implementation of the initial condition and the side wall condition is described in the following sections.

3 Method of Solution

We divide the flow domain equally into M elements of length Δy along the y axis and approximate the water height λ and velocity v by piece-wise-constant functions of y, i.e., λ and v are constants over an element. As defined before, Dt is the time step in the numerical calculation of the motion of a vessel. Dt is further discretized into much smaller equal time intervals (time steps), $\Delta\tau=Dt/N_1$, with N_1 being the number of time steps. λ and v at each time instant within Dt are then obtained by solving the initial boundary value problem, i.e., Eqs. (7) and (8) with the initial condition Eq. (9) and the boundary condition Eq. (10), in a time stepping fashion.

The main difficulty of finding the solution to Eqs. (7) and (8) is handling of hydraulic jumps which almost inevitably appear. Prior to the appearance of a jump, the solution may be obtained numerically using the method of characteristics. However, the method breaks down when the characteristic lines converge, which implies the formation of a jump.

Glimm's method (Chorin [16]) is used to solve Eqs. (7) and (8) and simulate hydraulic jumps in shallow water flows. The method consists of two steps. First, for each element, an analytical solution of a local Riemann problem (or equivalently a dam-breaking problem) at the end of each time interval $\Delta\tau$ is obtained by solving the initial value problem using the solution at the previous time step (i.e., the beginning of this time interval) as the initial condition. Then, the solution as piece-wise constant functions for the whole space domain is constructed using a random sampling procedure to sample a series of the obtained local explicit solutions of the Riemann problems. This gives the solution for the water height $\lambda=\eta+h$ and the flow velocity v for each element at the end of the time interval $\Delta\tau$. The process repeats for the next time interval, thus giving the solution at all time instants in Dt for all the elements. It has been proven that the solution obtained in this time-stepping fashion converges to the exact solution to Eq. (7) and Eq. (8) as the number of time steps and the number of the spatial grid points increase (Chorin [16]).

Glimm's method is attractive because it can handle relatively complex flows with multiple hydraulic jumps without any special treatment of the discontinuities and can handle the cases where the deck can be partially dry. The method is unconditionally stable and numerical errors can be quantified if the Courant-Friedrichs-Levy (CFL) condition (defined in Eq. (19)) is met. Theoretical stability analysis and numerical experiences have shown that for a best accuracy in tracking discontinuities it is best to have the CFL condition just barely satisfied (Tannehill et al. [23], Wigton [24]). In the following, we will show how this condition is satisfied in our version of the Glimm's method.

3.1 Time-Stepping of the Solution. The technique of operator splitting (Tannehill et al. [23]) is used to remove the inhomogeneous term $f(y)$ on the right-side of Eq. (7). At each time instant, we solve the following homogeneous equations,

$$\frac{\partial v}{\partial \tau}+v\frac{\partial v}{\partial y}+a(y,\tau)\frac{\partial \lambda}{\partial y}=0 \tag{11}$$

$$\frac{\partial \lambda}{\partial \tau}+v\frac{\partial \lambda}{\partial y}+\lambda\frac{\partial v}{\partial y}=0 \tag{12}$$

Downloaded 03 Jun 2010 to 171.66.16.150. Redistribution subject to ASME license or copyright; see http://www.asme.org/terms/Terms_Use.cfm

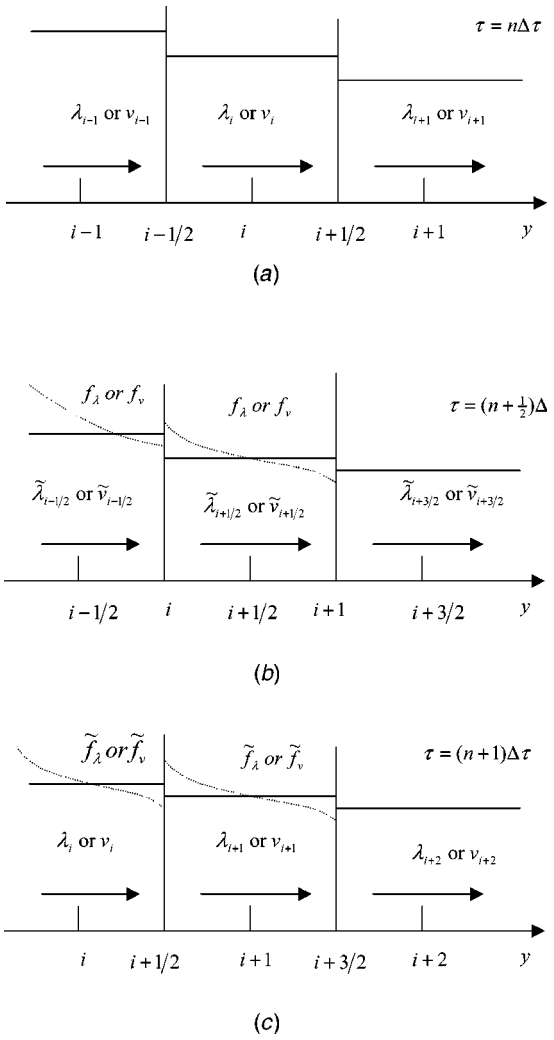

Fig. 3 Time stepping of the flow solution for Element *i*. (*a*) Flow state at $\tau = n\Delta\tau$; (*b*) intermediate flow state at $\tau = (n+1/2)\Delta\tau$; (*c*) flow state at $\tau = (n+1)\Delta\tau$

and then correct the solution to the homogeneous equations with the inhomogeneous equation,

$$\frac{\partial \nu}{\partial \tau} = f(y,\tau) \tag{13}$$

The solution obtained using the splitting technique is the solution to Eqs. (7) and (8) (Tannehill et al. [23]).

First, we seek the solution to the homogeneous equations, Eq. (11) and Eq. (12). Assume that the solution to the homogeneous equations at time $n\Delta\tau$,

$$U_i^n = \begin{Bmatrix} \lambda_i \\ \nu_i \end{Bmatrix} \quad \text{for} \quad \left(i-\frac{1}{2}\right)\Delta y < y < \left(i+\frac{1}{2}\right)\Delta y \tag{14}$$

is known (Fig. 3(*a*)). In Eq. (14), i is the element index indicating the mid-point of the ith element, while n is the time step index indicating the nth time instant. When $n=0$, i.e., at the beginning of Dt, the solution to Eq. (7) and Eq. (8) is used for (λ_i, ν_i) in Eq. (14). The objective is to find the solution to the homogeneous Eq. (11) and Eq. (12) at time $(n+1)\Delta\tau$ with U_i^n in Eq. (14) as the initial condition. Figure 3(*a*) shows the solution at $n\Delta\tau$ for elements $i-1$, i and $i+1$. Notice that it has been assumed that the solutions are piece-wise-constant functions of y.

The procedure of finding the solution to Eq. (11) and Eq. (12) consists of two steps:

Step 1:

For grid point $i+1/2$ which is the end point of the element i and also the starting point of element $i+1$, a local Riemann problem is solved. The local Riemann problem is an initial-value problem of an imagined dam-breaking governed by Eq. (11) and Eq. (12) with the initial condition,

$$U(y,n\Delta\tau) = \begin{cases} U_{i+1}^n & y > (i+1/2)\Delta y \\ U_i^n & y < (i+1/2)\Delta y \end{cases} \tag{15}$$

for which an analytical solution exists (Stoker [8]). For every grid point, e.g., point $i+1/2$, let $f_\nu(y,(n+1/2)\Delta\tau)$ and $f_\lambda(y,(n+1/2)\Delta\tau)$ be the analytical solution (corresponding to ν and λ, respectively) to the local imagined dam-breaking problem. The analytical solution within element i, being shown in Fig. 3(*b*) by the dotted line, is used to construct an intermediate solution, $\tilde{U}_{i+1/2}^{n+1/2}$, shown by the solid horizontal line between grid nodes i and $i+1$. $\tilde{U}_{i+1/2}^{n+1/2}$ is determined by

$$\tilde{U}_{i+1/2}^{n+1/2} = \begin{cases} \tilde{\nu}_{i+1/2}^{n+1/2} = f_\nu\left[\left(i+\frac{1}{2}+r_n\right)\Delta y, \left(n+\frac{1}{2}\right)\Delta\tau\right] \\ \tilde{\lambda}_{i+1/2}^{n+1/2} = f_\lambda\left[\left(i+\frac{1}{2}+r_n\right)\Delta y, \left(n+\frac{1}{2}\right)\Delta\tau\right] \end{cases} \tag{16}$$

where r_n is a random number from [0,1/2]. Solving the local Riemann problems for all the grid nodes $i+1/2$ for $i = 1,2,\ldots\ldots,M-1$, we obtain the intermediate solution over the whole domain at time $\tau=(n+1/2)\Delta\tau$, (Fig. 3(*b*)). The discontinuities in the solution have been shifted a distance of half element length.

Step 2:

This step advances the solution to time $\tau=(n+1)\Delta\tau$ using the intermediate solution obtained in Step 1 as the initial condition. Similarly, a sequence of local Riemann problems are solved for every point of the discontinuities (now at $i+1$). The analytical solution to the Riemann problem, $\tilde{f}_\nu(y,(n+1)\Delta\tau)$ and $\tilde{f}_\lambda(y,(n+1)\Delta\tau)$, for point $i+1$ is shown in Fig. 3(*c*) (dotted line). Finally, the solution for element $i+1$ is determined in a similar way by

$$U_{i+1}^{n+1} = \begin{cases} \nu_{i+1}^{n+1} = \tilde{f}_\nu[(i+1+\tilde{r}_n)\Delta y, (n+1)\Delta\tau] \\ \lambda_{i+1}^{n+1} = \tilde{f}_\lambda[(i+1+\tilde{r}_n)\Delta y, (n+1)\Delta\tau] \end{cases} \tag{17}$$

with a different random number $\tilde{r}_n$ from $[-1/2,0]$. The final solution is shown in Fig. 3(*c*) by the horizontal solid line.

These two steps advance the solution to the homogeneous equations, Eq. (11) and Eq. (12) from time $\tau=n\Delta\tau$ to time $\tau=(n+1)\Delta\tau$.

Repeating the two steps for every $\Delta\tau$ until the solution to the homogeneous equations is obtained for $\tau=N_l\Delta\tau=Dt$. The homogeneous solution at $\tau=Dt$, denoted as ν_i^o, is corrected to obtain the final solution to Eq. (7) and Eq. (8) at this time instant with the use of the inhomogeneous equation, Eq. (13),

$$\nu_i = \nu_i^o + \int_t^{t+Dt} \frac{\partial \nu}{\partial \tau} dt = \nu_i^o + \int_t^{t+Dt} f(y,t)dt. \tag{18}$$

The time integration in the above equation can be easily carried out using a simple Runge-Kutta method.

Two measures are employed to ensure that the numerical solution is stable and the waves propagate correctly. The first measure is that the following Courant-Friedrichs-Levy (CFL) condition (Tannehill et al. [23]),

$$\frac{\Delta y}{2\Delta\tau} > (|\nu| + C) \tag{19}$$

is satisfied for every element. In Eq. (19), $|\nu|$ and C are the local velocity and celerity of the flow respectively. The local celerity is approximated with the shallow water wave velocity $C=\sqrt{g\lambda}$.

Downloaded 03 Jun 2010 to 171.66.16.150. Redistribution subject to ASME license or copyright; see http://www.asme.org/terms/Terms_Use.cfm

When the CFL condition is satisfied, the waves generated by the local dam breaks will not propagate more than one half of the element length in one time step. The second measure is that it is necessary that the sequence of the random numbers $\{r_n\}$ approaches a uniform distribution in the interval $(-1/2,1/2)$ as rapidly as possible. If the sequence were completely random, then there would have been a finite probability in numerical calculations that stationary discontinuities or boundaries may move, or that a moving discontinuity may propagate in the wrong direction during some short time intervals. The possibility of either of these occurrences can be eliminated if the random sequence alternates so that during the one half time step $r_n>0$ and the next half time step $\tilde{r}_n<0$ (a more extensive discussion is given by Chorin [16]).

3.2 Numerical Implementation of the Boundary Condition at Walls. To enforce the nonpenetration condition, Eq. (10), on the walls at the two ends of the flow domain, we replace the walls with one virtual element to the left end of the domain and one virtual element to the right end of the domain. The flow states of the virtual elements are chosen so that there is no flow exchange between a virtual element and its adjacent real element. Here, we demonstrate how this is done for the right wall. The left wall is treated in a similar manner.

Refer to Fig. 4(*a*) the center of the last element is located at point marked M while the right wall is located at the point marked $M+1/2$. The added virtual element has its center at the point $M+1$. At time $\tau=n\Delta\tau$, the flow state of element M, denoted as ν_l and λ_l, are known. The flow state of the virtual element, denoted as ν_r and λ_r, is chosen so that

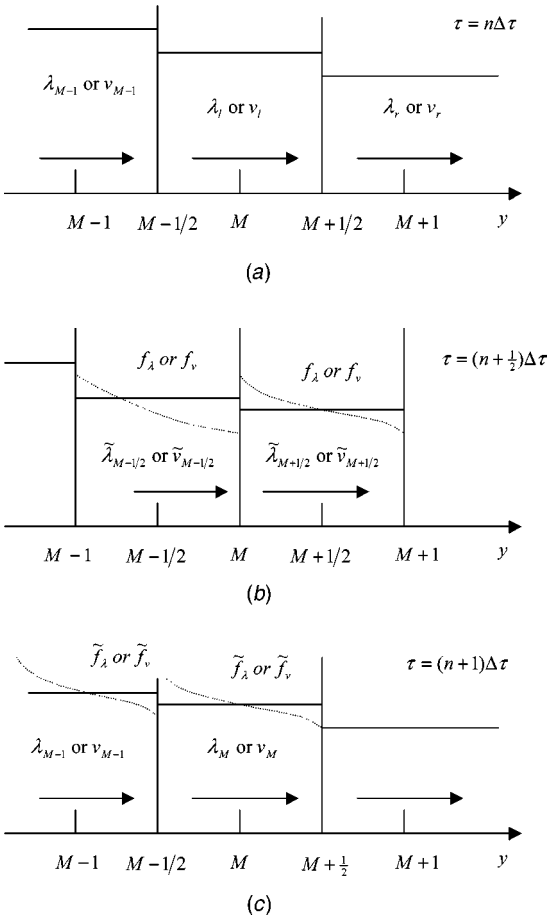

Fig. 4 Time stepping of the flow solution for the element at the end of the flow domain. (*a*) Flow state at $\tau=n\Delta\tau$; (*b*) intermediate flow state at $\tau=(n+1/2)\Delta\tau$; (*c*) flow state at $\tau=(n+1)\Delta\tau$

$$\begin{cases} \dfrac{\nu_l+\nu_r}{2}=V_w \\ \lambda_r=\lambda_l \end{cases} \tag{20}$$

or

$$\begin{cases} \nu_r=2V_w-\nu_l \\ \lambda_r=\lambda_l \end{cases} \tag{21}$$

The flow state of element M can then be advanced to time $\tau=(n+1)\Delta\tau$ using the above described two-step procedure with ν_r and λ_r in Eq. (21) as the initial condition. In the first step, the analytical solution to the local Riemann problem about point $M+1/2$ is obtained and used to construct the flow state at $\tau=(n+1/2)\Delta\tau$ between point M and point $M+1$ using Eq. (16) with a random number r_n from [0,1/2]. Meanwhile, the flow state at time $\tau=(n+1/2)\Delta\tau$ between point $M-1$ and point M has also been constructed using the analytical solution to the Riemann problem about point $M-1/2$. Figure 4(*b*) illustrates the analytical solutions of the Riemann problems about point $M-1/2$ and point $M+1/2$ and the flow states at time $\tau=(n+1/2)\Delta\tau$ on both sides of point M. In the second step, the flow state of element M at time $\tau=(n+1/2)\Delta\tau$ is obtained using the solution to the Riemann problem about point M with the flow states on both sides from the first step as the initial condition and a random number $\tilde{r}_n$ from $[-1/2,0]$. Figure 4(*c*) illustrates the corresponding solution to the Riemann problem and the flow state of element M. It is not necessary to advance the flow state of element $M+1$ to time $\tau=(n+1/2)\Delta\tau$ since it is a virtual element outside the flow domain. The flow state of the virtual element at time $\tau=(n+1)\Delta\tau$ will be chosen according to Eq. (21) and used for the time stepping of the flow state of the last element for the next time step.

Actually, the time stepping of the elements at the domain ends is carried out in the exactly same way as those inner elements when the two virtual elements are added. The flow states of the virtual elements are chosen according to Eq. (21) so that the nonpenetration condition is satisfied.

3.3 Impacting Forces. Once the water height is sought, the linearized impact pressure exerted on the bottom of the tank can be calculated using the following formula (Zhou [21]),

$$p(y,z,t)|_{z=z_0}=\rho a(y,z_0,t)\lambda(y,t) \tag{22}$$

The impact pressure exerted on the walls can be calculated using

$$p(y,z,t)|_{y=y_0}=\rho a(y_0,z,t)(\lambda,(y_0,t)-h-z) \tag{23}$$

In Eq. (22) and Eq. (23), (y, z) is the coordinate of a point where the pressure is of interest in the deck-flow coordinate system Z_d-yz. ρ is the water density.

The forces exerted on the bottom and walls can be obtained by integrating the pressure over the wetted area,

$$\vec{F}(y,z,t)=-\int_s\int p(y,z,t)\vec{n}ds \tag{24}$$

and the moment about the origin is:

$$\vec{M}(y,z,t)=-\int_s\int p(y,z,t)\vec{r}\times\vec{n}ds \tag{25}$$

where $\vec{n}$ is unit exterior normal to the boundary and $\vec{r}$ is the position vector of a point on the boundary from the origin.

4 Numerical Results

The numerical algorithm described in the previous section is examined with three problems: 1) dam-breaking, 2) water slosh-

Downloaded 03 Jun 2010 to 171.66.16.150. Redistribution subject to ASME license or copyright; see http://www.asme.org/terms/Terms_Use.cfm

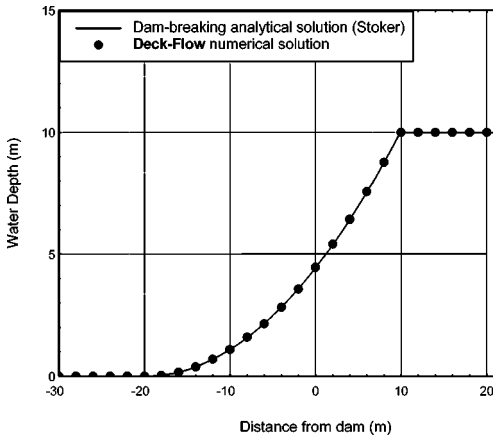

Fig. 5 Comparison of water depth of dam-breaking problem

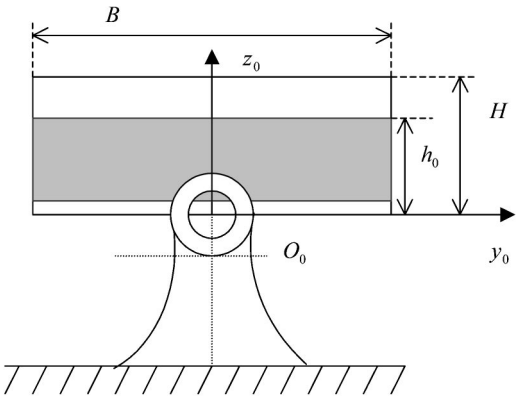

Fig. 7 Fluid oscillation in an oil tank

ing in a rolling tank, and 3) water impacting due to the breaking of a water reservoir. The results of the investigations are presented in the following.

4.1 Dam-Breaking Problem. As a first check, Glimm's method is used to solve the dam-breaking problem for which an analytical solution exists (Stoker [8]). Initially, the water height is 10.0 m on right side of the dam and there is no water on the left side. The water on the right side extends to infinite (to the right) and the dry left side of the bottom extends to infinite (to the left). The solution after the dam breaks is sought using the numerical procedure.

Recall that in Glimm's method, the same analytical solution approach is applied locally (for each spatial interval) at each time step to the imagined dam-breaking problems and the solutions of the local dam-breaking problems used to construct the global solution. Because of this, the numerical solution should recover the analytical solution very well globally for this problem as long as the discretizations in time and space are fine enough.

Figure 5 compares the numerical and analytical values of the water height at the time $t=1.0$ second. Figure 6 compares the numerical and analytical values of the velocity at the same time instant. A ''perfect'' correlation between the numerical and analytical results is found as expected.

4.2 Water Sloshing in a Rolling Tank. Water sloshing in a two-dimensional tank undergoing a forced oscillation is considered. The tank has a width of B and is initially leveled and filled with water of a depth h_0. The tank oscillates about the origin of the $O_0-y_0z_0$ system as depicted in Fig. 7.

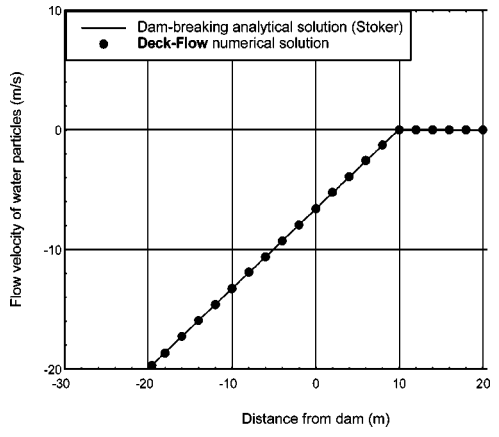

Fig. 6 Comparison of velocity of dam-breaking problem

According to the theoretical analysis by Verhagen and van Wijngaarden [6], a resonance of the oscillation of the water in the tank occurs if the frequency of the excitation (the roll motion of the tank) is near the natural frequency of a weak jump which depends upon the fluid depth:

$$\omega_0=\frac{\pi}{B}\sqrt{gh_0} \tag{26}$$

It was observed in the experiment by Verhagen and van Wijngaarden [6] that a hydraulic jump was generated when the excitation frequency was near $\omega=\omega_0$ and the hydraulic jump traveled periodically back and forth between the walls of the tank.

For oscillations near the natural frequency, linear theories for the water sloshing fail because they are not able to handle the hydraulic jumps and would give a solution of infinite amplitude. We use Glimm's method to simulate the water sloshing. The experimental measurement (Verhagen and van Wijngaarden [6]) is available for validating the numerical solution. In the experiment, the tank width was $B=1.20$ m and the water depth initially was $h_0=0.09$ m. The tank was moved, with the roll angle being,

$$\phi=\phi_0\sin(\omega_0 t-\theta_0) \tag{27}$$

where,

ϕ_0 : the amplitude of roll oscillation;
θ_0 : the initial roll angle;
ω_0 : the natural frequency, $\omega_0=2.46\ \mathrm{s}^{-1}$.

This experimental configuration is used in the numerical simulation.

In the numerical calculations, the tank width is equally divided into N_y elements. The total simulation time is set to be $T=13.0$ seconds long enough to reveal the characteristics of the flow. The time step for which the motion of the tank is calculated is *Dt*. *Dt* is further divided into $\Delta\tau=Dt/N_1$ in Glimm's method for the time stepping of the shallow water flow solution. The time marching step number N_1 within *Dt* is determined according to the CFL condition to satisfy the stability criteria. Within the time interval *Dt*, the acceleration of the tank is held constant, implying the body force due to the acceleration of the tank is held unchanged during the time stepping for the time interval *Dt*.

Like in any numerical method, two important parameters (the resolution of geometric discretization and the time step size) may affect the accuracy of the numerical solutions using Glimm's method. The effects of these two parameters are examined and the results of the numerical investigation are presented in Section 4.2.1 and Section 4.2.2. It should be pointed out that in the numerical investigation we always keep the CFL condition satisfied so that the time stepping is stable.

Downloaded 03 Jun 2010 to 171.66.16.150. Redistribution subject to ASME license or copyright; see http://www.asme.org/terms/Terms_Use.cfm

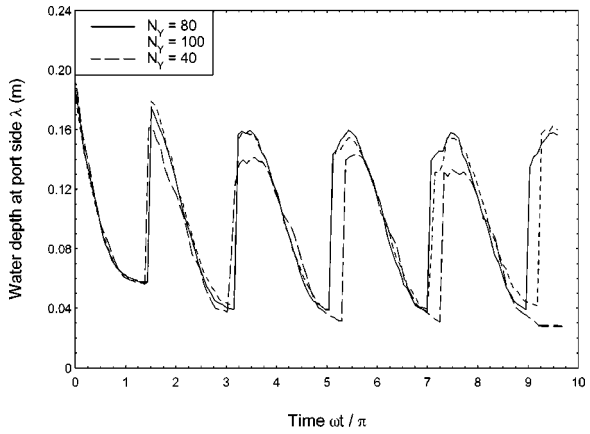

Fig. 8 Effect of resolution of Δy on the simulation of hydraulic jumps

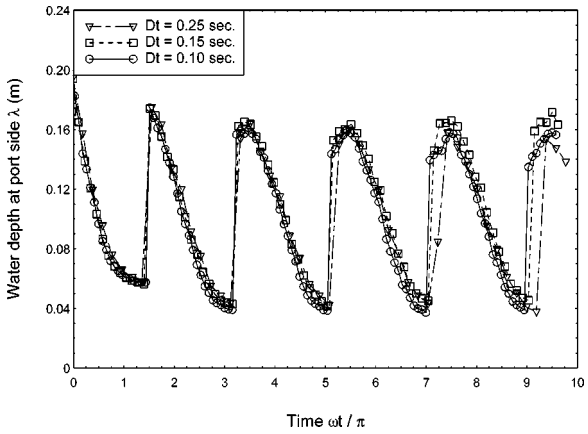

Fig. 10 Effect of the time step size *Dt* on the simulation of hydraulic jumps

4.2.1 Effect of the Resolution of Geometric Discretization. The effect of the resolution of geometric discretization on the numerical solution is examined by varying the number of the elements N_y while keeping *Dt* unchanged. Since the celerity of the local wave propagation varies in space and changes with time, the smaller time step size $\Delta\tau$ for the time stepping within *Dt* may vary to meet the stability requirement of the CFL condition. In the results presented below, the time step size *Dt* is 0.10 second.

Figure 8 shows the computed water height as a function of time at the location $y/B=0.492$ using three different grid resolutions ($N_y=40$, 80, and 100). Figure 9 shows the effect of $\Delta y(=B/N_y)$ on the sloshing moment exerted on the tank by the sloshing water. It demonstrates that the sloshing moment is less sensitive to the change of Δy than the water height.

4.2.2 Effect of the Time Step Size Dt. The effect of the time step size *Dt* on the numerical solution is examined by varying *Dt* while keeping Δy unchanged. Again, for the same reason, the time marching step number N_1 for the time stepping within *Dt* may vary to meet the stability requirement of the CFL condition. In the results presented below, the number of the spatial elements is $N_y=80$, *i.e.*, $\Delta y=0.015$ m. Three values of *Dt* (0.10, 0.15 and 0.25 seconds) are used.

Figure 10 shows the effect of *Dt* on the water height. As can be seen, the three curves are very close to each other for up to $\omega t/\pi=5$. After that, the curve with $Dt=0.25$ second gradually departs from the other two curves in the traveling velocity of the hydraulic jump in particular. The curves with the finer time steps ($Dt=0.10$ and 0.15 second) stay close for a longer time. This indicates that the numerical error in the jump traveling velocity, as well as the water height, accumulates as the time stepping proceeds. The larger *Dt* is, the higher the rate of the error accumulation. Such error accumulation is also very common in most of numerical time stepping procedures. Nevertheless, it is quite remarkable that the present algorithm remains stable for such a large time step *Dt* simulation.

Figure 11 shows the effect of *Dt* on the sloshing moments. As expected, the sloshing moment is much less sensitive to *Dt* since the sloshing moment is an integrated quantity. The rate of the error accumulation is, therefore, lower than that for the water height. Up to $t=13.0$ sec., the three curves are very close to each other.

4.2.3 Hydraulic Jump Traveling Between the Walls of the Tank. Figure 12 shows the water surface profile at six time instants ($t=9.25$, 9.50, 9.75, 10.0, 10.25, and 10.50 s), and the traveling of the hydraulic jump between the tank walls is clearly seen. The hydraulic jump occurs at around $t=9.25$ s, and travels toward the right wall. As the jump travels, the magnitude of the jump remains pretty much unchanged, but the water height changes so that the total fluid mass remains conserved. At around $t=10.0$ s, the jump reaches the wall, changes the direction of its movement, and moves back toward the left wall, as indicated by the profiles at $t=10.25$ s and $t=10.50$ s. This characteristics of the movement of the hydraulic jump in the sloshing tank, as observed in the experiment (Verhagen and van Wijngaarden [6]), is well captured by the numerical simulation.

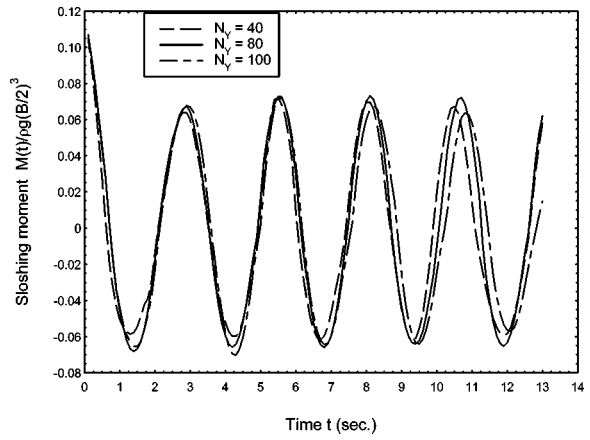

Fig. 9 Effect of resolution of Δy on the sloshing moment

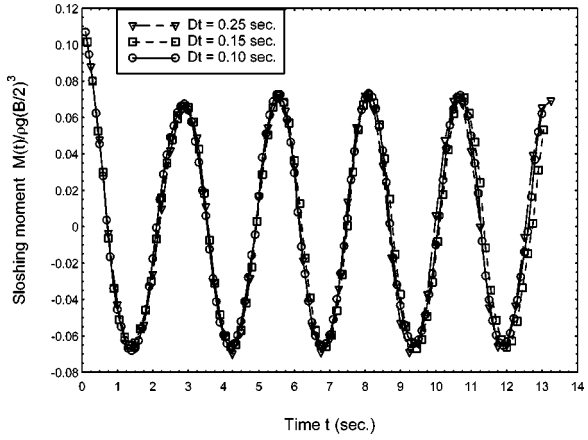

Fig. 11 Effect of the time step size *Dt* on the sloshing moment

Downloaded 03 Jun 2010 to 171.66.16.150. Redistribution subject to ASME license or copyright; see http://www.asme.org/terms/Terms_Use.cfm

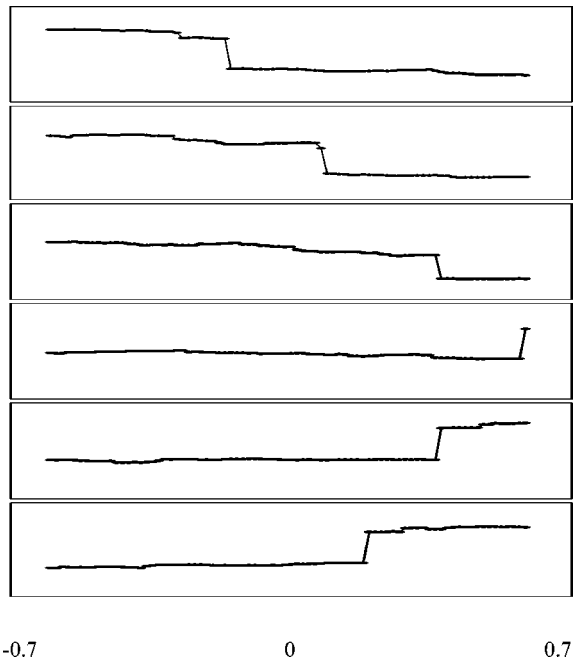

Fig. 12 Hydraulic jump traveling between the walls of a tank at $t=9.25$ s, 9.50s, 9.75s, 10.00s, 10.25s, and 10.50s. (Time increases from top to bottom; for each time, the horizontal axis ranges from −0.7 m to 0.7 and the vertical axis ranges from 0.0m to 0.2 m; $Dt=0.25$ s, $\omega_0=2.46$ s^{-1}, $h_0=0.09$ m)

4.2.4 Comparison of the Numerical Results With the Experimental Data. Validation of the present algorithm is carried out by comparing the numerical results with the available experimental data. Figure 13 shows the computed water height and the experimental measurement at the middle of the tank ($y/B=0$). The experimental data is available only for a relatively short period of time ($\omega t/\pi=0.5$ to 2.5). Figure 14 compares the calculation and the measurement for this time period. The agreement is fairly good, especially in the phase of the hydraulic jump.

Figure 15 shows the computed water height and the experimental measurement at the location, $y/B=0.492$, which is very close to the wall. Figure 16 compares the calculation and the measurement for the time period of $\omega t/\pi=0.5$ to 2.5. The computed height of the hydraulic jump is very close to the height measured. The discontinuity in the water elevation (the hydraulic jump) has been handled well in this algorithm. The predicted location of the jump matches closely with the observation. The jump in the measurements of the water height was not as sharp. This might be due to the effect of surface tension or viscosity of the real fluid that are not included in the present method. In fact, one should not expect the computed water height to match the measured water height perfectly, especially near the hydraulic jump, because the abrupt change in the water height is idealized mathematically with a

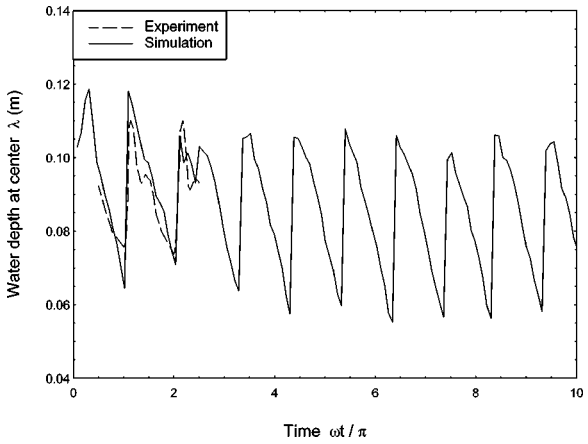

Fig. 13 Comparison of water surface elevation at center of the tank

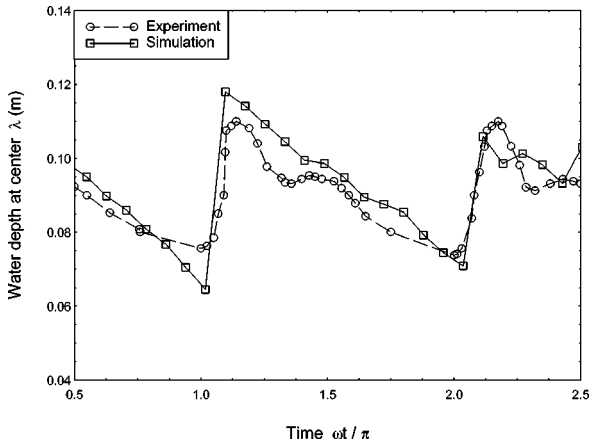

Fig. 14 Zoom view of the comparison of water surface elevation

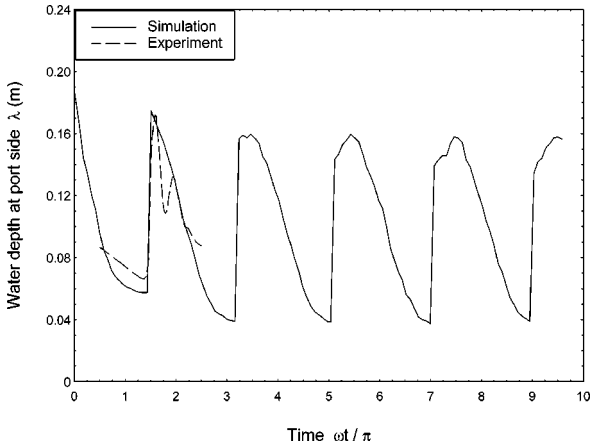

Fig. 15 Comparison of water surface elevation at port side of tank

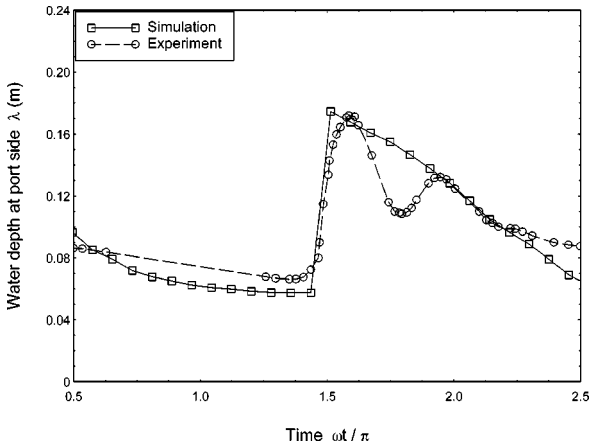

Fig. 16 Zoom view of the comparison of water surface elevation

Downloaded 03 Jun 2010 to 171.66.16.150. Redistribution subject to ASME license or copyright; see http://www.asme.org/terms/Terms_Use.cfm

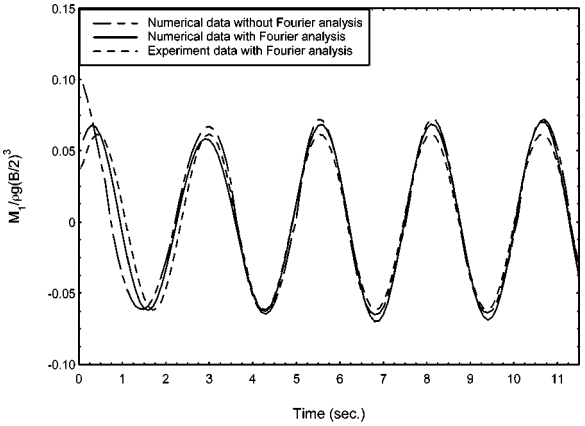

Fig. 17 Comparison of rolling moment of first order component

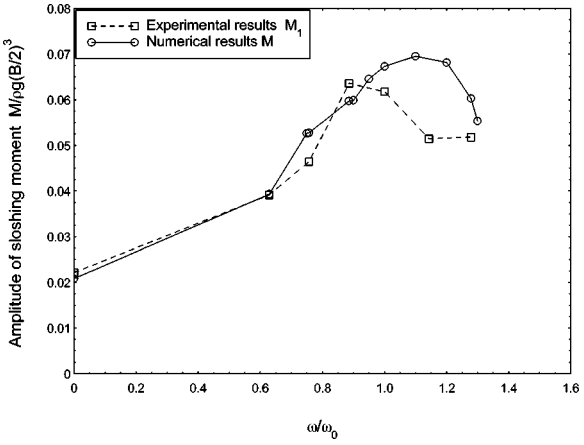

Fig. 19 Amplitude frequency response function

discontinuity in the height. In reality, the water surface is always rounded on the both sides of the jump due to the effects of viscosity and surface tension.

Next, we compare the computed sloshing moment with the experimental data. Due to the complexity of the flow motion of the real fluid, the sloshing moment contains many frequency components. However, the dominant frequency is the first-order frequency, i.e., the natural sloshing frequency. Verhagen and van Wijngaarden [6] gave an estimation of the amplitude of the first-order sloshing moment M_1 and the phase difference ψ_1 based on a Fourier analysis of the experimental data. Therefore, the computed sloshing moment is filtered using Fourier analysis before a meaningful comparison with the experiment results can be made. Figure 17 compares the first-order components of the computed and measured sloshing moments. The agreement is excellent.

We also include the original computed sloshing moment (without Fourier analysis). As seen, the difference in amplitude between the total moment and the first order component is small, confirming that the first-order component is indeed dominant.

Figure 18 shows the comparison of the sloshing moments at $\omega/\omega_0=1.0$ and $\omega/\omega_0=1.10$. As mentioned before, at the frequency near $\omega=\omega_0$, a resonance and a hydraulic jump will occur, thus producing a large rolling moment. As seen from Fig. 18, the generated moment has a distinguish period and amplitude, which appears mainly due to the back and forth movements of the hydraulic jump.

Finally, we compare the frequency response function for the sloshing moment. Figure 19 shows the amplitude of the computed sloshing moment as a function of the excitation frequency. We also include the first order component of the experiment data. As seen, the magnitudes are very close to each other for the excitation frequency less than the sloshing natural frequency. A significant discrepancy is noticed when the excitation frequency is greater than the natural frequency. Also noticed is that the peak response from the measurement occurs at a frequency slightly less than the natural frequency while the computed peak response occurs at a frequency a little higher than the natural frequency. The discrepancy may be due to the effects of high frequency components. Further investigation is needed to determine the causes.

4.3 Water Impacting Due to Breaking of a Water Reservoir. Glimm's method is then applied to the water impacting due to breaking of a water reservoir. In this problem, a rectangular water tank is initially divided with a vertical flap into two areas. The one on the right side of the flap is filled with water (reservoir area) and the other area is empty. We are interested in the water flow in the tank and the water impacting on the tank bottom and

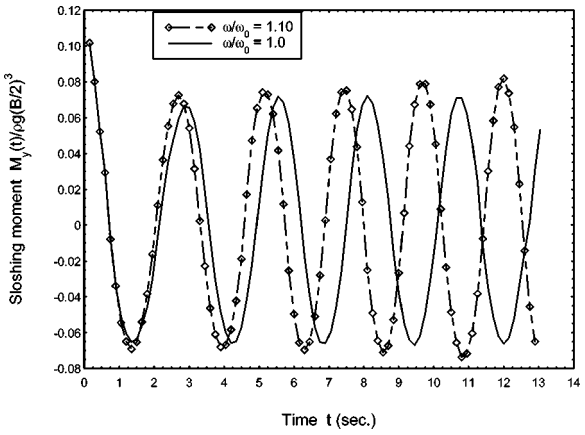

Fig. 18 Sloshing moment at the range near $\omega=\omega_0$

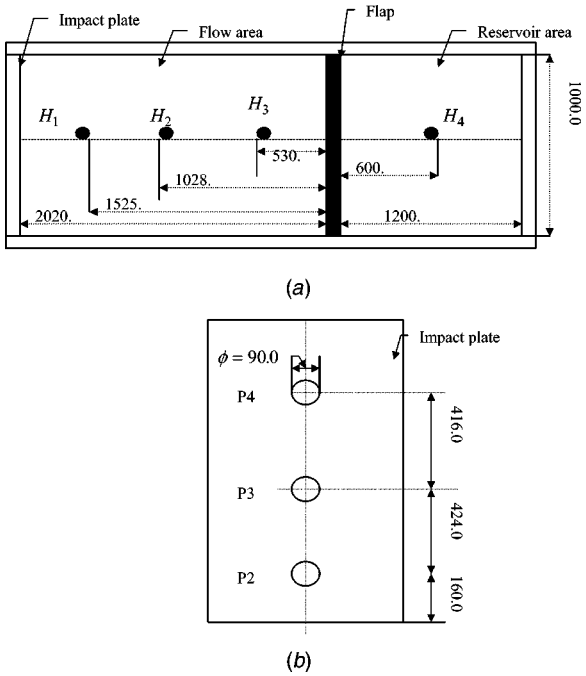

Fig. 20 Configuration of the experimental setup for the breaking of the water reservoir. (*a*) The locations of water depth probes (in mm); (*b*) the locations of the impact pressure transducers (in mm)

Downloaded 03 Jun 2010 to 171.66.16.150. Redistribution subject to ASME license or copyright; see http://www.asme.org/terms/Terms_Use.cfm

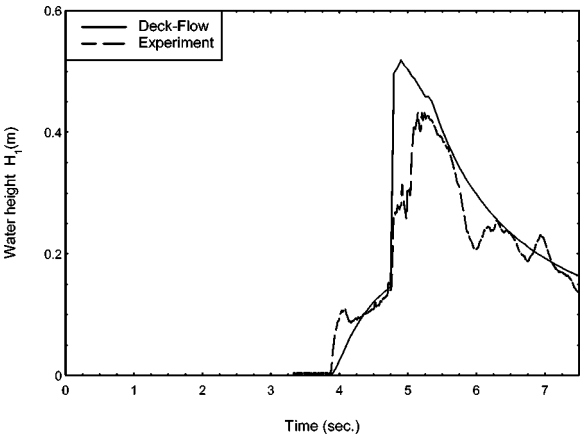

Fig. 21 Water height at H_1

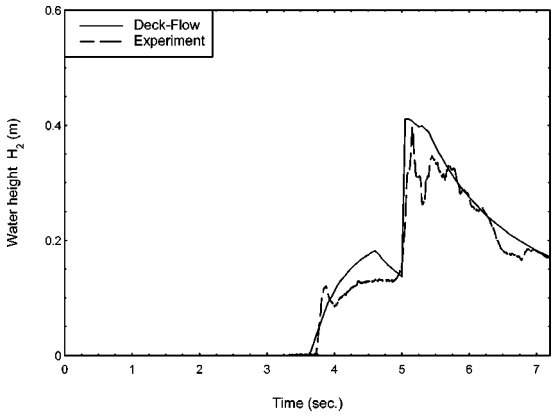

Fig. 22 Water height at H_2

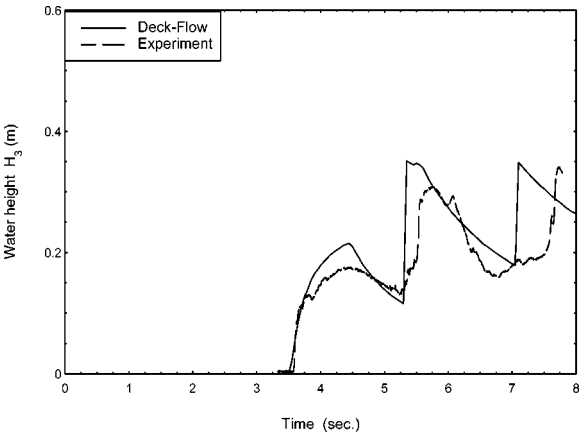

Fig. 23 Water height at H_3

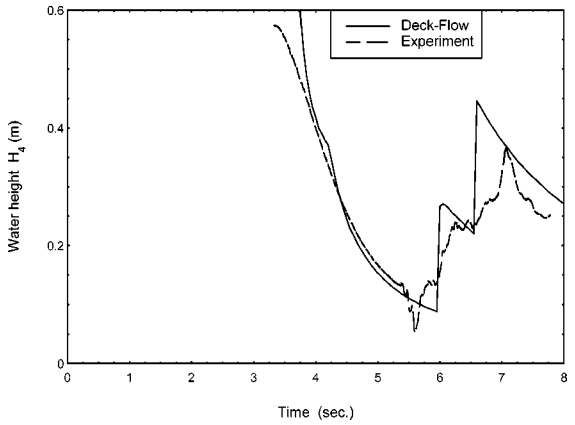

Fig. 24 Water height at H_4

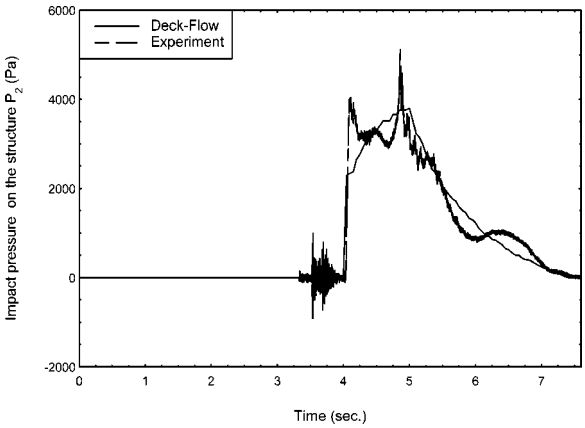

Fig. 25 Impact pressure at P_2

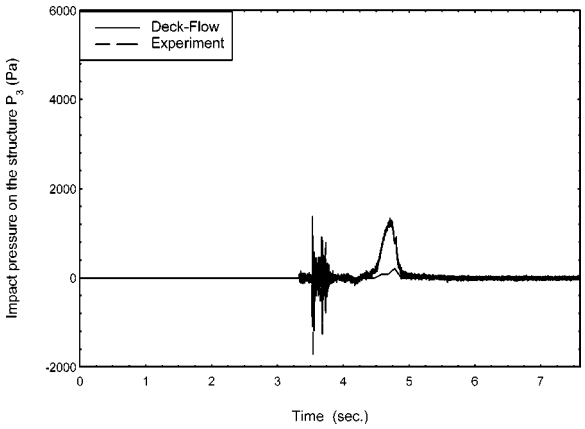

Fig. 26 Impact pressure at P_3

the tank wall on the left end after the flap is suddenly lifted. At the moment when the flap is lifted, the vertical wall of the water in the reservoir crashes into the dry area, resulting in a flow flushing over the bottom of the tank and a splashing of a volume of high speed water on the left wall. When the water hits the wall, it causes a large impact on the wall.

The calculation presented here uses the same configuration of the problem setup used in the experimental study by Buchner and van Ballegoyen [10], see Fig. 20. The dimension of the tank is shown in Fig. 20. The initial water height in the reservoir was 0.6 m. In the experimental study, water height probes were placed at four locations marked as H1, H2, H3, and H4 in Fig. 20(*a*). Three pressure transducers were placed on the wall of a plate at the locations marked as P2, P3 and P4, Fig. 20(*b*). The water height at the four locations on the bottom and the pressure at the three locations on the wall were measured simultaneously.

Like in the water sloshing problem, a numerical investigation on the effects of the grid spacing Δy and the time step size Dt was conducted, and converged solutions were obtained for the water reservoir breaking problem. For the results presented in this paper,

Downloaded 03 Jun 2010 to 171.66.16.150. Redistribution subject to ASME license or copyright; see http://www.asme.org/terms/Terms_Use.cfm

the total simulation time length is $T_N = 8.0$ seconds. The simulation used a time step size of $Dt = 0.10$ s and a grid space of $\Delta y = 0.01$ m. The smaller time step size was again determined automatically in the calculation according to the CFL condition to ensure the stability. The pressure formula reduces to $p = \rho g(\lambda - z)$ in this case since the water tank is stationary.

Figures 21–24 show the comparisons of the water height at the four locations. Generally speaking, the agreement is fairly good. Especially, the numerical simulation is able to capture the occurrence of the first big hydraulic jump at the right time and right place. There is a noticeable discrepancy in water height between the calculation and the measurement. But, again, one should not expect that the computed water height would match well with the measured for the reasons mentioned earlier.

Figures 25 and 26 show the comparisons of the pressure at locations P2 and P3. As seen, the trend of the computation fits closely to that of the experiment measurement. In the experimental data, there are very high frequency components, which might very likely come from the structural vibration of the tank as a response to the impact. The computation under-predicts the impact pressure at the higher location, Fig. 25. This may be due to the omission of the flow velocity terms in the pressure formula; the contribution from the velocity terms may become very significant and cannot be ignored.

5 Conclusions and Discussions

Numerical investigation on Glimm's method has been conducted carefully. The convergence tests have been carried out for three shallow water flow problems. The numerical solutions have been compared with the analytical solution (the dam-breaking problem) and the experimental data (the water sloshing problem and the breaking of water reservoir problem). Our experience with Glimm's method indicated that two measures in our version of Glimm's method are critical in obtaining stable and converged results. The first measure is meeting the CFL condition for every smaller time step $\Delta\tau$ within the big step Dt. The second measure is making the sequence of the random numbers $\{r_n\}$ approach a uniform distribution in $(-1/2, 1/2)$ as rapidly as possible, which is achieved by alternating the sequence such that $r_n > 0$ for the first half of the time step and $r_n < 0$ for the second half step.

Based on the numerical investigation and the comparisons with the experimental data, the following conclusions can be drawn,

1 The present time stepping procedure using Glimm's method is stable as long as the CFL condition is met.

2 Numerical solutions converge as the time step size decreases and the spatial grid density increases.

3 The numerical solution matches almost perfectly the analytical solution in both the water height and flow velocity for the dam-breaking problem for which the analytical solution exists. This indicates that the numerical algorithm is correctly implemented in the computer code.

4 The capability of Glimm's method in handling the problems where part of the domain is dry has been demonstrated through the numerical investigation with the three problems.

5 In general, the numerical results compare fairly well with the experimental data for the water sloshing and the breaking of water reservoir problems. The numerical simulation predicts the occurrence of hydraulic jumps at right time and right location. It also gives correct movement of hydraulic jumps (the traveling direction and speed) and very well preserves the sharp shape of the jumps. The computed sloshing moment on the water tank compares very well with the experimental data.

6 The numerical computation under-predicts the impact pressure at the higher location on the wall in the water reservoir breaking problem. Improvement of the accuracy in the impact pressure calculation may be possible by including the flow velocity terms in the pressure formula.

The results for the water sloshing problem presented in this paper show a significant improvement over those by Pantazopoulous and Adee [19] but only a slight improvement over those by Dillingham [18]. However, our results, for both the water sloshing and water impacting problems, are supported by the more thorough investigation on the Glimm's method in terms of the numerical convergence tests and validation using experimental data.

Further investigation is needed to determine the causes of the discrepancies between the computational results and the experimental measurements in Figs. 16, 19, 21–24 and 26. The possible causes may include ignoring the viscosity and surface tension of the fluid, and the effect of the elasticity of the tank walls, etc.

Extension of the Glimm's method to three-dimensional shallow water problems is relatively straightforward although the formulation and the computations may be tedious. Chorin [16] discussed the Glimm algorithm for the multidimensional problems.

As compared to finite difference methods or boundary element methods, the time stepping procedure using Glimm's method is stable and accurate for shallow water problems, especially when hydraulic jumps occur. Unlike the boundary element method in Faltinsen [12], the Glimm's method requires no artificial damping to keep the solution from going unbounded. In contrast to some finite difference methods (Tannehill et al. [23]), the Glimm's method introduces little numerical damping and is able to maintain the sharpness of the hydraulic jumps. However, the Glimm's method will fail if the motion of the fluid is so violent that the free surface waves turn over. In this case, the water surface is a multivalue function. A boundary element method like that in Faltinsen [12] would not suffer such difficulty.

References

[1] Buchner, B., 1995, "On the Impact of Green Water Loading on Ship and Offshore Unit Design," The Sixth International Symposium on Practical Design of Ships and Mobile units (PRADS), September.

[2] De Kat, J. O., 1996, "Dynamics of a ship with partially flooded component," Second Workshop on Stability and Operational Safety of Ships, Osaka, Nov. 18–19.

[3] Graham, E. W., and Rodriguez, A. M., 1962, "The characteristics of fuel motion which affect airplane dynamics," Journal of Applied Mechanics. **123**, no. 9, pp. 381–388.

[4] Abramson, H. N. (editor), 1966, *The Dynamic Behavior of Liquids in Moving Containers*, NASA SP 106, Washington, DC.

[5] Pilipchuk, V. N., and Ibrahim, R. A., 1997, "The Dynamics of a Nonlinear System Simulating Liquid Sloshing Impact in Moving Structures," J. Sound Vib., **205**, No. 5, pp. 593–615.

[6] Verhagen, J. H. G., and Wijngaarden, L. Van, 1965, "Non-linear Oscillations of Fluid in a Container," J. Fluid Mech., **22**, Part 4, pp. 737–751.

[7] Hamlin, N. A., Lou, Y. K., Maclean, W. M., Seibold, F., and Chandras, L. M., 1986, "Liquid Sloshing in Slack Tanks - Theory, Observations, and Experiments," SNAME Transactions, **94**, pp. 159–195.

[8] Stoker, J. J., 1957, "Water Waves," *Pure and Applied Mathematics*, Vol. **9,** *The Mathematical Theory with Applications*, R. Courant, L. Bers, and J. J. Stoker, eds., Interscience, New York.

[9] Yih, C-S., 1977, *Fluid Mechanics*, West River Press.

[10] Buchner, B., and van Ballegoyen, G., 1997, "F(P)SO Green Water Loading," Vol. A1, Discussion Report, MARIN Report No. 1.13644, Dec.

[11] Faltinsen, O. M., 1974, "A Nonlinear Theory of Sloshing in Rectangular Tanks," J. Ship Res., **18**, No. 4, pp. 224–241.

[12] Faltinsen, O. M., 1978, "A Numerical Method of Sloshing in Tanks with Two-dimensional Flow," J. Ship Res., **22**, No. 3, pp. 192–202.

[13] Lou, Y. K., Wu, M. C., and Lee, C. K., 1985, "Further Studies on Liquid Sloshing," Maritime Administration Report No. MA-RD-760-85009, March.

[14] Lee, Se Hyuk, et al., 1995, "Simulation of 3-D Sloshing and Structural Response in Ship's Tanks Taking Account of Fluid-structure Interaction," SNAME Transactions, **103**, pp. 321–342.

[15] Glimm, J., 1965, "Solutions in the Large for Nonlinear Hyperbolic Systems of Equations," Commun. Pure Appl. Math, **18**, pp. 697–715.

[16] Chorin, A. J., 1976, "Random Choice Solution of Hyperbolic Systems," J. Comput. Phys., **22**, No. 4, pp. 517–533.

[17] Chorin, A. J., 1977, "Random Choice Methods with Application to Reacting Gas Flow," J. Comput. Phys., **25**, No. 3, pp. 253–272.

[18] Dillingham, J., 1981, "Motion Studies of a Vessel with Water on Deck," Marine Technology, **18**, No. 1, pp. 38–50.

[19] Pantazopoulous, M. S. and Adee, B. H., 1987, "Three Dimensional Shallow Water Waves in an Oscillating Tank," Proc. American Society of Civil Eng. Conf. Coastal Hydrodynamics, University of Delaware, Newark, Del., June 28-July 1, pp. 399-412.

[20] Pantazopoulous, M. S., 1988, "Three-dimensional Sloshing of Water on Decks," Marine Technology, **25**, No. 4, pp. 253–261.

Downloaded 03 Jun 2010 to 171.66.16.150. Redistribution subject to ASME license or copyright; see http://www.asme.org/terms/Terms_Use.cfm

[21] Zhou, Z., 1998, ''A Nonlinear 3-D Approach to Simulate Green Water Dynamics on Deck,'' MARIN Report No. 14580-WD, June.
[22] Zhou, Z., de Kat, J. O., and Buchner, B., 1999, ''A Nonlinear 3-D Approach to Simulate Green Water Dynamics on Deck,'' Proc. 7th International Symposium on Numerical Ship Hydrodynamics, Report No. 82000-NSH 7, May, France.
[23] Tannehill, J. C., Anderson, D. A., and Pletcher, R. H., 1997, *Computational Fluid Mechanics and Heat Transfer*, 2nd ed., Taylor & Francis.
[24] Wigton, L., 1979, ''Glimm's Method for Humans,'' Lecture Notes prepared for course on numerical method, Department of Mechanical Engineering, University of California, Berkeley, Ca.

Downloaded 03 Jun 2010 to 171.66.16.150. Redistribution subject to ASME license or copyright; see http://www.asme.org/terms/Terms_Use.cfm

Computational Evaluation of the Periodic Performance of a NACA 0012 Fitted With a Gurney Flap

James C. Date
e-mail: jamesd@ship.soton.ac.uk

Stephen R. Turnock
e-mail: steve@ship.soton.ac.uk

School of Engineering Sciences,
Fluid Structure Interactions Research Group,
University of Southampton,
Highfield, Southampton SO17 1BJ,
United Kingdom

A detailed computational investigation into the periodic two-dimensional performance of a NACA 0012 section fitted with 2 and 4 percent h/c Gurney flaps operating at a Reynolds number of 0.85×10^6 is presented. The aim of the work was to determine the suitability of the incompressible Reynolds-averaged Navier-Stokes (RANS) formulation in modeling the vortex shedding experienced by lifting sections with blunt, sharp edged features. In particular, whether under-converged steady state calculations could be used for section design performance evaluation in place of the computationally intensive time accurate flow simulations. Steady, periodic, and time-averaged two-dimensional lift and drag coefficients, as well as vortex shedding frequency, were predicted and compared with the available experimental data. Reasonable agreement was found, once sufficiently fine grids had been generated, and the correct time step determined for the time accurate simulations. [DOI: 10.1115/1.1427927]

1 Introduction

A Gurney flap is a short thin flap of height, *h*, fitted perpendicular to the pressure surface at the trailing edge of a wing. The most common application of this device is in racing-car spoilers, where it is used to increase the down-force. The blunt, sharp edged affect of the Gurney induces an effective camber disproportionate to its size, increasing the C_L for a given incidence, as well as maximum C_L. The penalty for these increases in C_L is an augment in the zero-lift C_D. Effects similar to these are experienced by high performance ship rudder sections [1]. Of considerable interest is how the lift augment can be maintained while minimizing the zero-lift drag. Early research into the performance affect of fitting a Gurney, and the flow structure resulting was conducted by Liebeck [2] and Neuhart et al. [3]. Recent experimental work by Jeffrey [4] and Jeffrey et al. [5,6] using Laser Doppler Anemometry (LDA), coupled with force and pressure measurements, has furthered the understanding of Gurney flap flows, and provided a rich source of validation data for computational fluid dynamics (CFD) simulations. CFD modeling of Gurneys has been limited, mainly due to computational resource constraints and difficulties associated with the periodic vortex street produced by the Gurney.

Fripp and Hopkins [7] and Jeffrey [4] used panel methods to model sections fitted with Gurney flaps. The Gurney was modelled through the definition of a modified section, with a ''virtual'' trailing edge, representing the streamlines bounding the recirculation regions upstream and downstream of the Gurney. Fripp, and Hopkins [7], reported disappointing results following comparison with experimental data. Jeffrey [4] managed to obtain reasonable agreement between the computational and experimental results for 2 and 4 percent Gurneys fitted to a NACA 0012 section. Although this approach has obvious weaknesses, it can be used as a qualitative tool for assessing Gurney flap performance, while being simple to develop and computationally inexpensive.

RANS investigations have been carried out by Ashby [8], Ross et al. [9], and Jang et al. [10]. All these investigations modeled the Gurney directly, yielding time-averaged data through a quasi-steady solution approach. At this point, it is deemed necessary to explain what is meant by a ''quasi-steady'' solution. Although the flow about a Gurney is unsteady due to the vortex shedding, it is typical to solve these problems as though they were steady, i.e., the time derivatives in RANS equations are set to zero. This provides details of average properties, commonly referred to as a quasi-steady state solution, rather than details of the flow transients. Quasi-steady computations are much easier and faster than time-accurate computations. Applying this solution approach to unsteady problems can, however, neglect important flow phenomena, resulting in incorrect performance prediction. In order to address this problem, both quasi-steady and time-accurate computations have been carried out to determine if this is the case.

Ashby [8] carried out both experimental and computational studies of lift-enhancing tabs on a multi-element aerofoil (NACA 63_2-215ModB). The computational study was conducted using a two-dimensional incompressible RANS code, implementing both the Spalart-Allmaras one-equation and Baldwin-Barth one-equation turbulence models. The computed results predicted all of the trends observed in the experimental data reasonably well. The time-averaged flow field, indicated by computed streamlines, were found to be consistent with the flow field hypothesized by Leibeck [2] and observed by Neuhart and Pendergraft [3].

Jang et al. [9] carried out computational studies of Gurney flaps fitted to a NACA 4412 aerofoil. The computational study was conducted using a two-dimensional incompressible RANS code, again implementing the Baldwin-Barth one-equation turbulence model. The trends observed in this study were shown to agree well with the available experimental results. Although not all of the flow physics was captured in the wake downstream of the Gurney flap, enough of the major flow disturbances caused by the application of the Gurney flap were, giving rise to results consistent with those found by experiment.

Ross et al. [10] also carried out both experimental and computational studies of lift-enhancing tabs on the multi-element aerofoil (NACA 63_2-215 ModB). The computational study was conducted using the same two-dimensional incompressible RANS code as used by Jang et al. [9], implementing the Baldwin-Barth one-equation turbulence model. While the computed lift and drag results did not exactly match those found by experiment, they did, however, manage to indicate the correct trend in the aerodynamic forces resulting from the addition of the Gurney flap to the geometry. Ross et al. [10] do not explicitly state the reasons for the departure of their computational lift and drag predictions from the experimentally measured values, contrary to the earlier findings of Jang et al. [9]. There are a number of possible explanations for this. First, the Gurney flapped single element aerofoil modeled by

Contributed by the Fluids Engineering Division for publication in the JOURNAL OF FLUIDS ENGINEERING. Manuscript received by the Fluids Engineering Division December 8, 2000; revised manuscript received September 13, 2001. Associate Editor: I. Celik.

 Copyright © 2002 by ASME

Downloaded 03 Jun 2010 to 171.66.16.150. Redistribution subject to ASME license or copyright; see http://www.asme.org/terms/Terms_Use.cfm

Jang et al. [9] allowed high quality computational grids to be produced around the section, whereas the complex multi-element aerofoil geometry modeled by Ross et al. [10] resulted in grids of a lower quality. Other likely causes might have been associated with the applicability of the Baldwin-Barth turbulence model for the modeling of more complex flows and possible uncertainties in the experimental data obtained by both researchers. Wilcox [11] specifically mentions that the Baldwin-Barth turbulence model can produce nonphysical diffusion in numerical computations around multi-element aerofoils, while also being renowned for under predicting skin friction drag, especially for attached boundary layers.

Although the RANS studies discussed above yielded results broadly similar to those found by experiment, a number of aspects of the computational modeling of Gurney flapped sections using RANS techniques have not been fully addressed. As yet no researchers have investigated the effect of wake grid resolution on the predicted flow physics found aft of the Gurney flap, or compared quasi-steady RANS computations with full time accurate flow predictions.

The aim of this work has been to apply the standard k-ε two-equation turbulence model in both quasi-steady and time accurate calculations and to compare the results with each other and experimental data. As with all other computations implementing turbulence models, the debate as to the best turbulence model for a specific application was ever present in this research. Although the standard k-ε turbulence model was known to be poor at predicting flows with adverse pressure gradients (similar to the Baldwin-Barth turbulence model) and hence separated flows, it was used because the authors were interested in assessing its performance for high lift section design purposes, rather than its absolute accuracy. Wake grid resolution and time step sensitivity studies were conducted to assess their influence on the computed flow, in order to establish confidence in the results obtained.

2 Investigation

In this study, both quasi-steady state and full time accurate two-dimensional computations were carried out on a Gurney flapped NACA 0012 section. Prior to the Gurney flap investigation, a full boundary location and grid dependence study was conducted on a bare NACA 0012 section. Subsequently, a wake grid dependence study was conducted on the NACA 0012+4 percent Gurney to investigate the effect of the wake grid on the quasi-steady solution, in particular its effect on flow structure and performance prediction.

Quasi-steady computed performance data for a NACA 0012 fitted with a 2 and 4 percent Gurney was then compared with the experimental data obtained by Jeffrey [4], using the optimum grid obtained from the wake study. The quasi-steady flow about the NACA 0012+4 percent Gurney was also compared the experimental flow structure obtained by Jeffrey [4]. A time accurate periodic flow investigation was carried out on the NACA 0012 +4 percent Gurney only. This involved a time step study to examine the effect of time step size on the solution, followed by validation against the experimental data of Jeffrey [4]. The time-averaged periodic data was also compared with the quasi-steady results to determine if the quasi-steady solution approach captured the same time-averaged flow physics. Steady-state solutions were also obtained for an unflapped NACA 0012 operating at the same flow conditions as the Gurney flapped NACA 0012 sections. This was done as a comparison to show how well the solver predicted the effect of fitting a Gurney. These computations were also validated against the data obtained by Jeffrey [4].

2.1 Validation Data. The experimental results obtained by Jeffrey [4] were used for validation. These tests were carried out in a wind tunnel on a wing section of chord $c=0.32$ m and span $b=1.6$ m, at a free stream velocity of $U_\infty=40$ m/s, corresponding to a Reynolds number of between $0.77-0.89\times10^6$ and Mach number of less than 0.11. The variation in the Reynolds number of these tests was caused by variations in the ambient pressure and temperature. The wind tunnel turbulence level was measured, and found to be of the order of 0.2 percent. Transition was fixed at 5 percent x/c from the leading edge. The low Mach numbers of these tests make them suitable for the validation of the computed incompressible results obtained from the RANS code. Jeffrey [4] presents time-averaged c_l, C_L, c_d, C_D versus α, surface pressures, LDA flow field data and LDA spectral flow field information. Calculations of the uncertainties of the data were made. The accuracy of the inclinometer used to set the incidence angle of the wings was ±0.1 degrees. An uncertainty of ±0.0087 in the C_L and ±0.00078 in the C_D was calculated. The surface pressure measurements were found to have an uncertainty of ±0.0013 in the C_p.

2.2 Grid Generator, Flow Solver and Compute Facility Details. The eight block, C-Grid topology grids were produced using the multi-block grid generator FLEXIMESH [12]. The commercial RANS solver CFX-4.3 was used for the research presented. CFX-4.3 is a structured multi-block, fully implicit finite volume flow code produced by AEA Technologies [13]. A variation upon the Rhie-Chow [14] solution algorithm is implemented within CFX-4.3. In all computations third order (convection terms) QUICK differencing, and SIMPLEC pressure correction were used. Quadratic second order time differencing in conjunction with fixed time stepping, was used for all time accurate calculations. The two-equation $k-\varepsilon$ turbulence model, implementing a wall function, was tested using the standard constants [11]. All computations were carried out using one 300 Mhz MIPS processor on an Origin 2000.

2.3 Computational Model and Boundary Conditions. Two Gurney flapped and one unflapped NACA 0012 sections were modeled using the RANS code, having a chord, $c=0.32$ m, span, $b=1.6$ m and flap heights of 2 and 4 percent. These models were run at a Reynolds number of 0.85×10^6 which equated to an inflow velocity of $U_\infty=40$ m/s, based on an air of density $\rho_{\text{air}}=1.204$ kg/m^3 and laminar viscosity $\mu_{\text{air}}=1.811\times10^{-5}$ m^2/s. The inlet turbulence parameters k and ε were set to zero. The mass source residual stopping convergence criteria, was set at 1.0×10^{-3} kg/s in all computations. This convergence level was determined from a mass source residual versus c_l and c_d convergence study on an un-flapped NACA 0012 section. The outer boundary conditions used were; an inlet with a prescribed $u=U_\infty\cos(\alpha)$ and $v=U_\infty\sin(\alpha)$ velocity on the forward part of the C-Grid and upper, lower and far field pressure boundaries of pressure $p=0$. The NACA 0012 section was modeled as a no-slip wall, and the Gurney flap was represented by two no-slip wall surfaces back-to-back. It was deemed unnecessary to model the Gurney thickness, as its effect was considered insignificant and would only serve to further complicate the grid generation process.

3 Results

3.1 NACA 0012 Boundary Location and Grid Dependence Study. A boundary location sensitivity study was conducted on an unflapped NACA 0012 at an angle of incidence of 8 degrees and Reynolds number of 6.0×10^6 appropriate for the data given in [15]. The grids were generated such that the number of cells around the section, and the cell size on the body and on the outer boundary, remained constant for all the boundary locations tested. This was done to ensure that any variations in c_l and c_d were solely due to the boundary location changes and not any grid quality effects. The outer boundaries were positioned between 2 and 15 chord lengths away from the section, and the effect on the computed c_l and c_d was noted. The results from this study can be seen in Table 1. It is evident that at 15 chord lengths the variations

Downloaded 03 Jun 2010 to 171.66.16.150. Redistribution subject to ASME license or copyright; see http://www.asme.org/terms/Terms_Use.cfm

Table 1 NACA 0012 boundary location study

r/c	$c_l \times 10^{-1}$	$c_d \times 10^{-1}$	c_l (% Change)	c_d (% Change)
2	7.700	0.265	-	-
5	7.957	0.209	3.3	21.1
10	8.056	0.191	1.2	8.6
15	8.071	0.189	0.1	1.0

Table 2 NACA 0012 grid dependence study

$n_\xi \times n_\eta$	y^+	$c_l \times 10^{-1}$	$c_d \times 10^{-1}$	α (deg)
474×25	270-765	0.0	0.106	0.0
474×27	118-398	0.0	0.101	0.0
474×29	65-200	0.0	0.098	0.0
474×32	39-99	0.0	0.096	0.0
474×34	20-49	0.0	0.096	0.0
44×32	26-197	7.020	0.347	8.0
118×32	26-197	8.149	0.164	8.0
244×32	26-197	8.148	0.166	8.0
494×32	26-195	8.150	0.168	8.0
494×24	20-196	8.086	0.178	8.0
494×49	36-197	8.164	0.162	8.0
494×99	35-195	7.884	0.213	8.0

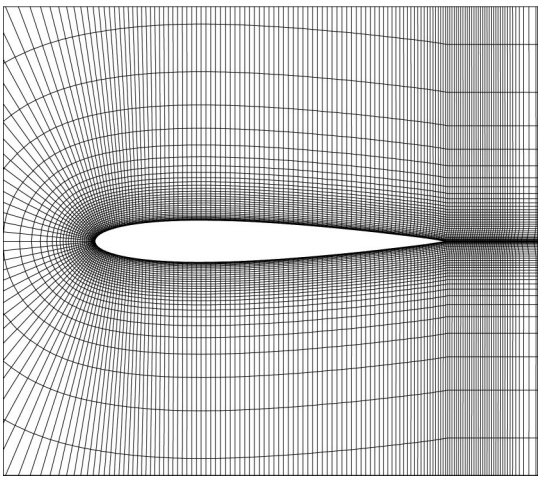

Fig. 1 Four percent Gurney, fine grid (Grid 4)

in the predicted c_l and c_d are small. Based on these findings, the outer boundaries in all subsequent investigations were placed 15 chord lengths away from the section.

A decoupled dependence study was conducted on the NACA 0012. Dependence of the solution to changes in near wall grid node location, number of nodes around the section (n_ξ) and number of nodes radiating (n_η) from the section was sought. It should be noted that the hyperbolic stretching function of Eiseman [16] was used in order to ensure the refined grids produced were of similar form. Wake grid dependence was not investigated since a detailed study would later be carried out for the Gurney flapped NACA 0012. However, a fine grid was propagated in the wake direction ($n_\xi = 49$), and held fixed throughout the near wall, radial and chordwise studies. A total of 12 grids were tested, the results of which can be seen in Table 2. Based on these findings, and in order to have a sufficiently fine grid in the wake the 494×99 grid was used for all subsequent calculations with the first grid node located $0.000625c$ away from the aerofoil ($y^+ = 39-99$).

3.2 Wake Grid Dependence Study. It was necessary for a wake grid dependence study to be carried out. A refined grid based on the one obtained in the NACA 0012 dependence study was taken and the wake distribution aft of the Gurney was refined successively producing four grids. The propagation parameters were chosen such that the majority of the grid nodes were located near to the Gurney. The finest (Grid 4) is shown in Fig. 1, for clarity every second grid line has been plotted. The flow over the four grids was then solved at an incidence of $\alpha = 0$ degrees. The computed mean c_l, c_d along with their uncertainties U_s due to iterative non-convergence, as defined by Stern et al. [17], are compared in Table 3. The computed c_l, c_d quasi-steady values referred to in the subsequent work are the mean values calculated near the end of the simulation.

It is evident that the c_l does not seem to follow a limiting trend with increasing wake grid density. This is somewhat expected, since the lift force is predominately affected by the flow over the section and not what is occurring in the wake. Although the c_d does not seem to have fully converged to a limiting value, it is evident that the predicted drag is affected by the wake grid density. Increased numbers of cells in the wake region allow more accurate resolution of the pressures aft of the flap and hence the predicted drag force. However, the small gains in accuracy in the computed drag resulting from the increased wake density do not seem to warrant the large simulation times. It can be seen from Table 3 that the computations on coarse grid (Grid 1) produces a fully converged steady state solution, i.e., lowest iterative uncertainty and mass source residual (MSR). Although the uncertainty of the predicted c_l is seen to be converging, it is not similarly small for Richardson Extrapolation to be used to evaluate the uncertainty due to grid refinement. It is also evident that the c_d uncertainty is not converging because of the large mass source residual associated with the quasi-steady assumption, and difficulties with the stability of the numerical solver in trying to reduce this further.

The streamlines plotted for the coarse grid (Grid 1) in Fig. 2 show the formation of the double vortex structure hypothesized by Liebeck [2] (Fig. 3). Figure 4 shows the interpolated mean streamlines derived by Jeffrey [4] from his LDA measurements. It is evident on comparing Fig. 2 and Fig. 4 that the coarse grid computations over predict the double vortex length by approximately 15 percent. The streamlines plotted for the fine grid (Grid 4) in Fig. 3 indicate the formation of a periodic vortex structure. It is evident that the captured flow physics is highly dependent on the wake grid resolution aft of the Gurney flap, confirming what was initially postulated but not confirmed, by Jang et al. [10]. It was found that as the grid in the wake region was refined, the steady state solutions failed to converge, instead oscillating about some

Table 3 Four percent Gurney quasi-steady wake grid study

Grid	n_ξ	Mean c_l $\times 10^{-1}$	Mean c_d $\times 10^{-1}$	$c_l U_s$ $\times 10^{-1}$	$c_d U_s$ $\times 10^{-1}$	Mean MSR (kg/s)	CPU Time (min)
1	37	6.517	0.304	0.0006	0	0.001	140
2	59	6.533	0.315	0.1377	0.004235	0.7	177
3	79	6.538	0.320	0.1036	0.008175	0.5	193
4	99	6.501	0.338	0.0293	0.008995	0.5	200

Downloaded 03 Jun 2010 to 171.66.16.150. Redistribution subject to ASME license or copyright; see http://www.asme.org/terms/Terms_Use.cfm

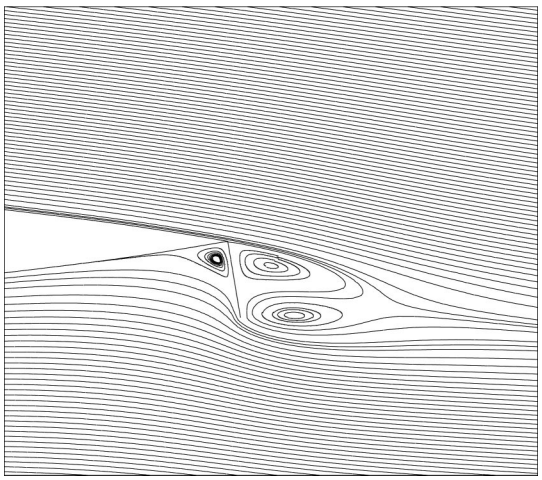

Fig. 2 Four percent Gurney, coarse grid (Grid 1) streamlines

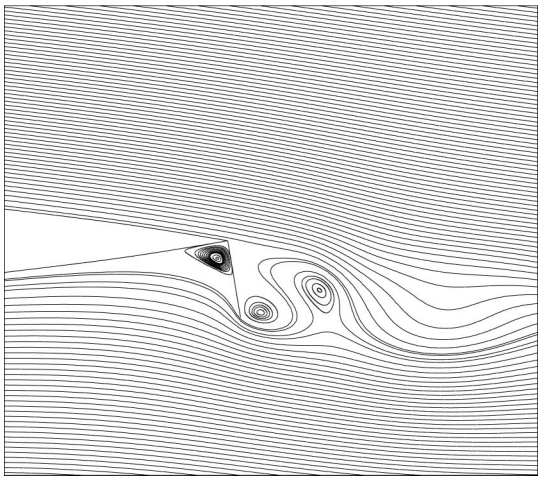

Fig. 3 Four percent Gurney, fine grid (Grid 4) streamlines

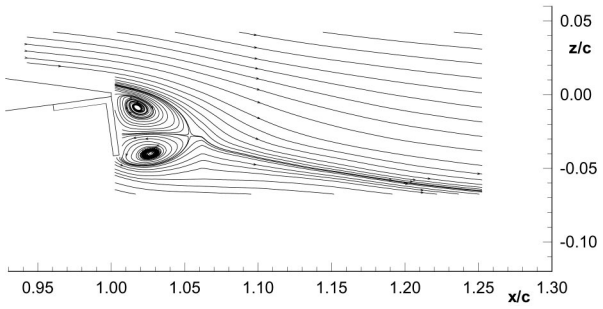

Fig. 4 Four percent Gurney, experimental streamlines, Jeffrey [4]

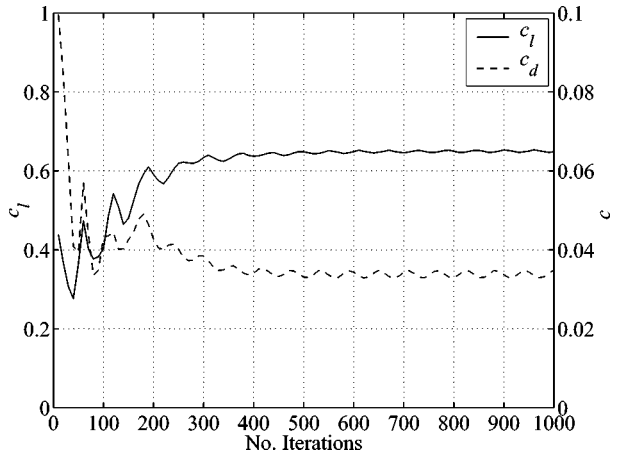

Fig. 5 Four percent Gurney quasi-steady c_l and c_d convergence history

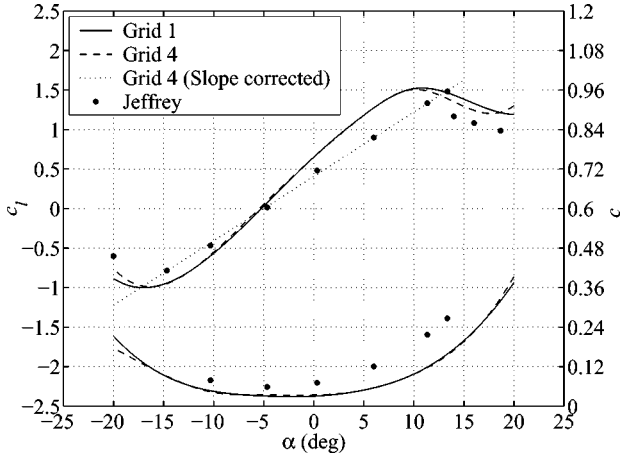

Fig. 6 Four percent Gurney quasi-steady c_l, c_d Vs α

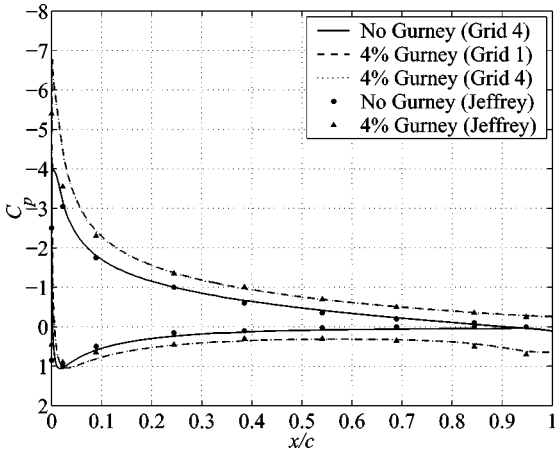

Fig. 7 Four percent Gurney quasi-steady Cp distribution, $\alpha = 10$ deg

mean mass source residual value. This also resulted in oscillations in the predicted c_l and c_d about some mean or quasi-steady value as shown in Fig. 5.

Numerically the steady-state solution is converging as if it was at one time step in a periodic flow. If the flow field is output early on in the simulation for the fine grid (Grid 4), before the solver manages to resolve the unsteadiness in the flow, the same double vortex structure as per the coarse grid is produced. As a final investigation the coarse (Grid 2) and fine grid (Grid 4) were run over a range of incidences, $-20 \leqslant \alpha \leqslant 20$ degrees. The results from this study are shown in Fig. 6. It can be seen that there is little difference in the c_l and c_d curves of both grids except around stall, with the coarse grid (Grid 1) predicting a later onset. The effect of wake grid distribution on the section pressure distribution was also plotted for the coarsest (Grid 1) and finest (Grid 4) grids at an angle of incidence 10 degrees in Fig. 7. As can be seen,

Downloaded 03 Jun 2010 to 171.66.16.150. Redistribution subject to ASME license or copyright; see http://www.asme.org/terms/Terms_Use.cfm

there is no noticeable difference in the pressure plots for both grids, supporting the conclusions obtained from the previous c_l comparison.

Although the wake dependence study indicated that the wake grid density only has a small effect on the computed c_l and c_d, it was decided that the fine wake grid (Grid 4) would be used in all subsequent quasi-steady, and time accurate calculations at the expense of increased solution times. This decision was made because the fine grid (Grid 4) was considered to form a closer numerical representation of the physical flow, allowing the unsteadiness to be captured in the later time accurate calculations. The total number of cells in the fine grid (Grid 4) was 68508.

3.3 Quasi-Steady Performance Results. The quasi-steady c_l and c_d were validated against the C_L and C_D obtained by Jeffrey [4] for the NACA 0012+4 percent Gurney over a range of incidences past stall. The quasi-steady pressure distribution was also compared with the experimental data obtained by Jeffrey [4], at an angle of incidence of $\alpha=10$ degrees. In order to assess the proficiency of the RANS code in predicting the effect of fitting different size Gurneys, both an unflapped NACA 0012 and a NACA 0012+2 percent Gurney were also modeled over a range of incidences past stall. Typically the quasi-steady computations took between 2 and 5 hours to converge to an oscillating state, depending on the angle of incidence.

It was decided that the computed c_l data would be compared directly with the measured C_L, data obtained by Jeffrey [4]. This decision was taken because comparing the data with the c_l derived through integration of the experimental pressures around the section was felt to be inadequate, since it fails to take account of any forces acting on the Gurney flap itself. Although this was akin to comparing two-dimensional data ($AR=\infty$) with three-dimensional data ($AR=5$), it was considered the best option, other than making empirical corrections to the data. Figure 6 compares the computed data with the experimental data.

As expected when carrying out a comparison of this type, there is a decrease in lift slope from the two-dimensional computed data to the three-dimensional experimental data. However, when the two-dimensional lift slope from the computed data is corrected to a finite aspect ratio ($AR=5$) using the finite aspect ratio correction [15] in Eq. (1), the lift slopes are in agreement, not withstanding the limitations of applying Eq. (1) to flows with large regions of separation.

$$\frac{dC_L}{d\alpha}=\frac{\dfrac{dc_1}{d\alpha}}{1+\dfrac{1.9}{AR}} \tag{1}$$

Table 4 shows the lift slope corrected data. Agreement of the experimental and corrected computational lift slopes seems to suggest that the two-dimensional section c_l curve is correct. However, the predicted stall angle and maximum c_l are governed by limitations of standard $k-\varepsilon$ turbulence model with wall function, as stall is approached. The model gives poor prediction of the onset of flow separation from surfaces under the action of adverse pressure gradients.

The computed c_d was compared with the measured C_D found by Jeffrey [4] and not the c_d found though integration of the

Table 4 Lift slope data

Gurney	CFX $\frac{dc_l}{d\alpha}(\mathrm{AR}=\infty)$	CFX Corrected $\frac{dC_L}{d\alpha}(\mathrm{AR}=5)$	Jeffrey [4] $\frac{dC_L}{d\alpha}(\mathrm{AR}=5)$
None	0.0983	0.0712	0.0714
2%	0.1124	0.0814	0.0811
4%	0.1129	0.0818	0.0827

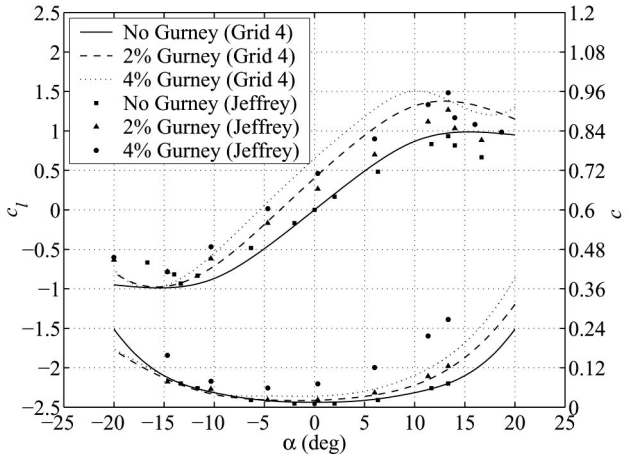

Fig. 8 Two and four percent Gurney quasi-steady c_l, c_d Vs α

surface pressures as again the effect of the flap and the skin friction contribution is neglected. However, at low angles of incidence, both the two-dimensional computed data, and the experimental three-dimensional data should be similar, since the induced drag component is small. Figure 6 compares the computed data with the experimental data. It is noticeable that even at low angles of incidence the computed data severely under predicts the drag experienced by the section, even at point of zero-lift. However, the likely reason for this difference can only be deduced upon comparison of the c_d drag curve for the NACA 0012+2 percent Gurney with its experimental equivalent in Fig. 8. It can be seen that there is closer agreement between the computed and experimentally derived data for the NACA 0012+2 percent Gurney. A possible explanation for this has been proposed. It is thought that the large upstream low pressure recirculation produced in front of the Gurney flap in the experiment (even at the zero-lift incidence) promotes the development of vortices close to the trailing-edge. This might explain why the smaller Gurney flap model has a better correlation with the experimental data than the larger Gurney flap case. Discrepancies in the predicted drag may also occur because the CFD simulation assumes the flow is fully turbulent, neglecting the laminar-turbulent transition occurring near the leading edge and the drag associated with tripping the flow in the experiments.

The computed quasi-steady pressure distribution for the NACA 0012+4 percent Gurney along with the steady-state pressure distribution about an un-flapped NACA 0012 section at an angle of incidence of $\alpha=10$ degrees was compared with Jeffreys data [4] in Fig. 7. The Gurney flaps influence on the pressure distribution around the NACA 0012 section is evident when the data for the un-flapped NACA 0012 section is compared to its flapped counterpart. The Gurney unquestionably increases the pressure difference between the suction and pressure surfaces, especially in the vicinity of the trailing edge. There is generally good agreement between the computed and experimental data, with the largest differences in the pressure distribution occurring near the leading edge. These large differences are likely to be due to the poor prediction of boundary-layer growth resulting from the use of the standard k-ε turbulence model.

The effect of flap size on the c_l and c_d was investigated. Facilitating this, further computations were carried out on an unflapped NACA 0012 and a NACA 0012+2 percent Gurney. The data obtained are plotted in Fig. 8. The computed two-dimensional data are compared with the experimental three-dimensional results and the lift slopes corrected to a finite aspect ratio ($AR=5$) in Table 4. It is apparent from Fig. 8 that the trends of increasing c_l

Downloaded 03 Jun 2010 to 171.66.16.150. Redistribution subject to ASME license or copyright; see http://www.asme.org/terms/Terms_Use.cfm

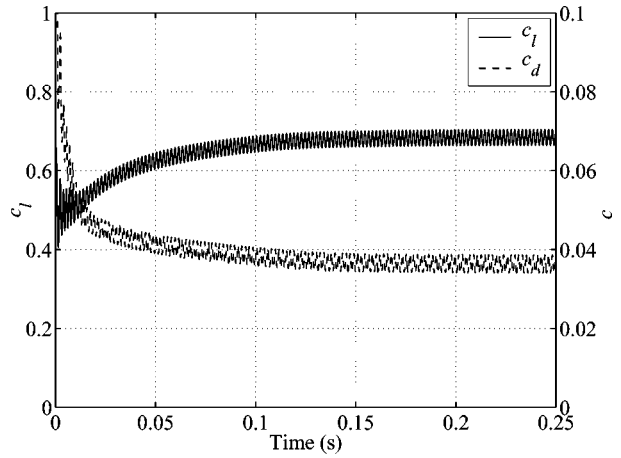

Fig. 9 Four percent Gurney periodic force evolution, $\Delta t = 0.000025$

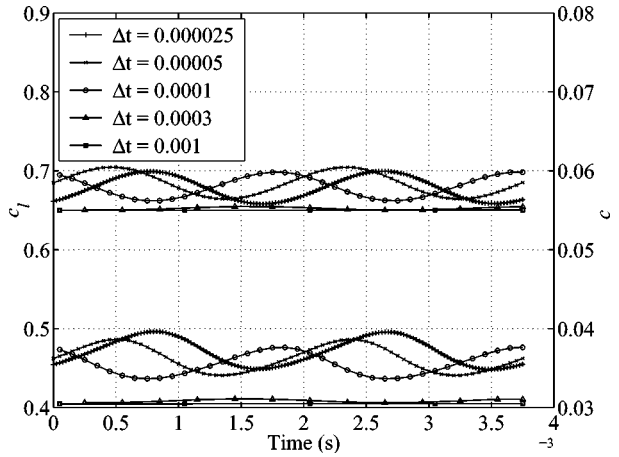

Fig. 10 Four percent Gurney periodic response over two cycles

and c_d with increasing flap height are correctly reproduced in the computations. The computed lift slopes also show good agreement with the experimental lift slopes.

3.4 Periodic Performance. A study into the periodic performance of the Gurney flapped NACA 0012 section was conducted. In order to keep the number of large time accurate simulations to a minimum, only the NACA 0012+4 percent Gurney was modeled. The aim of this investigation was to obtain information on the flow transients caused by the Gurney flap and to identify if the RANS code is capable of predicting the principle vortex shedding frequency and periodic performance. Comparison of the time-averaged performance data with the data obtained from the quasi-steady investigation was used to assess the applicability of the quasi-steady approach.

The selection of the correct real time step is the most important parameter after grid resolution to affect the solution of periodic flows. To highlight this, a study was conducted to determine the optimum time step needed to capture the vortex shedding behind the Gurney. Computations were carried out on the fine grid (Grid 4) used in the previous quasi-steady computations, at an incidence of $\alpha = 0$ degrees. Solutions were obtained using various time steps and the time step dependency of the solutions was investigated.

An initial estimate of the smallest time step needed was made using the residence time approach [18]. Knowing the smallest cell size in the wake region $\Delta x = 0.001$ m and freestream velocity $U_\infty = 40$ m/s, an approximation of the required time step was made. This gave the estimate of the smallest time step to be $\Delta t = 0.000025$ s. An estimate of the total simulation time was made, based on the domain size and freestream velocity. The time taken for the fluid to travel from the inlet to the downstream outlet was calculated as 0.25 s. Based on these onerous conditions at least 10000 time steps were estimated for the whole simulation. Figure 9 shows the evolution of the c_l and c_d as the simulation progresses.

It is evident that the solution is highly oscillatory at the beginning of the computation and slowly converges to a regular oscillating solution as the vortex shedding becomes better resolved. Figure 9 confirms the estimate of the total simulation time, as up until 0.2 s in the solution is still converging. Figure 10 shows the periodic c_l and c_d near the end of the simulation over a period of approximately two cycles. Looking at the number of 0.000025 s time steps used in evaluating the periodic performance over one cycle in Fig. 10, it would be pertinent to assume that an excessive number have been used. To investigate if this was in fact the case further solutions were carried out using larger time steps of 0.00005, 0.0001, 0.0003, and 0.001 s. The results from this study are also plotted in Fig. 10.

As can be seen all but the two largest time steps of 0.0003 and 0.001 s succeeded in predicting the periodic performance of the section. It is evident from the plots of c_l and c_d for these two larger time steps that the solver has essentially solved the problem as if the flow was at a steady state. On comparison of the periodic response curves in Fig. 10 and the time-averaged (zero, a_0 and normalized first harmonic, a_1/a_0) performance data in Table 5 it is evident that the predicted performance is approximately the same for time steps 0.000025, 0.00005, 0.0001 s, all except for the lift curve produced using the smallest time step of 0.000025 s which has a slight offset.

Although the response curves shown in Fig. 10 were plotted using the data taken from the same time interval near the end of the simulation, all the curves are out of phase. These phase shifts occur because of the way in which the vortex shedding is resolved as the solution progresses. Table 5 shows the amount of CPU time taken in all for the time step studies to complete. These computations are extremely intensive, with the small time step case taking 230 hours to solve.

Although satisfactory time accurate results have been obtained in this instance, the numerical basis of the RANS approach must not be forgotten. As highlighted by Lasher and Taulbee [19] if the time scale of a periodic flow feature overlaps with the time scale of the turbulence, what exactly has been time-averaged by the RANS equations? In this case there is still a clear distinction

Table 5 Four percent Gurney time stepping results

Δt (s)	f_p (Hz)	Mean $c_l \times 10^{-1}$ (a_0)	$c_l(a_1/a_0) \times 10^{-1}$	Mean $c_d \times 10^{-1}$ (a_0)	$c_d(a_1/a_0) \times 10^{-1}$	CPU Time (hrs)
0.000025	526	6.812	0.348	0.369	0.650	230
0.00005	526	6.844	0.359	0.363	0.661	115
0.0001	526	6.801	0.274	0.356	0.562	104
0.0003	416	6.525	0.039	0.309	0.129	57
0.001	-	6.497	-	0.305	-	13

Downloaded 03 Jun 2010 to 171.66.16.150. Redistribution subject to ASME license or copyright; see http://www.asme.org/terms/Terms_Use.cfm

between the periodic flow and turbulence. Although not investigated in this work, useful information might be gained as to the turbulence time and length scales from analysis of the calculated k and ε values.

4 Comparison of Periodic Performance With Experimental and Quasi-Steady Data

Following the detailed time step study, the time-averaged c_l and c_d were assessed against those obtained by Jeffrey [4] and compared with those found in the quasi-steady investigation over a range of incidences. The computed principle shedding frequency was validated against the LDA measured value of Jeffrey [4]. The time-averaged pressure distribution was also validated against Jeffrey's [4] data at an angle of incidence of $\alpha=10$ degrees. It was decided, based on the data obtained in the time step study, that a time step of 0.0001 s would be used in all the computations, providing a compromise between accuracy and CPU time. Typically, these time accurate computations took between 100 and 150 hours to converge to an oscillating state depending on the angle of incidence.

Table 6 shows the calculated principle shedding frequency and Strouhal number at angles of incidence of $\alpha=-5$, 0, $+10$ degrees using a time step of 0.0001 s. It can be seen that only the $\alpha=0$ and -5 degrees incidence angle computations managed to capture the periodic vortex shedding. The $+10$ degree incidence angle case along with all the other incidence angle computations failed to capture the periodic vortex shedding. It is likely that this occurred because the wake grid at these incidence angles (which would be approximately at the same angle as the aerofoil to the inflow) failed to have enough resolution to capture the unsteadiness. This problem could have been resolved by propagating the fine wake grid in the anticipated wake direction, however this was not investigated. The $\alpha=-5$ degrees incidence case managed to capture the periodic vortex shedding because at this angle the vortex street was displaced closer toward the wake grid centerline, where the grid was of a sufficient resolution to capture the vortex shedding. It can be seen from Table 6 the computed principle shedding frequency and Strouhal number for the $\alpha=0$ degrees incidence case compares extremely well with the measured values found by Jeffrey [4] in his LDA experiments.

As with the quasi-steady comparison of c_l and c_d, the computed time-averaged c_l and c_d was also compared directly with the measured C_L and C_D data obtained by Jeffrey [4]. Figure 11 compares the time-averaged data with the experimental data and quasi-steady state data. It is apparent that the computed time-averaged c_l is identical to that obtained in quasi-steady state investigation and hence shows the same correlation with the experimental data. Correction to finite aspect ratio, using the same method as applied to the quasi-steady data would therefore give the same close correlation. It is apparent that the time-averaged c_d is identical to that obtained in quasi-steady state investigation and hence shows the same correlation with the experimental data not withstanding the high mass source residual for the quasi-steady calculations.

The computed periodic pressure distribution at an angle of incidence $\alpha=10$ degrees was compared with the experimental data obtained by Jeffrey [4] and the results obtained in the quasi-steady investigation. For the pressure distributions at the maximum (1/4 shedding cycle) and minimum (3/4 shedding cycle) and time-averaged values it was found that there was little change in the pressure distribution over the shedding cycle, with only small noticeable changes ($\Delta C_p<1.2$ percent) in the pressure distribution occurring in the trailing-edge region ($x/c>0.7$). The time-averaged pressure distribution was found to be identical to that obtained in the quasi-steady investigation in Fig. 7, showing the same close correlation with the experimental results.

Table 6 Four percent Gurney principle shedding frequency and Strouhal No.

α (deg)	CFX f_p	Jeffrey [4] f_p	CFX St	Jeffrey [4] St
0	526	485-490	0.168	0.155-0.157
-5	526	-	0.168	-
$+10$	-	440-445		0.141-0.142

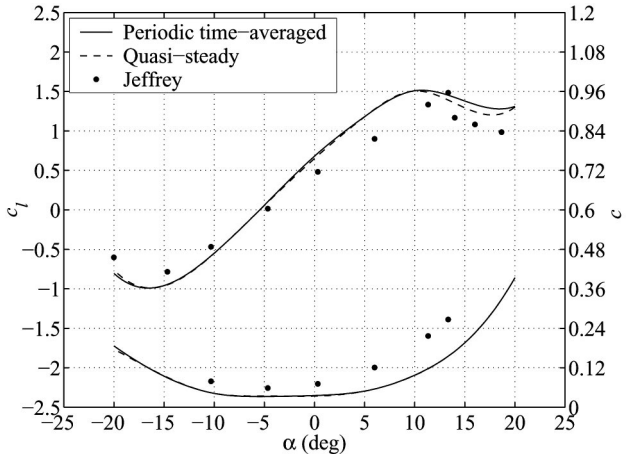

Fig. 11 Four percent Gurney quasi-steady and periodic time-averaged c_l, c_d vs α

5 Conclusions

A detailed investigation of the quasi-steady and periodic performance of a NACA 0012 fitted with 2 and 4 percent Gurney flaps was conducted using a RANS solver implementing the two-equation k-ε turbulence model with wall function.

The quasi-steady wake resolution sensitivity analysis highlighted that although the wake grid resolution has an affect on the flow physics captured within it, the mean performance remained largely unchanged. The predicted quasi-steady performance for both the coarsest and finest grids was found to correlate well with the experimental data. The correct trends in performance resulting from the addition of different size Gurney flaps was also observed.

The time accurate performance investigation highlighted the importance of selecting the correct time step necessary to resolve the periodicity in the wake region. The time-averaged performance was found to be identical to the performance predicted by the quasi-steady solution approach, showing the same correlation with the experimental data. The principle vortex shedding frequency was also found to correlate favorably.

The quasi-steady solution approach used here and in other investigations was confirmed as producing the same performance predictions as the full time accurate simulations, however, at 1/30th of the computing cost. Hence, for practical applications when periodic section performance is of secondary importance, the quasi-steady solution approach can be used to obtain estimates of performance. However, care should be taken during grid dependence investigations involving quasi-steady and time accurate solution approaches as has been shown because the local grid size can have a significant influence on the predicted flow, and this may prevent asymptotic force convergence.

The detailed validation studies presented here have shown that the typical grid resolution needed for accurate two-dimensional section performance prediction is of the order of 70,000 cells. Assuming that a similar level of grid resolution would be required in the third dimension, an estimate of total number of cells needed to model a low aspect ratio wing can be made. It is thought that 21 million cells would probably be needed to resolve the three-dimensional flow features to the same degree of accuracy as those

Downloaded 03 Jun 2010 to 171.66.16.150. Redistribution subject to ASME license or copyright; see http://www.asme.org/terms/Terms_Use.cfm

in the two-dimensional study presented here. Even with this number of cells there is no guarantee that grid convergence would be achieved.

Acknowledgments

The authors wish to acknowledge the support of Hamworthy KSE, Fleets Corner Poole, Dorset, U.K.

Nomenclature

AR = aspect ratio
a_n = Cosine Fourier series coefficients ($n=0,1$)
b = wing span
c = reference chord
d = base height, measured normal to chordline
c_d = section drag coefficient
C_D = wing drag coefficient
c_l = section lift coefficient
C_L = wing lift coefficient
C_p = pressure coefficient
f_p = principle vortex shedding frequency
h = Gurney flap height
k = turbulent kinetic energy
n_ξ = no. cells around the section
n_η = no. cells radiating from the section
n_ζ = no. cells in the wake direction
r = boundary location distance
St = Strouhal number, $f_p d/U_\infty$
t = time
u, v = velocity components in x, y axes system
U_s = uncertainty due to iterative nonconvergence
U_∞ = freestream velocity
x, y = coordinate system: $x+ve$ downstream, $y+ve$ up
α = incidence
ρ_{air} = density of air
μ_{air} = laminar viscosity of air
ε = rate of dissipation of turbulent kinetic energy

References

[1] Bingham, V. P., and Mackey, T. P., 1987, ''High-Performance Rudders—with Particular Reference to the Schilling Rudder,'' Marine Technology, **24**, No. 4, Oct., pp. 312–320.
[2] Liebeck, R. H., 1978, ''Design of Subsonic Airfoils for High Lift,'' J. Aircr., **15**, No. 9, Sept., pp. 547–561.
[3] Neuhart, D. H., and Pendergraft, O. C., 1988, ''A Water Tunnel Study of Gurney Flaps,'' NASA TM 4071, Nov.
[4] Jeffrey, D. R. M., 1998, ''An Investigation into the Aerodynamics of Gurney Flaps,'' Ph.D. thesis, University of Southampton, Southampton, U.K., Mar.
[5] Jeffrey, D. R. M., Zhang, X., and Hurst, D. W., 2000, ''Aerodynamics of Gurney flaps on a single-element high-lift wing,'' J. Aircr., **37**(2), pp. 295–302.
[6] Jeffrey, D. R. M., Zhang, X., and Hurst, D. W., 2001, ''Some Aspects of the Aerodynamics of Gurney Flaps on a Double-Element Wing,'' ASME J. Fluids Eng., **123**, Mar., pp. 99–104.
[7] Fripp, A. G., and Hopkins, W. B., 1991, ''Experimental Investigation and Computer Modelling of Flow around Aerofoils with Gurney Flaps,'' Ph.D. Final Year B.Eng. Project, University of Bristol, Bristol, U.K., Mar.
[8] Ashby, D., 1996, ''Experimental and Computational Investigation of Lift-Enhancing Tabs on Multi-Element Airfoil,'' NASA-CR-201482, June.
[9] Jang, C. S., and Ross, J. C., and Cummings, R. M., 1992, ''Computational Evaluation of an Airfoil with a Gurney Flap,'' Proceedings, 10th AIAA Applied Aerodynamics Conference, Palo Alto, C.A., June., pp. 801–809.
[10] Ross, J. C., Storms, B. L., and Carrannanto, P. G., 1995, ''Lift-Enhancing Tabs on Multi-Element Airfoils,'' J. Aircr., **32**, No. 3, May–June., pp. 649–655.
[11] Wilcox, D. C., 1998, ''Turbulence Modelling for CFD,'' D.C.W. Industries, Edition 2.
[12] Rycroft, N. C., 1997, ''Three-Dimensional Multi-block Grid Generation-Fleximesh,'' Ship Science Report, Department of Ship Science, Southampton University, Southampton, U.K., No. 101., Nov.
[13] CFX-4.3, Flow Solver Guide, 1998, AEA Technology, Harwell Laboratory, Oxfordshire, U.K.
[14] Rhie, C. M., and Chow, W. L., 1983, ''Numerical Study of the Turbulent Flow Past an Airfoil with Trailing Edge Separation,'' AIAA J., **21**, No. 11, pp. 1525–1532.
[15] Abbott, I. H., and Von Doenhoff, A. E., 1959, *Theory of Wing Sections*, Dover Publications Inc.
[16] Eiseman, P. R., 1979, ''A Multi-Surface Method of Coordinate Generation,'' J. Comput. Phys., **33**, pp. 118–150.
[17] Stern, F., Wilson, R. V., Coleman, H. W., and Paterson, E. G., 1999, ''Verification and Validation of CFD Simulations,'' Proceedings of the 3rd ASME/JSME Joint Fluids Engineering Conference, July 18–23, San Francisco, Ca.
[18] Shaw, C. T., 1992, *Using Computational Fluid Dynamics*, Prentice Hall, N.Y.
[19] Lasher, W. C., and Taulbee, D. B., 1992, ''On the Computation of Turbulent Backstep Flow,'' Int. J. Heat Fluid Flow, **13**, No. 1, Mar., pp. 30–40.

Downloaded 03 Jun 2010 to 171.66.16.150. Redistribution subject to ASME license or copyright; see http://www.asme.org/terms/Terms_Use.cfm

The Effect of Finite Amplitude Disturbance Magnitude on Departures From Laminar Conditions in Impulsively Started and Steady Pipe Entrance Flows

E. A. Moss
Professor

A. H. Abbot
Graduate Student

School of Mechanical Engineering,
University of the Witwatersrand,
Johannesburg, Private Bag 3,
WITS 2050,
South Africa

The aim of this study was to investigate first departures from laminar conditions in both impulsively started and steady pipe entrance flows. Wall shear stress measurements were conducted of transition in impulsively started pipe flows with large disturbances. These results were reconciled in a framework of displacement thickness Reynolds number and a velocity profile shape parameter, with existing measurements of pipe entrance flow instability, pipe-Poiseuille and boundary layer flow responses to large disturbances, and linear stability predictions. Limiting critical Reynolds number variations for each type of flow were thus inferred, corresponding to the small and gross disturbance limits respectively. Consequently, insights have been provided regarding the effect of disturbance levels on the stability of both steady and unsteady pipe flows. [DOI: 10.1115/1.1445137]

1 Introduction

This study is concerned with the onset of instability and transition in two ostensibly similar systems—steady pipe entrance flows and spatially fully developed pipe flows impulsively started from rest. These flows share the common feature that each has velocity profiles which evolve, in space and time, respectively, from uniform toward parabolic shapes. Both limiting velocity profile shapes are unconditionally stable to axisymmetric and nonaxisymmetric infinitesimal disturbances: the latter pipe-Poiseuille limit was first shown by Lessen et al. [1] to possess this property for *both* types of disturbances (see also Salwen and Grosch [2]; Salwen et al. [3]), while the former represents a limiting boundary layer of zero thickness. At intermediate stages (Reynolds number dependent) the flows may become unstable during the boundary layer growths. Although for steady and unsteady flows, velocity profiles vary with space and time respectively, linear stability depends merely on velocity profile shape, provided the respective effects of spatial and temporal development are insignificant for the two flows. The former effect was shown to be true in Abbot and Moss [4], while the latter is valid provided the time scale of the unstable disturbance is significantly smaller than the diffusive time scale of the developing flow, an issue that is addressed in Section 3 of this paper. In mathematically formulating the two problems, while the spatial growth of disturbances might be more physically appropriate for the first case and the temporal growth for the second, Gaster [5] has established that the alternatives degenerate to the same case in the infinitesimal disturbance stability limit.

A number of analytical investigations of steady pipe entrance flow stability have been performed (for example; Huang and Chen [6]; Garg [7]; da Silva and Moss [8]; Abbot and Moss [4]), of which the results of Abbot and Moss most closely approach the accepted asymptotic limit of $\mathrm{Re}_{\delta^*}=520$ for zero pressure gradient boundary layers on a flat plate, applicable at the pipe inlet limit. This was first determined by Jordinson [9] and later refined by Davey (unpublished; see Drazin and Reid [10]) to $\mathrm{Re}_{\delta^*}=519.06$. (The displacement thickness Reynolds number is defined as $\mathrm{Re}_{\delta^*}\equiv U_0\delta^*/\nu$, with $\delta^*\equiv$displacement thickness; $U_0\equiv$cross-sectional mean velocity; $\nu\equiv$fluid kinematic viscosity.) However this flow system is still unresolved, to the extent that the only substantial experimental study by Sarpkaya [11] yields results at much lower critical Reynolds numbers than analysis.

Studies of departures from laminar conditions in pipe flows monotonically accelerated from rest (Van de Sande et al. [12], Lefebvre and White [13]; Moss [14]) have been largely experimental, except for the predictions of Abbot (1995) for flows exponentially accelerated after an impulsive start, for which an impulsively started flow is a limiting case. Of the measurements, Lefebvre and White, and Moss observed *local* transition, rather than turbulent structures *washed down* from the inlet after startup. (In fact the latter author observed both modes of transition and accounted for them in a formal way.) It is noteworthy that no published work in unsteady (nonpulsatile and nonoscillatory) pipe flows has thusfar produced even a qualitative correlation with analytical stability results.

The purpose of this paper is to attempt to reconcile the stability characteristics of steady entrance pipe flows and impulsively started flows (far from the pipe inlet), through the use of the hypothesis that finite amplitude disturbances give rise to critical Reynolds numbers lower than those predicted by the linear theory.

2 Experimentation

The test rig used in the current investigation (Moss [14]), is shown in Fig. 1. It comprised a stainless steel pipe, 15.6 mm in diameter, mounted vertically and supplied by a constant head tank via a simple sharp edged inlet, which did not prevent the intermittent occurrence of turbulence in the tube at a steady state Reynolds number of about 2400 (effectively a disturbed inlet). A quick-acting solenoid valve allowed a close approximation to an impulsively started flow with a final Reynolds number which was dictated by the opening of a high-accuracy needle valve. Both valves were positioned at the end of the pipe, approximately 1.5 m below a Disa type 55R47 glue-on shear stress probe situated 291 diameters from the pipe inlet. The working fluid was kerosene and flow rate was measured by an orifice meter located below the test section.

Contributed by the Fluids Engineering Division for publication in the JOURNAL OF FLUIDS ENGINEERING. Manuscript received by the Fluids Engineering Division February 16, 1999, revised manuscript received November 7, 2001. Associate Editors: S. Banerjee and J. Katz.

 Copyright © 2002 by ASME

Downloaded 03 Jun 2010 to 171.66.16.150. Redistribution subject to ASME license or copyright; see http://www.asme.org/terms/Terms_Use.cfm

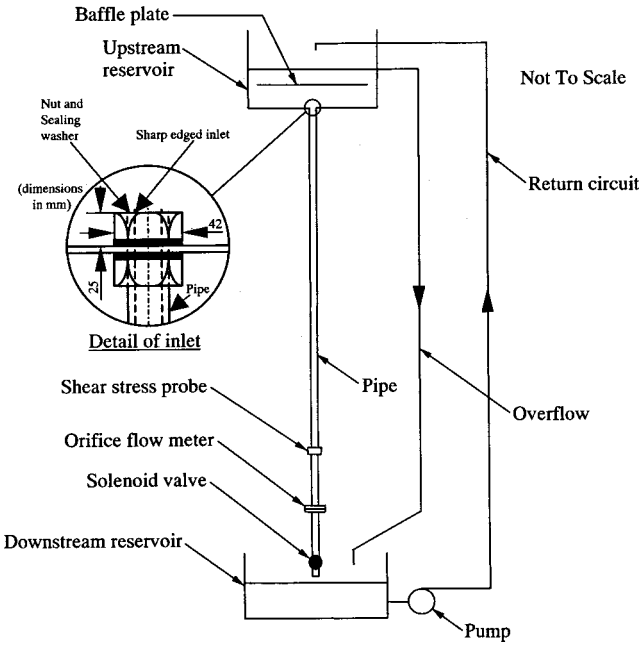

Fig. 1 Schematic of test rig used in the current investigation

The analogue output of the shear stress probe was directed into a digital oscilloscope triggered by the solenoid valve. The cross-sectional mean velocity U_0 at transition was obtained from the flowrate measured using a simple orifice meter. Transition was found to occur at diminishing times with increasing flow velocity, and beyond $U_0 \simeq 1.2$ m/s (a Reynolds number based on pipe diameter of about 12,500) occurred during the flow acceleration: experimental data were disregarded for comparison purposes beyond that point. Therefore, transition was observed in an environment with U_0 constant, but the boundary layer (and hence shear stress) changing with time. This distinguishes the current work from that of Van de Sande et al. [12], who observed transition in a pipe system in which the flow (and hence U_0) in addition to τ_w were changing with time. Intermittent turbulence for the present study occurred in the tube at a steady-state Reynolds number ($\mathrm{Re} \equiv U_0 d/\nu$; $d \equiv$ pipe diameter) of about 2400, while no turbulence was observed for Reynolds numbers less than about 2200. This trend may be reconciled with the results of Rubin et al. [15] who introduced strong disturbances into pipe-Poiseuille flows, establishing that a Reynolds number of approximately 2200 (corresponding to the minimum Reynolds numbers at which so-called *puffs* are sustained) was required to ensure survival in their downstream path. Accordingly, this point may be regarded as the *large disturbance pipe-Poiseuille stability limit* (i.e. any increase in the magnitude of disturbances would not further reduce the Re at which they are sustained).

Figure 2 is a typical voltage trace obtained from the shear stress probe. An initial period of laminar flow occurs (characterized by an abrupt increase in shear stress as the flow starts up, followed by a steady decrease as vorticity diffuses away from the pipe wall) which is followed by three successsive and discrete events at the measuring station, clarified in Moss [14]: (i) the natural or *local* occurrence of transition to turbulence at A, arising from a turbulent front moving in the upstream direction as successive sites become unstable; (ii) A turbulent to laminar interface at B as the structure observed in (i) is washed downstream by (iii) the inlet-generated laminar to turbulence interface observed at C. Figure 3 shows the variation of wall shear stress with final cross-sectional mean velocity just prior to transition, embracing all of the tests which were conducted.

3 Results and Discussion

In attempting to reconcile the current unsteady measurements with analytical data it should be noted that the onset of *transition* was measured, while patterns of *instability* to infinitesimal disturbances were predicted. Thus comparisons were necessarily made circumspectly, emphasizing asymptotic features. The current stability curves were established for axisymmetric disturbances: this may be justified by the fact that the purpose of this paper is to emphasize first order effects, in the context of the fact that the only experimental study of steady entrance flows has been shown to be minimally dependent on whether the applied disturbances are axisymmetric or nonaxisymmetric in nature (Sarpkaya [11]). It should be emphasized that Sarpkaya used a large contraction ratio with a very smooth transition at the inlet (see his Plate 1), and was thus able to sustain laminar flow at a steady state Reynolds number of 24,000. As will be noted later, differences between the inlet geometries of Sarpkaya's test facility and the current one largely explain deviations between the respective sets of data, particularly at lower values of S.

The present transition data are plotted in Fig. 4 as a variation of displacement thickness Reynolds number [$\mathrm{Re}_{\delta^*} \equiv \mathrm{Re}\,\delta^*/(2R)$] with dimensionless time ($\bar{t} \equiv \nu t/R^2$), where ν and R are fluid kinematic viscosity and pipe radius respectively. The displacement thickness was obtained by first computing variations of δ^*/R with the parameter $S[\equiv \tau_w d/(\mu U_0)]$. Thereafter these data were used as a "lookup table" into which measured values of S were passed to obtain interpolated values of δ^*/R for the measured data; i.e. the assumption was made that the same direct correspondence between δ^*/R and S exists for the experimental as for the computed data. There are strong indications from Fig. 4 that critical values of Re_{δ^*} are bounded for both high and low values of $\bar{t}$:

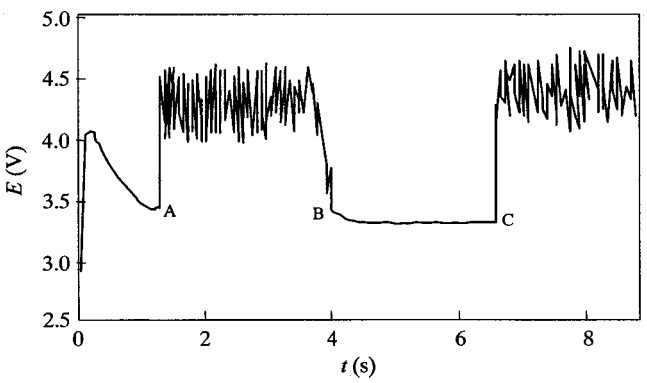

Fig. 2 Typical voltage variation with time, as an output of the shear stress probe

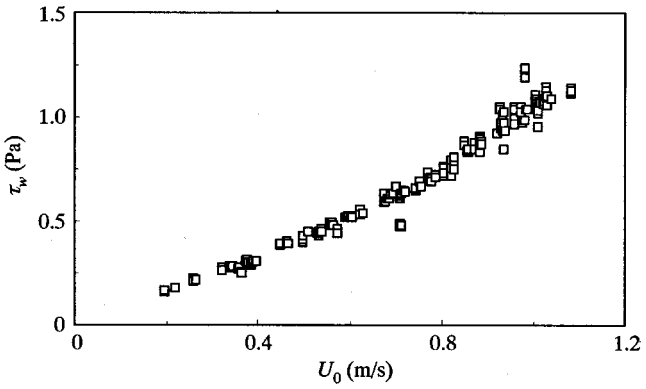

Fig. 3 Variations of wall shear stress with cross-sectional mean velocity immediately prior to transition

Downloaded 03 Jun 2010 to 171.66.16.150. Redistribution subject to ASME license or copyright; see http://www.asme.org/terms/Terms_Use.cfm

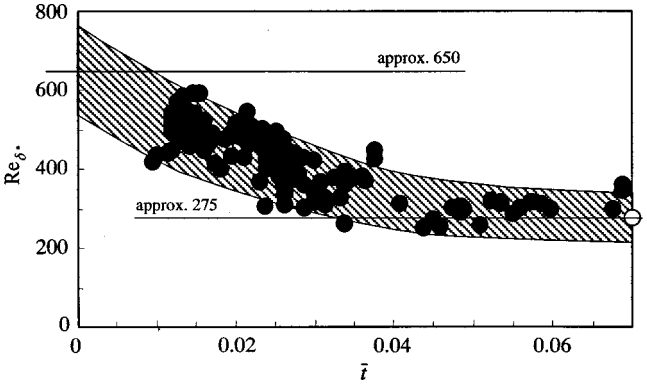

Fig. 4 Variation of displacement thickness Reynolds number with dimensionless time, showing departures from laminar flow for the current experiments

within the uncertainties (approximated by the cross-hatched area) imposed by the scatter of the data, the median values of Re_{δ^*} are given by 650 ± 115 and 275 ± 65 as $\bar{t}\rightarrow 0$ and ∞, respectively.

Figure 5 shows Sarpkaya's [11] stability data plotted as a variation of displacement thickness Reynolds number (Re_{δ^*}) with dimensionless axial distance ($\bar{x}\equiv 2xR/\mathrm{Re}$). In this instance, measured values of the Reynolds number Re were multiplied by computational predictions of $\delta^*/(2R)$ at the various values of $\bar{x}$ to obtain critical values of Re_{δ^*} which are bounded (and tend toward a value of about 410) as $\bar{x}\rightarrow 0$, but appear to be unbounded as $\bar{x}\rightarrow\infty$. It is noteworthy that the scatter of the data increases with $\bar{x}$, toward the pipe-Poiseuille limit.

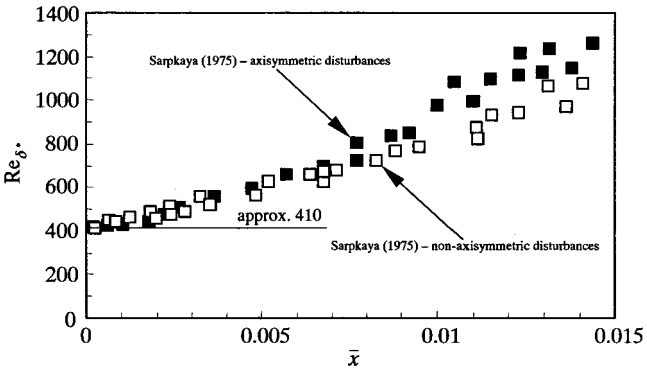

Fig. 5 Variation of displacement thickness Reynolds number with dimensionless axial co-ordinate, showing the experimental onset of instabilities (Sarpkaya [11]) for axisymmetric and non-axisymmetric disturbances

The data in Figs. 4 and 5 need to be contextualized by comparison with computational predictions. In the first instance, Sarpkaya's [11] stability measurements predictions and the present transition results are plotted (Fig. 6) in the framework of Re versus S. The parameter S defined earlier was used because, (i) like other parameters such as δ^*/R, it is directly representative of velocity profile shape, and (ii) it could be easily obtained from the current measurements of shear stress. It may be regarded as a *velocity profile shape parameter* for any particular *class* of pipe flows, although it is not unique among different classes. For example, in the case of impulsively started pipe flows far from the pipe inlet, equal values of S guarantee equal shapes of velocity profile: however the same values of S for an entrance flow, say, might imply slightly different shapes of velocity profile. Superimposed on the experimental data are the computations of Abbot [16] and Abbot and Moss [4] for impulsively started flows and steady pipe entrance flows respectively (axisymmetric disturbances). Both analyses exhibit limits corresponding to uniform (as $S\rightarrow\infty$) and parabolic (as $S\rightarrow 8$) velocity profiles that are stable at all Reynolds numbers to infinitesimal disturbances. Deviations between the computational predictions for the two cases are a direct consequence of slightly differing velocity profile shapes for the same values of S. Both sets of experimental data fundamentally diverge from their respective linear predictions for all values of S; they also differ substantially from each other for low values of S, but appear to show a similar pattern as S increases. As previously noted, the current data appear to be approaching $\mathrm{Re}\simeq 2200$ (i.e., the large amplitude stability limit for pipe-Poiseuille flows) as $S\rightarrow 8$, while Sarpkaya's data have a similar *trend* to the predictions, insofar as they appear to be unbounded in this same limit.

Figure 7 shows the same data as Fig. 6, now plotted in a framework of Re_{δ^*} versus S. Superimposed as individual points are the predicted linear stability limits as $S\rightarrow\infty$ for the two types of flow. Although critical Re's in this limit are infinite, critical Re_{δ^*}'s are bounded. For a steady entrance flow the classical, zero pressure gradient Blasius boundary layer limit is given by $Re_{\delta^*}=519.06$, while for its unsteady counterpart the error function boundary layer limit of $Re_{\delta^*}=1675$ pertains to impulsively accelerated

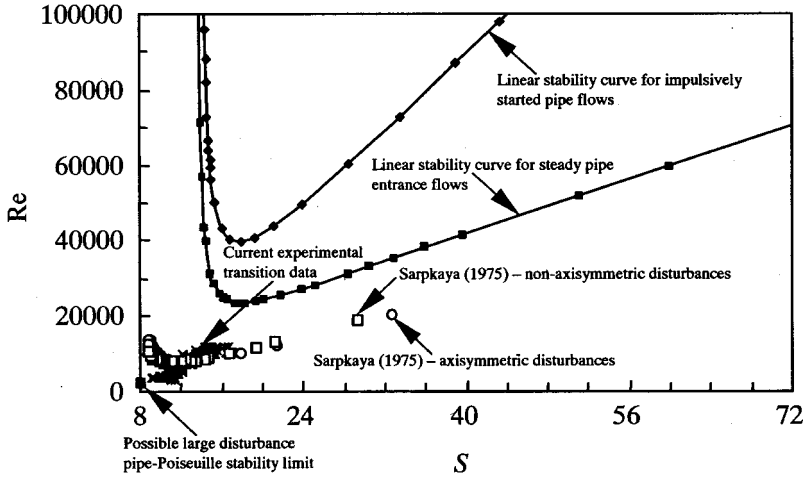

Fig. 6 Variation of Reynolds number with velocity profile shape parameter, showing:- the current transition data for impulsively started pipe flows flows; Sarpkaya's [11] stability measurements for steady pipe entrance flows; the respective linear stability predictions for each type of flow; and the possible large disturbance pipe-Poiseuille limit

Downloaded 03 Jun 2010 to 171.66.16.150. Redistribution subject to ASME license or copyright; see http://www.asme.org/terms/Terms_Use.cfm

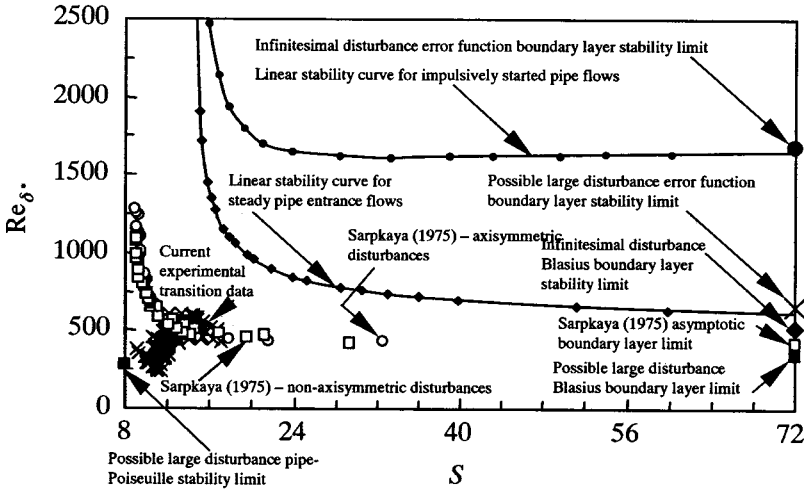

Fig. 7 Variation of displacement thickness Reynolds number with velocity profile shape parameter, showing: The current transition data for impulsively started pipe flows flows; Sarpkaya's [11] stability measurements for steady pipe entrance flows; the respective linear stability predictions and boundary layer limits for each type of flow; the possible large disturbance pipe-Poiseuille limit; the possible large disturbance Blasius boundary layer limit; and the possible large disturbance error function boundary layer limit

boundary layer flows over a flat plate in the absence of spatial development (Abbot [16]). Therefore, while the two types of flow are ostensibly similar as $\bar{x}$, $\bar{t} \rightarrow 0$ insofar as they both exhibit uniform velocity profiles, in fact their limiting velocity profile shapes close to the pipe wall differ significantly—with commensurately different stability characteristics.

In the context of other experimental work showing the effects of large disturbances on stability, it was noted previously that as $S \rightarrow 8$ (pipe-Poiseuille flows), approximate critical values of Re and Re_{δ^*} are, respectively, 2200 (from Rubin et al. [15]) and 275 (the product of 2200 and the dimensionless displacement thickness of value 0.125)—plotted as the *possible large disturbance pipe-Poiseuille stability limit* in Figs. 6 and 7. As $S \rightarrow \infty$ (corresponding to $\bar{x} \rightarrow 0$), steady pipe entrance flows behave like classical boundary layers, for which there is well-established evidence in the literature (for example Mayle [17]) that as the level of free-stream turbulence intensity increases the transition Reynolds number based on displacement thickness diminishes. Critical values as low as $Re_{\delta^*} \simeq 340$—plotted as the *possible large disturbance boundary layer stability limit* in Fig. 7 have been observed just before the start of transition (see Abu-Ghannan and Shaw, [18]). Although for boundary layers the variation of critical Re_{δ^*} with disturbance level appears to be asymptoting at this point, it is a subject of debate in the literature as to whether or not a lower value exists.

From the above rationale it is apparent that as $S \rightarrow 8$ and $S \rightarrow \infty$ for steady pipe entrance flows critical values of Re_{δ^*} have the approximate ranges $\infty \geqslant Re_{\delta^*} \geqslant 275$ and $340 \geqslant Re_{\delta^*} \geqslant 519.06$, respectively: for each limiting value of S the upper and lower values of Re_{δ^*} refer to flows subjected to infinitesimal and large disturbances respectively. Therefore it is inferred that critical values of displacement thickness Reynolds number are much more

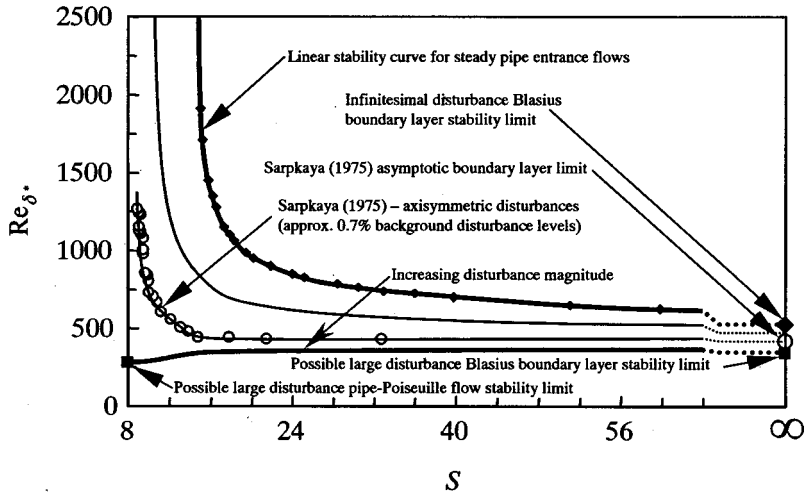

Fig. 8 Variation of displacement thickness Reynolds number with velocity profile shape parameter, showing asymptotic limits, the experimental data of Sarpkaya [11], and the expected qualitative dependence of steady pipe flow entrance stability on disturbance level

Downloaded 03 Jun 2010 to 171.66.16.150. Redistribution subject to ASME license or copyright; see http://www.asme.org/terms/Terms_Use.cfm

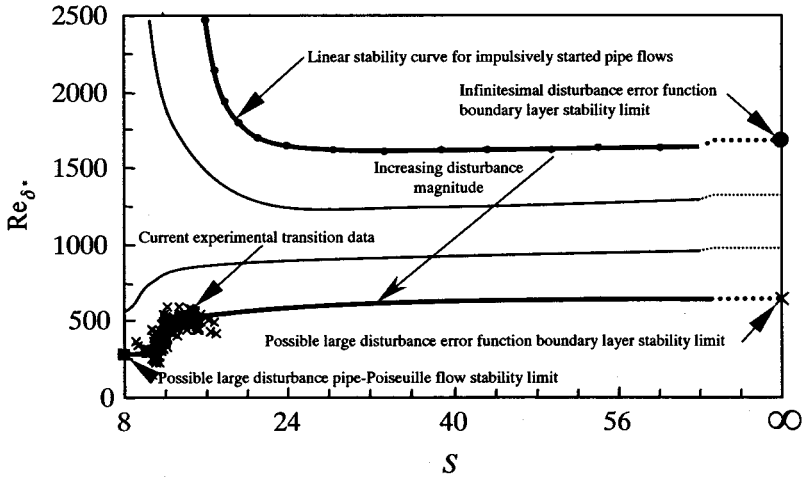

Fig. 9 Variation of displacement thickness Reynolds number with velocity profile shape parameter, showing asymptotic limits, the current experimental data, and the expected qualitative dependence of impulsively started pipe flow stability on disturbance level

sensitive to disturbance magnitude for small values of S than for large. Sarpkaya's data may be broadly reconciled with this logic and framework, because in the range $\infty \geqslant \mathrm{Re}_{\delta^*} \geqslant 8$, they fall within the infinitesimal and large amplitude disturbance limits.

As discussed previously, impulsively started flows in the pipe-Poiseuille limit ($S \rightarrow 8$) share the large and infinitesimal disturbance stability characteristics of their steady entrance flow counterparts. However, as $S \rightarrow \infty$ (corresponding to $\bar{x}, \bar{t} \rightarrow 0$), impulsively started flows have an infinitesimal disturbance limit given by $\mathrm{Re}_{\delta^*}=1675$, rather than the value of 519.06 for steady pipe entrance flows. While the large disturbance limit for the latter flow is given by $\mathrm{Re}_{\delta^*} \simeq 340$, there has thusfar been no prior indication in the literature of a corresponding measured stability limit for the latter (error function) velocity profile.

The current experimental data were subject to large disturbances of an unknown magnitude, and approach the approximate values $\mathrm{Re}_{\delta^*}=275$ and 650 as $S \rightarrow 8$ and ∞, respectively (see Fig. 4). In view of the fact that the former value may be interpreted as the large amplitude stability limit for pipe-Poiseuille flows, it seems reasonable to deduce that the latter is its counterpart for error function boundary layer flows. This result is significant because it would be difficult to achieve experimentally by any other means. However its validity depends on the assumption that the disturbance levels in this limit were similar to those which the pipe-Poiseuille limit were exposed to—or at least of a sufficient magnitude to ensure that any increase in disturbance size would not have further reduced the value of the displacement thickness Reynolds number at which departures from laminar flow occurred.

In broad terms the first transition observed in the present study was local in the sense that it occurred as part of a turbulent structure moving rapidly upstream. In addition, it was probably of a bypass kind in which transition took place abruptly in the presence of finite disturbances. Although ''natural'' transition occurring via the growth of Tollmien-Schlichting (T-S) waves is thought to be fundamentally different from bypass transition, the start of both processes is characterized by a departure from laminar flow: for the former case this takes the form of linear instability, while for the latter it is the onset of transition itself. Therefore representation of the two extremes on a common set of axes is appropriate, and in fact an ideal way to ascertain a global picture of the manner in which steady entrance and impulsively started pipe flows respond to finite disturbances.

While the computations of neutral stability for impulsively started flows take cognizance of instantaneous velocity profile shape, they ignore the effects of unsteadiness. This may be justified for such systems, provided the viscous time scale ($t_{viscous}$) governing the velocity profile development is much greater than the time scale ($t_{disturb}$) of the unstable disturbance. In fact a simple analysis shows that the ratio (β) is given to a good approximation by

$$\beta \equiv \frac{t_{viscous}}{t_{disturb}} = \frac{\bar{\alpha}_{\delta^*}\bar{c}}{2\pi}\mathrm{Re}_{\delta^*}$$

where the dimensionless wave number and wave celerity are defined by $\bar{\alpha}_{\delta^*} \equiv \alpha\delta^*$ and $\bar{c} \equiv c/U_0$, respectively. Computations of β gave values in the approximate range $28 \geqslant \beta \geqslant 20$, vindicating the assumption that neutral stability curves for this flow system depend mainly on velocity profile shape.

On the basis of the evidence presented, Figs. 8 and 9 were constructed as being broadly representative of the manner in which the two classes of system respond to finite amplitude disturbances. In both instances linear stability curves are shown (the infinitesimal disturbance limit), while possible large disturbance limits for $S \rightarrow \infty$ and $S=8$ are given in each case as individual points; other variations are qualitative, with the exception of curves passing through the current data and those of Sarpkaya [11], which have been included as appropriate for the respective cases of impulsively started and steady entrance pipe flows.

4 Conclusions and Recommendations for Future Work

The following has emerged during the course of this investigation:

(i) The Reynolds number based on displacement thickness (Re_{δ^*}) and dimensionless shape parameter [$S \equiv \tau_w U_0/(\mu d)$] represent a suitable framework for viewing computational predictions and measurements of the stability of impulsively started pipe flows and steady pipe entrance flows on a single set of axes.

(ii) All of the experiments yielded lower critical Reynolds numbers than their respective predictions, attributable to the magnitude of the initial disturbances, which were clearly much lower in the case of Sarpkaya's [11] experiments for steady pipe entrance flows (lowest $\mathrm{Re} \simeq 24{,}000$ for intermittent turbulence) than the current ones for impulsively started pipe flows (lowest $\mathrm{Re} \simeq 2400$ for intermittent turbulence).

(iii) As $S \rightarrow 8$ (the pipe-Poiseuille limit), critical values of Re_{δ^*} for the current experiments approach the well-established large

Downloaded 03 Jun 2010 to 171.66.16.150. Redistribution subject to ASME license or copyright; see http://www.asme.org/terms/Terms_Use.cfm

disturbance stability limit of $\mathrm{Re}_{\delta^*} \simeq 275$ with a scatter of ± 65, while as $S \to \infty$ they approach the limit given by $\mathrm{Re}_{\delta^*} \simeq 650 \pm 115$. It is thus inferred that this latter value approximates the large disturbance error function stability limit, subject to scatter in the experimental data.

(iv) Critical values of displacement thickness Reynolds number for steady pipe entrance flows subjected to *infinitesimal* disturbances have the range $519.06 \leqslant \mathrm{Re}_{\delta^*} \leqslant \infty$ (for $\infty \geqslant S \geqslant 8$ corresponding to $0 \leqslant \bar{x} \leqslant \infty$), while the approximate range $275 \leqslant \mathrm{Re}_{\delta^*} \leqslant 340$ applies for *large* disturbances over the same range of S and $\bar{x}$.

(v) Critical values of displacement thickness Reynolds number for impulsively started pipe flows subjected to *infinitesimal* disturbances have the range $1675 \leqslant \mathrm{Re}_{\delta^*} \leqslant \infty$ (for $\infty \geqslant S \geqslant 8$ corresponding to $0 \leqslant \bar{t} \leqslant \infty$), while the approximate range $275 \leqslant \mathrm{Re}_{\delta^*} \leqslant 650$ applies for *large* disturbances over the same range of S and $\bar{t}$.

(vi) Critical values of Re_{δ^*} as $S \to \infty$, for steady pipe entrance flows in the Blasius boundary layer limit are much less sensitive to disturbance magnitude than for impulsively started pipe flows in the error function boundary layer limit.

(vii) For both steady pipe entrance flows and impulsively started pipe flows, critical values of Re_{δ^*} as $S \to 8$ are far more sensitive to disturbance magnitude than they are in the limit $S \to \infty$.

(viii) Future experiments need to be designed and conducted in order to further quantify the effect of finite disturbances on the stability of both steady pipe entrance flows and impulsively started pipe flows; future computations should take cognizance of the effects of nonaxisymmetric disturbances on the stability of these flows.

Acknowledgments

The authors are grateful to the reviewers for critical but constructive comments, which have materially improved the substance of this paper.

References

[1] Lessen, M., Sadler, S. G., and Liu, T. Y., 1968, "Stability of pipe Poiseuille Flow," Phys. Fluids, **11**, pp. 1404–1409.

[2] Salwen, H., and Grosch, C. E., 1972, "The stability of Poiseuille flow in a pipe of circular cross-section," J. Fluid Mech., **54**, Part 1, pp. 93–112.

[3] Salwen, H., Cotton, F. W., and Grosch, C. E., 1980, "Linear stability of Poiseuille flow in a circular pipe," J. Fluid Mech., **98**, Part 2, pp. 273–284.

[4] Abbot, A. H., and Moss, E. A., 1994, "The existence of critical Reynolds numbers in pipe entrance flows subjected to infinitesimal axisymmetric disturbances," Phys. Fluids, **6**, No. 10, pp. 3335–3340.

[5] Gaster, M., 1962, "A note on the relation between temporally-increasing and spatially-increasing disturbances in hydrodynamics stability," J. Fluid Mech., **14**, pp. 222–224.

[6] Huang, L. M., and Chen, T. S., 1974, "Stability of the developing pipe flow subjected to non-axisymmetric disturbances," J. Fluid Mech., **63**, Part 1, pp. 183–193.

[7] Garg, V. K., 1981, "Stability of developing flow in a pipe: non-axisymmetric disturbances," J. Fluid Mech., **110**, pp. 209–216.

[8] da Silva, D. F., and Moss, E. A., 1993, "The stability of pipe entrance flows subjected to axisymmetric disturbances," ASME J. Fluids Eng., **116**, pp. 61–65.

[9] Jordinson, R., 1970, "The flat plate boundary layer. Part 1. Numerical Integration of the Orr-Sommerfeld equation," J. Fluid Mech., **43**, Part 4, pp. 801–811.

[10] Drazin P. G., and Reid W. M., 1981, *Hydrodynamic Stability*, Cambridge University Press, Cambridge.

[11] Sarpkaya, T., 1975, "A note on the stability of developing laminar pipe flow subjected to axisymmetric and non-axisymmetric disturbances," J. Fluid Mech., **68**, Part 2, pp. 345–351.

[12] Van de Sande E., Belde A. P., Hamer B. J. G., and Hiemstra W., 1980, "Velocity profiles in accelerating pipe flows started from rest," *Proc. of the Third Int. BHRA Conf. on Pressure Surges, Canterbury, England*, pp. 1–14.

[13] Lefebvre, P. J., and White, F. M., 1989, "Experiments on transition to turbulence in a constant-acceleration pipe flow," ASME J. Fluids Eng., **111**, pp. 428–432.

[14] Moss, E. A., 1989, "The identification of two distinct laminar to turbulent transition modes in pipe flows accelerated from rest," Exp. Fluids, **7**, pp. 271–274.

[15] Rubin Y., Wygnanski I., and Haritonidis J. H., 1979, "Further observations on transition in a pipe," *IUTAM Conf. on Laminar-Turbulent Transition, Stuttgart, Germany*, pp. 17–26.

[16] Abbot A. H., 1995, "The transition to turbulence in strongly accelerated pipe flows," *PhD thesis*, University of the Witwatersrand, Johannesburg.

[17] Mayle, R. E., 1991, "The role of laminar-turbulent transition in gas turbine engines," ASME J. Turbomach., **113**, pp. 509–519.

[18] Abu-Ghannan, B. J., and Shaw, R., 1980, "Natural transition of boundary layers—the effects of turbulence, pressure gradient and flow history," J. Mech. Eng. Sci., **22**, No. 5, pp. 213–221.

Downloaded 03 Jun 2010 to 171.66.16.150. Redistribution subject to ASME license or copyright; see http://www.asme.org/terms/Terms_Use.cfm

Franz Durst
Professor of Fluid Mechanics and
Director of the Institute
e-mail: durst@lstm.uni-erlangen.de

Jun-Mei Shi
Research Scientist of CFD Group
e-mail: shi@lstm.uni-erlangen.de

Michael Breuer
Senior Research Scientist and
Head of CFD Group
e-mail: breuer@lstm.uni-erlangen.de

Lehrstuhl für Strömungsmechanik,
Universität Erlangen-Nürnberg
Cauerstr. 4, D-91058 Erlangen, Germany

Numerical Prediction of Hot-Wire Corrections Near Walls

A thorough numerical investigation was performed for the two-dimensional convective heat transfer of a circular cylinder in a Couette flow close to a wall in order to study the hot-wire near-wall correction. A finite-volume Navier-Stokes solver enhanced by local block refinement and multigrid acceleration guaranteed highly accurate and efficient computational results. Unlike all previous numerical simulations, a more realistic model was used in the present study by taking the heat transfer in the solid wall into account to bridge the discrepancy between the previous theoretical models and the real situation. The computed results from the present investigation show good agreement with experimental data in the literature. Reference correction curves for hot-wire anemometers with respect to different wall materials (e.g., aluminum, glass, Perspex, air, etc.) were obtained.
[DOI: 10.1115/1.1429636]

1 Introduction

Hot-wire anemometry (HWA) is a well-developed measurement technique widely used in experimental fluid mechanics. It measures the local, time-resolved velocity in a flow field utilizing the calibration relationship between the convective heat loss from the wire and the local flow velocity, which must be determined in advance in a known flow field, normally in a uniform free-stream flow. In general, the heat transfer rate of a hot-wire in a free stream depends not only on the flow velocity, but additionally on various geometrical and design factors such as the diameter and length of the wire, the dimensions of the wire supports, the connection of the wire to the supporting prongs and the orientation of the probe to the flow velocity, on fluid properties such as density, viscosity, Prandtl number, etc., and on the wire overheat ratio, i.e., the temperature difference between the wire and the fluid. However, if a large length-to-diameter ratio is used for a hot-wire and if the orthogonality between the wire and the velocity direction is assured, some of the above-mentioned influences can be reduced. As a result, the heat transfer of a hot-wire in measurements can be treated as a problem of two-dimensional convective heat transfer of a heated cylinder.

Although the hot-wire measurement technique can be considered as well developed through numerous investigations (see, e.g., Bruun [1]), its application to perform reliable near-wall measurements is still connected to open questions. It is well known that a hot-wire generally measures a larger apparent velocity than the true value, thus corrections are needed when it is applied in the proximity of a cooler solid wall. This is known as the wall effect. Many efforts have been made in the last half century to investigate the influencing factors responsible for this measurement deviation and to set up a suitable correction procedure for near-wall measurements (see, e.g., Bhatia et al. [2]). A brief literature survey is given in the next section to bring together the existing knowledge on this topic. However, the problem remains so far unsolved since contradictory results exist in the literature and our understanding on the physics behind the wall effect on hot-wire measurements is still far from satisfactory.

It is clear, at least since the work of Polyakov and Shindin [3], that the thermal conductivity of the wall material has a strong effect on the hot-wire reading and it is generally agreed that the required hot-wire corrections close to highly conducting walls are larger than those close to wall materials with low thermal conductivities (see, e.g., Bruun [1]). However, Bhatia et al. [2] reported that wall materials such as glass or plywood do not require corrections at all, in contradiction to the findings of Polyakov and Shindin [3]. Another surprising result is from the recent numerical investigation by Lange et al. [4]. They predicted that the apparent velocity measured by a hot-wire is smaller than the real value in the proximity of a perfectly insulated wall, thus an opposite correction to that for a highly conducting wall is needed. Although the recent work of Chew et al. [5,6] confirms the tendency of the results of Polyakov and Shindin [3], the confusion about the physical cause for the wall effect in the case of poorly conducting walls remains unsolved. Chew et al. [5] suggested the flow distortion due to the presence of the hot-wire close to a wall as the major cause of the wall effect. In contrast, Bhatia et al. [2] and Lange et al. [4] proposed the heat conduction in the solid wall as the major influence.

The existing controversies can be resolved by means of numerical simulations since they can provide detailed field information on the flow and heat transfer around the hot-wire and in the solid wall. In the previous numerical studies (Bhatia et al. [2]; Chew et al. [5], Lange et al. [4]) known to the authors, the conjugated heat transfer in the solid wall was not taken into account. In fact, due to the simplifications introduced in their theoretical models, only two extreme cases, i.e., a perfectly conducting wall and a perfectly insulated wall, were considered in these studies. The discrepancies between numerical results and experimental data can only be resolved by means of a more realistic theoretical model. Moreover, it is also necessary to take the conjugate heat conduction in the solid wall into account in the numerical study to get a better understanding on the effect of the wall thermal conductivity on the hot-wire measurement. These considerations motivated the work reported in this paper.

In the present work, a detailed numerical investigation of the convective heat transfer of a heated cylinder in a near-wall laminar flow was carried out. Unlike the previous numerical studies, the conjugate problem consisting of the convective heat transfer of the cylinder and the heat transfer in the solid wall was solved. This enabled us to study in detail the influence of different wall materials. A very efficient finite-volume Navier-Stokes solver (FASTEST) for block-structured colocated grid arrangements with a local grid refinement scheme was employed for the numerical investigations (Perić [7], Barcus et al. [8], Perić [9], Durst et al. [10], Durst and Schäfer [11]). A detailed description of the mathematical model together with the discretization procedure for the governing equations is provided in Section 3. The computational domain and the boundary conditions are discussed in Section 4. Numerical results together with conclusive findings are presented

Contributed by the Fluids Engineering Division for publication in the JOURNAL OF FLUIDS ENGINEERING. Manuscript received by the Fluids Engineering Division January 7, 2000; revised manuscript received September 13, 2001. Associate Editor: U. Ghia.

 Copyright © 2002 by ASME

Downloaded 03 Jun 2010 to 171.66.16.150. Redistribution subject to ASME license or copyright; see http://www.asme.org/terms/Terms_Use.cfm

in Section 5. Good agreement with experimental data was found for wall materials with both high and low thermal conductivities. In addition to realistic wall materials (aluminum, glass, Perspex, air), two artificial wall materials with 10 percent and 1 percent of the thermal conductivity of air were also investigated for theoretical interest. As expected, the numerical investigations not only yielded useful correction data for HWA measurements close to different wall materials but also threw new light on this problem.

2 Literature Survey on Hot-Wire Heat Transfer Close to a Wall

The need for correction in HWA measurements near walls has been known since the early applications of this velocity measurement technique. A good review of the literature on this subject before 1980 can be found in Bhatia et al. [2]. Among the earlier investigations, the work of Wills [12], which was one of the first to deal with the corrections for constant-temperature HWA probes, has attracted wide attention. Since the time constant for constant-temperature HWA is small compared with the time-scale of turbulence, Wills [12], following up the suggestion of Reichardt [13], expected that corrections based on the known velocity distribution in a well-defined laminar channel flow can be applied to measurements in turbulent boundary layer flows if the friction velocity U_τ is the same as in the calibration flow facility. However, without any physical explanation, only half of the laminar correction was proposed by Wills [12] for turbulent flow measurements based on a comparison of his experimental data measured in the viscous sublayer of turbulent channel flow with the expected velocity profile, i.e., $U^+=Y^+$. Here $U^+=U/U_\tau$ and $Y^+=YU_\tau/\nu$ are nondimensional velocity and wire-to-wall distance, respectively.

Although differences in corrections between laminar and turbulent flow were also reported by some other earlier investigators, a recent experimental study by Chew et al. [6] confirmed the experimental finding of Zemskaya et al. [14] that the same velocity corrections are needed for hot-wire measurements in a laminar or a turbulent flow if the wall shear stress is the same in both flows. In addition, all numerical simulations (Bhatia et al. [2], Chew et al. [5], Lange et al. [4]), which implemented a laminar flow model to investigate the HWA wall correction, also achieved acceptable agreement with experimental data obtained under turbulent flow conditions in the case of highly heat-conducting walls.

Using dimensional analysis, Wills [12] concluded that the additional heat loss of a hot-wire in the vicinity of a solid wall depends on the Reynolds number of the wire ($\mathrm{Re}_D=U_0D/\nu$, where U_0 is the velocity at the location of the wire, D is the wire diameter and ν is the fluid viscosity) and the ratio of the wire-to-wall distance to the wire radius. The thermal conductivity ratio of the wall material and the fluid ($k_w^*=k_w/k_{air}$) was also pointed out as an important influencing parameter. However, no further efforts were made to analyze this effect.

Later, Kostić and Oka [15] and Hebbar [16] obtained velocity correction curves for hot-wire measurements based on their experiments in turbulent flows in a channel and over a flat plate, respectively. Their results suggested the existence of a universal correction expressed in terms of a function, $\Delta U^+=f(Y^+)$, where ΔU^+ is the velocity correction, i.e., difference between the apparent velocity and the real value ($U_{\mathrm{appa}}-U_0$) normalized by U_τ. This finding implies that the effect of the friction velocity U_τ on the HWA correction is negligible, which was verified by the numerical results of Bhatia et al. [2] (which also suggested a universal correction) and later by those of Chew et al. [5]. It should be pointed out that the wall materials in both experimental studies were not given, implying that the important influence of wall materials on the hot-wire near-wall measurement was not recognized by them.

Contesting the universal correction which is exclusively determined by the wire-to-wall distance Y^+, Zemskaya et al. [14] reported a strong influence of the wire diameter, whose influence range extends beyond $Y^+=2$. The diameter effect was confirmed by the more complete experimental study of Krishnamoorthy et al. [17], which was carried out with an aluminum wall. Their results show that the velocity correction needed at a given Y^+ increases with increasing wire diameter and with increasing overheat ratio. The dependence on the wire diameter was supported by the numerical results of Chew et al. [5], whereas all the available numerical studies (Bhatia et al. [2], Chew et al. [5], Lange et al. [4]), which were performed with a two-dimensional model, predicted no apparent or a very weak effect of the overheat ratio.

The additional heat loss to the prongs ($3D$ effect) was attributed by Chew et al. [6] as the cause of this contradiction. They measured the velocity distribution near an aluminum wall using a 5 μm wire with different length-to-diameter ratios ($L/D=200$, 250, and 400) and different overheat ratios τ ranging from 1.1 to 1.8. The results obtained for $L/D=200$ (the same as used by Krishnamoorthy et al. [17]) showed a similar dependence on the overheat ratio to that reported by Krishnamoorthy et al. [17], while this influence disappears in the case of a lower overheat ratio equal to 1.1 or with a larger length-to-diameter ratio ($L/D \geqslant 250$). This recent work of Chew et al. [6] is one of the most systematic experimental investigations of the wall effect on HWA measurement, including the influence of prong length, wire diameter, wall conductivity and the overheat ratio. Their data confirm again the wire diameter influence mentioned above.

Based on measurements with two different walls made of copper (high thermal conductivity) and textolite (low thermal conductivity), Polyakov and Shindin [3] reported that the wall effect is larger in the vicinity of a highly conducting wall than a wall of low conductivity. This finding is also confirmed by the numerical simulation of Chew et al. [5] and their experimental investigation with an aluminum and a Perspex wall (Chew et al. [6]). In the case of highly conducting walls, general agreement could be reached from a number of numerical (Bhatia et al. [2], Chew et al. [5], Lange et al. [4]) and experimental (Krishnamoorthy et al. [17], Janke [18], Chew et al. [6]) investigations that velocity corrections are needed for HWA measurements in the range $Y^+ \lesssim 4-6$. In contrast, a great contradiction still exists with respect to the case of poorly or ''non-conducting'' wall materials. Bhatia et al. [2] concluded from their computations that no correction is necessary for a poorly conducting wall. However, this is directly contradictory to the results of Polyakov and Shindin [3]. It also contradicts the results of Ligrani and Bradshaw [19], which were obtained with subminiature hot-wire sensors in the vicinity of a mirror glass wall, and those of Chew et al. [5,6]. Further confusion arose from the most recent numerical findings by Lange et al. [4] that a hot-wire will read out a smaller apparent velocity than the true value, i.e., an opposite velocity correction is needed in the case of an adiabatic wall. In support of their findings, their results for a perfectly conducting wall showed good agreement with the available experimental data measured in the vicinity of metal walls. It has to be pointed out, despite the numerous investigations mentioned above, the influence of the thermal conductivity of the wall material is still not fully clear. In fact, the effect of this influencing factor has so far not been quantitatively analyzed.

Hence, the above summary of the literature shows that, as concluded in Bruun's book on HWA (Bruun [1]), no universal correction procedure has so far been established, because of the various parameters that influence this correction. The literature survey also shows that the physical causes of the wall effect, especially the influence of the wall material, are not well understood. There are still strong contradictions and quantitative discrepancies among experimental data and numerical results. A more extensive numerical investigation is required in order to resolve the discrepancies and to clarify the existing confusions.

An improved theoretical model has to be applied in the numerical simulation to take the influence of the real thermal conductivity of the wall material into account. Therefore, the conjugate problem consisting of the flow and heat transfer around the cylin-

Downloaded 03 Jun 2010 to 171.66.16.150. Redistribution subject to ASME license or copyright; see http://www.asme.org/terms/Terms_Use.cfm

der and the heat transfer in the solid wall was solved in this work, which enabled us to study in detail the influence of different wall materials.

3 Numerical Method

3.1 Theoretical Model and Governing Equations. In the present study, a continuum approach is used. The fluid is assumed to be incompressible (the density does not vary with the pressure) while the variation of the fluid properties (ρ, μ, k and c_p) under different temperatures is taken into account. The nondimensional governing equations expressing the conservation of mass, momentum and energy for steady two-dimensional flow of an incompressible fluid are, in Cartesian coordinates, as follows:

$$\frac{\partial(\rho^* U_i^*)}{\partial x_i^*} = 0, \tag{1}$$

$$\frac{\partial(\rho^* U_i^* U_j^*)}{\partial x_i^*} = -\frac{\partial P^*}{\partial x_j^*} + \frac{1}{\mathrm{Re}} \frac{\partial}{\partial x_i^*}\left[\mu^*\left(\frac{\partial U_j^*}{\partial x_i^*} + \frac{\partial U_i^*}{\partial x_j^*}\right)\right] + \frac{\mathrm{Gr}}{\mathrm{Re}^2} T^*, \tag{2}$$

$$c_p^* \frac{\partial(\rho^* U_i^* T^*)}{\partial x_i^*} = \frac{1}{\mathrm{Re}\,\mathrm{Pr}} \frac{\partial}{\partial x_i^*}\left[k^* \frac{\partial T^*}{\partial x_i^*}\right] + \frac{Ec}{\mathrm{Re}} \Phi^*, \tag{3}$$

where $i,j = 1,2$ and Φ^* is the normalized viscous dissipation function, given by

$$\Phi^* = \mu^*\left(\frac{\partial U_i^*}{\partial x_j^*} + \frac{\partial U_j^*}{\partial x_i^*}\right)\frac{\partial U_i^*}{\partial x_j^*}. \tag{4}$$

Considering the flow characteristics in the viscous sublayer around the cylinder, the friction velocity $U_\tau = \sqrt{\tau_w/\rho_\infty}$ and the molecular diffusion length $l_c = \nu_\infty / U_\tau$ are introduced as characteristic quantities for the normalization. ρ^*, μ^*, k^* and c_p^* are density, dynamic viscosity, thermal conductivity and specific heat at constant pressure normalized by the corresponding values at the ambient temperature T_∞, i.e., ρ_∞, μ_∞, $k_{f,\infty}$ and $c_{p,\infty}$, respectively. T^* is normalized by the temperature difference between the cylinder and the undisturbed oncoming flow $(T_W - T_\infty)$.

The resultant nondimensional parameters relevant to the considered flow problem are as follows:

Reynolds number: $\mathrm{Re} = U_c l_c / \nu_\infty = 1$

Grashof number: $\mathrm{Gr} = l_c^3 g \beta_\infty \rho_\infty^2 (T_W - T_\infty)/\mu_\infty^2$

Prandtl number: $\mathrm{Pr} = \mu_\infty c_{p,\infty} / k_{f,\infty}$

Eckert number: $\mathrm{Ec} = U_\tau^2 / c_{p,\infty}(T_W - T_\infty)$

where g is the gravitational acceleration, β_∞ the coefficient of volumetric thermal expansion evaluated at the ambient temperature T_∞.

For the solid wall, the system of governing Eqs. (1)–(3) reduces to a diffusion equation describing the heat conduction in the wall. In the case of a steady-state problem as considered here, the heat conduction in solids is described by a Laplace equation and only the ratio of the thermal conductivity of the solid to the fluid k_w^* remains as a relevant parameter in this part of the integration domain.

The fluid considered was air at an inflow (ambient) temperature of $T_\infty = 20°\mathrm{C}$. Two hot-wire temperatures $T_W = 21$ and $100°\mathrm{C}$ were investigated, corresponding to the overheat ratio[1] $\tau = T_W[K]/T_\infty[K] = 1.003$ and 1.27, respectively. A small overheat ratio of $\tau = 1.003$ is not of interest for practical applications of hot-wire measurements. It was used as a test case to evaluate the effect of the overheat ratio. In case of $\tau = 1.003$, the temperature dependence of the fluid properties can be neglected. Consequently, the nondimensional fluid properties (ρ^*, μ^*, k^* and c_p^*) are set to unity. Otherwise, these quantities were calculated by means of quadratic functions of temperature, whose coefficients were obtained based on VDI-Wärmeatlas [20], and were updated in each new iteration. Considering the dimensions and temperatures involved in the present investigation, natural convection and viscous dissipation effects are small. Therefore, the last terms in Eqs. (2) and (3) were neglected. A detailed justification for neglecting these physical effects can be found elsewhere (Lange [21], Lange et al. [22]).

3.2 Discretization and Solution Procedure. For the spatial discretization of Eqs. (1)–(3), a finite-volume method with a colocated arrangement of the variables was employed, as described by Demirdžić and Perić [23]. Equations (2) and (3) were integrated over each control volume (CV), leading to a balance equation for the fluxes through the CV faces and the volumetric sources. The convection and diffusion contributions to the fluxes were evaluated using a central differencing scheme of second-order accuracy, which for the convective part was implemented using the deferred-correction approach proposed by Khosla and Rubin [24]. An evaluation of the discretization accuracy based on the numerical results is given in the next section.

For the pressure calculation, a pressure correction equation was used instead of Eq. (1) and was solved iteratively with Eq. (2) following the well-known SIMPLE algorithm proposed by Patankar and Spalding [25]. Convergence was achieved when the maximum sum of the normalized absolute residuals in all equations was reduced by six orders of magnitude. Details of the discretization and the pressure-velocity coupling can be found elsewhere (Perić et al. [26], Demirdžić and Perić [23]).

The solver for the linearized system of equations is a parallel variant of the strongly implicit method of Stone [27] based on an incomplete LU decomposition. A nonlinear multigrid scheme was employed for convergence acceleration (see, e.g., Hortmann et al. [28]). For parallel computations, a block-structured grid partitioning and a message-passing strategy were used as described in Durst and Schäfer [11].

In order to improve the accuracy of the numerical results without a decrease in efficiency and to optimize the utilization of the available computational resources, a local grid refinement technique was employed. For the local refinement procedure, the computational domain was divided into blocks and each block was discretized with a different mesh density. After refinement, each block remained fully structured, hence retaining the very efficient implementation of the code (Durst et al. [10], Lange [21]).

The numerical code was verified by extensive predictions for the flow and heat transfer around a heated two-dimensional cylinder under free-stream conditions in the range $10^{-4} \leqslant \mathrm{Re}_D \leqslant 10^2$ (Lange [21], Lange et al. [22]), which also partly provide calibration data (Nu_∞ versus Re_D) for the present study.

4 Computational Domain, Boundary Conditions, and Numerical Grids

In the present study, a heated infinite cylinder parallel to a wall and normal to the flow is employed to represent the hot-wire. To simulate the flow conditions in the part of a boundary layer in the vicinity of a wall, a Couette flow with a constant ambient temperature was prescribed at the inflow boundary (see Fig. 1). The upper boundary was assumed to be undisturbed and a zero gradient boundary condition for a fully developed flow was assigned at the outflow boundary.

A hot-wire with a diameter of $D = 5\ \mu\mathrm{m}$ was studied here. The wire-to-wall distance Y is in the range $10 \leqslant Y/D \leqslant 300$. For each value of Y/D, several inflow velocity gradients were applied, based on which the friction velocity varies in the range $0.006 \leqslant U_\tau \leqslant 0.307\,[\mathrm{m/s}]$. As a result, the resulting nondimensional wall distances ($Y^+ = [YU_\tau]/\nu$) cover a range from 0.1 to 10 in the computations. The Reynolds numbers Re_D based on the cylinder diameter and the undisturbed inflow velocity at the location of the wire are very low in this investigation, namely in the range

[1]The overheat ratio τ should not be confused with τ_w, the molecular momentum transport term at the wall.

Downloaded 03 Jun 2010 to 171.66.16.150. Redistribution subject to ASME license or copyright; see http://www.asme.org/terms/Terms_Use.cfm

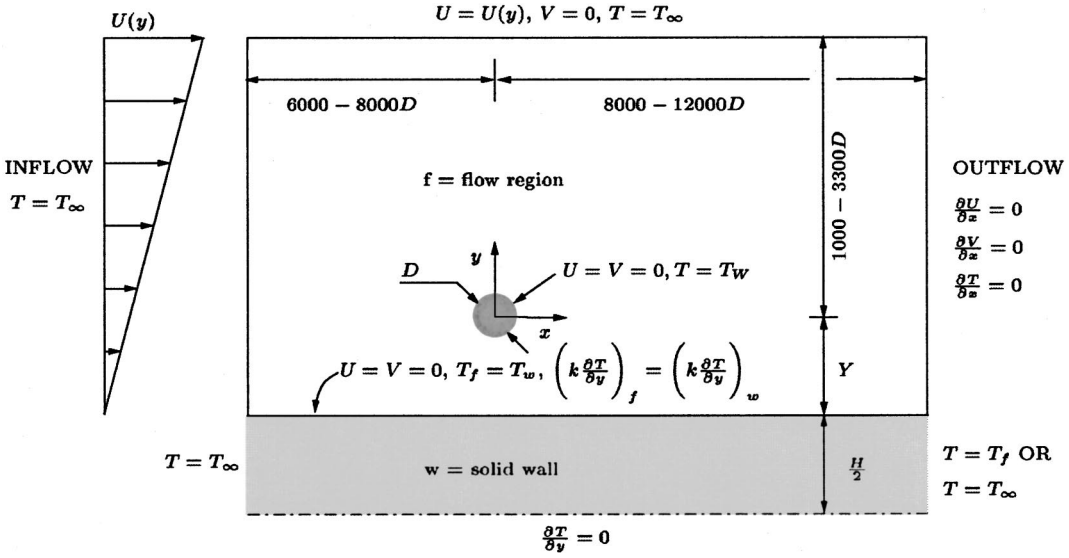

Fig. 1 Computational domain and boundary conditions

0.001–1, which is typical for HWA near-wall measurements. Based on some numerical tests, the computational domain was normally extended between $1000\,D$ and $3300\,D$ to the wall to ensure the accuracy of the results.

The heat transfer in the solid wall was coupled to the flow region by means of the temperature continuity and the heat flux conservation at the interface. The ambient temperature was prescribed for both lateral boundaries of the wall block at the inflow and the outflow locations, physically corresponding to the case of an infinitely long solid wall. Tests were also made with an alternative lateral boundary condition by assuming the downstream lateral wall temperature to be equal to that of the fluid at the interface, which corresponds to the case that the solid wall is ended and surrounded by the fluid at this boundary. Negligible differences were found for the cylinder Nusselt number and for the flow and temperature field in the region of interest with both types of boundary conditions when the domain was extended to $6000\,D$ upstream and $10000\,D$ downstream of the cylinder. Hence good accuracy of the simulations could be guaranteed. Walls of $600\,D$, or 3 mm in thickness, and with different thermal conductivities (aluminum, $k_w^*=9186$; glass, $k_w^*=29.6$; Perspex, $k_w^*=7.2$; air, $k_w^*=1$; and two artificial materials with $k_w^*=0.01$ and 0.1) were investigated. The computational domain together with corresponding boundary conditions are summarized in Fig. 1.

The computational grids consisted of five multigrid levels in the present study. In order to ensure a high accuracy of the numerical results, grids were locally refined around the cylinder. As a result, more than 500 grid points at the cylinder surface ($D=5\ \mu$m) and about 160,000 grid points for the total domain were applied on the finest grid level. As an example, a zoomed view of the grid and the core region on the third multigrid level for the case of $Y/D=100$ are shown in Fig. 2. With this resolution, reliable numerical results for the mean Nusselt number, which is defined as

$$\mathrm{Nu}=-\frac{1}{2\pi}\oint\left.\frac{\partial T^*}{\partial\left(\frac{r}{D}\right)}\right|_W \mathrm{d}\theta \tag{5}$$

where r and θ are coordinate components of a polar system located at the center of the cylinder, can be obtained. Evaluations for the discretization error were carried out with the help of the following formula (Ferziger and Perić [29])

$$p_n=\frac{\ln\left(\frac{\mathrm{Nu}_{n-1}-\mathrm{Nu}_{n-2}}{\mathrm{Nu}_n-\mathrm{Nu}_{n-1}}\right)}{\ln 2}$$

where the subscript n denotes the grid level. Based on the results of Nu, the order of the discretization accuracy were found to be $p_5\approx 1.9$ in the case of $\tau=1.003$ where the temperature dependence of the fluid properties was neglected. In the case of $\tau=1.27$ the variation of the fluid properties under different temperatures was taken into account, the problem becomes strongly nonlinear and one finer multigrid level (totally six levels) was additionally needed to obtain monotonic convergence (Nu decreases with increasing grid level n) on three continuous grid levels for the pur-

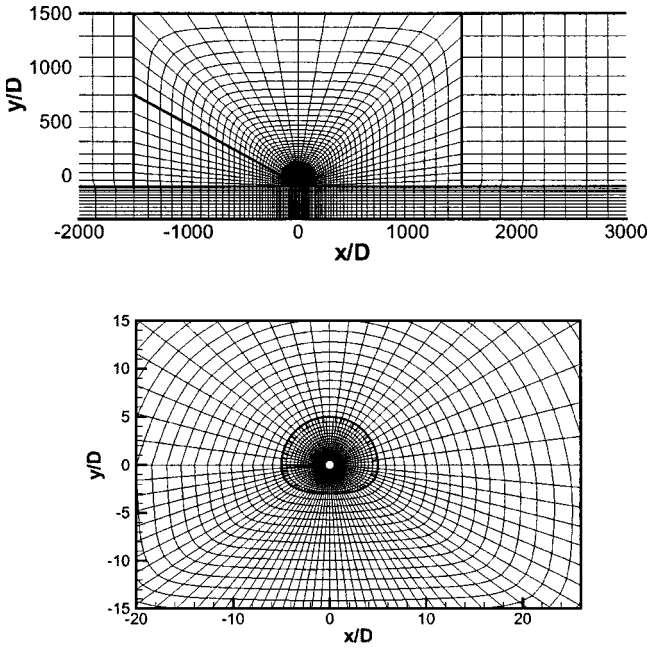

Fig. 2 Example of a computational grid ($Y/D=100$) and zoom of the locally refined region at the third grid level (of a total of five multigrid levels)

Downloaded 03 Jun 2010 to 171.66.16.150. Redistribution subject to ASME license or copyright; see http://www.asme.org/terms/Terms_Use.cfm

pose of the discretization error analysis, which yielded $p_6=1.7-1.95$. Hence, the second-order accuracy of the CDS spatial discretization was preserved in the present study. According to the numerical tests with six multigrid levels, a maximum decrease of 0.1 percent in the results of Nu were found from the fifth to the sixth grid level in the case of a mirror glass wall. The effect of the grid resolution is much stronger in the case of an aluminum wall, where a maximum decrease of about 0.29 percent was observed. That might cause a maximum discretization error of about 1.5 percent in the corresponding results of U^+_{appa} or C_U (defined in Section 5) on the fifth grid level. Therefore, in this case (aluminum wall) the numerical results of Nu were corrected by employing the Richardson extrapolation method (see, e.g., Ferziger and Perić [29]) to remove the discretization error. Noting that an error of 1–2 percent might occur in hot-wire measurements, the present numerical results should be acceptable.

5 Results for Different Heat Conductivities of the Wall Material

As in experimental measurements, the computed value of the Nusselt number Nu was transformed into a corresponding value of the velocity based on the improved numerical calibration curves of Nu_∞ versus Re_D compared with the previous work of Lange [21] which were obtained by simulations for flow and heat transfer around a cylinder under free-stream conditions. Accordingly, the predicted apparent velocity U_{appa} was determined. The actual local velocity U_0 is known from the inflow boundary condition. Following Lange et al. [4], the velocity correction results are also presented here by employing the correction factor C_U, defined as

$$C_U=\frac{U_0}{U_{\text{appa}}}=\frac{U_0^+}{U_{\text{appa}}^+} \tag{6}$$

which is the fraction of the hot-wire signal that corresponds to the actual value of the velocity. A transformation between this representation and the most common form in the literature, $\Delta U^+ = U^+_{\text{appa}}-U_0^+=U_0^+(C_U^{-1}-1)$ can be made since the real velocity distribution (U_0^+ versus Y^+) is known (see Fig. 11 in Appendix). The present study is concentrated on the wall thermal conductivity effect on the hot-wire near-wall correction. The effect of the wire diameter was not investigated here. The same wire diameter as in the present study ($D=5\ \mu$m) was used in all references cited for the validation of the numerical results except Polyakov and Shindin [3], $D=1-10\ \mu$m, Hebbar [16], $D=3.8\ \mu$m and Ligrani and Bradshaw [19], $D=0.625\ \mu$m.

5.1 Results for Walls With High Conductivities. The numerical results of the velocity correction factor C_U in the case of an aluminum wall ($k_w^*=9186$; $\tau=1.27$ and 1.003) are shown in Fig. 3. The results of $\tau=1.003$ were obtained to evaluate the effect of the overheat ratio. Similar to the previous numerical results (Bhatia et al. [2], Chew et al. [5], Lange et al. [4]), a weak dependence of the velocity correction on the overheat ratio was observed in Fig. 3. Tests were also performed for different thermal conductivities with k_w^* varying from 7000 to 10,000, but no obvious change was found in the numerical results. That suggests that the hot-wire correction is not sensitive to the wall material in case of highly conducting walls. Therefore, experimental data with different highly conducting wall materials can be used for comparison.

Several experimental results and the numerical results of Lange et al. [4] for a perfectly conducting wall are plotted for comparison. The experimental data were extracted from their papers and the data of Kostić and Oka [15] and Hebbar [16] were redisplayed by means of interpolation. The wall material used in Kostić and Oka [15] and Hebbar [16] were not given while it was copper ($k_w^*>10{,}000$) in Polyakov and Shindin [3] and aluminum in Krishnamoorthy et al. [17] and Chew et al. [6], which is the same as in the present investigation. The overheat ratios in Krishnamoorthy et al. [17] ($\tau=1.27$ and 1.006, respectively) are very close to those of the present study. Thus their results serve as the most suitable reference data for the present simulation.

As can be seen in Fig. 3, the experimental data are highly scattered due to different experimental conditions (e.g., D, τ). Fairly good agreements are observed between the present results and the experimental data of Polyakov and Shindin [3] and of Krishnamoorthy et al. [17] at the lower end of Y^+ ($Y^+<1$). In the range $Y^+>1.5$ the experimental results can be distinguished into two classes. The results for C_U in Krishnamoorthy et al. [17] are obviously higher than those of the other class (Kostić and Oka [15], Polyakov and Shindin [3], Hebbar [16], Chew et al. [6]), among which a general agreement can be seen. The present numerical results agree favorably well with those of Krishnamoorthy et al. [17], whose measurement conditions are closest to the

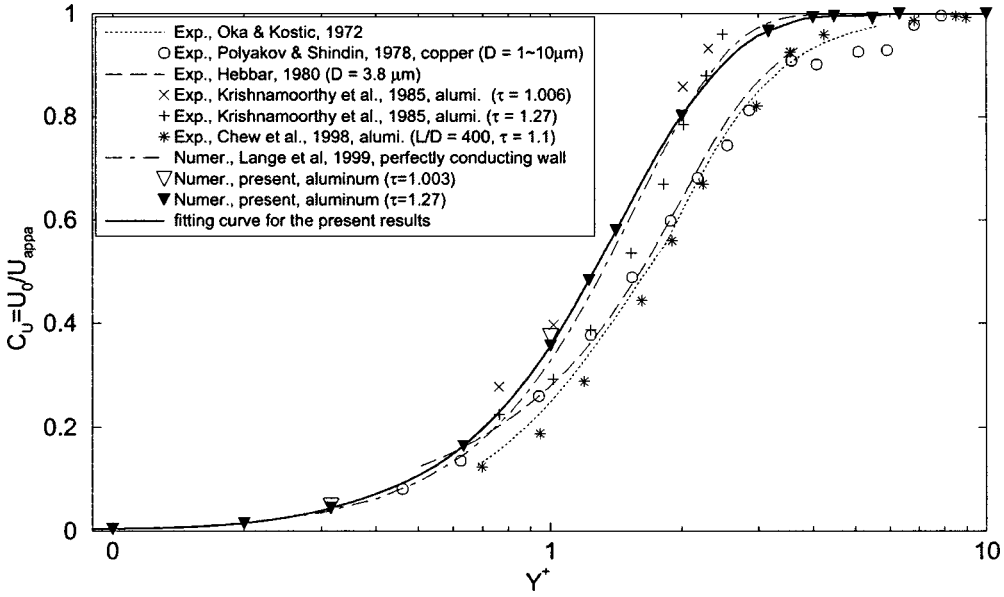

Fig. 3 Comparison of numerical and experimental values of the velocity correction factor C_U in cases of highly conducting walls, $D=5\ \mu$m if not given

Downloaded 03 Jun 2010 to 171.66.16.150. Redistribution subject to ASME license or copyright; see http://www.asme.org/terms/Terms_Use.cfm

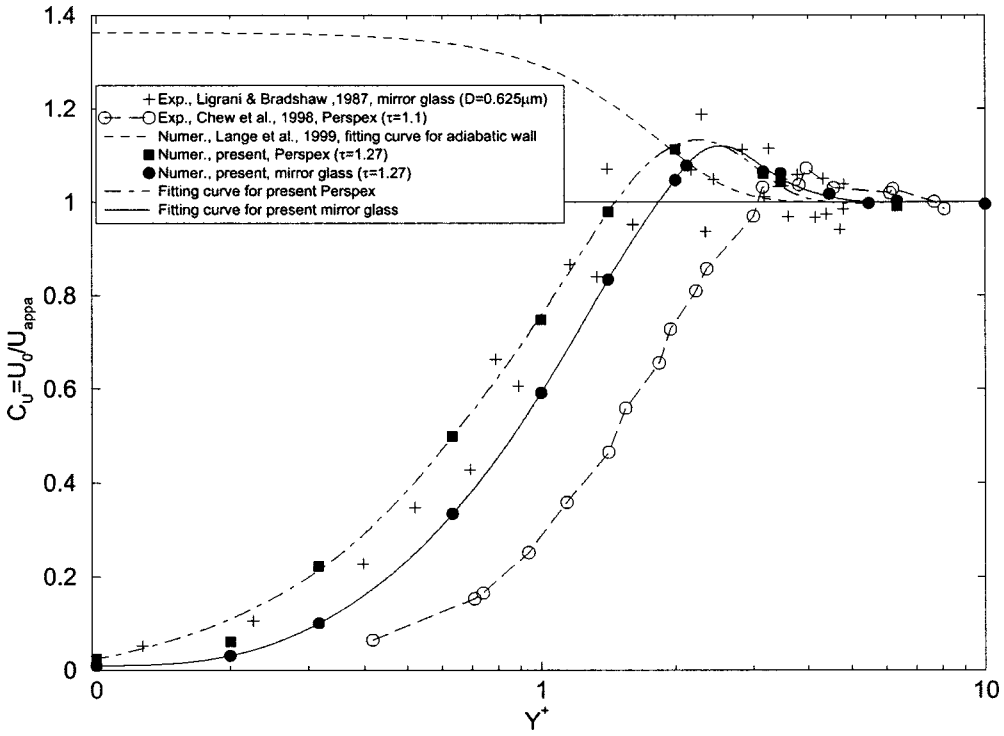

Fig. 4 Comparison of numerical and experimental values of the velocity correction factor C_U in cases of walls with low conductivities

present simulation. The general agreement between the present computed velocity corrections and experimental data obtained in turbulent flows confirms again that the velocity correction curve established under the laminar flow condition could be applied to measurements in turbulent near-wall flows.

It is interesting to note that, the differences between the present results and the fitting curve of Lange et al. [4] for a perfectly heat conducting wall is minor. That implies, that the isothermal boundary condition at the fluid-wall interface (T_w=const) employed in the previous numerical investigations (e.g., Lange et al. [4]) is a good simplification to model the influence of the highly conducting wall on the hot-wire measurements. The discrepancy is mainly due to the fact that the calibration data used by Lange et al. [4] has been improved in the present study. In addition, the computational domain in their simulations ($3000\,D$ downstream of the wire) is not large enough according to the present study.

Although favorable agreements with the measurements of Krishnamoorthy et al. [17] are reached, it should be pointed out that the computed velocity correction factor C_U for $\tau=1.27$ is obvious larger than all the corresponding experimental data in the range $1<Y^+<2$. In other words, the heat loss rate and the apparent velocity reading of a hot-wire U^+_{appa} in this range are under predicted in the present study. It might be caused by the two-dimensional model used in the numerical simulations, in which the additional lateral heat loss of the wire was not included. In case of $Y^+<2$ the data of C_U from Chew et al. [6] are lower than all other results. On checking their measurement condition, it is found that the channel used in Chew et al. [6] was 1.6 mm in height, i.e., only 320 times the wire diameter. As a result, the heat convection of the wire may additionally be subjected to the hydrodynamic and thermal influence of the upper wall. This effect is expected to be larger at lower wire Reynolds number Re_D, i.e., lower Y^+ when Y/D is kept unchanged.

The additional heat transferred to the wall is thought to be the dominant cause of deviations in the HWA measurements in the proximity of a highly heat-conducting wall, as was recognized by previous investigators (see e.g., Bruun [1]). This perception was also the justification for the neglect of any flow field distortion in the computations of Bhatia et al. [2]. Detailed information on the local heat transfer behavior around the wire probe and at the fluid-wall interface were analyzed in Shi et al. [30] to allow a better understanding of the mechanism of the wall correction.

5.2 Results for Walls With Low Conductivities. The required velocity correction for HWA measurement decreases with decreasing thermal conductivity of the wall material, resulting in larger values of C_U for a given Y^+ position of the wire, as shown in Fig. 4, where the predicted results for mirror glass ($k^*_w=29.6$) and Perspex ($k^*_w=7.2$) are presented. The experimental data of Chew et al. [6] (Perspex) and Ligrani and Bradshaw [19] (mirror glass, $D=0.625\,\mu$m) were extracted[2] and redisplayed in the corresponding form of the numerical results for comparison. In addition, the numerical results of Lange et al. [4] for the extreme case of an adiabatic wall are also plotted. In Fig. 4, the present computed C_U data for a mirror glass wall are smaller than the corresponding results of Ligrani and Bradshaw [19] for $Y^+<2$, however, the qualitative agreement is reasonably good in the entire range of Y^+. The smaller deviations from $C_U=1$ found in Ligrani and Bradshaw [19] corresponding to smaller required velocity corrections may be due to the small wire diameter ($D=0.625\,\mu$m) they used. As pointed out in Section 5.1, the results of Chew et al. [6] contain the influence of the upper wall due to the small channel size. The thermal conductivity of the wall material was not reported in both experimental studies, which, however, has a significant effect on the required velocity correction according to the present results. The wall thickness was also not given. In comparison with the case for highly conducting walls, more experimental investigations are required not only to evaluate

[2]Although we were careful with the data extraction, minor errors may still be introduced. However, they should have no consequence to the conclusion of the present work.

Downloaded 03 Jun 2010 to 171.66.16.150. Redistribution subject to ASME license or copyright; see http://www.asme.org/terms/Terms_Use.cfm

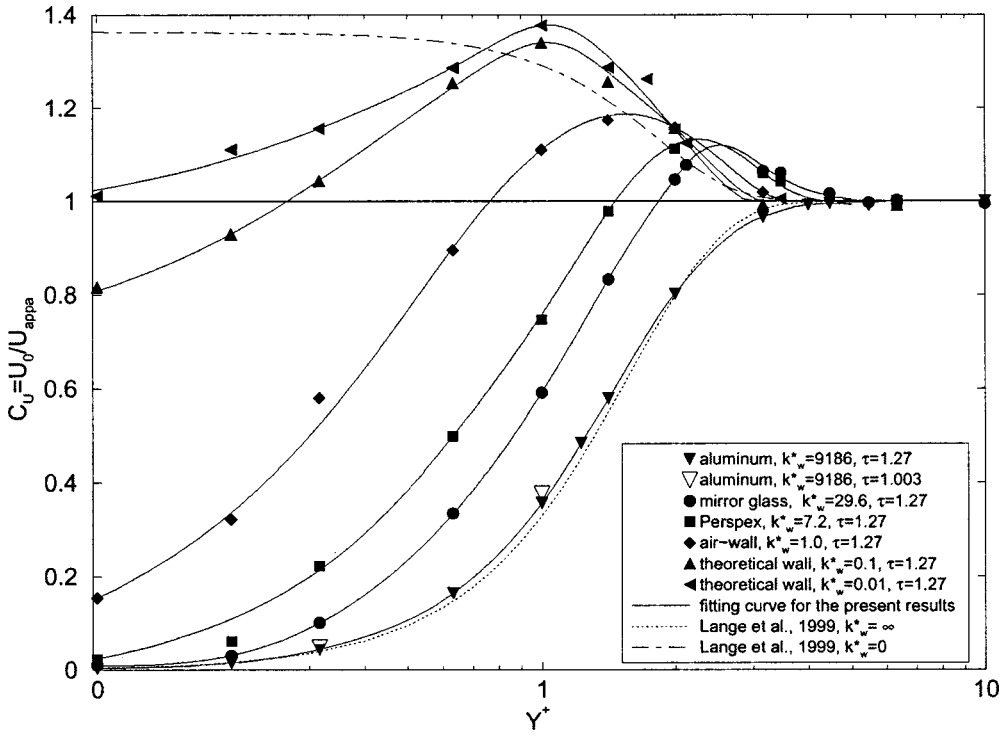

Fig. 5 Summary of the numerical values of the velocity correction factor C_U for different wall materials

the present numerical results, but also to improve the understanding of the physics behind the hot-wire corrections required near walls of low conductivity.

It is interesting to note the small "hump" in the C_U versus Y^+ curve where $C_U>1$ occurs (negative velocity corrections $\Delta U^+<0$ are needed) in both experimental (Ligrani and Bradshaw [19] Chew et al. [6]) and numerical results. As mentioned in the literature survey, great confusion exists concerning the HWA measurement correction close to walls of low conductivities. The common understanding in the literature (see e.g., Bruun [1]) is that positive velocity corrections ($\Delta U^+>0$, i.e., $C_U<1$) are needed in the case of "nonconducting" wall materials for $Y^+\lesssim 2$. Owing to this understanding, great confusion arose among hot-wire experts when Lange et al. [4] predicted that negative corrections ($\Delta U^+<0$, i.e., $C_U>1$) are needed for hot-wire measurements close to an perfectly heat-insulated wall. Therefore, the same "hump" phenomenon observed in the experimental data of Ligrani and Bradshaw [19] and Chew et al. [6] is not only a support for the present numerical results but also encourage the authors further to reveal the physical mechanism, which is discussed in detail in Shi et al. [30].

For theoretical interest, numerical investigations were carried out for wall materials with the same heat conductivity as the fluid ($k_w^*=1$) and two artificial materials with $k_w^*=0.1$ and 0.01. All the numerical results are presented in Fig. 5 together with the results of Lange et al. [4].

It is interesting to see in Fig. 5 that the computed corrections for the three materials further confirm the existence of the "hump" in the $C_U(Y^+)$ distribution. This phenomenon for the two artificial materials ($k_w^*=0.1$ and 0.01) is so evident that they also serve to validate the trend of the numerical finding of Lange et al. [4] for the extreme case of an adiabatic wall ($k_w^*=0$). In contrast to this finding, the numerical work of Chew et al. [5] did not report a negative velocity correction ($\Delta U^+<0$ or $C_U>1$) in the case of an adiabatic wall.

All previous experimental and numerical investigations on this topic simply classified the wall materials into "nonconducting" (low conductivities) walls and highly conducting walls. According to the present results, summarized in Section 5.1, the classification for the case of highly conducing walls is acceptable since no obvious difference is found for the numerical values of the velocity correction factor C_U when the thermal conductivity of the wall material varies from 7000 to 10,000. However, such a classification is insufficient for "nonconducting" wall materials. As shown in Fig. 5, the quantitative dependence of the velocity correction on the thermal conductivity of the wall material is very clear for different poorly conducting walls. For example, mirror glass ($k_w^*=29.6$) and Perspex ($k_w^*=7.2$) are normally both treated as "nonconducting" materials whereas quite different values of the velocity correction factor C_U are predicted for the two wall materials in the present work.

Based on the distribution of the numerical velocity correction factor $C_U(Y^+)$, the critical distance Y_{ct}^+, below which velocity correction is required for hot-wire measurements, can be determined. This value is about $Y_{ct}^+\lesssim 4.5$ both for an aluminum wall or for the poorly conducting walls of mirror glass or Perspex. However, with decreasing wire-to-wall distance negative velocity corrections ($C_U>1$, i.e., $\Delta U^+<0$) are first needed and then positive values ($C_U<1$, i.e., $\Delta U^+>0$) in the case of poorly conducting walls. The range of Y^+ for negative corrections depends on the thermal conductivity of the wall material. For example, this range is larger for a Perspex wall ($1.5<Y^+<4.5$) than a mirror glass wall ($2.0<Y^+<4.5$).

It is worth mentioning the results for a wall with $k_w^*=1$. In such a case, the required velocity corrections of the hot-wire measurement are normally expected to be very small, i.e., $C_U\approx 1$, because the conductivity of the fluid is the same as that of the wall. However, as clearly demonstrated in Fig. 5, instead of a small correction, the predicted apparent velocity is about two times the expected value at $Y^+\approx 0.32$ (resulted from $Y/D=100$ and $\mathrm{Re}_D=0.001$). Now, the remaining open question arises again, whether

Downloaded 03 Jun 2010 to 171.66.16.150. Redistribution subject to ASME license or copyright; see http://www.asme.org/terms/Terms_Use.cfm

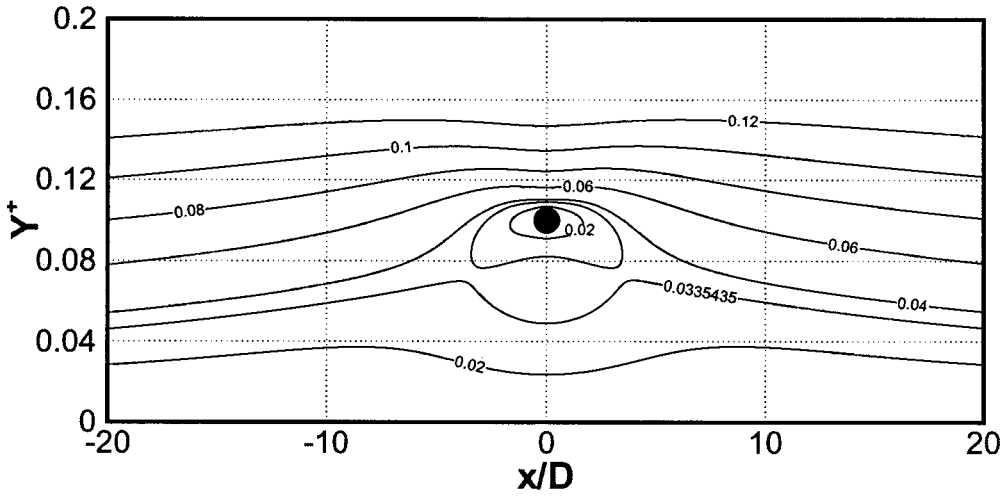

Fig. 6 Total velocity ($V^+=\sqrt{u^2+v^2}/U_\tau$) around the wire for $Y/D=10$ and Re=0.001, resulting in $Y^+=0.1$, and for $k_w^*=1$

such large measurement deviations in this case are really caused by the flow distortion from the interaction between the cylinder and the wall as suggested by Chew et al. [6] for the case of walls with low conductivities. This problem will be addressed now.

The flow distortion around the cylinder due to the presence of a wall is obvious in Fig. 6, where contours of the total velocity values ($V^+=\sqrt{u^2+v^2}/U_\tau$) are plotted. The undisturbed inflow velocity is known by reference to $V^+=Y^+$. However, no strong flow acceleration is found close to the cylinder. Instead, the v-component of the velocity is found to be restricted by the wall when the wire-to-wall distance is reduced (not presented here). Therefore, the flow distortion (convection) is not a dominant effect on the enhanced heat loss from the wire. On the contrary, as Lange et al. [4] pointed out, the small Peclet numbers (Pe=Re Pr) that characterize this kind of flow reflect precisely the minor role played by the convective heat transfer compared with the heat transferred by conduction. Moreover, the interpretation of Chew et al. [6] failed to explain the ''overshoot'' phenomenon observed by Lange et al. [4] for the extreme case of an adiabatic wall and also by the present simulations and some experimental investigations (Ligrani and Bradshaw [19], Chew et al. [6]) for poorly conducting walls. In fact, the real physical mechanism of the ''overshoot'' phenomenon and the large measurement distortions in the proximity of a wall with $k_w^*=1$ can be understood by a detailed analysis of the conjugate heat transfer around the wire in the fluid flow and in the wall, which is discussed in the next section.

6 Mechanism Responsible for Different Wall Correction Behaviors of Hot-Wire Measurements

The above results show clearly the dominant influence of the wall thermal conductivity. Therefore, it is important to analyze the heat transfer process between the fluid and the solid wall, which is exactly the point simplified in the theoretical models of the previous numerical simulations (Bhatia et al. [2], Chew et al. [5], Lange et al. [4]). As discussed below, the temperature distributions at different Y^+ show clearly the important influence of the temperature wake and the heat exchange process between the fluid and the solid wall on the heat loss rate from a wire. Based on this finding, the distinct behaviors of the velocity correction $C_U(Y^+)$ corresponding to different thermal conductivities of wall materials and at different Y^+ locations could be explained.

The ''temperature wake-wall'' interaction and the heat exchange process between the fluid and the solid wall that correspond to different wall effects on the hot-wire measurement at various Y^+ locations are shown schematically in Fig. 7.

When a hot-wire comes close to a wall, i.e., within certain values of Y^+, heat transfer from the fluid into the wall material occurs in the region of the temperature wake of the wire far downstream (refer to Fig. 7(*a*)) even when the wire has not become subject to the wall effect. The heat flux from the fluid is then transferred in both the upstream and downstream directions in the solid wall and back into the fluid when the fluid temperature at the interface is lower than that in the solid wall. This ''temperature wake-wall'' interaction and the heat ''feedback'' process through heat transfer in the solid wall will have no evident effect on the hot-wire heat loss unless it occurs close enough to the wire location when the wire-to-wall distance reaches below a certain value of Y_{ct}^+. This distance depends directly on the thermal conductivity of the wall material. For example, based on the results in Fig. 5, Y_{ct}^+ is about 5.5 for aluminum and about 4.0 for mirror glass. As an example for this case, the ''temperature wake-wall'' interaction and the heat feedback process are clearly observed in Fig. 8 for a wire located at $Y/D=100$ from a mirror glass wall with $\mathrm{Re}_D=1$ resulting in $Y^+=10$, where the wall effect on the hot-wire measurement is still negligible ($C_U\approx 1$ in Fig. 4).

This process has a two-way effect on the heat loss from the hot-wire. The enhancing effect is obvious for materials with $k_w^*>1$ since the heat transfer in the region close to a wire can be enhanced owing to the heat transfer process in the solid wall compared with the combined effect of diffusion and convection in a free stream so that the heat transfer rate of the wire is increased. However, a restraining effect may also arise when the heat flux

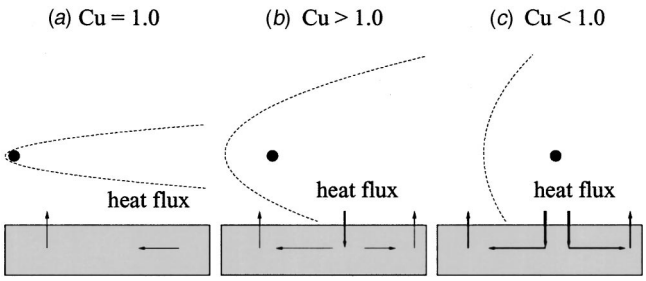

Fig. 7 Schematic temperature influence region of a hot-wire and the heat exchange process between the fluid and the solid wall at various wire-to-wall distances Y^+

Downloaded 03 Jun 2010 to 171.66.16.150. Redistribution subject to ASME license or copyright; see http://www.asme.org/terms/Terms_Use.cfm

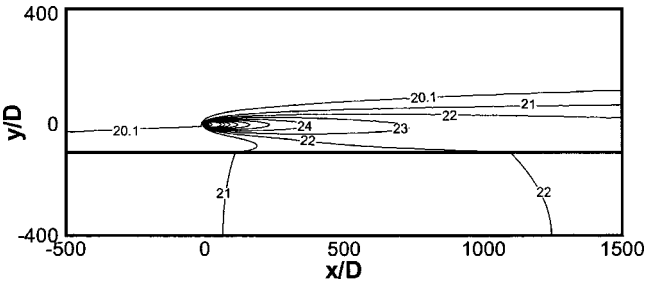

Fig. 8 Isotherms (°C) around the wire and in the wall with a wire-to-wall distance $Y^+=10$ (mirror glass, $k_w^*=29.6$, $Y/D=100$ and $Re_D=1$), $C_U\approx1$

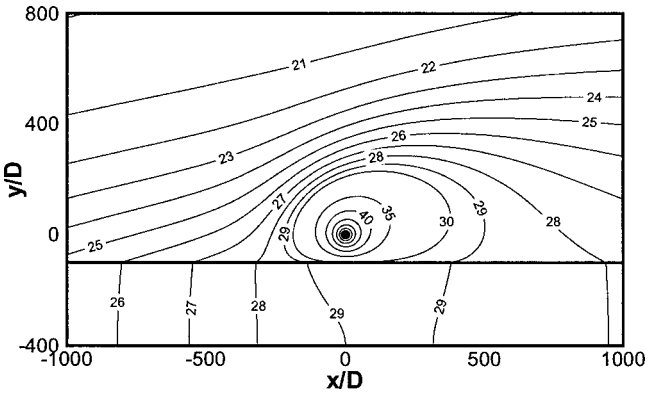

Fig. 10 Isotherms (°C) around the wire and in the wall with a wire-to-wall distance $Y^+=0.63$ (mirror glass, $k_w^*=29.6$, $Y/D=100$ and $Re_D=0.004$), $C_U<1$

from the temperature wake downstream far away from the wire transfers partly upstream in the solid wall and comes back into the fluid flow in the vicinity of the wire location, or especially in the vicinity upstream of the wire when Y^+ decreases (Fig. 7(*b*)). In such a case, the flow around the wire is heated by the feed-back heat flux from the wall, and as a result the heat loss rate of the wire is reduced, which is illustrated in Fig. 9 (mirror glass, $Y/D=100$ and $Re_D=0.1$, resulting in $Y^+\approx3.2$). This restraining effect is the physical cause responsible for the surprising ''velocity correction factor overshoot'' phenomenon ($C_U>1$) obtained for the ''nonconducting'' walls (Fig. 5). For highly conducting walls, the heat from the fluid transfers far away from the wire location owing to the high thermal conductivity of the wall material. As a result, the restraining effect arising from the heat ''feed-back'' process always plays a negligible role, hence the velocity correction factor C_U remains below unity (Fig. 3).

When Y^+ is further reduced (Fig. 7(*c*)), the temperature wake-wall interaction begins in the close proximity of the wire. Moreover, a large heat flux transfers directly from the heated fluid around the wire into the wall owing to its higher conductivity than the fluid, hence the temperature gradient around the wire is greatly increased. The heat transfers far away from the wire location in the wall, both upstream and downstream. The upstream heat transfer in the wall is especially enhanced by the large cooling effect of the oncoming unheated flow. As an example, Fig. 10 displays clearly the direct ''wire-wall'' heat interaction at a distance of $Y^+=0.63$ close to a mirror glass wall resulting from $Y/D=100$ and $Re_D=0.004$, where the higher wall temperature gradients in the upstream direction indicate an enhanced heat transfer in that direction. The enhancing effect becomes dominant and more heat is lost from the wire than under the free-stream condition as Y^+ decreases further. As a result, $C_U<1$ is observed.

Now the ''hump'' in the $C_U(Y^+)$ distributions for wall materials with low conductivities is easily understood. It reflects the dynamic transition from the restraining effect to the enhancing effect with decreasing Y^+. For decreasing thermal conductivity of the wall, the restraining effect increases, hence the ''hump'' in the $C_U(Y^+)$ distribution increases (see Fig. 4).

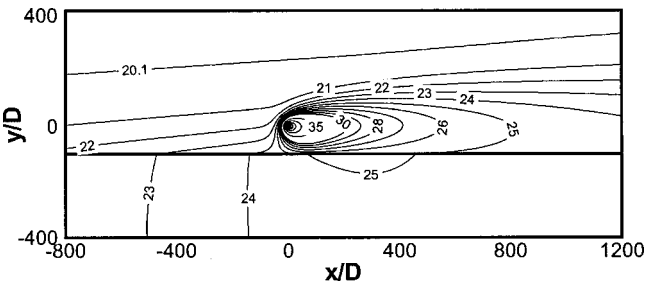

Fig. 9 Isotherms (°C) around the wire and in the wall with a wire-to-wall distance $Y^+=3.16$ (mirror glass, $k_w^*=29.6$, $Y/D=100$ and $Re_D=0.1$), $C_U>1$

7 Conclusions and Final Remarks

Numerical simulations were carried out to study the influence of the thermal conductivity of the wall material on the hot-wire wall correction. The conjugate heat transfer in the solid wall was taken into account, which leads to a significant improvement of the results for poorly conducting materials. Materials with different thermal conductivities were investigated. Reasonable agreement with the measurement data in the literature was achieved for both highly and poorly conducting materials. Based on the present results, the following conclusions can be drawn:

- In the case of highly conducting walls, the velocity corrections needed for HWA near-wall measurements are not sensitive to the wall material, but a strong dependence on the thermal conductivity of the wall material is found in the case of poorly conducting walls.
- The wall effect can not only enhance heat transfer from the wire, as recognized in previous studies, but can also have a restraining effect on the heat loss from the wire when the wire is located at a certain range of Y^+ values from poorly conducting walls, due to the heat feed-back from the wall.
- The heat exchange process between the fluid and the wall is the most important physical mechanism for the hot-wire corrections required near walls both of high and low thermal conductivity. In numerical studies, the Dirichlet temperature boundary condition $T_w=T_\infty$ at the fluid-wall interface, corresponding to $k_w=\infty$, is a good approximation for cases of highly conducting walls. In case of walls of low conductivity, on the other hand, it is not realistic to model the wall effect by means of the Neumann temperature boundary condition $\partial T/\partial n|_w=0$ at the fluid-wall interface, which physically corresponds to $k_w=0$. Instead, the conjugate heat transfer in the solid wall has to be included in the mathematical model.

Acknowledgments

This work was supported by a fellowship from the German Academic Exchange Program (DAAD) to J.-M. Shi and by a research grant from the Bavarian Consortium for High-Performance Scientific Computing (FORTWIHR), which are gratefully acknowledged. The authors also acknowledge that Dr.-Ing C. F. Lange (Dept. of Mechanical Engineering, University of Alberta, Canada) took part in the implementation of the coupling proce-

Downloaded 03 Jun 2010 to 171.66.16.150. Redistribution subject to ASME license or copyright; see http://www.asme.org/terms/Terms_Use.cfm

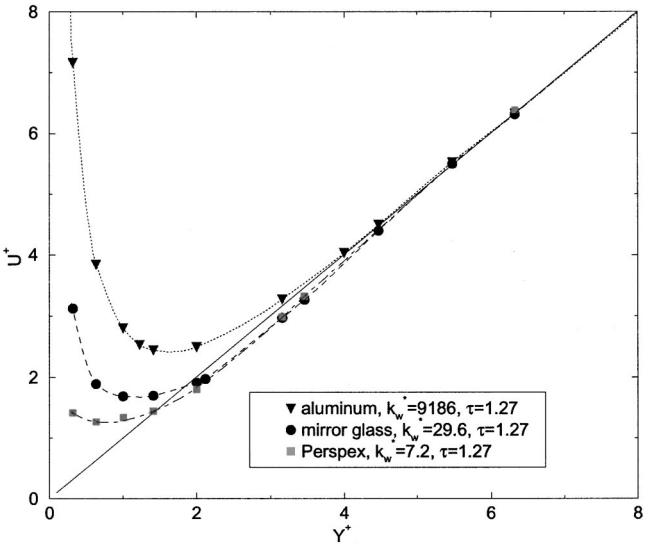

Fig. 11 Predicted apparent velocity values for a hot-wire close to walls of different materials

dure in FASTEST. Finally, we would like to thank Prof. U. Ghia and Prof. P. Bradshaw for valuable comments for the revision of the paper.

Nomenclature

C_D = drag coefficient
c_p = specific heat at constant pressure
C_U = velocity correction factor
D = cylinder diameter
Ec = Eckert number
g = gravitational acceleration
Gr = Grashof number
H = thickness of the solid wall
k = thermal conductivity
L = length of the wire
Nu = Nusselt number
P = pressure
Pr = Prandtl number
$\dot{q}$ = specific heat flux
Re = Reynolds number
T = temperature
U_i = Cartesian velocity components
U_τ = friction velocity
x_i = Cartesian coordinates
Y = wire-to-wall distance
β = coefficient of volumetric thermal expansion
μ = dynamic viscosity
ν = kinematic viscosity
ρ = fluid density
τ = overheat ratio
τ_w = wall shear stress
Φ = viscous dissipation function

Indices:

0 = actual value
appa = apparent value
c = characteristic quantities
ct = critical value
∞ = free-stream
f = flow region
w = solid wall
W = at the cylinder surface
$*$ = nondimensional quantity
$+$ = in wall units

Appendix

Following the suggestion of one referee, the numerical results in cases of realistic wall materials (aluminum, mirror glass and Perspex) are redisplayed in Fig. 11 in the form of U^+ versus Y^+ for reference.

References

[1] Bruun, H. H., 1995, *Hot-Wire Anemometry*, Oxford University Press, Oxford.
[2] Bhatia, J. C., Durst, F., and Jovanović, J., 1982, "Corrections of hot-wire anemometer measurements near walls," J. Fluid Mech., **122**, pp. 411–431.
[3] Polyakov, A. F., and Shindin, S. A., 1978, "Peculiarities of hot-wire measurements of mean velocity and temperature in the wall vicinity," Lett. Heat Mass Transfer, **5**, pp. 53–58.
[4] Lange, C. F., Durst, F., and Breuer, M., 1999, "Wall effects on heat losses from hot-wires," Int. J. Heat Mass Transf., **20**, pp. 34–47.
[5] Chew, Y., Shi, S., and Khoo, B., 1995, "On the numerical near-wall corrections of single hot-wire measurements," Int. J. Heat Fluid Flow, **16**, pp. 471–476.
[6] Chew, Y. T., Khoo, B. C., and Li, B. C., 1998, "An investigation of wall effects on hot-wire measurements using a bent sublayer probe," Meas. Sci. Technol., **9**, pp. 67–85.
[7] Perić, M., 1985, "A Finite Volume Method for the Prediction of Three-dimensional Fluid Flow in Complex Ducts," Ph. D. thesis, Imperial College, London.
[8] Barcus, M., Perić, M. and Scheuerer, G., 1988. A control volume based full multi-grid procedure for the prediction of two-dimensional, laminar, incompressible flows. *Notes on Numerical Fluid Mechanics*, M. Deville, ed., Vol. 20, pp. 9–16. Braunschweig, Vieweg.
[9] Perić, M., 1990, "Analysis of pressure-velocity coupling on non-orthogonal grids," Numer. Heat Transfer, Part B, **17**, pp. 63–82.
[10] Durst, F., Lange, C. F., and Schäfer, M., 1995, "Local block refinement using patched grids for the parallel computation of viscous flows," Technical Report LSTM 445/N, LSTM, Universität Erlangen-Nürnberg, Erlangen.
[11] Durst, F., and Schäfer, M., 1996, "A parallel blockstructured multigrid method for the prediction of incompressible flows," Int. J. Numer. Methods Fluids, **22**, pp. 549–565.
[12] Wills, J. A. B., 1962, "The correction of hot-wire readings for proximity to a solid boundary," J. Fluid Mech., **12**, pp. 388–396.
[13] Reichardt, H., 1940, "Die Wärmeübertragung in turbulenten Reibungsschichten," Angew. Math. Mech., **20**, pp. 297–328.
[14] Zemskaya, A., Levitskiy, V. N., Repik, Y. U., and Sosedko, Y. P., 1979, "Effect of the proximity of the wall on hot-wire readings in laminar and turbulent boundary layers," Fluid Mech.-Sov. Res., **8**, pp. 133–141.
[15] Kostić, Z., and Oka, S., 1972, "Influence of wall proximity on hot-wire velocity measurements," DISA Information, **13**, pp. 29–33.
[16] Hebbar, K. S., 1980, "Wall proximity corrections for hot-wire readings in turbulent flows," DISA Information, **25**, pp. 15–16.
[17] Krishnamoorthy, L. V., Wood, D. H., Antonia, R. A., and Chambers, H. J., 1985, "Effect of wire diameter and overheat ratio near a conducting wall," Exp. Fluids, **3**, No. 3, pp. 121–127.
[18] Janke, G., 1987, "Hot wire in wall proximity," G. Comte-Bellot and J. Mathieu, eds., *Advances in Turbulence*, pp. 488–498, Springer, Berlin.
[19] Ligrani, P. M., and Bradshaw, P., 1987, "Subminiature hot-wire sensors: Development and use," J. Phys. E, **20**, pp. 323–332.
[20] Verein Deutscher Ingenieure 1994, *VDI-Wärmeatlas* (7th ed.), VDI, Düsseldorf.
[21] Lange, C. F., 1997, "Numerical Predictions of Heat and Momentum Transfer from a Cylinder in Crossflow with Implications to Hot-Wire Anemometry," Ph. D. thesis, Institute of Fluid Mechanics, Friedrich-Alexander University of Erlangen-Nürnberg.
[22] Lange, C. F., Durst, F., and Breuer, M., 1998, "Momentum and heat transfer from cylinders in laminar flow at $10^{-4} \leqslant Re \leqslant 200$," Int. J. Heat Mass Transf., **41**, pp. 3409–3430.
[23] Demirdžić, I., and Perić, M., 1990, "Finite volume method for prediction of fluid flow in arbitrary shaped domains with moving boundaries," Int. J. Numer. Methods Fluids, **10**, pp. 771–790.
[24] Khosla, P. K., and Rubin, S. G., 1974, "A diagonally dominant second-order accurate implicit scheme," Comput. Fluids, **2**, pp. 207–209.
[25] Patankar, S. V., and Spalding, D. B., 1972, "A calculation procedure for heat, mass and momentum transfer in three-dimensional parabolic flows," Int. J. Heat Mass Transf., **15**, pp. 1787–1806.
[26] Perić, M., Kessler, R., and Scheuerer, G., 1988, "Comparison of finite-volume numerical methods with staggered and colocated grids," Comput. Fluids, **16**, pp. 389–403.
[27] Stone, H. L., 1968, "Iterative solution of implicit approximations of multi-dimensional partial differential equations," SIAM (Soc. Ind. Appl. Math.) J. Numer. Anal., **5**, pp. 530–558.
[28] Hortmann, M., Perić, M., and Scheuerer, G., 1990, "Finite volume multigrid prediction of laminar natural convection: Bench-mark solutions," Int. J. Numer. Methods Fluids, **11**, pp. 189–207.
[29] Ferziger, J. H., and Perić, M., 1999, *Computational Methods for Fluid Dynamics*, Springer, Berlin.
[30] Shi, J.-M., Breuer, M., and Durst, F., 2002, "Wall effect on heat transfer from a micro cylinder in near-wall shear flow," Int. J. Heat Mass Transf., **45**, pp. 1309–1320.

Downloaded 03 Jun 2010 to 171.66.16.150. Redistribution subject to ASME license or copyright; see http://www.asme.org/terms/Terms_Use.cfm

Numerical Simulation of Polymer Flow Into a Cylindrical Cavity

Amit Kumar
Former Graduate Student

P. S. Ghoshdastidar[1]
Professor
Mem. ASME
e-mail: psg@iitk.ac.in

Department of Mechanical Engineering,
Indian Institute of Technology Kanpur,
Kanpur, U.P.208016
India

In this paper, new finite-difference based detailed general methodologies are presented for numerical simulation of injection mold-filling during the production of a long cylindrical object. The polymer considered is low density polyethylene (LDPE) following power-law viscosity model for nonzero shear rate zone. However, where shear rate becomes zero, "zero-shear viscosity" value has been used. Three cases have been considered, namely; (i) isothermal filling at constant injection pressure; (ii) isothermal filling at constant flow rate and; (iii) nonisothermal filling at constant flow rate. For (iii), the viscosity of LDPE is also a function of temperature. The material of the mold is steel. For the nonisothermal filling, the concept of melt-mold thermal contact resistance coefficient has been incorporated into the model. The length and diameter of the body in all three cases have been taken as 0.254 m and 0.00508 m, respectively. The results show excellent agreement with the corresponding analytical solutions for the first two cases showing the correctness of the numerical method. The simulation results for nonisothermal filling are reported for the first time for this particular geometry and lend insight into various important aspects of mold-filling including injection pressure versus time, and effects of flow rates on melt temperature fields at various axial locations as well as on frozen skin layer.
[DOI: 10.1115/1.1445796]

Keywords: Injection Molding, Polymer Flow, Numerical Simulation

1 Introduction and Literature Review

Injection molding is one of the most common processing methods for thermoplastics. Nowadays one sees a multitude of different types of injection molded products in homes, vehicles, offices, and factories. These include combs, syringes, paint brush handles, crash helmets, telephones, soft drink glasses, gearwheels, brief cases, television housings, typewriters—the list is almost endless.

In the injection molding process, a thermoplastic in the form of granules or powder, passes from a feed hopper into a barrel where it is heated until it becomes soft. It is then forced through a nozzle into a relatively cold mold which is clamped tightly closed. After the plastic is cooled and solidified, the article is ejected and the cycle is repeated. The major advantages of the process include its versatility in molding a wide range of products, the ease with which automation can be introduced, the possibility of high production rates, and the manufacture of articles with close tolerances (Crawford [1]).

To improve the mold design and process control in this area, increasing reliance is being placed on computer-aided design, manufacture, and engineering. The quality of an injection molded part is affected by many factors, which include geometric parameters associated with the mold design and the cooling system design as well as process parameters such as molding conditions during filling phase.

Numerous mathematical models have been proposed and extensively developed by various research groups for the analysis of different stages of the injection molding process. Serious research on injection molding started in the early fifties (Kamal et al. [2]). An empirical equation for capillary flow, coupled with a quasi-steady approximation and a correlation to calculate the filling time associated with the molding process were developed. A numerical model for disk type geometry was given by Kamal and Kenig [3] who proposed an integrated mathematical treatment of the filling, packing, and cooling stages of the injection molding cycle. Wu et al. [4] also presented a model for simulation of filling of a disk shaped cavity. The transport equations for a power-law fluid were used to solve the transient and nonisothermal problem of the filling of the cavity.

A finite-difference/finite element simulation was presented by Hieber and Shen [5]. In this paper, a detailed formulation was given for simulating the injection mold filling of thin cavities of arbitrary planer geometry. The modeling is in terms of generalized Hele-Shaw flow for an inelastic, non-Newtonian fluid under nonisothermal conditions. Chiang et al. [6] employed a unified theoretical model to simulate the filling and post filling stages of the injection molding process. Implementation of such a model is based on hybrid finite element/finite difference numerical solution of the generalized Hele-Shaw flow of a compressible viscous fluid under nonisothermal conditions.

Hetu et al. [7] reported a 3D finite element method for the simulation of the filling stage in injection molding of industrial parts. Recent trends are seen in the direction of obtaining optimum molding conditions. Pandelidis and Zou [8] addressed the problem of automatic optimization of gate location and presented a methodology for molding condition optimization in a companion paper (Pandelidis and Zou [9]). Choi et al. [10] presented a method for optimizing process parameters of injection molding with Neural Network application in the process simulation environment. In their study, a learning system was developed to generate an optimum set of process parameters at the design stage with minimum number of CAE runs. While the work of Hetu et al. [7] dealt with irregular geometry and finite-element simulation, the present work treated a simple but important geometry and solves the mold filling problem by developing novel, general finite-difference based methodologies and showed new results that lent insight into non-isothermal polymer flow into a cylindrical cavity.

1.1 Objectives of the Present Study. The objectives of the present study are to investigate numerically the mold filling for the production of a cylindrical object of length, 0.254 m and diameter, 0.00508 m. Three cases have been considered, namely: (i) isothermal filling at constant injection pressure; (ii) isothermal

[1]Corresponding Author.

Contributed by the Fluids Engineering Division for publication in the JOURNAL OF FLUIDS ENGINEERING. Manuscript received by the Fluids Engineering Division December 6, 1999; revised manuscript received October 15, 2001. Associate Editor: P. E. Raad.

 Copyright © 2002 by ASME

Downloaded 03 Jun 2010 to 171.66.16.150. Redistribution subject to ASME license or copyright; see http://www.asme.org/terms/Terms_Use.cfm

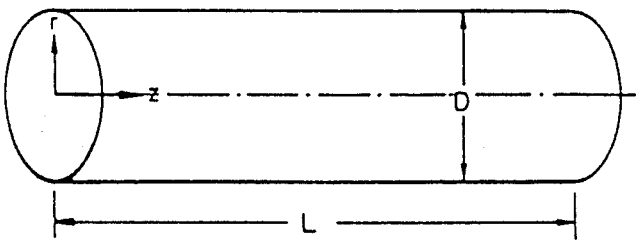

Fig. 1 Cylindrical cavity to be filled by polymer melt

filling at constant flow rate; and (iii) nonisothermal filling at constant flow rate. The main aims are (a) to develop a new numerical approach based on finite-difference which can be useful to other researchers and (b) to gain insight into the aspects of polymer flow into a long cylindrical cavity.

2 Isothermal Filling

The first two cases fall under the category of isothermal filling, which corresponds to the situation when the ratio of heat generated by viscous dissipation to that lost by heat transfer to cold walls is close to unity and therefore, fair estimates of filling time can be obtained by assuming isothermal flow.

For the first two cases the quasi-steady, fully developed, and incompressible flow of a polymer (in this case, LDPE) melt along a cylindrical cavity of diameter D and length L (Fig. 1) under isothermal condition takes place. While in case (i), the melt is injected at constant injection pressure and hence the flow rate Q decreases as the mold fills, in case (ii), the constant flow rate is maintained and hence the injection pressure is increased as the cavity fills.

2.1 Problem Formulation. In injection molding simulations the inertial terms in the momentum equation are negligible in comparison to the pressure and viscous terms. Therefore, the simple Stokes flow form of the momentum equation may be used. The polymer is Non-Newtonian and assumed to follow power-law viscosity model for nonzero shear rate zone. It is well known that low density polyethylene (LDPE) exhibits power-law behavior over limited ranges of shear rate (Han [11]). In the range of shear rates considered in the present work, the assumption of power-law viscosity model for molten LDPE is a valid one. However, where shear rate becomes zero, ''zero-shear rate viscosity'' value has been used. For both cases the flow is quasi-steady, fully developed, and incompressible. Cylindrical polar coordinates r and z are appropriate for describing the axisymmetric flow in which case there are no variations with respect to the angular coordinate, θ and $V_\theta = 0$. Fully developed flow implies that $\partial V_z / \partial z = 0$. From the equation of continuity it can be deduced that $V_r = 0$. Since the

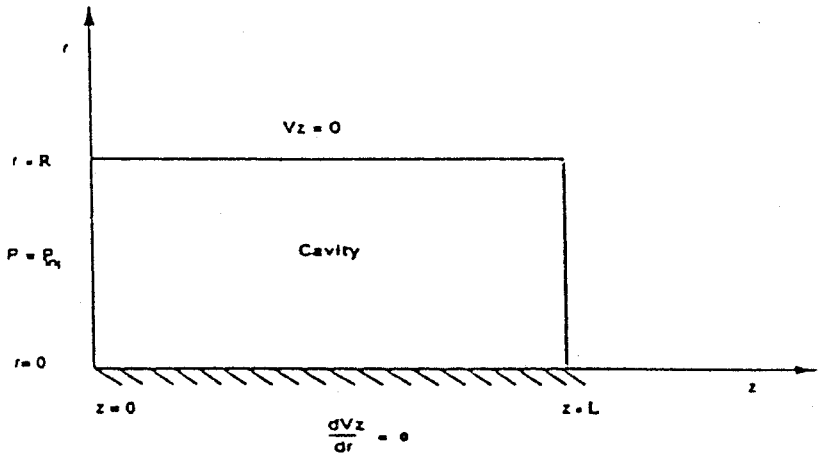

Fig. 2 The computational domain for isothermal filling

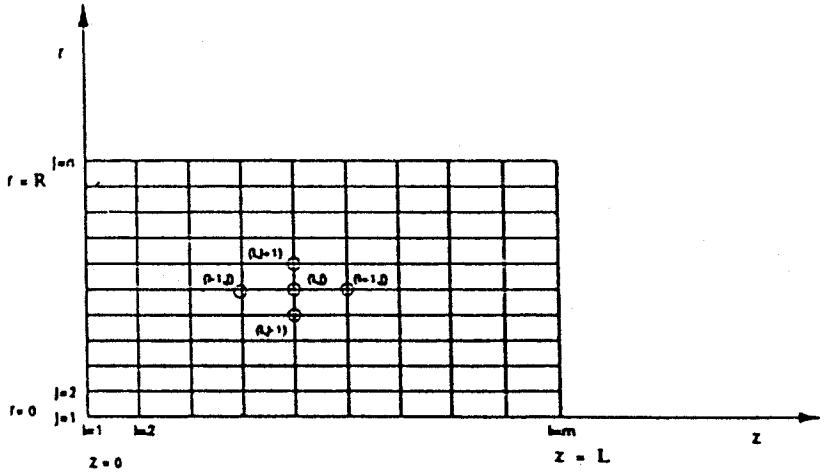

Fig. 3 The grid and the grid points in the computational domain

Downloaded 03 Jun 2010 to 171.66.16.150. Redistribution subject to ASME license or copyright; see http://www.asme.org/terms/Terms_Use.cfm

problem is thermally and geometrically symmetric about the longitudinal axis, only one half of the physical domain is considered. The computational domain is shown in Fig. 2. From the three components of the equation of motion is it is apparent that $\partial p/\partial r=0$ and $\partial p/\partial\theta=0$. Therefore, only *z*-momentum equation needs to be solved. Since the flow is isothermal, the solution of energy equation is not necessary. For both the cases, the governing differential equation and boundary conditions are same.

2.2 Governing Differential Equation.

$$\frac{\partial p}{\partial z}=\frac{1}{r}\frac{\partial}{\partial r}(r\tau_{rz}) \tag{1}$$

$$\text{where}\quad \tau_{rz}=\mu\frac{\partial V_z}{\partial r} \tag{1a}$$

$$\text{and}\quad \mu=m(|\partial V_z/\partial r|)^{n-1} \tag{1b}$$

"*m*" in Eq. 1(b) is called Consistency Index (see Nomenclature for its unit) and represents the Newtonian viscosity (that is, corresponding to $n=1$). Therefore, the values of *n* different from unity describe the deviation from Newtonian fluids. In the case of many polymer solutions and melts, *n* is usually less than unity (Han [11]). For $\partial V_z/\partial r=0$, zero shear-rate viscosity value is used. Clearly, *p* is a function of only *z*, whereas the right hand side of Eq. (1) is a function of only *r*. Therefore, $\partial p/\partial z$ must be constant.

2.3 Boundary Conditions. B.C.1: At $r=0$, $\partial V_z/\partial r=0$ (axisymmetry)
B.C.2: At $r=R$, $V_z=0$ (no-slip)
The pressure at the melt front is always zero because the atmospheric pressure prevails there (Guceri [12]).

2.4 Details of Finite-Difference Formulation. From Eq. (1), using L'Hopital's rule, we get

$$\text{for}\quad r=0,\quad \frac{\partial p}{\partial z}=2\mu\frac{\partial^2 V_z}{\partial r^2} \tag{2}$$

$$\text{where}\quad \mu=\mu_0$$

where μ_0 is the viscosity at zero shear rate.
For $r>0$, Eq. (1) reduces to

$$\frac{\mu}{r}\frac{\partial V_z}{\partial r}+\mu\frac{\partial^2 V_z}{\partial r^2}+\frac{\partial\mu}{\partial r}\frac{\partial V_z}{\partial r}-\frac{\partial p}{\partial z}=0 \tag{3}$$

where μ is defined in Eq. 1(b).

Equations (2) and (3) are discretized using finite-difference scheme. A uniform grid is used (Fig. 3). The details of the finite-difference scheme are shown below.

Grid Points: $j=1$ *for* $i=2$ *to* ***m***. These grid points lie on the center axis ($r=0$) and hence Eq. (2) applies here.
Since at $r=0$, $\partial V_z/\partial r=0$, using image-point technique, we have

$$\frac{V_{z,i,j+1}-V_{z,i,j-1}}{2\Delta r}=0\Rightarrow V_{z,i,j+1}=V_{z,i,j-1}$$

Since $p_{\text{melt front}}=0$, $p_{i,j}=0$ $(i\geqslant 2)$. Also, $p_{1,j}=p_{\text{inj}}$. Using backward difference for $\partial p/\partial z$, central difference for $\partial^2 V_z/\partial r^2$ and using $V_{z,i,j+1}=V_{z,i,j-1}$ and $p_{i,j}=0(i>\text{or}=2)$ and $p_{l,j}=p_{\text{inj}}$ from above, the discretized form of Eq. (2) becomes

$$4\frac{\mu_0}{(\Delta r)^2}V_{z,i,j}-4\frac{\mu_0}{(\Delta r)^2}V_{z,i,j+1}-\frac{p_{\text{inj}}}{z}=0 \tag{4}$$

Grid Points: $j=2$ *to* $n-2$, $i=2$ *to* ***m***. The discretized form of Eq. (3) takes the following form using backward difference for $\partial p/\partial z$, central difference for $\partial^2 V_z/\partial r^2$ and $p_{i,j}=0(i\geqslant 2)$ and $p_{l,j}=p_{\text{inj}}$.

$$V_{z,i,j-1}\left(-\frac{\mu_{i,j}}{2(\Delta r)r_{i,j}}+\frac{\mu_{i,j}}{(\Delta r)^2}-\frac{\mu_{i,j+1}-\mu_{i,j-1}}{4(\Delta r)^2}\right)+V_{z,i,j}\left(-2\frac{\mu_{i,j}}{(\Delta r)^2}\right)+V_{z,i,j+1}\left(\frac{\mu_{i,j}}{2(\Delta r)r_{i,j}}+\frac{\mu_{i,j}}{(\Delta r)^2}+\frac{\mu_{i,j+1}-\mu_{i,j-1}}{4(\Delta r)^2}\right)+\frac{p_{\text{inj}}}{2}=0 \tag{5}$$

Grid Points: $j=n-1$, $i=2$ *to* ***m***. From the boundary condition at $r=R$, $V_z=0$ which implies that $V_{z,i,j+1}=0$. Therefore, from Eq. (5), the following discretization equation is obtained.

$$V_{z,i,j-1}\left(-\frac{\mu_{i,j}}{2(\Delta r)r_{i,j}}+\frac{\mu_{i,j}}{(\Delta r)^2}-\frac{\mu_{i,j+1}-\mu_{i,j-1}}{4(\Delta r)^2}\right)+V_{z,i,j}\left(-2\frac{\mu_{i,j}}{(\Delta r)^2}\right)+\frac{p_{\text{inj}}}{z}=0 \tag{6}$$

It should be noted that $z=z_{i,1}$ $(i\geqslant 2)$

2.5 Average Velocity of the Melt, Fill Time, and Volumetric Flow Rate. The average velocity of the melt over any cross-section of the cylindrical cavity is calculated from the following expression.

$$V_{z,\text{avg}}=\frac{\int_0^R V_z 2\pi r dr}{\pi R^2} \tag{7}$$

The fill time is computed from

$$t=\sum_{i=2}^{m-1}\Delta t_i \tag{8}$$

$$\text{where}\quad \Delta t_i=\frac{\Delta z}{V_{z,\text{avg},i}} \tag{8a}$$

The volumetric Flow Rate (Q) is calculated from

$$Q=(\pi R^2)V_{z,\text{avg}} \tag{9}$$

3 Methods of Solution

3.1 For Isothermal Filling at Constant Injection Pressure: Case (i). From Eq. 1(b), it is evident that the knowledge of the velocity profile is needed to calculate viscosity. Therefore, the velocity profile is guessed at the station $i=2$. This in turn is used to compute viscosity value at the grid points from $j=2$ to *n* from Eq. 1(b). For $j=1$, $\mu=\mu_0$ at the given melt temperature is used. Subsequently, the set of linear algebraic Eqs. (4)–(6) having a tridiagonal coefficient matrix is solved using Thomas algorithm. The new velocity profile is again used to calculate the new viscosity values and the aforesaid procedure is repeated till there is virtually no change in the old and new velocity profiles. The converged velocity profile is then used to compute the average melt velocity, the fill time and the volumetric flow rate from the Eq. (7), Eq. (8), and Eq. (9), respectively. The computation now starts at $i=3$ separated from the previous station by Δz with the guessed profile same as the profile at $i=2$ and the aforesaid procedure described for $i=2$ is repeated. The computation continues for $i=4,5,6$, and so on till the end of the cavity is reached.

3.2 For Isothermal Filling at Constant Flow Rate: Case (ii). In this case the flow rate is constant and known. The solution gives us the injection pressure required at a particular time to achieve the desired flow rate. The correct injection pressure at a given time is obtained iteratively by the application of the Newton-Raphson Method (Jaluria [13]). The basic concept is as follows. If Q is the flow rate, then for the correct p_{inj} we can write

Downloaded 03 Jun 2010 to 171.66.16.150. Redistribution subject to ASME license or copyright; see http://www.asme.org/terms/Terms_Use.cfm

$$F(p_{\text{inj}}) = \int_0^R V_z 2\pi r dr - Q = 0 \tag{10}$$

That is, p_{inj} is the root of Eq. (10). Now, following the Newton-Raphson method, the following can be written.

$$p_{\text{inj,improved}} = p_{\text{inj,guess}} - \frac{F(p_{\text{inj,guess}})}{(F(p_{\text{inj,guess}} + \Delta p_{\text{inj}}) - F(p_{\text{inj,guess}}))/\Delta p_{\text{inj}}} \tag{11}$$

Δp_{inj} is taken as a small interval. The procedure is repeated till $|p_{\text{inj,improved}} - p_{\text{inj,guess}}| \leqslant \varepsilon$.

The solution starts at $i=2$ with guessed velocity profile and injection pressure. Then the set of linear simultaneous Eqs. (4)–(6) are solved by Thomas algorithm as before. Newton-Raphson method is now applied to obtain converged p_{inj} and hence, converged velocity profile. Then the solution moves on to $i=3,4,5$ and so on till the end of the cavity is reached.

It is important to note that for both case (i) and case (ii), computation starts from a small distance away from the inlet, since the Eqs. (4)–(6) can be solved for $z>0$. That is why, in the present study, Δz is taken very small in order to calculate the fill time to the closest possible accuracy. It is, however, possible to take a tiny value of initial Δz and then increase Δz to save computational time. That is, a nonuniform Δz is allowed in this method.

4 Nonisothermal Filling of Cavity at Constant Flow Rate: Case (iii)

4.1 Physical Problem. In this case, the ratio of heat generated by viscous dissipation to that lost by heat transfer to cold walls is much greater than unity which gives rise to nonuniform temperature in the melt. The mold is kept at a temperature T_{mold}. The material of the mold is steel. The polymer melt enters at a temperature T_i. The injection pressure p_{inj} is gradually increased so that the flow rate Q in the cavity is constant.

4.2 Problem Formulation. Since the viscosity of the polymer melt is dependent on the shear rate as well as temperature, the momentum (axial) and energy equations are coupled and are to be solved simultaneously. Half of the physical domain is shown in Fig. 4. The computational domain is the cavity.

4.3 Governing Differential Equations. Momentum (axial) equation:

$$\frac{\partial p}{\partial z} = \frac{1}{r}\frac{\partial}{\partial r}(r\tau_{rz}) \tag{12}$$

$$\text{where} \quad \tau_{rz} = \mu \frac{\partial V_z}{\partial r} \tag{12a}$$

$$\text{and} \quad \mu = m\left|\frac{\partial V_z}{\partial r}\right|^{n-1} e^{-b(T-T_{\text{ref}})} \tag{12b}$$

For $\partial V_z/\partial r = 0$, $\mu = \mu_0 e^{-b(T-T_{\text{ref}})}$ is used. μ_0 is the zero shear-rate viscosity value. $T_{\text{ref}} = 160°\text{C}$.

Energy Equation:

Neglecting axial conduction,

$$\rho c_p V_z \frac{\partial T}{\partial z} = k\frac{1}{r}\frac{\partial}{\partial r}\left(r\frac{\partial T}{\partial r}\right) + \mu\left(\frac{\partial V_z}{\partial r}\right)^2 \tag{13}$$

4.4 Boundary Conditions.

$$\text{B.C.1: at } r=0, \quad \frac{\partial V_z}{\partial r} = 0 \text{ (axisymmetry)}$$

$$\text{B.C.2: at } r=0, \quad \frac{\partial T}{\partial r} = 0 \text{ (axisymmetry)}$$

$$\text{B.C.3: at } r=R, \quad V_z = 0 \text{ (no-slip)}$$

$$\text{B.C.4: at } r=R, \quad -k\frac{\partial T}{\partial r} = h(T - T_{\text{mold}})$$

The pressure at the melt front is always zero as the atmospheric pressure prevails there.

4.5 Explanation for B.C.4. Even if the thermal contact resistance between the melt and the mold cavity can be assumed negligible, an interface condition between the melt and the mold is implemented. It is similar to heat transfer between two solids with imperfect contact. "h" in Eq. (14) is similar to contact conductance. The assumption is justified by the fact that in mold flows frozen skin layers are likely to be formed (see the Results and Discussion). The variation in the heat transfer at the interface is a complex phenomenon that depends on many factors such as surface roughness, geometry, mold coating, and polymer composition. From the model point of view, the interface modeling adds flexibility. It facilitates the coupling between the flow equations and heat transfer. The condition specified at the interface is such that the heat flux must be conserved across the discontinuity. This is expressed as:

$$q'' = h(T_{\text{melt}} - T_{\text{mold}}) \tag{14}$$

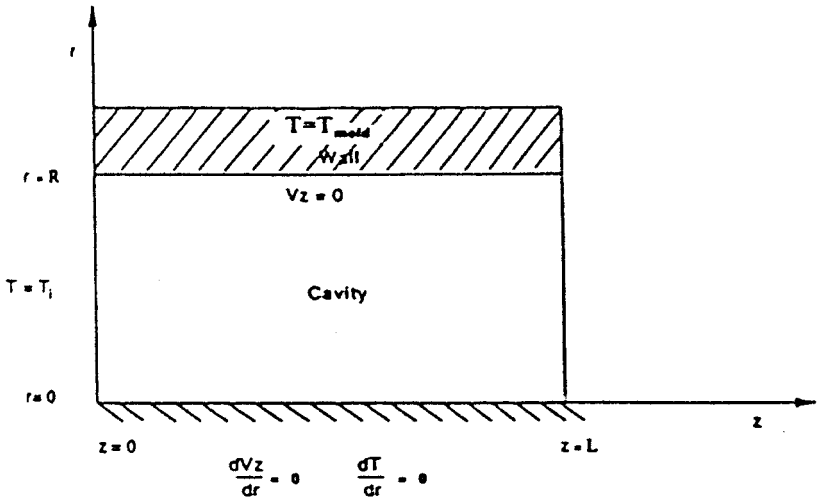

Fig. 4 The half physical domain for nonisothermal filling

Downloaded 03 Jun 2010 to 171.66.16.150. Redistribution subject to ASME license or copyright; see http://www.asme.org/terms/Terms_Use.cfm

The melt-mold thermal contact resistance coefficient, h, is determined experimentally (Kamal et al. [14]). In the present work, a suitable value for h is taken as 2×10^8 W/m$^2\cdot$K (Hetu et al. [7]).

4.6 Details of Finite Difference Formulation. The discretization of the momentum equation is same as described in Section 2.4 for isothermal cases, only difference being the expressions used to calculate the viscosity which are given below.

$$\text{For } r=0, \quad \mu=\mu_0 e^{-b(T-T_{\text{ref}})} \tag{15a}$$

$$\text{For } r>0, \quad \mu=m\left|\frac{\partial V_z}{\partial r}\right|^{n-1} e^{-b(T-T_{\text{ref}})} \tag{15b}$$

Energy Equation:
For $r=0$, using L'Hopital's rule (since $\partial T/\partial r=0$) and also substituting $\partial V_z/\partial r=0$ in Eq. (13), we get

$$\rho c_p V_z\frac{\partial T}{\partial z}=2k\frac{\partial^2 T}{\partial r^2} \tag{16}$$

For $r>0$,

$$\rho c_p V_z\frac{\partial T}{\partial z}=k\left(\frac{1}{r}\frac{\partial T}{\partial r}+\frac{\partial^2 T}{\partial r^2}\right)+\mu\left(\frac{\partial V_z}{\partial r}\right)^2 \tag{17}$$

The energy equation being parabolic is solved using Explicit finite-difference scheme taking stability considerations into account. A uniform grid is used (Fig. 3).

Grid Points: $j=1$, $i=2$ *to* ***m***. These grid points lie on the center axis and hence Eq. (16) applies here. The discretized form of Eq. (16) using $T_{i,j+1}=T_{i,j-1}$ (resulting from the application of image-point technique) takes the following form.

$$T_{i+1,j}=\left(1-\frac{4k\Delta z}{\rho c_p V_{z,i,j}(\Delta r)^2}\right)T_{i,j}+\frac{4k\Delta z}{\rho c_p V_{z,i,j}(\Delta r)^2}(T_{i,j+1}) \tag{18}$$

Grid Points: $j=2$ *to* $n-1$, $i=2$ *to* ***m***. Equation (17) is valid at these grid points. The discretized form of Eq. (17) is as follows.

$$T_{i+1,j}=\left(1-\frac{2k\Delta z}{\rho c_p V_{z,i,j}(\Delta r)^2}\right)T_{i,j}+\frac{k\Delta z}{\rho c_p V_{z,i,j}}\left(\frac{T_{i,j+1}+T_{i,j-1}}{(\Delta r)^2}+\frac{1}{r_{i,j}}\frac{T_{i,j+1}-T_{i,j-1}}{2\Delta r}\right)+\frac{\mu_{i,j}\Delta z}{\rho c_p V_{z,i,j}}\left(\frac{V_{z,i,j+1}-V_{z,i,j-1}}{2\Delta r}\right)^2 \tag{19}$$

Grid Points: $j=n$, $i=2$ *to* ***m***. These grid points correspond to $r=R$ at which B.C.3 and B.C.4 are valid. Since $V_z=0$ (B.C.3) here, Eq. (17) takes the form

$$k\left(\frac{1}{r}\frac{\partial T}{\partial r}+\frac{\partial^2 T}{\partial r^2}\right)+\mu\left(\frac{\partial V_z}{\partial r}\right)^2=0 \tag{20}$$

Using image-point technique, that is, central difference approximation to B.C.4, we have

$$T_{i,j+1}=-\frac{2h\Delta r}{k}(T_{i,j}-T_{\text{mold}})+T_{i,j-1} \tag{21}$$

Substituting Eq. (21) into the discretized form of Eq. (20) containing backward difference expression for $\partial V_z/\partial r$ and noting that $V_{z,i,j}=0$ (no-slip), the following expression for $T_{i,j}$ is obtained.

$$T_{i,j}=\left(\frac{\frac{\mu_{i,j}}{2k}(V_{z,i,j-1})^2-T_{i,j-1}\left(\frac{\Delta r}{2r_{i,j}}-1\right)-T_{\text{mold}}\left(\frac{h(\Delta r)^2}{2kr_{i,j}}-\frac{h\Delta r}{k}\right)}{1-\frac{h(\Delta r)^2}{2kr_{i,j}}}\right) \tag{22}$$

Note that in the above the index i actually corresponds to $i+1$. This means that $T_{i+1,j}$ is calculated from Eq. (22) by using the previously calculated value of $T_{i+1,j-1}$ obtained from Eq. (19).

4.7 Average Melt Temperature. Once the temperature and velocity profiles at any z-location is obtained, the average melt temperature is calculated using the concept of mixing-cup temperature (Holman [15]) as given below.

$$T_{\text{avg}}=\frac{\int_0^R \rho 2\pi r dr V_z c_p T}{\int_0^R \rho 2\pi r dr V_z c_p} \tag{23}$$

The trapezoidal rule has been used to evaluate the above integral.

4.8 Stability Criteria. Since the energy equation is parabolic, the following restriction regarding Δz has to be imposed in order to obtain a stable solution by the Explicit method.

$$\text{For } r=0, \quad \Delta z\leqslant\frac{\rho c_p V_{z,i,j}(\Delta r)^2}{4k} \tag{24}$$

$$\text{For } r>0(\text{but}\neq R), \quad \Delta z\leqslant\frac{\rho c_p V_{z,i,j}(\Delta r)^2}{2k} \tag{25}$$

The smaller of the two minimum Δz's obtained from Eq. (24) and Eq. (25) is taken.

4.9 Method of Solution. Since the energy equation is parabolic (as the z-coordinate behaves like a time coordinate), a solution marching in the axial (z-direction) is required which means that the inlet melt temperature is needed to initiate the computation. As the energy equation contains the viscous dissipation term, to start the solution, the velocity profile is guessed first at the station $i=2$. The injection pressure also has to be guessed. Then using the guessed velocity profile, the energy equation is solved to obtain a new temperature profile which is subsequently used to calculate the viscosity of the melt. The next step is to solve the momentum equation and calculate the new velocity. Newton-Raphson method is applied to get a converged p_{inj}, and the velocity profile for the particular temperature (which was obtained from the guessed velocity profile to begin with). Using the current velocity profile the energy equation is solved to get the current temperature profile. Again the previous and current velocity and temperature profiles are compared to see whether significant change has occurred or not. In case the convergence criteria for both velocity and temperature are not satisfied, the procedure is repeated with the new velocity and temperature profiles until in successive iterations no change is observed in both velocity and temperature. The solution then moves on to the next z-station using the freshly calculated temperature at the previous z-station and so on till the end of the cavity is reached. The pressure distribution in the melt at the end of filling is calculated from Eq. (26).

Downloaded 03 Jun 2010 to 171.66.16.150. Redistribution subject to ASME license or copyright; see http://www.asme.org/terms/Terms_Use.cfm

$$p_{i+1}=p_i+\left(\frac{\partial p}{\partial z}\right)\Delta z, \quad i=1 \text{ to } m-2 \tag{26}$$

where $\partial p/\partial z=-p_{\text{inj}}(t)/L$ (since $p_m=0$ and p versus z is linear). Also, $p_1=p_{\text{inj}}(t)$ where $p_{\text{inj}}(t)$ is the final injection pressure, that is, the injection pressure at the end of the filling process.

5 Results and Discussion

Mold filling simulation requires the calculation of the detailed velocity and temperature profiles throughout the mold flow region, including the position and shape of the advancing front. This helps the analyst to determine orientation distribution affecting the article morphology, which evolves upon cooling and solidification. Such a model will facilitate the theoretical mold design as well as optimizing molding conditions for specific property requirements.

In the present research numerical results are shown for isothermal and nonisothermal filling of a cylindrical cavity of length 25.4 cm (0.254 m) and diameter 5.08 mm (.00508 m). The material of the object is LDPE (low density polyethylene). Sufficient numerical experiments have been done to obtain the optimum grid size. For the isothermal cases 101×101 grid points have been used, the first and second numbers signifying number of grid points in r and z-directions, respectively. For the nonisothermal case, 31×181 grid points have been taken. For the sake of brevity only one grid independence test for a given case of nonisothermal filling is shown in Fig. 15. It may be noted that the present work addresses the issue of "stability" by choosing to think of z as a time scale and selecting Δz to be sufficiently small as not to cause the Explicit scheme to become unstable. The approach involves a number of iterative procedures to ensure "convergence" in velocity and temperature profiles, not to mention the nonlinear viscosity. Decreasing Δr by a factor of 2 would require that Δz be dropped by a factor of 4. The grid independence test is conducted by fixing the number of grid points in the z-direction at 181 and changing the number of grid points in the r-direction from 11 to 61 in steps of 10. It is clearly seen from Fig. 15 that the optimum number of grid points is 31×181 and the solution becomes unstable when the number of grid points in the r-direction is 61 as expected from the stability analysis. All computations have been carried out on HP-9000 computer system of IIT Kanpur.

5.1 Case (i): Isothermal Filling at Constant Injection Pressure. The input data for this case are shown in Table 1. The property values of the polymer melt have been taken from Tadmor and Gogos [16]. Values of z and Q are listed for various times in Table 2. The excellent match with the corresponding analytical solutions (Tadmor and Gogos [16]) which are given below shows the correctness of the numerical solution.

Table 1 Input data for case (i)

m	9360(N s^n/m^2)
n	0.41
P_{inj}	15.6 (MPa)
T_i	160°C
μ_0	6300(N s/m^2)

$$z(t)=\left(\frac{1+n}{1+3n}\right)^{n/(1+n)} R\left(\frac{p_{\text{inj}}}{2m}\right)^{1/(1+n)} t^{n/(1+n)} \tag{27a}$$

$$Q(t)=\pi R^3\left(\frac{1+n}{1+3n}\right)^{n/(1+n)}\left(\frac{n}{1+n}\right)\left(\frac{p_{\text{inj}}}{2m}\right)^{1/(1+n)}\frac{1}{t^{1/(1+n)}} \tag{27b}$$

The results clearly indicate that we should expect a very high flow rate and quick filling initially, followed by a rapid drop in Q and long filling times for the remainder of the cavity. Figure 5 shows that z versus t plot for the present numerical solution. It is clear that $\partial z/\partial t$ is high in the beginning whereas with increasing time $\partial z/\partial t$ drops off rapidly. This is obvious because with increasing z, Q decreases at a fast rate. Figure 6 shows the plot of Q versus z. It essentially reproduces Table 2 in the graphical form.

Figure 7 depicts the half melt velocity profile at various z-locations indicated by percent filling distance. It is clear that the profile is initially parabolic but turns to flat as the cavity is filled

Table 2 Values of t and Q at various z-locations

Z	$t_{\text{anal.}}$	$t_{\text{numl.}}$	$Q_{\text{anal.}}$	$Q_{\text{numl.}}$
0.035	1.00×10^{-3}	$.97\times10^{-3}$	$.207\times10^{-3}$	$.217\times10^{-3}$
0.106	$.169\times10^{-1}$	$.143\times10^{-1}$	$.359\times10^{-5}$	$.437\times10^{-5}$
0.150	.147	.146	$.601\times10^{-5}$	$.606\times10^{-5}$
0.200	.394	.391	$.298\times10^{-5}$	$.302\times10^{-5}$
0.250	.850	.847	$.173\times10^{-5}$	$.174\times10^{-5}$
0.254	.897	.893	$.166\times10^{-5}$	$.168\times10^{-5}$

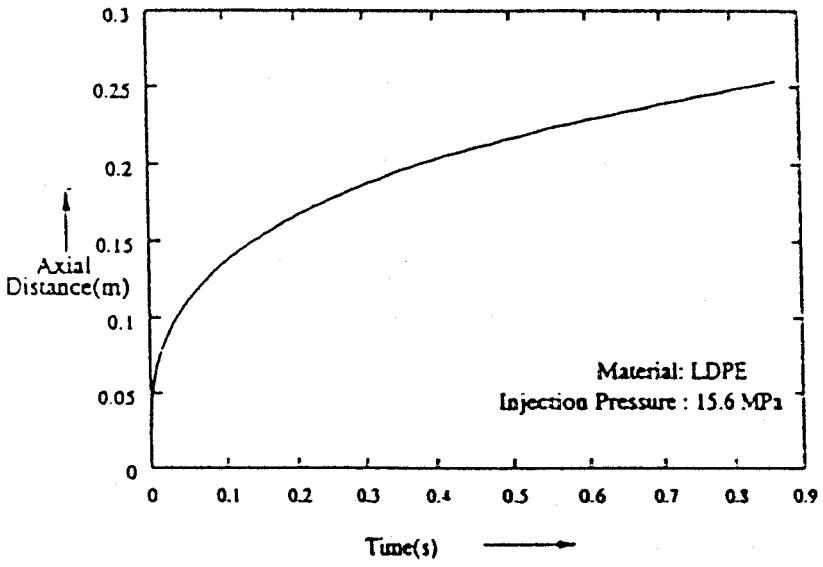

Fig. 5 The position of advancing melt front as a function of time for constant injection pressure isothermal filling

Downloaded 03 Jun 2010 to 171.66.16.150. Redistribution subject to ASME license or copyright; see http://www.asme.org/terms/Terms_Use.cfm

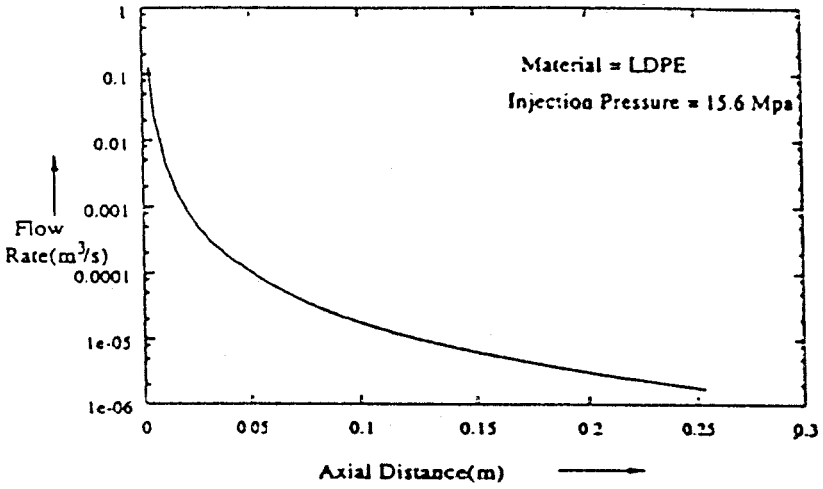

Fig. 6 Flow rate versus distance for constant injection pressure isothermal filling

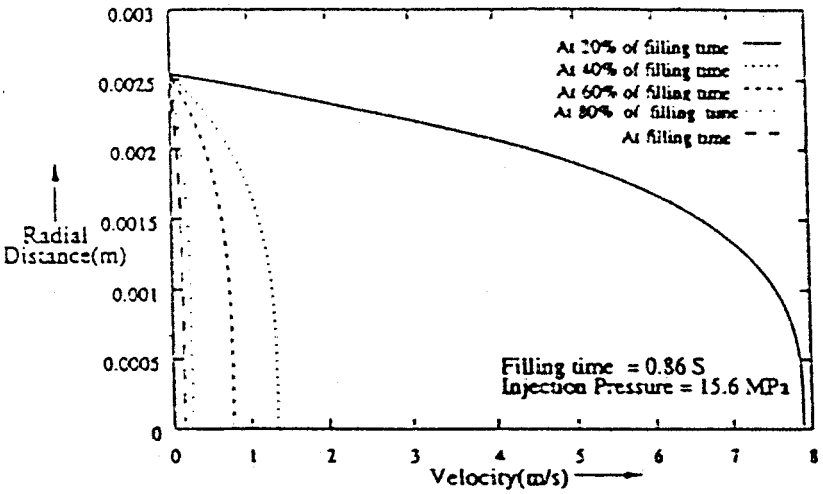

Fig. 7 Half melt velocity profile at various z-locations for constant injection pressure isothermal filling

more and more. Thus the shape of the melt front flattens out with increasing axial distance. It is also seen that the magnitude of the maximum velocity (located at the center axis) decreases with increasing z.

5.2 Case (ii): Isothermal Filling at Constant Flow Rate. The input data for the case are shown in Table 3. The property values of the polymer melt have been taken from Tadmor and Gogos [16]. Figure 8 shows the plot of injection pressure versus time. It is observed that an applied pressure linearly increasing with time is required. This is because with time the melt tends to slow down and therefore, to maintain constant flow rate, the injection pressure is continuously increased. This linear trend can be easily justified from the analytical solution (Tadmor and Gogos [16]) for $Q(t)$ which is given as follows.

Table 3 Input data for case (ii)

m	9360(N s^n/m^2)
n	0.41
Q	$.515\times10^{-2}$ (m^3/s)
T_i	160°C
μ_0	6300 (N s/m^2)

$$Q(t)=\frac{\pi R^3}{s+3}\left(\frac{Rp_{\text{inj}}}{2mz(t)}\right)^s \tag{27c}$$

Note that Eq. (27*c*) is the original equation from which Eq. (27*a*) and Eq. (27*b*) follow. Now, if $Q(t)$ is constant, then p_{inj} must be linearly proportional to $z(t)$ since R, m, $s(=1/n)$ are constants. Table 4 shows a comparison of injection pressure versus time of the present and the analytical solution. The agreement is excellent. In actual practice, variable injection pressure is more common since it is easy to implement and has a better control over the filling time.

5.3 Case (iii): Nonisothermal Filling at Constant Flow Rate. In practical situations, isothermal filling is difficult to achieve. Therefore, we turn our attention to the scenario where the mold is kept at a fixed temperature and the melt is losing heat to the mold. The input data for this case are shown in Table 5.

Figure 9 shows a comparison of injection pressure versus time for nonisothermal and isothermal filling. It is evident that the injection pressure increases nonlinearly with time for the nonisothermal filling. This is because of the fact that in the case of non-isothermal filling momentum equation is coupled with the energy equation through the viscosity which is a function of strain rate as well as temperature. Also, it is seen that the requirement of

Downloaded 03 Jun 2010 to 171.66.16.150. Redistribution subject to ASME license or copyright; see http://www.asme.org/terms/Terms_Use.cfm

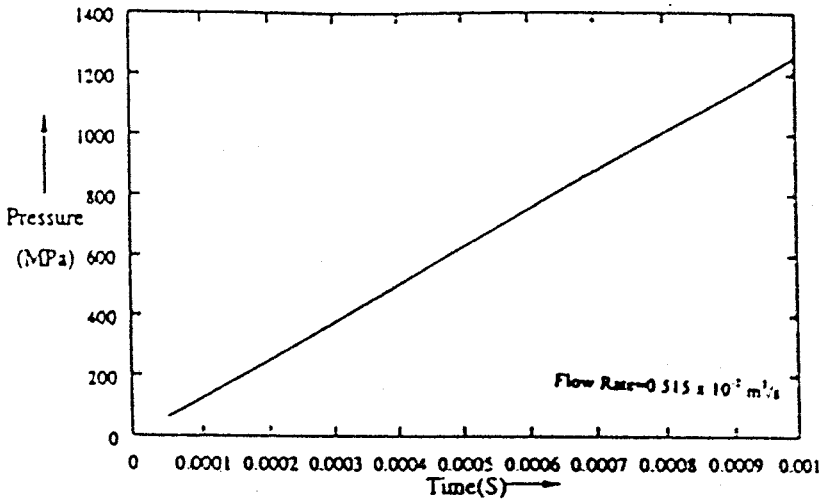

Fig. 8 Plot of injection pressure versus time for constant flow rate isothermal filling

Table 4 Comparison of $P_{inj,anal}$ and $P_{inj,numl}$

t (s)	$P_{inj,anal.}$ (MPa)	$P_{inj,numl.}$ (MPa)
$.100\times10^{-3}$	124.34	125.61
$.500\times10^{-3}$	629.05	626.23
$.600\times10^{-3}$	753.54	754.86
$.700\times10^{-3}$	880.67	880.67
$.800\times10^{-3}$	1004.48	1006.82
$.900\times10^{-3}$	1133.29	1132.15
$.100\times10^{-2}$	1259.32	1258.10

Table 5 Input data for case (iii)

m	9360(N s^n/m^2)
n	0.41
b	0.01 ($°C^{-1}$)
ρ	525 (kg/m^3)
c_p	2300 (J/kg°C)
k	0.335(W/m°C)
h	2×10^8(W/m^2°C)
μ_0	6300 (N s/m^2)
T_i	200°C
T_{mold}	60°C
Mold Material	Steel

injection pressure rise versus time is much less in the case of nonisothermal filling because of the effect of viscous heat generation in the melt which raises the temperature and hence decreases the viscosity of the melt. As a result, less injection pressure is required to push the melt through the cavity. The viscosity decreases more toward the end of the cavity due to higher average temperature and hence dp_{inj}/dt also decreases thus producing a flatter curve as the time increases. However, this trend is valid for high flow rate case (0.515×10^{-2} m^3/s) which corresponds to the present figure (Fig. 9) under discussion.

Figure 10 shows the melt temperature field at various z-locations for $Q=0.515\times10^{-4}$ m^3/s. The layer near the center is virtually isothermal throughout filling, which is due to the fact

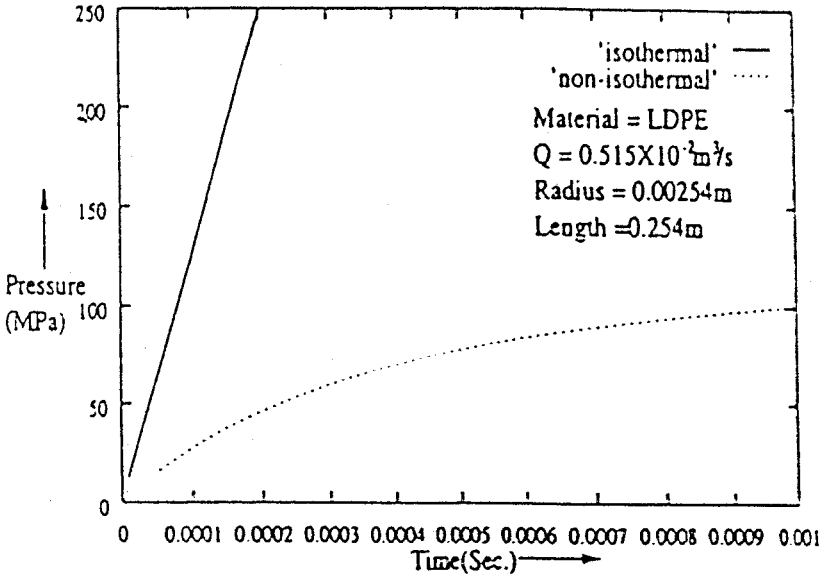

Fig. 9 Comparison of injection pressure versus time for nonisothermal and isothermal filling at constant flow rate

Downloaded 03 Jun 2010 to 171.66.16.150. Redistribution subject to ASME license or copyright; see http://www.asme.org/terms/Terms_Use.cfm

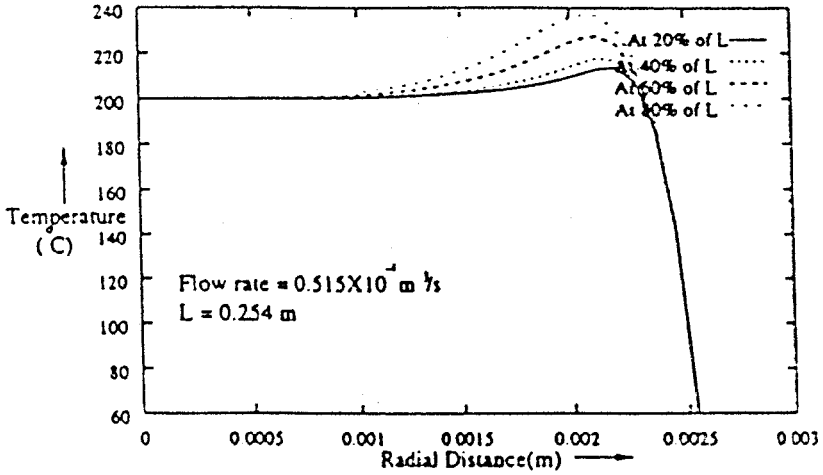

Fig. 10 Melt temperature fields at various *z*-locations for $Q=0.515\times10^{-4}$ m³/s for nonisothermal flow (case (iii))

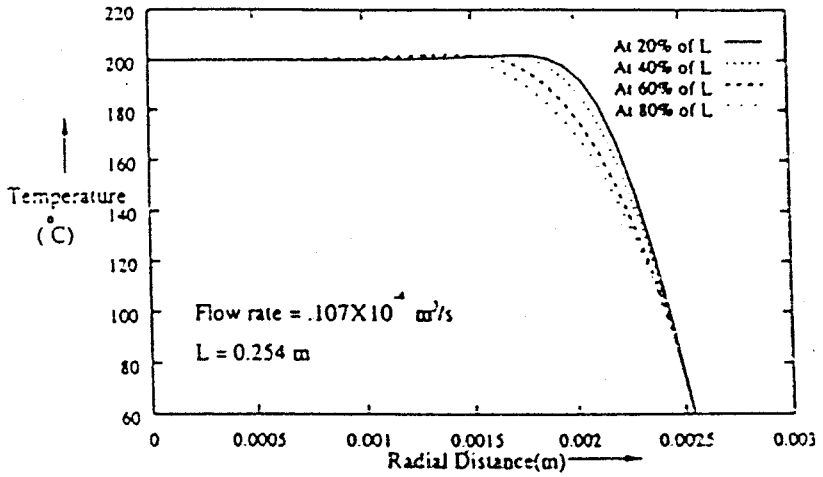

Fig. 11 Melt temperature fields at various *z*-locations for $Q=0.107\times10^{-4}$ m³/s for nonisothermal flow (case (iii))

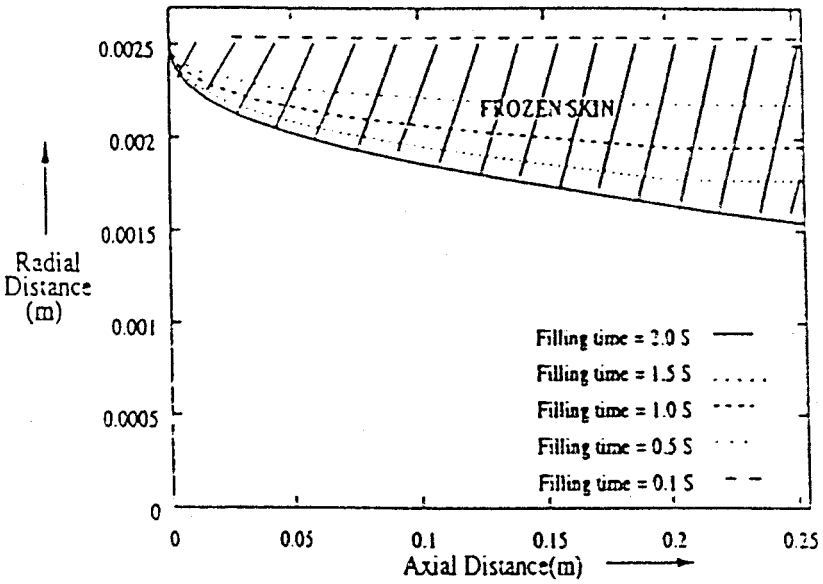

Fig. 12 Frozen skin layers for various flow rates for nonisothermal flow (case (iii))

Downloaded 03 Jun 2010 to 171.66.16.150. Redistribution subject to ASME license or copyright; see http://www.asme.org/terms/Terms_Use.cfm

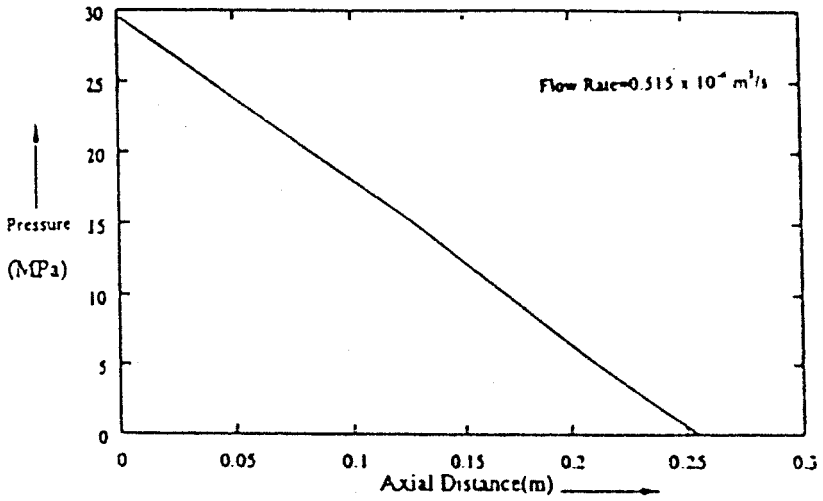

Fig. 13 Pressure distribution in the cavity after filling for nonisothermal flow (case (iii))

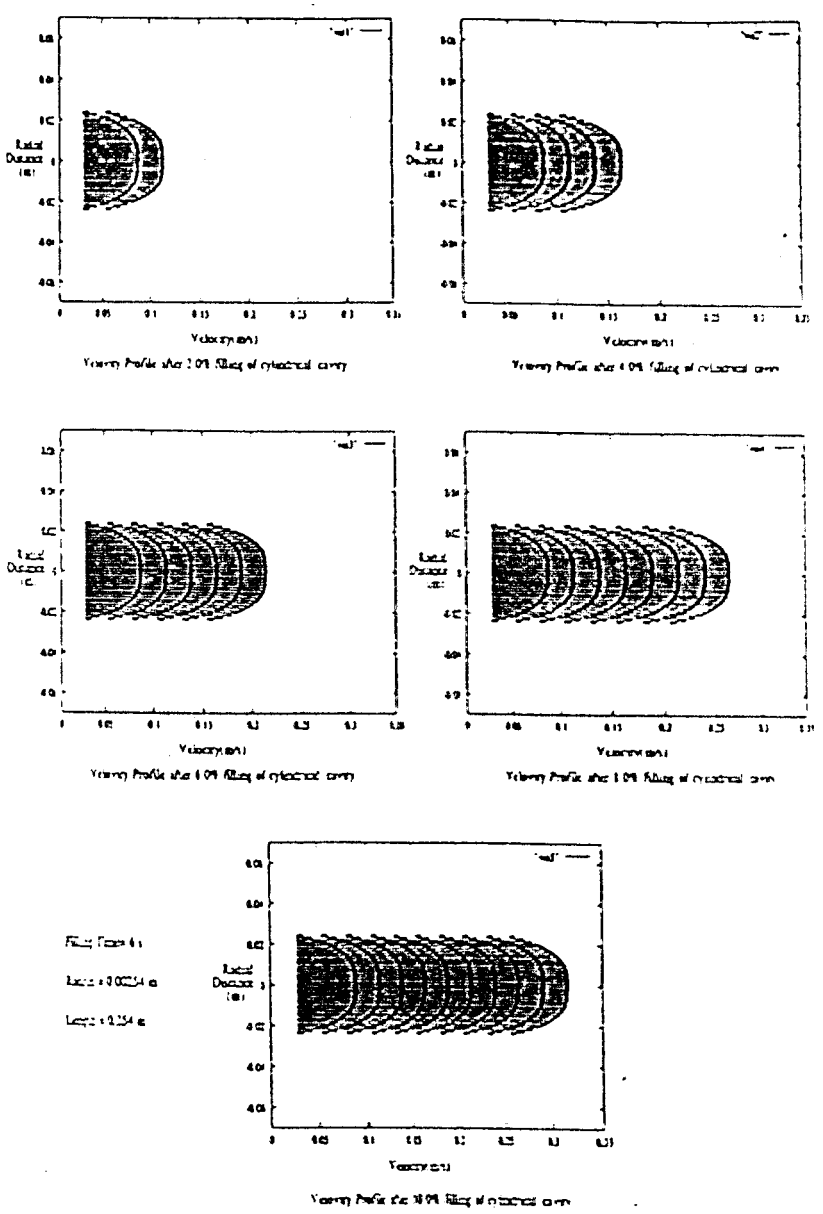

Fig. 14 Melt velocity profiles at different locations during filling for nonisothermal flow (case (iii))

Downloaded 03 Jun 2010 to 171.66.16.150. Redistribution subject to ASME license or copyright; see http://www.asme.org/terms/Terms_Use.cfm

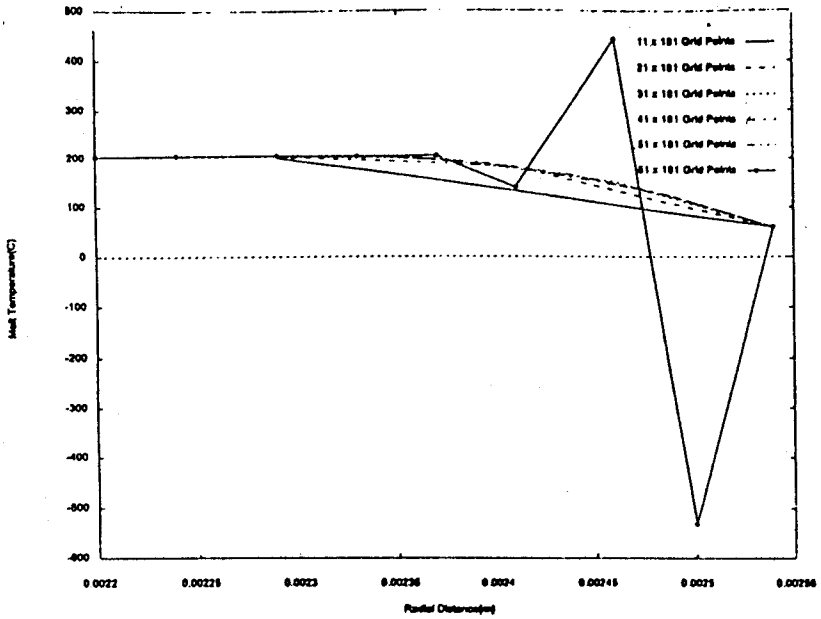

Fig. 15 Grid independence test for one case of nonisothermal filling of the cavity ($Q=0.515\times10^{-4}$ m^3/s, $T_i=200^0$ C, $T_{mold}=60^0$ C, $z=0.0113$ m, i.e., at 4.448% of the total length of the cavity)

that the velocity gradients are zero and the thermal conductivity of the melt is low. As one approaches the wall of the cavity, the temperature increases with radial position, it goes through a maximum and then decreases to low values. The maximum is a result of the competition between the viscous heat dissipation and heat conduction. The level of the largest is nearly 238°C. As stated above, the temperature rapidly drops at larger radial positions. This is due to the fact that in this region the melt has resided in the cold cavity, and near the wall, for a longer period of time.

Figure 11 shows similar plot as in Fig. 10 but for $Q=0.107\times10^{-4}$ m^3/s, that is, for a much lower flow rate. It is interesting to see that no peak appears in this case. The average temperature at 80 percent of filling is lower than that at 20 percent of filling which means that the temperature of the melt decreases as it flows towards the end of the cavity. This is because of the fact that at low flow rates the velocity profile is flatter and hence viscous dissipation is less and therefore, the maximum temperature is not encountered. The reason why the melt becomes colder as it reaches the end is due to the high residence time in the cavity arising out of the low flow rate and greater loss of heat to the cold mold.

From Fig. 10 it is observed that very near the wall the temperature of the melt is below 180°C, where the viscosity of LDPE is so high that the fluid exhibits virtually no flow. Thus, for the above regions a ''frozen skin'' layer is formed during filling. This layer is seen to form much earlier for lower flow rate case (Fig. 11), that is, near $r=0.002$ m.

Figure 12 shows the frozen layer is smallest for the highest flow rate and vice-versa. The ''frozen skin'' layer is not desirable in that it contributes to the ''molded in'' strains in the molded article. The frozen layer can be effectively reduced or eliminated by higher injection pressure (resulting in higher flow rate), higher melt temperature and to a lesser but appreciable, degree by increasing mold temperature.

Figure 13 shows the pressure distribution in the cavity after filling. As expected, p versus z profile is linear with negative pressure gradient. Figure 14 shows the location of the melt front at various times. The velocity profile remains invariant because of constant flow rate and fully developed nature of the flow.

The results for the case of nonisothermal filling are new and have not been found in earlier literature. To the best of the present authors' knowledge, no experimental data are available for the case of nonisothermal filling problem presented here. Therefore, a comparison of the numerical results with experiment could not be done (see a discussion on the issue of numerical uncertainty in Section 5 with reference to Fig. 15).

6 Conclusions

In this paper, numerical simulation of the mold filling for the production of a cylindrical object is presented. The material of the object is LDPE. Novel finite-difference based general methodologies have been developed. Three cases have been considered, namely; (i) isothermal filling at constant injection pressure; (ii) isothermal filling at constant flow rate; and (iii) nonisothermal filling at constant flow rate. The results show excellent agreement with the corresponding analytical solutions for the first two cases showing the correctness of the numerical method. The simulation results for nonisothermal filling are new for this particular geometry and show physically realistic trends and lend insight into various important aspects of mold-filling including injection pressure versus time, and effects of flow rates on melt temperature fields at various axial locations as well as on frozen skin layer.

Nomenclature

b = temperature coefficient of viscosity (°C^{-1})
c_p = specific heat at constant pressure (J/kg·K)
D = diameter (m)
h = melt-mold thermal contact resistance coefficient (W/m^2·K)
k = thermal conductivity (W/m·K)
L = length (m)
m = consistency index (N·s^n/m^2), also number of grid points in z-direction
n = power-law index, also number of grid points in r-direction
p = pressure (N/m^2 or Pa)
p_{inj} = injection pressure (N/m^2 or Pa)
q'' = heat flux (W/m^2)
Q = flow rate (m^3/s)

Downloaded 03 Jun 2010 to 171.66.16.150. Redistribution subject to ASME license or copyright; see http://www.asme.org/terms/Terms_Use.cfm

r = radial coordinate (m)
Δr = grid spacing in r-direction (m)
R = radius (m)
T = temperature (°C)
T_{avg} = average temperature of the melt (°C)
T_i = inlet melt temperature (°C)
T_{ref} = reference melt temperature for nonisothermal flow (°C), Eq. (12*b*)
T_{mold} = mold temperature (°C)
t = filling time (s)
V_z = velocity of the melt in the z-direction (m/s)
$V_{z,avg}$ = average velocity of the melt over any cross-section (m/s)
z = axial coordinate (m)
Δz = grid spacing in z-direction (m)

Greek Letters

α = thermal diffusivity (m^2/s)
ε = a very small value ($=10^{-6}$)
μ = viscosity ($N\cdot s/m^2$)
μ_0 = viscosity at zero shear rate ($N\cdot s/m^2$)
ρ = melt density (kg/m^3)
τ_{rz} = shear stress (N/m^2)

Subscripts

i = grid index in z-direction, also inlet
inj = injection
j = grid index in r-direction
melt = for melt
mold = for mold
ref = reference

Special Symbol

Δ = increment

References

[1] Crawford, R. J., 1989, *Plastics Engineering*, Pergamon Press, 2nd Edition.
[2] Kamal, M. R., Mashelkar, R. A., and Mujumdar, A. S., 1989, *Transport Phenomena in Polymer Systems-2*, Wiley Eastern Ltd., pp. 133–217.
[3] Kamal, M. R., and Kenig, S., 1972, "The Injection Molding of Thermoplastics," Polym. Eng. Sci., **12**, pp. 294–302.
[4] Wu, P. C., Huang, C. F., and Gogos, C. G., 1974, "Simulation of Mold Filling Process," Polym. Eng. Sci., **14**, No. 14, pp. 223–230.
[5] Hieber, C. A., and Shen, S. F., 1980, "A Finite-Element/Finite-Difference Simulation of the Injection Molding Filling Process," J. Non-Newtonian Fluid Mech., **7**, pp. 1–32.
[6] Chiang, H. H., Hieber, C. A., and Wang, K. K., 1991, "A Unified Simulation of the Filling and Post Filling Stages in Injection Molding, Part I: Formulation," Polym. Eng. Sci., **31**, No. 2, pp. 116–123.
[7] Hetu, J. F., Gao, D. M., Garcia-Rejon, A., and Salloum, G., 1998, "3D Finite Element Method for the Simulation of the Filling Stage in Injection Molding," Polym. Eng. Sci., **38**, No. 2, pp. 223–236.
[8] Pandelidis, Ioannis, and Zou, Qin, 1990, "Optimization of Injection Molding Design. Part I: Gate Location Optimization," Polym. Eng. Sci., **30**, No. 10, pp. 873–882.
[9] Pandelidis, Ioannis, and Zou, Qin, 1990, "Optimization of Injection Molding Design. Part II: Molding Condition Optimization," Polym. Eng. Sci., **30**, No. 10, pp. 882–892.
[10] Choi, G. H., Lee, K. D., and Chiang, N., 1994, "Optimization of Process Parameters of Injection Molding with Neural Network Application in a Process Simulation Environment," Ann. CIRP, **43**, No. 1, pp. 449–452.
[11] Han, Chang Dae, 1976, *Rheology in Polymer Processing*, Academic Press, New York.
[12] Guceri, Selcuk I., 1989, "Finite Difference Solution of Field Problems" *Computer Modeling of Polymer Processing*, Charles L. Tucker III, ed., Hanser Publishers, pp. 142–236.
[13] Jaluria, Yogesh, 1988, *Computer Methods in Engineering*, Allyn and Bacon, Inc.
[14] Kamal, M. R., Mutel, A. T., Garcia-Rejon, A., and Salloum, G., 1991, SPE ANTEC Tech. Papers, Vol. 37, p. 483.
[15] Holman, J. P., 1997, *Heat Transfer*, McGraw-Hill, ed., 8th Edition.
[16] Tadmor, Zehev and Gogos, Costas G., 1979, *Principles of Polymer Processing*, Wiley, New York.

Downloaded 03 Jun 2010 to 171.66.16.150. Redistribution subject to ASME license or copyright; see http://www.asme.org/terms/Terms_Use.cfm

The Effects of Compression and Pore Size Variations on the Liquid Flow Characteristics in Metal Foams

K. Boomsma
ASME Member

D. Poulikakos
ASME Fellow

Laboratory of Thermodynamics in Emerging Technologies,
Institute of Energy Technology,
Swiss Federal Institute of Technology,
ETH Center, 8092 Zurich, Switzerland

Open-cell aluminum foams were investigated using water to determine their hydraulic characteristics. Maximum fluid flow velocities achieved were 1.042 m/s. The permeability and form coefficient varied from $2.46\times10^{-10}\,m^2$ and 8701 m^{-1} to $3529\times10^{-10}\,m^2$ and 120 m^{-1}, respectively. It was determined that the flowrate range influenced these calculated parameters, especially in the transitional regime where the permeability based Reynolds number varied between unity and 26.5. Beyond the transition regime where $Re_K \gtrsim 30$, the permeability and form coefficient monotonically approached values which were reported as being calculated at the maximum flow velocities attained. The results obtained in this study are relevant to engineering applications employing metal foams ranging from convection heat sinks to filters and flow straightening devices. [DOI: 10.1115/1.1429637]

Introduction

This study investigates the hydraulic characteristics of a liquid flowing through a rigid, open-cell, metal foam. The metal foam is an intricately detailed structure, which is manufactured from a variety of molten aluminum processes (Fig. 1(*a*) and Fig. 1(*b*) in uncompressed form and Fig. 1(*c*) and Fig. 1(*d*) in compressed form). The structure of the metal foam opens itself to many applications due to its large surface area to volume ratio and high permeability. The list of possible applications includes lightweight high-strength structural applications, mechanical energy absorbers, filters, pneumatic silencers, containment matrices and burn rate enhancers for solid propellants, flow straighteners, catalytic reactors, heat sinks, and heat exchangers. In addition to flow applications, thermally conductive porous media may also increase the thermal conductance of a solid-fluid system simply by their physical presence [1–3].

The use of open-cell metal foams in fluid-flow applications requires a thorough understanding of the pressure-drop behavior of the fluid flowing through the porous structure. Extensive work has been done to characterize the pressure-drop behavior of fluid flow through porous media, but these are often limited to packed granular beds or beds of packed spheres. An excellent review on the subject involving such granular materials can be found in [4]. As seen in Fig. 1, the structure of the open-cell metal foam is completely different from that encountered in packed beds of spheres. Because of these structural differences, the characterization of the pressure-drop through the open-cell metal foams requires a renewed research effort.

Theory

Different models have been developed in the past 150 years to characterize the fluid flow in a porous matrix on the basis of macroscopically measurable flow quantities. A thorough historical review of the work in porous media can be found in [5]. The first of these models can be traced back to Darcy's publication in 1856 [6]. He established the well-known Darcy's law which states that the pressure-drop per unit length for a flow through a porous medium is proportional to the product of the fluid velocity and the dynamic viscosity (later added by Krüger [7]), and inversely proportional to the permeability.

$$\frac{\Delta p}{L}=\frac{\mu}{K}v \tag{1}$$

However, Darcy's law is applicable only for relatively slow-moving flows, where the permeability-based Reynolds number is small.

$$\mathrm{Re}_K=\frac{\rho\sqrt{K}}{\mu}v<O(1) \tag{2}$$

The velocity term v in Eq. (1) can be either the Darcian velocity of the fluid flow, which is based on the cross-section dimensions of the channel

$$v_D=\frac{Q}{area_{cs}} \tag{3}$$

or the pore (filter) velocity, as given by the Dupuit-Forchheimer relation [8] which accounts for the presence of the solid phase in the channel by dividing the Darcy velocity by the volumetric void fraction of the medium (assuming an isotropic medium).

$$v_p=\frac{v_D}{\varepsilon} \tag{4}$$

Either velocity can be used in the characterization and derivation of the permeability, but one must state which velocity is used in the calculations [4,9,10].

As the flow velocity increases, the form drag becomes more prevalent and must be considered for an accurate description of the pressure-drop [11]. This effect is accounted by the addition of the form drag term C as suggested by Dupuit [12] which yields the following quadratic relation for the pressure-drop.

$$\frac{\Delta p}{L}=\frac{\mu}{K}v+\rho Cv^2 \tag{5}$$

This form drag compensation, C, may vary according to the porosity of the medium and the channel which contains it [13]. However, the porous medium container effects of a metal foam do not resemble those generated in packed beds of spheres. In a packed bed of spheres, the porosity of the bed increases exponentially to

Contributed by the Fluids Engineering Division for publication in the JOURNAL OF FLUIDS ENGINEERING. Manuscript received by the Fluids Engineering Division January 29, 2001; revised manuscript received August 24, 2001. Associate Editor: P. W. Bearman.

 Copyright © 2002 by ASME

Downloaded 03 Jun 2010 to 171.66.16.150. Redistribution subject to ASME license or copyright; see http://www.asme.org/terms/Terms_Use.cfm

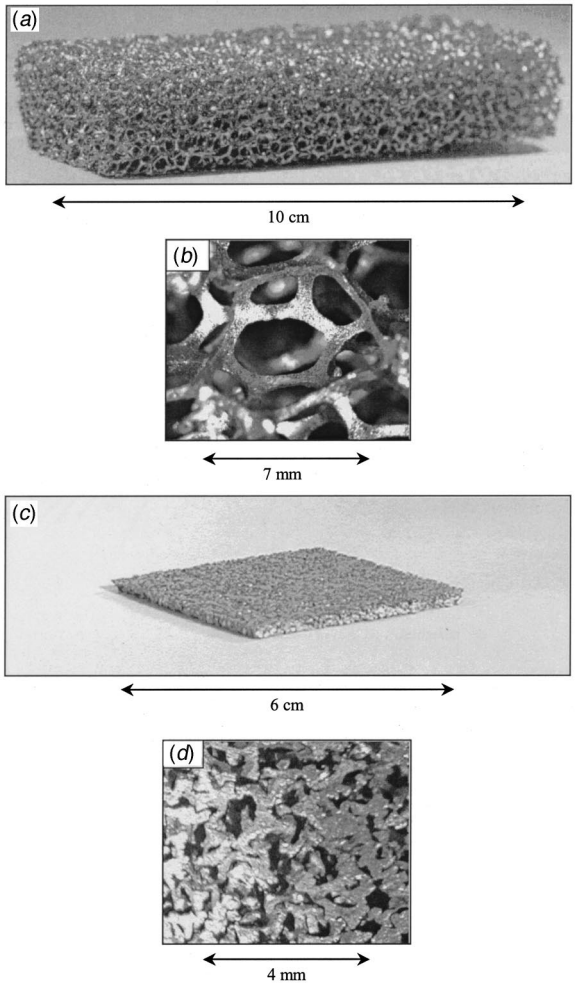

Fig. 1 (*a*) Aluminum foam block which measures 10.0 cm ×4.0 cm×1.5 cm, 92% porous (10 pores per linear inch =6.9 mm pore diameter); (*b*) magnified view of a single pore from Fig. 1 (*a*); (*c*) aluminum foam block as depicted in Fig. 1 (*a*), but compressed by a factor of four, which decreased the porosity from 92% to 76.1%; (*d*) magnified view of the foam in Fig. 1 (*c*).

the container wall [14] causing ''tunneling effects'' which may increase the permeability of the system [15]. This effect, however, is not applicable in the study of the hydraulic characteristics of metal foam because of the metal foam production process. The metal foam production process generates large quantities of liquid foam inside a container whose dimensions are much larger than the pore size. After the foam has been produced in bulk, it is then cut to specification, effectively eliminating any type of wall-interference on the final foam structure. A consistent porosity is thus maintained throughout the foam without the need for any porosity variation considerations [16].

There exists no general relationship between the permeability of a porous medium and porosity because the permeability is affected by the form of the solid structure [4]. Different mathematical models have been developed with varying degrees of success in order to predict the permeability of porous media using simplified structures, with the majority consisting of packed beds of spheres [15,17–19]. However, the structure of the metal foam confronted here is notably more complex than that of a packed bed of spheres. Although some models of flow through various representations of this complex structure have been developed with limited success [20–22], detailed experimentation is still required to accurately measure the permeability of the material.

The addition of the quadratic term in Eq. (5) has been proven to be applicable for packed beds of spheres for permeability based Reynolds number in the range $80>\mathrm{Re}_K>5$ by Dybbs and Edwards [23]. Fand et al. [9] confirmed this for randomly packed spheres, i.e., spheres of various diameters which composed the packed bed instead of spheres of equal diameter which pack regularly. Beyond this Re_K range, Lage et al. [24] demonstrated the existence of a third regime which requires a cubic velocity term for an accurate description of the pressure-drop in metal foams, which is in line with that considered by Forchheimer when studying large sets of hydraulic data from flow through porous media [25].

There are several ways by which the permeability, K, and the form coefficient, C, can be calculated through experimentation. One approach has been to modify Eq. (5) to bring it into linear form and then extrapolate to determine the coefficients as done by Givler and Altobelli [26]. However, this method has been shown to lack accuracy due to the extrapolation, and therefore a more direct and accurate way has been introduced by Antohe et al. [27] using a least-squares quadratic curve fit through the pressure-drop versus fluid-speed data points. A direct advantage of the least-squares curve fit using the form coefficient is the provision for an accurate uncertainty analysis, which is beneficial when analyzing and reporting quantities derived from experimental results. The least squares curve-fitting process works as follows. Making the following substitutions in Eq. (5),

$$A=\frac{\mu}{K} \tag{6}$$

and

$$B=\rho C \tag{7}$$

yields the following quadratic equation for the length-normalized pressure-drop

$$\frac{\Delta p}{L}=Av+Bv^2 \tag{8}$$

in which A and B are solved through the least squares curve fit technique. Applying the least-squares quadratic fit on Eq. (8) gives the following results for the coefficients A and B.

$$A=\frac{\left(\sum_{i=1}^{n}x_iy_i\right)\left(\sum_{i=1}^{n}x_i^4\right)-\left(\sum_{i=1}^{n}x_i^2y_i\right)\left(\sum_{i=1}^{n}x_i^3\right)}{\left(\sum_{i=1}^{n}x_i^2\right)\left(\sum_{i=1}^{n}x_i^4\right)-\left(\sum_{i=1}^{n}x_i^3\right)\left(\sum_{i=1}^{n}x_i^3\right)} \tag{9}$$

$$B=\frac{\left(\sum_{i=1}^{n}x_i^2y_i\right)\left(\sum_{i=1}^{n}x_i^2\right)-\left(\sum_{i=1}^{n}x_iy_i\right)\left(\sum_{i=1}^{n}x_i^3\right)}{\left(\sum_{i=1}^{n}x_i^2\right)\left(\sum_{i=1}^{n}x_i^4\right)-\left(\sum_{i=1}^{n}x_i^3\right)\left(\sum_{i=1}^{n}x_i^3\right)} \tag{10}$$

In these equations, the x_i's represent the various fluid flow velocities at which the data were taken and the y_i's represent the respective measured pressure-drop per unit length values. Knowing A and B, the permeability and inertia coefficient are obtained by backsolving Eq. (6) and Eq. (7).

Experimental Apparatus and Procedure

The experimental setup (Fig. 2) used to measure the pressure-drop for characterization of the metal foams consisted of a foam test housing, a pump to circulate the fluid, various flowrate measuring apparati, two pressure transducers for different pressure ranges, and degassed, deionized water as the working fluid. This setup models that which would use metal foam heat exchangers to cool electronics which dissipate large amounts of heat. The function of the foam test housing was to provide a secure means to

Downloaded 03 Jun 2010 to 171.66.16.150. Redistribution subject to ASME license or copyright; see http://www.asme.org/terms/Terms_Use.cfm

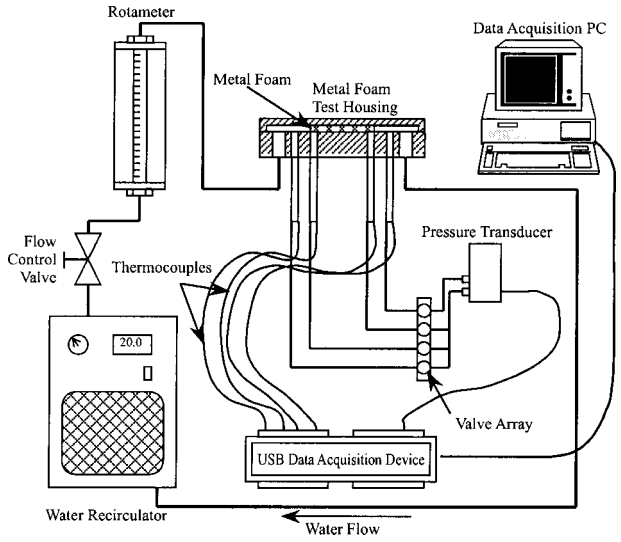

Fig. 2 Diagram of the experimental apparatus used to measure the pressure drop over various configurations of metal foam

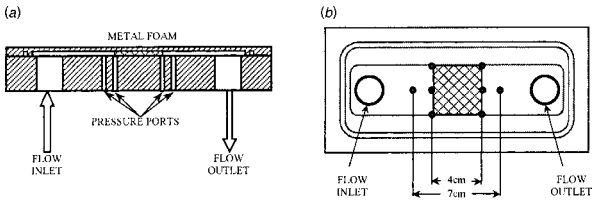

Fig. 3 (*a*) Metal foam test housing cross-sectional view of the inlet, outlet, and foam positioning during the pressure-drop characterization experiments. (*b*) Top view of the metal foam test housing with the lid removed for clarity.

hold the metal foam, to channel the fluid flow through the open-cell metal foam, and to provide a means to measure the pressure-drop across the foam. Figure 3(*a*) is a cross-section of the foam test housing showing the passage of the fluid through the housing and the foam. Figure 3(*b*) shows the same housing but from a top view without the lid for clarity, and allows one to see how the metal foam blocks were placed in relation to the pressure ports located in the bottom of the channel. The foam blocks (measuring 40.0 mm×40.0 mm×2.0 mm) were held securely by means of a tight fit inside the channel. After numerous experiments requiring the changing of the foam blocks by removing the lid, movement of the foam in the channel direction was never observed. The small ports which were drilled into the bottom of the channel were 0.4 mm in diameter and located before and after the foam test pieces, as shown in Fig. 3(*b*). These ports were attached to the pressure transducer through eight different valves which allowed each of the seven pressure ports to be measured directly against the reference port, which was the last port downstream of the water flow. All reported pressures were measured between the two outermost ports, spanning a distance of 7.0 cm. By conservation of mass, the incompressible liquid must accelerate as it enters the foam because the effective cross-sectional area of the channel is reduced by the physical presence of the foam in the channel. The opposite occurs when the liquid leaves the foam; the liquid velocity must decrease in order to compensate the increase in the effective cross-sectional area of the channel. Locating the pressure ports at a distance of 1.5 cm from the entrance and exit of the foam reduced the static pressure-altering effects of the fluid acceleration and deceleration. The six additional ports located at the edge of the foam block were used as a check for symmetry in the pressure. Discrepancies between the left and right hand sides of the pressure measurements during experimentation did not exceed 3%, and were therefore, neglected.

Two different pressure transducers were used depending upon the pressure range of interest. For the lower range, a Huba 692 differential pressure transducer was used for the pressure range between 0.0 and 0.200 bar with an accuracy of ±0.5% FS. For the higher pressure range, an Omega differential pressure transducer (PX81DO-050DT) was implemented for differential pressure measurements up to 3.45 bar with an accuracy of ±0.25% FS. The flowrate was measured with two flowmeters, the Omega FLR 1009 for a flowrate range from 0.0 l/min. to 0.500 l/min, and the Omega FLR 1012 for the flowrate range between 0.500 l/min. and 5.000 l/min. Each flowmeter was calibrated to within ±1.5% FS accuracy. For the larger flowrates attained in the uncompressed foam experiments, a Wisag 2000 rotameter was used for the flowrate range from 1.000 l/min. to 11.220 l/min with ±1% FS accuracy.

The acquisition of the signals from the sensors which included both pressure transducers and two electronic flowmeters was handled by a USB data acquisition device manufactured by IOTech. The device was attached via a USB port on a PC running Windows 98 which controlled the IOTech data acquisition device using LabVIEW software. With this configuration the pressure and flow data were viewed and recorded to the PC hard drive in real time.

A Neslab chiller (CFT-75) pumped water through the foam test housing. It also regulated the water temperature at 20.0°C to within ±0.5°C. The pressure-drop experiments were conducted from the low-end to the high-end of the flowrate range. As a check for hysteresis, selected experiments were performed from the high-end of the flowrate range to the low-end. No hysteresis was observed in these experiments when they were compared to the pressure measurement data taken by varying the flowrate from

Table 1 Compressed foam physical data

Foam	Compression	Name	Expected Porosity [%]	Measured Porosity [%]
5%	2	95-02	90.0	88.2
	4	95-04	80.0	80.5
	6	95-06	70.0	68.9
	8	95-08	60.0	60.8
8%	2	92-02	84.0	87.4
	3	92-03	76.0	82.5
	4	92-04	68.0	76.1
	5	92-05	60.0	72.2
	6	92-06	52.0	66.9

Uncompressed Foam Physical Data

Foam	Pore Diameter [mm]	Specific Surface Area [m^2/m^3]	Measured Porosity [%]
10 PPI	6.9	820	92.1
20 PPI	3.6	1700	92.0
40 PPI	2.3	2700	92.8

Downloaded 03 Jun 2010 to 171.66.16.150. Redistribution subject to ASME license or copyright; see http://www.asme.org/terms/Terms_Use.cfm

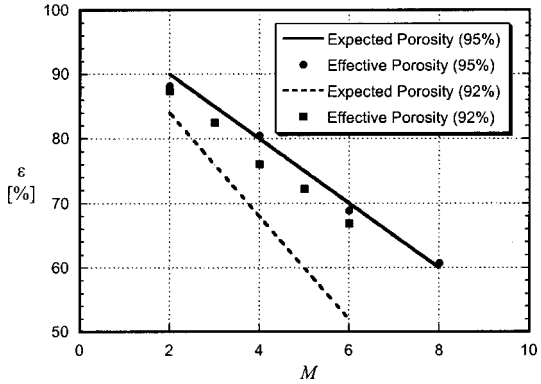

Fig. 4 The expected compressed metal foam porosities based on the precompression porosity and nominal compression factors are graphically compared against the measured values

low to high. Therefore, all data used in the calculations were taken as an average from four experimental trials, adjusting the flowrate from low to high. The temperature of the water during the experiments was held constant at $20.0 \pm 0.5°C$. Within the temperature range of 0.5°C, the physical properties of water do not vary enough to be considered in the calculations when compared to the uncertainties generated by the data acquisition equipment.

Metal Foam. Table 1 gives an overview of the physical properties of all foams which were tested. All foams were manufactured from 6101 aluminum alloy. To generate the array of compressed foam blocks in Table 1, 40 PPI foam (2.3 mm precompression pore diameter) of two different initial porosities, one of 92% and the other of 95%, were compressed by various factors ranging from two to eight. The notation used for the compressed foams works as follows: The first two digits of the foam's name designate the porosity of the foam in pre-compressed form. The second pair of numbers of the foam name after the hyphen signify the compression factor. For example, foam 95-05 designates a foam that was 95% porous in its uncompressed state and then compressed by a factor of six, which in the final compressed state, corresponds to finished foam of one-sixth of its original uncompressed height.

The procedure for compressing the foams, as explained by the manufacturer, allows the foam to expand freely on the open lateral sides of the compression device. By not restraining the lateral edges of the foam block while being compressed, the isotropicity of the aluminum in the foam is claimed to be held more consistent by avoiding mass accumulation along the edges of the compression device. However, as the foam is being compressed, whatever mass of foam extends beyond the original lateral dimensions is lost when the foam is machined to final tolerances, and hence, the measured porosity of the final compressed state of the foam may be higher than expected for a given compression factor because this solid portion of the original foam is lost. To measure the actual values of the porosity, each compressed foam block was weighed, and based on the nominal external measurements, an effective porosity was calculated and compared to an expected final porosity based on the foam's initial solid fraction and compression factor. The expected porosity was based on the simple physical relation for a change in volume, where M is the compression factor (ratio of the original uncompressed foam block height to the final compressed height) and ε is the void fraction of the material $(0 < \varepsilon \leq 1)$.

$$\varepsilon_{\text{compressed}} = 1 - M(1 - \varepsilon_{\text{uncompressed}}) \tag{11}$$

Figure 4 shows the expected porosity of the compressed foam blocks as lines with the actual porosity measurements represented as points. The final overall dimensions of the compressed foam blocks used in the pressure-drop experiments were 40.0 mm $\times$ 40.0 mm $\times$ 2.0 mm, with the cross-sectional area normal to the flow direction measuring 40.0 mm $\times$ 2.0 mm.

In Table 1, the physical characteristics of the three blocks of uncompressed foam are given. The foams are labeled by their characteristic pore diameter in inches (as specified by the manufacturer), which are 10, 20, and 40 pores per linear inch (PPI). However, due to the subjective nature of the pore counting, the uncompressed foams were viewed under a microscope and the pore diameters were measured by hand to an accuracy of ± 0.5 mm and tabulated in Table 1. This provides a more objective description of the actual foam geometry for comparison purposes. These foams have open pore diameters of 6.9 mm, 3.6 mm, and 2.3 mm, respectively. Each uncompressed foam block tested was 12.0 mm $\times$ 38.0 mm $\times$ 80.0 mm, with the flow cross-section measuring 12.0 mm $\times$ 38.0 mm. The blocks were cut to final external tolerances by an electro-discharge machining system to minimize deformation of the solid structure and to ensure uniform porosity to the outer edges of each block. The porosity of each block was calculated by dividing its weight by the volume, as measured by the external dimensions, and then comparing this value to the density of the solid metal, aluminum 6101. The surface area to volume ratio (specific surface area) is also tabulated for the uncompressed metal foam blocks in Table 1. This specific surface area data were provided by the foam manufacturer [28].

Results and Discussion

All data were calculated and reported on a Darcian flow velocity basis, as given by Eq. (3). This velocity accounts only for the channel dimensions, is independent of the porosity of the test material, and is practical for comparison against other data sets of porous media. The pressure-drop data for both the compressed and uncompressed foam blocks were taken and normalized on a length-scale basis, which was based on the respective lengths of the foam blocks of 40.0 mm for the compressed metal foams and 80.0 mm for the uncompressed metal foams. From these data, a quadratic curve was fitted through the data points for each foam block according to Eqs. (6)–(10).

Figure 5 shows the pressure-drop experimental data and the fitted curves in graphical form for the compressed blocks based on the Darcian velocity. Figure 5 is separated into (a) and (b) according to pre-compression porosities of 95% and 92%, respectively. The left-hand ordinate is the length-normalized pressure drop and the right-hand ordinate is the pressure drop for one 40-mm long aluminum foam block. By backsolving the constants A and B from the fitted curves as given in Eqs. (6) and (7), the permeability, form coefficient, and their respective uncertainties, were calculated for each foam block using the entire flowrate range tested for each foam block. This corresponded to a flowrate range of 0.00 l/min. to 5.00 l/min. (0.00 m/s to 1.04 m/s Darcian flow velocity) for the compressed foam. The only exception was foam 95-08. The maximum pressure for the pressure transducer (3.45 bar) was reached with a flow velocity of 0.729 m/s while testing the 95-08 foam block, and therefore, the maximum usable data pair (flow velocity, pressure) in the quadratic least-squares curve fit for foam 95-08 was obtained from this flow velocity value. However, the fitted pressure-drop curve for foam 95-08 was plotted over the entire flow velocity range from 0.00 m/s to 1.04 m/s in Fig. 5(a) for comparison purposes. Table 2 gives the permeability, the form coefficient, the A and B coefficients used in the curve fitting procedure, and their respective uncertainties for both the compressed and uncompressed foam blocks.

Reviewing the pressure-drop data from both the compressed and uncompressed foams, it becomes apparent that the flow through open-cell metal foams deviates from Darcy law flow behavior, i.e., the pressure-drop across the foam is a quadratic function of the flow velocity. It is of interest to compare the effects of compression on the permeability and form coefficient for each foam block, which are tabulated in Table 3. As seen in Fig. 5, the

Downloaded 03 Jun 2010 to 171.66.16.150. Redistribution subject to ASME license or copyright; see http://www.asme.org/terms/Terms_Use.cfm

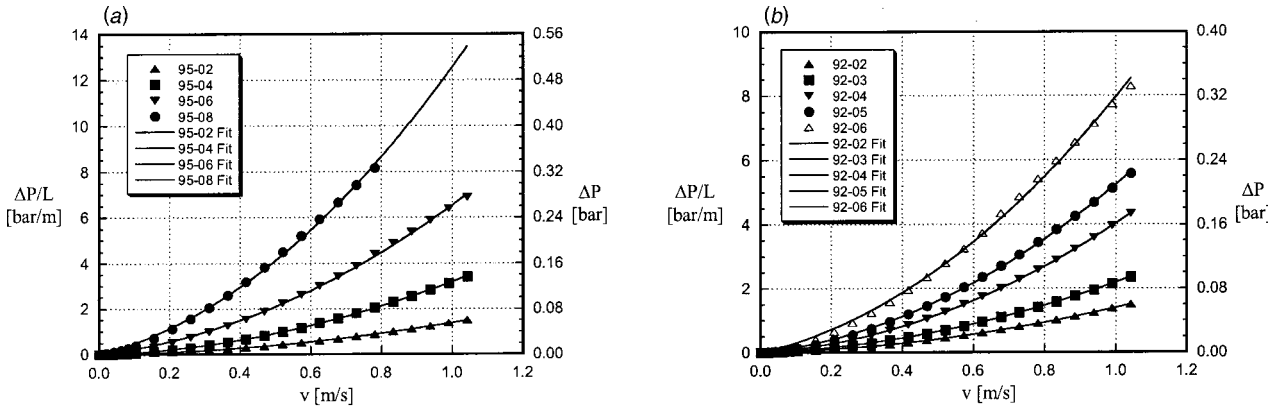

Fig. 5 (*a*) **The experimentally obtained pressure-drop data are plotted along with the fitted curves for the 95-series compressed foam blocks. The experimental uncertainty values are 0.22 bar/m in the length-normalized pressure measurement, 0.0088 bar in the actual pressure measurement, and 0.013 m/s in the fluid flow velocity measurement.** (*b*) **the experimentally obtained pressure-drop data are plotted along with the fitted curves for the 92-series compressed foam blocks. The experimental uncertainty values are 0.22 bar/m in the length-normalized pressure measurement, 0.0088 bar in the actual pressure measurement, and 0.013 m/s in the fluid flow velocity measurement.**

compression has a profound effect on the pressure-drop behavior of a compressed foam. Both foam sample series which were 95% and 92% porous before compression showed similar flow behavior with respect to the changes in the compression factor. For the 95% original porosity series, increasing the compression factor from two to four reduced the permeability from $44.4\times10^{-10}\,m^2$ to $19.7\times10^{-10}\,m^2$, or a relative reduction of 55.6%. Increasing the compression factor from two to six reduced the permeability to a value of $5.25\times10^{-10}\,m^2$, which is a reduction of 88.2%. For the last compressed foam block which was originally 95% porous, increasing the compression factor from two to eight reduced the permeability to $2.46\times10^{-10}\,m^2$, which is a significant reduction of 94.4%.

The other series of compressed foam blocks which where 92% porous before compression showed approximately the same sensitivity between the compression factor and the change in permeability. The first sample, which was compressed by a factor of two, had a measured permeability of $36.7\times10^{-10}\,m^2$. Increasing the compression factor from two to three reduced the permeability to $23.0\times10^{-10}\,m^2$, a reduction of 37.3%. Continuing from a compression factor of two to four, the permeability is reduced to $13.9\times10^{-10}\,m^2$, a reduction of 62.1%. This 62.1% reduction in the compressed foam permeability between a compression factor from two to four is compared with the change in permeability of the 95% porous series between the compression factors of two and four, which is similar at 55.6%. Increasing the compression factor from two to five with the 92% original porosity foam decreased the permeability to $8.07\times10^{-10}\,m^2$, a decrease of 78.0%. The highest compression ratio for the 92% foam series which was tested was six. The permeability at this level of compression was only $3.88\times10^{-10}\,m^2$, which is a reduction of 89.4% when compared to the permeability of the foam of the same initial porosity but with a compression factor of two.

Figure 6 shows a plot of the permeability based on the measured porosity of the compressed metal foam samples. There is no difference made in the plotting of data points between foams of 95% and 92% precompression porosity; all are placed on the same scale by their measured porosity in compressed form. In Fig. 6, the data plot a rather smooth curve. However, the dependence of the permeability on porosity becomes steeper at higher values of porosity. At the low end of the tested porosity range, foam 95-08, with a measured porosity of 60.8%, had a calculated permeability of $2.46\times10^{-10}\,m^2$. Comparing this to the next foam, 92-06, which had a measured porosity of 66.9%, the permeability increased to $3.88\times10^{-10}\,m^2$. An increase in porosity of 6.1% caused an increase in the permeability of 58%. This change in porosity and its associated change in permeability are contrasted to the difference between the two foams which had a compression factor of only two, namely 95-02 and 92-02. The foam 92-02 had a measured porosity of 87.4% and a permeability of $36.7\times10^{-10}\,m^2$. Increasing the porosity by a mere 0.8% to 88.6%, as characterized by foam 95-02, caused the permeability to increase to $44.4\times10^{-10}\,m^2$, an increase of 21%.

The form coefficient also varied with the compression of the

Table 2 Calculated from flow characteristics

Compressed Foam								
Foam	K [10^{-10} m^2]	C [m^{-1}]	A [bar·s/m^2]	B [bar·s^2/m^3]	ΔA [bar·s/m^2]	ΔB [bar·s^2/m^3]	σ_K [%]	σ_C [%]
95-02	44.4	1168	0.216	1.165	0.0291	0.0406	13.5	3.5
95-04	19.7	2707	0.487	2.698	0.0679	0.0946	14.0	3.5
95-06	5.25	4728	1.828	4.714	0.1386	0.1893	7.6	4.0
95-08	2.46	8701	3.893	8.675	0.3269	0.5849	8.4	6.7
92-02	36.7	1142	0.261	1.139	0.0298	0.0412	11.4	3.6
92-03	23.0	1785	0.417	1.780	0.0461	0.0640	11.1	3.6
92-04	13.9	3361	0.689	3.351	0.0856	0.1189	12.4	3.5
92-05	8.07	4073	1.189	4.061	0.1110	0.1529	9.3	3.8
92-06	3.88	5518	2.472	5.502	0.1707	0.2321	6.9	4.2
Uncompressed Foam								
Foam	K [10^{-10} m^2]	C [m^{-1}]	A [bar·s/m^2]	B [bar·s^2/m^3]	ΔA [bar·s/m^2]	ΔB [bar·s^2/m^3]	σ_K [%]	σ_C [%]
10 PPI	3529	120	0.003	0.119	0.0004	0.0098	13.5	8.2
20 PPI	1089	239	0.009	0.239	0.0012	0.0105	13.4	4.4
40 PPI	712	362	0.013	0.361	0.0018	0.0116	13.4	3.2

Downloaded 03 Jun 2010 to 171.66.16.150. Redistribution subject to ASME license or copyright; see http://www.asme.org/terms/Terms_Use.cfm

Table 3 Decrease in permeability [%]

Compression Factor	Foam Series	
M	95	92
2 to 3	--	37.3
2 to 4	55.6	62.1
2 to 5	--	78.0
2 to 6	88.2	89.4
2 to 8	94.4	--

metal foam blocks and the differing pre-compression porosities, ultimately being controlled by the porosity of the compressed metal foam. The form coefficient of the foams increased monotonically with decreasing porosity, with only one exception. Foam 95-02 was the most porous foam tested with a measured porosity of 88.2% and a form coefficient of 1168 m^{-1}. Foam 92-02, which was the second most porous compressed foam tested (87.4%) had a slightly lower form coefficient of 1142 m^{-1}. However, considering the calculated uncertainty of the form coefficients at 3.5%–3.6%, these two values of 1168 m^{-1} and 1142 m^{-1} overlap, thus giving reasonable answers when considering the monotonic increase of the form coefficient with decreasing porosity.

Figure 7 shows the pressure-drop data and associated fitted curves against the Darcian flow velocity for the uncompressed foam blocks. The left-hand ordinate gives the length-normalized pressure-drop, and the right-hand ordinate is the scale of the measured pressure-drop values across the 80 mm-long foam block. The flowrate varied from 1.00 l/min to 11.22 l/min (0.036 m/s to 0.410 m/s Darcian flow velocity) for the uncompressed foam blocks. Table 2 lists the permeability, form coefficient, and their respective uncertainties. The A and B coefficients used in the curve fitting are also listed.

The three aluminum foam blocks which were tested were of nearly the same porosity (within 0.8%). The only difference between the samples was the average pore diameter. Referring to Table 1, the porosities of these uncompressed aluminum foam blocks ranged from 92.0% to 92.8%, and the pore diameter varied from an average of 6.9 mm to 2.3 mm. The difference in pore diameter appeared to dramatically affect the permeability and form coefficient of the foams. Decreasing the pore diameter decreased the permeability and increased the form coefficient. The 10 PPI foam, which had a pore size of 6.9 mm, generated the least flow resistance with a permeability of 3529×10^{-10} m^2 and a form coefficient of 120 m^{-1}. In contrast, the 40 PPI foam with a pore size of 2.3 mm, had the greatest flow resistance with a permeability of 712×10^{-10} m^2 and a form coefficient of 362 m^{-1}. The

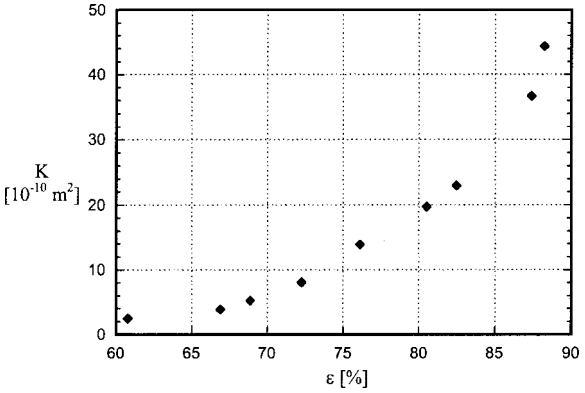

Fig. 6 The permeability of compressed foams is plotted against the values of the measured porosity. The uncertainty values for the permeabilities are gives in Table 2, and the uncertainty value of the measured porosity is estimated at a conservative 3%.

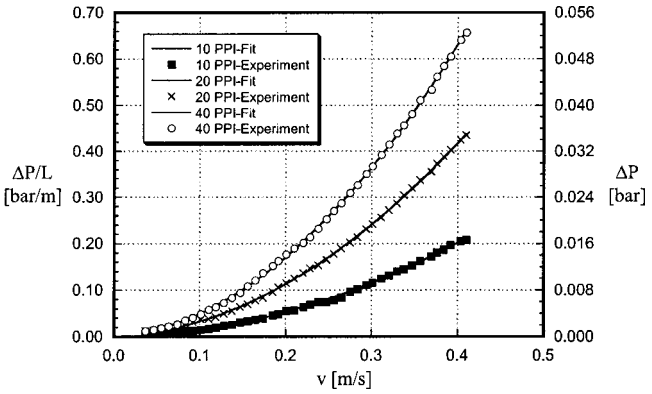

Fig. 7 Pressure-drop versus fluid flow velocity for the three uncompressed metal foams. The experimental uncertainty values are 0.0125 bar/m in the length-normalized pressure measurement, 0.001 bar in the actual pressure measurement, and 0.004 m/s in the fluid flow velocity measurement.

increase in flow resistance directly relates to the ''effective surface length'' as explained by Lage [5], which relates an increase in drag to the increase in the specific surface area.

Transition From Linear Darcy Regime. An important outcome of this study is the ability to determine when the pressure-drop across a metal foam leaves the linear Darcy regime and enters the form-dominated pressure-drop regime, characterized by the addition of the quadratic term to the linear Darcy law, Eq. (5). Making the substitution of Eqs. (6) and (7) into Eq. (8) and rearranging it into the following form, gives a graphical means by which the linear and nonlinear flow regimes can be separated.

$$\frac{\Delta P}{Lv} = A + Bv \tag{12}$$

The data from the pressure-drop experiments on the uncompressed foam were plotted in Fig. 8 according to Eq. (12) against the fluid flow speed. Figure 8 is separated into parts (a), (b), and (c) depending on the pore diameter as labeled by the foam manufacturer as 10 PPI, 20 PPI, and 40 PPI. In Table 1, these labels correspond to average pore diameters of 6.9 mm, 3.6 mm, and 2.3 mm, respectively. The discrete data points in Fig. 8 are the experimentally obtained data points, and the lines which are shown passing through the points are the second-order curves fitted to the pressure-drop data points using the curve-fitting technique described by Eqs. (5)–(10).

As expected from a quadratic relationship when the coefficients A and B of Eq. (12) are constant, the plotted line has a slope of B and a y-intercept of A. When B is equal to zero, the line is horizontal. This horizontal region describes the pressure-drop region where the form constant, C, is zero and the pressure-drop is governed entirely by Darcy's law, Eq. (1). These two regimes are seen by the discrete experimental points plotted in Fig. 8. In Fig. 8$(a-c)$, the experimental points form a horizontal line in the Darcian flow regime where the flow speeds are less than 0.101 m/s, 0.110 m/s, and 0.074 m/s, respectively. At flow velocities greater than these transitional flow velocity values, the experimental data points turn onto the curve-fitted line with a non-zero slope of B, which by Eq. (7), is the product of the fluid density, ρ, and the form coefficient, C.

The question arises as to which parameter best describes the transition of the pressure-drop from a linear to quadratic curve. A factor commonly used to determine the transition between flow regimes is the Reynolds number, which can be described in three different ways in the area of open-cell metal foams. The first method relates the Reynolds number to the square root of the permeability, K.

Downloaded 03 Jun 2010 to 171.66.16.150. Redistribution subject to ASME license or copyright; see http://www.asme.org/terms/Terms_Use.cfm

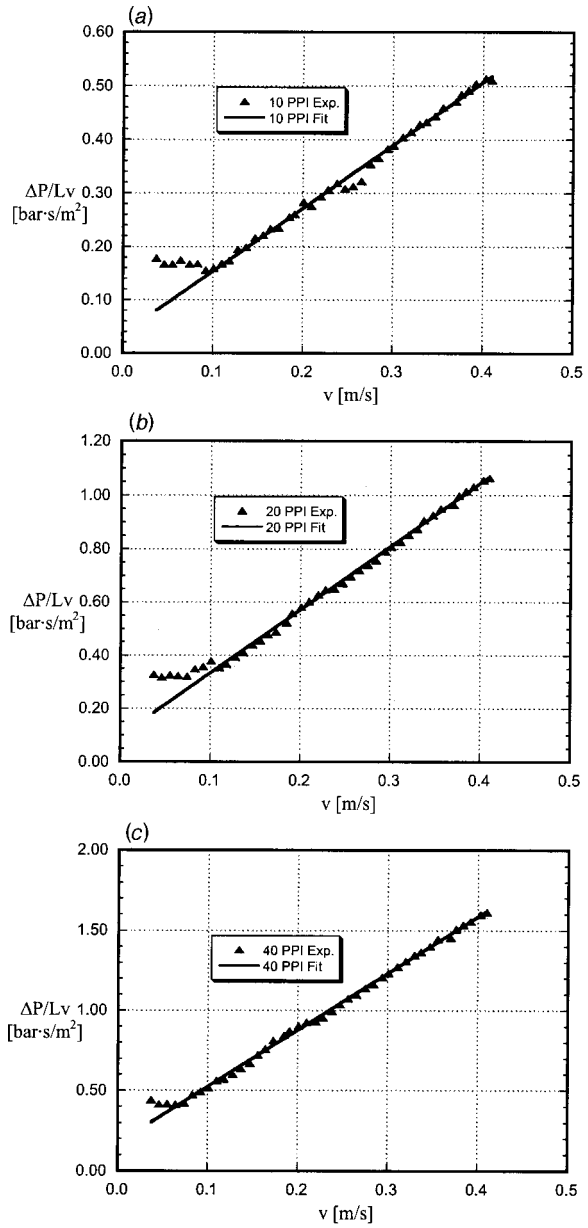

Fig. 8 (*a*) The quantity ($\Delta P/Lv$) for the 10 PPI foam (6.9 mm pore diameter) is plotted to show the pressure-drop deviation from Darcy's law at fluid flow velocities greater than 0.101 m/s. The discrete points represent the experimental data, and the straight line is the corresponding quadratic curve-fit. (*b*) The quantity ($\Delta P/Lv$) for the 20 PPI foam (3.6 mm pore diameter) is plotted to show the pressure-drop deviation from Darcy's law at fluid flow velocities greater than 0.110 m/s. The discrete points represent the experimental data, and the straight line is the corresponding quadratic curve-fit. (*c*) The quantity ($\Delta P/Lv$) for the 40 PPI foam (2.3 mm pore diameter) is plotted to show the pressure-drop deviation from Darcy's law at fluid flow velocities greater than 0.074 m/s. The discrete points represent the experimental data, and the straight line is the corresponding quadratic curve-fit.

$$\mathrm{Re}_K = \frac{\rho v \sqrt{K}}{\mu} \tag{13}$$

However, the value for K may be calculated by two different methods. One method uses the pressure-drop data points from a zero flow velocity value up to and including the velocity at which the transition to the quadratic regime takes place. The second method uses a larger flow velocity range which encompasses the transitional flow velocity by a subjective amount.

The third method bases the Reynolds number on the average pore diameter. In this method, the permeability, K, in Eq. (13) is replaced by the average pore diameter of the respective uncompressed open-cell aluminum foam, as tabulated in Table 1.

$$\mathrm{Re}_p = \frac{\rho v D_p}{\mu} \tag{14}$$

Table 4 Transitional Reynolds number in uncompressed aluminum foams

Foam	D_p [mm]	$v_{transition}$ [m/s]	Re_K (limited)	Re_K (full)	Re_p
10 PPI	6.9	0.101	26.5	62.4	725
20 PPI	3.6	0.110	22.3	37.8	412
40 PPI	2.3	0.074	14.2	20.5	177

Table 4 gives the Reynolds numbers at the transitional flow velocities using these three methods as described above. Using the permeability based on a maximum flow velocity which equals the transitional flow velocity (limited range), the flows for the three open-celled aluminum foams entered the quadratic pressure-drop relationship at Re values of 26.5, 22.3, and 14.2 for the 10 PPI, 20 PPI, and 40 PPI aluminum foams, respectively. These Re values correspond to fluid flow velocities of 0.101 m/s, 0.110 m/s, and 0.074 m/s. These velocities are contrasted to the maximum flow velocity tested, 0.410 m/s. This maximum velocity was used in the second method (full range) and generated a larger spread of transitional Re of 62.4, 37.8, and 20.5 for the 10 PPI, 20 PPI, and 40 PPI foams, respectively. Using the third and final method of relating the Re to the average pore diameter gave the widest range of transitional Re of 725, 412, and 177 for the 10 PPI, 20 PPI, and 40 PPI metal foams, respectively.

Even though each method produces transitional Re within its respective order of magnitude, the best approach from these data is first method, which uses the permeability calculated at the transitional flow velocity. This method provides the narrowest transitional Re number range ($\sim$O(10)) with an easily calculable scheme. The only drawback is that one must perform experiments just beyond the transition point in order to witness the deviation of the $(\Delta P/Lv)$ plot.

Permeability and Form Coefficient Flowrate Dependence. Previous works which investigated the hydraulic characteristics of highly porous media found that values for the permeability and form coefficient of the porous medium depend upon the flow velocity range over which they are calculated [27]. The permeability and form coefficient were calculated for each compressed and uncompressed foam by varying the flow velocity range over which the terms were calculated to investigate this dependence. For the compressed foam samples, each calculation used the range of flow velocities from the common minimum, 0.010 m/s, to varying maxima at which the data points are plotted. Figures 9 and 10 plot the permeability and form coefficient against the fluid flow velocity for the compressed foams, beginning at 0.010 m/s and continuing to 1.042 m/s.

Looking at the permeabilities plotted against the fluid flow velocity for the compressed foam blocks in Fig. 9, it becomes immediately apparent that the range over which the permeability is calculated affects its value. The relatively flat region of the permeability located near the low end of the range marks the linear pressure-drop flow regime where Darcy's law holds. The value of the permeability reaches a maximum at a value of the Darcian flow velocity of approximately 0.2 m/s. For example, at this flow velocity, foam 95-02 has a peak permeability of $175\times10^{-10}\,\mathrm{m}^2$. After this peak, all permeabilities decrease and level off to their respective values which are tabulated in Table 2 and were obtained using the entire flowrate range tested (up to 1.042 m/s fluid flow velocity). A possible explanation for this peak and the fol-

Downloaded 03 Jun 2010 to 171.66.16.150. Redistribution subject to ASME license or copyright; see http://www.asme.org/terms/Terms_Use.cfm

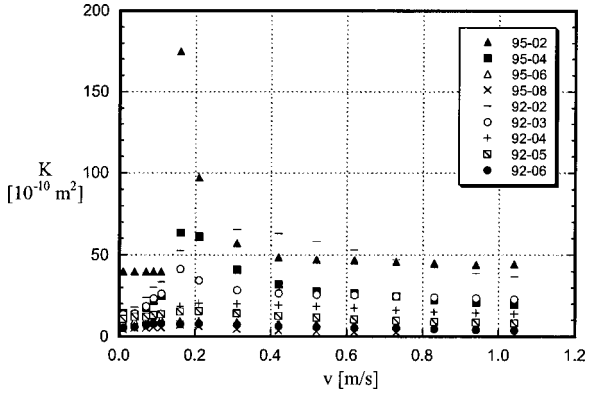

Fig. 9 Plot of the permeability, *K*, for the compressed aluminum foam blocks using a maximum flow velocity which corresponds to the velocity value at which the *K* value is plotted

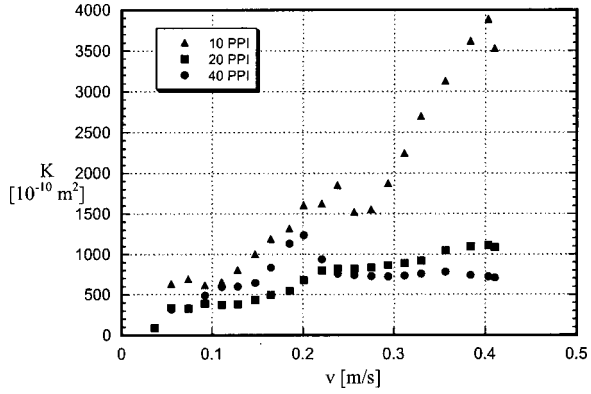

Fig. 11 Plot of the permeability, *K*, for the uncompressed aluminum foam blocks using a maximum flow velocity which corresponds to the velocity value at which the *K* value is plotted

lowing decrease in value may be offered by the least-squares method of calculating the permeability-based Reynolds number, Re_K. Forcing a curve fit onto data points which are comparably weighted in both the linear and quadratic regimes caused this peak to arise in the region of the transition points. When more points are accumulated in the quadratic region, i.e., as the fluid flow velocity continues to increase after the transition point, the majority of the curve-fitting points in the quadratic region then dominate and the permeability converges to its ultimate value.

The behavior of the form coefficients of the compressed foam samples in Fig. 10 mimicked the behavior of the changes in permeability in Fig. 9, which showed a trend of rising values until peaking at a fluid flow velocity of approximately 0.2 m/s. After this peak, the form coefficients of all foam blocks converged in a monotonic fashion to their respective values which were obtained by using the entire flowrate range (up to 1.042 m/s). These form coefficient values obtained from the calculation over the entire flowrate range are given in Table 2. This behavior in the lower flow velocity range may be explained by the same reasoning for the initial rise in the permeability, i.e., the flow is passing through the transition point into the quadratic-dominated flow regime. Forcing a curve fit onto the data points which are comparably weighted in both the linear and quadratic regimes caused these peaks to develop around the transition points.

The same permeability and form coefficient calculation process was used for the data sets of the uncompressed foam blocks. However, the flowrates spanned from 1.000 l/min. to 11.220 l/min., which corresponded to Darcian flow velocities from 0.037 m/s to 0.410 m/s. The permeability, which is plotted at the lowest flow velocity (0.037 m/s), is based only on that single data point. The rest of the calculated permeabilities include all data points between the lowest flow velocity of 0.037 m/s and up to and including the flow velocity at which the respective permeability value is plotted. Figure 11 plots the permeability based on an increasing maximum fluid flow speed. The permeabilities of the three uncompressed foams are nearly constant in the lower fluid flow speed range, up to the flow speed of approximately 0.1 m/s, which was previously explained as being the range in which the fluid enters the quadratic pressure-drop regime. The values of the permeability for the 20 PPI and 40 PPI foams peak at a fluid flow velocity of approximately 0.2 m/s, and then decline and remain somewhat steady for the rest of the flow speed range tested, up to 0.410 m/s. This behavior resembles the behavior of the compressed metal foams, as seen in Fig. 9, and indicates that the quadratic curve fits well to the data. The permeability of the 10 PPI foam, however, continued to rise after the transitional fluid flow velocity of 0.101 m/s, ultimately peaking just short of the maximum fluid flow speed tested, 0.410 m/s.

Figure 12 plots the form coefficients for the three uncompressed foams. The values of the form coefficient of all three foams start at a value of nearly zero and then increase up to a fluid flow velocity of approximately 0.2 m/s. Here the form coefficients obtain a maximum value and remain constant for the rest of the fluid flow speed tested, up to 0.410 m/s. As previously explained, decreasing the pore diameter consistently increased the flow resistance, and this change was also reflected in the changing form

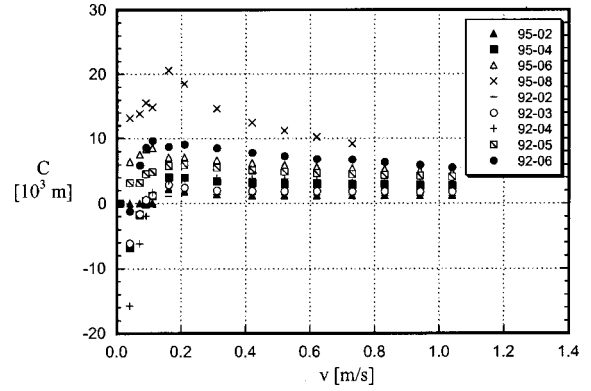

Fig. 10 Plot of the form coefficient, *C*, for the compressed aluminum foam blocks using a maximum flow velocity which corresponds to the velocity value at which the *C* value is plotted

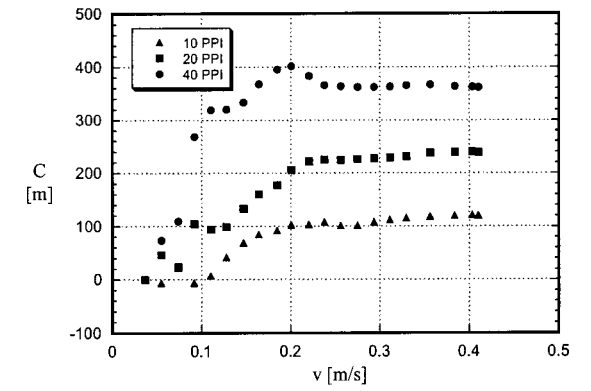

Fig. 12 Plot of the form coefficient, *C*, for the uncompressed aluminum foam blocks using a maximum flow velocity which corresponds to the velocity value at which the *C* value is plotted

Downloaded 03 Jun 2010 to 171.66.16.150. Redistribution subject to ASME license or copyright; see http://www.asme.org/terms/Terms_Use.cfm

coefficients. The 10 PPI foam, which had the largest pore diameter of 6.9 mm and the smallest specific surface area of 820 m^2/m^3, also had consistently the lowest form coefficient, with an ultimate value of 120 m^{-1}. The 40 PPI foam, which had the smallest pore diameter of 2.3 mm and the largest specific surface area of 2700 m^2/m^3, consistently generated the largest form coefficient, with an ultimate form coefficient value of 362 m^{-1}. This behavior was already witnessed in the discussion of Fig. 7, whereby increasing the surface area increased the total drag. The steadiness of the form coefficient beyond the fluid flow speed range of approximately 0.22 m/s indicates a good quadratic curve-fit to the data and validates the use of the quadratic pressure-drop relation, Eq. (5), as long as the flowrate range used in the calculation extends beyond the transition point.

Uncertainty Analysis

The uncertainties generated by the least-squares curve fit are given by the general formula for error propagation [29] applied to the least-squares curve fit equations, Eqs. (9) and (10), which yields the following equations for the uncertainty of the A and B coefficients of Eq. (8).

$$\Delta A = \sqrt{\sum_{i=1}^{n}\left(\frac{\partial A}{\partial x_i}\Delta x_i\right)^2 + \sum_{i=1}^{n}\left(\frac{\partial A}{\partial y_i}\Delta y_i\right)^2} \tag{15}$$

$$\Delta B = \sqrt{\sum_{i=1}^{n}\left(\frac{\partial B}{\partial x_i}\Delta x_i\right)^2 + \sum_{i=1}^{n}\left(\frac{\partial B}{\partial y_i}\Delta y_i\right)^2} \tag{16}$$

Each i term represents a single data pair (Darcy flow velocity and length-normalized pressure). The corresponding partial derivatives of Eqs. (9) and (10) were calculated and inserted into Eqs. (15) and (16) in order to obtain ΔA and ΔB. Backsolving A for K in Eq. (6) yields the uncertainty for the permeability. Assuming zero uncertainty for the dynamic viscosity, this gives the following relationship.

$$\sigma_K = \frac{\Delta A}{A} \times 100\% \tag{17}$$

The uncertainty of the form coefficient is given by backsolving Eq. (7) and applying the same error propagation technique as in Eqs. (15) and (16). Assuming zero uncertainty in the density term gives the uncertainty of the form coefficient as

$$\sigma_C = \frac{\Delta B}{B} \times 100\% \tag{18}$$

The uncertainties of the permeabilities and the form coefficients are tabulated in Table 2.

Conclusions

Open-cell metal foams were experimentally tested to evaluate their hydraulic characteristics using water. The experimental matrix of metal foams consisted of open-cell aluminum foams of various porosities and pore diameters in both compressed and uncompressed form. The characterization procedure involved solving for two terms, the permeability and the form coefficient. These two factors accurately described the pressure-drop vs. flow velocity behavior in porous media in general and were shown to be applicable to high porosity metal foams. From these experiments and the reduction of the data, several conclusions can be drawn.

1 The structural differences in the precompressed form between the originally 95% and 92% metal foams did not have a noticeable effect on the permeability. When comparing compressed foams with varying degrees of compression and initial porosities, the post-compression porosity governs the permeability and the resulting pressure-drop.

2 Similar compression factors had similarly weighted effects on both foams with 95% and 92% pre-compression porosity. Increasing the compression factor decreased the permeability of the foam by regular, incremental amounts, which were nearly equal for each of the two foam series.

3 The permeability of the compressed foams became more sensitive to changes in the porosity as the porosity increased.

4 Holding the porosity constant and decreasing the pore diameter increased the flow resistance in the uncompressed metal foams by reducing the permeability and increasing the form coefficient. This increase is attributed to the higher specific surface area generated by the smaller pore size.

5 The transition regime between the linear Darcy regime and the well-defined quadratic flow regime for all metal foams tested occurred in a Re_K range between unity and 26.5 based on the calculation of the permeability and form coefficient in this range.

6 The narrowest range of transitional Re_K was obtained when the permeability was calculated using a flowrate range from zero to the flow velocity at which the transition occurred.

7 Using different flow velocity regimes resulted in various permeability and form coefficient values. Whenever the permeability and the associated form coefficient for a high-porosity porous medium are stated, the flow velocity range over which these terms are calculated must also be specified for accuracy.

Acknowledgments

It is gratefully acknowledged that this research was supported jointly by the Swiss Commission for Technology and Innovation (CTI) through project no. 4150.2 and by the ABB Corporate Research Center, Baden-Dättwil, Switzerland. Helpful discussions with Dr. Fabian Zwick and Dr. Alexander Stuck of the ABB Corporate Research Center during the course of the work are also acknowledged.

Nomenclature

A = coefficient for curve fitting [$bar \cdot s \cdot m^{-2}$]
B = coefficient for curve fitting [$bar \cdot s \cdot m^{-3}$]
C = inertia coefficient [m^{-1}]
D = diameter [m]
K = permeability [m^2]
L = length [m]
M = compression factor
P = pressure [bar]
Q = volumetric flowrate [$m^3 s^{-1}$]
Re_K = permeability based Reynolds number [$\rho v K^{1/2} \mu^{-1}$]
Re_p = pore based Reynolds number [$\rho v D_p \mu^{-1}$]
v = velocity [ms^{-1}]

Greek

Δ = difference
ε = void fraction [range $1.0 \geqslant \varepsilon > 0.0$]
μ = dynamic viscosity [$kg \cdot m^{-1} s^{-1}$]
ρ = density [$kg \cdot m^{-3}$]
σ = uncertainty [%]

Subscripts

D = Darcy
K = permeability based
cs = cross-section
i = single, independent data point reference notation
p = pore diameter based

References

[1] Boomsma, K., and Poulikakos, D., 2001, "On the effective thermal conductivity of a three-dimensionally structured fluid-saturated metal foam," Int. J. Heat Mass Transf., **44**, pp. 827–836.
[2] Okuyama, M., and Abe, Y., 2000, "Measurement of Velocity and Temperature Distributions in a Highly Porous Medium," Journal of Porous Media, **3**, pp. 193–206.
[3] Schlegel, A., Benz, P., and Buser, S., 1993, "Wärmeübertragung und Druck-

Downloaded 03 Jun 2010 to 171.66.16.150. Redistribution subject to ASME license or copyright; see http://www.asme.org/terms/Terms_Use.cfm

abfall in keramischen Schaumstrukturen bei erzwungener Strömung,'' Wärme- und Stoffübertragung, **28**, pp. 259–266.
[4] Kaviany, M., 1995, *Principles of Heat Transfer in Porous Media*, Second ed., Springer-Verlag, New York.
[5] Lage, J. L., 1998, ''The Fundamental Theory of Flow Through Permeable Media from Darcy to Turbulence,'' *Transport Phenomena in Porous Media*, D. B. Ingham and I. Pop, eds., Elsevier Science, Oxford, pp. 1–30.
[6] Darcy, H., 1856, *Les Fontaines Publiques de la ville de Dijon*., Dalmont, Paris.
[7] Krüger, E., 1918, ''Die Grundwasserbewegung,'' Internationale Mitteilungen für Bodenkunde, **8**, pp. 105.
[8] Scheidegger, A. E., 1974, *The Physics of Flows Through Porous Media*, Third ed., University of Toronto Press, Toronto.
[9] Fand, R. M., Kim, B. Y. K., Lam, A. C. C., and Phan, R. T., 1987, ''Resistance to the Flow of Fluids through Simple and Complex Porous Media whose Matrices are Composed of Randomly Packed Spheres,'' ASME J. Fluids Eng., **109**, pp. 268–274.
[10] Macdonald, I. F., El-Sayed, M. S., Mow, K., and Dullien, F. A. L., 1979, ''Flow through porous media: The Ergun equation revisited,'' Ind. Eng. Chem. Fundam., **18**, pp. 199–208.
[11] Diedericks, G. P. J., and Du Plessis, J. P., 1997, ''Modeling of flow through homogeneous foams,'' Mathematical Engineering in Industry, **6**, pp. 133–154.
[12] Dupuit, J., 1863, *Etudes Theoriques et Pratiques sur le Mouvement des Eaux*., Dunod, Paris.
[13] Beckermann, C., and Viskanta, R., 1986, ''Forced convection boundary layer flow and heat transfer along a flat plate embedded in a porous medium,'' Int. J. Heat Mass Transf., **30**, pp. 1547–1551.
[14] Amiri, A., and Vafai, K., 1994, ''Analysis of dispersion effects and non-thermal equilibrium, non-Darcian, variable porosity incompressible flow through porous media,'' Int. J. Heat Mass Transf., **37**, pp. 939–954.
[15] Mehta, D., and Hawley, M. C., 1969, ''Wall effect in packed columns,'' I & EC Process Design and Development, **8**, pp. 280–282.
[16] Baumeister, J., 1997, ''Überblick: Verfahren zur Herstellung von Metallschäumen,'' presented at Symposium Metallschäume, J. Banhart, Verlag Metall Innovation Technologie, Bremen, pp. 3–14.
[17] Ergun, S., 1952, ''Fluid Flow through Packed Columns,'' Chem. Eng. Prog., **48**, pp. 89–94.
[18] Renken, K., and Poulikakos, D., 1988, ''Experiment and analysis of forced convective heat transport in a packed bed of spheres,'' Int. J. Heat Mass Transf., **31**, pp. 1399–1408.
[19] Poulikakos, D., and Renken, K., 1987, ''Forced Convection in a Channel Filled With Porous Medium, Including the Effects of Flow Inertia, Variable Porosity, and Brinkmann Friction,'' ASME J. Heat Transfer, **109**, pp. 880–888.
[20] Du Plessis, J. P., Montillet, A., Comiti, J., and Legrand, J., 1994, ''Pressure Drop Prediction for Flow through High Porosity Metallic Foams,'' Chem. Eng. Sci., **49**, pp. 3545–3553.
[21] Smit, G. J. F., and du Plessis, J. P., 1999, ''Modeling of non-Newtonian purely viscous flow through isotropic high porosity synthetic foams,'' Chem. Eng. Sci., **54**, pp. 645–654.
[22] Sodre, J. R., and Parise, J. A. R., 1997, ''Friction factor determination for flow through finite wire-mesh woven-screen matrices,'' ASME J. Fluids Eng., **119**, pp. 847–851.
[23] Dybbs, A., and Edwards, R. V., 1975, ''Department of Fluid, Thermal, and Aerospace Report,'' presented at Workshop on Heat and Mass Transfer in Porous Media, FTAS/TR (Case Western Reserve University), Springfield, VA., pp. 75–117.
[24] Lage, J. L., Antohe, B. V., and Nield, D. A., 1997, ''Two Types of Nonlinear Pressure-Drop Versus Flow-Rate Relation Observed for Saturated Porous Media,'' ASME J. Fluids Eng., **119**, pp. 700–706.
[25] Forchheimer, P., 1901, ''Wasserbewegung durch Boden,'' Z. Ver. Deutsch. Ing., **45**, pp. 1736–41 pp. 1781–1788.
[26] Givler, R. C., and Altobelli, S. A., 1994, ''A determination of the effective viscosity for the Brinkmann-Forchheimer flow model,'' J. Fluid Mech., **258**, pp. 355–370.
[27] Antohe, B. V., Lage, J. L., Price, D. C., and Weber, R. M., 1997, ''Experimental Determination of Permeability and Inertia Coefficients of Mechanically Compressed Aluminum Porous Matrices,'' ASME J. Fluids Eng., **119**, pp. 404–412.
[28] 1999, *Duocel Aluminum Foam Data Sheet*., ERG Material and Aerospace, Oakland.
[29] Taylor, J. R., 1997, *An Introduction to Error Analysis*, Second ed., University Science Books, Sausalito.

Downloaded 03 Jun 2010 to 171.66.16.150. Redistribution subject to ASME license or copyright; see http://www.asme.org/terms/Terms_Use.cfm

Sourith Sisavath
Xudong Jing
Chris C. Pain
Robert W. Zimmerman
e-mail: r.w.zimmerman@ic.ac.uk

Department of Earth Science and Engineering,
Imperial College of Science, Technology and Medicine,
London SW7 2BP,
United Kingdom

Creeping Flow Through an Axisymmetric Sudden Contraction or Expansion

Creeping flow through a sudden contraction/expansion in an axisymmetric pipe is studied. Sampson's solution for flow through a circular orifice in an infinite wall is used to derive an approximation for the excess pressure drop due to a sudden contraction/expansion in a pipe with a finite expansion ratio. The accuracy of this approximation obtained is verified by comparing its results to finite-element simulations and other previous numerical studies. The result can also be extended to a thin annular obstacle in a circular pipe. The "equivalent length" corresponding to the excess pressure drop is found to be barely half the radius of the smaller tube. [DOI: 10.1115/1.1430669]

1 Introduction

One of the most widely-encountered problems in industries involving the transport of fluids is the modification of the flow due to a sudden change in the pipe diameter. Knowledge of the additional pressure drop resulting from an abrupt diameter change is extremely important for a proper assessment of the pumping power required in ducts, which explains the large amount of literature on this topic. Since many industries are interested in the transport of non- Newtonian fluids such as paints or emulsions or, in the case of aeronautics, the flow of low-viscosity fluids at high Reynolds numbers, there have consequently been many studies of laminar flow of non-Newtonian fluids [1] or turbulent flow of Newtonian fluids [2]. However, there is a relative scarcity of studies involving flow of a *Newtonian* fluid through a sudden expansion in the *laminar* regime.

Nevertheless, the study of a laminar flow of a Newtonian fluid through a sudden expansion/contraction in an axisymmetric tube still presents some interest, from both a scientific and technical point of view. The determination of the additional pressure drop is indeed far from being resolved for a Newtonian fluid in the laminar regime. In fact, most existing experimental results do not agree with each other [3-5], and do not agree with the results of numerical studies [6,7]. Hence, further investigation of laminar flow of a Newtonian fluid through a sudden expansion seems warranted. Of particular interest is the creeping flow regime ($Re \rightarrow 0$), for which the problem of flow through a thin orifice has been solved analytically more than a century ago by Sampson [8]. The related problem of flow from an infinitely large reservoir into a circular tube of finite diameter has been investigated by Weissberg [9], but no similar analytical solution exists for the flow from a finite radius tube into another tube of smaller radius.

The purpose of the present study is to link the solution obtained by Sampson to the problem of flow through a sudden contraction/expansion, in order to find an approximation for the excess pressure drop generated by this geometry. We note that in the limit of creeping flow, and only in this limit, the problem of flow through an expansion is equivalent to flow through a contraction, and so no further distinction will be made between these two cases. A numerical study of this problem is also performed using the finite-element code FLUIDITY [10]. The results from this numerical study are used to assess the accuracy of our proposed approximate formula, and both are compared to previous studies. Due to the existing discrepancies in the experimental results, as mentioned earlier, our results are compared with previous *numerical* studies only.

Contributed by the Fluids Engineering Division for publication in the JOURNAL OF FLUIDS ENGINEERING. Manuscript received by the Fluids Engineering Division May 23, 2001; revised manuscript received October 18, 2001. Associate Editor: J. Marshall.

2 Analytical Considerations

The effects of a sudden expansion/contraction in an axisymmetric duct (Fig. 1) on creeping flow of a Newtonian fluid are investigated. This process is important for many industries, and interest has increased among petroleum engineers and hydrologists with the development of models representing porous rocks as network of pore throats connected at nodes [11]. Despite the apparent simplicity of the present problem, Sigli and Monnet [12] found that a closed-form solution for a circular tube with a finite expansion ratio is not attainable. Instead, analytical solutions in each tube had to be found independently, and then patched together at the ''interface'' by appropriate choice of the coefficients. The stream function thus obtained is consequently difficult to implement, due to the computation required to find the coefficients. As a closed-form solution is not possible, we will attempt to derive an approximate analytical expression for the excess pressure drop. As a starting point, we begin with the problem of flow through a small circular hole in an infinite plate (Fig. 2).

2.1 Thin Circular Orifice. Sampson [8] solved the problem of flow through a circular orifice of zero thickness in an infinite wall (Fig. 2) in the creeping flow regime for a Newtonian fluid, and gave the solution for the difference between the pressures at infinity, Δp_s. The correct result, without typographical error, was first given by Roscoe [13] as

$$\Delta p_s = \frac{3q\mu}{a^3}, \tag{1}$$

where q is the volumetric flowrate, μ is the viscosity of the fluid, and a is the radius of the orifice.

The relation between pressure difference and flowrate has been determined experimentally by different investigators, usually making no reference to Sampson's theoretical work. A review of these studies can be found in [14]. In particular, the work of Johansen [15], who studied the flow of castor oil through circular orifices situated within a pipe, confirms Sampson's result, although Johansen did not seem to be aware of the earlier theoretical work. For an orifice diameter as small as 0.090 of the diameter of the pipe, a factor of 2.99 can be obtained from the graphical presentation of Johansen's results; this is very close to the theoretical value of 3 that appears in Eq. (1).

 Copyright © 2002 by ASME

Downloaded 03 Jun 2010 to 171.66.16.150. Redistribution subject to ASME license or copyright; see http://www.asme.org/terms/Terms_Use.cfm

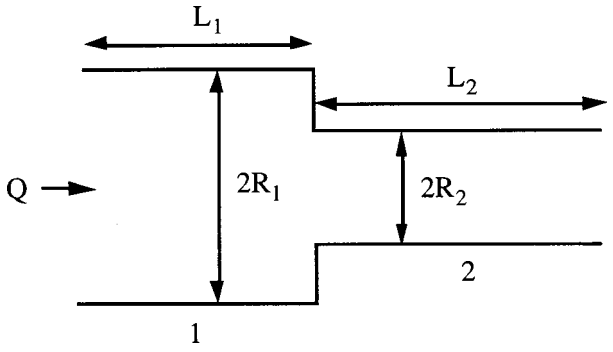

Fig. 1 Sudden contraction in an axisymmetric tube

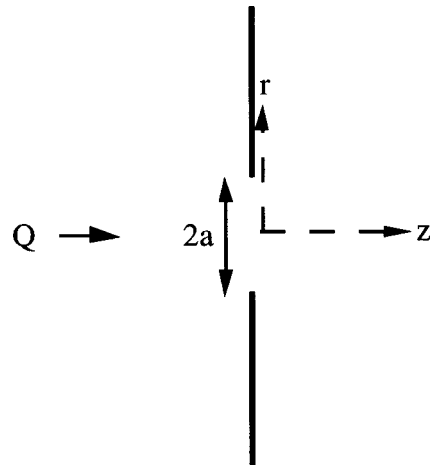

Fig. 2 Circular orifice of radius *a* and zero-thickness in an infinite space; the *z*-axis is an axis of rotation

2.2 Circular Orifice of Finite-Length in an Infinite Wall. Sampson's work has been extended to the case of an orifice of finite-length L (Fig. 3) by Dagan et al. [16]. They expressed the pressure drop through such an orifice as

$$\Delta p = \Pi(L)\frac{3q\mu}{a^3}, \tag{2}$$

where $\Pi(L)$ is a dimensionless function of the length L, with $\Pi(0)=1$, so as to agree with Sampson's solution for a thin orifice. The function $\Pi(L)$ was calculated numerically by matching the normal and tangential stresses at the pore opening. Dagan et al. [16] found that $\Pi(L)$ can be approximated with less than 1% error by the expression

$$\Pi(L) = 1 + \frac{8L}{3\pi a}. \tag{3}$$

This approximation was obtained by assuming Poiseuille flow throughout the tube in Fig. 3, and Sampson's solution outside. One interpretation of this result is that the pressure drop through an orifice of finite length is the sum of the pressure drop due to the Poiseuille pressure loss along the finite length of the tube, plus the pressure drop Δp_s calculated by Sampson that accounts for the expansion and contraction. This result is in agreement with similar work carried out by Weissberg [9], who studied the viscous dissipation near the ends of long round tubes. He expressed the pressure drop through such a tube as

$$\Delta p = \frac{8\mu q(L/a)}{\pi a^3} + \frac{c\mu q}{a^3}, \tag{4}$$

where c is a constant. For a thin orifice, i.e., $L/a=0$, Weissberg [9] rederived Sampson's solution and found a value of c equal to 3. In light of experimental results, he also hypothesized that the constant c is independent of the length-to-radius ratio L/a, and is equal to 3. Although he could not prove this previous assumption, he demonstrated, using Helmholtz's minimum-energy theorem, that $c<3.47$ for $L/a\to\infty$.

Due to the symmetry of the geometry, and the symmetry of the equations of creeping flow, the pressure drop Δp_∞ due to the entrance or exit from a tube of radius a into an infinite plane is therefore given by

$$\Delta p_\infty = \frac{3q\mu}{2a^3}, \tag{5}$$

which is exactly half the pressure drop through a thin orifice as found by Sampson.

2.3 Sudden Expansion/Contraction in an Axisymmetric Tube. We now consider flow from a finite radius tube into another finite radius tube (Fig. 1). Assuming that Poiseuille flow can be applicable to the entire tubing, the pressure drop $\Delta p_{1\to 2}$ between cross-section 1 and cross-section 2 (Fig. 1) can be decomposed into

$$\Delta p_{1\to 2} = \Delta p_{F1} + \Delta p_e + \Delta p_{F2}, \tag{6}$$

where Δp_{F1} and Δp_{F2} are the pressure losses due to fully-developed friction in the tubes of radius R_1 and R_2 respectively, i.e.,

$$\Delta p_{Fi} = \frac{8\mu}{\pi R_i^4} L_i q, \quad \text{for } i=1 \text{ or } 2, \tag{7}$$

and Δp_e is an excess pressure drop due to the contraction. This excess pressure drop was defined in [6] as the total pressure drop *minus* the pressure drop that would occur if the fluid were in fully-developed flow in each of the circular tubes.

In order to find an approximation for the excess pressure drop Δp_e, we consider again the case of a thin circular orifice mentioned in Section 2.1. Sampson [8] introduced a stream function ψ, defined in cylindrical coordinates as [14]

$$u_r = \frac{1}{r}\frac{\partial \psi}{\partial z}, \quad u_z = -\frac{1}{r}\frac{\partial \psi}{\partial r}, \tag{8}$$

where u_r and u_z are, respectively, the radial and axial velocity components. Oblate spheroidal coordinates (ξ,η,θ) were also in-

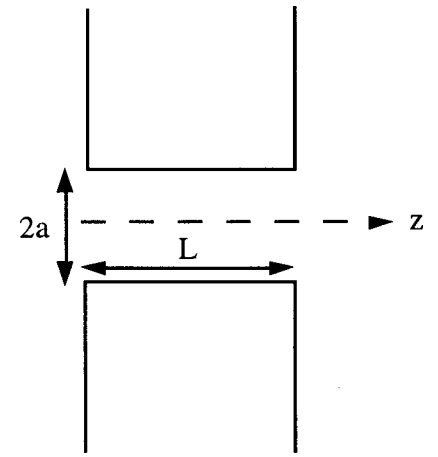

Fig. 3 Orifice of radius *a* and finite length, *L*

Downloaded 03 Jun 2010 to 171.66.16.150. Redistribution subject to ASME license or copyright; see http://www.asme.org/terms/Terms_Use.cfm

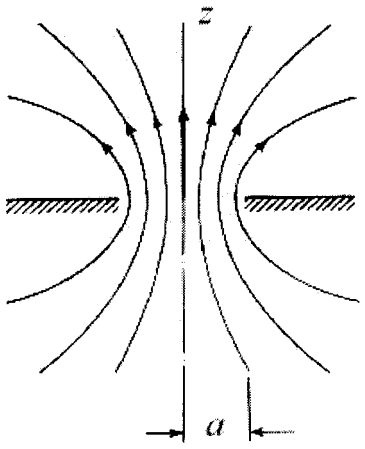

Fig. 4 Flow through the thin circular orifice of Fig. 2 (after [14])

troduced (see pp. 512-15 of [14]). These coordinates are obtained from the cylindrical coordinates (r,z,θ) by the transformation

$$z+ir=a\sinh(\xi+i\eta), \tag{9}$$

with $a>0$, $0\leqslant\xi<\infty$, $0\leqslant\eta\leqslant\pi$ and $0\leqslant\theta<2\pi$. The condition that the stream function must vanish along the tube axis requires that

$$\psi=0 \quad \text{for} \quad \cos\eta=1. \tag{10}$$

The boundary of the thin orifice is located at $\eta=\pi/2$, and it follows from the definition of the stream function that

$$\psi=-\frac{q}{2\pi} \quad \text{for} \quad \cos\eta=0. \tag{11}$$

For a thin orifice, Sampson [8] showed that the stream function ψ for flow through a circular hole in a plane wall is given by

$$\psi=-\frac{q}{2\pi}(1-\cos^3\eta). \tag{12}$$

The streamlines obtained from Eq. (12) are hyperbolas, as can be seen in Fig. 4. Close to the wall, the fluid actually flows along the wall orthogonal to the z-axis, i.e., orthogonal to the main flow direction. In this case, the excess pressure loss should be due to the additional pressure drop due to friction against this wall. As the friction is related to the area in contact with the fluid, the excess pressure loss Δp_e can indeed be assumed to be an increasing function of the cross-sectional area acting as an obstacle to the flow. In the limiting case of an infinitely large wall, with $R_1/R_2\rightarrow 0$, the maximum value of this pressure drop is therefore the value Δp_∞ found in Section 2.2. *Assuming* proportionality between the cross-sectional area and the excess pressure drop, the excess pressure drop Δp_e through a contraction can then be written as

$$\Delta p_e=\Delta p_\infty\left(1-\frac{R_1^2}{R_2^2}\right). \tag{13}$$

This is the only expression that gives an excess pressure drop proportional to the obstruction area, and which reduces to the correct values in the two limiting cases. As $R_1/R_2\rightarrow 1$, it correctly gives zero excess pressure drop, whereas for $R_1/R_2\rightarrow 0$ it reduces to Sampson's result. Moreover, as Δp_∞ is its maximum value, Eq. (13) also respects Weissberg's upper bound [9] mentioned in Section 2.2.

Equation (13) can be nondimensionalized with respect to $\rho U_1^2/2$, where ρ is the density of the fluid and U_1 is the average velocity of the fluid in the smaller tube, to yield

$$\frac{\Delta p_e}{\rho U_1^2/2}=\frac{6\pi[1-(R_1^2/R_2^2)]}{\mathrm{Re}}, \tag{14}$$

where the Reynolds number is defined as $\mathrm{Re}=\rho U_1 D_1/\mu$, with D_1 being the diameter of the smaller tube. This result is qualitatively consistent with experimental observations that show the dimensionless pressure drop to be inversely proportional to the Reynolds number for low Reynolds numbers [4,5]. These researchers therefore expressed their results in the form

$$\frac{\Delta p_e}{\rho U_1^2/2}=\frac{K'}{\mathrm{Re}}, \tag{15}$$

where the coefficient K' is called the Couette coefficient. According to the present approximation, Eq. (13), the Couette coefficient is given by

$$K'=6\pi\left(1-\frac{R_1^2}{R_2^2}\right). \tag{16}$$

In the context of rock pores, a parameter called the *hydraulic conductance* is often used to quantify the capacity of a pore to conduct fluid [17]. The hydraulic conductance C of the system located between section 2 and 1, as indicated in Fig. 1, can be defined as

$$q=\frac{C}{\mu}\Delta p_{1\rightarrow 2}. \tag{17}$$

The pressure drop $\Delta p_{1\rightarrow 2}$ is obtained from Eq. (6). The expansion/contraction therefore introduces an excess conductance C_e that is *connected in series* with the two conductances obtained from the Hagen-Poiseuille equation for the tubes 1 and 2, and therefore *decreases* the overall conductance. Using Eq. (13), this excess conductance can be expressed as

$$C_e=\frac{2R_1^3}{3[1-(R_1^2/R_2^2)]}. \tag{18}$$

3 Numerical Simulations

3.1 Numerical Method for a Sudden Expansion. In order to assess the accuracy of Eq. (13), numerical calculations have been carried out to calculate the excess pressure drop induced by a sudden expansion, for several diameter ratios, using the general purpose CFD code FLUIDITY [10]. This code is capable of numerically solving the Navier-Stokes equations using iterative solutions methods. In the present case, since our focus is on the creeping flow regime ($\mathrm{Re}=0$), FLUIDITY was used to solve the Stokes equations. The finite element mesh generator GEM [18] was used to describe the geometry of the cylindrical tube with a sudden expansion. The output is a list of elements, nodal coordinates and other items in the format required by the code FLUIDITY. The computational grids were generated using patched blocks, one for the inlet pipe, and two for the larger outlet pipe. The mesh spacing was uniform, although this is not a requirement of the program, and square grids were used. Optimization of the number of grids was not a goal of this study, and so no attempt was made to use nonuniform mesh spacing with more mesh points concentrated near the expansion plane, as was done by Oliveira and Pinho [19].

All the velocity components were set to zero at the wall, to satisfy the no-slip and no-penetration boundary conditions. As the geometry is axisymmetric, the radial component of the velocity was set to zero along the centerline. In the inlet pipe, the flow was allowed to develop from an initial plug velocity profile into a Poiseuille parabolic profile well before reaching the expansion plane, by using a long inlet pipe having $L_1/R_1=10$. The outlet pipe was also chosen to be long enough ($L_2/R_1=15$) to allow the velocity to regain a parabolic profile after the expansion plane.

Downloaded 03 Jun 2010 to 171.66.16.150. Redistribution subject to ASME license or copyright; see http://www.asme.org/terms/Terms_Use.cfm

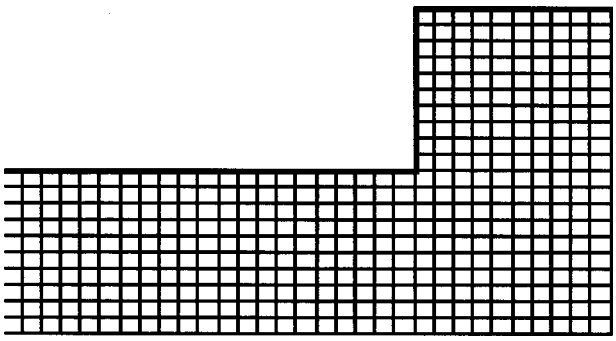

Fig. 5 Grid generated for a sudden expansion of $R_2/R_1=2$, and for $n=1$. The radius R_1 is subdivided into $10n$ intervals

3.2 Grid Testing. In order to validate our simulations, the configuration $R_2/R_1=4$ was investigated in detail. The pressure was calculated at $z/R_1=-3$ and $z/R_1=14$, with z being the axial coordinate along the main flow direction, and the origin being located at the expansion plane. The velocity and the pressure were calculated at various radial positions. The velocity profile was found to be parabolic, the radial velocity component was essentially zero, and the pressure was uniform at these two locations. It can be shown that these facts imply that the flow is fully-developed, in the sense that dp/dx is constant.

A series of tests with different grid sizes was conducted in order to verify the convergence of the results. The radius R_1 of one unit length was subdivided into $10n$ intervals (Fig. 5). The problem studied is axisymmetric, i.e., so there is no component of the velocity in the θ-direction. Hence, the problem can be treated as a 2D problem in a finite-element scheme, and square elements were used. For this type of grid, the length of the inlet duct ($L_1/R_1=10$) and outlet duct ($L_1/R_1=15$) were subdivided into $100n$ and $150n$ intervals, respectively. Table I shows that the pressure drop seems to have converged by the third level of refinement, i.e., by $n=4$.

The same procedure was applied to expansions having diameter ratios of 1.2, 1.4, 1.6, 1.8, 2.0, 2.6, 3, 3.5 and 5.0, chosen because these values were considered by previous investigators [6,7]. For these diameter ratios, refinement of the grid to $n=3$ was sufficient to ensure accuracy of better than 1%. However, for large expansion ratios the length L_2 had to be increased in order to guarantee fully-developed flow in the outlet duct. Indeed, for a diameter ratio of 5, an outlet duct of length $L_2/R_1=25$ was needed in order to obtain a uniform pressure over the outlet plane. The excess pressure drop Δp_e was calculated by subtracting the Poiseuille loss from the pressure drop calculated numerically, using Eq. (6).

4 Estimation of the Couette Coefficient

The validity of the results obtained with $n=4$ will now be compared with the finite-volume simulations carried out by Oliveira et al. in [7]. These investigators performed simulations for Re=0.5, 1.0, 2. 0, 3.5, and 5.0, for diameter ratios of 1.5, 2.0, 2.6, 3.0 and 4.0 (Table 2). In order to compare their results to our creeping flow results, we have extrapolated their Couette coefficients down to Re=0, for each diameter ratio. This was done by fitting a least-squares straight line through the values. However, as the curve of Couette coefficient versus Re is almost perfectly linear in this range, essentially the same values would be found at Re=0 if we had merely extrapolated from the two values at Re =1 and 0.5. The discrepancy between our values and their (extrapolated) values is generally only a few percent, reaching about 5.5% for an expansion ratio of 4:1.

Table 1 Number of grids and convergence of the results for a 1:14 expansion

n	Number of cells	Change in pressure drop between $n-1$ and n
1	7,000	-
2	28,000	−0.45%
3	63,000	−0.26%
4	112,000	+0.10%

Table 2 Couette coefficients obtained numerically in [7], for different values of Re. The next-to-last row shows the values found by extrapolation to Re=0. Last row shows values obtained in the present work, using $n=4$ grid refinement.

Re	R_2/R_1 = 1.5	2.0	2.6	3.0	4.0
5.0	2.07	5.60	7.44	8.05	8.76
3.5	4.31	8.11	9.99	10.5	11.2
2.0	6.62	10.7	12.7	13.2	13.9
1.0	8.20	12.5	14.5	15.1	15.8
0.5	8.99	13.4	15.5	16.1	16.8
0.0 (extrap)	9.73	14.3	16.3	16.9	17.6
present	9.48	14.2	16.4	17.3	18.7

Note that Oliveira et al. decomposed the total pressure drop Δp as

$$\Delta p=\Delta p_R+\Delta p_I+\Delta p_F, \tag{19}$$

where Δp_R is the reversible pressure *increase*, Δp_I is the irreversible pressure drop, and Δp_F is the fully-developed pressure drop obtained with Eq. (7). The reversible pressure increase corresponds to the Bernoulli effect, associated with the decrease of the velocity across the expansion. The irreversible pressure drop includes the inefficient dissipation of energy as the fluid decelerates. The excess pressure drop Δp_e used in the present study is therefore the sum of their reversible and irreversible pressure drops.

The Couette coefficients calculated using FLUIDITY ($n=4$) are plotted as a function of the diameter ratio in Fig. 6, where they are compared to the values obtained using the approximation (16), the values extrapolated to Re=0 from [7], along with the results obtained by Vrentas and Duda [6] using finite differences. The agreement between all three sets of numerical results is reasonably good. As found in [6], extrapolation of the excess pressure drop obtained for a diameter ratio of 4 to larger expansion ratios introduced little error, since the excess pressure drop has nearly

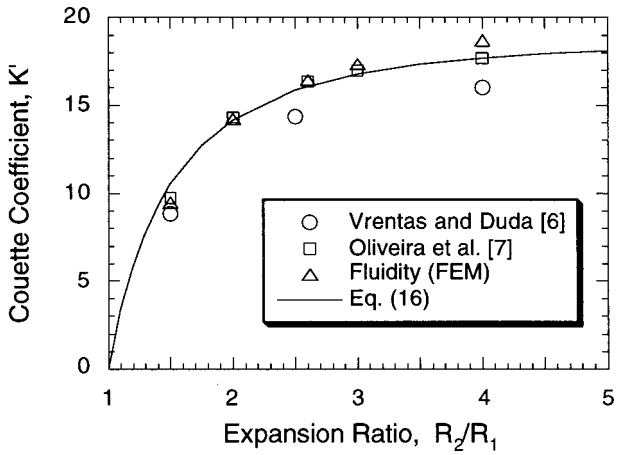

Fig. 6 Couette coefficient K' as a function of the expansion ratio

Downloaded 03 Jun 2010 to 171.66.16.150. Redistribution subject to ASME license or copyright; see http://www.asme.org/terms/Terms_Use.cfm

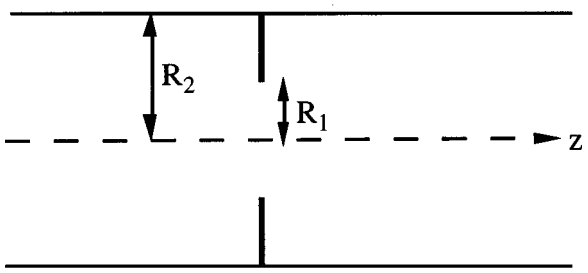

Fig. 7 Thin circular orifice in an axisymmetric tube

reached its asymptotic value of $6\pi=18.85$ when $R_2/R_1=4$. It also appears that the accuracy of Eq. (16) is best for a diameter ratio $R_2/R_1>1.5$, for which the discrepancy with the other numerical results is less than 10%. For $R_2/R_1>2$, the estimations of the Couette coefficient provided by Eq. (16) are within 5% of the results obtained with FLUIDITY or from [7].

The agreement between the results deteriorates for $R_2/R_1<1.5$. This is to be expected, as the approximation is based on the assumption that the fluid flows along the wall orthogonal to the z-axis, which is less true for expansion/contractions of small diameter ratio. However, although the *relative* error for the excess pressure drop becomes substantial for $R_2/R_1<1.5$, the excess pressure drop is so small in this case that its accurate estimation is not really of much practical interest.

The effect of a sudden expansion or contraction is in a sense equivalent to adding an additional length of tubing into the system. In order to be able to encompass the case of an infinite expansion ratio, we will quantify this in terms of an additional length of the tube having the diameter of the *smaller* tube. Assuming a Poiseuille pressure loss in this additional section of tubing, Eq. (15) allows us to express this equivalent length L_e in terms of the Couette coefficient, as follows:

$$\frac{L_e}{R_1}=\frac{K'}{32}. \tag{20}$$

For small values of the Couette coefficient, which is to say for small diameter ratios, the additional length is negligible. The *maximum* value of the equivalent length corresponds to the limiting case $R_2/R_1\to\infty$, and is given by

$$\left(\frac{L_e}{R_1}\right)_{\max}=\frac{6\pi}{32}\simeq 0.6. \tag{21}$$

The pressure drop due to a sudden contraction/expansion therefore adds, at most, an equivalent length that is barely half the radius of the smaller tube.

5 Extension to a Thin Circular Orifice in an Axisymmetric Tube

The results obtained by Dagan et al. [16] also suggest that Eq. (14) can be applied to the problem of thin orifice in an axisymmetric tube of finite radius (Fig. 7). As the phenomenon is symmetric for creeping flow, it follows from Section 2 that the excess pressure drop Δp_d due to a thin annular disk can be approximated as

$$\frac{\Delta p_d}{\rho U_1^2/2}=\frac{12\pi[1-(R_1^2/R_2^2)]}{\mathrm{Re}}. \tag{22}$$

Davis [20] studied the effect of an annular obstacle on the creeping flow in an axisymmetric tube. Using a Fredholm integral equation formulation, the value of the dimensionless pressure drop, $R_1\Delta p_d/32\mu U$, was calculated for different diameter ratios. The velocity U corresponds to the axial Poiseuille velocity far from the orifice. This allows us to compare the excess pressure drop obtained using Eq. (22) with Davis's results. Very good agreement, with less than 3% discrepancy, was obtained for R_1/R_2 lying between 0.4 and 0.6, as shown in Fig. 8. The disagreement is more significant for more extreme values of the contraction ratio. For a very slight constriction, i.e., $R_1/R_2\to 1$, the value of the excess pressure drop is, however, so small as to not be of much practical interest. For severe constrictions, e.g., a diameter ratio R_1/R_2 of 0.25, the discrepancy between the two studies is as high as 31%. However, our previous comparison with the results obtained in [7] for the same diameter ratio showed good agreement of the excess pressure drops. The results obtained by Vrentas and Duda [6] using a finite difference method also agree with Oliveira et al.'s results. Moreover, plotting the results as in Fig. 8 shows that Davis's values do *not* tend asymptotically towards Sampson's solution as $R_1/R_2\to 0$.

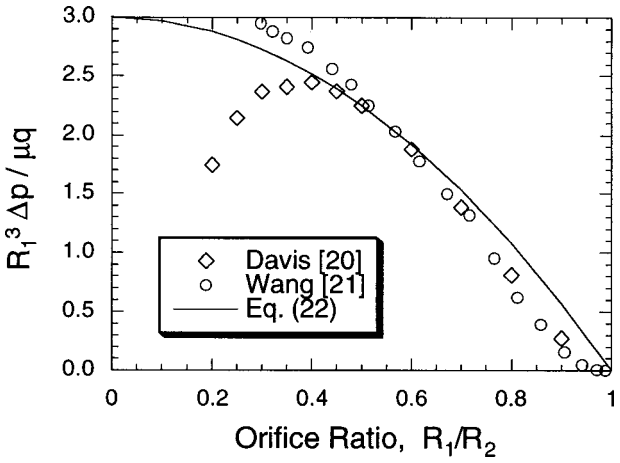

Fig. 8 Dimensionless pressure drop for a thin circular orifice in an axisymmetric tube

Flow through a thin annular disk was also studied by Wang [21], using eigenfunction expansions and a matching method; his results are also displayed in Fig. 8. Although Wang's results are difficult to extract accurately from his original curve as $R_1/R_2\to 0$, his results show clearly that the excess pressure drop tends towards Sampson's solution as $R_1/R_2\to 0$. Wang [21] also concluded that Sampson's solution was an accurate approximation for the excess pressure drop for $R_1/R_2>0.2$. The results obtained by Davis [20] for large contraction ratios therefore seem to have been corrupted by substantial numerical errors.

6 Discussion

Assuming that the excess pressure drop in the creeping regime is mainly due to friction against the wall orthogonal to the direction of the flow, an approximation [Eq. (13)] based on early work of Sampson [8] on flow through an orifice, was found for the excess pressure drop due to a sudden contraction/expansion in an axisymmetric tube. Very good agreement can be obtained with previous numerical investigations [6,7], and also with finite-element calculations using the code FLUIDITY [10], for diameter ratios larger than 2. For expansion/contraction diameter ratios less than 1.5, the approximation is less accurate. However, the additional pressure drop generated by such a slight diameter variation is probably too small to be of practical interest. The approximation for the excess pressure drop can also, to a certain extent, be used for estimating the excess pressure drop due to a thin annular disk [20,21]. This suggests that Sampson's analysis for a thin orifice in an infinite plane can be extended for flow through a sudden contraction/expansion in an axisymmetric tube. The approximation found in this study presents the advantage of being

Downloaded 03 Jun 2010 to 171.66.16.150. Redistribution subject to ASME license or copyright; see http://www.asme.org/terms/Terms_Use.cfm

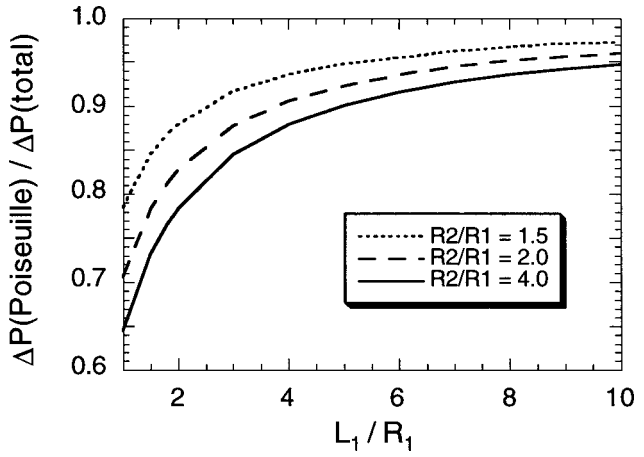

Fig. 9 Relative importance of the excess pressure drop as a function of tube length, for the case $L_1=L_2$

linked to Sampson's results, and of being simple to implement, when compared to existing correlations [7] or to computationally extensive methods such as finite-elements.

As mentioned in Section 3.2, the additional pressure drop generated by the sudden expansion/contraction represents a small percentage of the total pressure drop. However, this result is due to the lengths of tubing considered. Using the concept of ''excess momentum loss factor'' introduced by Azzam and Dullien [22], we consider the ratio β defined as

$$\beta = \frac{\Delta p_{HP}}{\Delta p_{1\to 2}}, \tag{23}$$

where Δp_{HP} is the Poiseuille loss along the two tubes of lengths L_1 and L_2. For simplicity, the particular case $L_1=L_2$ was considered and the value of β was calculated for various diameter ratios and lengths of tubing, L_1. The value of $\Delta p_{1\to 2}$ was calculated using Eq. (7) for various diameter ratios, and the excess pressure drop was calculated using the approximation (13). As the length of the tube decreases, the ratio β decreases, as shown in Fig. 9. For a given diameter ratio, the excess pressure drop can represent less than 5%, or more than 30%, of the total pressure drop, depending on the length of the tubes considered. This result is in agreement with the numerical results of Azzam and Dullien [22]. This discussion is also closely related to the notion of equivalent length introduced in Section 4. Obviously, the equivalent length added by the excess pressure drop becomes more substantial when the tubes considered are short. This equivalent length was, however, found to be at most barely half than the radius of the smaller tube.

No comparison to experimental results was performed, owing to the discrepancies between existing experimental studies. Some experimental studies found an excess pressure drop [3-5] that was much higher (by up to one order of magnitude) than predicted by numerical and theoretical studies, and it is difficult to explain this discrepancy without questioning the reliability of these experimental studies. Nevertheless, the pressure drop measurements performed by Young et al. [23] for contraction in arteries, and also the experimental results obtained in [22], indicate no excessive additional pressure drop due to contraction or expansion. The data presented in these two studies do not, however, allow a sufficiently accurate estimation of the excess pressure drop for a proper comparison with the present study. Further experimental investigations need to be conducted at very low Reynolds number in order to resolve the existing disagreements. However, the stability of the flow necessary for the pressure measurements requires a long system of tubing for the flow to recover a parabolic Poiseuille profile after the expansion/contraction. This makes an accurate measurement of the excess pressure drop very difficult, as its contribution to the total pressure drop becomes smaller, as shown in Fig. 9.

Acknowledgments

The authors thank J. S. Vrentas of Pennsylvania State University, and P. J. Oliveira of the University of Beira Interior (Portugal), for helpful discussions of this problem.

References

[1] Hammad, K. J., Volkan Ötügen, M., Vradis, G. C., and Arik, E. B., 1999, ''Laminar Flow of a Nonlinear Viscoplastic Fluid through an Axisymmetric Sudden Expansion,'' ASME J. Fluids Eng., **121**, pp. 488–495.
[2] Stielmeier, M., Tropea, C., Weiser, N., and Nitsche, W., 1989, ''Experimental Investigation of the Flow through Axisymmetric Expansions,'' ASME J. Fluids Eng., **111**, pp. 464–471.
[3] Astarita, G., and Greco, G., 1968, ''Excess Pressure Drop in Laminar Flow through Sudden Contraction,'' Ind. Eng. Chem. Fundam., **7**, pp. 27–31.
[4] Sylvester, N. D., and Rosen, S. L., 1970, ''Laminar Flow in the Entrance Region of a Cylindrical Tube,'' AIChE J., **16**, pp. 964–972.
[5] Edwards, M. F., Jadallah, M. S. M., and Smith, R., 1985, ''Head Losses in Pipe Fittings at Low Reynolds Numbers,'' Chem. Eng. Res. Des., **63**, pp. 43–50.
[6] Vrentas, J. S., and Duda, J. L., 1973, ''Flow of a Newtonian Fluid through a Sudden Contraction,'' Appl. Sci. Res., **28**, pp. 241–260.
[7] Oliveira, P. J., Pinho, F. T., and Schulte, A., 1998, ''A General Correlation for the Local Loss Coefficients in Newtonian Axisymmetric Sudden Expansions,'' Int. J. Heat Fluid Flow, **19**, pp. 655–660.
[8] Sampson, R. A., 1891, ''On Stokes's Current Flow,'' Philos. Trans. R. Soc. London, Ser. A, **182**, pp. 449–518.
[9] Weissberg, H. L., 1962, ''End Correction for Slow Viscous Flow through Long Tubes,'' Phys. Fluids, **5**, pp. 1033–1036.
[10] Pain, C. C., 2000, ''Brief Description and Capabilities of the General Purpose CFD Code FLUIDITY,'' Internal Report, Imperial College of Science, Technology and Medicine, London.
[11] Ioannidis, M., and Chatzis, I., 1993, ''Network Modeling of Pore Structure and Transport Properties of Porous Media,'' Chem. Eng. Sci., **48**, pp. 951–972.
[12] Sigli, D., and Monnet, P., 1982, ''Some New Aspects of the Slow Flow of a Viscous Fluid through an Axisymmetric Duct Expansion or Contraction. I–Numerical Part,'' Appl. Sci. Res., **39**, pp. 215–232.
[13] Roscoe, R., 1949, ''The Flow of Viscous Fluids around Plane Obstacle,'' Philos. Mag., **40**, pp. 338–351.
[14] Happel, J., and Brenner, H., 1986, *Low Reynolds Number Hydrodynamics*, Martinus Nijhoff, Dordrecht.
[15] Johansen, F. C., 1930, ''Flow through Pipe Orifice at Low Reynolds Numbers,'' Proc. R. Soc. London, Ser. A, **126**, pp. 231–245.
[16] Dagan, Z., Weinbaum, S., and Pfeffer, R., 1982, ''An Infinite-Series Solution for the Creeping Motion through an Orifice of Finite Length,'' J. Fluid Mech., **115**, pp. 505–523.
[17] Sisavath, S., Jing, X. D., and Zimmerman, R. W., 2001, ''Laminar Flow through Irregularly-Shaped Pores in Sedimentary Rocks,'' Transp. Porous Media, **45**, pp. 41–62.
[18] de Oliveira, C. R. E., 2000, ''GEM: A Finite Element Mesh Generator and Data Preparation Program for Radiation Transport Codes,'' Internal Report, Imperial College of Science, Technology and Medicine, London.
[19] Oliveira, P. J., and Pinho, F. T., 1997, ''Pressure Drop Coefficient of Laminar Newtonian Flow in Axisymmetric Sudden Expansions,'' Int. J. Heat Fluid Flow, **18**, pp. 518–529.
[20] Davis, A. M. J., 1991, ''Creeping Flow through an Annular Stenosis in a Pipe,'' Q. Appl. Math., **49**, pp. 507–520.
[21] Wang, C. Y., 1996, ''Stokes Flow through a Tube with Annular Fins,'' Eur. J. Mech. B **15**, pp. 781–789.
[22] Azzam, M. I. S., and Dullien, F. A. L., 1977, ''Flow in Tubes with Periodic Step Changes in Diameter: a Numerical Solution,'' Chem. Eng. Sci., **32**, pp. 1445–1455.
[23] Young, D. F., Cholvin, N. R., and Roth, A. C., 1975, ''Pressure Drop across Artificially Induced Stenoses in the Femoral Arteries of Dogs,'' Circ. Res., **36**, pp. 735–743.

Downloaded 03 Jun 2010 to 171.66.16.150. Redistribution subject to ASME license or copyright; see http://www.asme.org/terms/Terms_Use.cfm

Journal of Fluids Engineering

Technical Briefs

Normal Stresses on the Surface of a Rigid Body in an Oldroyd-B Fluid

N. A. Patankar
Assistant Professor, Department of Mechanical Engineering, Northwestern University, IL 60208

P. Y. Huang
Postdoctoral Researcher

D. D. Joseph
Russell J. Penrose Professor

Department of Aerospace Engineering and Mechanics, University of Minnesota, MN 55455

H. H. Hu
Associate Professor, Department of Mechanical Engineering and Applied Mechanics, University of Pennsylvania, PA 19104

In this note we present a proof showing that the contribution from the extra stress tensor to the normal component of the stress on the surface of a moving rigid body in an incompressible Oldroyd-B fluid is zero. [DOI: 10.1115/1.1436095]

Introduction

A proof showing that the contribution from the extra stress tensor to the component of stress normal to the surface of a rigid body, in an incompressible Oldroyd-B fluid, is zero was briefly proposed by Huang et al. [1]. In this note we present a more complete proof based on the property of frame indifference of the constitutive equation of an Oldroyd-B fluid.

Consider a rigid body moving with some translational velocity $\mathbf{V}$ and angular velocity $\mathbf{\Omega}$ in an incompressible Oldroyd-B fluid at time t. The stress $\boldsymbol{\sigma}$ at a point in the fluid is given by

$$\sigma = -p\mathbf{I} + \mathbf{T} \tag{1}$$

where p is the pressure, $\mathbf{I}$ is the identity tensor and $\mathbf{T}$ is the extra-stress tensor. For an Oldroyd-B fluid the extra-stress is given by the following constitutive equation

$$\mathbf{T} + \lambda_1 \overset{\nabla}{\mathbf{T}} = \eta\left(\mathbf{A} + \lambda_2 \overset{\nabla}{\mathbf{A}}\right) \tag{2}$$

Contributed by the Fluids Engineering Division of THE AMERICAN SOCIETY OF MECHANICAL ENGINEERS. Manuscript received by the Fluids Engineering Division March 11, 2001; revised manuscript received August 23, 2001. Associate Editor: J. Marshall.

where $\mathbf{A} = (\nabla\mathbf{u} + \nabla\mathbf{u}^{\mathrm{T}})$ is the rate-of-deformation tensor, η is the viscosity, λ_1 is the relaxation time and λ_2 is the retardation time. Hats on the stress and rate-of-deformation tensors denote the upper-convected time derivative.

One of the main axioms of mechanics is the requirement that material response be independent of the observer. This is the condition of frame indifference or material objectivity. The extra-stress tensor $\mathbf{T}$ is frame indifferent if during any change in observer it transforms according to (Gurtin [2])

$$\mathbf{T}^* = \mathbf{Q}\mathbf{T}\mathbf{Q}^{\mathrm{T}} \tag{3}$$

where $\mathbf{T}$ and $\mathbf{T}^*$ are the extra-stress tensors with respect to the two observers, say unstarred and starred, respectively. $\mathbf{Q}(t)$ is a rotation tensor which transforms the starred axes to the unstarred axes. It can be verified that the constitutive equation for $\mathbf{T}$, given in (2), satisfies the condition of frame indifference given by (3) (Bird [3]). Hence, observers in different frames of reference should conclude the same about the state of extra stress at any point in an Oldroyd-B fluid. We therefore choose a frame of reference translating and rotating with the rigid body in order to study the state of stress on its surface. The rigid body is stationary with respect to this moving frame.

Define an orthogonal curvilinear coordinate system (ξ_1, ξ_2, ξ_3) such that the coordinates ξ_1 and ξ_2 are along the surface of the stationary rigid body and ξ_3 is normal to the surface. Let the origin be at any point of interest on the surface of the rigid body. We assume that the surface of the rigid body is smooth so that the normal and tangent directions can be defined. By the no-slip condition, the fluid velocity on the surface of the rigid body is zero ($\mathbf{u} = \mathbf{0}$). The no-slip condition also implies

$$\frac{\partial \mathbf{u}}{\partial \xi_1} = \mathbf{0} \quad \text{and} \quad \frac{\partial \mathbf{u}}{\partial \xi_2} = \mathbf{0} \tag{4}$$

at any point on the surface. Let u_1, u_2, u_3 be the components of velocity in each of the coordinate directions ξ_1, ξ_2, ξ_3, respectively. The no-slip condition and the divergence-free constraint for the velocity together imply that

$$\frac{\partial u_3}{\partial \xi_3} = 0 \tag{5}$$

Due to the no-slip condition and (5) the velocity gradient tensor $\mathbf{L}$ at any given point on a rigid body becomes

$$\mathbf{L} = \begin{bmatrix} 0 & 0 & \dfrac{1}{h_3}\dfrac{\partial u_1}{\partial \xi_3} \\ 0 & 0 & \dfrac{1}{h_3}\dfrac{\partial u_2}{\partial \xi_3} \\ 0 & 0 & 0 \end{bmatrix} = \begin{bmatrix} 0 & 0 & L_{13} \\ 0 & 0 & L_{23} \\ 0 & 0 & 0 \end{bmatrix} \tag{6}$$

where h_3 is a scale factor for the curvilinear coordinate ξ_3 and the orthogonal bases are along the three coordinate directions, respectively. The extra-stress tensor is

$$\mathbf{T} = \begin{bmatrix} T_{11} & T_{12} & T_{13} \\ T_{12} & T_{22} & T_{23} \\ T_{13} & T_{23} & T_{33} \end{bmatrix} \tag{7}$$

 Copyright © 2002 by ASME

Downloaded 03 Jun 2010 to 171.66.16.150. Redistribution subject to ASME license or copyright; see http://www.asme.org/terms/Terms_Use.cfm

Using the no-slip condition, (6) and (7), the constitutive equation can be written as

$$\begin{bmatrix} T_{11} & T_{12} & T_{13} \\ T_{12} & T_{22} & T_{23} \\ T_{13} & T_{23} & T_{33} \end{bmatrix} + \lambda_1 \left(\frac{\partial}{\partial t} \begin{bmatrix} T_{11} & T_{12} & T_{13} \\ T_{12} & T_{22} & T_{23} \\ T_{13} & T_{23} & T_{33} \end{bmatrix} - \begin{bmatrix} 2L_{13}T_{13} & L_{13}T_{23}+L_{23}T_{13} & L_{13}T_{33} \\ L_{13}T_{23}+L_{23}T_{13} & 2L_{23}T_{23} & L_{23}T_{33} \\ L_{13}T_{33} & L_{23}T_{33} & 0 \end{bmatrix} \right) = \eta \begin{bmatrix} 0 & 0 & L_{13} \\ 0 & 0 & L_{23} \\ L_{13} & L_{23} & 0 \end{bmatrix} + \eta\lambda_2 \left(\frac{\partial}{\partial t} \begin{bmatrix} 0 & 0 & L_{13} \\ 0 & 0 & L_{23} \\ L_{13} & L_{23} & 0 \end{bmatrix} - \begin{bmatrix} 2L_{13}^2 & 2L_{13}L_{23} & 0 \\ 2L_{13}L_{23} & 2L_{23}^2 & 0 \\ 0 & 0 & 0 \end{bmatrix} \right) \tag{8}$$

The equation for the normal component of the extra stress on the surface of the rigid body is given by

$$T_{33} + \lambda_1 \frac{\partial T_{33}}{\partial t} = 0 \tag{9}$$

This equation represents a linear initial value problem for T_{33}. $T_{33}=0$ at all times, if its value at the initial instant is zero. For any nonzero initial value, T_{33} will exponentially decay to zero with a time constant equal to λ_1.

At a given instant, the value of the normal component of extra stress on the rigid surface, with respect to an observer in any other frame of reference, can be calculated using (3). Let $\mathbf{n}^*$ denote a unit normal vector on the surface of the rigid body at a given point with respect to a new observer and $\mathbf{n}$ denote a unit normal at the same point with respect to an observer moving with the body. The two normal vectors are related by

$$\mathbf{n}^* = \mathbf{Q}\mathbf{n} \tag{10}$$

where $\mathbf{Q}$ is the rotation tensor. Let $\mathbf{T}^*$ be the extra stress tensor with respect to the new observer. The normal component of extra stress with respect to the new observer is given by

$$T_N^* = \mathbf{n}^*\mathbf{T}^*\mathbf{n}^* \tag{11}$$

Using (3), (10) and the fact that tensor $\mathbf{Q}$ is orthogonal and preserves inner products

$$T_N^* = \mathbf{Q}\mathbf{n}\mathbf{Q}\mathbf{T}\mathbf{n} = \mathbf{n}\mathbf{T}\mathbf{n} = T_{33}. \tag{12}$$

Thus we see that the value of the normal component of extra stress in any frame is the same as that inferred by an observer moving with the body.

The above results can also be proved using the Oldroyd-B model in its integral form. The well-known result that the normal component of extra stress on a rigid surface in an incompressible Newtonian fluid is zero can be obtained as a special case of (8). Consider any incompressible fluid with the constitutive model of the following form

$$a_1\mathbf{A} + a_2\overset{\nabla}{\mathbf{A}} + a_3\mathbf{T} + a_4\overset{\nabla}{\mathbf{T}} = \mathbf{0} \tag{13}$$

where a_1, a_2, a_3, and a_4 are constants or some scalar functions of the invariants of $\mathbf{A}$ and $\mathbf{T}$. All such fluids will have a zero normal component of extra stress on a rigid body surface. This is because these models will give rise to a homogeneous equation for T_{33} on the surface of a rigid body similar to the one obtained for the Oldroyd-B fluid. The consequence of zero normal component of extra stress on the rigid surface is that the normal force acting on a solid boundary in such fluids is caused only by pressure, where the pressure is as defined in (1).

Caswell [4] had considered the kinematics and state of stress on a surface at rest. He assumed a general form of the constitutive equation for viscoelastic fluids and arrived at several conclusions regarding the state of stress on a surface at rest. His results when applied to Oldroyd-B fluids in contact with moving surfaces would lead to the same conclusion as ours. This note is an attempt to propose another method to derive the result. The forms of the equations obtained in deriving the result have direct relevance to the forms of equations encountered in the simulation of moving particles in Oldroyd-B fluids [1]. We have frequently used the above result to validate our codes for moving particles in Oldroyd-B fluids [5].

Acknowledgment

We acknowledge the support from NSF under the KDI/NCC grant NSF/CTS-98-73236. NAP acknowledges the support from Northwestern University through the startup funds.

References

[1] Huang, P. Y., Hu, H. H., and Joseph, D. D., 1998, "Direct Simulation of the Sedimentation of Elliptic Particles in Oldroyd-B Fluids," J. Fluid Mech., **362**, pp. 297–325.

[2] Gurtin, M. E., 1981, *An Introduction to Continuum Mechanics*, Academic Press, San Diego.

[3] Bird, R. B., Armstrong, R. C., and Hassager, O., 1987, *Dynamics of Polymeric Liquids*, Vol. 1, Wiley-Interscience, New York.

[4] Caswell, B., 1967, "Kinematics and Stress on a Surface of Rest," Arch. Ration. Mech. Anal., **26**, pp. 385–399.

[5] Hu, H. H., Patankar, N. A., and Zhu, M. Y., 2001, "Direct Numerical Simulations of Fluid-Solid Systems using the Arbitrary-Lagrangian-Eulerian Technique," J. Comput. Phys., **169**, pp. 427–462.

Total Unsteadiness Downstream of an Axial Flow Fan With Variable Pitch Blades

Sandra Velarde-Suárez
Associate Professor

Rafael Ballesteros-Tajadura
Associate Professor
e-mail: rballest@correo.uniovi.es

Carlos Santolaria-Morros
Professor

Eduardo Blanco-Marigorta
Associate Professor

Universidad de Oviedo, Área de Mecánica de Fluidos,
Campus de Viesques, 33271 Gijón, Asturias,
Spain

Variable pitch axial flow fans are widely used in industrial applications to satisfy variable operating conditions. The change of the blade pitch leads to a different rotor geometry and has a major influence on the unsteady operation of the machine. In this work, an experimental research on an axial flow fan with variable pitch blades has been carried out. First of all, the fan performance curves has been obtained. Then the flow field has been measured at ten radial locations both at the inlet and exit rotor plane using hot wire anemometry. Velocity components and total unsteadiness were determined and analyzed in order to characterize the influence of pitch blade and operating conditions on the flow structure.

[DOI: 10.1115/1.1427926]

Contributed by the Fluids Engineering Division of THE AMERICAN SOCIETY OF MECHANICAL ENGINEERS. Manuscript received by the Fluids Engineering Division November 3, 2000; revised manuscript received September 10, 2001. Associate Editor: Y. Tsujimoto.

Copyright © 2002 by ASME

Downloaded 03 Jun 2010 to 171.66.16.150. Redistribution subject to ASME license or copyright; see http://www.asme.org/terms/Terms_Use.cfm

Introduction

In recent years, much research effort has been concerned with the study of the unsteadiness generated in axial flow turbomachinery. Some researchers have shown encouraging results and provided useful data for further study [1–3]. Despite a number of experimental and computational efforts in studying the unsteady phenomena in axial compressors, in the literature there are few relevant works regarding flow unsteadiness in axial fans.

Many industrial ventilation systems require a wide operating range. One of the most efficient methods to fulfill the regulation purpose in axial flow fans is to provide variable pitch blades [4,5]. However, the aerodynamic behavior of the fan changes in such a way that the stall margin is modified and the maximum efficiency is reduced. The pitch variation implies that the blade geometry is not as well adapted to the resulting flow as in the design setting. This situation modifies not only the mean flow field but the unsteady flow pattern characteristics.

In this work, an experimental research on an axial flow fan with variable pitch blades has been carried out. First, the fan performance curves have been obtained. Then the flow field has been measured at ten radial locations at the rotor exit using hot wire anemometry. Velocity components and total unsteadiness were determined and analyzed in order to characterize the influence of pitch blade and operating conditions on the flow structure.

Fan Performance

The fan analyzed is an eight-blade rotor based on the NACA-65 family, and designed in order to provide a free vortex distribution of the absolute tangential velocity component. The rotor has a 600 mm tip diameter and a 380 mm hub diameter. The tip clearance is 2% of the blade height. Other relevant data are listed in Table 1. In this paper blade pitch refers to the blade setting (i.e., a fixed angular position of the blade) at the hub. The rotor has the possibility of manually changing the blade pitch. In all the subsequent experiments, the rotational speed was 3000 rpm.

Figure 1 represents total to total pressure coefficient $\psi=(P_2-P_1)/(0.5\rho U_t^2)$ and efficiency against the flow coefficient $\varphi=V_m/U_t$ for three blade pitches: 52.5, 48, and 57 deg (with respect to the tangential direction), which correspond to the design geometry (“Nom.” in the figures) and variations of −4.5 and 4.5 deg, respectively (“Nom.−4.5 deg” and “Nom.+4.5 deg” in the figures). The uncertainty has been estimated in ±2% for the flow rate and ±1.4% for the total pressure. This figure shows how either the pressure and the flow rate increase as the blade pitch increases. The design geometry provides the highest efficiency, showing a little reduction as the blade pitch is modified, and we can work in the enveloping curve of all the efficiency curves. Using this regulation method, an important increment on the operative range of flow rates is obtained. The maximum efficiency values obtained (slightly higher than 80%) are typical for this kind of machines. The relatively large tip clearance (2% of blade height), needed to permit blade movements, could be the origin of efficiency losses up to 2% [6].

Table 1 Rotor blade characteristics (design)

R (m)	Solidity	Pitch (Deg.)	Camber (Deg.)	Thickness (% relative to chord)
0.19	1.052	52.50	42.97	12.0
0.20	0.989	47.68	36.80	10.5
0.21	0.934	43.50	32.00	9.2
0.22	0.884	39.79	27.80	8.1
0.23	0.838	36.82	25.20	7.3
0.24	0.796	34.28	23.30	6.6
0.25	0.760	32.18	21.80	6.1
0.26	0.726	30.28	20.70	5.8
0.27	0.694	28.82	19.80	5.5
0.28	0.665	28.00	19.20	5.2
0.29	0.639	27.58	18.85	5.1
0.30	0.615	27.40	18.66	5.0

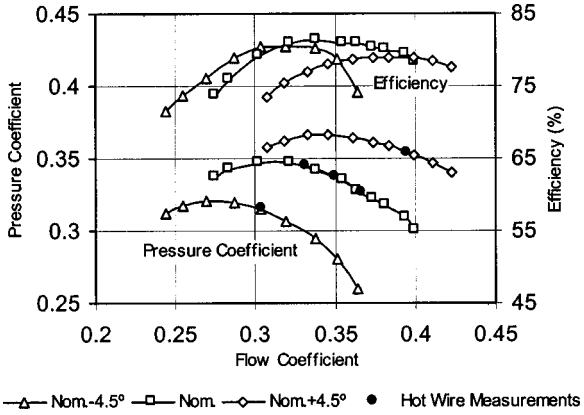

Fig. 1 Fan performance curves

Flow Field Measurements

Hot wire techniques were used in order to measure the velocity field at rotor exit. Details of the measurement procedure, calibra-

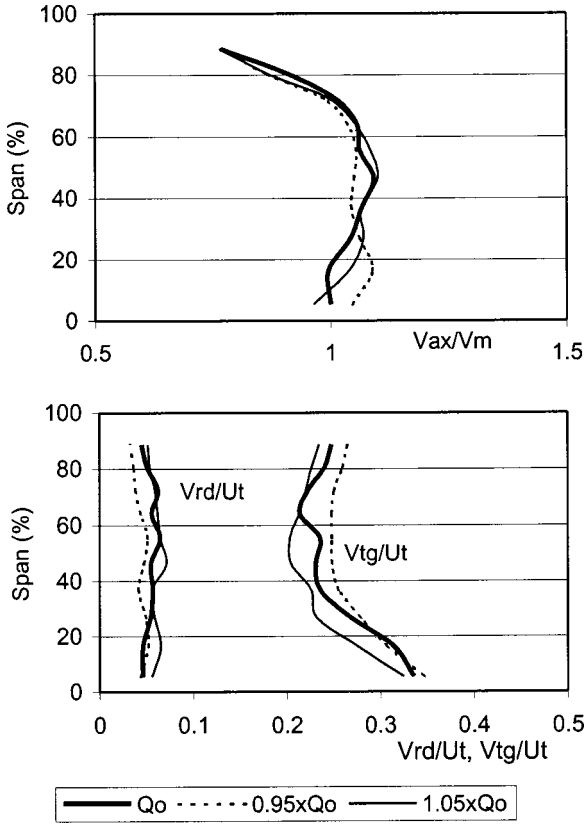

Fig. 2 Radial distribution of the velocity components at rotor exit (design pitch angle)

Downloaded 03 Jun 2010 to 171.66.16.150. Redistribution subject to ASME license or copyright; see http://www.asme.org/terms/Terms_Use.cfm

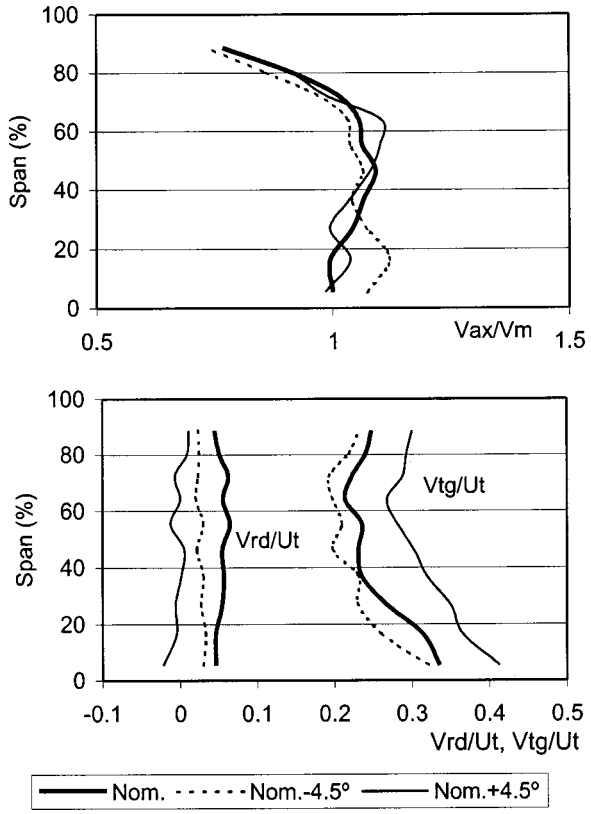

Fig. 3 Radial distribution of the velocity components at rotor exit (best efficiency point)

tion, and uncertainties have been published in [7,8]. The probe uncertainty has been estimated in 1 deg in the center of the measurement range and 3 deg at the borders. The uncertainty of the absolute velocity value has been estimated in 1.7% in the center and up to 5% near the borders. The flow field measurements have been taken for the best efficiency point (Qo) of each blade pitch tested, and for a lower and higher flow rate: $0.95\times Q$o and $1.05\times Q$o. The measurement plane is 142 mm downstream the blade axis.

Figures 2 and 3 show the radial distributions of the velocity components at rotor exit for the three operating points and pitch blade angles reported above. The axial component has been normalized with respect to the mean axial velocity V_m in each par-

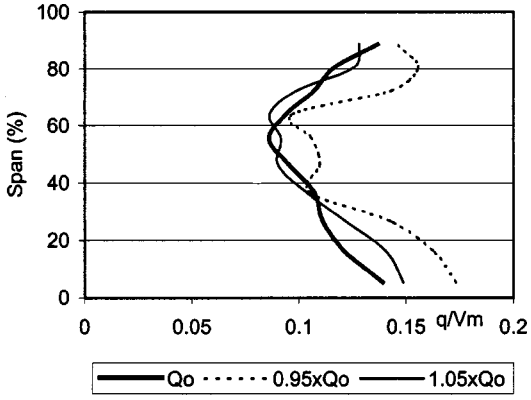

Fig. 4 Radial distribution of the total unsteadiness parameter at rotor exit (design pitch angle)

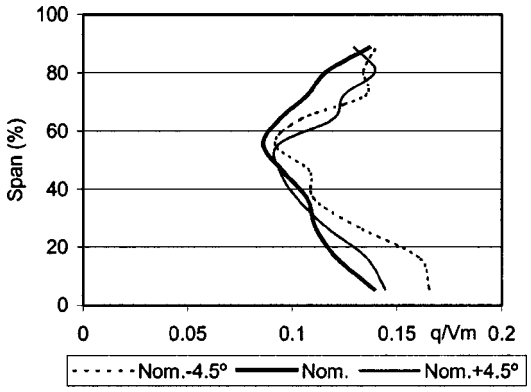

Fig. 5 Radial distribution of the total unsteadiness parameter at rotor exit (best efficiency point)

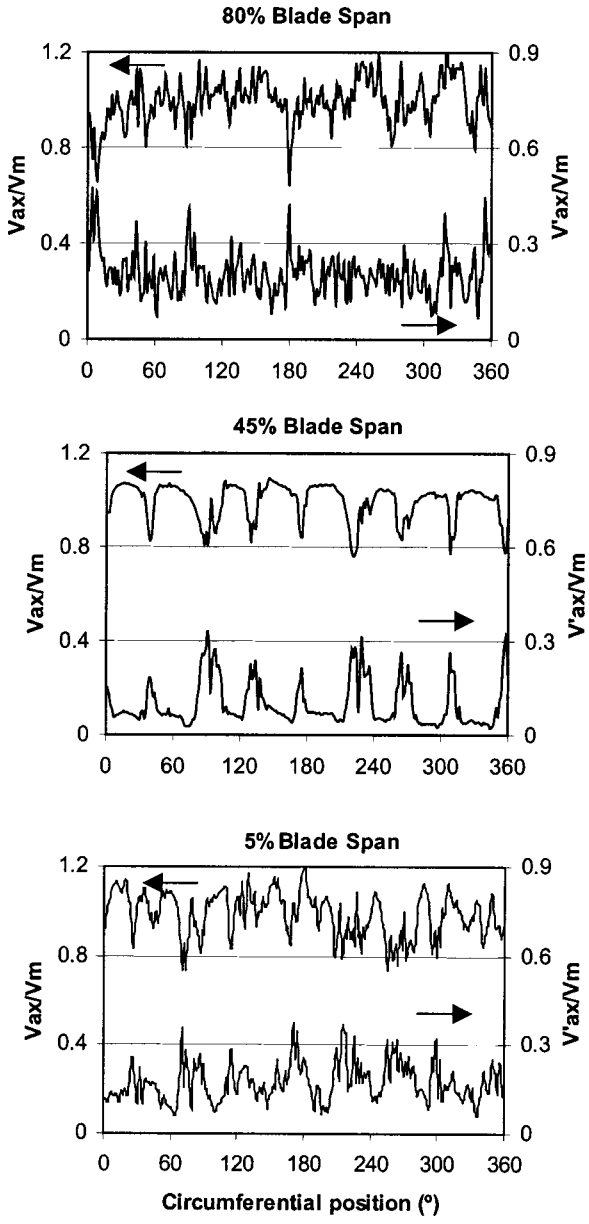

Fig. 6 Blade-to-blade distribution of the axial component of velocity and phase-locked total unsteadiness at rotor exit (nominal pitch blade angle, best efficiency point)

Downloaded 03 Jun 2010 to 171.66.16.150. Redistribution subject to ASME license or copyright; see http://www.asme.org/terms/Terms_Use.cfm

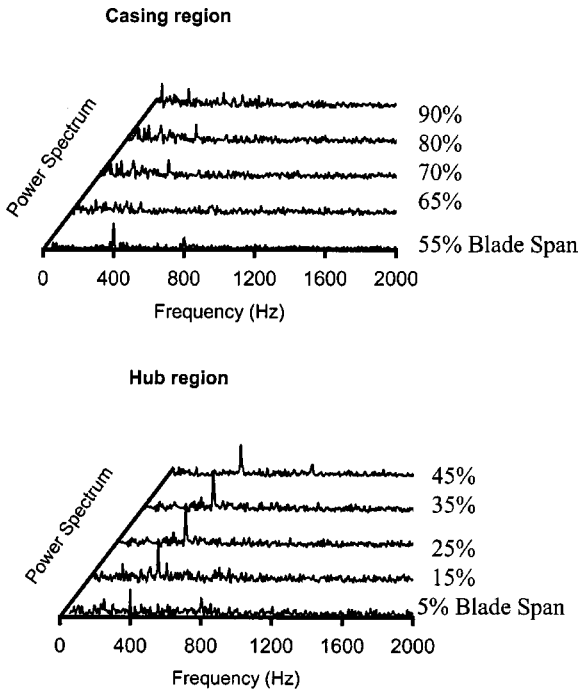

Fig. 7 Power spectra of the axial component of velocity fluctuation at rotor exit (Nom. −4.5 deg, best efficiency point)

ticular test condition, and the radial and tangential components with respect to the tip blade velocity, U_t. The axial component is quite uniform except in the tip region. The tangential component decreases from hub to mid-span, presenting a free vortex distribution modified by the blockage in the casing viscous region.

Figures 4 and 5 represent the radial distributions at rotor exit of the total unsteadiness parameter q divided by V_m, where q is defined as:

$$q = \frac{\sqrt{V'^2_{ax} + V'^2_{tg} + V'^2_{rd}}}{2} \tag{1}$$

and V'_{ax}, V'_{tg}, and V'_{rd} are the axial, tangential, and radial rms fluctuating velocity components. Generally speaking, total unsteadiness formation is mainly caused by real turbulence and flow perturbations generated by the rotor wake velocity deficit. In addition, unsteadiness due to vortex shedding, sawing movements of tip leakage vortices, fluttering of separated flows, and unsteadiness of separation points may also contributed to the total unsteadiness [1]. The analysis of blade-to-blade distribution of total unsteadiness and power spectra of velocity fluctuation allows differentiating the wake velocity deficit effect from other small-scale fluctuations due to the above mentioned phenomena.

In Figs. 4 and 5 high levels of total unsteadiness appear in the hub and casing regions. The lowest levels correspond to the nominal pitch angle and the best efficiency point. The unsteadiness flow pattern shown presents very similar characteristics to the results obtained from axial compressors in Refs. [1–3].

Figure 6 represents the blade-to-blade distribution of the axial velocity component and total unsteadiness at three spanwise locations of the rotor exit, for the nominal pitch blade angle and the best efficiency point. At midspan the axial component of velocity presents a clear jet-wake structure with high levels of unsteadiness in the blade wakes. At the hub region, this structure is not so clear and the zone with high levels of unsteadiness at the wakes is wider. At the casing region, the periodic structure of the flow is masked by small-scale fluctuations, and high levels of unsteadiness appear in all the blade pitch, not only in the blade wakes.

The power spectra of axial component of velocity fluctuation at rotor exit for the Nom.−4.5 deg pitch blade and best efficiency point are shown in Fig. 7. Although noise spectra from this kind of fans frequently exhibit strong second harmonics, these velocity spectra show a little harmonic structure. The power spectra at midspan contain relatively large-scale systematic unsteadiness which originates within blade wakes (note that the blade passing frequency is 400 Hz). The power spectrum increases gradually toward the hub and blade passing frequency is noticeable very close to the hub surface. On the other hand, within the casing region high levels of unsteadiness at the low frequency range below the blade passing frequency are observed. These levels are possibly created by the unstable tip leakage vortices. The blade passing frequency is partially masked by the small-scale unsteadiness.

Further investigations are still needed to clarify the influence of the stator on the propagation of all this unsteadiness and how far downstream do these effects persist.

Conclusions

The performance and flow characteristics of an axial fan with variable pitch blades have been analyzed. The variation of the blade pitch has proved to be a good regulation method, which provides a valuable increase on the range of operation while the maximum efficiency does not experience a significant reduction with respect to the nominal geometry.

High levels of total unsteadiness have been observed at the hub and casing regions. These levels were higher for off-design operating conditions and pitch blade angles different from the nominal one.

At midspan the flow field contains relatively large-scale systematic unsteadiness, which originates within the blade wakes. In the hub region, this periodic effect is also noticeable and low levels of small-scale fluctuations appear. The high levels of unsteadiness observed near the casing mainly consist of unstable tip leakage vortices and small-scale turbulence inside the casing viscous region.

Acknowledgments

This work was supported by the Research Project "Modelado del comportamiento del flujo no estacionario subsónico en la interacción entre haces fijos y móviles de turbomáquinas axiales," Ref. DPI2000-0702-C02-01, CICYT, Spain.

References

[1] Goto, A., 1992, "Three-dimensional flow and mixing in an axial flow compressor with different rotor tip clearances," ASME J. Turbomach., **114**, pp. 675–685.
[2] Moore, J., and Moore, J. G., 1998, "Turbulence energy and spectra downstream of an axial compressor rotor," AIAA Paper No. 98-2550.
[3] Liu, B., Moore, J. G., and Moore, J., 1998, "Total unsteadiness downstream of an axial compressor rotor," AIAA Paper No. 98-0967.
[4] Marples, J., "A Discussion of Fan Air Quantity Control with Particular Respect to Axial Flow Fans and Variable Pitch Mechanisms," Proceedings of the BHRA International Conference on Fan Design & Applications, paper K2, pp. 445–459, Guilford, England, 1982.
[5] O'Neill, A. C., "Variable Pitch Axial Flow Fans," Proceedings of the BHRA International Conference on Fan Design & Applications, paper K3, pp. 461–499, Guilford, England, 1982.
[6] Wallis, R. A., 1993, *Axial Flow Fans and Ducts*, Krieger Publishing Company, Malabar, Florida.
[7] Ballesteros, R., Blanco, E., and Santolaria, C., 1995, "Blade Pitch Influence at the Exit Flow Field of an Axial Flow Fan," ASME Paper No. 95-GT-191.
[8] Blanco, E., Ballesteros, R., and Santolaria, C., 1998, "Angular range and uncertainty analysis of non-orthogonal crossed hot wire probes," ASME J. Fluids Eng., **120**, pp. 90–94.

Downloaded 03 Jun 2010 to 171.66.16.150. Redistribution subject to ASME license or copyright; see http://www.asme.org/terms/Terms_Use.cfm

Comparison of the Numerical and Experimental Flowfield Downstream of a Plate Array

D. W. Guillaume
Department of Mechanical Engineering, California State University, Los Angeles, Los Angeles, CA 90032

J. C. LaRue
Department of Mechanical and Aerospace Engineering, University of California, Irvine, Irvine, CA 92697

The findings of a numerical solution of the flowfield downstream of a six-plate array are compared to a previous experimental study. In both studies, the chord-to-thickness ratio, c/t, is 6.67, the Reynolds number, Re, is 500, and the spacing-to-thickness ratio, H/t, is 3.67. Consistent with experimental results, the numerical simulation shows that the recirculation zones formed at the trailing edges of the surfaces that form channels in the plate array are in-phase. Also consistent, they are nearly 180 deg out-of-phase with the recirculation zones formed at the trailing edges of the surfaces of adjacent channels. Comparison of the locations of recirculation zones and peaks in the downstream variation in axial velocity confirms that "vortex pumping" is described by 1) the axial velocity increase on the midplane of the channel in the region where the separation between pairs of recirculation zones is a minimum and 2) the axial velocity decrease in the region where the separation between pairs of recirculation zones is a maximum. [DOI: 10.1115/1.1436094]

Introduction

Arrays of vanes—flat or curved—are commonly used to condition flow fields. Examples include turning vanes in ducts and swirl vanes in gas turbine combustors. In addition to controlling the flow, vanes also generate large scale vortical structures that affect the flow field.

There is a dearth of reported studies on the effects of plate arrays on a flowfield. The studies that are available typically focus on the phenomenon called ''flopping'' which is the spontaneous change in relative base pressure and wake size behind an individual plate in the array. For example, Hayashi et al. [1] study flopping using two-, three-, and four-plate arrays with $0.014 \leqslant c/t \leqslant 0.114$, where c/t is the plate chord-to-thickness ratio, and $6\times10^3 \leqslant \mathrm{Re}_c \leqslant 1.9\times10^4$, where the characteristic length is the chord, and with plate-separation to plate-thickness ratios, H/t, of $0 \leqslant H/t \leqslant 3.75$. They find flopping to occur with the two-plate array only when $H/t=2.75$. For the two-plate arrays with $H/t \neq 2.75$ they find that some plates have wide wakes and others exhibit narrow wakes downstream from their trailing. This pattern of wide and narrow wakes is called ''quasi-stable'' (Guillaume and LaRue [2]).

Miau et al. [3,4] study the flow downstream of two-plate arrays with $1.4 \leqslant H/t \leqslant 3.0$, $c/t=0.150$, and $1.3\times10^3 \leqslant \mathrm{Re} \leqslant 1.2\times10^4$. They find flopping for $1.5 \leqslant H/t \leqslant 1.85$ with $1.3\times10^3 \leqslant \mathrm{Re} \leqslant 1.2\times10^4$ and quasi-stable wake behavior for $1.85 \leqslant H/t < 2.6$, but stable wakes for $H/t > 2.6$.

Contributed by the Fluids Engineering Division of THE AMERICAN SOCIETY OF MECHANICAL ENGINEERS. Manuscript received by the Fluids Engineering Division January 9, 2001; revised manuscript received October 15, 2001. Associate Editor: I. Celik.

In summary, Hayashi et al. [1], for $0.014 \leqslant c/t \leqslant 0.114$, and $6\times10^3 \leqslant \mathrm{Re}_c \leqslant 1.9\times10^4$, report that flopping and quasi-stable behavior can be avoided if $H/t > 3.25$ and Miau et al. [4], for $c/t=0.150$, and $1.3\times10^3 \leqslant \mathrm{Re}_c \leqslant 1.2\times10^4$, report that these behaviors can be avoided if $H/t > 2.6$. Both studies agree that the wakes downstream of a plate array with $H/t > 3.5$ are stable and equal in size.

Background

Guillaume and LaRue [5] use smoke visualization to study a six-plate array and observe that the mean separation between streaklines for the flow downstream of adjacent channels is negatively correlated. Consistent with this observation, they use two hot-wire anemometers to show that the vortices shed at the trailing edges of the bounding surfaces that form a channel in the plate array are in-phase, but they are nearly 180 deg out-of-phase with the vortices shed at the trailing edges of the bounding surfaces of adjacent channels. They also observe that axial velocity, relative to the freestream, on the midplane of the channel periodically increases and decreases in a pattern that is nearly 180 deg out-of-phase with the periodic increase and decrease in the relative axial velocity observed on the midplane of the adjacent channels. Power spectra for a mean upstream velocity of 2.0 m/s show that the vortices are shed at a frequency of 128 Hz which corresponds to a period of 0.0078 s.

Based on these observations, Guillaume and LaRue [5] hypothesize that the relative increase in mean velocity occurs in the region between each pair of vortices and the relative decrease in mean velocity occurs in the region not near the vortex pair. They define this periodic increase and decrease in the midplane velocity between adjacent plates as vortex pumping. They propose that the synchronous shedding of vortices at the trailing edges of the channel surfaces with the 180 deg out-of-phase shedding of vortices between adjacent channels leads to vortex pumping which is consistent with the negative correlation of the fluctuating velocity measured on the midplanes between adjacent channels.

Although the mechanism of this flow is unknown, it is important to note that flow visualization shows that pressure and viscous stress gradients exist between the plates that form the channel. Guillaume and LaRue [5] hypothesize that as the flow first develops, the first vortex shed entrains the flow down the channel and triggers, via these gradients, the neighboring plate to shed a vortex down the same channel. This is followed by an alternating shedding pattern and produces the in-phase pattern.

The goals of the present study are to 1) show that a commercial CFD program can confirm that the recirculation zones (i.e., vortex structures) shed at the trailing edges of the bounding surfaces that form a channel in the plate array are in-phase, but they are nearly 180 deg out-of-phase with the recirculation zones shed at the trailing edges of the bounding surfaces of adjacent channels and 2) verify the hypothesis that since the relative increase and decrease in mean velocity occur, respectively, in the regions near a recirculation zone pair and in regions far from a recirculation zone pair, the change in velocity can be used to imply the presence of vortex pairs and the cause of the vortex pumping flow pattern.

Numerical Model

The flowfield around and downstream of the plate array is modeled as a laminar flow since the Reynolds number used in this study, based the plate thickness, is 500 (Fox and McDonald [6]). The Semi-Implicit Method for Pressure-Linked Equations, i.e., SIMPLE, family of algorithms is used to iterate for values of pressure and velocity as implemented in FLUENT. Since the values of pressure and velocity are stored at the centers of the control

 Copyright © 2002 by ASME

Downloaded 03 Jun 2010 to 171.66.16.150. Redistribution subject to ASME license or copyright; see http://www.asme.org/terms/Terms_Use.cfm

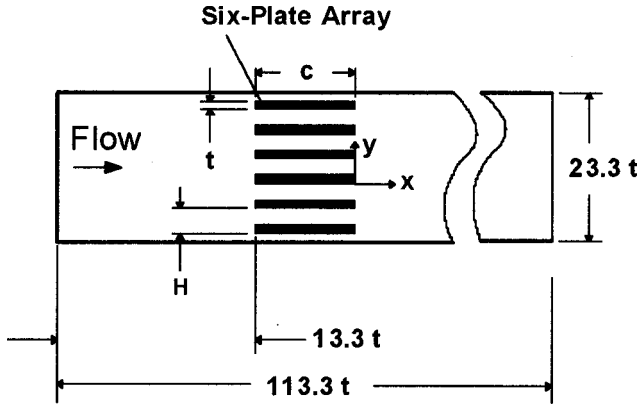

Fig. 1 Schematic of the test setup illustrating the definitions of the symbols and the coordinate system employed

volume, a second order discretization scheme, which uses the lower order terms of a Taylor expansion, is used to interpolate the values at the faces of each control volume. The solution is taken to converge when the sum of the normalized residuals of pressure and velocity is less than 1×10^{-3}.

A two-dimensional model with rectangular cells is used with a computational domain that extends 113.3t or 30.9H (419 cells) in the downstream direction and 23.3t or 3.36H (319 cells) in the transverse direction. The leading edge of the plate array is positioned 13.3t from the inlet boundary and the array has 6 plates with $c/t=6.67$ and $H/t=3.67$ (Fig. 1). The inlet boundary condition is taken to be a simple plug flow with a velocity of 2 m/sec in the downstream direction and the outlet boundary condition is taken to be uniform at atmospheric pressure. In order to obtain a converged solution, the time step is set initially to 0.00001 s for the first 10 iterations and then it is set to 0.001 sec for the subsequent iterations. To check for grid dependence, the simulation was repeated using a grid with twice the number of cells. Since no change in the solution was observed, the original solution is not grid dependent.

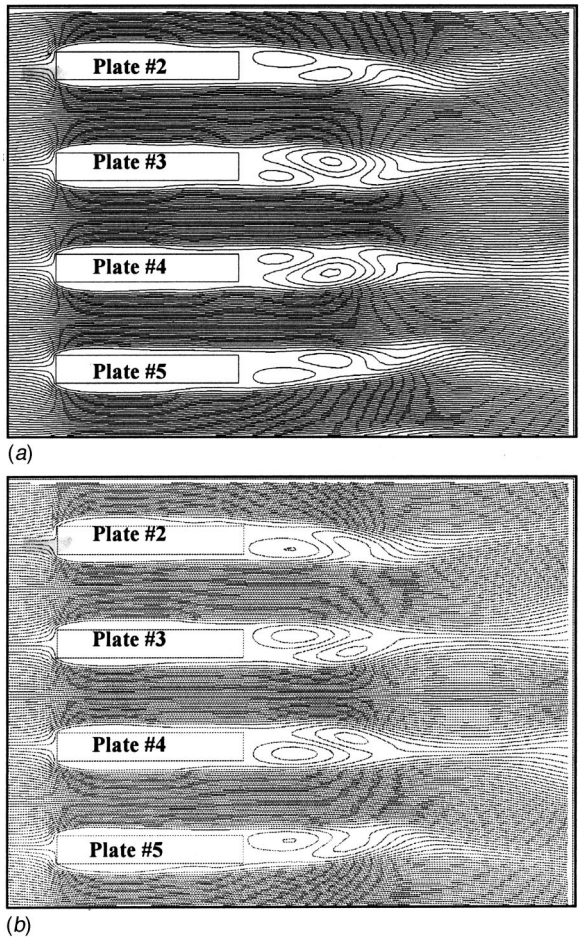

Fig. 2 Streamlines from the numerical model that show the recirculation zones downstream of the channels formed between plates 2 and 3, plates 3 and 4, and plates 4 and 5. Figure 2(*a*) is at $t=0.2235$ seconds and Fig. 2(*b*) at $t=0.2275$ seconds, i.e., 0.004 s later

Results

Results are presented for 1) the recirculation zones downstream of the plate array and for 2) the vortex pumping observed between adjacent channels.

Recirculation Zones. Figure 2(*a*) shows the streamlines about the four center plates at an equivalent time of 0.2235 seconds. For the channel formed between plates 3 and 4, the numerical prediction shows that the recirculation zones downstream and below the centerplane of plate 3 are in phase with the recirculation zones downstream and above the centerplane of plate 4. For the adjacent channel which is formed between plates 4 and 5, the recirculation zones downstream and below the centerplane of plate 4 are in-phase with the recirculation zones downstream and above the centerplane of plate 5. Further, the recirculation zone downstream and above the centerplane of plate 4, i.e., the bottom surface of the upper channel, and the recirculation zone downstream and above the centerplane of plate 5, i.e., the bottom surface of lower adjacent channel, are nearly 180 deg out-of-phase.

Figure 2(*b*) shows the streamlines about the four center plates of the array at an equivalent time of 0.2275 seconds, i.e., 0.004 s later. The recirculation zones below the centerplane and near the trailing edge of plate 3 and above the centerplane and near the trailing edge of plate 4 remain in-phase but have moved downstream. New recirculation zones that are in-phase have formed above the centerplane and near the trailing edge of plate 5 and below the centerplane of plate 4. Thus, consistent with results of Guillaume and LaRue [5], the recirculation zones downstream of the bounding surfaces of each channel are in-phase but are 180 deg out-of-phase with the recirculation zones downstream of the bounding surfaces of adjacent channels.

Vortex Pumping. Figure 3 is a series of plots of the downstream variation in the axial velocity for $0.2235\leqslant t\leqslant0.2275$ calculated at $0\leqslant x/t\leqslant20$ on the midplane and downstream of adjacent channels formed between plates 3 and 4 and plates 4 and 5. At $t=0.2235$, the variation of the axial velocity downstream of the channel formed between plates 3 and 4 shows peaks at about $x/t=1.1$ and 5.3 and a valley at about 3.3. The streamline plot of Fig. 2(*a*) shows a pair of recirculation zones near the upper and lower surfaces that form this channel (i.e., the recirculation zone is below the centerplane of plate 3 and above the centerplane of plate 4) at x/t locations of about 1.1 and 5.3. Thus the relative increase in axial velocity corresponds to the minimum spacing between the pair of recirculation zones about the midplane of the channel. At $x/t=3.3$, Fig. 2(*a*) shows that the pair of recirculation zones is not near the upper and lower surfaces that form this channel (i.e., the recirculation zone is above the centerplane of plate 3 and below the centerplane of plate 4). Thus the relative

Downloaded 03 Jun 2010 to 171.66.16.150. Redistribution subject to ASME license or copyright; see http://www.asme.org/terms/Terms_Use.cfm

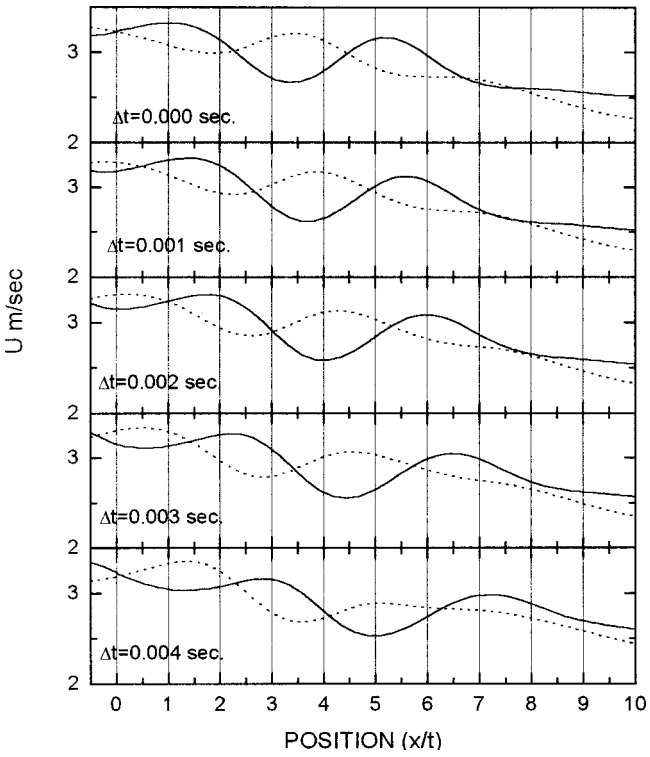

Fig. 3 Plots of the downstream variation in the axial velocity for $0.2235<t<0.2275$ and $0<x/t<20$ on the midplane of adjacent channels. The velocity variation observed between plates 3 and 4 is represented by —— and the velocity variation observed between plates 4 and 5 is represented by — — —

decrease in axial velocity again corresponds to the maximum spacing between the pair of recirculation zones about the midplane of the channel.

Likewise, the downstream variation of the axial velocity on the centerplane of the channel formed by plate 4 and 5 shows a velocity peak at approximately $x/t=3.5$ and valleys at about $x/t=1.6$ and 5.5. Figure 2(*a*) shows a pair of recirculation zones that have a minimum spacing about the midplane of this channel at approximately $x/t=3.5$ and pairs of recirculation zones that have a maximum spacing about the midplane of this channel at approximately $x/t=1.6$ and 5.5 which again corresponds to the relative increase in axial velocity.

This velocity increase and decrease that corresponds to the locations of recirculation zone pairs is also apparent in Figs. 2(*a*) and 2(*b*). About the midplane of a channel, the separation between streamlines is decreased where the separation between recirculation zones is a minimum and the separation is increased where the separation between recirculation zones is a maximum. A decrease in streamline separation implies a velocity increase whereas an increase in separation implies a velocity decrease.

Thus consistent with the vortex pumping hypothesis of Guillaume and LaRue [5], the relative increase and decrease in mean velocity occurs in the region where the separation of pairs of recirculation zones about the midplane of a channel is a minimum and a maximum, respectively.

The locations of the velocity peaks on the centerplane and downstream of the channel formed by plates 3 and 4 are approximately out-of-phase with the locations of the velocity peaks calculated on the centerplane and downstream of the channel formed between plates 4 and 5. At 2 m/s, the distance between these peaks corresponds to a period of 0.008 which is consistent with the shedding period observed by Guillaume and LaRue [5]. This corresponds to a Strouhal number of 0.24.

Figure 3 shows the downstream variation of the axial velocity on the midplane of the channel formed between plates 3 and plate 4 for $0.000\leqslant\Delta t\leqslant 0.004$ s. Velocity peaks occur at about $x/t=3.1$ and valleys at about $x/t=1.1$ and 5.0. These correspond to the locations of the pairs of recirculation zones shown in Fig. 2(*b*). Likewise the downstream variation of the axial velocity on the midplane of the channel formed between plates 4 and 5 shows peaks at about $x/t=1.5$ and 5.1 and a valley at about $x/t=3.5$. This is again consistent with the locations of the recirculation zone pairs shown in Fig. 2(*b*). Thus, at a time difference of 0.004 s, the velocity peaks on the midplane of a channel occur at nearly the same locations where a valley occurred at $\Delta t=0.000$ s. This 180 deg phase change is consistent with both the streamlines shown in Figs. 2(*a*) and 2(*b*) and the vortex shedding measurements of Guillaume and LaRue [5].

Summary

The numerical results shown in Figs. 2(*a*) and 2(*b*) indicate that the recirculation zones formed at the trailing edges of the bounding surfaces that form a channel in the plate array are in-phase, but at the same downstream location, they are nearly 180 deg out-of-phase with the vortices shed at the trailing edges of the bounding surfaces of adjacent channels. This demonstrates that FLUENT can predict the vortex shedding behavior that is experimentally observed downstream of a plate array. Further, a comparison of the locations of the recirculation zone pairs observed in the streamline plots with the locations of velocity peaks in the corresponding downstream variation in axial velocity confirms the mechanism that causes vortex pumping. Specifically, the axial velocity on the midplane between adjacent plates increases and decreases in regions where the separation between a pair of recirculation zones about the midplane of the channel is, respectively, a minimum and a maximum. Thus the numerical results show that the formation of recirculation zone pairs at the trailing edges of the plate array cause vortex pumping.

References

[1] Hayashi, M., Sakurai, A., and Ohya, Y., 1986, "Wake Interference of a Row of Normal Flat Plates Arranged Side by Side in a Uniform Flow," J. Fluid Mech., **164**, pp. 1–25.

[2] Guillaume, D. W., and LaRue, J. C., 1999, "Investigation of the Flopping Regime of Two-, Three-, and Four-Cylinder Arrays," Exp. Fluids, **27**, pp. 137–144.

[3] Miau, J. J., Wang, H. B., and Chou, J. H., 1992, "Intermittent Switching of Gap Flow Downstream of Two Flat Plates Arranged Side by Side," J. Fluids Struct., **6**, pp. 563–582.

[4] Miau, J. J., Wang, H. B., and Chou, J. H., 1996, "Flopping Phenomenon of Flow Behind Two Plate Placed Side-by-Side Normal to the Flow Direction," Fluid Dyn. Res., **17**, pp. 311–328.

[5] Guillaume, D. W., and LaRue, J. C., 2000, "Synchronous Vortex Shedding (Vortex Pumping) Downstream of Flat Plate Array," ASME J. Fluids Eng., **122**, pp. 183–185.

[6] Fox, R. W., and McDonald, A. T., 1992, *Introduction to Fluid Mechanics*, Fourth Edition, Wiley, New York, pp. 437–449.

Downloaded 03 Jun 2010 to 171.66.16.150. Redistribution subject to ASME license or copyright; see http://www.asme.org/terms/Terms_Use.cfm

Flow Characteristics of the Molecular Pump of Holweck Type in the Slip Regime

Yeng-Yung Tsui

Yuan-Sheng Su

Department of Mechanical Engineering,
National Chiao Tung University,
Hsinchu 300, Taiwan R.O.C.

Hong-Ping Cheng
Department of Air-Conditioning
and Refrigeration Engineering,
National Taipei University of Technology,
Taipei 100, Taiwan R.O.C.

A computational method is used to analyze the viscous flow in the spiral grooves of the molecular drag pump of Holweck type. The flow is assumed in the slip flow regime and, thus, the slip boundary condition is imposed at walls. Tests are conducted to examine the effects of clearance gap, spiral angle, channel height, number of channels, and rotating speed. The appearance of clearance brings about lower pressure gradient between side walls of the channel and, thus, reduces the pressure rise in the channel. Testing on spiral angle and channel height indicates that these parameters need to be optimized to achieve better performance. Results also reveal that increase of rotating speed is an effective way to promote compression ratio. In calculations, pressure rise is enhanced when the number of channel is decreased. However, it should be understood that by reducing channel number the cross-sectional area of the channel is decreased, which has the effects of reducing the pressure rise. [DOI: 10.1115/1.1431268]

1 Introduction

The turbomolecular pump has advantages of high pumping speed and low ultimate pressures while the molecular drag pump provides high compression ratio and has high discharge pressure. Therefore, it is beneficial to combine these two pumps to form hybrid pumps. To analyze the flow in molecular pumps either the transmission probability method [1] or the DSMC method [2] is often employed. However, the working pressures for the molecular drag pump can reach 10^3 Pa, at which the flow falls in the viscous flow regime. Thus, the CFD method is a better way for analysis.

In this study, a finite volume method is used to investigate the flow in the grooves (or flow channels) of a molecular drag pump. A geometrical parameter greatly affecting pumping performance is the clearance gap between the rotator and the housing. This clearance will be taken into account in the calculation. Another important geometrical parameter is the angle of the flow channel. In the molecular pump of Gaede type the flow channel is in the direction of rotation. But a certain angle exists between the rotational direction and the flow channel in the pumps of Holweck type and Siegbahn type. The effects of the channel angle will be examined in detail. Also considered are channel height, number of channels together with rotating speed. In order to better depict the flow affected by the geometrical parameters a momentum balance over the entire flow channel is undertaken.

Contributed by the Fluids Engineering Division of THE AMERICAN SOCIETY OF MECHANICAL ENGINEERS. Manuscript received by the Fluids Engineering Division July 7, 2000; revised manuscript received August 10, 2001. Associate Editor: Y. Matsumoto.

2 Mathematical Method

The grooves of the flow channels are sited on a rotating shaft. To deal with the spiral channels body-fitted, curvilinear grids are adopted. Since the frame of reference is situated on the rotating shaft, the centrifugal force and the Coriolis force raised are taken into account in formulation. In calculations the discharge pressure at the outlet is fixed at 133 pa. At this level of pressure the flow is in the slip flow regime. The slip flow velocity V_0 at the solid wall is usually expressed as

$$V_0 = V_w + \frac{2-f}{f}\lambda\left(\frac{dV}{dy}\right)_w, \tag{1}$$

where V_w is the velocity of the solid wall itself, λ the mean free path of gas molecules, and f the accommodation coefficient for molecules colliding with the wall. Usually, the accommodation coefficient is close to 1. The value of unity is adopted in the following calculations.

Difference equations are obtained by the finite volume method through integrating the governing equations over each grid cell volume. Convection terms are approximated by the second-order linear upwind difference [3] while the diffusion terms by the central difference. All the variables are placed on each cell center. To avoid checkerboard oscillations caused by the non-staggered grid arrangement the momentum interpolation practice of Rhie and Chow [4] is utilized to calculate the mass flux through each cell face. Although there are a number of grooves on the rotor, only one groove is considered in simulation and periodic conditions are imposed at the clearance boundary between adjacent grooves (see Fig. 1). In implementing the periodic condition both the mass flux and the momentum flux must be conserved across the periodic boundaries. The calculation of the momentum flux through each boundary cell face is treated in the same way as that for the internal cell face using the momentum interpolation method [4]. All other variables, including pressure and velocity etc., can be obtained through linear interpolation between the grid points on the two sides of the periodic boundaries.

3 Results and Discussion

A schematic drawing of the pump is illustrated in Fig. 1. Unless stated otherwise, there are six grooves on the rotor. The axial length (L) of the rotor is 115 mm and the outer diameter (D) is 137.6 mm. The height (H) of the flow channel is 4.06 mm and the width (W) at the bottom of the channel is 52.5 mm. The clearance gap (G) between the rotor and the housing is 0.65 mm. The spiral angle (α) of the channel is 15 deg. The rotor rotates at 18000 rpm. In calculations the pressure at the exit of the pump was fixed at 133 Pa and a mesh with 102*27*33 nodes was used.

A comparison of the pressure rise across the channel between predictions and measurements [5] is given Fig. 2. In this figure, P_1 and P_2 represent the average pressures at the inlet and the outlet, respectively. It is obvious that the pressure rise is reduced when there exists a clearance gap. It is also evident from the figure that with the gap simulated the agreement with the measurements is improved.

Since the frame of reference is placed on the rotator, the housing surface moves relative to the flow channel. The inclination of the channel to the moving surface causes pressure built up not only in the channel direction, but in the transverse direction also. To illustrate the relation between the pressure rise across the pump and the pressure difference between the side walls the flow channel is straightened as given in Fig. 3 and a momentum balance is made over the entire channel in the axial direction:

$$(P_2 - P_1)A \approx (P_p - P_s)A_w \cos\alpha - F_x, \tag{2}$$

Downloaded 03 Jun 2010 to 171.66.16.150. Redistribution subject to ASME license or copyright; see http://www.asme.org/terms/Terms_Use.cfm

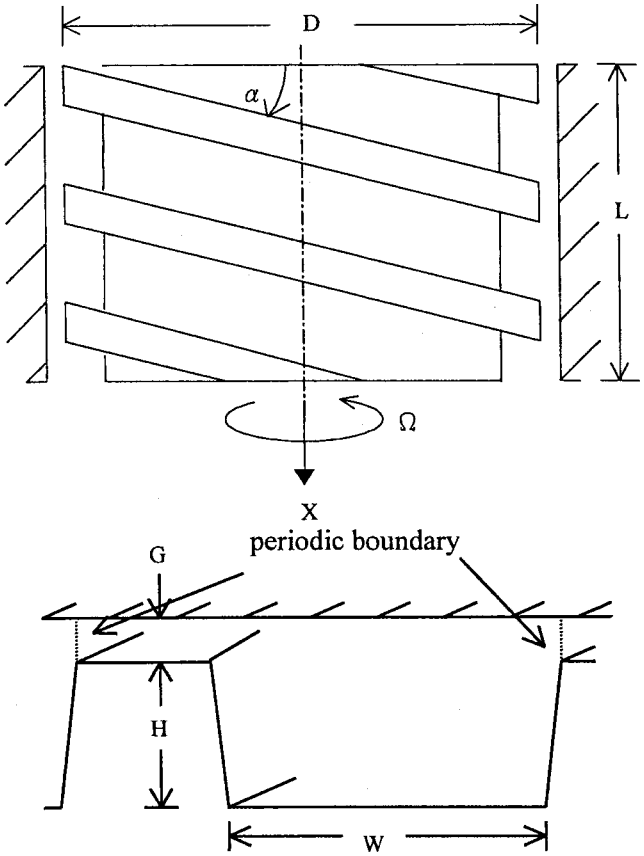

Fig. 1 A schematic drawing of the pump and the flow channels

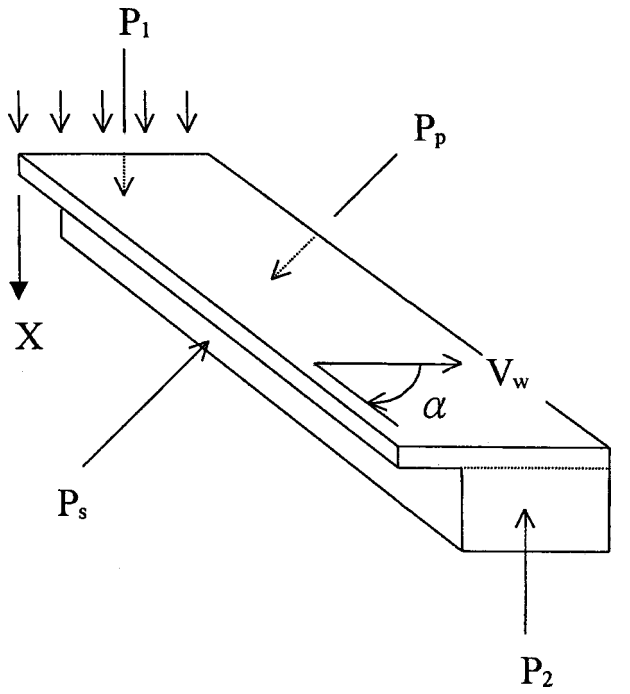

Fig. 3 Illustration of the momentum balance over the entire flow channel

where P_p and P_s denote the average pressures over the pressure and suction side walls, A and A_w designate the cross-sectional area of the channel and the side-wall area, and F_x represents the frictional force exerted by the solid walls in the axial direction. It is noted that the difference between the inlet and outgoing momentum fluxes is ignored. It is clear from this equation that the pressure rise across the channel is directly linked to the pressure difference between side walls and the spiral angle.

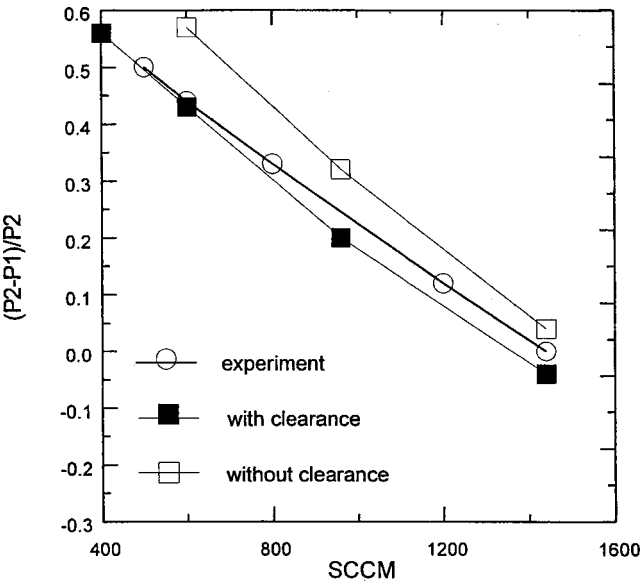

Fig. 2 Comparison of the pressure rise with measurements

Effects of Clearance Gap G. The axial variation of the average pressures for clearance heights of 0.5, 0.65, and 0.8 mm for the flow rate of 400 sccm is presented in Fig. 4(*a*). As expected, the pressure rise decreases with the increase of the height. This is definitely attributed to the leaking flow in the clearance gap, which results in reduction of the pressure difference between side walls as seen in Table 1 and, in turn, the decrease of the pressure rise along the channel.

Effects of Spiral Angle α. As given in Table 2, the pressure difference between side walls increases with the spiral angle because the transverse component of the moving wall velocity also increases. At 90 deg the wall is moving in the direction normal to the channel, i.e., the channel is in the direction of the axis, which creates the largest pressure difference. However, it should be noted that the value of $\cos\alpha$ decreases as the spiral angle increases. In addition, the side wall area A_w also decreases because the length of the channel is shortened. As a consequence, there exists an optimum spiral angle to generate maximum pumping performance. According to Fig. 4(*b*), the optimum angle is in the range 20–25 deg.

Effects of Channel Height H. When the height of the channel is increased, the mean velocity in the channel decreases because the overall flow rate needs to be conserved. Therefore, more momentum is transferred from the moving wall to the flow. However, on the other side, it is easy to cause reverse flow due to the adverse pressure gradient prevailing in the channel, which can cause large pressure loss. Examination of Fig. 4(*c*) reveals that the pressure rise is enhanced as the height is increased to 4.5 mm, followed by deteriorating for the case with 6 mm height. An effective way to improve pumping performance is to gradually reduce the height along the channel. As an example, the channel height, originally fixed at 4.06 mm, is decreased from 6 mm at

Downloaded 03 Jun 2010 to 171.66.16.150. Redistribution subject to ASME license or copyright; see http://www.asme.org/terms/Terms_Use.cfm

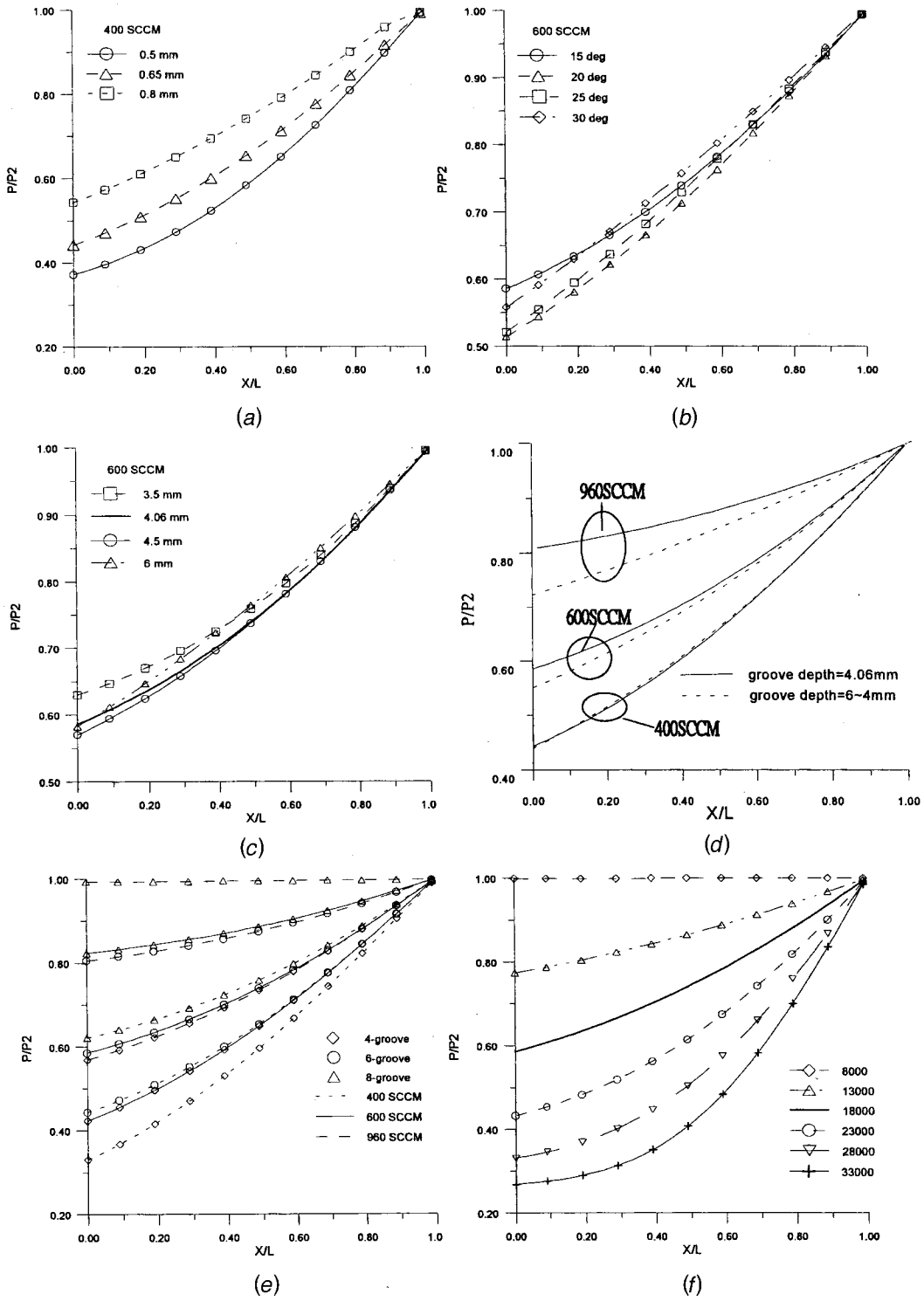

Fig. 4 Pressure variation along the channel for (*a*) various clearances; (*b*) various spiral angles; (*c*) various channel heights; (*d*) a linear reduction of channel height from 6mm to 4 mm; (*e*) various channel numbers; (*f*) various rotational speeds

Table 1 Side wall pressures for various clearances (400 sccm)

	0 mm	0.5 mm	0.65 mm	0.8 mm
P_p (nt/m^2)	87.1	96.7	102.3	110.1
P_s (nt/m^2)	75.4	87.2	95.9	103.9

Table 2 Side wall pressures for various spiral angles (600 sccm)

	15 deg	20 deg	25 deg	30 deg	90 deg
P_p (nt/m^2)	102.3	103.5	104.9	107.1	143.9
P_s (nt/m^2)	95.9	91.6	87.0	86.4	112.6

Downloaded 03 Jun 2010 to 171.66.16.150. Redistribution subject to ASME license or copyright; see http://www.asme.org/terms/Terms_Use.cfm

Table 3 Side wall pressures for various channel numbers (600 sccm)

	4-groove	6-groove	8-groove
P_p (nt/m^2)	93.9	102.3	119.9
P_s (nt/m^2)	76.7	95.9	116.4

inlet to 4 mm at outlet in a linear fashion in Fig. 4(*d*). The pressure rise is greatly increased for the two large flow rates of 600 and 960 sccm.

Effects of Channel Number. The numbers of channels selected for test are 4, 6, and 8. The channel number determines the width of the channel. For wider channels there are more spaces for the transverse pressure gradient to develop. It results in increase of pressure difference between the two sided walls, evidenced in Table 3. Consequently, the pressure rise through the channel increases with decrease of channel number as seen in Fig. 4(*e*). However, it should be pointed here that the reduction of channel number leads to increase of cross-sectional area A. According to Eq. (2), the pressure rise may be decreased by increasing the area A if the side-wall pressure difference is increased by a relatively small extent.

Effects of Rotating Speed Ω. The pressure variation for a number of rotating speeds is presented in Fig. 4(*f*). The speed of the moving wall is linearly related to the rotating speed. When the rotating speed becomes higher, more momentum is transferred to the gas via shear force at the moving wall and more effective pumping is obtained. A logarithmic correlation between the pressure rise and the rotating speed for the considered speed range can be found:

$$(P_2 - P_1)/P_2 = 0.552^*(\log \Omega) - 4.68, \tag{3}$$

4 Conclusions

A numerical analysis has been conducted to examine the viscous flow in the slip flow regime in the spiral grooves of a molecular drag pump of the Holweck type. A summary of main findings is given as follows.

1. The momentum balance indicates that the pressure rise across the channel is directly related to the pressure difference between the two side walls and the spiral angle of the channel.
2. The flow in the clearance gap between the housing and the rotator leads to reduction of pressure gradient between side walls. This, in turn, causes deterioration of pumping performance.
3. The merit of large spiral angle is the generation of greater pressure difference between side walls. However, the side wall area together with the projection of the side wall pressures in the axial direction are decreased. Therefore, the spiral angle needs to be optimized.
4. By increasing the channel height the flow velocity is decreased and more momentum is transferred to the gas from the wall. But large heights may cause reverse flow. A good strategy is to have large height at inlet and small height at outlet.
5. The decrease of channel number brings about wider channel. This has two contradictory impacts: one is to increase pressure rise in the channel by increasing the side-wall pressure difference and the other to decrease pressure rise due to the increase of cross-sectional area. However, for the cases tested the former has larger impact.
6. By increasing rotating speed more momentum is transferred to the gas and, thus, the pumping performance is enhanced.

Acknowledgment

The authors wish to acknowledge the support provided by the Precision Instrument Development Center of the National Science Council, R.O.C.

References

[1] Kruger, C. H., and Shapiro, A. H., 1960, "Vacuum Pumping with a Bladed Axial-Flow Turbo-Machine," 7th Nat. Symp. Vac. Techn. Transaqct., pp. 6–12.
[2] Bird, G. A., 1994, *Molecular Gas Dynamics and the Direct Simulation of Gas Flows*, Clarendon Press, Oxford.
[3] Tsui, Y.-Y., Wu, P.-W., and Liao, C.-W., 1994, "Flow Modeling in Turbofan Mixing Duct," Numer. Heat Transfer, Part A, **26**, pp. 219–236.
[4] Rhie, C. M., and Chow, W. L., 1983, "A Numerical Study of the Turbulent Flow Past an Isolated Airfoil with Trailing Edge Separation," AIAA J., **21**, pp. 1525–1532.
[5] Nanbu, K., and Igarashi, S., 1992, "Three-Dimensional Low-Density Flows in the Spiral Grooves of a Turbo-Molecular Pump," Comput. Fluids, **21**, pp. 221–228.

Downloaded 03 Jun 2010 to 171.66.16.150. Redistribution subject to ASME license or copyright; see http://www.asme.org/terms/Terms_Use.cfm